INTERACTION BETWEEN FLOOR SLABS AND SHEAR WALLS IN TALL BUILDINGS

YANG CHEE WONG, C.Eng., M.I.C.E.

A Thesis presented for the degree of

Doctor of Philosophy

of the

University of Strathclyde, Glasgow,

in the

Department of Civil Engineering.

1979

ACKNOWLEDGEMENTS

The author is indebted to Professor A. Coull, B.Sc., Ph.D., F.R.S.E., F.I.C.E., F.I.Struct.E., F.A.S.C.E., Regius Professor of Civil Engineering, University of Glasgow, formerly Professor of Structural Engineering, University of Strathclyde, for his supervision, guidance and encouragement during the course of the study and in the preparation of the thesis.

The work was carried out in the University of Strathclyde, and the author would like to thank Dr. J. Marshall, B.Sc., Ph.D., A.R.C.S.T., M.I.C.E., M.I.Struct.E., for his advice on various aspects of finite element computation.

Thanks are also due to Messrs. J. Morrin and W. Leighton for their assistance in the construction and testing of the experimental models.

The author is grateful to his wife Hooi Hoon for her assistance in the preparation of the drawings, and most important of all, for her patience, understanding and endurance through the long trying years of the author's study.

Thanks are due to Mrs. G. Stewart for her neat and diligent typing of the manuscript.

ABSTRACT

The interaction between floor slabs and the vertical elements in a tall building structure results in a more efficient lateral load resisting system. The study examines the structural behaviour of the floor slab in the following situations:

(i) Slab coupling a pair of shear walls in a cross-wall structure under cantilever bending action.

(ii) Slab in composite action with a lintel beam connecting a pair of shear walls.

(iii) Slab restraining a centre core against torsional warping.

(iv) Slab coupling a centre core to a peripheral framed tube in a hull-core structure under cantilever bending action.

(v) Slab connecting a row of columns in a flat-plate frame structure under lateral loading.

The resistance of the floor slab against the deformation of the vertical elements, and the actions induced in the slab in the various situations are determined by finite element and influence coefficient techniques. The finite element technique idealises the slab-wall structure as an assembly of plate and shell elements and uses an established stiffness analysis to determine the displacements, forces and stress resultants in the slab. The influence coefficient technique approximates the interaction forces between the slab and walls as a system of discrete nodal forces which are determined from the solution of compatibility equations written in terms of plate influence coefficients and prescribed wall displacements.

The results of parameter studies are presented in a series of design curves and tables to enable the effective slab stiffness and slab actions to be readily determined

for a wide range of structural configurations.

Experimental tests on small-scale shear wall-slab models are carried out to substantiate the general accuracy of the theoretical methods of analysis.

NOTATION

The principal symbols used in various chapters are listed below. Other subsidiary symbols are defined where they appear locally in the text.

CHAPTER 2

(i) Plate Theory

D	Plate flexural rigidity
E	Young's modulus
M_x, M_y, M_{xy}	Bending and twisting moments per unit width of plate
Q_x, Q_y	Shearing forces per unit width of plate
V_x, V_y	Kirchhoff's supplemented shears
a, b	Plate dimensions
t	Plate thickness
x, y	Co-ordinate axes
z	Distance from neutral plane
ν	Poisson's ratio
σ_x, σ_y	Normal stresses
$\tau_{xy}, \tau_{xz}, \tau_{yz}$	Shear stresses

(ii) Vlasov's Theory

B_z	Bimoment at distance z from origin
G	Shear modulus
I_w	Sectorial moment of inertia
J	St. Venant torsional moment of inertia
M_s, M_n	Concentrated in-plane and out-of-plane bending moments
P	Concentrated axial force
S_w	Sectorial static moment
T	Applied torque
T_v	St. Venant torsional moment
T_w	Flexural torsional moment
h_s	Wall thickness
u	Longitudinal displacement
z, s	Longitudinal and tangential co-ordinate axes

$t(z)$	Intensity of distributed torque
$p(s)$	Intensity of distributed axial load
$\mathbb{W}$	Sectorial co-ordinate
θ	Torsional rotation
σ, τ	Normal and shear stresses

(iii) Finite Element Theory

u, v, w	Displacements in x, y, z directions
x, y, z	Orthogonal co-ordinate axes
[B]	Strain matrix
[C]	Matrix relating generalised parameters to nodal displacements
[D]	Elasticity matrix
[K]	Structure stiffness matrix
[N]	Matrix of interpolation functions
[P]	Matrix of displacement functions
[S]	Stress matrix
[k]	Element stiffness matrix
$[k_\alpha]$	Generalised element stiffness matrix
{F}	Element nodal forces
{L}	Consistent element nodal loads
{R}	Complete nodal force vector
{q}	Distributed loads
{u}	Internal displacements
$\{\Delta\}$	Complete displacement vector
$\{\alpha\}$	Generalised displacement parameters (constants)
$\{\delta\}$	Element nodal displacements
$\{\epsilon\}$	Element 'strains'
$\{\sigma\}$	Element 'stresses'

(iv) Influence Coefficient Theory

D	Plate flexural rigidity
H	Distance between axes of rotation of coupled walls
K	Coupling stiffness of slab
L	Clear opening between walls
M_a	Wall moment

M_{xi}, M_{yi}	Concentrated moments in x and y directions at node i
P_i	Concentrated force at node i
W	Length of wall
X	Total length of floor slab
Y	Bay width of floor slab
Y_e	Effective coupling width of floor slab
Z	Width of wall flange
a,b	Plate dimensions
w	Transverse slab deflection
x,y	Co-ordinate axes
$(f_{rs})_{ij}$	Influence coefficient
[F]	Flexibility matrix
{R}	Unknown nodal forces
{δ}	Nodal displacements

CHAPTERS 3, 4 AND 5

B	Core opening width
C	Slab overhang width
D	Plate flexural rigidity
D'	Core lintel depth
E	Young's modulus
F	Storey height
H	Overall height of shear wall
K	Rotational coupling stiffness of slab
K_δ	Translational coupling stiffness of slab
K_a	Double area under curve of bending moment factor
K_q	Shear modification factor
K*	Coupling stiffness of slab with 'flexible' walls
K'	Coupling stiffness of slab with crack
L	Clear opening width between walls or corridor width
L*	Flexible span of connecting beam corrected for junction flexibility
M, M_o	Wall moment
M_x, M_y, M_{xy}	Bending and twisting moments per unit width of slab

$\bar{M}_x$, $\bar{M}_y$	Bending moment factors of slab
M_a	Averaged bending moment per unit width of slabs
Q, Q_o	Shear force in coupling beam
Q_x, Q_y	Shearing forces per unit width of slab
$\bar{Q}_x$, $\bar{Q}_y$	Shearing force factor of slab
Q_a	Average shearing force per unit width of slab
Q_1	Positive shear at critical section for punching shear
Q_3	Positive shear in effective shear zone
Q_c	Critical design shear
W	Length of cross wall
X	Length of slab panel or depth of cross wall building
Y	Width of slab panel or bay width
Y_e	Effective coupling width of slab
Y_e^*	Effective coupling width of slab with flexible walls
Z	Width of wall flange or box core
Z*	Effective flange width of 'flexible' flanged walls
a	Half length of slab panel
b	Half width of slab panel
d	Effective depth of slab
e	Effective span extension for slab coupling 'flexible' walls
h	Wall thickness
t	Slab thickness
u	Critical peripheral distance for punching shear
v, v_c	Design and permissible punching shear stress respectively
w	Transverse deflection of slab
$w_{,x}$, $w_{,y}$	Slopes in x and y directions respectively
$w_{,xx}$, $w_{,yy}$, $w_{,xy}$	Curvatures and twist in slab
x, y	Co-ordinate axes
α	Characteristic stiffness parameter of coupling medium

σ_A, σ_B	Maximum fibre stresses at bottom of shear wall
ν	Poisson's ratio
Θ	Wall rotation
$\emptyset$	Relative rotations of ends of coupling beam at inner wall edges
λ	Length of crack in slab

CHAPTER 6

A^*	Effective shear area of coupling beam
A_w	Cross section area of web of composite coupling beam
D	Plate flexural rigidity
E	Young's modulus
G	Shear modulus
H	Overall height of coupled shear walls
I, I*	Actual and reduced second moments of area (M.I.)
I_c, I_c^*	Actual and reduced composite M.I. of coupling beam
I_w, I_w^*	Actual and reduced M.I. of web of composite coupling beam
K	Coupling stiffness of composite coupling beam
L	Clear span of coupling beam
L*	Effective flexible span of coupling beam
L_a	Distance between centroidal axes of coupled walls
M	Wall moment
M_x, M_y	Bending moments per unit width of slab
N_x, N_y, N_{xy}	Membrane and shear stresses in slab
Q	Vertical reaction or lintel shear
W	Wall length
Y	Width of slab or bay width
Y_e	Effective flange width of composite coupling beam
b	Width of lintel beam
d	Depth of lintel beam
e	Eccentricity between lintel and slab neutral axes

t	Slab thickness
u, v, w	Displacements in x,y,z directions respectively
x, y, z	Co-ordinate axes
α	Characteristic coupling stiffness parameter
δ	Relative axial displacements of coupled walls
Θ	Wall rotation
$\Theta_x, \Theta_y, \Theta_z$	Rotations about x, y and z axes respectively
	Nodal displacement vector
$[K_B], [K_S]$	Standard and eccentric space frame stiffness matrices
$[T]$	Eccentric transformation matrix
$[Z]$	Eccentric transformation sub-matrix

CHAPTER 7

A_b	Cross-sectional area of connecting beam
B	Width of core
B_w	Bimoment resultant
B_o	Bimoment at bottom of core
D	Depth of core
D^*	Plate flexural rigidity
E	Young's modulus
G	Shear modulus
H	Overall height of core structure
I_w	Sectorial moment of inertia of core
I_b	Moment of inertia of connecting beam
J	St. Venant torsional moment of inertia of core
K_w	Warping stiffness of slab
L	Width of core opening
M_{si}, M_{ni}	In-plane and out-of-plane concentrated moments respectively
P	Concentrated torque at top of core
P_i	Concentrated axial force in core
S	Slab width from core wall to facade
X	Length of slab panel in cross-wall structure
Y	Width of slab panel in cross-wall structure
Y_e	Effective width of slab
d	Depth of connecting beam

h	Storey height
m	Intensity of uniformly distributed torque
n	Maximum intensity of triangular distributed torque
q(z)	Intensity of distributed shear in continuous medium at height z
t(z)	Intensity of distributed torque at height z
z	Vertical axis of core
α	Characteristic torsional coupling stiffness parameter
Θ	Torsional rotation of core
Θ'	Rate of twist or torsional warping (= $d\Theta/dz$)
ν	Poisson's ratio
$\mathcal{W}$	Sectorial co-ordinate
$\mathcal{S}$	Double core area (=2BD)

CHAPTER 8

A_c	Cross-sectional area of frame column
C_w	Frame panel flexural stiffness parameter
D	Plate flexural rigidity
E	Young's modulus
E_c, E_s	Young's moduli for column and slab materials respectively
H	Storey height
I	Second moment of area
I_c, I_s	Second moments of area of column and unit slab strip respectively
J_c	Torsional constant of spandrel beam
K	Rotational stiffness of slab
L	Slab span from core wall to frame panel
M	Wall moment
M_x, M_y	Bending moments per unit width of slab
S	Column spacing
V_x, V_y	Distributed reactions per unit width of slab
Y	Overall width of slab
Y_e	Effective width of slab

a	Half depth of core
b	Half width of core
t	Slab thickness
x, y	Co-ordinate axes
β	Structural parameter
ν	Poisson's ratio
θ	Rotation of core cross-section
$\lambda_a, \lambda_i, \lambda_j$	Relative axial, flexural and torsional stiffness parameters of frame panel

CHAPTER 9

A	Length of slab panel
B	Width of slab panel
B_e	Effective width of slab
D	Plate flexural rigidity
K	Rotational stiffness of slab
M	Column moment
U	Column depth
V	Column width
a	Half length of slab
b	Half width of slab
x, y	Co-ordinate axes
ν	Poisson's ratio

CHAPTER 10

D	Plate flexural rigidity
E	Young's modulus
K	Coupling stiffness of slab
L	Clear opening width between walls
M_1	Applied wall moment
M_i, M_e	Internal and external bending moments
P	Applied load
W	Length of wall section
Y	Width of slab
Y_e	Effective slab width
Z	Width of wall flange
c	Distance between centroid axes of walls
t	Slab thickness

ν	Poisson's ratio
θ_1	Wall rotation
ϵ_x, ϵ_y	Surface strains in x and y directions respectively

CONTENTS

CHAPTER 1

INTRODUCTION

1.1 STRUCTURAL SYSTEMS

In recent years, with increasing costs of land in city centres, architectural trends have changed towards high-rise construction to meet the growing demand for office space and housing generated by industrial and population growths. The challenge of building upwards has been met by the development of new structural systems and construction techniques which have contributed to the rapid increase in the number of tall buildings throughout the world. The continuing demand for the construction of tall buildings in the face of rising material and labour costs has made it increasingly more important to achieve a more efficient design for the tall building through a better understanding of the behaviour of the structure and its components.

A major problem in the design of a tall building is the provision of adequate strength and stiffness to resist the lateral loads which may arise due to wind, seismic or blast effects. The provision of adequate strength in the structure is, of course, a fundamental requirement as it ensures the stability and safety of the building. The stiffness requirement is intended to limit the building's deflection and oscillatory motion produced by lateral forces to acceptable levels to ensure the servicibility of the building. Excessive lateral deflection affects the stability of the structure and causes cracking of non-structural partitions and glazing which may lead to serious maintenance problems. Perceptible oscillatory motion causes discomfort to occupants and may affect the usefulness or rental value of the building.

The lateral stiffness of a tall building may be provided by two basic types of structural units, namely the rigid frame and the shear wall. The rigid frame

derives its lateral stiffness from the rigidity of its joints, and is relatively flexible compared with a shear wall. For the structure to be economical, the frames and shear walls must be arranged to perform a dual function of supporting vertical as well as lateral loads. Shear walls should also be arranged to perform a non-structural function, that of partitioning or enclosing space. Ideally the structural system designed for vertical loads should not require extra strengthening for it to function adequately also as a lateral load resisting system for the building.

In current structural systems[1] the rigid frame unit and the shear wall unit are used in various forms and combinations. Frame buildings and shear wall buildings generally use respectively the rigid frame unit and the shear wall unit in parallel assemblies. The core-supported structure and the framed tube structure are examples in which shear walls and rigid-frames are used in tubular assemblies. In the framed tube structure, the frame panels consist of closely spaced columns tied by deep spandrel beams to form an exterior grid. Structural systems produced using frame and shear wall units in combinations are the shear wall-frame system consisting of parallel assemblies of frames and shear walls, and the hull-core or tube-in-tube system consisting of a central shear core within an exterior framed tube.

1.2 INTERACTION BETWEEN COMPONENTS

The vertical elements in a building structure are connected together through the floor slabs which serve primarily to collect and distribute vertical and lateral loads to the vertical elements which eventually transfer the loads down to the foundations. The slab, however, also performs a less obvious but important function of coupling the vertical elements and forcing them to interact thereby producing an overall lateral load response of greater stiffness than the aggregate response provided by

independent actions. A more efficient structural system can therefore be obtained by considering the coupling action of the slab.

An efficient structural system which derives much of its lateral stiffness from the coupling action of the floor slab is the cross-wall structure, which has found considerable favour among planners for the construction of multi-storeyed apartment buildings. The system consists of continuous one-way slabs spanning between parallel assemblies of load bearing walls which resist lateral as well as gravity loads. Architectural planning often produces plan forms with apartments laid out on both sides of a central corridor along the length of the building.

The cross-wall structure resists the lateral loads by the cantilever actions of the shear walls, which result in rotations of wall cross-sections. The free bending of a pair of in-line shear walls is resisted by the slab, which is forced to bend out-of-plane under the differential vertical shearing action imposed by the pair of walls across the corridor. The reaction of the slab induces opposite axial forces into the walls thereby reducing greatly the wind moments and resultant stresses and deflections in the walls. A more efficient design can therefore be achieved by considering the coupling action of the slab.

Another structural system in which the interaction between the slab and the vertical elements results in a more efficient structure is the centre core structure which has become popular for the construction of multi-storeyed office buildings. In this system, the shear walls are arranged in the form of a core, enclosing lifts, stairs, utilities and other services grouped together in a central area in the building. The centre core may serve alone in supporting the floor system and in resisting lateral loads, as in a suspension or cantilevered core structure, or may act in conjunction with peripheral columns as in a hull-core structure. In reinforced concrete systems, the floor

slab may be of flat slab, waffle slab or ribbed slab construction, depending on floor span and type of building.

The practical layout of services in a centre-core building often result in a box-shaped core made up of a number of independent shear walls connected together by lintel beams or floor slabs across the wall openings. When resisting lateral loads which produce a pure bending action, the various core walls undergo a parallel rotation of cross-sections at the same level. The parallel rotation of a pair of walls which produces a differential vertical shearing action across the wall opening is resisted by the connecting slab as in a cross-wall structure. In the hull-core system, however, coupling occurs also between the centre core and the exterior frames. Apart from constraining the core and the exterior framed tube to deflect equally, resulting in a sharing of lateral loads, the slab also restrains the core against the cantilever bending action which produces bending and differential shearing across the floor span. The coupling action induces in the normal frame panels vertical axial forces which reduce the shear lag effect in column loads produced by framed tube action, and also increase the moment of resistance of the structure due to the large lever-arm effect.

Under torsional loading the centre core behaves as a thin-walled tube of open section, and undergoes warping of cross-sections, which results in differential vertical wall displacements across an opening. The floor slab restrains the warping by being forced to deform out-of-plane where it connects rigidly to the core. The restraining action stiffens the core against torsional rotations and reduces the longitudinal warping deformations and base stresses in the core walls. As in the case of pure bending action, when external frames are present, torsional coupling occurs further between the core and the exterior frames and results in a structure of greater stiffness.

In the cross-wall and centre-core structures, although

the lateral stiffness is increased considerably by the interaction between the slab and shear walls, the essential lateral stability of the structure is derived from the inherent flexural stiffness of the shear walls. A structural system which relies solely on the interaction between the slab and the vertical elements to provide the lateral stability is the flat plate structure frequently used for multi-storeyed office buildings of medium height (10 to 15 storeys). The system consists of orthogonal rows of columns connected by flat slabs. The slab in this case provides the portal bracing which forces individual columns to act as members of a rigid frame. The flat plate structure comes under the general classification of frame buildings which include systems with waffle slab and joist-slab floors.

The structural analysis and design of a slab coupled shear wall, centre core or frame system may readily be performed using the techniques developed for beam-coupled systems, provided that the equivalent width of the slab which acts effectively as a wide coupling beam, or its corresponding structural stiffness can be assessed. Unlike a beam however, the coupling stresses are not uniform across the width of a slab. Heavy shearing actions are induced in the coupling slab giving rise to severe stress concentrations around the inner edges of the restrained wall or column. In order to design the slab safely, the magnitude and distribution of these stresses must be known. The interactive shearing forces at the slab-wall or slab-column junction must also be accurately known to allow the local detailing of highly stressed regions in the vertical element.

1.3 PREVIOUS WORK

It is only relatively recently that systematic studies have been made of the nature of the interaction between laterally loaded walls and floor slabs and of the relative importance of the various parameters affecting stresses and

deformations. The first theoretical investigation on the coupling of cross-walls by floor slabs was carried out by Qadeer and Stafford Smith[2] who used a finite difference technique to evaluate the bending stiffness of a slab panel coupling a pair of plane walls. The bending stiffness was evaluated essentially by imposing on the slab at the wall positions transverse deflections produced by an assumed unit parallel wall rotation, and evaluating the slab reactions and hence the resultant wall moment by a plate analysis. Values of bending stiffness and effective width were obtained for a range of slab proportions and wall opening widths and tests were conducted on small-scale models to support the theoretical results. The distribution of coupling actions in the slab was also evaluated by the same investigators.[3] Values of stress resultants were presented for various locations on the slab, but unfortunately the results cannot be interpreted sensibly because the vital distances have not been normalised and units have not been given for them. A similar investigation was carried out by Chang[4] who has presented curves showing the sectional variation of bending moments in a non-dimensional form for various slab proportions.

The coupling of plane walls by floor slabs was investigated by a finite element technique by Petersson.[5] A 'mixed' type of rectangular bending element with corner deflections and side bending-moments as variables was employed for the finite element analysis. Small-scale models were tested to support the theoretical results.

The above mentioned investigations were restricted to plane walls of zero thickness. The influence of finite wall thickness on the bending stiffness of the slab was investigated by Black, Pulmano and Kabaila[6] using a conforming quadrilateral bending element developed by Veubeke[34] for the finite element analysis of the slab.

More recently the influence of orthogonal walls acting as flanges in tee-shaped, ell-shaped and box-shaped walls has been examined experimentally by Coull and El Hag[7]

and by El-Buluk.[8] Slab stresses were measured both by the Moire interference technique and directly by strain gauges. A finite element study on the influence of flange walls was reported by Tso and Mahmoud[9] very recently since the completion of a similar study by the author.[10]

Very little investigation appears to have been carried out on the warping interaction between floor slabs and shear cores. The only investigation known to the author was carried out by Stafford Smith and Taranath[11-13] who showed how the warping stiffness of a slab could be evaluated by a finite element technique in a torsional analysis of a slab-coupled core structure. The warping stiffness was evaluated in an essentially similar manner to the evaluation of bending stiffness for a slab in a cross-wall structure. Transverse displacements produced by a unit torsional warping (defined as the rate of twist in the core and considered as a generalised displacement term), and assumed to vary according to Vlasov's law of sectorial areas[14] were imposed on the slab. The slab reactions and resultant bimoment (a generalised force term corresponding to the torsional warping displacement term) were evaluated by a finite element analysis of the slab to give the warping stiffness of the slab.

Although the coupling action of a slab in a flat plate frame is very similar to that in a cross-wall structure, since a shear wall is, in essence, a very deep column, past investigations for the two structural systems have been pursued independently, and by different investigators. The earliest investigation on the relative influence of various structural parameters on the bending stiffness of a slab in a flat plate frame was carried out by Khan and Sbarounis.[15] The rotational stiffness and effective width of slab were evaluated for a range of column and slab proportions by small-scale model tests in conjunction with approximate slab analyses using a beam-grid analogy. Since the experimental and theoretical techniques employed were relatively unsophisticated, the

results obtained are of limited accuracy.

The relative influence of column stiffness, boundary conditions and relative column-slab sizes on the rotational stiffness of a slab panel was evaluated by Aalami[16] using a finite difference technique, and subsequently by Mehrain and Aalami[17] using a finite element technique. The results are limited to square columns and square slab panels.

The effective width of a slab was evaluated for a wide range of geometrical ratios by Pecknold[18] and by Allen and Darvall[19,20] using a closed form series solution which, unfortunately, does not account properly for the important column-slab boundary conditions in the plate analysis.[21]

1.4 SCOPE OF WORK

The work described in this thesis is concerned with the evaluation of effective width, bending or warping stiffness and stress distribution for slabs interacting with the vertical elements (walls or columns) in cross-wall, centre-core and flat-plate-frame structures. The finite element technique and an influence coefficient technique are employed in the investigation to obtain the relevant design information. The finite element technique uses established element formulations, but the influence coefficient technique is developed here for the first time. A paper on the latter technique has been accepted for publication in a forthcoming ACI symposium volume.[81] Elastic behaviour of the structure is assumed throughout the investigation.

In Chapter 2 of this thesis, the fundamentals in the theories for plate bending and warping torsion in open-section thin-walled beams are summarized so that reference to other texts is unnecessary. The general procedure of the finite element method and special features of the established element formulations are briefly described. The influence coefficient technique is developed and influence functions are derived by the classical plate Levy method of solution.

The influence of various structural parameters on the interaction between the slab and shear walls in the cross wall structure is investigated by the finite element method in Chapter 3. Plane walls, flanged walls and box cores are considered. Design curves and empirical equations are presented to enable the rapid evaluation of effective width or slab stiffness for lateral load analysis in practical situations. Curves are also presented to enable the calculation of slab stresses for the slab design.

In Chapter 4, the influence coefficient technique is applied to the analysis of the slab in the cross wall structure. The convergence characteristics, accuracy, and computing efficiency of the technique are evaluated by comparing the results obtained by the technique with the theoretical and experimental results available in the literature and those obtained by the finite element method in Chapter 3.

In Chapter 5, the effects of local elastic wall deformation on the coupling performance of the slab are evaluated by a finite element technique for a range of wall configurations. Curves are presented to enable the flexibility effects to be included in the evaluation of slab stiffness.

In Chapter 6, the influence of a slab on the bending stiffness of a lintel beam coupling a pair of plane walls is examined. The problem is of interest since in practical shear wall structures, walls are frequently coupled by lintel beams monolithic with a floor slab. A finite element technique is employed to evaluate the effective flange width of a lintel beam for various wall, slab and lintel geometrical ratios.

The relative influence of various structural parameters on the warping stiffness of a slab enclosing a centre core is investigated in Chapter 7. Box cores with single and double openings are considered. A finite element technique is employed to evaluate the slab

stiffness. Curves are presented to enable the effective width for an equivalent beam to be rapidly evaluated for the torsional analysis of a core structure.

In Chapter 8, the bending stiffness of a slab coupling a centre core to an exterior frame is investigated. Finite element and influence coefficient techniques are employed in the investigation. Tables are presented to enable the bending stiffness and effective width of slab to be rapidly evaluated for various geometrical ratios.

The influence of various structural parameters on the rotational stiffness and effective width of slab in a flat plate frame is investigated by the influence coefficient technique in Chapter 9. A comprehensive set of Tables is presented to enable the rapid evaluation of rotational stiffness or effective width of slab for frame analysis in practical situations.

An experimental investigation carried out to support the theoretical investigations on slabs coupling cross-walls is described in Chapter 10. Effective widths and slab stresses are obtained in the tests using small-scale perspex models.

Aspects of computing and salient features of the computer programs written during the course of the work are described in Chapter 11.

The closing chapter summarizes the main conclusions reached in this thesis and indicates possible areas for future investigation.

CHAPTER 2

THEORY

2.1 INTRODUCTION

Shear walls and floor slabs consist essentially of two-dimensional plane elements. When resisting lateral loads in a cross-wall structure, shear walls undergo in-plane bending and floor slabs undergo out-of-plane bending. Since the thickness of the wall is small, in comparison with the wall height or depth, the wall is subjected to a state of plane stress, in bending. However, as the depth of the wall is small in relation to its total height, the overall wall behaviour may be approximately described by ordinary beam theory. The thickness of the floor slab is small compared to the floor span. The transverse displacement, induced in the slab are small compared to the slab thickness, and in-plane strains in the slab are generally negligible. The bending action of the floor slab may therefore be described by small deflection thin plate theory.

Shear cores consist essentially of thin open-section box-shaped shear walls. Under torsional loading, a shear core undergoes warping of its cross sections. Vlasov's theory of thin walled beams which accounts for warping torsion may be used to describe the torsional behaviour of a shear core.

In this chapter, the fundamentals in the theory of plate bending and in Vlasov's theory of warping torsion are briefly described mainly to introduce the terminologies and important mathematical relationships which will be referred to later in the thesis. The finite element procedure and the influence coefficient technique, which are the analytical tools employed throughout the investigation of slab-wall interaction, are then described.

2.2 THEORY OF PLATE BENDING

The basic theory of plates is fully treated in the standard text by Timoshenko and Woinowsky-Krieger.[22] The

salient features of the theory, applicable to the bending of thin elastic isotropic plates with small deflection are here briefly reviewed.

2.2.1 FUNDAMENTAL ASSUMPTIONS

The fundamental assumptions made in the development of the theory are as follows:

1. Plane sections of the plate before bending remain plane after bending.
2. The middle surface of the plate remains a neutral plane (i.e. unstrained) during bending.
3. The normal stresses in the direction transverse to the plate can be disregarded.

2.2.2 DEFLECTION, SLOPES AND CURVATURES

The displacement of a bent plate is uniquely described by the transverse deflection w at all points on the middle surface of the plate. Taking the x-y plane as the middle plane of the plate before bending, the slopes of the middle surface in the x- and y-directions are given respectively by

$$i_x = \frac{\partial w}{\partial x} \quad \text{and} \quad i_y = \frac{\partial w}{\partial y}$$

The curvatures of the middle surface in the x- and y-directions are given respectively by

$$\frac{1}{r_x} = \frac{-\partial^2 w}{\partial x^2} \quad \text{and} \quad \frac{1}{r_y} = \frac{-\partial^2 w}{\partial y^2},$$

and the twist of the middle surface is given by

$$\frac{1}{r_{xy}} = \frac{\partial^2 w}{\partial x \partial y}$$

2.2.3 STRESS RESULTANTS

The bending moments per unit length, M_x and M_y, and the twisting moments per unit length, M_{xy} and M_{yx} (Fig. 2.1(a)) are related to the curvatures and twist by

$$M_x = -D\left(\frac{\partial^2 w}{\partial x^2} + \nu \frac{\partial^2 w}{\partial y^2}\right)$$

$$M_y = -D\left(\frac{\partial^2 w}{\partial y^2} + \nu \frac{\partial^2 w}{\partial x^2}\right)$$

$$M_{xy} = -M_{yx} = D(1-\nu)\frac{\partial^2 w}{\partial x \partial y} \qquad (2.1)$$

where ν is the Poisson's ratio and D is the flexural rigidity of the plate, defined by

$$D = \frac{E\,t^3}{12(1-\nu^2)}$$

in which E is the modulus of elasticity, and t is the plate thickness.

The transverse shearing forces per unit length, Q_x and Q_y, (Fig. 2.1(a)) are given by

$$Q_x = \left(\frac{\partial M_{yx}}{\partial y} + \frac{\partial M_x}{\partial x}\right) = -D\frac{\partial}{\partial x}\left(\frac{\partial^2 w}{\partial x^2} + \frac{\partial^2 w}{\partial y^2}\right)$$

$$Q_y = \left(\frac{\partial M_y}{\partial y} + \frac{\partial M_{xy}}{\partial x}\right) = -D\frac{\partial}{\partial y}\left(\frac{\partial^2 w}{\partial x^2} + \frac{\partial^2 w}{\partial y^2}\right) \qquad (2.2)$$

The Kirchhoff supplemented shearing forces per unit length, V_x and V_y, at the plate edges are given by

$$V_x = \left(Q_x - \frac{\partial M_{xy}}{\partial y}\right) = -D\frac{\partial}{\partial x}\left[\frac{\partial^2 w}{\partial x^2} + (2-\nu)\frac{\partial^2 w}{\partial y^2}\right]$$

$$V_y = \left(Q_y - \frac{\partial M_{xy}}{\partial x}\right) = -D\frac{\partial}{\partial y}\left[\frac{\partial^2 w}{\partial y^2} + (2-\nu)\frac{\partial^2 w}{\partial x^2}\right] \qquad (2.3)$$

2.2.4 STRESSES

The normal stresses and shearing stresses (Fig. 2.1(b)) at a transverse distance z from the middle surface can be obtained from the stress resultants by the following expressions

$$\sigma_x = 12\ M_x \frac{z}{t^3}$$

$$\sigma_y = 12\ M_y \frac{z}{t^3}$$

$$\tau_{xy} = 12\ M_{xy} \frac{z}{t^3} \qquad (2.4)$$

$$\tau_{xz} = \frac{3}{2}\ \frac{Q_x}{t}\ (1 - \frac{4z^2}{t^2})$$

$$\tau_{yz} = \frac{3}{2}\ \frac{Q_y}{t}\ (1 - \frac{4z^2}{t^2}) \qquad (2.5)$$

2.2.5 STRAIN ENERGY

The strain energy in a plate due to bending and twisting is given by

$$U = \frac{D}{2} \iint \left\{ (\frac{\partial^2 w}{\partial x^2} + \frac{\partial^2 w}{\partial y^2})^2 - 2(1-\nu) \left[\frac{\partial^2 w}{\partial x^2} \cdot \frac{\partial^2 w}{\partial y^2} - (\frac{\partial^2 w}{\partial x \partial y})^2 \right] \right\} dx\,dy \qquad (2.6)$$

where the integration is performed over the area of the plate.

2.2.6 GOVERNING PLATE EQUATION

In a plate bent by a uniformly distributed lateral load of intensity q, considerations of compatibility, equilibrium and material properties of a small element leads to the governing biharmonic equation for the plate deflection

$$\frac{\partial^4 w}{\partial x^4} + 2\ \frac{\partial^4 w}{\partial x^2 \partial y^2} + \frac{\partial^4 w}{\partial y^4} = \frac{q}{D} \qquad (2.7)$$

A solution of the governing equation satisfying the known boundary conditions provides a complete solution for the plate bending problem.

2.2.7 BOUNDARY CONDITIONS

Boundary conditions in terms of displacements or stress resultants are usually known at edge supports or

along lines of symmetry or antisymmetry (inflexion). The commonly encountered boundary conditions are briefly discussed.

(a) Simply Supported Edge

Along the simply supported edge x = a, the deflection and bending moment M_x are both zero. The reduced boundary conditions are, since $\partial^2 w/\partial y^2 = 0$,

$$\begin{aligned} w &= 0 \\ \frac{\partial^2 w}{\partial x^2} &= 0 \end{aligned} \qquad \text{at } x = a \qquad (2.8)$$

(b) Clamped Edge

Along the clamped edge x = a the deflection and normal slope are both zero, and the boundary conditions are

$$\begin{aligned} w &= 0 \\ \frac{\partial w}{\partial x} &= 0 \end{aligned} \qquad \text{at } x = a \qquad (2.9)$$

(c) Free Edge

Along the free edge x = a the moment M_x and the supplemented shear V_x are both zero. The boundary conditions are

$$\begin{aligned} &\frac{\partial^2 w}{\partial x^2} + \nu \frac{\partial^2 w}{\partial y^2} = 0 \\ &\frac{\partial^3 w}{\partial x^3} + (2-\nu) \frac{\partial^3 w}{\partial x \partial y^2} = 0 \end{aligned} \qquad \text{at } x = a \qquad (2.10)$$

(d) Line of Symmetry (or Continuous Edge)

Along the line of symmetry x = a, the normal slope and supplemented shear V_x are both zero. The reduced boundary conditions are, since $\partial^3 w/(\partial x \partial y^2) = 0$,

$$\begin{aligned} \frac{\partial w}{\partial x} &= 0 \\ \frac{\partial^3 w}{\partial x^3} &= 0 \end{aligned} \qquad \text{at } x = a \qquad (2.11)$$

(e) The Line of Antisymmetry (or inflexion)

The boundary conditions are identical to those of the simply supported edge.

2.2.8 THEORETICAL METHODS OF SOLUTION

There is no known general method by which the governing plate equation (2.7) can be solved directly. All known methods introduce some form of approximation to obtain an indirect solution. Classical methods[22] assume a plausible form of solution which may be expressed in terms of polynomial or transcendental series containing unknown constants or functions. The unknown constants or functions are then determined to satisfy the governing plate equation and the known boundary conditions. Classical solutions are restricted to plates with simple geometry and regular boundary conditions; but, being of closed form, they yield accurate results with relatively little computational effort, and also allow the solution of other problems by superposition.

Numerical techniques may be used to solve complicated plate problems which cannot be handled by classical methods. Available techniques approximate either the mathematical solution of the plate equation or the physical behaviour of the plate through a discretisation process yielding a large set of simultaneous linear algebraic equations which normally require a computer for solution. The finite difference[24,25] and finite element methods[26,27] are the best-known numerical techniques under these two categories.

2.3 TORSION OF THIN-WALLED OPEN SECTIONS

A thin-walled beam of open section subjected to torsion undergoes twisting about its axis and warping of its cross-sections. The warping arises from differences in the longitudinal displacements of points on the contour of the section. Any axial constraint which prevents the free warping of the section induces longitudinal stresses

in the beam. The rate of twist along the beam becomes non-uniform. Since St. Venant's theory does not allow for longitudinal stresses and is applicable only for uniform torsion, it becomes inadequate for describing the behaviour of the thin-walled open section under non-uniform or restrained torsion.

A suitable theory which accounts for non-uniform torsion is Vlasov's theory of thin walled beams. Since the development of the theory is fully described in the standard text[23] only the salient features of the theory will be described in this section.

2.3.1 WARPING DISPLACEMENTS

In Vlasov's theory, it is assumed that the cross-sectional shape of the section cannot distort and that the shear strain of the middle surface of the section is negligible. By considering the kinematics of rigid contour displacements of cross-sections, and the condition of zero shear strain in an element of the middle surface, it can be shown that the longitudinal displacement of a point P(z,s), (Fig. 2.2(a)) is given by

$$u_{z,s} = - \frac{d\theta}{dz} \; W_s \qquad (2.12)$$

where $d\theta/dz$ is the rate of twist and W_s is the sectorial co-ordinate of the point P. The quantity $d\theta/dz = \theta'(z)$, which serves as a measure of the warping of the section may be considered as a generalised displacement quantity referred to simply as the torsional warping.

2.3.2 WARPING STRESSES

The stresses at a section are assumed to consist only of longitudinal direct stresses and tangential shear stresses. By considering the stress-strain relationship described by Hooke's law, the longitudinal direct stress at point P(z,s) can be shown to be given by

$$\sigma_{z,s} = - E_1 \frac{d^2\theta}{dz^2} W_s \qquad (2.13)$$

where $E_1 = E/(1 - \nu^2)$, and E and ν are respectively Young's modulus and Poisson's ratio.

The tangential shear stress distribution across the wall thickness is assumed to be obtained by the superposition of a uniform membrane shear stress distribution on a linear St. Venant shear stress distribution (Fig. 2.2 (b)). By considering the equilibrium of a shell element, the membrane shear stress at the point P(z,s) can be shown to be given by

$$\tau_{z,s} = E_1 \frac{d^3\theta}{dz^3} \frac{S_{w,s}}{h_s} \qquad (2.14)$$

where h_s is the wall thickness, and $S_{w,s}$ is the sectorial static moment given by

$$S_{w,s} = \int_o^s w \, dA$$

with $dA = h \, ds$.

2.3.3 WARPING STRESS RESULTANTS

The longitudinal direct stresses σ_z at a cross-section at z give rise to a generalised stress-resultant termed the bimoment B_z which may be derived by virtual work as

$$B_z = \int_A \sigma_{z,s} w_s \, dA \qquad (2.15)$$

Substituting for $\sigma_{z,s}$ from equation (2.13), B_z can be expressed as

$$B_z = - E_1 I_w \frac{d^2\theta}{dz^2} \qquad (2.16)$$

where I_w is the sectorial moment of inertia defined by

$$I_w = \int_A w^2 \, dA$$

Using equations (2.13) and (2.16) the longitudinal direct stress $\sigma_{z,s}$ may be expressed in terms of the bimoment B_z as,

$$\sigma_{z,s} = \frac{B_z}{I_w} \omega_s \qquad (2.17)$$

The membrane shear stresses τ_z at the section at z give rise to a flexural torsional moment T_w about the shear centre given by

$$T_w = \int_A (\tau_{z,s} h_s) r_s \, ds = \int_A (\tau_{z,s} h_s) \, d\omega \qquad (2.18)$$

where r_s is the normal distance from the centre of rotation to the tangential line at the point (z,s).

Substituting for $\tau_{z,s}$ given by equation (2.14), T_w may be expressed as

$$T_w = - E_1 I_w \frac{d^3\theta}{dz^3} \qquad (2.19)$$

The membrane shear stress $\tau_{z,s}$ may be expressed in terms of the flexural torsional moment T_w by

$$\tau_{z,s} = - \frac{T_w}{I_w} \frac{S_{w,s}}{h_s} \qquad (2.20)$$

The St. Venant torsional moment T_v is given by

$$T_v = G J \frac{d\theta}{dz} \qquad (2.21)$$

where G is the shear modulus, given by

$$G = \frac{E}{2(1+\nu)}$$

and J is the St. Venant moment of inertia given by

$$J = \frac{\alpha}{3} \sum b h^3$$

where b and h are respectively the width and thickness of the individual plates which make up the beam and α is a coefficient close to unity.

The St. Venant shear stress is zero at the middle surface and has a maximum value at the external surface given by

$$\tau_v = \frac{T_v}{J} h \qquad (2.22)$$

2.3.4 GOVERNING DIFFERENTIAL EQUATION

For torsional equilibrium, the sum of the flexural torque T_w and the St. Venant torque T_v is equal to the applied torque T at a section, i.e.

$$T_w + T_v = T$$

By substituting equations (2.19) and (2.21) in the above equilibrium equation and differentiating once with respect to z, the governing differential equation for torsion is given

$$E_1 I_w \frac{d^4\theta}{dz^4} - G J \frac{d^2\theta}{dz^2} = t(z) \qquad (2.23)$$

where t(z) is the intensity of the applied torque at position z. The solution of the above fourth order governing differential equation satisfying the boundary conditions at the ends of the beam provides a complete solution for the torsional analysis of the beam.

2.3.5 BIMOMENT RESULTANT OF EXTERNAL LOADS

The bimoment resultant of longitudinal forces acting on a section of the beam may be obtained by two theorems:

(a) "A bimoment caused by an external force in a direction parallel to the axis of a beam is equal to the product of this force and the principal sectorial co-ordinate of the point of its application."

(b) "A bimoment caused by a bending moment acting in a plane parallel to the longitudinal axis of the beam is equal to the product of this moment and distance of its plane from the shear centre of the beam."

The mathematical expressions for the bimoment resultants for various forms of loading are as follows:

(a) Distributed load of intensity p(s), (Fig. 2.2(c))

The bimoment is given by

$$B_w = \int p W \, ds \qquad (2.24)$$

(b) Concentrated force P_z at point s = k, (Fig. 2.2(d))

The bimoment is given by

$$B_w = P_z \; W_k \tag{2.25}$$

(c) Concentrated in-plane moment M_s at point s = k, (Fig. 2.2(e))

The bimoment is given by

$$B_w = M_s \left(\frac{dW}{ds}\right)_k \tag{2.26}$$

where dW/ds is the rate of change in the tangential direction s of the sectorial co-ordinate function.

(d) Concentrated out-of-plane M_n at point s = k, (Fig. 2.2(f))

The bimoment is given by

$$B_w = M_n \left(\frac{dW}{dn}\right)_k \tag{2.27}$$

where dW/dn is the rate of change in the normal direction n of the sectorial co-ordinate function.

2.4 THE FINITE ELEMENT METHOD

2.4.1 GENERAL PROCEDURE

In the general procedure of the finite element method, the continuous plate is divided into a number of small elements, usually triangular, rectangular or quadrilateral in shape (Fig. 2.3(a)). These elements are inter-connected together at their corners or nodal points, and, at these points, continuity of displacements and equilibrium must be established.

Consider a typical quadrilateral element e with nodal points i, j, k and l (Fig. 2.3(b)). Various degrees of freedom may be associated with each nodal point. These degrees of freedom consist usually of independent displacement components and their derivatives (u, v, w, $\frac{\partial u}{\partial x}$, $\frac{\partial v}{\partial x}$, $\frac{\partial w}{\partial x}$, etc.). Denoting the 'm' nodal displacements of node i as a vector

$$\{\delta_i\} = \begin{Bmatrix} \delta_1^i \\ \delta_2^i \\ \cdot \\ \cdot \\ \cdot \\ \delta_m^i \end{Bmatrix} \qquad (2.28)$$

the displacements of the element e can be referred to as

$$\{\delta\}^e = \begin{Bmatrix} \delta_i \\ \delta_j \\ \delta_k \\ \delta_l \end{Bmatrix}$$

Corresponding to each nodal 'displacement' δ_j^i, there exists a generalised 'force' f_j^i. Again denoting the nodal forces at node i as

$$\{F_i\} = \begin{Bmatrix} f_1^i \\ f_2^i \\ \cdot \\ \cdot \\ \cdot \\ f_m^i \end{Bmatrix} \qquad (2.29)$$

the nodal forces of the element may be referred to simply as

$$\{F\}^e = \begin{Bmatrix} F_i \\ F_j \\ F_k \\ F_l \end{Bmatrix}$$

The nodal forces may be related to the nodal displacements by

$$[F]^e = [k]^e \{\delta\}^e, \qquad (2.30)$$

where $[k]^e$ represents a stiffness matrix of element e. This matrix is composed of l x l sub-matrices $[k_{ii}]$,

$[k_{ij}]$, ... $[k_{ll}]$, each of m x m terms.

Once the stiffness matrices of the elements are established, the formulation of the whole problem can be easily completed.

Consider a joint i to which p elements are connected. If at this joint external forces $\{R_i\}$ are acting, a set of equilibrium equations can be written for the joint as

$$\{R_i\} = \{F_i\}^1 + \{F_i\}^2 + \ldots. \{F_i\}^p = \sum_{e=1}^{p} [k_{ij}]^e \{\delta\}^e \qquad (2.31)$$

Establishing equilibrium at all the joints in the structure leads to a system of equations which may be represented simply as

$$\{R\} = [K]\{\Delta\} \qquad (2.32)$$

in which

$\{R\} = \begin{Bmatrix} R_1 \\ \cdot \\ \cdot \\ \cdot \\ \cdot \\ \cdot \end{Bmatrix}$ lists all the external nodal forces,

$\{\Delta\} = \begin{Bmatrix} \delta_1 \\ \cdot \\ \cdot \\ \cdot \\ \cdot \\ \cdot \end{Bmatrix}$ lists all the nodal displacements,

and $[K]$ is the structure stiffness matrix built up by adding the stiffnesses of elements adjacent to each node. The system of equations can be solved once the known support displacements have been substituted.

The internal stresses in an element can be related to the nodal displacements. These will be given as

$$\{\sigma\}^e = [S]^e \{\delta\}^e \qquad (2.33)$$

where $[S]^e$ is the element stress matrix. The solution of the problem is seen to hinge on the determination of the element stiffness matrix $[k]^e$ and the stress matrix $[S]^e$.

2.4.2 DERIVATION OF ELEMENT CHARACTERISTICS

(a) Stiffness and Stress Matrices

In order that the finite element idealisation may provide a reasonable representation of the actual continuum. each element must be required to deform similarly to the deformation developed in the corresponding region of the continuum. This can be accomplished by specifying for each element suitable deformation patterns which will provide internal compatibility within the element and at the same time achieve full compatibility of displacements along element boundaries. The deformation patterns may be assumed in the form of polynomial functions with unknown constants which can be regarded as generalised co-ordinates. The number of independent functions specified must agree with the number of nodal degrees of freedom for the element. The internal displacements $\{u\}$ may be expressed in terms of the displacement functions $[P]$ thus,

$$\{u\} = [P]\{\alpha\} \tag{2.34}$$

where $\{\alpha\}$ is a column of constants. By substituting the co-ordinates of each nodal point in turn, the nodal displacements $\{\delta\}^e$ are evaluated in terms of the nodal constants, thus:

$$\{\delta\}^e = [C]\{\alpha\} \tag{2.35}$$

in which $[C]$ is a square matrix simply written in terms of the co-ordinates of the nodes. The unknown constants can then be evaluated in terms of the nodal displacements as

$$\{\alpha\} = [C]^{-1}\{\delta\}^e \tag{2.36}$$

This allows the internal displacements to be related to the nodal displacements thus

$$\{u\} = [P][C]^{-1}\{\delta\}^e = [N]\{\delta\}^e \tag{2.37}$$

where $[N]$ now contains interpolation functions.

The element strains $\{\epsilon\}$ may be evaluated from the

appropriate derivatives in the displacement functions and expressed as

$$\{\varepsilon\} = [B]\ \{\alpha\} = [B]\ [C]^{-1}\ \{\delta\}^e \qquad (2.38)$$

The element stresses $\{\sigma\}$ are related to the element strains by

$$\{\sigma\} = [D]\ \{\varepsilon\} = [D]\ [B]\ [C]^{-1}\ \{\delta\}^e \qquad (2.39)$$

where [D] is the elasticity matrix written in terms of the elastic material properties of the element. The product matrix ($[D]\ [B]\ [C]^{-1}$) is seen to represent the stress matrix $[S]^e$.

The element stiffness matrix may now be established by applying the principle of virtual work. During virtual displacements $\{\bar{\delta}\}^e$, the external work done by the nodal forces is

$$W_e = (\{\bar{\delta}\}^e)^T\ \{F\}^e \qquad (2.40a)$$

The internal work done is given by the product of the actual stresses $\{\sigma\}$ and the internal virtual strains $\{\bar{\varepsilon}\}$ thus

$$W_i = \int_{vol} \{\bar{\varepsilon}\}^T \{\sigma\}\ dv \qquad (2.40b)$$

where $\{\bar{\varepsilon}\} = [B]\ [C]^{-1}\ \{\bar{\delta}\}^e$

and dv is the differential volume of the element.

Equating the external work to the internal work gives

$$(\{\bar{\delta}\}^e)^T\ \{F\}^e = (\{\bar{\delta}\}^e)^T \int_{vol} ([B]\ [C]^{-1})^T\ \{\sigma\}\ dv$$

As this relationship is valid for any value of virtual displacement, the equality of the multipliers must exist. Substituting Eq. (2.39) then gives

$$\{F\}^e = \int_{vol} ([B]\ [C]^{-1})^T\ [D]\ [B]\ [C]^{-1}\ \{\delta\}^e\ dv$$

$$= \left[([C]^{-1})^T \left\{ \int_{vol} [B]^T [D]\ [B] dv \right\} [C]^{-1} \right]\ \{\delta\}^e \qquad (2.41)$$

The whole expression within the square bracket can then be interpreted as the element stiffness matrix $[k]^e$. The central portion under the integral is commonly referred

to as the generalised stiffness matrix $[k_\alpha]^e$. The integration required to evaluate $[k_\alpha]^e$ has to be performed over the entire volume of the element.

For certain simple elements, the stiffness and stress matrices may be evaluated explicitly. In general it is more convenient to perform the various matrix operations and integration numerically on a computer.

(b) Consistent Load Vector

In the formulation of the general finite element procedure, it was assumed that the external loads applied to the plate were concentrated at the nodes. With loads which are distributed over the volume of the element, a consistent method of assigning these loads to the respective nodal points may be established using virtual work.

During any displacement, the work done by the assigned nodal loads is equal to the corresponding work done by the actual distributed loading. The work done by a set of nodal loads $\{L\}$ during virtual displacements $\{\bar{\delta}\}^e$ is

$$W_n = (\{\bar{\delta}\}^e)^T \{L\} \qquad (2.42a)$$

and the corresponding work done by the distributed loading $\{q\}$ is

$$W_d = \{\bar{u}\}^T \{q\} dv = \int_{vol} ([P][C]^{-1}\{\bar{\delta}\}^e)^T \{q\}\, dv \qquad (2.42b)$$

On equating the two expressions, and considering unit virtual displacement,

$$\{L\} = ([C]^{-1})^T \int_{vol} [P]^T \{q\}\, dv \qquad (2.43)$$

2.4.3 PLATE BENDING AND PLANE STRESS ELEMENT CHARACTERISTICS

The procedure for deriving the element stiffness and stress matrices and the consistent load vector has been described in general terms and is applicable to any class of elastic continum problems such as plane stress and plane strain, plate bending, shells and solids. The application of the general procedure to plate bending and

plane stress problems will now be shown in more specific detail, where features unique to a particular class of problem are involved.

In the following sections, a subscript comma after a displacement notation is taken to indicate partial differentiation of the displacement function with respect to the subscript variables following the comma ; for example,

$$w_{,x} = \frac{\partial w}{\partial x} \quad ; \quad w_{,y} = \frac{\partial w}{\partial y} \quad ;$$

$$w_{,xx} = \frac{\partial^2 w}{\partial x^2} \quad ; \quad w_{,xy} = \frac{\partial^2 w}{\partial x \partial y} \quad ; \quad w_{,yy} = \frac{\partial^2 w}{\partial y^2} \quad ; \text{ etc.}$$

(a) Plate Bending Element

The deformation of a plate, under the usual thin plate theory, is uniquely defined by the transverse deflection w at all points on the middle surface. The deformation pattern for the element can be written in the form of Eq.(2.34) as

$$w = [P] \{\alpha\}$$

in which [P] is a row vector of co-ordinate functions and $\{\alpha\}$ is a column of constants.

The nodal displacement parameters in Eq. (2.28) consist essentially of the deflection w and two slopes, $w_{,x}$ and $w_{,y}$, and may include higher derivatives of w, if more than three degrees of freedom are considered at each node. The total number of degrees of freedom for the element must of course match the number of unknown constants in $\{\alpha\}$.

The actual strains in the plate can be defined in terms of the middle-plane curvatures, by the usual assumption of linear strain variation across the plate thickness. Similarly the actual stresses can be found in terms of the moment stress-resultants (cf. Eq.(2.4)). For the purpose of analysis, the generalised 'strains' in Eq. (2.38) may be represented by

$$\{\varepsilon\} = \begin{Bmatrix} -w_{,xx} \\ -w_{,yy} \\ 2w_{,xy} \end{Bmatrix}$$

and the generalised 'stresses' in Eq. (2.39) by

$$\{\sigma\} = \begin{Bmatrix} M_x \\ M_y \\ M_{xy} \end{Bmatrix}$$

since the product of the appropriate components in $\{\varepsilon\}$ and $\{\sigma\}$ gives the correct internal work done across the plate thickness.

The bending moments are related to the curvatures by Eq. (2.1), for an isotropic plate. The elasticity matrix in Eq. (2.39) is then defined by

$$[D] = \frac{Et^3}{12(1-\nu^2)} \begin{bmatrix} 1 & \nu & 0 \\ \nu & 1 & 0 \\ 0 & 0 & \frac{(1-\nu)}{2} \end{bmatrix}$$

in which t is the plate thickness, E is the modulus of elasticity, and ν is Poisson's ratio.

The integration required for the evaluation of the generalised stiffness matrix in Eq. (2.41) is now performed over the area of the element, thus

$$[k_\alpha] = \int [B]^T [D] [B] \, dx \, dy$$

(b) Plane Stress Element

In a plane-stressed continuum the displacement field is given uniquely by the u and v displacements in the x and y cartesian co-ordinate directions. The deformation pattern for the element can then be written in the form of Eq. (2.34) thus,

$$\begin{Bmatrix} u \\ v \end{Bmatrix} = [P] \{\alpha\}$$

in which [P] is a matrix of co-ordinate functions and $\{\alpha\}$ is a column of unknown constants.

The nodal displacement parameters in Eq. (2.28) consist of the two essential displacement components u and v and may include first and second derivatives of u and v depending on the number of degrees of freedom considered for each node.

The state of strain at any point is defined by three strain components ϵ_x, ϵ_y and γ_{xy}, and these are related to the displacements by

$$\begin{Bmatrix} \epsilon_x \\ \epsilon_y \\ \gamma_{xy} \end{Bmatrix} = \begin{Bmatrix} u_{,x} \\ v_{,y} \\ u_{,y} + v_{,x} \end{Bmatrix}$$

The state of stress, similarly is described by three stress components, thus

$$\{\sigma\} = \begin{Bmatrix} \sigma_x \\ \sigma_y \\ \tau_{xy} \end{Bmatrix}$$

The stress-strain relationships expressed in Eq. (2.39) then provides the definition of the elasticity matrix thus,

$$[D] = \frac{E}{1-\nu^2} \begin{bmatrix} 1 & \nu & 0 \\ \nu & 1 & 0 \\ 0 & 0 & \frac{(1-\nu)}{2} \end{bmatrix}$$

The generalised stiffness matrix $[k_\alpha]$ is now evaluated by integrating the infinitesimal internal work done, over the volume of the element, thus

$$[k_\alpha] = \int [B]^T [D] [B] \, t \, dxdy$$

2.4.4 SPECIFIC ELEMENT FORMULATIONS

For a particular class of problem, the element characteristics are dictated by the choice of the element shape, nodal displacement parameters and displacement functions, which allow an endless number of possibilities.

The formulation of the established elements which have been used for the present study will now be described.

2.4.4.1 Rectangular Bending Element RB12

This plate bending element, commonly referred to as the ACM (Adini-Clough-Melosh) rectangle,[28] has three kinematic degrees of freedom, consisting of the transverse deflection w and two rotations θ_x and θ_y, at each corner node. The displacement field for the element is assumed in the form of an incomplete 4th order polynomial expansion in x and y containing 12 unknown constants thus

$$w = [\,1 \;\; x \;\; y \;\; x^2 \;\; \ldots \;\; xy^2 \;\; y^3 \;\; x^3y \;\; xy^3\,] \begin{Bmatrix} \alpha_1 \\ \alpha_2 \\ \vdots \\ \alpha_{12} \end{Bmatrix} \qquad \text{(a)}$$

(10 complete 3rd order polynomial terms)

The displacement field chosen ensures continuity of deflections, but not of normal slopes, along inter-element boundaries. The derivation of the element stiffness and 'stress' matrices and element load vector follows the standard procedure. The explicit forms of these matrices are given in Ref. 26.

In plate bending problems, the shear stress resultants Q_x and Q_y (and sometimes the Kirchoff supplemented shear V_x and V_y) often have to be evaluated, particularly in regions of concentrated loading. To enable the calculation of these quantities, a shear 'stress' matrix may be derived along similar lines to those followed in the derivation of the bending 'stress' matrix. If the shear stress resultants are listed as

$$\{\tau\} = \begin{Bmatrix} Q_x \\ Q_y \end{Bmatrix}$$

and third derivatives of w listed as

$$\{\mu\} = \begin{Bmatrix} -w_{,xxx} \\ -w_{,yyy} \\ -w_{,xyy} \\ -w_{,xxy} \end{Bmatrix}$$

the expressions for shear stress resultants in Eq. (2.2) can be written simply as

$$\{\tau\} = [\bar{D}]\{\mu\}$$

in which

$$[\bar{D}] = \frac{Et^3}{12(1-\nu^2)} \begin{bmatrix} 1 & 0 & 1 & 0 \\ 0 & 1 & 0 & 1 \end{bmatrix}$$

for isotropic material. The derivatives in $\{\mu\}$ can be evaluated directly from the displacement functions in Eq. (a) in the form

$$\{\mu\} = [\bar{B}]\{\alpha\}$$

The coefficient vector $\{\alpha\}$, by the standard procedure, is evaluated in terms of the nodal displacement vector $\{\delta\}^e$ in the form

$$\{\alpha\} = [C]^{-1}\{\delta\}^e$$

The shearing forces can then be evaluated in terms of the nodal displacements thus,

$$\{\tau\} = ([\bar{D}][\bar{B}][C]^{-1})\{\delta\}^e$$

where the product matrix within the brackets represents the shear 'stress' matrix. To obtain the 'stress' matrix for calculating the Kirchhoff supplemented shears V_x and V_y, it is only necessary to re-define the matrix $[\bar{D}]$ as

$$[\bar{D}] = \frac{Et^3}{12(1-\nu^2)} \begin{bmatrix} 1 & 0 & (2-\nu) & 0 \\ 0 & 1 & 0 & (2-\nu) \end{bmatrix}$$

2.4.4.2 Triangular Bending Element TB^9

This plate bending element, introduced by Bazeley, Cheung, Irons and Zienkiewicz,[29] is one of the first successful triangular element with the three basic kinematic degrees of freedom w, θ_x and θ_y, at each corner node. The displacement field chosen for the element is expressed in area co-ordinates in a form containing 9 unknown constants thus,

$$w = \beta_1\zeta_1 + \beta_2\zeta_2 + \beta_3\zeta_3 + \beta_4(\zeta_2^2\zeta_1 + \tfrac{1}{2}\zeta_1\zeta_2\zeta_3) + \ldots\ldots$$

$$\beta_9(\zeta_1^2\zeta_3 + \tfrac{1}{2}\zeta_1\zeta_2\zeta_3)$$

The 9 independent functions for the displacement field are terms from a complete linear polynomial expansion, plus a combination of terms from an incomplete cubic polynomial expansion, in area co-ordinates. The displacement field adopted ensures continuity of w but not of normal slopes along element boundaries.

The area co-ordinates (ζ_1, ζ_2, ζ_3) are an alternative system of intrinsic co-ordinates which are used to locate a point P, relative to the triangle, by specifying the three areas A_1, A_2 and A_3 (Fig. 2.5), as ratios of the area of the triangle, A, thus

$$\zeta_1 = A_1/A, \quad \zeta_2 = A_2/A \text{ and } \zeta_3 = A_3/A$$

The area co-ordinates are related to the cartesian x-y system by the following expressions:

$$x = \sum_{i=1}^{3} \zeta_i x_i \ , \ y = \sum_{i=1}^{3} \zeta_i y_i \text{ and } 1 = \sum_{i=1}^{3} \zeta_i$$

where (x_i, y_i) are nodal cartesian co-ordinates.

The derivation of the element stiffness and 'stress' matrices and the element load vector follows the standard procedure, but, in the process, cartesian derivatives and area integrals are evaluated using the following rules:

$$\frac{\partial}{\partial x}\left[f(\zeta_1, \zeta_2, \zeta_3)\right] = \frac{1}{2A} \sum_{i=1}^{3} b_i \frac{\partial f}{\partial \zeta_i}$$

$$\frac{\partial}{\partial y}\left[f(\zeta_1, \zeta_2, \zeta_3)\right] = \frac{1}{2A} \sum_{i=1}^{3} a_i \frac{\partial f}{\partial \zeta_i}$$

and $$\iint \zeta_1^l \zeta_2^m \zeta_3^n \, dxdy = \frac{l!\ m!\ n!}{(l+m+n)!} 2A$$

where $a_i = x_k - x_j$

$b_i = y_j - y_k$

and A = area of triangle i j k

The explicit forms for the element stiffness and 'stress' matrices are given in Ref. 30.

2.4.4.3 Refined Rectangular Bending Element RB24

This is a refined version of a rectangular bending element proposed by Wegmuller.[31] Six degrees of freedom are chosen at each corner node for the element (Fig. 2.6). In addition to the usual deflection w and two slopes $w_{,x}$ and $w_{,y}$ commonly adopted in simple elements, three curvature terms $w_{,xx}$; $w_{,yy}$ and $w_{,xy}$ are introduced as nodal parameters resulting in a 24-degree-of-freedom element which permits the choice of a higher-order polynomial for better approximation of the displacement field. The chosen displacement functions consist of 24 terms of an incomplete 6th order polynomial and the element is not a fully compatible element. The displacement field is represented as

$$w(x,y) = \underbrace{[\,1 \;\; \xi \;\; \eta \;\; \xi^2 \;\; \ldots\ldots \;\; \xi^4\eta \;\; \eta^5}_{\text{21 complete 5th order polynomial terms}} \;\; \xi^5\eta \;\; \xi^3\eta^3 \;\; \xi\eta^5\,] \begin{Bmatrix} \alpha_1 \\ \alpha_2 \\ \vdots \\ \alpha_{24} \end{Bmatrix}$$

in which $\xi = x/a$ and $\eta = y/b$.

The 24 unknown constants $\alpha_1 - \alpha_{24}$ can be evaluated in terms of the nodal displacement components in the usual way, but the matrix $[C]$ (Eq.(2.35)) is difficult to invert explicitly. The generation and subsequent inversion of this matrix, however, can easily be performed numerically on the computer. Following the standard procedure, the element stiffness matrix may be evaluated in the form

$$[k] = ([C]^{-1})^T \; [k_\alpha] \; [C]^{-1} \qquad \text{(b)}$$

The generalised element stiffness matrix $[k_\alpha]$ can be evaluated explicitly using the simple integration formula

$$\iint_A x^i y^j \, dA = a.b \int_{-1}^{+1}\int_{-1}^{+1} \xi^i \eta^j \, d\xi \, d\eta$$

$$= \begin{cases} \dfrac{4ab}{(i+1)(j+1)} & \text{if i and j are both even,} \\ 0 & \text{otherwise} \end{cases}$$

The explicit form is given in Appendix A2.1 for easy reference, since this was not included in the literature.

Since curvature terms are included as nodal displacement parameters, the bending and twisting moments at the nodal points can be evaluated directly using the moment-curvature relationship in Eq. (2.1), and there is no need to evaluate the usual 'stress' matrix, unless the stress resultants at other points are required, in which case, a 'stress' matrix may be evaluated in accordance with Eq. (2.39).

2.4.4.4 Refined Triangular Bending Element TB18

This is a refined fully compatible triangular plate bending element developed by Bell.[32] The element has at each corner node six degrees of freedom consisting of the transverse deflection w, the two slopes $w_{,x}$ and $w_{,y}$ and three curvatures $w_{,xx}$, $w_{,xy}$ and $w_{,yy}$ (Fig. 2.7(a)). The 18-degree-of-freedom element is derived from a 21-degree-of-freedom element (Fig. 2.7(b)) by eliminating three degrees of freedom associated with normal slopes at three mid-side nodes.

The displacement field assumed for the 21-degree-of-freedom element is based on a complete 21-term fifth-order polynomial expansion in x and y, which ensures complete inter-element displacement and slope compatibility. With the origin of the co-ordinate system at the centroid of the element, the displacement field is written in terms of 21 unknown constants as

$$w = \underbrace{[\,1 \;\; x \;\; y \;\; x^2 \;\; \ldots\ldots \;\; x^2y^3 \;\; xy^4 \;\; y^5\,]}_{21\ \text{Terms}} \begin{Bmatrix} \alpha_1 \\ \alpha_2 \\ \vdots \\ \alpha_{21} \end{Bmatrix}$$

The 21 constants α_1 to α_{21} can be determined in terms of the 21 degrees of freedom given by $\{\delta\} = \left\{\frac{\delta_c}{\delta_s}\right\}$ in which

$$\{\delta_{ci}\}^T = [w \;\; w_{,x} \;\; w_{,y} \;\; w_{,xx} \;\; w_{,xy} \;\; w_{,yy}]_{i=1,2,3}$$

at the three corner nodes and $\{\delta_{sm}\}^T = [w_{,n}]_{m=4,5,6}$ at the three mid-side nodes.

Following the standard procedure, the stiffness matrix for the 21-degree-of-freedom element can be evaluated in the form

$$[k_{21}] = ([C]^{-1})^T [k_\alpha] [C]^{-1}$$

in which the generalised stiffness matrix $[k_\alpha]$ may be evaluated explicitly[33] and the generation and inversion of [C] performed numerically by computer.

The presence of mid-side nodes in the 21-degree-of-freedom element results in a disproportionately large increase in the bandwidth of the structure stiffness matrix. In order to obtain a more efficient element, the three mid-side nodes are eliminated by imposing a cubic variation of the edge normal slope which maintains inter-element displacement compatibility, and allows the mid-side nodal displacements $\{\delta_s\}$ to be expressed in terms of the corner displacements $\{\delta_c\}$ in the form

$$\{\delta_s\} = [H] \{\delta_c\}$$

The stiffness matrix for the 18 d.o.f. element is then obtained by the following transformation

$$[k_{18}] = [I_{18} \vdots H] [k_{21}] \begin{bmatrix} I_{18} \\ \hdashline H \end{bmatrix}$$

where $[I_{18}]$ is an 18 x 18 unit matrix.

2.4.4.5 Quadrilateral Bending Element QB16

This is a conforming quadrilateral plate bending element developed by Veubeke.[34] The element has 16 degrees of freedom consisting of the deflection and two slopes at each corner node and an edge normal slope at each mid-side node (Fig. 2.8(b)). The displacement field for the complete element is built up from complete cubic deflection fields in four triangular regions delimited by the edges of the quadrilateral and its diagonals which

serve as oblique co-ordinate axes for assembling the fields (Fig. 2.8(a)).

The complete cubic deflection field for the first triangular region with vertices 1, 2 and 0 is written as

$$w = \alpha_1 + \alpha_2 x + \alpha_3 y + \alpha_4 x^2 + 2\alpha_5 xy + \alpha_6 y^2 + 4(\alpha_7 x^3 + \alpha_8 x^2 y + \alpha_9 xy^2 + \alpha_{10} y^3)$$

The ten coefficients $\alpha_1 - \alpha_{10}$ can be determined in terms of the displacement components for the region, which are

$$(w_o \; \phi_o \; \psi_o \;\; w_1 \; \phi_1 \; \psi_1 \;\; w_2 \; \phi_2 \; \psi_2 \;\; \phi_{12}) = \{q_1\}^T$$

where $\phi = \partial w/\partial x$ and $\psi = \partial w/\partial y$.

The bending strain energy involving curvature terms and area integration can be evaluated from the deflection field explicitly in the form

$$U_1 = \tfrac{1}{2} \{q_1\}^T [K_1] \{q_1\}$$

in which the matrix $[K_1]$ represents the stiffness matrix of the first field.

For the second region with vertices 2, 3 and 0, the coefficients α_1, α_2, α_3, α_5, α_6, α_9 and α_{10} from the first field are retained to preserve continuity of w, $\partial w/\partial y$ and $\partial w/\partial x$ along the interface x=0, and new values α_4', α_7' and α_8' introduced for the remaining coefficients. The ten coefficients and the stiffness matrix $[K_2]$, expressed in terms of the displacement vector of the second field, which is

$$(w_o \; \phi_o \; \psi_o \;\; w_3 \; \phi_3 \;\; \psi_3 \;\; w_2 \; \phi_2 \;\; \psi_2 \;\; \phi_{23}) = \{q_2\}^T,$$

are readily evaluated from the results of the first field by simply replacing the co-ordinates and displacement parameters of node 1 with values for node 3 and replacing ϕ_{12} with ϕ_{23}.

For the third region with vertices 1, 4 and 0, identity of deflection and slopes with field 1 along the interface y=0 is obtained by retaining the coefficients

α_1, α_2, α_3, α_4, α_5, α_7 and α_8, and introducing new coefficients α_6', α_9' and α_{10}'. The ten coefficients and the stiffness matrix $[K_3]$, now related to the displacement vector

$$(w_o \; \phi_o \;\; \psi_o \;\; w_1 \; \phi_1 \;\; \psi_1 \;\; w_4 \; \phi_4 \;\; \psi_4 \;\; \phi_{41}) = \{q_3\}^T,$$

are again easily evaluated from results of the first field with appropriate changes in co-ordinates and displacement parameters.

Finally for the fourth region with vertices, 3, 4 and O, the coefficients α_1, α_2, α_3, α_4, α_5, α_6', α_7', α_8', α_9' and α_{10}' are adopted so that field 4 conforms with fields 2 and 3 at the interfaces. With displacement parameters

$$(w_o \; \phi_o \;\; \psi_o \;\; w_3 \; \phi_3 \; \psi_3 \;\; w_4 \; \phi_4 \; \psi_4 \;\; \phi_{34}) = \{q_4\}^T,$$

the coefficients and the stiffness matrix $[K_4]$ are evaluated from results of field 1 by parameter changes between node 1 and node 3, between node 2 and node 4 and between ϕ_{12} and ϕ_{34}.

The four partial stiffness matrices $[K_1]$ - $[K_4]$ are combined into a single matrix $[J]$ referred to the 19 displacement parameters

$$(w_o \; \phi_o \; \psi_o \; \ldots\ldots \; \phi_{12} \; \phi_{23} \; \phi_{34} \; \phi_{41}) = \{p\}^T,$$

by direct energy addition.

The 19 displacement parameters in $\{p\}$, however, are not independent since they depend on 16 coefficients $\alpha_{i(1,2,3\ldots10)}$, $\alpha'_{i(4,6,7,8,9,10)}$. The three displacement parameters w_o, ϕ_o ψ_o for the internal node can be evaluated in terms of displacements for other nodes, and the 16 coefficients expressed in terms of the 16 external displacement parameters

$$(w_1 \; \phi_1 \;\; \psi_1 \; \ldots\ldots \; \phi_{12} \; \phi_{23} \; \phi_{34} \; \phi_{41}) = \{q\}^T$$

On expressing $(w_o \; \phi_o \; \psi_o)$ in terms of $\{q\}$,

$$(w_o \; \phi_o \; \psi_o)^T = [M] \; \{q\},$$

$\{p\}$ is related to $\{q\}$ by

$$\{p\} = \begin{bmatrix} \frac{M}{---} \\ I_{16} \end{bmatrix} \{q\}$$

where $[I_{16}]$ is a 16 x 16 unit matrix.
The matrix [J] can now be transformed into a proper stiffness matrix given by

$$[K] = [N]^T [J] [N]$$

where $[N] = \begin{bmatrix} \frac{M}{---} \\ I_{16} \end{bmatrix}$

The oblique slopes $\emptyset$ and ψ in the displacement vector are inconvenient for the assembly of different elements. At corner nodes, slopes should be referred to a common cartesian reference frame and at mid-side nodes it is convenient to refer to the edge normal slope. The new set of cartesian displacement components

$$\{r\}^T = (w_1 \ \eta_1 \ \xi_1 \ \ w_2 \ \eta_2 \ \xi_2 \ \cdots \ \eta_{12} \ \eta_{23} \ \eta_{34} \ \eta_{41}),$$

can be related to the original set of oblique displacements by a transformation given by

$$\{q\} = [P] \{r\}$$

in which [P] is evaluated from the geometry of the element. The final operational stiffness matrix is then obtained by an orthogonal transformation of [K], thus

$$[R] = [P]^T [K] [P]$$

The relevant matrices required for the construction of the stiffness matrix for the element have been evaluated explicitly in Ref. 34. The construction of the 'stress' matrix, however, is not mentioned in this reference. The author's derivation of the 'stress' matrix is presented in Appendix A2.2.

2.4.4.6 Triangular Plane Stress Element TP6

This element first introduced by Turner et al.[35] is commonly referred to as the constant strain triangle. Two basic degrees of freedom, consisting of displacements u

and v in the x and y directions respectively, are associated with each corner node resulting in a 6 degree-of-freedom element. The displacement functions assumed for the element consist of linear polynomials given by

$$u = \alpha_1 + \alpha_2 x + \alpha_3 y$$

$$v = \alpha_4 + \alpha_5 x + \alpha_6 y$$

The linear deformation patterns ensure inter-element displacement compatibility. The derivation of element properties is fairly straightforward and follows the standard procedure described. The stiffness and stress matrices are given in explicit form in most text books on the finite element method.

2.4.4.7 Rectangular Plane Stress Element RP8

This plane stress element has 8 degrees of freedom consisting of plane displacements u and v in the x and y directions respectively, at its four corner nodes. The derivation of element properties as first presented by Cheung[36] contained an error in the displacement functions, which was subsequently corrected by Marshall.[37] The corrected version shows improved accuracy in practical applications.

The displacement functions are assumed initially in the forms involving 10 unknown constants, thus

$$u(x,y) = \alpha_1 + \alpha_2 x + \alpha_3 y + \alpha_4 xy + \alpha_9 y^2$$

$$v(x,y) = \alpha_5 + \alpha_6 x + \alpha_7 y + \alpha_8 xy + \alpha_{10} x^2$$

Then, by making use of equilibrium conditions within the element, the constants α_9 and α_{10} are expressed in terms of α_8 and α_4, as,

$$\alpha_9 = - \frac{1+\nu}{2(1-\nu)} \alpha_8$$

$$\alpha_{10} = - \frac{1+\nu}{2(1-\nu)} \alpha_4$$

The displacement functions are now written in terms of

8 constants, namely,

$$u(x,y) = \alpha_1 + \alpha_2 x + \alpha_3 y + \alpha_4 xy - \frac{1+\nu}{2(1-\nu)} \alpha_8 y^2$$

$$v(x,y) = \alpha_5 + \alpha_6 x + \alpha_7 y + \alpha_8 xy - \frac{1+\nu}{2(1-\nu)} \alpha_4 x^2$$

The derivation of the stiffness matrix from here onwards follows the standard procedure and the explicit forms for the stiffness and stress matrices can be found in Ref.37.

2.4.4.8 Rectangular Flat Shell Element RS24

This element is obtained by combining the bending element RB12 with the plane stress element RP8 so that the flexural as well as the membrane characteristics are incorporated in the same element, which can then be used in a general spatial situation. Since the bending and membrane actions in a flat element are uncoupled, when local deformations are small, the stiffness matrix for the flat shell element can be built up from the constituent bending and membrane stiffnesses in a relatively straightforward manner.

(a) Stiffness Matrix Assembly

In the plane stress element the nodal displacements and corresponding nodal forces are defined respectively by

$$\{\delta_i^p\} = \begin{Bmatrix} u_i \\ v_i \end{Bmatrix} \text{ and } \{F_i^p\} = \begin{Bmatrix} F_{ui} \\ F_{vi} \end{Bmatrix}$$

and in the bending element by

$$\{\delta_i^b\} = \begin{Bmatrix} w_i \\ \theta_{xi} \\ \theta_{yi} \end{Bmatrix} \text{ and } \{F_i^b\} = \begin{Bmatrix} F_{wi} \\ M_{xi} \\ M_{yi} \end{Bmatrix}$$

Combining the plane stress element with the bending element then results in an element with five degrees of freedom at each node. A sixth kinematic degree of freedom possible in a general spatial element consists of the in-plane rotation θ_z, which in practice is very small and may

be entirely left out of the element nodal description, as in the case of the plane stress element. However, for convenience in subsequent matrix operations, it is desirable to include Θ_z in the nodal displacement vector, as a fictitious rotational degree of freedom, associated with a fictitious couple M_z.

Now, if the nodal displacements and nodal forces in the shell element are defined respectively as

$$\{\delta_i\} = \begin{Bmatrix} u_i \\ v_i \\ w_i \\ \Theta_{xi} \\ \Theta_{yi} \\ \Theta_{zi} \end{Bmatrix} \quad \text{and} \quad \{F_i\} = \begin{Bmatrix} F_{ui} \\ F_{vi} \\ F_{wi} \\ M_{xi} \\ M_{yi} \\ M_{zi} \end{Bmatrix}$$

then the stiffness matrix of the shell element consists of sub-matrices which are assembled from the plane stress and bending stiffness submatrices as follows

$$[k_{ij}] = \left[\begin{array}{cc|ccc|c} [k_{ij}{}^p] & & 0 & 0 & 0 & 0 \\ (2x2) & & 0 & 0 & 0 & 0 \\ \hline 0 & 0 & & & & 0 \\ 0 & 0 & & [k_{ij}{}^b] & & 0 \\ 0 & 0 & & (3x3) & & 0 \\ \hline 0 & 0 & 0 & 0 & 0 & k_{ij}{}^f \end{array}\right]$$

in which $[k_{ij}{}^p]$ is the plane stress element stiffness sub-matrix

$[k_{ij}{}^b]$ is the bending element stiffness sub-matrix

and $k_{ij}{}^f$ is a fictitious in-plane rotational stiffness coefficient

(b) Fictitious Stiffness Coefficients

The fictitious stiffness coefficients, strictly, should be set to zero, but since this will lead to

numerical difficulties in the solution when adjoining elements are co-planar, the set of fictitious stiffness coefficients are given finite values, defined arbitrarily by a stiffness relationship which preserves local equilibrium thus,

$$\begin{Bmatrix} M_{zi} \\ M_{zj} \\ M_{zk} \\ M_{zm} \end{Bmatrix} = \alpha E t A \begin{bmatrix} 1.5 & -0.5 & -0.5 & -0.5 \\ & 1.5 & -0.5 & -0.5 \\ & & 1.5 & -0.5 \\ \text{Symmetric} & & & 1.5 \end{bmatrix} \begin{Bmatrix} \theta_{zi} \\ \theta_{zj} \\ \theta_{zk} \\ \theta_{zm} \end{Bmatrix}$$

where E is the elasticity modulus, t and A are the element thickness and area, and α is some coefficient which can be judiciously chosen to ensure that results are not significantly affected by the fictitious stiffness introduced, when elements are not co-planar. A value of $\alpha = 10^{-6}$ was found to be satisfactory for the author's solutions for wall/slab interaction problems.

(c) Co-ordinate Transformation

The stiffness matrix just assembled is based on a local co-ordinate system which has been used for the derivation of the plane stress and bending components. For the assembly of elements and solution of the equilibrium equations, the co-ordinates have to be transformed to a global system. Denoting global quantities by a bar over the symbol, the displacements and forces at a node transform from global to local system by a matrix [L] as follows:

$$\{\delta_i\} = [L] \{\bar{\delta}_i\} \quad \text{and} \quad \{F_i\} = [L] \{\bar{F}_i\} ,$$

in which

$$[L] = \begin{bmatrix} \lambda & 0 \\ 0 & \lambda \end{bmatrix} ,$$

[λ] being a matrix of direction cosines given by

$$[\lambda] = \begin{bmatrix} C_{x\bar{x}} & C_{x\bar{y}} & C_{x\bar{z}} \\ C_{y\bar{x}} & C_{y\bar{y}} & C_{y\bar{z}} \\ C_{z\bar{x}} & C_{z\bar{y}} & C_{z\bar{z}} \end{bmatrix}$$

where $C_{x\bar{x}}$ denotes the cosine of the angle between the x and $\bar{x}$ axes, etc.

The transformation of the complete displacement and load vectors for a rectangular element can therefore be written as

$$\{\delta\}^e = [T]\{\bar{\delta}\}^e \quad \text{and} \quad \{F\}^e = [T]\{\bar{F}\}^e$$

in which

$$[T] = \begin{bmatrix} L & 0 & 0 & 0 \\ 0 & L & 0 & 0 \\ 0 & 0 & L & 0 \\ 0 & 0 & 0 & L \end{bmatrix}$$

By the rules of orthogonal transformation, the stiffness matrix for the shell element in the global system is then given by

$$[\bar{k}] = [T]^T [k] [T],$$

which may be evaluated simply by operating on the (3 x 3) sub-matrices $[k_{rs}]$ thus

$$[\bar{k}_{rs}] = [\lambda]^T [k_{rs}][\lambda] \quad , (r=1,2,..8), (s=1,2...8)$$

(d) Direction Cosines

The direction cosines need to be established in terms of the global nodal co-ordinates. With the local x-axis directed along the element side ik (Fig. 2.9), the direction cosines of the x-axis are defined by the unit vector

$$\{v_x\} = \begin{Bmatrix} C_{x\bar{x}} \\ C_{x\bar{y}} \\ C_{x\bar{z}} \end{Bmatrix} = \frac{1}{I_{ik}} \begin{Bmatrix} \bar{x}_{ki} \\ \bar{y}_{ki} \\ \bar{z}_{ki} \end{Bmatrix}$$

with $$l_{ik} = \sqrt{\bar{x}_{ki}^2 + \bar{y}_{ki}^2 + \bar{z}_{ki}^2}$$

and $$\bar{x}_{ki} = \bar{x}_k - \bar{x}_i, \text{ etc.}$$

Similarly, the direction cosines of y-axis are defined by

$$\{V_y\} = \begin{Bmatrix} C_{y\bar{x}} \\ C_{y\bar{y}} \\ C_{y\bar{z}} \end{Bmatrix} = \frac{1}{l_{ij}} \begin{Bmatrix} \bar{x}_{ji} \\ \bar{y}_{ji} \\ \bar{z}_{ji} \end{Bmatrix}$$

with $$l_{ji} = \sqrt{\bar{x}_{ji}^2 + \bar{y}_{ji}^2 + \bar{z}_{ji}^2}$$

The z-axis is normal to the plane of the element, defined by the sides ik and ij, and the direction cosines are defined by the vector cross-product

$$\{V_z\} = \begin{Bmatrix} C_{z\bar{x}} \\ C_{z\bar{y}} \\ C_{z\bar{z}} \end{Bmatrix} = \{V_x\} \times \{V_y\} = \frac{1}{I_{ik} I_{ij}} \begin{Bmatrix} \bar{y}_{ki}\bar{z}_{ji} - \bar{z}_{ki}\bar{y}_{ji} \\ \bar{z}_{ki}\bar{x}_{ji} - \bar{x}_{ki}\bar{z}_{ji} \\ \bar{x}_{ki}\bar{y}_{ji} - \bar{y}_{ki}\bar{x}_{ji} \end{Bmatrix}$$

The solution of the equilibrium equations yields nodal displacements in the global directions. These have to be transformed back to the local co-ordinate system, to allow the calculation of stresses, using the stress matrices derived for the plane stress and bending elements.

2.4.4.9 Triangular Flat Shell Element TS18

This triangular flat shell element is derived by combining the non-conforming bending element TB9 with the constant strain triangle TP6. Previous studies[38] have reported the satisfactory performance of this element in many practical situations.

The stiffness matrix for the element is built up from the membrane and bending components in a similar manner to that described for the rectangular flat shell element. In this case the fictitious stiffness coefficients are defined by the stiffness relationship

$$\begin{Bmatrix} M_{zi} \\ M_{zj} \\ M_{zm} \end{Bmatrix} = \alpha E t A \begin{bmatrix} 1 & -0.5 & -0.5 \\ & 1 & -0.5 \\ \text{symm.} & & 1 \end{bmatrix} \begin{Bmatrix} \theta_{zi} \\ \theta_{zj} \\ \theta_{zm} \end{Bmatrix}$$

The co-ordinate transformation described for the rectangular element is also applicable to the triangular element, but here the direction cosines are evaluated in the following manner:

Assuming that the local x-axis is directed along the element side ij (Fig. 2.10), the direction cosines for the x-axis are, as before, given by the unit vector

$$\{V_x\} = \{V_{ij}\} = \begin{Bmatrix} C_{x\bar{x}} \\ C_{x\bar{y}} \\ C_{x\bar{z}} \end{Bmatrix} = \frac{1}{l_{ij}} \begin{Bmatrix} \bar{x}_{ji} \\ \bar{y}_{ji} \\ \bar{z}_{ji} \end{Bmatrix}$$

$$\text{with } l_{ij} = \sqrt{\bar{x}_{ji}^2 + \bar{y}_{ji}^2 + \bar{z}_{ji}^2}$$

The plane of the triangle is defined by the sides ij and im. The unit vector for the side im is given by

$$\{V_{im}\} = \frac{1}{l_{im}} \begin{Bmatrix} \bar{x}_{mi} \\ \bar{y}_{mi} \\ \bar{z}_{mi} \end{Bmatrix},$$

$$\text{with } l_{im} = \sqrt{\bar{x}_{mi}^2 + \bar{y}_{mi}^2 + \bar{z}_{mi}^2}$$

The z-axis is normal to the plane of the triangle and its direction cosines are defined by the vector cross product

$$\{V_z\} = \{V_{ij}\} \times \{V_{im}\} = \begin{Bmatrix} C_{z\bar{x}} \\ C_{z\bar{y}} \\ C_{z\bar{z}} \end{Bmatrix} = \frac{1}{2A} \begin{Bmatrix} \bar{y}_{ji}\bar{z}_{mi} - \bar{z}_{ji}\bar{y}_{mi} \\ \bar{z}_{ji}\bar{x}_{mi} - \bar{x}_{ji}\bar{z}_{mi} \\ \bar{x}_{ji}\bar{y}_{mi} - \bar{y}_{ji}\bar{x}_{mi} \end{Bmatrix}$$

with A = area of triangle ijm

The y-axis is normal to the x and z axes, and its direction cosines are given by the vector cross product

$$\{V_y\} = \{V_z\} \times \{V_x\} = \begin{Bmatrix} C_{y\bar{x}} \\ C_{y\bar{y}} \\ C_{y\bar{z}} \end{Bmatrix} = \begin{Bmatrix} C_{z\bar{y}}C_{x\bar{z}} - C_{z\bar{z}}C_{x\bar{y}} \\ C_{z\bar{z}}C_{x\bar{x}} - C_{z\bar{x}}C_{x\bar{z}} \\ C_{z\bar{x}}C_{x\bar{y}} - C_{z\bar{y}}C_{x\bar{x}} \end{Bmatrix}$$

2.5 THE SERIES INFLUENCE COEFFICIENT METHOD

Finite difference[3,4] and finite element methods[5,6,9] have been used to solve the complicated plate problem posed by a floor slab interacting with a pair of shear walls. These numerical methods are characterised by relatively complicated computer programming, tedious data preparation, large computer core requirements and lengthy computing time, which make their use in a normal design office unattractive or even impractical. An alternative approach based on an influence coefficient method which offers a distinct advantage in terms of computational effort is presented in this section.

2.5.1 METHOD OF ANALYSIS

2.5.1.1 Idealisation

A typical layout of a segment of a shear wall-slab building is shown in Fig. 2.10. When a pair of coupled walls undergo parallel rotation when bending under lateral loading, the floor slab, which is rigidly connected to the walls, is forced to bend out of plane, resisting the independent bending of the walls. The transverse deflection of the slab and the displacement of the wall must be equal where the two members interconnect. If plane sections of the wall remain plane in bending, the deflection of the slab at points along the wall connection is known from the rotation of the wall. The transfer of moment from wall to slab gives rise to continuously distributed interaction forces along the connection. In order to study its interaction with the wall, the slab can be considered in isolation with an unknown distribution of reactive pressure which produces a known deflection

pattern at the wall position, the determination of this reactive pressure providing the necessary force/ displacement relationship to give a measure of the slab coupling stiffness and effective width.

The exact distribution of reactive pressure on the slab cannot be readily determined, and it is necessary to introduce simplifying assumptions to render the problem amenable to solution. In common with the finite element solution, the distributed reactive pressure is replaced by a system of concentrated forces and moments acting at a discrete set of nodes as shown in Fig. 2.11. It is intuitively expected that a progressively more accurate representation of the actual continuous pressure occurs as the number of nodes is increased.

In order to simplify the problem further, the panel of floor slab to be analysed is assumed to be simply supported along the two edges normal to the direction of bending. In a slab coupling a series of internal shear walls (or columns in more common situations), the simply supported edges correspond directly to the line of inflection passing through the axes of rotation of the walls (or columns) and also along the line of contraflexure at mid-span. In a slab coupling only two shear walls, the slab edges, if terminated on spandrel girders, as is frequently the case, can be considered simply supported. Even without the spandrel girder, association of the free edge with conditions of a simply supported one need not introduce any significant error in the analysis since very little bending of the slab occurs in the portion remote from the corridor area and its immediate neighbourhood, as indicated by previous theoretical and experimental studies.[3,4,8,40] A slightly better and more convenient location for the assumed simply supported edges for this case, however, appears to be at the positions of the wall centroidal axes, since very little deflection occurs along a slab section at this position (cf. Fig. 2.12). The remaining two slab edges parallel to the direction of

bending can be continuous, free, simply supported or clamped, as applicable to the real situation.

2.5.1.2 Solution Method

Consider now the slab simply supported along two opposite edges and arbitrarily supported along the remaining two edges, and subjected to the system of unknown concentrated forces acting at a set of discrete wall nodes as shown in Fig. 2.13. For generality, the two walls are assumed to be dissimilar. The forces $\{R\}_i$ at a node 'i' in general consist of a point load P_i and two moments M_{xi} and M_{yi}. The displacements $\{\delta\}_i$ then consist of the transverse deflection w_i and two rotations w_{xi} and w_{yi} to provide the necessary correspondence between forces and displacements. The influence coefficient $(f_{rs})_{ij}$, which defines the displacement component s_i at node 'i' due to a unit force component r_j at node 'j', allows the net displacement at any node 'i' due to the complete system of loading to be evaluated by superposition, thus,

$$\{\delta\}_i = [F_{i1} \quad F_{i2} \quad F_{i3} \cdots\cdots F_{in}] \begin{Bmatrix} R_1 \\ R_2 \\ \cdot \\ \cdot \\ R_n \end{Bmatrix} \qquad (2.44)$$

in which $[F_{ij}]$ is a 3 x 3 flexibility submatrix containing the influence coefficients $(f_{rs})_{ij}$. These influence coefficients may readily be evaluated from influence functions derived from classical plate theory. The establishment of compatibility between the displacement produced by the system of unknown forces and the linear displacements imposed by an assumed arbitrary parallel wall rotation leads to a system of simultaneous equations,

$$[F] \quad \{R\} = \{\delta\} \qquad (2.45)$$

which may be solved for the unknown forces, to give,

$$\{R\} = [F]^{-1} \quad \{\delta\} \qquad (2.46)$$

The set of calculated forces at the wall nodes constitutes a resultant wall moment about the centroidal axis. Thus,

referring to Fig. 2.14

$$M_a = \sum_{i=1}^{n} (P_i x_i + M_{xi}) \qquad (2.47)$$

and the slope Ø becomes

$$Ø = w_{xa} + w_{xb} + \frac{1}{H} (w_a - w_b) \qquad (2.48)$$

The coupling stiffness of the slab K is then defined as

$$K = \frac{M_a + M_b}{D\ Ø} \qquad (2.49)$$

in which D is the flexural rigidity for the plate.

By equating the stiffness of the coupling slab to the stiffness of an equivalent coupling beam of uniform effective width, and having a depth equal to the slab thickness, the effective width Y_e of the slab may be shown to be, in non-dimensional terms,

$$\frac{Y_e}{Y} = \frac{K}{6(1-\nu^2)} \left(\frac{L}{H}\right)^2 \left(\frac{L}{Y}\right) \qquad (2.50)$$

Although the method of analysis has been described for slabs coupling walls which are undergoing parallel rotation, it is equally applicable to slabs coupling walls undergoing differential axial displacements due to axial forces, since both forms of related movement are identical (cf. Fig. 2.15).

2.5.2 DERIVATION OF INFLUENCE COEFFICIENTS: GENERAL PROCEDURE

2.5.2.1 Green's Function For Plate

The solution of the governing plate equation (2.7) for a rectangular plate simply supported on two opposite edges is most conveniently obtained following Levy's method.[22] If the supported edges are defined by x = o and x = a, the deflection function for the plate is taken in the form of an infinite harmonic series,

$$w = \sum_{m=1}^{\infty} Y_m \sin \frac{m\pi x}{a} \qquad (2.51)$$

in which the coefficients Y_m are functions only of the coordinate 'y'. The series satisfies automatically the boundary conditions at the simply supported edges. The functions Y_m can be chosen in a form to satisfy the differential equation, containing four unknown constants which are chosen to satisfy the remaining boundary conditions on the other panel edges. The solution may then be obtained to any level of accuracy by summing up enough terms in the series solution.

The various influence functions required for the evaluation of the influence coefficients and stresses can be obtained from the single Green's function $G(x,y,\xi,\eta)$ which defines the deflection at a point (x,y) due to the influence of a unit load at another point (ξ,η) on the plate. In deriving the Green's function for a plate, it is necessary to deal with loading in the form of a single point load. When using the Levy technique, a single point load P can be represented[21] as a sinusoidal line load along the line $y = \eta$ in the form,

$$P = \sum_{m=1}^{\infty} E_m \sin \frac{m\pi x}{a} \qquad (2.52)$$

in which E_m is a constant which can be evaluated for the particular loading position using Fourier analysis.[39] The line load divides the plate into two parts, each having no distributed surface loading q; the deflection of each part satisfies the governing differential equation (2.7) with the right hand side equal to zero. The deflection functions for the two segments 1 and 2 may be expressed in the form

$$w_1 = \sum_{m=1}^{\infty} \frac{E_m}{2D} \left(\frac{a}{m\pi}\right)^3 \left\{ A_m \operatorname{ch} \frac{m\pi y}{a} + B_m \frac{m\pi y}{a} \operatorname{sh} \frac{m\pi y}{a} + C_m \operatorname{sh} \frac{m\pi y}{a} + D_m \frac{m\pi y}{a} \operatorname{ch} \frac{m\pi y}{a} \right\} \sin \frac{m\pi x}{a} \qquad (y \leq \eta) \qquad (2.53)$$

and

$$w_2 = \sum_{m=1}^{\infty} \frac{E_m}{2D} \left(\frac{a}{m\pi}\right)^3 \left\{ P_m \, ch \frac{m\pi y}{a} + Q_m \frac{m\pi y}{a} sh \frac{m\pi y}{a} \right.$$

$$\left. + R_m \, sh \frac{m\pi y}{a} + S_m \frac{m\pi y}{a} ch \frac{m\pi y}{a} \right\} \sin \frac{m\pi x}{a}$$

$$(y \geq \eta) \qquad (2.54)$$

where sh and ch are used to denote the hyperbolic functions sinh and cosh.

Considering the m^{th} harmonic, the eight constants A_m - D_m, and P_m - S_m, may be determined from the four known boundary conditions at the edges y = o and y = b, and another four from the continuity conditions at the load line $y = \eta$. The continuity conditions are given by the continuity of the deflection, normal slope and normal curvature across the load line, and a discontinuity in the shear force equal to the applied line loading given by equation (2.52). The solution is a standard procedure in classical plate theory.[22] Substitution of the constants evaluated in terms of the coordinates (ξ, η) of the point load into equations (2.53) and (2.54) allows the deflection function to be expressed in the form

$$w_p = P.G(x, y, \xi, \eta) \qquad (2.55)$$

2.5.2.2 Deflection Influence Functions for Concentrated Moments M_x and M_y

The concentrated moment M_x acting at the point (ξ, η) may be replaced by a couple consisting of a pair of point loads of magnitude $M_x/\Delta x$, acting at the points (ξ, η) and $(\xi + \Delta x, \eta)$. The deflection function for the combined point loading may be obtained by superposition from equation (2.55) to give

$$w_{mx} = \frac{M_x}{\Delta x} \left[G(x, y, \xi + \Delta x, \eta) - G(x, y, \xi, \eta) \right]$$

In the limit, as Δx approaches zero, the loading reduces to that of a concentrated moment and the deflection function is given by

$$w_{mx} = M_x \frac{\partial}{\partial \xi} G(x, y, \xi, \eta) \qquad (2.56)$$

Proceeding in the same manner, the deflection function for a concentrated moment M_y is given by

$$w_{my} = M_y \frac{\partial}{\partial \eta} G(x, y, \xi, \eta) \qquad (2.57)$$

2.5.2.3 Rotation Influence Functions

The influence functions for rotations in the x- and y-directions at a point (x,y) due to a concentrated load or moment at another point (ξ, η) are obtained by taking derivatives with respect to 'x' or 'y' of the deflection influence functions for the loading considered. The rotation functions are then given by the following expressions,

Concentrated load P:-

$$w_{p,x} = \frac{\partial}{\partial x} w_p = P \frac{\partial}{\partial x} G(x, y, \xi, \eta) \qquad (2.58)$$

$$w_{p,y} = \frac{\partial}{\partial y} w_p = P \frac{\partial}{\partial y} G(x, y, \xi, \eta) \qquad (2.59)$$

Concentrated moment M_x:-

$$w_{mx,x} = \frac{\partial}{\partial x} w_{mx} = M_x \frac{\partial^2}{\partial x \partial \xi} G(x, y, \xi, \eta) \qquad (2.60)$$

$$w_{mx,y} = \frac{\partial}{\partial y} w_{mx} = M_x \frac{\partial^2}{\partial y \partial \xi} G(x, y, \xi, \eta) \qquad (2.61)$$

Concentrated moment M_y:-

$$w_{my,x} = \frac{\partial}{\partial x} w_{my} = M_y \frac{\partial^2}{\partial x \partial \eta} G(x, y, \xi, \eta) \qquad (2.62)$$

$$w_{my,y} = \frac{\partial}{\partial y} w_{my} = M_y \frac{\partial^2}{\partial y \partial \eta} G(x, y, \xi, \eta) \qquad (2.63)$$

The general form of the flexibility submatrix $[F_{ij}]$ of equation (2.44) is assembled from the displacement functions of equations (2.55) to (2.63) as

$$[F_{ij}] = \begin{bmatrix} w_p & w_{mx} & w_{my} \\ w_{p,x} & w_{mx,x} & w_{my,x} \\ w_{p,y} & w_{mx,y} & w_{my,y} \end{bmatrix}$$

with unit values of P, M_x and M_y, and with $x = x_i$, $y = y_i$, $\xi = x_j$, $\eta = y_j$.

With the flexibility submatrix in this form, the complete flexibility matrix [F] in equation (2.45) is easily built up by entering the coordinates of the nodes taken in pairs by permutation. With the reciprocal properties of Green's function, only the upper triangular half of the flexibility matrix [F] need be evaluated, the lower half being reproduced from symmetry.

2.5.2.4 Stress Influence Functions

Once the deflection functions are established, the general functions for calculating plate moments and stresses due to the various forms of concentrated loading may be obtained from the standard stress resultant-curvature relationships (Equations (2.1)-(2.5)). The curvatures and twists may be obtained by double differentiation of the deflection functions.

2.5.3 DERIVATION OF INFLUENCE FUNCTIONS FOR SPECIFIC CASES

2.5.3.1 Influence Functions for a Plate with Two Continuous Edges

The derivation of the various displacement influence functions in explicit form is illustrated for the particular case of a plate with two continuous edges. The plate may thus be used to represent the most common practical situation of a typical internal panel of a coupling slab, or its symmetric half or quadrant in a regular cross-wall structure.

(a) Continuous Edges at y = o and y = b

Proceeding in the manner described earlier, the load function E_m of equation (2.52) is found by Fourier analysis to be,

$$E_m = \frac{2P}{a} \sin \frac{m \pi \xi}{a} \qquad (2.64)$$

The boundary conditions at the continuous edges are,

$$\frac{\partial w_1}{\partial y} = 0, \quad \frac{\partial^3 w_1}{\partial y^3} = 0 \quad \text{at } y = o,$$

$$\frac{\partial w_2}{\partial y} = 0, \quad \frac{\partial^3 w_2}{\partial y^3} = 0 \quad \text{at } y = b \qquad (2.65)$$

The continuity conditions of deflection, slope, and curvature, and the change in shear force across the load line $y = \eta$ are given by

$$w_1 = w_2 \ , \quad \frac{\partial w_1}{\partial y} = \frac{\partial w_2}{\partial y} \ , \quad \frac{\partial^2 w_1}{\partial y^2} = \frac{\partial^2 w_2}{\partial y^2}$$

and

$$\left(\frac{\partial^3 w_1}{\partial y^3} + \frac{\partial^3 w_1}{\partial x^2 \partial y}\right) = \left(\frac{\partial^3 w_2}{\partial y^3} + \frac{\partial^3 w_2}{\partial x^2 \partial y}\right) - \frac{q}{D} \qquad (2.66)$$

On substituting equations (2.53) and (2.54) into (2.65) and (2.66), equating corresponding harmonics, and solving, the eight constants are found to be,

$$A_m = \frac{1}{\mathrm{sh}\,\alpha} \left\{ \frac{\alpha\, \mathrm{ch}\beta}{\mathrm{sh}\,\alpha} + \beta\, \mathrm{sh}(\alpha - \beta) + \mathrm{ch}(\alpha - \beta) \right\}$$

$$B_m = - \frac{\mathrm{ch}(\alpha - \beta)}{\mathrm{sh}\,\alpha}$$

$$C_m = D_m = 0$$

$$P_m = \frac{1}{\mathrm{sh}\,\alpha} \left\{ \frac{\alpha\, \mathrm{ch}\beta}{\mathrm{sh}\,\alpha} - \beta\, \mathrm{ch}\,\alpha\ \mathrm{sh}\beta + \mathrm{ch}\,\alpha\ \mathrm{ch}\beta \right\}$$

$$Q_m = - \frac{\mathrm{ch}\,\alpha\, \mathrm{ch}\beta}{\mathrm{sh}\,\alpha}$$

$$R_m = \beta\, \mathrm{sh}\beta - \mathrm{ch}\beta$$

$$S_m = \mathrm{ch}\beta$$

where $\alpha = \frac{m\pi b}{a}$ $\beta = \frac{m\pi\eta}{b}$

Considering only the portion of the plate defined by $y < \eta$ for illustration, the influence functions defined in equations (2.55) to (2.63) become,

$$w_p = \frac{Pa^2}{\pi^3 D} \sum_{m=1}^{\infty} \frac{1}{m^3} \left[A_m C'_m + B_m \gamma_m S'_m \right] \sin \frac{m\pi\xi}{a} \sin \frac{m\pi x}{a}$$

$$w_{mx} = \frac{M_x a}{\pi^2 D} \sum_{m=1}^{\infty} \frac{1}{m^2} \left[A_m C'_m + B_m \gamma_m S'_m \right] \cos \frac{m\pi\xi}{a} \sin \frac{m\pi x}{a}$$

$$w_{my} = \frac{M_y a}{\pi^2 D} \sum_{m=1}^{\infty} \frac{1}{m^2} \left[A'_m C'_m + B'_m \gamma_m S'_m \right] \sin \frac{m\pi\xi}{a} \sin \frac{m\pi x}{a}$$

$$w_{p,x} = \frac{Pa}{\pi^2 D} \sum_{m=1}^{\infty} \frac{1}{m^2} \left[A_m C'_m + B_m \gamma_m S'_m \right] \sin \frac{m\pi\xi}{a} \cos \frac{m\pi x}{a}$$

$$w_{p,y} = \frac{Pa}{\pi^2 D} \sum_{m=1}^{\infty} \frac{1}{m^2} \left[A_m S'_m + B_m (S'_m + \gamma_m C'_m) \right] \sin \frac{m\pi\xi}{a} \sin \frac{m\pi x}{a}$$

$$w_{mx,x} = \frac{M_x}{\pi D} \sum_{m=1}^{\infty} \frac{1}{m} \left[A_m C'_m + B_m \gamma_m S'_m \right] \cos \frac{m\pi\xi}{a} \cos \frac{m\pi x}{a}$$

$$w_{mx,y} = \frac{M_x}{\pi D} \sum_{m=1}^{\infty} \frac{1}{m} \left[A_m S'_m + B_m (S'_m + \gamma_m C'_m) \right] \cos \frac{m\pi\xi}{a} \sin \frac{m\pi x}{a}$$

$$w_{my,x} = \frac{M_y}{\pi D} \sum_{m=1}^{\infty} \frac{1}{m} \left[A'_m C'_m + B'_m \gamma_m S'_m \right] \sin \frac{m\pi\xi}{a} \cos \frac{m\pi x}{a}$$

$$w_{my,y} = \frac{M_y}{\pi D} \sum_{m=1}^{\infty} \frac{1}{m} \left[A'_m S'_m + B'_m (S'_m + \gamma_m C'_m) \right] \sin \frac{m\pi\xi}{a} \sin \frac{m\pi x}{a}$$

in which, for simplicity, the functions introduced are defined as,

$$S'_m = \text{sh}\,\frac{m\pi y}{a} \qquad C'_m = \text{ch}\,\frac{m\pi y}{a} \qquad \gamma_m = \frac{m\pi y}{a}$$

and the constants A'_m and B'_m are the derivatives of A_m and B_m with respect to η, given by,

$$A'_m = \frac{1}{\text{sh}\,\alpha}\left[\frac{\alpha\,\text{sh}\beta}{\text{sh}\,\alpha} - \beta\,\text{ch}(\alpha-\beta)\right]$$

$$B'_m = \frac{\text{sh}(\alpha-\beta)}{\text{sh}\,\alpha}$$

Analogous expressions may readily be derived for the plate region defined by $y > \eta$.

(b) Continuous Edges at $y = \pm b/2$

When an interior floor panel is required to be represented as its full width, it may be more convenient to locate the x-axis along the centre-line of the plate, in which case, the continuous edges are now at $y = \pm b/2$. With a transfer of axis, the eight constants A_m - S_m then become

$$A_m = \frac{1}{\text{sh}\,\alpha'}\left[\frac{\alpha'\text{ch}\beta}{\text{sh}\,\alpha'} + \beta\,\text{sh}(\alpha'-\beta) + \text{ch}(\alpha'-\beta)\right]$$

$$B_m = -\frac{\text{ch}(\alpha'-\beta)}{\text{sh}\,\alpha'}$$

$$C_m = \frac{1}{\text{ch}\,\alpha'}\left[\frac{\alpha'\text{sh}\beta}{\text{ch}\,\alpha'} + \beta\,\text{sh}(\alpha'-\beta) + \text{ch}(\alpha'-\beta)\right]$$

$$D_m = -\frac{\text{ch}(\alpha'-\beta)}{\text{ch}\,\alpha'}$$

$$P_m = \frac{1}{\text{sh}\,\alpha'}\left[\frac{\alpha'\text{ch}\beta}{\text{sh}\,\alpha'} - \beta\,\text{sh}(\alpha'+\beta) + \text{ch}(\alpha'+\beta)\right]$$

$$Q_m = \frac{-\text{ch}(\alpha'+\beta)}{\text{sh}\,\alpha'}$$

$$R_m = \frac{1}{\text{ch}\,\alpha'}\left[\frac{\alpha'\text{sh}\beta}{\text{ch}\,\alpha'} + \beta\,\text{sh}(\alpha'+\beta) - \text{ch}(\alpha'+\beta)\right]$$

$$S_m = \frac{\text{ch}(\alpha'+\beta)}{\text{ch}\,\alpha'}$$

in which $\alpha' = \frac{m\pi b}{2a}$

2.5.3.2 Influence Functions For Plates with Other Edge Supports

The integration constants for other forms of support at the edges y = o, y = b, are given for completeness in Appendix A2.3.

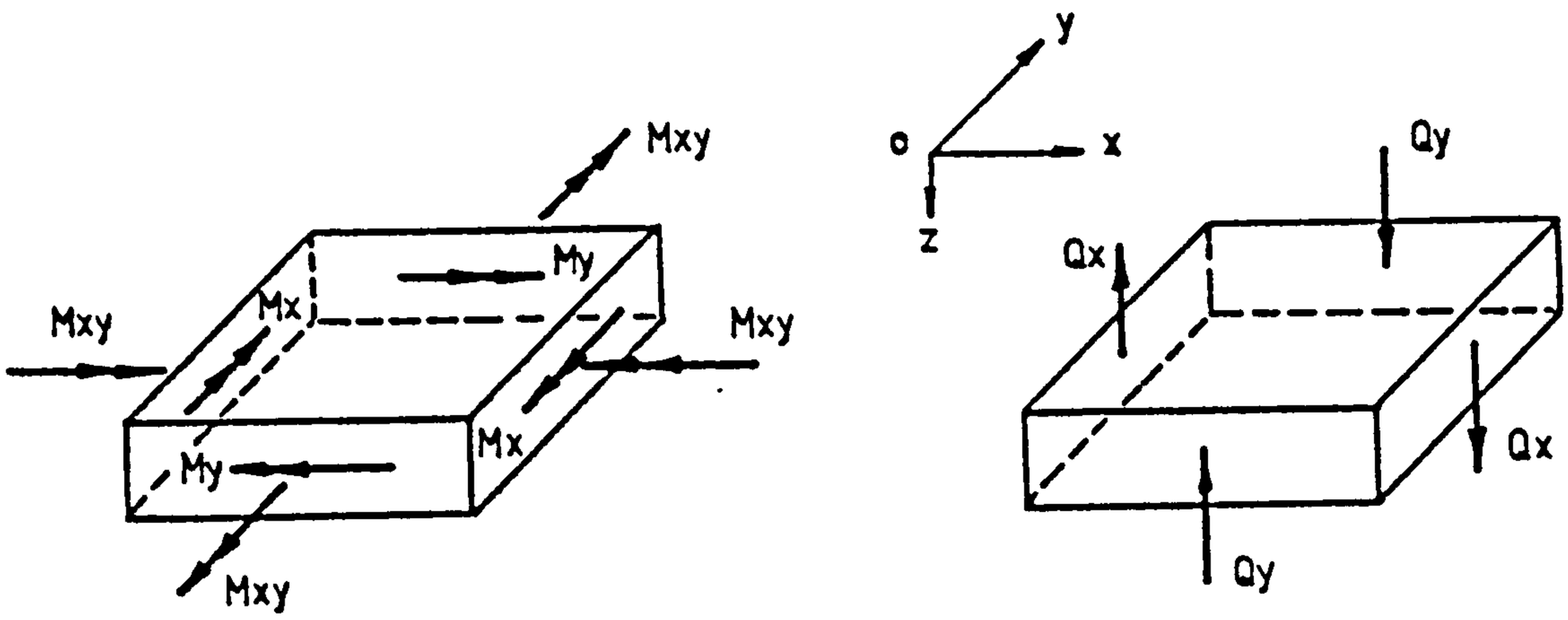

(a)

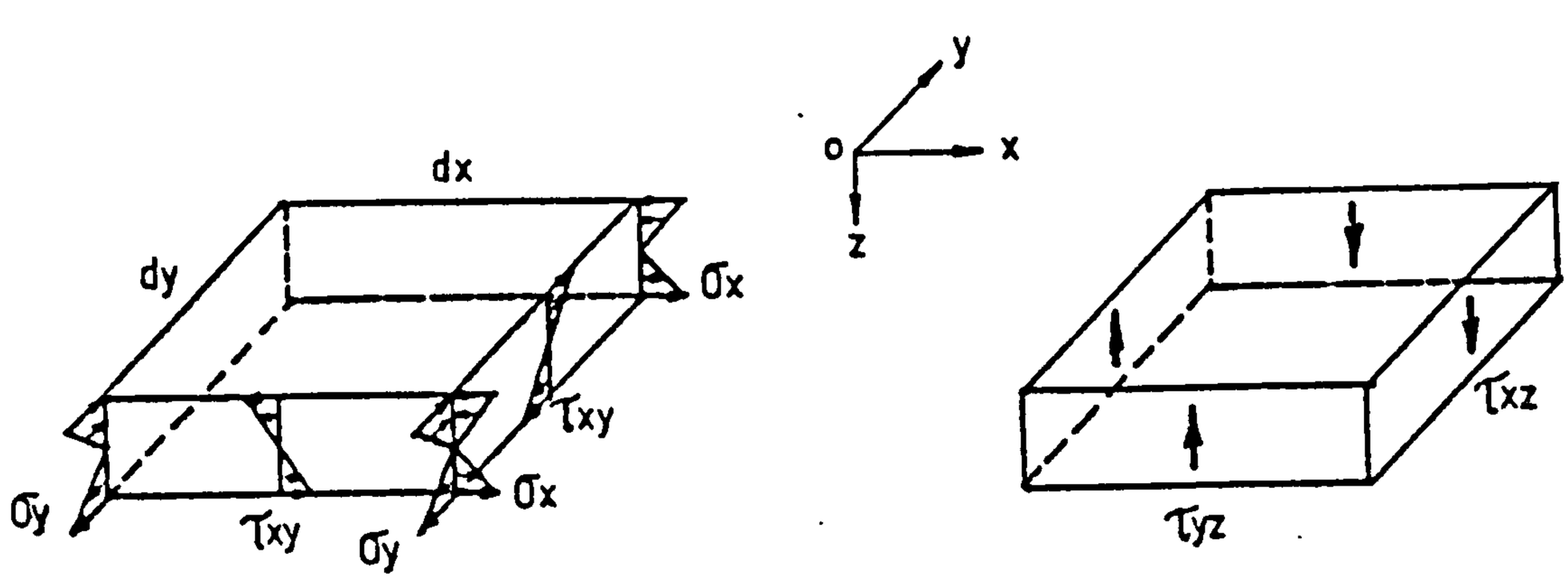

(b)

Fig. 2.1 (a) Stress-Resultants and (b) Plate Stresses

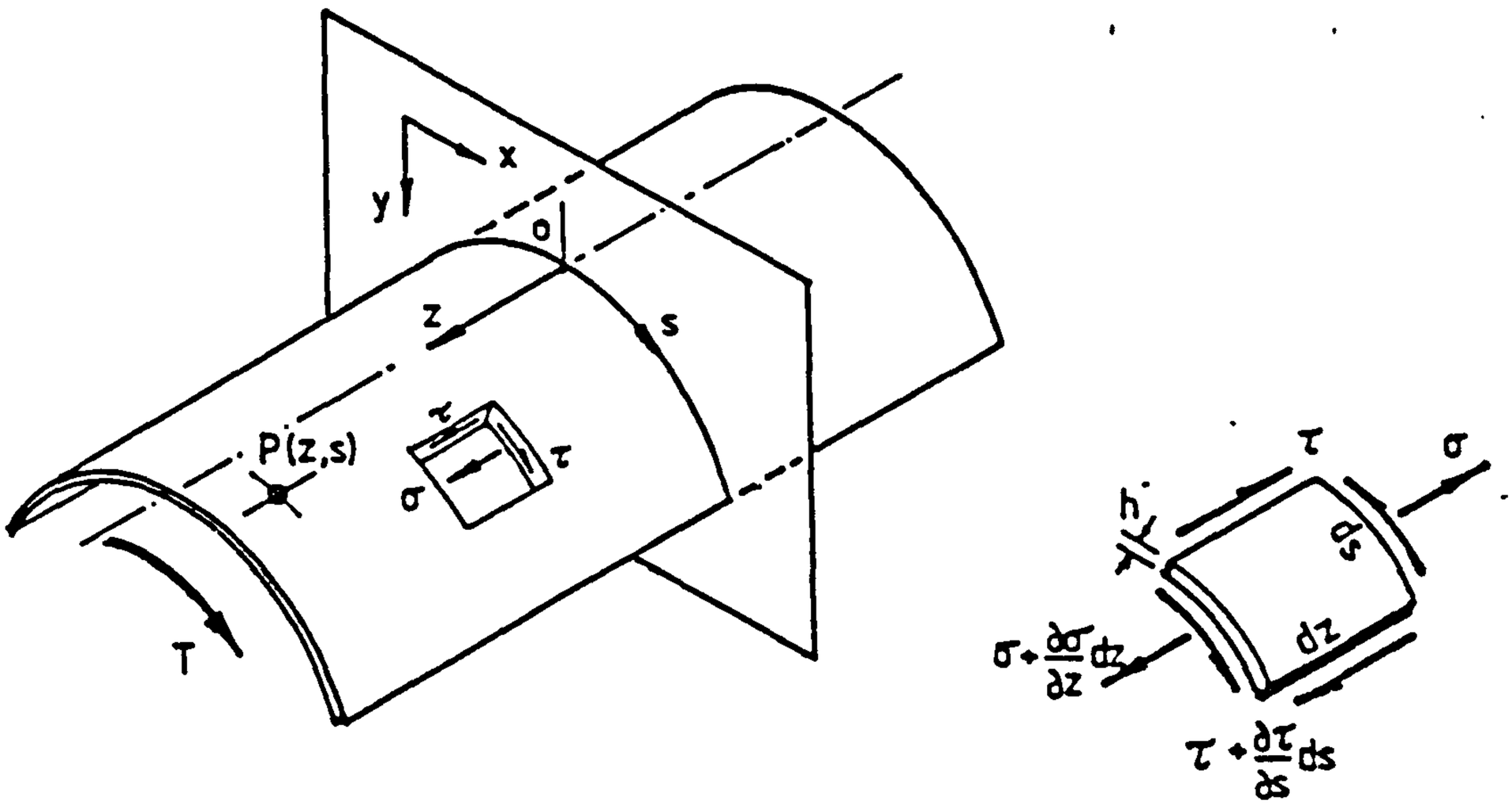

(a) An Open Section Thin Walled Beam

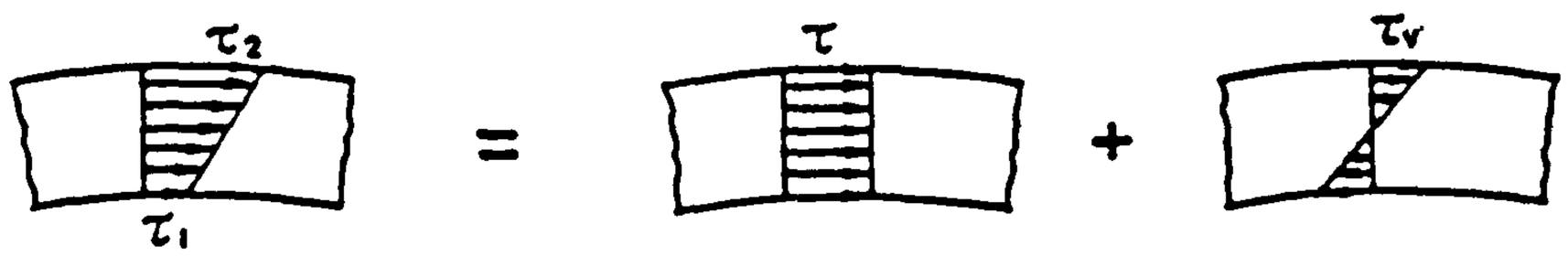

(b) Tangential Shear Stresses

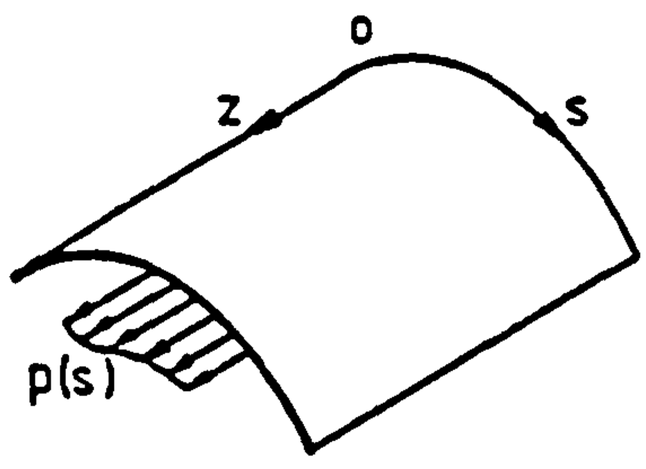

(c) Distributed Load

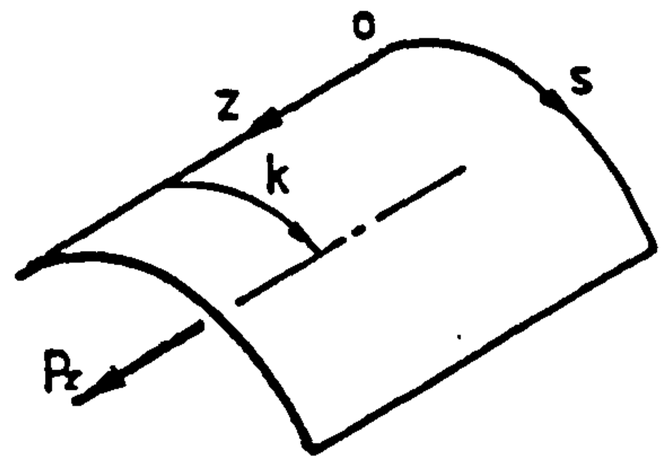

(d) Concentrated Force

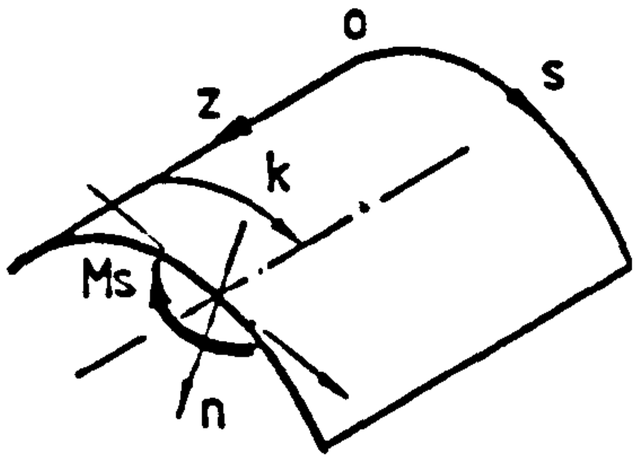

(e) In-plane Moment

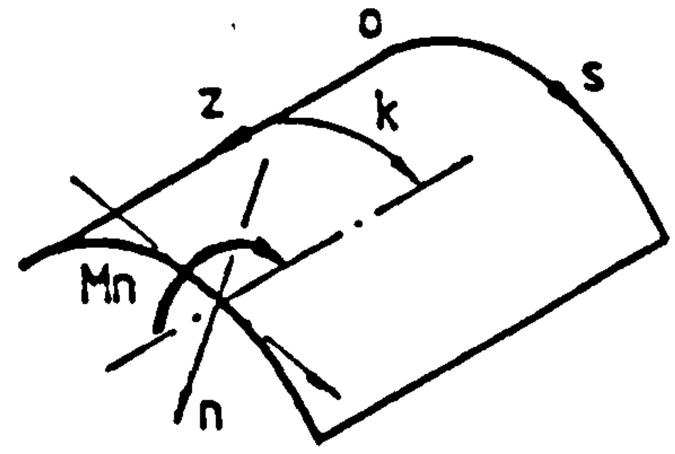

(f) Out-of-plane Moment

Fig. 2.2 An Open Section Thin-Walled Beam, Stresses and Forms of Longitudinal Loading

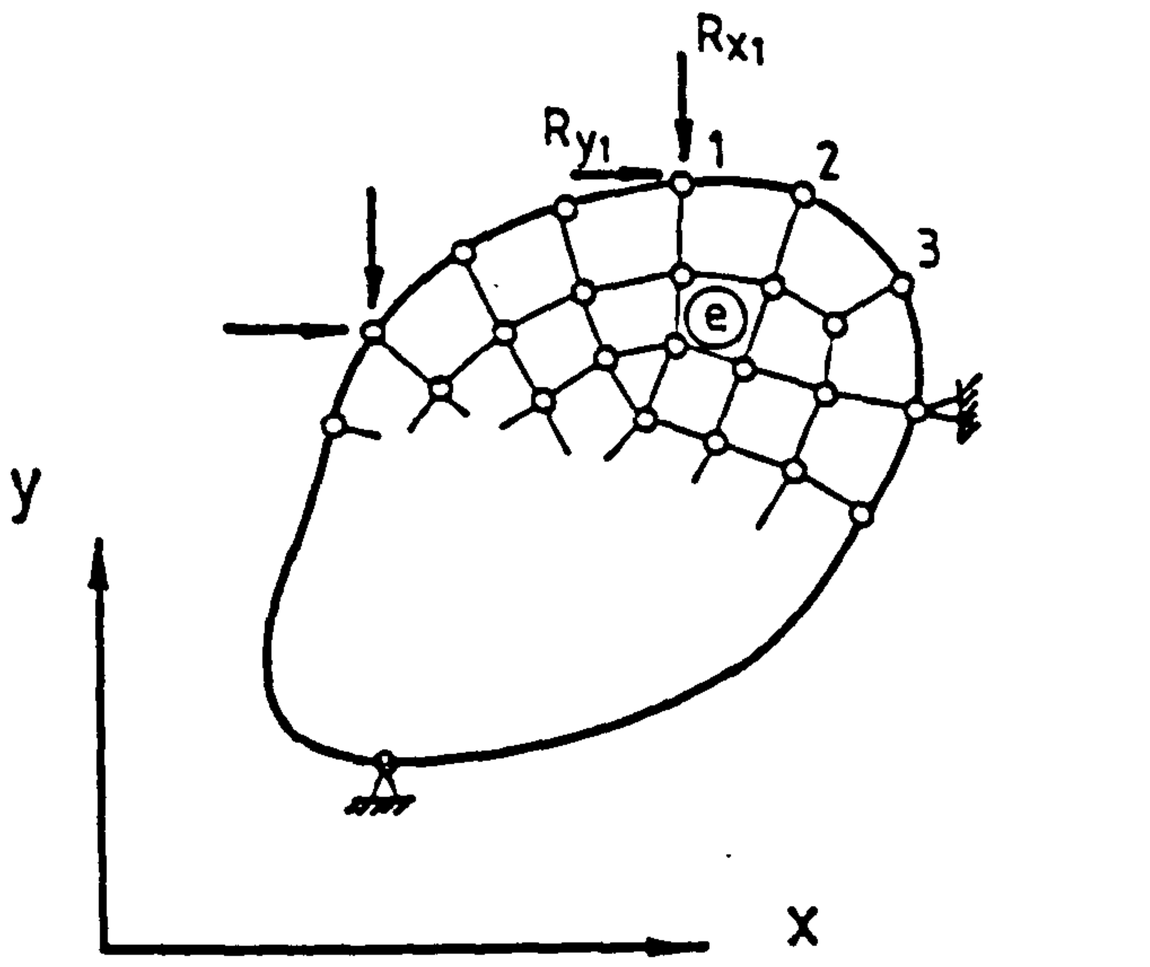

(a)

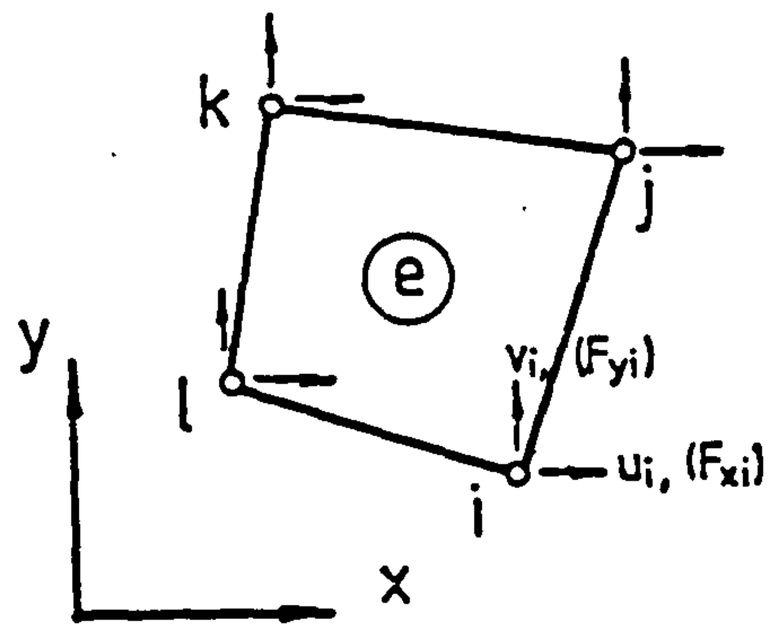

(b)

Fig. 2.3 (a) Finite Element Discretisation of Continum, and
(b) A Typical Element

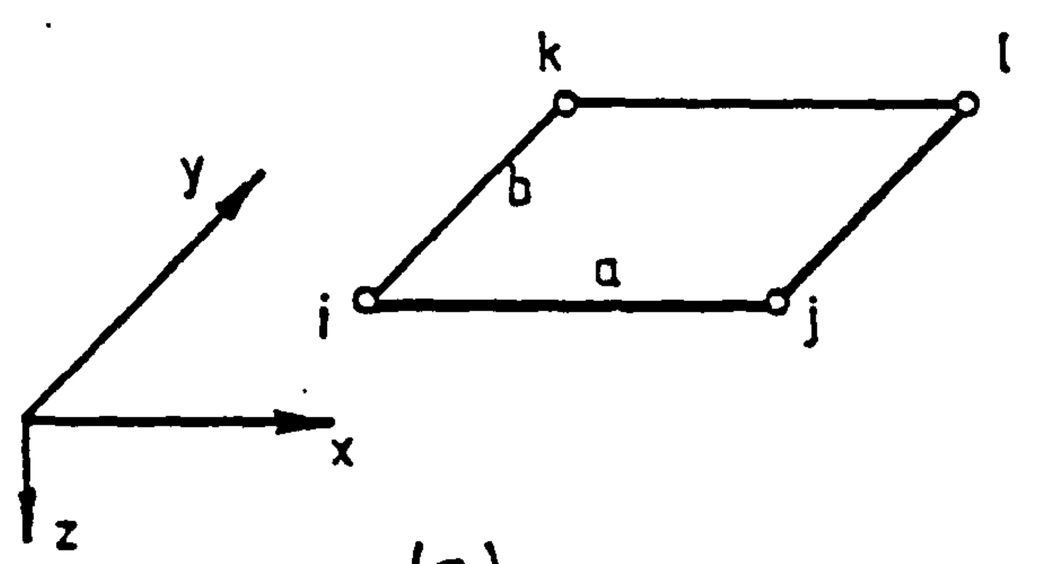

(a)

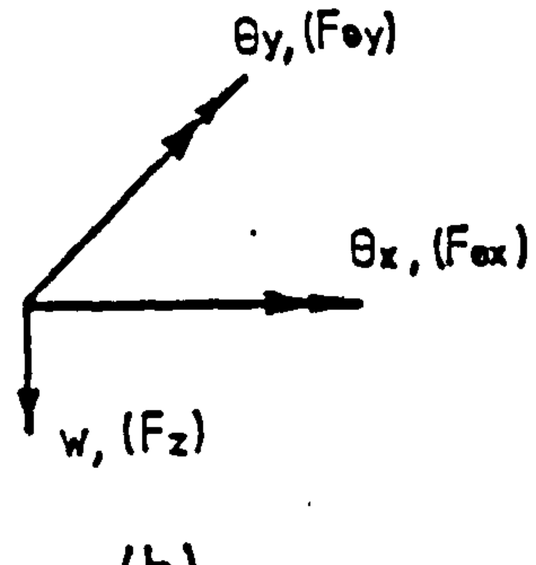

(b)

Fig. 2.4 (a) The Simple Rectangular Bending Element and
(b) The Nodal Displacements and Forces

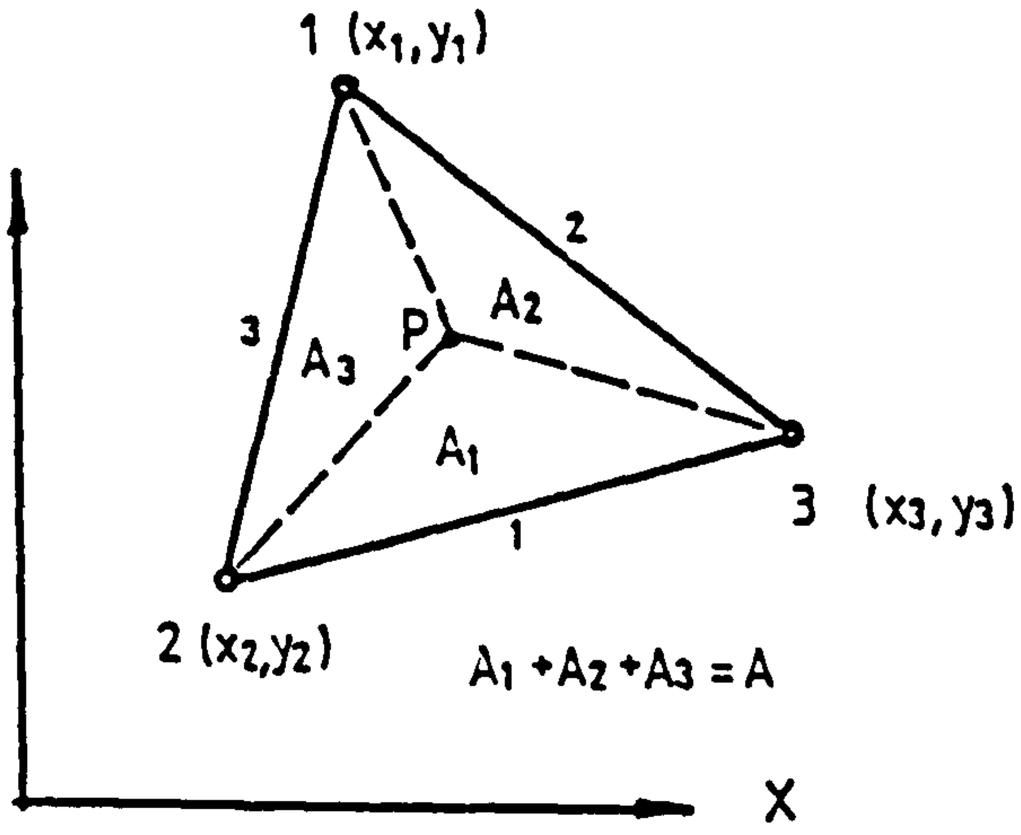

Fig. 2.5 Area Co-ordinates

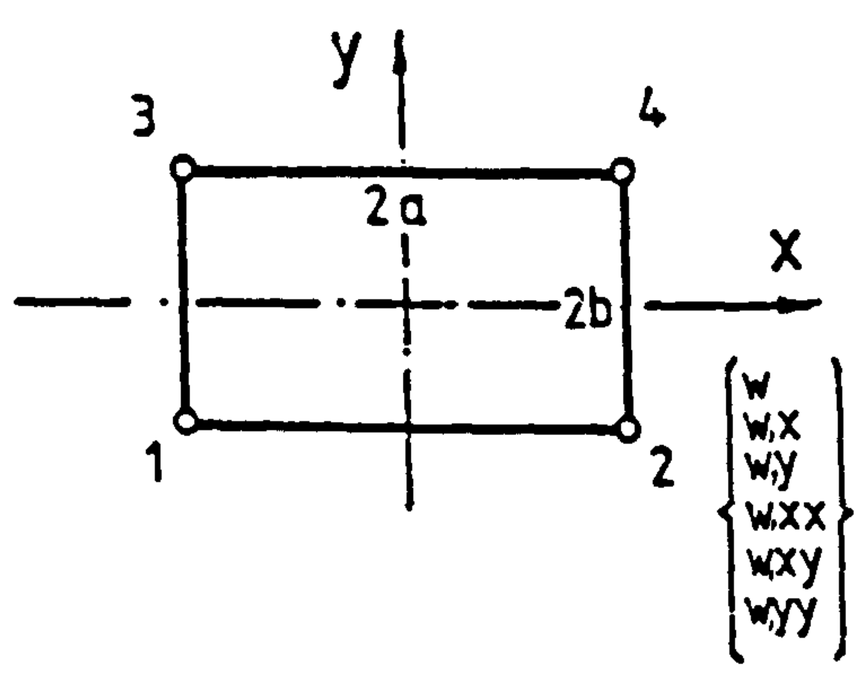

Fig. 2.6 The Refined
Bending Element

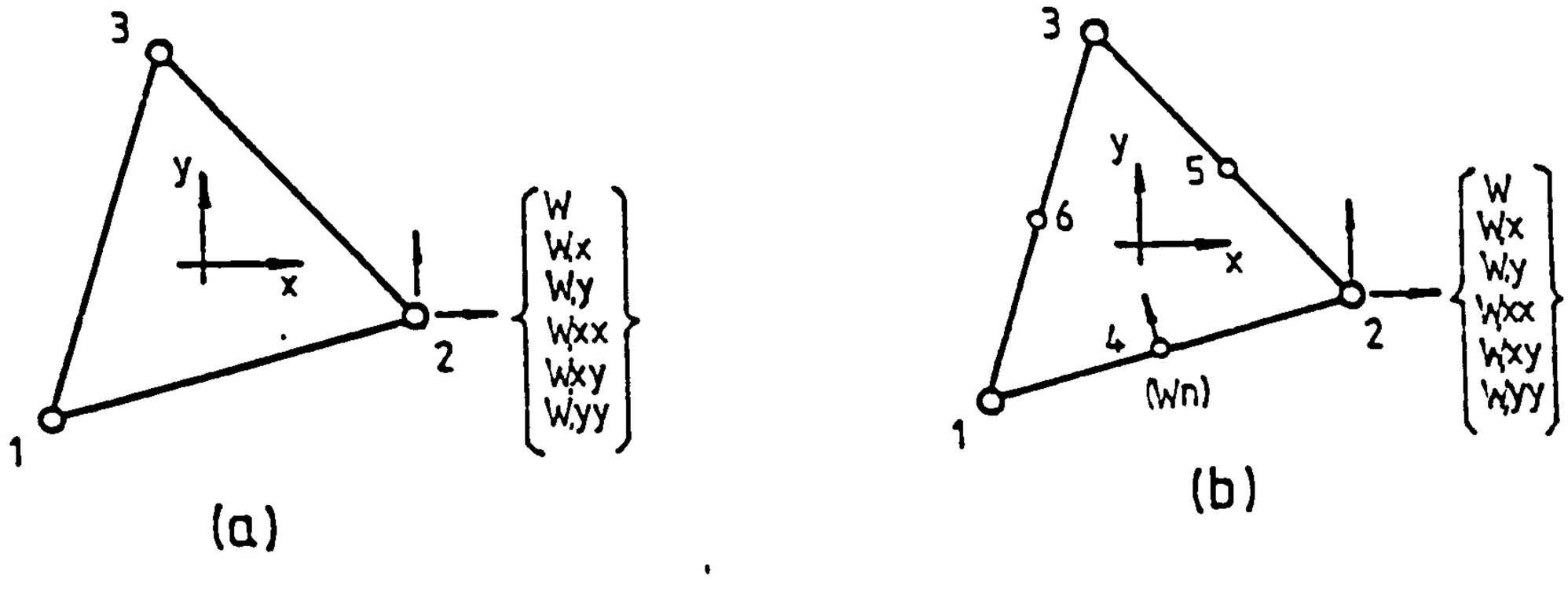

Fig. 2.7 The Refined Triangular Bending Element.
(a) 18 D.O.F. Version (b) 21 D.O.F. Version

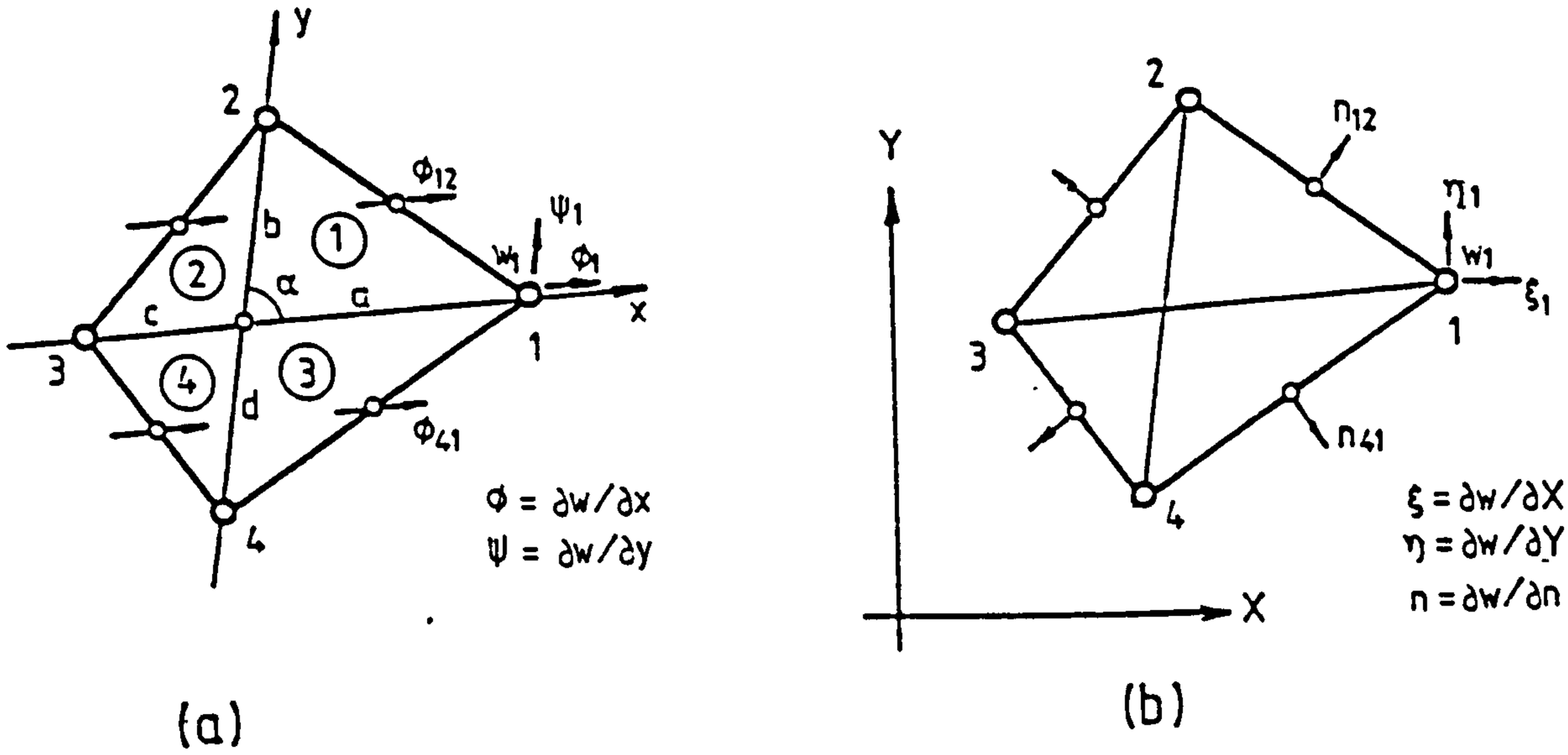

Fig. 2.8 The Quadrilateral Bending Element and Displacement Parameters in (a) Oblique Co-ordinate System, and (b) Cartesian Co-ordinate System

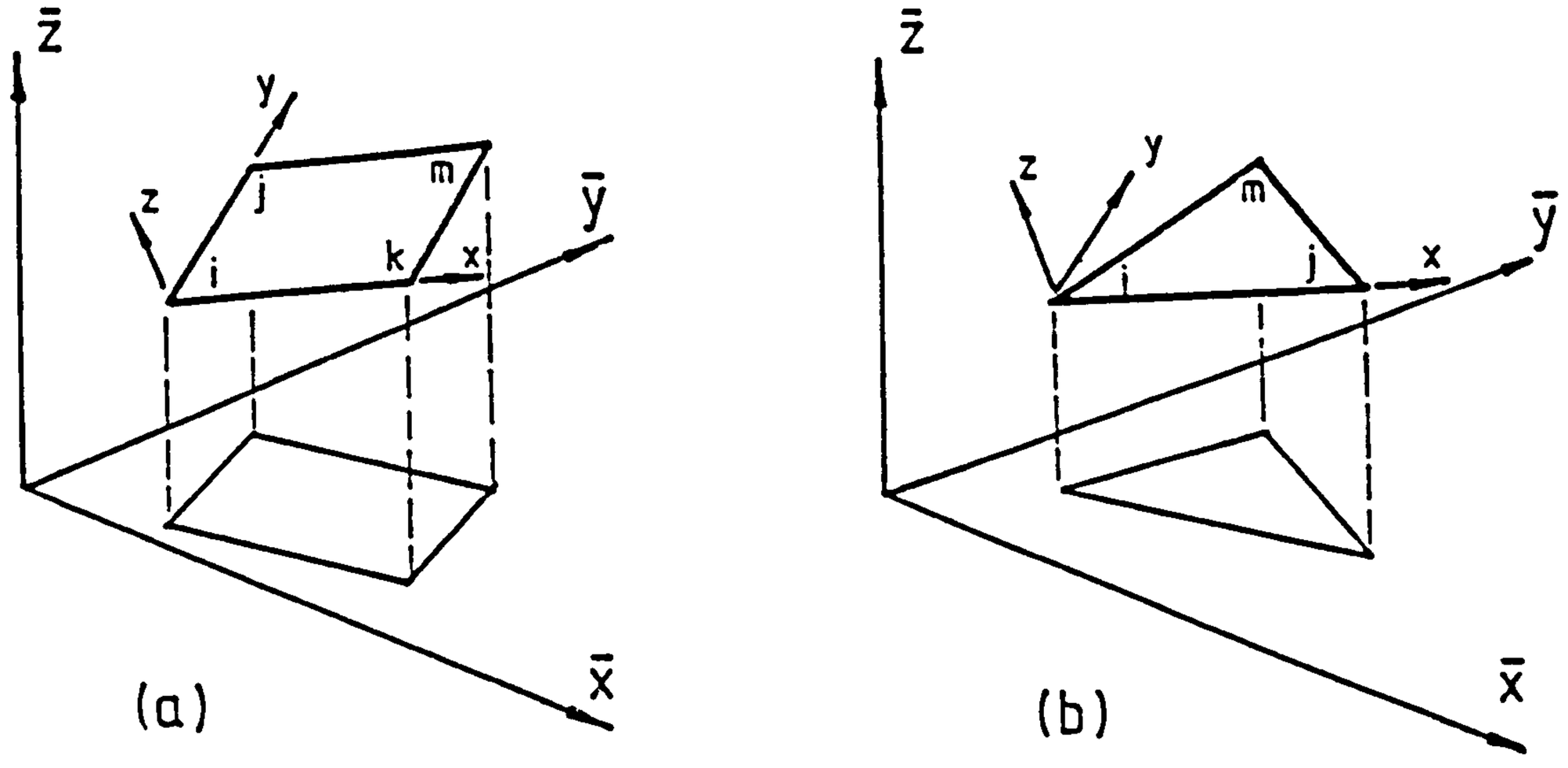

Fig. 2.9 Local and Global Co-ordinate Axes for
(a) Rectangular Flat Shell Element, and
(b) Triangular Flat Shell Element

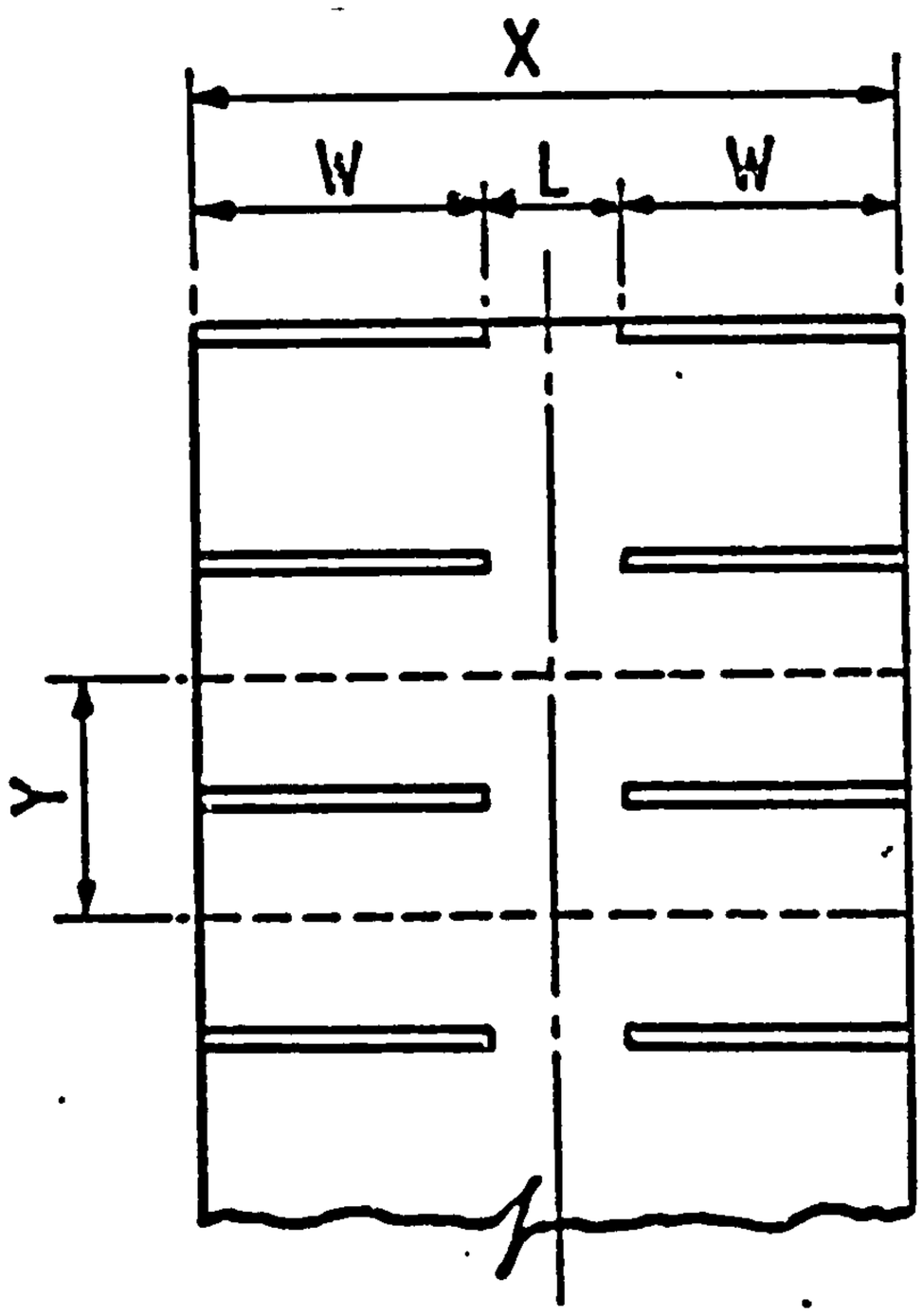

Fig. 2.10 Typical Floor Plan of Cross-Wall Structure

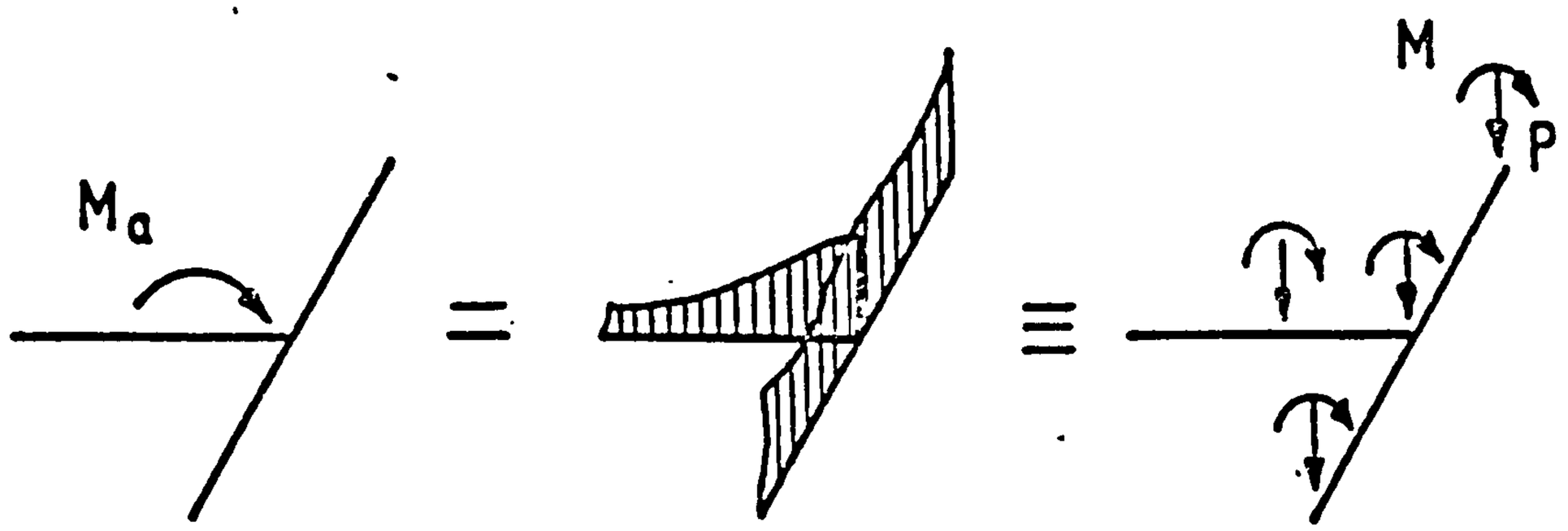

Fig. 2.11 Representation of Moment Transfer Between Wall and Slab by Discrete Forces

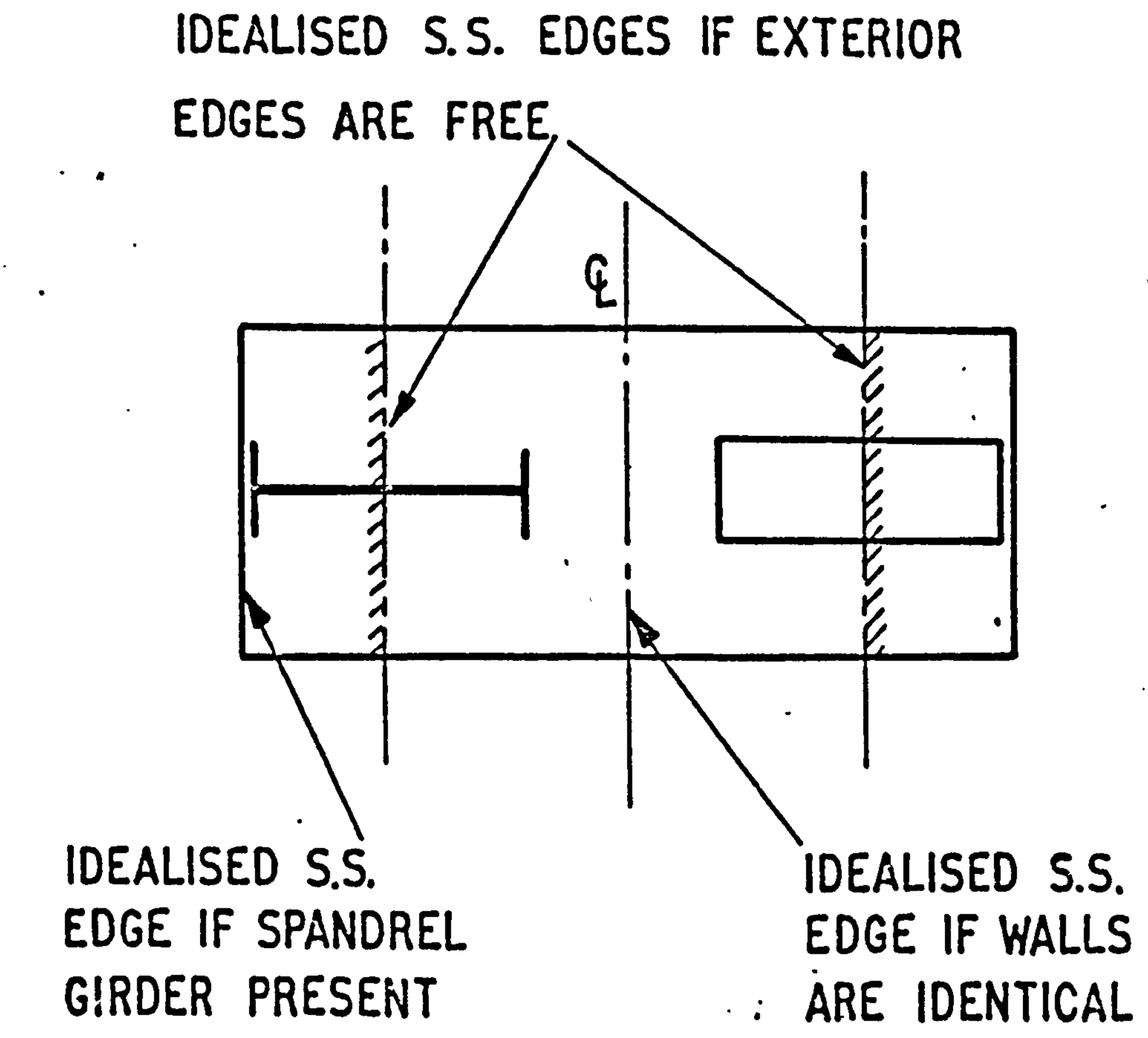

Fig. 2.12 Typical Floor Plan with Dissimilar Coupled Walls

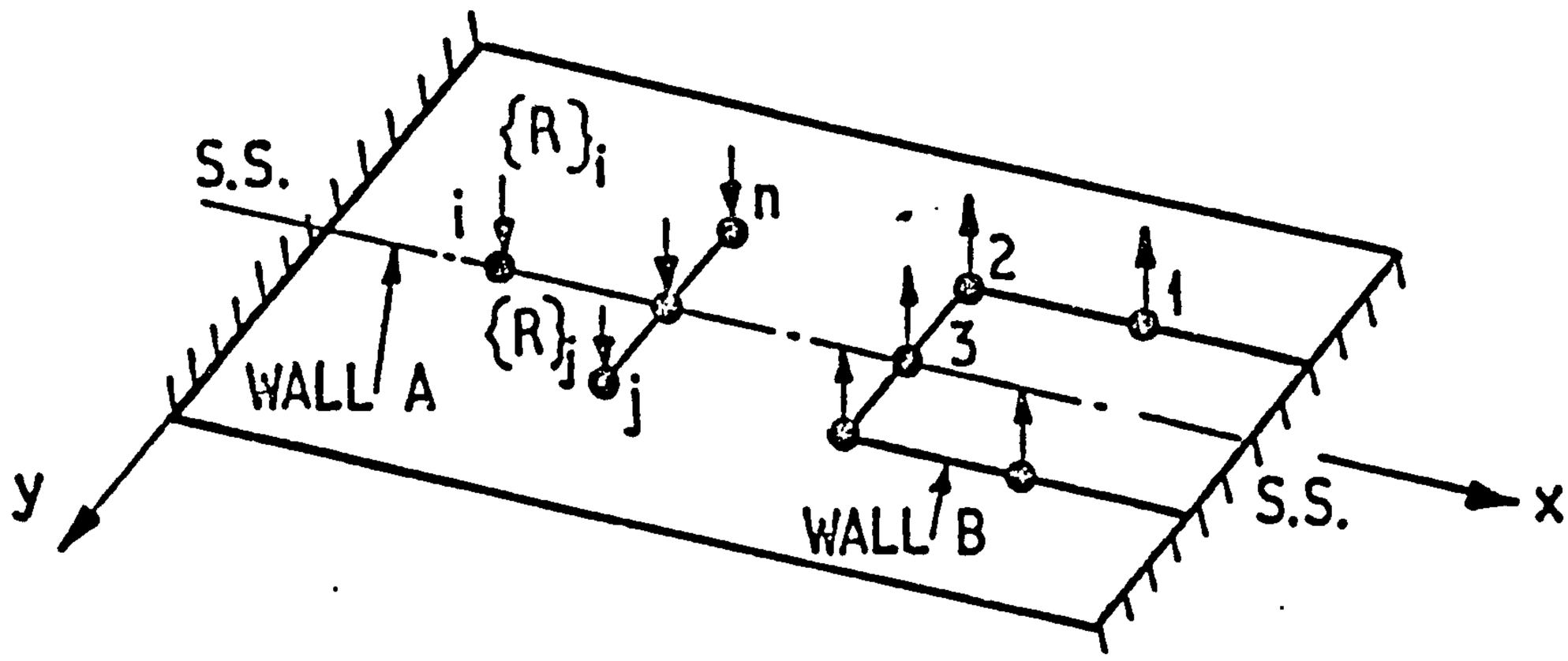

Fig. 2.13 Idealised Slab with Concentrated Forces

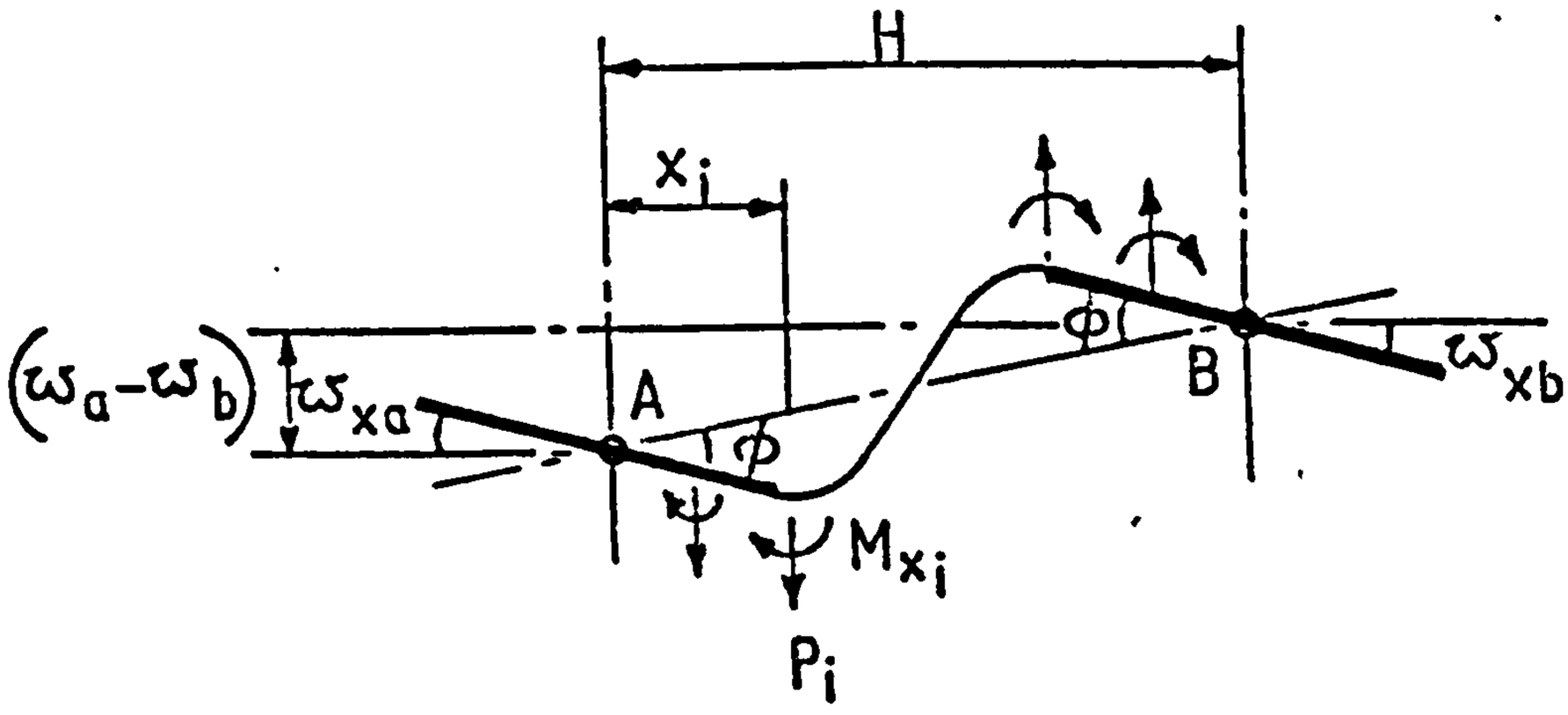

Fig. 2.14 Forces and Displacements in Coupling Slab

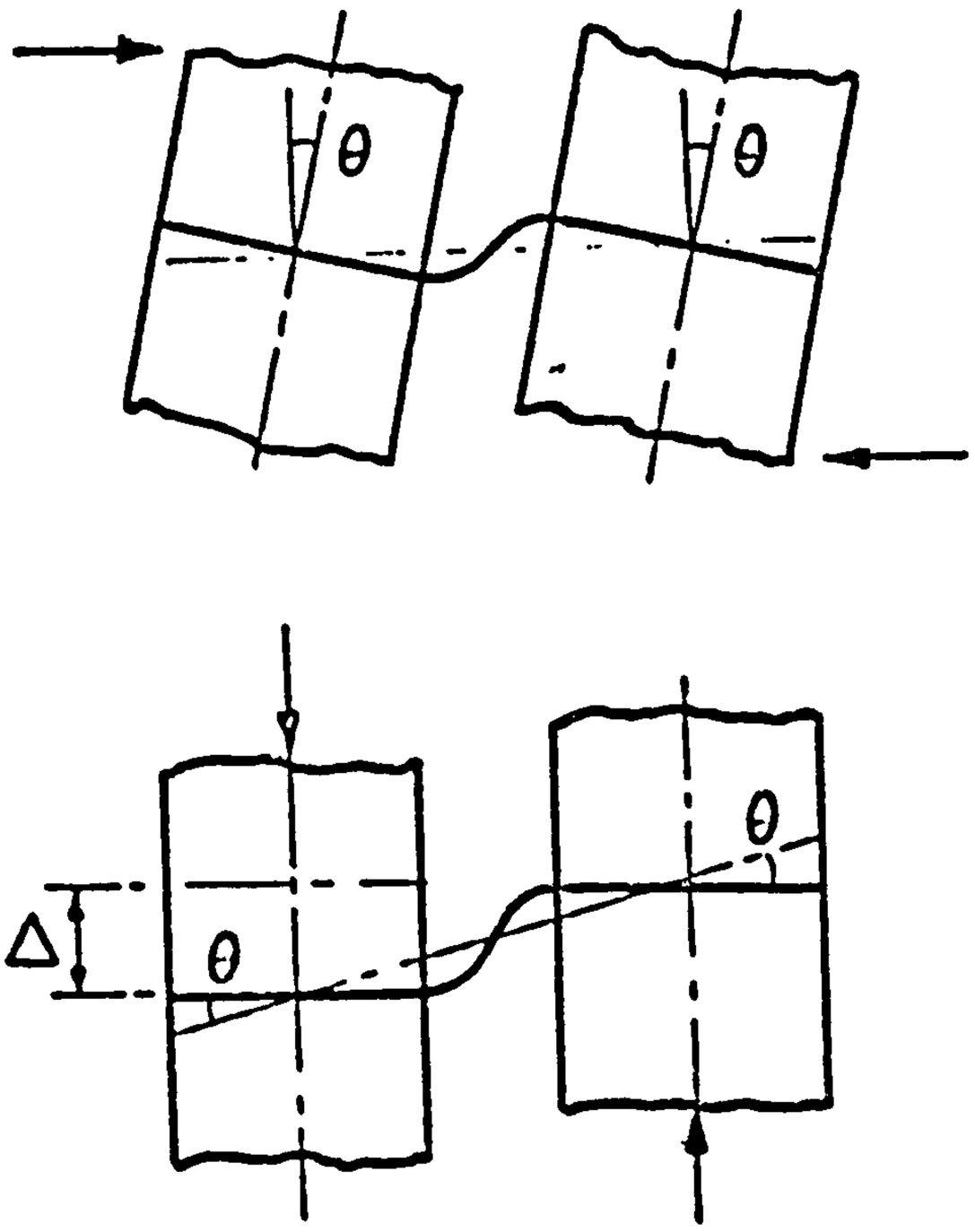

Fig. 2.15 Similarity of Action of Slabs Undergoing (a) Parallel Rotation, and (b) Differential Axial Displacements

CHAPTER 3

INTERACTION BETWEEN FLOOR SLABS AND SHEAR WALLS IN CROSS WALL STRUCTURES (Investigation By Finite Element Method)

3.1 INTRODUCTION

The cross-wall structure is a popular form of construction for multi-storeyed apartment buildings. Fig. 3.1 shows a typical floor plan of a slab block in which self-contained apartment units are arranged side by side along the length of the building. This arrangement naturally results in parallel assemblies of division walls running perpendicular to the face of the building, with intersecting longitudinal walls along the corridor and facade enclosing the living spaces. The cross-walls are employed as load bearing walls in addition to serving architectural requirements, since their disposition favours an efficient distribution of both gravity and lateral loads to the structural elements. The longitudinal corridor and facade walls are provided with openings for access to the living areas and balconies, and for window framing. If they are also designed to be load bearing, these longitudinal walls act effectively as flanges for the primary cross-walls. In addition to the structural partition walls, shear walls are used to enclose lift shafts and stair wells to form the open section box structures which act as strong points in the building. Thus in practice, shear walls of various shapes, planar, flanged or box-shaped, may be coupled together by floor slabs in cross-wall structures.

In this Chapter the finite element method is employed to establish the slab coupling stiffness and effective width, and the distribution of bending moments and shearing forces in the slab for a range of shear wall structures, with combinations of plane, T-shaped, L-shaped and box shaped wall elements (Fig. 3.3, (a) - (k)).

3.2 SHEAR WALL/SLAB INTERACTION

Fig. 3.2(a) shows a segment of an idealised floor plan of a cross-wall structure consisting of regularly spaced pairs of shear walls connected through the floor slab. A typical interior slab panel bounded by lines of symmetry located mid-way between wall panels is considered in the study of the wall/slab interaction. The end panel with the gable walls contains only half the slab in an interior panel and is considered a special case in the study.

The shear walls resist the lateral loads on the structure, due to wind or earthquake, by cantilever bending action, in which the inplane bending of the walls results in rotations of wall cross-sections. The free bending of a pair of shear walls is resisted by the floor slab which is forced to rotate and bend out of plane where it connects rigidly to the shear walls (Fig. 3.2(b)). Due to the large wall depth considerable differential shearing action is imposed on the connecting slab which develops transverse reactions to resist the wall deformation. The effect of the wall slab interaction is to reduce the lateral deflections and stresses in the walls below those which would exist if the walls behave as independent cantilevers.

Another situation in which the slab interacts with the pair of shear walls arises due to vertical wall movements which result from unequal loading on the walls or from differential foundation settlement. The effect on the slab produced by the relative vertical movement is however similar to that produced by the parallel wall rotation as shown in Fig. 3.2(c).

3.2.1 COUPLING STIFFNESS OF SLAB

The resistance of the floor slab against the displacements imposed by the shear walls is a measure of its coupling stiffness, which has to be determined in order to study the behaviour of the coupled shear walls. The coupling stiffness of the slab can be defined in terms of the displacements at its ends and the forces producing them.

Thus referring to Fig. 3.2, (d) and (e), the stiffness of the slab may be defined as a rotational stiffness M/θ or as a translational stiffness Q/δ since both stiffnesses are related. Due to non-uniform bending across the slab width, the force-displacement relationship can only be evaluated from a two-dimensional plate-bending analysis. For convenience, the rotational and translational slab stiffnesses may be evaluated in the form of non-dimensional stiffness factors given by

$$K = \frac{M}{D\theta} \qquad (3.1a)$$

and

$$K_\delta = \frac{Q}{\delta} \cdot \frac{L^2}{D} \qquad (3.1b)$$

where K and K_δ are respectively the rotational and translational stiffness factors and D is the plate rigidity.

3.2.2 EFFECTIVE WIDTH OF SLAB

For the purpose of overall analysis, it is convenient to assume that a strip of slab acts effectively as a beam in coupling a pair of walls. The effective stiffness of the slab can then be defined simply in terms of the geometric and material characteristics of the equivalent beam. The effective width of slab can be established by equating the rotational or translational stiffness of the slab to that of the equivalent beam. Using area-moment principles, the rotational and translational stiffnesses of the equivalent beam can be written respectively as

$$\frac{M}{\theta} = \frac{6EI}{L^3}(L + W)^2 \qquad (3.2a)$$

and

$$\frac{Q}{\delta} = \frac{12EI}{L^3} \qquad (3.2b)$$

where L and W are respectively the corridor width and wall length, and $I = Y_e t^3/12$ in which Y_e is the effective slab width and t is the slab thickness.

The effective width can then be expressed in terms of the rotational or translational stiffness factors in non-

dimensional form as

$$\frac{Y_e}{Y} = \frac{K}{6(1-\nu^2)} \left(\frac{L}{Y}\right)\left(\frac{L}{L+W}\right)^2 \qquad (3.3a)$$

or

$$\frac{Y_e}{Y} = \frac{K}{12(1-\nu^2)} \left(\frac{L}{Y}\right) \qquad (3.3b)$$

where Y is the full width of the slab panel and ν is Poisson's ratio.

3.2.3 FINITE ELEMENT ANALYSIS OF SLAB

The study of wall/slab interaction involves basically the analysis of slab actions in resisting the deformation imposed by the pair of shear walls undergoing parallel wall rotation or differential vertical movement. The finite element method is used in this study to analyse the slab actions. For analysis the slab is assumed to be homogeneous, isotropic and linearly elastic and plane sections of the walls are assumed to remain plane where the slab interacts with the walls.

In the finite element analysis the slab is discretised into an assembly of plate bending elements following a suitable mesh pattern which has been shown by a convergence study to yield accurate results. The mesh is generally graded such that the region close to the inner edge of the wall, where stress gradients are expected to be high, is sub-divided more finely than other parts of the slab. Depending on the element type, the mesh may be rectangular or triangular, the latter being conveniently obtained by sub-dividing a rectangular mesh along a diagonal. Conditions of symmetry and anti-symmetry in respect of displacement patterns may be used to reduce the computational effort. In a typical interior slab panel with identical coupled walls for instance, the displacements are symmetric about the longitudinal centreline and anti-symmetric about the transverse centreline, in which case, the actual analysis may be performed for a typical quadrant of the slab panel. Fig. 3.4 shows a typical

finite element idealisation of the slab coupling a pair of plane walls. The element nodes are numbered consecutively in one direction along the set of mesh lines with the smaller number of sub-divisions, commencing from an edge of the slab. The numbering scheme adopted facilitates data generation and also ensures that the band-width of the assembled structure stiffness matrix is minimised for an efficient solution.

The element stiffness matrices are generated from geometric and material data and are assembled into an overall structure stiffness matrix forming a set of equilibrium equations which may be solved for the unknown nodal displacements once the boundary conditions are prescribed. The prescribed boundary conditions consist of known displacements at the slab edges or lines of symmetry and anti-symmetry and at the wall nodes. Since only those displacement components which correspond to the nodal displacement parameters for the particular element can be incorporated in the solution, when using lower order elements (RB12, TB9 and QB16) only known values of the deflection w and slopes $w,_x$ and $w,_y$ are prescribed, whereas when using refined elements (RB24 and TB18) known curvatures $w,_{xx}$, $w,_{xy}$ and $w,_{yy}$ are also prescribed in addition to the deflection and slopes. At the longitudinal slab edges, which are lines of symmetry, the transverse slope $w,_y$ and twist $w,_{xy}$ are zero. At the corridor edge, which is a line of anti-symmetry, the deflection w, the transverse slope $w,_y$ and the curvatures $w,_{xx}$ and $w,_{yy}$ are zero. The displacements prescribed for the wall nodes can be due either to a unit parallel wall rotation or to a unit relative vertical wall movement since in each case the slab is subjected to the same form of deformation relative to the walls. If parallel wall rotation is prescribed, then the longitudinal slope $w,_x$ is of unit value at all the wall nodes and the deflection w varies linearly with distance x from the centre of rotation. On the other hand, if relative vertical wall movement is

prescribed, the deflection w is of constant value and the longitudinal slope $w,_x$ is zero at the wall nodes. In each case, the transverse slope $w,_y$ is zero at all the wall nodes and the curvature $w,_{xx}$ is zero at only the interior wall nodes. The boundary conditions for the typical slab coupling a pair of plane walls undergoing unit parallel rotation are shown in Fig. 3.4. The bracketed items shown are applicable to refined elements only.

The equilibrium equations are solved by a Gaussian elimination scheme to yield the unknown nodal displacements. Once the nodal displacements have been calculated, the stress resultants may be computed from the stress matrix relationship (Equation (2.33)) while the reactions at the restrained nodes may be computed from the element stiffness relationship (Equation (2.30)). The reactions at a set of wall nodes provide the static equivalent wall moment M and shear force Q transferred from the wall to the slab when the wall undergoes the relative displacements assumed in the slab analysis. Evaluation of the appropriate force-displacement relationship gives the coupling stiffness of the slab, from which the effective width of the slab may be calculated from equation (3.3a) or (3.3b).

3.3 ELEMENT EVALUATION

Various plate bending elements which have been successfully developed can be used in the finite element analysis of the floor slab. The performance of an element, as measured by the accuracy of results obtainable with a particular computational effort, however, varies from element to element depending on the sophistication of the element formulation and on the type of slab problem being solved. Since a comprehensive parameter study of floor slabs coupling shear walls requires an extensive use of finite element analysis, it is necessary to select from the vast repetoire of elements available an efficient

element for implementation to ensure that results can be obtained to an acceptable level of accuracy with minimal computational effort. The relative performance of various elements is evaluated to assist in the selection of the best element for the parameter study.

3.3.1 STANDARD CONVERGENCE RESULTS

The relative efficiency of various elements has often been evaluated on the basis of convergence results for a test problem involving a simply supported or clamped plate under uniform or central point loading. Fig. 3.5, (a) and (b), show the comparison of convergence results obtained by a number of elements described in the literature.[26,41] The elements compared have been designated with the numerals indicating the total number of degrees of freedom for the element. TB18 and RB24 are higher order or refined triangular and rectangular elements proposed respectively by Bell[32] and Wegmuller.[31] These two elements contain curvature terms in their nodal degrees of freedom. QB16 and QB19 are conforming or compatible quadrilateral elements assembled from triangular sub-elements and have been developed respectively by Veubeke[34] and by Clough and Felippa.[42] HCT9 and RB16 are compatible triangular and rectangular elements developed respectively by Hsieh, Clough and Tocher[43] and by Bogner, Fox and Schmidt,[8] while TB9 and RB12 are incompatible triangular and rectangular elements described by Zienkiewicz and Cheung.[45,30] The convergence results obtained by the various elements have been compared on the basis of equal numbers of rectangular divisions of the half edge for the plate. The results for elements TB18 and RB24 for the case of the clamped plate have been obtained by the author as these could not be found in the literature available to the author. The rest of the results have been reproduced from various published sources.

It is seen from the comparison of convergence results that generally the more sophisticated elements give the

better results in both cases of simply and clamped plates. The results obtained by the refined triangular and rectangular elements TB18 and RB24 and by the compatible rectangular element RB16 are remarkably accurate even with a very coarse mesh division. The results obtained by the quadrilateral elements QB16 and QB19 are less accurate than the results obtained by the first three elements but are more accurate than the results obtained by the three simpler elements, HCT9, TB9 and RB12. QB16 appears to give better results, compared to QB19. The results obtained by the compatible triangular element HCT9 are worst in both cases.

3.3.2 CONVERGENCE RESULTS FOR COUPLING SLAB PROBLEM

The choice of a suitable element to be used for the parameter study of the coupling slab could apparently be made on the basis of the convergence results just discussed. However it is recognised that the same order of performance indicated for the various elements under the ideal conditions of the test problem may not necessarily be reproduced in more complex situations. It appears logical to base the selection of the desirable element on the element performance under similar conditions associated with the actual parameter study. Towards this end, five of the more attractive elements, viz. TB18, RB24, QB16, TB9 and RB12 are selected for evaluation of their relative performance in the slab coupling problem. The computer programs for the implementation of the first four elements were written by the author. The program for the last element was modified from a finite element program suite in the Department of Civil Engineering, Strathclyde University.

Two typical cases of slab coupling have been considered for the element evaluation. In the first case, the slab couples plane walls, and in the second case it couples flanged (T-shaped) walls. The four patterns of mesh division of the slab for convergence study are shown in

Fig. 3.6. The mesh refinement adopted follows a monotonic sequence. The mesh for the triangular elements is obtained by sub-dividing the rectangular mesh along a diagonal. The walls were assumed to be of zero thickness in the discretisation of the slab. Due to double symmetry of the problem, only a quarter of the slab panel was considered in the analysis.

The numerical results for the effective width Y_e/Y obtained by the various elements are shown graphically in Fig. 3.5, (c) and (d). The rectangular mesh division along the shorter side of the slab quadrant has been used as the common base for comparing the results obtained by various elements so that the presentation is consistent with that for the square plate problem.

When discussing relative accuracies of various finite element solutions, the 'exact' theoretical solution should be available as a reference datum for comparing various results. Unlike the case of a square plate, an 'exact' solution for the present problem of a coupling slab does not exist. However, the 'true' result may be extrapolated from the sets of finite element approximations using Richardson's extrapolation[46] provided the nature of the approximation error is known.

The principal error in the finite element solution arises from the discretisation process. For the Adini-Clough-Melosh rectangular element (RB12) under uniformly distributed loading, Waltz et al.[47] have shown that the principal discretisation error in deflections is of order h^2 and errors in slopes are of order h^4 where h is the characteristic mesh length. Ramstad[33] has applied the Richardson h^2-extrapolation to the case of a simply supported square plate under uniform loading and obtained remarkably accurate and consistent 'true' values of deflections and stresses, by extrapolating between any two sets of finite element results obtained for various mesh sizes of this particular element.

For the slab coupling problem, the h^2-extrapolation

failed to give a consistent value of the effective width Y_e/Y when different mesh combinations were tried for each of the element type. This is not too surprising since the distributed loading which is essential for the type of error approximation assumed in the h^2-extrapolation is not involved in the present situation. When the discretisation error in the calculation of Y_e/Y for the coupling slab problem was assumed to be of order h and the Richardson (h, h^2)-extrapolation (Appendix A3.1) was used, very consistent 'true' values of Y_e/Y were obtained by extrapolating between any three mesh combinations for each element type. The extrapolated 'true' values of Y_e/Y based on (2,4,8) mesh combinations are shown in the last comumns of Tables 3.1, (a) and (b), for the plane wall and flanged wall cases. The discrepancy between the highest and lowest extrapolated 'true' value of Y_e/Y does not exceed 0.2% for the plane wall configuration and 0.35% for the flanged wall configuration. The mean extrapolated 'true' values of Y_e/Y for both cases have been marked in Fig. 3.5, (a) and (b), to give a better indication of the accuracy and convergence of the various elements. The extrapolated values in both cases are seen to be consistent with the graphical trend of results, providing a further indication of the validity of the method of extrapolation adopted.

3.3.3 DISCUSSION OF CONVERGENCE RESULTS

The results of this convergence study indicate a number of interesting points. Contrary to expectation, the results obtained by both the refined elements TB18 and RB24 are rather poor compared to the results obtained by the simpler elements. The accuracy of results obtained by the two simplest incompatible elements TB9 and RB12, even with the coarsest mesh, is remarkable. There appears to be little difference between the performance of elements TB9 and RB12, both of which gave the best results in each case. The results obtained by the quadrilateral element QB16 are nearly as accurate as that obtained by TB9 or RB12 for the

case of flanged walls, but for the case of plane walls, the results of QB16 are substantially less accurate than the results of TB9 or RB12. The trend of results indicating improved element performance with sophistication in element formulation, shown by the standard square plate convergence study, appears to be completely reversed in this convergence study on a coupling slab. The results obtained by the various elements converge to the 'true' values of Y_e/Y for each case from above.

Another desirable characteristic to be evaluated for the different elements is their relative efficiency in terms of computer time required for the analysis. Tables 3.2, (a) and (b), show the computing times in seconds, clocked for the various operations in the finite-element program-runs on the ICL 1904S computer, for the plane wall problem with mesh 3 and mesh 4 discretisations. The superiority of the simple elements over the refined elements is even more striking in this comparison. The refined elements TB18 and RB24 both take more than five times the amount of total computing time required by their simpler counterparts TB9 and RB12. The break down of the total run-times indicates that the refined elements, when compared with the simple elements, consume a very large amount of computer time in the element stiffness matrix generation and in the solution of the equilibrium equations. The quadrilateral element QB16 takes nearly three times more total computing time than the rectangular element RB12, which is marginally more efficient than the triangular element TB9. The higher time clocked by QB16 arises from the solution of a larger number of equilibrium equations compared to RB12.

The convergence study indicates that among the five bending elements considered, the two simplest elements RB12 and TB9 are the better elements to be used for the study of slabs coupling shear walls. The triangular element TB9 is seen to be marginally less efficient than the rectangular element RB12 in terms of convergence and

computing time. In stress calculations, TB9 is generally less accurate than RB12 due to lower order of displacement function assumed in its formulation. Other considerations in favour of RB12 include the simple data preparation for the computer run, as well as the ease with which this element could be combined with a satisfactory plane-stress element to form a spatial or flat shell element suitable for use in the study of local elastic deformation effects in shear walls coupled by the floor slab.

3.4 PLANAR WALL CONFIGURATION

The planar wall configuration, consisting of a pair of plane walls coupled in-plane by the floor slab, is most commonly encountered in cross-wall buildings built on the double loaded corridor scheme. Common architectural layouts result in building depths of 12 to 18 m (40 to 60 ft) and bay sizes of 3 to 9 m (10 to 30 ft). Wall thicknesses range from 150 to 380 mm (6 to 15 in.) and floor depths from 140 to 250 mm ($5\frac{1}{2}$ to 10 in.). In certain layouts, the floor slab extends beyond the facade line. The slab overhang in most cases is unlikely to exceed about 2 m (6 ft).

The factors which have an influence on the effective width of the coupling slab have, in previous theoretical and experimental studies, been identified as the overhang width C, the wall length W, the wall opening or corridor width L, the slab width Y and the wall thickness h. Although the influence of these factors have been examined theoretically by the finite difference[2-4] and finite element[5,6] methods, a similar study using the finite element method is conducted as a part of a more extensive programme of investigation into various aspects of shear wall-slab interaction. Since Qadeer's results[2] differ considerably (in some cases up to 30% difference) from the results obtained by Black et al.,[6] the results obtained from the present study could serve as a check on the reliability of previous results.

Following the method of analysis outlined in Section 3.2.3, results have been obtained showing the influence of various parameters on the coupling stiffness or effective width of slab for an interior bay bounded by lines of symmetry located mid-way between wall assemblies. The finite element analyses were performed using mesh patterns with between 88 and 104 element sub-divisions, depending on the slab geometry. As indicated by the convergence results described in Section 3.3.2, the mesh patterns adopted should yield relatively accurate results. A typical mesh pattern adopted has been shown in Fig. 3.4. Although the final results are expressed in non-dimensional forms to be of general application, in the parameter study, a slab thickness of 228.6 mm (9 in.) was assumed throughout. The slab panel length (a building depth) was generally taken as 15.25 m (50 ft), with other dimensions varied as required for parameter study. Young's modulus and Poisson's ratio for concrete were assumed as 2.07×10^7 kN/m^2 (4.32×10^5 kip/ft^2) and 0.15 respectively. The numerical results obtained are discussed in the following sections.

3.4.1 NUMERICAL RESULTS FOR EFFECTIVE WIDTH

3.4.1.1 Effect of Slab Overhang

Values of slab stiffness factor K and effective width Y_e/Y obtained from the finite element analyses are shown in Table 3.3(a) for slabs having a fixed aspect ratio Y/X of 0.4 and in Table 3.3(b) for slabs having a fixed wall-opening ratio L/X of 0.6. It is seen from the results that increasing the overhang ratio for a slab increases marginally the slab's coupling stiffness. This effect is relatively more significant for slabs with larger values of the ratios L/X and Y/X. Nevertheless, the influence of slab overhang is generally so small that for practical purpose it may be neglected. Neglecting the effects of the ratio C/X in the worst case examined (L/X = 0.6, Y/X = 0.8), is seen to result in an underestimation of the

slab stiffness of less than 5%.

The general trend of results obtained appears consistent with Qadeer's[2] and El-Hag's[40] results. In view of its insignificant influence, the slab overhang is disregarded in further investigations of slab-wall coupling.

3.4.1.2 Effect of Wall Length

In examining the influence of wall length on the effective coupling by the floor slab, two of the other variables, namely, the wall opening L and the slab width Y, are kept constant while the wall length W is varied. As a result of varying W, the floor length X is varied accordingly. Since the rotational stiffness of the equivalent beam, as defined, is affected directly by the change in the lever arm distance between wall centres as the wall length is varied, the results for the stiffness factor K will not give a clear picture of the actual influence of wall length on the effective coupling slab width. Therefore in order to assess more succinctly the influence of wall length, reference is made only to the results obtained for the effective width Y_e/Y.

The variation of Y_e/Y with the ratio of wall length to wall opening, W/L, is shown in Fig. 3.7 for the two ratios L/Y examined. The trend of results is seen to be very similar for both cases, for L/Y = 0.5 and L/Y = 1.5. The effective width increases with the increase in wall length. The variation of Y_e/Y is rapid for W/L less than 0.3 but becomes insignificant when W/L is larger than 0.5. Since in practical cross-wall structures W/L is unlikely to be less than 0.5, it appears that in most cases the effect of variation in wall length may be disregarded in the evaluation of effective slab width, as long as the influence of the ratio L/Y is considered. Similarly, the effect of dissimilar wall lengths in a pair of coupled walls may also be disregarded if the ratio of the shorter wall length to the wall opening is greater than 0.5.

3.4.1.3 Effect of Slab Width

To illustrate the influence of slab width more clearly, the effective width Y_e and the slab width Y are normalised with respect to the standard panel length X. Fig. 3.8 shows graphically the variation of Y_e/X as a function of Y/X for various wall opening ratios L/X. The effective width is seen to increase with the slab width, as expected, since a wider slab should provide a greater restraint than a narrower slab against bending induced by the coupled walls. The influence of slab width is strongly felt when the slab width Y/X is smaller than the wall opening width L/X (i.e. when $Y/L < 1$), but when Y/X is larger than L/X the influence of slab width diminishes rapidly. Increasing the slab width beyond a value of three times the wall opening width appears to have practically no effect on the effective slab width for a particular wall opening width.

3.4.1.4 Effect of Wall-Opening Width

The results discussed in the preceding section are re-plotted in Fig. 3.9 to show the variation of effective width Y_e/X as a function of the wall opening width L/X for various slab widths Y/X. By comparing Fig. 3.9 with Fig. 3.8, it becomes immediately obvious that the two sets of curves are practically similar for the range of variables considered. The influence of L/X on Y_e/X for a particular value of Y/X is seen to be practically identical to the influence of Y/X on Y_e/X for the same value of L/X. This reciprocal influence of L and Y can also be noted by referring to the numerical results in Table 3.4, which show that the values of L and Y may be interchanged without affecting practically the effective width Y_e (c.f. Note the symmetry of the tabulated results about the diagonal L/Y = 1). This interesting reciprocal relationship between L and Y will be exploited in the presentation of simple design curves and empirical equations in a later section (3.4.1.7).

3.4.1.5 Design Curves for Effective Width

To enable the rapid calculation of effective widths to be achieved, curves are presented in Fig. 3.10(a) showing the variation of effective width Y_e/Y as a function of wall opening ratio L/X for various slab aspect ratios Y/X. The numerical results from which the curves have been drawn are given in Appendix A3.2 for further reference. The results presented have been obtained assuming zero wall thickness in the analysis. The finite wall thickness in actual structures will influence the stiffness and effective width of the slab to an extent depending on the relative wall and slab dimensions. For relatively thin walls, the effective slab widths obtained from the curves in Fig. 3.10(a) should prove sufficiently accurate for practical purpose. For walls with appreciable thickness, the effective slab widths can still be evaluated satisfactorily from the same set of curves, with certain modifications, as will be shown in a subsequent section (3.4.1.9).

The curves account for the influence of slab width, wall opening width and wall length. The curves for various slab aspect ratios Y/X have been spaced at rather close intervals to facilitate accurate visual interpolation where necessary when the actual value of Y/X for the particular problem falls between any two curves. However, interpolation between curves is not strictly necessary. As shown in Section 3.4.1.2, the influence of variations in wall length can practically be disregarded when the wall length ratio W/L is larger than 0.5, or, alternatively, when L/X is less than 0.5. Therefore the value of the slab length X for the particular problem can be arbitrarily adjusted so that the new value of Y/X corresponds to the value for the nearest curve, and the correct effective width Y_e/Y is given by this curve at the new value of L/X.

The effective width values have been evaluated assuming a value of Poisson's ratio of 0.15 for concrete.

The slab stiffness factor K is not sensitive to small differences in values of Poisson's ratio. The effective width Y_e/Y is however influenced by the value of ν as can be seen from equations (3.3a) and (3.3b). If desired, the value of Y_e/Y obtained from the design curves may be approximately corrected for the actual value of ν by multiplying by a factor $(1 - 0.15^2)/(1 - \nu^2)$.

3.4.1.6 Generalised Design Curve for Effective Width

Although the presentation of design curves in the usual form shown in Fig. 3.10(a) already allows a fairly rapid evaluation of the effective width for any practical floor slab coupling a pair of plane walls, it is possible to simplify further the presentation of design information to allow an even more rapid evaluation of the effective width. As was first suggested by Michael[48] and is shown by the results in Section 3.4.1.4, the effective width Y_e/Y is essentially a function of the wall-opening to slab-width ratio L/Y only. The series of design curves presented in Fig. 3.10(a) can therefore be approximated by a single generalised curve of Y_e/Y versus L/Y as shown in Fig. 3.11(a). This generalised curve is fairly accurate for practical purpose. With slab and wall proportions such that $(L/X + Y/X) \leq 1$, which covers most practical cases, values of Y_e/Y obtained by the generalised curve and by the more accurate series of design curves are practically identical. For such cases the generalised curve should prove more convenient to use than the previous series of curves. In exceptional cases where $(L/X + Y/X) > 1$ and L/X is also larger than 0.4, the effective widths Y_e/Y evaluated by the generalised curve are overestimated, generally by less than 10%. For such cases, if a more accurate estimate of Y_e/Y is required, this could be obtained from the more accurate series of design curves in Fig. 3.10(a).

3.4.1.7 Empirical Design Equation for Effective Width

The generalised design curve in Fig. 3.11(a) can be separated into two distinct sections defined by the limits $0 \leq L/Y \leq 1$ and $1 \leq L/Y \leq \infty$. Values of Y_e/Y given by the second section of the generalised curve, which may be termed the reciprocal section, can in fact be obtained from the first section of the generalised curve, which may be termed the normal section, by making use of the reciprocal relationship between L and Y. As shown by the numerical results discussed in Section 3.4.1.4, values of L and Y may be interchanged without sensibly affecting the value of Y_e for the slab. Therefore when the ratio L/Y exceeds unity, the reciprocal of this ratio can be used to evaluate the effective width ratio Y_e/L for the reciprocal section, from the normal section of the generalised curve. If the normal section of the curve is represented by the equation $Y_e/Y = F(L/Y)$, where F denotes a function, the reciprocal section will be represented correspondingly by $Y_e/L = F(Y/L)$.

The normal section of the curve can be represented to an acceptable level of accuracy by the simple empirical relationship,

$$\frac{Y_e}{Y} = \frac{L}{Y}\left(1 - 0.4\,\frac{L}{Y}\right) , \quad 0 \leq \frac{L}{Y} \leq 1 \qquad (3.4)$$

The reciprocal section is then represented, simply by interchanging L and Y, by the equation

$$\frac{Y_e}{L} = \frac{Y}{L}\left(1 - 0.4\,\frac{Y}{L}\right), \quad 0 \leq \frac{Y}{L} \leq 1 \qquad (3.5)$$

Multiplying equation (3.5) by $\frac{L}{Y}$, the reciprocal equation becomes simply

$$\frac{Y_e}{Y} = 1 - 0.4\left(\frac{L}{Y}\right)^{-1} , \quad 1 \leq \frac{L}{Y} \leq \infty \qquad (3.6)$$

Equations (3.4) and (3.6) now represent the generalised design curve over the complete range

$0 \leq L/Y \leq \infty$. The value of Y_e/Y given by the reciprocal equation approaches unity when L/Y becomes infinitely large. This is consistent with the fact that a long narrow strip of slab will behave essentially as a beam.

In order to illustrate the accuracy of the empirical representation of the generalised design curve, the empirical curve given by equations (3.4) and (3.6) is compared with the generalised design curve in Fig. 3.11(b). It can be seen that the empirical curve gives an almost perfect fit to the generalised design curve. By comparing numerical values of Y_e/Y obtained by the empirical equations with the corresponding accurate values taken from Appendix A3.2 discrepancies are seen to be generally less than 4% for the range of L/Y from 0.1 to 6.0 which is covered by the finite element results.

3.4.1.8 Effect of Finite Wall Thickness

Fig. 3.12, (a) and (b), show the variation of effective width Y_e/Y as a function of wall thickness ratio h/Y for a range of wall opening ratios L/X and slab aspect ratios Y/X. The numerical results from which the curves have been drawn are given in Appendix A3.3 for further reference.

It is seen from the curves of Y_e/Y that the thickness of the wall has a considerable stiffening effect on the slab. For the range of h/Y less than 0.5, Y_e/Y increases almost linearly with the increase in h/Y. The influence of wall thickness is seen to be relatively more significant with smaller wall opening ratios L/X. With slabs in which the wall opening is small compared to the slab width ($L/Y < 1/4$), an increase in the wall thickness produces an equal increase in the effective width generally when h/Y is less than 0.5.

The results presented in this Section are also applicable to the case of coupled box-cores without openings on the inner edges, since the displacements imposed on the slab by a thick solid wall and by a box-core of the same

peripheral dimensions are identical.

3.4.1.9 Empirical Method to Account for Influence of Wall Thickness

It has been suggested by Michael[48] that the influence of wall thickness may be accounted for simply by including an additional slab width equal to the wall thickness in the effective width calculated for zero wall thickness. This simple procedure is seen to be valid generally for $L/Y < 1/4$ and $h/Y < 1/2$. With larger ratios of L/Y, this procedure overestimates the stiffening effect of the wall thickness considerably when the walls are thick in relation to the slab width. A more general procedure is suggested here to account for the influence of wall thickness in the evaluation of effective width. As illustrated in Fig. 3.13 (below), the slab of width Y coupling a pair of walls with wall thickness h is assumed to be made up of an effective wall strip of width h and a reduced slab panel of width $Y' = (Y-h)$ coupling a pair of walls of zero thickness. The effective width Y_e' is obtained for the reduced slab panel and the effective wall strip is added to give the effective width Y_e for the actual slab.

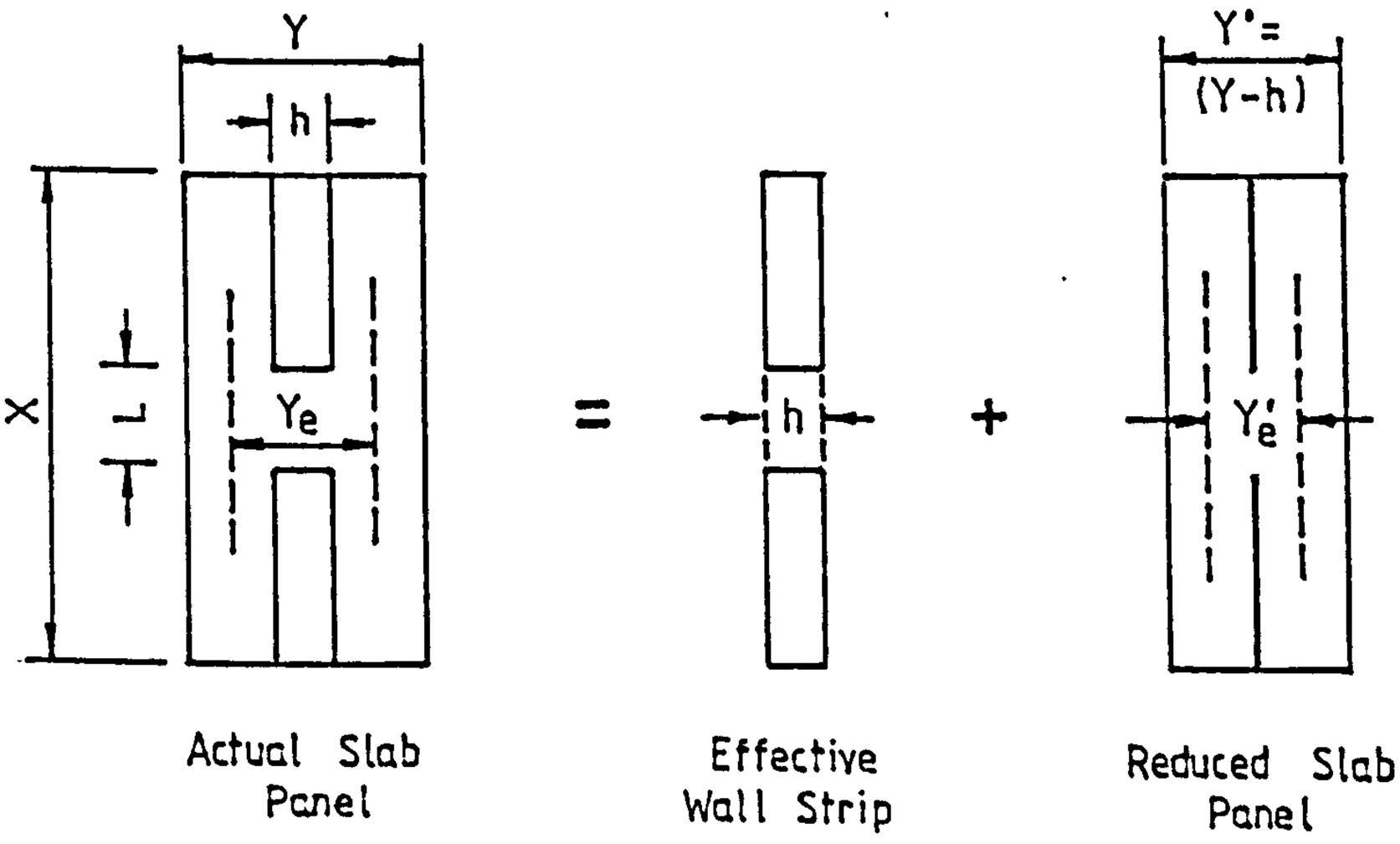

Fig. 3.13

3.4.1.9.1 Numerical Examples

In order to illustrate the application of the suggested empirical method and to indicate the relative accuracy of the approximation, two numerical examples are considered.

Example No. 1:

It is required to evaluate the effective width of a slab of aspect ratio Y/X = 0.4 coupling a pair of thick walls with thickness ratio h/Y = 0.5 and wall opening ratio L/X = 0.4.

The reduced slab width Y'/Y	= 1-h/Y	= 0.5
The reduced span/width ratio L/Y'	= 0.4/(0.4x0.5)	= 2.0
From the generalised design curve in Fig.3.11(a),		
	Y_e'/Y'	= 0.79
$\therefore$ The effective width Y_e'/Y	= 0.79 x 0.5	= 0.395
The effective wall strip h/Y		= 0.500
$\therefore$ The total effective width $Y_e/Y = Y_e'/Y + h/Y$		= 0.895

Comparing this value with the accurate value of 0.911 from Appendix A3.3, the relative error is seen to be -1.8%. Using Michael's procedure the effective width Y_e/Y would be evaluated as 0.61 + 0.5 = 1.11 which is 22% in error.

Example No. 2:

The relative proportions of the slab and wall for this example are Y/X = 0.4, L/X = 0.2, h/Y = 0.125.

The reduced slab width Y'/Y	= 1 - 0.125	= 0.875
The reduced span/width ratio L/Y'	= 0.2/(0.4x0.875)	= 0.57
From Fig. 3.11(a) the effective width Y_e'/Y'		= 0.43
$\therefore$ The effective width Y_e'/Y	= 0.43 x 0.875	= 0.376
The effective wall strip h/Y		= 0.125
$\therefore$ The total effective width Y_e/Y		= 0.501

Comparing this value with the accurate value of 0.507 given in Appendix A3.3 the relative error is seen to be -1.2%. Using Michael's procedure the effective width Y_e/Y would be evaluated as 0.39 + 0.125 = 0.515 which is +1.6% in error.

It is seen from the worked examples that results obtained by the suggested method are accurate to within 2% in both cases. Although only two examples are shown in this Section, the range of variables covered in the examples is sufficiently wide to provide a convincing check on the general accuracy of the suggested method.

3.4.1.10 Empirical Design Equations which Account for Finite Wall Thickness

The empirical equations (3.4) and (3.6) representing the generalised design curves for evaluating the effective widths Y_e/Y for slabs with walls of zero thickness may be modified to include the influence of finite wall thickness. In accordance with the simple procedure suggested to account for the influence of finite wall thickness, the effective width Y_e of the actual slab panel may be considered as being made up of an effective wall strip of width h plus the effective width Y_e' of a reduced slab panel of width Y', the effective width Y_e/Y can then be expressed as

$$\frac{Y_e}{Y} = \frac{h}{Y} + \frac{Y'}{Y}\left(\frac{Y_e'}{Y'}\right) \qquad (3.7)$$

The effective width Y_e'/Y' of the reduced slab panel may be represented by the empirical equations (3.4) and (3.6) with Y_e' and Y' in place of Y_e and Y respectively. Therefore equation (3.7) may be written as

$$\frac{Y_e}{Y} = \frac{h}{Y} + \frac{Y'}{Y} \cdot \frac{L}{Y'}\left[1 - 0.4\,\frac{L}{Y'}\right] \qquad 0 \le \frac{L}{Y'} \le 1 \qquad (3.8)$$

$$\text{and} \quad \frac{Y_e}{Y} = \frac{h}{Y} + \frac{Y'}{Y}\left[1 - 0.4\left(\frac{L}{Y'}\right)^{-1}\right] \qquad 1 \le \frac{L}{Y'} \le \infty \qquad (3.9)$$

In order to demonstrate the accuracy of the empirical equations, values of Y_e/Y obtained by the empirical equations and by the finite element method (Results in Appendix A3.3) are compared for a slab of aspect ratio Y/X = 0.4, with various wall thickness ratios h/Y and two

wall opening ratios L/X of 0.1 and 0.4, in Table 3.5 which also shows the relevant quantities Y'/Y and L/Y' required in the empirical equations. The results obtained by the simple empirical equations are seen to have been evaluated to within 3% of the accurate finite element results for walls of finite thickness. The results being compared cover a wide range of ratios L/X and h/Y. The general accuracy of the empirical equations however is unaffected by the range of variables considered.

3.4.1.11 End-Bay Results

The end bay occurs at the two gable ends of the building block where the gable walls are coupled by the floor slab on one side of the wall only (Fig. 3.2(a)). With the asymmetric coupling of the slab, gable walls will generally undergo some out-of-plane bending which will affect the coupling stiffness of the slab to some extent depending on the wall stiffness. The edge of the slab across the wall opening is free. Since the gable edge of the slab is less restrained against transverse rotation than a continuous edge, the coupling stiffness of the end-bay slab can be expected to be less than half the stiffness of the internal-bay slab.

In evaluating the coupling stiffness and effective width of the end-bay slab, two cases of wall stiffness are considered. The first case assumes that the gable walls are so stiff that they do not bend out-of-plane. The second case considers the finite stiffness of a wall of 304.8 mm (12 in.) thickness. The flexural stiffness of the wall is incorporated in the finite element analysis as a rotational spring stiffness for each wall node. In the discretisation of the slab, the wall connection is, as usual, represented as a line connection.

The numerical results for the effective width Y_e/Y for end bays of various proportions are shown in Table 3.6. It is seen from the results that the assumption of infinitely stiff walls overestimates the effective width of the slab, but in the worst case considered (L/X = 0.1

and Y/X = 0.2) the effective width is overestimated by only about 7%. It appears that for practical purpose the out-of-plane flexibility of the gable walls could be disregarded in the calculation of effective width or stiffness of the end-bay slab. The effective width for the case of rigid gable walls have been plotted in Fig. 3.10(b) as design curves. Comparing the results for an end bay and an interior bay, it is seen that the effective width for an end bay varies between 44% and 47% of the effective width for an interior bay, depending on the configuration. The corresponding figure obtained by Qadeer and Smith[2] was 42%. As a convenient rule, the effective width for the end bay may be assumed as 45% of the effective width for the interior bay.

3.4.2 NUMERICAL RESULTS FOR STRESS RESULTANTS

3.4.2.1 General Distribution Pattern

Fig. 3.14, (a) to (e), show in perspective the general distribution of bending and twisting moments and shearing forces in a typical quadrant of a slab coupling a pair of plane walls of zero thickness undergoing unit rotation as shown in Fig. 3.14(f). The coupling action of the slab results in a distribution of stress resultants with large variations in values throughout the slab. Very large moments and shears are induced in the slab around the coupled end of the wall, but away from this critical region, the stress resultants diminish rapidly in both the longitudinal (x) and transverse (y) directions. The significant coupling actions are induced mainly in the corridor area. The portion of the slab some distance away from the corridor remains practically unstressed, or unaffected by the coupling action. This explains why an increase in wall length beyond a certain range does not affect significantly the coupling stiffness of the slab (Section 3.4.1.2).

3.4.2.2 Problem of Singular Stress Resultants

The presence of severe stress concentrations calls for careful interpretation of calculated critical stress-resultant values. If the calculated stress-resultant values are to be used directly for the design of the slab section, it is obviously necessary to ensure that the calculated peak stress-resultants are theoretically finite and have been evaluated with sufficient accuracy in the numerical solution of the slab problem. The results of the convergence study reported in Section 3.3.2 are therefore re-examined with particular attention to the convergence of calculated critical stress resultants around the coupled end of the wall in the slab.

Fig. 3.15(a) shows quantitatively the variations of bending moment M_x along a critical transverse slab section passing through the inner edge of the wall which have been evaluated using various element mesh-division of the slab. The results were obtained with the element RB12 which has been used throughout the parameter study. It can be seen from the comparison of various results that whereas values of M_x calculated at other points converge to definite finite values, the bending moment calculated at the tip of wall diverges with mesh refinement. It may be concluded from the calculation of extremely large and divergent bending moment values that a theoretical stress singularity exists in the slab at the coupled end of the wall. The presence of the stress singularity in the coupling slab may also be inferred from the results of various investigations into similar mixed boundary-value plate-bending problems such as bending of cracked plates[49], plates partially supported along an edge[50] or plates with an internal line support[51], which show that the bending moments and shearing forces become singular, or theoretically infinite, at the point where there is an abrupt change of boundary conditions.

The finite width of the wall has not been represented in the discretisation of the slab on which the convergence results are based. With the finite width of the wall

correctly represented, the results of a convergence study, though they are not shown here, indicate that large divergent stress resultants now are obtained in the slab at the corners of the coupled wall-end. That the stress resultants at these points are singular can again be inferred from analytical results for similar problems such as the bending of a slab supported by a rigid column of finite width[22], or the bending of a slab with a rectangular opening.[52]

It should be obvious from the results of various other mathematically similar 'singular' plate problems that the singular stress resultants are predicted in the slab at the coupled end (corners) of the wall as a consequence of the use of thin-plate theory and boundary conditions associated with an infinitely rigid wall-support for the solution of the problem. Since the stress resultants in the coupling slab at the singular points are theoretically unbounded, any finite stress-resultant values furnished at these points by a numerical solution based on thin-plate theory must be considered incorrect or meaningless. Previous investigators[3,4] who used the finite difference technique to study the coupling slab actions have not commented on this important fact, and have presented finite stress-resultant values which were supposed to be correct at the theoretically singular points.

3.4.2.3 Interpretation of Results at the Singular Points

The problem of stress singularity and the apparent difficulty of obtaining meaningful results at the singular points in the coupling slab are not of great practical consequence, for while the stress concentration in slabs may be a physical reality, the existence of infinite stresses at a point is obviously a mathematical fiction. The infinitely large stresses predicted in the coupling slab, in practice, will be limited by local elastic deformation, material yielding or stress redistribution in the critically stressed areas in the wall and slab. It is therefore more

practical to consider the net distributed forces in a finite slab strip, rather than the extremely large stresses at a point, as a basis for the design of the slab section. With this approach to slab design, it is possible to interpret more meaningfully the finite element results for stress resultants in the critical region.

It has been mentioned that the peak critical longitudinal bending moment M_x in the coupling slab evaluated in the finite element analysis has no apparent meaning. This is so only if the calculated peak bending-moment stress-resultant is considered by itself. However, when considered together with calculated bending-moment stress-resultant values at other points along a transverse section, it gives a correct statical balance between the integrated internal bending moment and the external applied moment at the section. The integrated bending moment evaluated in the critical zone using calculated bending-moment stress-resultant values is therefore correct although the peak stress-resultant value by itself is not. The calculated peak bending moment M_x at the critical node should therefore only be used in conjunction with the calculated bending-moment value at the adjacent node to give an estimate of the net bending moment distributed in the critical strip bounded by the nodes.

The peak critical transverse bending moment M_y is also evaluated in the finite element analysis as a finite value which provides equilibrium between the internal transverse bending moment and the external bending moment, at the critical longitudinal slab section, and should therefore be interpreted in the same manner as that suggested for the critical bending moment M_x.

3.4.2.4 Calculation of Stress-Resultant Factors

The coupling-slab stress resultants calculated for the arbitrary unit wall displacements assumed in the slab analysis may be expressed in the form of non-dimensional stress-resultant factors to facilitate the calculation of

stress resultants due to any other wall displacements. These factors define the coupling stress resultants in a slab of unit corridor (or wall-opening) width L and unit flexural rigidity D, induced either by a unit relative wall rotation Ø at the coupled wall end or by a unit relative axial wall displacement δ (Fig. 3.16). If M_i and Q_i represent respectively the calculated bending moments and shearing forces in the slab analysis, then the stress-resultant factors $\bar{M}_i$ and $\bar{Q}_i$ are given by

$$\bar{M}_i = \frac{M_i}{D}\frac{L}{\text{Ø}} \quad \text{and} \quad \bar{Q}_i = \frac{Q_i}{D}\frac{L^2}{\text{Ø}} \tag{3.10a}$$

or $$\bar{M}_i = \frac{M_i}{D}\frac{L^2}{\delta} \quad \text{and} \quad \bar{Q}_i = \frac{Q_i}{D}\frac{L^3}{\delta} \tag{3.10b}$$

Fig. 3.16

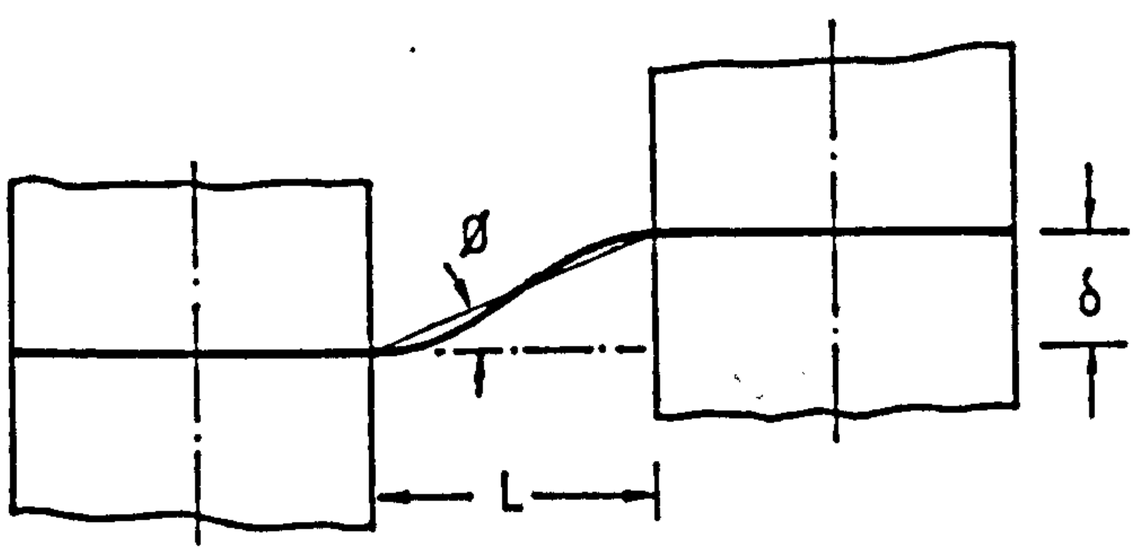

The stress-resultant factors may be expressed in a form involving the effective width Y_e and the wall reaction or lintel shear Q. It can be shown that for the equivalent beam,

$$\text{Ø} = \frac{Q\,L^2}{12(1-\nu^2)D\,Y_e}$$

Therefore the stress-resultant factors may be expressed as

$$\bar{M}_i = \frac{12(1-\nu^2)Y_e}{Q\ L}\cdot M_i \quad \text{and} \quad \bar{Q}_i = \frac{12(1-\nu^2)Y_e}{Q}\cdot Q_i \tag{3.11}$$

Observing that $QL/(2Y_e)$ and Q/Y_e represent respectively the maximum average bending moment M_a and

the average shearing force Q_a in the equivalent beam, expressions (3.11) may be re-written as

$$\bar{M}_i = 6(1-\nu^2)\frac{M_i}{M_a} \quad \text{and} \quad \bar{Q}_i = 12(1-\nu^2)\frac{Q_i}{Q_a} \qquad (3.12)$$

It is seen from expressions (3.11) and (3.12) that once the stress-resultant factors $\bar{M}_i$ and $\bar{Q}_i$ for the slab are known, the actual stress resultants (M_x, Q_x, etc.) produced by the system of forces calculated in a coupled wall analysis may be easily determined. In the slab-coupled wall analysis using the continuous connection technique, for instance, the lintel shear Q is calculated directly from established equations or design curves.[53] The slab stress resultants, M_x and Q_x, for instance, can then be easily calculated using expression (3.11) thus,

$$M_x = \frac{Q\,L}{12(1-\nu^2)Y_e} \cdot \bar{M}_x \quad \text{and} \quad Q_x = \frac{Q}{12(1-\nu^2)Y_e} \cdot \bar{Q}_x \qquad (3.13)$$

3.4.2.5 Design Stress-Resultant Contour-Diagrams

In Section 3.4.1.2 it was shown that provided the wall length to wall opening ratio W/L is greater than 0.5 the effective slab width is practically unaffected by variations in wall length. Considering the form of distribution of stress resultants in the slab discussed in Section (3.4.2.1), it is obvious that the stress-resultant factors which are of significant values are likewise unaffected by variations in wall length. Therefore, when evaluating stress-resultant factors for practical coupling-slabs it is necessary to consider only the influence of the wall-opening to slab-width ratio L/Y.

Fig. 3.17 to 3.21 show the contours of bending-moment factors $\bar{M}_x$ and $\bar{M}_y$ for slabs with practical ratios Y/L ranging from 1 to 4 and with a wall thickness ratio h/L of 0.1. The contours in each diagram are shown over a typical quadrant of the slab, and these have been reproduced from the computer plots of the finite element results

obtained with a very fine mesh in the region of stress concentration (Fig. 3.22). The contours of stress-resultant factors allow a rapid and accurate evaluation of bending moments M_x and M_y at any point on the slab, induced by any coupled-wall action, and may be used during the final design stage for the design or detailing of the slab reinforcement.

In all the contour diagrams, the stress-resultant value at the critical wall corner has been indicated. Since the stress resultant at this point is theoretically infinite, the value indicated in each diagram should be interpreted in the manner described in Section 3.4.2.3. In measuring off distances to the respective contours, it should be noted, from the definition of stress-resultant factors, that the wall-opening width L is represented as a unit distance in the contour diagrams.

3.4.2.6 Generalised Curve For Critical Bending Moments

In the early stages of design or feasibility study of the structural system it is the stresses at critical slab sections which are of immediate interest to the designer who is required to establish fairly quickly realistic member sizes for the structure. A knowledge of the approximate variation of longitudinal bending moment M_x at a critical transverse slab section is usually sufficient to allow the adequacy of the chosen slab thickness to be established.

Fig. 3.23 shows, for slabs of various normalised widths Y/L, the variation of bending-moment factor $\bar{M}_x$ along the critical transverse slab section through the inner edge of the plane wall (zero thickness). It can be seen from the curves for various ratios of Y/L that the variation of $\bar{M}_x$ within a distance given approximately by y/L = 0.25 from the wall is practically unaffected by variations in the slab width. Outside this critical region, the variation of $\bar{M}_x$ is influenced by the slab width but the bending-moment factors are so small compared to values in the critical region that the influence of

slab width becomes of little practical significance. For practical purposes, the bending-moment curves for various ratios of Y/L may be approximated by a generalised curve shown by the broken line in Fig. 3.23. This generalised bending-moment curve allows the variation of $\bar{M}_x$ to be obtained conveniently for any slab by truncating the tail of the curve at the limit of the slab width. The generalised curve for $\bar{M}_x$ is presented in better detail in Fig. 3.24. Values of ordinates at various non-dimensional distances ξ (= y/L) have been inserted along the curve for convenience in the evaluation of $\bar{M}_x$. The value of $\bar{M}_x$ at ξ = 0, which is given as 20.0 should only be used in conjunction with the adjacent values shown to give an estimate of the bending moment in the most critically stressed slab-strip as explained in Section 3.4.2.3. The integrated bending moments at various slab strips, $\bar{M}_x . \Delta\xi$, have been evaluated and tabulated below the curve of $\bar{M}_x$ to facilitate the calculation of steel ratios, if required, for the slab.

The generalised curve of $\bar{M}_x$ may also be used to evaluate approximately the effective width of any slab for checking purposes. Since the integration of the bending stress resultant M_x at the transverse section must equal the value of the external moment, the area under the curve of $\bar{M}_x$ may be evaluated to obtain the moment-rotation relationship leading to the calculation of effective slab width. If the double-area under the truncated curve of $\bar{M}_x$ for the slab of width Y is K_a, then it can be shown using expression (3.12) that

$$\frac{Y_e}{Y} = \frac{1}{6(1-\nu^2)} \left(\frac{L}{Y}\right) K_a \qquad (3.14)$$

To facilitate the calculation of effective width in this way, the curve for K_a has been included in Fig. 3.24 with the generalised curve for $\bar{M}_x$.

In order to illustrate the use of the curve for K_a for the calculation of effective widths an example is now shown.

Example:

It is required to evaluate the effective width for a slab with the following data:
X = 15.25 m (50 ft), Y = 6.1 m (20 ft), L = 1.525 m (5 ft)

The limit of the curve K_a is $\xi = 0.5\ Y/L = 2.0$.
The ordinate of the curve K_a at this point is 5.1.
Therefore the effective width $\frac{Y_e}{Y} = \frac{1}{6\,(1+0.15^2)} \times \frac{5}{20} \times 5.1$

$= 0.217$

Comparing this figure with the accurate value of 0.218 from Appendix A3.2 the effective width is seen to be underestimated by only ½%.

3.4.2.7 Shear Transfer Between Wall and Slab

The general distribution of shearing forces Q_x and Q_y throughout the slab induced by coupling action has been shown in Fig. 3.14, (d) and (e). The shearing force distribution in the vicinity of the wall boundary is now examined in more detail.

Fig. 3.25, (b) and (c), show respectively the variations of the shearing forces (stress resultants) Q_y and Q_x along two perpendicular sections A and B passing through the toe of the wall (Fig. 3.25(a)). The numerical values of the shearing forces have been evaluated at the nodal points in a finite element analysis. The shearing forces Q_y along the wall boundary apparently represent the continuously distributed shear transferred from the wall to the slab, which in the finite element analysis has been discretised as nodal point reactions. It is seen from Fig. 3.25(b) that the distribution of Q_y is consistent with the distribution of nodal reactions. Obviously, for equilibrium, the integration of Q_y over the length of the wall must equal the sum of the nodal reactions.

The shearing forces Q_x and Q_y at the inner edge of the wall are theoretically infinite, but have been evaluated as arbitrary finite values which vary according to the finite

element discretisation of the slab. While it is possible, as has been shown, to make use of similarly arbitrary values of bending moments M_x and M_y to provide a valid estimate of the integrated bending moments disposed around the singular point, it is not possible in this case to get from the calculated values of Q_x and Q_y a meaningful estimate of the shear forces disposed in the critical region because of the discontinuity in the shear distribution at a point between the singular and adjacent nodes. The convergence study has shown that the shear discontinuity always exists between the singular and the adjacent node, and that the calculated positive and negative shearing stress-resultants at the respective nodes are divergent (apparently to maintain equilibrium) with refinement of element mesh around the singular point. The shearing stress resultants are arbitrarily calculated not only at the node at the critical end of the wall, but also at adjacent nodes in the slab, and the apparent finite width over which the critical positive shearing forces are distributed is also arbitrary because in the limit of mesh refinement this will be reduced to a point. With these limitations on the calculated shear distribution, it is not possible to evaluate quantitatively the actual form of shear transfer between wall and slab, though we may conclude from the form of shear distribution indicated that the shear transfer must be effected essentially as a very large reaction distributed, in practice, over a finite wall length at the inner edge of the wall, together with much smaller opposite reactions distributed over the rest of the wall. This form of shear transfer is consistent with observed punching shear failures in coupling slabs.[54]

3.4.2.8 Critical Peripheral Slab Section For Shear

Fortunately, for design purpose it is not absolutely essential to know the exact values of shearing forces at points in the slab very close to the wall since at these points the shear forces are carried primarily by a strut

and tie action of the concrete and steel with the shear resistance of the slab acting only as a secondary load carrying medium (Fig. 3.25(d)). The critical slab section which has to be checked or designed against shear failure is located at some critical distance u from the face of the wall where frame action in carrying shear is no longer possible. At such sections in the coupling slab, the shearing forces predicted by thin-plate theory are finite and values calculated by the finite element method using sufficiently fine mesh divisions are quite satisfactory for design purpose.

Recommendations for the location of the critical section for shear near column supports in flat slab structures are given in various design Codes,[55,56] and these recommendations are assumed applicable for shear wall-slab structures since both types of structure involve the same form of punching shear failure in the slab. The critical distance u for ultimate strength design is usually given in terms of the effective depth d or the overall depth t of the slab depending on the code in use, and the shear at failure is assumed uniformly distributed over a peripheral section located at this critical distance from the face of the support.

3.4.2.9 Shear Distribution at a Typical Peripheral Section

Fig. 3.26 shows the distribution of normalised shearing forces or shearing-force factors $\bar{Q}_x$ and $\bar{Q}_y$ along a peripheral section located at a distance of u/L = 0.1 from the face of the wall in a slab of normalised width Y/L = 2. This distance represents a practical location for the critical shear section required by most codes when applied to the design of cross wall-slab structures. To show that the shear stress distributions obtained from the finite element analysis are accurate, a check is made of the equilibrium relationship between internal stress-resultants around the peripheral section and the external forces applied by the wall. The distributions of

normalised bending and twisting moments $\bar{M}_x$ and $\bar{M}_{yx}$ along the peripheral section have been included for this purpose. The equilibrium with respect to shears and moments at the wall axis for a symmetric half panel (Fig. 3.27) are established by the following relationships:

$$\int_o^b \bar{Q}_x \, d\eta + \int_o^a \bar{Q}_y \, d\zeta = \bar{Q}_o \qquad (3.15a)$$

and

$$\int_o^b \bar{M}_x \, d\eta + \int_o^a \bar{M}_{xy} \, d\zeta + c. \int_o^b \bar{Q}_x \, d\eta + \int_o^a \bar{Q}_y \, \zeta \, . \, d\zeta = \bar{M}_o \qquad (3.15b)$$

where $\bar{Q}_o$ and $\bar{M}_o$ refer to the external shear force and moment applied by the wall and a, b, c, η and ζ are non-dimensional distances normalised with respect to the corridor width L. The numerical results for the various terms in the above equilibrium equations are shown in Fig. 3.27 from which it can be seen that the equilibrium of shears and moments are established to an acceptable degree of accuracy at the peripheral section.

The equilibrium check at the peripheral section provides simultaneously an insight into the relative significance of various slab actions in resisting the applied wall moment. As shown in equation (3.15b) the applied wall moment is resisted at the peripheral section by a combination of bending, twisting and shearing forces. The results of the equilibrium check indicate that the applied wall moment is resisted at the typical peripheral section primarily by vertical shearing action (more than 80%) and very little by the bending and twisting actions.

3.4.2.10 Dimensions of Critical Shear Section

It will be obvious from the shearing force distribution that the design of the slab section against possible shear failure will be critically governed by the

substantially higher positive shear distributed over a relatively small section at the front of the peripheral section. For the purpose of design it is convenient to assume that the critical shear at failure is uniformly distributed over a critical section. With the shear distribution shown in Fig. 3.26 an obvious choice of the critical section is to consider the whole U-shaped section acted on by the positive shearing forces around the inner edge of the wall as the critical section. Depending on the design Code adopted in practice, the corners of the U-shaped critical section may be taken as square or rounded (Fig. 3.26) to be consistent with similar provisions for flat-slab design. The rounded corners, in this instance, provide a more realistic approximation of uniform shear distribution, since an approximately radial dispersion of the critical shear is indicated by the shape of the actual shear distribution curve. The open ends of the U-shaped section in either case can be extended to the point where the calculated shearing force changes sign. This point is at a distance of approximately 0.5 u measured back from the front (inner) edge of the wall, and so the length of each leg of the U-shaped section may be taken as 1.5 u. As shown by the shear distributions for various peripheral sections (Fig. 3.28) and for various slab widths Y/L (Fig. 3.29), this convenient side-length for the critical section is consistent for all possible locations of the critical section. The overall length of the critical section can therefore be generally taken as h+5u for the square-cornered critical section and $h+(1+\pi)u$ for the round-cornered section, h being the wall thickness.

3.4.2.11 Shear Modification Factors

The positive shear force developed in the critical shear section as shown by the various shear distribution curves in Fig. 3.28 and 3.29 is substantially greater than the applied shear force and varies in value with the location of the peripheral section and with the slab width

Y/L. The ratio of the critical positive shear force Q_1 to the applied shear force Q_o, which may be considered as a shear modification factor, has been calculated for various locations of the peripheral section in slabs of normalised widths Y/L = 1, 2 and 4 for walls of zero thickness. The curves showing the variation of the shear modification factor K_q with the peripheral distance u/L are presented in Fig. 3.30, and may be used conveniently as design curves for evaluating the critical shear at any location of the critical section.

3.4.2.12 Influence of Finite Wall Thickness on Shear Distribution

The shearing force distributions on which the derivation of the critical shear section and the shear modification factors have been based do not account for the influence of finite wall thickness. To illustrate the influence of wall thickness, the shear distribution for a wall of zero thickness and for a wall with a thickness ratio h/L = 0.1, are compared at a peripheral section at u/L = 0.1 in Fig. 3.31. It can be seen from the comparison that the distributions of $\bar{Q}_y$ along the sides of the peripheral section for the two cases are almost identical, while the distributions of $\bar{Q}_x$ along the front end of the peripheral section show some significant differences between absolute values. The effect of considering the wall thickness and a wider peripheral section is seen to result in lower shearing forces in front of the wall. The total positive shear force distributed over the front ends of the two peripheral sections however do not show much significant difference in the comparison of areas under the shear distribution curves. A comparison of shear modification factors which are of more relevance for practical shear strength design shows a difference of approximately 6%, with the value for the wall of zero thickness on the higher side. Since neglecting the effects of wall thickness in the calculation of shear modification factors will result

in a slightly conservative estimate of the critical design shear force in the slab, the design curve for shear modification factors presented in Fig. 3.30 should be quite satisfactory for design purpose when walls are not exceptionally thick (say h < u).

3.4.2.12.1 Application of Critical Section and Stress Modification Factor

To illustrate the application of the critical section and the shear modification factor, typical punching shear calculations consistent with the design Codes CP110 and ACI 318-71 are now shown.

Example:

The floor slab coupling a pair of plane walls in a 20-storeyed, 52 m (170 ft) high cross-wall structure which has been analysed separately for wind effects is considered. The typical dimensions of the slab are

Y = 6 m (20 ft), X = 15.25 m (50 ft), L = 1.525 m (5 ft)

The wall thickness h and the slab thickness t are both 200 mm (8 in.).
The effective depth of the slab d is 170 mm (6.75 in.)
The maximum lintel shear at an ultimate wind load of 1.68 kN/m^2 (35 lb/ft^2) has been calculated as Q_o = 67.5 kN (15.2 kip).

(a) Design to CP110:

The critical section is located at u = 1.5 t from the face of the wall and corners for the critical section are rounded. The length of the critical section is therefore $h + (1 + \pi)\ 1.5\ t$, and the shear area is $[h + (1+\pi)1.5\ t]d$.

The critical distance u/L = 1.5 x 0.2/1.5 = 0.2
The slab width ratio Y/L = 4.0
The shear modification factor K_q from Fig. 3.30 is

$$K_q = 1.25$$

The critical shear stress is then

$$v = \frac{K_q \times Q_o}{[h + (1+\pi)1.5t]d} = \frac{1.25 \times 67.5 \times 10^3}{[200 + 4.14 \times 1.5 \times 200]170}$$

$$= 0.34 \text{ N/mm}^2$$

This value should not exceed the permissible shear stress determined in accordance with Cl. 3.4.5 (CP110) and Tables 5 and 14 (CP110). Assuming a Grade 25 concrete and 0.25% steel area the permissible shear stress is given by

$$\xi_s v_c = 1.10 \times 0.35 = 0.39 \text{ N/mm}^2$$

which is 1.15 times the design shear stress.

(b) Design to ACI 318-71:

The critical section is located at u = 0.5d and the corners of the critical section are square. The shear area is then (h + 2.5d)d.

Working in fps units,

The critical distance u/L = 0.5 x 6.75/60 = 0.06

The shear modification factor from Fig. 3.30 is $K_q = 1.92$

The critical shear stress is then

$$v = \frac{1.92 \times 15.2 \times 10^3}{(8 + 2.5 \times 6.75)6.75} = 173.8 \text{ lb/in}^2$$

This should not exceed the permissible ultimate shear stress of $4\sqrt{f'_c}$, otherwise special provision has to be made to increase the shear capacity of the slab.

Assuming the same Grade of concrete as above, and taking the cylinder crushing strength f'_c as 0.78 times the cube strength of concrete,

$$f'_c = 0.78 \times 25 \times 145 = 2827 \text{ lb/in}^2$$

The permissible ultimate shear stress is then

$$v_c = 4\sqrt{f'_c} = 4\sqrt{2827} = 212.7 \text{ lb/in}^2$$

which is 1.22 times the design shear stress.

It is seen from the above calculations that although the shape and location of the critical shear section assumed in accordance with CP110 are distinctly different

from those assumed in accordance with ACI 318-71 the ratios of design ultimate shear stress to permissible ultimate shear stress from the two different calculations are not substantially different.

3.5 FLANGED WALL CONFIGURATION

Flanged shear walls occur frequently in cross-wall structures as a result of making the corridor or facade longitudinal walls of similar construction to the cross walls to satisfy the need for additional load bearing area or simply for the purpose of convenience in building construction. Depending on planning requirements, various arrangements of flanged walls may be encountered in cross-wall structures.

3.5.1 NUMERICAL RESULTS FOR EFFECTIVE WIDTH

3.5.1.1 Coupled Flanged Walls with External Flanges

In this wall configuration the flanges are at the exterior or facade ends of the cross-walls (Fig. 3.3(c)). Since the slab actions induced by the coupled walls are mainly confined to the corridor area and its immediate vicinity, the external wall flanges are not expected to have much influence on the coupling stiffness of the slab.

Table 3.7 shows the effective width Y_e/Y, obtained for slabs with external flanged walls, compared with the corresponding results for plane walls. The effective width Y_e/Y for the slab with a small aspect ratio $Y/X = 0.2$ is seen to be unaffected by the presence of the external wall flanges. For the slab with a larger aspect ratio $Y/X = 0.4$, the effective width increases marginally with the increase in the flange width ratio Z/Y. In the extreme case considered ($Y/X = 0.6$, $L/X = 0.6$ and $Z/Y = 0.75$), the presence of the external wall-flanges increases the effective width of the slab by less than 4%. For practical purposes, therefore, the influence of external wall-flanges can be safely disregarded.

3.5.1.2 Coupled Flanged Walls with Internal Flanges (T-Shaped Walls)

The wall flanges for this configuration are at the coupled (corridor) ends of the cross-walls. The pair of walls considered in a typical slab panel are identical and symmetrical with respect to the panel centrelines (Fig. 3.3(d)). Since in plane-wall configurations the finite wall thickness has a considerable influence on the stiffness of the coupling slab, the width of the internal wall-flanges can be expected to have a strong influence on the effective width of the slab.

Fig. 3.32, (a) to (d), show the variation of effective width Y_e/Y as a function of the wall opening ratio L/X for various flange-width ratios Z/Y. The numerical results for drawing these curves are given in Appendix A3.4. It is seen from the curves that the flange width has a considerable influence on the effective width of the slab. To illustrate the influence of flange width more clearly, the results have been re-plotted in Fig. 3.33, (a) to (d), to show the variation of Y_e/Y as a function of Z/Y for various ratios of L/X. By comparing these curves with the curves presented in Fig. 3.12, (a) and (b), for slabs coupling thick walls, it is seen that the influence of the flange width and the influence of the wall thickness are practically identical. This can also be seen by comparing Appendix A3.4 with Appendix A3.3, which shows more clearly that the effective slab width for flanged walls is marginally less than that for plane walls, where the flange width and the wall thickness are equal.

The curves presented in Fig. 3.32, (a) to (d), or the curves presented in Fig. 3.33, (a) to (d), may be used as design curves for the rapid evaluation of effective widths. In using these curves, the need to interpolate between values of Y/X can again be avoided by arbitrarily adjusting the value of X for the particular slab so that the adjusted value of Y/X coincides with the nearest value of a set of curves, as suggested in section 3.4.1.5.

3.5.1.3 Generalised Design Curves

The four sets of curves presented in Fig. 3.32, (a) to (d), may be generalised into a more convenient set of design curves by disregarding the negligibly small influence of wall length in the evaluation of effective slab widths. The generalised set of curves showing the variation of effective width Y_e/Y as a function of L/Y for various flange width ratios Z/Y is presented in Fig. 3.34. The generalised curves are accurate compared to the curves which account for the influence of wall length, when the wall and slab proportions are such that $[L/X + (Y-Z)/X] \leq 1$ which is obtained in most practical cases. In unusual cases where $[L/X + (Y-Z)/X]$ is greater than unity and L/X is also greater than 0.4, the effective widths obtained by the generalised curves are over-estimated, generally less than 10%, compared to values obtained by the more accurate sets of curves.

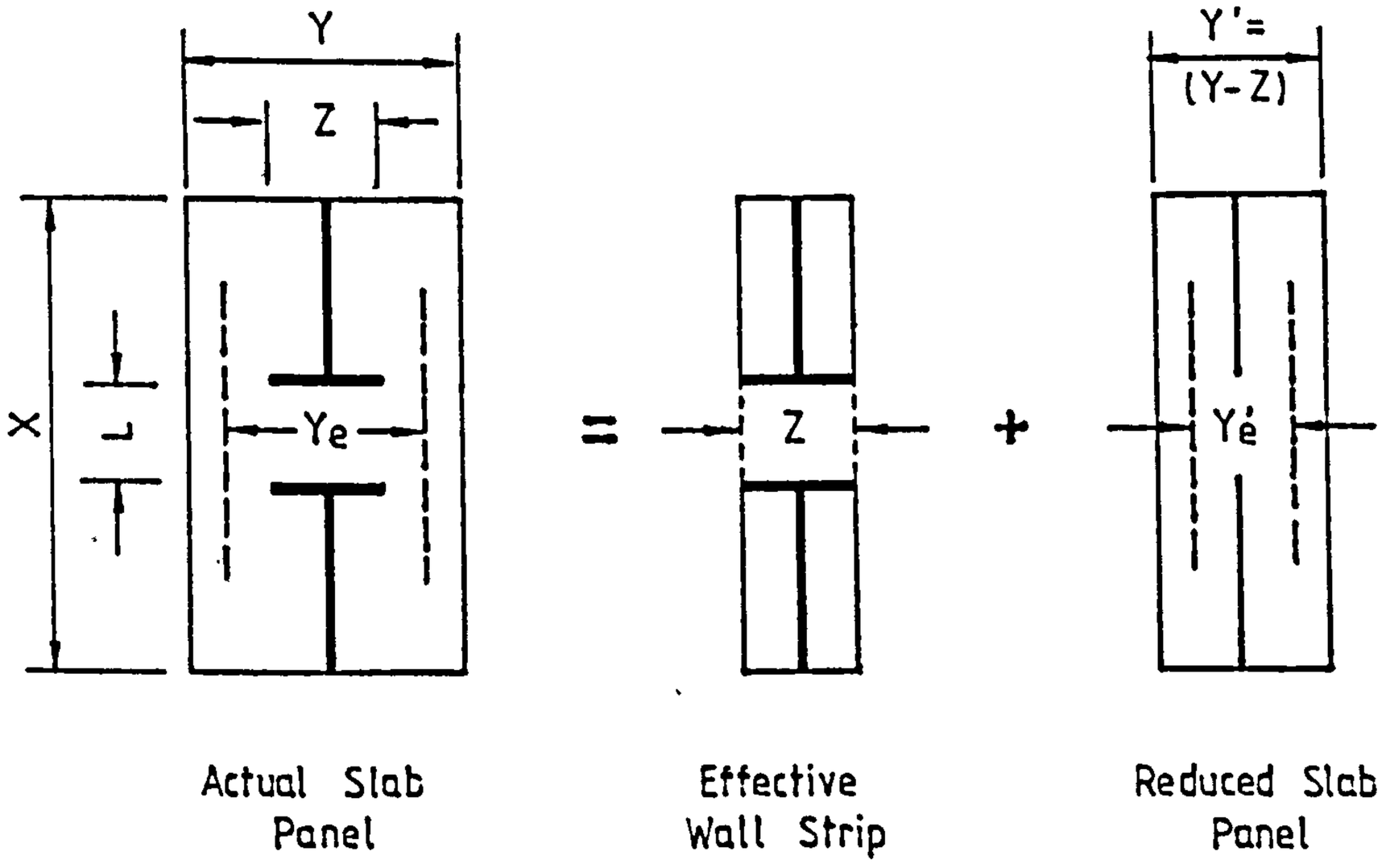

Fig. 3.35

3.5.1.4 Empirical Method to Account For the Influence of Flange Width

Since the influence of the flange width and the influence of finite wall thickness are practically identical, the simple method suggested in Section 3.4.1.9,

to account for the influence of wall thickness, is also applicable to the case of the flange wall to account for the corresponding influence of flange width, using the basic design curves presented for plane walls of zero thickness. As shown in Fig. 3.35 the effective slab width Y_e is assumed to be made up of an effective wall strip equal in width to the flange width Z, plus the effective width Y'_e of a reduced slab panel with plane walls of zero thickness.

As an illustration of the application of the proposed method of evaluating the effective slab width for flanged wall configurations, an example is shown.

Example:

It is required to find the effective width of a slab of aspect ratio Y/X = 0.6 coupling a pair of flanged walls with flange width ratio Z/Y = 0.75 and wall-opening ratio L/X = 0.2.

The reduced slab width Y'/Y = 1-Z/Y = 0.25

The reduced span/width ratio L/Y' = 0.2/0.6/0.25 = 1.33

From Fig. 3.34, the effective width Y'_e/Y' = 0.69

The effective width Y'_e/Y = 0.69 x 0.25 = 0.173

The effective wall strip = 0.750

$\therefore$ The total effective width Y_e/Y = 0.923

Comparing this value with the accurate value of 0.939 from Appendix A3.4 or from Fig. 3.32(c), the relative error is seen to be -1.7%. Using Michael's procedure, the effective Y_e/Y would be evaluated as 0.28 + 0.75 = 1.03 which is +9.7% in error.

3.5.1.5 Empirical Equations For Evaluating the Effective Slab Width

The empirical equations (3.8) and (3.9) presented in Section 3.4.1.10 for the coupled thick planar wall configuration are also applicable to the flanged wall configuration, with a change of the variable h with the new variable Z. The empirical equations for the flanged wall configuration can then be written as

$$\frac{Y_e}{Y} = \frac{Z}{Y} + \frac{Y'}{Y} \cdot \frac{L}{Y'} \left[1 - 0.4 \frac{L}{Y'} \right], \quad 0 \leq \frac{L}{Y'} \leq 1 \qquad (3.16)$$

and

$$\frac{Y_e}{Y} = \frac{Z}{Y} + \frac{Y'}{Y} \left[1 - 0.4 \left(\frac{L}{Y'}\right)^{-1} \right] \quad , \quad 1 \leq \frac{L}{Y'} \leq \infty \qquad (3.17)$$

In order to illustrate the accuracy of the empirical equations when applied to the flanged wall configuration, the empirical results previously compared with 'thick wall' finite element results in Table 3.5 are now compared in Table 3.8 with the finite element results obtained for flanged wall configurations. The empirical results are seen to have been evaluated to within 2½% accuracy in relation to the accurate finite element results.

3.5.2 NUMERICAL RESULTS FOR STRESS RESULTANTS (FLANGED WALL CONFIGURATION)

3.5.2.1 General Distribution Pattern

Fig. 3.36, (a) to (e), show in perspective the typical variation of bending, twisting and shearing stress resultants throughout a symmetric quadrant of a floor slab coupling a pair of flanged walls subjected to unit rotation as shown in Fig. 3.36(f). The corresponding stress-resultant contours are shown in Fig. 3.37, (a) to (e), with the typical element discretisation of the slab in Fig. 3.37(f). These two sets of diagrams have been presented to give a general picture of the overall distribution of stress resultants in the slab and to indicate critical areas of high stress concentration which require detailed examination. In the perspective and contour presentations, each stress-resultant component has been multiplied by a separate scaling factor which reduces the stress-resultant values to a convenient range for plotting. Therefore when comparing visually the relative magnitudes of bending or shear stress resultants in the two orthogonal directions, the scaling factors must be taken into account.

It can be seen from the diagrams that a large portion of the slab some distance back from the corridor edge is practically free of bending and shearing actions. The

significant coupling actions arise mainly in the corridor area with high concentrations of bending moments and shearing forces occurring around the tips of the flange. The bending moments M_x and M_y and the longitudinal shearing force Q_x are higher in the strip of corridor slab directly coupling the wall flanges than elsewhere outside this region. The twisting moment M_{xy} and the transverse shear force Q_y, on the other hand, arise mainly in the area outside the direct coupling strip. Comparing peak values, it can be seen that the transverse bending moment M_y and shearing force Q_y are much less significant than the longitudinal stress resultants M_x and Q_x.

3.5.2.2 Stress-Resultant Singularity

The possibility of a stress-resultant singularity occurring in the slab at the tip of the wall flange is now examined by referring, in particular, to the distribution of longitudinal bending moment along the critical transverse slab section at the inner edge of the flange wall. Fig. 3.15(b) shows the variation of M_x obtained using various mesh divisions of the slab in the convergence study (Section 3.3.2). The results clearly show that whereas values of M_x calculated at other points converge to finite values, the value of M_x calculated at the critical point on the flange tip diverges with mesh refinement, indicating the possibility of stress-resultant singularity at this point. The stress-resultant values around the flange tip should therefore be interpreted in the manner described in Section 3.4.2.3 for plane walls.

3.5.2.3 Design Curves For Critical Bending Moment Factors

Curves showing the variation of the longitudinal bending moment factor $\bar{M}_x$ along the critical transverse slab section at the inner edge of the flange-wall ($x = -0.5L$) for slabs with various wall-opening to slab-width ratios L/Y and flange width ratios Z/Y are presented in Fig.3.38, (a) to (f). The six sets of curves have been drawn with

distances normalised with respect to the half panel width (ζ = y/(0.5Y)). On comparing each set, it can be seen that the curves for various flange width ratios are very similar in form. If the curves were re-drawn with the tip of the flange as the origin for the ζ-axis, all the curves in a set would practically coincide over the greater part of the curve. For the first five sets of curves with L/Y less than 1, $\bar{M}_x$ generally remains constant for each curve at a value of 6.0 along the flange until close to the flange tip where it increases rapidly, reaching a peak at the flange tip. Beyond the end of the flange, $\bar{M}_x$ decreases very rapidly to a relatively low value a short distance from the flange tip and thereafter the decrease in $\bar{M}_x$ is very gradual. For the last set of curves with L/Y = 1, values of $\bar{M}_x$ along the flange are generally higher than 6.0 when the flange width ratio Z/Y is small. The peak values of $\bar{M}_x$ for each set of curves are also higher with smaller ratios of Z/Y. Comparing values of $\bar{M}_x$ at corresponding points in the slabs with different corridor or wall-opening widths L, it can be seen that at points outside the flange area $\bar{M}_x$ is higher for larger ratios of L/Y.

3.5.2.4 Generalised Curve for Critical Bending Moment Factor $\bar{M}_x$

The six sets of curves for $\bar{M}_x$, and similar curves which can be drawn for other ratios of L/Y (which, for conciseness are not included), may be used as design curves if desired, to evaluate relatively accurately the critical bending moments which may influence the design of the floor slab. However, because of the large number of individual curves involved and the need to interpolate between them at times, these curves become less suitable to use when critical bending moments have to be evaluated rapidly, but only approximately in the preliminary stages of design. Since the curves of $\bar{M}_x$ for various ratios of L/Y and Z/Y are very similar in form, particularly when they are plotted

with the flange tip as origin and the distances are normalised with respect to L instead of 0.5Y, it is possible to approximate the whole series of curves by a single generalised curve which is applicable, for practical purposes, to slabs with any normal ratios of L/Y and Z/Y, and is therefore more convenient to use. The generalised design curve which shows the variation of $\bar{M}_x$ with the normalised distances ξ (ξ = y/L) from the flange tip is presented in Fig. 3.39. To obtain the distribution of $\bar{M}_x$ for a slab of width Y with flange width Z and wall opening L, the generalised curve is simply truncated at the points $\xi_1 = -0.5Z/L$ and $\xi_2 = 0.5(Y-Z)/L$ corresponding respectively to the centreline and an edge of the slab.

The peak value of $\bar{M}_x$ at the origin of the generalised design curve has been taken as 8.5, this being the approximate average for the range of slabs considered. Although this value may appear to differ considerably from individually calculated peaks in some cases, it must be remembered that any such calculated peak on its own is quite arbitrary in absolute value because of the stress singularity. The average peak value of 8.5, when used in conjunction with the adjacent values indicated on the generalised curve, however gives an accurate estimate of the total moment in the region of the stress concentration.

The generalised design curve for $\bar{M}_x$ can also be used for the evaluation of effective slab width following the procedure outlined in Section 3.4.2.6. For this purpose, the segmental areas $\bar{M}_x . \Delta\xi$ have been tabulated beneath each segment of the curve of $\bar{M}_x$ and these may be easily summed over the appropriate length of the curve for the particular slab. The area integrals $K_{a1} = 2\int_{-\xi_1}^{o} \bar{M}_x \, d\xi$ and $K_{a2} = 2\int_{o}^{\xi 2} \bar{M}_x \, d\xi$ evaluated numerically from the summation of segmental areas have been plotted as supplementary design curves along with the generalised curve.

To illustrate the use of the design curves presented in Fig. 3.39 a numerical example is now shown.

Example:

It is required to evaluate approximately the effective width and critical bending moments for a slab with the following dimensions:

L = 1.525 m (5 ft), Y = 6.1 m (20 ft) and z = 1.525m (5 ft)

The normalised distances from the flange tip to the slab centreline and to the slab edge are respectively

$$\xi_1 = -0.5 \quad \text{and} \quad \xi_2 = +1.5$$

The area integrals at these points of the curves of K_a are

$$K_{a1} = 6.3 \text{ and } K_{a2} = 4.3$$

From equation (3.14) the effective slab width is therefore

$$\frac{Y_e}{Y} = \frac{1}{6(1-0.15^2)} \times \frac{5}{20} \times (6.3 + 4.3) = 0.452$$

Comparing this figure with the accurate value of 0.460 given in Appendix A3.4, the discrepancy is seen to be -1.74%.

The generalised curve of $\bar{M}_x$ truncated at the points $\xi = -0.5$ and $\xi = +1.5$ gives the distribution of $\bar{M}_x$ for the slab.

3.5.2.5 Critical Shear Distribution

In Section 3.5.2.1 it was shown that concentrations of shearing forces are developed in the slab around the interior edges of the wall flanges. Although these shearing forces may not under normal circumstances lead to dramatic punching shear failures in the slab, since this type of failure has seldom been reported, it is desirable as a matter of precaution to ascertain the level of stress which may arise at areas of stress concentration under working or ultimate load conditions. A convenient design procedure is suggested in this section for punching shear calculation for the slab coupling flanged-walls, using the same concept of a critical section and shear modification factors suggested for slabs coupling plane-walls.

3.5.2.6 The Shear Distribution at a Peripheral Section

Fig. 3.40 shows the normalised shearing force (shearing-force factor) distribution at various peripheral slab sections encompassing a flanged wall with a normalised flange width of Z/L = 1, the slab being considered, having a normalised slab width of Y/L = 2. Referring, for illustration, to the shear distribution curve for u/L = 0.05 it can be observed that the highest positive shearing forces $\bar{Q}_x$ and $\bar{Q}_y$ for the particular peripheral section are confined within a small region at the corner of the peripheral section. Over a considerable length of the peripheral section in front of the flange, the positive shearing force $\bar{Q}_x$ remains relatively low, at an approximate value of 12.0, this value being incidentally the value of the effective shearing force obtained by distributing the applied shear uniformly over the effective slab width (see equation 3.1[illegible]). Around the corner and along the side of the peripheral section, the critical positive shearing force $\bar{Q}_y$ changes to a negative shearing force at a point approximately 1.25 u from the corner.

3.5.2.7 Dimensions of the Critical Shear Section

For the purpose of design it is convenient to assume that the positive shear in each half of the slab is uniformly distributed in two distinct zones instead of being distributed according to the theoretical shear distribution curve. The critical design shearing forces can be assumed uniformly distributed over a critical section near the end of the flange. The shearing force in the remaining front portion of the peripheral section can be assumed at a value equal to the effective shearing force, i.e. at a value of $12(1-\nu^2)$. The critical shear section can be taken as L-shaped with maximum dimensions of 2u x 1.5u (Fig. 3.40). These recommended dimensions, it will be observed, are consistent for other peripheral sections. The corner of the L-shaped critical section may be taken as square or rounded to be consistent with

similar recommendations for flat slab or flat plate structures given by the design Codes.

3.5.2.8 Influence of Slab Width and Flange Width on Shear Distribution

The critical section suggested for shear design has been derived by considering the shear distribution at peripheral sections in a slab with a particular slab width ratio Y/L and a flange width ratio Z/L. To illustrate the influence of slab width and flange width on the shear distribution at a peripheral section, the peripheral shear distribution curves defined by u/L = 0.1 for slabs with different half flange-width ratios ξ_1 = 0.5Z/L and flange-opening ratios ξ_2 = 0.5(Y-Z)/L are compared in Fig. 3.41. By comparing the shear distribution for the case of ξ_1 = 0.25 and ξ_2 = 0.5 with the shear distribution for the case of ξ_1 = 0.5 and ξ_2 = 0.5, it is seen that changing the flange width ratio ξ_1 merely changes the length of the shear distribution curve for $\bar{Q}_x$ over the uniform effective shearing-force region, the shear distribution curve for the critical shearing force region remaining practically unaffected by the change in the flange width. By comparing the case of ξ_1 = 0.5 and ξ_2 = 0.5 with the case of ξ_1 = 0.5 and ξ_2 = 1.0, on the other hand, it is seen that increasing the slab width increases substantially the positive shearing forces in the critical section. The form of shear distribution and the shape of the critical shear distribution curve in all three cases are however very similar, indicating that the critical design shear section suggested in Section 3.5.2.7 is quite general and is applicable to slabs of any width with walls of any flange width Z which is not smaller than twice the critical peripheral distance u.

3.5.2.9 Shear Modification Factors

The total positive shear at the peripheral section is in excess of the applied shear and only a portion of the

positive shear is distributed over the critical section. In order to facilitate the calculation of critical shears for design, shear modification factors may be calculated for various locations of the critical section using the peripheral shear distribution curves. It has been shown that along the middle front portion of the peripheral section, the positive shearing forces are sensibly uniformly distributed, with a value approximately equal to the effective shearing force. Since this portion of the slab is fully effective in coupling the flanges, a change in the flange width produces a change only in the positive shear in this "effective shear zone", equal in value to the change in the applied shear force required to induce unit wall displacements. The positive shear in the "critical shear zone" remains practically unchanged as long as the flange is sufficiently wide ($Z > 2u$). Therefore if the critical shear is expressed in terms of the portion of the applied shear with which it is associated, the resulting shear modification factor will be less influenced by the flange width.

Denoting the shear in the "effective shear zone" as Q_3, the shear modification factor K_q can be expressed as

$$K_q = (Q_1 - Q_3)/(Q_o - Q_3)$$

where Q_1 and Q_o, as before, represent respectively the total positive shear in the peripheral section and the total external applied shear.

In the calculation of shear modification factors Q_1 is obtained from the numerical integration of the positive areas under the actual curves of $\bar{Q}_x$ and $\bar{Q}_y$ for a peripheral section, and Q_3 is obtained simply from the idealised effective shear distribution.

The shear modification factors evaluated for various peripheral sections in slabs with flange opening width ratios $\xi_2 = 0.25$, 0.5 and 1 are presented in Fig. 3.42. The shear modification factor is seen to be influenced by the flange opening width ξ_2 relatively more with smaller peripheral distances u/L. Although results are not shown,

the influence of flange width ratio ξ_1 has been found to be negligible in the evaluation of shear modification factors.

3.5.2.10 Application of Critical Section and Shear Modification Factor

In order to illustrate the application of the critical shear section and the shear modification factors, typical punching shear calculations consistent with the requirements of the British and American Codes, CP110 and ACI 318-71, are now shown for the slab coupling a pair of flanged walls in a 30-storeyed, 78 m (255 ft) high cross-wall structure which has been separately analysed for wind load effects.

The characteristic dimensions for the slab are

L = 1.525 m (5 ft), Y = 6.1 m (20 ft), X = 15.25 m (50 ft) and Z = 3.05 m (10 ft).

The walls are 200 mm (8 in.) thick throughout.
The effective slab width Y_e is 4.2 m (14 ft), (cf. Fig. 3.32(b)).
The overall and effective depth of slab are

t = 200 mm (8 in.) and d = 170 mm (6.75 in.)

The calculated maximum lintel shear under an ultimate wind load of 1.68 kN/m^2 (35 lb/ft^2) is Q_o = 136.6 kN (30.73 kip).

(a) Design to CP110:

The critical shear section is located at u = 1.5t = 0.3 m. The shear in the effective shear zone is

$Q_3 = (Z-2u)Q_o/Y_e = (3 - 2 \times 0.3) \times 136.6/4.2 = 78.06$ kN.

The normalised critical distance u/L = 0.3/1.5 = 0.2
The flange opening ratio ξ_2 = 1.0
From Fig. 3.42, the shear modification factor K_q = 1.1
The critical design shear is therefore

$$Q_c = 1.1 \times (136.6 - 78.1) = 64.35 \text{ kN}$$

The length of the critical section on one half of the slab is

$$p = \frac{u}{2}(3 + \pi) = \frac{0.3}{2} \times (3 + \pi) = 0.92 \text{ m}$$

The critical punching shear stress is then

$$v = \frac{64.35 \times 10^3}{2 \times 920 \times 170} = 0.21 \text{ N/mm}^2$$

which is only about half the value of the permissible ultimate shear stress for a Grade 25 concrete and 0.25% steel area (cf. Section 3.4.2.12.1).

(b) Design to ACI 318-71:

The critical section for shear is located at

$u = 0.5d = 0.5 \times 6.75 = 3.375$ in.

$$\therefore \frac{u}{L} = \frac{3.38}{60} = 0.06$$

The shear in the effective shear zone is

$Q_3 = (10 - 2 \times 0.281) \times 30.73/14 = 20.72$ kip

The flange opening ratio $\xi_2 = 1.0$

From Fig. 3.42, the shear modification factor $K_q = 1.70$.
The critical design shear is therefore

$Q_c = 1.7 \times (30.73 - 20.72) = 17.02$ kip

The length of the critical section is $3.5u = 11.81$ in.
The critical shear stress is then

$$v = \frac{17.02 \times 10^3}{2 \times 11.81 \times 6.75} = 106.8 \text{ lb/in}^2$$

which again is about half the value of the permissible ultimate shear stress of $4\sqrt{f'_c}$ for a grade 25 concrete.

It would appear from the above example calculations that under normal circumstances the possibility of punching shear failure in slabs coupling flanged walls is quite remote.

3.6 COUPLED PLANAR-FLANGED (T-SHAPED) WALL CONFIGURATION

The slab in this configuration couples a plane wall to a flanged wall having an internal flange (Fig. 3.3(e)). Since the walls being coupled are dissimilar, the rotational stiffnesses of the slab evaluated at its ends

will not be equal. For the substitution of the slab by a uniform equivalent beam, the averaged rotational stiffness is taken to be the effective value.

The stiffness of the slab will no doubt be influenced by the width of the wall flange and by the finite thickness of the plane wall. For the investigation described in this section the plane wall is assumed to be of zero thickness. However, as will be shown in a subsequent section, the influence of the planar wall thickness can be accounted for by a simple procedure similar to that described for symmetrically coupled thick planar walls (Section 3.4.1.9).

3.6.1 NUMERICAL RESULTS FOR EFFECTIVE WIDTH

3.6.1.1 Design Curves for Effective Width

The numerical results obtained for the effective width Y_e/Y for a wide range of slab aspect ratios Y/X, wall opening ratios L/X and flange width ratios Z/Y are presented in Fig. 3.43, (a) to (d), as design curves. Tabulated results are given in Appendix A3.5 for further reference. The design curves show the variation of Y_e/Y as a function of L/X for various ratios of Z/Y and Y/X. To illustrate more clearly the influence of the flange width ratio Z/Y, the results have also been plotted in the form shown in Fig. 3.44, (a) and (b). It can be seen from these curves that increasing the flange width ratio Z/Y increases the effective width ratio Y_e/Y, the influence of flange width diminishing with larger flange width ratios. With small wall opening ratios L/X, increasing the value of Z/Y beyond a certain critical width does not produce any further increase in Y_e/Y.

3.6.1.2 Generalised Design Curves

The generalised set of design curves showing the variation of Y_e/Y as a function of L/Y for various ratios Z/Y is presented in Fig. 3.45.

The curves approach a zero value for Y_e/Y when L/Y reduces to zero and are asymptotic to the line $Y_e/Y = 1$. On comparing these curves with the corresponding set in Fig. 3.34 for the configuration with two flanged walls, it is seen that the omission of one flange from a wall results in a disproportionately large reduction in the effective width of the slab when the ratio L/Y is small.

The generalised curves are accurate compared to the design curves which account for the influence of wall length, presented in Fig. 3.43, (a) to (d), when the slab and wall proportions are such that $(L/X + Y/X) \leq 1$. Where the sum of (L/X + Y/X) exceeds 1.0, and L/X is also greater than 0.4, the effective widths defined by the generalised curves are generally higher than the values obtained from the more accurate sets of curves, but in the worst case discrepancies are not likely to exceed 10%. In most practical cases, the wall opening ratio is unlikely to exceed 0.4 and the generalised set of design curves should then prove more convenient to use than the previous sets of curves.

3.6.2 NUMERICAL RESULTS FOR STRESS RESULTANTS

3.6.2.1 General Distribution Pattern

The general distribution of bending moments and shearing forces in a slab coupling a plane with a flanged wall (T-shaped) is illustrated in Fig. 3.46. The contours show that large bending moments and shearing forces are concentrated around the coupled end of the plane wall. The stress resultants on the flanged-wall side of the slab are comparatively low. The longitudinal bending moment M_x decreases gradually along the flange wall away from the panel centreline (or longitudinal axis), as coupling of the flange becomes less effective. It is seen from the zero-value contour for M_x that the line of inflexion does not deviate significantly from the mid-span position over the portion of the slab where coupling is most effective. Hence the assumption of a uniform equivalent beam with a

mid-span point of contraflexure for the analysis of the walls coupled by the slab would not appear to be unreasonable, although the actual width of slab effectively stressed varies considerably across the wall opening.

3.6.2.2 Critical Bending Moment Factor $\bar{M}_x$

The curves showing the variation of longitudinal bending moment factors $\bar{M}_x$ along two critical transverse sections passing through the coupled ends of the plane wall and flanged wall are presented in Fig. 3.47, (a) to (f), for slabs with various ratios L/Y. The distribution of $\bar{M}_x$ along the critical section on the side of the plane wall is seen to be affected very little by the variation of flange width on the opposite wall. For walls with small flange width ratios, a distinct peak is observed in the bending moment distribution curve at the tip of the flange. Since it is likely that the bending moments at this point and also at the tip of the plane wall are theoretically infinite, it would be logical to interpret the peak bending moment values in the manner described in Section 3.4.2.3.

3.6.2.3 Generalised Design Curves for Critical Bending Moment Factors

The curves described in the above section may be used for the design of the critical slab sections, but they are not convenient to use because of the large number of curves involved. Since the bending moment distribution in the most effective coupling zone of the slab is practically unaffected by variations in slab width, the six sets of curves for various ratios L/Y may be generalised by a single set of curves which is applicable for all ratios L/Y provided that these ratios are not greater than 1.0. The generalised set of curves showing the variation of critical bending moment $\bar{M}_x$ with normalised distance ξ (= y/L) for various flange width ratios Z/L are presented in Fig. 3.48. To obtain the approximate distribution of $\bar{M}_x$ for any slab, the tail of the generalised curve for the

appropriate flange width ratio is simply truncated at the point corresponding to the actual limit of the slab width.

3.7 COUPLED FLANGED WALLS WITH UNEQUAL FLANGES (T-SHAPED)

In this configuration the slab couples two flanged walls with internal flanges of unequal width (Fig. 3.3(f)). Only a limited amount of numerical results have been obtained for this configuration of walls using the finite element method since the effective slab width, it will be shown, can easily be obtained quite accurately from the results presented for the planar-flanged wall configuration using a similar approach suggested for the coupled thick wall configuration.

3.7.1 NUMERICAL RESULTS FOR EFFECTIVE WIDTH

Table 3.9 shows the values of effective width Y_e/Y, obtained by the finite element method, for a slab of aspect ratio $Y/X = 0.6$ coupling flanged walls with a fixed opening ratio $L/X = 0.4$ and with various combinations of flange widths Z_1/Y and Z_2/Y. These results have been presented essentially to provide a measure of the accuracy of an empirical procedure suggested to account for the influence of unequal flange widths.

3.7.1.1 Empirical Method to Account for Unequal Flanges

The effective width Y_e of the slab coupling a pair of flange walls with flange widths Z_1 and Z_2 is assumed to be made up of an effective wall strip equal in width to the smaller flange width Z_1, plus the effective width Y'_e evaluated for a slab panel with a reduced width $Y' = (Y-Z_1)$ coupling a plane wall to a flanged wall of reduced flange width $Z' = (Z_2-Z_1)$, as shown in Fig. 3.49 (next page).

The effective width Y'_e for the reduced slab panel can be directly obtained from the generalised design curves presented in Fig. 3.45. An example is presented to illustrate the application of the method.

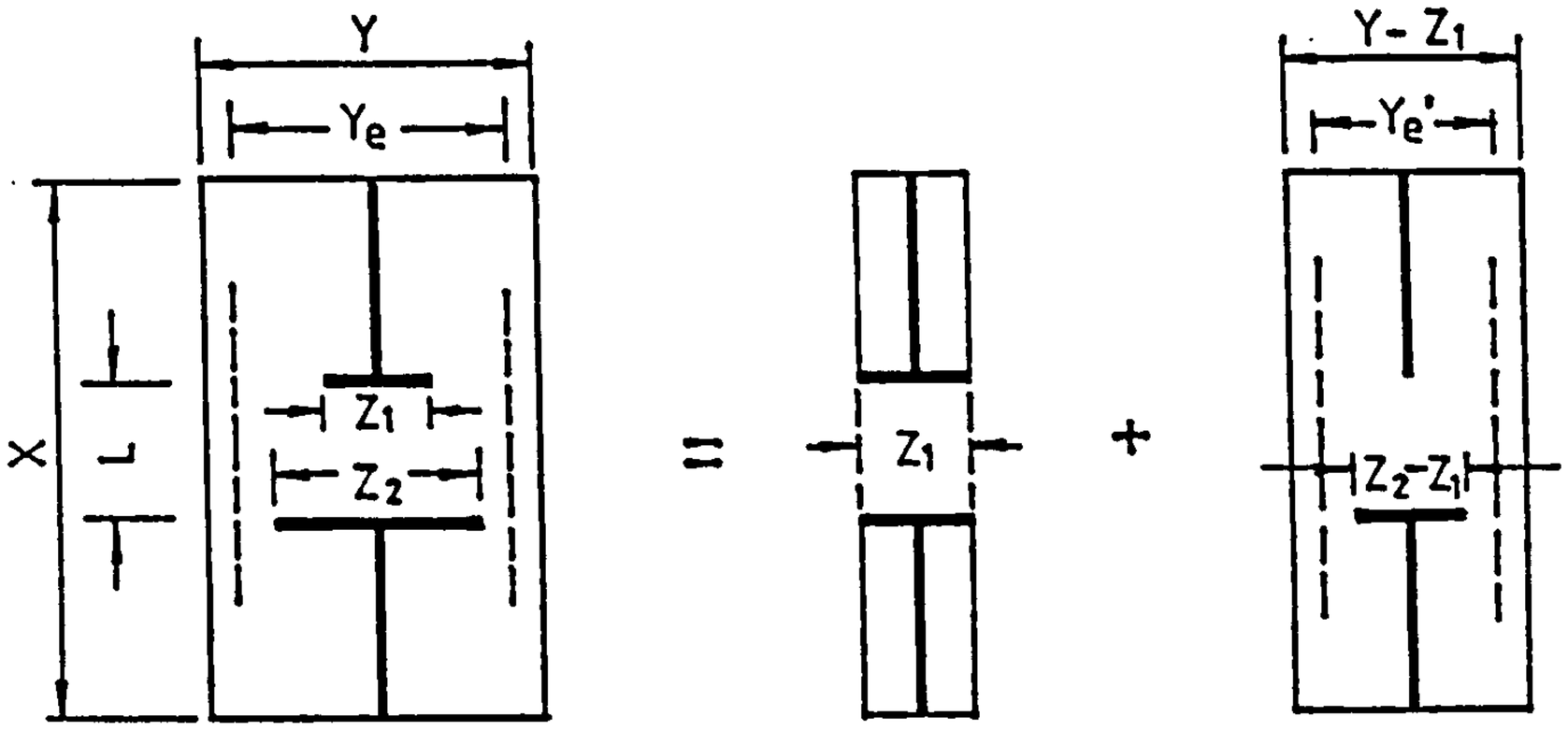

Fig. 3.49

Example:

It is required to evaluate the effective slab width for a structure with the following geometrical ratios:

$Y/X = 0.6$, $L/X = 0.4$, $Z_1/Y = 0.167$, $Z_2/Y = 0.333$.

The reduced slab width $Y'/Y = 1 - Z_1/Y = 0.833$.

The reduced flange width $Z'/Y = 0.333 - 0.167 = 0.167$

The reduced flange width ratio $Z'/Y' = 0.167/0.833 = 0.20$

The reduced span width ratio $L/Y' = 0.4 \times \frac{1}{0.6} \times \frac{1}{0.833}$

$= 0.80$

From Fig. 3.45 the effective width $Y'_e/Y' = 0.61$

$\therefore$ The effective width $Y'_e/Y = 0.61 \times 0.833 = 0.508$

The effective wall strip $Z_1/Y = \underline{0.167}$

$\therefore$ The total effective width $Y_e/Y = \underline{0.675}$

Comparing this figure with the accurate value of 0.670 from Table 3.9, the relative error is seen to be +0.75%.

To illustrate the general accuracy of the empirical method, values of Y_e/Y for various flange combinations obtained by the empirical method are compared, in Table 3.10, with the accurate results from Table 3.9. It is seen from the comparison that using the empirical method

in conjunction with the generalised design curves for planar-flanged wall configurations, the effective widths Y_e/Y are evaluated to within 1% of the accurate finite element results. Since the influence of finite wall thickness in plane walls and the influence of flange width are essentially similar, the suggested empirical method is also applicable to configurations consisting of coupled plane walls of unequal thickness (Fig. 3.3(g)) or a plane wall of finite thickness coupled to a flanged wall (Fig. 3.3(h)).

3.8 COUPLED L-SHAPED FLANGED WALL CONFIGURATION

The L-shaped flanged walls may be coupled in three different configurations. In the configuration shown in Fig. 3.3(i) the cross walls or web walls are coupled in-line with opposing flanges while in the configuration shown in Fig. 3.3(j) the webs are coupled off-line with opposing flanges. The effective widths of the slabs in these two configurations may be obtained directly from the results presented for coupled T-shaped flanged walls or from the results presented for coupled thick planar walls or box cores since both sets of results are essentially similar. In the third L-shaped wall configuration shown in Fig. 3.3(k), the webs are coupled in-line but the flanges are off-set or skew coupled. The investigation which has been carried out is concerned only with this arrangement of walls.

3.8.1 NUMERICAL RESULTS FOR EFFECTIVE WIDTH

3.8.1.1 Design Curves for Effective Width

The numerical results obtained for the effective width Y_e/Y for slabs with various aspect ratios Y/X, wall opening ratios L/X and flange width ratios Z/Y are presented in Fig. 3.50, (a) to (c), as design curves and are also tabulated in Appendix A3.6 for further reference. The design curves show the variation of Y_e/Y as a function of L/X for various ratios Z/Y and Y/X. Fig. 3.51, (a) to

(c), show the numerical results plotted in a different form to illustrate the influence of flange width more clearly. It is seen that although the flanges are not directly cross-coupled they still have a considerable influence on the coupling stiffness of the slab. By comparing the results obtained for the L-shaped wall configuration with the results for the planar-flanged wall configuration (Section 3.6.1.1), an interesting feature is revealed. It is seen that with the same total flange width in the coupled walls, the effective slab widths in the coupled L-shaped wall configuration and in the planar-flanged wall configuration are practically identical for any set of ratios L/X, Y/X and Z/Y. Therefore the generalised design curves presented for the planar-flanged wall configuration may also be used to evaluate the effective slab widths for L-shaped wall configurations if the flange width ratios Z/Y indicated on the curves are halved to correspond to the flange width of the L-shaped walls.

3.8.2 NUMERICAL RESULTS FOR STRESS RESULTANTS

3.8.2.1 General Distribution Pattern

Fig. 3.52, (a) to (e), show the contours of bending moments and shearing forces in a typical floor slab coupling a pair of L-shaped flanged walls subjected to a differential axial wall displacement. The contours indicate clearly that large coupling actions are concentrated around the junction between the flange wall and the web wall on each side of the corridor. At the ends of the wall flanges, the slab actions are lower. These results are in contrast to those obtained for the coupled T-shaped wall configuration described in Section 3.5.2.1, which show concentrations of slab actions at the tip of the flange wall but not at the junction of the walls. The lower slab actions induced near the ends of the flanges in the L-shaped walls reflect the lack of

direct flange wall coupling across the corridor or wall opening. The contours indicate that as usual the significant coupling actions are induced in the corridor area with some actions spreading back a small distance from the corridor edge.

3.8.2.2 Curves For Bending Moment Factor $\bar{M}_x$

To facilitate the calculation of the critical bending moments required for the design of the slab section, curves showing the variation of bending moment factors $\bar{M}_x$ along the critical transverse slab section immediately in front of the flange wall are presented in Fig. 3.53, (a) to (h), for various slab-width and flange-width ratios. It can be seen from the curves that the bending moment distribution on the half of the critical section defined by ξ positive is practically unaffected by the variation of flange width when the ratio L/Y is less than 1.0. Two distinct peaks can be seen in each curve and these occur at the ends of the flange wall. The bending moments at these points are likely to be theoretically singular judging from the shape of the curve, and from the results presented earlier for other flanged wall configurations. By comparing the various sets of curves it is seen that with a constant slab width Y the bending moment factors $\bar{M}_x$ are higher with larger wall opening widths L.

3.8.2.3 Generalised Design Curve For Critical Bending Moment Factors

With a small degree of approximation, the 8 sets of curves for $\bar{M}_x$ presented in Fig. 3.53 may be generalised to a more convenient set of curves shown in Fig. 3.54. The generalised curves show the variation of $\bar{M}_x$ with the normalised distance ξ (= y/L) for various flange width ratios Z/L and may be used to obtain the distribution of $\bar{M}_x$ in a slab of any width by truncating the tail of the appropriate generalised curve at the points corresponding to the actual limits of the slab width.

The generalised set of curves may also be used indirectly to evaluate the effective width of the slab as a check against the value obtained directly from the design curves for Y_e/Y presented earlier. To illustrate the use of the generalised curve for this secondary purpose, a numerical example is now shown.

Example:

It is required to evaluate the effective width of a slab with the following typical dimensions

Y = 6.1m (20 ft), L = 3.05m (10 ft) and X = 15.25m (50 ft)

The flange width ratio Z/L = 0.5

The limits of the slab width are $\xi_1 = -1.0$ and $\xi_2 = +1.0$

The ordinates of the generalised curve for Z/L = 0.5 from $\xi = -1.0$ to $\xi = +1.0$ are tabulated below

$\pm\xi$	0	0·06	0·13	0·25	0·38	0·50	0·63	0·75	0·88	1·0
$\bar{M}_x(-\xi)$	10.8	6.7	5.7	4.7	4.4	4.7	2.6	1.8	1.2	0.8
$\bar{M}_x(+\xi)$	10.8	6.6	4.4	2.9	2.0	1.5	1.2	1.0	0.8	0.6

The area under the curve evaluated from the above results using the trapezoidal rule is, $K_a = 6.14$.

The effective slab width from equation (3.14) is then

$$\frac{Y_e}{Y} = \frac{1}{6(1-\nu^2)} \times \frac{10}{20} \times 6.14 = 0.523$$

The accurate value of Y_e/Y obtained from the design curve in Fig. 3.50 is 0.524.

3.9 COUPLED BOX CORE CONFIGURATION

3.9.1 COMPARISON OF RESULTS WITH THICK WALL CONFIGURATION AND FLANGED WALL CONFIGURATION

The slab in this configuration couples a pair of closed box-shaped core walls (Fig. 3.3(b)). Since the

assumption of beam theory to describe the behaviour of the core disallows local elastic out-of-plane bending of the core walls, the assumed displacements imposed on the coupling slab by a hollow core and a solid wall of similar peripheral dimensions are identical. The coupling stiffness of the slab in each case is therefore similar and the results presented for the thick coupled plane wall configuration in Section 3.4.1.8 are also applicable to the coupled box-core configuration. The design curves and empirical equations presented for the coupled flanged wall (T-shaped) configuration discussed in Sections 3.5.1.2 to 3.5.1.5 may similarly be used for the coupled box-core configuration since the influence of flange width and finite plane-wall thickness or box-core width, have been shown to be essentially similar in the evaluation of the effective slab widths.

3.9.1.1 Influence of Core Opening

Box-cores, particularly those serving as lift shafts, are provided with large openings for access into the core. The presence of large corridor access openings alters the core to an open section with a connecting lintel at each floor. The stiffness of the coupling slab can be expected to be influenced by the core opening to a certain extent depending on the location and size of the opening and on the flexibility of the connecting lintels. It may be expected from the similarity of results obtained for the coupled thick planar wall configuration and for the coupled flanged wall configuration that the core opening located in a side wall (or web wall) will not have any significant influence on the coupling stiffness of the slab. The influence of the core opening in the corridor wall (or flange wall) is investigated in this study.

In the analysis of the slab-wall interaction, it is assumed that the core walls are infinitely rigid in relation to the slab and lintel. Although the lintel is in fact a part of the core wall, in the analysis it is

considered as an integral part of the floor slab connected to the core. In order to keep the finite element analysis of the slab as simple as possible, the lintel is represented by prismatic beam elements which are connected to the plate elements for the slab along their centroidal axes. Although the actual eccentric connection between lintel and slab is not being represented in this way, this should not affect the results for the slab significantly as the action of the slab on the beam is mainly a torsional action in this case.

Values of effective width Y_e/Y have been evaluated for slabs of various aspect ratios Y/X, coupling a pair of square cores with various core opening ratios B/Z and lintel depth ratios D'/Z and with fixed ratios L/X and Z/X. The numerical results which are tabulated in Appendix A3.7 are presented graphically in Fig. 3.55, (a) to (c). These Figures show the variation of Y_e/Y as a function of B/Z for various ratios D'/Z and Y/X. It is seen from the curves that the effective slab width reduces as the core opening size, defined by B/Z and D'/Z, is increased. The influence of core opening is relatively more significant with larger core width ratios Z/Y and is not significant when the core opening width B/Z is less than 0.5. At this value of B/Z the reduction of effective width in the slab due to a full height core opening (D'/Z = 0) is seen to be less than 6% in the worst affected case (Y/X = 0.4). The influence of core opening becomes increasingly more significant when B/Z increases beyond 0.5. With a full core opening (B/Z = 1, D'/Z = 0) the effective width of the worst affected slab is seen to be reduced by about 25% by the presence of the core opening.

3.9.2 DISTRIBUTION OF STRESS RESULTANTS

Fig. 3.56, (a) to (f), and 3.57, (a) to (f), show the distributions of stress resultants in a slab coupling a pair of box cores undergoing unit rotation. By comparing these two sets of diagrams with the corresponding sets for the T-shaped flanged wall configuration, presented in

Section 3.5.2.1 it can be seen that the general patterns of stress-resultant distribution are very similar in the two different configurations, though minor differences between absolute values of stress resultants may be observed from the different scaling factors (or multipliers) for corresponding perspective diagrams. Hence the numerical results for slab actions which have been presented for the coupled T-shaped flanged wall configuration may also be applied in the case of the coupled box-core configuration for practical purposes.

3.10 EFFECT OF ORTHOTROPIC SLAB PROPERTIES

In the elastic analysis of slab coupling, it has been usual practice to regard the floor slab as an isotropic plate. In a practical concrete floor slab, the different steel ratios in two directions impart orthotropic properties to the slab. In other less usual forms of floor construction such as voided slabs, ribbed slabs or pseudo slabs (consisting of precast beams and in situ concrete infill), the orthotropic properties of the floor arise principally from differences in structural geometry of the floor cross-sections. The results which have been obtained assuming isotropic slab properties are, strictly, incorrect when applied to an orthotropic slab. The degree of approximation involved in the application of isotropic slab results to actual floor slabs will depend on the degree of orthotropy present in the slab. An investigation is thus carried out to assess the influence of orthotropic properties on the stiffness and effective width of a coupling slab.

3.10.1 METHOD OF ANALYSIS

The flexural behaviour of an orthotropic plate is governed by four constants D_x, D_y, D_1 and D_{xy}, representing the flexural rigidities in two orthogonal directions, the cross coupling rigidity and the torsional rigidity.[22] In practical cases, these constants can be evaluated

approximately in terms of the material and geometric properties of the orthotropic plate. In applying the finite element method to the analysis of the orthotropic plate, the constants are simply incorporated in the elasticity matrix [D] in the element stiffness calculation and in the stress calculation (cf. Section 2.4.3).

The influence of orthotropic slab properties on the effective coupling slab width is investigated for a slab of aspect ratio Y/X = 0.4, with various wall opening ratios in a plane wall configuration. In the analysis, the flexural rigidity D_x in the direction of wall bending is kept at a constant value of 2.7×10^4 kN-m (2×10^4 kip-ft), corresponding to E = 2.07×10^7 kN/m^2 (4.32×10^5 kip/ft^2), ν = 0.15 and t = 0.25 m (0.8159 ft), while the flexural rigidity D_y is varied to give ratios of D_y/D_x ranging from 1/8 to 8. For reinforced concrete, the cross coupling and torsional rigidities D_1 and D_{xy} may be evaluated in terms of D_x and D_y as[22]

$$D_1 = \nu \sqrt{D_x D_y} \quad \text{and} \quad D_{xy} = \frac{1-\nu}{2} \sqrt{D_x D_y}$$

These expressions are strictly valid only for solid slabs, the usual form of floor construction in cross wall buildings, but serve the present purpose of assessing the effects of orthotropy.

3.10.2 DISCUSSION OF RESULTS

The effective widths Y_e/Y obtained from the finite element analyses for the various cases are shown in Table 3.11. The effective width Y_e/Y is seen to increase with the ratio of transverse to longitudinal flexural rigidity D_y/D_x. The influence of orthotropy is more significant with smaller wall opening ratios.

In order to appreciate the significance of the results obtained, it is necessary to have an idea of the likely range of flexural rigidity ratios found in practice. Fig. 3.58 shows approximate values of D_x/D_y for four common forms of orthotropic slab with various geometric

proportions. These values have been evaluated using approximate formulae given in various references.[22,57,58] When calculating D_y for the solid slab, the transverse steel (distribution steel) has been neglected for convenience. For the other three cases, the effects of steel reinforcements have been completely disregarded in the calculation of D_x and D_y.

It is seen that for solid slabs and voided slabs, D_x/D_y is unlikely to exceed a value of 1.5, and for such cases the results in Table 3.11 indicate that the effective widths calculated assuming isotropic and orthotropic properties will not differ by more than 10%. For pseudo-slabs, the likely range of D_x/D_y is from 2 to 5. The effective widths calculated assuming isotropic behaviour for such slabs could be underestimated or overestimated by 10 to 40% depending on the direction of orthotropy and the geometric proportions of the slab. For one-way ribbed slabs, the ratio of D_x/D_y is unlikely to be less than 10. Errors in the calculation of effective widths for such cases could thus be quite large if isotropic slab behaviour is assumed.

Errors in the calculation of effective width usually result in much smaller errors in the estimation of the lateral stiffness of the coupled wall system. With the usual form of solid slab construction for cross-wall structures, it appears that the effects of orthotropy due to different steel ratios in the principal directions, could be safely disregarded in the calculation of effective slab width. In unusual cases where effects of orthotropy are likely to be significant in the calculation of effective widths, Table 3.11 could be used in conjunction with results obtained for isotropic slabs, to give a better estimate of the correct effective widths.

3.11 EFFECT OF A CRITICAL TRANSVERSE CRACK IN SLAB COUPLING A PAIR OF PLANE WALLS

Elastic studies of wall slab interaction have shown a severe concentration of slab stresses, induced by

coupling action, around the coupled ends of plane walls. Unless the slab has been adequately reinforced locally, these extremely large stresses will result in local cracking of the concrete with yielding or complete failure of the reinforcing steel. This will lead to a significant reduction in the overall coupling stiffness of the slab, since flexural resistance is lost at the most effective part of the slab. Cracking, on the other hand, may cause a re-distribution of coupling action to other parts of the slab and bring into active participation those areas that were previously ineffective, and so there may be some compensating effect on the loss of coupling stiffness at the crack. In this section, the influence of a transverse crack on the coupling performance of a slab in a plane wall configuration is investigated. The crack in the slab is assumed to be located at the inner edge of the wall.

3.11.1 METHOD OF ANALYSIS

The crack in a plate can be represented in the finite element discretisation by assigning two nodes to each mesh point on the line of the crack to define the dislocated element edges on either side of the crack. When the crack extends over a part of the coupling slab panel the nodal representation of the crack results in an irregular nodal numbering pattern over part of the slab. This means that every time the length of crack is changed, a different nodal pattern is created requiring a substantially different set of input data for the computer analysis. In a parameter study concerned about the effects of various crack lengths on the slab performance, the amount of effort required to prepare and verify new input data for every case analysed would be substantial. To minimise the amount of data preparation required for the investigation, the crack was imagined initially to extend across the whole slab width so that the nodal definition of imaginary crack resulted in a regular nodal numbering

pattern throughout the plate being discretised. Then by introducing a fictitious link element to connect each pair of nodes across the imaginary crack and by giving the fictitious link elements either a zero stiffness or a very large stiffness, a cracked or an uncracked section could be simulated at the link position.

The stiffness properties of the fictitious link element was defined by the element stiffness matrix

$$[k_l] = \begin{bmatrix} k_w & 0 & 0 & -k_w & 0 & 0 \\ & k_x & 0 & 0 & -k_x & 0 \\ & & k_y & 0 & 0 & -k_y \\ & & & k_w & 0 & 0 \\ & \text{symmetric} & & & k_x & 0 \\ & & & & & k_y \end{bmatrix}$$

in which k_w, k_x and k_y are arbitrary stiffness terms set either to zero or to large number to prevent or to allow force transfer across the imaginary crack. It was recognised that using too large a number for the stiffness terms for the rigid link could lead to numerical instability in the finite element solution, while by using an insufficiently large number, the full rigid connection may not be effectively simulated at an uncracked section. It was found by comparing results obtained using fictitious link elements against results obtained without the use of link elements that the smallest number required for the stiffness terms in $[k_l]$ to simulate an uncracked section was 10^6. It was also found that using a number as large as 10^{12} for the rigid link stiffness terms did not cause any numerical difficulty with the solution. For the parameter study a value of 10^{10} was used for the stiffness terms to simulate a rigid link.

3.11.2 DISCUSSION OF RESULTS

The influence of crack length ratio λ/Y on the coupling stiffness and effective width of slab has been

investigated for a slab with an aspect ratio Y/X = 0.4 and various wall opening ratios. The results obtained are given in Appendix A3.8. Values of rotational stiffness factor K' for the cracked slab have been expressed as a ratio of the 'uncracked' value K and are plotted in Fig. 3.59(a) against the crack length ratio λ/Y. It is seen from the results that the reduction in slab stiffness due to the presence of a crack is more significant for slabs with smaller wall opening ratios. The extension of the crack produces a larger loss of slab stiffness in the earlier stages. At the stage where the crack extends over 10% of the slab width ($\lambda/Y = 0.1$), the stiffness of the slab with L/X = 0.1 has been reduced by 40%. For the slab with L/X = 0.4 the corresponding reduction is only 15%.

The influence of a crack on the distribution of longitudinal bending moment factor $\bar{M}_x$ at the critical transverse section is illustrated in Fig. 3.59(b) for the slab with Y/X = 0.4 and L/X = 0.2. The curves for various crack length ratios show clearly the concentration of bending action around the crack tip. It is a well known fact that the bending stress resultant at the crack tip in the plate is theoretically infinite, but in the finite element solution this stress resultant has been evaluated to a finite value which has to be interpreted in the manner discussed in section 3.4.2.3. It is seen from the curves that the distribution of $\bar{M}_x$ in the uncracked portion of the slab is affected very little by the presence of a crack except around the crack tip.

3.12 COMPARISON OF RESULTS

In this section the theoretical results obtained by the author are compared with various theoretical and experimental results obtained by other investigators.

3.12.1 COMPARISON BETWEEN THEORETICAL RESULTS

3.12.1.1 Effective Slab Width in Plane Wall Configuration

The results for the effective slab width obtained by the author using the finite element method (RB12 element) and the empirical equations are compared, in Fig. 3.60(a) and (b), with the results obtained by other investigators using finite element and finite difference techniques. All the results being compared are based on coupled plane walls of zero thickness.

The results of Black, Pulmano and Kabaila[6] were obtained using Veubeke's conforming quadrilateral element[34] (QB16). Peterssons results[5] were obtained using a 'mixed' rectangular finite element with corner deflection and edge moments as unknown variables. The results of Tso and Mahmoud[9] were obtained using a partially conforming triangular element with deflections and slopes as corner variables. Qadeer and Stafford Smith's results[2] were obtained by a finite difference solution.

It can be seen from the comparison that the author's empirical and finite element results lie between Petersson's results and the results of Black et al. Tso and Mahmoud's results, which are available only for the case of Y/X = 0.25, are in close agreement with the author's results. The finite difference results appear to underestimate the effective widths, given by the various finite element results. In extreme cases, the finite difference results are as much as 30% below the author's finite element results. One possible explanation for the significantly lower finite difference results is that in the finite difference solution, compatibility of slope in the direction of wall rotation, at the wall/slab junction, has not been enforced and this could result in additional flexibility at the coupled edges of the wall.

3.12.1.2 Effective Slab Width in Flanged Wall Configuration

The author's finite element results for the effective width of slabs coupling walls with two flanges, one flange

and no flanges are compared in Fig. 3.61 with the corresponding results interpolated from the design curves presented by Tso and Mahmoud.[9] The results being compared are based on configurations with slab aspect ratio Y/X = 0.4, flange width ratio Z/Y = 0.5 and wall thickness ratio h/Y = 0.05. It is seen from the curves that the author's results are in close agreement with Tso and Mahmoud's results for all three cases considered.

In fig. 3.62, (a)-(c), the author's empirical results for flanged wall configurations with various flange width ratios are compared with the results of Tso and Mahmoud.[9] The plane wall configuration has been included as the limiting case of the flanged wall configuration when the flange width is reduced to the thickness of the cross-wall. It can be seen from the curves that the empirical results are generally in very close agreement with the results of Tso and Mahmoud in all cases. Where discrepancies between the empirical and the finite element results are largest (Y/X = 0.3, L/X = 0.05, Z/X = 0.2 and 0.1), Tso and Mahmoud's results are seen to be more suspect than the empirical results because when L/X is reduced to zero the effective slab width should reduce to the width of the wall flange, which is shown by the empirical results but not so by Tso and Mahmoud's results. The cases considered cover a very wide range of wall and slab geometric ratios, but the accuracy of the empirical equations is shown to be consistent throughout.

3.12.1.3 Effective Slab Width in Thick Wall or Box Core Configurations

Values of effective width calculated by the empirical equations for slabs which couple plane walls of finite thickness or box cores are compared with the finite element results obtained by Black, Pulmano and Kabaila,[6] in Fig. 3.63, (a)-(c). It is seen that the empirical results are in reasonably close agreement with the finite element results, but are generally lower. The latter results can be expected to overestimate the correct effective widths

by a few per cent due to the use of rather coarse meshes for the discretisation of the slabs. For the particular case of Y/X = 0.5, Z/W = 0.5, and L/X = 0.2, which has been analysed by the author, as a check, using the same element that was used by Black et al., but with a very fine element sub-division of the slab (120 elements, 695 degrees of freedom), the result given by Black et al. was found to be 4½% higher than the author's finite element result (shown by a cross in Fig. 3.63(a)). The empirical result for this case is about 3% below the more accurate finite element result.

3.12.2 COMPARISON BETWEEN FINITE ELEMENT RESULTS AND EXPERIMENTAL RESULTS

3.12.2.1 Effective Slab Width in Plane Wall Configuration

Fig. 3.64(a) shows a comparison of the theoretical values of effective slab width in plane wall configuration, with experimental results obtained by Petersson,[5] El-Hag,[40] El-Buluk[8] and by the author. All the experimental results were obtained from tests on small scale perspex slab models with steel sections attached to simulate the coupled walls. The method of loading the slab model and monitoring the response, however, differed between various investigations. In El-Hag's and El-Buluk's tests the slab was attached to the tops of the wall sections which were pivoted at their bases. When the slab was displaced horizontally by an applied load the walls rotated about their bases and induced bending in the slab (Fig. 3.64(b)). In Petersson's tests a pair of slabs were sandwiched between steel wall-pieces at their ends which were displaced axially by applying opposite co-axial forces to the wall sections (Fig. 3.64(c)). In the author's tests, which are described more fully in Chapter 10, the half slab section to which a steel wall section was attached, was simply supported at the external edge of the wall and at the slab edge corresponding to the corridor centre-line. The wall section was rotated about its supported end by

an applied vertical load at its inner edge (Fig. 3.64(d)).

The material constants for the perspex in Petersson's models were $E = 2500\ N/mm^2$ and $\nu = 0.36$, while those for the other investigations were $E = 2900\ N/mm^2$ and $\nu = 0.35$. The latter sets of values were also used in the finite element analysis from which the theoretical results were obtained.

The wall thickness to slab width ratio, h/Y, varied between 0.05 and 0.2 in Petersson's models, but in the other models this ratio was kept at a constant value of 0.025. For the theoretical investigation, the effect of finite wall thickness was disregarded.

It is seen from the comparison that Petersson's and the author's experimental results are in close agreement with the theoretical results, but El-Hag's and El-Buluk's experimental results are significantly lower than the theoretical results, especially with small L/Y ratios. If the influence of finite wall thickness were considered in the theoretical analyses, all the experimental results would appear to be lower than the theoretical results. With large L/Y ratios, Petersson's and the author's experimental results are slightly higher than the theoretical results, indicating the stiffening effect of finite wall thickness not included in the theoretical results, but with very small ratios L/Y, the experimental results are lower than the theoretical results, and may be due to the flexibility effects produced by transverse shear deformation and local elastic deformation of the slab under the heavily loaded wall tip. In the case of El-Hag's and El-Buluk's results, additional flexibility effects could be produced by slackness of joints in the apparatus and the difficulty of achieving a tight fit of the slab between the steel wall shapes. Within the limits of experimental errors, reasonably good agreement is obtained between the theoretical and experimental results, generally.

3.12.2.2 Distribution of Slab Moments in Plane Wall Configuration

The distributions of bending stresses in a slab coupling a pair of plane walls, evaluated by the finite element method are compared with the experimental results obtained by El-Buluk,[8] in Fig. 3.65, (a) and (b). The experimental results were evaluated by strain measurements on a small scale perspex slab model attached to steel sections which simulated the coupled walls. The theoretical results were obtained using the RB12 element for the finite element analysis. The finite thickness of the wall was disregarded and the wall represented as a line of nodes in the idealisation of the slab.

It can be seen from the comparison that the theoretical and experimental results for M_x and M_y are generally in good agreement except at points close to the tip of the wall where significant differences between the two results can be observed. The theoretical distribution of M_x shows two distinct peaks in the bending moment curve a small distance on either side of the wall line. The location of the strain gauges unfortunately did not permit the evaluation of bending moments at these critical positions for comparison with the theoretical results. However, accepting that the experimental values do not vary abruptly between gauge points, reasonably good agreement is obtained between theoretical and experimental results, in respect of the nett moment distributed over the middle portion of the slab section.

The theoretical distribution of the transverse bending moment M_y shows a significantly higher peak in the bending moment curve than the experimental results, at the point on the wall line. This discrepancy arises principally through the idealisation of the wall as a line in the theoretical analysis. The finite wall thickness, in effect, provides a certain amount of transverse stiffening to the slab and so the transverse bending moment measured at the point in question is expected to be lower than the theoretical value.

3.12.2.3 Distribution of Slab Moments in L-Shaped Wall Configuration

The comparison between the author's finite element results with El-Buluk's experimental results for bending moment distributions in a slab coupling a pair of L-shaped flanged walls, is shown by Fig. 3.66, (a) and (b). The experimental results were evaluated by the same procedure described for the plane wall configuration.

It is seen that the theoretical and experimental results for the longitudinal and transverse bending moments, M_x and M_y respectively generally agree reasonably well. The experimental moments on the side of the slab without the wall flange (Y-negative side) are in very close agreement with the theoretical values, but at certain points in front of the flange on the other side of the slab, the experimental moments are distinctly lower than the theoretical results and appear to be influenced by the flexibility of the wall flange in the model.

3.12.2.4 Slab Displacement Patterns

Fig. 3.67, ((a)-(c)) to 3.70 ((a)-(c)) show contours of deflection and slopes in slabs coupling walls of various shapes. The contours were produced by computer from results evaluated by the finite element method. The contours of slopes θ_x and θ_y for the various wall configurations have been compared with Moirĕ fringe patterns obtained by El-Hag[40] from experiments on perspex models, and a close resemblance between the theoretical and experimental contour patterns has been noted in every case. The relevant Moirĕ fringe patterns can be found in El-Hag's thesis [40] (pages 169-172).

3.13 EFFECT OF SLAB COUPLING ON OVERALL BEHAVIOUR

The lateral load behaviour of a pair of shear walls coupled by floor slabs can be conveniently assessed using the continuous connection method of analysis, which has been produced by assuming that the discrete system of connections formed by lintel beams or floor slabs may be

replaced by an equivalent continuous medium. Based on this theory, explicit expressions for evaluating the deflections and stresses in a coupled wall system, subjected to standard forms of loading, have been derived.[59,60] These expressions are characterised by the parameter αH, which has been found useful for describing the overall behaviour of the coupled-wall system. A study by Marshall[61] has indicated that when αH exceeds 13, the walls are effectively coupled and behave essentially as a homogeneous solid cantilever. When αH is less than 0.8 coupling is ineffective and the walls behave as two independent cantilevers. For αH between these limits, the behaviour of the coupled walls depends on the stiffness of the connecting medium.

Fig. 3.71, (a) to (d), show the variation of the characteristic parameter αH with the wall opening ratio L/X, for four wall configurations. In order to illustrate the effectiveness of slab coupling, critical wall deflections and stresses, based on an effective width of slab acting as the coupling medium, have been expressed as ratios of corresponding quantities calculated assuming that the walls behave as independent cantilevers. The variations of the coupled/uncoupled ratios for the maximum deflection δ at the top, and maximum tensile and compressive stresses, σ_A and σ_B, at the bottom of the walls, with the wall opening ratios L/X, have been included in the Figures to illustrate the correspondence between these ratios and αH. All the results shown are based on a 20-storeyed building of 61 m (200 ft) height and 15.25 m (50 ft) depth with cross walls at 6.1 m (20 ft) centres. The wall flanges are of 3.05 m (10 ft) width, and wall and slab thicknesses are 305 mm (12 in.) and 228 mm (9 in.) respectively. The wind loading on the structure is assumed to be uniformly distributed.

It is seen from the various diagrams that the effectiveness of slab coupling varies with the shape of the walls, coupling being relatively more effective with plane walls than with flanged walls. The value of αH

is seen to be less than 3 when L/X is larger than 0.2 and varies between 5 and 6 when L/X is 0.1, generally. Pearce and Matthews,[62] in a report to the Department of the Environment, have suggested that when αH is less than 4, coupling could be ignored and the walls designed as separate walls. The results from the examples considered in this section certainly do not substantiate this contention, for with αH slightly less than 4, the coupling effect is seen to reduce the maximum deflection δ and the maximum stress σ_B at the inner edge of the wall by 60 to 70 per cent, depending on wall configuration. Even with a much smaller value of αH, say $\alpha H = 1.5$, the results in Fig. 3.71, (a) to (d), indicate that the maximum wall deflection δ is reduced by at least 40 per cent and the maximum wall stress σ_B by at least 30 per cent in any of the buildings considered. It is seen that throughout the range of wall-opening ratios considered, significant coupling of the walls is provided by the floor slab.

3.14 CONCLUSIONS

A numerical investigation based on the finite element method has been carried out to determine the variation of effective slab width and distribution of stress resultants with various structural parameters. The slab overhang, the absolute wall length and the external wall flanges have been shown to have negligible effect on the effective slab widths for practical cross-wall structures. The effective slab width is influenced essentially by the corridor to slab width ratio and also by the wall thickness to slab width ratio in the case of plane walls, or the flange width to slab width ratio in the case of flanged walls (including box cores).

Design curves have been presented to enable the rapid evaluation of effective slab widths in practical situations. Simple empirical equations have also been suggested for this purpose when the walls being coupled are similar in shape. Contour diagrams and curves showing the sectional

variation of critical bending moment factors have been presented to enable the rapid evaluation of slab stresses induced by coupling action. A design method has been suggested for checking against punching shear failure in the coupling slab.

The accuracy of the numerical results have been confirmed by comparing them with theoretical and experimental results from other investigations.

The influence of orthotropic slab properties on the coupling stiffness of the slab has been assessed. The usual assumption of isotropic properties for reinforced concrete coupling slabs is not likely to result in significant errors in the evaluation of slab stiffness or effective width.

The presence of slab cracks across the inner ends of the coupled wall has been shown to result in a substantial reduction in the coupling stiffness of the slab, especially when the wall opening ratio is small.

The effectiveness of slab coupling on the overall performance of the coupled wall system has been shown by worked examples on typical cross-wall buildings.

TABLE 3.1 CONVERGENCE CHARACTERISTICS OF DIFFERENT ELEMENTS

(a) Slab Coupling Plane Walls
(L/X = 0.4, Y/X = 0.4)

Element Type	Effective Width Y_e/Y				
	Mesh 1 (1 x 2)	Mesh 2 (2 x 4)	Mesh 3 (4 x 8)	Mesh 4 (8 x 16)	Richardson's Extrapolation (2,4,8)
TB9	0.6418	0.6322	0.6158	0.6111	0.6087
RB12	0.6636	0.6279	0.6160	0.6122	0.6098
QB16	0.7327	0.6663	0.6374	0.6234	0.6097
TB18	0.9225	0.7563	0.6780	0.6427	0.6100
RB24	0.8485	0.7164	0.6603	0.6344	0.6099

(b) Slab Coupling Flanged Walls
(L/X = 0.4, Y/X = 0.4, Z/Y = 0.5)

Element Type	Effective Width Y_e/Y				
	Mesh 1 (1 x 2)	Mesh 2 (2 x 4)	Mesh 3 (4 x 8)	Mesh 4 (8 x 16)	Richardson's Extrapolation (2,4,8)
TB9		0.9308	0.9149	0.9035	0.8898
RB12		0.9227	0.9053	0.8975	0.8903
QB16		0.9349	0.9119	0.9014	0.8916
TB18		1.0565	0.9743	0.9335	0.8929
RB24		1.0178	0.9547	0.9236	0.8928

TABLE 3.2 COMPUTING TIMES* IN SECONDS FOR DIFFERENT ELEMENT TYPES IN ANALYSIS OF SLAB COUPLING PLANE WALLS

(a) Mesh 3 - (4 x 8 mesh)

Program Function	Element Type				
	TB9	RB12	QB16	TB18	RB24
Input Data	2	1	2	2	2
Form Elem. Stiff. Mat.	1	1	5	52	35
Assem. Struct. Stiff. Mat.	2	1	2	3	3
Solve Equations	3	3	7	16	16
Calculate Stresses	4	3	8	8	6
Total Time (sec)	12	9	24	81	62

(b) Mesh 4 - (8 x 16 mesh)

Program Function	Element Type				
	TB9	RB12	QB16	TB18	RB24
Input Data	4	2	4	4	3
Form Elem. Stiff. Mat.	1	1	5	51	35
Assem. Struct. Stiff. Mat.	5	5	10	16	15
Solve Equations	21	22	69	146	146
Calculate Stresses	12	8	14	19	16
Total Time (sec)	43	38	102	236	215

*Mill Time on ICL 1904S Computer

TABLE 3.3 EFFECT OF OVERHANG RATIO C/X ON STIFFNESS FACTOR K AND EFFECTIVE WIDTH Y_e/Y

(a) Y/X = 0.4

L/X		C/X			
		0.0	0.04	0.08	0.12
0.2	K	41.6170	41.6188	41.6194	41.6196
	Y_e/Y	0.3942	0.3942	0.3942	0.3942
0.4	K	11.0338	11.0385	11.0404	11.0412
	Y_e/Y	0.6143	0.6146	0.6147	0.6147
0.6	K	5.0187	5.0305	5.0375	5.0404
	Y_e/Y	0.7220	0.7237	0.7247	0.7251

(b) L/X = 0.6

Y/X		C/X			
		0.0	0.04	0.08	0.12
0.4	K	5.0187	5.0305	5.0375	5.0404
	Y_e/Y	0.7220	0.7237	0.7247	0.7251
0.5	K	6.2011	6.3116	6.3524	6.3723
	Y_e/Y	0.5947	0.6053	0.6092	0.6112
0.8	K	6.8263	7.0059	7.0965	7.1435
	Y_e/Y	0.4910	0.5039	0.5105	0.5138

TABLE 3.4 EFFECT OF SLAB WIDTH Y/X ON EFFECTIVE SLAB WIDTH Y_e/X

Y/X \ L/X	Effective Width Y_e/X					
	0.1	0.2	0.3	0.4	0.5	0.6
0.1	0.0616	0.0788	0.0851	0.0893	0.0914	0.0935
0.2	0.0781	0.1216	0.1437	0.1567	0.1648	0.1710
0.3	0.0840	0.1447	0.1829	0.2075	0.2238	0.2358
0.4	0.0870	0.1569	0.2080	0.2440	0.2696	0.2879
0.5	0.0891	0.1641	0.2240	0.2697	0.3039	0.3280
0.6	0.0907	0.1687	0.2345	0.2874	0.3284	0.3572
0.7	0.0921	0.1719	0.2414	0.2993	0.3453	0.3774
0.8	0.0934	0.1742	0.2463	0.3077	0.3572	0.3918
1.0	0.0936	0.1757	0.2504	0.3154	0.3688	0.4061

TABLE 3.5 COMPARISON BETWEEN EMPIRICAL AND FINITE ELEMENT RESULTS FOR THICK WALL CONFIGURATION

L/X	h/Y	Y'/Y	L/Y'	Y_e/Y Empirical	Y_e/Y F.Element	Percentage Difference
0.1	0.000	1.000	0.250	0.2250	0.2175	+3.45%
	0.125	0.875	0.286	0.3464	0.3405	+1.73%
	0.250	0.750	0.333	0.4667	0.4656	+0.24%
	0.375	0.625	0.400	0.5850	0.5891	-0.70%
	0.500	0.500	0.500	0.7000	0.7099	-1.39%
	0.750	0.250	1.000	0.9000	0.9271	-2.92%
0.4	0.000	1.000	1.000	0.6000	0.6101	-1.66%
	0.125	0.875	1.143	0.6938	0.7031	-1.32%
	0.250	0.750	1.333	0.7750	0.7825	-0.96%
	0.375	0.625	1.600	0.8438	0.8523	-1.00%
	0.500	0.500	2.000	0.9000	0.9109	-1.20%
	0.750	0.250	4.000	0.9750	0.9955	-2.06%

TABLE 3.6 EFFECTIVE WIDTH OF SLAB FOR END BAY OF COUPLED PLANE WALL CONFIGURATION

Effective Width Y_e/Y					Wall Stiff-ness
Y/X \ L/X	0.1	0.2	0.4	0.6	
0.2	0.1780	0.2807	0.3699	0.4024	Infinite Stiffness
0.4	0.0987	0.1764	0.2764	0.3298	
0.6	0.0692	0.1259	0.2131	0.2654	
0.8	0.0542	0.0978	0.1699	0.2151	
0.2	0.1653	0.2708	0.3608	0.4006	305 mm (12 in.) thick wall
0.4	0.0921	0.1685	0.2663	0.3208	
0.6	0.0651	0.1204	0.2046	0.2568	
0.8	0.0514	0.0937	0.1630	0.2027	

TABLE 3.7 COMPARISON OF EFFECTIVE WIDTHS Y_e/Y BETWEEN EXTERNAL FLANGED WALL CONFIGURATION AND PLANE WALL CONFIGURATION

		Plane Walls	External Flanged Walls	
Y/X	Z/Y / L/X	0.000	0.375	0.750
0.2	0.1	0.3903	0.3903	0.3903
	0.2	0.6082	0.6082	0.6082
	0.4	0.7836	0.7836	0.7836
	0.6	0.8550	0.8550	0.8552
0.6	0.1	0.1511	0.1511	0.1512
	0.2	0.2812	0.2817	0.2819
	0.4	0.4790	0.4836	0.4849
	0.6	0.5953	0.6149	0.6189

TABLE 3.8 COMPARISON BETWEEN EMPIRICAL AND FINITE ELEMENT RESULTS FOR FLANGED WALL CONFIGURATION

L/X	Z/Y	Y_e/Y Empirical	Y_e/Y F.Element	Percentage Difference
0.1	0.125	0.3464	0.3388	+2.24
	0.250	0.4667	0.4603	+1.39
	0.375	0.5850	0.5804	+0.79
	0.500	0.7000	0.6985	+0.21
	0.750	0.9000	0.9176	-1.92
0.4	0.125	0.6938	0.6950	-0.17
	0.250	0.7750	0.7666	+1.10
	0.375	0.8438	0.8325	+1.36
	0.500	0.9000	0.8918	+0.92
	0.750	0.9750	0.9906	-1.57

TABLE 3.9 EFFECTIVE WIDTH OF SLAB FOR COUPLED FLANGED WALLS WITH UNEQUAL FLANGES

Y/X = 0.6, L/X = 0.4

Z_2/Y \ Z_1/Y	0	0.083	0.167	0.250	0.333
0	0.4790				
0.083	0.5089	0.5462			
0.167	0.5362	0.5773	0.6112		
0.250	0.5609	0.6048	0.6413	0.6732	
0.333	0.5793	0.6321	0.6696	0.7024	0.7312

TABLE 3.10 COMPARISON BETWEEN EMPIRICAL AND FINITE ELEMENT RESULTS FOR COUPLED FLANGED WALLS WITH UNEQUAL FLANGES

Y/X = 0.6, L/X = 0.4

Z_1/Y	Z_2/Y	Values of Y_e/Y		Percentage Difference
		Empirical Method	Finite Element	
0.083	0.167	0.578	0.577	+0.17
0.083	0.250	0.606	0.605	+0.17
0.083	0.333	0.633	0.632	+0.16
0.167	0.250	0.642	0.641	+0.16
0.167	0.333	0.675	0.670	+0.75
0.250	0.333	0.700	0.702	-0.28

TABLE 3.11 EFFECTIVE WIDTH OF SLAB Y_e/Y FOR VARIOUS ORTHOTROPIC RATIOS D_y/D_x

Plane Wall Configuration, Y/X = 0.4

L/X \ D_y/D_x	$\frac{1}{8}$	$\frac{1}{4}$	$\frac{1}{2}$	1	2	4	8
0.1	0.1363	0.1593	0.1862	0.2175	0.2535	0.2944	0.3401
0.2	0.2537	0.2950	0.3410	0.3942	0.4447	0.4998	0.5545
0.4	0.4437	0.5019	0.5593	0.6140	0.6647	0.7105	0.7514

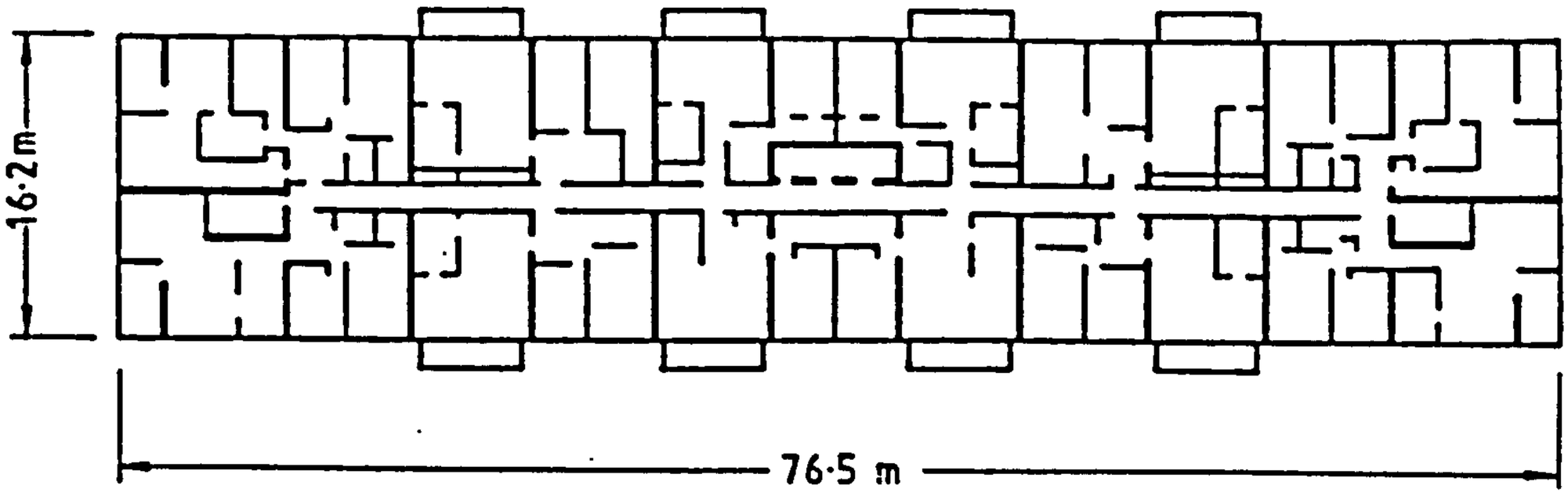

Fig. 3.1 Typical Floor Plan of Apartment Building

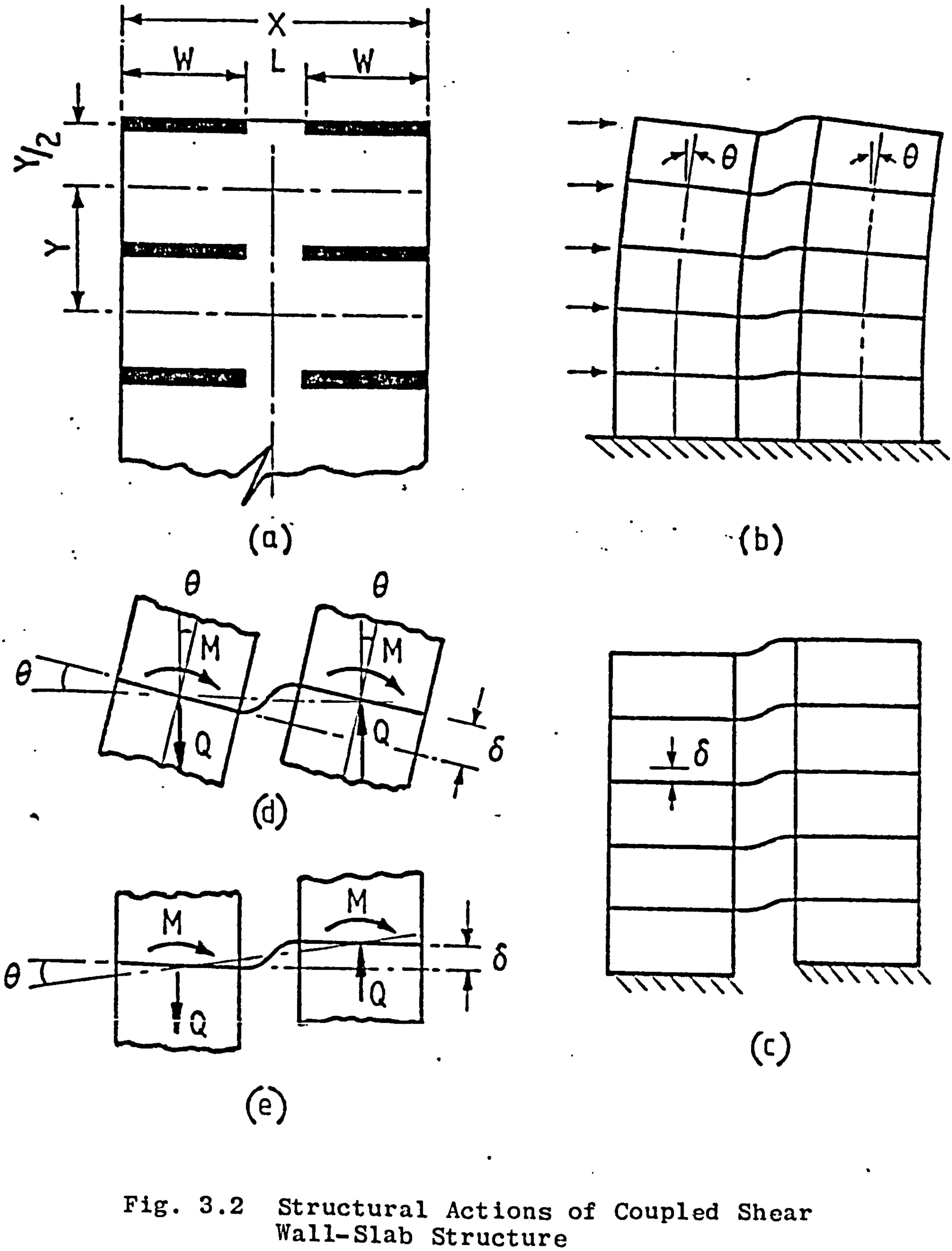

Fig. 3.2 Structural Actions of Coupled Shear Wall-Slab Structure

Unequal Flanged Walls

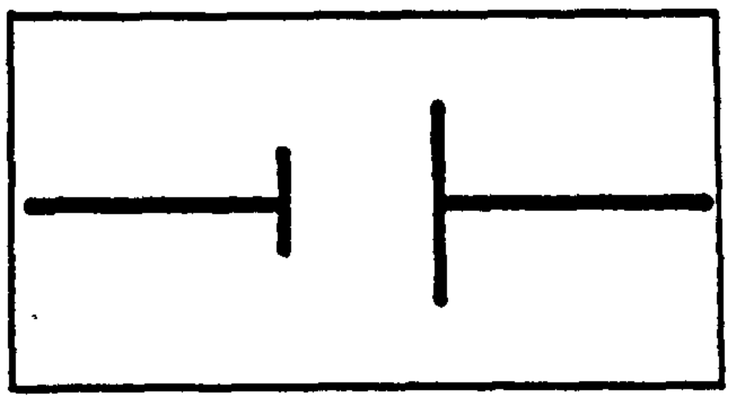

(f)

Box Cores with Openings

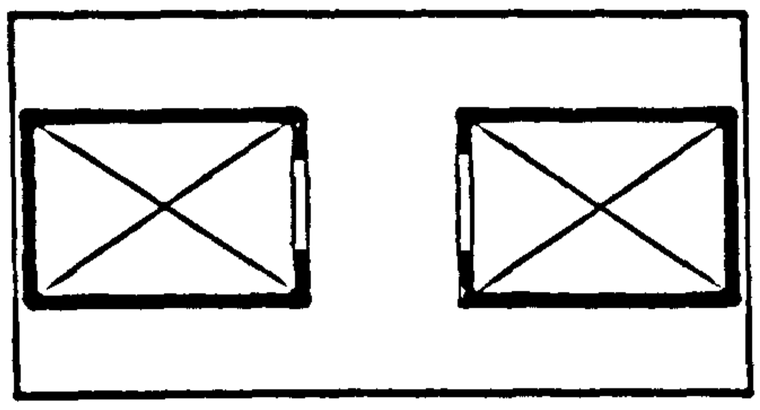

(l)

Thin Planar - Flanged Walls

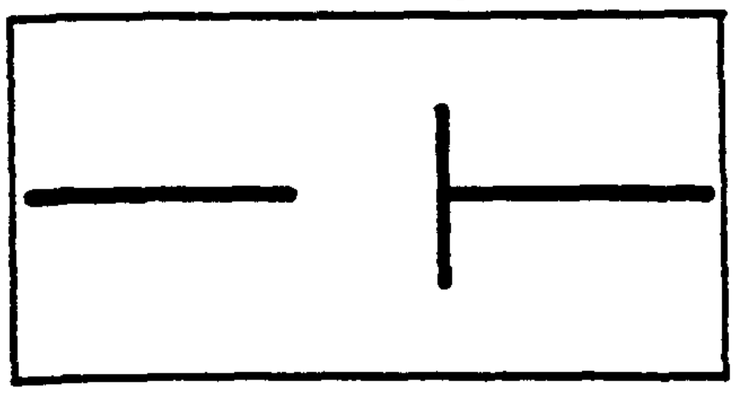

(e)

L - Shaped Flanged Walls
(Offset Flanges, In-line Webs)

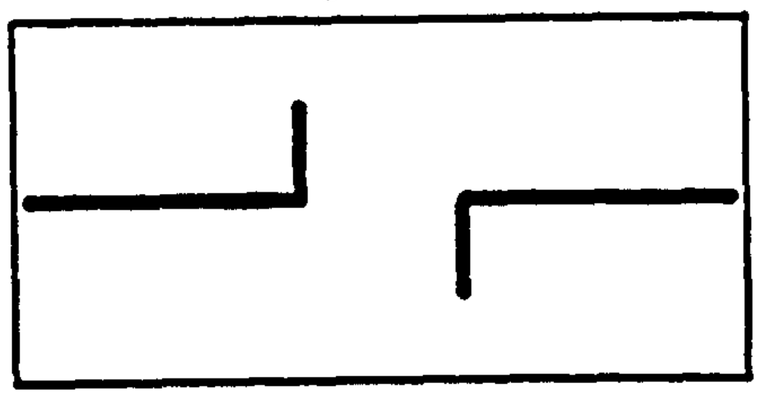

(k)

Internal Flanged Walls

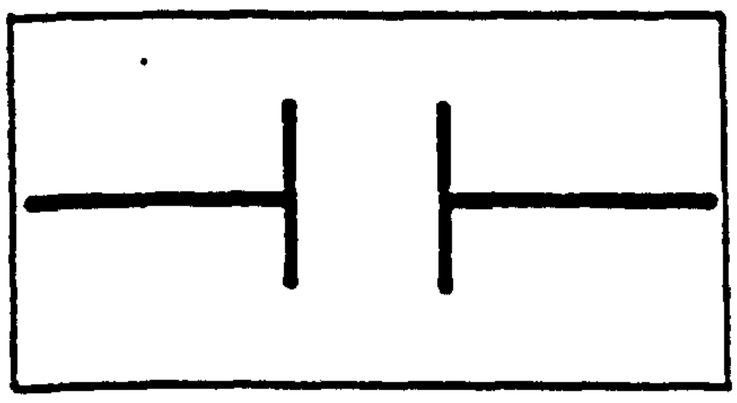

(d)

L - Shaped Flanged Walls
(Opposing Flanges, Off-line Webs)

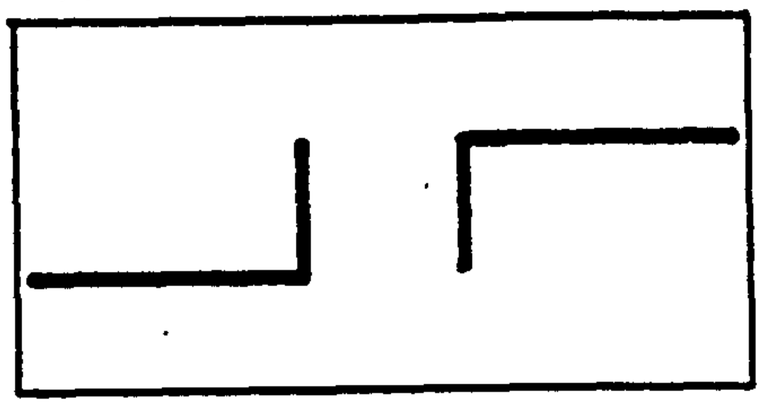

(j)

External Flanged Walls

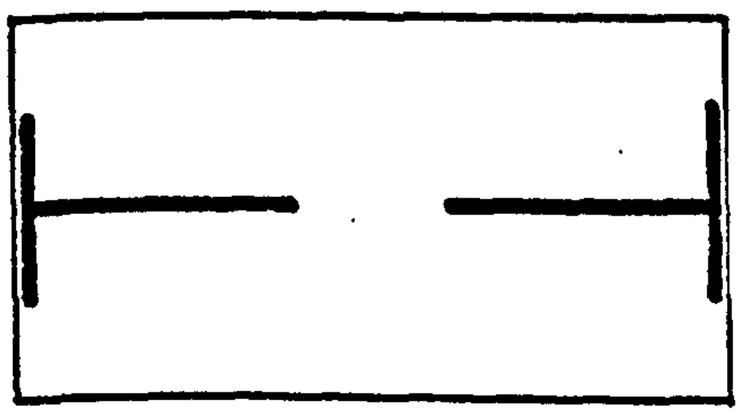

(c)

L- Shaped Flanged Walls
(Opposing Flanges, In-line Webs)

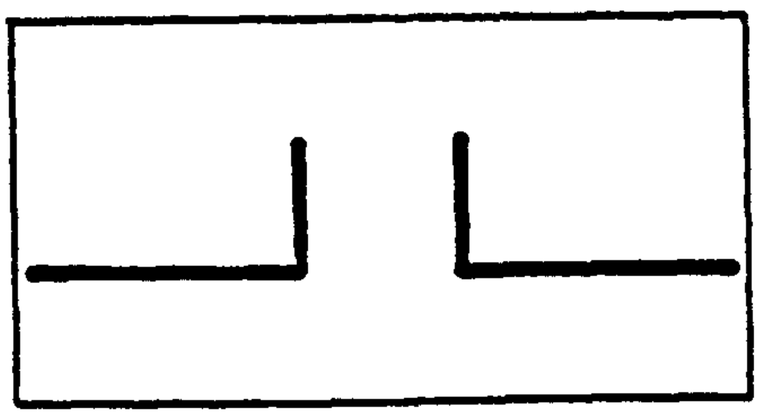

(i)

Thick Planar Walls
or Box Cores

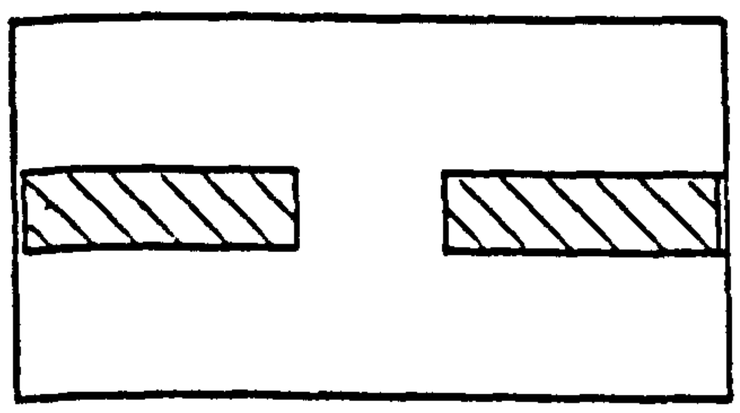

(b)

Thick Planar - Flanged Walls
or Box Core - Flanged Walls

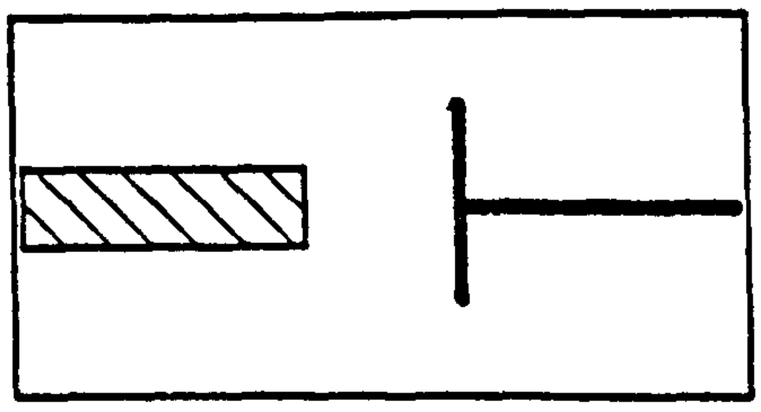

(h)

Thin Planar Walls

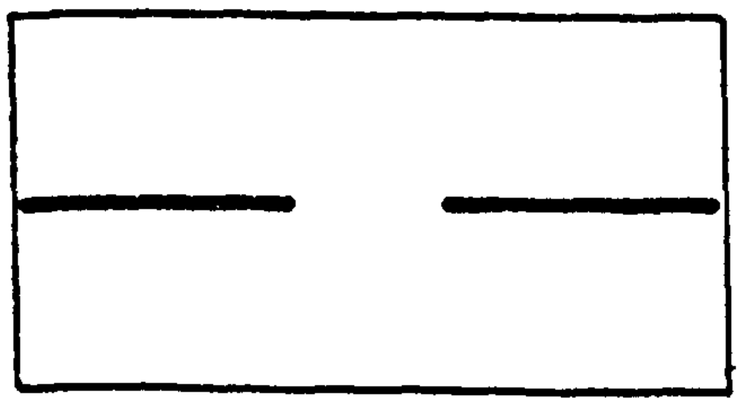

(a)

Unequal Thick Planar Walls
or Unequal Box Cores

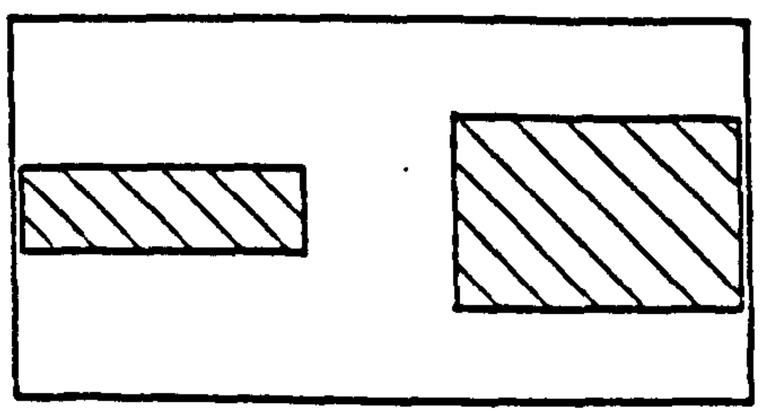

(g)

Fig. 3.3 Coupled Shear Wall Configurations

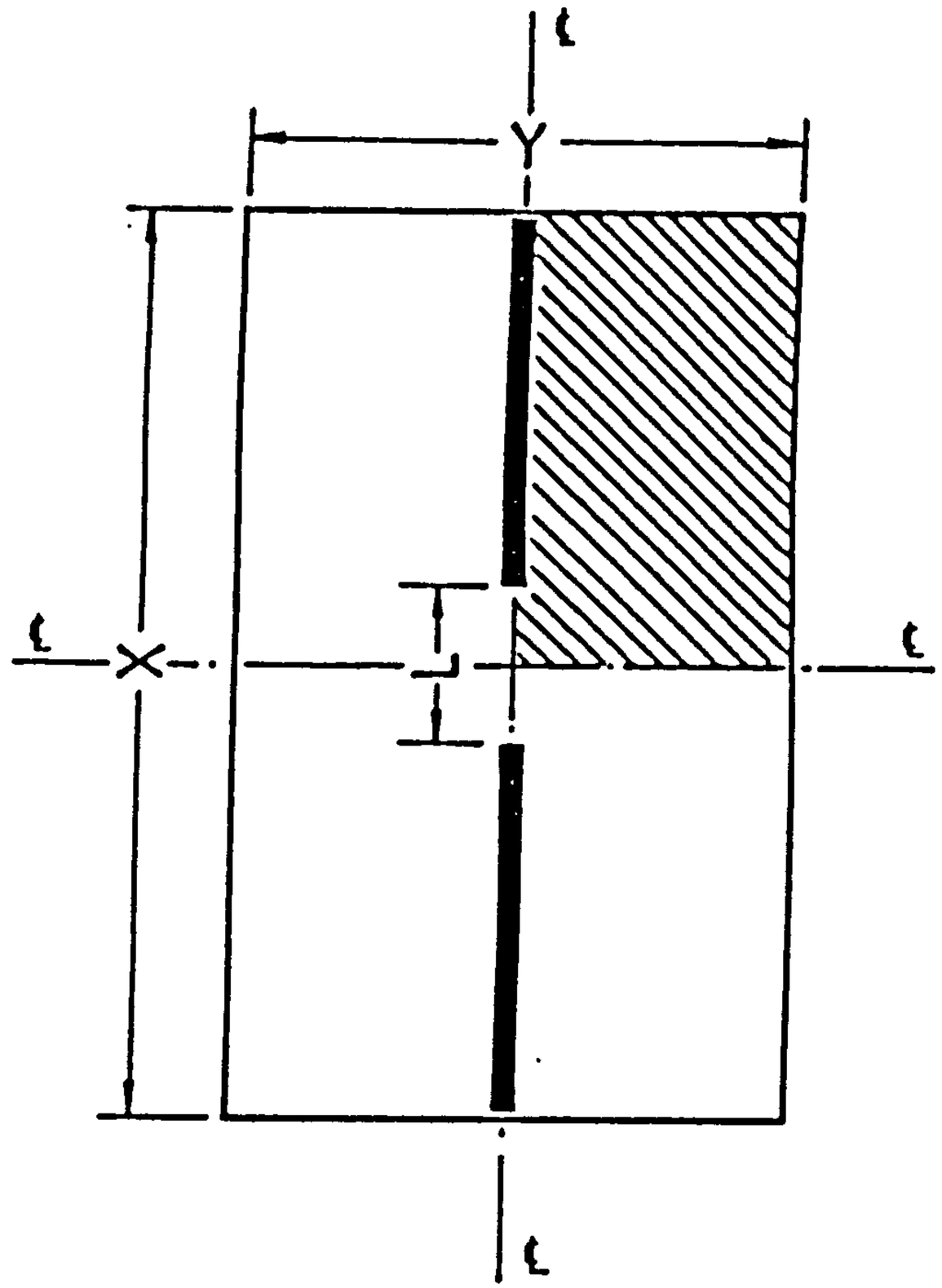

Typical Slab Panel

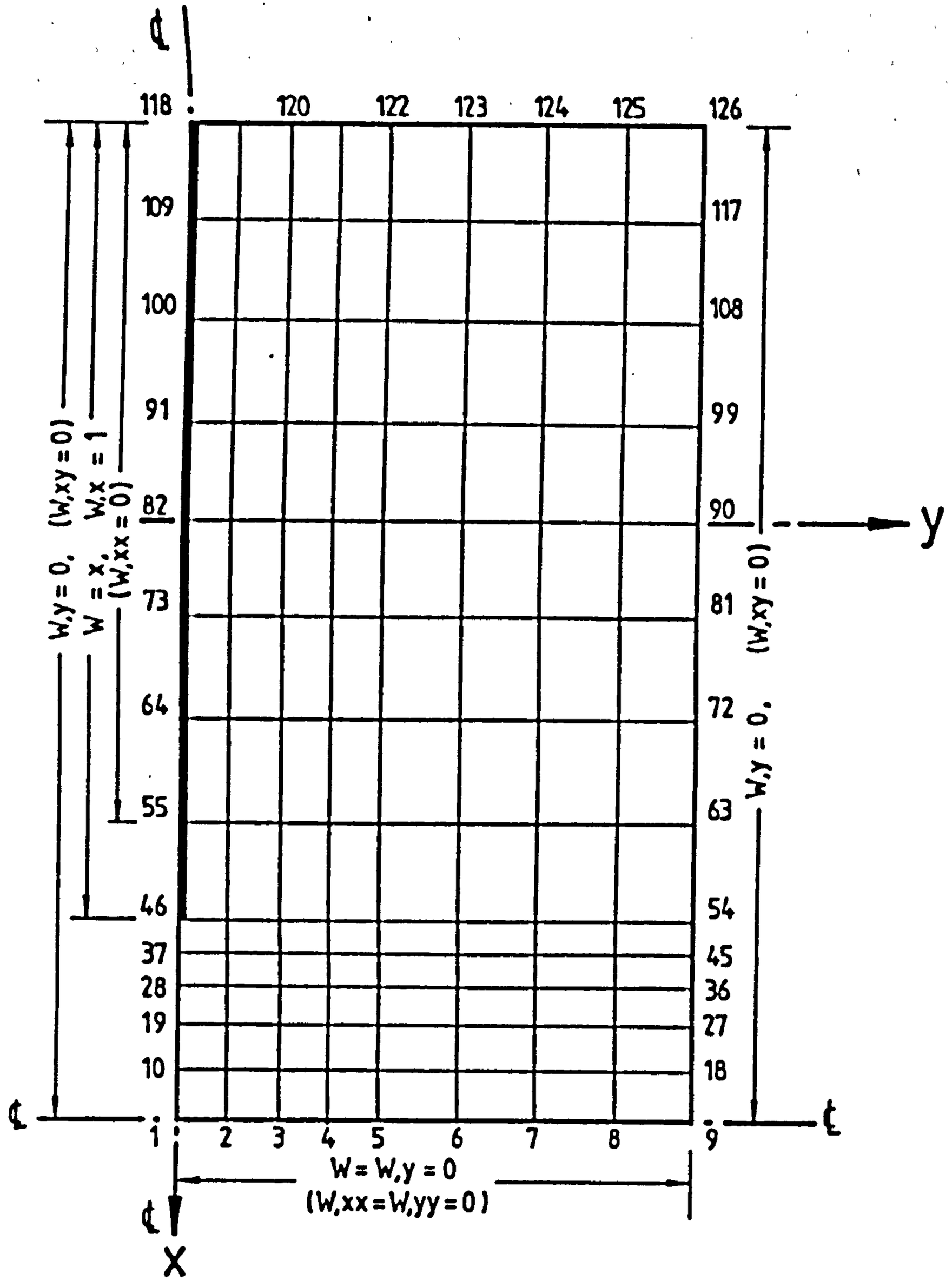

Finite Element Idealisation

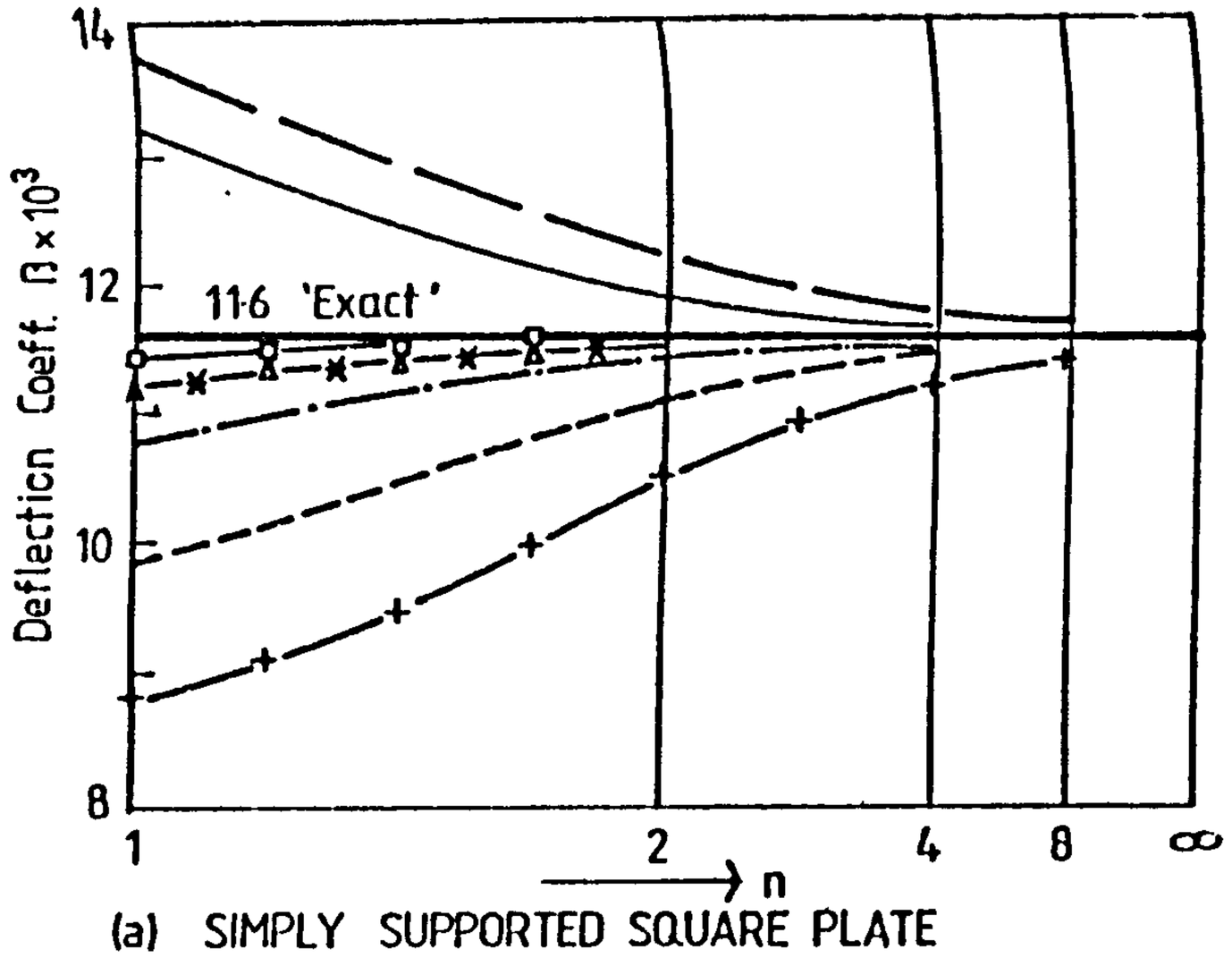

(a) SIMPLY SUPPORTED SQUARE PLATE

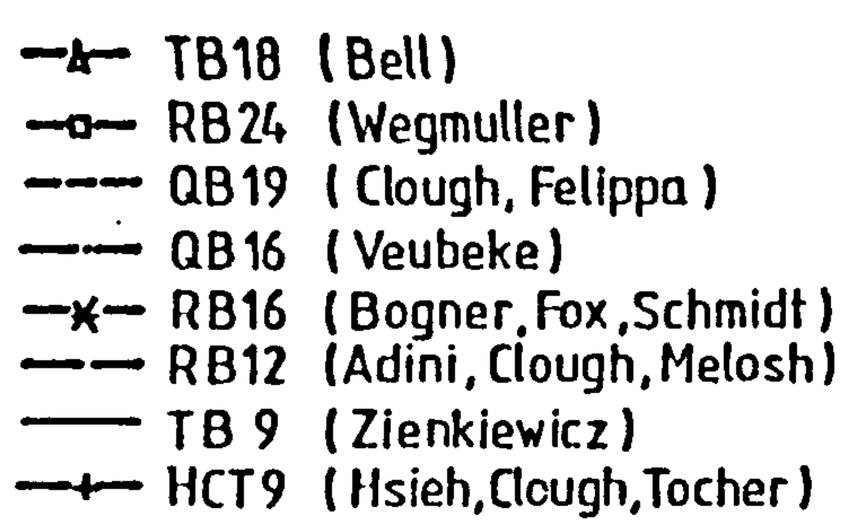

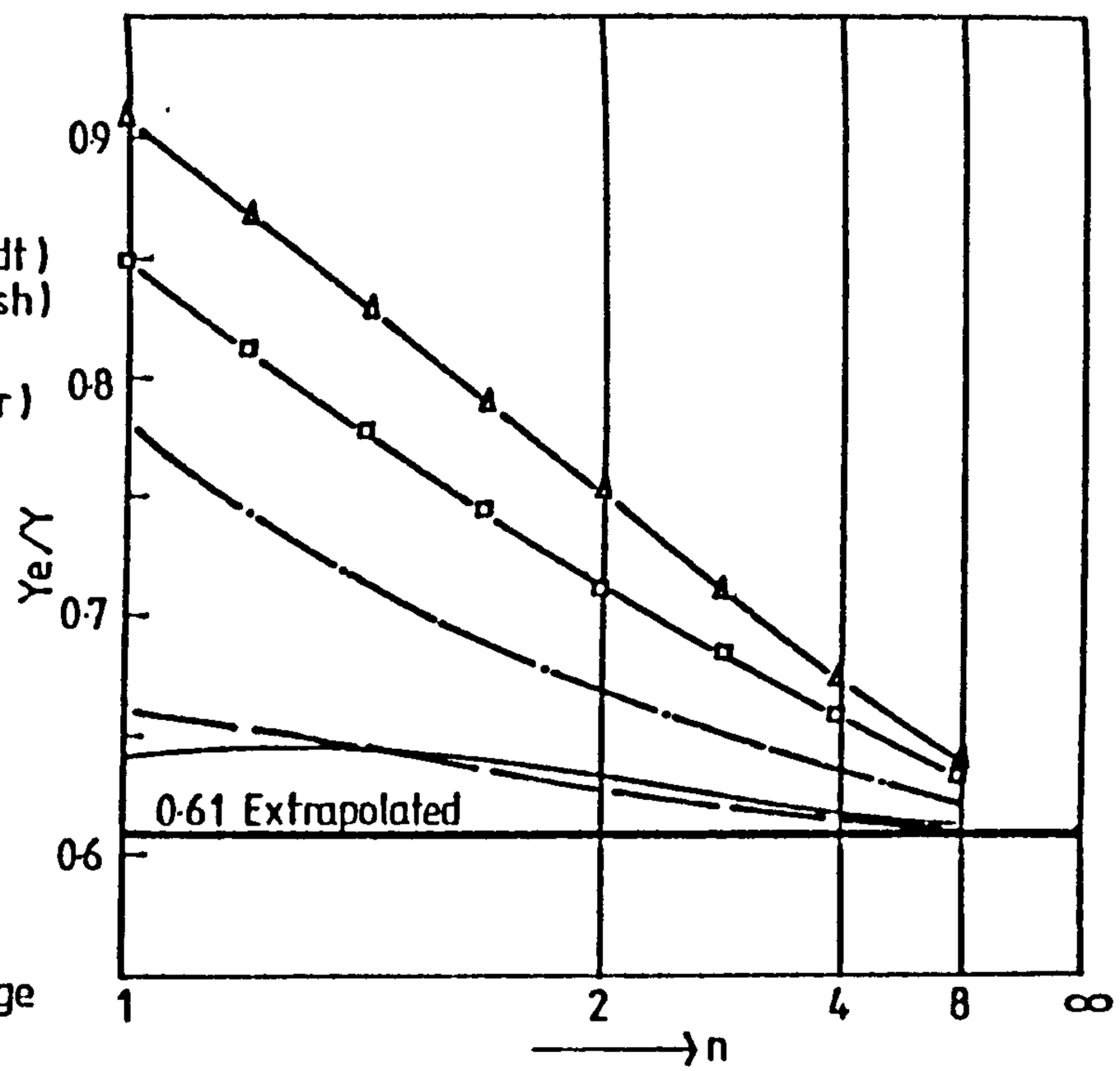

(c) SLAB COUPLING PLANE WALLS

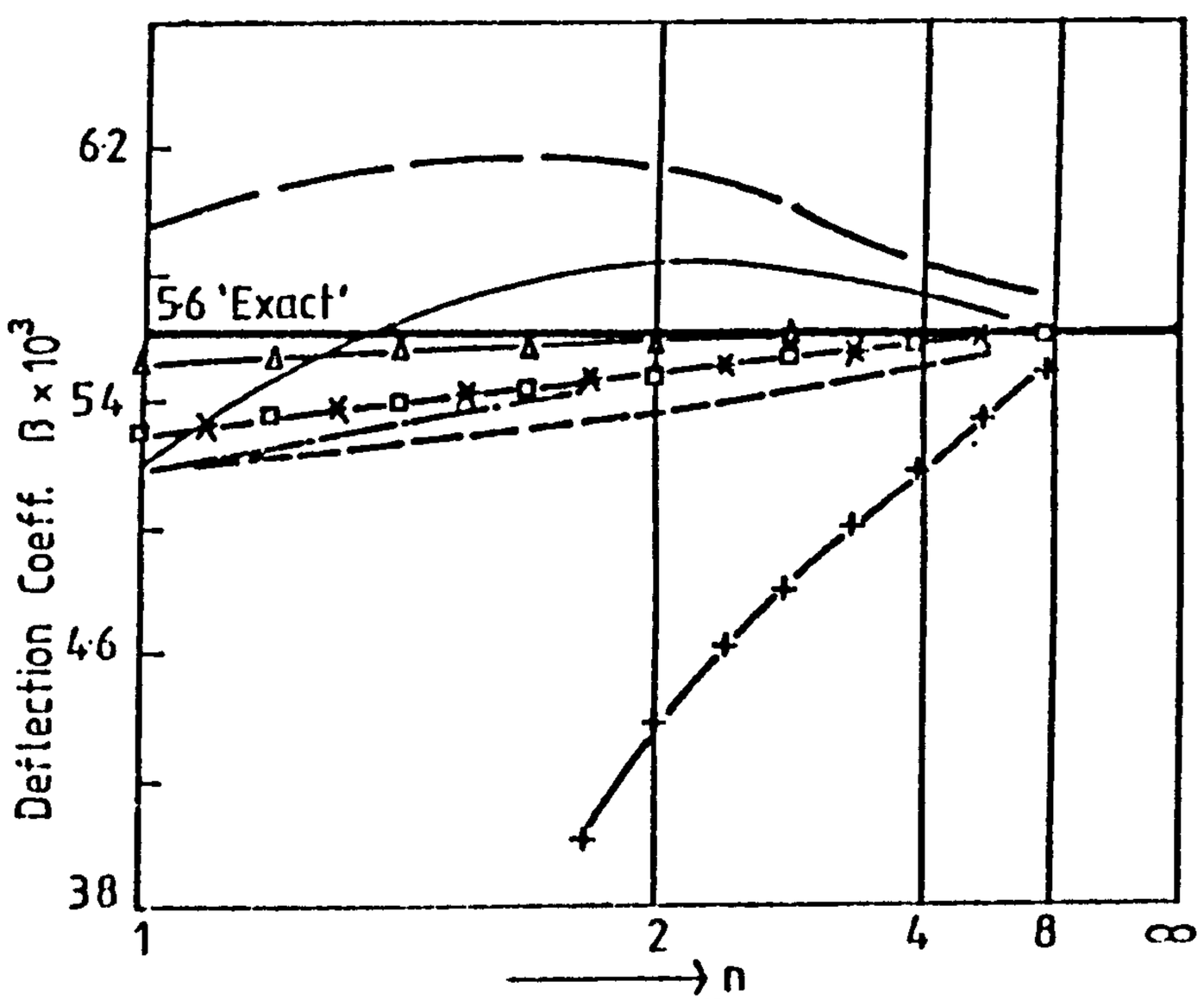

(b) CLAMPED SQUARE PLATE

n = number of divisions of half edge

$\beta = \frac{wD}{PL^2}$

P = central point load

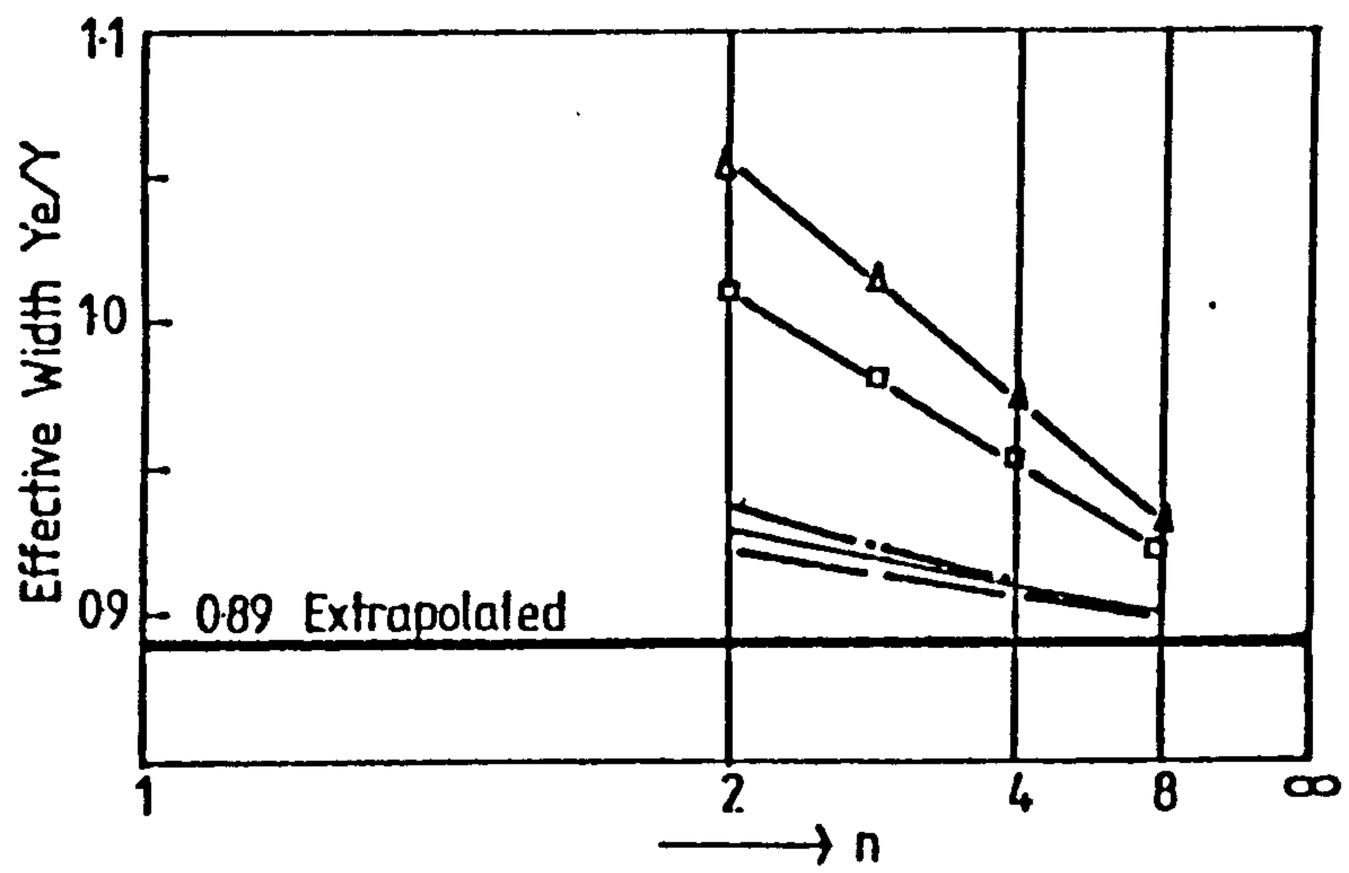

(d) SLAB COUPLING FLANGE WALLS

Fig. 3.5 Convergence Results for Various Plate Bending Elements

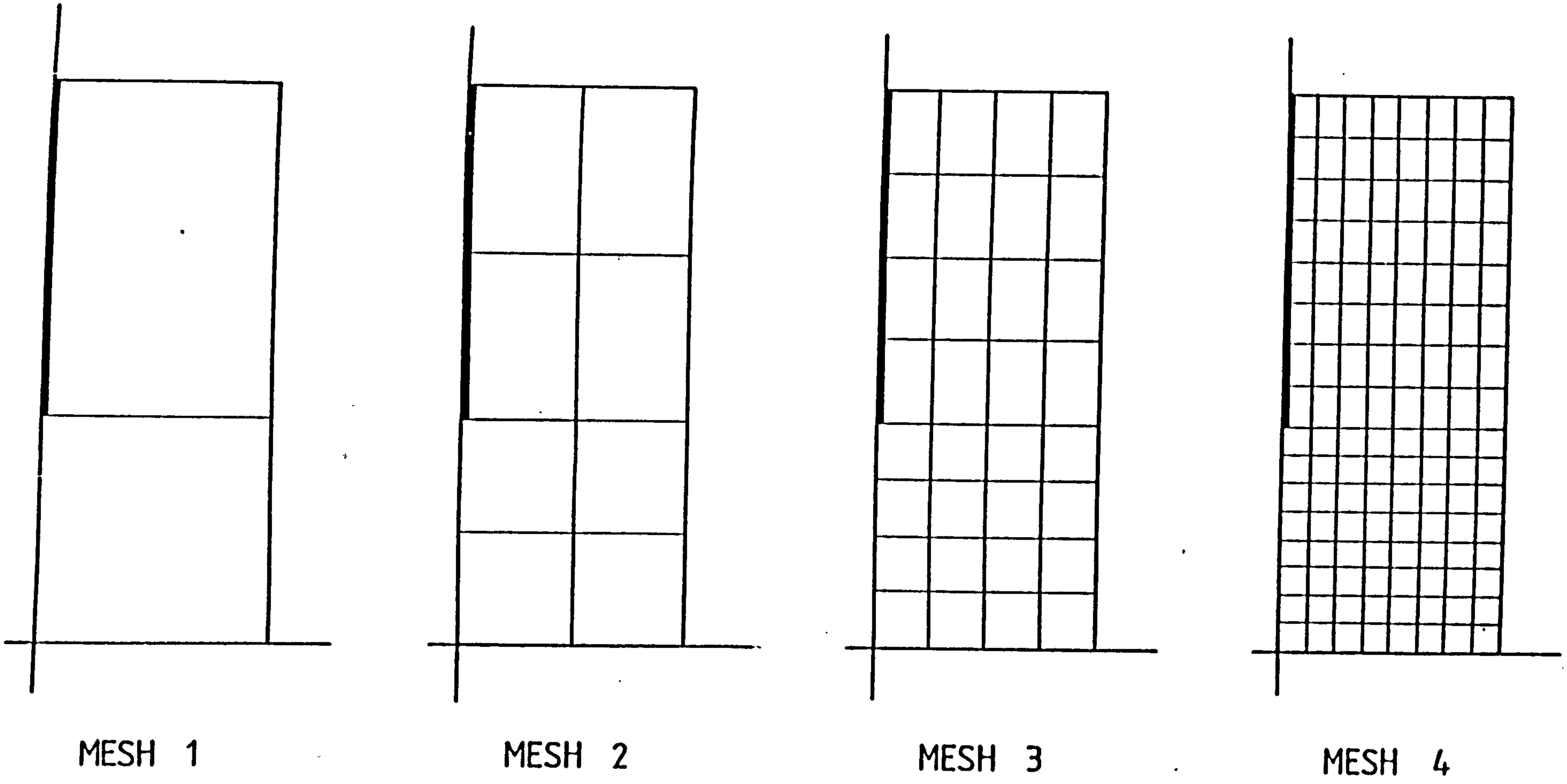

Fig. 3.6 Element Mesh Divisions for Coupling Slab in Convergence Study

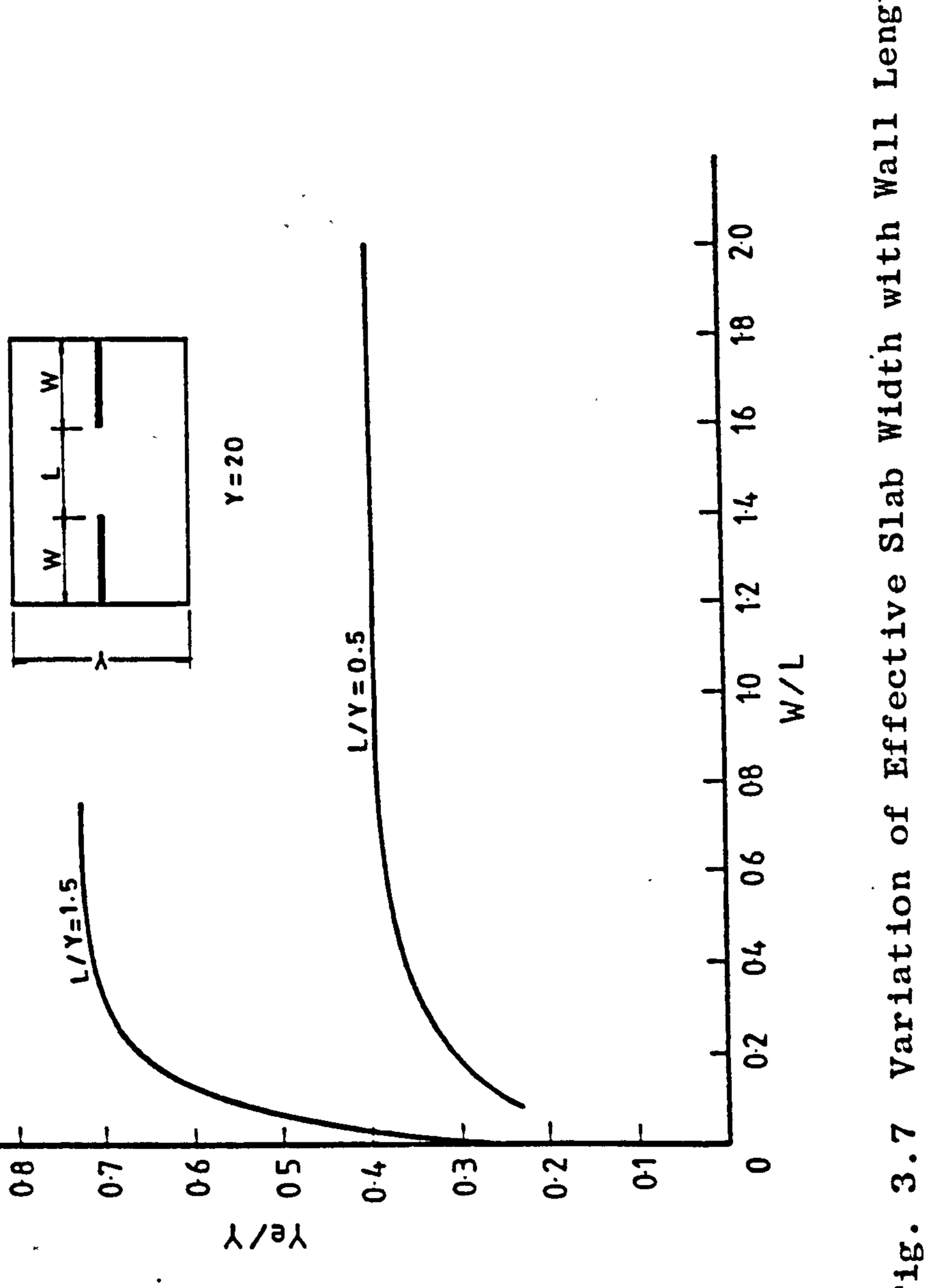

Fig. 3.7 Variation of Effective Slab Width with Wall Length

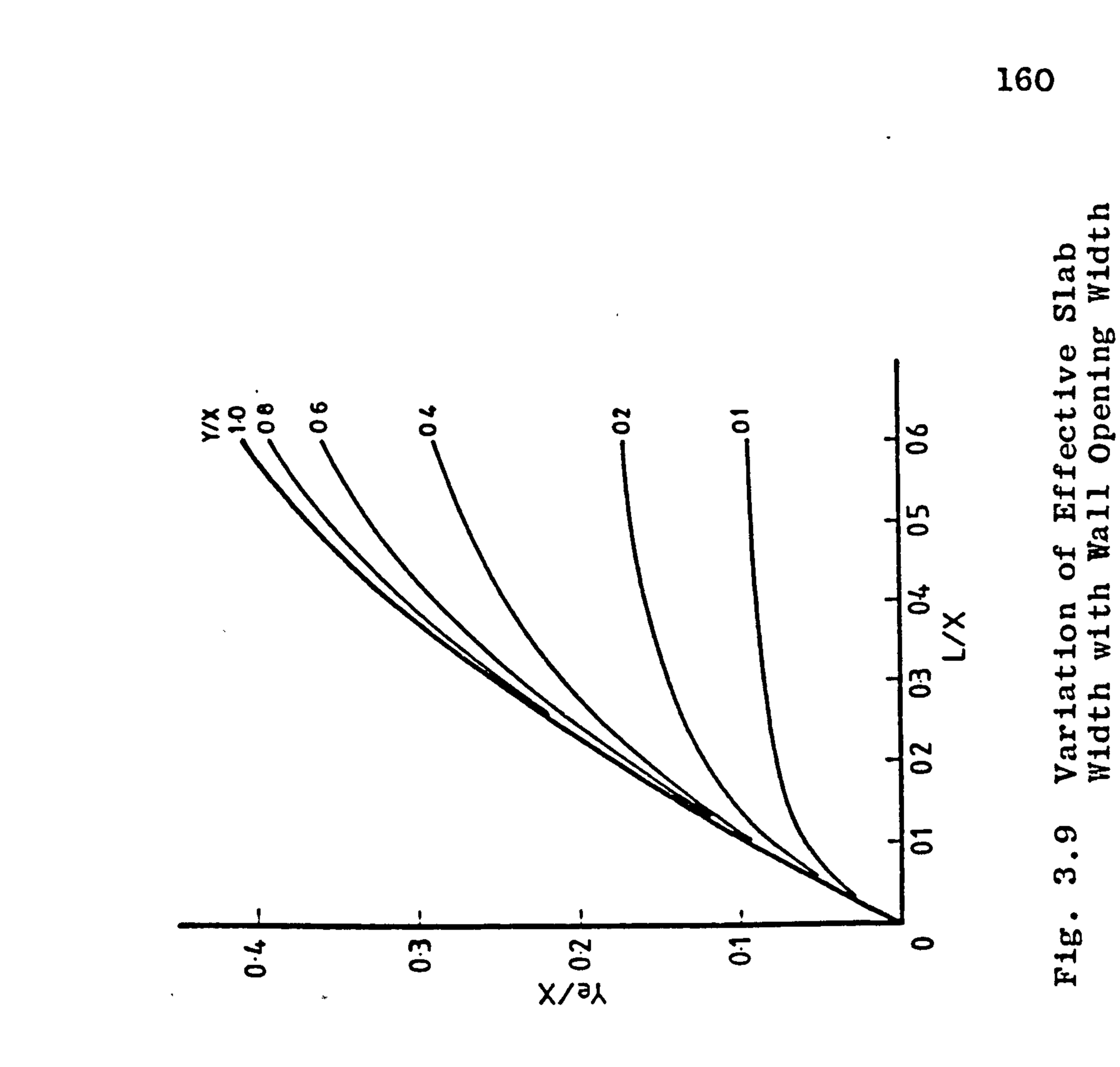

Fig. 3.9 Variation of Effective Slab Width with Wall Opening Width

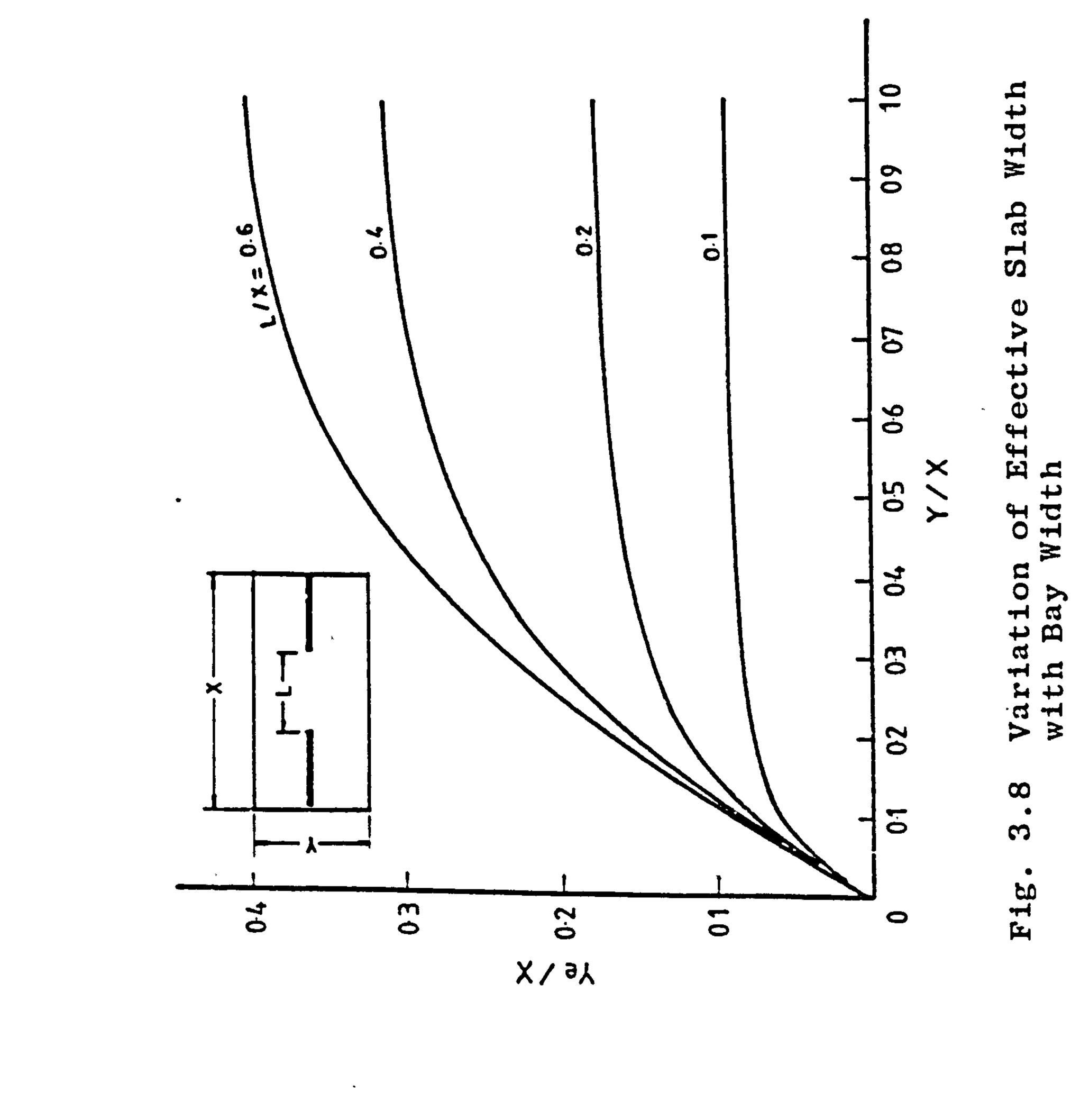

Fig. 3.8 Variation of Effective Slab Width with Bay Width

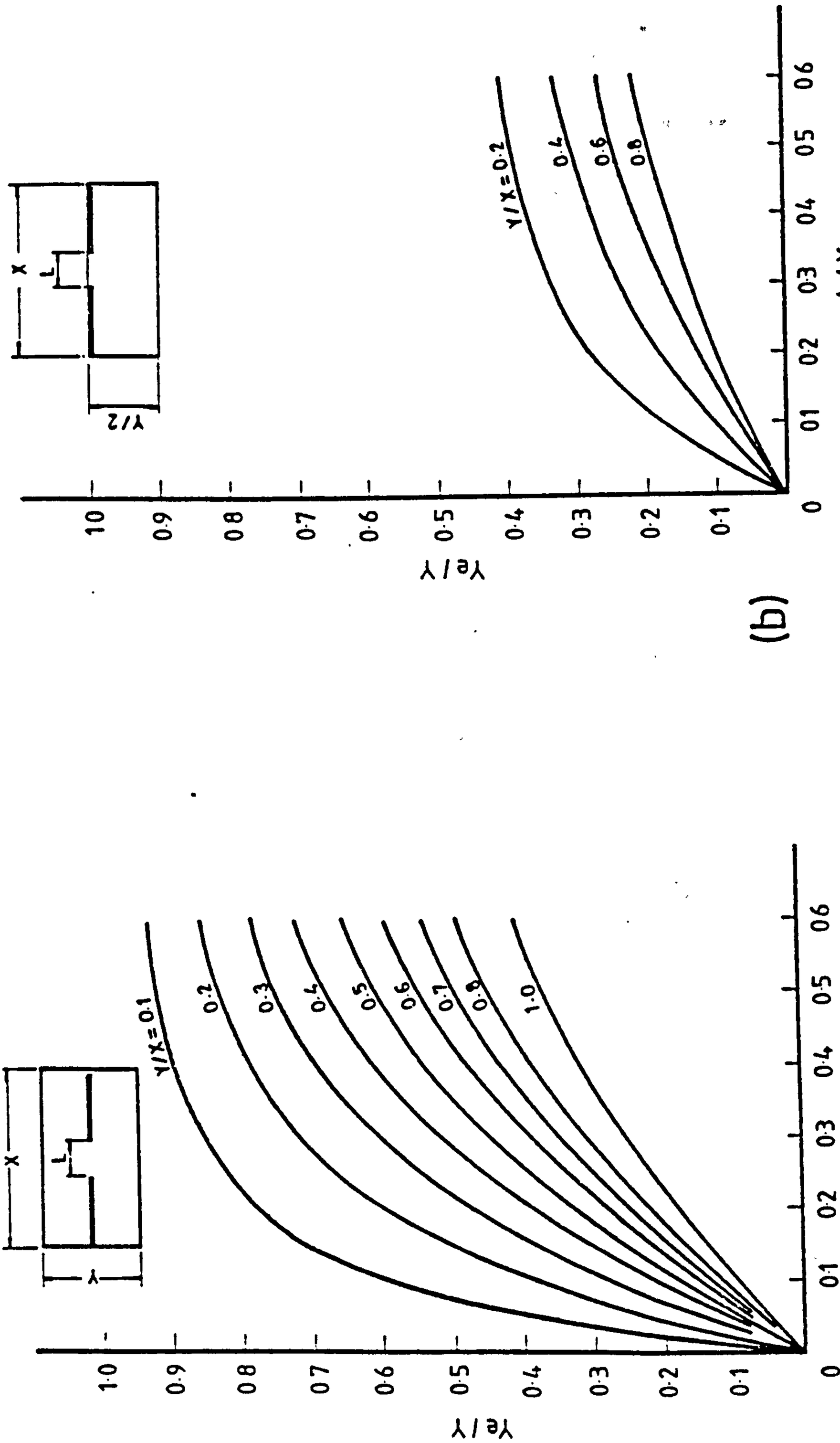

Fig. 3.10 Design Curves for Effective Slab Width for (a) Interior Bay and (b) End Bay of Plane Wall Configuration

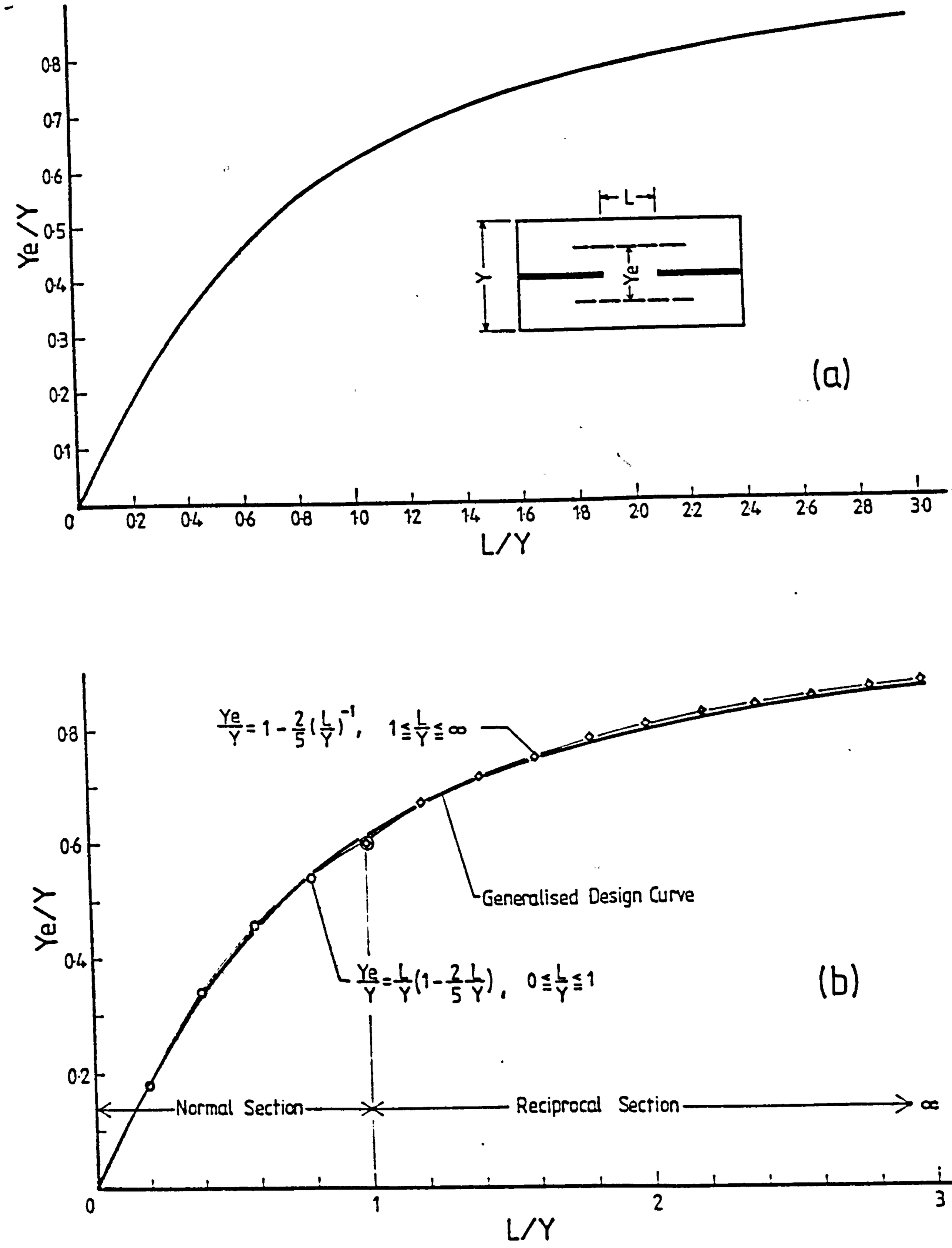

Fig. 3.11 (a) Generalised Design Curve and (b) Empirical Curve, for Effective Slab Width for Plane Wall Configuration

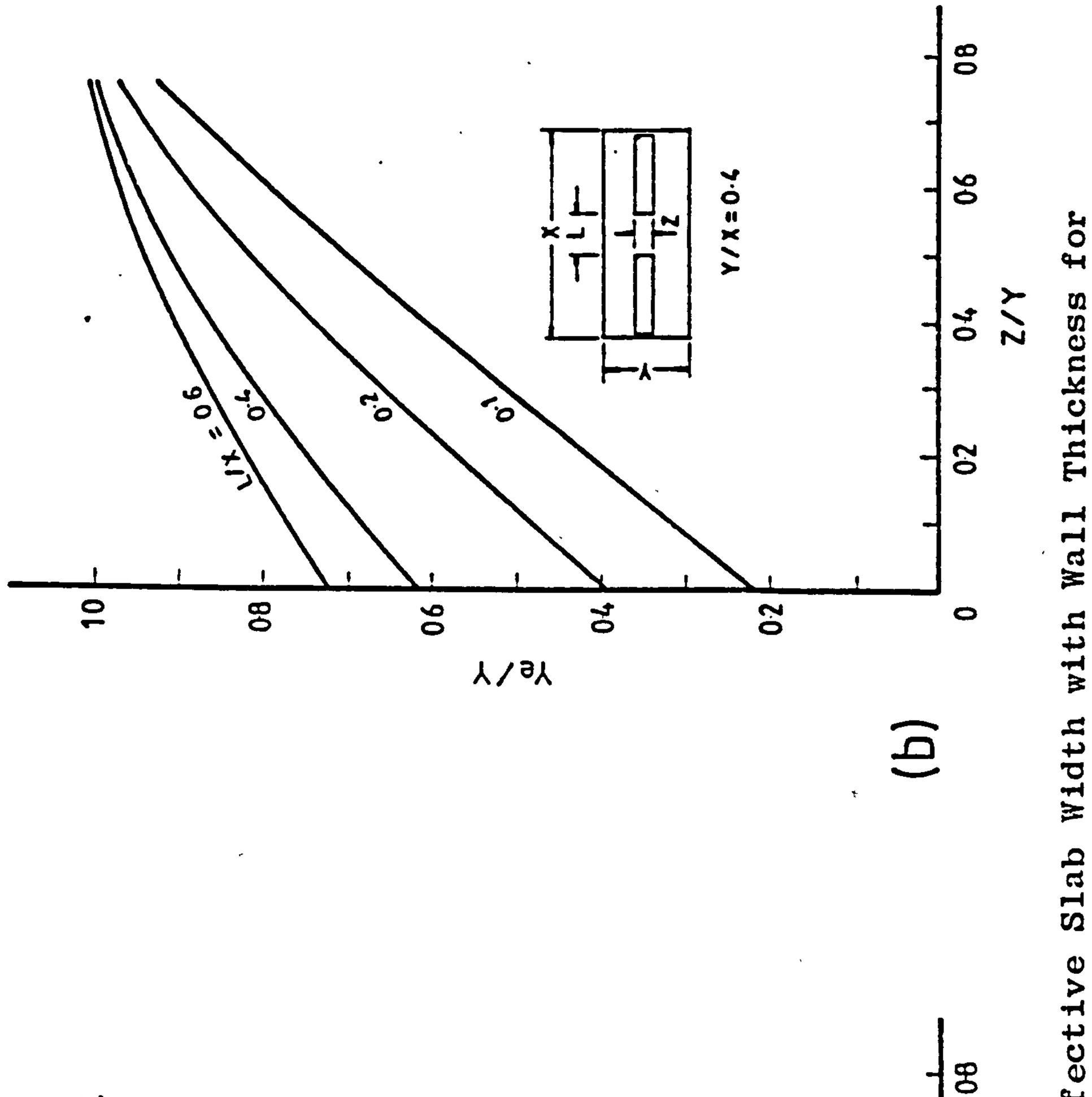

Fig. 3.12 Variation of Effective Slab Width with Plane Wall Configuration

NOTE :

The term 'STRESS' is used in the context of a stress resultant.

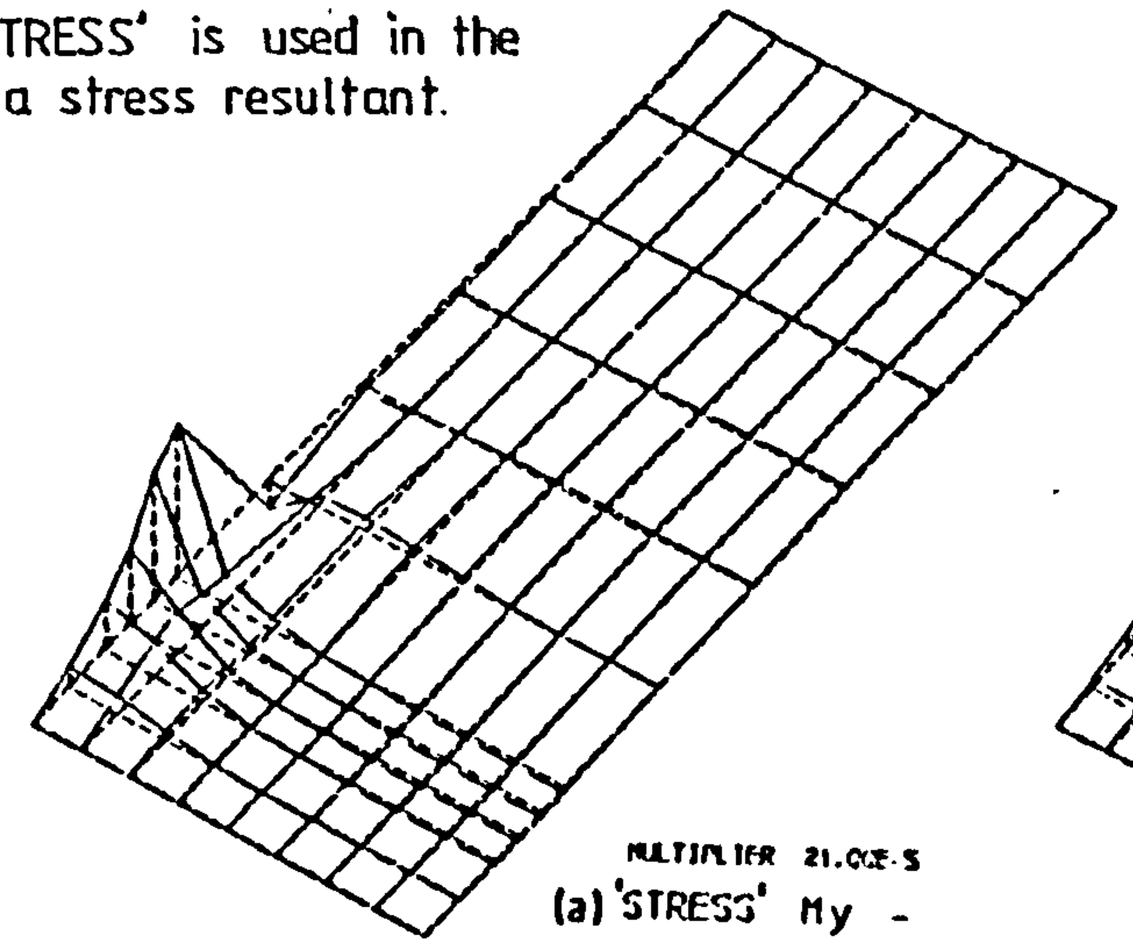

(a) 'STRESS' My -

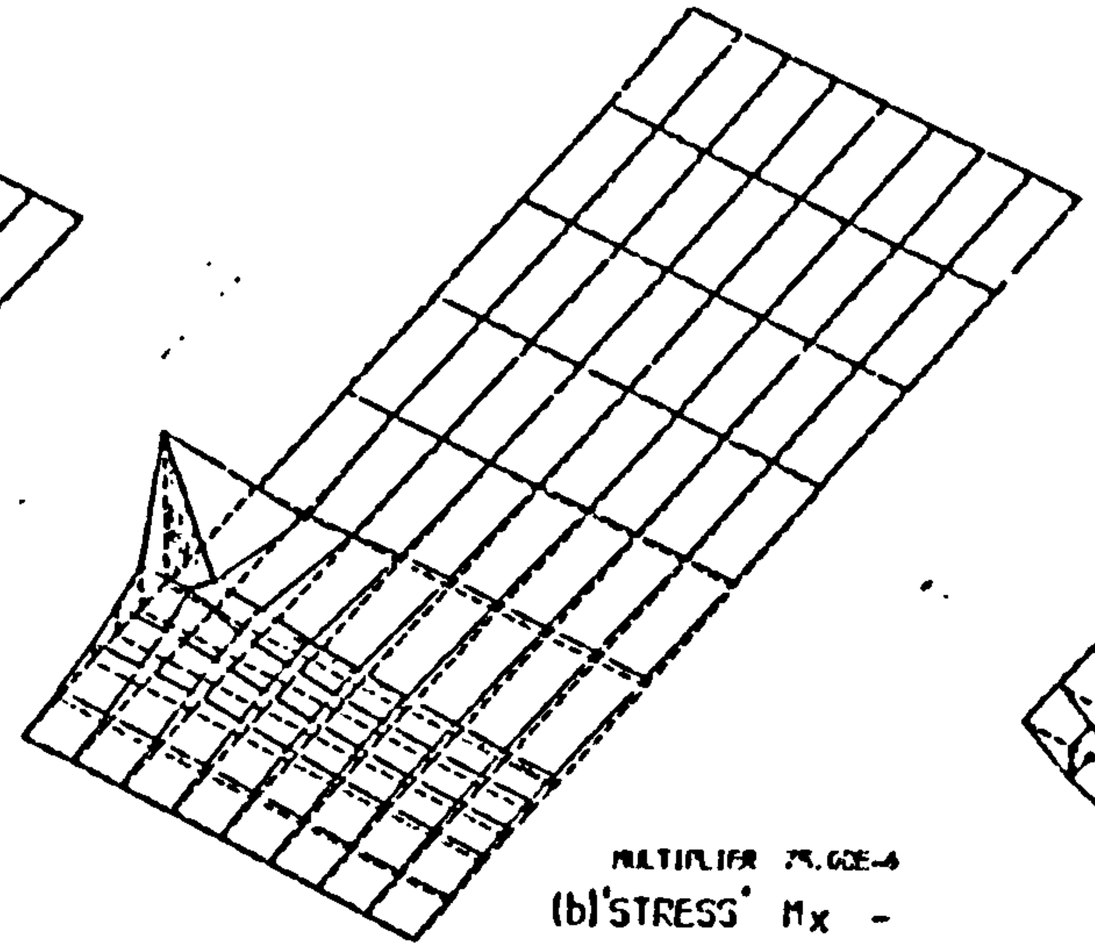

(b) 'STRESS' Mx -

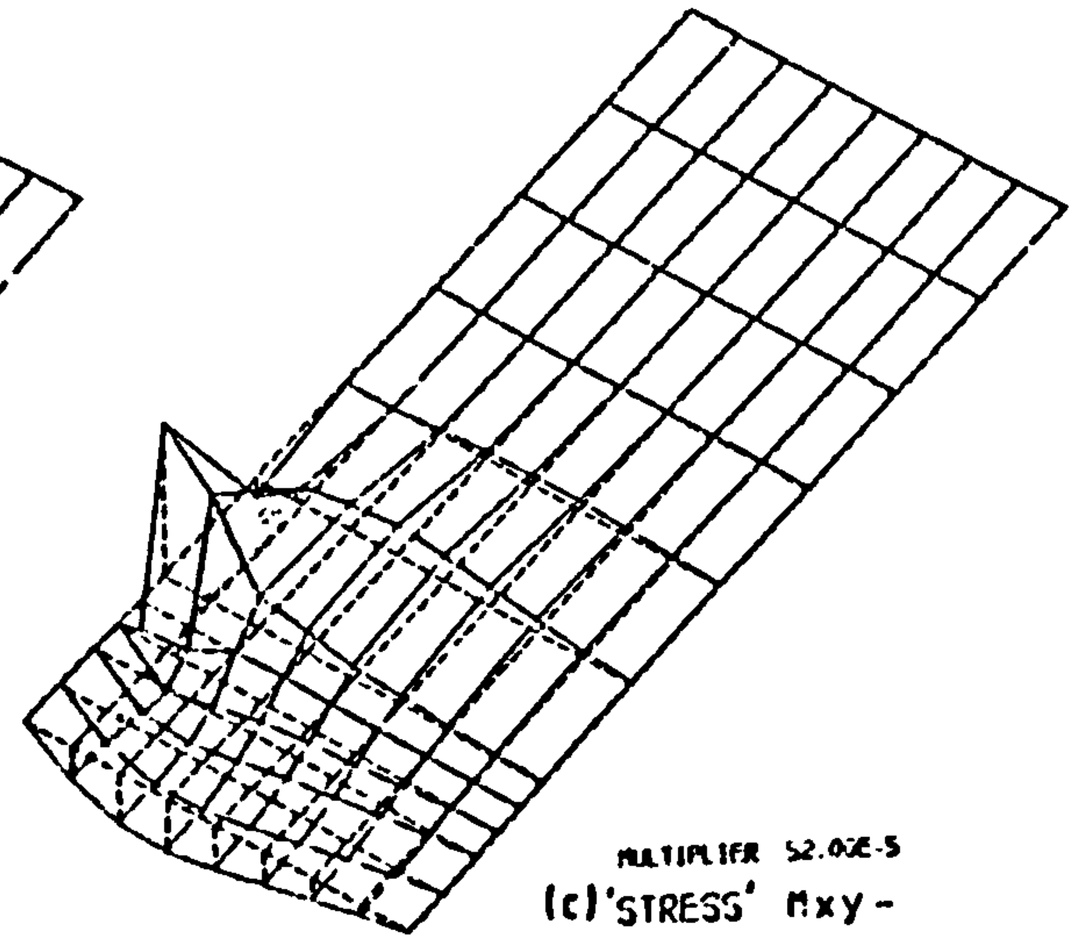

(c) 'STRESS' Mxy -

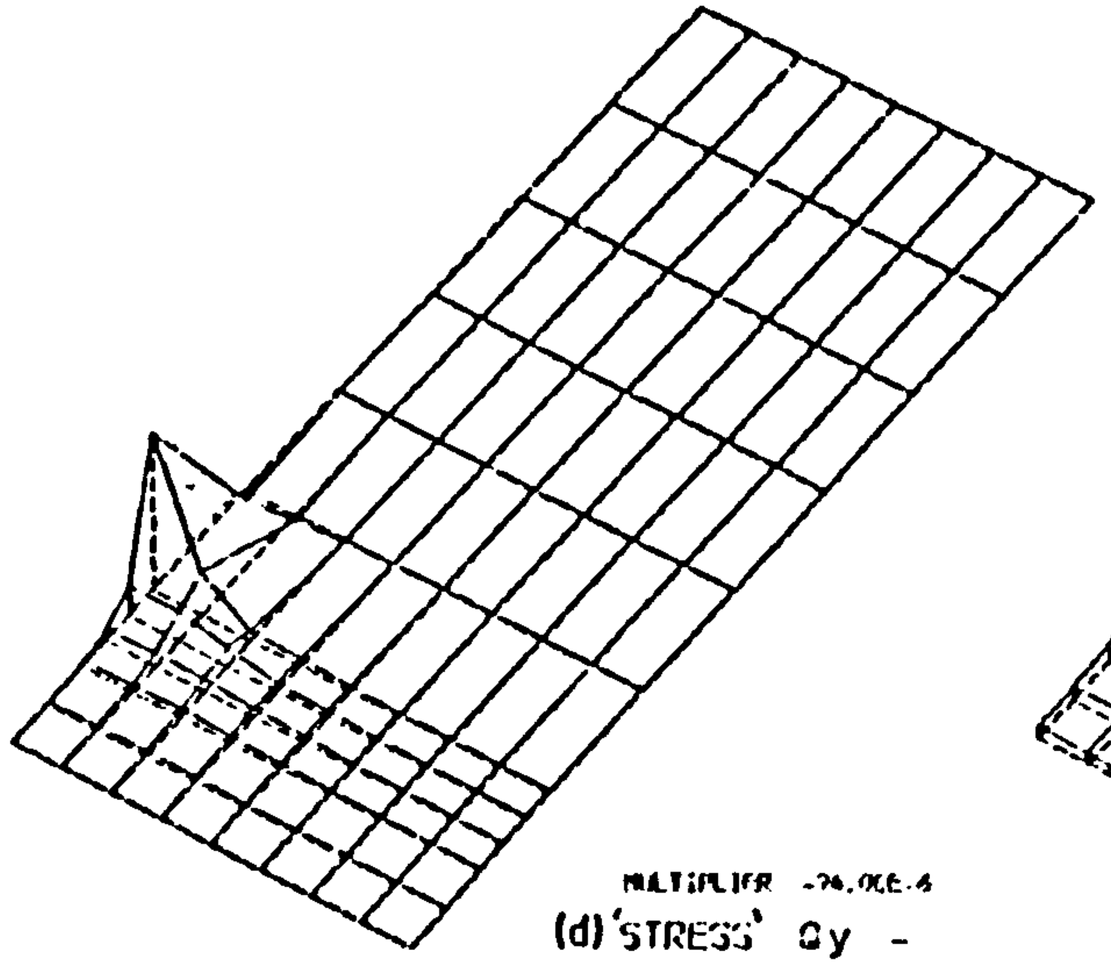

(d) 'STRESS' Qy -

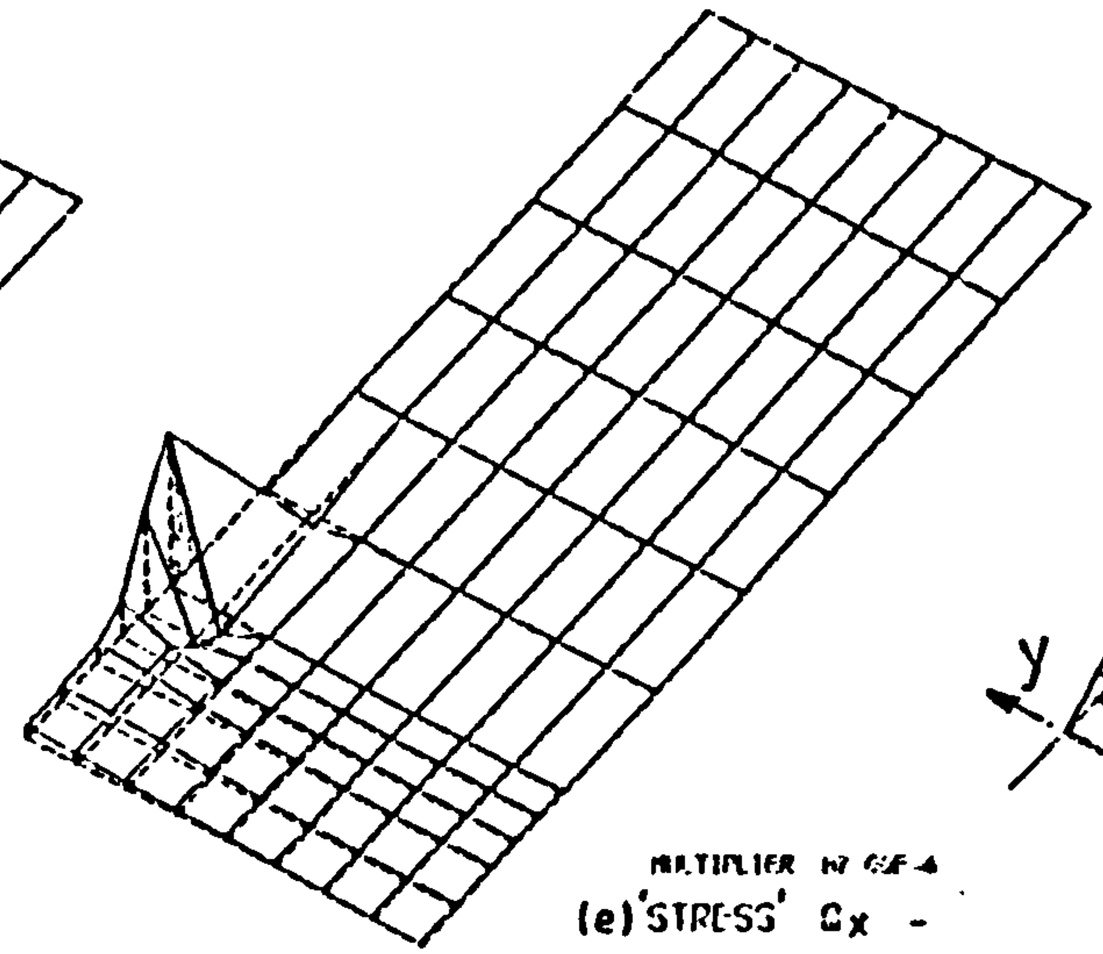

(e) 'STRESS' Qx -

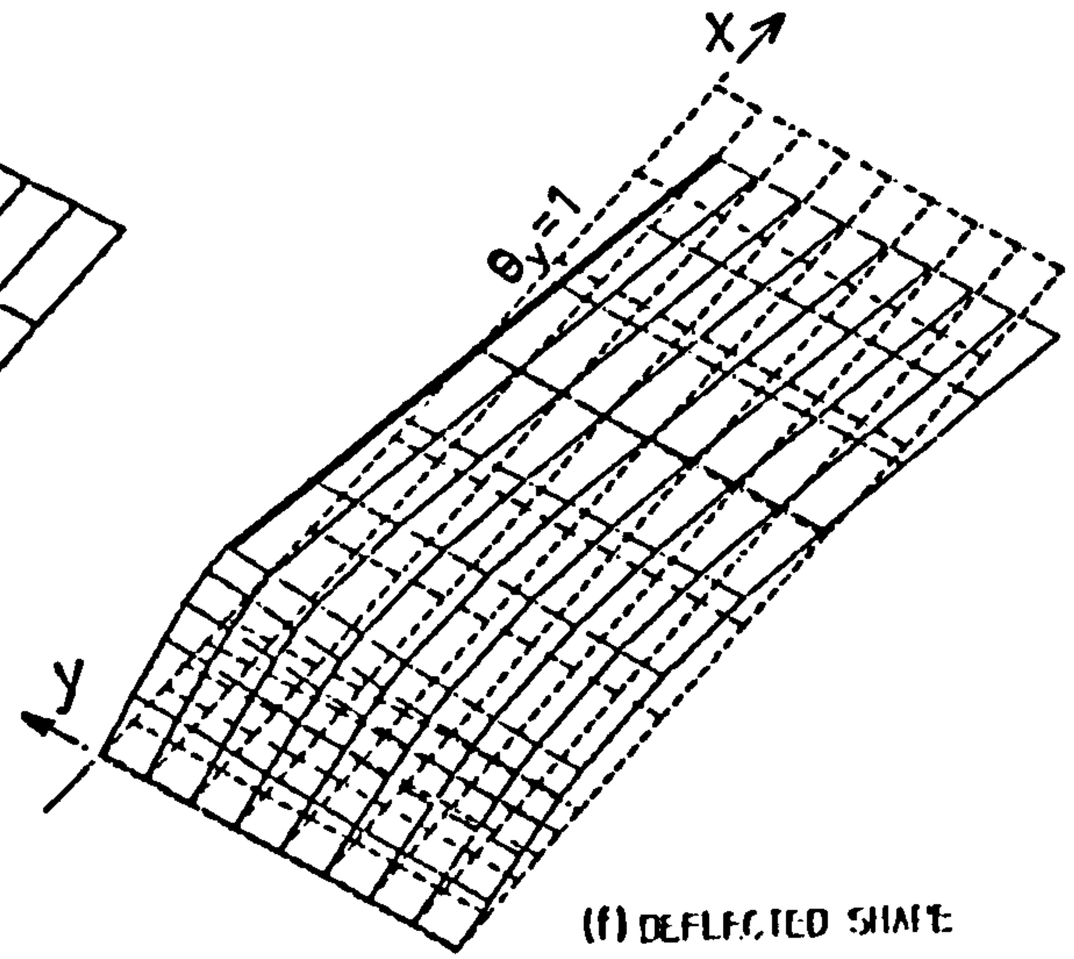

(f) DEFLECTED SHAPE

Fig. 3.14 General Distribution of Slab Actions in Plane Wall Configuration

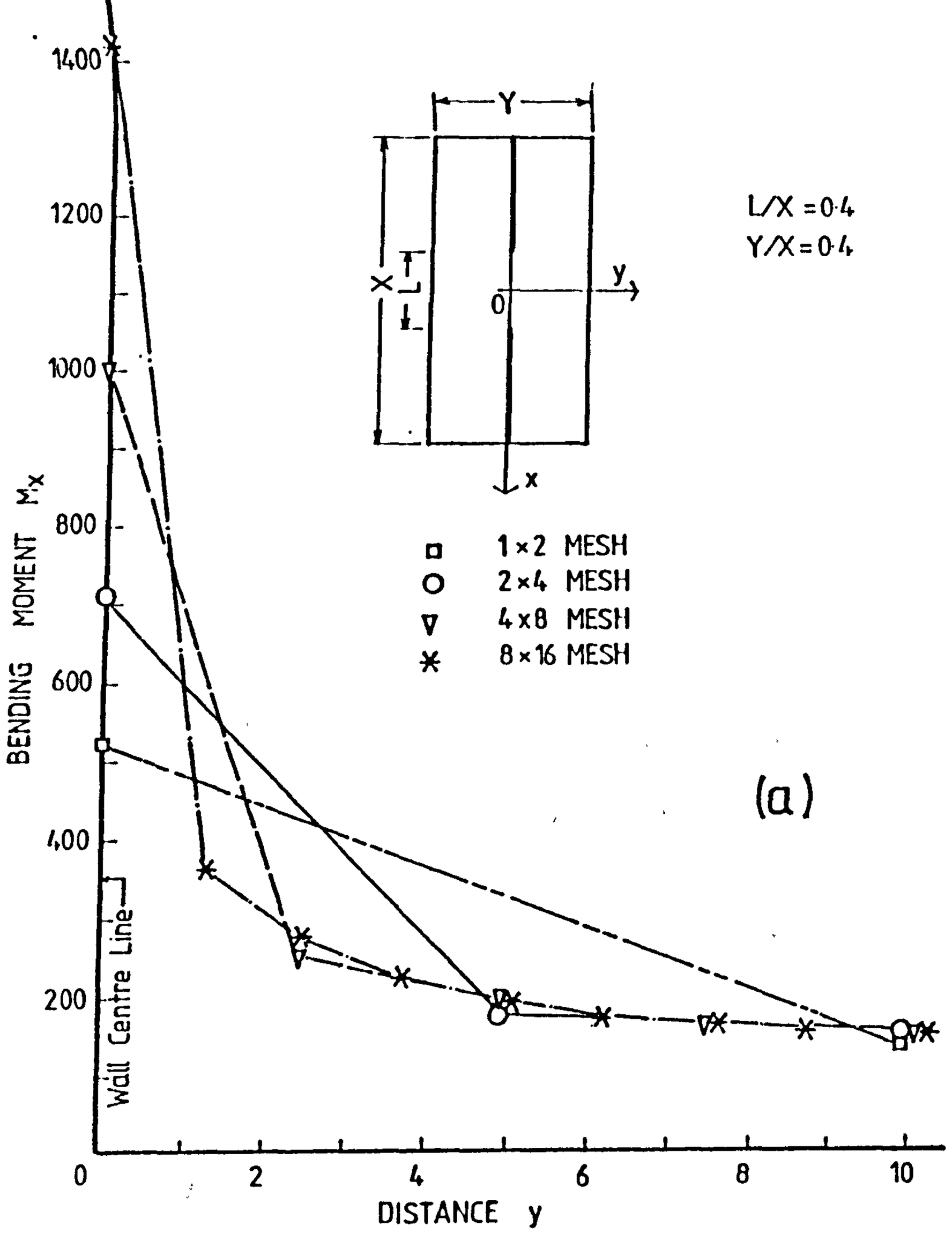

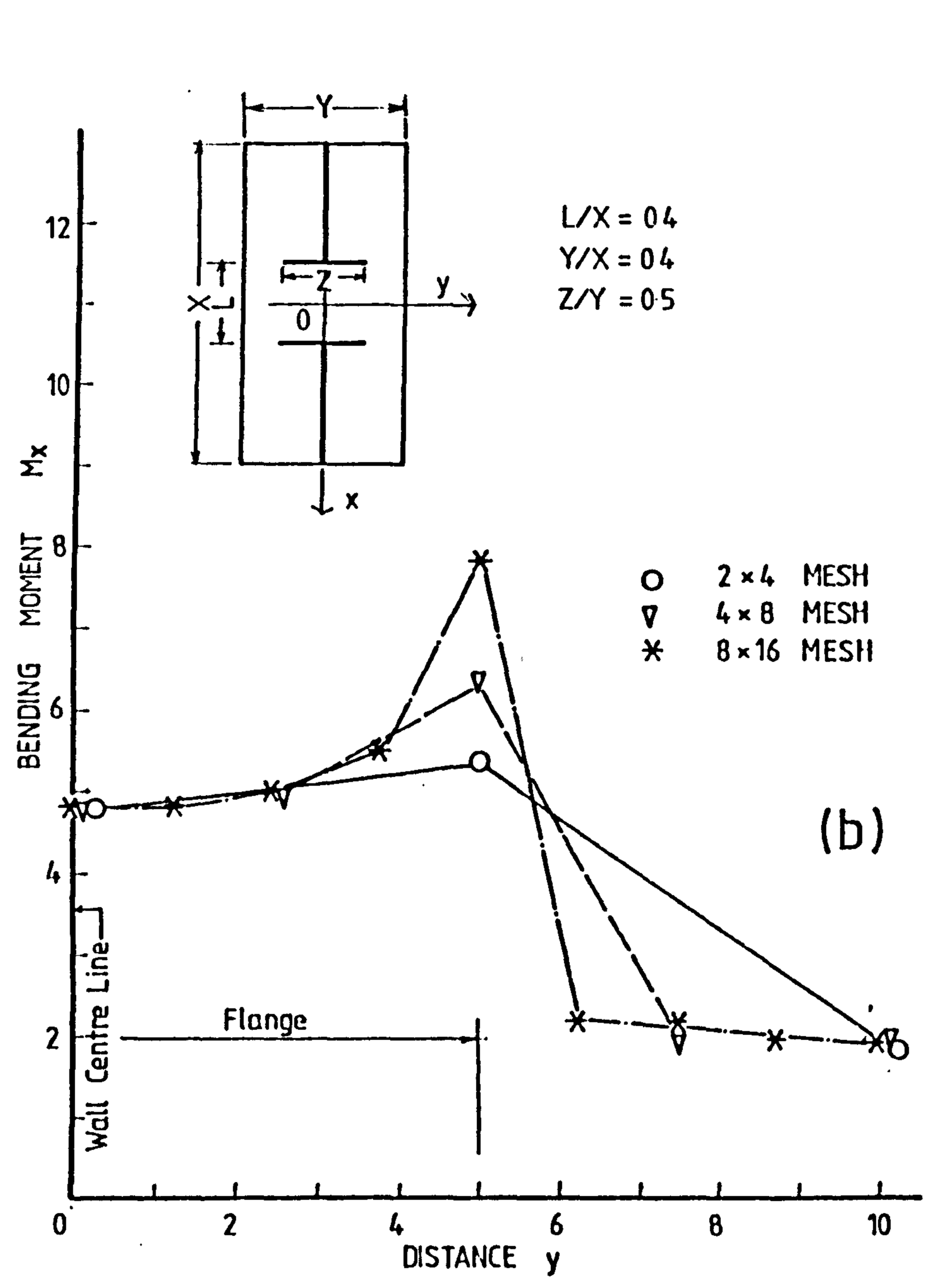

Fig. 3.15 Convergence Results for Longitudinal Bending Moments at Critical Transverse Slab Section for (a) Plane Wall Configuration and (b) Flanged Wall Configuration

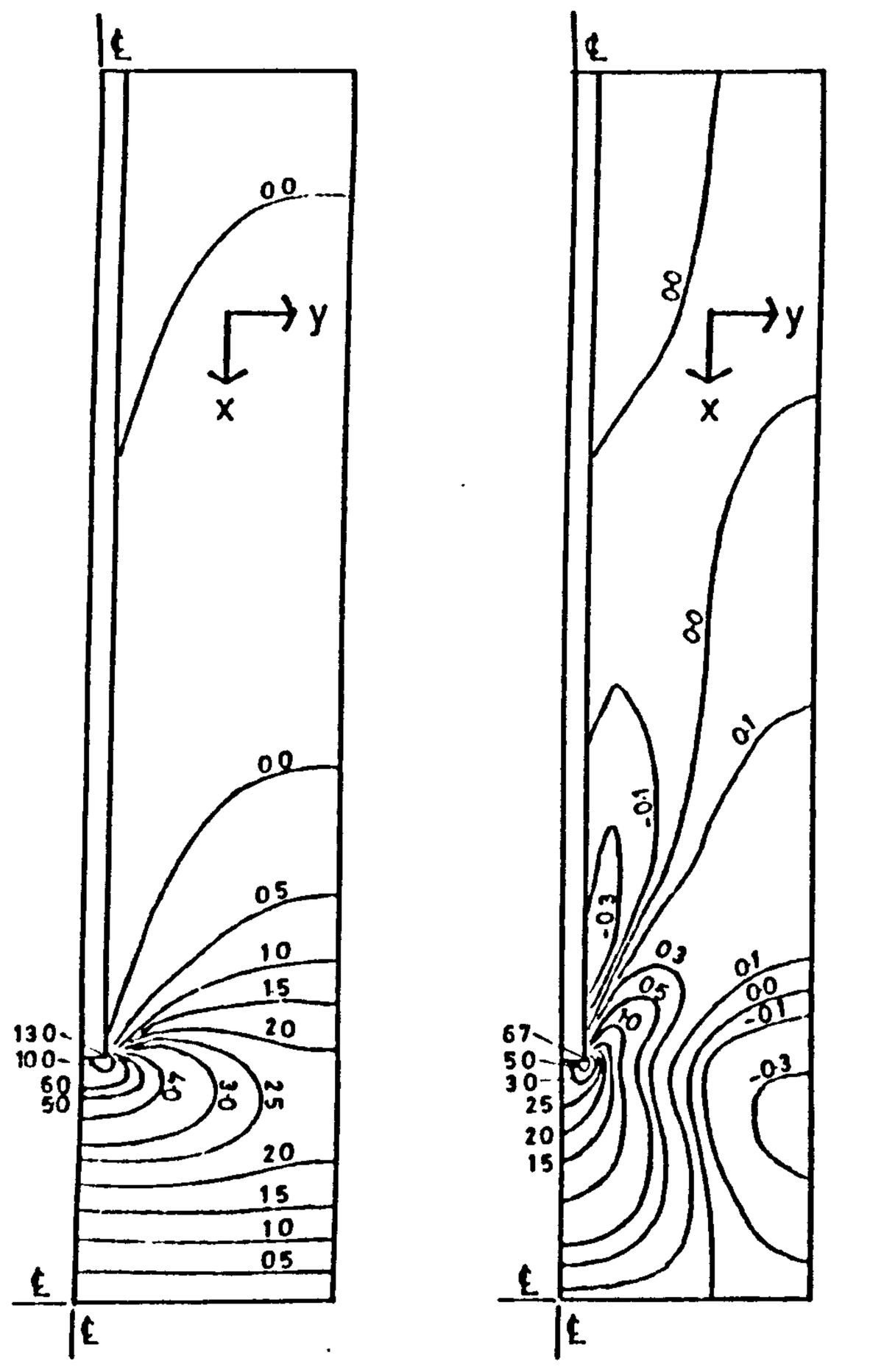

(a) BENDING MOMENT $\bar{M}_x$ (b) BENDING MOMENT $\bar{M}_y$

Fig. 3.17 Bending Moment Contours for Slab in Plane Wall Configuration (Y/L = 1)

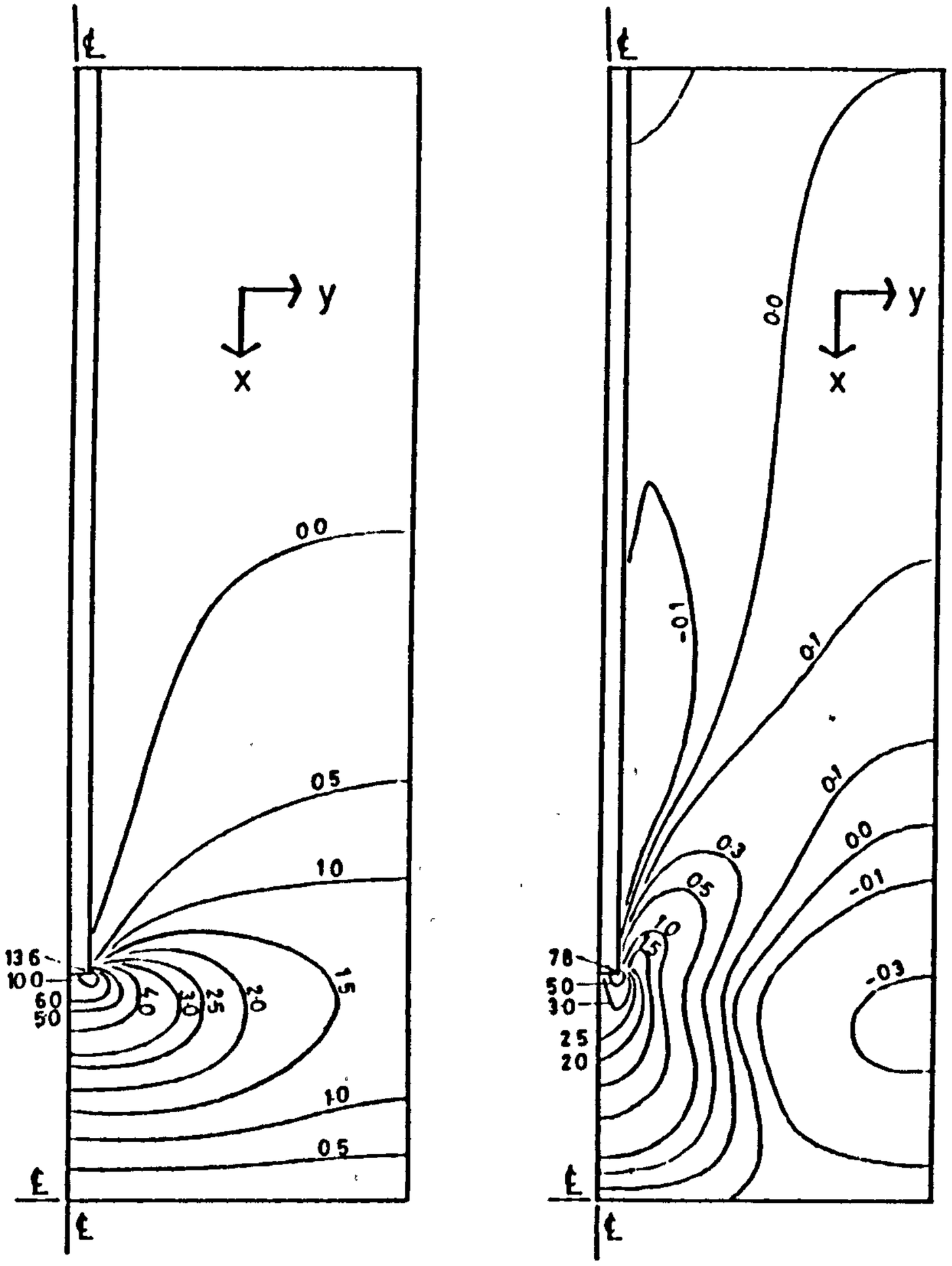

(a) BENDING MOMENT $\bar{M}_x$ (b) BENDING MOMENT $\bar{M}_y$

Fig. 3.18 Bending Moment Contours for Slab in Plane Wall Configuration (Y/L = 1.5)

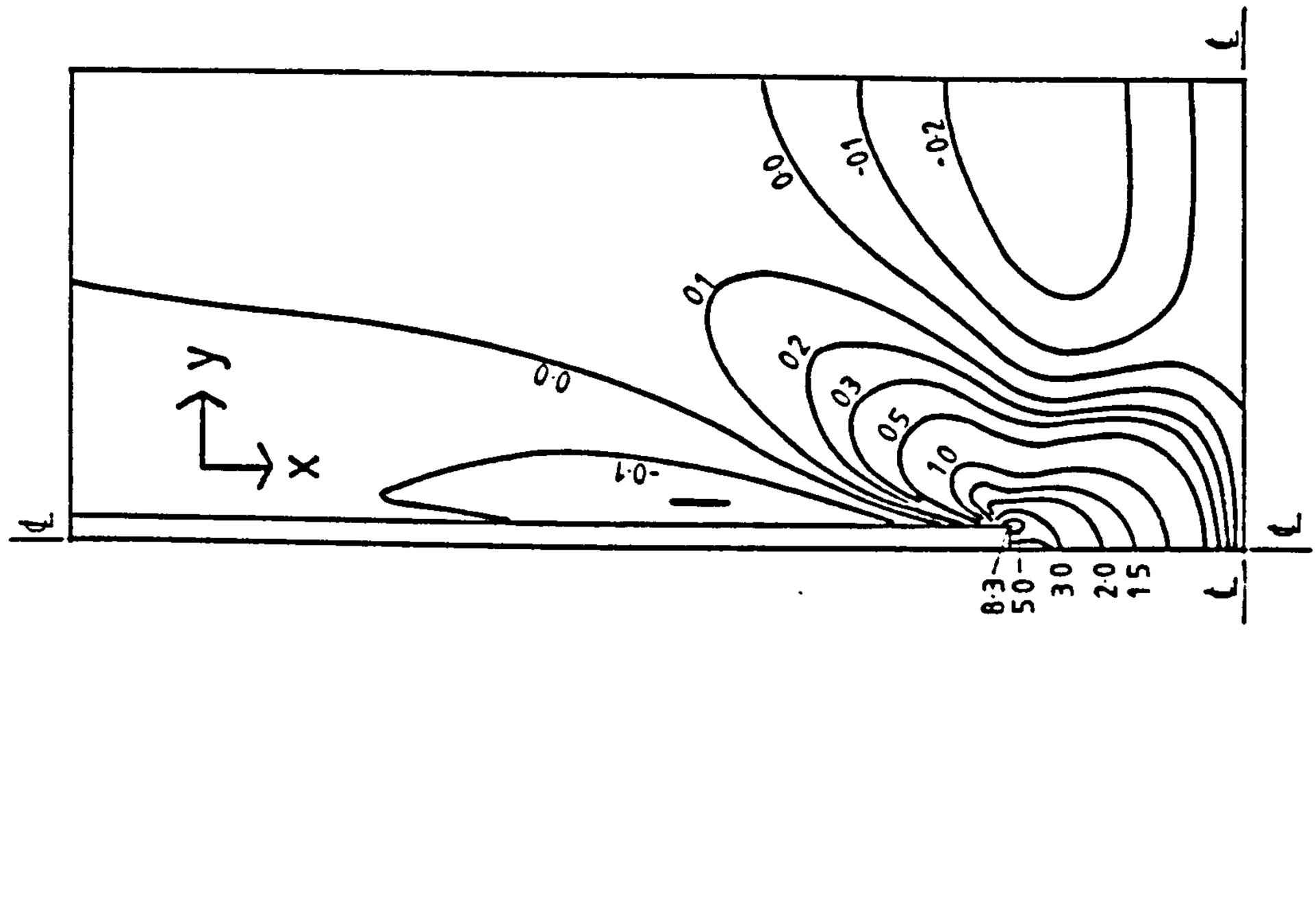

Fig. 3.19 Bending Moment Contours for Slab Configuration (Y/L = 2)

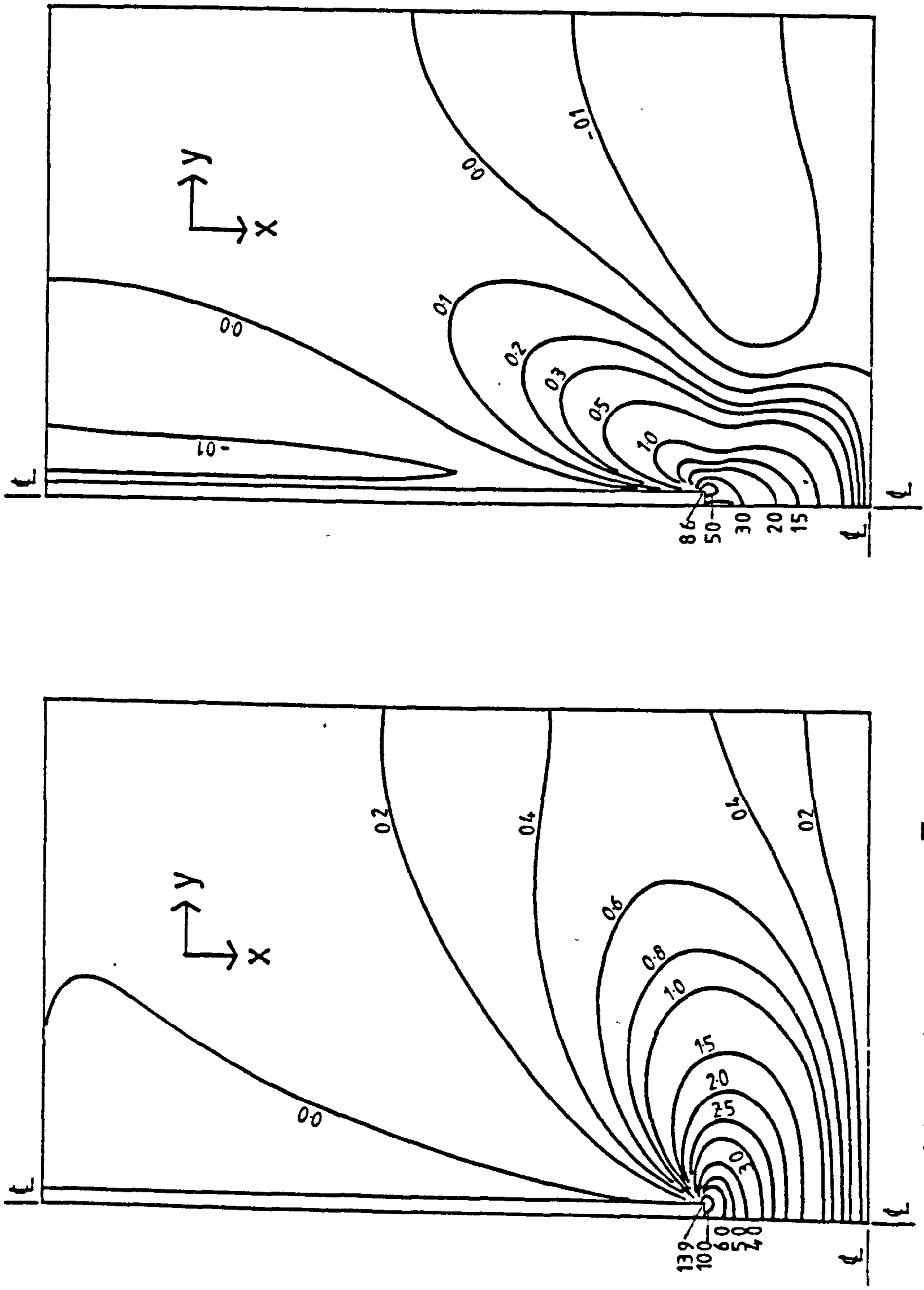

(a) BENDING MOMENT M_x

(b) BENDING MOMENT M_y

Fig. 3.20 Bending Moment Contours for Slab in Plane Wall Configuration (Y/L = 3)

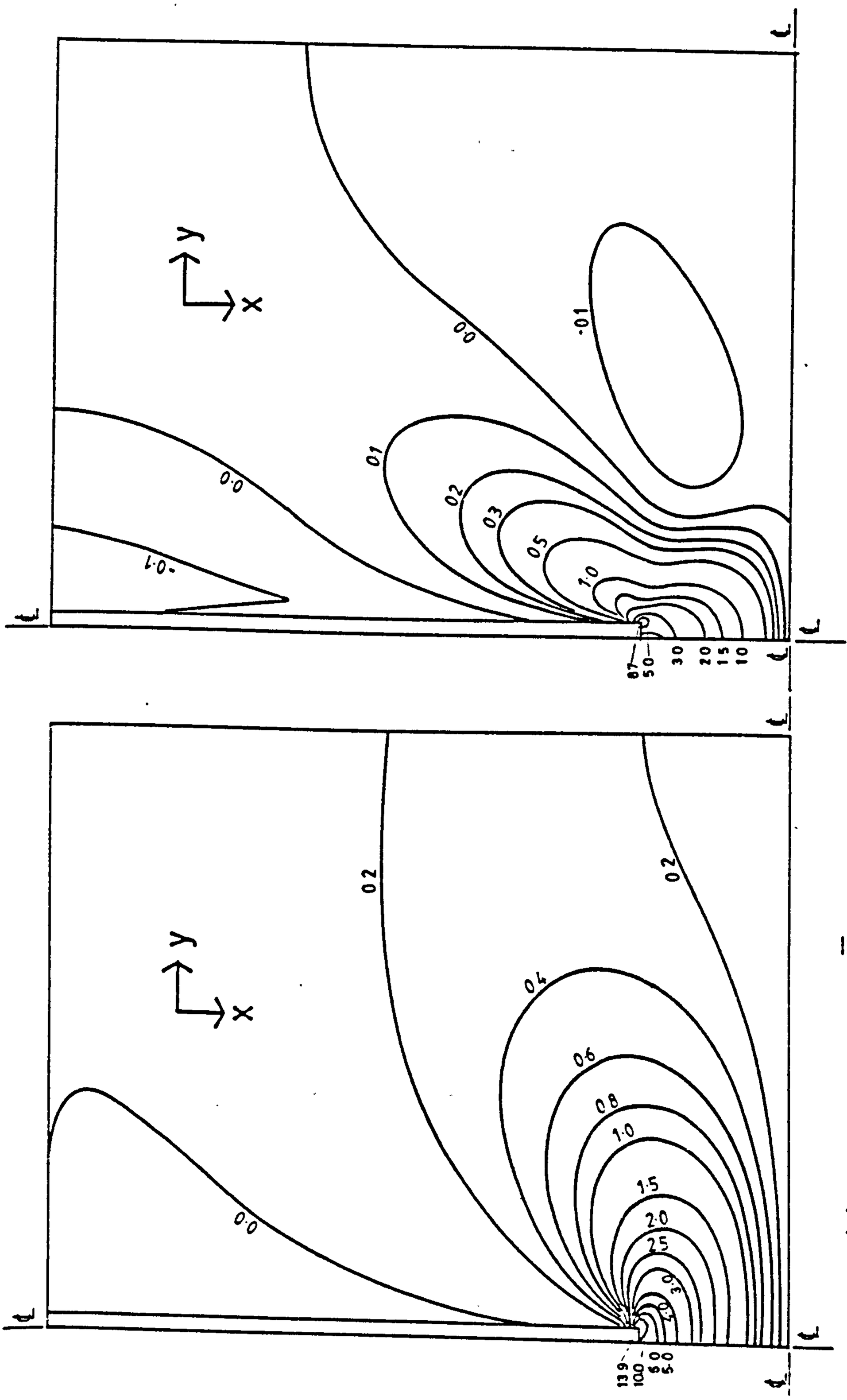

(b) BENDING MOMENT $\bar{M}_y$

(a) BENDING MOMENT $\bar{M}_x$

Fig. 3.21 Bending Moment Contours for Slab in Plane Wall Configuration (Y/L = 4)

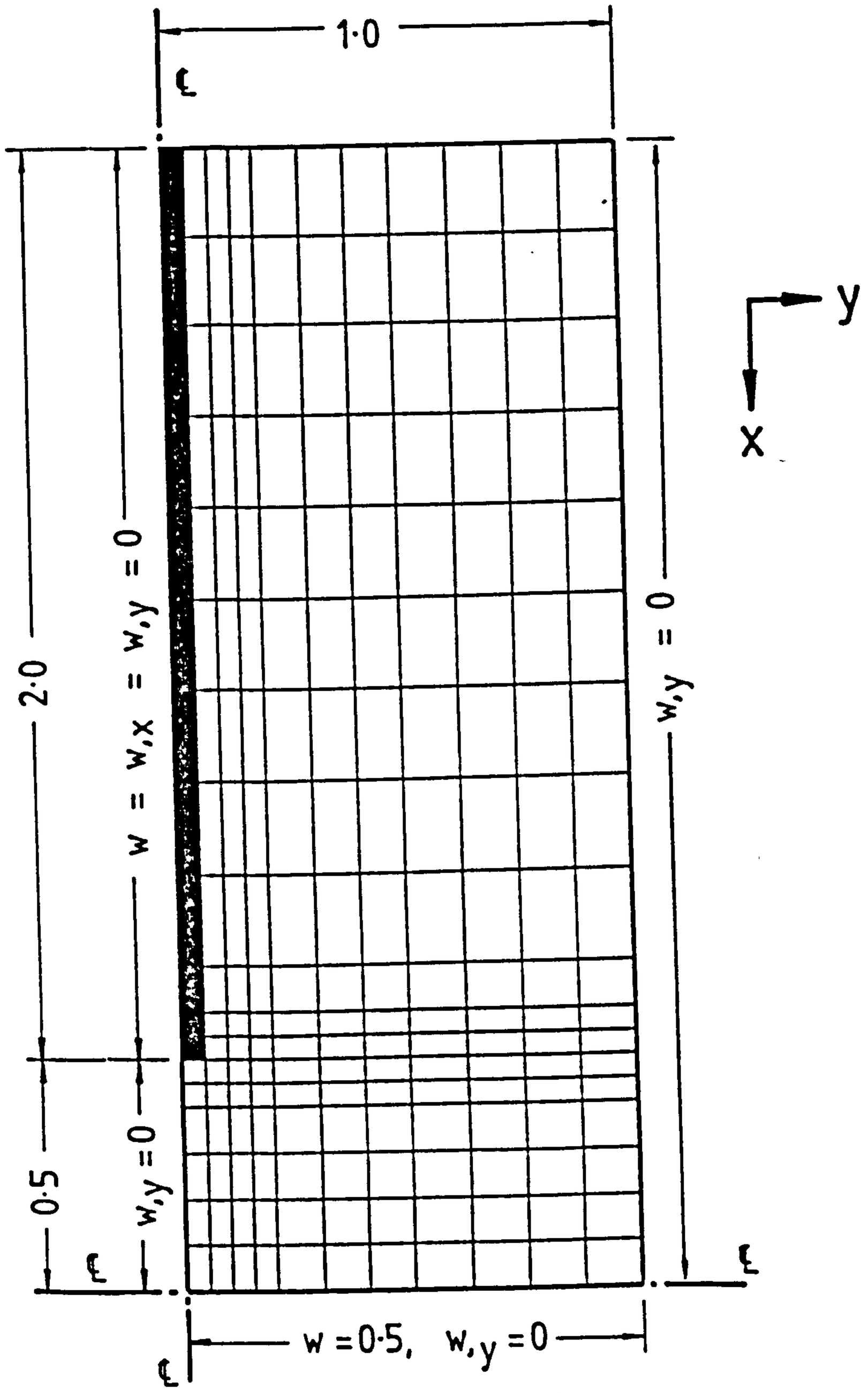

Fig. 3.22 Typical Finite Element Mesh for Contour Diagrams

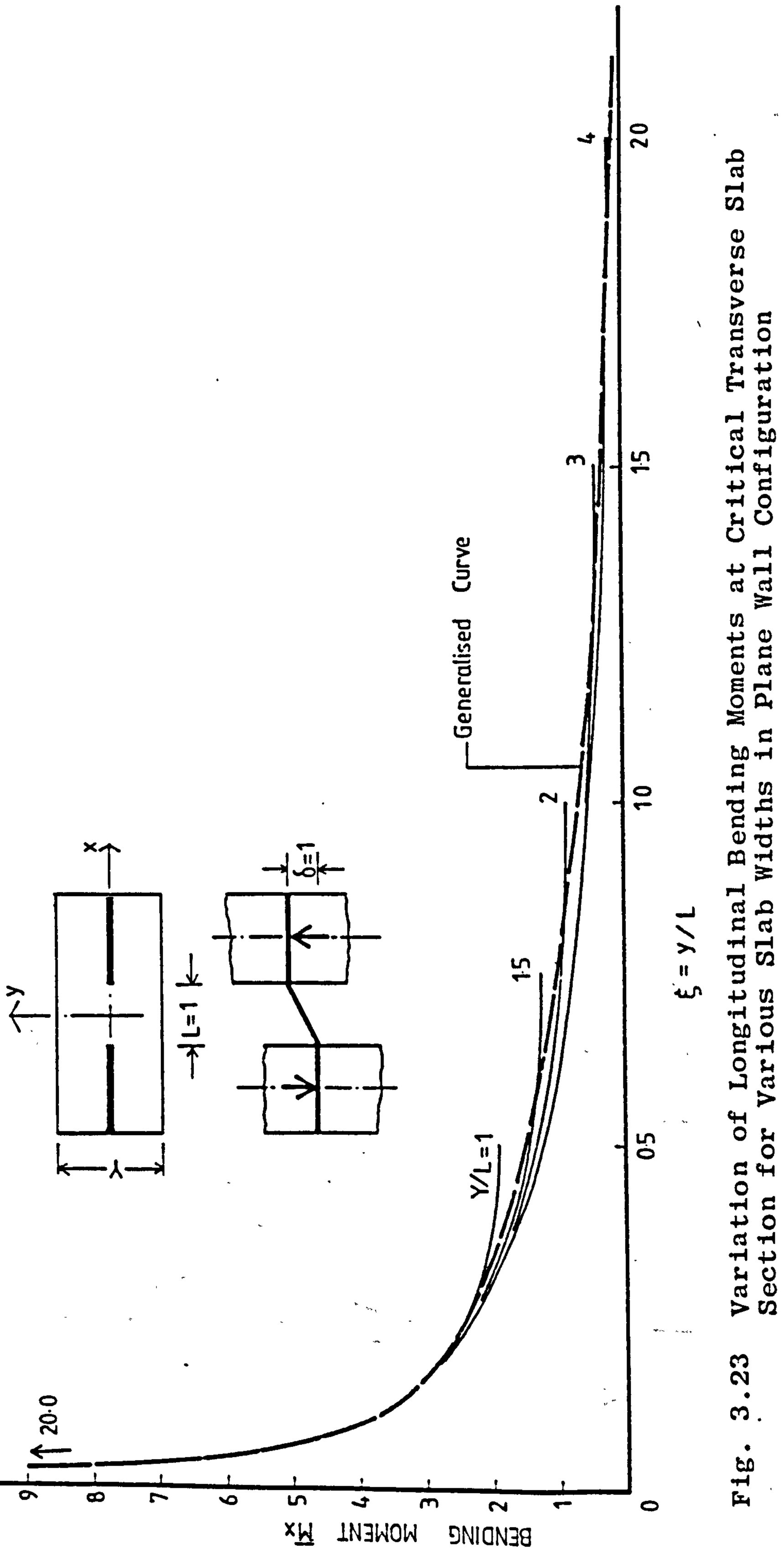

Fig. 3.23 Variation of Longitudinal Bending Moments at Critical Transverse Section for Various Slab Widths in Plane Wall Configuration

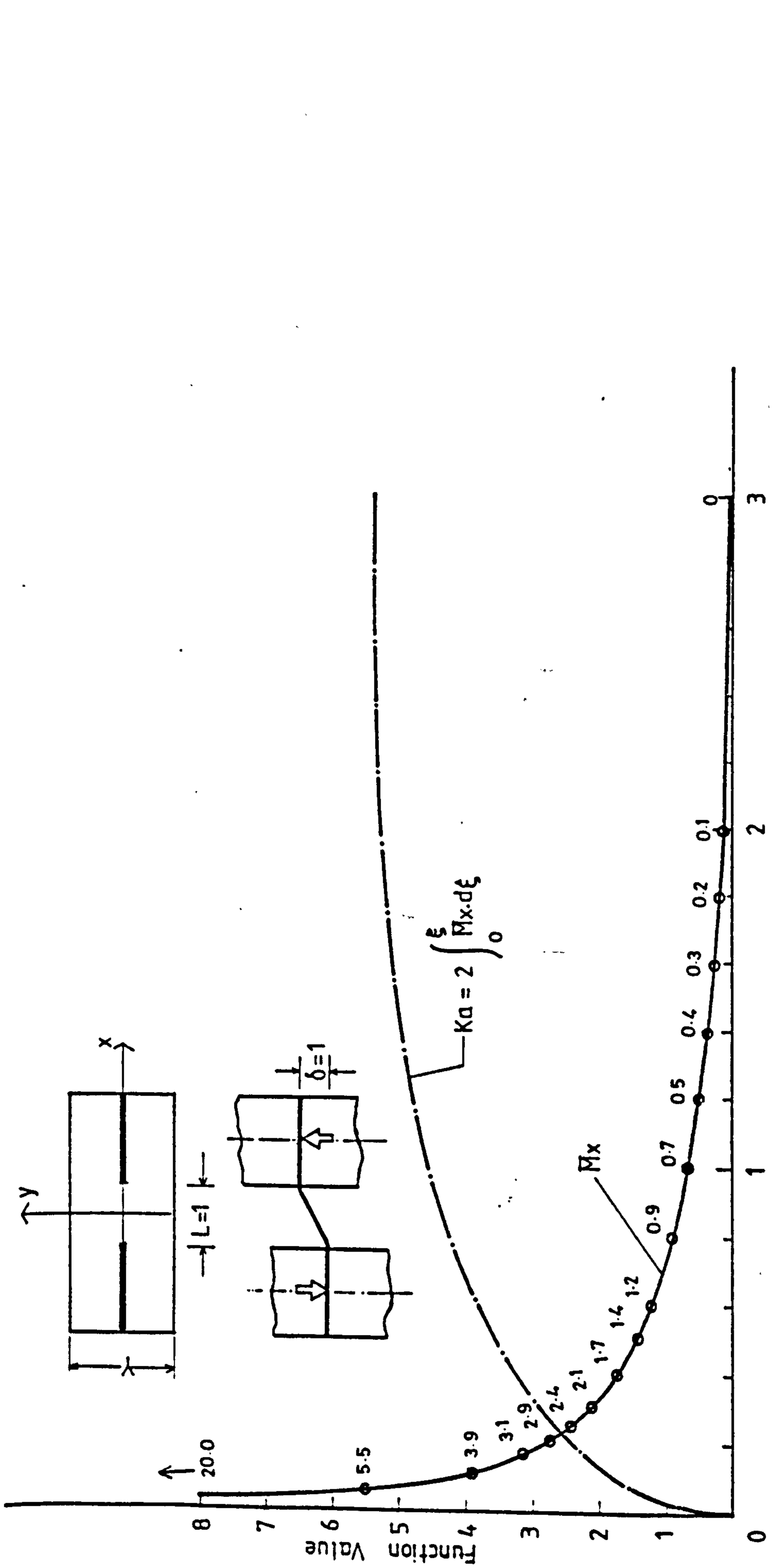
Longitudinal Bending Moments at Critical
Plane Wall Configuration
Transverse Slab Section for Plane
Generalised Design Curves for Longitudinal
Fig. 3.24
$\xi = y/L$
$\bar{M}x$
$Ka = 2\int_0^{\xi} \bar{M}x \cdot d\xi$
Function Value
$\bar{M}x \cdot \Delta\xi$
$\Sigma \bar{M}x \cdot \Delta\xi$
$\Delta\xi$
L=1
δ=1
λ
x
y

(a) Finite Element Idealisation of Slab

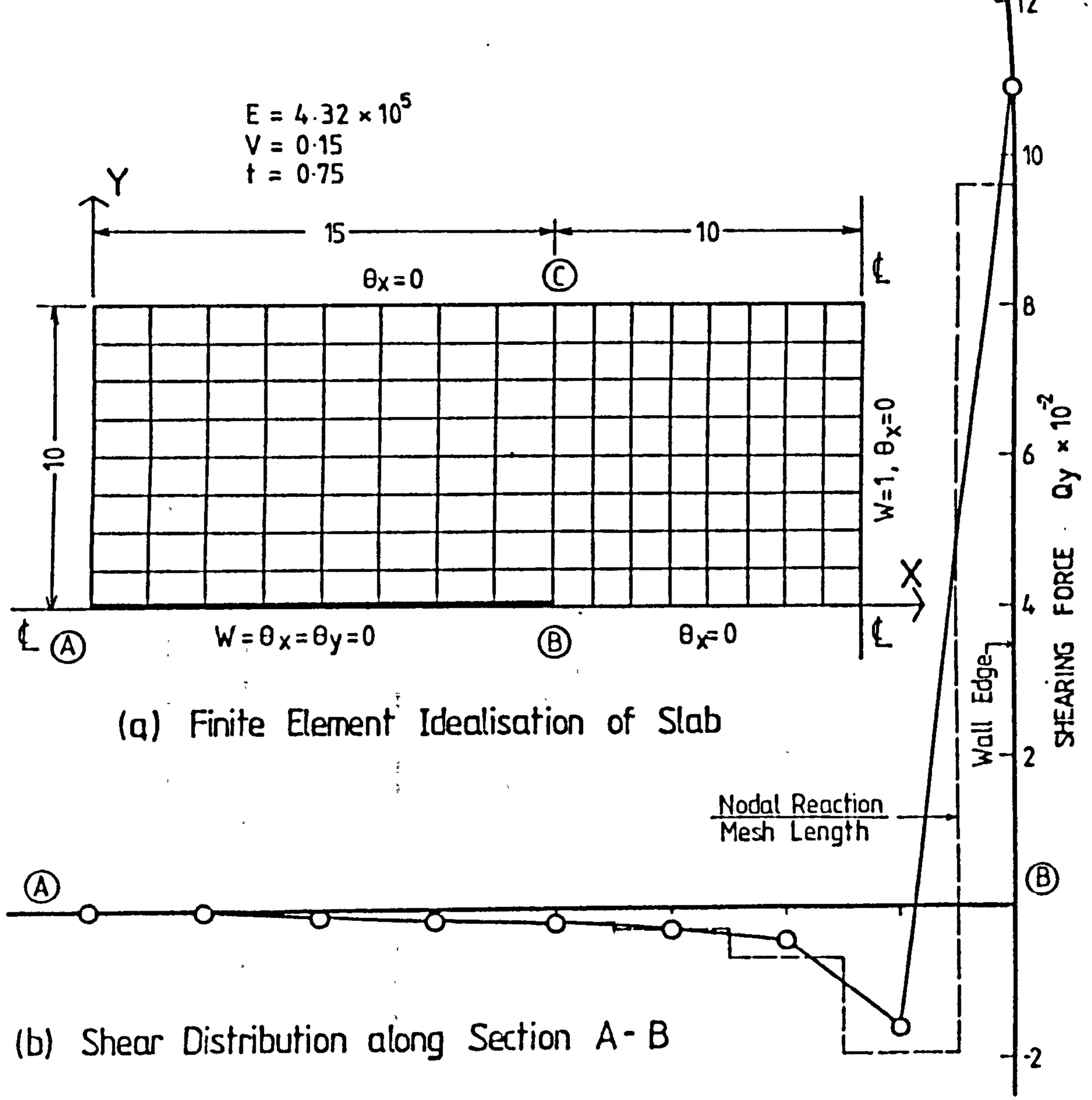

(b) Shear Distribution along Section A - B

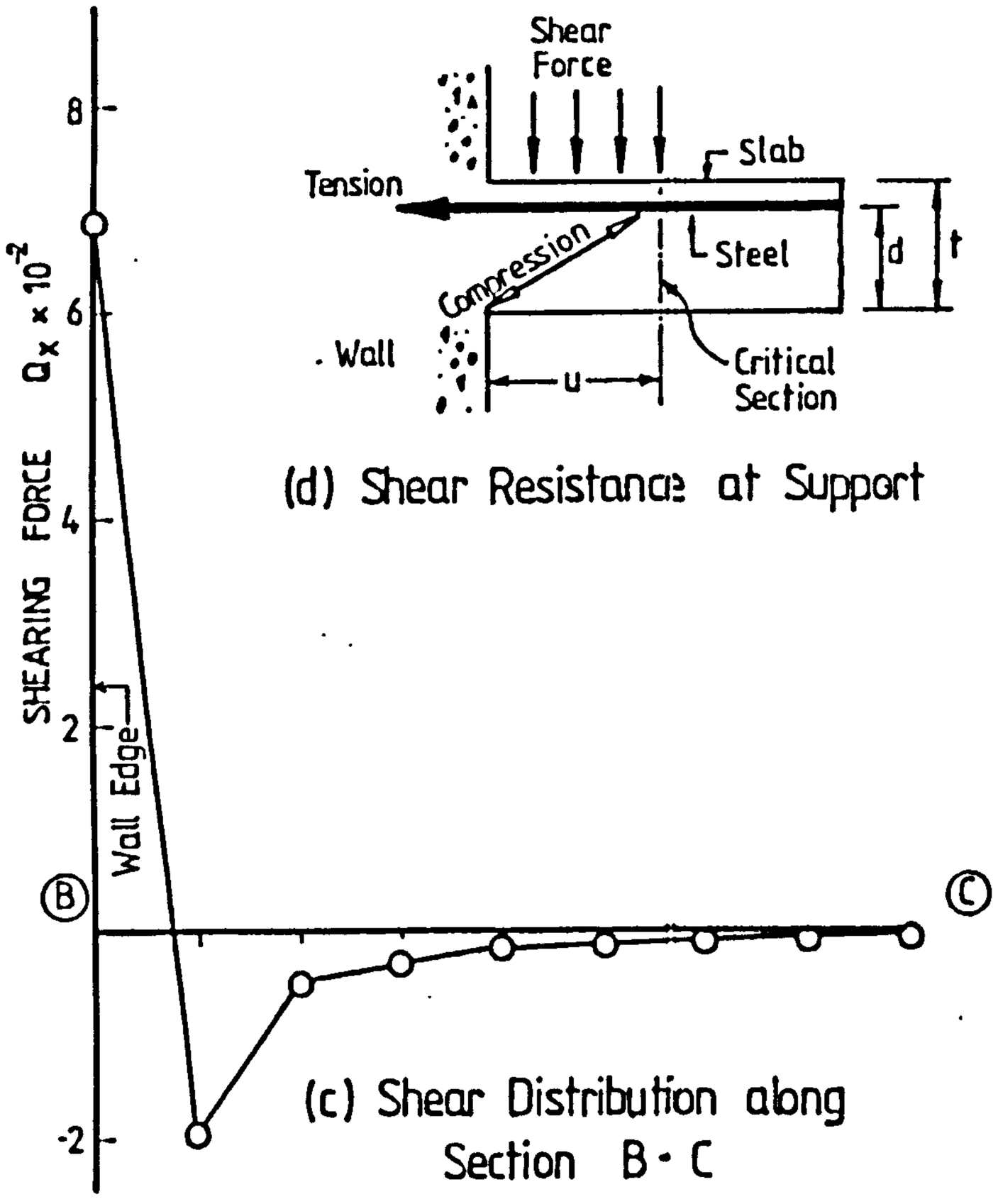

(c) Shear Distribution along Section B - C

(d) Shear Resistance at Support

Fig. 3.25 Shear Distribution at Wall Support

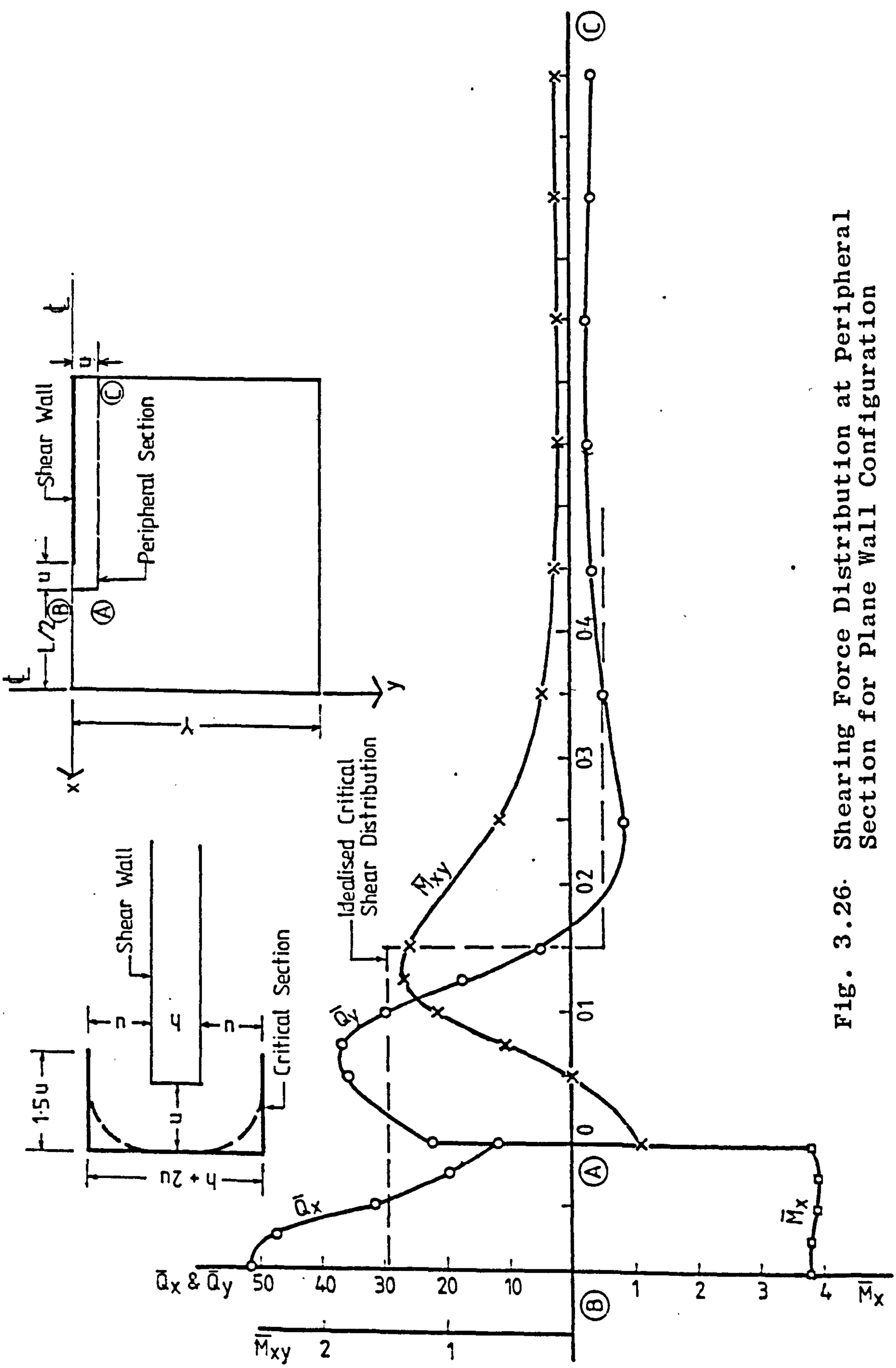

Fig. 3.26. Shearing Force Distribution at Peripheral Section for Plane Wall Configuration

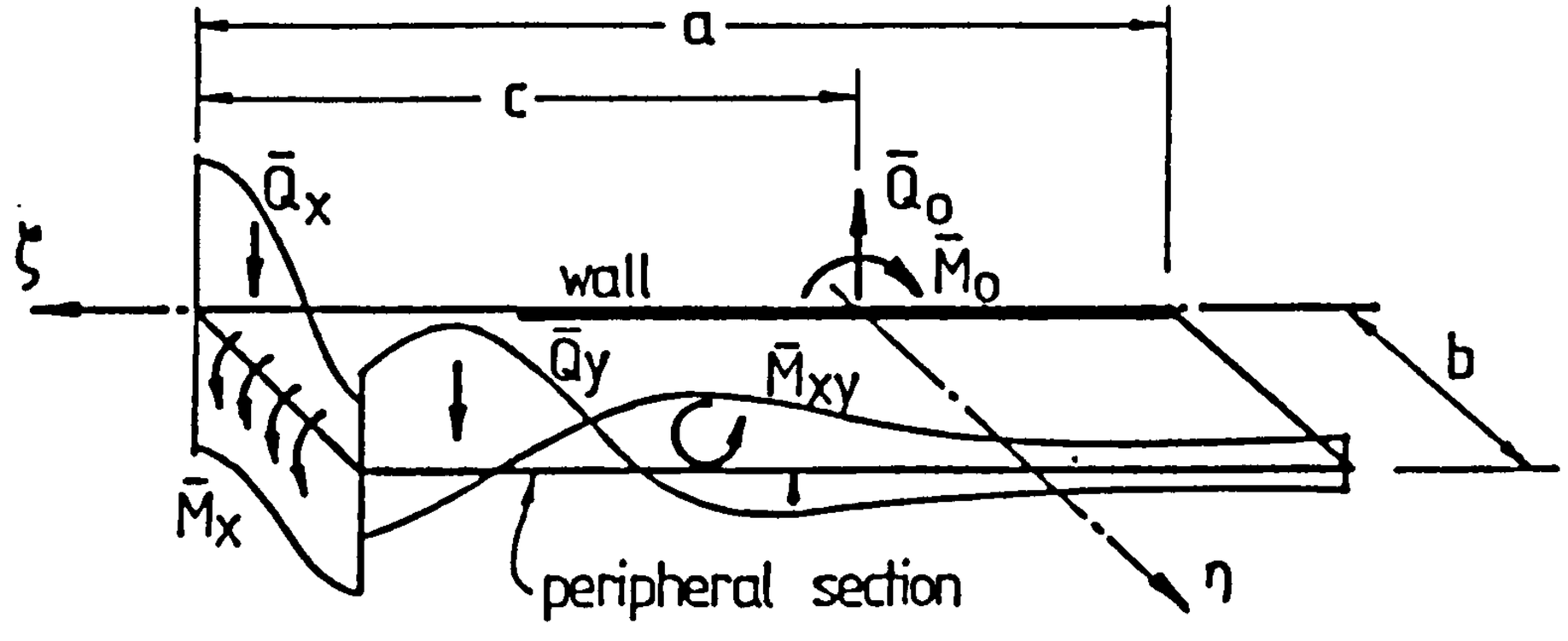

EQUILIBRIUM CHECK ON SHEARS

$\int_o^b \bar{Q}_x \, d\eta$	=	3·236
$\int_o^a \bar{Q}_y \, d\zeta$	=	1·222
$\sum$	=	4·458
$\bar{Q}_o$	=	4·460

EQUILIBRIUM CHECK ON MOMENTS

$\int_o^b c.\bar{Q}_x \, d\eta$	=	1·537
$\int_o^a \zeta \, \bar{Q}_y \, d\zeta$	=	1·616
$\int_o^b \bar{M}_x \, d\eta$	=	0·388
$\int_o^a \bar{M}_{xy} \, d\zeta$	=	0·270
$\sum$	=	3·811
$\bar{M}_o$	=	3·903

Fig. 3.27 Equilibrium of Force Actions at Peripheral Section

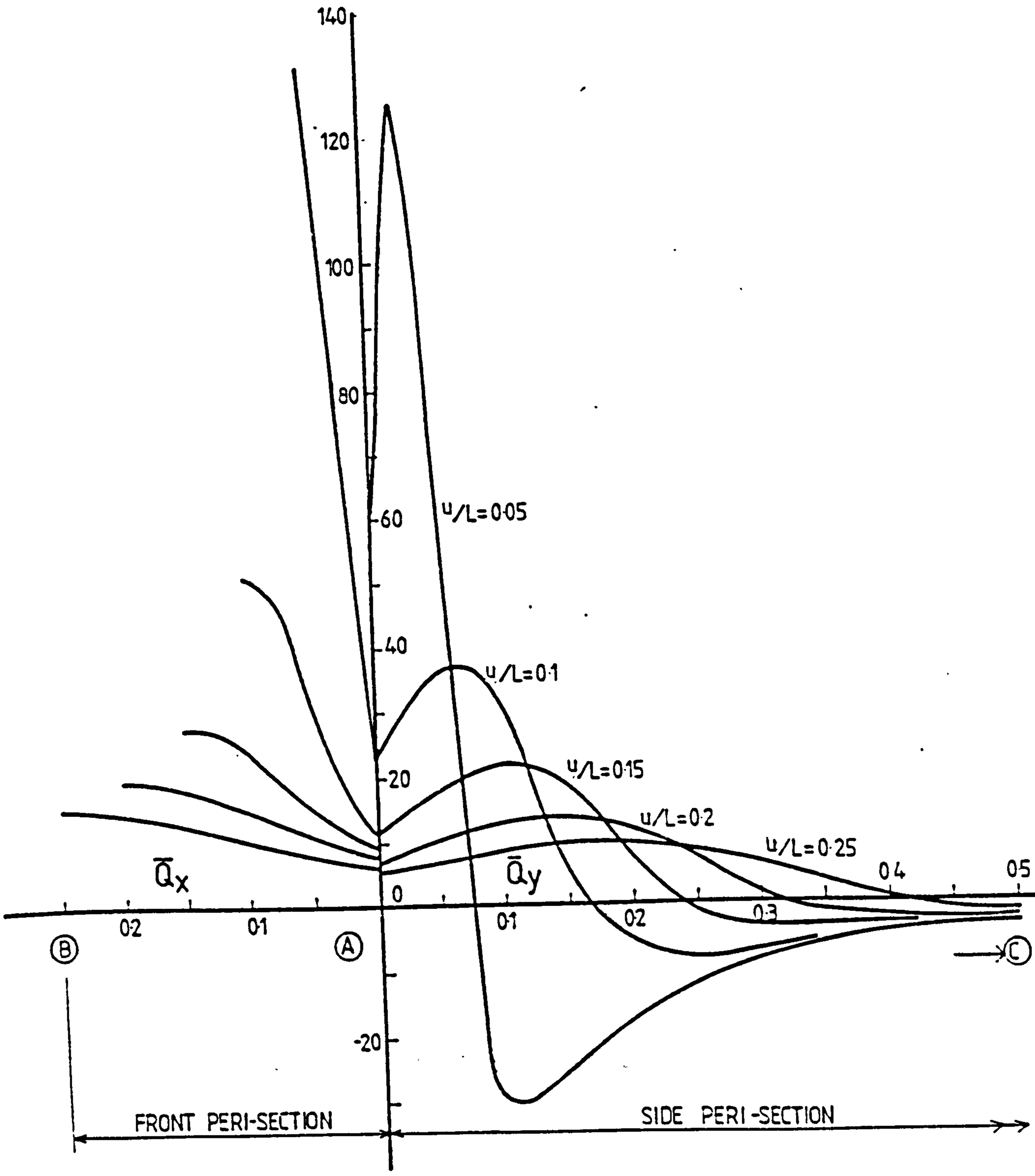

Fig. 3.28 Shearing Force Distributions at Various Peripheral Sections

u/L	Y/L	Q1	Q2	Q0	Q1/Q0
0·1	1·0	6·715	-3·119	3·596	1·868
	2·0	7·614	-3·061	4·553	1·672
	4·0	7·790	-2·956	4·934	1·579
0·2	1·0	4·900	-1·306	3·594	1·363
	2·0	5·831	-1·278	4·553	1·281
	4·0	6·136	-1·202	4·934	1·244

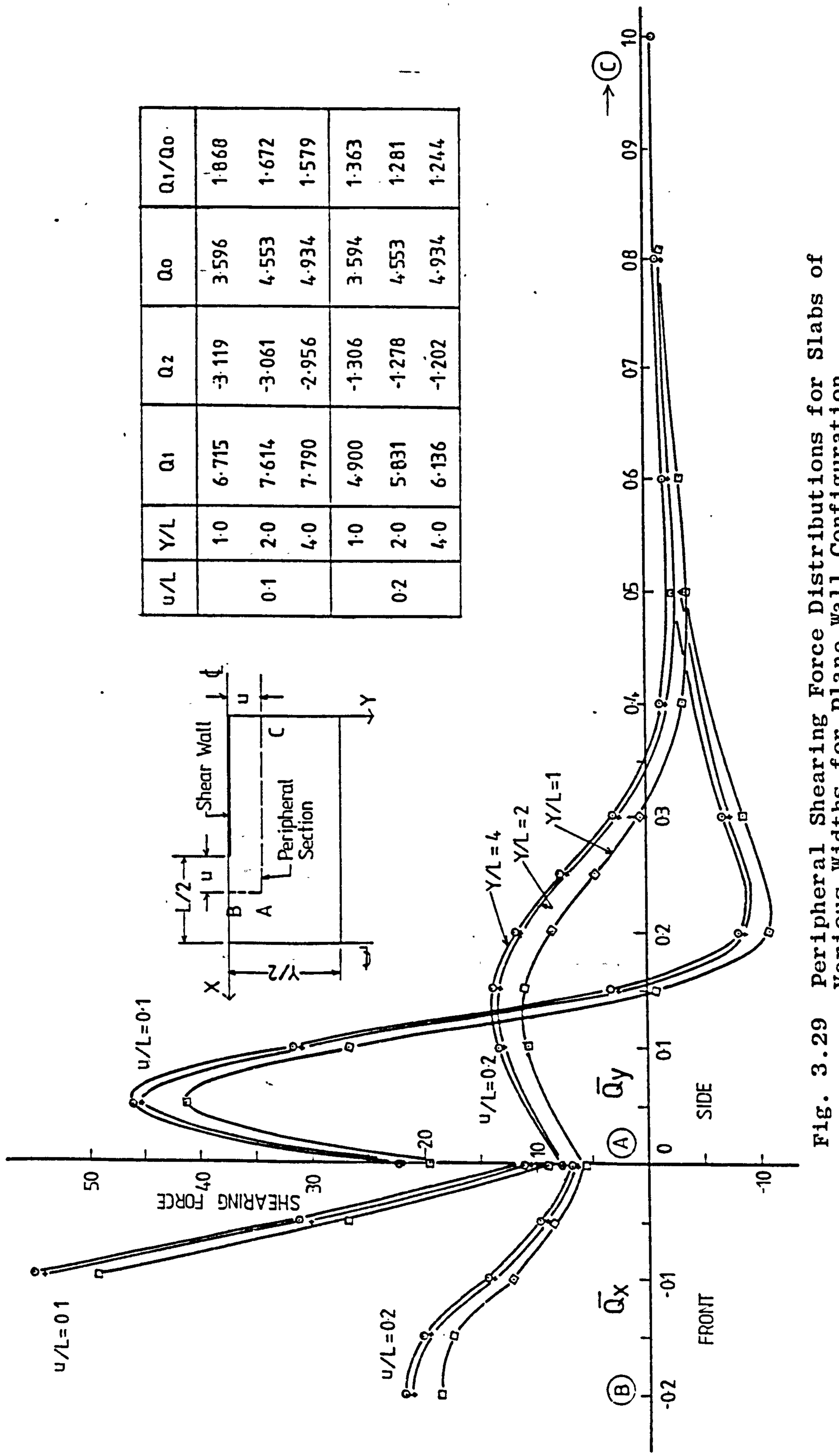

Fig. 3.29 Peripheral Shearing Force Distributions for Slab Various Widths for Plane Wall Configuration

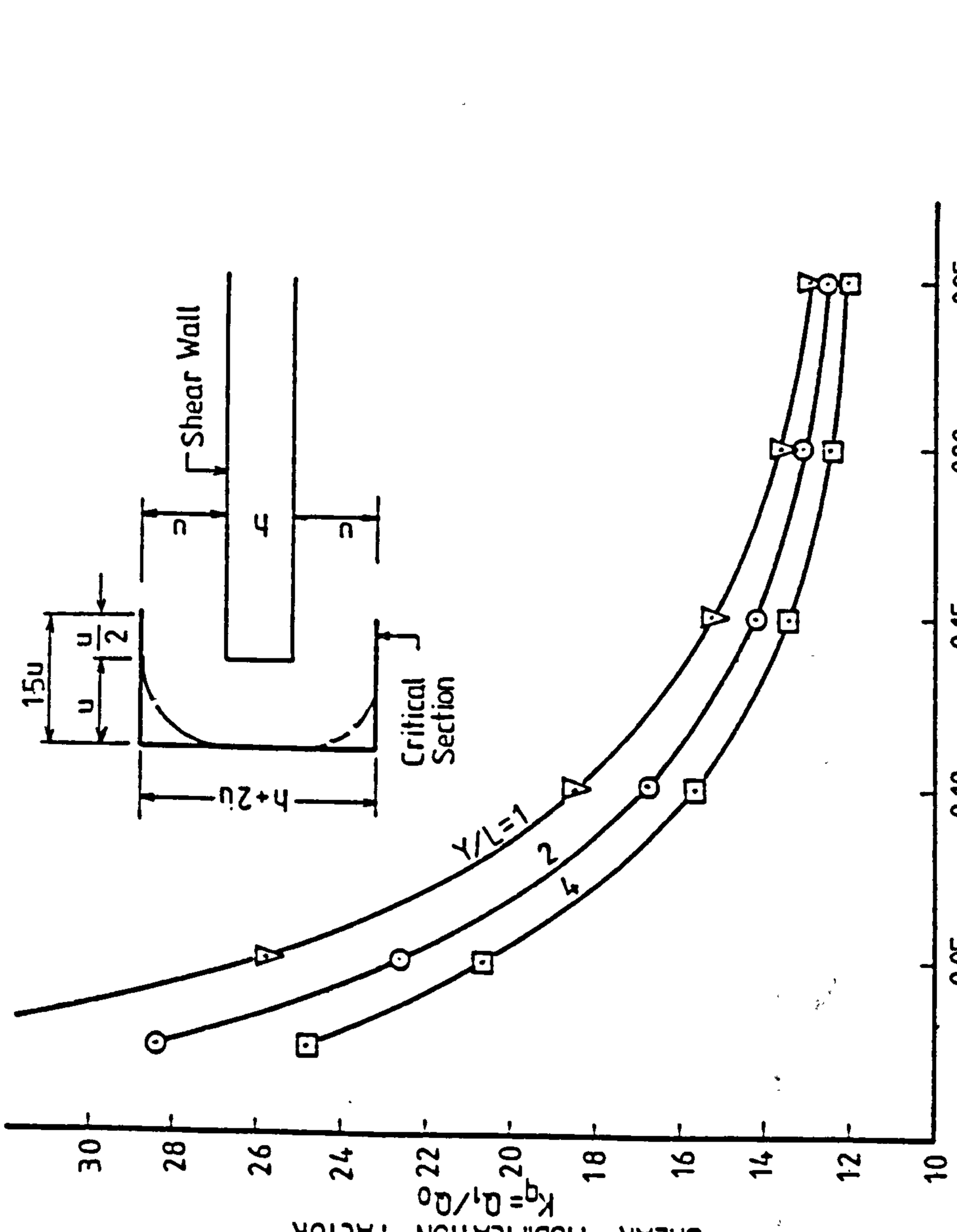
Shear Wall
h
n
n
15u
u
u/2
h+2u
Critical Section
Y/L=1
2
4
SHEAR MODIFICATION FACTOR
$K_q = Q_1/Q_o$
30
28
26
24
22
20
18
16
14
12
10
0·05
0·10
0·15
0·20
0·25
PERIPHERAL DISTANCE u/L
DESIGN CURVE FOR SHEAR MODIFICATION FACTOR
(PLANE WALL CONFIGURATION)

FIG. 3.30

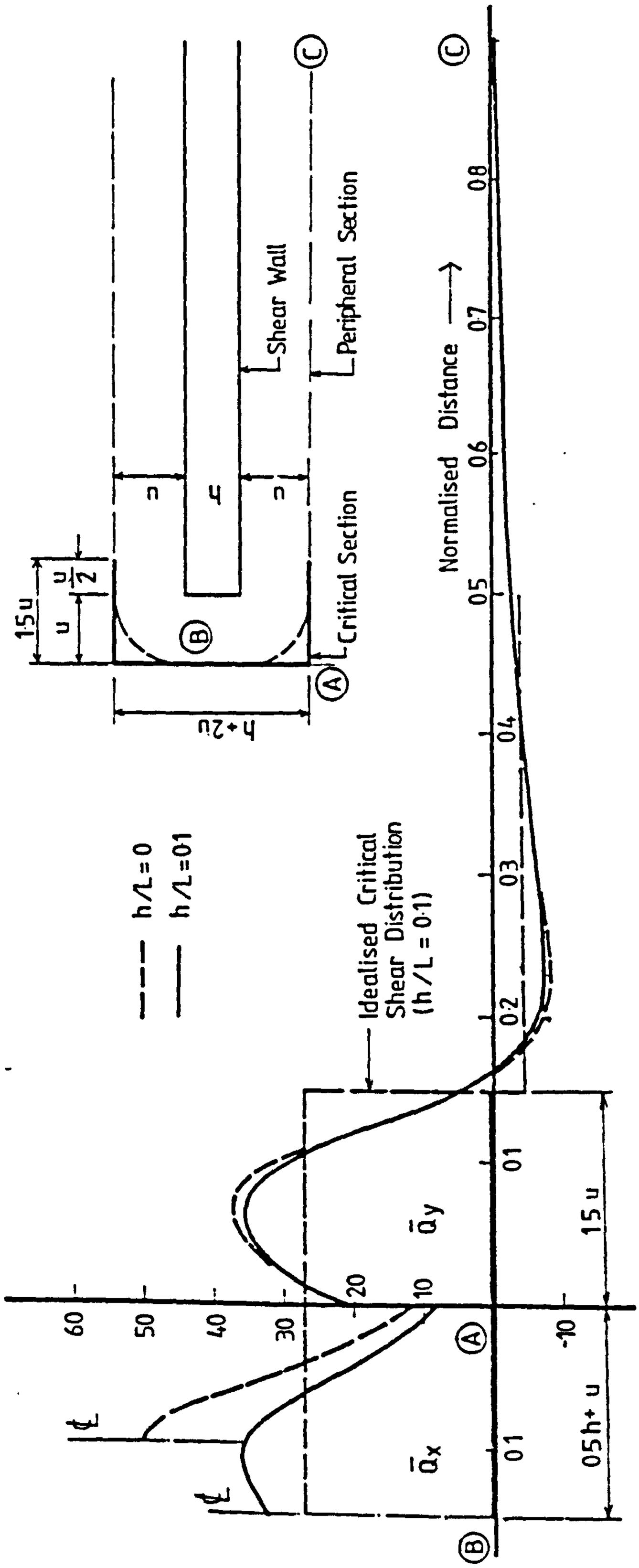

Fig. 3.31 Effect of Finite Wall Thickness on Peripheral Shearing Force Distribution

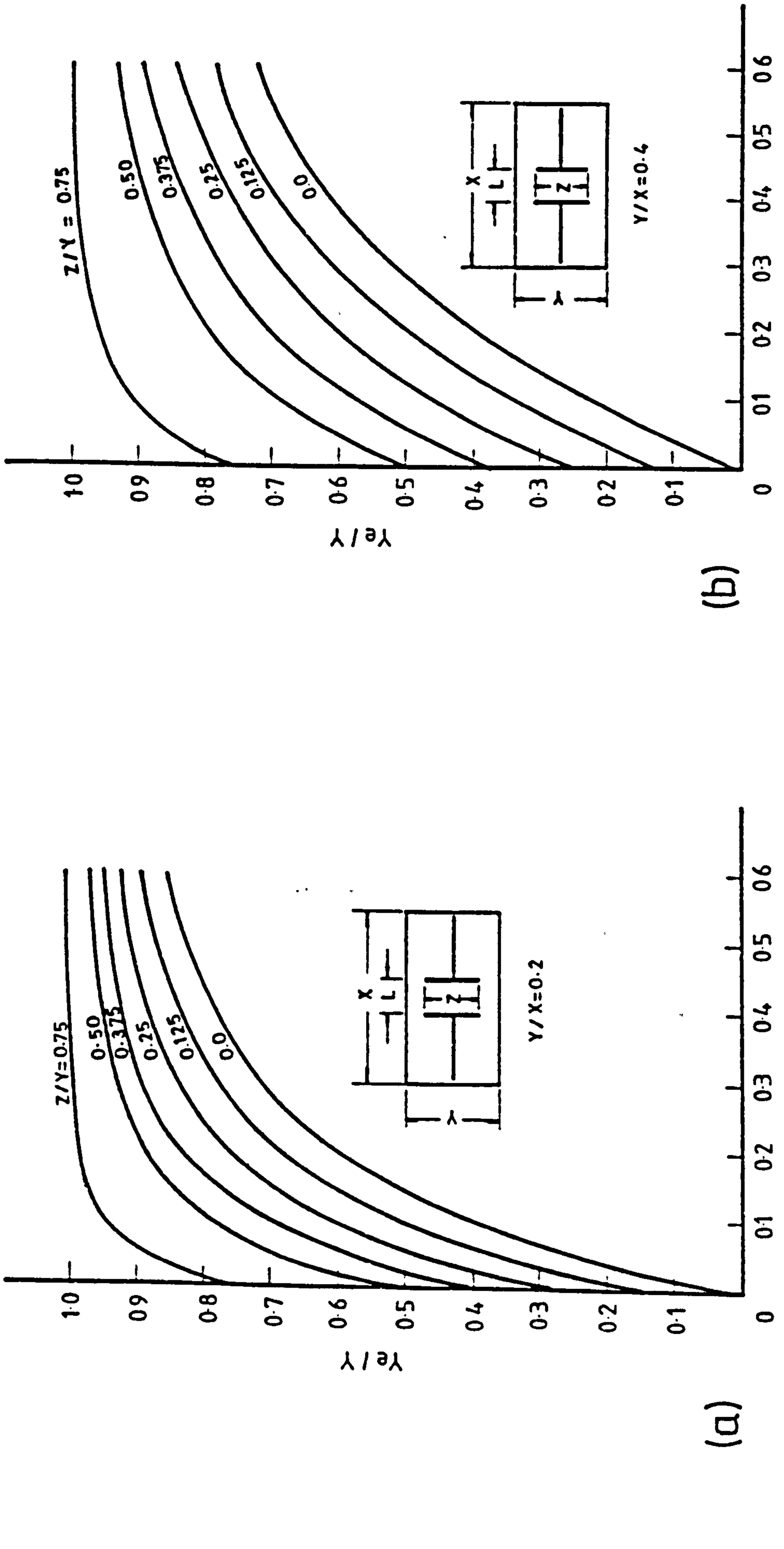

Fig. 3.32 Effective Slab Width for T-shaped Flanged Wall Configuration

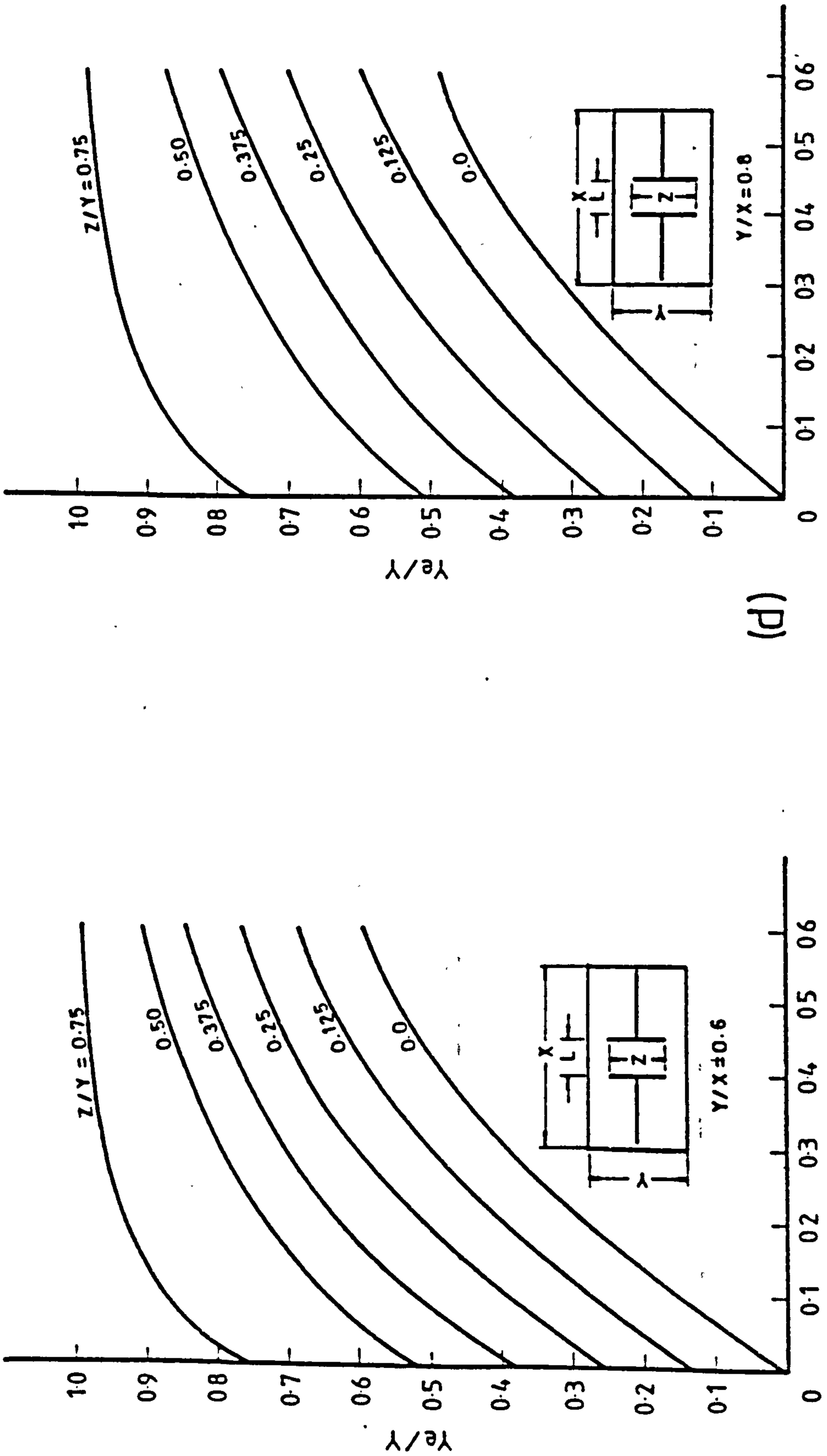

Fig. 3.32 (Contd) Design Curves for Effective Slab Width for T-shaped Flanged Wall Configuration

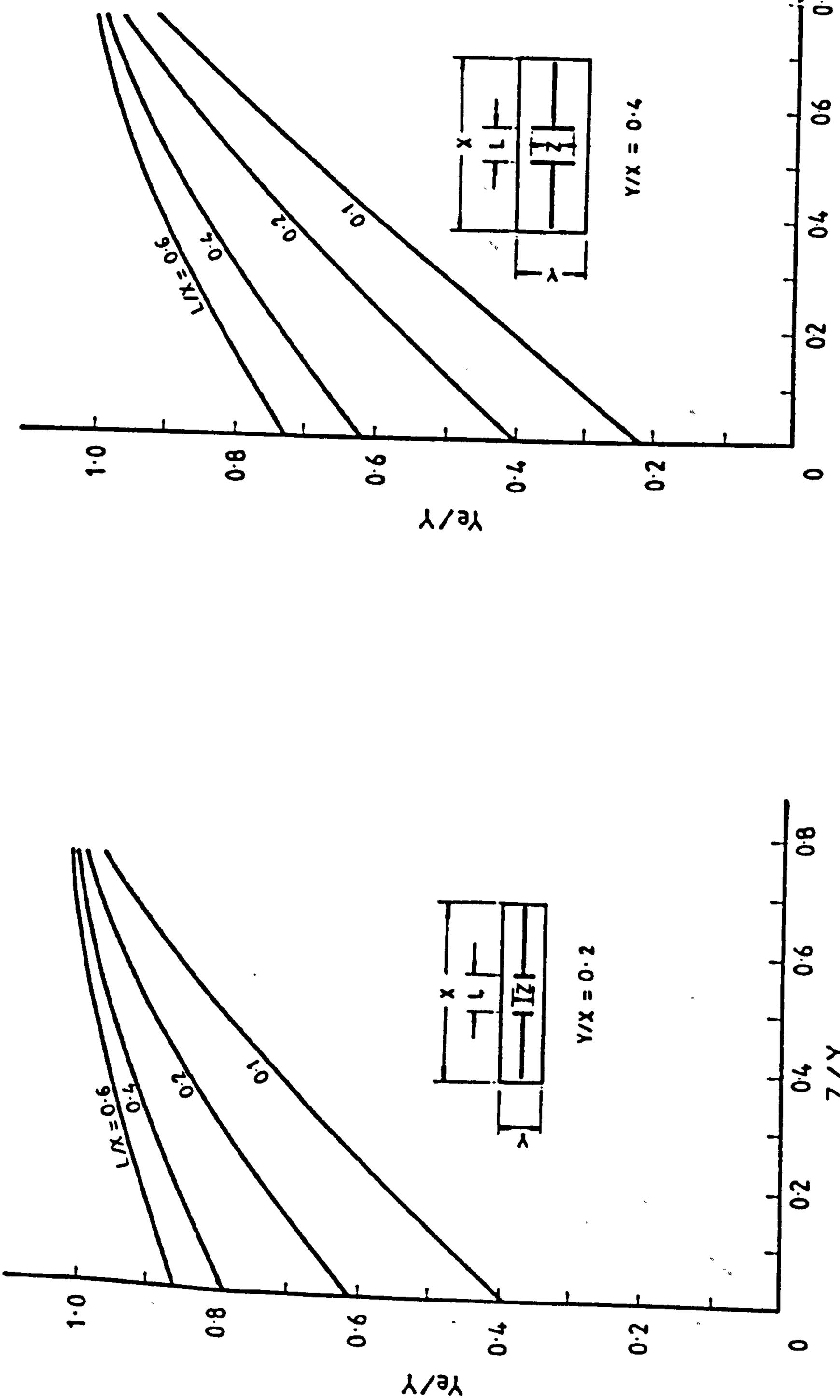

Fig. 3.33 Variation of Effective Slab Width with Flange Width for Flanged Wall Configuration

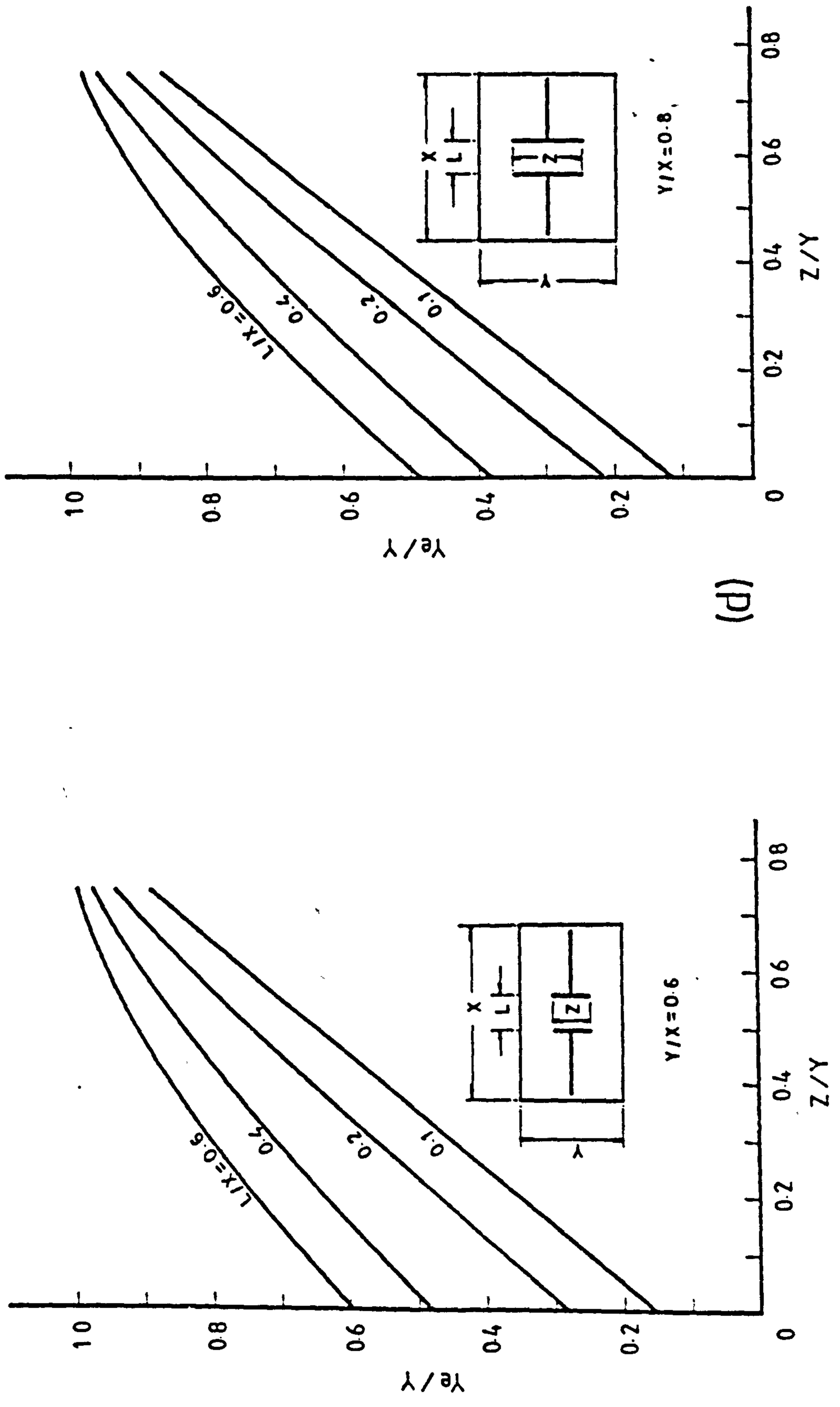

Fig. 3.33 (Contd) Variation of Effective Slab Width with Flange Width for Flanged Wall Configuration

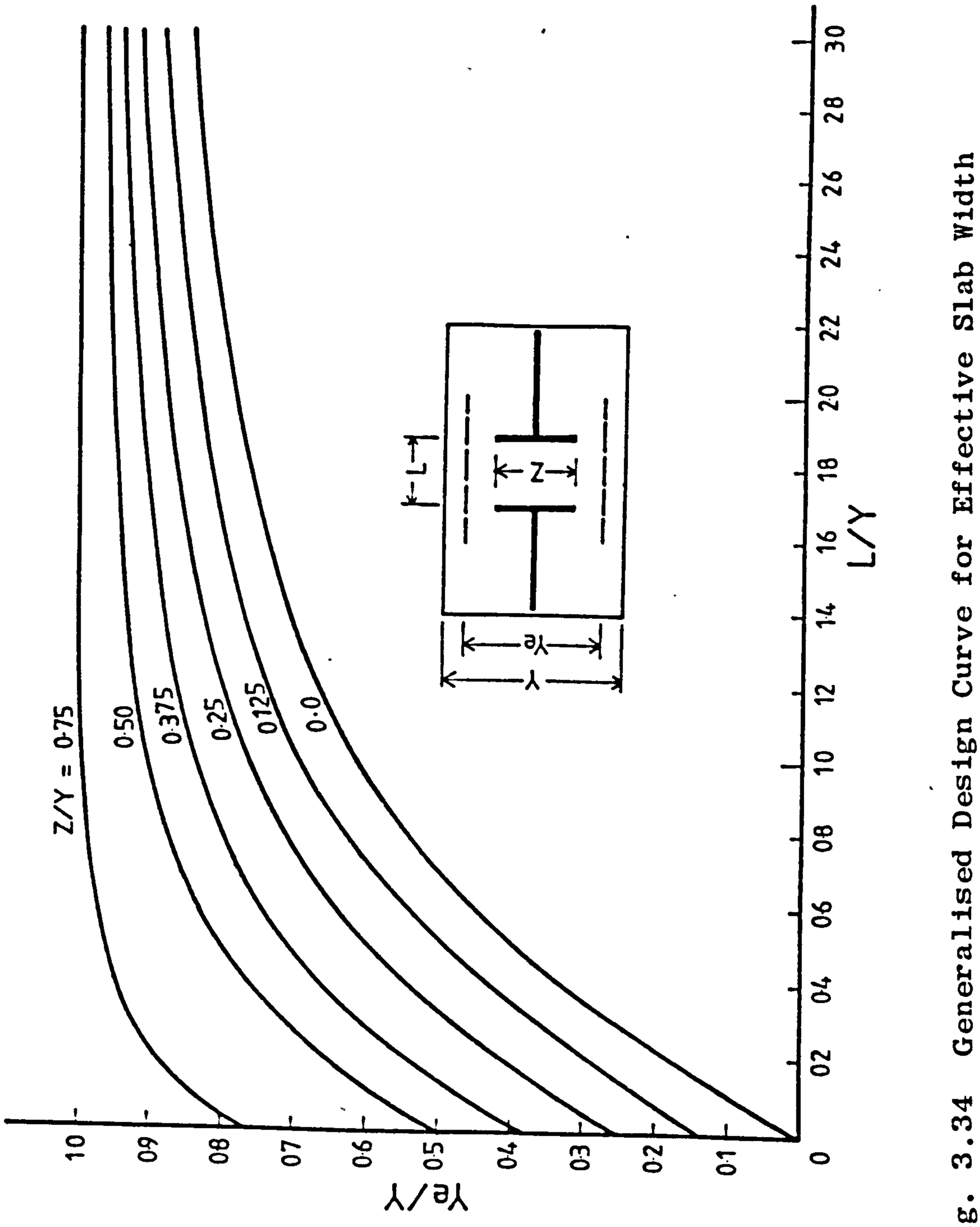

Fig. 3.34 Generalised Design Curve for Effective Slab Width for Flanged Wall Configuration

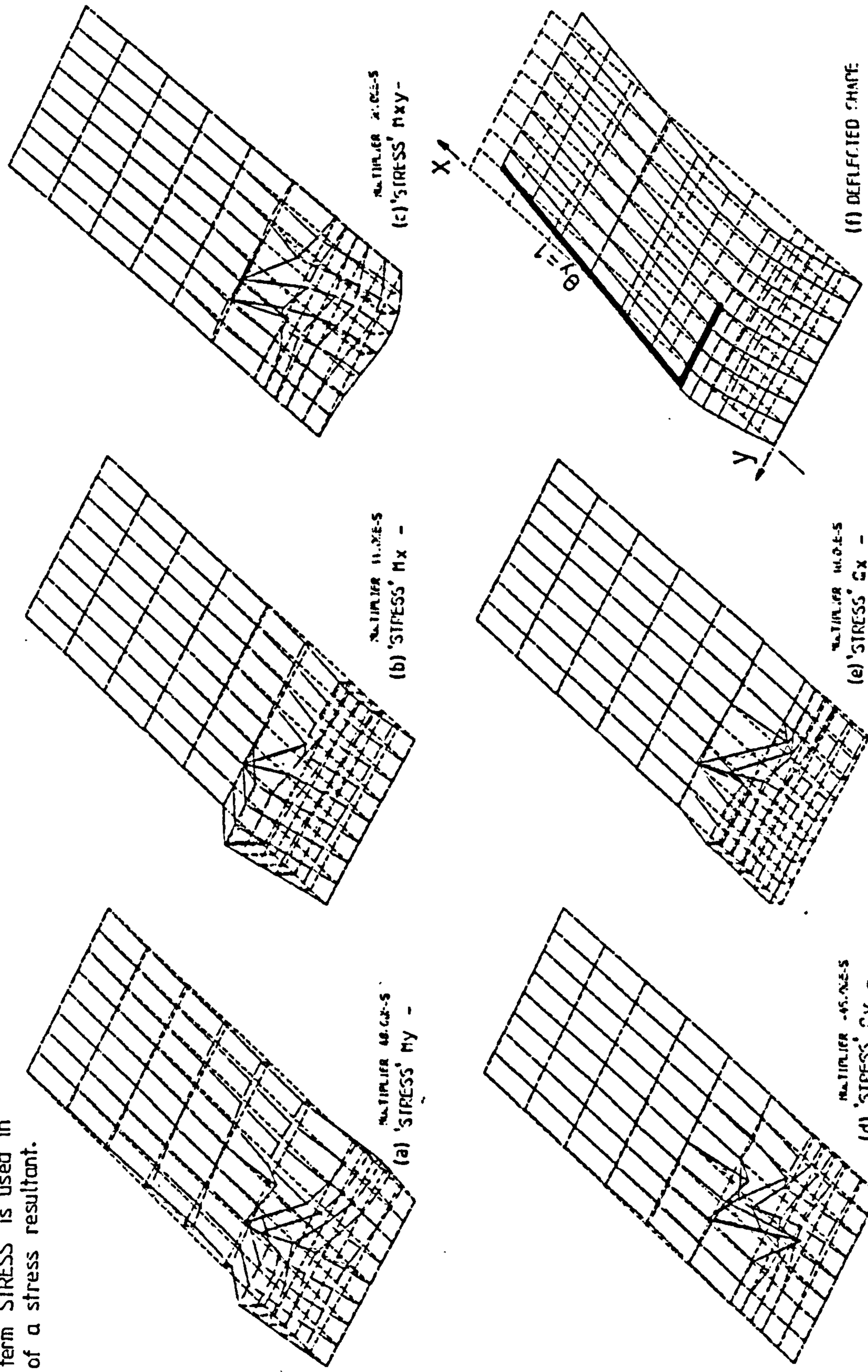

NOTE: The term 'STRESS' is used in the context of a stress resultant.

Fig. 3.36 General Distribution of Slab Actions in Flanged Wall Configurations

NOTE: The term 'STRESS' is used in the context of a stress resultant.

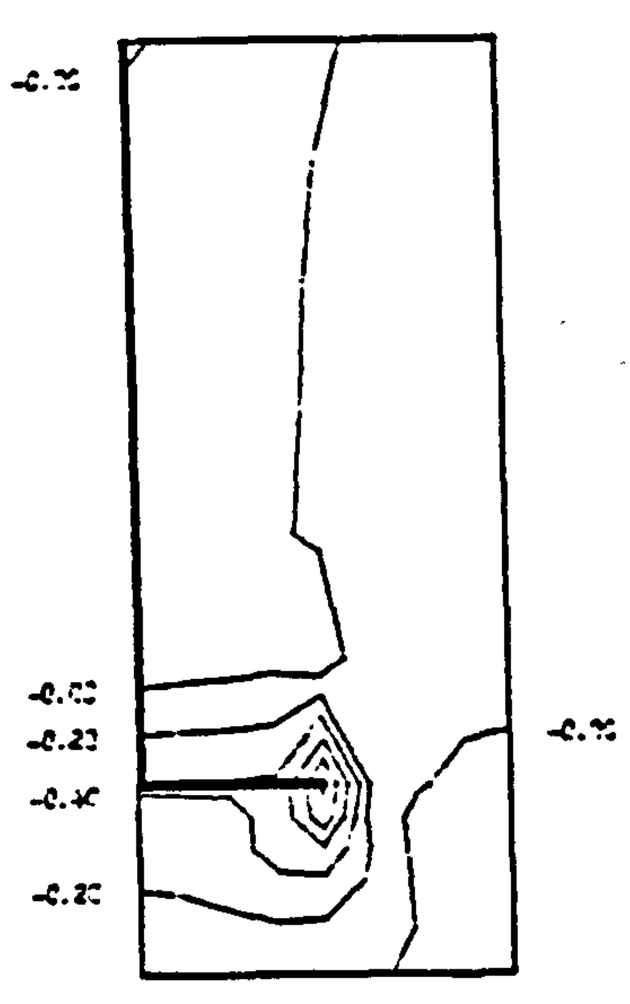

(a) 'STRESS' CONTOURS My

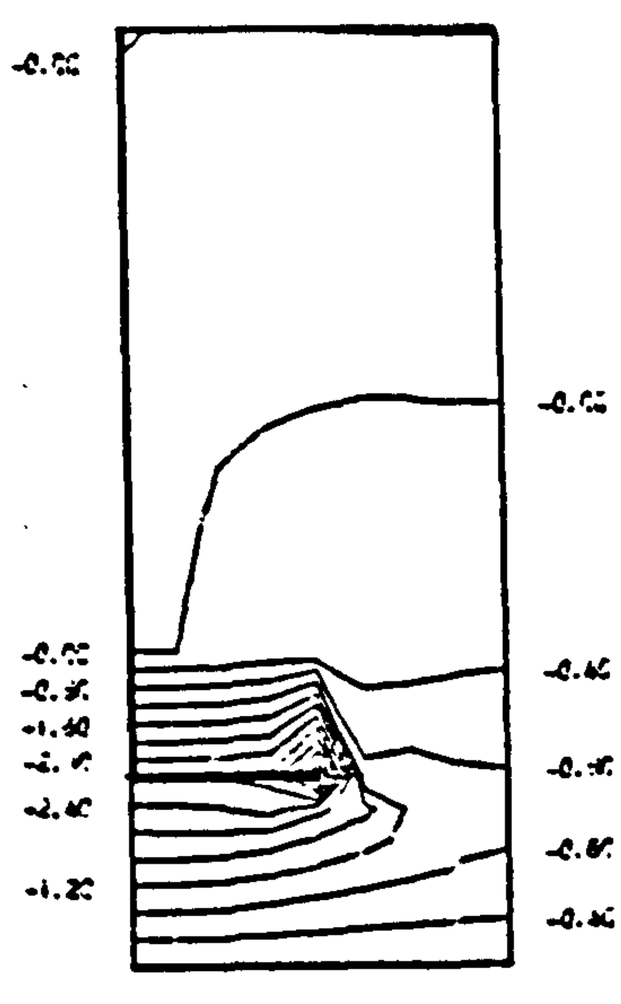

(b) 'STRESS' CONTOURS Mx

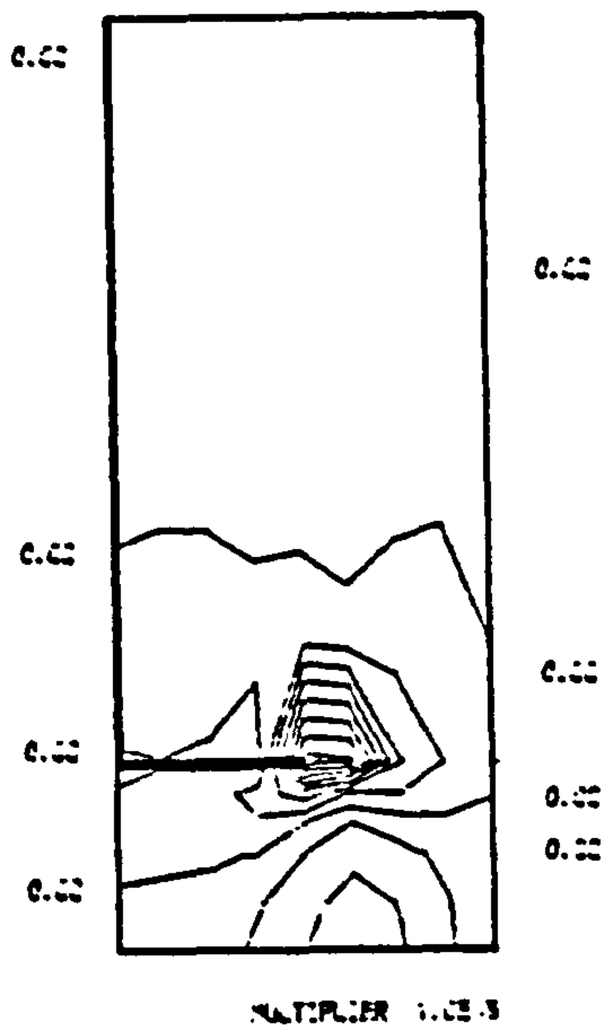

(c) 'STRESS' CONTOURS Mxy

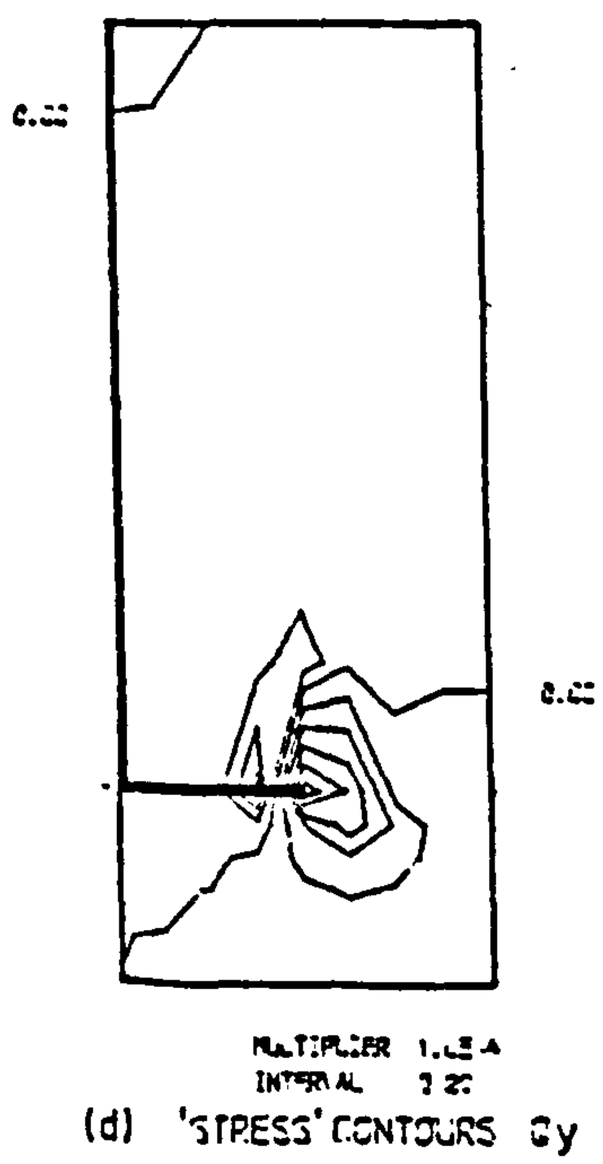

(d) 'STRESS' CONTOURS Qy

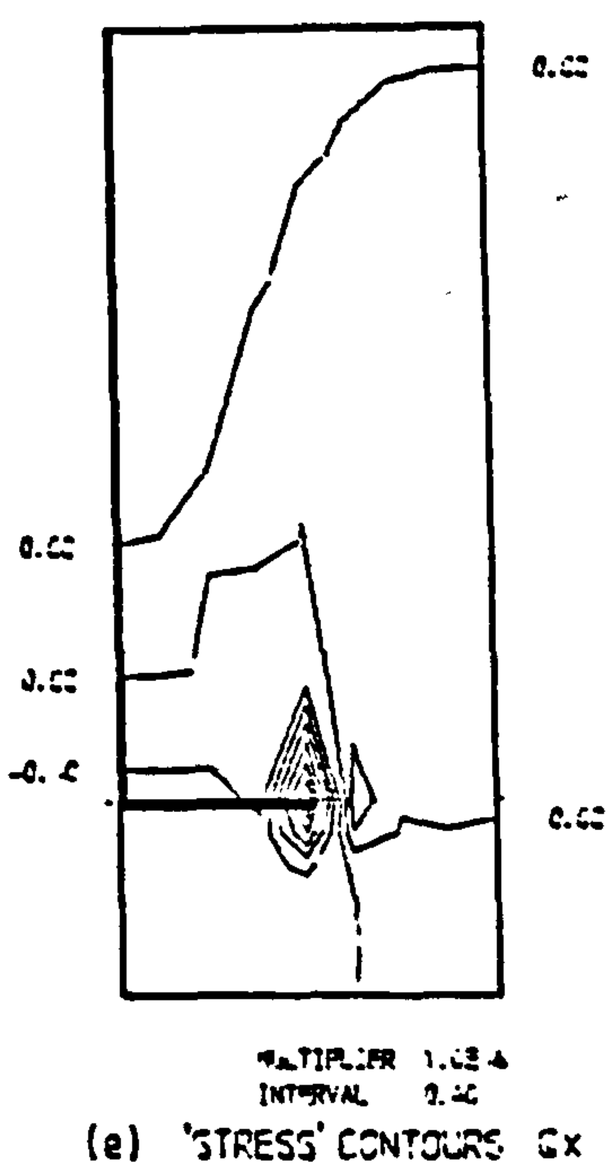

(e) 'STRESS' CONTOURS Qx

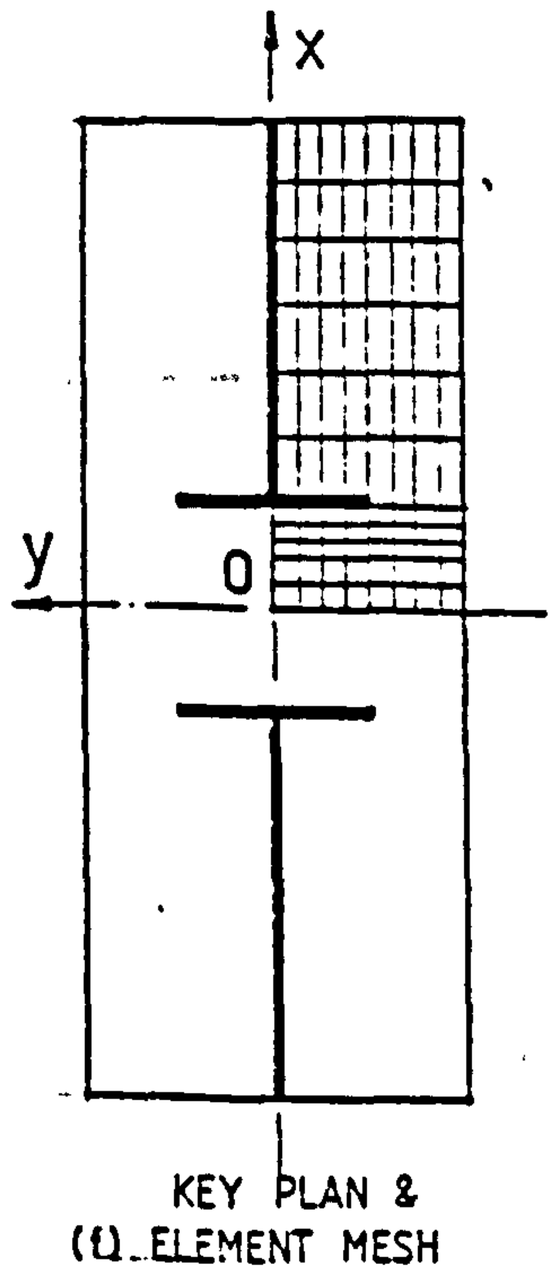

KEY PLAN & (f) ELEMENT MESH

Fig. 3.37 Contours of Stress Resultants in Slab for Flanged Wall Configuration

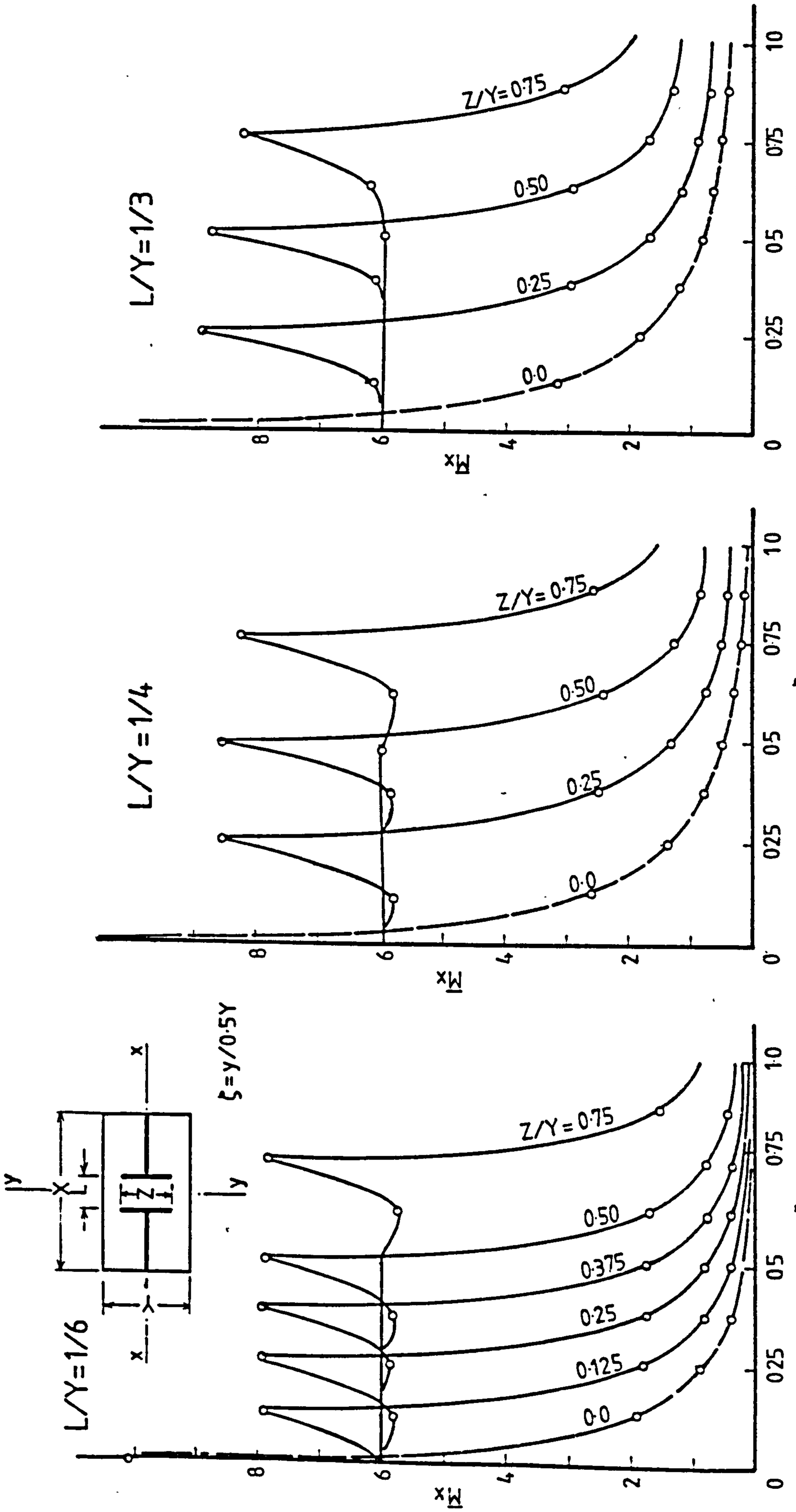

Fig. 3.38 Variation of Longitudinal Bending Moments at Critical Transverse Slab Section for Flanged Wall Configuration

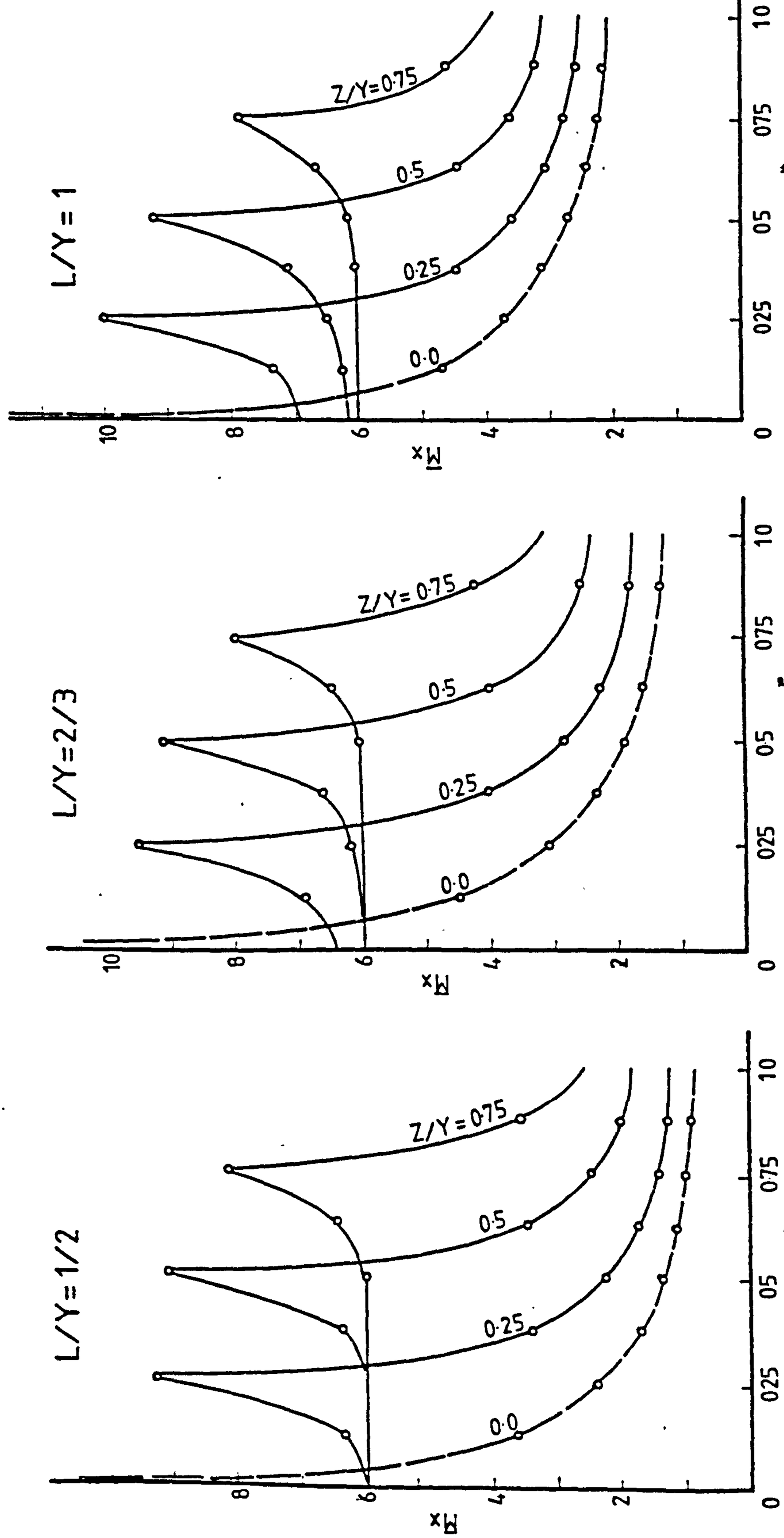

Fig. 3.38 (Contd) Variation of Longitudinal Bending Moments at Critical Transverse Slab Section for Flanged Wall Configuration

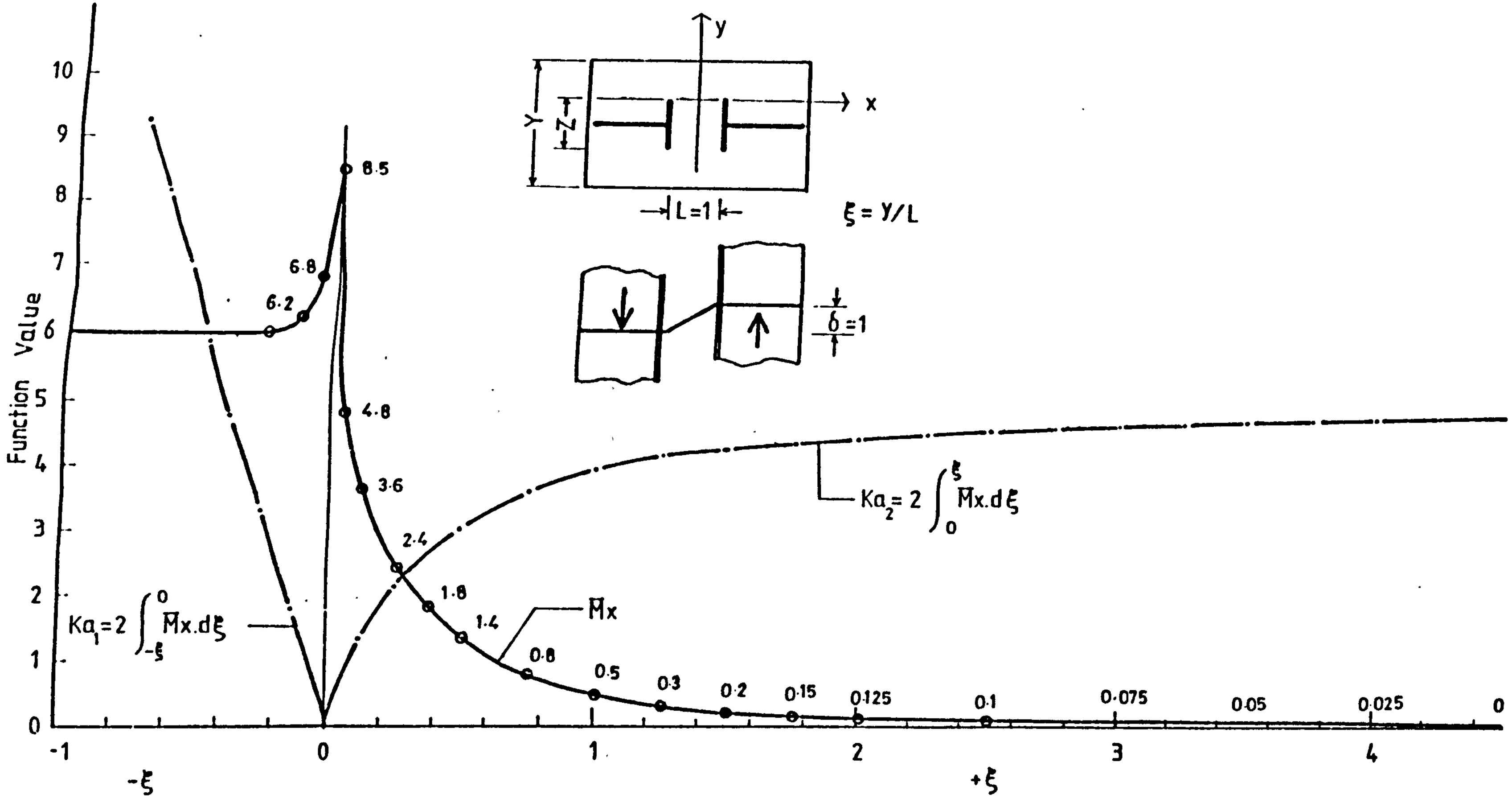

M̄x·Δξ																		
	1·50	1·50	1·50	0·75	0·88	0·68	0·38	0·26	0·20	0·28	0·16	0·10	0·06	0·08	0·06	0·04	0·03	0·02	0·01

Fig. 3.39 Generalised Design Curve for Longitudinal Bending Moments at Critical Transverse Slab Section for Flanged Wall Configuration

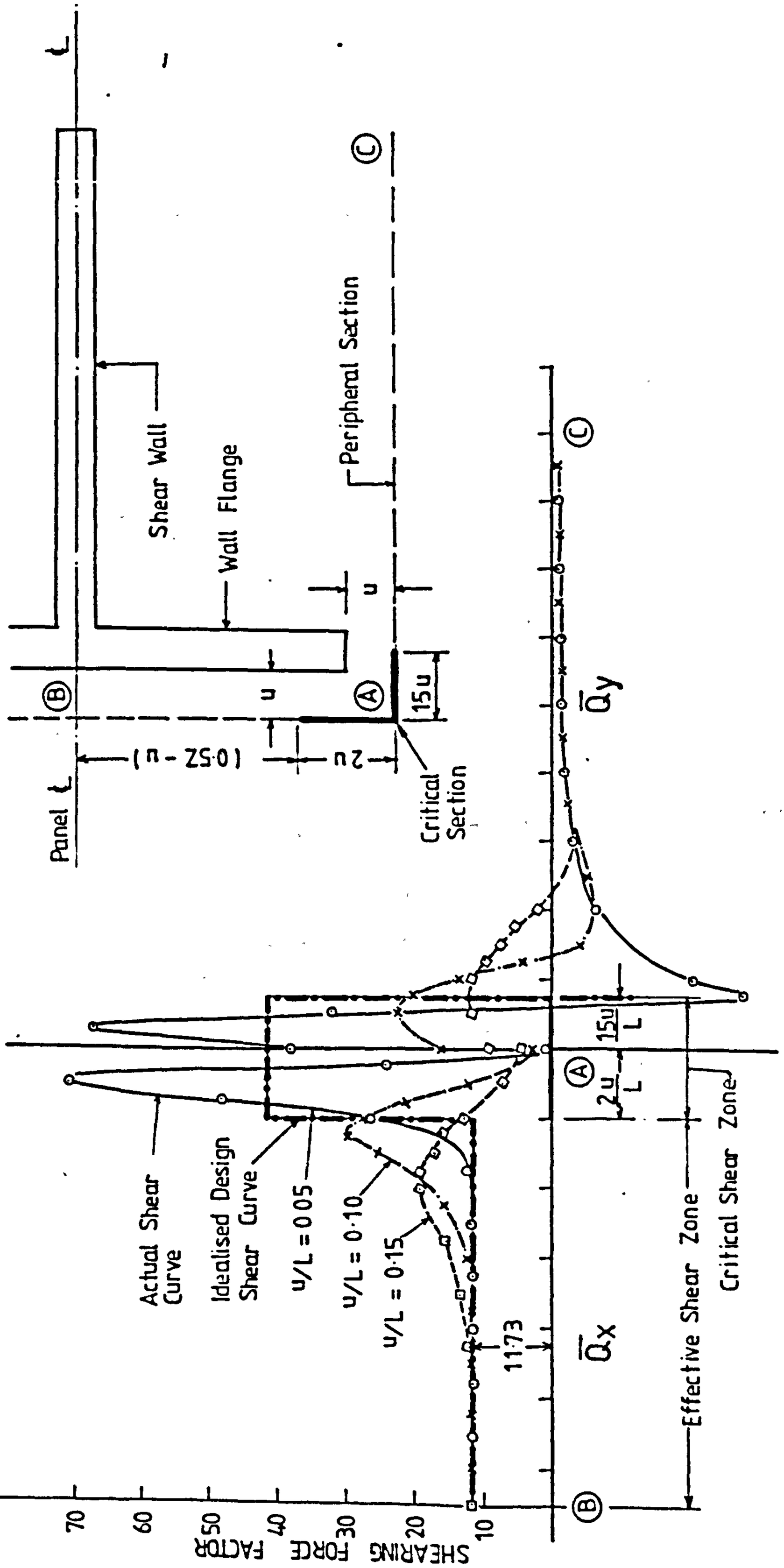

Fig. 3.40 Shearing Force Distributions at Peripheral Sections for Flanged Wall Configuration

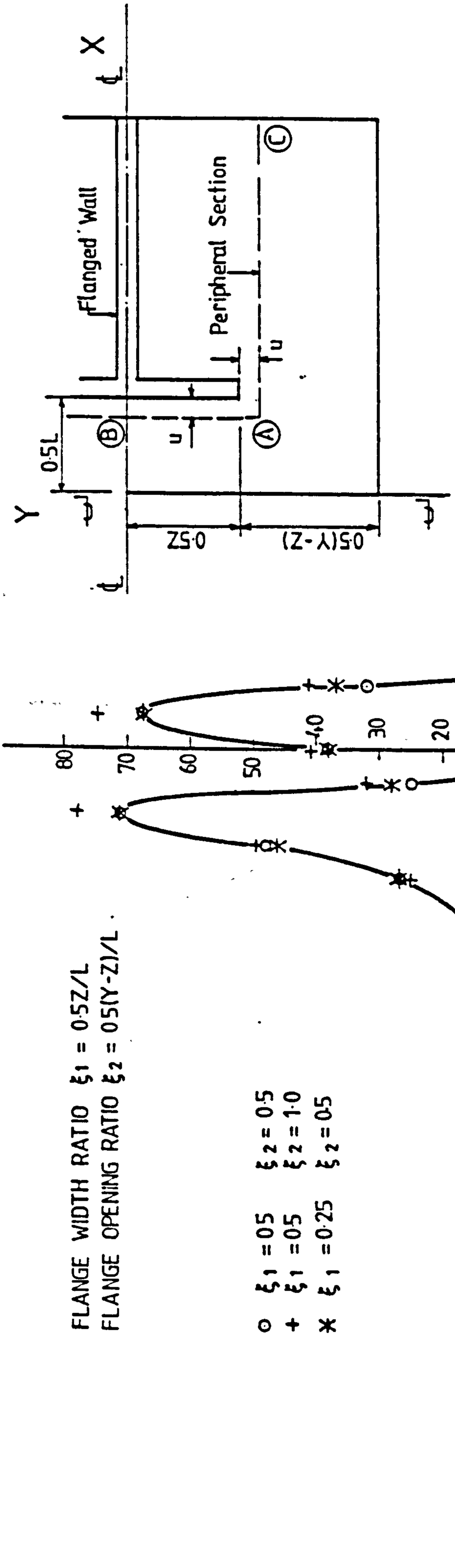

Fig. 3.41 Influence of Flange Width and Slab Width on Peripheral Shear Distribution for Flanged Wall Configuration

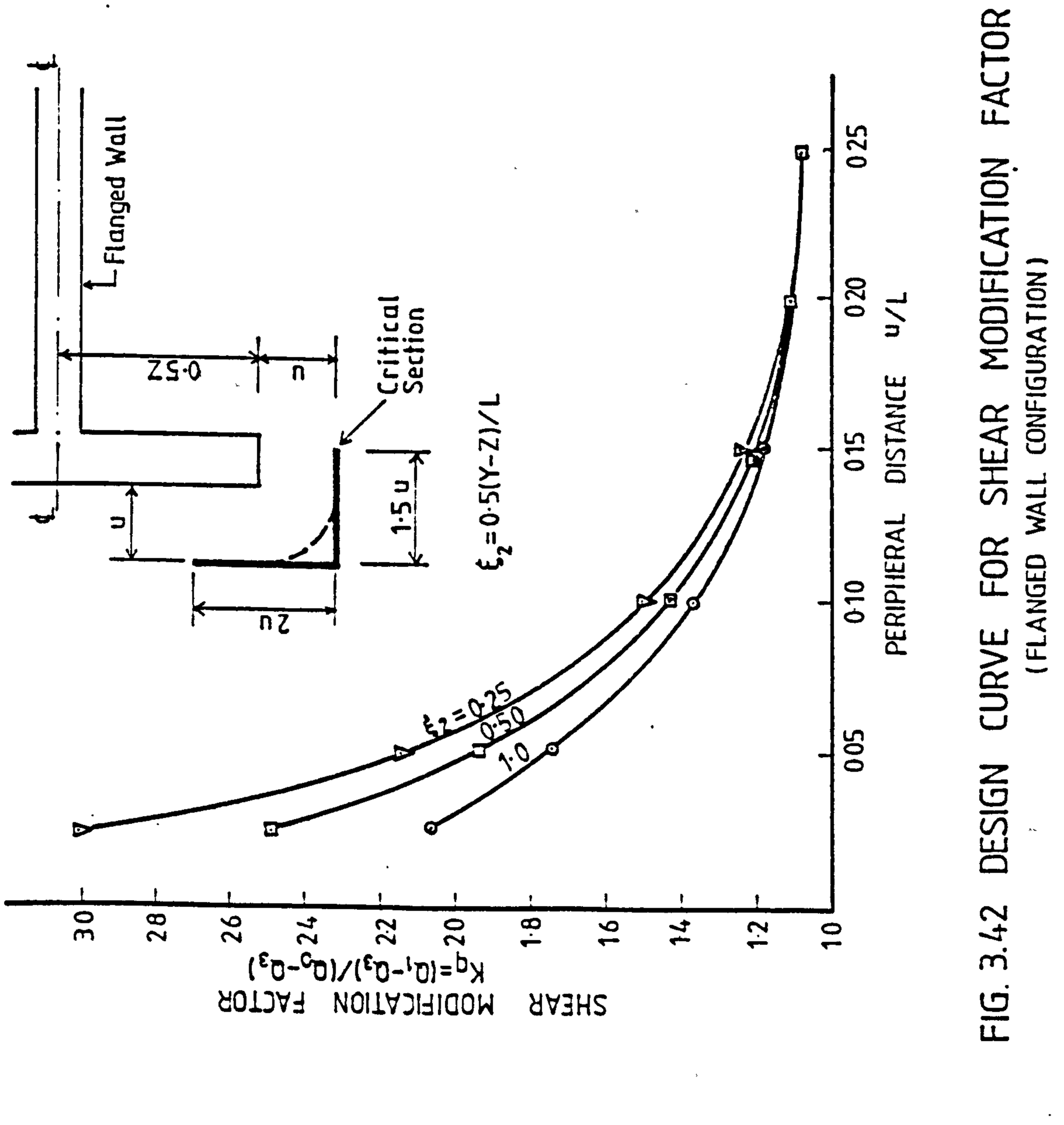

FIG. 3.42 DESIGN CURVE FOR SHEAR MODIFICATION FACTOR
(FLANGED WALL CONFIGURATION)

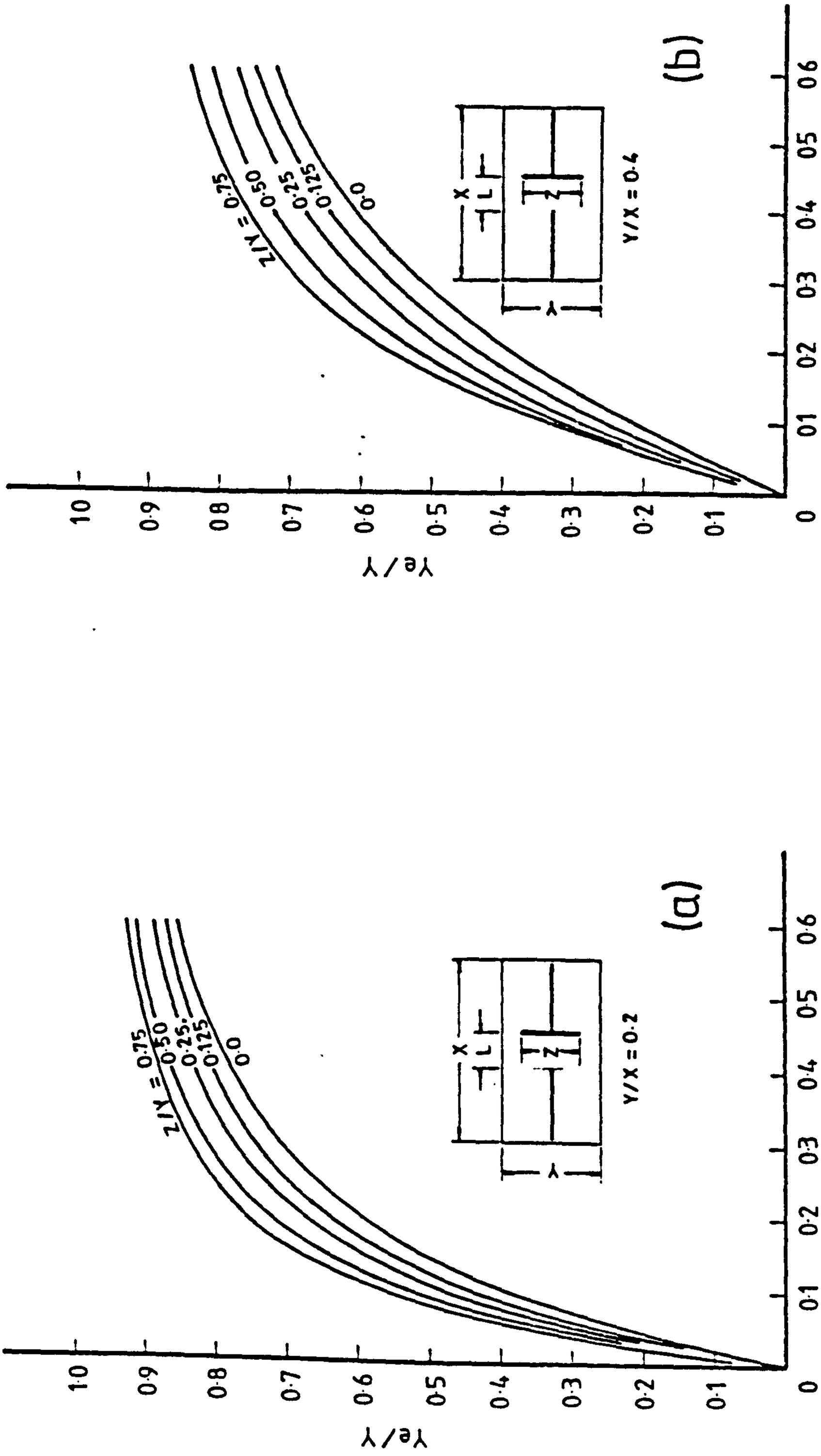

Fig. 3.43 Design Curves for Effective Slab Width for Planar/Flanged Wall Configuration

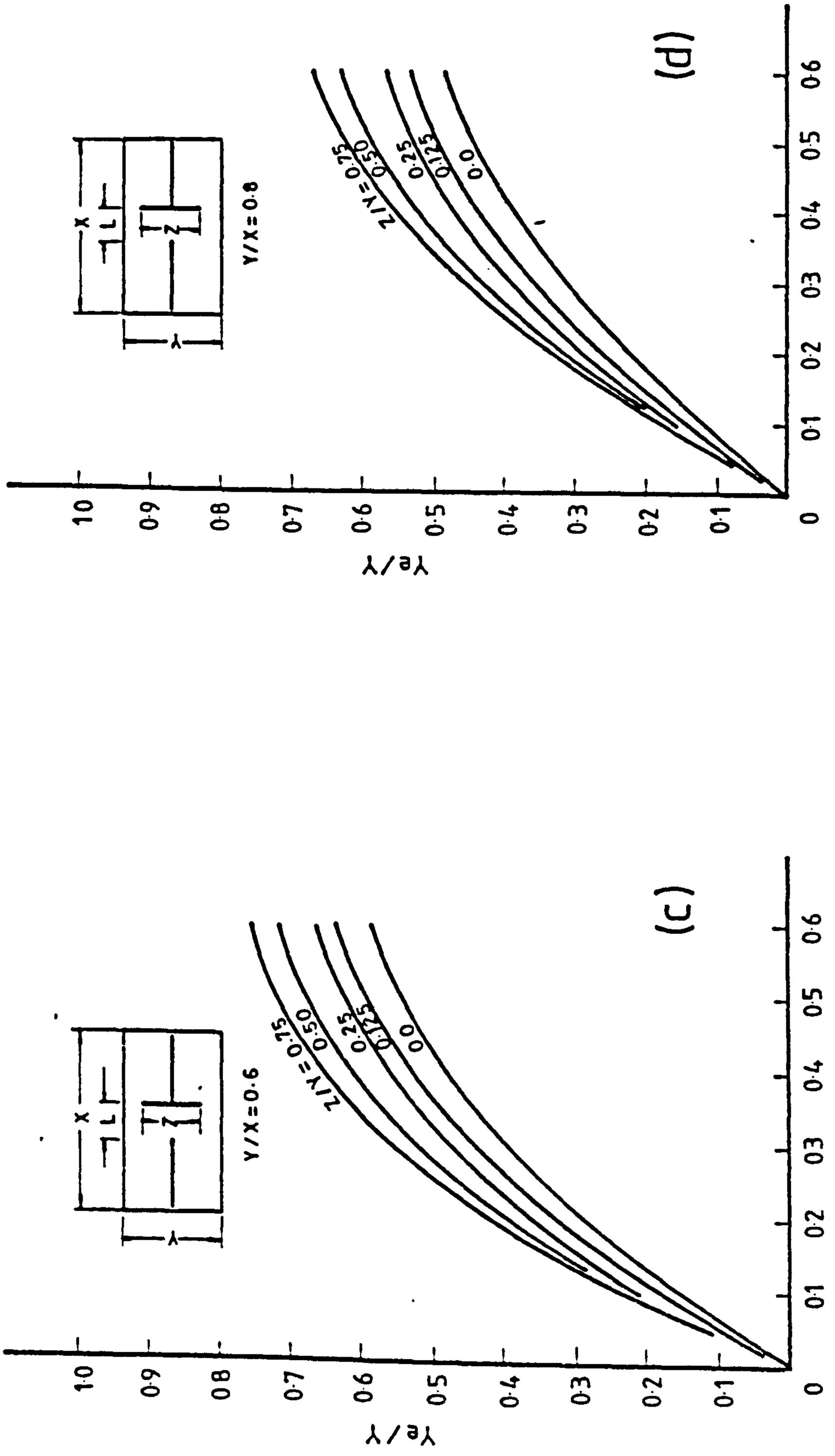

Fig. 3.43 (Contd) Design Curves for Effective Slab Width for Planar/Flanged Wall Configuration

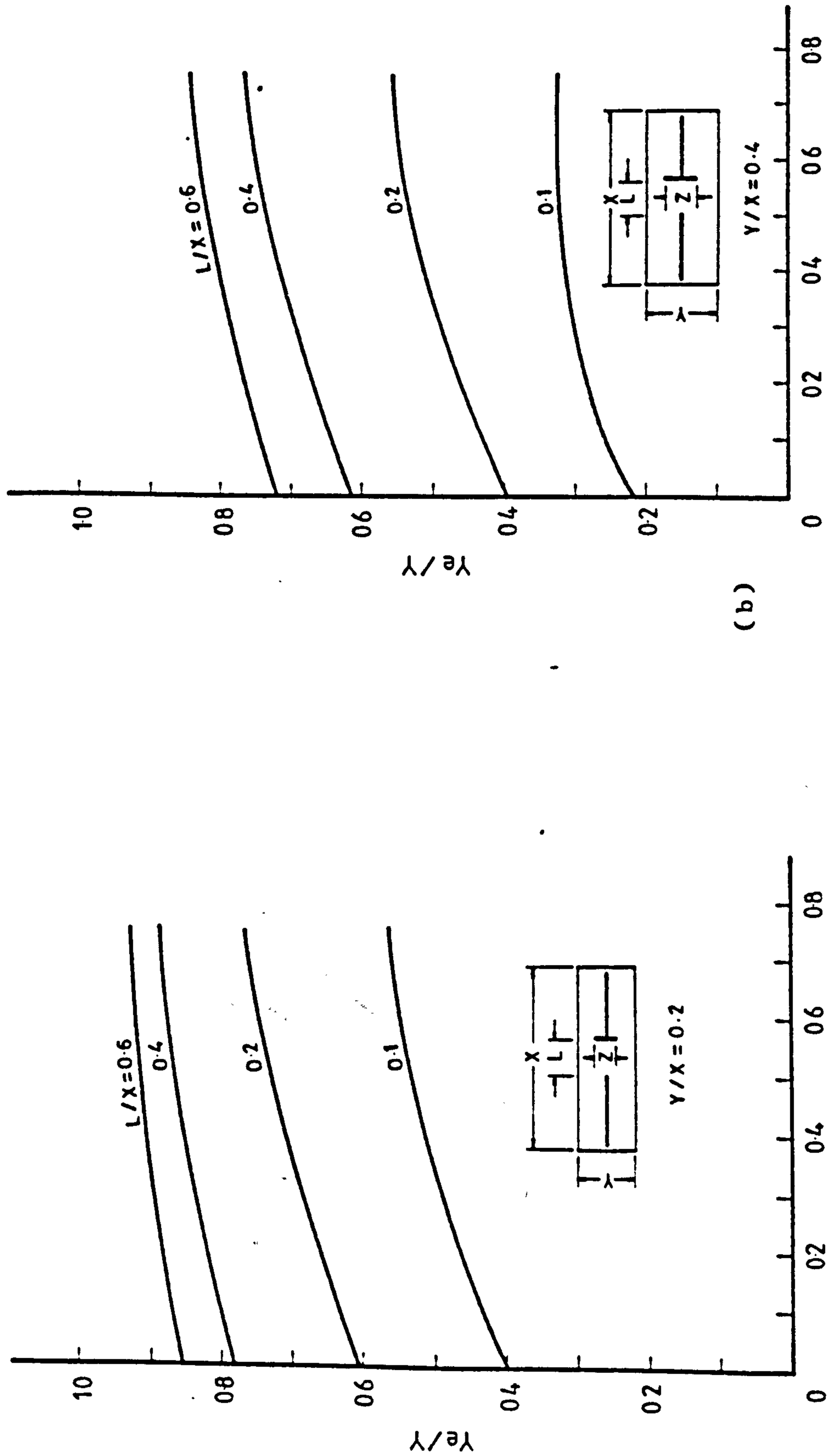

Fig. 3.44 Variation of Effective Slab Width with Flange Width for Planar/Flanged Wall Configuration

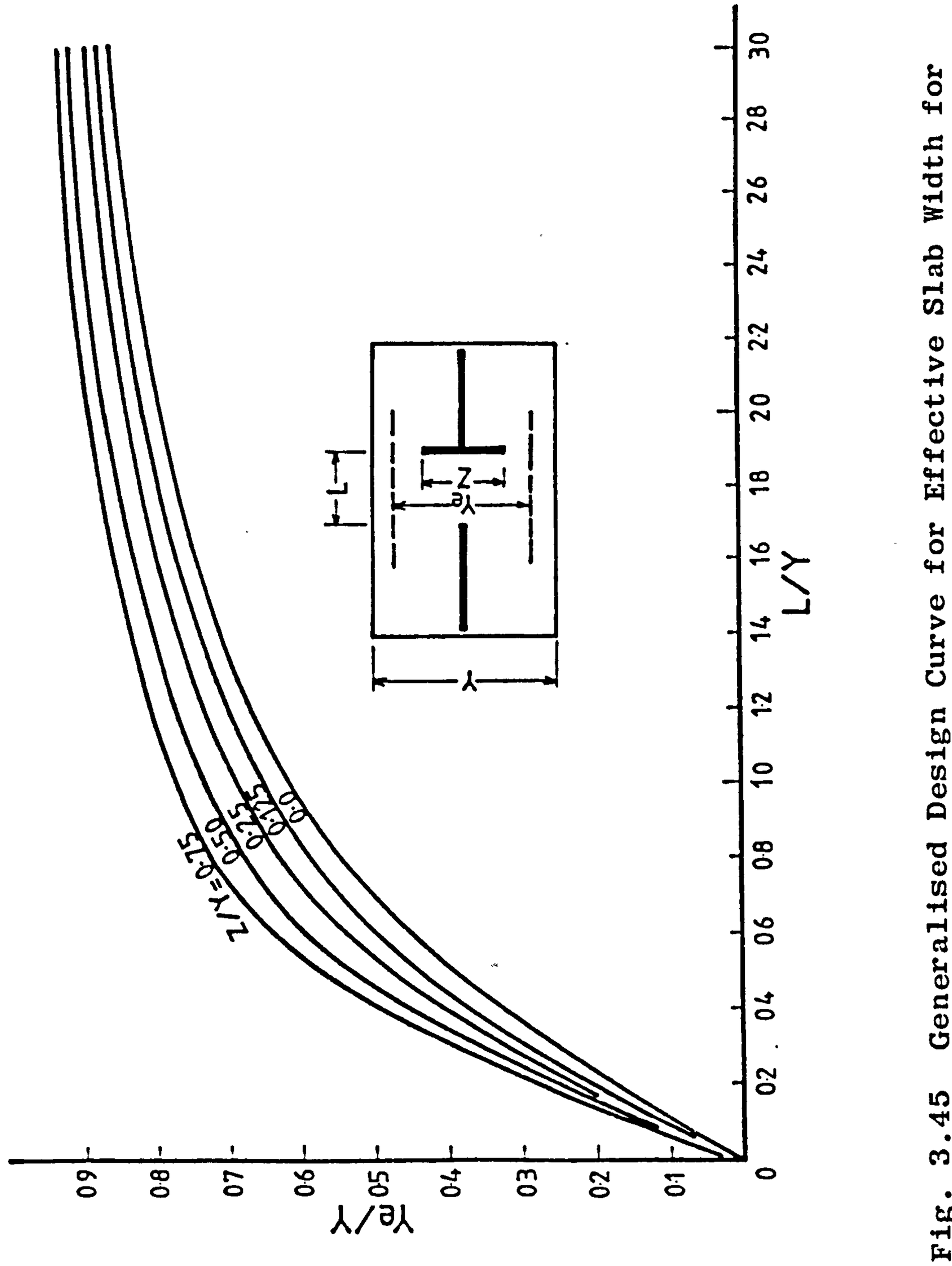

Fig. 3.45 Generalised Design Curve for Effective Slab Width for Planar/Flanged Wall Configuration

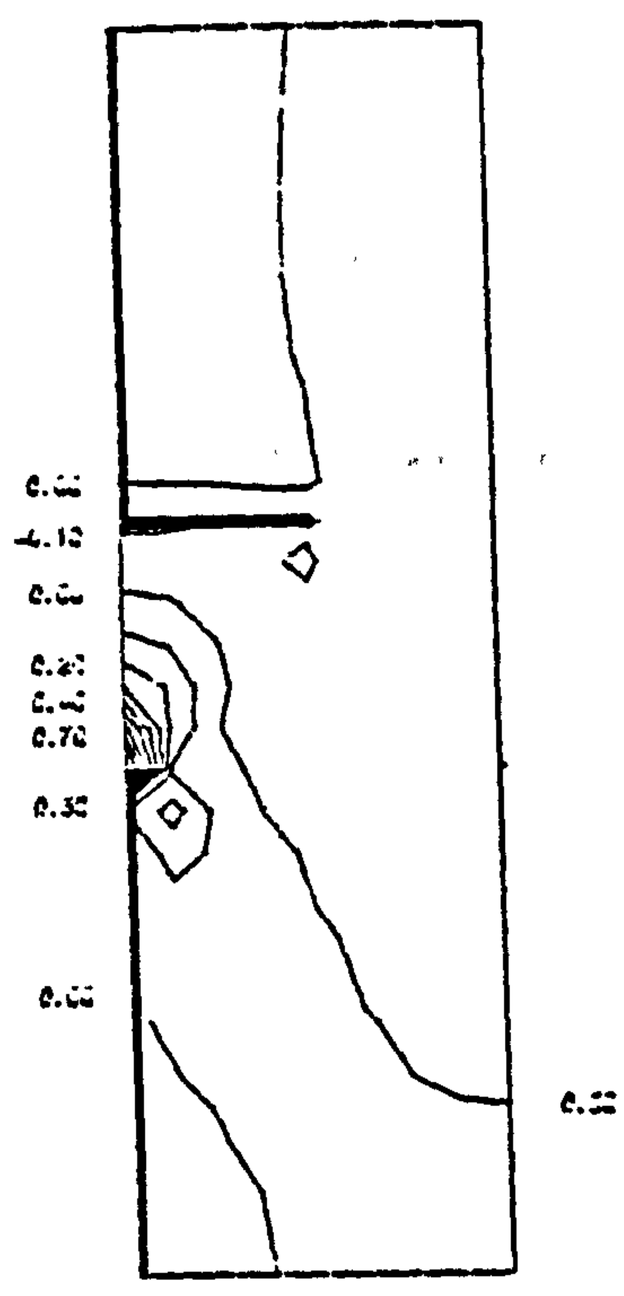

(a) 'STRESS' CONTOURS My

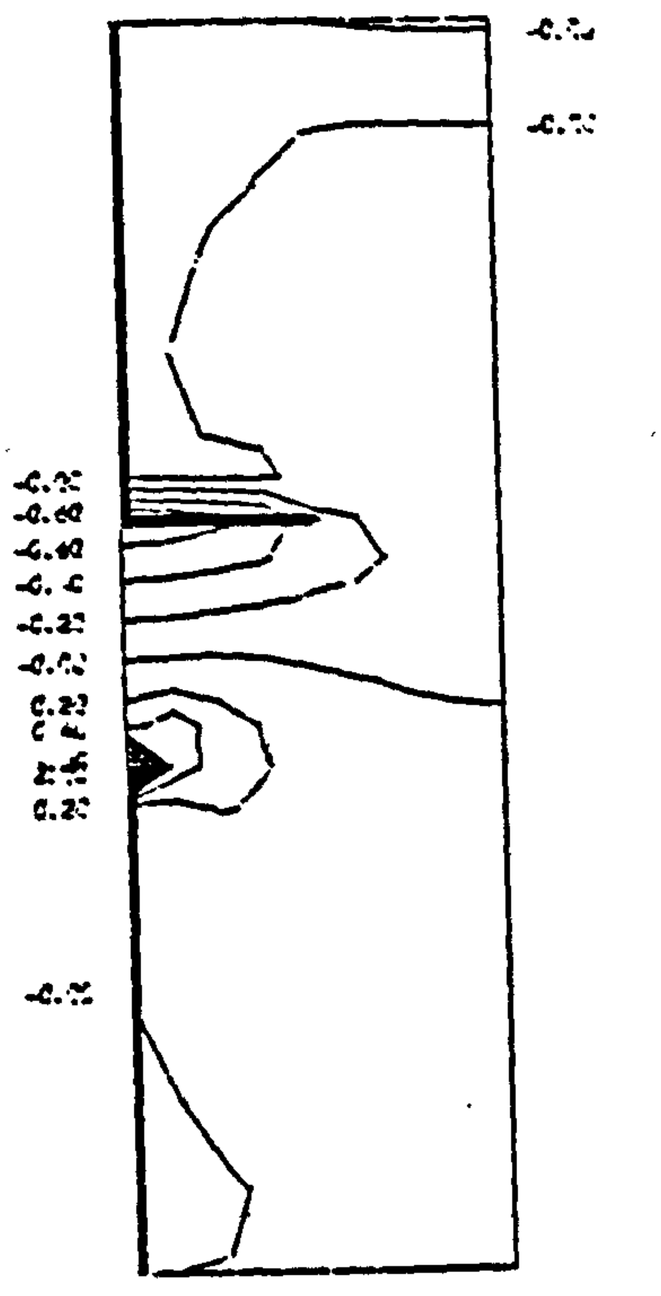

(b) 'STRESS' CONTOURS Mx

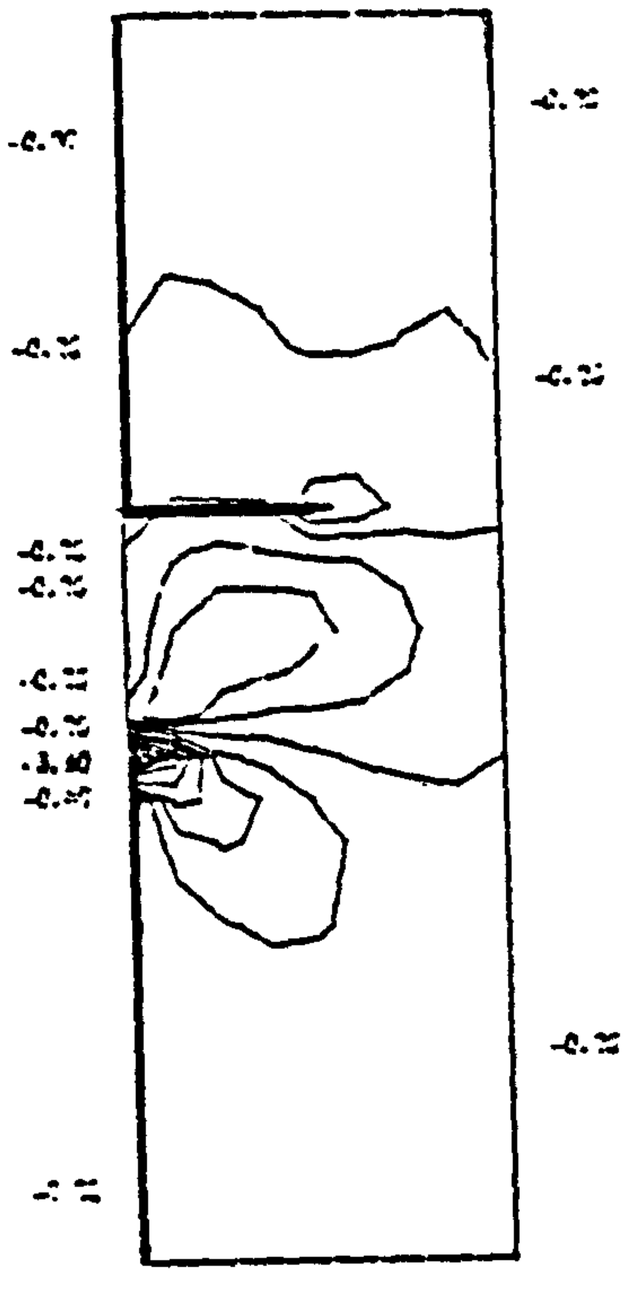

(c) 'STRESS' CONTOURS Mxy

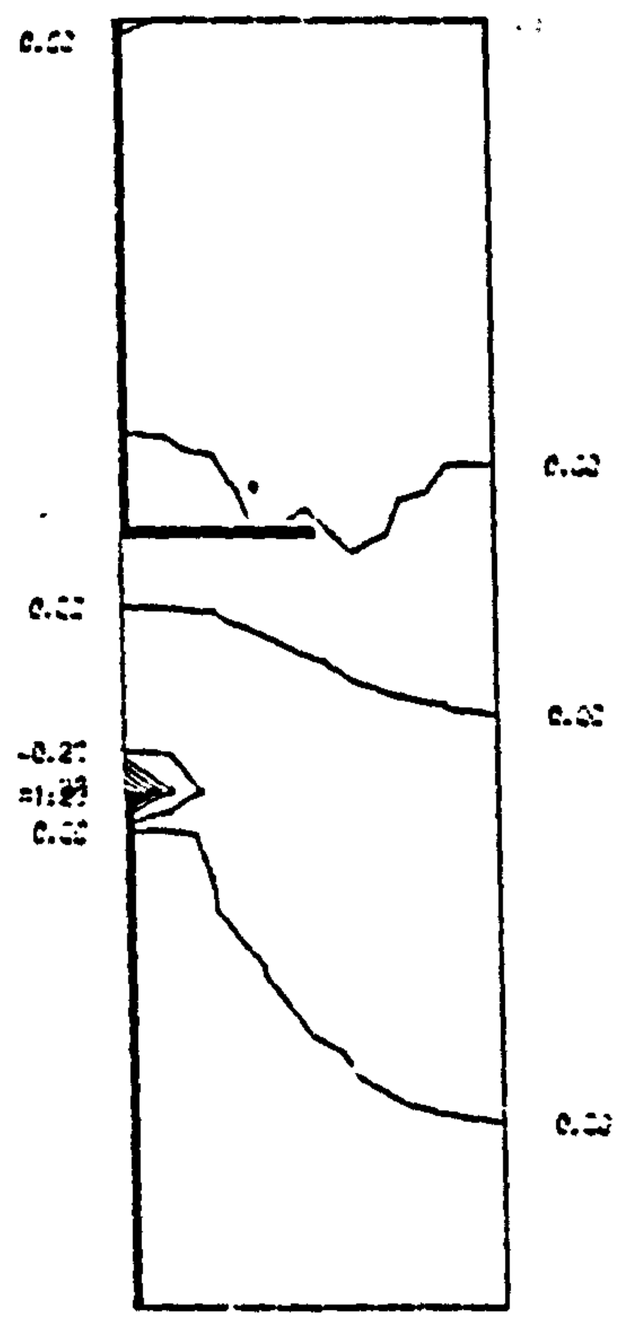

(d) 'STRESS' CONTOURS σy

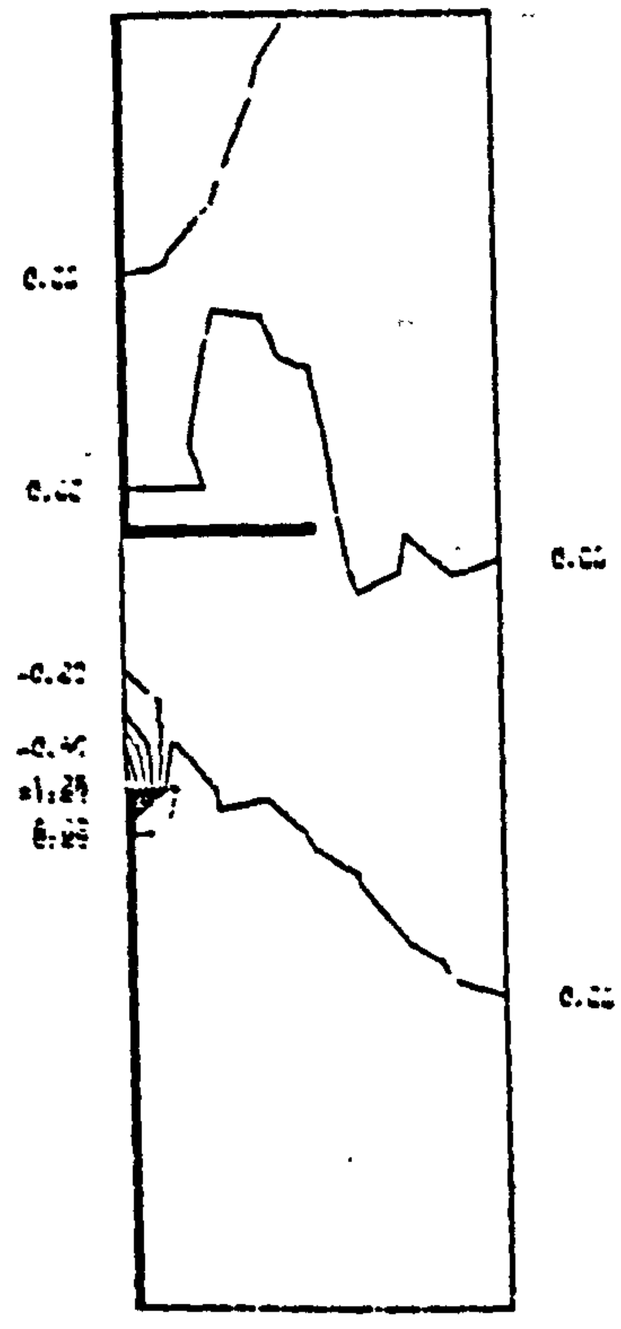

(e) 'STRESS' CONTOURS σx

NOTE:
The term 'STRESS' is used in the context of a stress resultant.

Fig. 3.46 Contours of Stress Resultants in Slab for Planar/Flanged Wall Configuration

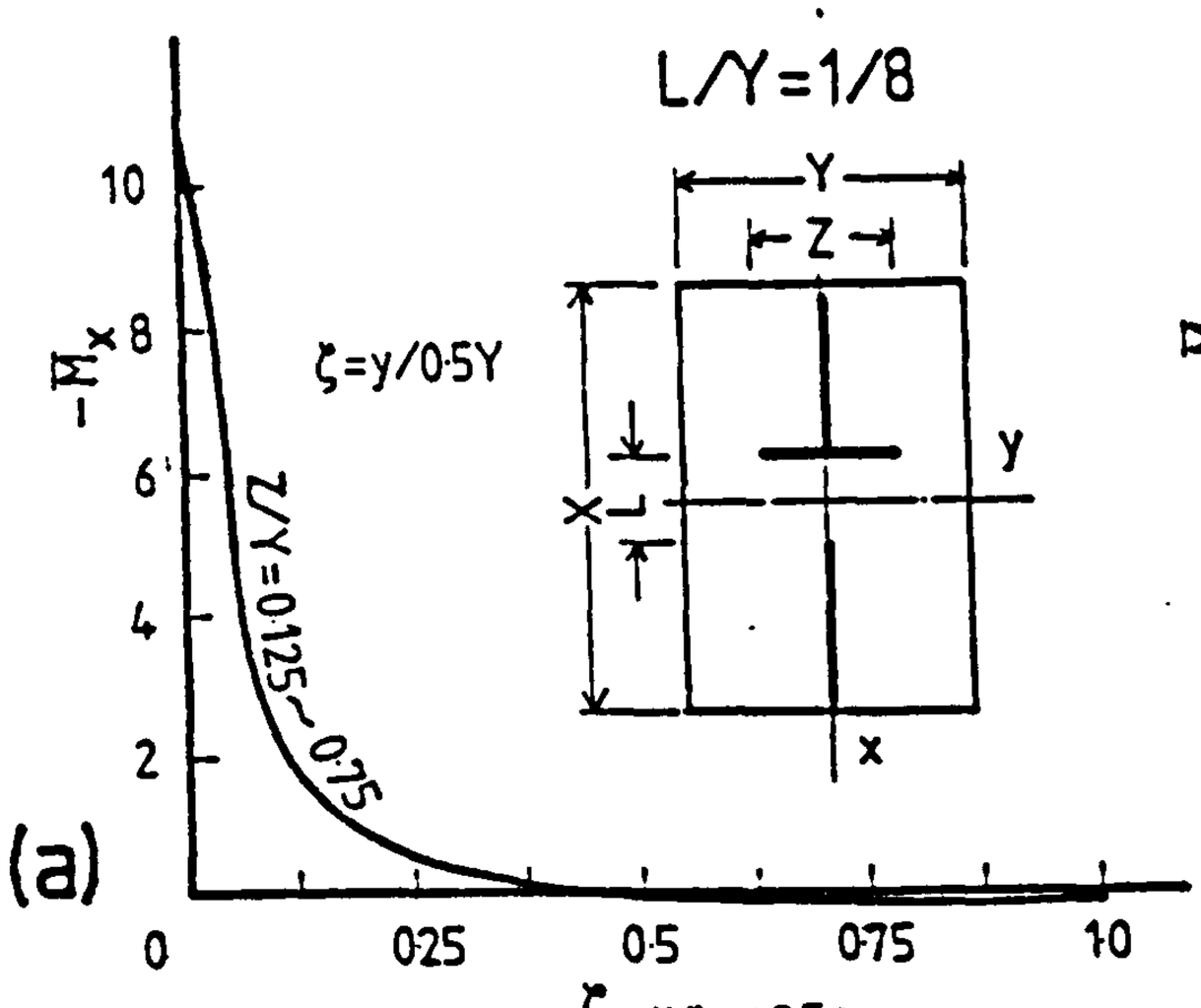

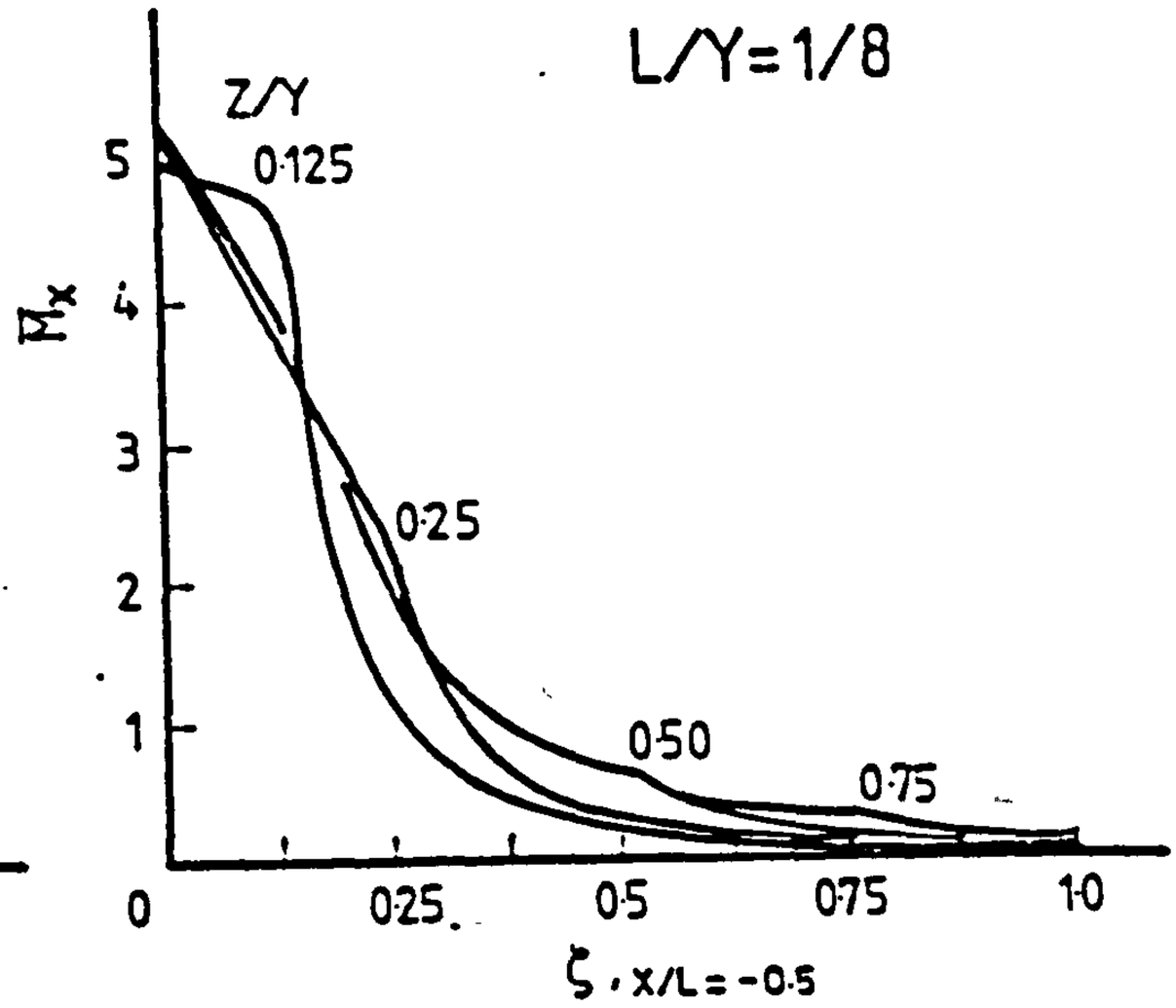

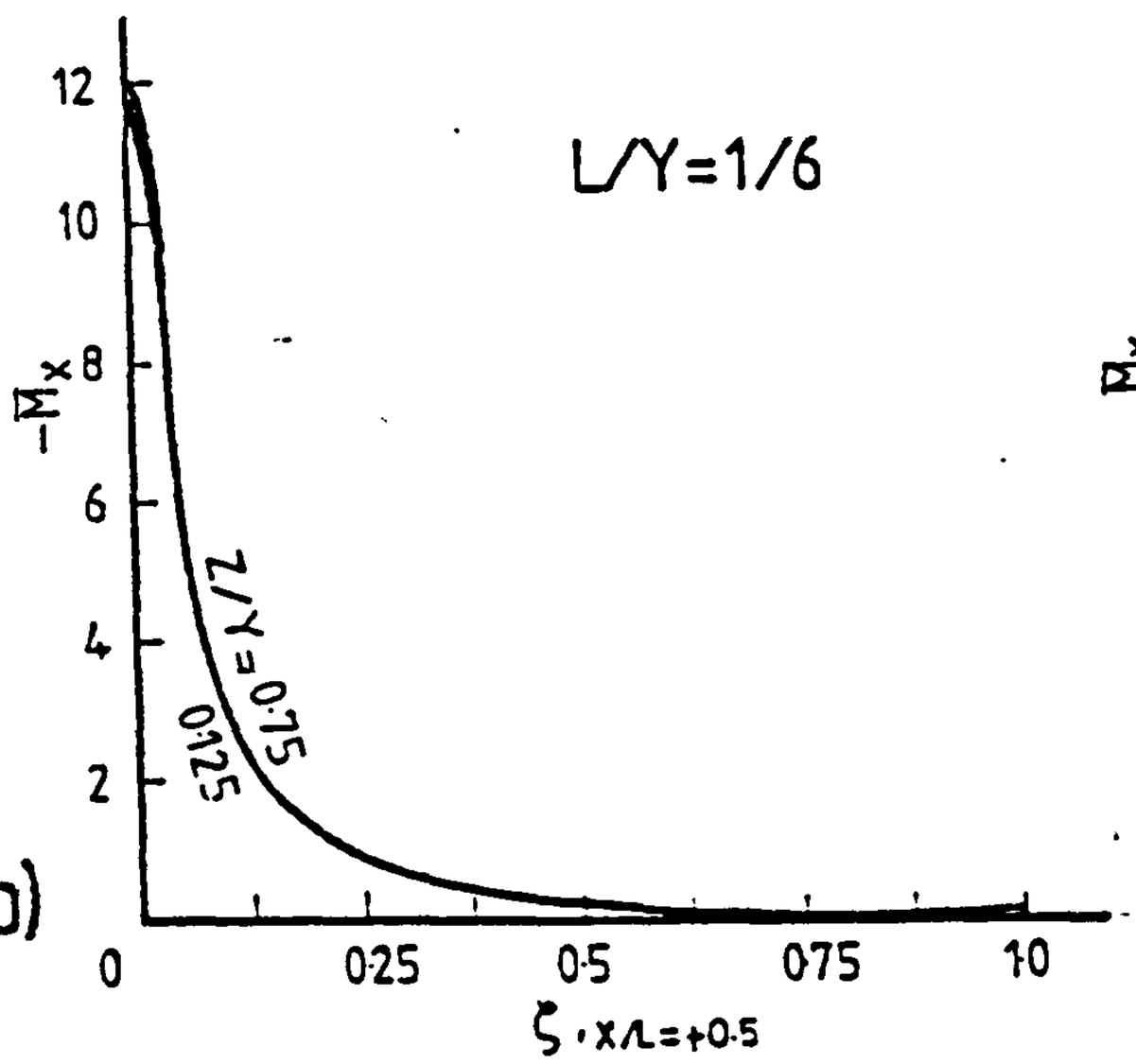

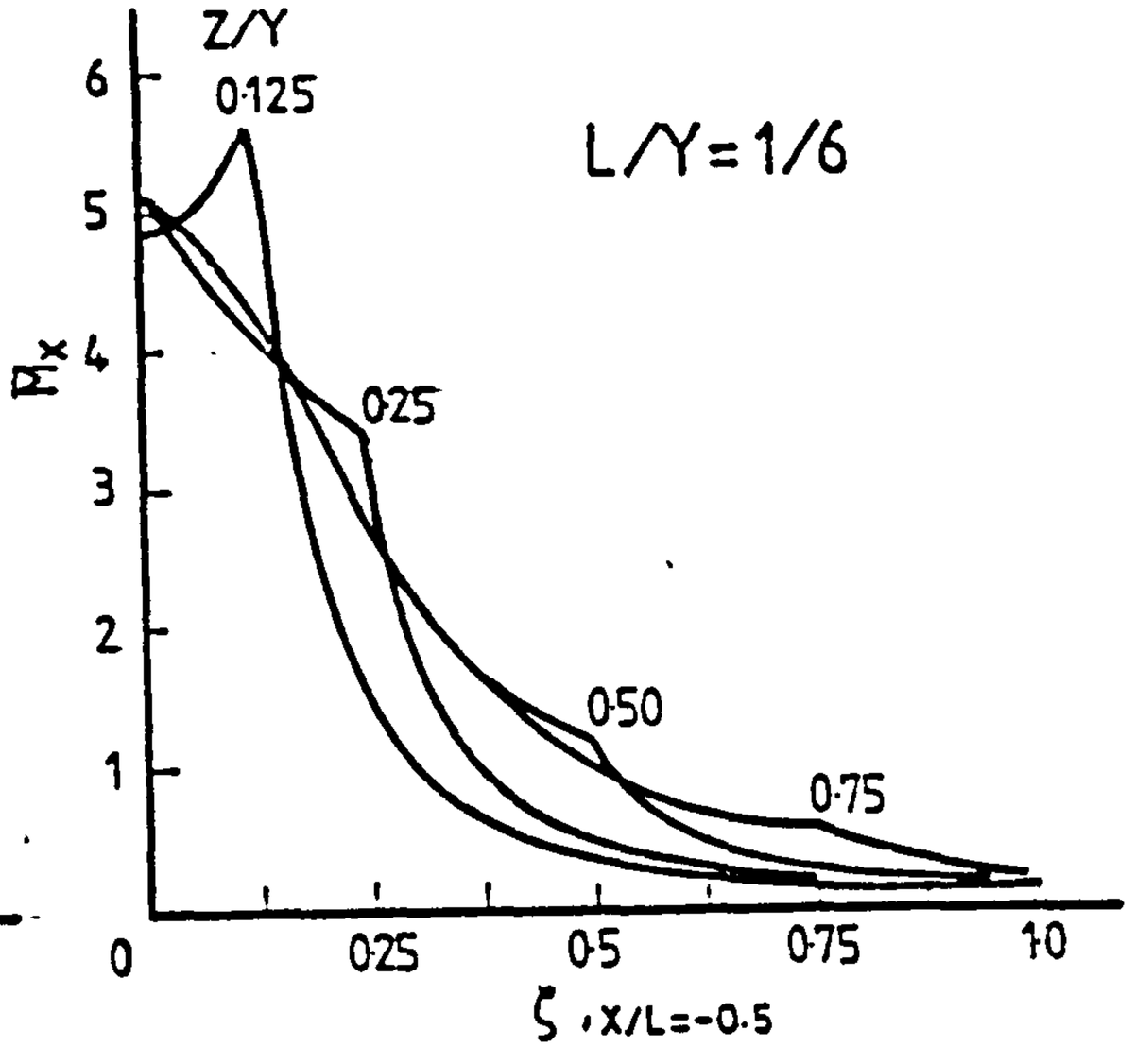

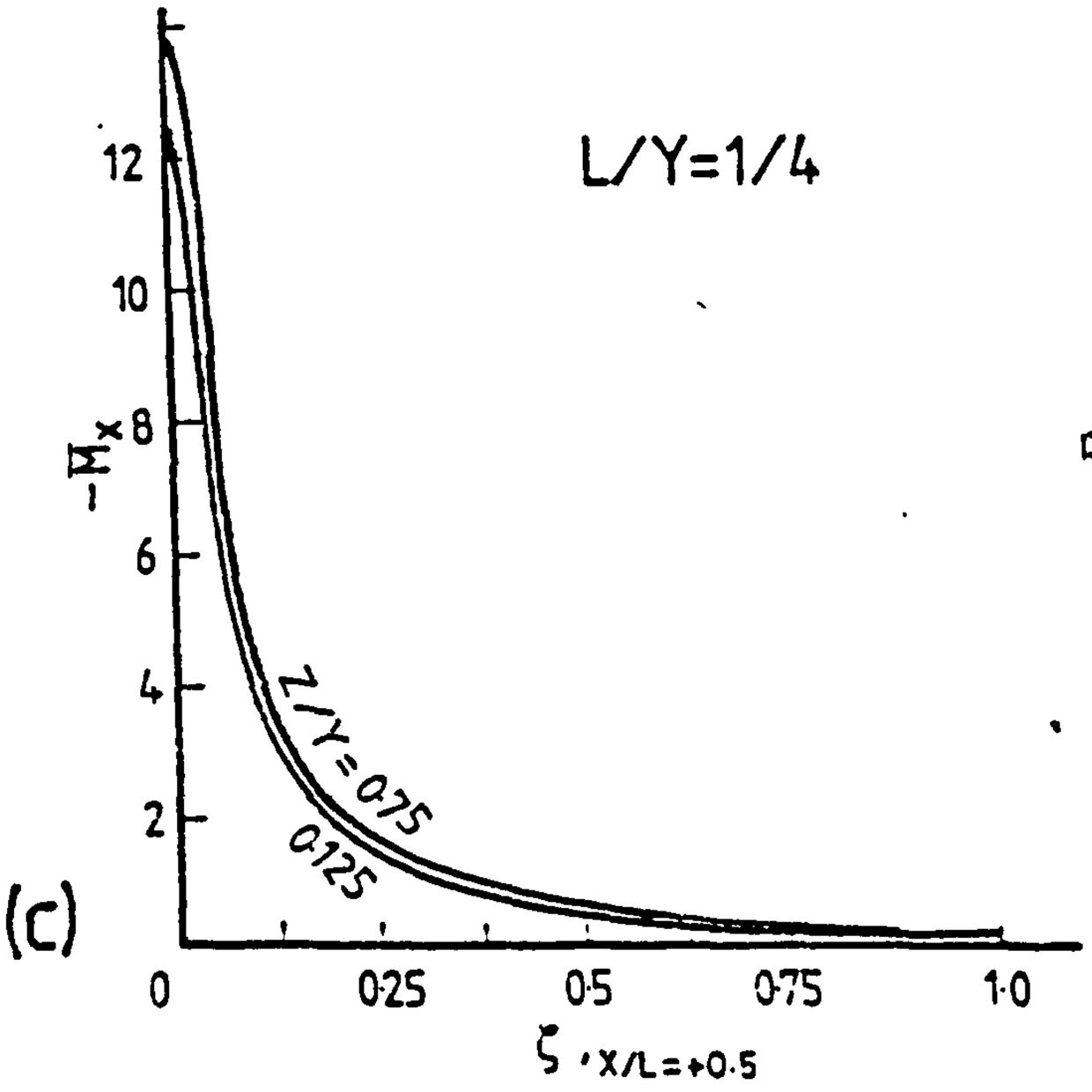

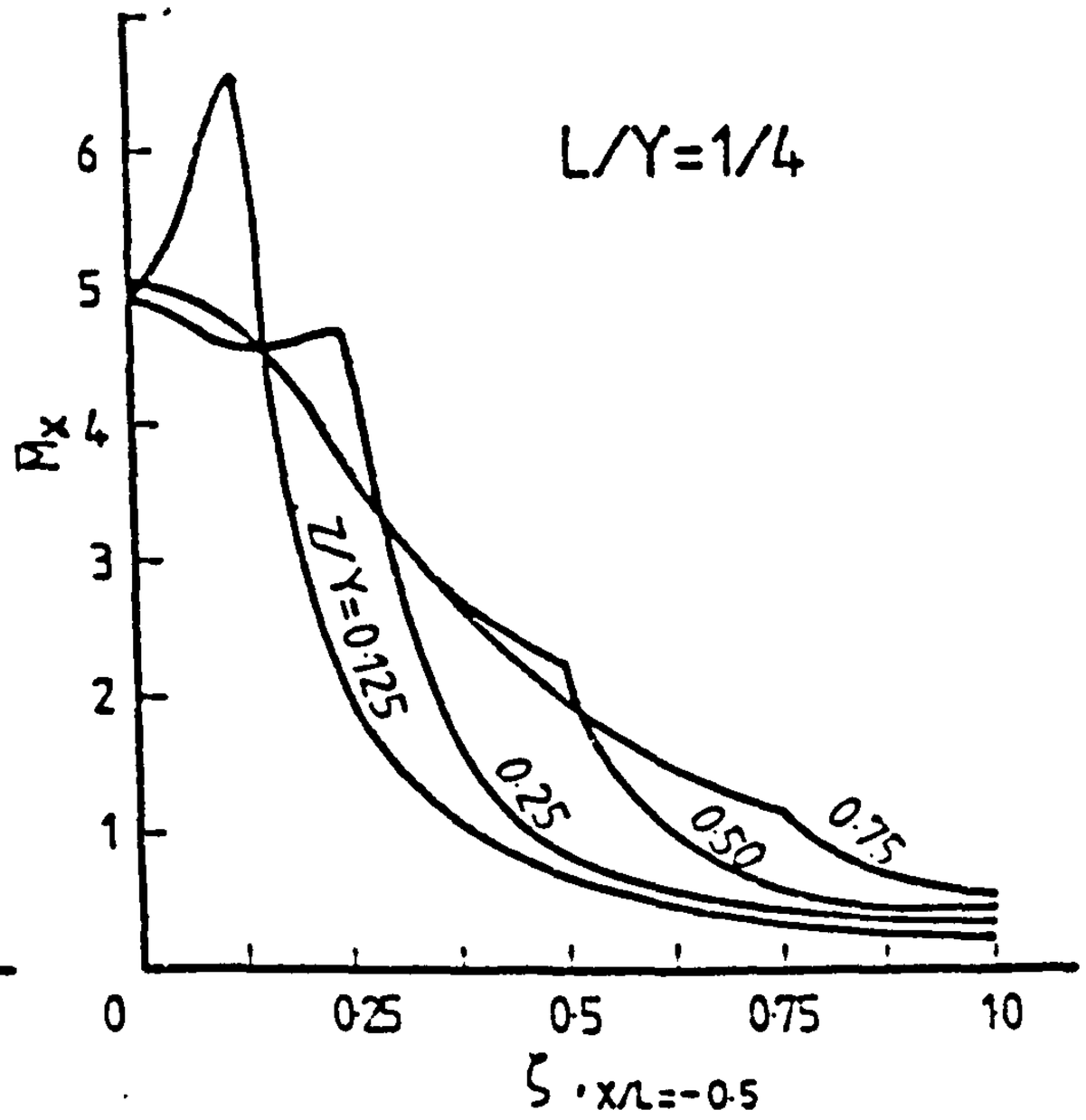

Fig. 3.47 Variation of Longitudinal Bending Moments at Critical Transverse Slab Sections for Planar/ Flanged Wall Configuration

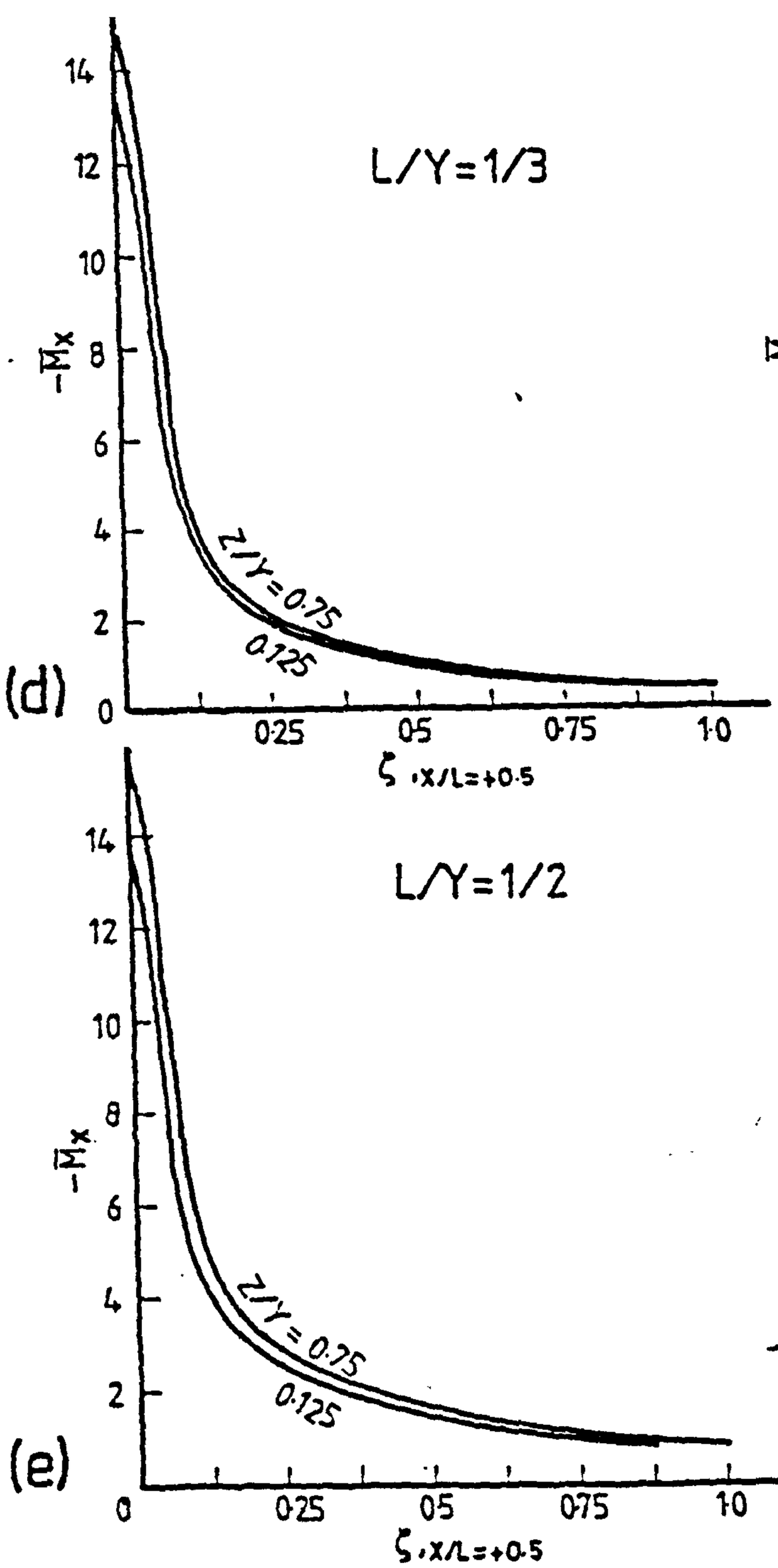

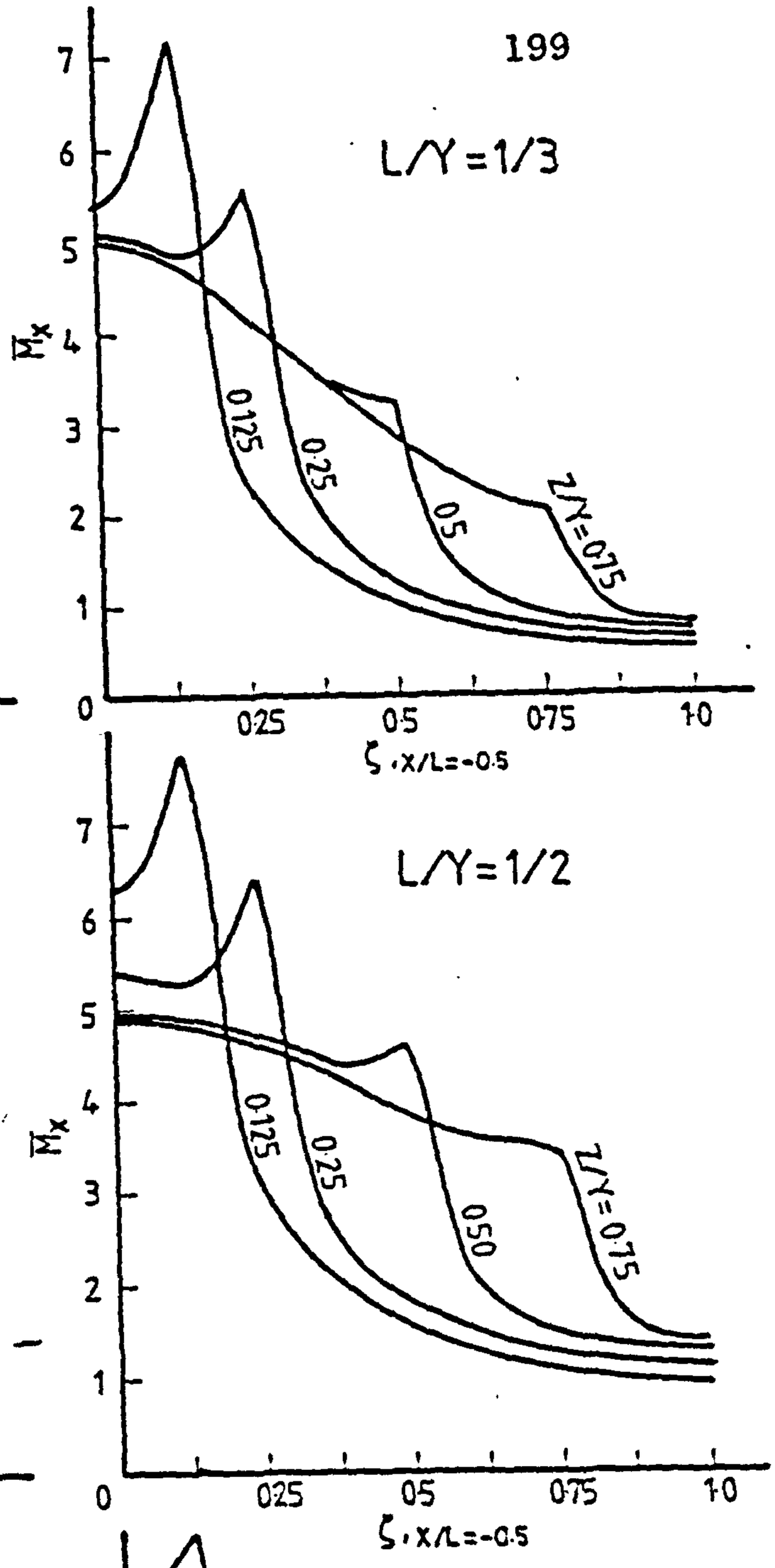

Fig. 3.47 (Contd) Variation of Longitudinal Bending Moments at Critical Transverse Slab Sections for Planar/ Flanged Wall Configuration

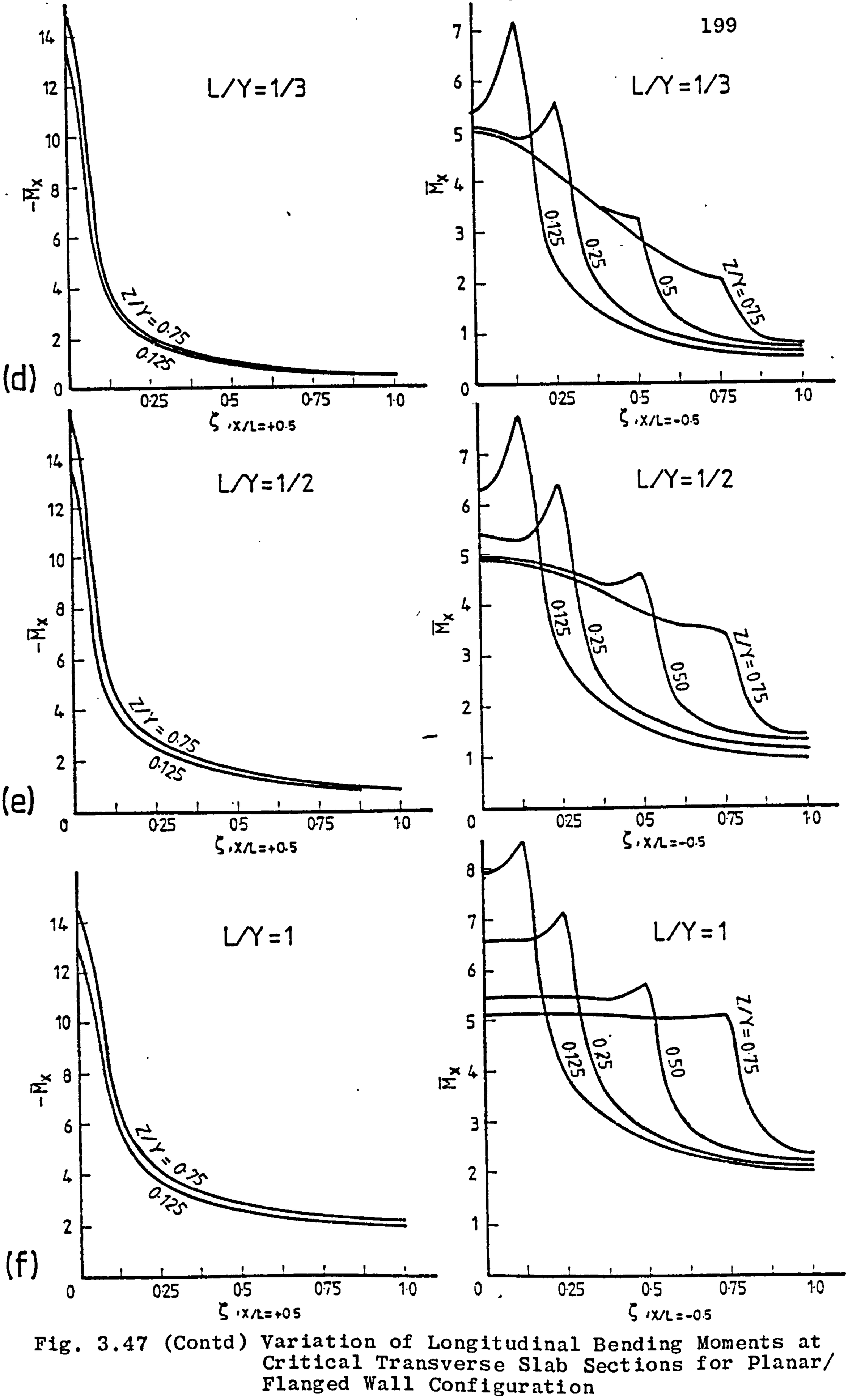

Fig. 3.47 (Contd) Variation of Longitudinal Bending Moments at Critical Transverse Slab Sections for Planar/ Flanged Wall Configuration

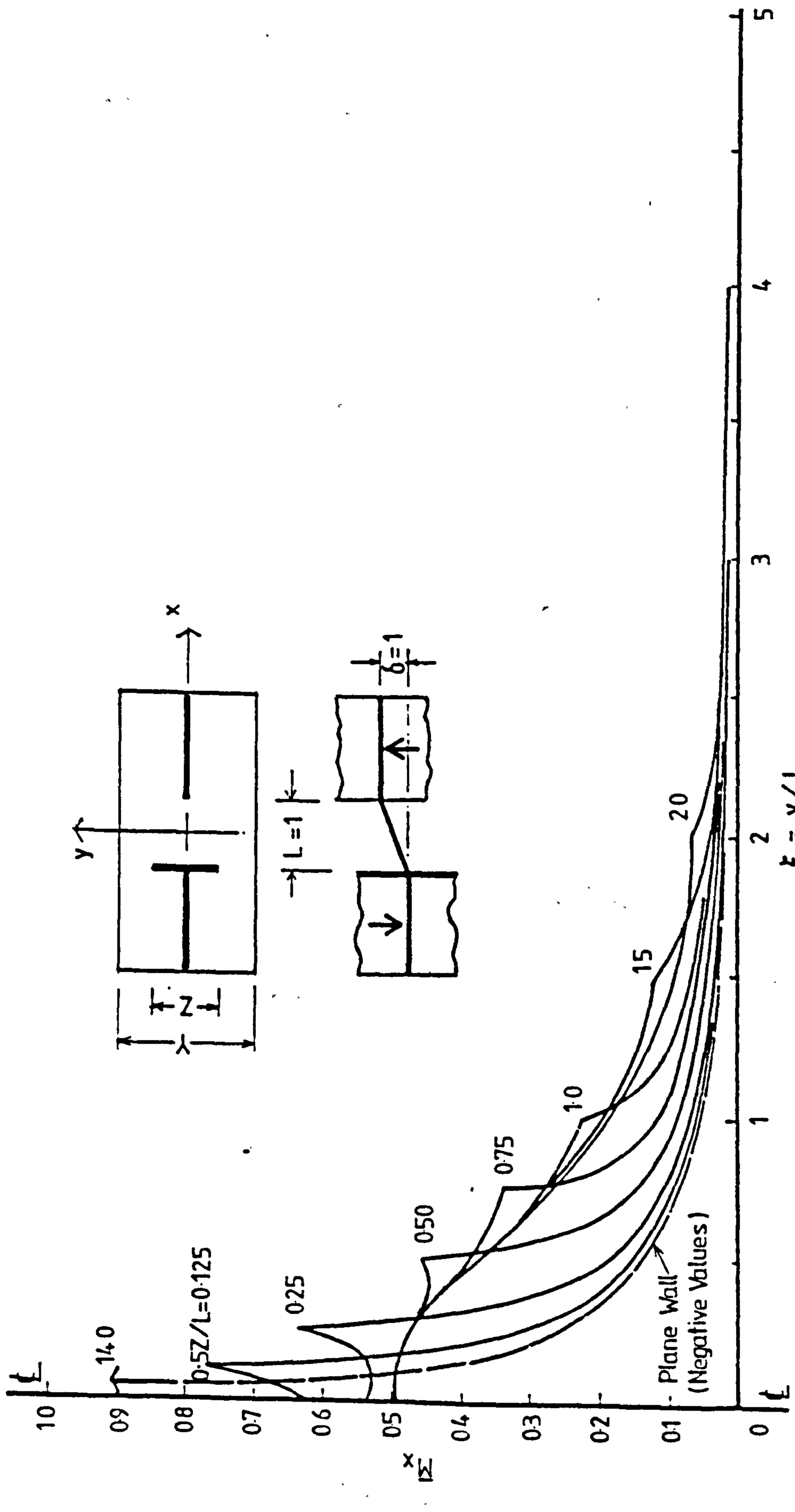

Fig. 3.48 Generalised Design Curve for Longitudinal Bending Moment Critical Transverse Slab Section for Planar/Flanged Wall Configuration

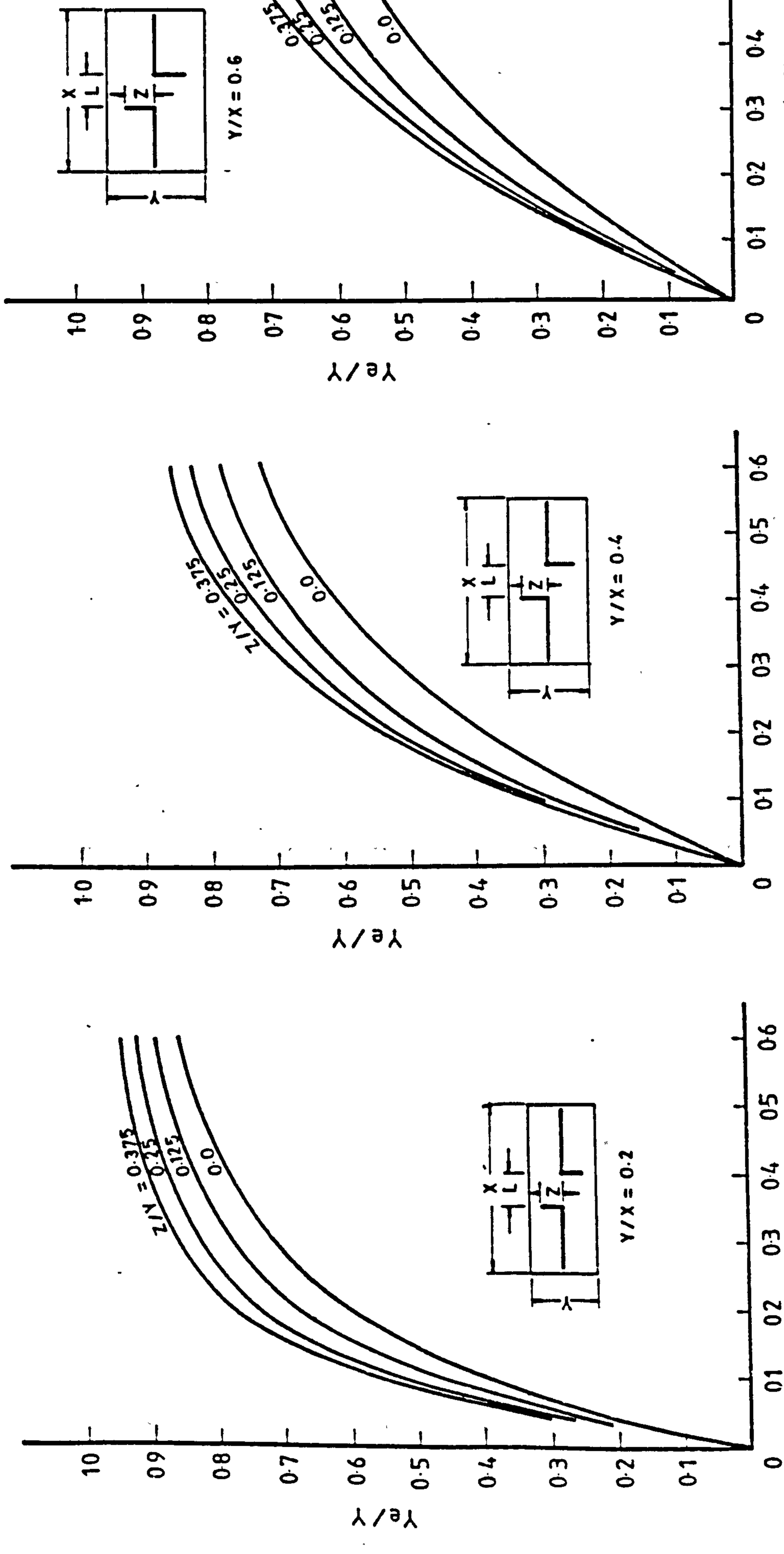

Fig. 3.50 Design Curves for Effective Slab Width for L-shaped Wall Configuration

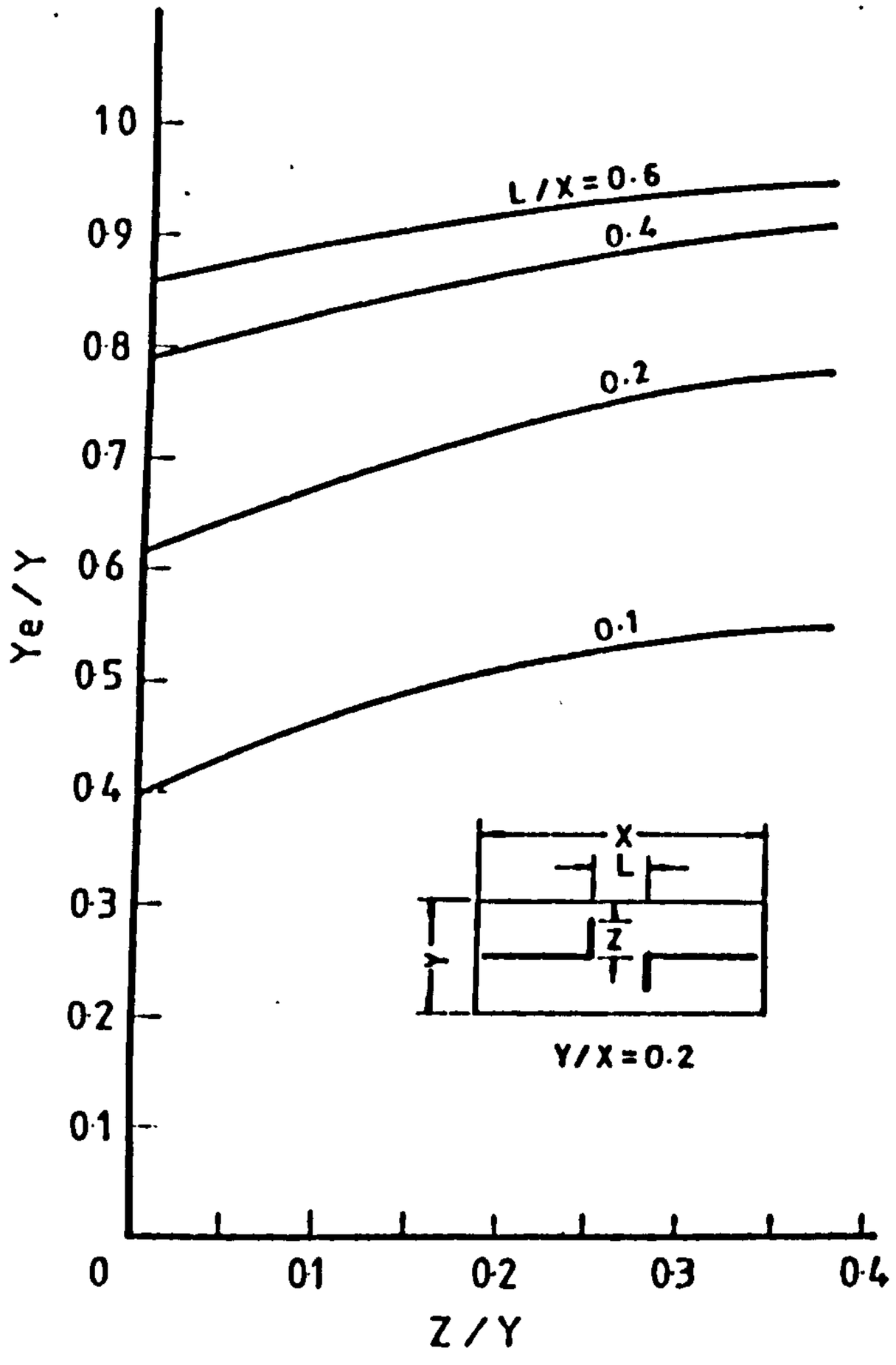

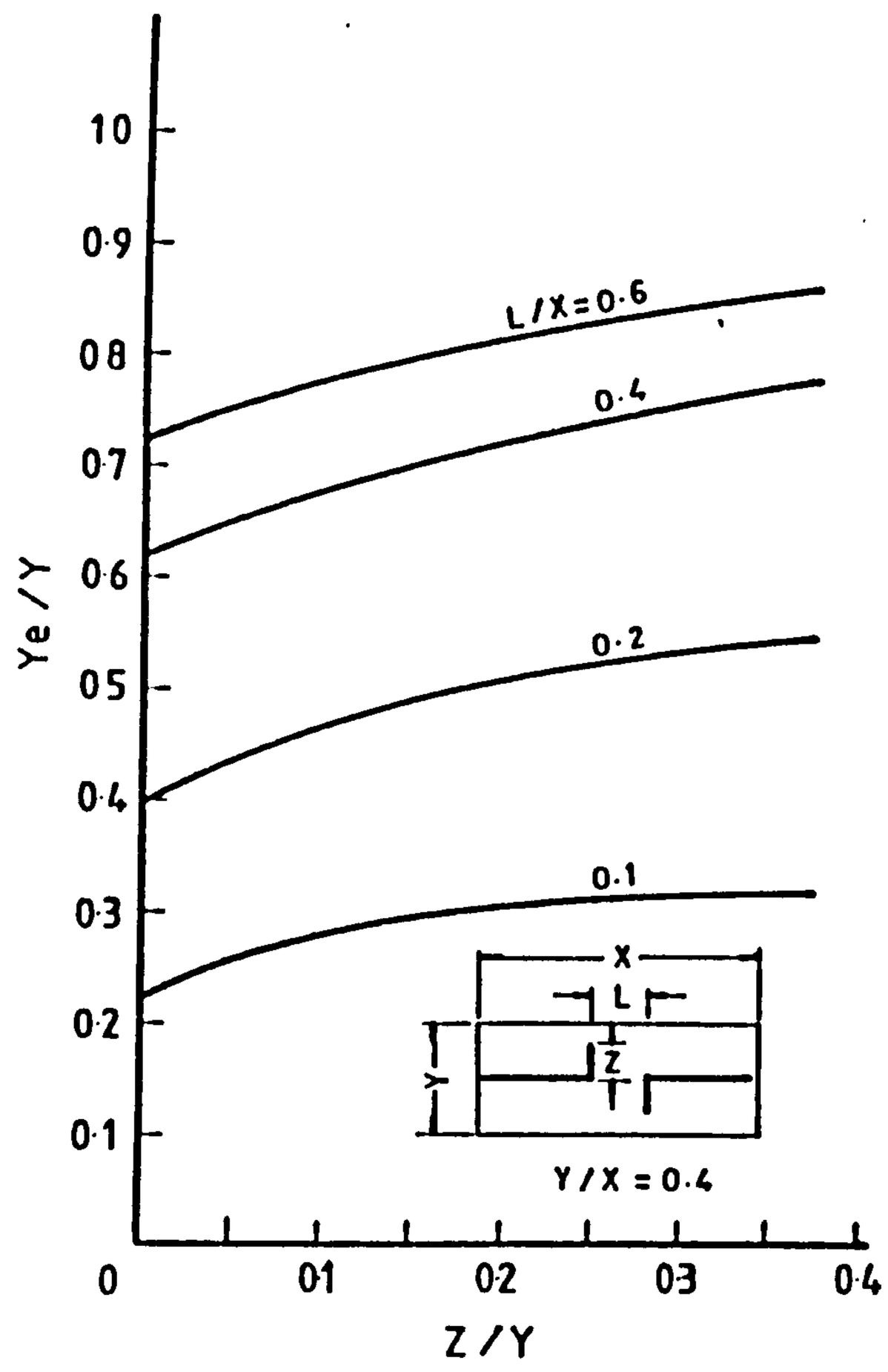

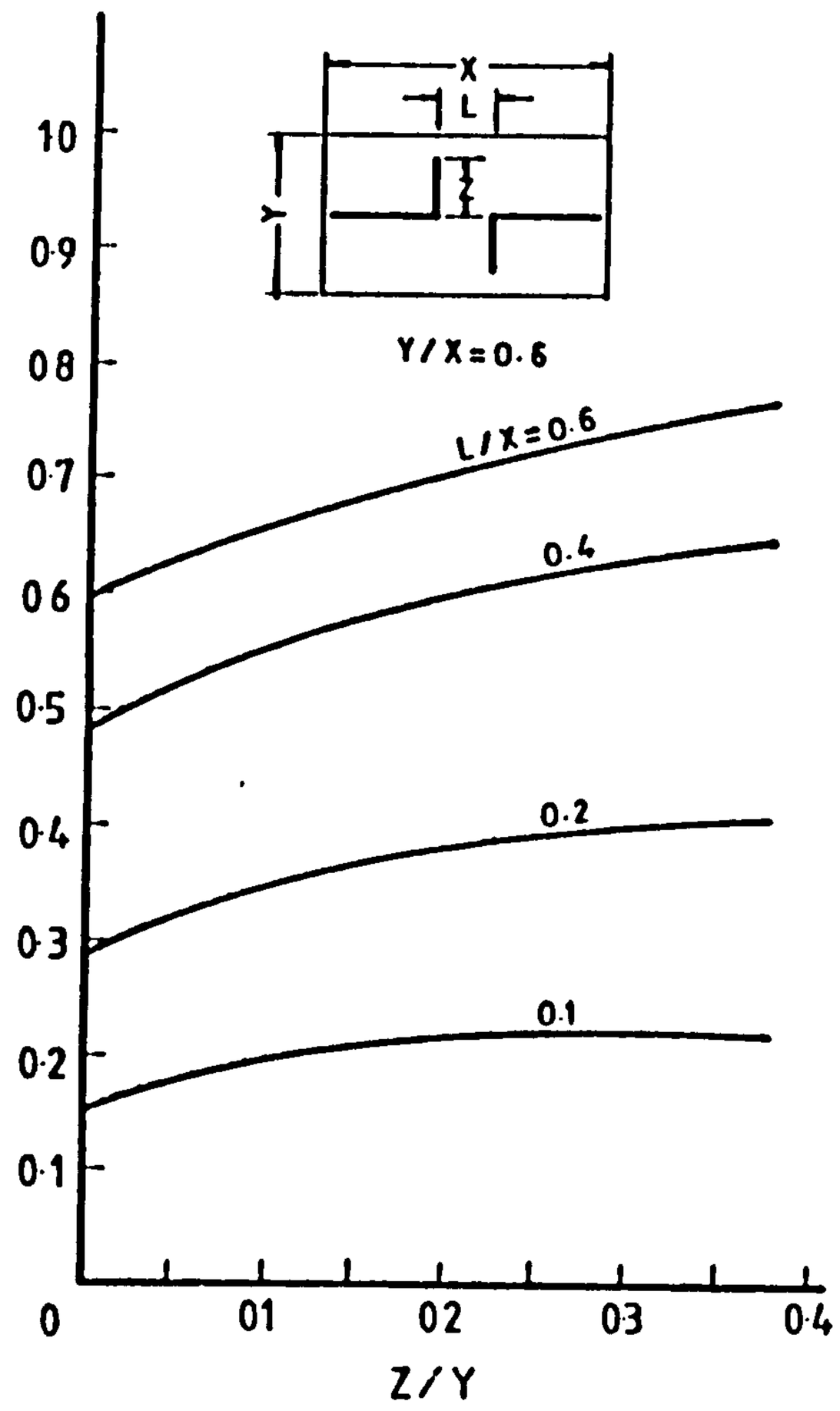

Fig. 3.51 Variation of Effective Slab Width with Flange Width for L-Shaped Wall Configuration

NOTE: The term 'STRESS' is used in the context of a stress resultant.

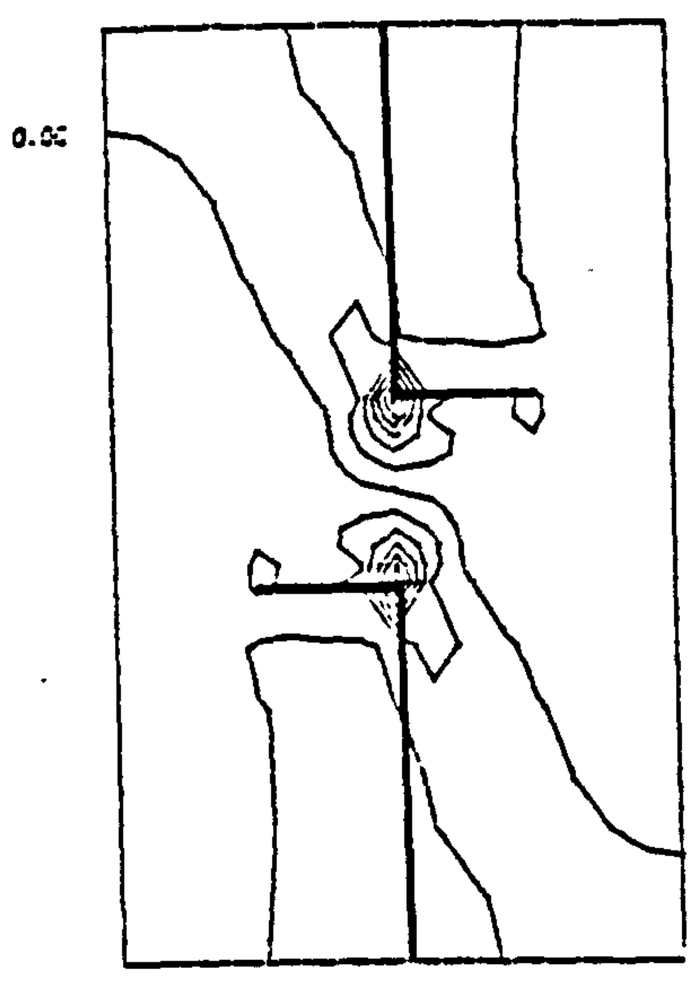

MULTIPLIER 1.0E-2
INTERVAL 1.00

(a) STRESS CONTOURS My

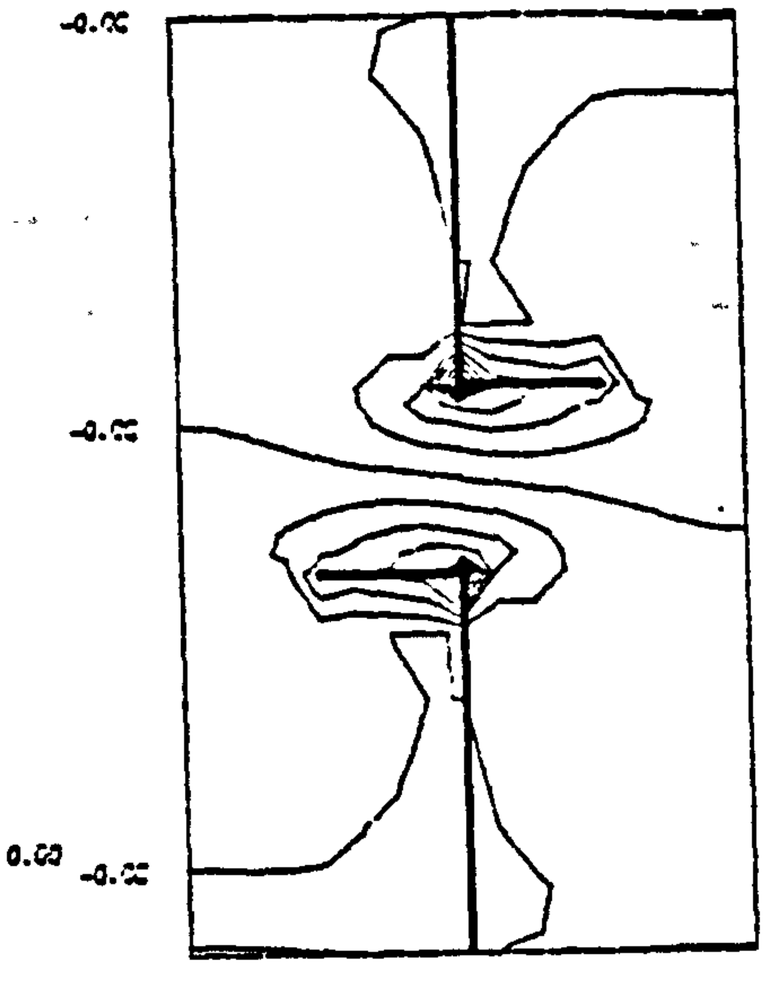

MULTIPLIER 1.0E-3
INTERVAL 2.00

(b) STRESS CONTOURS Mx

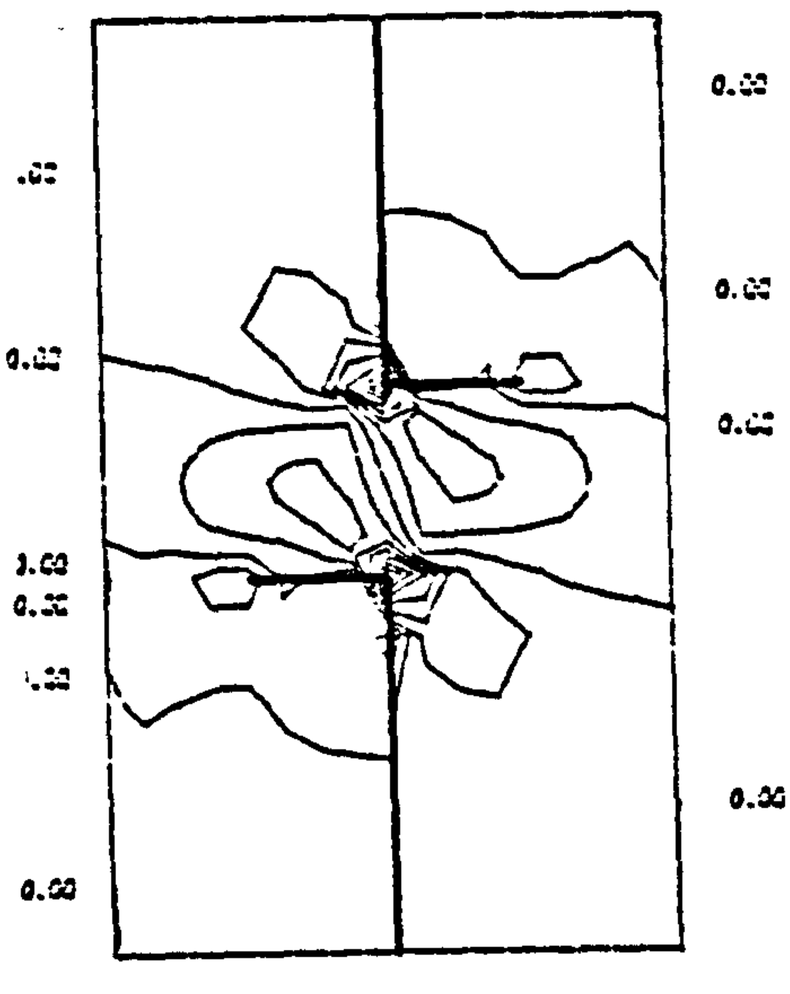

MULTIPLIER 1.0E-2
INTERVAL 0.50

(c) STRESS CONTOURS Mxy

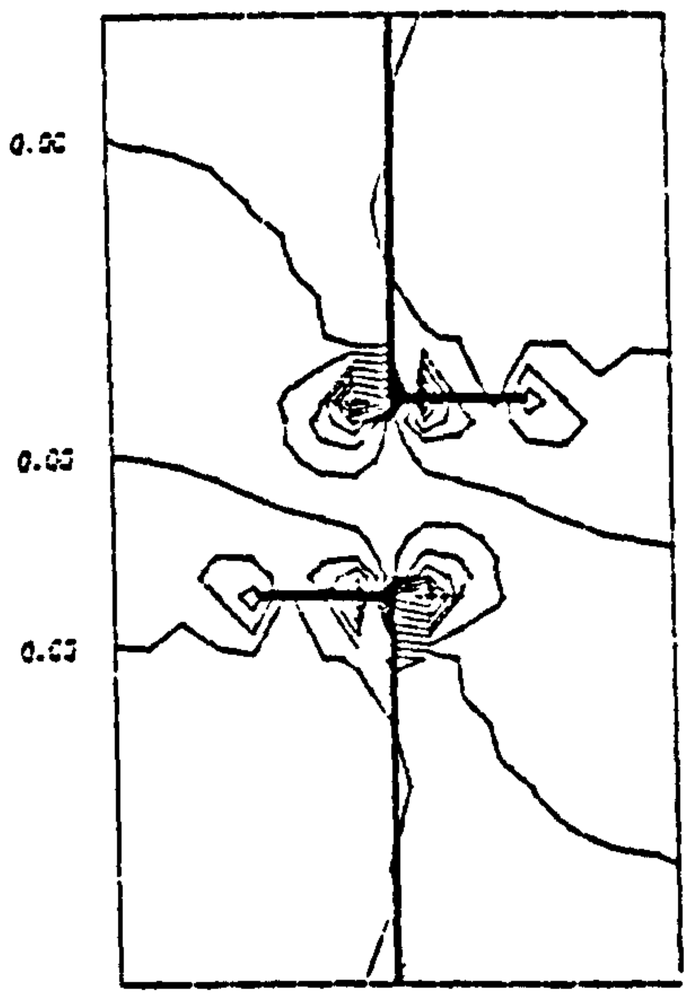

MULTIPLIER 1.0E-2
INTERVAL 0.50

(d) STRESS CONTOURS Qy

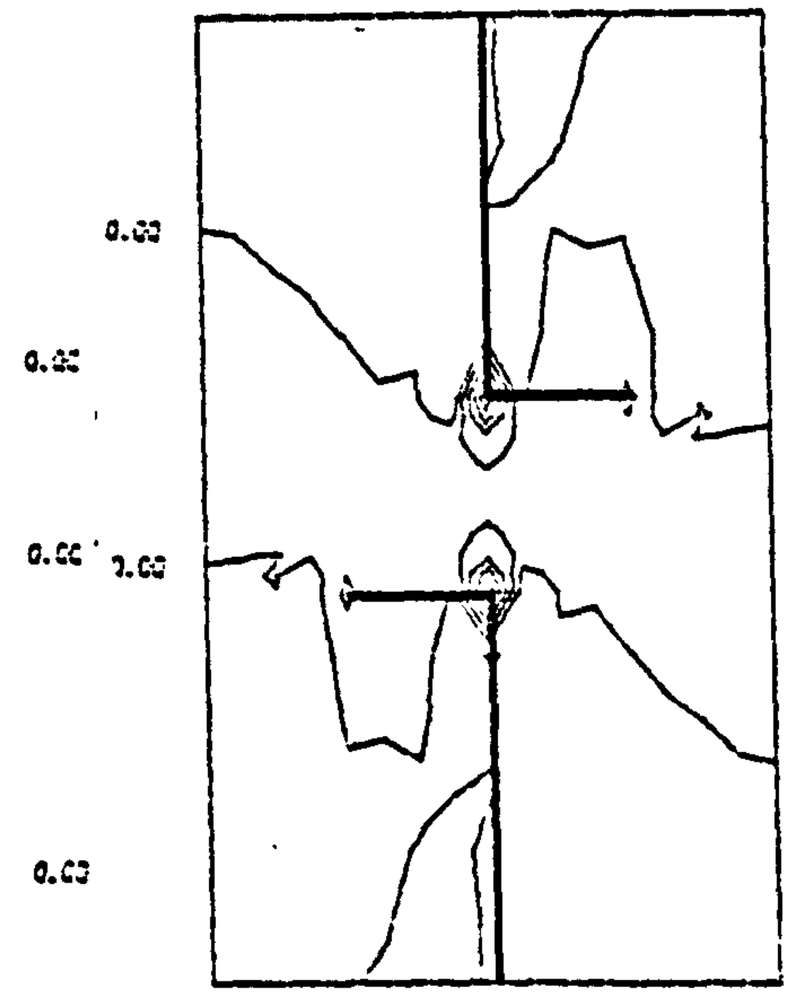

MULTIPLIER 1.0E-2
INTERVAL 2.00

(e) STRESS CONTOURS Qx

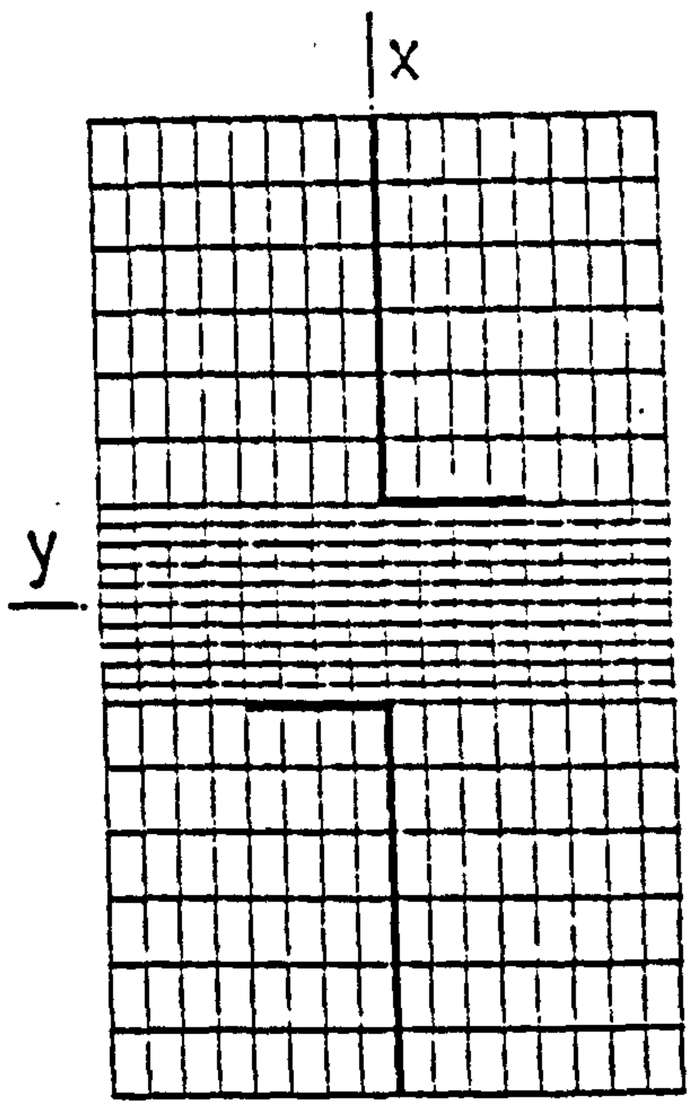

(f) FINITE ELEMENT MESH

Fig. 3.52 Contours of Stress Resultants in Slab for L-shaped Wall Configuration

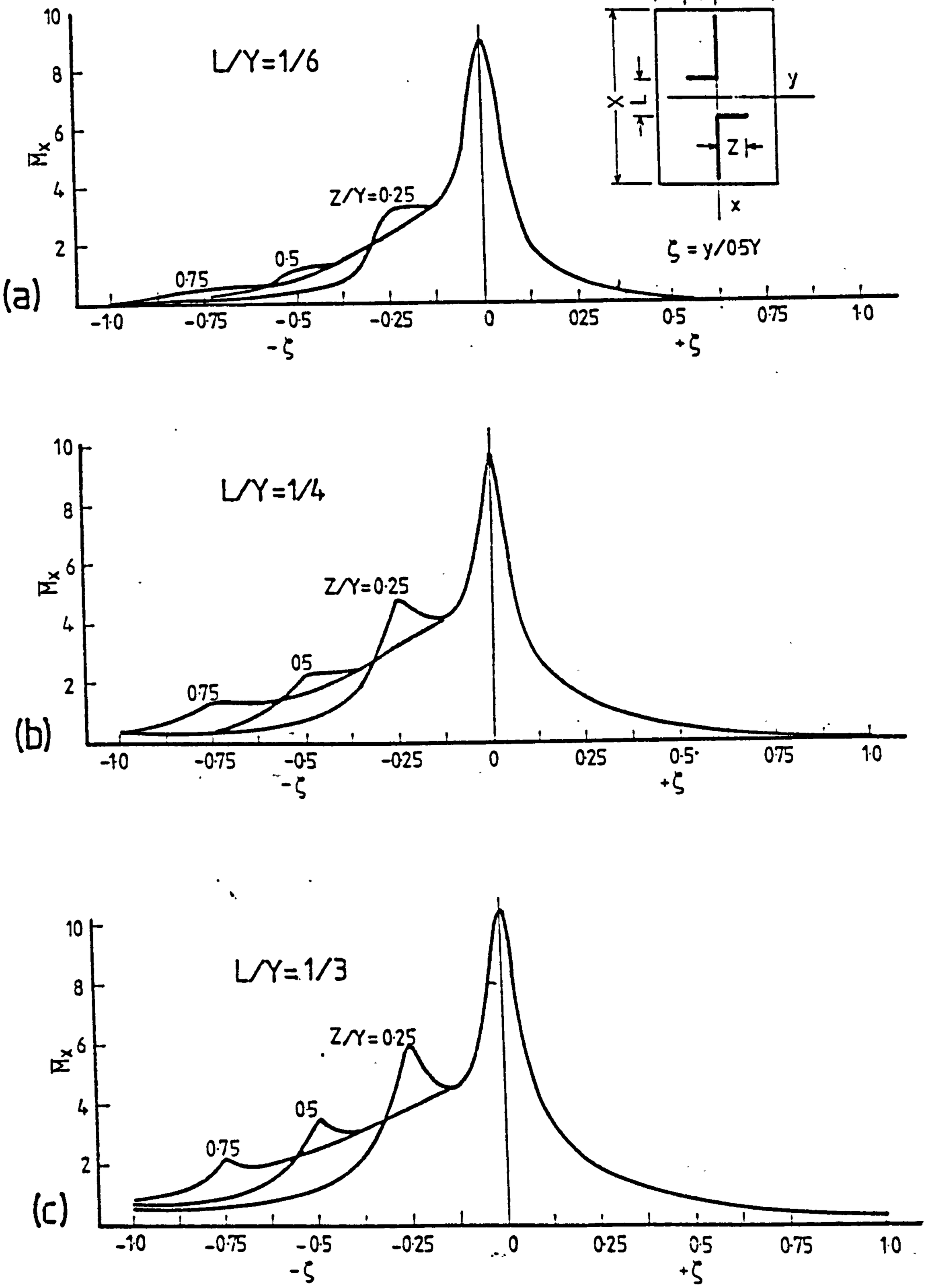

Fig. 3.53 Variation of Longitudinal Bending Moments at Critical Transverse Slab Section for L-Shaped Wall Configuration

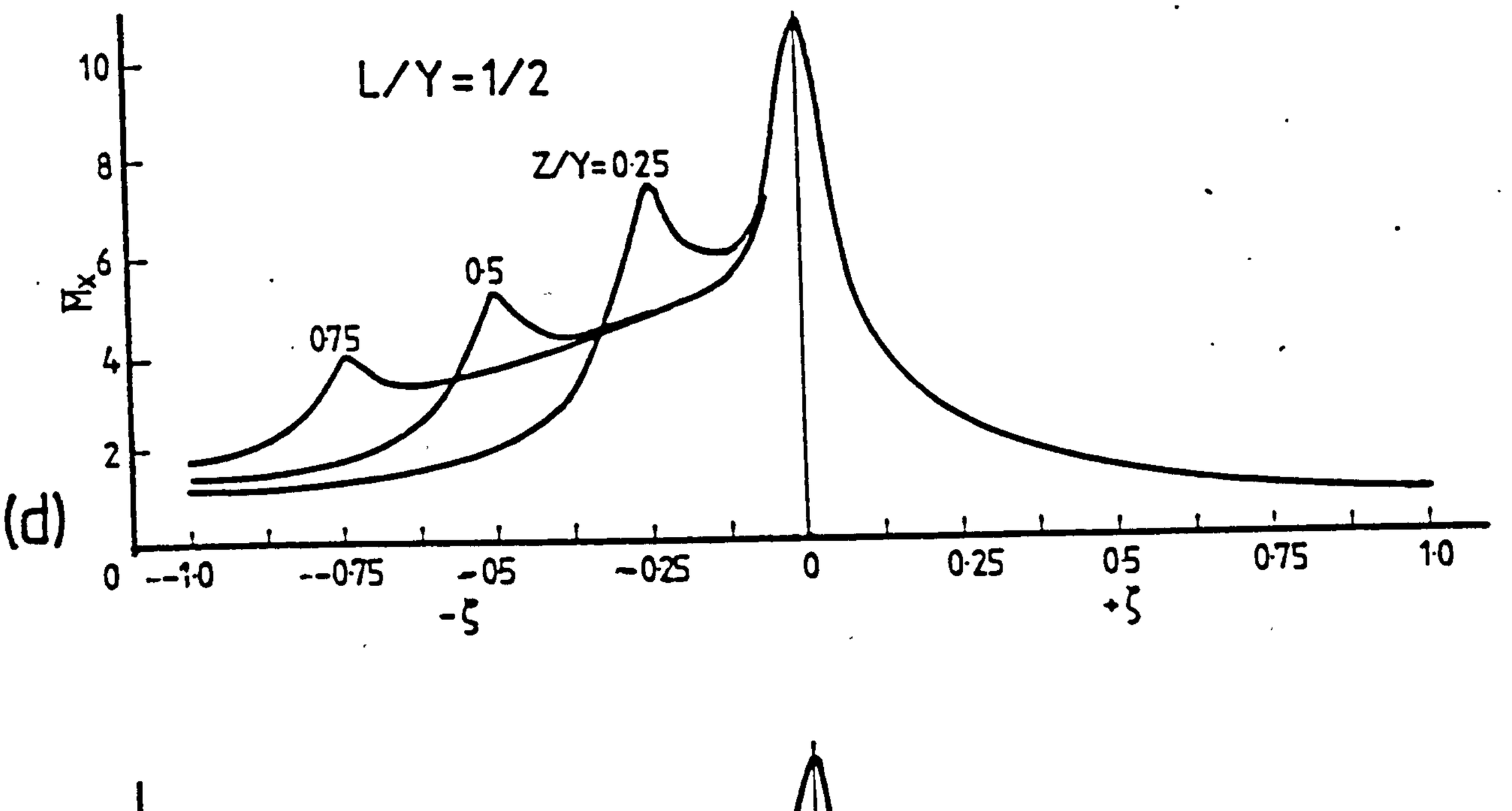

(d)

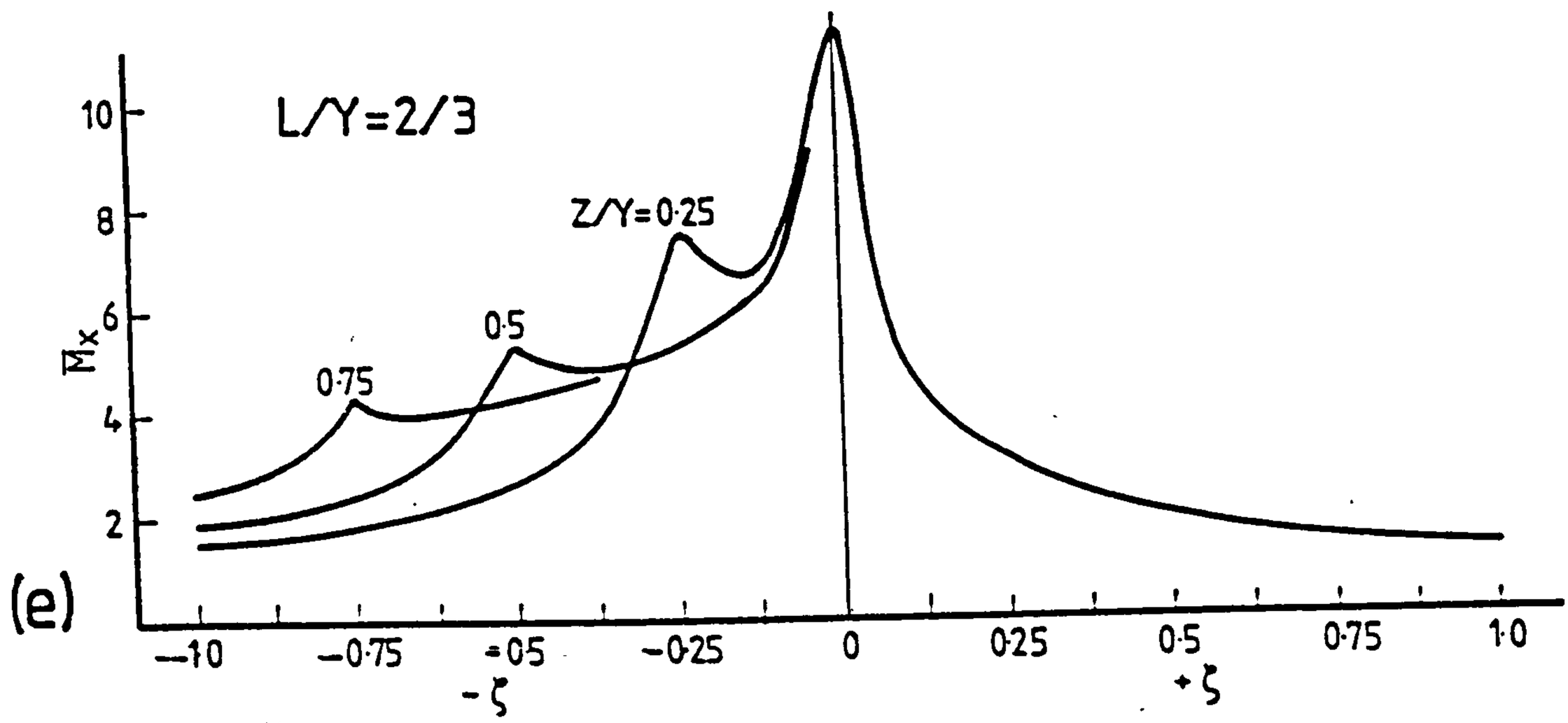

(e)

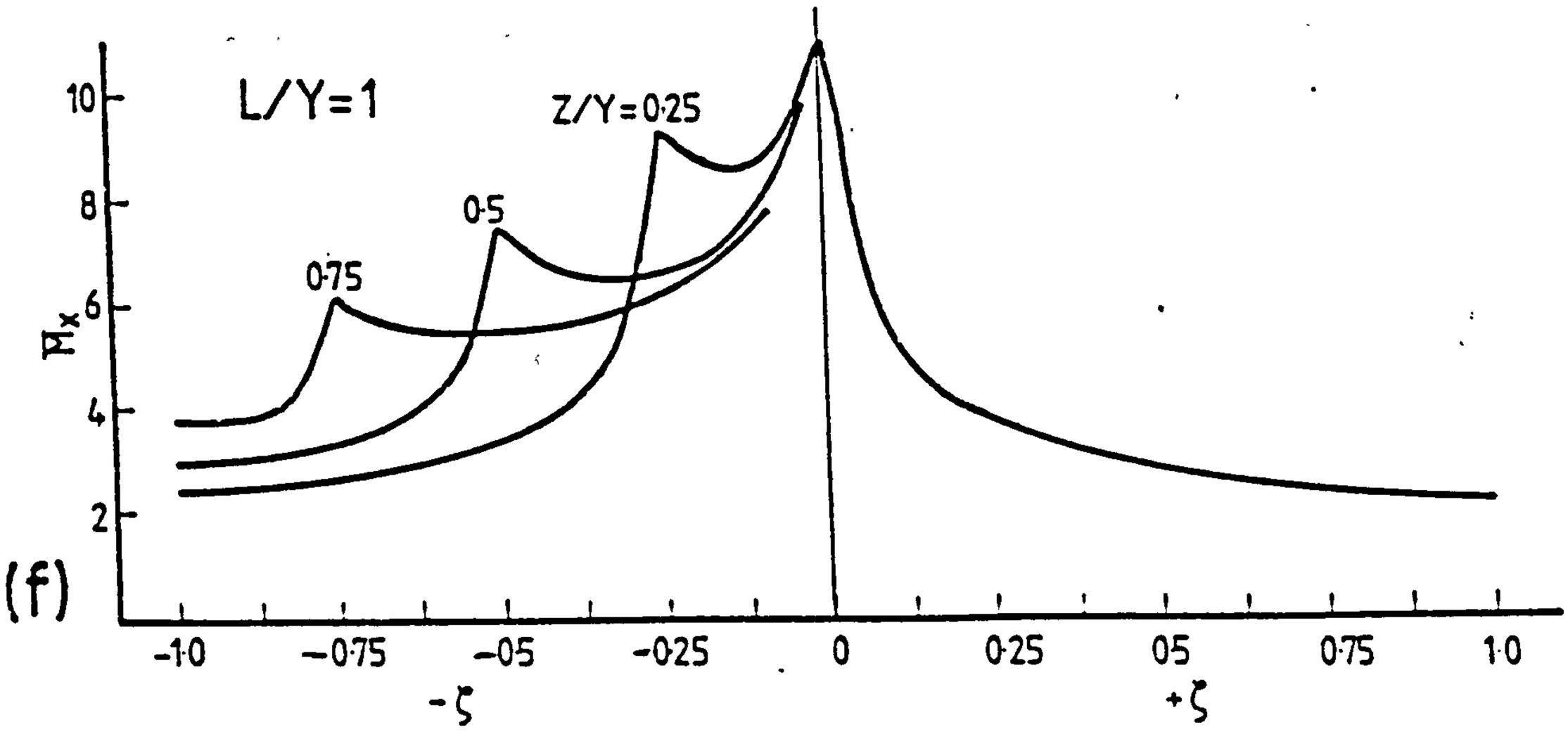

(f)

Fig. 3.53 (Contd) Variation of Longitudinal Bending Moments at Critical Transverse Slab Section for L-Shaped Wall Configuration

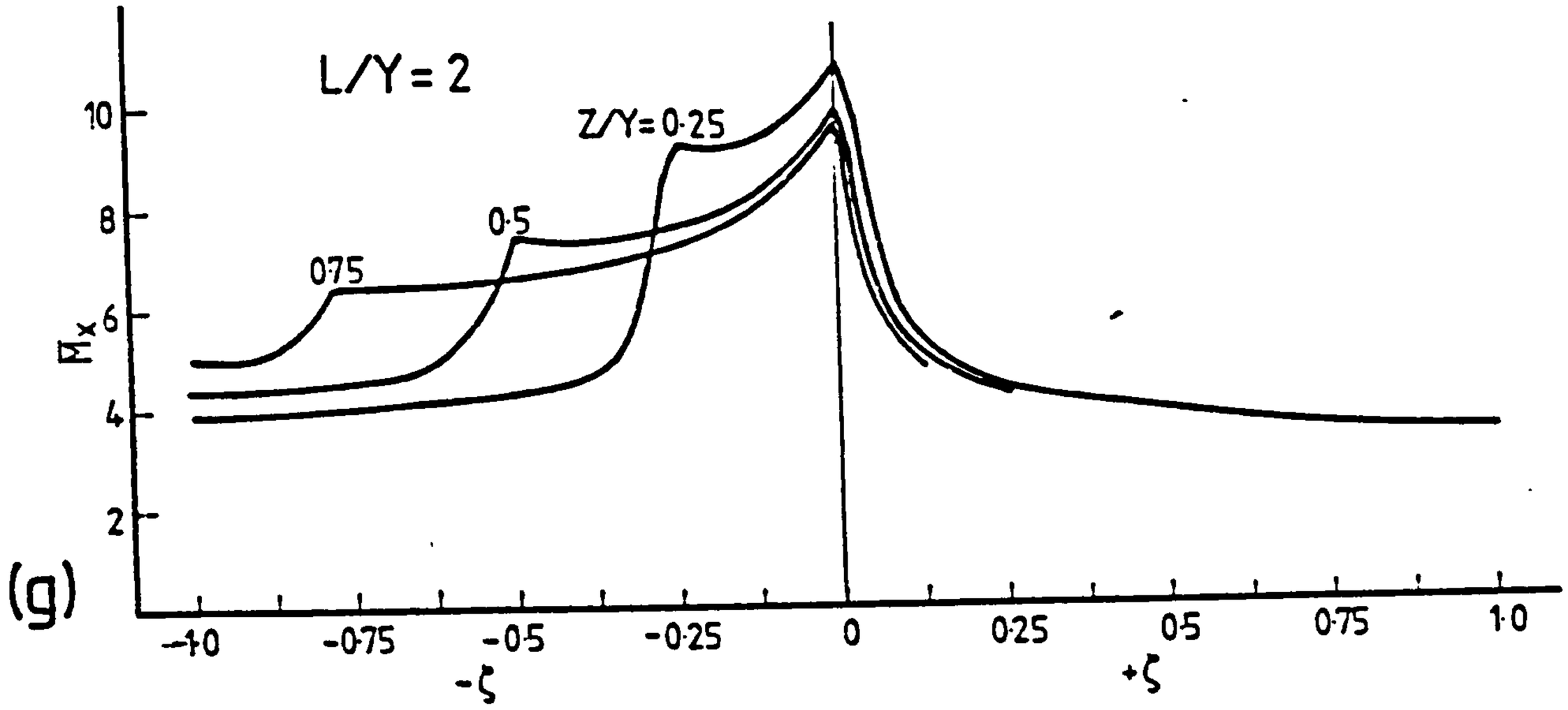

(g)

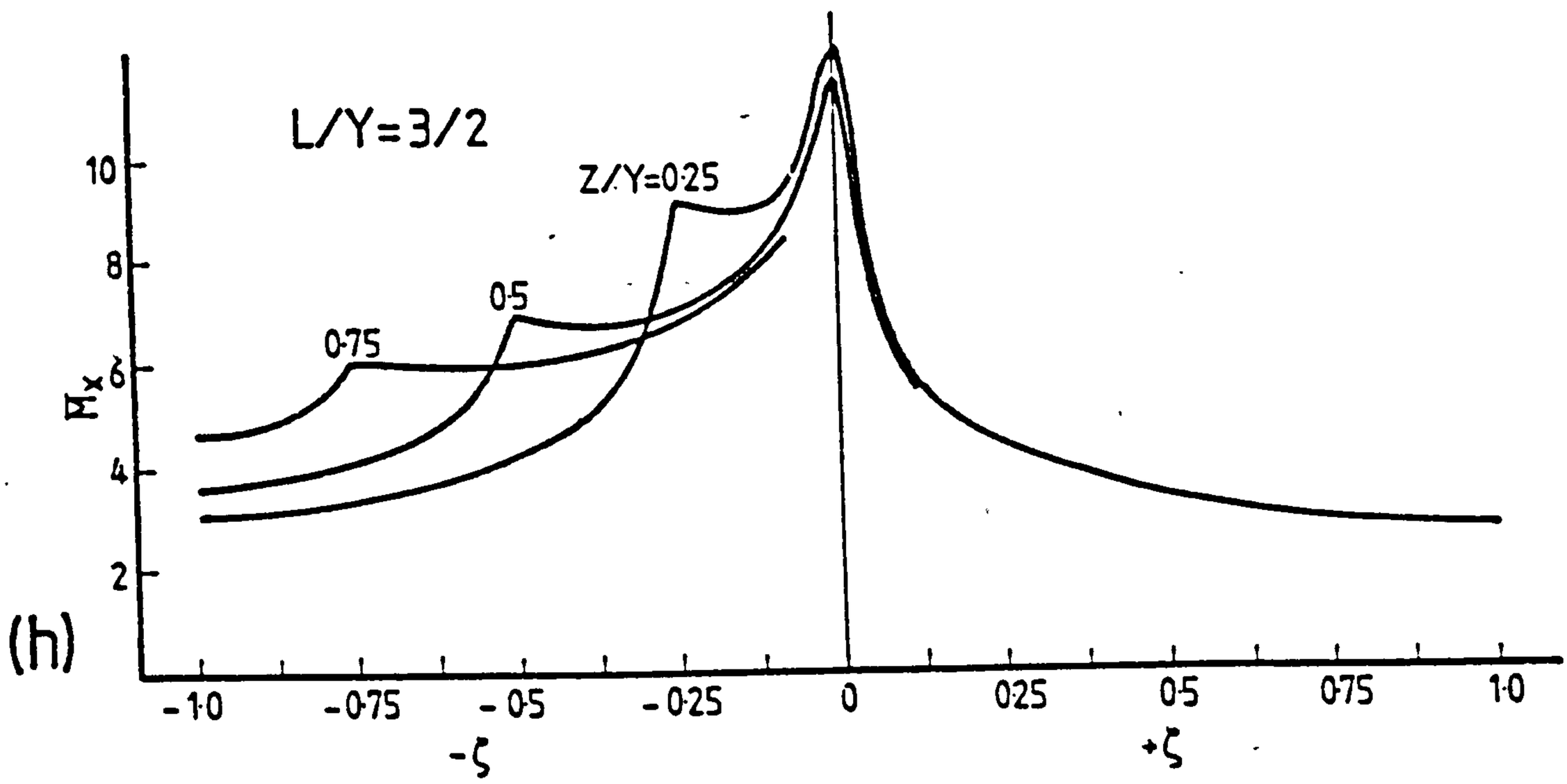

(h)

Fig. 3.53 (Contd) Variation of Longitudinal Bending Moments at Critical Transverse Slab Section for L-Shaped Wall Configuration

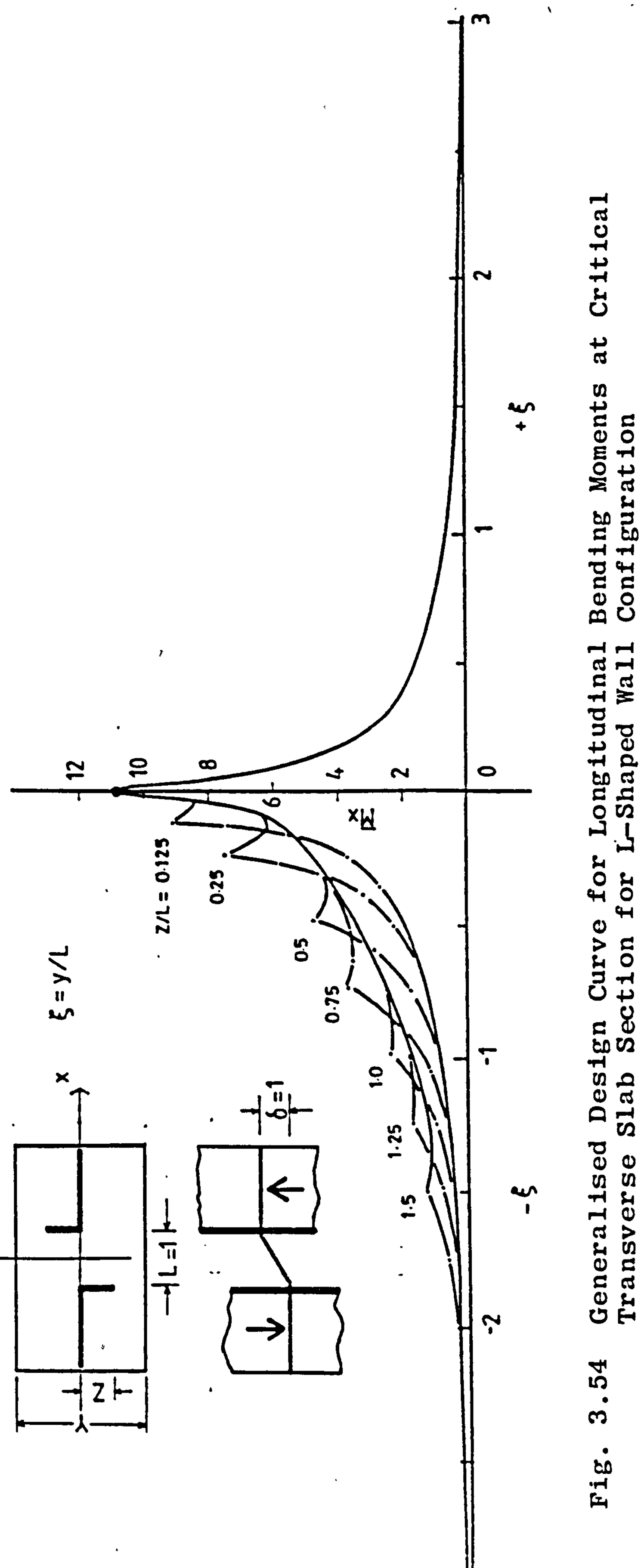

3.54 Generalised Design Curve for Longitudinal Bending Moments at Critical Transverse Slab Section for L-Shaped Wall Configuration

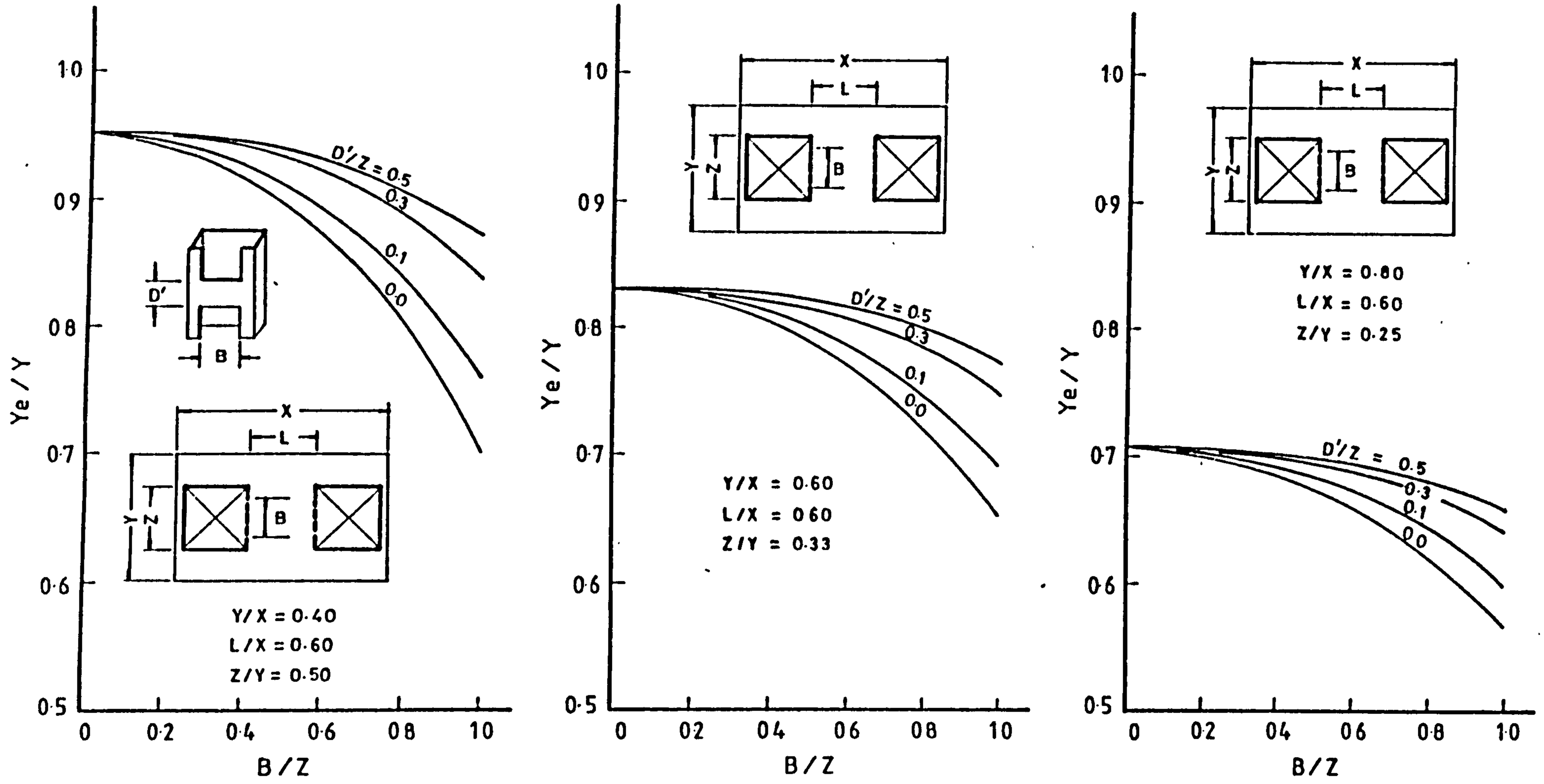

Fig. 3.55 Variation of Effective Slab Width with Core Opening Width and Lintel Depth

NOTE:
The term 'STRESS' is used in the context of a stress resultant

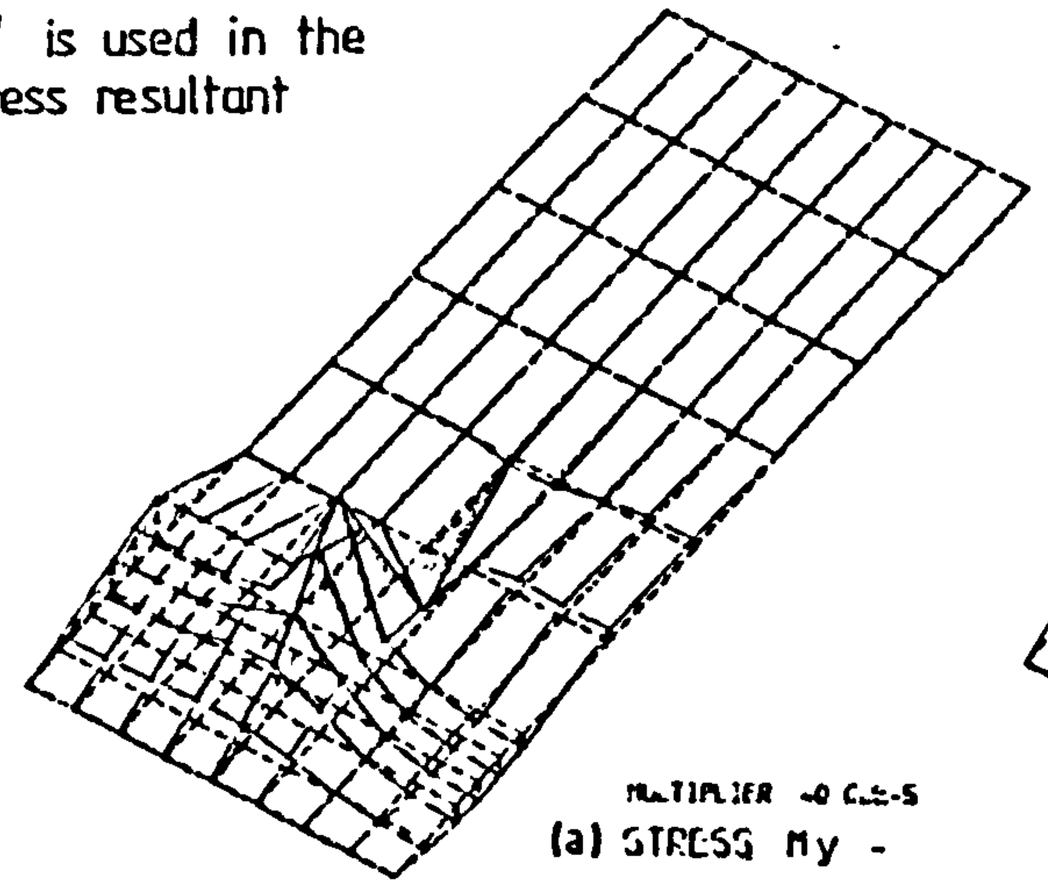

(a) STRESS My -

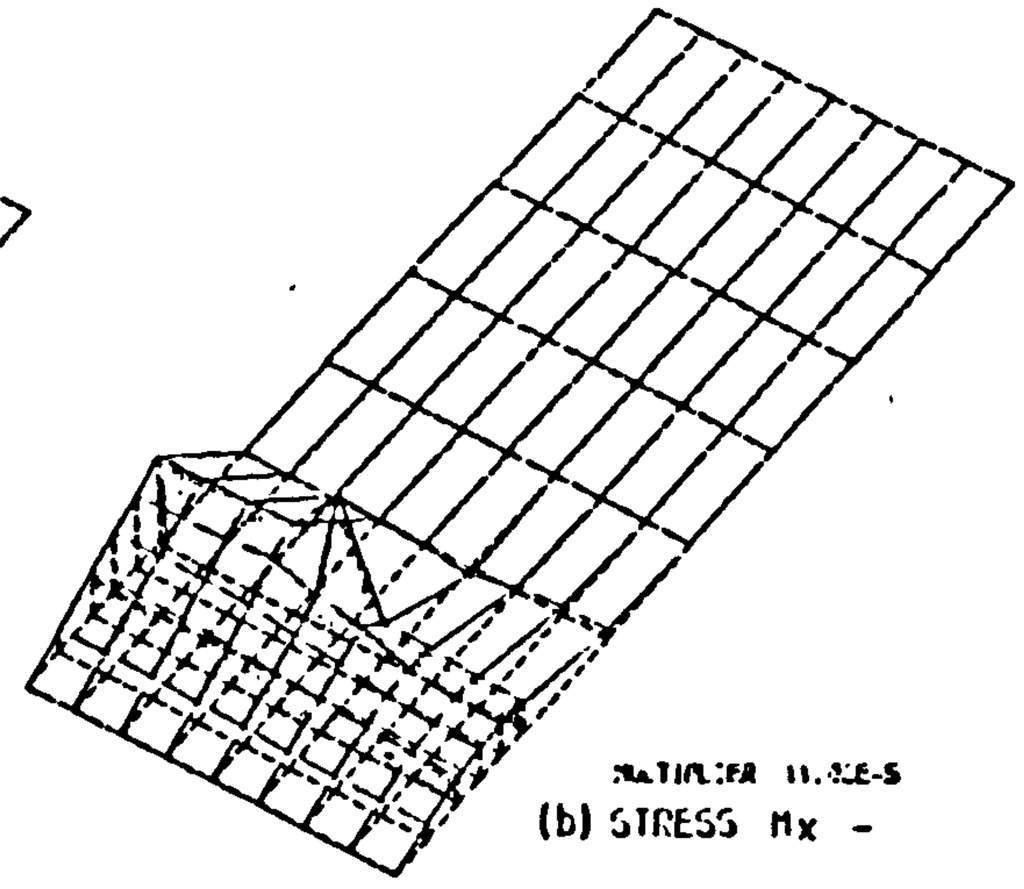

(b) STRESS Mx -

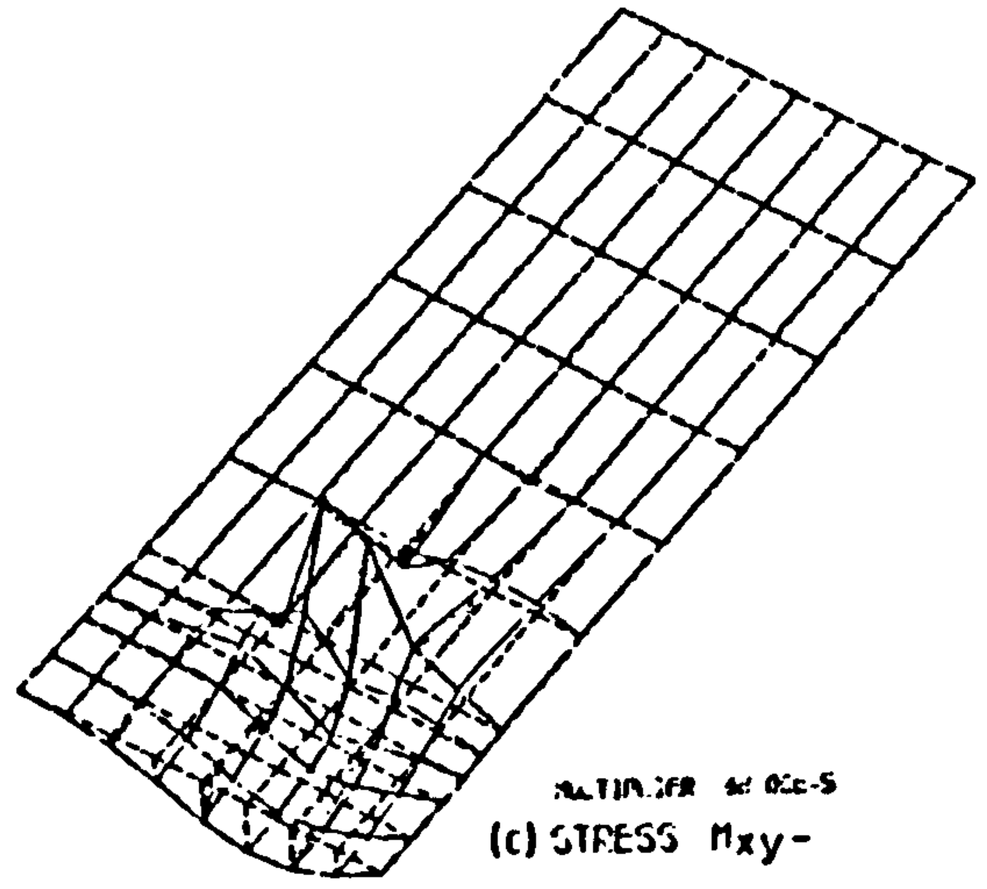

(c) STRESS Mxy -

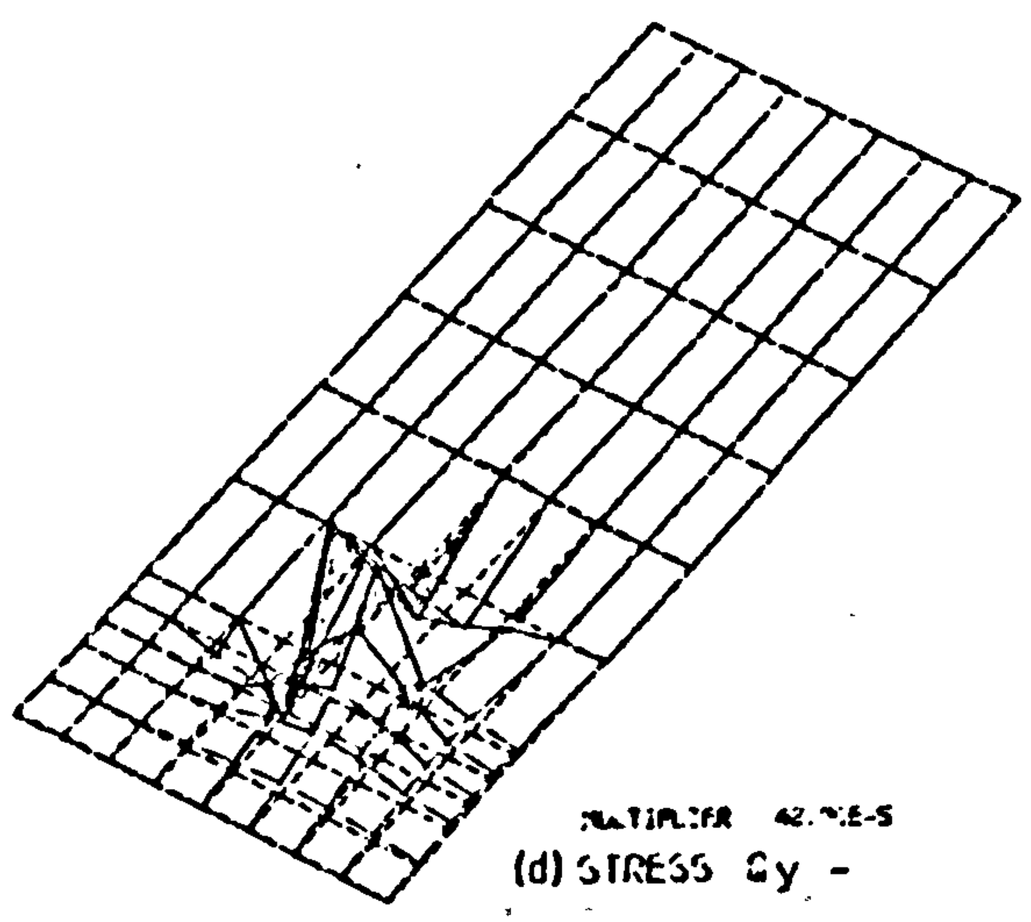

(d) STRESS Qy -

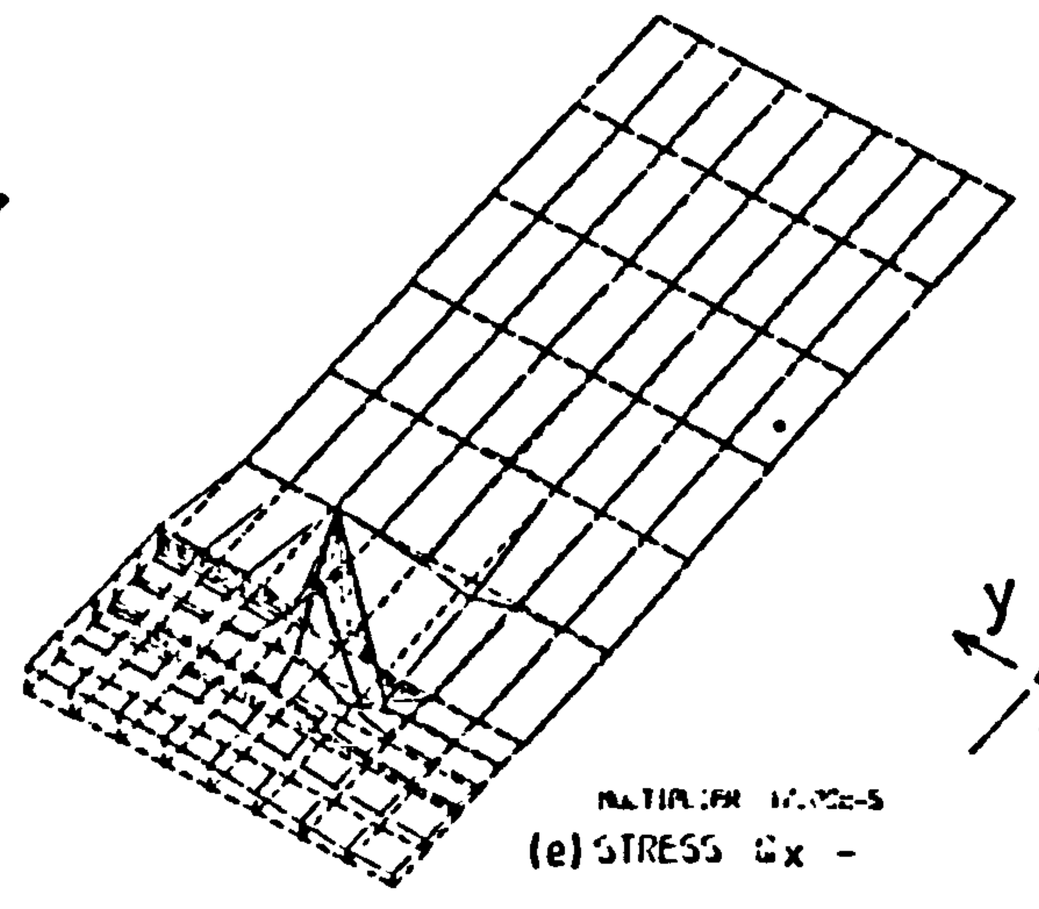

(e) STRESS Qx -

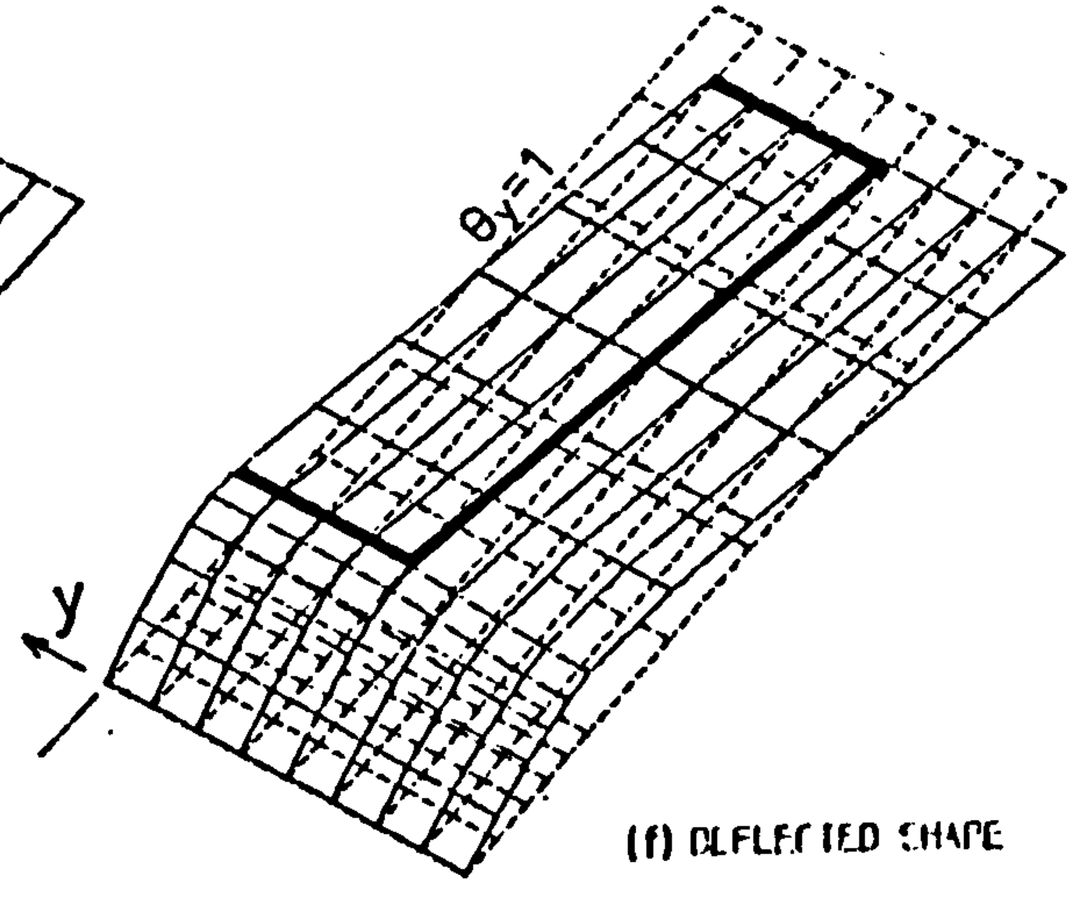

(f) DEFLECTED SHAPE

Fig. 3.56 General Distribution of Slab Actions in Box-Core Configuration

NOTE: The term 'STRESS' is used in the context of a stress resultant.

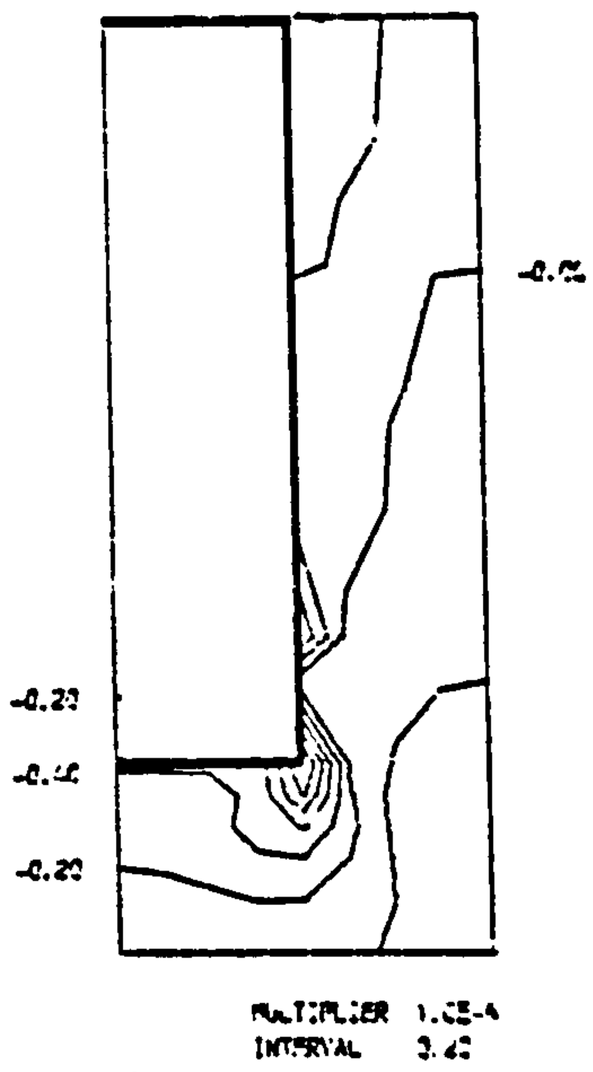

(a) STRESS CONTOURS My

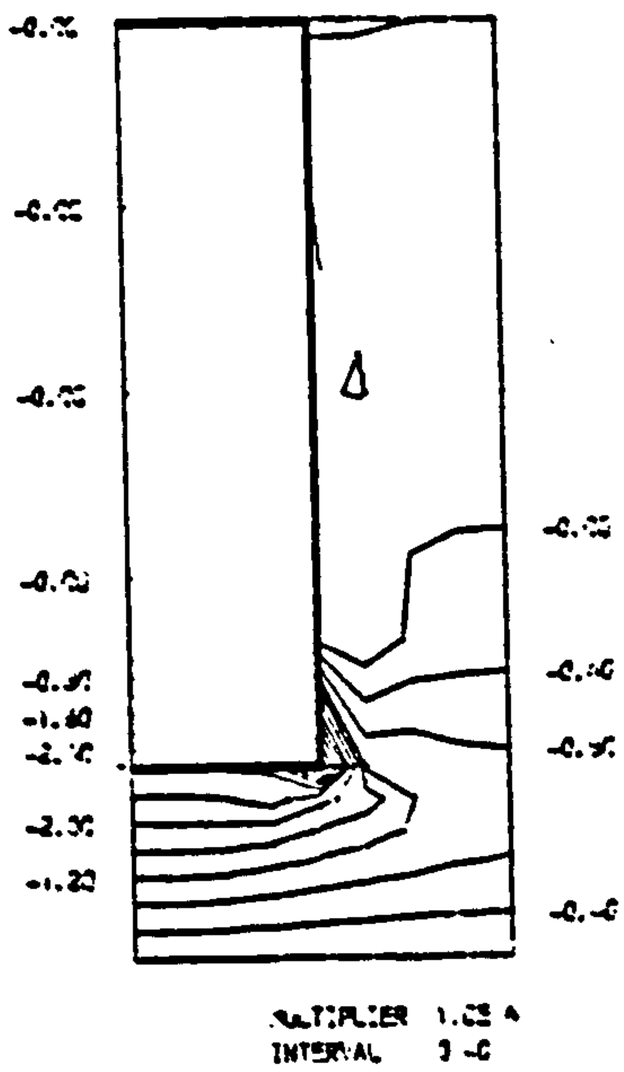

(b) STRESS CONTOURS Mx

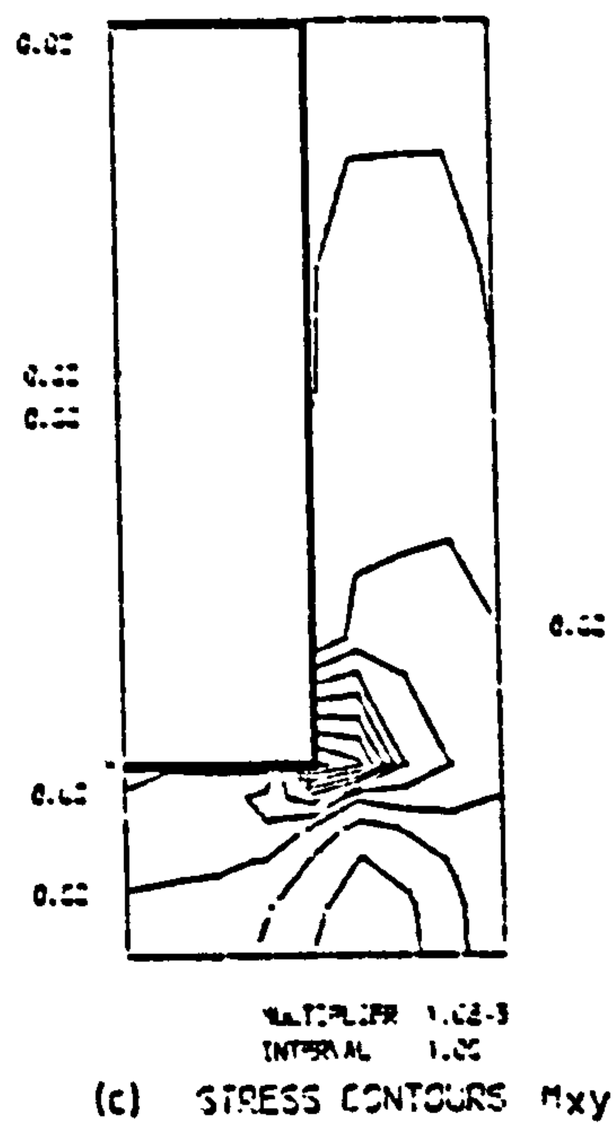

(c) STRESS CONTOURS Mxy

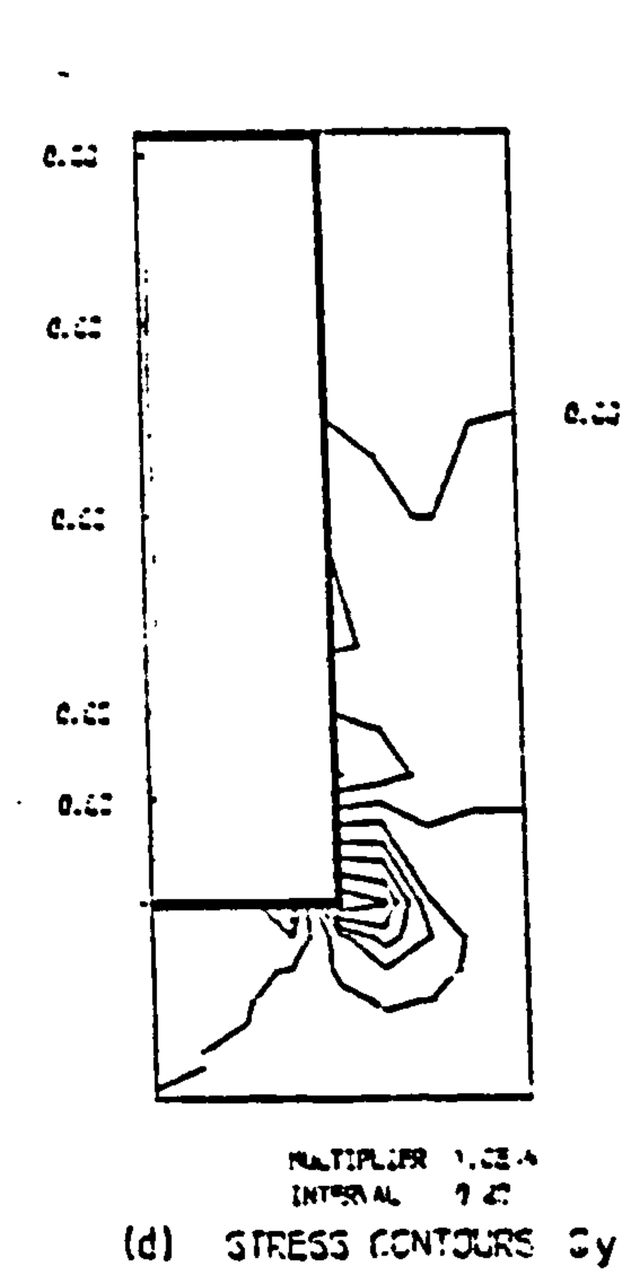

(d) STRESS CONTOURS Sy

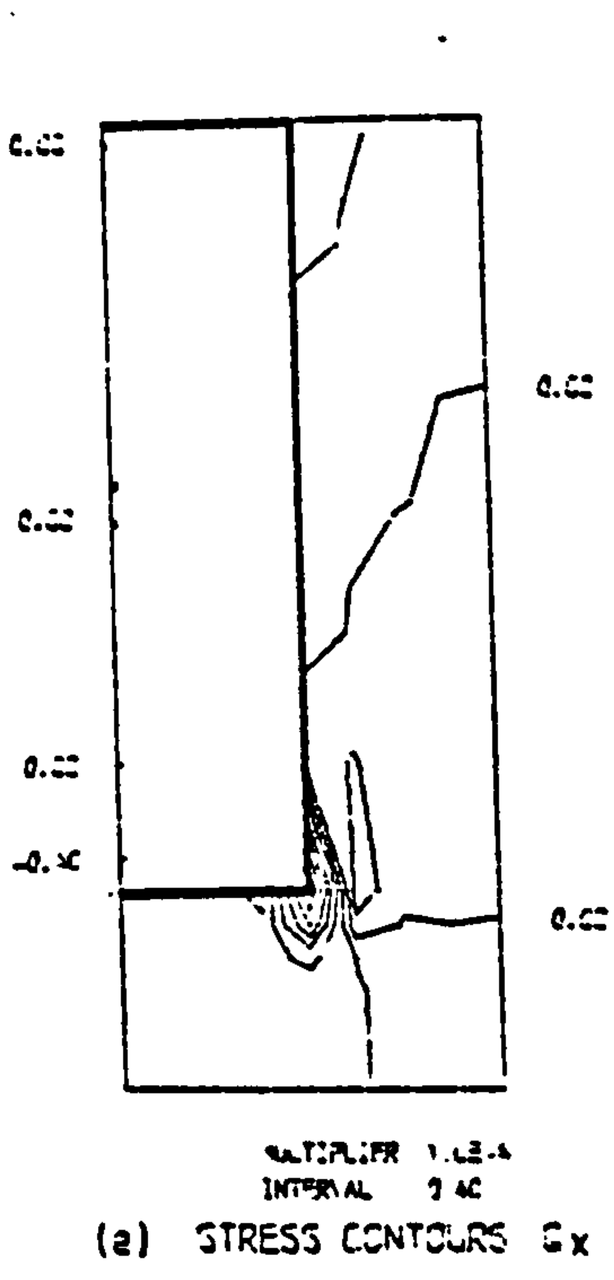

(e) STRESS CONTOURS Sx

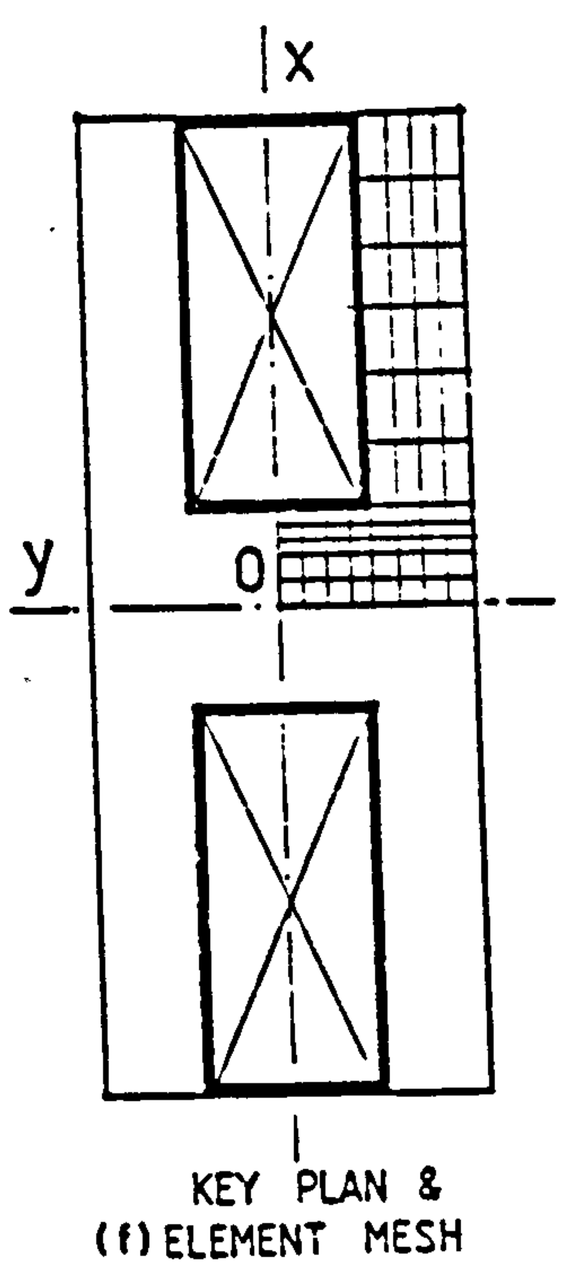

KEY PLAN &
(f) ELEMENT MESH

Fig. 3.57 Contours of Stress Resultants in Slab for Box-Core Configuration

ρ	Dx/Dy
1%	1·10
4%	1·23

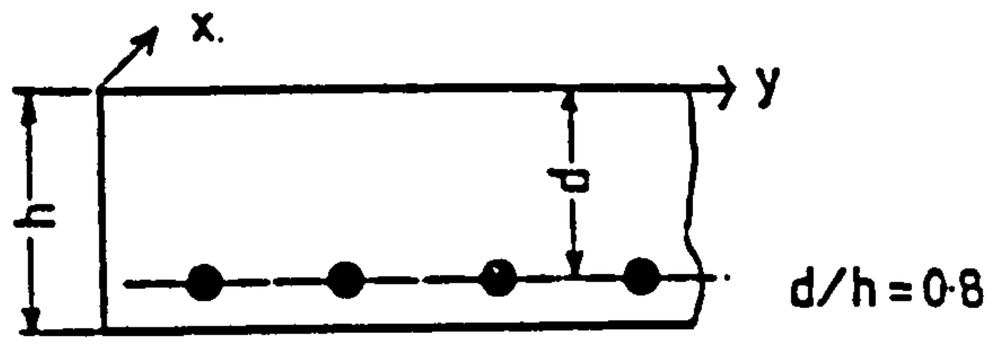

Solid Slab

d/h	Dx/Dy
0·50	1·10
0·75	1·47

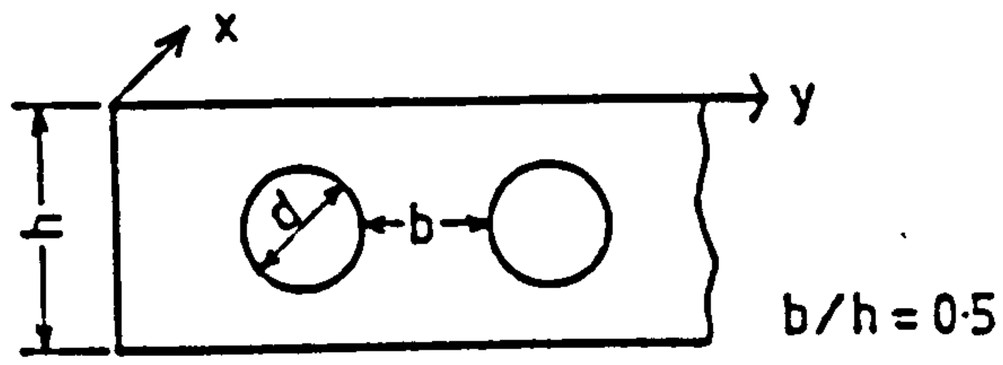

Voided Slab

c/h	Dx/Dy
0·20	1·95
0·40	4·63

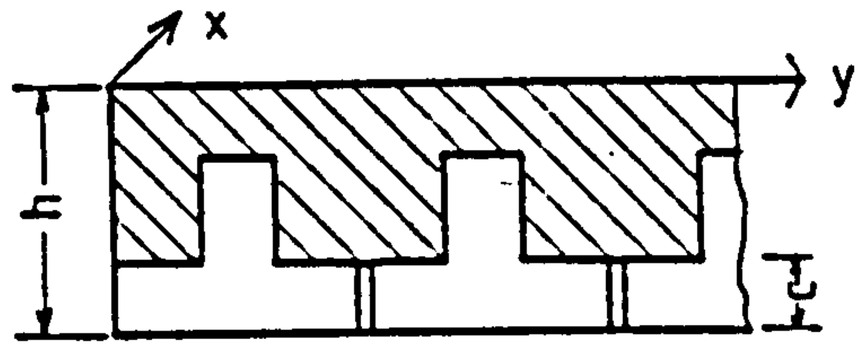

Pseudo-Slab

t/h	Dx/Dy
0·3	12·31
0·2	41·17

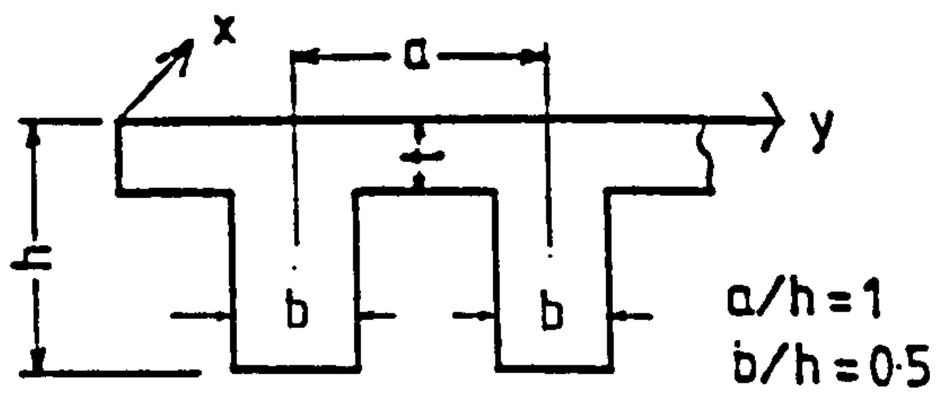

Ribbed Slab

Fig. 3.58 Forms of Orthotropic Slab and Flexural Rigidity Ratios

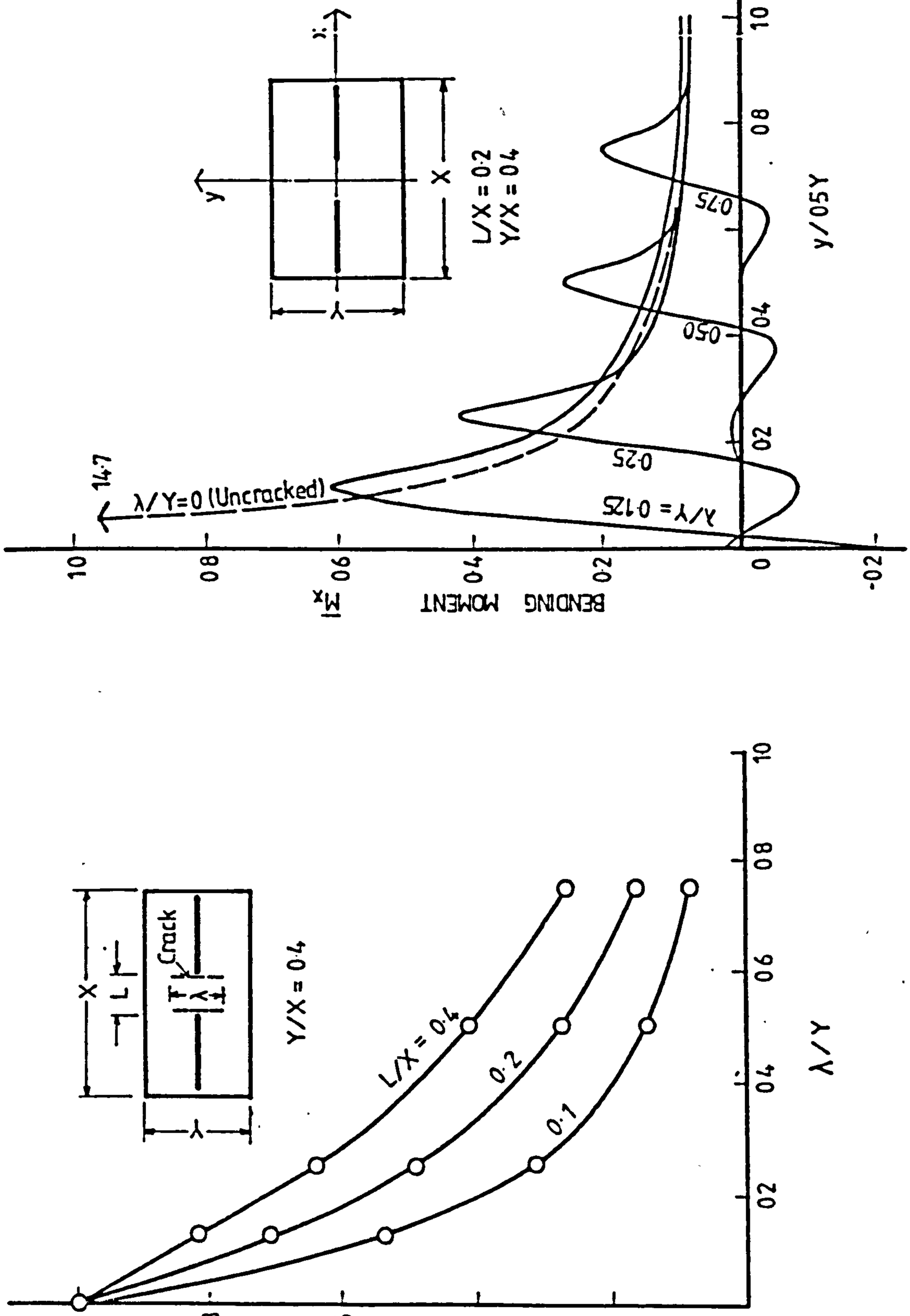

3.59 Influence of Crack Length on (a) Slab Stiffness Ratio and (b) Longitudinal Bending Moments at Critical Transverse Slab Section

Fig.

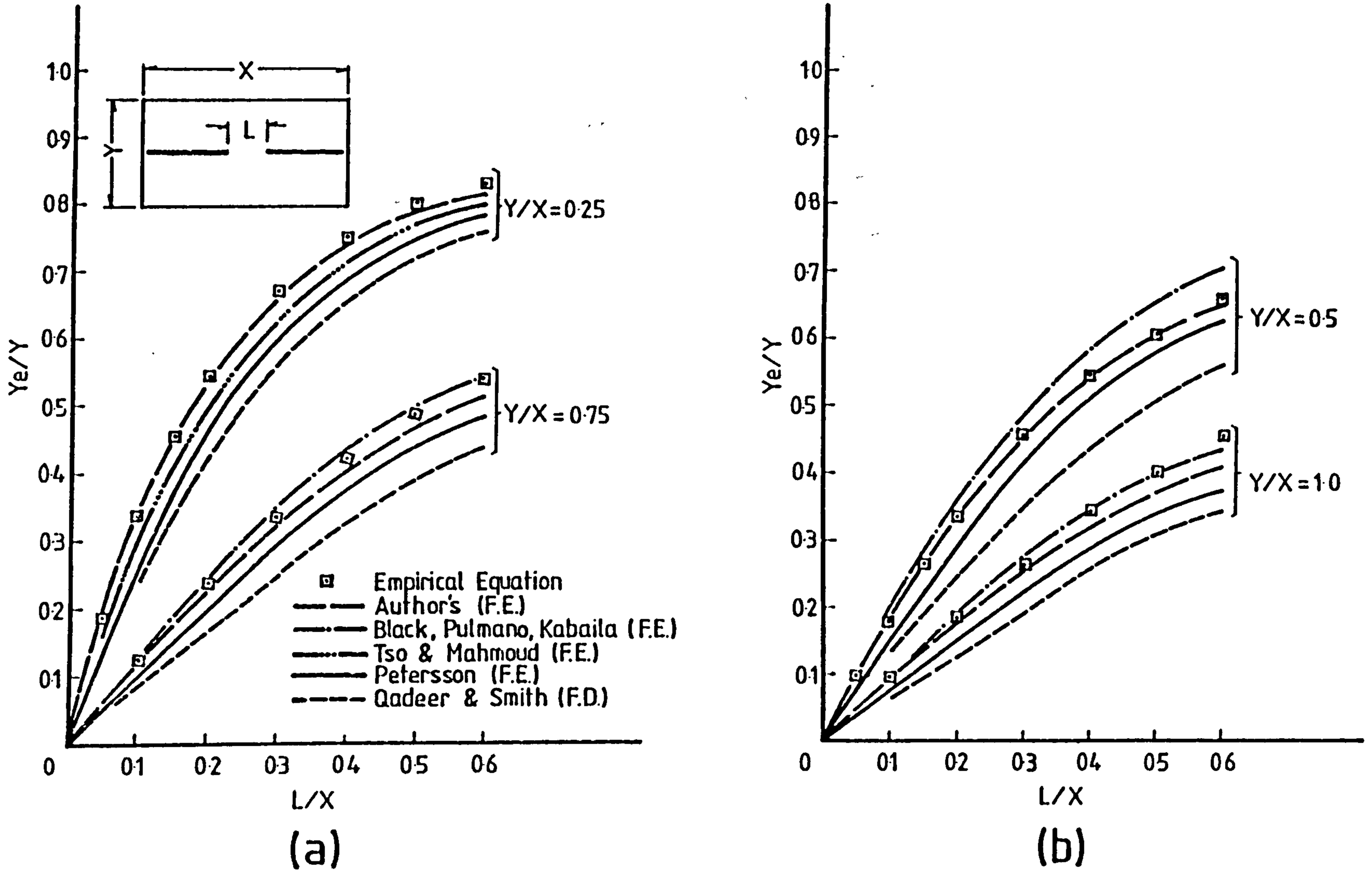

Fig. 3.60 Comparison Between Theoretical Effective Widths Determined by Author and by Other Investigators, for Plane Wall Configuration

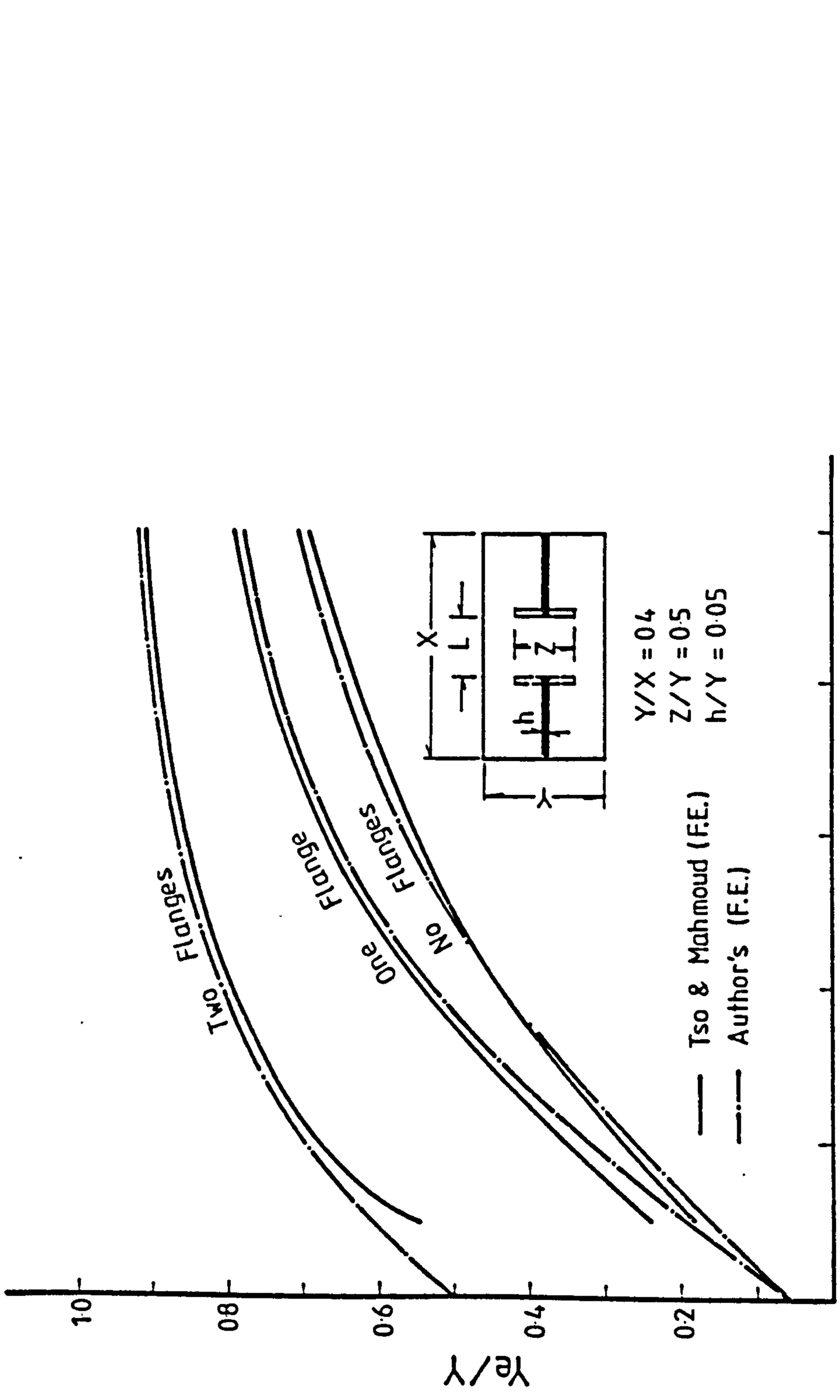

Fig. 3.61 Comparison Between Effective Widths Obtained by Author's and Tso and Mahmoud's Finite Element Solutions, for Flanged Wall Configuration

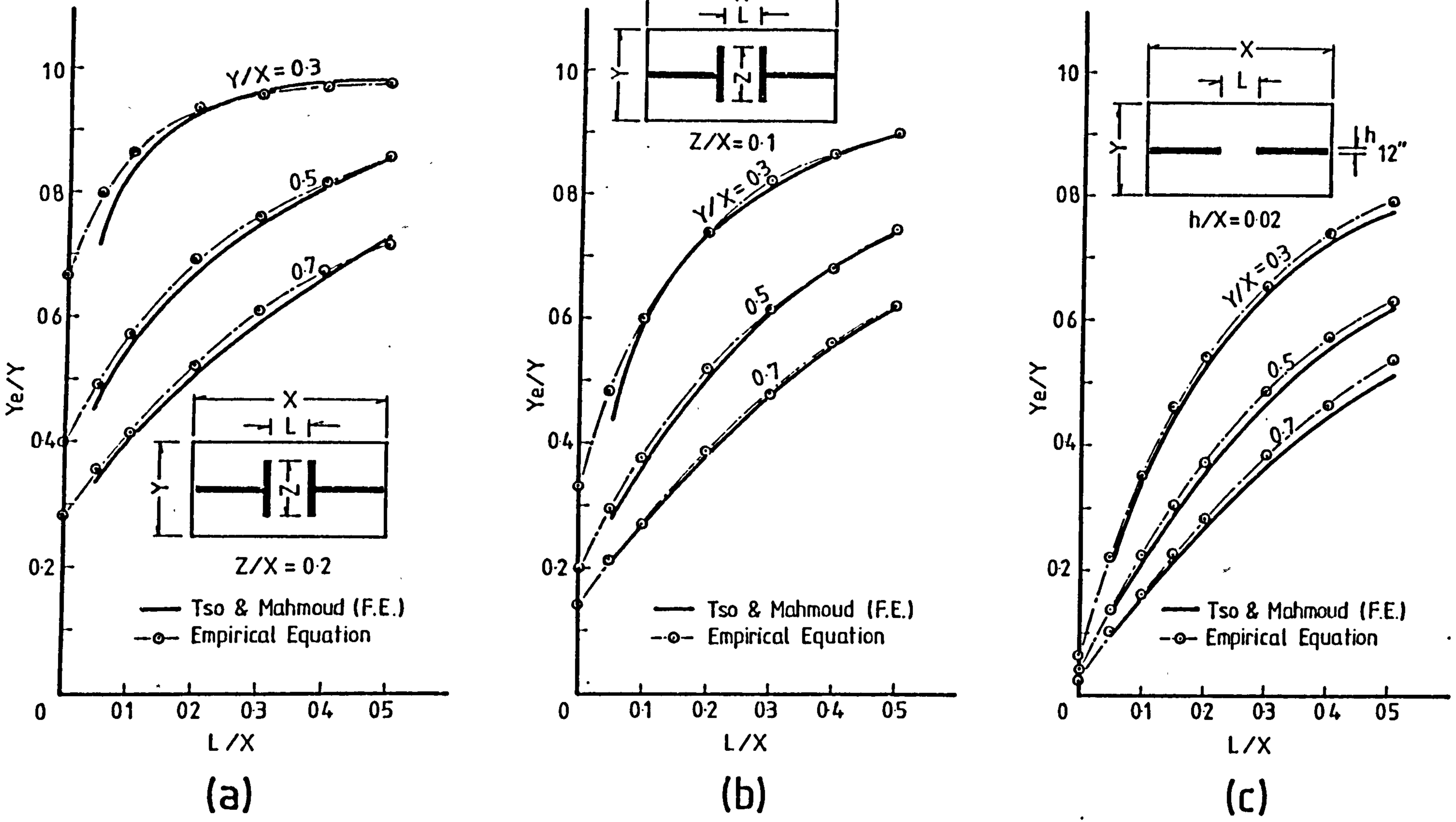

Fig. 3.62 Comparison Between Effective Widths Determined by Author's Empirical Equations and by Tso and Mahmoud's Finite Element Solution, for Flanged Wall Configuration

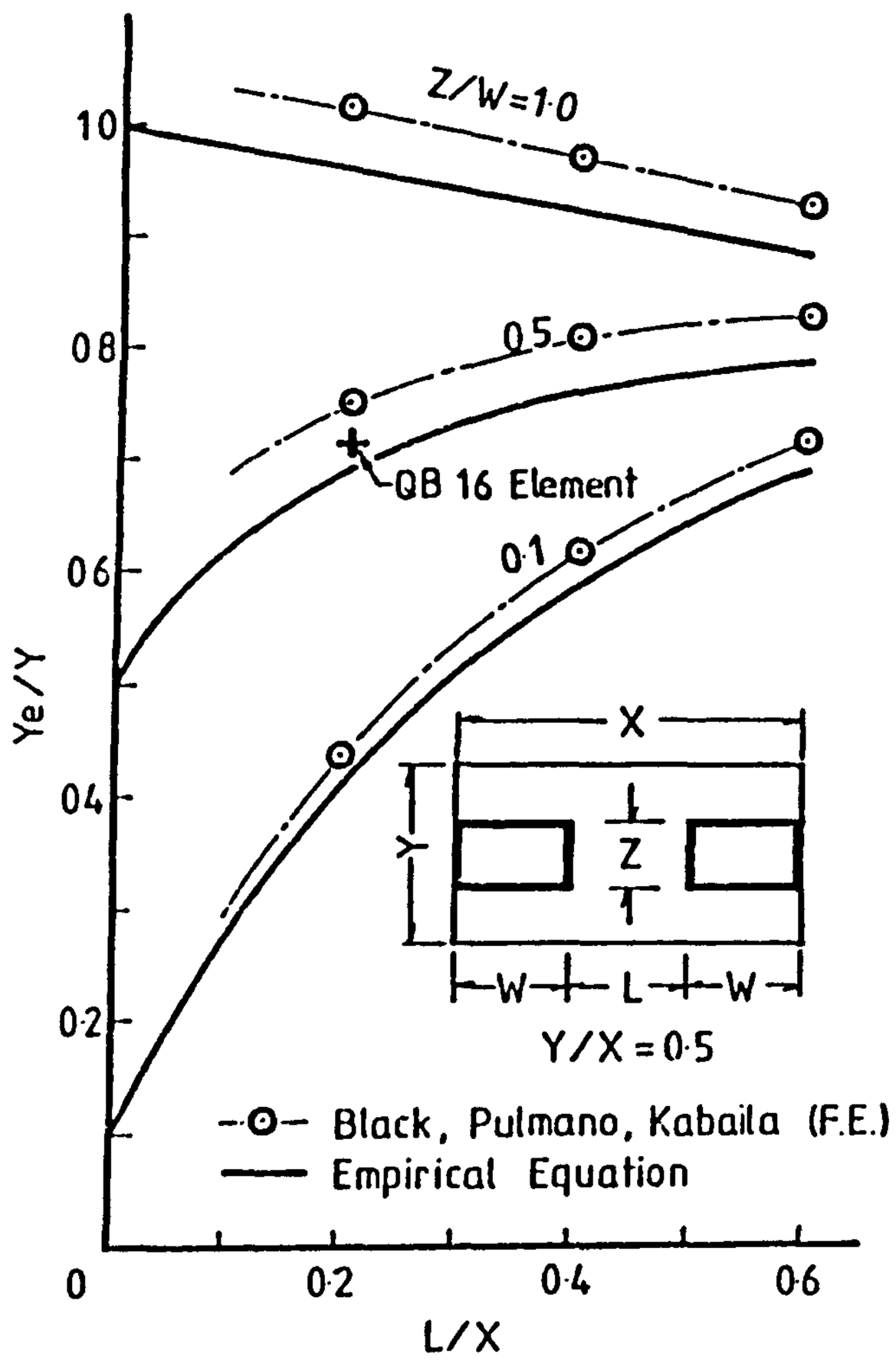

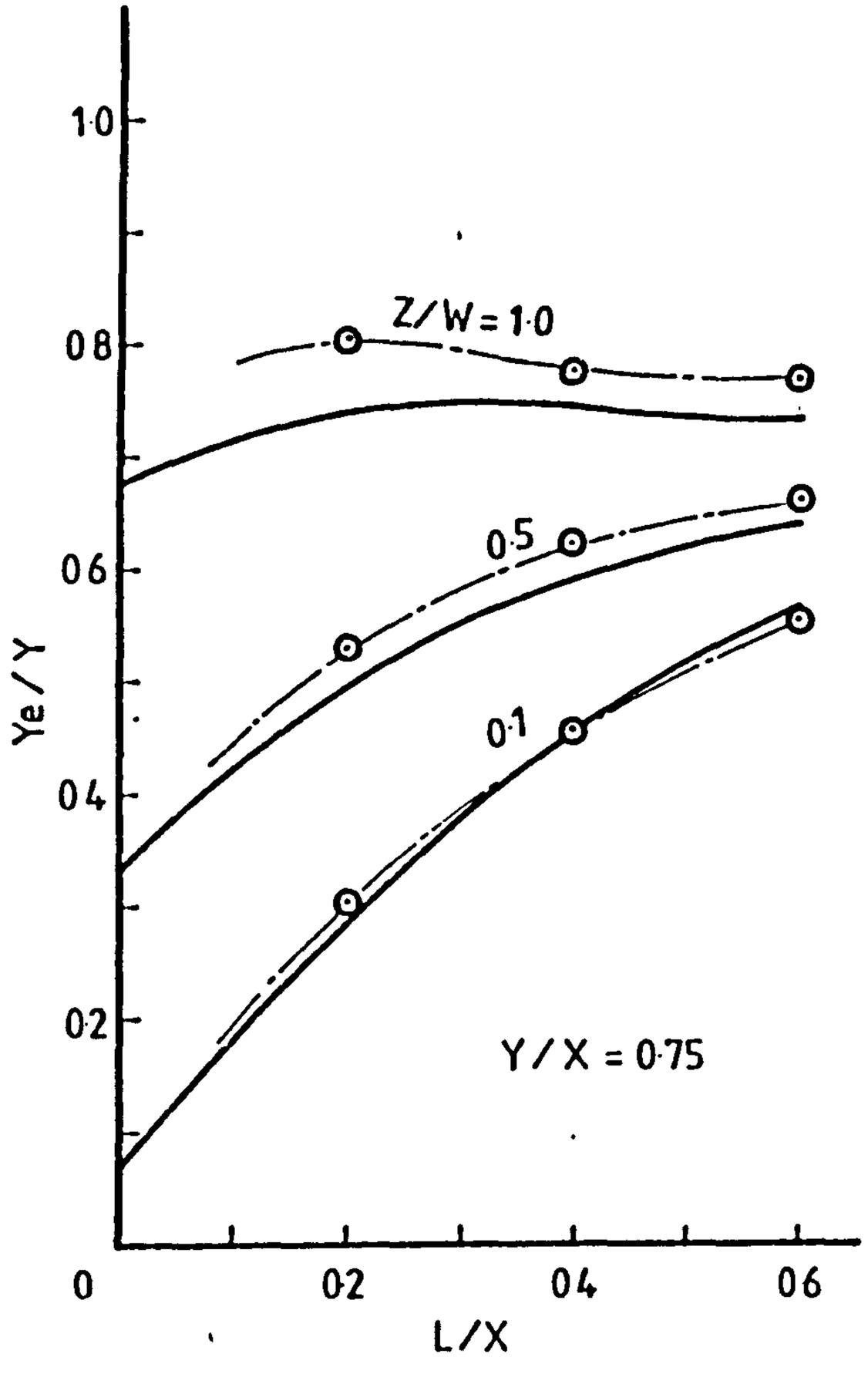

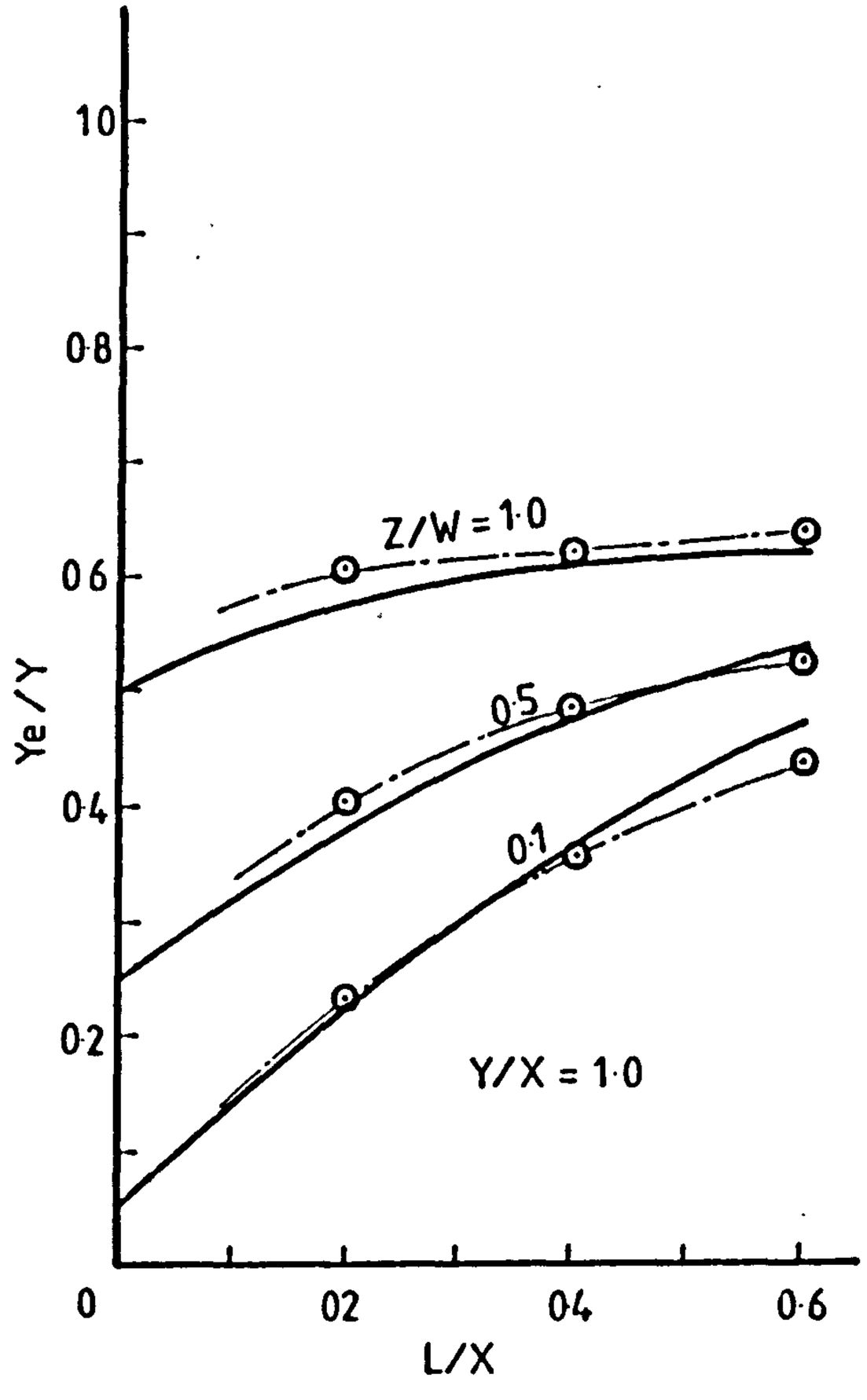

Fig.3.63 Comparison Between Effective Widths Determined by Author's Empirical Equations and by Black, Pulmano and Kabaila's Finite Element Solution, for Thick Wall or Box Core Configuration

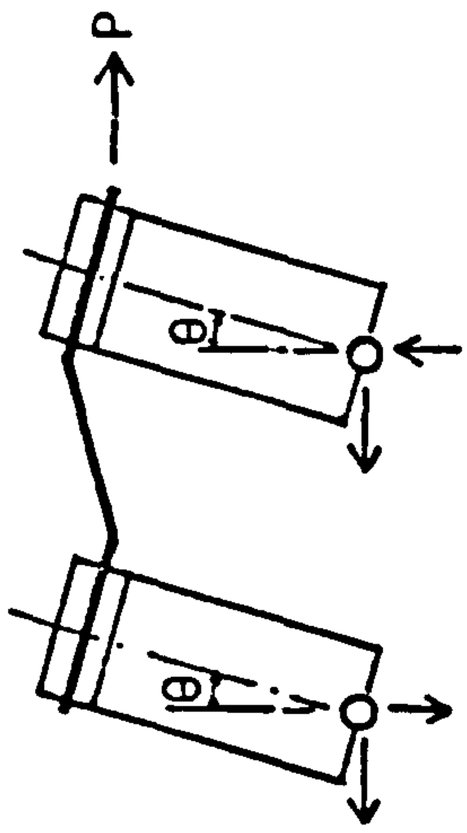

(b)

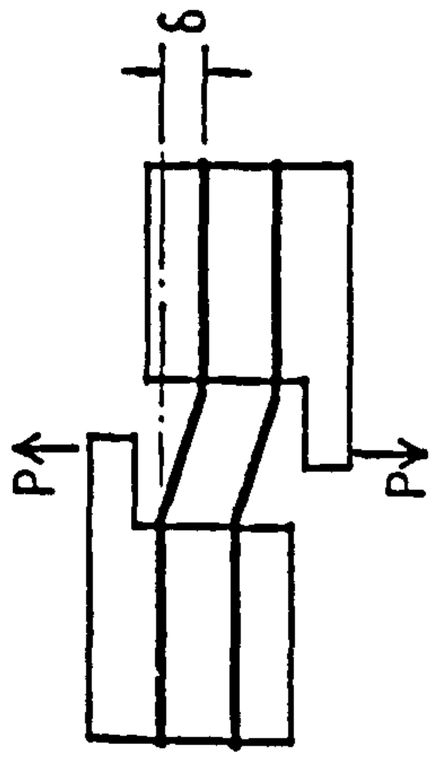

(c)

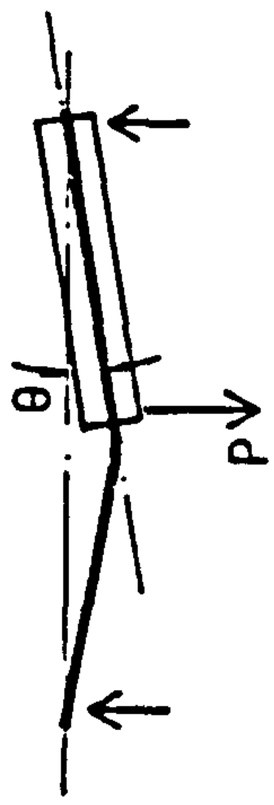

(d)

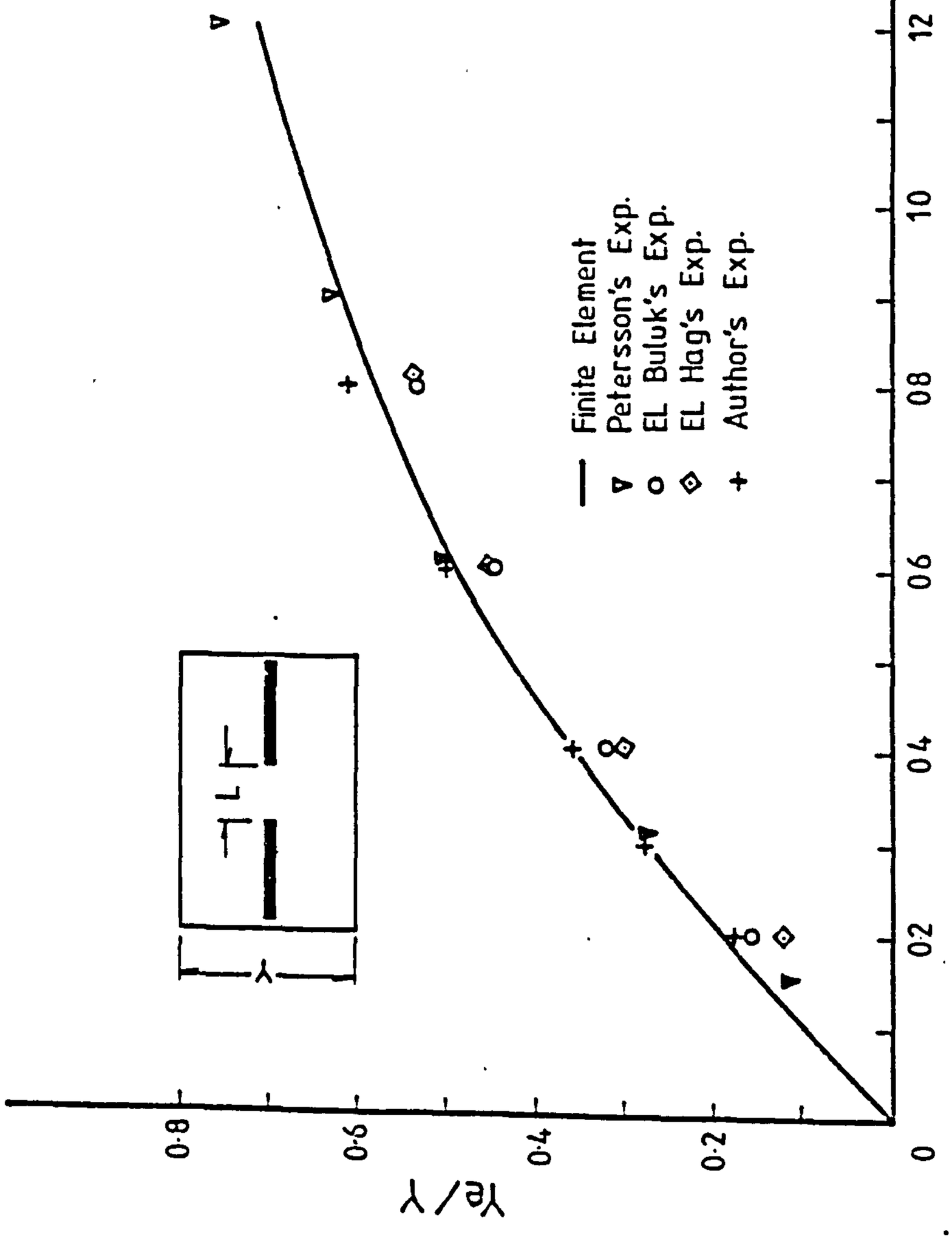

(a)

Fig. 3.64 Comparison Between Effective Widths Determined by Finite Element Solution and by Experiment, for Plane Wall Configuration

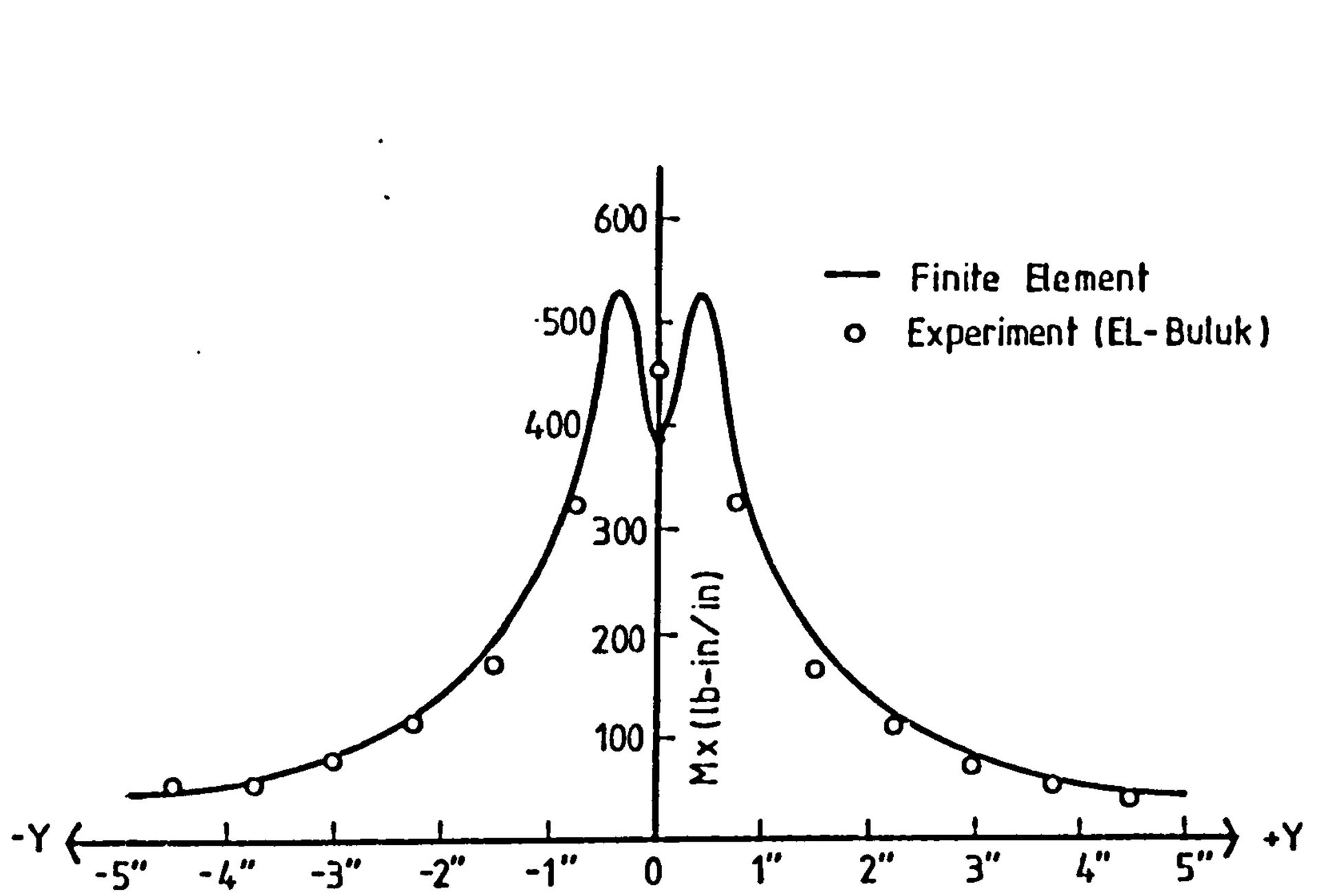

(a) Distribution Of Moment Mx At Section X=-1·6" Due To Unit Wall Rotation

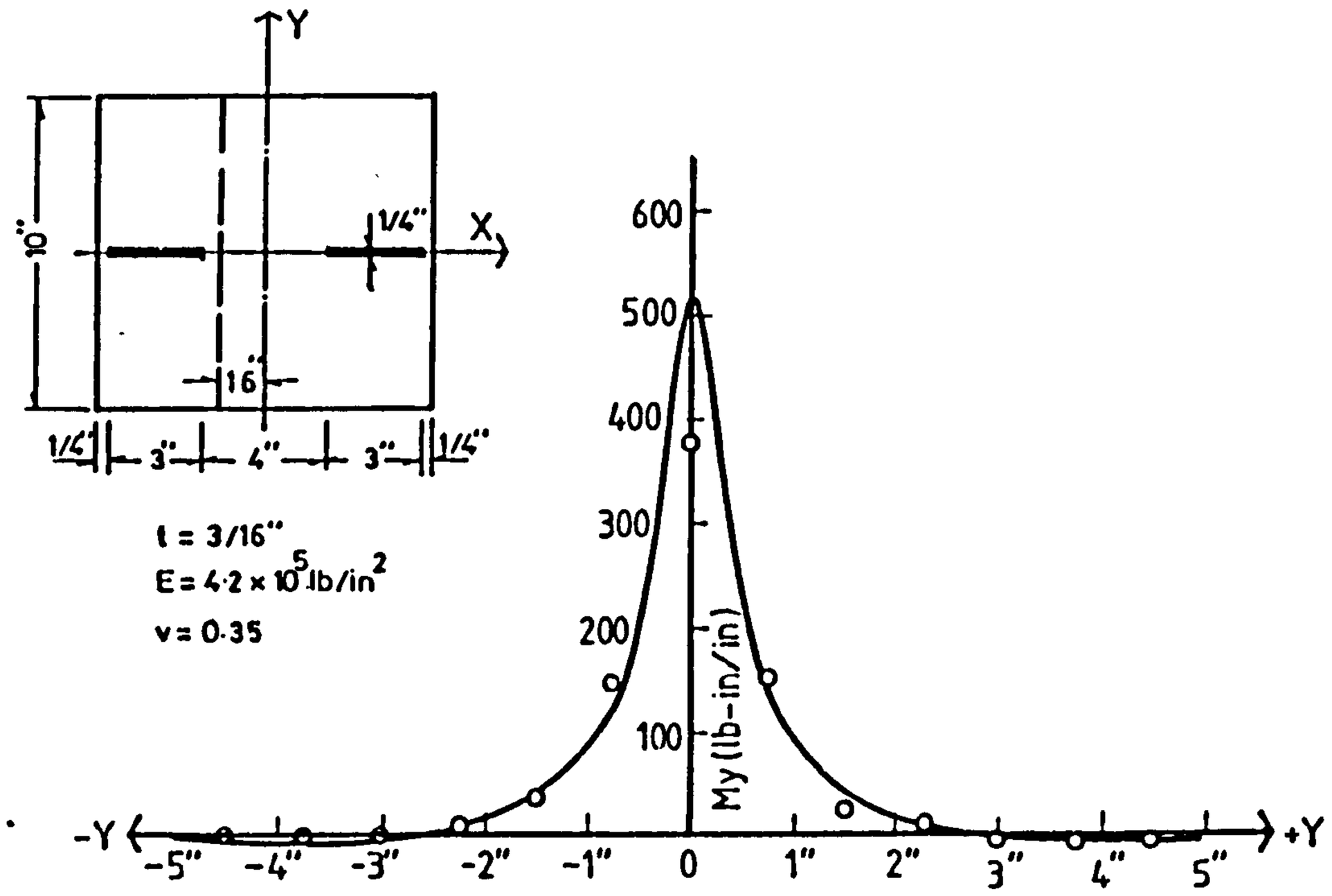

(b) Distribution Of Moment My At Section X=-16" Due To Unit Wall Rotation

Fig. 3.65 Comparison Between Slab Moments Determined by Finite Element Solution and by Experiment, for Plane Wall Configuration

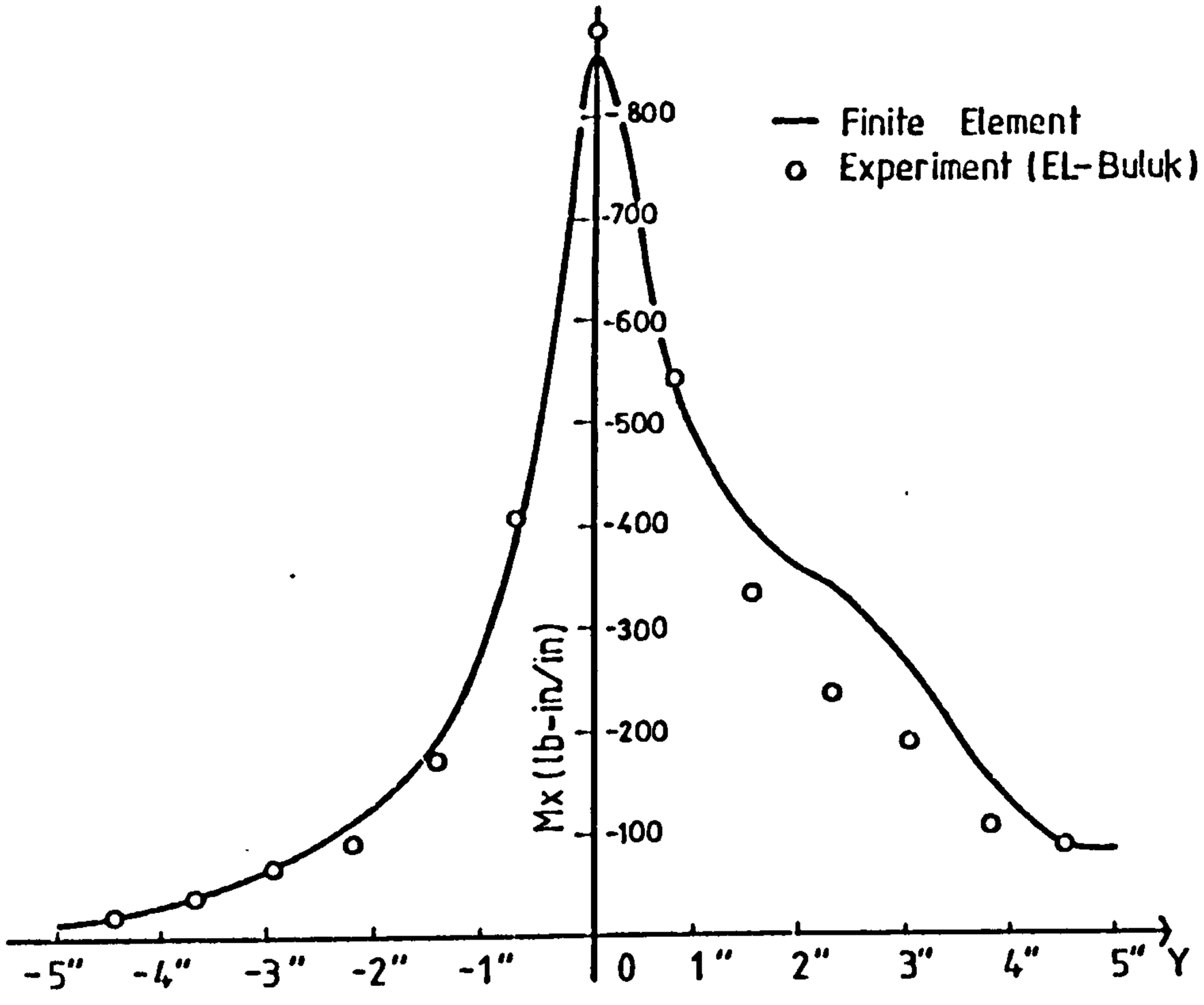

(a) Distribution Of Moment Mx At Section X=1·6" Due To Unit Wall Rotation

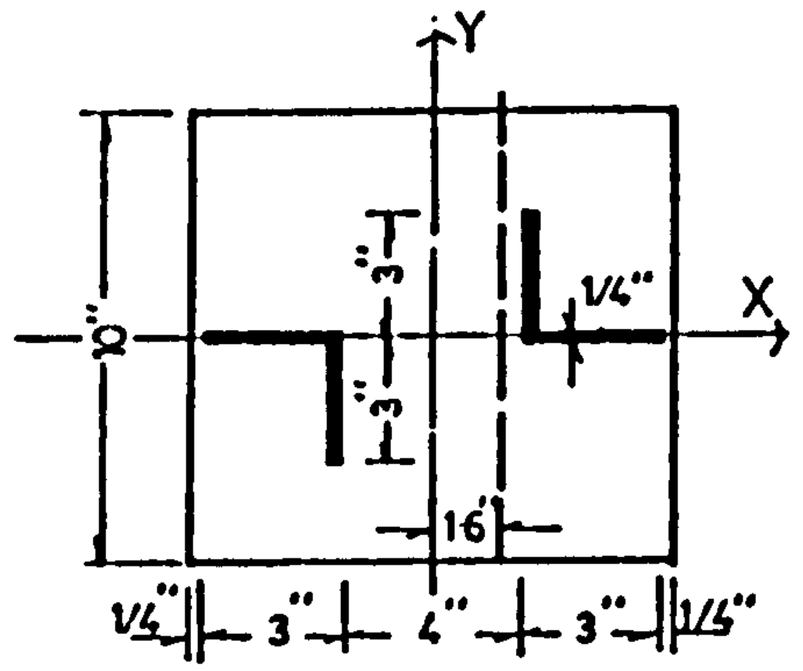

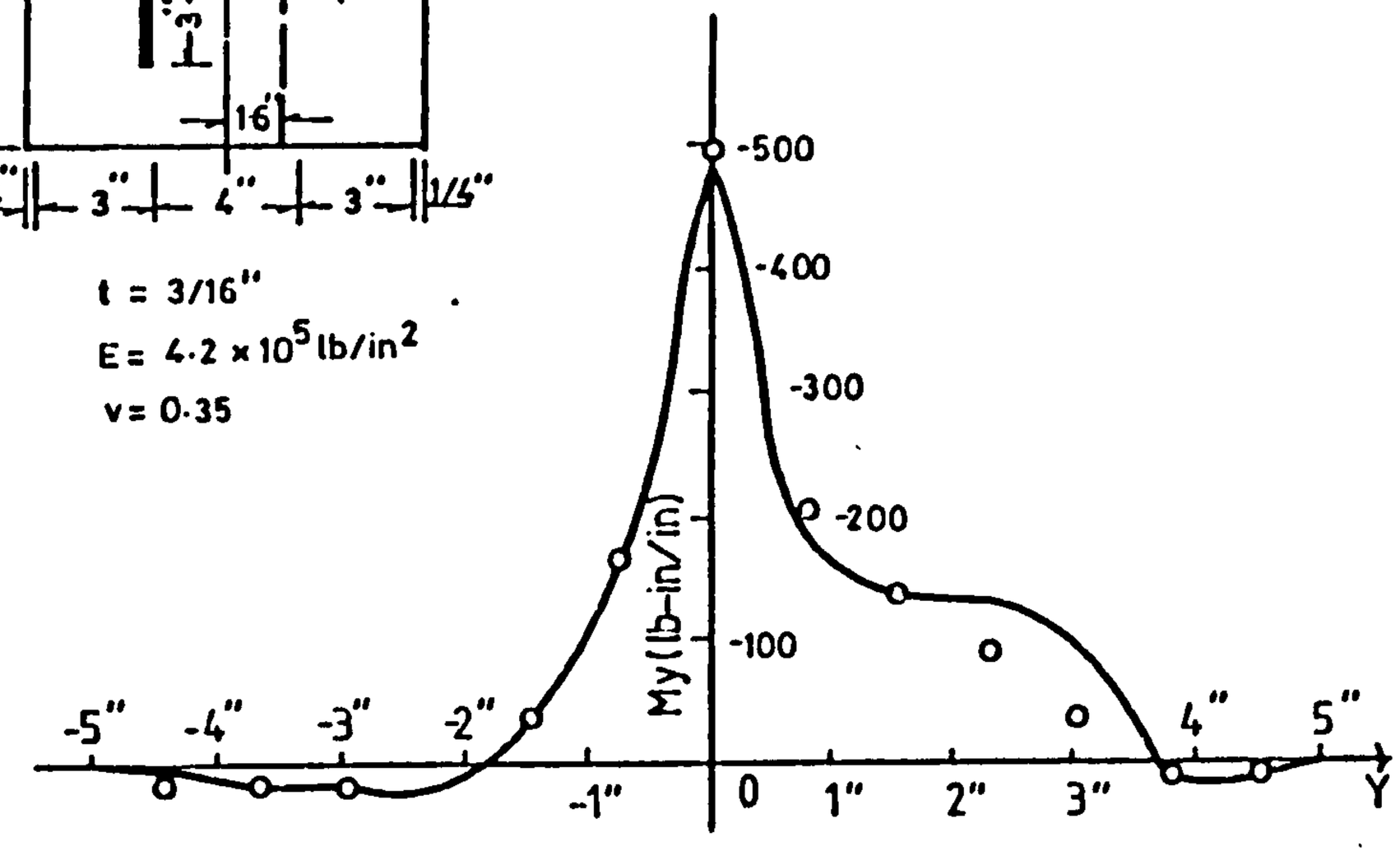

(b) Distribution Of Moment My At Section X=1·6" Due To Unit Wall Rotation

Fig. 3.66 Comparison Between Slab Moments Determined by Finite Element Solution and by Experiment, for L-Shaped Wall Configuration

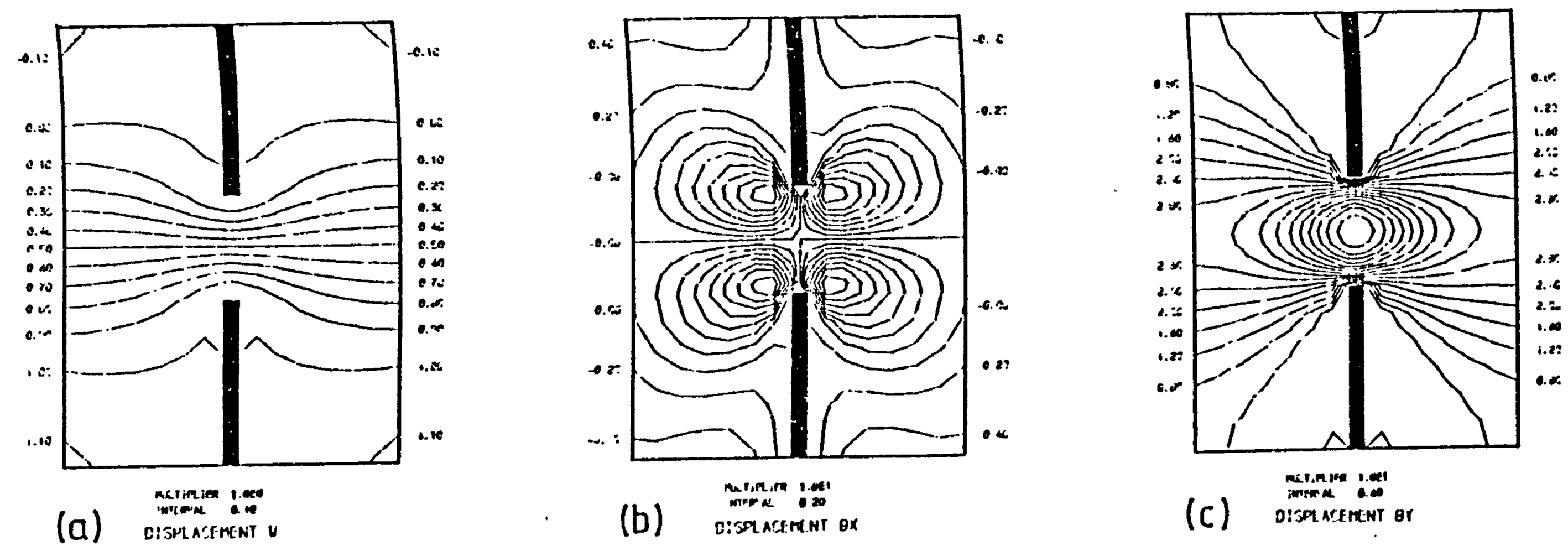

Fig. 3.67 Contours of Deflection and Slopes in Slab for Plane Wall Configuration

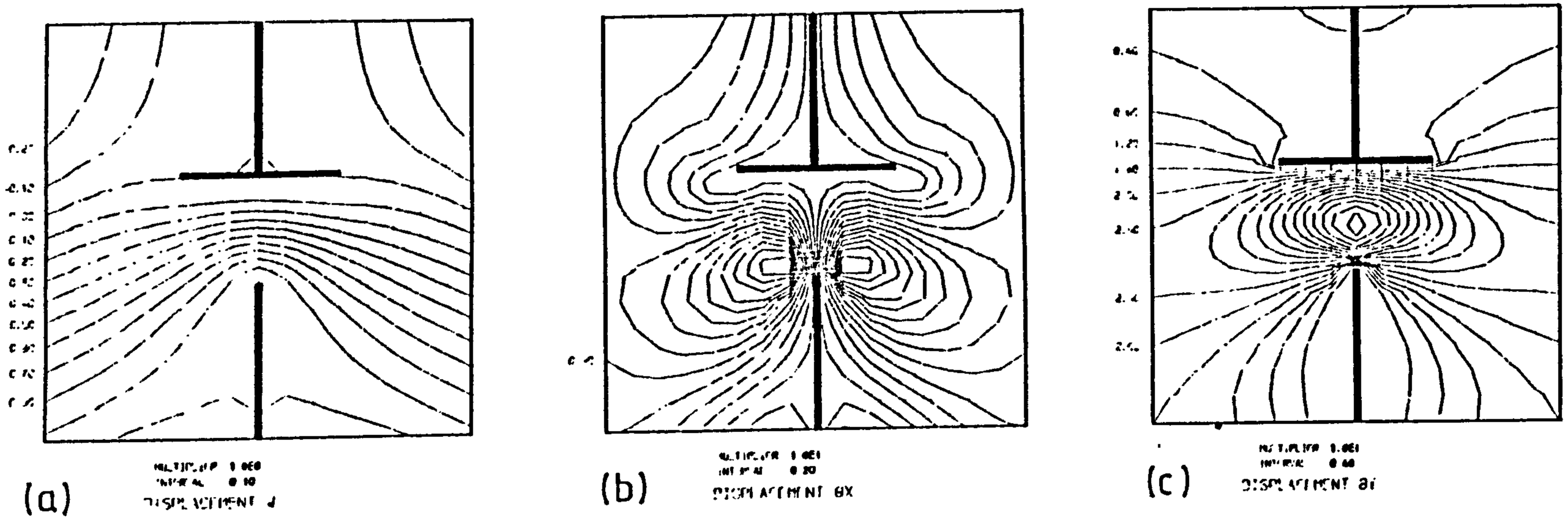

Fig. 3.68 Contours of Deflection and Slopes in Slab for Planar/ Flanged Wall Configuration

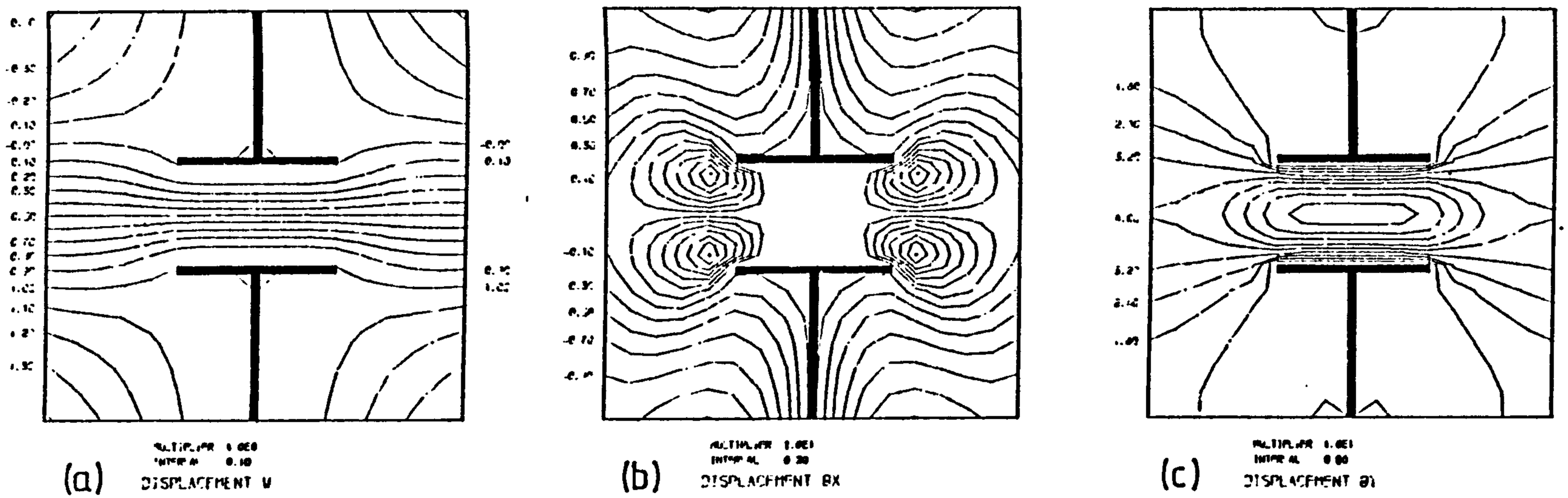

Fig. 3.69 Contours of Deflection and Slopes in Slab for Flanged Wall Configuration

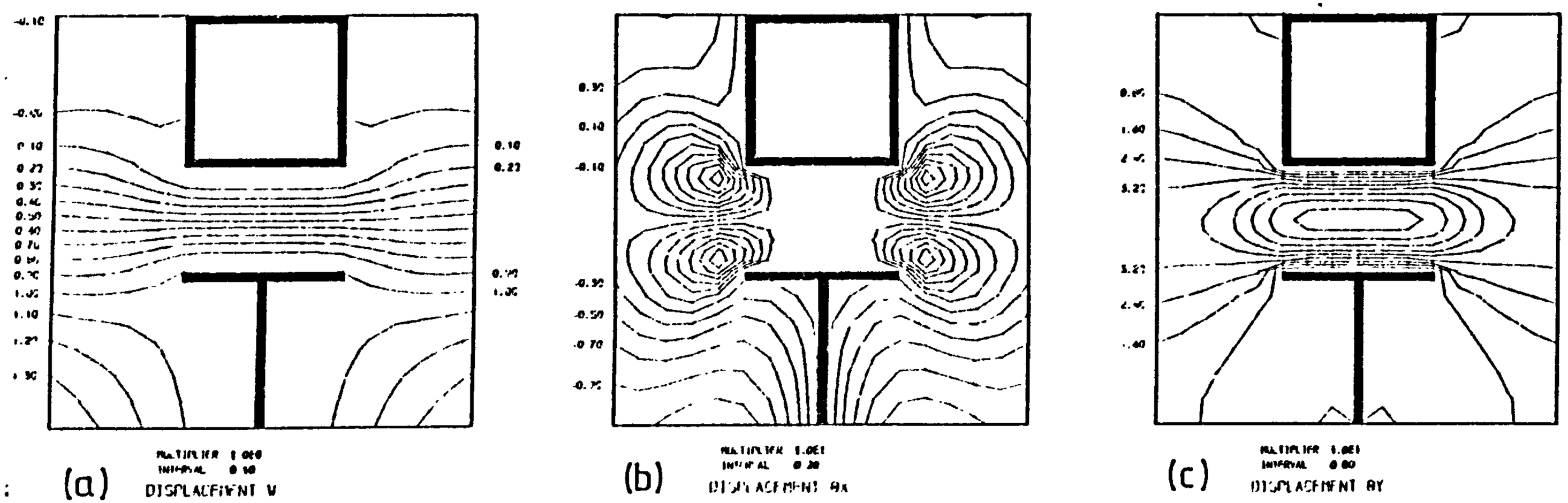

Fig. 3.70 Contours of Deflection and Slopes in Slab for Flanged Wall/Box Core Configuration

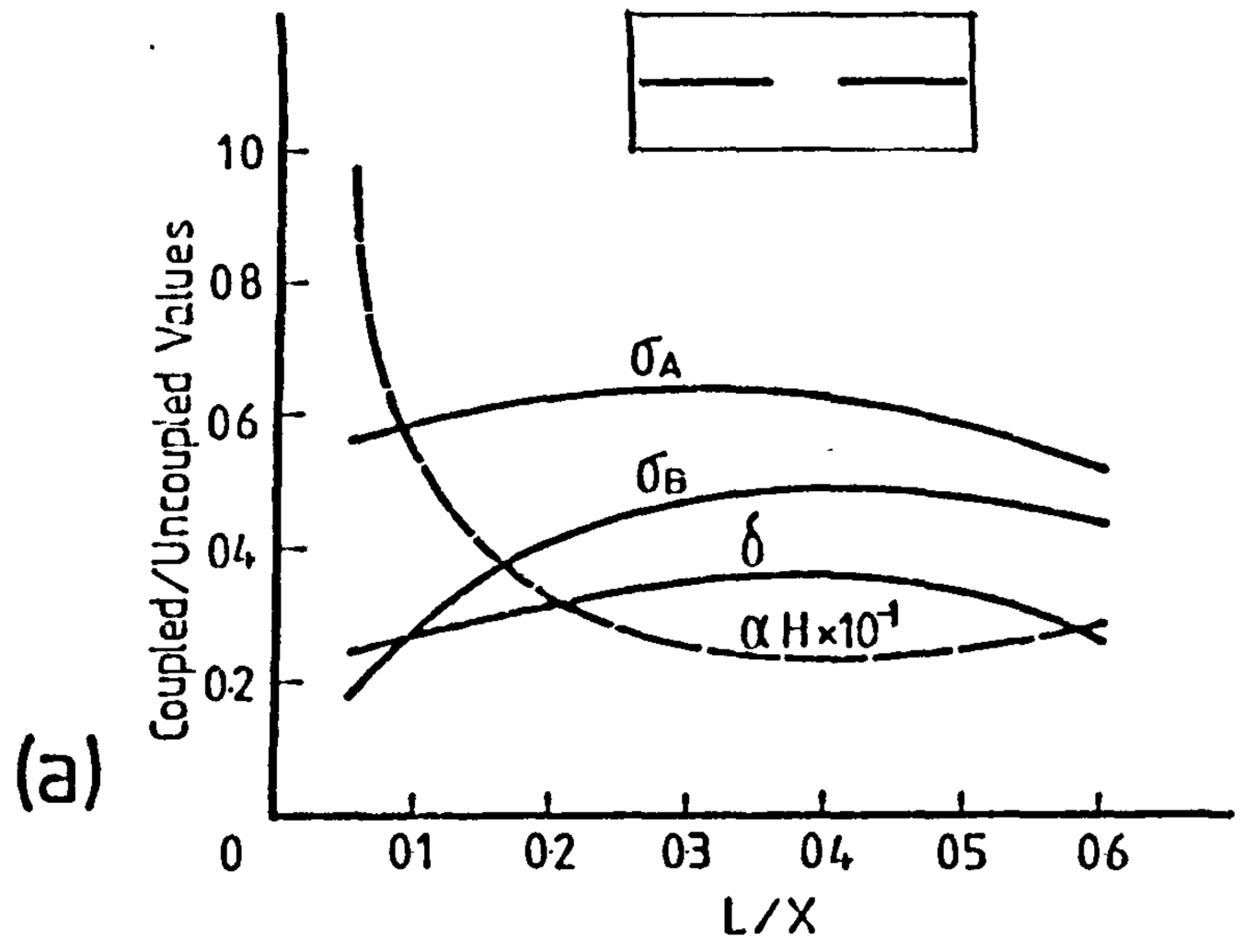

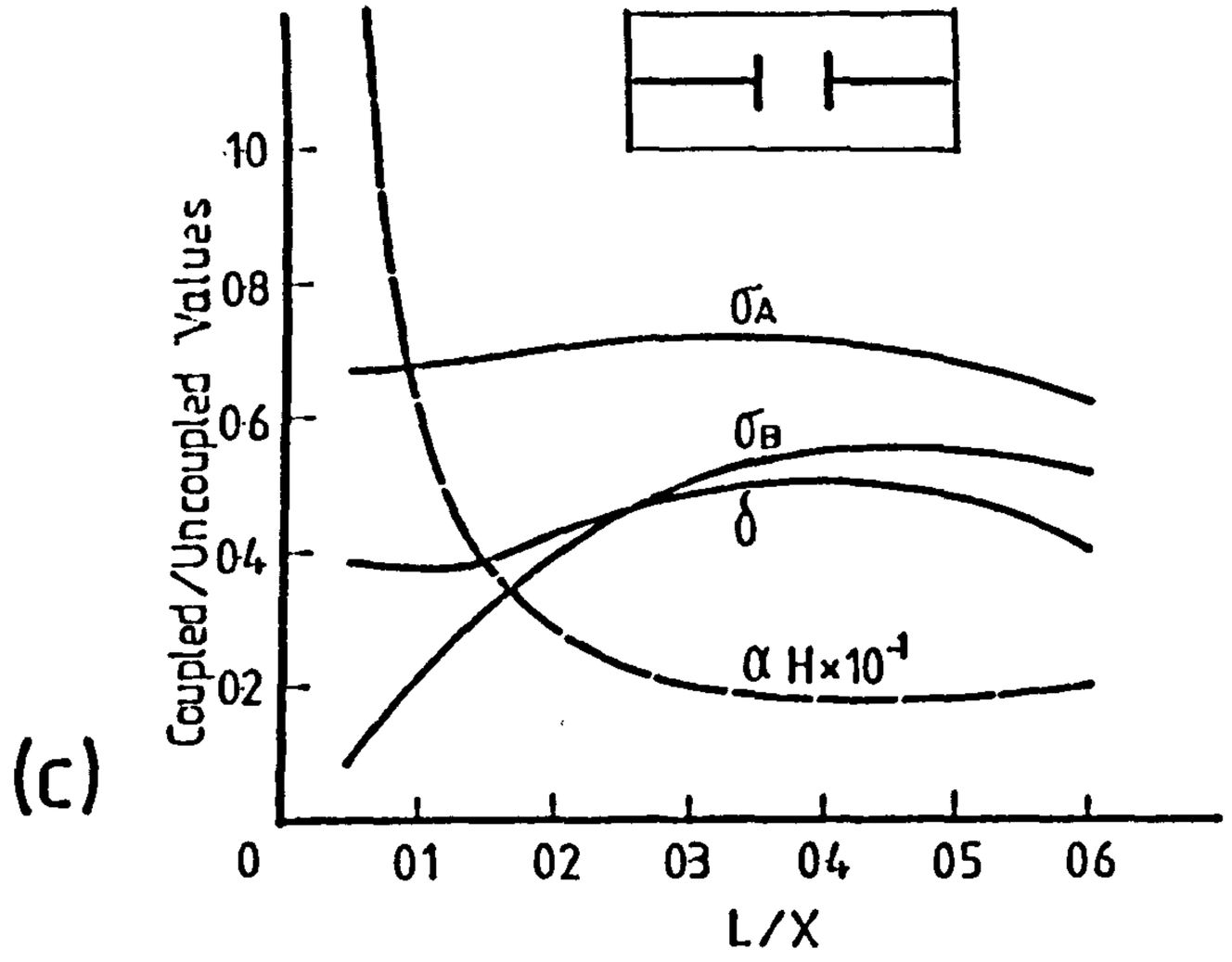

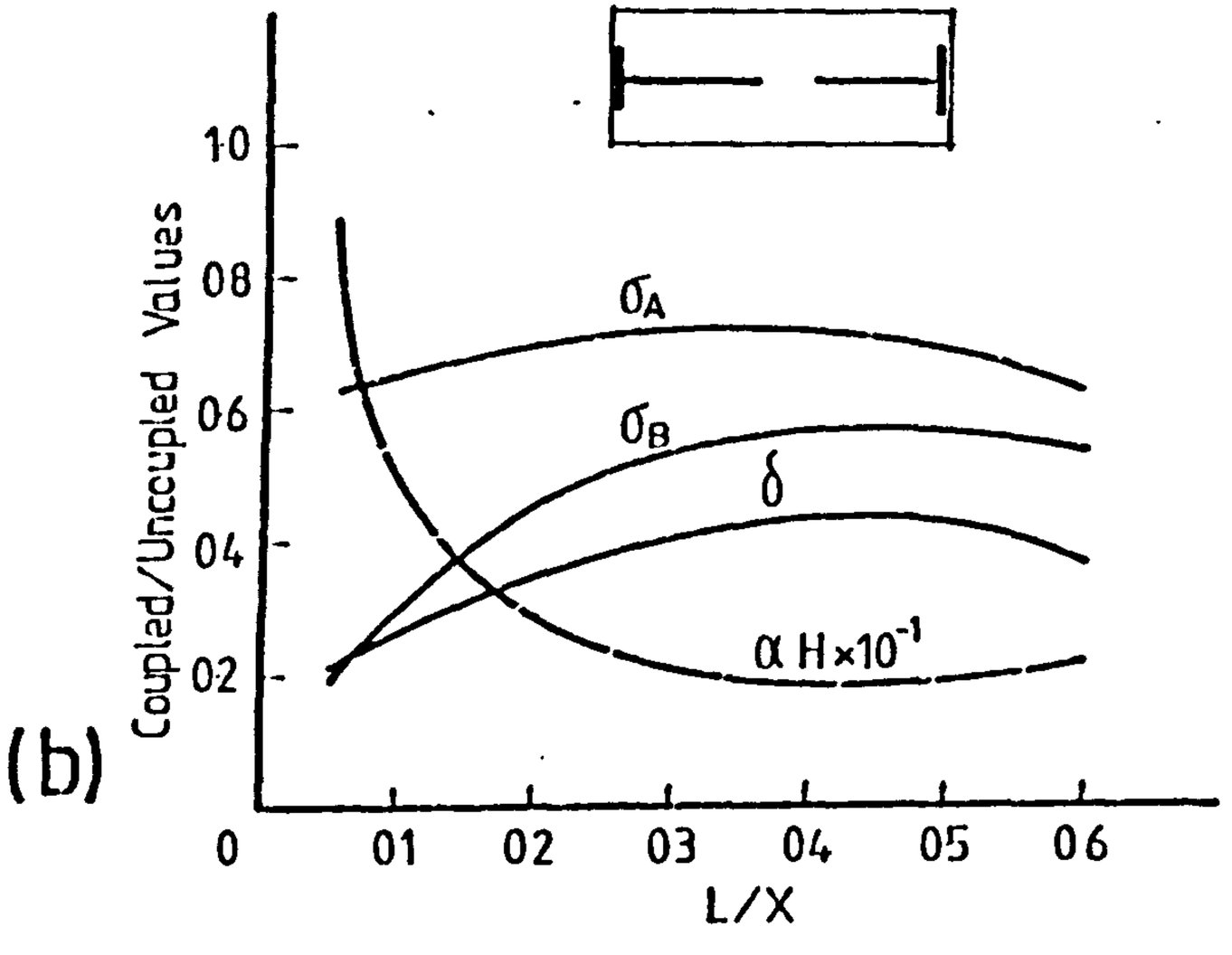

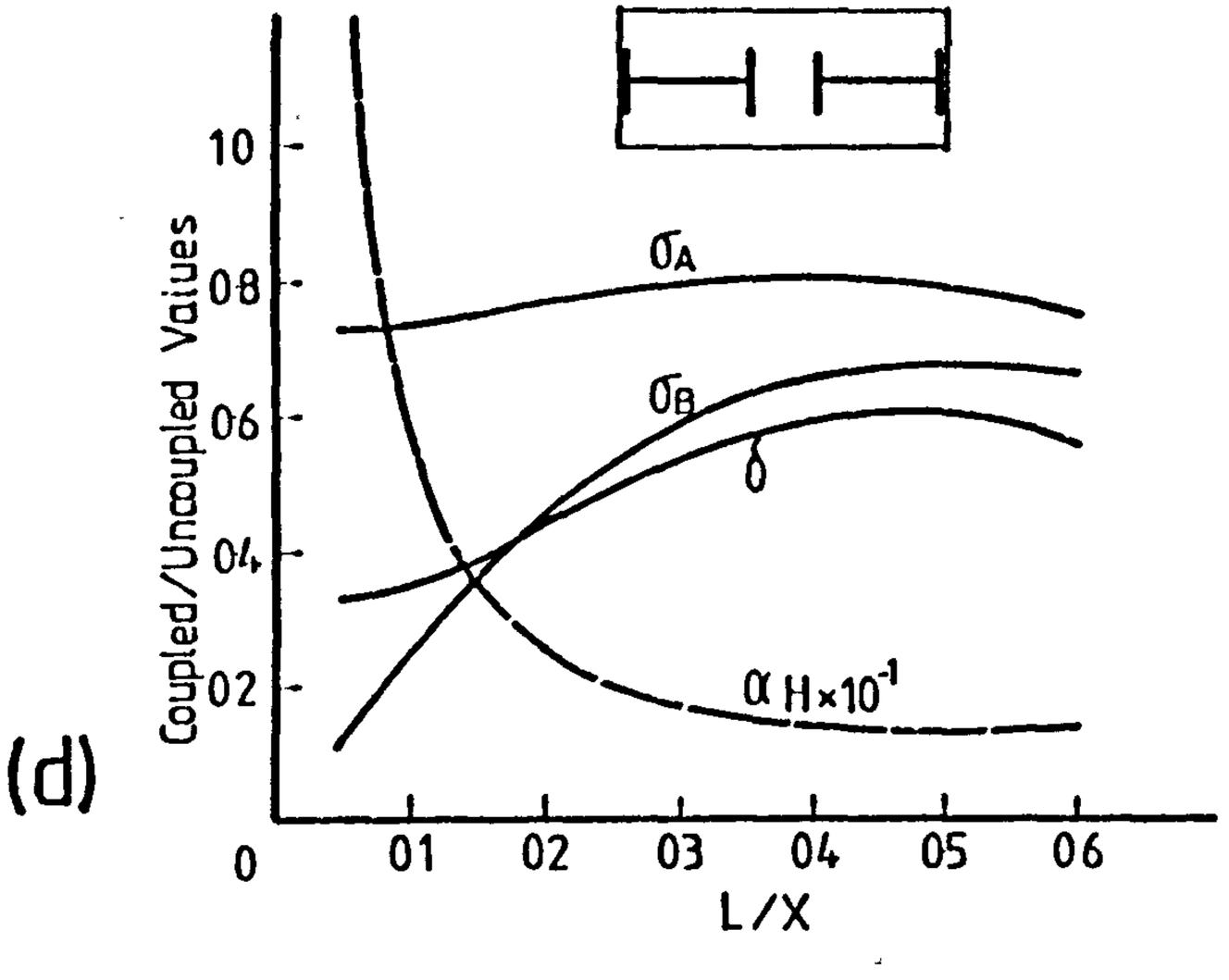

Fig. 3.71 Effect of Slab Coupling on Maximum Wall Deflection and Fibre Stresses for Various Wall Configurations

CHAPTER 4

INVESTIGATION OF FLEXURAL INTERACTION BETWEEN FLOOR SLABS AND SHEAR WALLS BY THE INFLUENCE COEFFICIENT METHOD

4.1 INTRODUCTION

The influence coefficient technique for the analysis of the interaction between floor slabs and shear walls in cross-wall structures was developed in Chapter 2. The practical application of the technique requires an investigation of such aspects as the number of nodes required, the influence of moments as well as direct loads in the representation of the distributed interactions, and the number of terms required for satisfactory convergence of the infinite series. This has been carried out as part of an investigation of the accuracy of the technique, which has been achieved by comparing the results obtained with those available in the published literature. Using the technique, a comprehensive parameter study on wall-slab interaction has been carried out as a confirmation of an earlier investigation based on the finite element method, and as further proof of the accuracy and versatility of the technique. The numerical results obtained are discussed in this Chapter.

4.2 CONVERGENCE STUDY

The influence functions have been expressed in the form of an infinite harmonic series which may be truncated after a relatively small number of terms since the series converge rapidly. In order to examine the influence of series truncation on the convergence of the solution, numerical studies were performed on two representative examples of a flexible and a stiff continuous slab (that is, one with widely spaced and closely spaced walls respectively) coupling a pair of plane walls.

The influence on the convergence of the form of

discretisation of the continuous wall-slab moment transfer with various discrete force components and number of nodal points was also examined, for both plane wall and flanged wall configuration.

In the analysis, only a quadrant of the floor panel was considered on account of symmetry. The idealised simply supported edge replacing the actual free edge was located along the section through the axis of rotation of the plane wall, whilst the set of nodes for a wall section were always evenly spaced, with a node at the critical node tip (cf. Fig. 4.15(a)). The other two edges were continuous.

Fig. 4.1(a) and 4.1(b) illustrate the convergence characteristics of the solution by showing the variation of the effective coupling width with the number of terms used in the influence series, for the flexible slab, whilst Fig. 4.1(c) and 4.1(d) show the corresponding results for the stiff slab. The results in Fig. 4.1(b) and 4.1(d) were obtained using only interacting vertical point loads to simulate the wall/slab interactions, whilst those in Fig. 4.1(a) and 4.1(c) were obtained with concentrated moments included with the discrete point loads.

The results of an accurate finite element analysis have been included to provide a relative measure of the accuracy of the influence coefficient solution. Two different elements, the Adini-Clough-Melosh rectangular element (RB12) and the Veubeke quadrilateral element (QB16), were used, but the results differed by less than 1%.

The results indicate that when only interacting point loads are used in the solution, convergence to a stable solution is very rapid if a small number of nodes is employed. The converged result for the flexible slab using only two nodes (i.e. two unknowns in the solution) is only 5% below the accurate finite element result. However, for the stiff slab associated with a much larger wall and narrower corridor opening, the converged result using two nodes is 22% below the accurate value. Even

when 16 nodes are used, the result has not improved to better than 5% below the finite element result.

There is a remarkable improvement in convergence to a more accurate solution, though at a less rapid rate, when concentrated moments are included with the interacting point loads. Considering the more critical case of a stiff slab, the nearly stable results using 40 harmonics and with only one node (i.e. two unknowns) is just 5% below the finite element value; with two nodes (four unknowns) the result has improved to 2½% below the finite element value. Thereafter, an increase in the number of nodes does not produce any significant difference in the result (Fig. 4.2). For the more flexible slab, which shows less rapid convergence with regard to series truncation, the use of two nodes with point loads and moments gives results obtained when using 40 and 100 harmonics which do not differ by more than 1%.

On the other hand, if more nodes are used than are strictly necessary, numerical instability in the solution could be encountered unless a large number of terms in the infinite series is taken to give a more accurate evaluation of the influence coefficients.

For practical purposes, it appears that the use of one node, and including both interacting forces and moments, and taking 20 harmonics, should prove sufficiently accurate for analysing most slabs coupling plane walls.

Fig. 4.3 shows the influence of the number of nodes used for the web and flange sections of the coupled wall on the convergence of the solution. In defining web and flange nodes for a tee-shaped wall section, the node at the flange/web junction is considered a web node, whilst the number of web and flange nodes is that included in the quadrant of the floor panel analysed (cf. Fig. 4.15(c)). In this study, 40 terms of the infinite series were used to calculate the influence coefficients, and at each node three force components, consisting of a point load and two point moments M_x and M_y, were considered for the equivalent

discrete interactive forces. The results from a finite element analysis were again used as a relative measure of the accuracy attained by the series solution.

The results indicate that the number of flange nodes used has a much greater influence on the accuracy of the results than do web nodes. For the particular flange-panel width considered, the use of at least 4 flange nodes was necessary to obtain a result within 5% of the finite element value. With 8 flange nodes, the series solution gave a result 1% higher than the finite element value. Provided that a sufficient number of flange nodes are included, it appears that the use of just one web node, at the web/flange junction will give satisfactory accuracy.

The effect of neglecting the less significant moment component M_y in the discretised nodal forces, thereby relaxing the enforcement of slope compatibility in the direction normal to the main direction of bending, was also examined. The results obtained, using various numbers of flange nodes, indicated that in the worst case omission of the moment component M_y resulted in the reduction in the calculated effective width of only $\frac{1}{2}$%. For practical purposes, therefore, only the point loads and point moments M_x need be considered for the discretised nodal forces in order to reduce the number of unknowns in the solution.

4.3 COMPARISON BETWEEN RESULTS OBTAINED BY SERIES SOLUTION AND BY OTHER INVESTIGATIONS

(a) Plane walls.

The results for the effective coupling width obtained using the present method have been compared in Fig. 4.4 with those from a number of other theoretical investigations, using the finite element and finite difference techniques, for slabs coupling plane walls. The results of Black, Pulmano and Kabaila[6] were obtained using a conforming quadrilateral element and the solution of some 200 finite element equations for each analysis.

Petersson's results[5] were obtained using a "mixed" finite element with corner deflections and side moments as unknown variables, approximately 500 equations being solved for each analysis. The author's finite element results were obtained using the rectangular element RB12 and a solution of roughly 320 equations. Qadeer and Stafford Smith's results[2] were obtained using the finite difference technique and a mesh division involving the solution of approximately 320 equations. In contrast, the results obtained using the present method were based on 4 discrete nodes with 8 unknown forces, using 40 harmonics for the evaluation of the influence coefficients.

It can be seen that the results from the present method agree well with the finite element solutions, lying between the two extremes. The finite difference results appear to underestimate the effective width, and this may be due to the fact that complete compatibility of slope in the critical direction of bending has not been enforced at the wall-slab intersection. This is similar to the effect of using only interacting point loads without point moments in the present method.

(b) Flanged walls.

Calculated values of the effective widths of slabs coupling flanged walls are compared in Fig. 4.5 with the corresponding results obtained by Tso and Mahmoud,[9] and by the author from the finite element method. The results of Tso and Mahmoud for the particular slab of aspect ratio Y/X = 0.4 were interpolated from their design curves for aspect ratios of 0.3, 0.5 and 0.7 using Lagrangian interpolation. It appears that Tso and Mahmoud's finite element results were obtained from a solution of 100 to 200 equations, and the author's results from 300 to 400 equations, depending on the parameters involved. In contrast, the results obtained by the present method required the solution of between 8 and 24 equations.

The curves indicate that the results obtained from the present method agree closely with both finite element solutions for the three cases of coupled walls without flanges, with one flange, and with two flanges.

(c) Walls of finite thickness, and box cores

The previous results were obtained from analyses which assumed that the walls could be treated as line elements of zero thickness. This is generally satisfactory for practical purposes, but it is of interest to examine the influence of the finite thickness of the wall. If the walls are very thick, the analysis will yield results equivalent to that for coupled box cores. Fig. 4.6 shows the comparison between the present results and those obtained by Black, Pulmano and Kabaila[6] using various finite element divisions requiring the solution of between 50 and 200 equations. The present results were obtained using 2 web nodes and 4 flange nodes, the "flange" being assumed to act along the inner edge of the wall. Inter-acting point loads and moments in the two orthogonal directions were considered at each node in order to enforce deflection and slope compatibility in both the main bending and transverse directions.

It is seen that the present results agree very well with those from the finite element method, but are generally lower. In the worst case, the discrepancy is less than 8%. However, it was observed by Black, Pulmano and Kabaila that their results could generally be expected to contain errors of up to 4%, and the maximum error may be much less. As a check, the author performed an analysis using the same element used by Black et al., with a very fine mesh (120 elements and 695 degrees of freedom) and obtained a value of effective width less than ½% higher than the influence coefficient solution, and 4½% lower than Black's result for the particular case of a slab defined by Y/X = 0.5, L/X = 0.2 and h/W = 0.5.

(d) Slab moments.

Fig. 4.7 shows a comparison of the critical bending moments in the slab along a transverse section through the inner (corridor) edge of the wall with the values obtained by Chang[4] using a finite difference solution. Good agreement is reached between the more important bending moments $\bar{M}_x$ in the main direction of bending, except at the critical tip of the wall where a theoretical stress singularity exists for a wall of zero thickness. For the less important transverse moment $\bar{M}_y$, although the absolute agreement between the two solutions is not nearly as good, the general shapes of the stress distribution are similar.

Fig. 4.8 shows a comparison of the bending moment distribution along the longitudinal centre line of a slab coupling a pair of plane walls of finite thickness with the results obtained by Black, Pulmano and Kabaila[6] using the finite element method. The series solution was obtained using three nodes and 40 harmonics. The results obtained by the two different methods are practically identical along almost the whole section, except at the wall face where the moment distribution is discontinuous. Since the series solution approximates the discontinuous moment distribution by a continuous curve the bending moment value calculated at the wall face should be interpreted as the average of the values on either side of the wall face. Therefore, if this average value is doubled to obtain the bending moment immediately outside the wall, then the series solution and finite element solution will be in excellent agreement.

(e) Comparison with experimental results.

Tests have been carried out on perspex slabs with steel inserts to simulate the wall cross-sectional shapes by Petersson,[5] El-Hag[40] and El-Buluk.[8] Fig. 4.9 shows the comparison of effective width values determined by the series solution and by Petersson's experiments. The series solutions were obtained using four nodes and 40 harmonics,

the finite width of the steel inserts being disregarded. The agreement between the theoretical and experimental results is generally good. With a small wall opening ratio L/X of 0.125, the transverse shear deformation in the slab and the flexibility of the wall-slab connection are expected to have an appreciable influence on the experimental results, and consequently the experimental results are slightly lower than the theoretical results. With a larger wall opening ratio of 0.25 these flexibility effects are less significant, and the stiffening effect of the finite wall thickness begins to show up. In this case the experimental results are slightly higher than the theoretical results.

Fig. 4.10 shows the comparison of theoretical longitudinal and transverse bending moments at a specific section with the experimental results obtained by El-Buluk.[8] The series solution was again obtained using four nodes and 40 harmonics, and the finite width of the wall inserts was disregarded. Very close agreement is obtained between the theoretical and experimental values of the transverse moments M_y throughout the section. The correspondence between theoretical and experimental values of longitudinal moments M_x appears less good at points close to the wall. The double peaks in the bending moment curve have also been shown by the finite element results (Fig. 3.65), but unfortunately the location of the strain gauges in El-Buluk's experiments does not permit a direct comparison of moments at critical points, Nevertheless the trend of results indicates reasonably good agreement between theory and experiment in respect of the integrated moment in the critical region near the wall.

4.4 PARAMETER STUDY ON WALL-SLAB INTERACTION

The simple data preparation and modest computer requirements for carrying out a series solution have allowed a fairly comprehensive parameter study on wall-slab interaction to be completed relatively easily. The

numerical results from the study are given in Appendices A4.1-A4.5. The main results are summarised in Fig. 4.11 to 4.14.

Fig. 4.11(a) shows the variation of effective width Y_e/Y with wall opening ratio L/X for various slab aspect ratios Y/X. The results are based on coupled plane walls of zero thickness. The corresponding results for walls with a relative wall thickness h/X of 1/50 are shown in Fig. 4.11(b). Both sets of results were evaluated using four nodes and 40 harmonics in the series solution (Fig. 4.15, (a) and (b)).

The above curves are applicable to cases where the coupled walls are relatively thin. The effective width values for thick walls or box cores with no corridor access openings are practically identical to those for coupled T-shaped flanged walls presented in Fig. 4.12(a-d). These results were evaluated using two web nodes and between one and six flange nodes depending on the flange width, and taking 40 harmonics for the series solution performed on a symmetric slab quadrant (Fig. 4.15,(c) and (d)).

Fig. 4.13(a-d) show the results for coupled planar-flanged wall configurations. The analysis of coupling action was performed on a symmetric half of the slab panel. The plane wall was represented by four nodes and the flanged wall by two web nodes and between one and six flange nodes depending on the flange width (Fig. 4.15(e)). The influence coefficients were evaluated to 60 harmonics in anticipation of the slower convergence associated with a smaller aspect ratio b/a and with a more acute displacement pattern when both walls are considered.

The curves for effective widths for slabs coupling a pair of L-shaped flanged walls with interior flanges on opposite sides of the wall line are shown in Fig. 4.14(a-c). Due to the absence of symmetry conditions in the principal directions, the analysis of the slab was performed on a full panel. Each wall was represented by four web nodes

and between one and four flange nodes (Fig. 4.15(f)). Again 60 harmonics were taken for the evaluation of influence coefficients.

4.4.1 COMPARISON BETWEEN SERIES SOLUTION AND FINITE ELEMENT SOLUTION

(a) Effective Widths

The curves presented in Fig. 4.11-4.14 are very similar to the design curves evaluated by the finite element method in Chapter 3 (cf. Fig. 3.10, 3.32, 3.43 and 3.50). Effective width values given by the two sets of curves generally differ by less than 10%. The comparison of typical curves for various wall configurations is illustrated in Fig. 4.16. It is seen that generally the effective width values obtained by the series solution are slightly higher than the finite element results.

(b) Stress Resultants

Fig. 4.17 shows a comparison of the bending moments in the slab along a transverse section through the inner edge of the wall evaluated by the series solution and by the finite element solution. The bending moments have been expressed in the non-dimensional form of moment factors defined in Chapter 3 (Section 3.4.2.4). The results are based on walls of zero thickness, and four nodes and 40 harmonics were used in the series solution. It is seen that except at points very close to the tip of the wall where the bending moments are theoretically infinite, the agreement between the two solutions is very close and the two curves are almost indistinguishable throughout most of the range. Although results have been shown only for one section across the slab, the results for other sections and other slab proportions have been found to yield the same degree of accuracy.

Fig. 4.18, (a) to (e), illustrate the comparison between the series solution and the finite element solution

for distributions of bending and twisting moments and shearing forces at various longitudinal sections through a slab coupling a pair of plane walls with finite wall thickness. Four nodes and 40 harmonics were again used for the series solution. The finite element solution used a relatively refined mesh pattern consisting of 270 elements. Close agreement is achieved between the two solutions for all the stress resultants at various sections. The close approximation of the discontinuous distribution of $\bar{M}_x$ at the section y/b = 0 (Fig. 4.18(a)) by a continuous curve evaluated by the series solution is worth noting in particular.

4.5 CONCLUSIONS

The influence coefficient method has been tested for both convergence and accuracy against available data and has been shown to furnish accurate results for both slab stiffness and stress resultants with a considerable saving on computational effort. When evaluating influence coefficients from the infinite harmonic series some 20 to 40 terms are adequate for practical purposes. When modelling the interaction forces between slab and wall greater accuracy is obtained when both point loads and point moments are included. Results of sufficient accuracy can be obtained using a very small number of nodes to represent the wall. A parameter study carried out by the influence coefficient method not only establishes the versatility of the technique but also confirms the results of an earlier investigation by the finite element method.

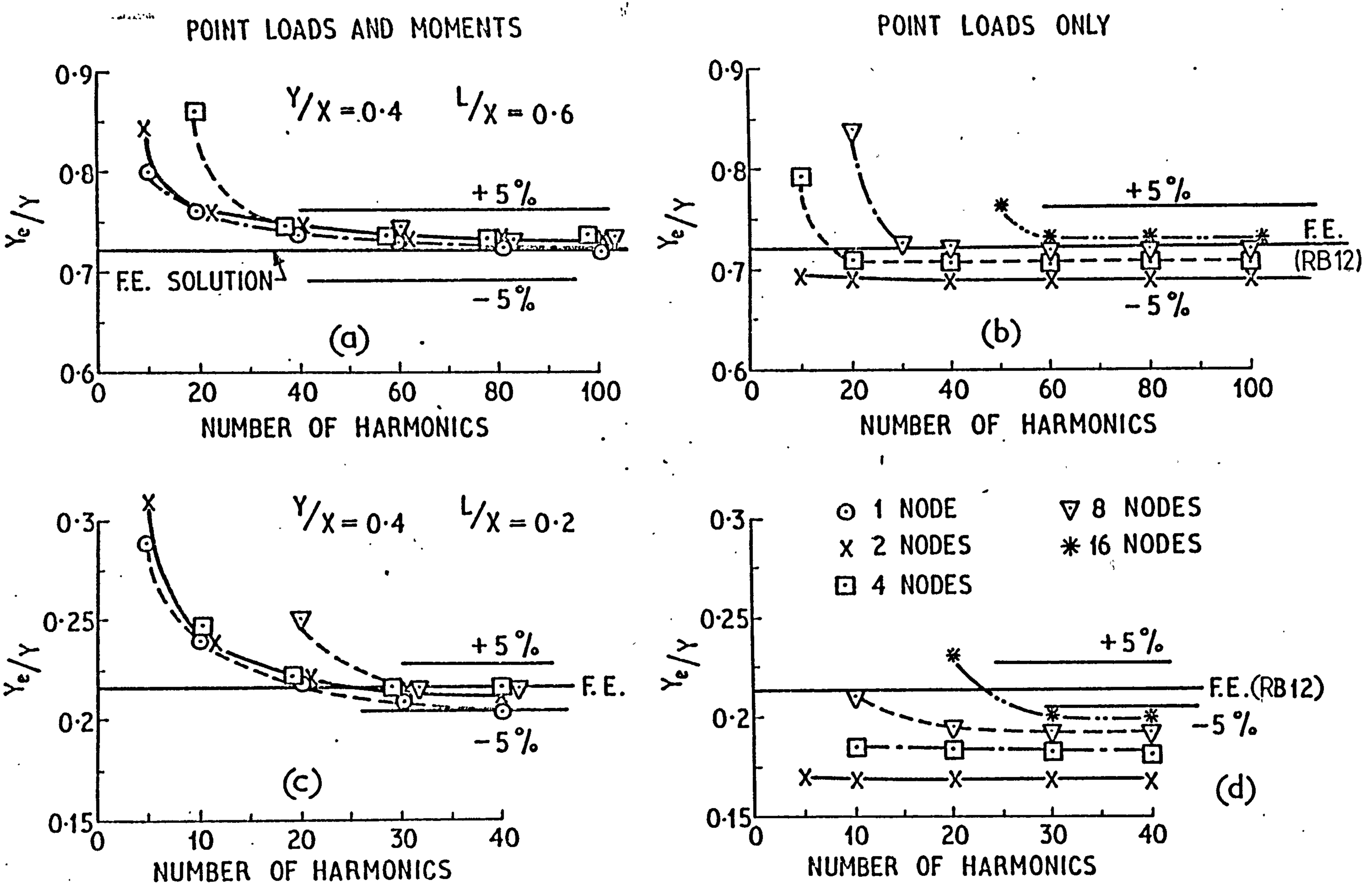

Fig. 4.1 Influence of Number of Nodes and Number of Harmonics on Convergence of Solution for Effective Width, when Interacting Loads and Moments, and Loads Only, Are Considered.

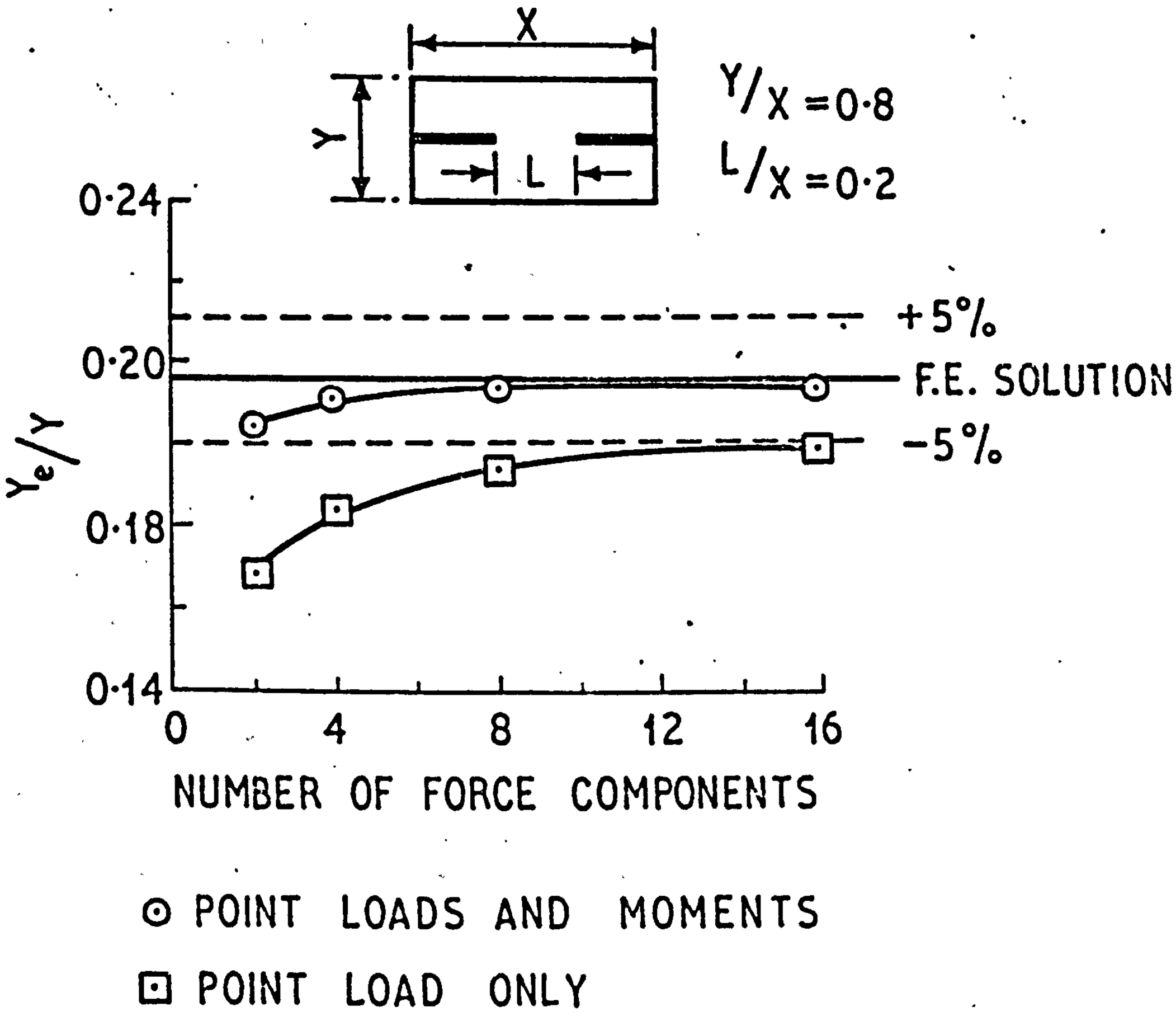

Fig. 4.2 Influence of Number of Interaction Force Components and Number of Nodes on Convergence

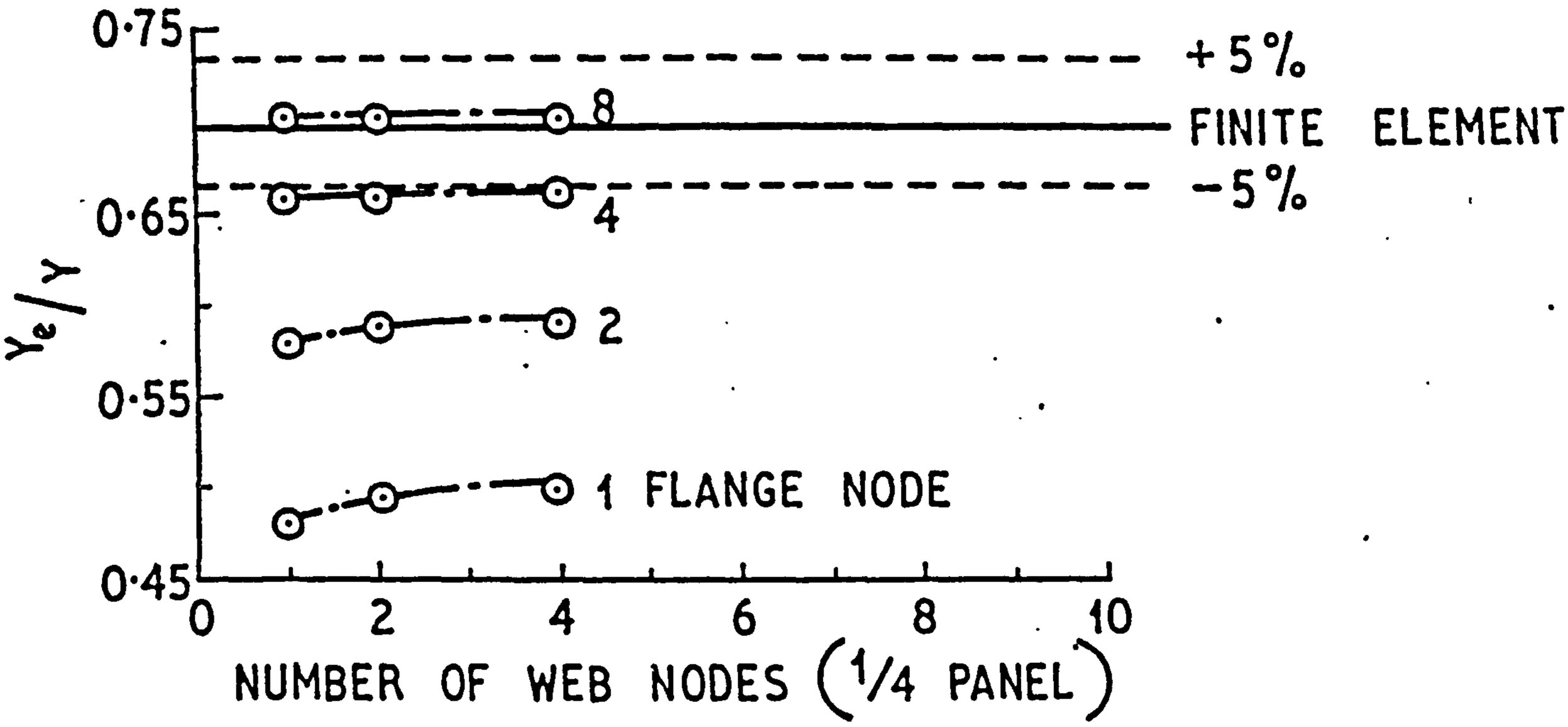

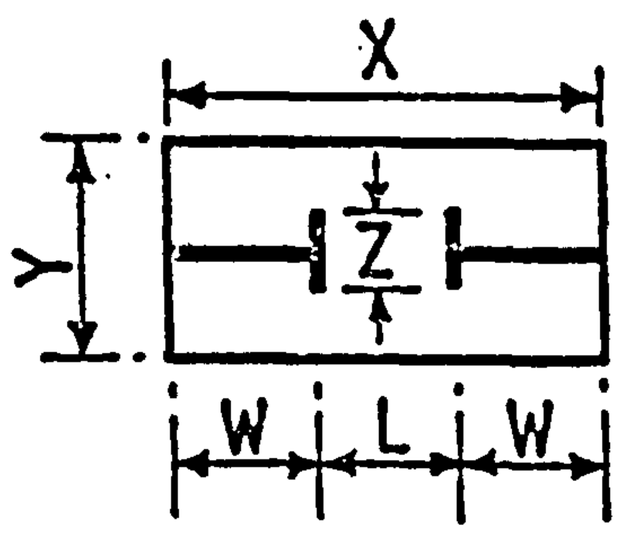

$Y/X = 0.8$

$L/X = 0.2$

$Z/Y = 0.5$

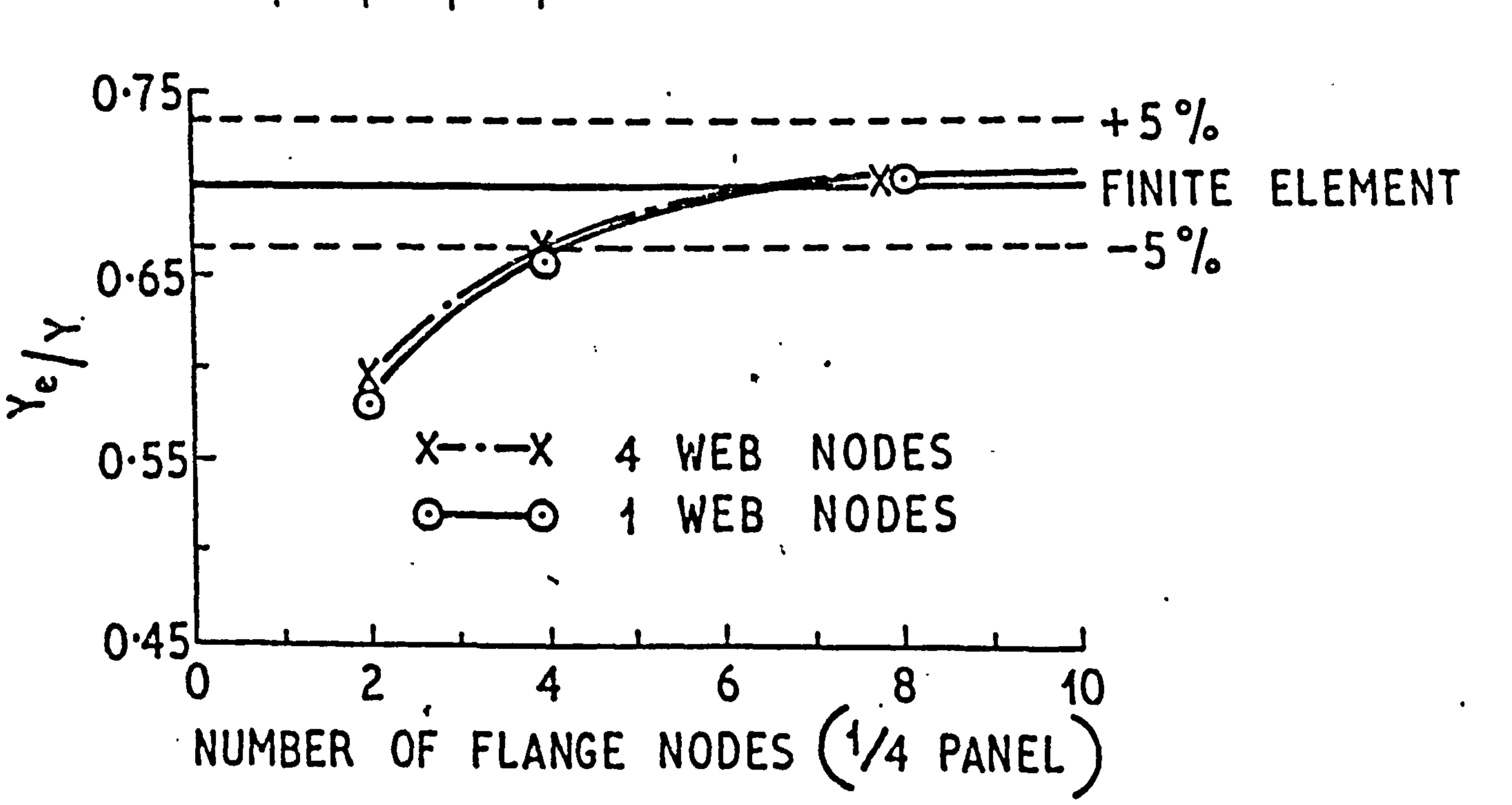

Fig. 4.3 Influence of Number of Flange and Web Nodes on Convergence for Tee-shaped Walls

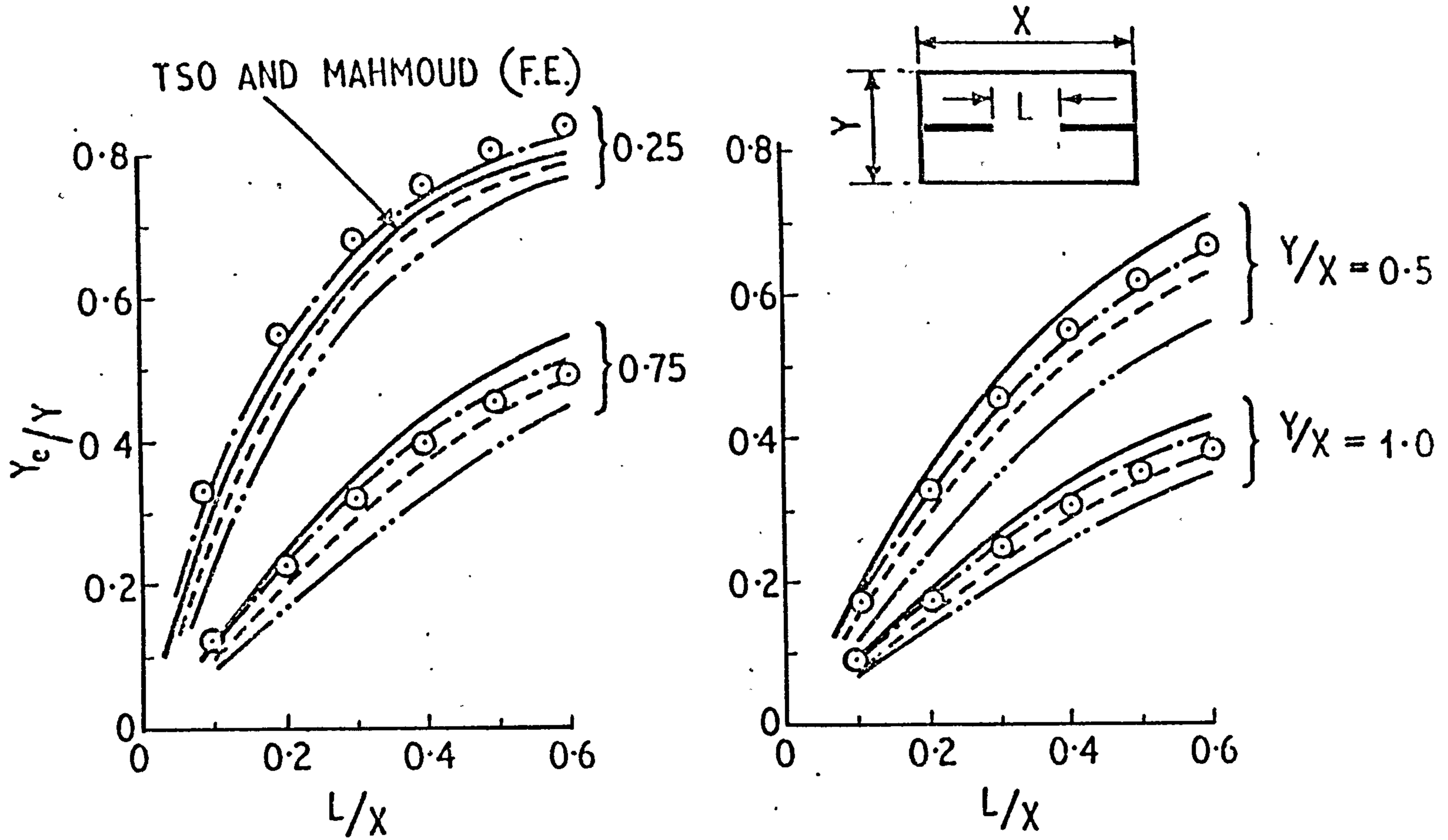

Fig. 4.4 Comparison Between Effective Widths Determined by Series Solution, Finite Difference Solution, and Finite Element Solutions for Plane Walls

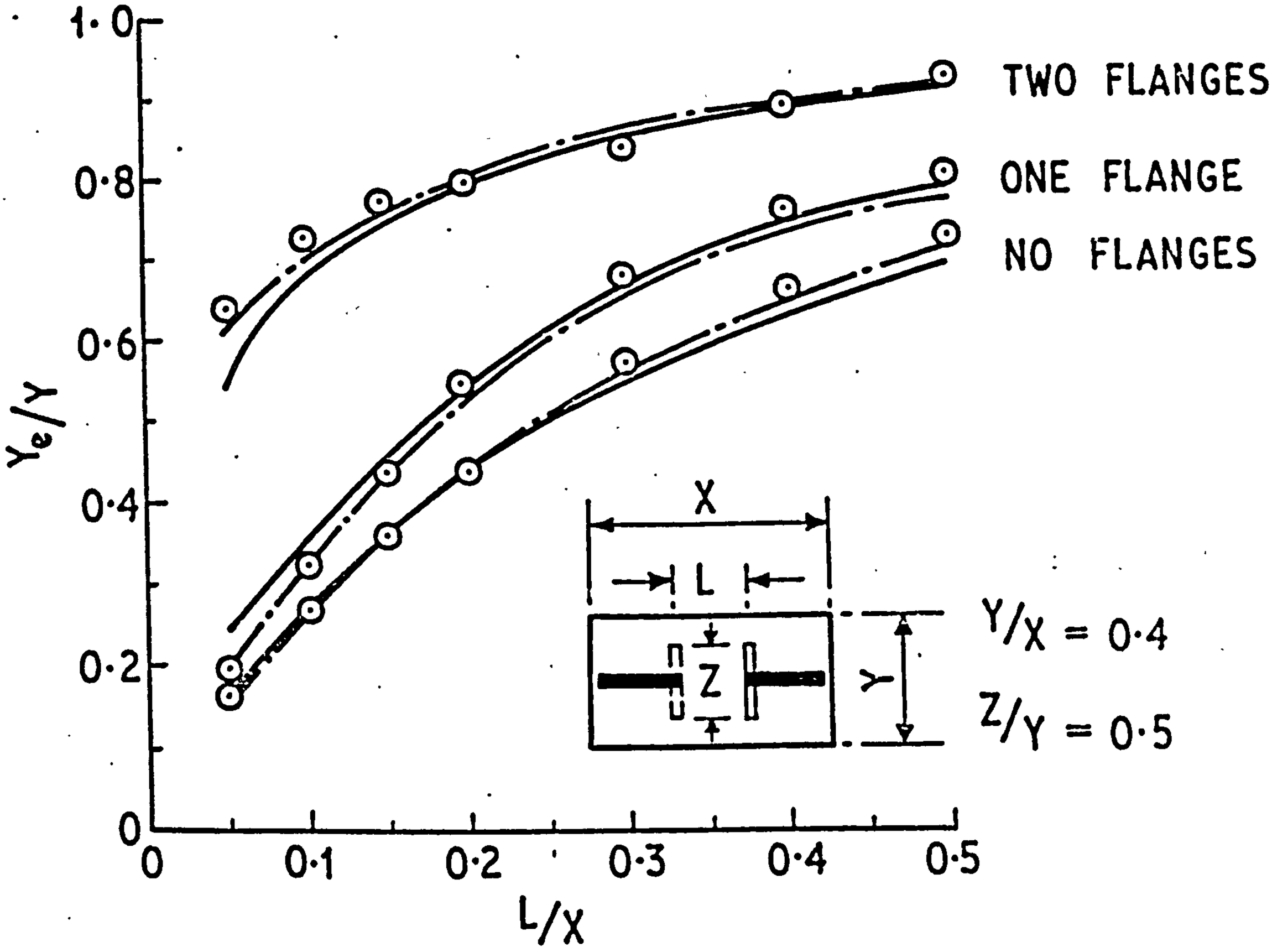

⊙ SERIES SOLUTION

——— TSO AND MAHMOUD (F.E.)

—·— AUTHORS' F.E. (RB12)

Fig. 4.5 Comparison Between Series Solution and Finite Element Solutions for Plane Walls

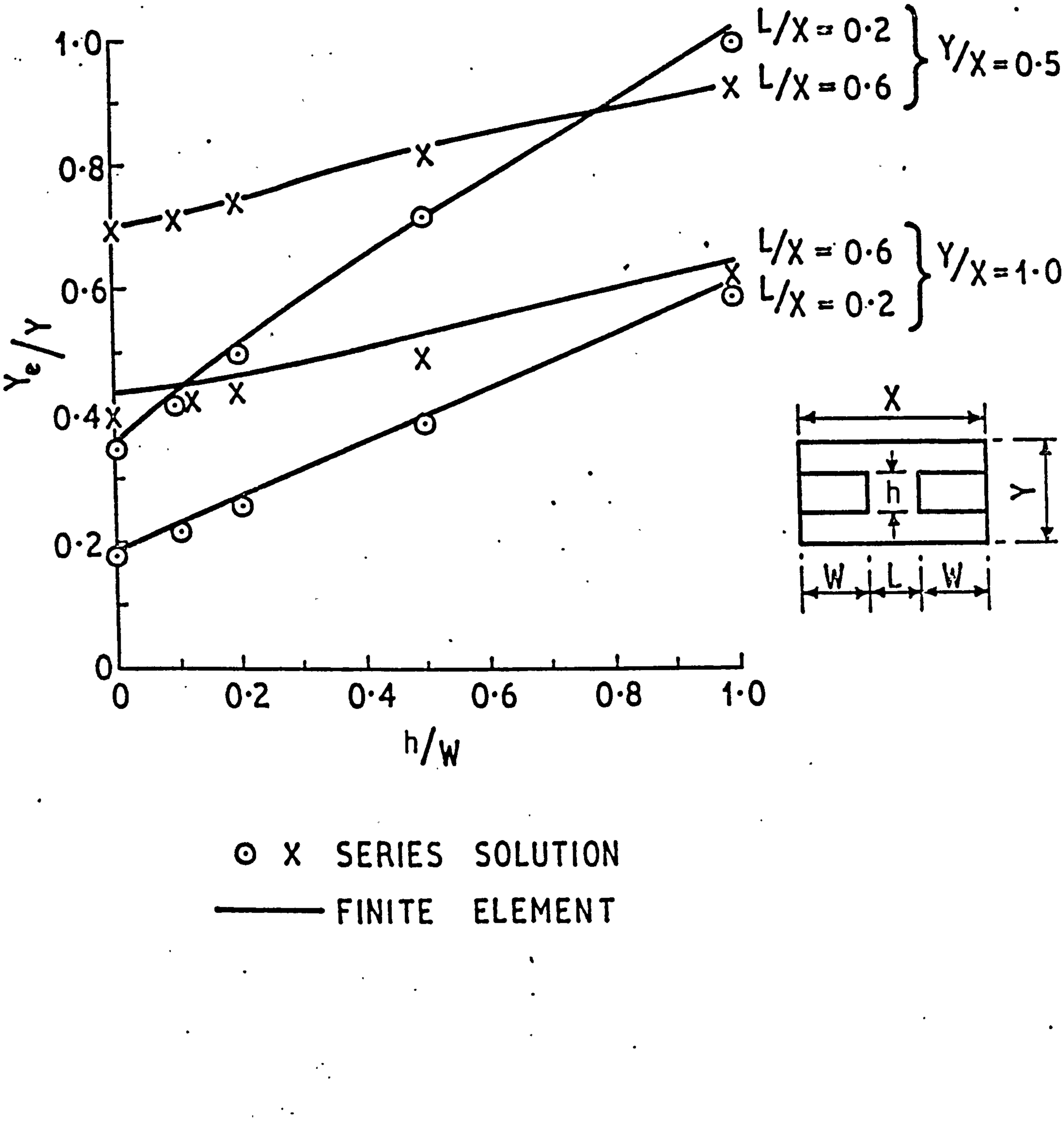

Fig. 4.6 Comparison Between Series Solution and Finite Element Solution for Thick Walls

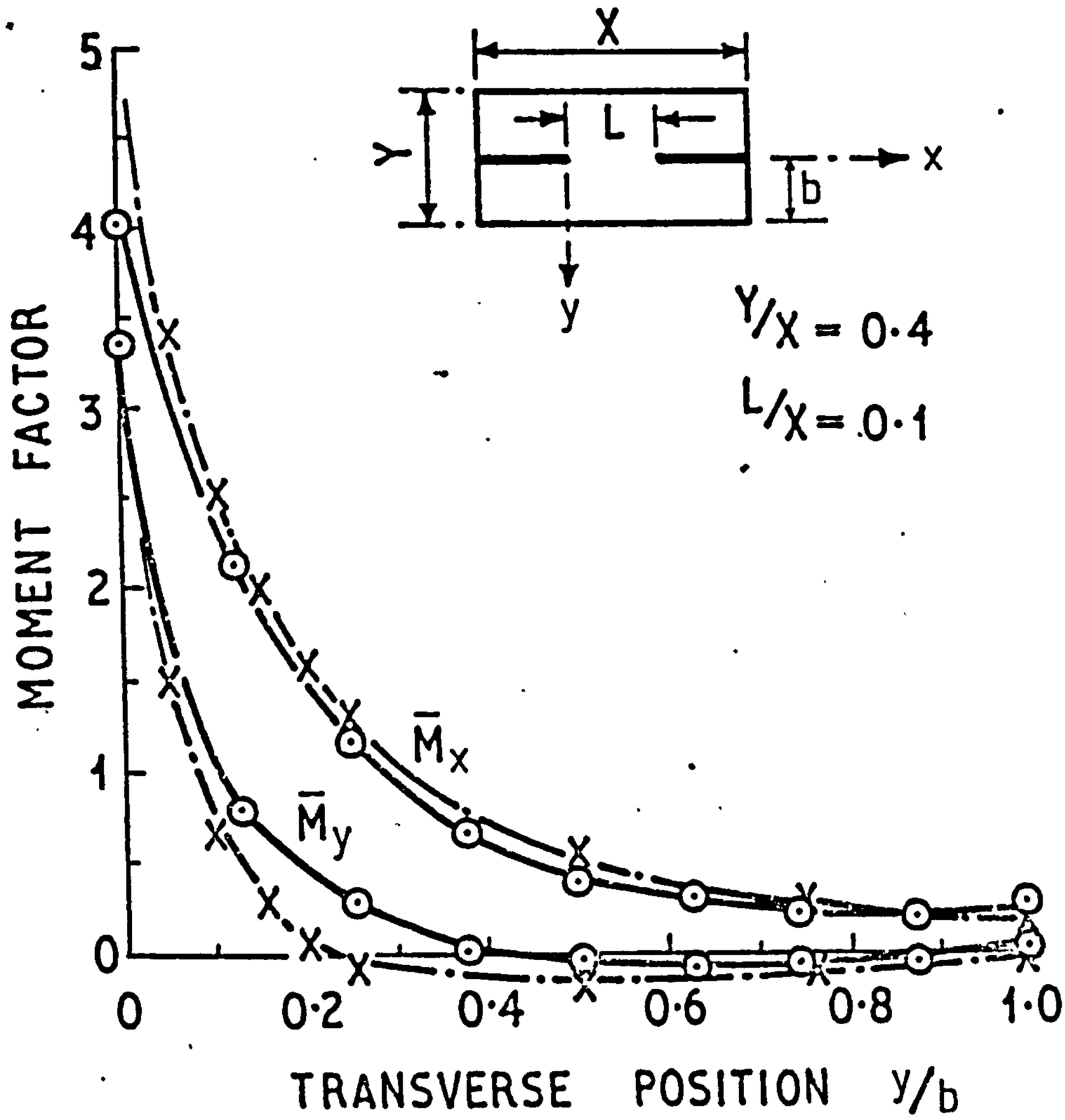

Fig. 4.7 Comparison Between Slab Moments Obtained by Series Solution and Finite Difference Solution

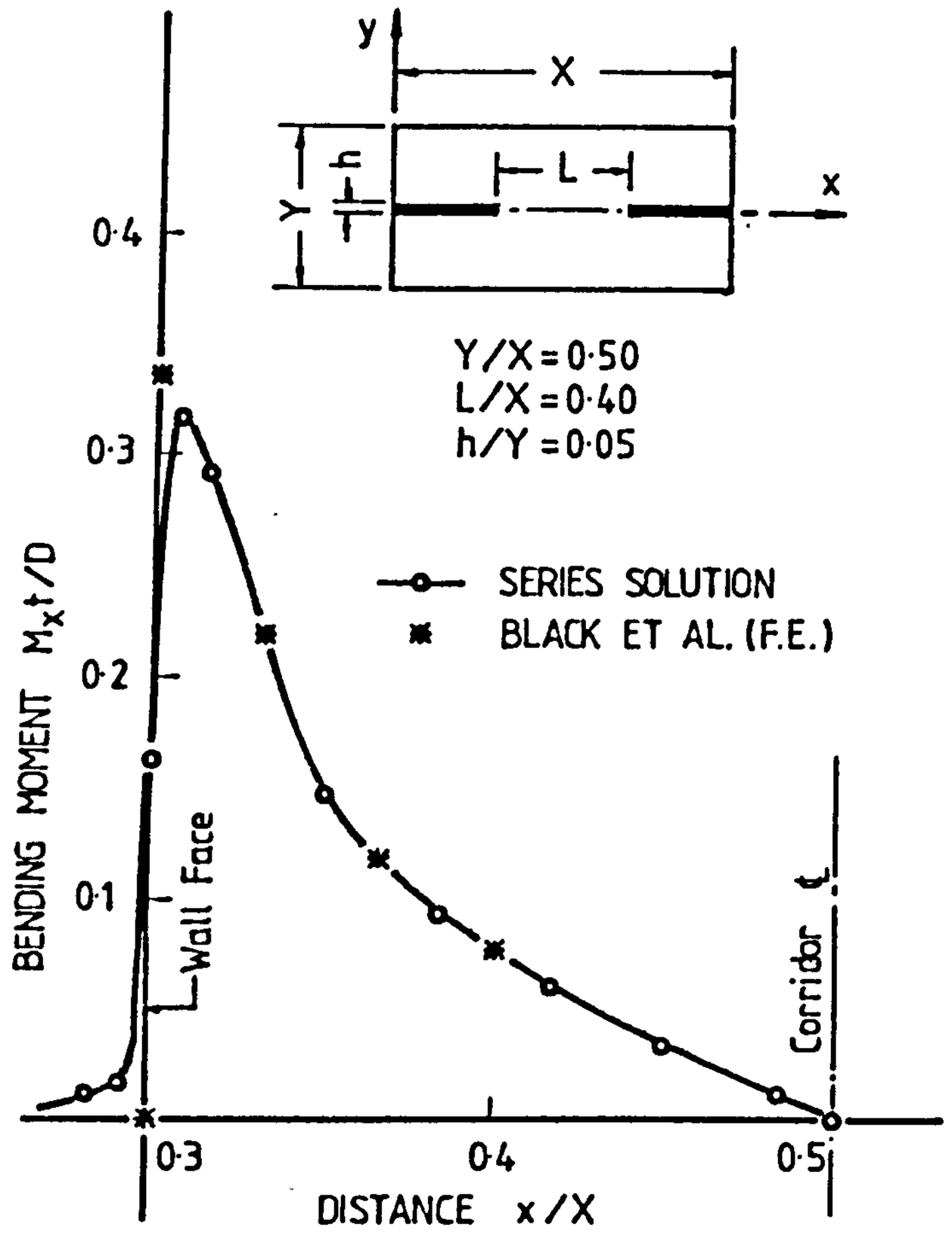

Fig. 4.8 Comparison Between Slab Moment Obtained by Series Solution and Finite Element Solution

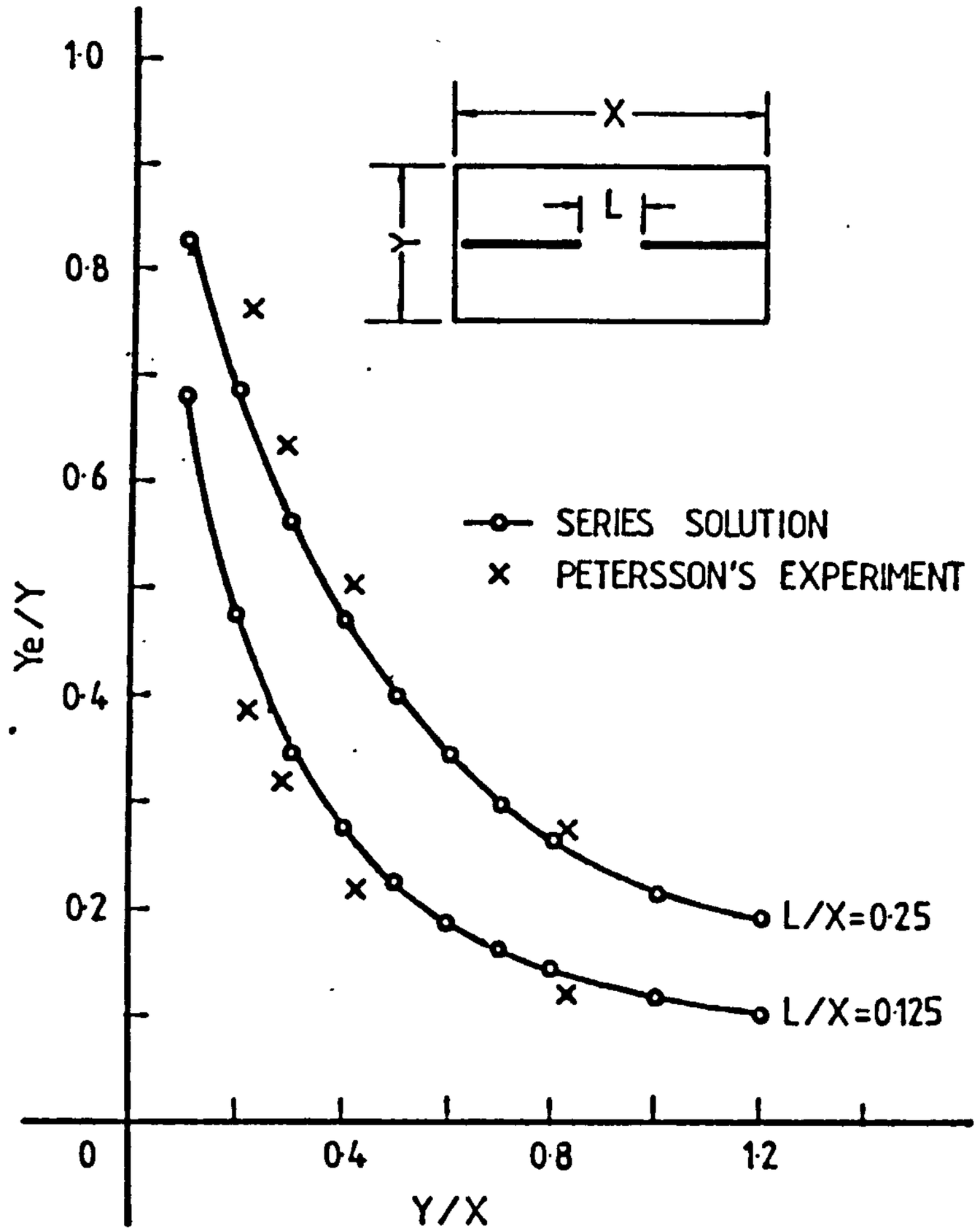

Fig. 4.9 Comparison Between Effective Widths Obtained by Series Solution and by Experiment

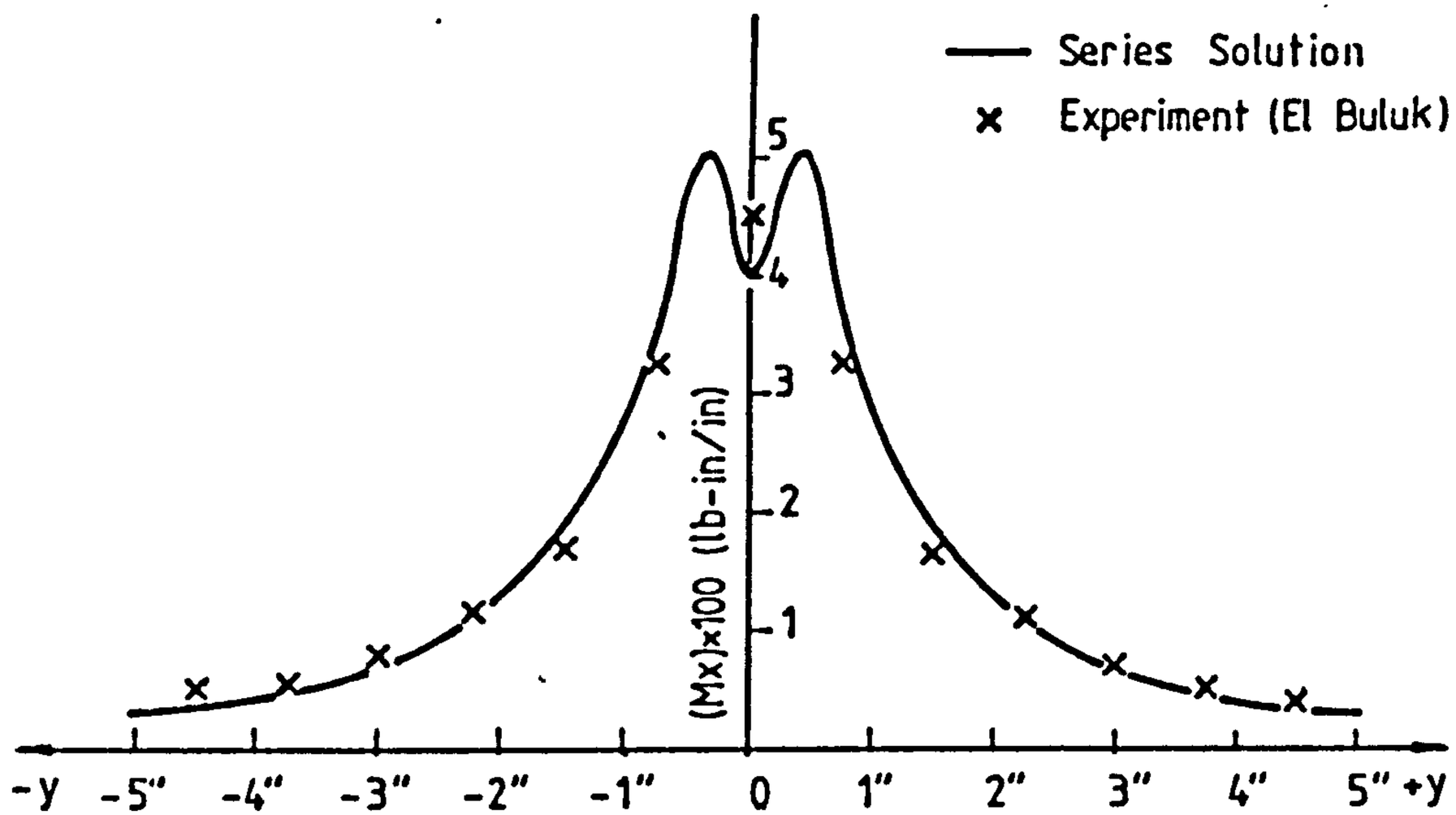

(a) Distribution Of Moment Mx At Section x = -1·6" Due To Unit Wall Rotation

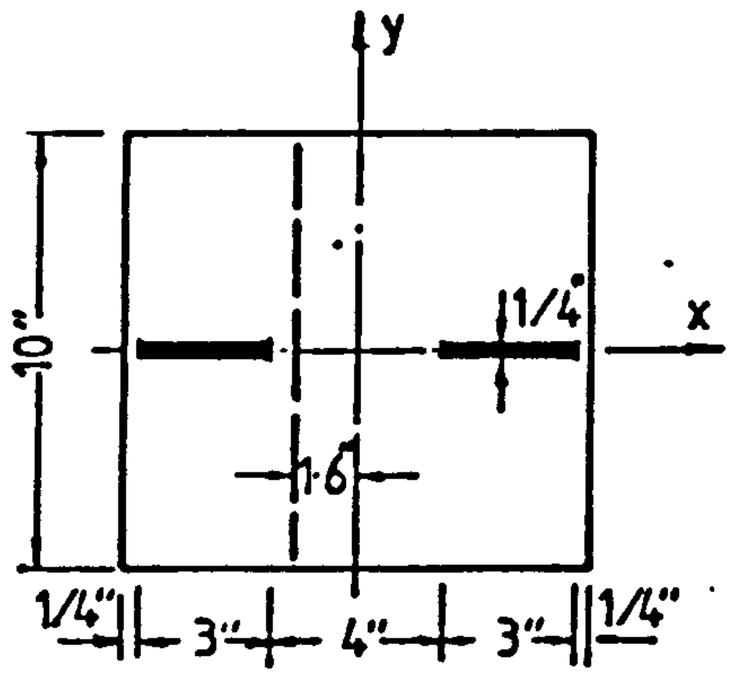

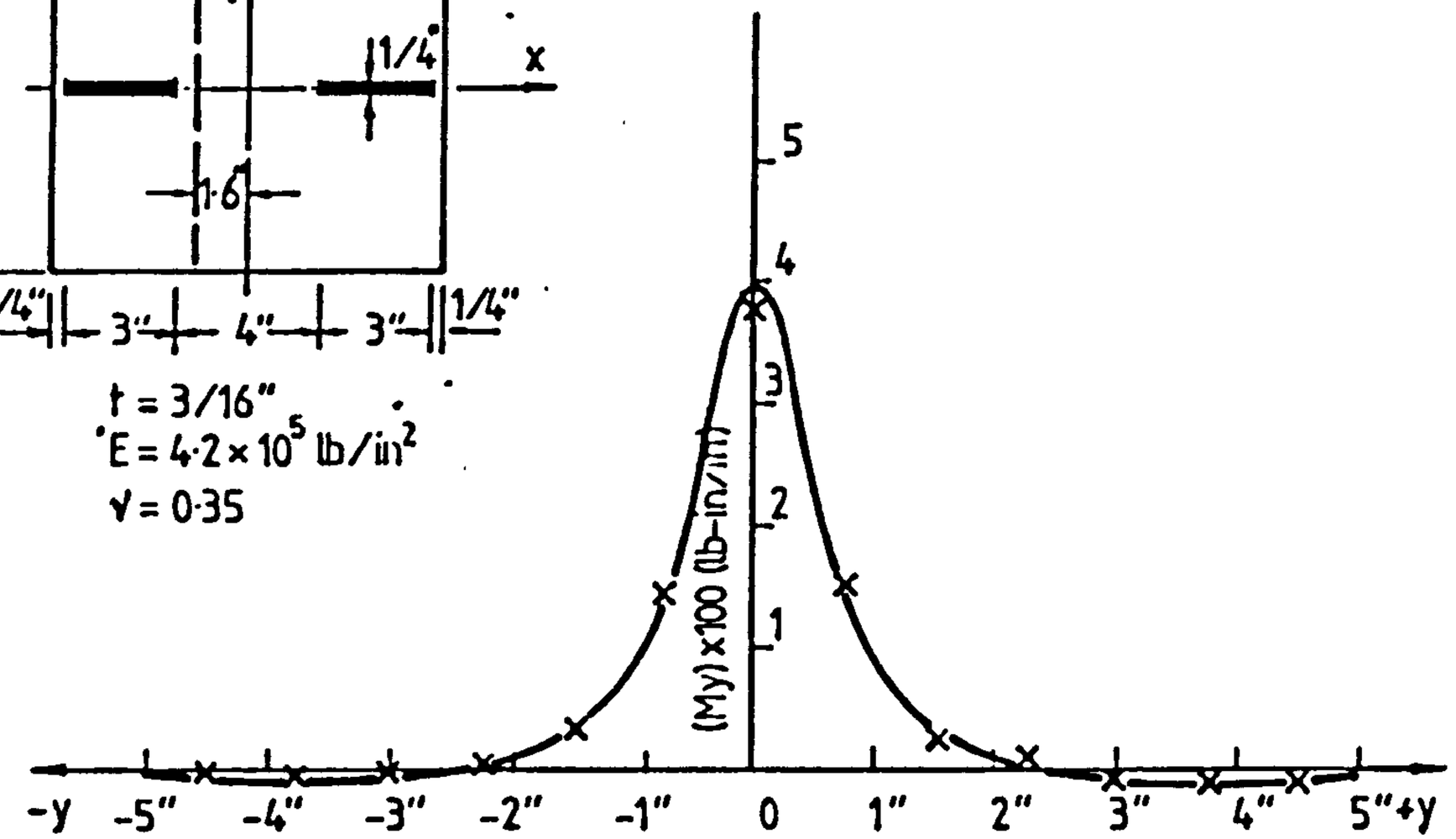

(b) Distribution Of Moment My At Section x = -1·6" Due To Unit Wall Rotation

Fig. 4.10 Comparison Between Slab Moments Obtained by Series Solution and by Experiment

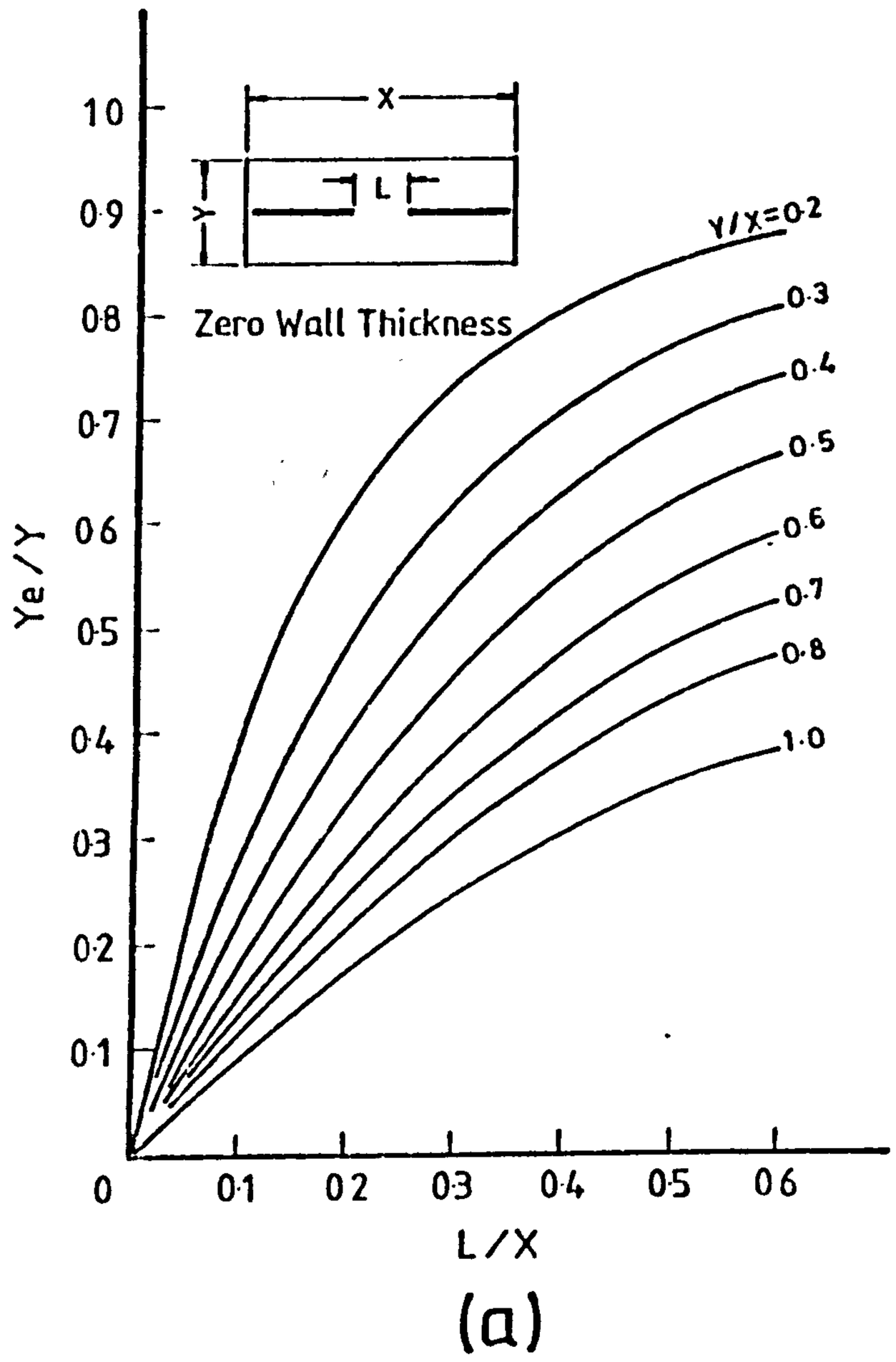

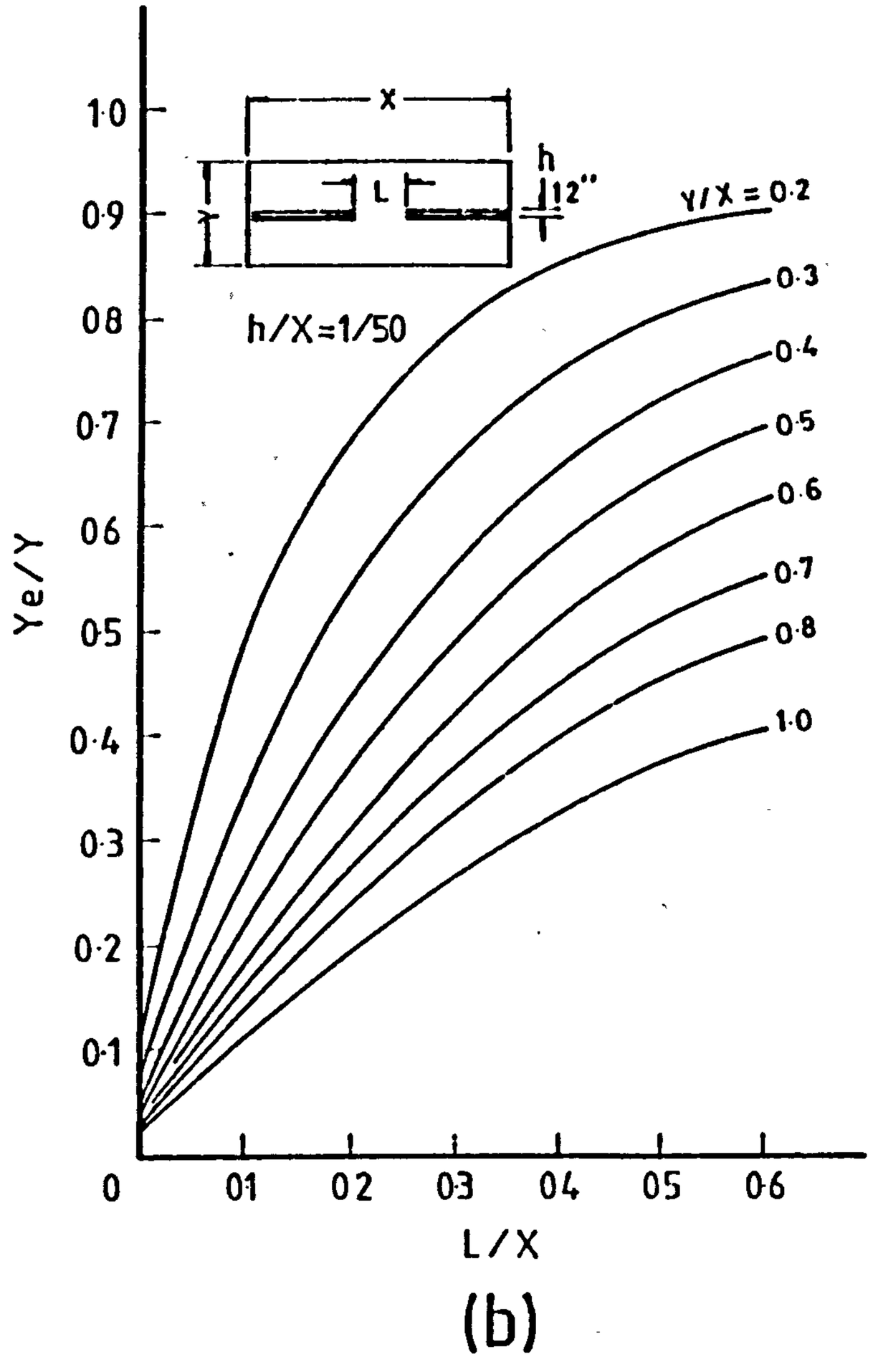

Fig. 4.11 Design Curves for Effective Width in Plane Wall Configuration (a) Walls of Zero Thickness, and (b) Walls of Finite Thickness

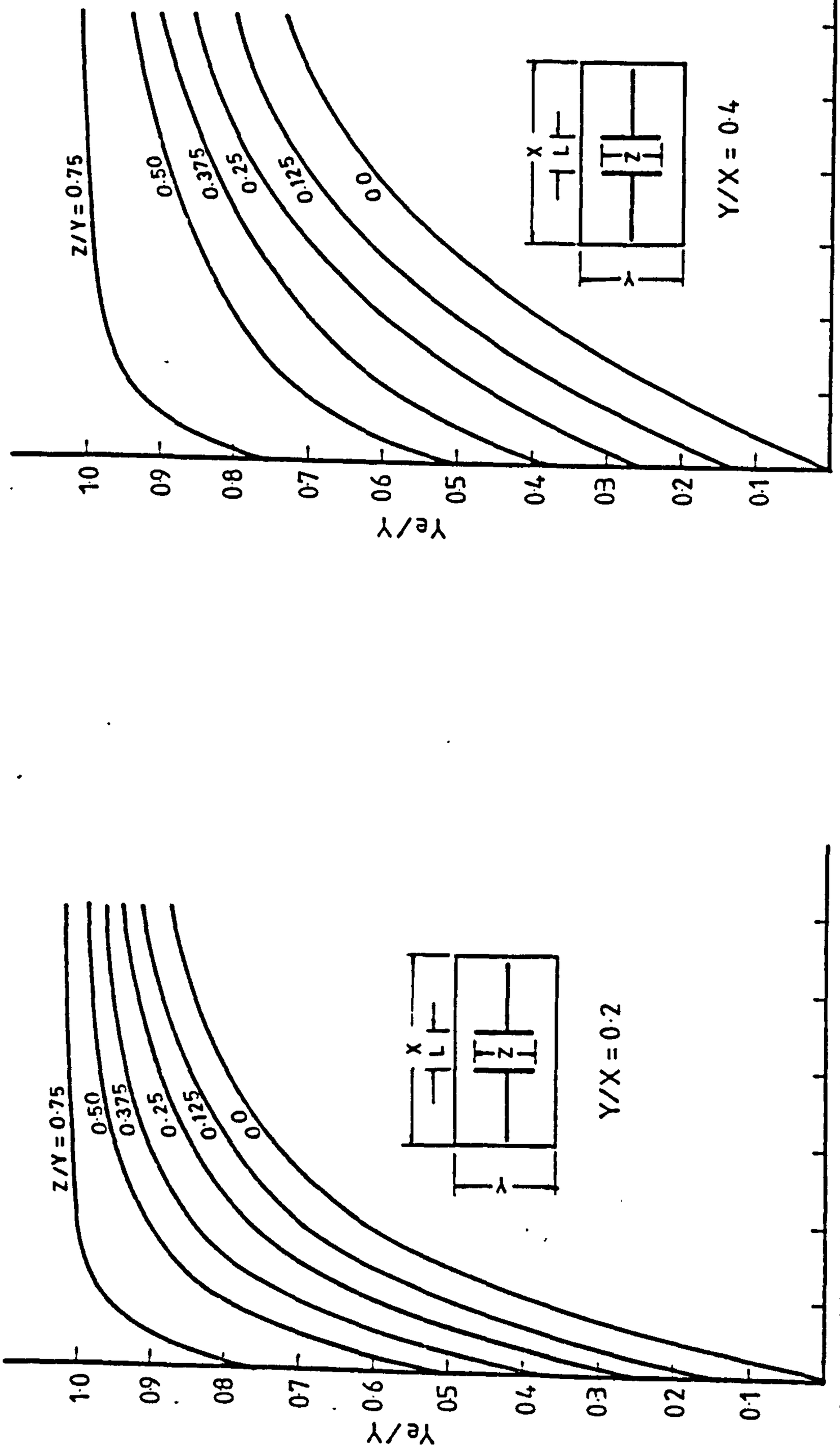

Fig. 4.12 Design Curves for Effective Width in Tee-shaped Flanged Wall Configurations

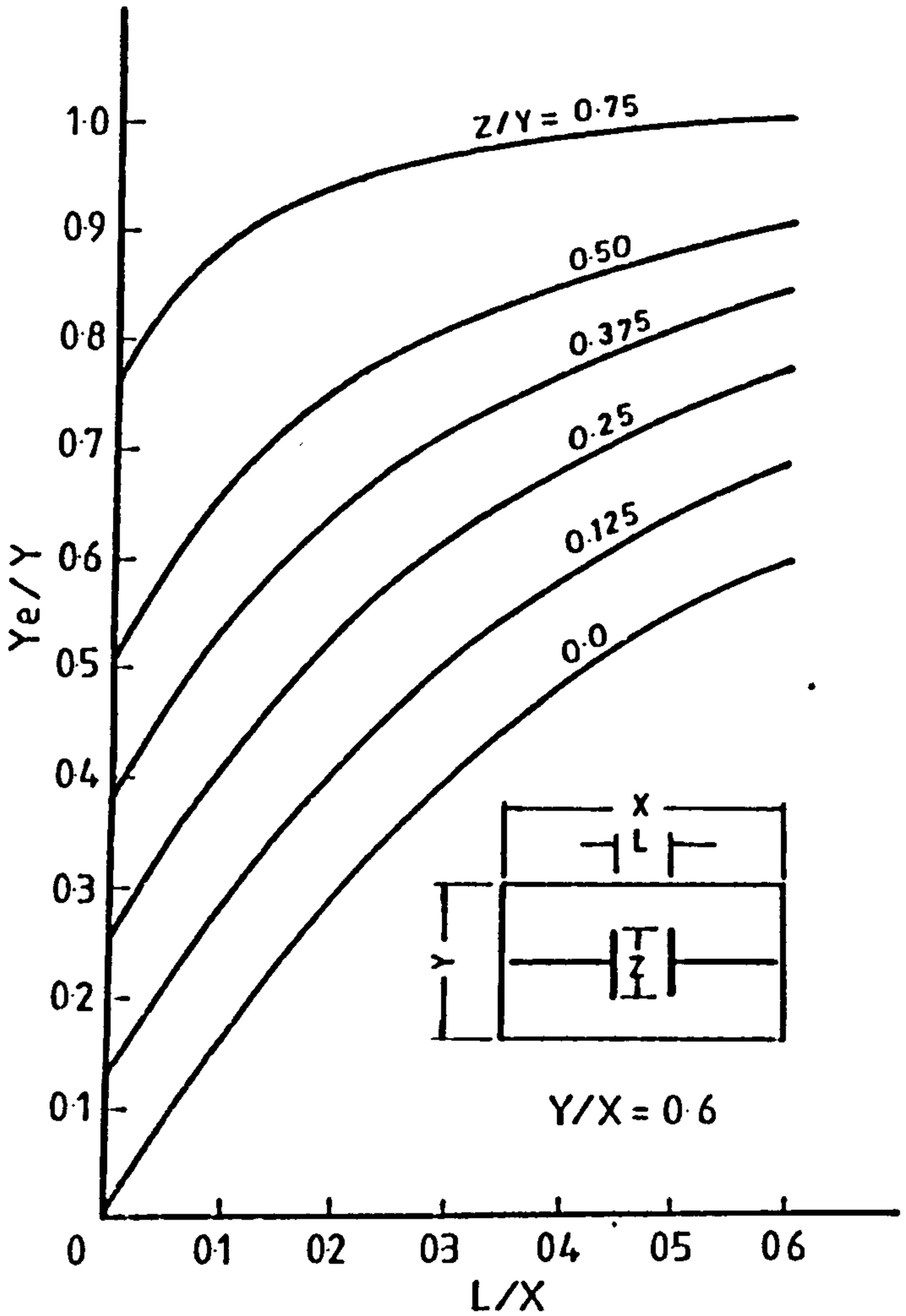

(c)

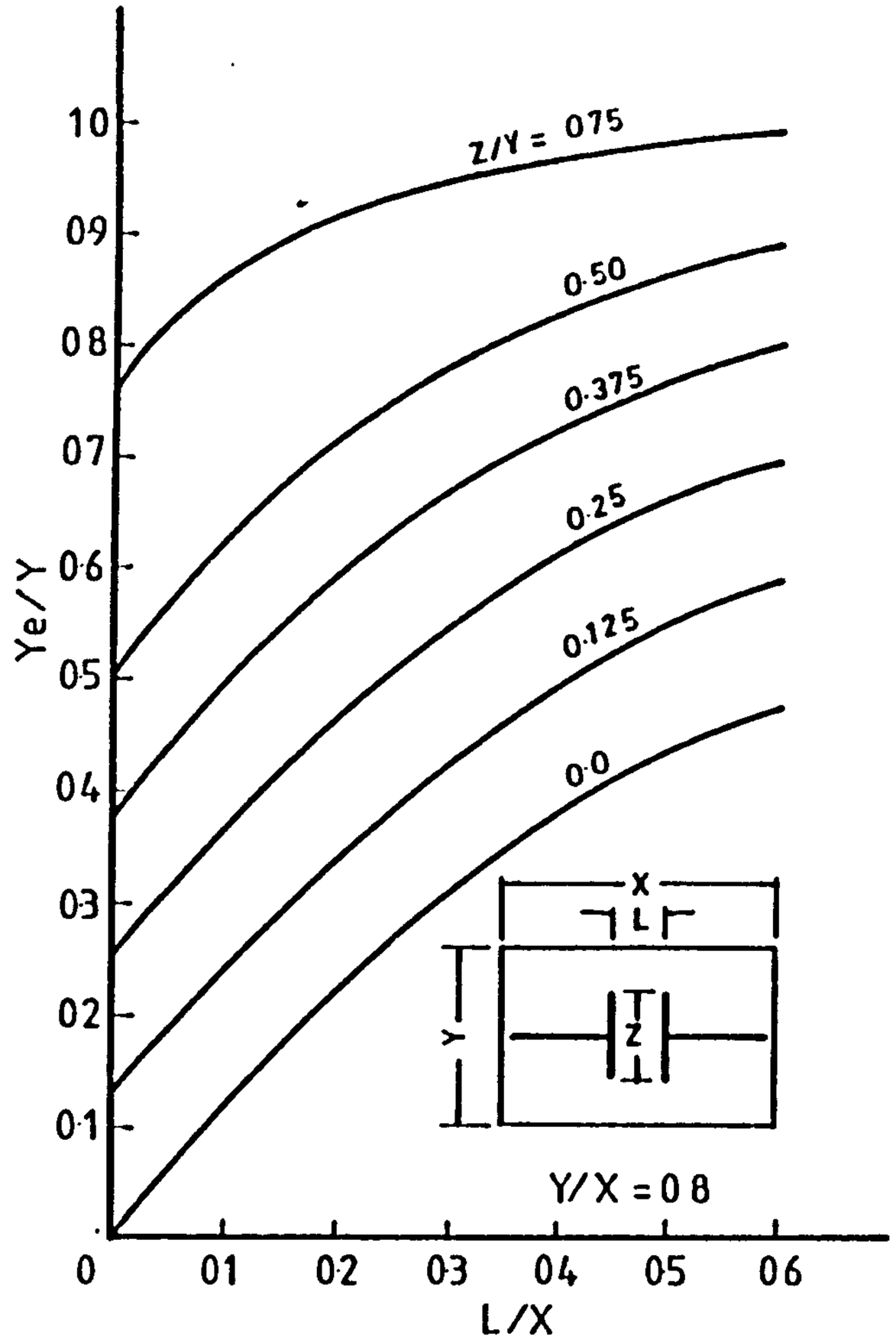

(d)

Fig. 4.12 (contd) Design Curves for Effective Width in Tee-shaped Flanged Wall Configurations

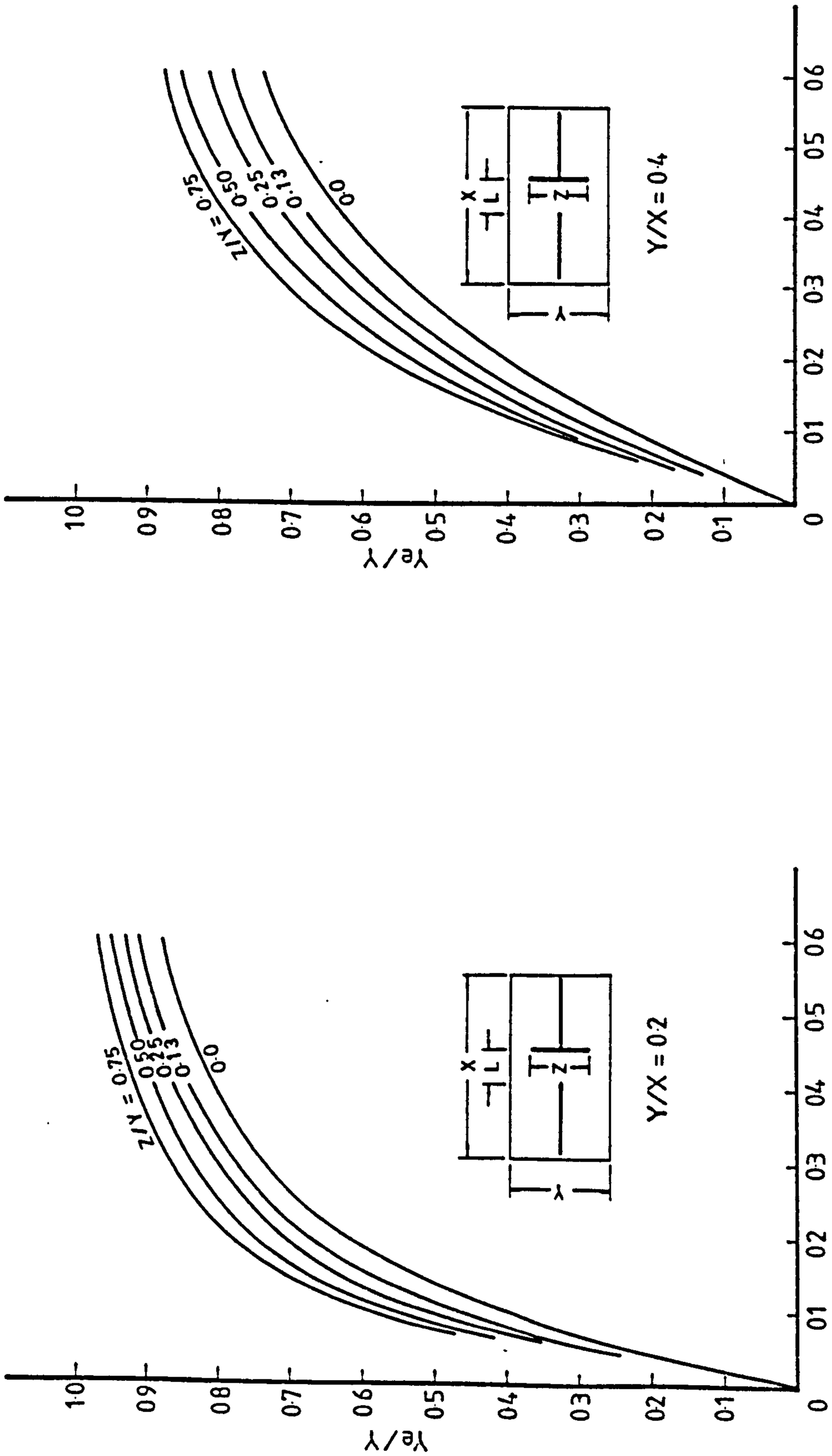

Fig. 4.13 Design Curves for Effective Width in Planar-flanged Wall Configuration

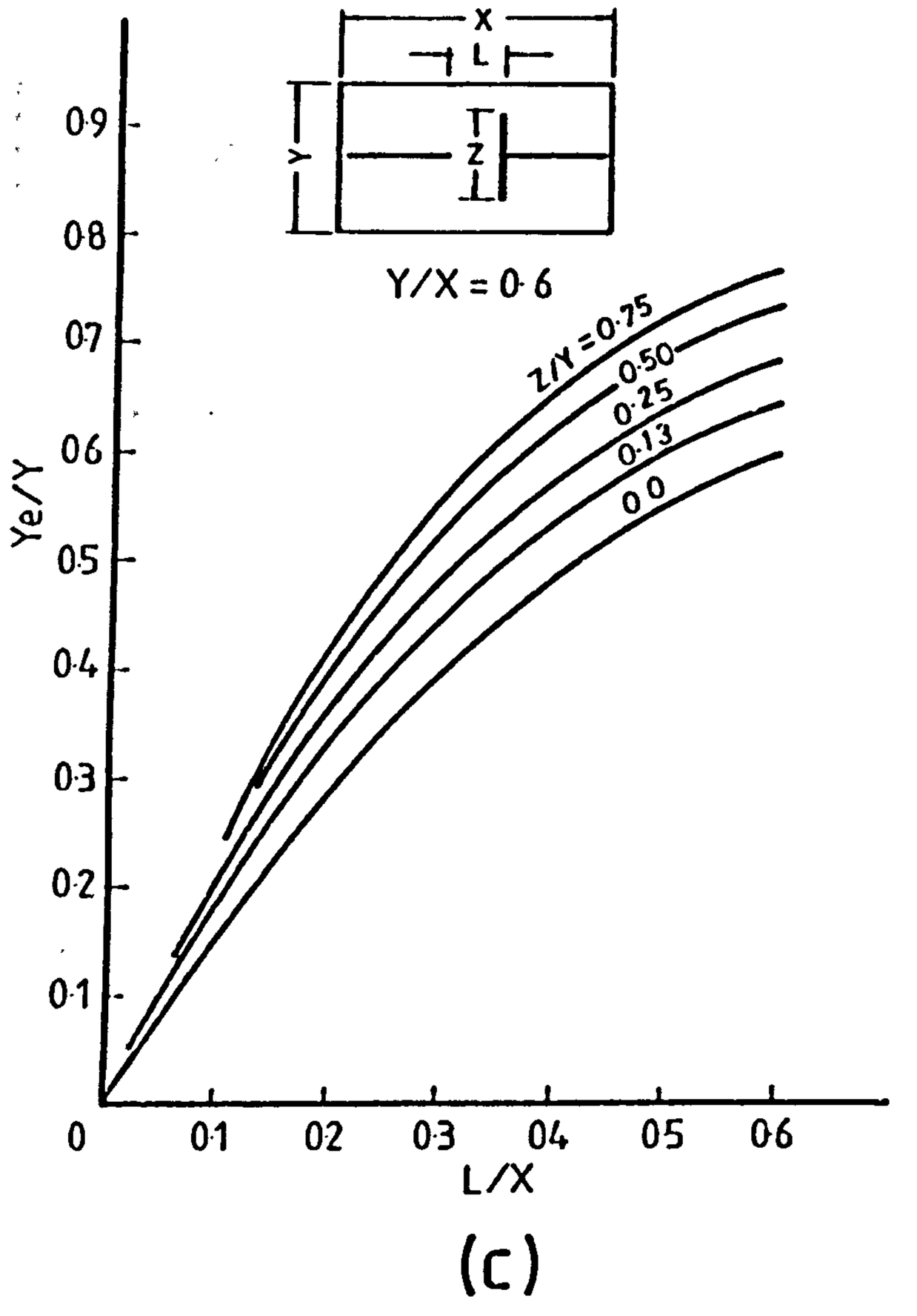

(c)

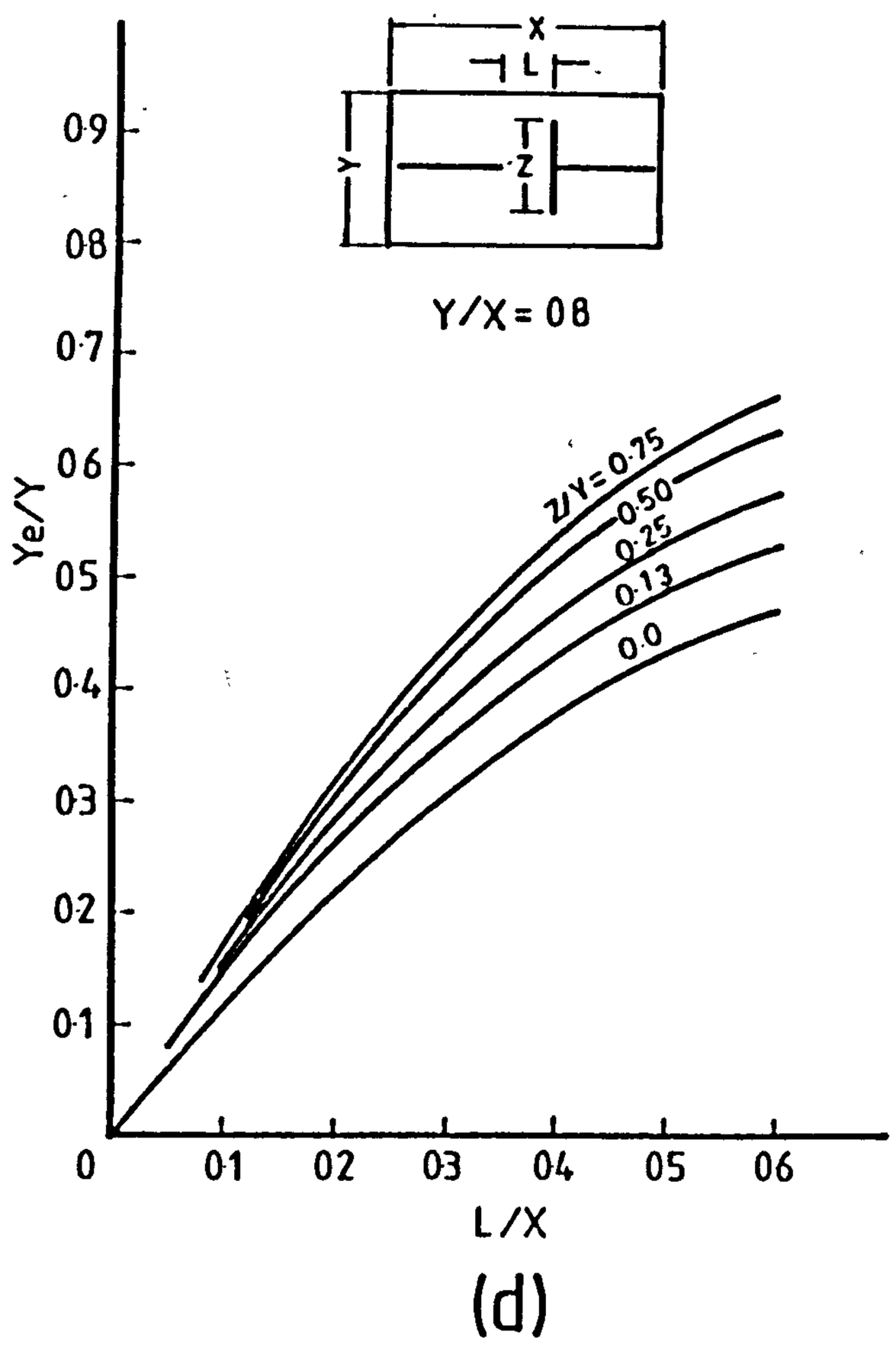

(d)

Fig. 4.13 (contd) Design Curves for Effective Width in Planar-flanged Wall Configuration

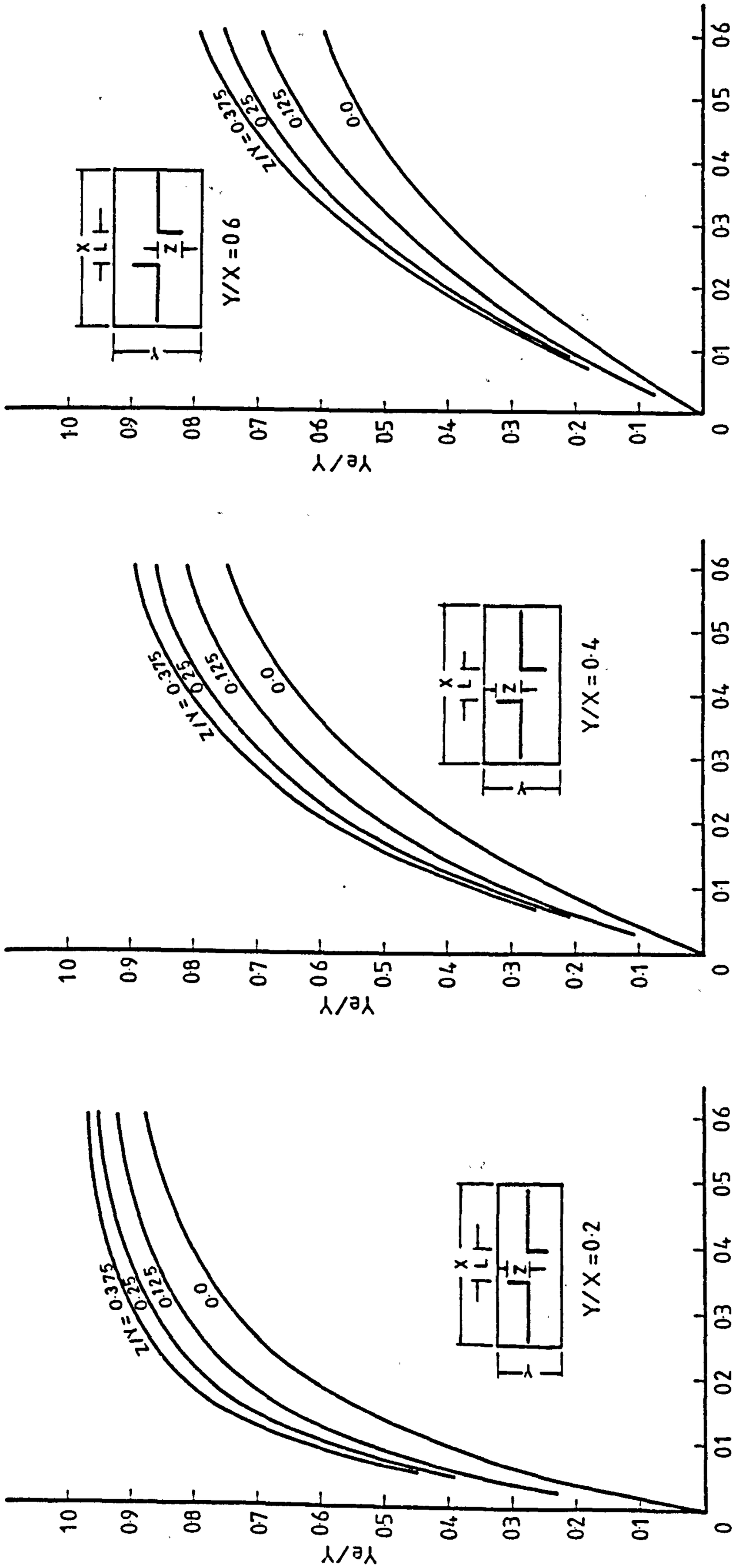

Fig. 4.14 Design Curves for Effective Width in L-shaped Flanged Wall Configuration

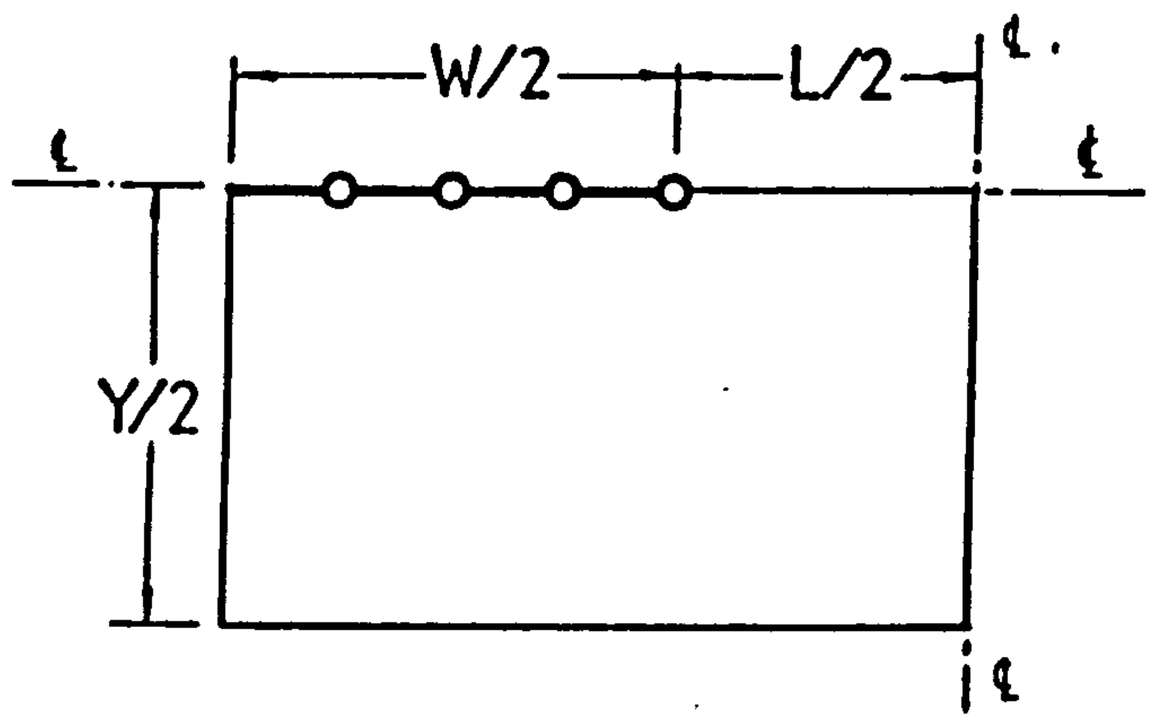

(a) Plane Walls of Zero Thickness

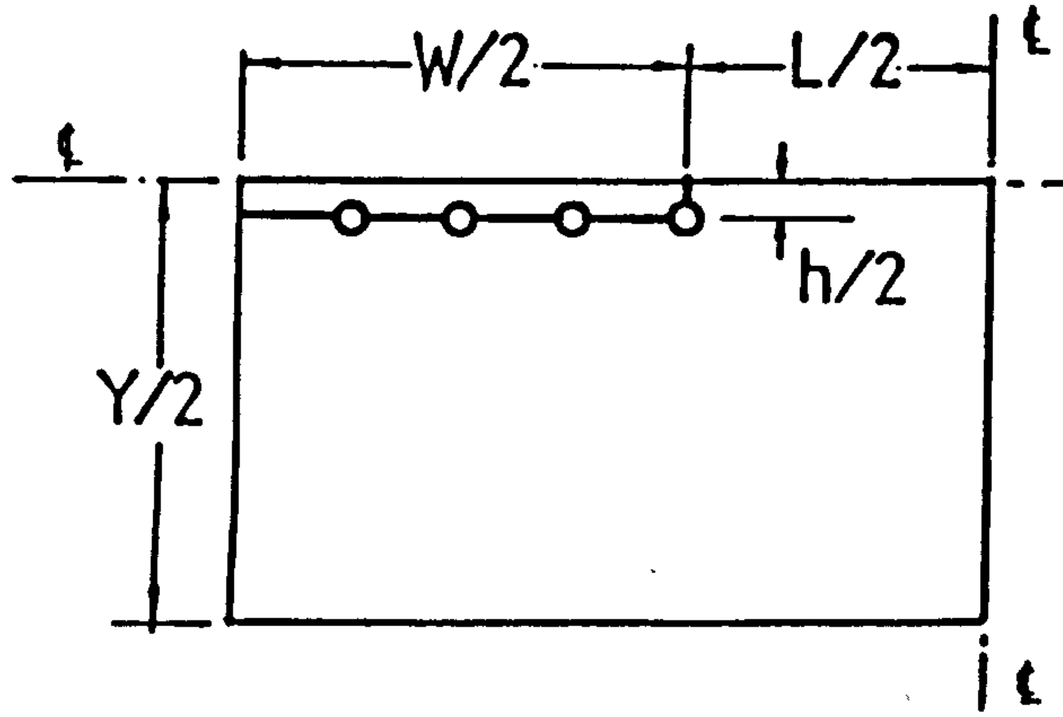

(b) Plane Walls of Finite Thickness

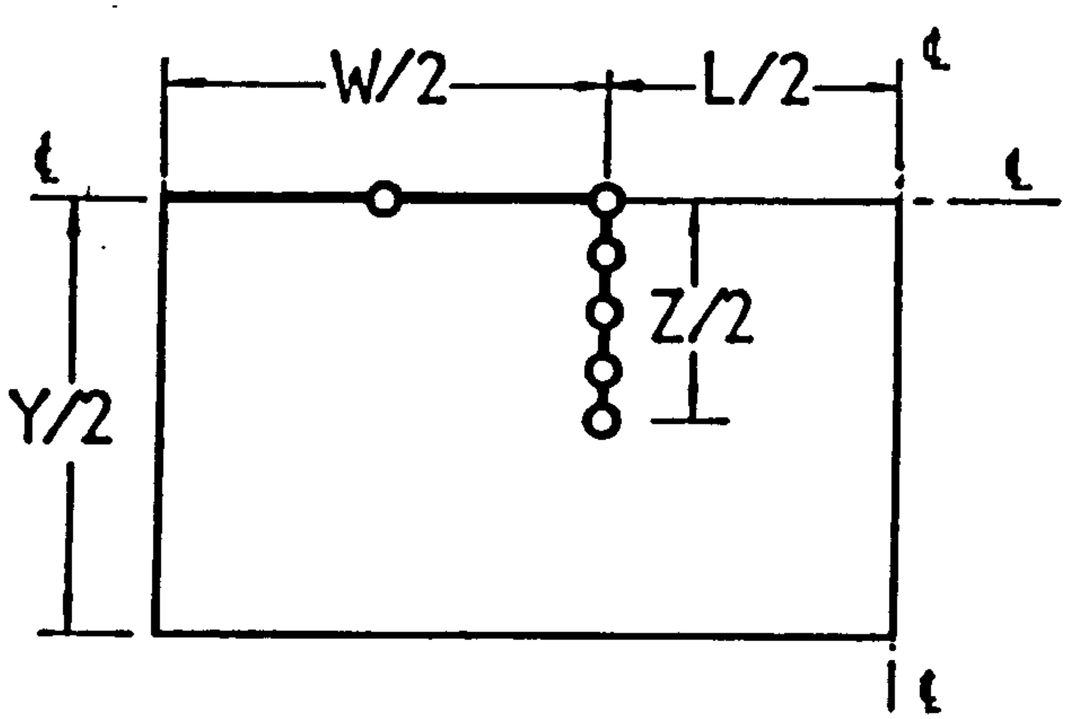

(c) T-Shaped Flanged Walls

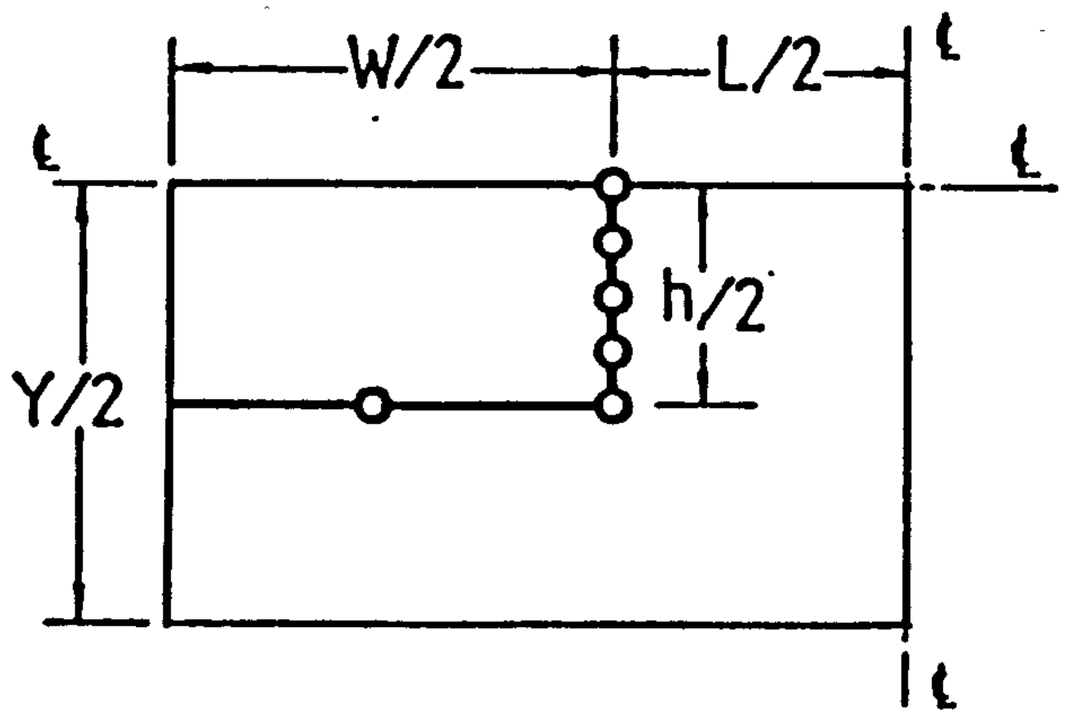

(d) Thick Walls or Box Cores

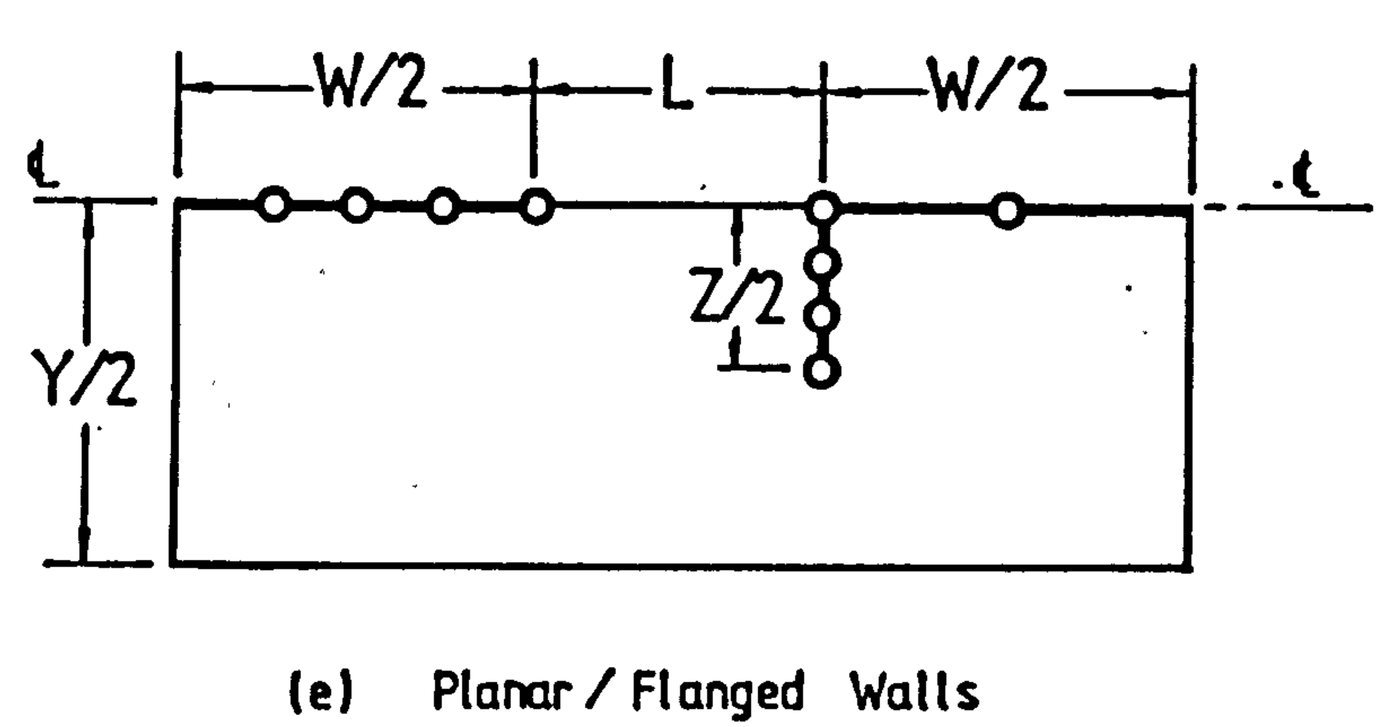

(e) Planar / Flanged Walls

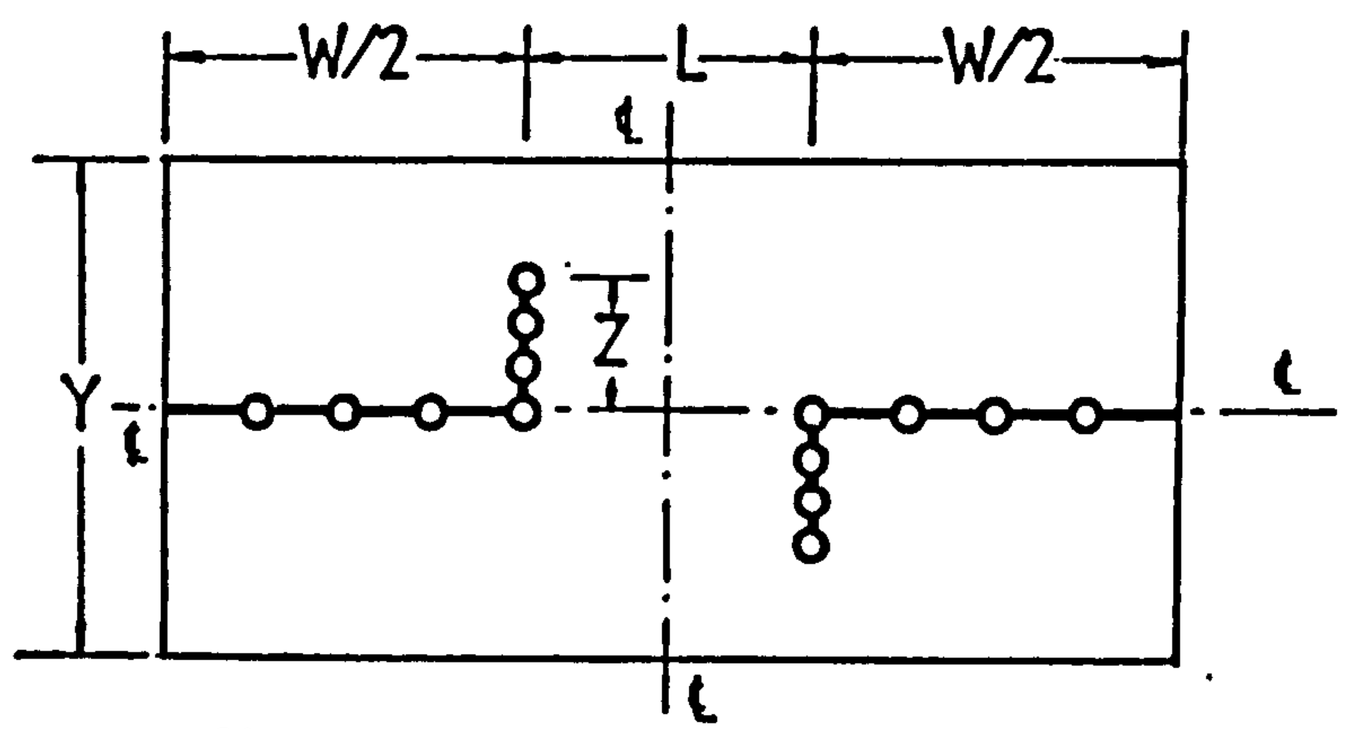

(f) L-Shaped Flanged Walls

Fig. 4.15 Nodal Representation of Wall in Various Configurations

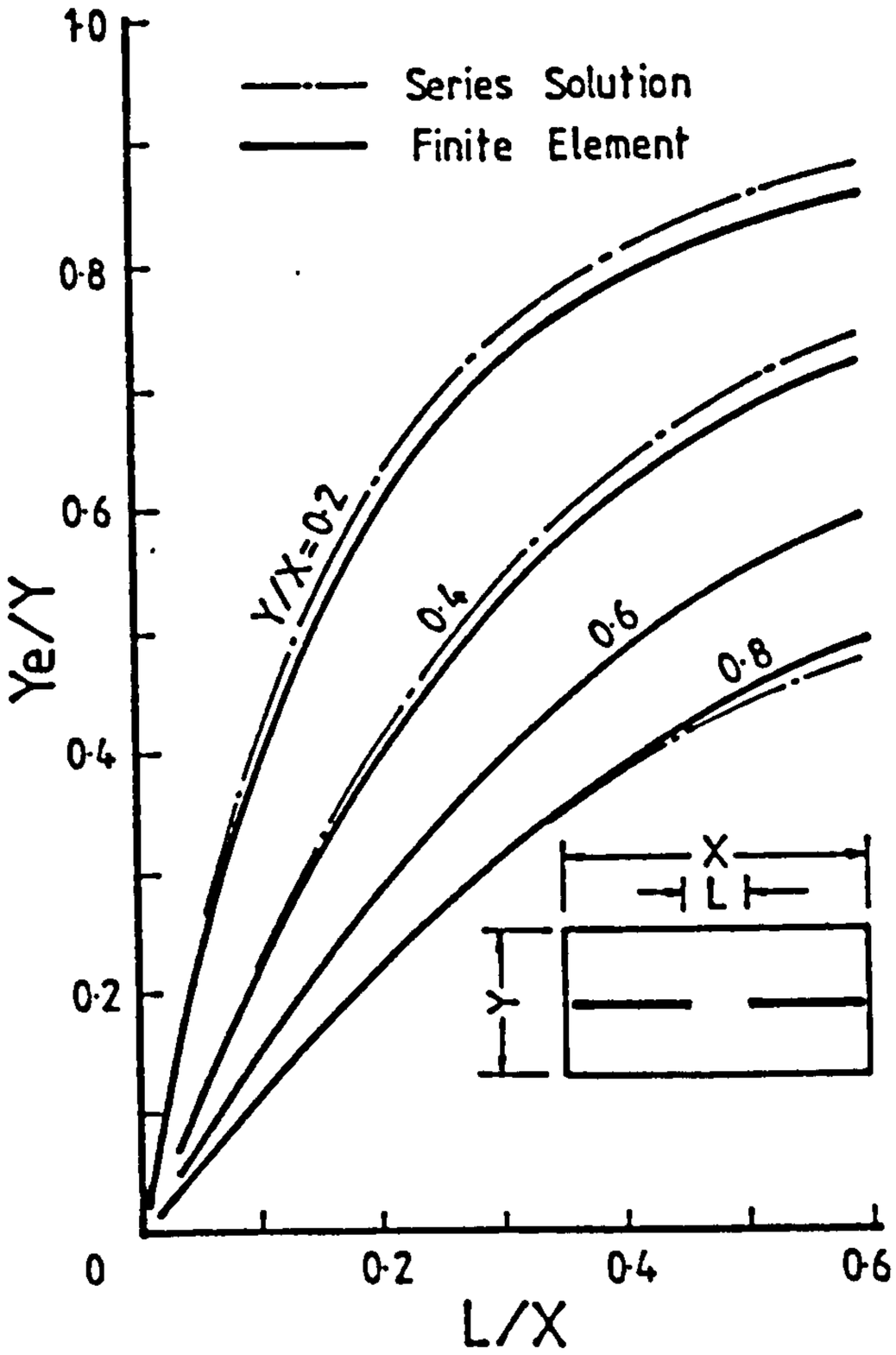

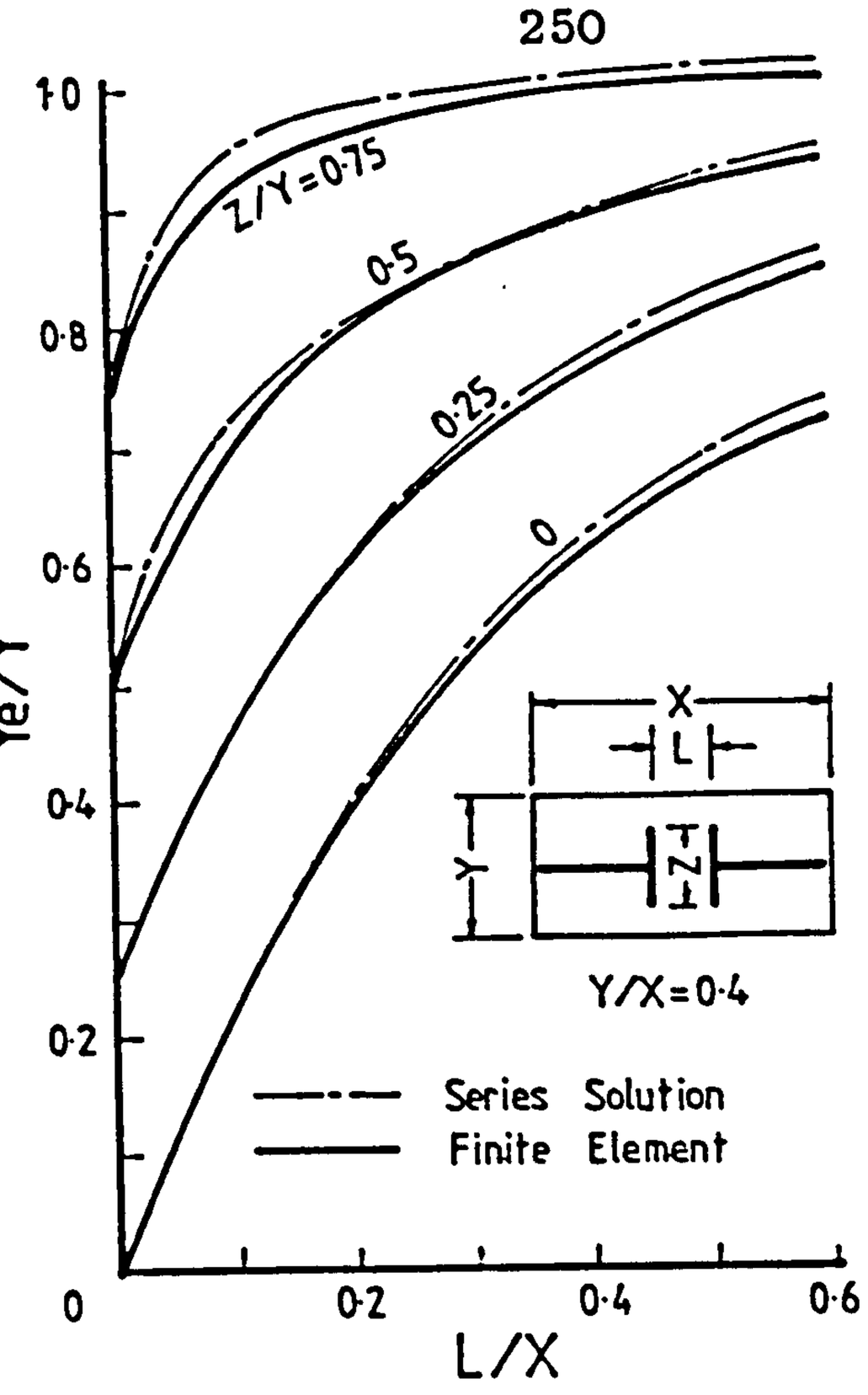

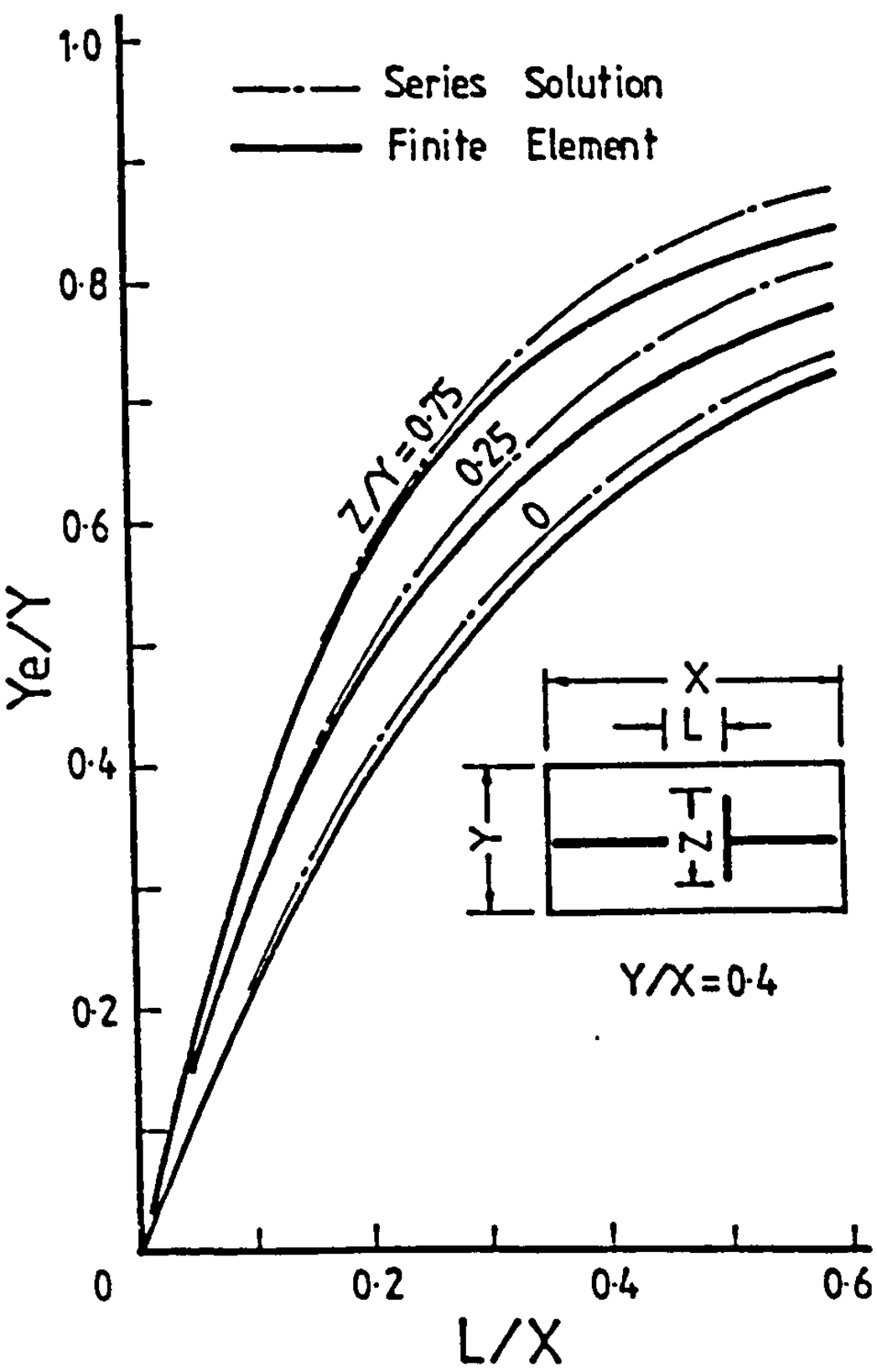

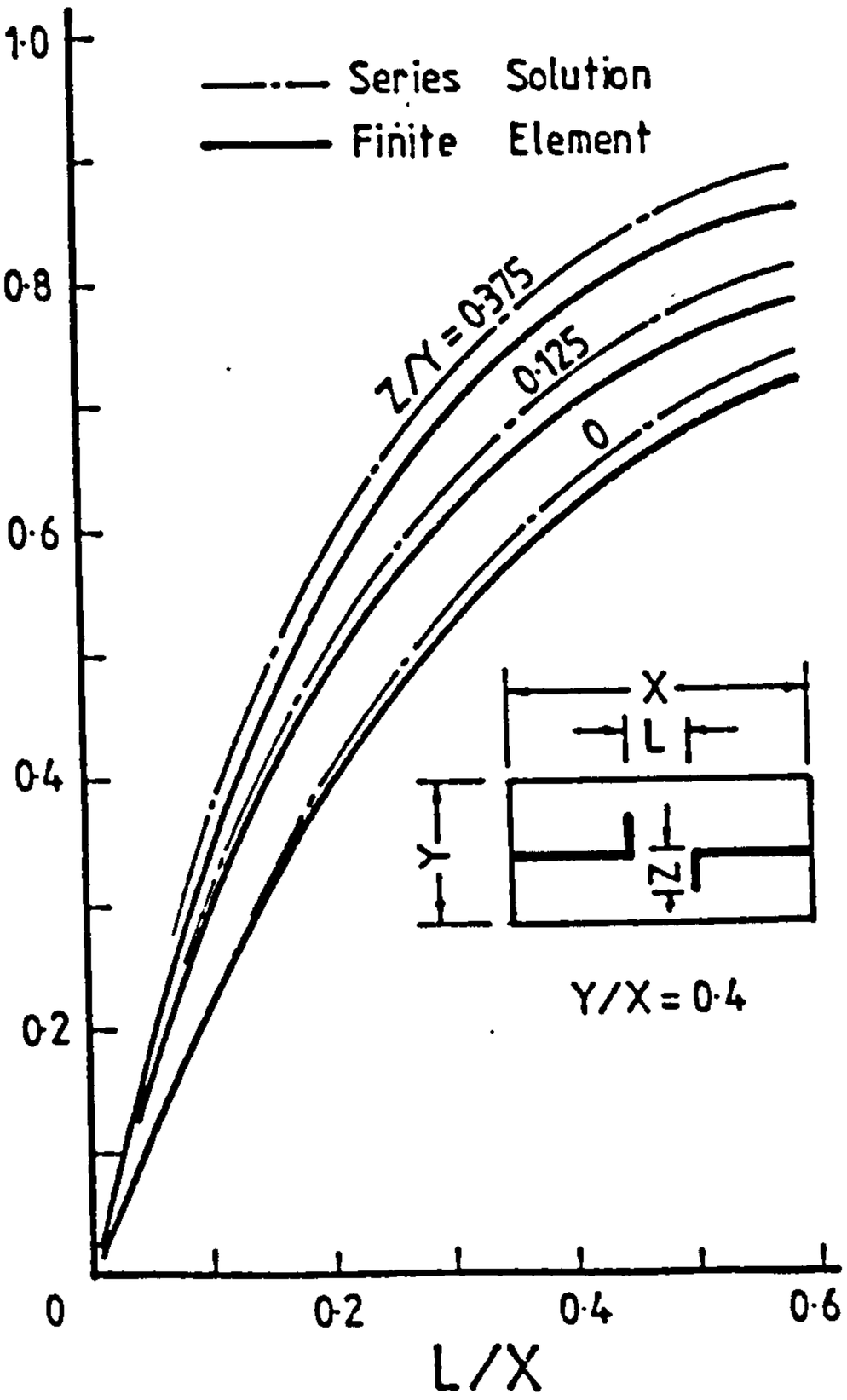

Fig. 4.16 Comparison Between Design Curves for Effective Width Obtained by Series Solution and Finite Element Solution

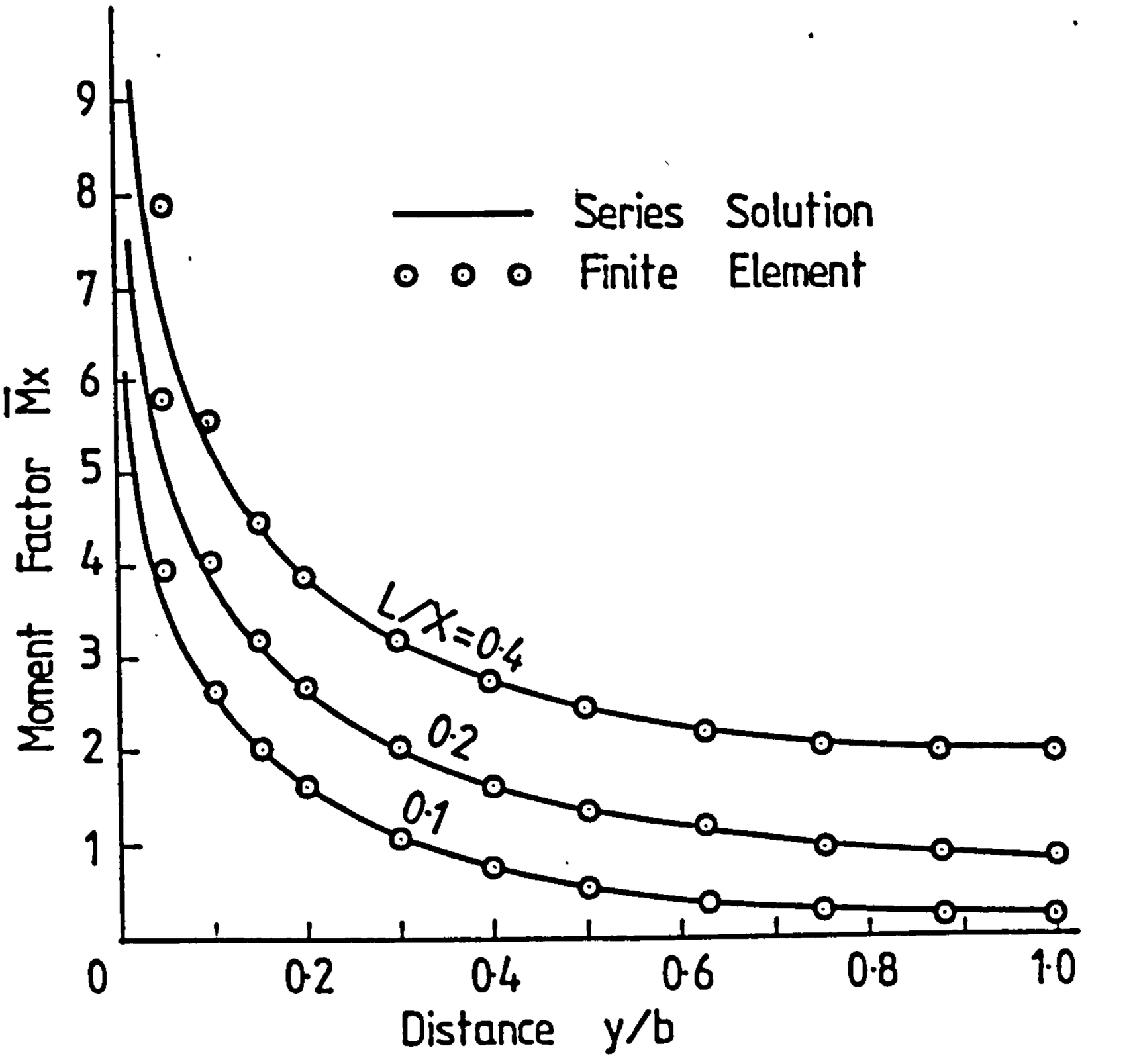

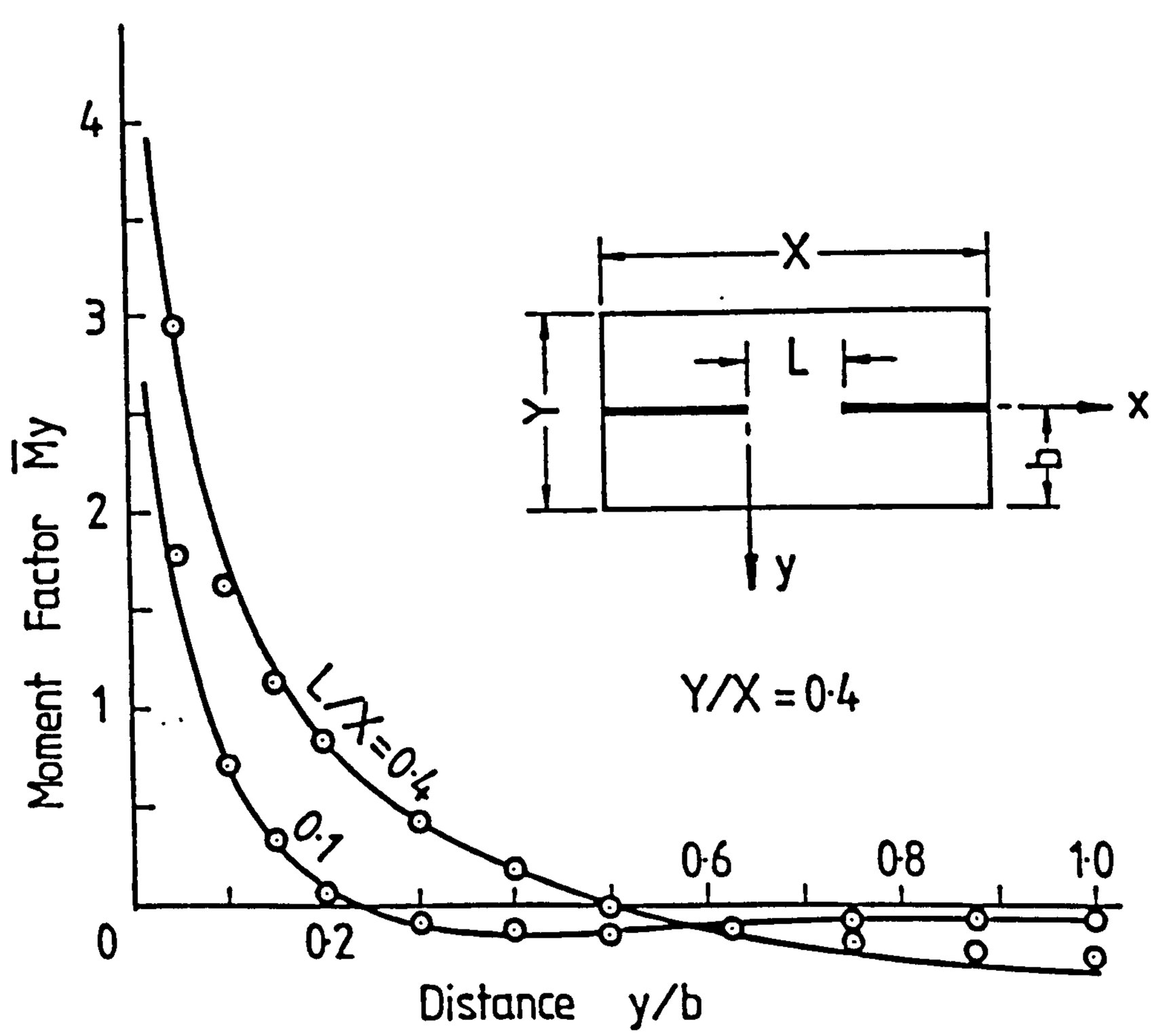

Fig. 4.17 Comparison Between Moment Factors Obtained by Series Solution and Finite Element Solution

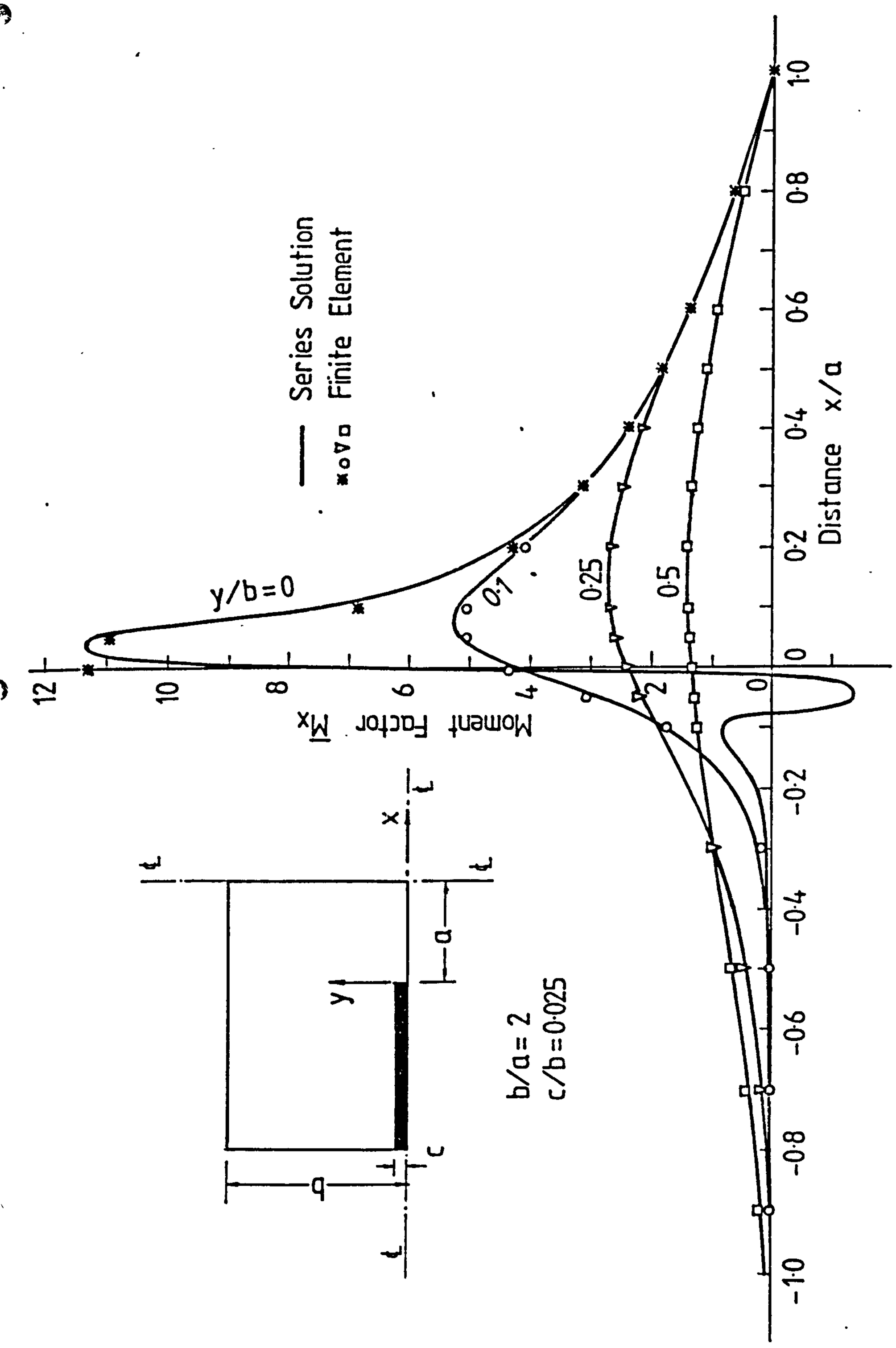

Fig. 4.18(a) Distribution of Longitudinal Bending Moments at Various Longitudinal Sections

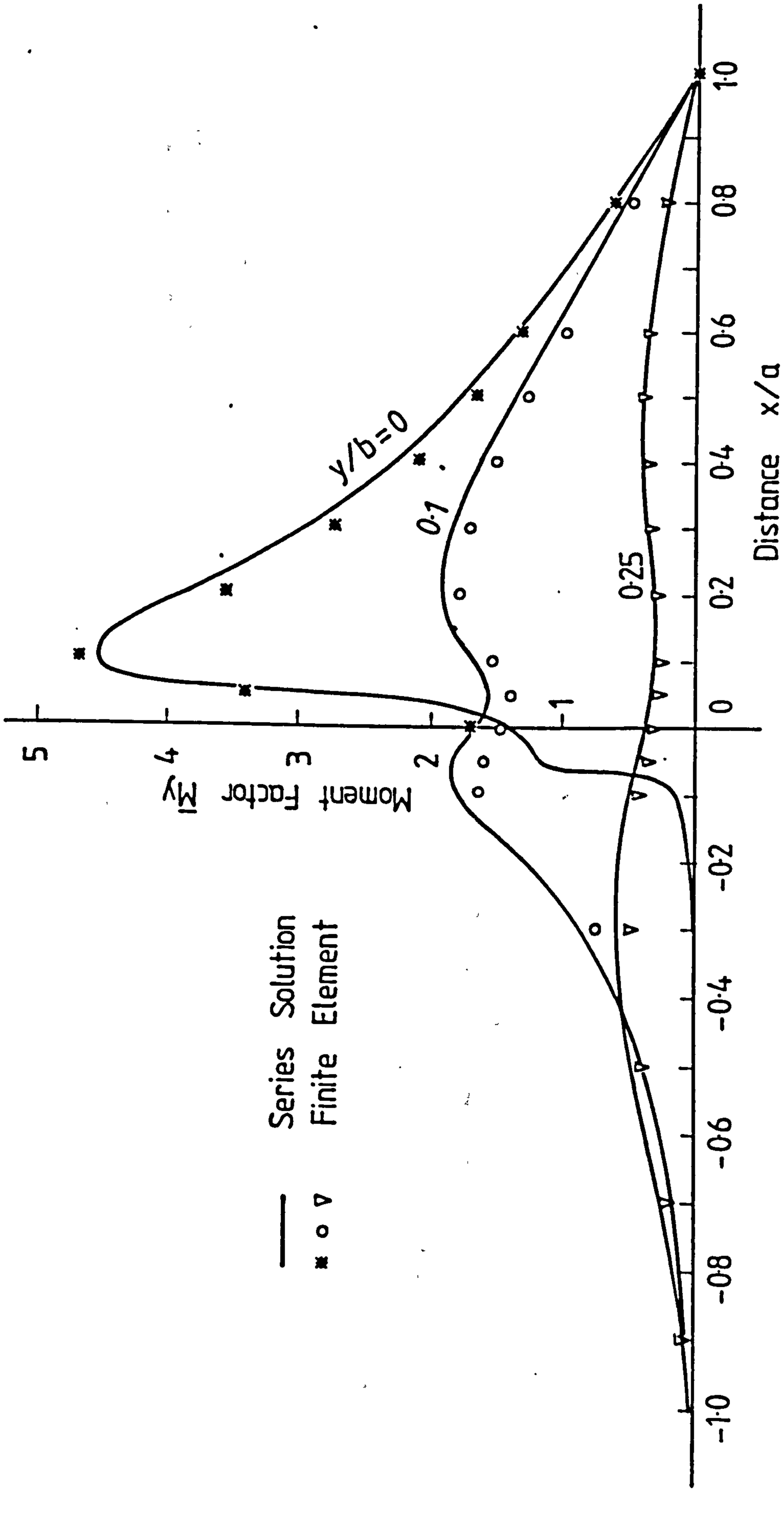

Fig. 4.18(b) Distribution of Transverse Bending Moments at Various Longitudinal Sections

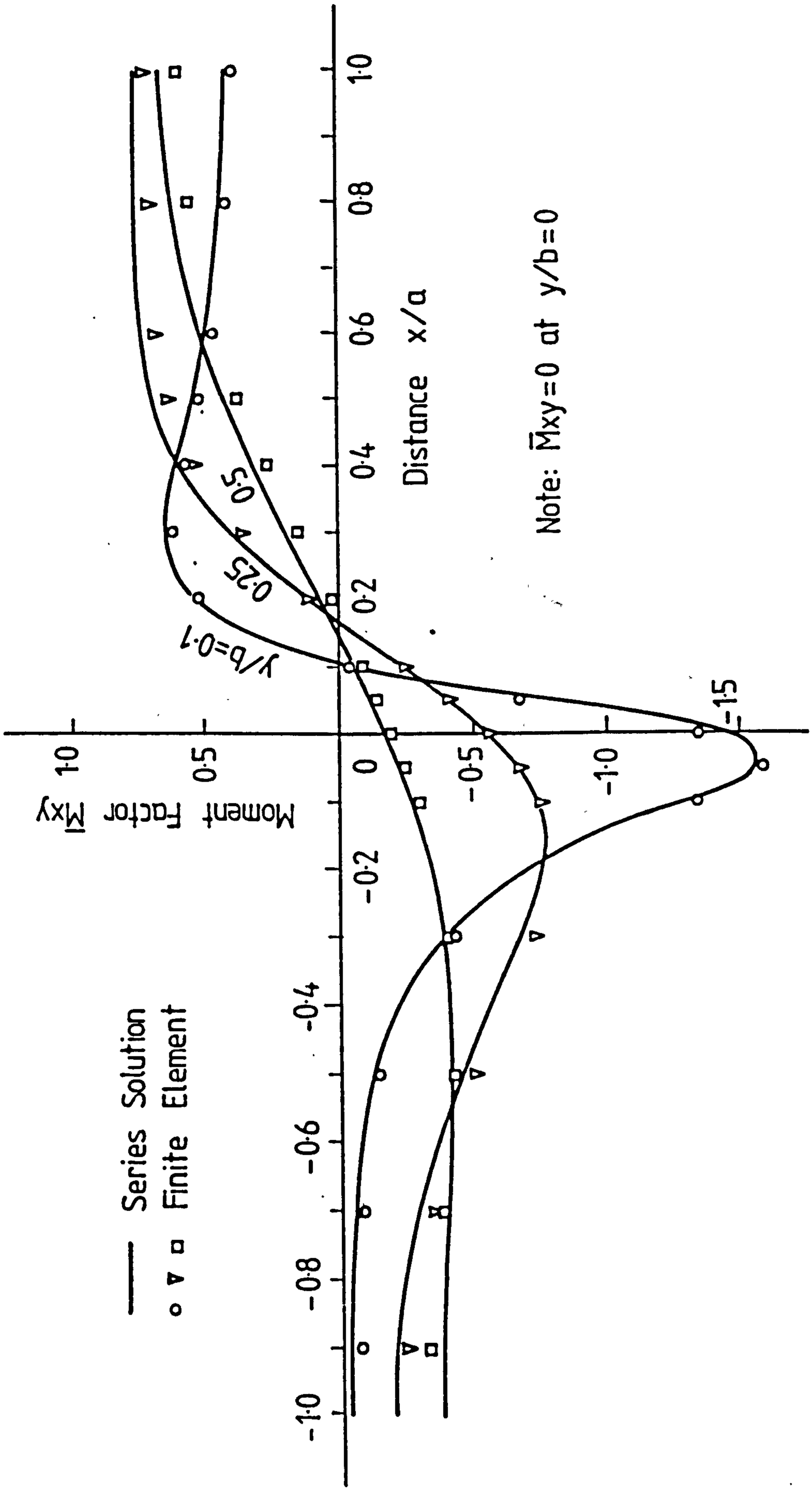

Fig. 4.18(c) Distribution of Twisting Moments at Various Longitudinal Sections

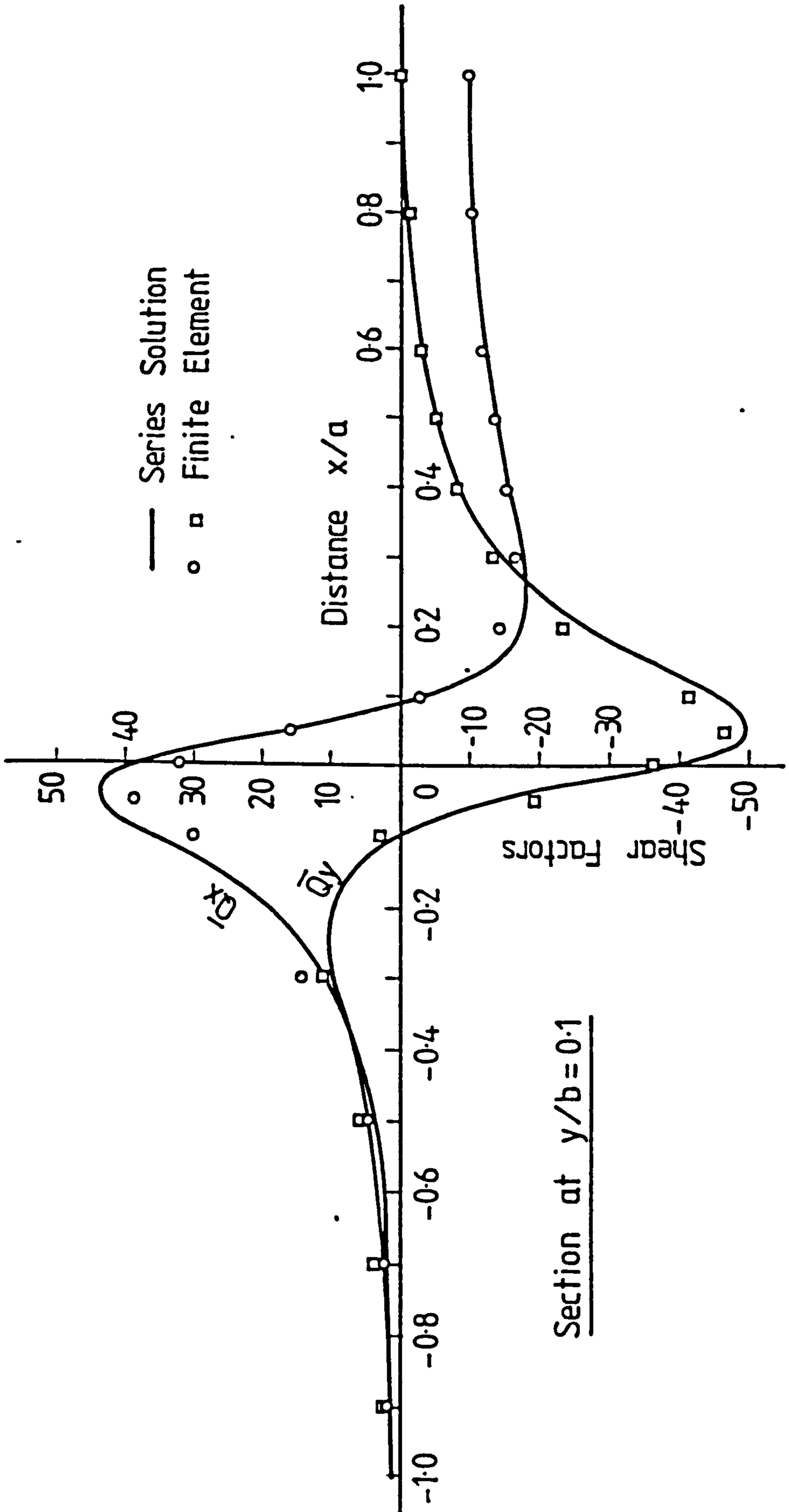

Fig. 4.18(d) Distribution of Shearing Forces at a Longitudinal Section

CHAPTER 5

EFFECTS OF LOCAL ELASTIC WALL DEFORMATION ON THE INTERACTION BETWEEN FLOOR SLABS AND SHEAR WALLS

5.1 INTRODUCTION

Methods of coupled wall analysis commonly use the engineer's theory of bending to describe the behaviour of wall sections under the action of lateral loads and coupling forces. The theory assumes that plane sections of the wall remain plane in bending, which implies that local deformations and stress concentrations do not arise in the wall. Following this simplifying assumption, the axial displacement of points on the wall/slab junction can be readily calculated from a knowledge of the wall rotation. This has allowed the analysis of wall/slab interaction to be conveniently carried out by considering only the slab in the analysis as described in Chapter 3. The results thus obtained have shown the presence of highly concentrated reactions at the coupled edges of the shear walls, due to the coupling action of the slab. In practice, such concentration of forces must lead to local elastic deformation in the wall. In coupled plane-walls, the local elastic deformations consist of only in-plane deformations. With coupled flanged walls, in addition to local in-plane deformation, out-of-plane bending of the relatively flexible wall flanges must also occur.

The flexibility of the slab/wall junction produced by the local elastic wall deformation reduces the coupling action of the slab. This would lead to higher cantilever wall stresses and deflections compared to values calculated assuming no local wall deformation. Therefore, neglecting the effects of local wall deformation when evaluating the coupling stiffness of the floor slab can lead to results which err on the unsafe side for the wall system. Also, by overestimating the coupling action of the floor slab, the design of the slab section, if

controlled by lateral load effects, may become too conservative, resulting in a wasteful use of materials, which can contribute significantly to the overall building cost since the wastage is repeated at a large number of floors in a multistorey building. It is therefore important to be able to evaluate the effects of local elastic wall deformation and to account for these effects in the calculation of the slab stiffness and slab stresses.

In this chapter the numerical results, obtained by the finite element method, showing the relative influence of various structural parameters on the wall/slab junction flexibility and on the coupling action of the slab are discussed. Design curves which allow the rapid evaluation of effective slab width and critical bending moment distribution for slabs coupling plane walls, T-section flanged walls and box cores, taking into account the effects of local elastic wall deformation, are presented. The significance of local elastic wall deformation effects in the design of the structure is illustrated by worked examples for typical cross-wall multistoreyed buildings.

5.2 METHOD OF ANALYSIS

The study of the wall-slab interaction which takes into account the effects of local elastic wall deformation can only be satisfactorily carried out by considering the wall and slab components together as an integral unit in the analysis. By assuming that the most significant elastic wall deformations due to the coupling action of the slab are localised in an area close to the wall slab junction, it is sufficient to consider only a section of each wall extending approximately one floor height above and below the floor slab in the analysis. The finite element method is again used to analyse the wall-slab interaction. Because of the spatial nature of the wall slab assembly it is necessary to use for the finite element analysis flat shell elements capable of representing in-plane as well as bending deformations which arise due to the interaction

of the various plate components. By taking advantage of the symmetry and anti-symmetry conditions which exist in the plan configuration, the actual analysis for the complete interior wall/slab panel can be reduced to the analysis of a typical quarter-panel as shown in Fig. 5.1(a). By further taking advantage of the anti-symmetry condition with respect to wall deformation above and below the floor slab, one section of the wall can be omitted by doubling the stiffness of the other wall section and by restraining the slab against horizontal translation (Fig. 5.1(b)).

To evaluate the coupling stiffness of the slab against unit wall rotation, an arbitrary vertical deflection δ is imposed at the slab edge representing the line of inflexion at the centre of the corridor, while the remote ends of the wall are fully restrained (Fig.5.1(c)). The reaction Q at this edge is evaluated in the finite element analysis and the resultant moment of this reaction about the wall axis is calculated as

$$M = Q\, l_a$$

where $l_a = (L + W)/2$, and L and W are respectively the corridor width and wall length. Neglecting the effects of overall wall axial deformation and overall wall bending rotation at the wall-slab junction, which are found to be negligibly small in relation to the displacements in the slab, the effective slab rotation Θ is calculated simply as

$$\Theta = \delta / l_a$$

The slab stiffness factor K^* is then expressed as

$$K^* = \frac{M}{D\Theta}$$

and the effective slab width Y_e^*/Y is, from equation (3.3a),

$$\frac{Y_e^*}{Y} = \frac{K^*}{6(1-\nu^2)} \cdot \frac{L}{Y} \left(\frac{L}{L+W}\right)^2 \qquad (5.1)$$

where Y is the full slab width and ν is Poisson's ratio.

In order to provide a measure of the flexibility produced by local elastic wall deformation, the corresponding results for the case of a 'rigid wall' (no local elastic wall deformation) have to be evaluated. This can be done simply by re-analysing the same wall/slab panel with additional fixity conditions prescribed at the wall/slab junction, or more economically, by a separate analysis of the slab using only plate bending elements, as described in Chapter 3. If K and Y_e are respectively the slab stiffness factor and effective slab width evaluated for the case of a'rigid wall', then the junction flexibility may be conveniently measured by the stiffness ratio K^*/K $(= Y_e^*/Y_e)$.

The slab stiffness factor K^* or K refersto relative rotations of the ends of the equivalent beam, measured at the centre-line of the cross-wall. With an asymmetric wall section, for instance a T-section, the centre line of the cross-wall does not coincide with the centroidal axis of the whole section. The slab stiffness, referred to the centroidal axes, may be obtained from the results, referred to the centre line axes, simply by the relationship

$$\frac{K_c^*}{K^*} = \left(\frac{l_c}{I_a}\right)^2 \qquad (5.2)$$

where l_c is the distance from the centre of the corridor to the centroidal axis of the wall, and K_c^* is the slab stiffness referred to the centroidal axes.

5.3 ELEMENT EVALUATION

Two simple flat shell elements which have been successfully used for the analysis of various spatial or shell structures are examined in this study to assess their suitability for the present investigation on elastic wall/slab interaction allowing for local elastic wall deformation effects. Element RS24, which is built up from the rectangular bending element RB12 and the plane-

stress element RP8, has been used by Zienkiewicz and Cheung[26] in the analysis of arch dams and by Rockey and Evans[63] in the analysis of folded plate structures. The second element, TS18, formed by combining the triangular bending element TB9 with the constant-strain triangular plane-stress element TP6, has been used successfully in the analysis of various shell structures, by Parekh.[38]

The desirable convergence characteristics of the bending elements RB12 and TB9, and their superior performance over more refined elements, for the study of slab coupling, have been demonstrated in Chapter 3. The convergence characteristics of the plane stress elements RP8 and TP6, when used in the standard cantilever beam problem, have been reported in the literature. The superior performance of the rectangular element over the triangular element is generally accepted. In the present investigation on wall/slab interaction, the plane-stress element is to be used in a situation quite different from the standard beam problem. The element is now required to model the state of deformation in an elastic continuum subjected to concentrated loads applied within the continuum. The performance of the two plane-stress elements have therefore to be evaluated under the present conditions. In order to simplify the computation of exact values of deformation and stresses against which the finite element results could be compared, a standard problem of a half-plane subjected to a unit tangential point load at the straight edge is considered for the evaluation of the elements. This problem is considered reasonably representative of the slab-coupled plane-wall problem, where the most significant slab reaction on the wall consists of a concentrated force at the inner edge of the wall.

For the finite element analysis of the half-plane, a finite rectangular area enclosing the load point is considered. The boundaries of the area considered are assumed sufficiently remote from the influence of the point load such that deformations along the boundaries are

negligible. Two different mesh divisions are considered to give an indication of the convergence of the finite element solution. The two mesh divisions are shown together in Fig. 5.2. By taking advantage of the skew symmetry with regard to deformation or stresses above and below the normal axis y, only one half of the area above or below the y-axis is actually analysed. The influence of the other half is represented by doubling the values of the element stiffness matrices for the first half and by restraining points on the y-axis against horizontal displacements.

To check the relative accuracy of various finite element results, the distribution of displacements and stresses at a number of sections, evaluated by the finite element method, are compared with results from an elasticity solution.[64] Fig. 5.2 shows the comparison of results for the vertical displacement $\delta_{x,x=0}$ along the y-axis, the horizontal displacement $\delta_{y,y=0}$ along the free edge, the vertical stress $\sigma_{x,x=-2.5}$ along a horizontal section at x = -2.5, and the vertical stress $\sigma_{x,y=0}$ along the free edge.

In the elasticity solution,[64] the stresses are calculated according to the equation

$$\sigma_x = \frac{2P}{\pi} \frac{x^3}{(x^2+y^2)^2}$$

where P is the point load.

The displacements are calculated from the expressions

$$\delta_{x,x=0} = \frac{P}{\pi E} \left\{ (1+\nu) - (1-\nu) \frac{\pi}{2} + 2 \log \frac{y}{d} \right\}$$

and $$\delta_{y,y=0} = \frac{P}{E} \frac{(1-\nu)}{2} (1 - \frac{x}{d})$$

which are derived by assuming a point on the x-axis at distance d from the origin to be fully restrained from displacements in the x and y directions.[64] E and ν in the above expressions are respectively Young's modulus and Poisson's ratio.

It is seen from Fig. 5.2 that the numerical values of displacements and stresses obtained with both elements converge towards the elasticity solution, as the mesh size is reduced. Values of the displacements $\delta_{x,x=0}$ and $\delta_{y,y=0}$ at all points except the singular point beneath the load, calculated with the fine mesh rectangular element, agree very well with the elasticity solution. Corresponding values of stresses $\sigma_{x,x=-2.5}$ and $\sigma_{x,y=0}$ obtained by these two solutions also agree reasonably well. In the case of the fine mesh triangular element, it is seen that although the finite element values of $\delta_{x,x=0}$ agree very well with the elasticity solution, values of $\delta_{y,y=0}$, especially near the point load, show rather poor agreement with the results from the elasticity solution. The stress $\sigma_{x,y=0}$ obtained by the triangular element show very poor agreement with the elasticity solution near the point load, but elsewhere good agreement is obtained between the two results.

It can be seen that, generally, the rectangular element RP8 gives a better performance than the triangular element TP6. When a reasonably fine mesh is used in the discretisation of the continuum, the rectangular element can give reasonably accurate results for displacements as well as for stresses, and is therefore suitable for use, when combined with the bending element RB12, in the investigation of local elastic wall deformation effects in slab-coupled wall systems.

For the numerical investigations described in the following sections, the rectangular shell element RS24 is used as the primary element in the finite element analysis. The triangular element TS18 is used as a secondary element where required to provide a transition between fine and coarse rectangular element mesh patterns.

5.4 COUPLED PLANE-WALL CONFIGURATION

5.4.1 VARIABLES TO BE CONSIDERED

The local elastic deformation in plane walls, due to the coupling action of floor slabs, consist only of in-plane deformations. Since for a unit wall rotation, the magnitude of the reaction, transferred from the slab to the wall, depends on the slab thickness, and the amount of wall deformation under load is dependent on wall thickness, the relative slab and wall thicknesses must have an important influence on the extent of local elastic wall deformation and on the effective coupling stiffness of the slab. The wall dimensions, viz., the height and length, can be expected to have some influence on the coupling stiffness of the slab, since the wall-slab junction deformation is affected to a certain extent by the proximity of the wall boundaries. The corridor opening width and the slab width both influence strongly the coupling stiffness of the slab as shown in the previous Chapter. The effect of local elastic wall deformation can be expected to vary for different corridor opening ratios and slab aspect ratios.

5.4.2 CONVERGENCE WITH MESH DIVISION

In order to provide some guidance on the choice of suitable mesh divisions for the parameter study, three different mesh divisions ranging from coarse to fine, as reflected in the sub-division of the wall, are considered for the discretisation of the wall/slab panel having the characteristic ratios L/X = 0.2, Y/X = 0.4 and F/W = 0.5. The wall and slab thicknesses are taken as h = 305 mm (12 in.) and t = 229 mm (9 in.) respectively, with the building width X = 15.25 m (50 ft.). The three element mesh divisions for the wall/slab panel analysed are shown in Fig. 5.3. For Mesh 2 and Mesh 3, the sub-division of the wall is varied in mesh size, with the finest mesh in the region where the slab reaction is most highly concentrated.

Values of slab stiffness factor K^*, and effective width Y_e^*/Y, obtained from the finite element analyses are shown in Table 5.1, from which it can be seen that the results for the three different mesh divisions are almost identical. It may be noted that the results obtained do not indicate monotonic convergence with respect to mesh size. This often happens when non-conforming elements are used for the finite element analysis. Since the results for the three mesh divisions are in very close agreement, it is unlikely that further mesh refinement will produce any substantial change in the results. It appears clear that there is not much point in sub-dividing the wall more finely than in Mesh 2. Although the results obtained from Mesh 1 are as good as the results for the finer meshes, the sub-division of the wall appears disproportionately coarse in comparison with the sub-division of the slab. Mesh 2, on the other hand, gives a more balanced sub-division of the wall and slab and also has reasonable computer requirements. Mesh patterns similar to Mesh 2 will therefore be used in the parameter study.

5.4.3 COMPARISON OF RESULTS OBTAINED BY RECTANGULAR AND TRIANGULAR ELEMENTS

In order to provide a check on the convergence results obtained by the rectangular elements an analysis of the wall/slab panel is performed using the triangular shell element TS18. The triangular mesh division of the wall/slab panel corresponds to Mesh 2 in the convergence study, with the sub-division of the rectangular mesh into two triangles along a diagonal. Values of K^* and Y_e^*/Y obtained by the two different elements are compared below:

Element Type	K^*	Y_e^*/Y
Rectangular Element RS24	34.071	0.3227
Triangular Element TS18	34.466	0.3264

It is seen from the comparison that the results for the

triangular element are just over 1% higher than the results for the rectangular element. The close agreement between the results obtained by two different elements may be taken as an indication of the reliability of the results.

5.4.4 INFLUENCE OF STOREY HEIGHT

In this investigation, three storey heights defined by F/X = 0.1, 0.2 and 0.3 are considered for a wall/slab configuration with L/X = 0.2, Y/X = 0.4 and t/h = 0.75, X being taken as 15.25 m (50 ft) and h as 0.305 m (1 ft). The slab stiffness factor K^* and the effective width Y_e^*/Y evaluated for the three storey-heights are compared in Table 5.2 in which is also shown the corresponding results for the case of rigid walls. It is seen from the results that varying the storey height over the practical range considered has very little effect on the coupling stiffness of the slab. The difference between values of K* or Y_e^*/Y for the smallest and largest storey heights is less than 1%. The flexible-wall results are approximately 80% of the rigid-wall results.

5.4.5 INFLUENCE OF WALL LENGTH

In this investigation, three wall lengths with W/L = 0.5, 0.75 and 1.0 are considered for slabs with a constant ratio Y/L of unity and with slab to wall thickness ratios t/h of 0.5 and 0.75. The corridor opening width L and the wall thickness h are respectively taken as 6.10 m (20 ft) and 0.305 m (1 ft.). The results obtained for the effective width Y_e^*/Y for the various cases are shown in Table 5.3, in which are also shown the results for the case of rigid walls. It can be seen from the results that for the range of ratios W/L greater than 0.5, the influence of wall length on the effective width is very small. The difference between the results for W/L = 0.5 and W/L = 0.75 is of the order of $1\frac{1}{2}$%, the result for W/L = 1.0 being practically identical to that for W/L = 0.75.

5.4.6 INFLUENCE OF WALL AND SLAB THICKNESSES

The influence of wall thickness and the influence of slab thickness on the effective coupling of locally deformable walls is investigated for a typical wall/slab configuration with L/X = 0.2 and Y/X = 0.4, X being taken as 15.25 m (50 ft). The storey height F for the wall is taken as 3.05 m (10 ft) in all cases. The wall thickness and the slab thickness, expressed respectively as $\eta = 50h/X$ and $\xi = 50\ t/X$ for convenience, are varied over the range $\eta = 0.5$ to 2.0 and $\xi = 0.125$ to 2.0 to cover all likely wall and slab dimensions encountered in practical buildings. Four slab/wall thickness ratios given by t/h = 0.25, 0.5, 0.75 and 1.0 are obtained by various combinations of the slab and wall thicknesses to enable the influence of this parameter to be examined. The finite element discretisation of the wall/slab panel follows Mesh 2 shown in Fig. 5.3.

The numerical values of the slab stiffness factor K* and the effective width Y_e^*/Y evaluated for the various cases are shown in Appendix A5.1. Values of the stiffness ratio K*/K representing the ratio of 'flexible' wall coupling stiffness to the 'rigid' wall coupling stiffness have also been included in the same Appendix. The variation of K*/K as a function of η is shown graphically in Fig. 5.4(a) for various values of ξ and t/h. It can be seen from the curves that with a constant slab thickness ξ, K*/K increases with increasing wall thickness η, whereas with a constant wall thickness η, K*/K decreases with increasing values of slab thickness ξ and slab wall thickness ratio t/h.

The values of K*/K for all combinations of η and ξ can in fact be plotted on a single curve showing K*/K as function of $\xi/\eta^{1/3}$ as shown in Fig. 5.4(b). This follows from the fact that the slab reaction varies cubically with the slab thickness, and the elastic wall deformation varies directly with the slab reaction and inversely with the wall thickness. It can be seen from Fig. 5.4(b) that

K^*/K decreases with increasing values of $\xi/\eta^{1/3}$. According to this reasoning, the effects of local elastic wall deformation should vanish as the slab thickness approaches zero or as the wall thickness becomes infinitely large, which means that K^*/K should approach unity when $\xi/\eta^{1/3}$ approaches zero. Although the curve in Fig. 5.4(b) indicates this trend most of the way from $\xi/\eta^{1/3} = 1.6$ to 0.5, K^*/K approaches a maximum value of approximately 0.92 instead of unity. This inconsistency may be due to the influence of numerical errors introduced into the finite element solution when the disparity between the slab thickness and wall thickness becomes too large. The inconsistent portion of the curve, however, is of no practical significance, since in practice the value of $\xi/\eta^{1/3}$ is seldom less than 0.5, at which value the effects of local elastic wall deformation are practically negligible.

5.4.7 INFLUENCE OF SLAB WIDTH AND CORRIDOR OPENING WIDTH

Having established that the stiffness ratio K^*/K varies with the single parameter $\xi/\eta^{1/3}$ instead of with two independent parameters ξ and η for a particular wall slab configuration, it is now easier to examine the influence of the two remaining parameters, namely, the slab aspect ratio Y/X and the corridor opening ratio L/X, simultaneously with the variation of $\xi/\eta^{1/3}$. For this investigation, it is convenient to consider unit value of η, i.e. $50h/X = 1$. The other variables are varied over a wide range of values covering most practical situations. The building width X and storey height F, are again taken as 15.25 m (50 ft) and 3.05 m (10 ft) respectively for this investigation. The finite element discretisation of the wall/slab panel uses between 159 and 201 nodes depending on the structural dimensions.

The values of the slab stiffness factor K^* and the effective width Y_e^*/Y evaluated from the finite element analyses are shown in Appendices A5.2,(a) and (b), respectively. The corresponding results for the case of

rigid walls have also been included in these Appendices to provide a measure of the flexibility produced by local elastic wall deformation. Curves showing the variation of Y_e^*/Y as a function of L/X for various values of $\xi/\eta^{1/3}$ and Y/X are presented in Fig. 5.5(a)-(c). These may be used as design curves to evaluate directly the effective widths of slabs coupling 'flexible'walls which allow for local elastic wall deformation. It can be seen from the curves that Y_e^*/Y decreases almost linearly with the increase in the value of $\xi/\eta^{1/3}$ for most of the range of the ratios L/X and Y/X.

Values of the stiffness ratio K*/K (evaluated from the results of Appendix A5.2(a) or (b)) are shown in Table 5.4 from which it can be seen that K*/K is influenced significantly by $\xi/\eta^{1/3}$ and L/X but not by Y/X. The variations of K*/K, averaged over the range of ratios Y/X considered, as a function of $\xi/\eta^{1/3}$ for various ratios L/X, and as a function of L/X for various values $\xi/\eta^{1/3}$ are shown graphically in Fig. 5.6(a). These curves may be used in conjunction with the design curves for Y_e/Y presented for the case of rigid walls in Chapter 3, to evaluate more accurately the effective slab width which accounts for the effects of local elastic wall deformation. It can be seen from the variation of K*/K with L/X that the effects of local elastic wall deformation become more significant when the wall-opening ratio becomes smaller. With very narrow corridor openings, (i.e., with L/X < 0.2) there is a substantial reduction in the coupling stiffness of the slab produced by the local wall deformation.

5.4.8 DESIGN CURVE FOR STIFFNESS RATIO

In Fig. 5.6(a) the variation of K*/K with the various parameters has been described by a series of curves. In evaluating the stiffness ratios for specific slabs, the need to interpolate between the curves generally makes the use of these curves rather inconvenient. By a proper combination of the principal variables which influence the

variation of K*/K, it is possible to reduce the number of curves required to describe the variation of K*/K fully to just one single curve. If the values of K*/K for various combinations t, h and L from Table 5.4 are plotted as a function of $t/(L^2h)^{1/3}$, all the plotted points will be seen to lie very close to a single curve which is shown in Fig. 5.6(b). This seems to follow from the fact that the end reactions of a flexural member subjected to a constant end rotation vary inversely as the square of the span length and directly as the cube of the member thickness, and from the fact that the elastic wall deformation varies directly with the slab reaction and inversely with the wall thickness.

The curve of K*/K against $t/(L^2h)^{1/3}$ shown in Fig. 5.6(b) becomes much more convenient to use as a design curve than the previous sets of curves shown in Fig. 5.6(a). As mentioned previously, K*/K is practically unaffected by the variation in slab aspect ratio Y/X. Therefore the design curve in Fig. 5.6(b) may be used for all practical slab aspect ratios. It may be noted from the trend of the curve that K*/K approaches zero when $t/(L^2h)^{1/3}$ becomes very large amd K*/K attains a value of unity when $t/(L^2h)^{1/3}$ is zero.

5.4.9 EFFECTIVE SPAN EXTENSION

The wall/slab junction flexibility due to the local elastic wall deformation may be accounted for in the calculation of the lateral stiffness of the coupled wall system by evaluating the stiffness of the coupling slab either from the 'flexible wall' effective slab width given by the curves in Fig. 5.5(a) to (c) or from the 'rigid wall' effective slab width in conjunction with the stiffness ratio given by the curve in Fig. 5.6(b). In either case, the actual clear opening between the walls is used as the span of the equivalent coupling beam in the stiffness calculation. Another convenient way of allowing for the additional wall/slab junction flexibility, when

the 'rigid wall' effective slab width is used in the stiffness calculation for the coupled wall system, is to allow an effective extension of the clear span of the equivalent coupling beam. For beam-coupled wall systems Michael[65] and Bhatt[66] have shown that the effective span extension could be approximately taken as equal to the beam depth. Such a simple approximation, it will be shown, cannot be applied to the case of slab coupled wall systems.

The effective span extension can be related to the stiffness ratio K*/K as follows:-

The stiffness factor of the coupling slab is given by

$$K = 6(1-\nu^2)\, z^2 Y_e / L^3$$

where z = (L+W), the distance between wall centroids. With similar values for z and for Y_e in both the 'flexible wall' and 'rigid wall' cases, the stiffness ratio can be expressed as

$$K^*/K = (L/L^*)^3 \qquad (5.3)$$

in which L* is the extended 'flexible' span of the equivalent beam, given by

$$L^* = L + e$$

where e is the effective span extension.
The effective span extension may then be expressed as

$$\frac{e}{L} = \left(\frac{K}{K^*}\right)^{1/3} - 1 \qquad (5.4)$$

The effective span extension is seen to be influenced by the clear span L, the wall thickness h and the slab thickness t. Since Michael's approximation when applied to the coupling slab would apparently consider only the influence of the slab thickness t, it is seen to be inapplicable in this case. The curve of e/L against $t/(L^2 h)^{1/3}$ has been included in Fig. 5.6(b) as a supplementary design curve.

5.4.10 INFLUENCE OF LOCAL ELASTIC WALL DEFORMATION ON CRITICAL BENDING MOMENTS IN SLAB

Curves showing the distribution of longitudinal bending moment factors $\bar{M}_x$ (cf. Section 3.4.2.4) along the critical transverse slab section through the coupled end of the wall, for 'flexible' wall configurations with various t/h, L/X and Y/X ratios are shown in Fig. 5.7(a) to (f). The curve for the case of 'rigid' wall has been included in each set of curves for the purpose of comparison. The curves for various slab/wall thickness ratios are based on results obtained assuming a constant wall thickness h = 0.305 m (1 ft) and a constant slab length X = 15.25 m (50 ft). In the finite element analysis for each case, the wall and slab were idealised as interconnected along a line of nodes at the intersection of their middle planes.

It is seen from the various sets of curves that the critical bending moment distribution is strongly influenced by the slab/wall thickness ratio. With normal slab/wall thickness ratios ranging from 0.5 to 1.0, the effects of wall/slab junction flexibility result in a substantial reduction in the slab moment factors, especially in the critical region around the coupled ends of the wall. The reduction in critical moment factors is seen to be strongly influenced by the corridor opening ratio, but not by the slab aspect ratio. This is in agreement with observations on the reduction of slab stiffness due to local wall deformation effects.

The curves for the 'flexible' wall cases may be used to evaluate, more realistically than is possible with curves for 'rigid' wall cases, the critical bending moments required for the preliminary design of the slab section.

5.5 COUPLED FLANGED WALL (T-SECTION) CONFIGURATION

5.5.1 VARIABLES TO BE CONSIDERED

The variables, namely wall thickness, slab thickness, slab width and corridor opening width, which have been

considered for plane wall configurations must also have some influence on the local elastic wall deformation in flanged wall configurations. Since out-of-plane bending of the wall flanges occurs in addition to in-plane deformation when the slab interacts with the wall, the relative slab/wall flexural stiffness should have an important influence on the flexibility of the slab/wall junction. The wall flange becomes more flexible as the flange width increases, and therefore the influence of flange width ratio must also be considered in addition to the slab/flange thickness ratio. The effect of differences between web and flange wall thicknesses is not expected to be significant in the evaluation of slab/wall junction flexibility due to local elastic deformation effects, since the slab/wall interaction is effected principally at the directly-coupled flanges. Therefore, to minimise the number of variables which have to be considered, equal web and flange wall thicknesses are assumed in this investigation, since most practical flange walls are constructed as such.

5.5.2 FINITE ELEMENT DISCRETISATION

A typical finite element idealisation of the flanged wall/slab panel considered in this investigation is shown in Fig. 5.8. Symmetry conditions allow the analysis to be performed on the reduced structure shown. Rectangular and triangular flat shell elements are used together in the same analysis, the triangular elements being introduced to allow a transition from a coarse to a fine mesh formed by the rectangular elements. The coarsest mesh is used in regions where least coupling action is expected (i.e. in the wall web and in the slab behind the flange line). The finest mesh is used in the areas around the flange/slab junction where large rapidly varying stresses and deformations are expected. The use of varied rectangular mesh patterns with triangular mesh transitions allows the number of elements or nodes for the problem to be kept to

a reasonable minimum and eliminates the use of unduly elongated rectangular elements. Throughout the investigation, the number of nodes used in the discretisation varied between 142 and 156 nodes depending on the structural dimensions.

5.5.3 EFFECTIVE FLANGE WIDTH

The presence of local elastic wall deformation reduces the effective width of the floor slab. The reduction in the effective slab width may be imagined as being produced by an equivalent reduction in the flange width of a rigid flanged wall in which no local elastic wall deformation occurs. By comparing the value of the 'flexible wall' effective slab width with values for 'rigid' walls of various flange widths Z, an effective 'rigid' flange width Z* can be established for the 'flexible' wall. The use of an effective flange width then allows the correct effective slab width to be evaluated from design data presented for slabs with rigid flanged walls.

5.5.4 INFLUENCE OF STOREY HEIGHT

For plane wall configurations it has been shown in Section 5.4.4 that the wall/slab junction flexibility due to local elastic wall deformation is practically unaffected by variations in the storey height. For the flanged wall configuration it appears possible that variations in storey height may have some significant influence on the wall/slab junction flexibility because of bending of the wall flanges. In this investigation two practical storey heights F/X of 0.2 and 0.3 are assumed in the evaluation of the coupling stiffness of a slab in a typical flanged wall configuration with Y/X = 0.4, L/X = 0.2 and Z/Y = 0.5, X being assumed as 15.25 m (50 ft). The wall and slab thicknesses are assumed to be respectively 0.305 m (1 ft) and 0.229 m (0.75 ft). The numerical results obtained for K*, Y_e^*/Y and K*/K for the two cases are shown in Table 5.5. It is seen that the

results for the two different storey heights do not differ by more than ½%, indicating once again that the influence of storey height may be neglected in the evaluation of local elastic wall deformation effects on the coupling slab.

5.5.5 INFLUENCE OF WALL THICKNESS AND SLAB THICKNESS

The influence of wall thickness and slab thickness on wall/slab junction flexibility is investigated for a typical flanged wall configuration with Y/X = 0.4, L/X = 0.2 and Z/Y = 0.5, X being taken as 15.25 m (50 ft). Two slab/wall thickness ratios t/h of 0.5 and 1.0 are considered, and these ratios are made up of various combinations of slab thickness t and wall thickness h. The slab thickness and wall thickness are respectively varied over the range t = 0.153 m (0.5 ft) to 0.305 m (1.0 ft) and the range h = 0.153 m (0.5 ft) to 0.61 m (2.0 ft), covering most practical situations.

The numerical results obtained for the slab stiffness factor K*, the effective width Y_e^*/Y and the stiffness ratio K*/K are shown in Table 5.6 for the various wall and slab combinations. It is seen from these results that for a fixed slab/wall thickness ratio t/h, increasing the slab thickness t and the wall thickness h increases only marginally the flexibility of the wall/slab junction, the effect being relatively greater for the larger t/h ratio, where a 4% difference between the largest and smallest values of K*/K is noted. Since for a fixed slab/wall thickness ratio t/h, variations in the slab thickness t and wall thickness h do not affect the wall/slab junction flexibility significantly, compared to the influence of the slab/wall thickness ratio itself, only one value of the slab thickness t = 0.23 m (0.75 ft), will be considered when the influence of other parameters is investigated.

5.5.6 INFLUENCE OF SLAB/WALL THICKNESS RATIO

The influence of slab/wall thickness ratio t/h on wall/slab junction flexibility is investigated by varying

t/h over a wide range of values from 0.25 to 1.5, in the typical configuration described in the preceding section. Values of K*, Y_e^*/Y, K*/K and Z*/Z evaluated for the various cases are given in Appendix A5.3. The variations of Y_e^*/Y, K*/K and Z*/Z with t/h are shown graphically in Fig. 5.9(a).

It is seen from the curves that the slab/wall thickness ratio has a strong influence on junction flexibility; increasing the ratio t/h decreases the values of Y_e^*/Y, K*/K and Z*/Z. The influence of t/h is relatively more significant within the range t/h of 0.5 to 1.0. The effective flange width ratio Z*/Z is more sensitive than the stiffness ratio K*/K, to variations in the slab/wall thickness ratio t/h.

5.5.7 INFLUENCE OF CORRIDOR OPENING RATIO

The influence of the corridor-opening ratio L/X on wall/slab junction flexibility is investigated for configurations with constant values of Y/X = 0.4, Z/Y = 0.5 and t/h = 0.75. The corridor opening ratio L/X is varied over the range 0.1 to 0.6 covering most practical ratios. Values of K*, Y_e^*/Y, K*/K and Z*/Z evaluated for various ratios of L/X are given in Appendix A5.4. Fig. 5.9(b) shows the variations of Y_e^*/Y, K*/K and Z*/Z with L/X.

It is seen from the curves that the effects of junction flexibility become more significant when the corridor-opening ratio is reduced. The effective width Y_e^*/Y and the stiffness ratio K*/K decrease substantially when L/X is reduced from 0.6 to 0.1, but the effective flange width Z*/Z is not affected significantly by the variation of L/X over this wide range.

5.5.8 INFLUENCE OF FLANGE WIDTH RATIO

The influence of flange width ratio Z/Y on wall/slab junction flexibility is investigated in wall/slab configurations with constant typical values of Y/X = 0.4,

L/X = 0.2 and t/h = 0.75. Three flange width ratios Z/Y = 0.25, 0.5 and 0.75 are considered together with the limiting case of Z/Y = 0.0 which corresponds to a plane wall configuration. The numerical results for the quantities K*, Y_e^*/Y, K*/K and Z*/Z are shown in Appendix A5.5. The variations of the last three quantities with Z/Y are illustrated in Fig. 5.9(c).

It is seen from the curves that the local elastic wall deformation produces larger reductions in the effective width of the slab with larger flange width ratios. The stiffness ratio K*/K however remains substantially constant over the range of flange width ratios considered. The effective flange width Z*/Z is also not affected significantly by the flange width ratio when Z/Y is larger than about 0.25. With smaller ratios Z/Y, the effective flange width Z*/Z decreases rapidly with a reduction in flange width ratio Z/Y.

5.5.9 PRESENTATION OF DESIGN CURVES

It is clear that in evaluating the slab stiffness or effective width which accounts for the effects of local elastic wall deformation, the influence of the principal parameters t/h, L/X, Z/Y and Y/X will have to be considered. To enable the production of useful design curves for evaluating the correct design information rapidly, numerical results for the slab stiffness factor K*, the effective slab width Y_e^*/Y, the stiffness ratio K*/K and the effective flange width Z*/Z have been obtained for slab /wall configurations with a reasonably wide range of values for the principal parameters involved.

5.5.9.1 Design Curves For Evaluating the Effective Slab Width

The numerical values of K* and Y_e^*/Y obtained directly from the finite element analyses for the various cases investigated are shown in Appendices 5.6, (a) and (b). Curves showing the variation of Y_e^*/Y as a function of L/X

for various ratios of t/h are presented in Fig. 5.10, (a) to (f), for various ratios of Y/X and Z/Y. These six sets of curves may be used as design curves for evaluating directly the effective slab width, accounting automatically for the effects of local elastic wall deformation. By comparing the curves for various ratios of t/h with the curves for the case of a rigid wall, it is seen that for most practical buildings, where t/h generally varies between 0.75 and 1.0, the effects of local elastic wall deformation can result in a substantial reduction in the effective slab width, particularly when the corridor-opening ratio or the flange width ratio is large.

5.5.9.2 Generalised Design Curves For Evaluating Effective Slab Width

The curves presented in Fig. 5.10(a) to (f) account for the influence of wall length W and slab length X in the evaluation of the effective slab width. For most practical cases, the influence of these parameters may be neglected so that instead of considering Y_e^*/Y as a function of L/X and Y/X, it is necessary only to consider Y_e^*/Y as a function of L/Y, when the other variables t/h and Z/Y remain constant. The two sets of curves for Y/X = 0.4 and 0.6 with the same ratio Z/Y, showing the variation of Y_e^*/Y as a function of L/X, can therefore be represented by a single generalised set of curves for the particular ratio Z/Y, showing Y_e^*/Y as a function of L/Y, for various ratios t/h. The three sets of curves in Fig. 5.10(a), (b) and (c), for the case of Y/X = 0.4, may be converted to generalised sets simply by replacing the function L/X with the new function L/Y and by changing the scale of the horizontal axis in each set. The resulting generalised sets of curves are shown in Fig. 5.11(a), (b) and (c). These curves are now applicable to slabs with any normal ratios of Y/X, as can be seen by comparing values of Y_e^*/Y obtained from these curves with

values obtained from the curves for Y/X = 0.6 in Fig. 5.10 (d), (e) and (f).

5.5.9.3 Design Curves For Evaluating The Stiffness Ratio

The numerical results for the stiffness ratio K*/K (evaluated from the results in Appendices 5.6(a) and (b)), are shown in Table 5.7. It is seen from these results that with any set of values for L/X, t/h and Z/Y, the stiffness ratio K*/K is not affected significantly by the slab aspect ratio Y/X. The stiffness ratio is also not affected significantly by the flange width ratio Z/Y when t/h is 0.75 or less.

The curves showing the variation of K*/K with L/X and t/h for various Y/X and Z/Y ratios are shown in Fig. 5.12, (a) to (f). These curves, it will be noted, are similar in form to the curves presented in Fig. 5.6(a) for plane wall configurations. If desired, these curves may be used as design curves for evaluating the wall/slab junction flexibility due to the effects of local elastic wall deformation. The stiffness ratios evaluated from these curves can be used to correct the effective width evaluated from the curves presented for the case of rigid walls, in order to account for the effects of local elastic wall deformation.

5.5.9.4 Approximate Curves For Evaluating The Stiffness Ratio

In order to reduce the number of curves required to describe the variation of K*/K with the various parameters, values of K*/K obtained from Table 5.7 and from the curves in Fig. 5.12, (a) to (f), are plotted as a function of $(t/h)/(L/X)^{\frac{1}{2}}$ in Fig. 5.13, (a) to (f), for various ratios of Z/Y and Y/X. It can be seen from each diagram that the points plotted for all values of t/h from 0.375 to 1.5 and L/X from 0.1 to 0.6 are distributed in a narrow band which may be approximated reasonably well by a single curve drawn through the middle of the band, the approximation

being more accurate with larger flange width ratios. The approximate curves of K*/K against $(t/h)/(L/X)^{\frac{1}{2}}$ for various ratios Z/Y are presented in Fig. 5.14(a) for the case of Y/X = 0.4. These curves should prove more convenient to use as design curves than the more accurate sets of curves presented in Fig. 5.12(a) to (f), since interpolation between values of t/h and L/X is unnecessary when using the approximate curves to evaluate K*/K. The approximate curves are also reasonably accurate, giving values of K*/K which are generally within 5% of the accurate values given by the more accurate sets of curves. Similar approximate curves may be drawn for the case of Y/X = 0.6, but these curves will not be significantly different from the set presented for the case of Y/X = 0.4, since K*/K is not significantly influenced by the slab aspect ratio.

The set of curves for Y/X = 0.4 can be used indirectly for evaluating approximately the stiffness ratio for other slab aspect ratios. As was shown in Section 5.5.9.2, the influence of wall length W or slab length X can be neglected in the evaluation of effective slab width, and Y_e^*/Y is essentially a function of L/Y when t/h and Z/Y are constant. Therefore, with any particular slab, the value of X may be arbitrarily adjusted so that the ratio Y/X becomes 0.4. Then, if the adjusted value of X is used in the calculation of the factor $(t/h)/(L/X)^{\frac{1}{2}}$, the value of K*/K, obtained from Fig. 5.14(a), gives a reasonably good estimate of the stiffness ratio for the slab.

5.5.9.5 Design Curves For Evaluating the Effective Flange Width

The numerical results for the effective flange width Z*/Z for the various cases investigated are shown in Table 5.8. It is seen from these results that Z*/Z is influenced largely by the slab/wall thickness ratio and much less by the other three variables, L/X, Y/X and Z/Y. The curves

showing the variation of Z*/Z as a function of t/h, for various L/X and Z/Y ratios are presented in Fig. 5.14(b), for the case of Y/X = 0.4. For clarity, only three curves are drawn to represent the series of curves for combinations of L/X and Z/Y, since many of the curves overlap. These curves may be used as design curves, if desired, to evaluate the effective flange width for a pair of coupled flanged walls; after which use can be made of the design curves presented for the case of rigid walls, to evaluate the correct effective slab width.

Again, the curves of Z*/Z against t/h, if drawn for the case of Y/X = 0.6, will not be significantly different from the set for Y/X = 0.4. For most practical cases, the effective flange width ratio can be evaluated from the set of curves for Y/X = 0.4, by disregarding the influence of the slab aspect ratio.

5.5.10 INFLUENCE OF LOCAL ELASTIC WALL DEFORMATION ON CRITICAL BENDING MOMENTS IN THE SLAB

In order to illustrate the influence of local wall deformation on critical bending moments which may control the design of the slab section, curves are presented in Fig. 5.15, (a) to (i), showing the distribution of longitudinal bending moment factors $\bar{M}_x$ along the critical transverse slab section at the inner edge of the flanged wall, for configurations with a typical ratio Y/X of 0.4, but with various ratios of t/h, L/X and Z/Y. The curve for the case of a 'rigid' wall, which should be theoretically similar to the case of t/h = 0, has been included with each set of curves for 'flexible walls, for the purpose of comparison.

It is seen from the various curves that the effects of local wall deformation result in a significant reduction in the large bending moment factors in the slab, in front of the wall flanges. Since increasing the slab/wall thickness ratio increases the wall/slab junction flexibility, the reduction in bending moment factors becomes relatively

more significant with larger ratios t/h. Also, as the flanges are more flexible at the ends than at the centre where they are stiffened by the cross wall (web wall), the reduction in bending moment factors is relatively larger at points near the flange tip than at other points nearer the flange centre. The flange becomes more flexible as the flange width increases. This is seen to result in a larger reduction in bending moment factors near the flange tip, with a larger flange width ratio Z/Y. The reduction in bending moment factors near the flange centre is however unaffected significantly by the flange width ratio, but is seen to be significantly influenced by the corridor opening ratio L/X. This can be expected since the bending moment factors in this part of the slab would be influenced primarily by in-plane deformation of the web rather than by flexural deformation of the flange.

By comparing the sets of curves for various corridor opening ratios L/X, it is seen that the local wall deformation effects produce, at the flange centre position, a decrease in the bending-moment factor when L/X is small (L/X = 0.1 - 0.2) and an increase in the bending-moment factor when L/X is large (L/X = 0.4). This seems to be consistent with the fact that as the ends of the flange become flexible, the coupling action is redistributed towards the stiffer part of the flange at the centre. The load redistribution would result in an increase in the slab bending-moment factors at the centre of the flange, but with small ratios of L/X, this increase would be offset by the larger reduction in bending-moment factors due to in-plane deformation effects.

It is seen from the curves that with t/h = 1 and L/X = 0.1, which are not unusual ratios for certain classes of cross-wall structures, the effects of local elastic wall deformation could result in as much as 50% reduction in the bending moment factors over a considerable portion of the slab in front of the wall flanges. The curves presented in Fig. 5.15, (a) to (i), may be used to evaluate realistically the critical bending moments for the

preliminary design of the slab section.

5.6 COUPLED BOX-CORE CONFIGURATION

5.6.1 VARIABLES TO BE CONSIDERED

The slab coupling a pair of box-cores and the slab coupling a pair of flanged walls which have the same flange width as the box-cores, behave essentially alike, when the effects of local elastic wall deformation are disregarded. Since the local elastic wall deformations arise predominantly in the coupled wall flanges, the coupling stiffness of the slab in both configurations will be influenced by similar factors, though the relative influence of various parameters may not be exactly alike in both configurations.

5.6.2 FINITE ELEMENT DISCRETISATION

The discretisation of the core/slab panel for the finite element analysis follows a similar strategy described for the flanged wall configuration. A typical finite element idealisation of the structure considered in the investigation is shown in Fig. 5.16. The number of nodes used varied between 121 and 125 nodes depending on the structural dimensions.

5.6.3 INFLUENCE OF STOREY HEIGHT

The influence of storey height on core/slab junction flexibility due to local deformation effects is investigated by considering two extreme practical storey heights F/X of 0.2 and 0.3 for a typical core and slab configuration with L/X = 0.2, Y/X = 0.4 and Z/Y = 0.5. Three slab/wall thickness ratios t/h = 0.75, 1.0 and 1.5 are considered with each storey height since the influence of storey height is unlikely to be similar with different slab/wall thickness ratios.

Values of the stiffness factor K*, the effective slab width Y_e^*/Y and the stiffness ratio K*/K obtained for the

various cases are shown in Table 5.9. It is seen from these results that increasing the storey height F/X from 0.2 to 0.3 reduces slightly the stiffness ratio K*/K, this effect being relatively more pronounced for larger slab/wall thickness ratios. However the influence of variation in storey height over the range considered is generally too small to be of any real practical significance. In the worst case considered (t/h = 1.5), the numerical results obtained for the two storey heights differ by about 4% only. For subsequent investigations involving the influence of other parameters, therefore, a constant practical storey height of F/X = 0.2 only will be considered.

5.6.4 INFLUENCE OF SLAB AND WALL THICKNESSES

The effects produced by variations in slab and wall thicknesses, while maintaining a fixed slab/wall thickness ratio, is investigated for a typical configuration with L/X = 0.2, Y/X = 0.4, Z/Y = 0.5 and X = 15.25 m (50 ft). Two slab/wall thickness ratios, t/h of 0.5 and 1.0, which are obtained by various combinations of practical slab and wall dimensions, are considered.

Table 5.10 shows the numerical results obtained for the important quantities K*, Y_e^*/Y and K*/K for the various cases. It is seen from the results that with a fixed ratio t/h, varying the values for t and h over the practical range has only a small effect on the results for the slab. Increasing the values of t and h has the effect of slightly increasing the flexibility of the wall/slab junction or reducing the stiffness of the slab, although the effect generally is too small to be of real significance.

5.6.5 INFLUENCE OF SLAB/WALL THICKNESS RATIO

The influence of slab/wall thickness ratio is investigated by varying t/h over a wide range of values from 0.25 to 1.5 in the typical configuration described in the preceding section. The numerical results for the

various cases are given in Appendix A5.7. Curves showing the variation of Y_e^*/Y, K*/K and Z*/Z as functions of t/h are shown in Fig. 5.17(a). Comparing this figure with Fig. 5.9(a) for the flanged wall configuration, it is seen that the trends of the results in both cases are similar. Values of K*/K for the box-core configuration are generally 2 to 3% higher than corresponding values for the flanged wall configuration when t/h has a value of 1.0 or less.

5.6.6 INFLUENCE OF CORRIDOR-OPENING RATIO

The influence of the corridor-opening ratio on the wall/slab junction flexibility is investigated by varying L/X over the range of values from 0.1 to 0.6, in a slab with t/h = 0.75, Y/X = 0.4 and Z/Y = 0.5. The numerical results for the usual quantities evaluated for the various cases are given in Appendix A5.8. Fig. 5.17(b) shows the variations of Y_e^*/Y, K*/K and Z*/Z as functions of L/X. Again, by referring to the corresponding results presented for the case of the flanged wall configuration, it is seen that the trends of results are similar in both cases. Values of K*/K for the box-core configuration are generally 3 to 5% higher than corresponding values for the flanged wall configuration, for the range of L/X ratios considered.

5.6.7 PRESENTATION OF DESIGN CURVES

Design curves, which may be used independently or in conjunction with the curves presented for the case of rigid walls, may be prepared for evaluating rapidly the effective slab width which accounts for local elastic wall deformation effects. Numerical results showing the variations of the slab stiffness factor K*, the effective slab width Y_e^*/Y, the stiffness ratio K*/K and the effective flange width Z*/Z, with the slab/wall thickness ratio t/h and the corridor-opening ratio L/X, have been obtained for a typical box-core configuration with Y/X = 0.4 and Z/Y = 0.5. The numerical results are given in Appendix A5.9.

5.6.7.1 Design Curves for Evaluating the Effective Slab Width

Curves showing the variation of Y_e^*/Y as a function of L/X for various ratios of t/h in the typical configuration considered are presented in Fig. 5.18(a). These curves are essentially similar to the set of curves presented for the flanged wall configuration in Fig. 5.10(b). By comparing corresponding values of Y_e^*/Y given by both sets of curves, it is seen that discrepancies are generally less than 10%. The curves in Fig. 5.18(a) may be used as design curves for evaluating the effective slab width in a box core configuration with Z/Y = 0.5. With other flange width ratios, the effective slab width can presumably be approximated from the curves presented for flanged wall configurations since results for box-core and flanged-wall configurations are not likely to be significantly different.

5.6.7.2 Design Curves for Evaluating the Stiffness Ratio

Curves showing the variation of K*/K as a function of L/X and as a function of t/h for the configuration considered are shown in Fig. 5.18(b). These curves are seen to be similar to the curves for the flanged wall configuration (Fig. 5.12(b)). By plotting values of K*/K (Appendix 5.9) as a function of $(t/h)/(L/X)^{\frac{1}{2}}$ it is seen that all the points fall almost exactly on a single curve. The curve of K*/K against $(t/h)/(L/X)^{\frac{1}{2}}$ is presented in Fig. 5.18(c) as a design curve for evaluating rapidly the stiffness ratio for the slab. The corresponding curve for the case of the flanged wall configuration has been included for the purpose of comparison. It is seen that the curves for the box-core configuration and for the flanged wall configuration are not significantly different, except for large values of $(t/h)/(L/X)^{\frac{1}{2}}$. Within the most practical range of $(t/h)/(L/X)^{\frac{1}{2}}$ from 1 to 3, differences between corresponding values of the stiffness ratio K*/K given by the two curves generally do not exceed 5%. Again,

although the design curve for the box-core configuration is directly applicable only for slabs with an aspect ratio of Y/X = 0.4, it can be used indirectly for slabs with any other ratios of Y/X, if the value of X for the particular slab is arbitrarily adjusted to suit the curve, as described in Section 5.5.9.4. The design curve is however applicable only to configurations with Z/Y = 0.5. For other ratios of Z/Y, values of stiffness ratio K*/K may be approximated from the curves presented for the flanged wall configuration.

5.6.8 INFLUENCE OF LOCAL ELASTIC WALL DEFORMATION ON CRITICAL BENDING MOMENTS IN SLAB

The influence of local elastic wall deformation on critical bending moments in the slab coupling box-cores is illustrated in Fig. 5.19, (a) to (c). The curves show, for various wall/slab geometric ratios, the distribution of longitudinal bending moment factors $\bar{M}_x$ (cf. Section 3.4.2.4) at the critical transverse slab section through the coupled end of the core. The curves for the case of a rigid wall refer to the results obtained assuming no local elastic wall deformation.

It is seen from the curves that as the core walls become flexible, the bending-moment factors in front of the core are reduced below the values for the case of a rigid wall, to an extent depending on the ratios t/h and L/X. The reduction in bending-moment factors is relatively larger with a larger ratio t/h and a smaller ratio L/X.

By comparing these sets of curves with the corresponding sets for T-shaped flanged wall configurations in Fig. 5.15, (d) to (f), it is seen that although the corresponding curves for the case of a rigid wall are very similar, the corresponding 'flexible wall' curves for various ratios t/h are quite different. But the results shown by the curves for the box-core and for the flanged-wall configurations are both consistent with the fact that

at points where the wall flange is less stiffened by the wall web, the reduction in bending-moment factors is relatively more than that at points where the flange is stiffened by the web.

The results presented in Fig. 5.19, (a) to (c), relate to a particular ratio Y/X of 0.4 and a particular ratio Z/Y of 0.5. The reduction in critical bending-moment factors produced by the elastic wall deformation will vary according to the ratios Z/Y and Y/X. Although results have not been obtained to show quantitatively the relative influence of these factors, it can be expected that as the flange width Z is increased, either by increasing Z/Y while keeping Y/X constant, or by increasing Y/X while keeping Z/Y constant, the flange will become relatively more flexible at the centre, and will therefore produce a larger reduction in the bending-moment factors at the slab section.

5.7 RELATIVE INFLUENCE OF IN-PLANE AND OUT-OF-PLANE WALL DEFORMATIONS IN FLANGED WALLS AND BOX-CORES

The wall/slab junction flexibility in flanged wall or box core configurations is produced by the combined effects of local in-plane and out-of-plane wall deformations. To assess the relative influence of each mode of wall deformation, it is necessary to re-analyse the wall/slab panel previously considered, with the walls now restrained against one of the two modes of local deformation. This is easily achieved in the finite element analysis by prescribing zero displacement boundary conditions at the wall/slab junction nodes to simulate the necessary infinite in-plane or out-of-plane rigidity of the walls.

Table 5.11 shows the numerical results obtained for typical flanged-wall and box-core configurations. The results for the case where walls are assumed flexible in-plane and out-of-plane are compared with the results for the case where walls are assumed infinitely rigid in-plane but flexible out-of-plane. The results for the

third case where walls are assumed infinitely rigid in-plane and out-of-plane have also been included to provide a measure of the reduction in coupling slab stiffness due to the wall flexibilities. By comparing appropriate values of the quantity (1 - K*/K) which gives a measure of the reduction in slab stiffness, it can be seen that the out-of-plane flexibility of the walls accounts for approximately 94% of the total slab-stiffness reduction in all cases considered. The influence of in-plane wall deformation is seen to be insignificant compared to the influence of out-of-plane wall deformation in the configurations considered in which the flange width ratio Z/Y has a value of 0.5. With smaller flange width ratios, the influence of in-plane wall deformation should become relatively more significant.

5.8 INFLUENCE OF DOOR-OPENINGS IN WALLS ON THE EFFECTIVE SLAB WIDTH

Door openings in walls for internal circulation within the apartment are often encountered in cross-wall buildings. Such openings are usually small in width, compared to the dimensions of the wall, and will not significantly affect the overall lateral stiffness of the shear wall. When a pair of perforated walls is coupled by floor slabs (Fig. 5.20(a) and (b)), each perforated wall may be assumed to behave as a composite unit, in the lateral load analysis of the structure. If cross sections of the perforated wall at the wall/slab junctions are assumed to remain plane when the slab interacts with the wall, then the effective coupling slab width will be similar to that for unperforated coupled walls. When local elastic wall deformation is considered, the effective slab width will, to a certain extent, be influenced by the presence of the door opening, depending on its size and location. This influence is investigated in this section, for a typical wall/slab configuration.

5.8.1 FINITE ELEMENT IDEALISATION

The finite element idealisation of a quarter of the wall/slab panel is shown in Fig. 5.20(c). The wall considered extends one storey height above and below the floor slab. The extremities of the wall are assumed fixed when the slab edge corresponding to the corridor centreline or inflexion line is displaced vertically to produce the required relative wall displacement. The wall and slab are represented by rectangular flat shell elements. The door-opening is represented by elements having a near-zero thickness which is equal to 10^{-4} times the thickness of the unperforated wall. This technique allows the size and position of the door-opening to be conveniently varied without the need to change the element mesh pattern, and so reduces considerably the amount of data preparation otherwise required.

5.8.2 NUMERICAL RESULTS

In this investigation a typical wall/slab configuration with the following characteristic dimensions is considered:

Slab length X	= 15.25 m	(50 ft)
Slab width Y	= 6.10 m	(20 ft)
Corridor width L	= 3.05 m	(10 ft)
Storey height F	= 3.05 m	(10 ft)
Slab thickness t	= 0.23 m	(9 in.)
Wall thickness h	= 0.30 m	(12 in.)

A constant door opening width of 1.14 m (3.75 ft) is assumed and the distance 'a' from the inner edge of the wall to the edge of the opening is varied. Two door-opening heights are considered. In the first case the opening extends over a part of the wall height and a lintel of 0.61 m (2 ft) depth remains at each floor. In the second case, which is an extreme case, the opening extends over the full wall-height and the slab provides the only connection across the opening at each floor.

The numerical results for the slab stiffness factor K* and effective width Y_e^*/Y obtained by the finite element analyses for the various cases are shown in Table 5.12. The slab stiffness factors are all based on the unit relative wall rotation referred to the centre of the perforated wall. The results for the case of unperforated walls has been included for the purpose of comparison. The ratios of perforated-wall/unperforated-wall effective slab width are also shown in the Table of results.

It is seen from the results that when the door opening is located within the middle half of the wall (a > 1.525 m (5 ft)), the effective slab width is reduced by the presence of the opening by not more than 1%. When the opening is very near the edge of the wall (a = 0.381 m (1.25ft)), the effective slab width is reduced by about 6% for the case with the lintel, and by about 13% for the other case without the lintel. In most practical cases, the door opening is unlikely to be located closer than about 1 m (3 ft) from the inner edge of the wall. In such cases, it is seen from the trend of results obtained that the influence of door openings is unlikely to be significant in the calculation of effective slab width.

5.9 SIGNIFICANCE OF LOCAL ELASTIC WALL DEFORMATION

In order to show the significance of local elastic wall deformation effects on design quantities which normally control the structural design of the building, two typical cross-wall/slab buildings, one with coupled plane walls and the other with coupled flanged walls (T-Section) are considered. Both structures are of 20 storeys with storey heights of 3.05 m (10 ft) and building depth of 15.25 m (50 ft). The cross-walls are spaced at 6.1 m (20 ft) centres and wall openings (corridor opening) are of 1.525 m (5 ft) width in both buildings. Walls and slabs are of 228.6 mm (9 in.) thickness. The width of the wall flange is 3.05 m (10 ft.). The uniform wind loading on the structure is taken as 1.2 kN/m^2 (25 lb/ft^2) throughout the building height.

The relevant design quantities considered are the maximum lateral deflection δ at the top of the structure, the extreme fibre wall stresses σ_A and σ_B at the bottom of the shear wall, the maximum lintel shear Q_o and the critical bending moment in a 0.61 m (2 ft) wide slab-strip. The continuous connection method of coupled wall analysis as presented by Coull and Choudhury[59] and by Coull and Irwin[53] are used to calculate the relevant design quantities. The results evaluated for the case where local elastic wall deformation effects are disregarded (rigid wall) are compared with the results for the case where these effects are included (flexible wall), in Tables 5.13, (a) and (b).

It is seen from the numerical results for the two buildings that when the local elastic wall deformation is disregarded, in each case the effective slab width is overestimated by a large margin (over 60%), but this results in the wall deflection and wall stresses being underestimated, and the maximum lintel shear being over-estimated, by a much smaller margin. The critical slab moment however is quite seriously overestimated (more than 100% in the plane wall building).

5.10 CONCLUSIONS

A finite element approach has been described for the evaluation of local elastic wall deformation effects in shear wall/slab interactions. Numerical results obtained showing the relative influence of various structural parameters on the flexibility of the wall/slab junction, and on the effective coupling of walls by the slab, have been presented.

In plane wall configurations, the slab stiffness ratio varies principally with a single parameter $t/(L^2h)^{1/3}$. Design curves have been presented for the rapid evaluation of the stiffness ratio or the effective span extension in a practical situation. Either of these quantities can be used to correct the 'rigid wall' slab stiffness so as to include the local elastic wall deformation effects. The

presence of normal door-openings has very little effect on the stiffness of the slab.

In the T-Section flanged wall and box-core configurations, the wall/slab junction flexibility is produced mainly by local bending of the wall flanges. The stiffness ratio varies approximately as a function of $(t/h)/(L/X)^{\frac{1}{2}}$. Design curves for evaluating the stiffness ratio for these configurations have also been presented.

The critical bending moment factors in the slab are substantially reduced by the effects of local elastic wall deformation, depending primarily on the slab/wall thickness ratio.

When the local elastic wall deformation is disregarded, although the effective slab width is considerably over-estimated, the resulting errors in the calculation of maximum wall deflection and stresses and maximum lintel shear are relatively small. The resulting error in the calculation of critical slab moments on the other hand can be quite large.

TABLE 5.1 COUPLED PLANE WALL CONFIGURATION
(L/X = 0.2, Y/X = 0.4, F/W = 0.5, t/h = 0.075)

	Mesh 1 Coarse	Mesh 2 Medium	Mesh 3 Fine
K*	33.8832	34.0705	33.5573
Y_e^*/Y	0.3210	0.3227	0.3178

TABLE 5.2 INFLUENCE OF STOREY HEIGHT
Plane Wall Configuration
(L/X = 0.2, Y/X = 0.4, t/h = 0.75)

	Wall Height F/X			Rigid Wall
	0.1	0.2	0.3	
K*	34.3219	34.0705	34.0428	40.9695
Y_e^*/Y	0.3251	0.3227	0.3196	0.3881
K*/K	0.8377	0.8315	0.8235	1.0000

TABLE 5.3 INFLUENCE OF WALL LENGTH
Plane Wall Configuration (Y/L = 1)
Effective Slab Width Y_e^*/Y

W/L / t/h	0.5	0.75	1.0
0.5	0.5821	0.5715	0.5710
0.75	0.5559	0.5468	0.5490
Rigid Wall	0.6177	0.6101	0.6124

TABLE 5.4 VARIATION OF SLAB STIFFNESS RATIO K*/K WITH VARIOUS GEOMETRIC RATIOS

Plane Wall Configuration

Y/X	t/h / L/X	Stiffness Ratio K*/K			
		0.5	1.0	1.5	2.0
0.4	0.1	0.809	0.585	0.391	0.270
	0.2	0.888	0.757	0.597	0.472
	0.4	0.937	0.859	0.758	0.665
	0.6	0.956	0.902	0.832	0.766
0.6	0.1	0.793	0.569	0.390	0.275
	0.2	0.878	0.740	0.593	0.475
	0.4	0.931	0.853	0.752	0.669
	0.6	0.951	0.898	0.829	0.762
0.8	0.1	0.782	0.560	0.386	0.275
	0.2	0.872	0.738	0.598	0.485
	0.4	0.936	0.859	0.756	0.679
	0.6	0.947	0.878	0.825	0.757

TABLE 5.5 INFLUENCE OF STOREY HEIGHT ON SLAB COUPLING STIFFNESS

Flanged Wall Configuration (L/X = 0.2, Y/X = 0.4, Z/Y = 0.5)

F/X	K*	Y_e^*/Y	K*/K
0.2	70.28	0.6657	0.828
0.3	69.92	0.6623	0.824
Rigid Wall	84.87	0.8039	1.000

TABLE 5.6 INFLUENCE OF WALL AND SLAB THICKNESSES ON SLAB COUPLING STIFFNESS

Flanged Wall Configuration (L/X = 0.2, Y/X = 0.4, Z/Y = 0.5)

t (ft)	h (ft)	t/h	K*	Y_e^*/Y	K*/K
0.50	0.50	1.0	64.60	0.6120	0.76
0.75	0.75	1.0	62.85	0.5953	0.74
1.00	1.00	1.0	61.84	0.5858	0.73
0.50	1.00	0.5	78.45	0.7431	0.92
0.75	1.50	0.5	77.59	0.7349	0.91
1.00	2.00	0.5	76.82	0.7276	0.91

TABLE 5.7 VARIATION OF SLAB STIFFNESS RATIO K*/K WITH VARIOUS GEOMETRIC RATIOS

Flanged Wall Configuration

Y/X	L/X	Stiffness Ratio K*/K				
		t/h / Z/Y	1.5	0.75	0.50	0.375
0.4	0.1	0.25	0.57	0.76	0.86	0.90
		0.50	0.49	0.72	0.85	0.91
		0.75	0.42	0.68	0.84	0.91
	0.2	0.25	0.73	0.86	0.92	0.95
		0.50	0.64	0.83	0.91	0.95
		0.75	0.59	0.81	0.92	0.96
	0.4	0.25	0.84	0.92	0.96	0.97
		0.50	0.77	0.91	0.96	0.98
		0.75	0.72	0.89	0.96	0.98
0.6	0.1	0.25	0.53	0.73	0.85	0.90
		0.50	0.43	0.68	0.83	0.90
		0.75	0.36	0.65	0.83	0.90
	0.2	0.25	0.70	0.84	0.91	0.94
		0.50	0.58	0.79	0.90	0.94
		0.75	0.51	0.78	0.90	0.95
	0.4	0.25	0.81	0.91	0.95	0.97
		0.50	0.71	0.88	0.95	0.98
		0.75	0.66	0.87	0.95	0.97

TABLE 5.8 VARIATION OF EFFECTIVE FLANGE WIDTH Z*/Z WITH VARIOUS GEOMETRIC RATIOS

Flanged Wall Configuration

Y/X	L/X	t/h / Z/Y	Effective Flange Width Z*/Z			
			1.5	0.75	0.50	0.375
0.4	0.1	0.25	0.18	0.55	0.72	0.80
		0.50	0.24	0.58	0.78	0.86
		0.75	0.23	0.57	0.77	0.87
	0.2	0.25	0.20	0.58	0.75	0.82
		0.50	0.25	0.63	0.81	0.89
		0.75	0.26	0.63	0.81	0.90
	0.4	0.25	0.20	0.58	0.78	0.85
		0.50	0.25	0.65	0.84	0.91
		0.75	0.23	0.63	0.83	0.91
0.6	0.1	0.25	0.25	0.58	0.75	0.85
		0.50	0.25	0.59	0.79	0.88
		0.75	0.23	0.57	0.79	0.87
	0.2	0.25	0.30	0.65	0.80	0.88
		0.50	0.31	0.65	0.83	0.90
		0.75	0.28	0.65	0.83	0.91
	0.4	0.25	0.32	0.65	0.82	0.88
		0.50	0.30	0.68	0.85	0.93
		0.75	0.27	0.67	0.87	0.92

TABLE 5.9 INFLUENCE OF STOREY HEIGHT ON SLAB COUPLING STIFFNESS

Box-Core Configuration (L/X = 0.2, Y/X = 0.4, Z/Y = 0.5)

t/h	F/X	K*	Y_e^*/Y	K*/K
0.75/0.50	0.2	50.36	0.4770	0.580
	0.3	48.27	0.4573	0.556
0.75/0.75	0.2	66.99	0.6345	0.771
	0.3	64.87	0.6145	0.747
0.75/1.00	0.2	75.14	0.7118	0.865
	0.3	74.30	0.7038	0.855
Rigid Wall		86.88	0.8230	1.000

TABLE 5.10 INFLUENCE OF SLAB AND WALL THICKNESSES ON SLAB COUPLING STIFFNESS

Box-Core Configuration (L/X = 0.2, Y/X = 0.4, Z/Y = 0.5)

t (ft)	h (ft)	t/h	K*	Y_e^*/Y	K*/K	Z*/Z
0.50	0.50	1.0	68.48	0.6487	0.79	0.56
0.75	0.75	1.0	66.99	0.6345	0.77	0.54
1.00	1.00	1.0	65.28	0.6184	0.75	0.50
0.50	1.00	0.5	82.50	0.7815	0.95	0.89
0.75	1.50	0.5	81.81	0.7750	0.94	0.88
1.00	2.00	0.5	80.99	0.7671	0.93	0.85
Rigid Wall			86.88	0.8230	1.00	1.00

TABLE 5.11 RELATIVE INFLUENCE OF IN-PLANE AND OUT-OF-PLANE WALL DEFORMATIONS ON SLAB COUPLING STIFFNESS

Wall Condition		K*	Y_e^*/Y	1-K*/K	Slab/Wall Thickness Ratio t/h
In-plane	Out-of-plane				
Flanged Wall Configuration (Y/X = 0.6, L/X = 0.2, Z/Y = 0.5)					
Flexible	Flexible	68.00	0.4294	0.420	
Rigid	Flexible	70.96	0.4481	0.395	1.5
Rigid	Rigid	117.23	0.7403	0.000	
Flexible	Flexible	93.16	0.5881	0.206	
Rigid	Flexible	94.55	0.5971	0.193	0.75
Rigid	Rigid	117.23	0.7403	0.000	
Box Core Configuration (Y/X = 0.4, L/X = 0.2, Z/Y = 0.5)					
Flexible	Flexible	48.27	0.4573	0.444	
Rigid	Flexible	50.36	0.4770	0.420	1.5
Rigid	Rigid	86.88	0.8230	0.000	

TABLE 5.12 STIFFNESS FACTORS AND EFFECTIVE WIDTHS FOR SLABS COUPLING PERFORATED WALLS

d (ft)	a (ft)	K*	Y_e^*/Y	$\frac{\text{Perforated}}{\text{Unperforated}}$
2	1.25	32.186	0.3049	0.937
	2.50	33.310	0.3155	0.970
	3.75	33.753	0.3197	0.983
	6.25	34.011	0.3222	0.990
	10.00	34.313	0.3250	0.999
0	1.25	30.004	0.2842	0.874
	2.50	32.928	0.3119	0.959
	3.75	33.711	0.3193	0.982
Unperforated-Wall		34.334	0.3253	

Note: 1 ft. = 0.305 m

TABLE 5.13 EFFECT OF LOCAL ELASTIC WALL DEFORMATION ON DESIGN QUANTITIES FOR EXAMPLE BUILDINGS

(a) Building No. 1 - Plane Wall Configuration

Design Quantities	Rigid Walls	Flexible Walls	Percentage Diff.
Effective Slab Width Y_e (ft)	4.35	2.70	61.11
Top Deflection δ (in.)	0.478	0.538	-11.15
Wall Stress σ_A (lb/in^2)	311.06	329.39	- 5.56
Wall Stress σ_B (lb/in^2)	-132.82	-164.87	-19.44
Max. Lintel Shear Q_o (kip)	16.19	14.14	14.52
Bending Moment in Critical 2 ft. wide slab strip (kip-ft)	24.36	11.25	116.53

(b) Building No. 2 - Flanged Wall Configuration

Design Quantities	Rigid Walls	Flexible Walls	Percentage Diff.
Effective Slab Width Y_e (ft)	13.8	8.6	60.47
Top Deflection δ (in.)	0.396	0.419	-5.30
Wall Stress σ_A (lb/in^2)	260.70	269.48	-3.26
Wall Stress σ_B (lb/in^2)	-37.14	-49.64	-25.18
Max. Lintel Shear Q_o (kip)	23.98	20.67	16.01
Bending Moment in Critical 2 ft. Wide Slab Strip (kip-ft)	8.74	5.89	48.39

Note: 1 lb = 0.453 kg, 1 in. = 25.4 mm.

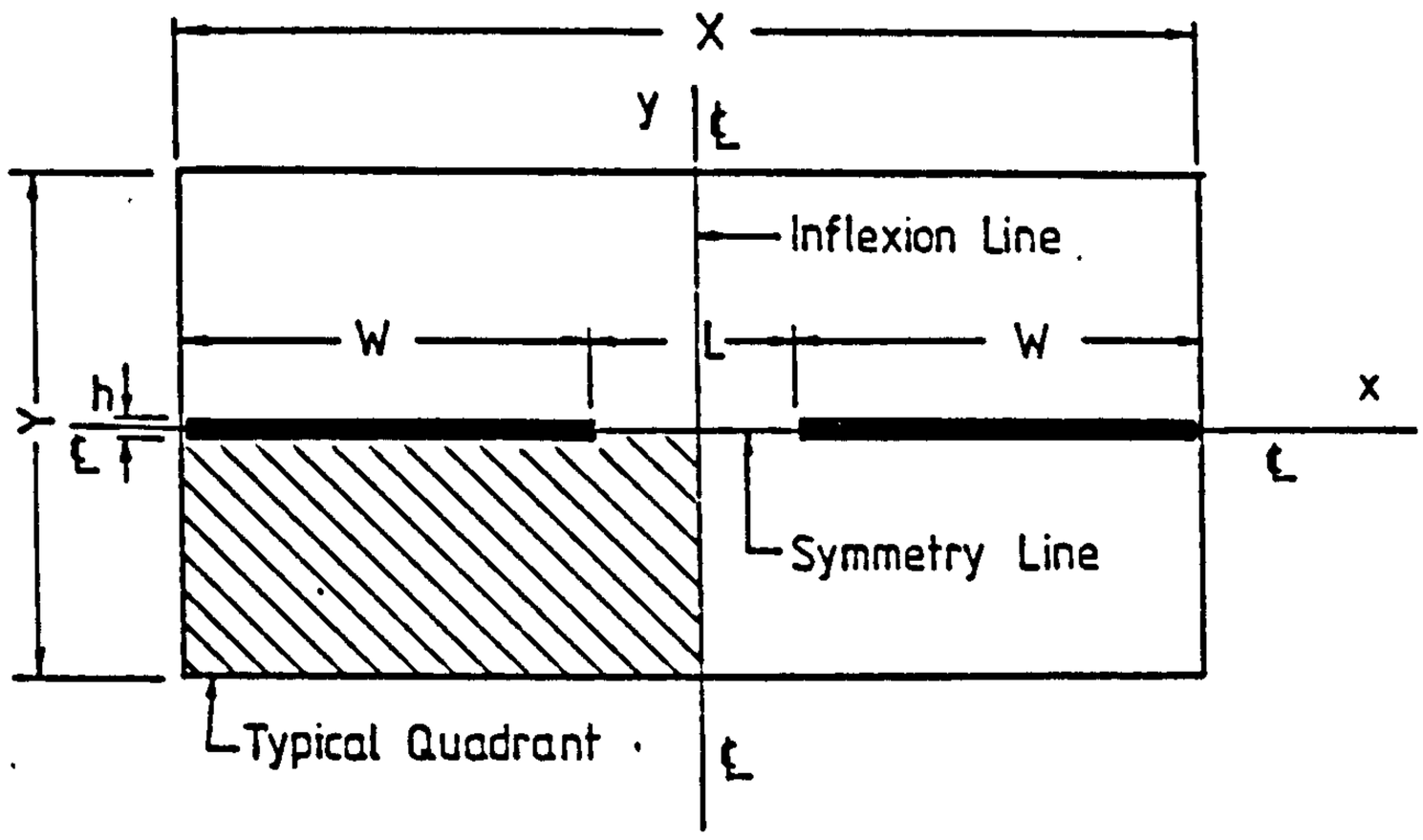

(a) Typical Interior Slab Panel

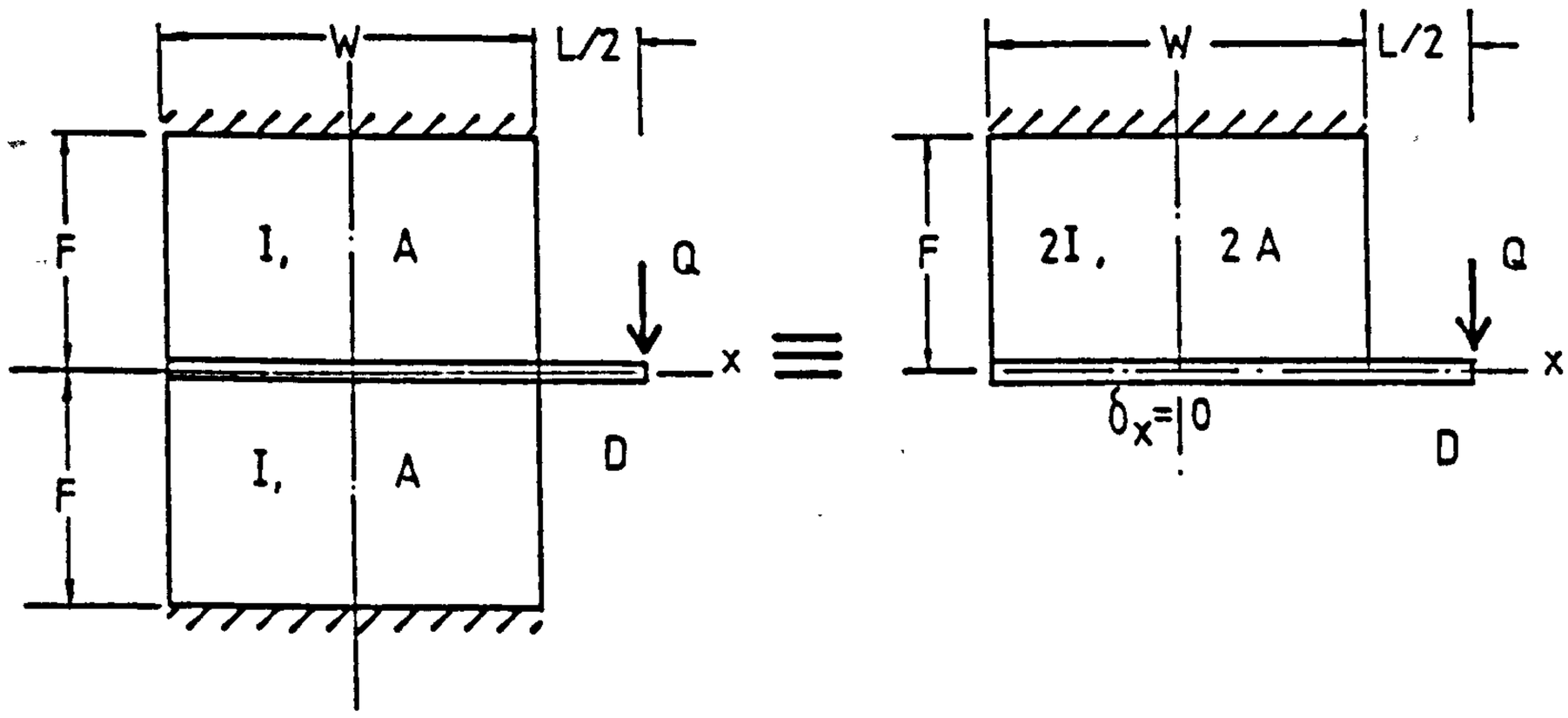

(b) Wall Anti-Symmetry Conditions

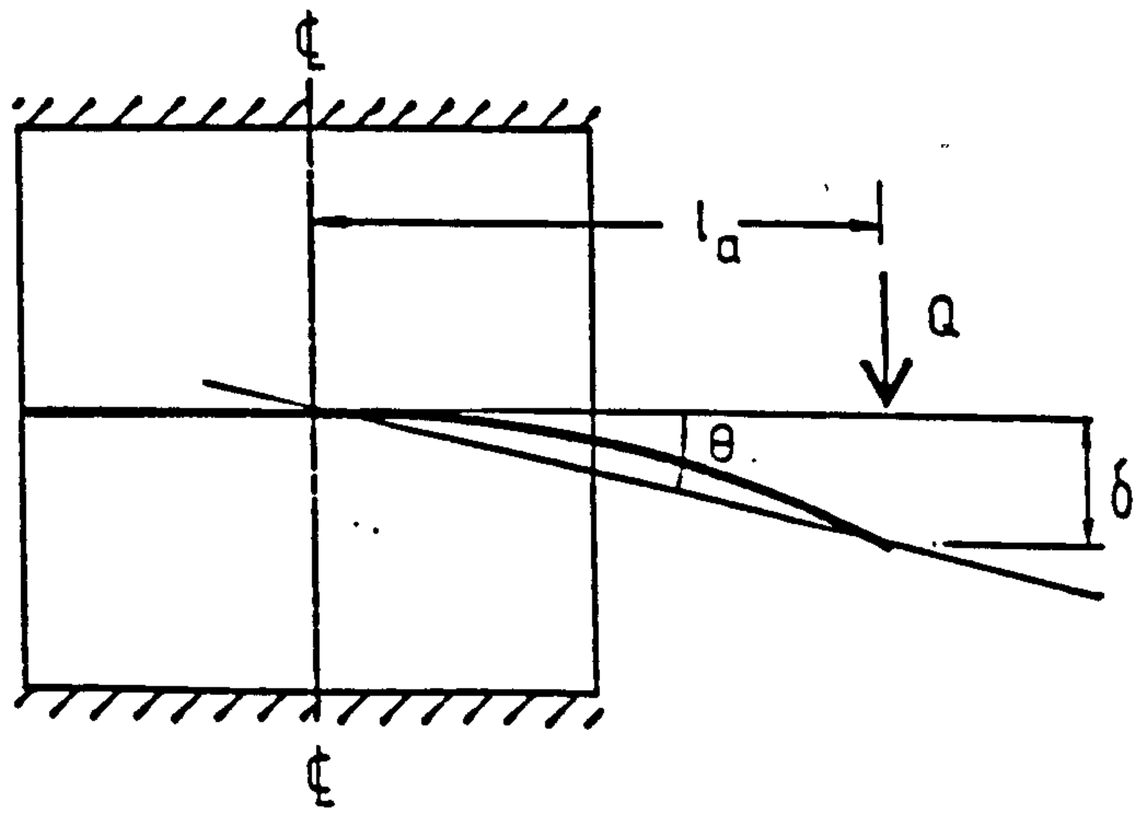

(c) Deformation of Slab

Fig. 5.1

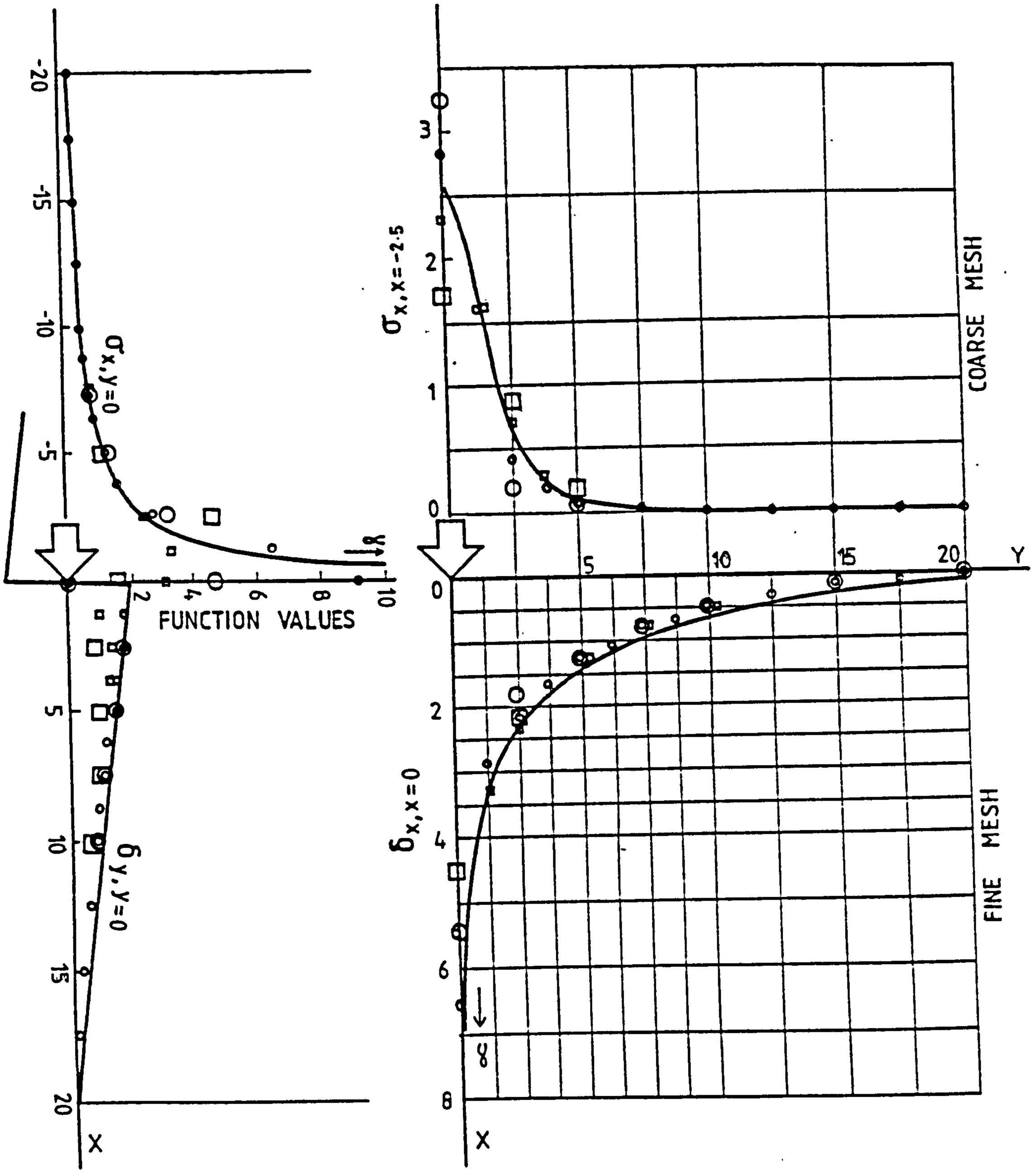

O COARSE MESH RP 8 FINITE ELEMENT
o FINE MESH RP 8 FINITE ELEMENT
□ COARSE MESH TP 6 FINITE ELEMENT
▫ FINE MESH TP 6 FINITE ELEMENT
— ELASTICITY SOLUTION

Fig. 5.2 Comparison Between Finite Element and Elasticity Solutions for Half-Plane with Tangential Point Load

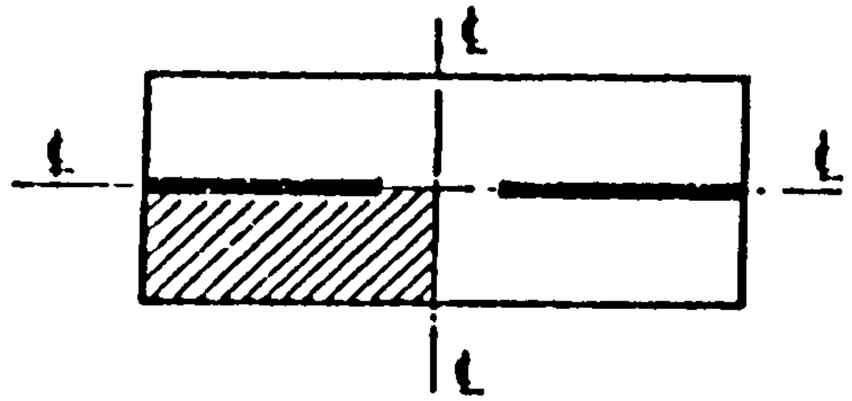

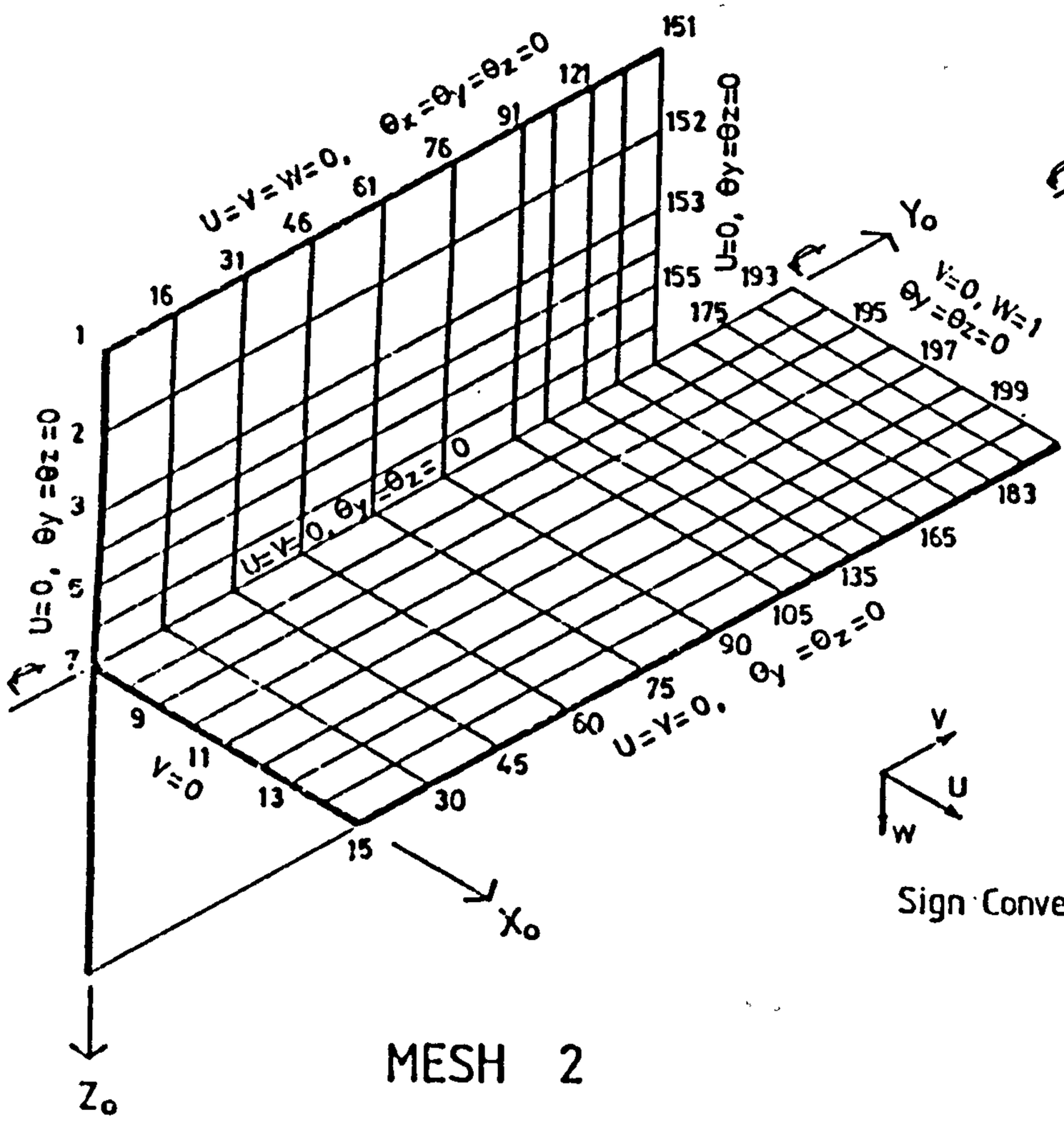

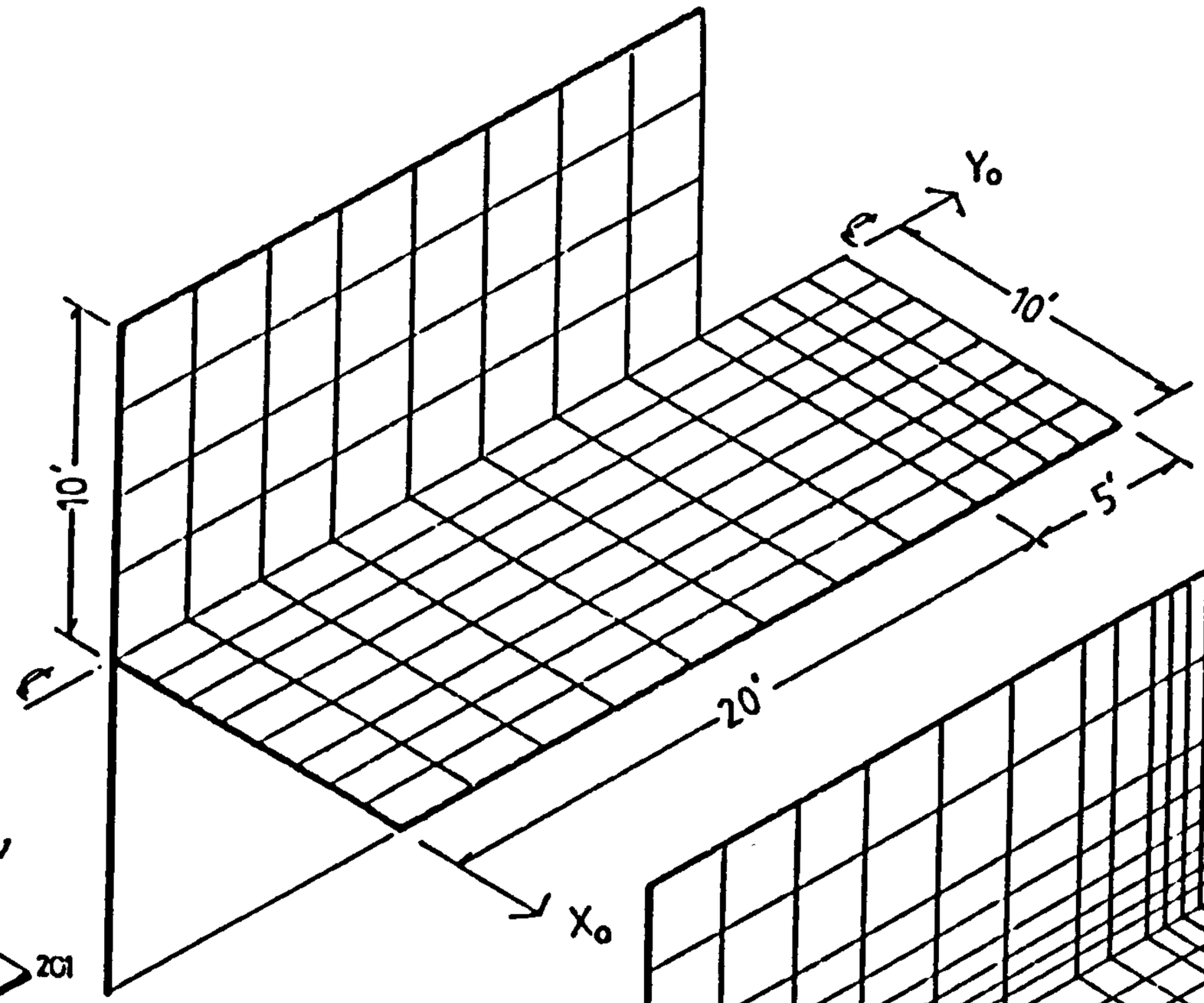

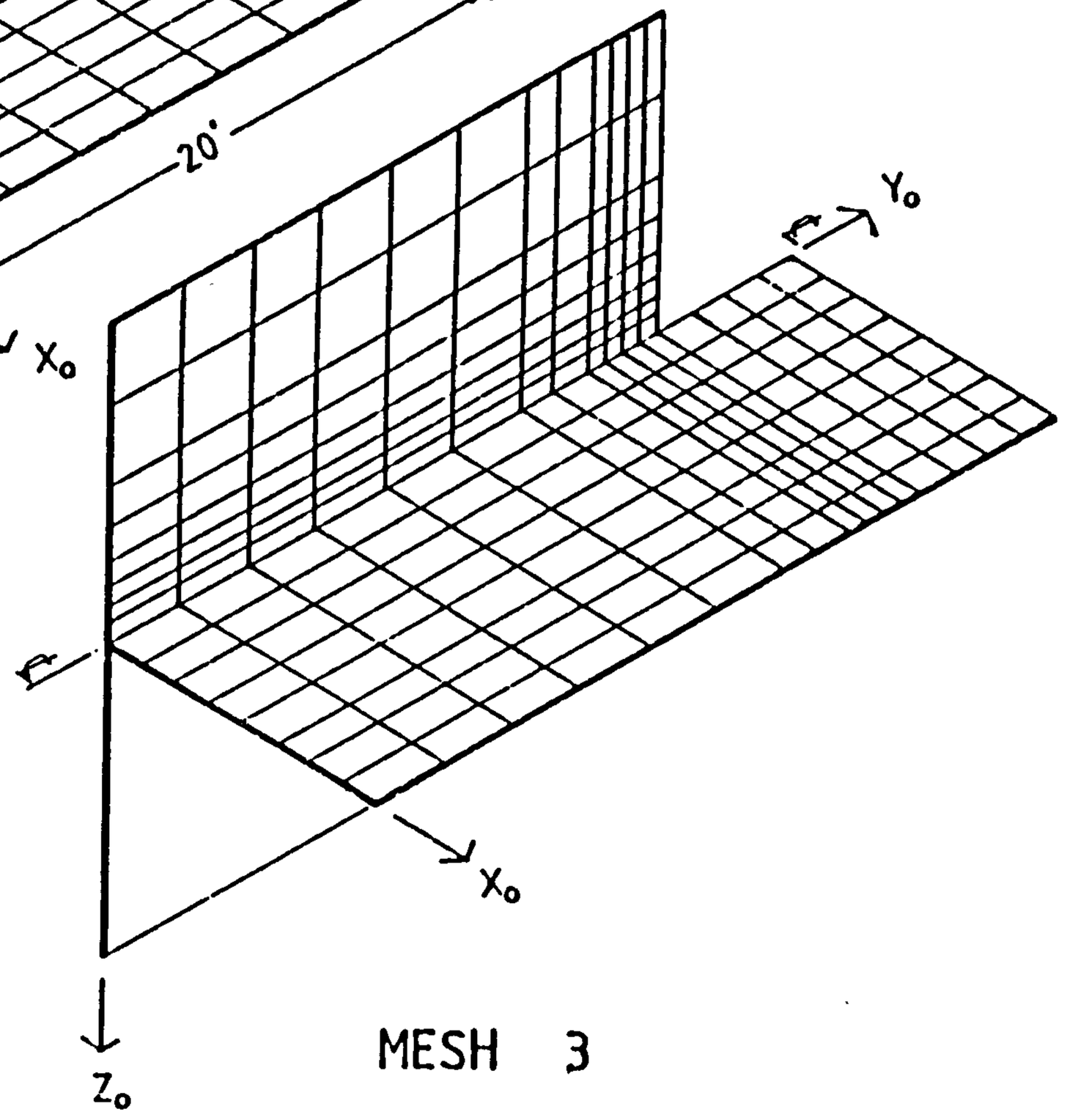

Fig. 5.3 Element Mesh Divisions for Convergence Study

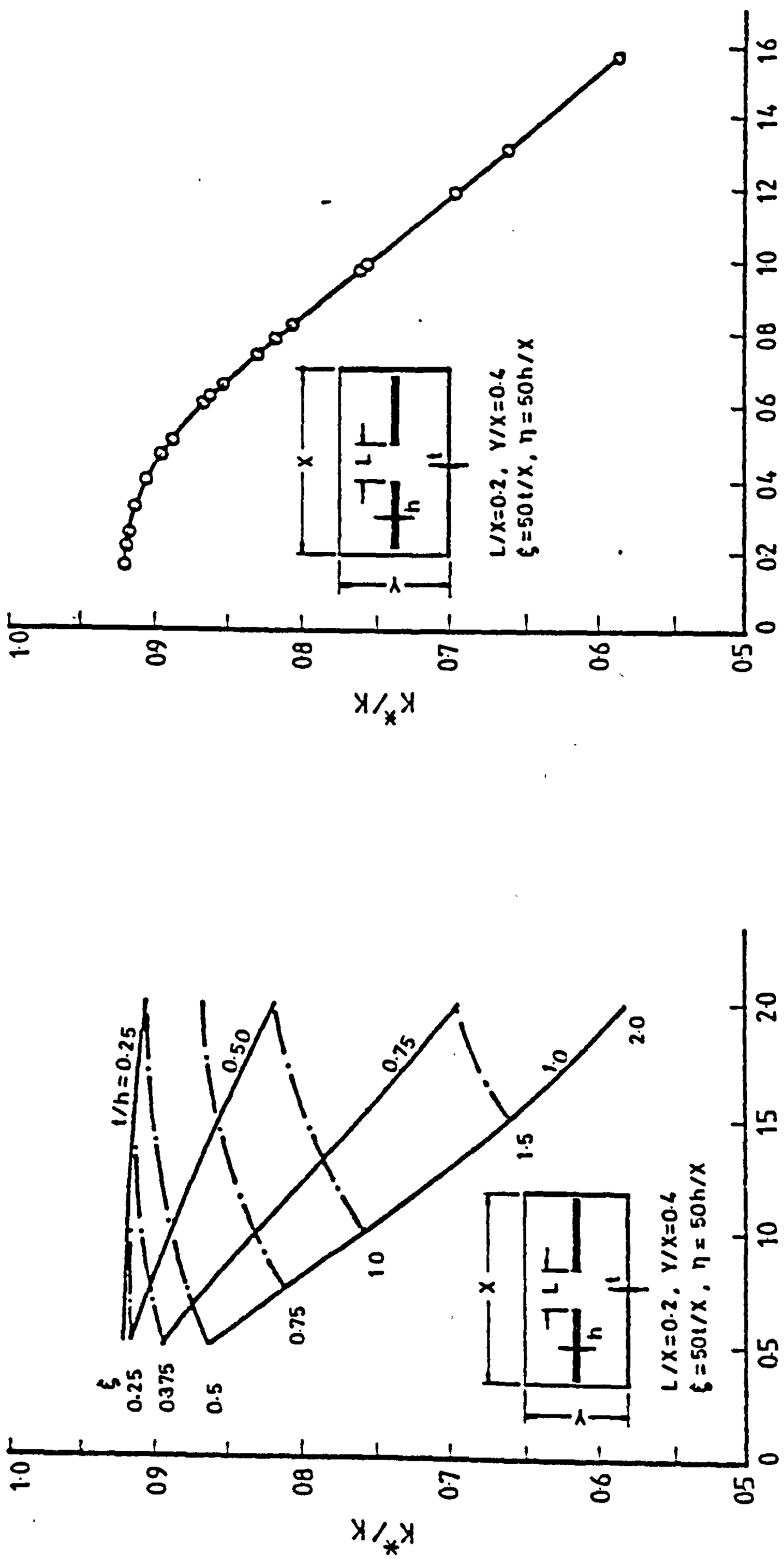

Fig. 5.4 Variation of Stiffness Ratio with (a) Slab and Wall Thickness Parameter (b) Slab/Wall Thickness Parameter

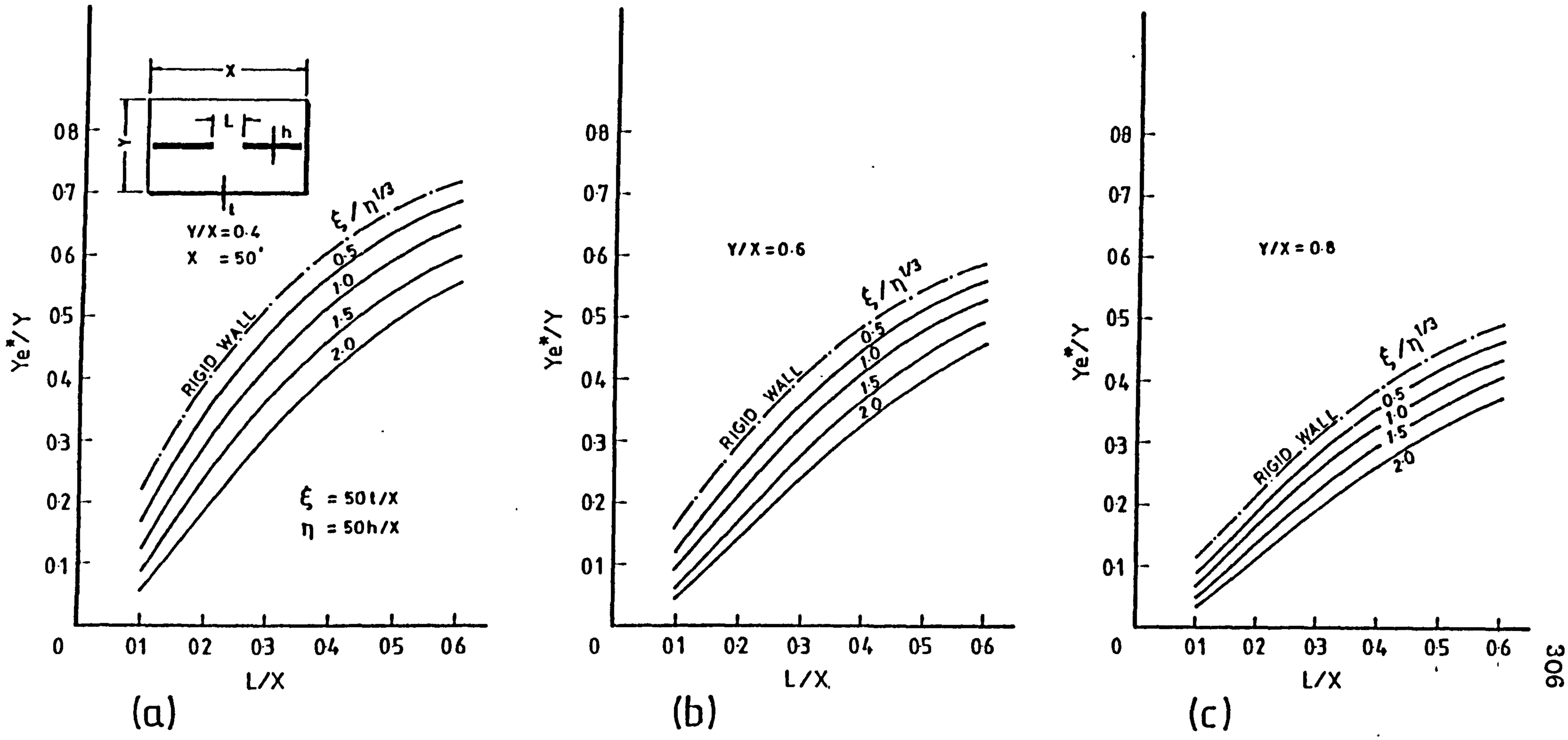

Fig. 5.5 Design Curves for Slab Effective Width in Plane Wall Configuration

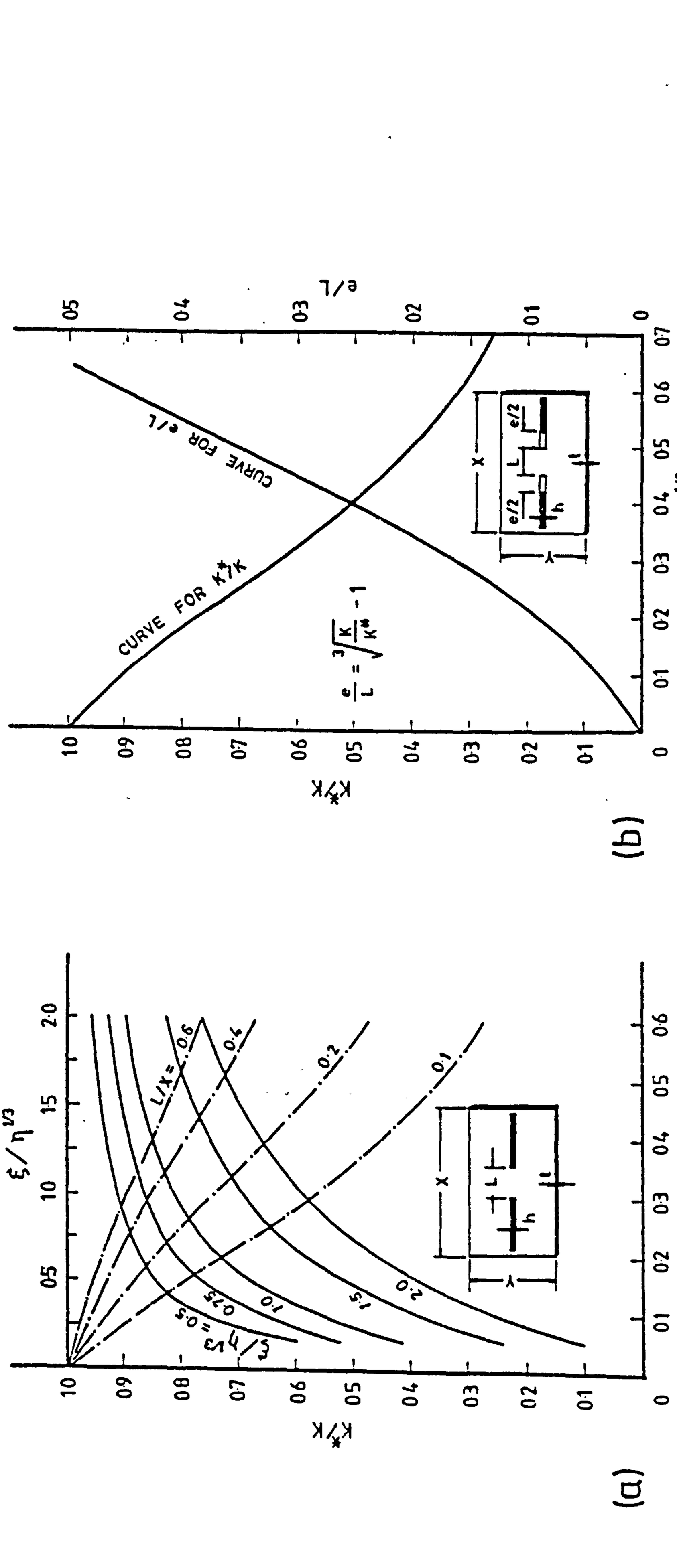

Fig. 5.6 (a) Variation of Stiffness Ratio with Corridor Opening Ratio and Wall Thickness Parameter in Plane Wall Configuration, (b) Design Curves For Stiffness Ratio and Effective Span Extension in Plane Wall Configuration

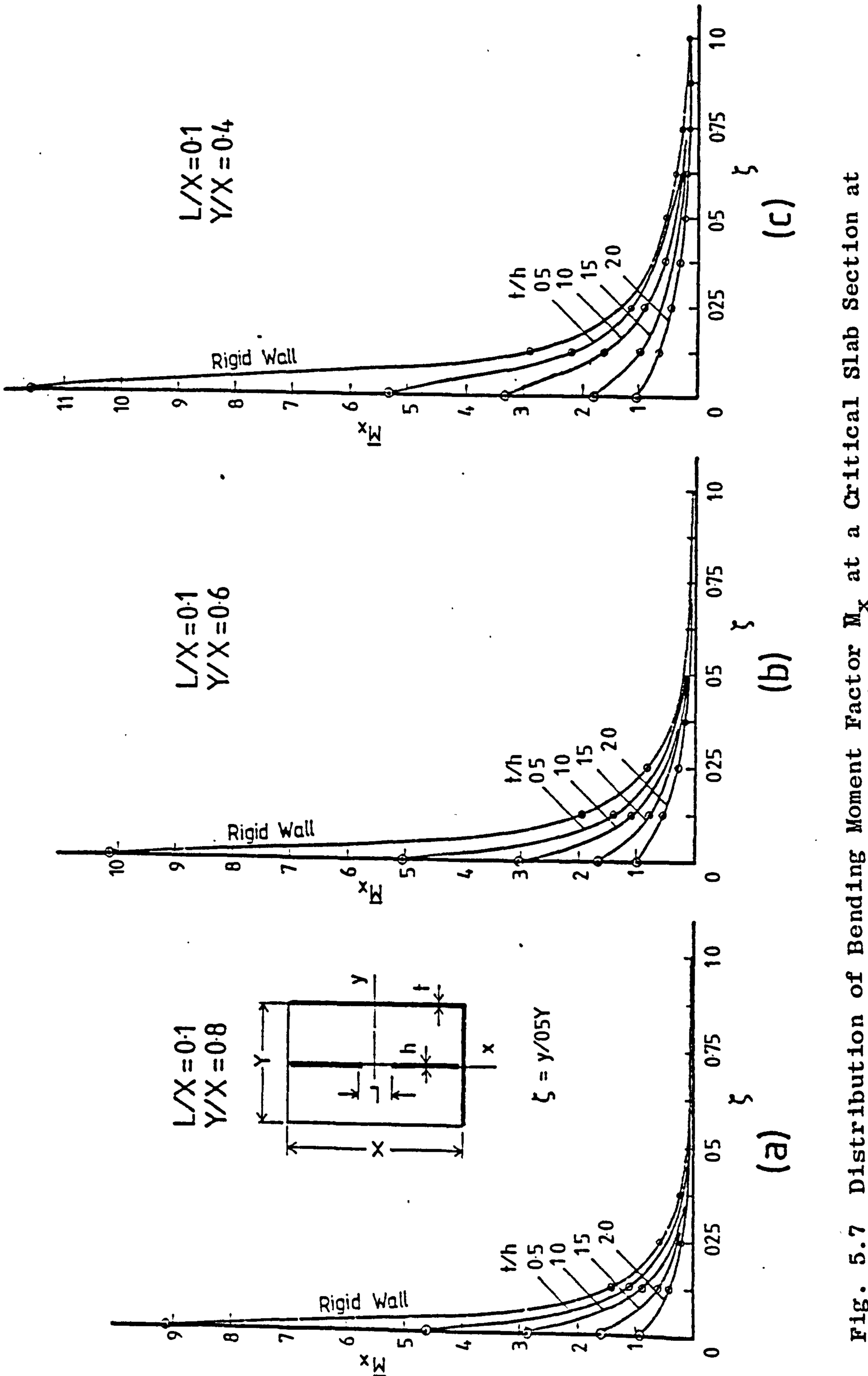

Fig. 5.7 Distribution of Bending Moment Factor M_x at a Critical Slab Section x = -L/2 in Plane Wall Configuration

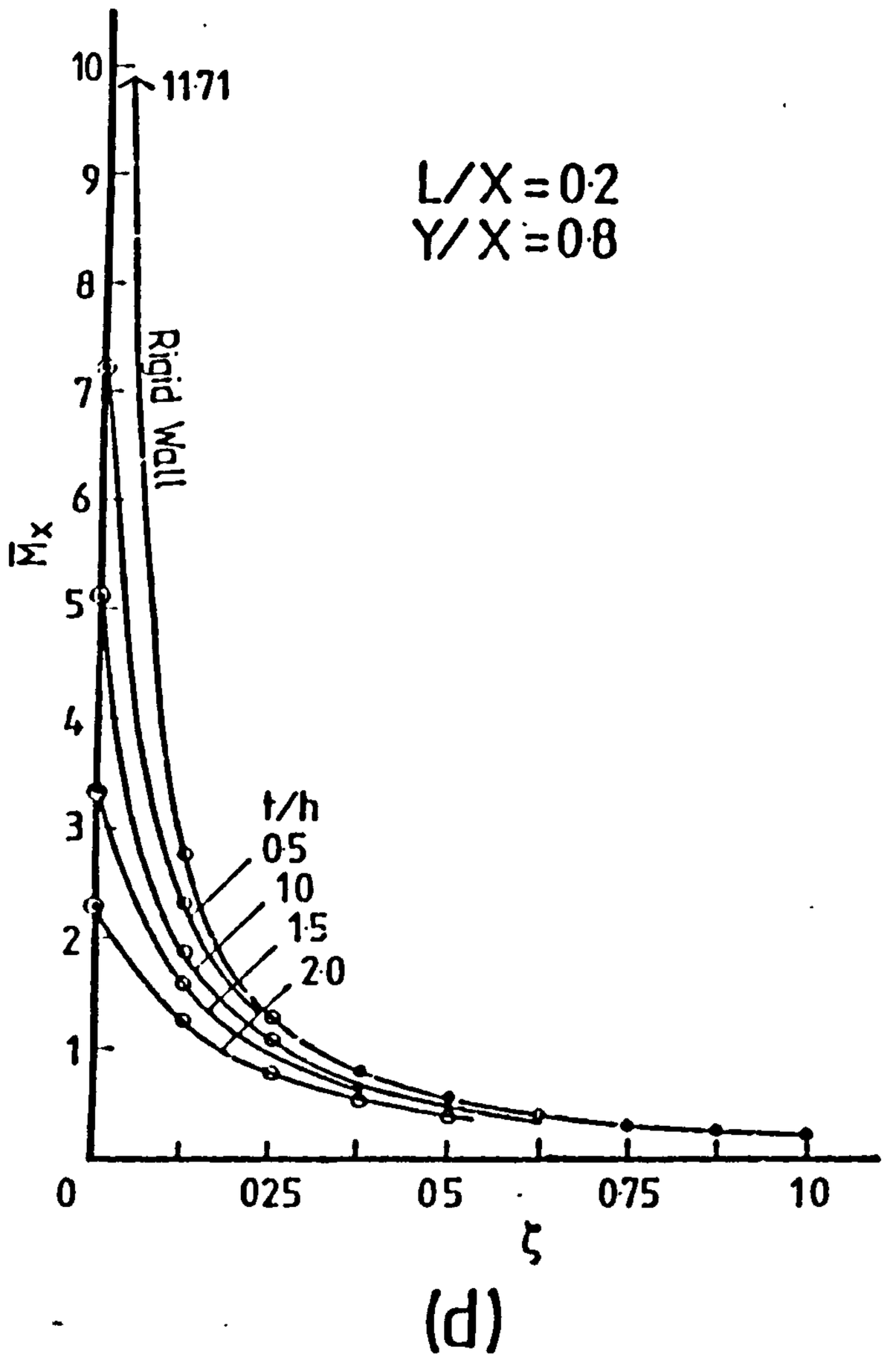

L/X = 0·2
Y/X = 0·8

(d)

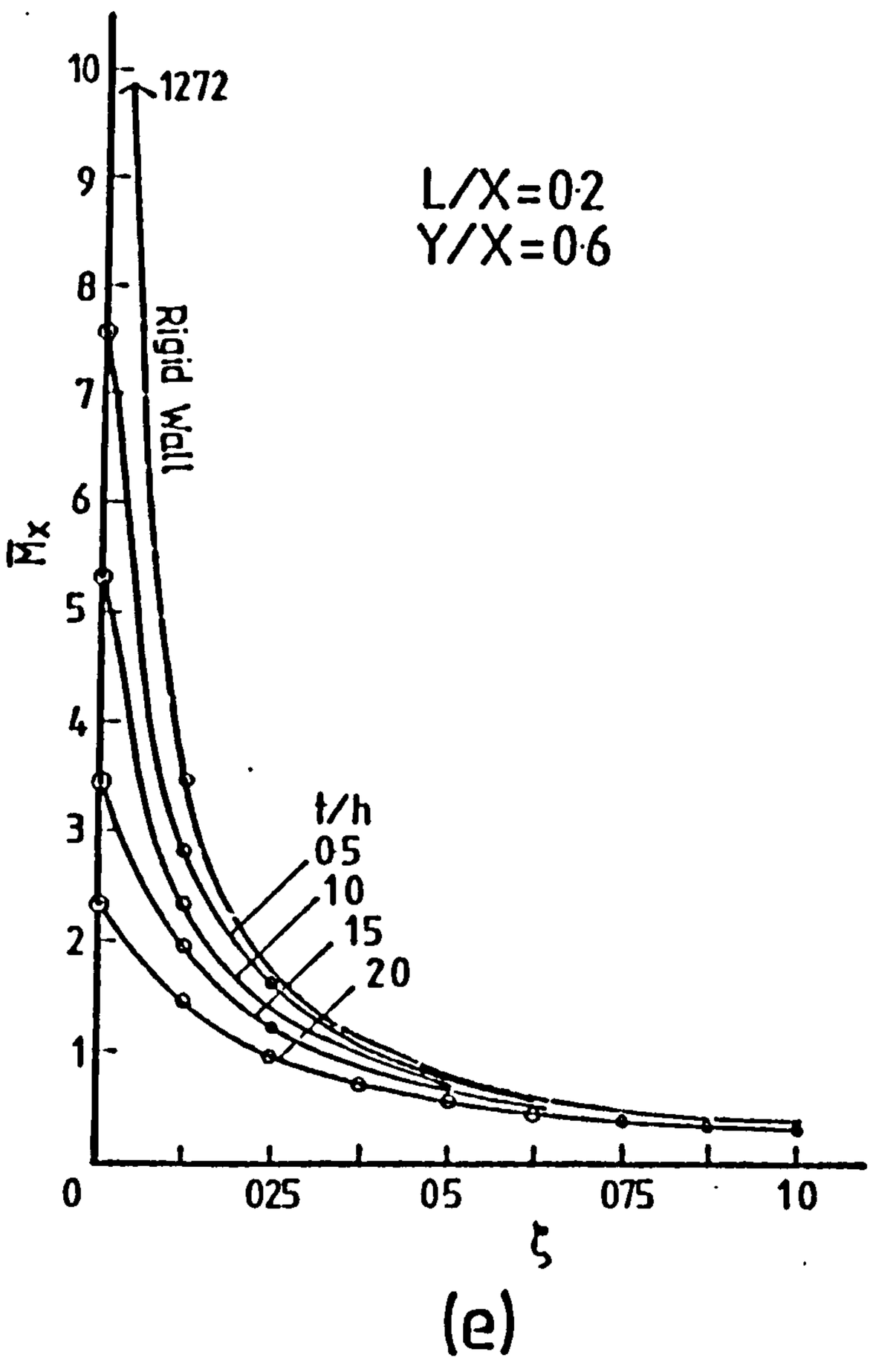

L/X = 0·2
Y/X = 0·6

(e)

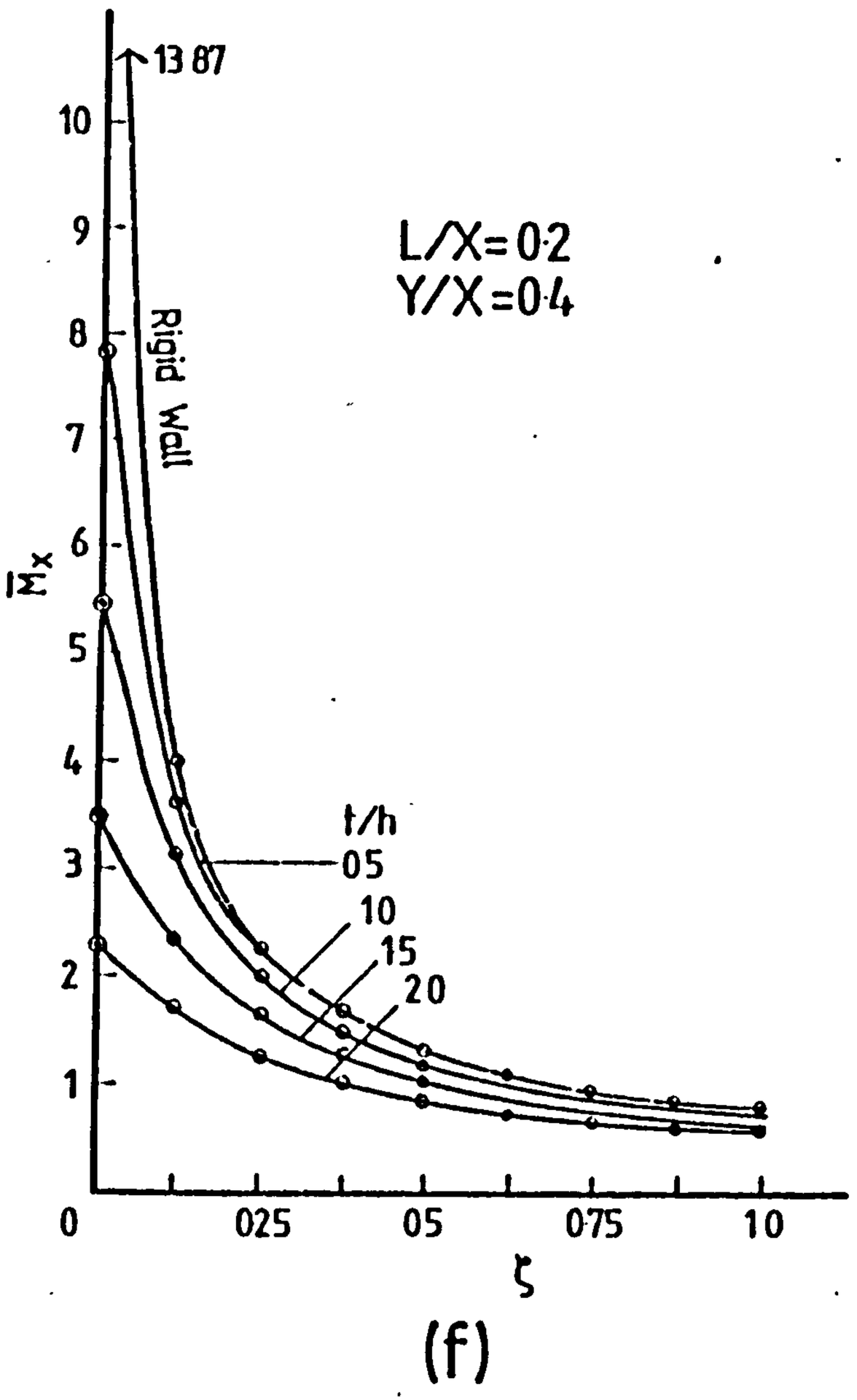

L/X = 0·2
Y/X = 0·4

(f)

Fig. 5.7 (contd) Distribution of Bending Moment Factor $\bar{M}_x$ at a Critical Slab Section at x = -L/2 in Plane Wall Configuration

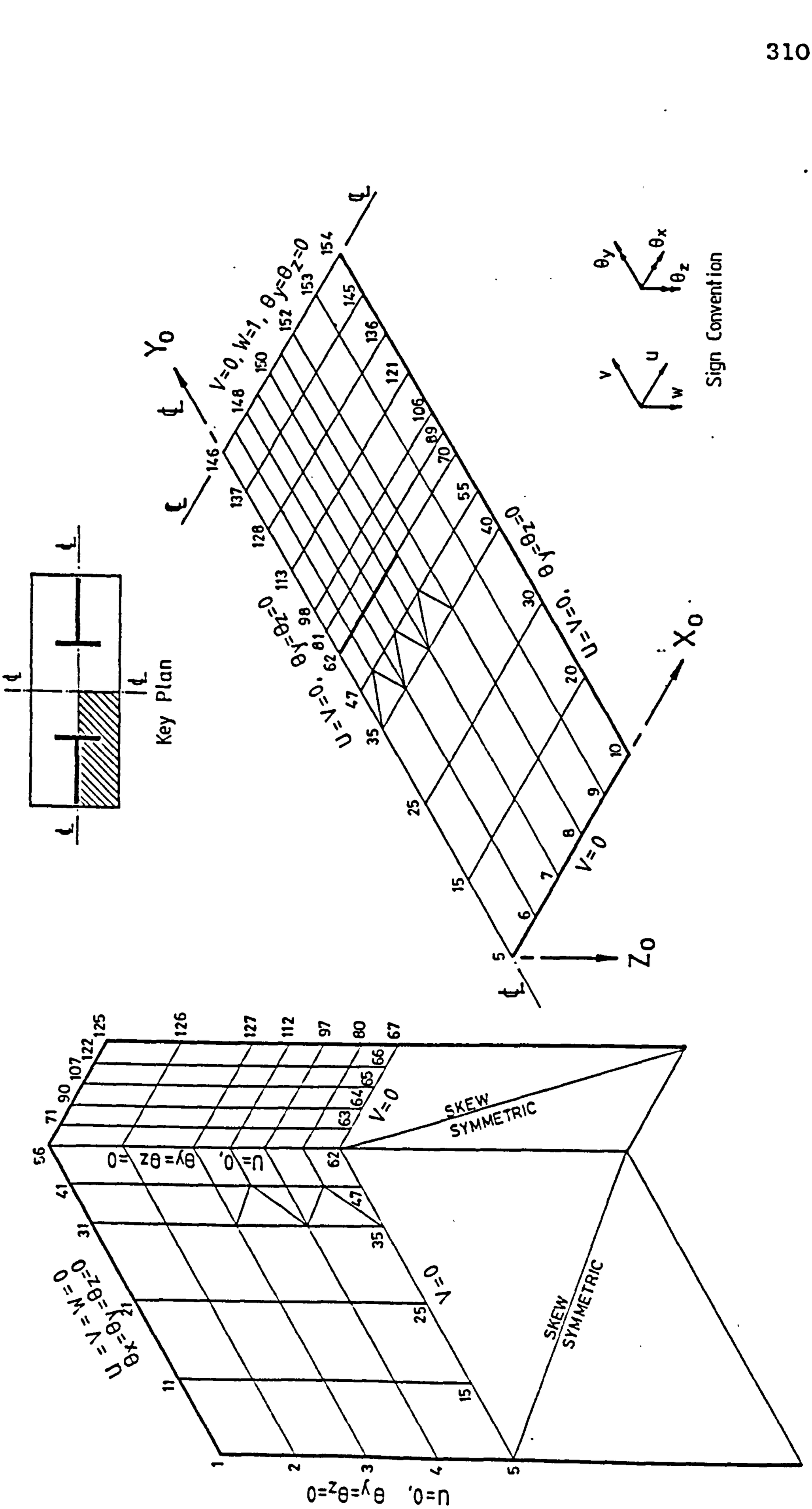

Fig. 5.8 Finite Element Idealisation of Flanged Wall / Slab Panel

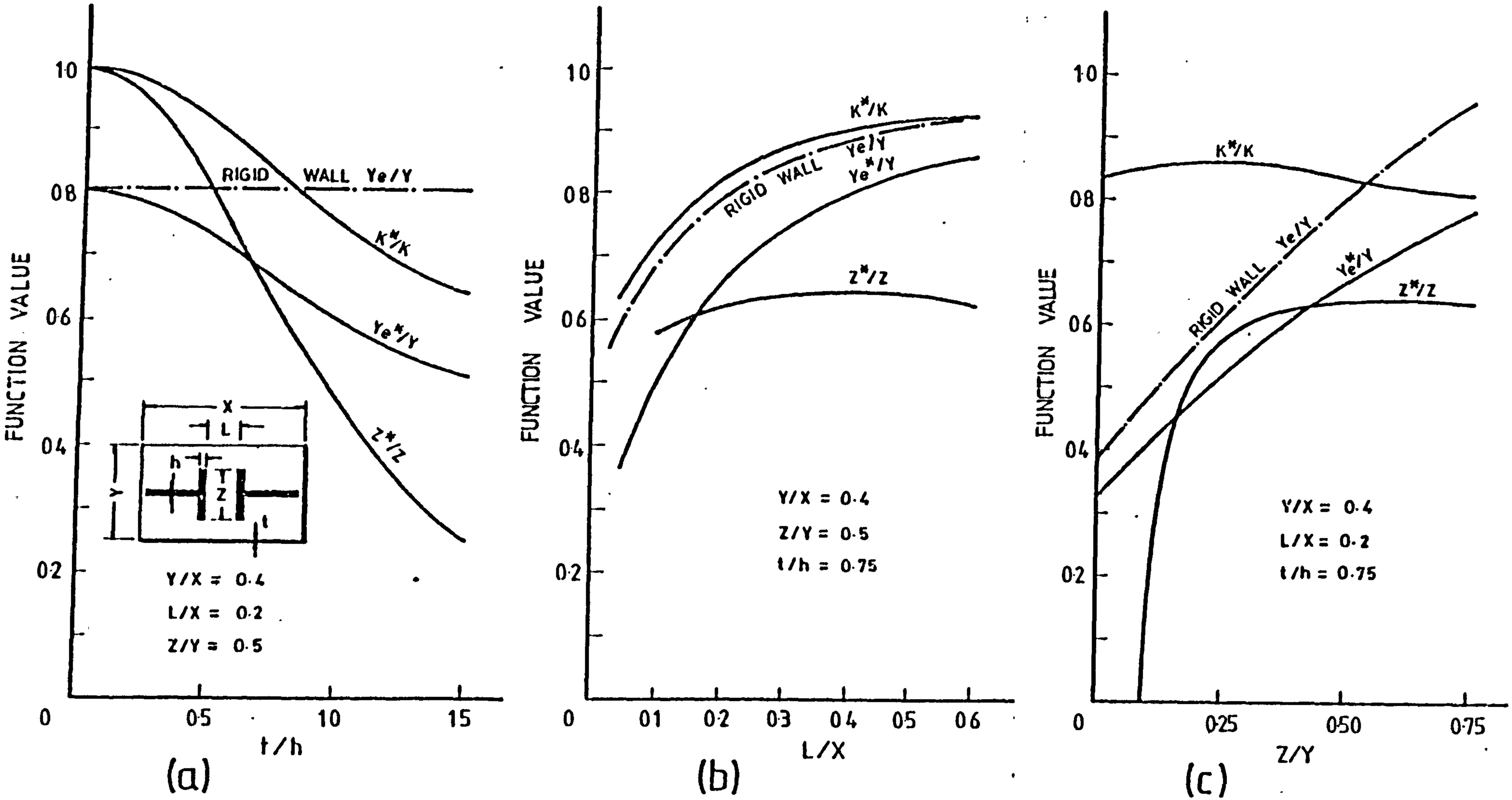

Fig. 5.9 Variations of Slab Effective Width, Stiffness Ratio and Effective Flange Width With (a) Slab/Wall Thickness Ratio, (b) Corridor Opening Ratio, and (c) Flange Width Ratio, in Flanged Wall Configuration

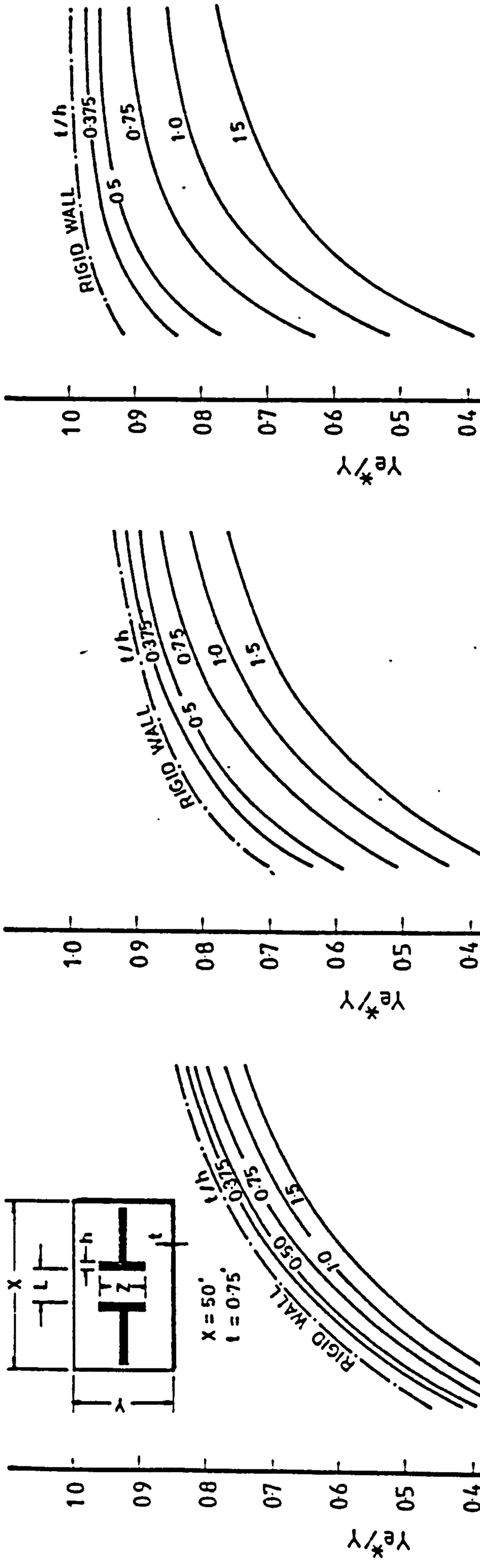

Fig. 5.10 Design Curves for Slab Effective Width in Flanged Wall Configuration

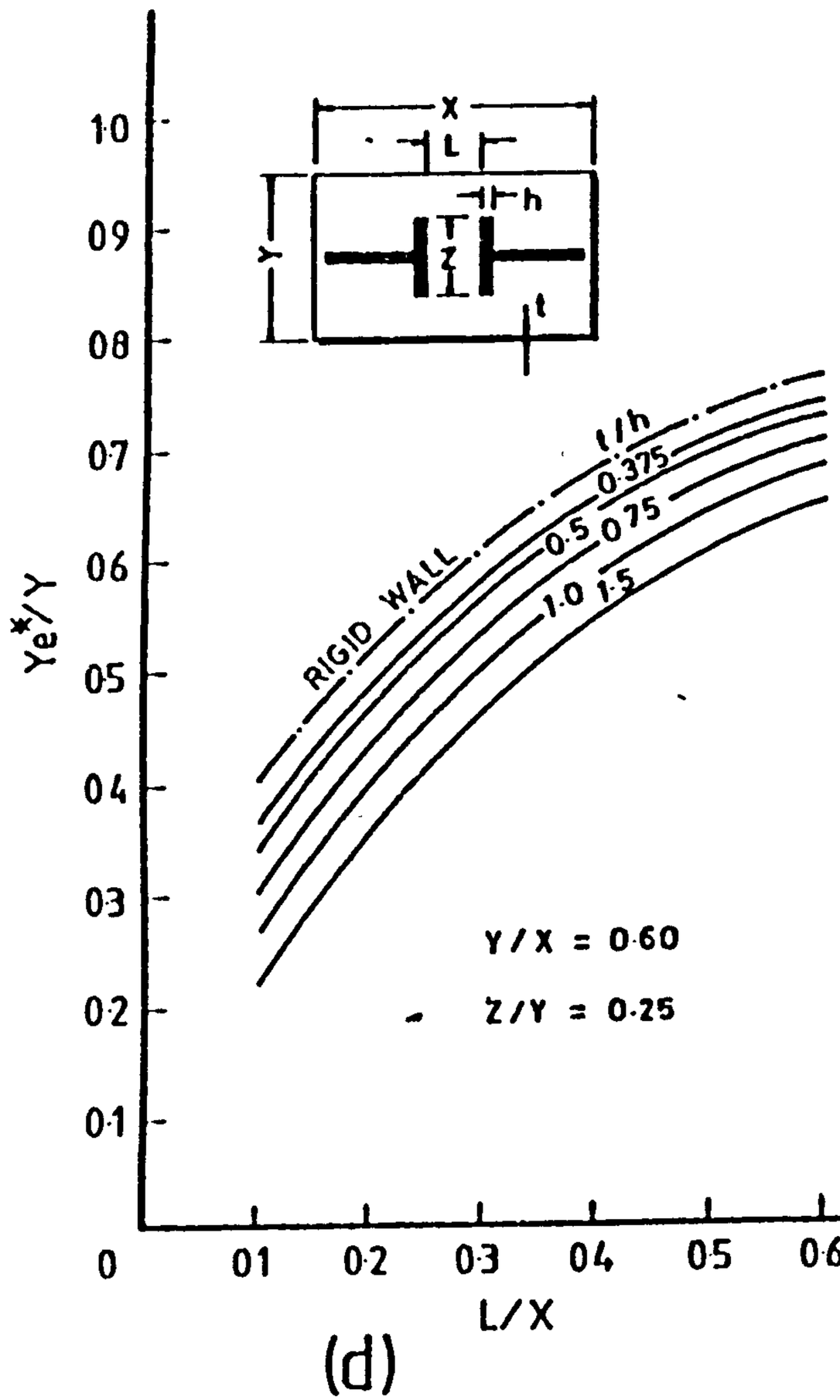

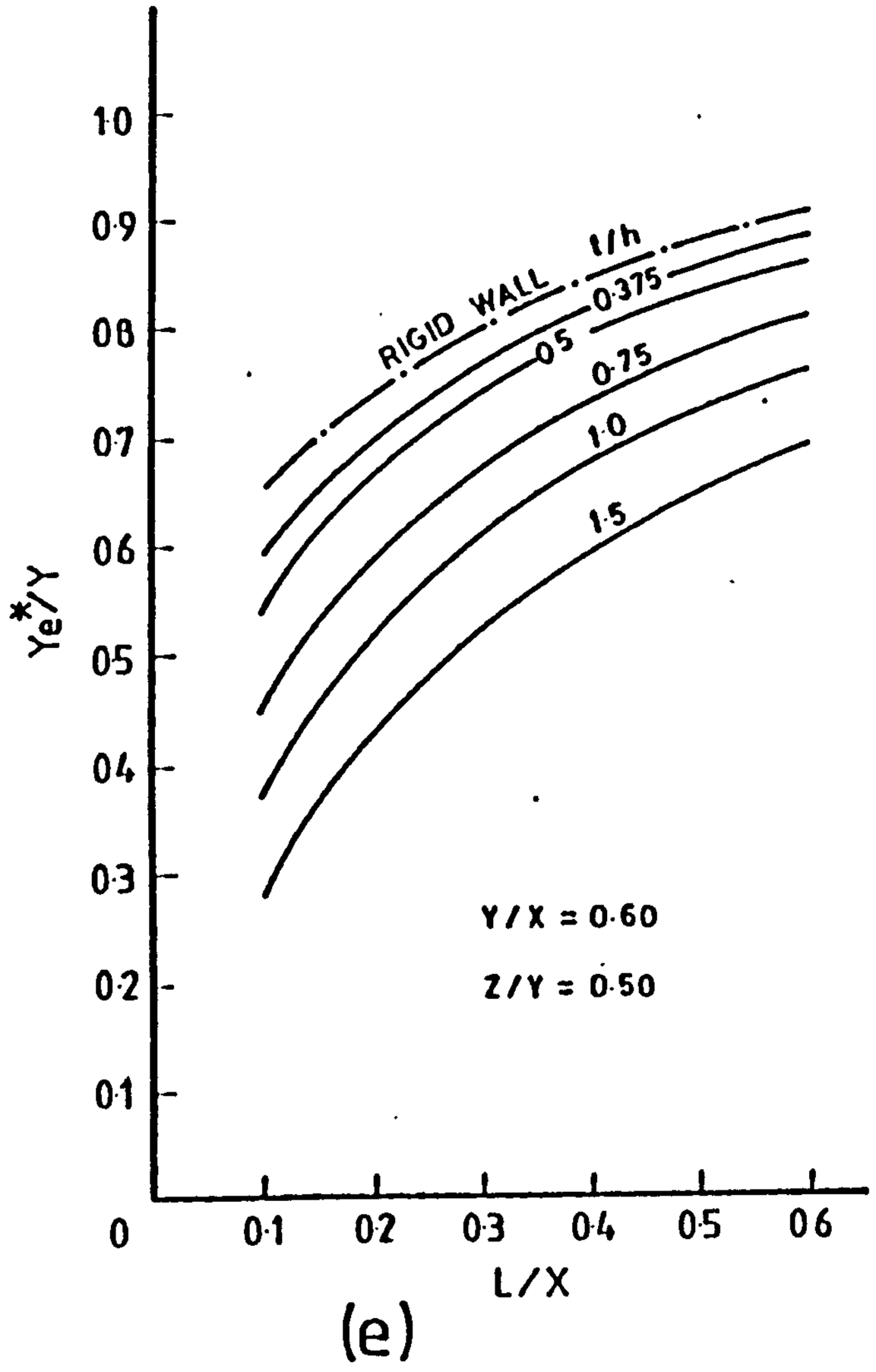

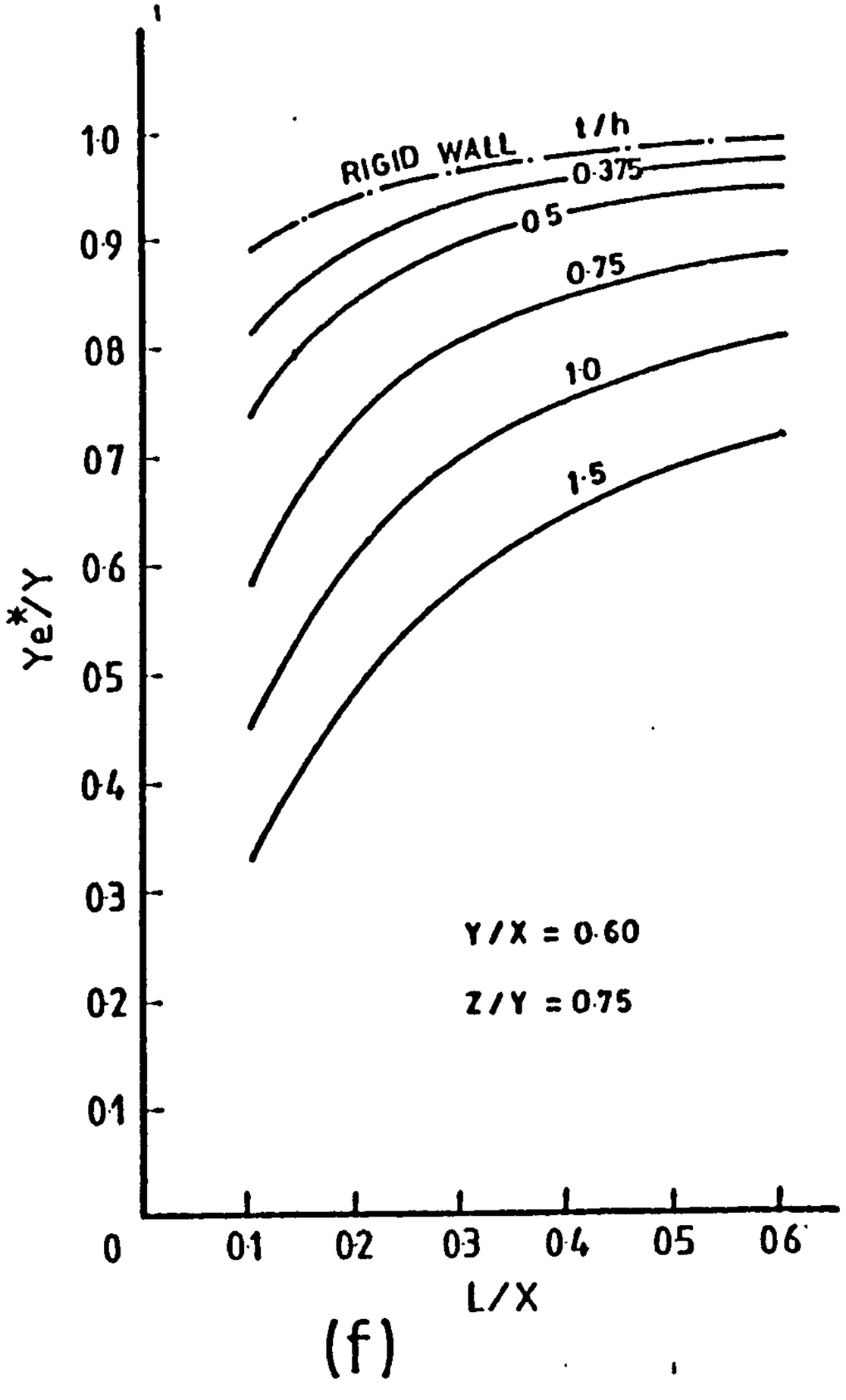

Fig. 5.10 (Contd) Design Curves for Slab Effective Width in Flanged Wall Configuration

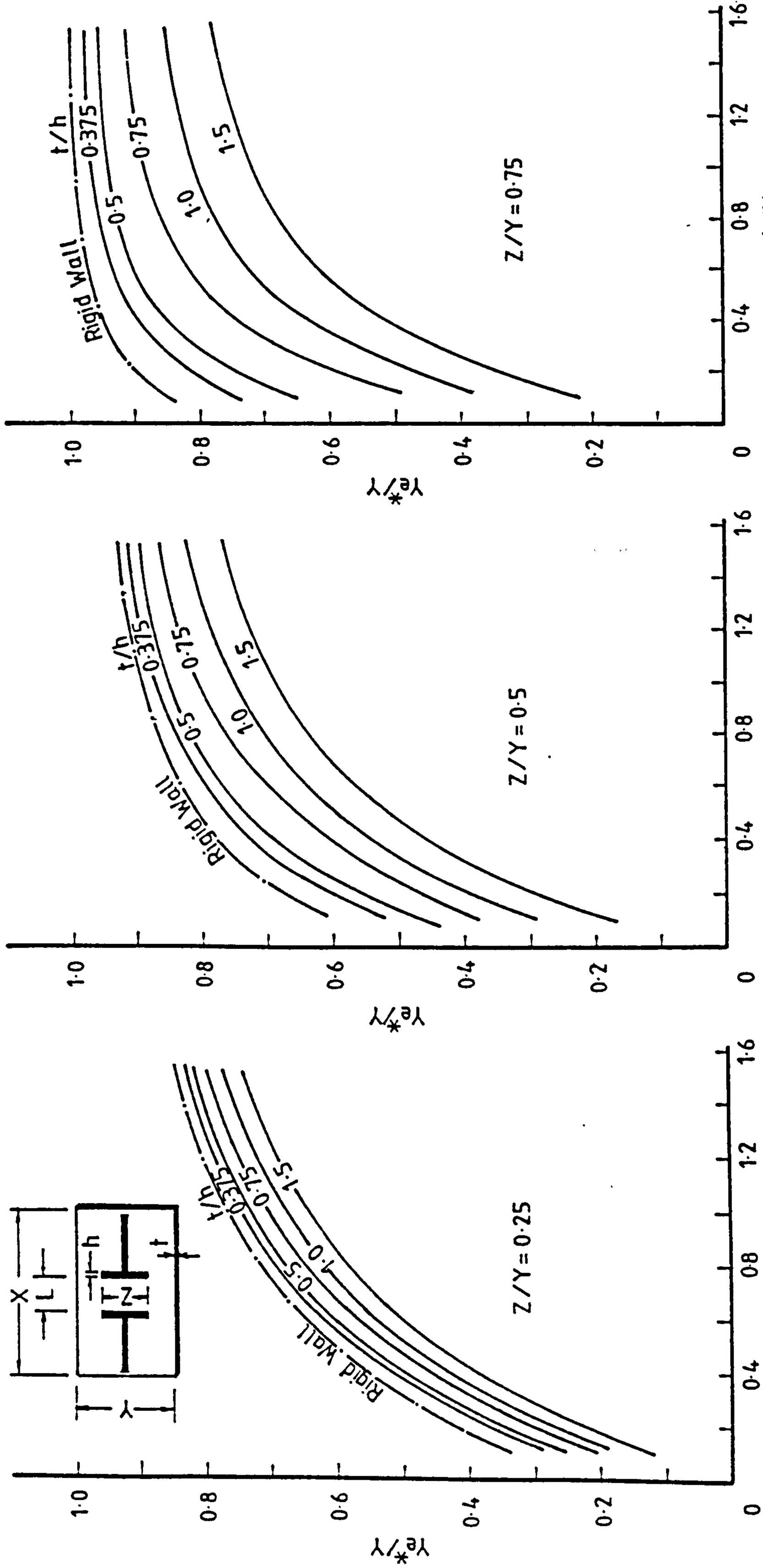

Fig. 5.11 Generalised Design Curves for Slab Effective Width in Flanged Wall Configuration with (a) Z/Y = 0.25, (b) Z/Y = 0.5, and (c) Z/Y = 0.75

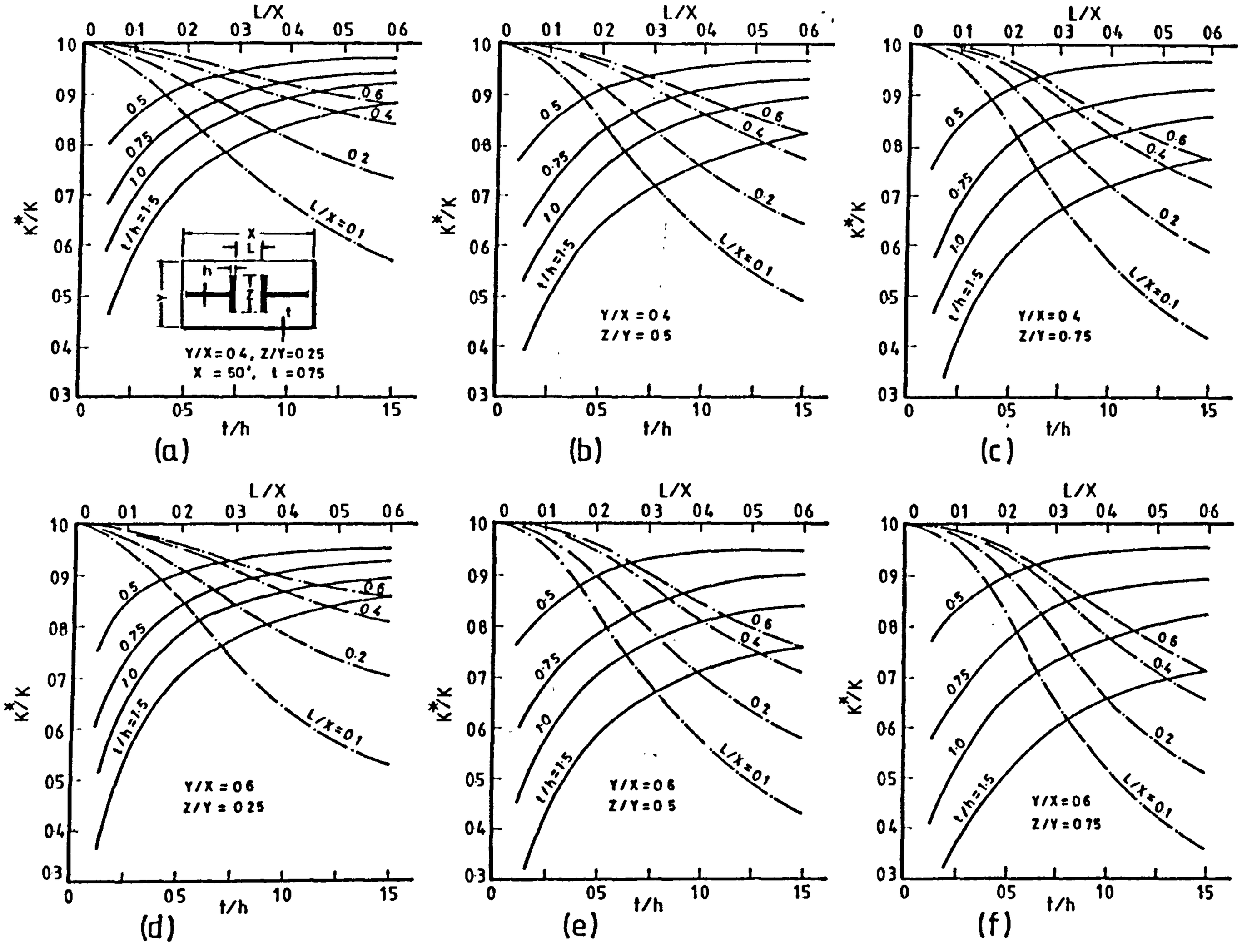

Fig. 5.12 Variation of Stiffness Ratio With Slab/Wall Thickness Ratio and With Corridor Opening Ratio, in Flanged Wall Configuration

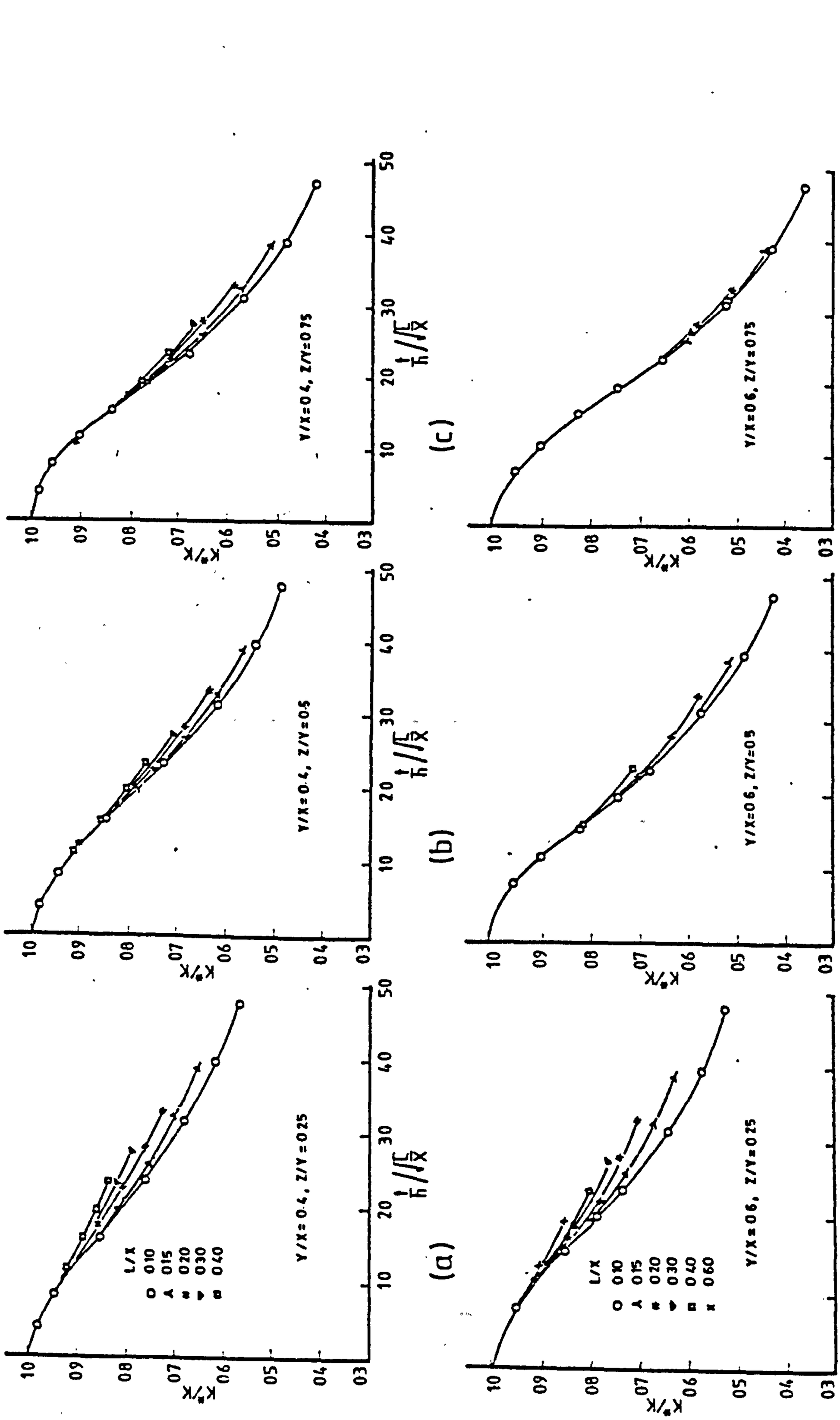

Fig. 5.13 Variation of Stiffness Ratio with the Parameter $(t/h)/(L/X)^{\frac{1}{2}}$

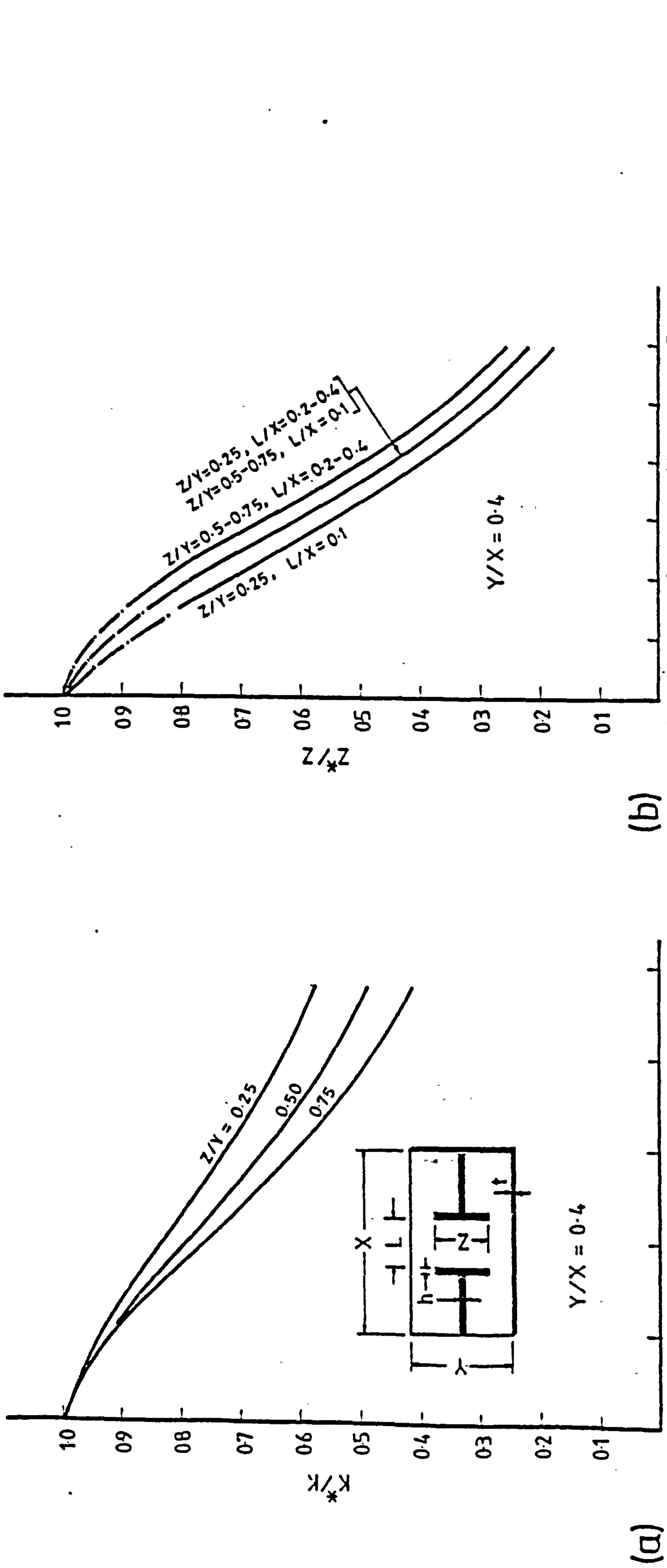

Fig. 5.14 Approximate Design Curves for (a) Stiffness Ratio, and (b) Effective Flange Width, in Flanged Wall Configuration

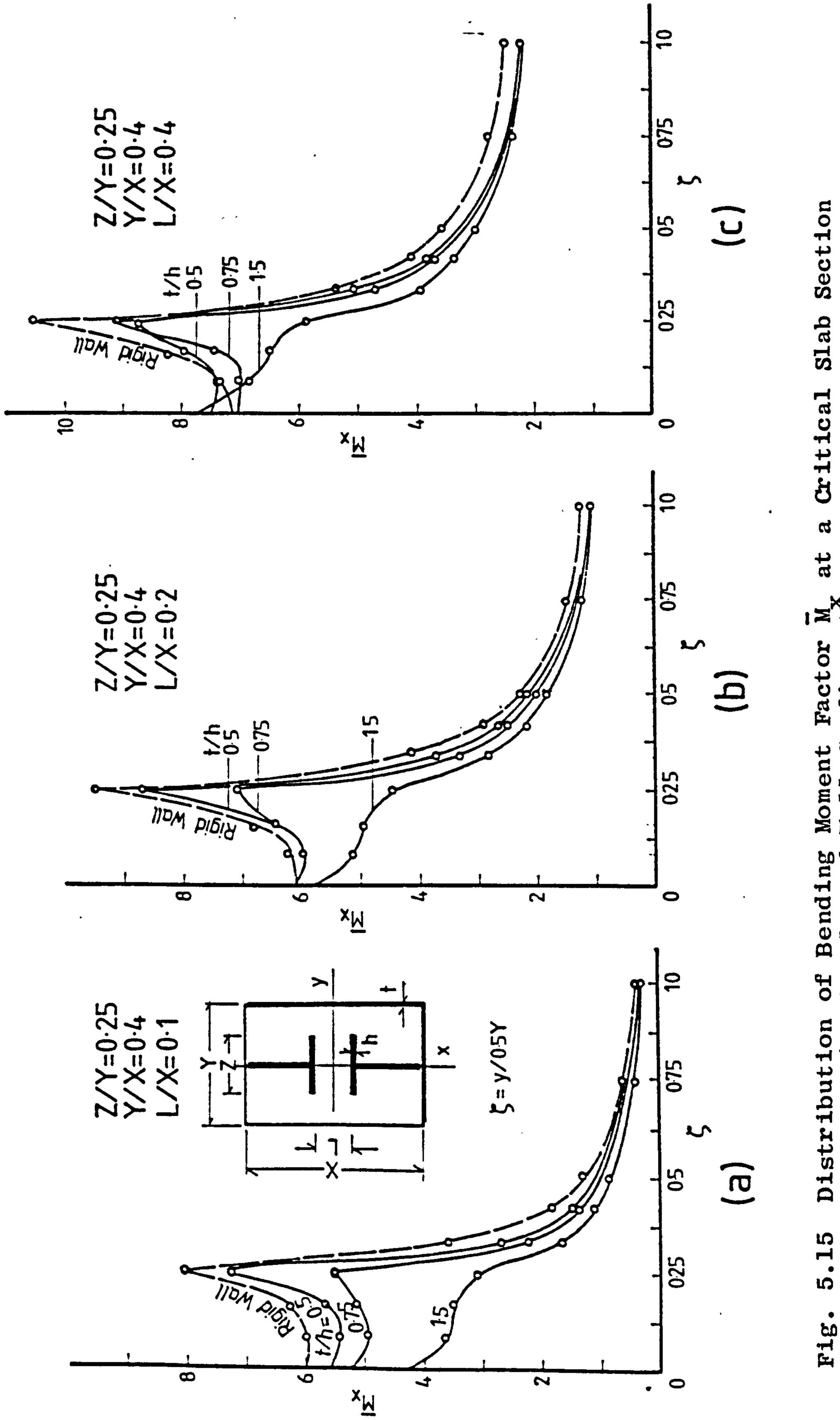

Fig. 5.15 Distribution of Bending Moment Factor $\bar{M}_x$ at a Critical x = -L/2, in Flanged Wall Configuration

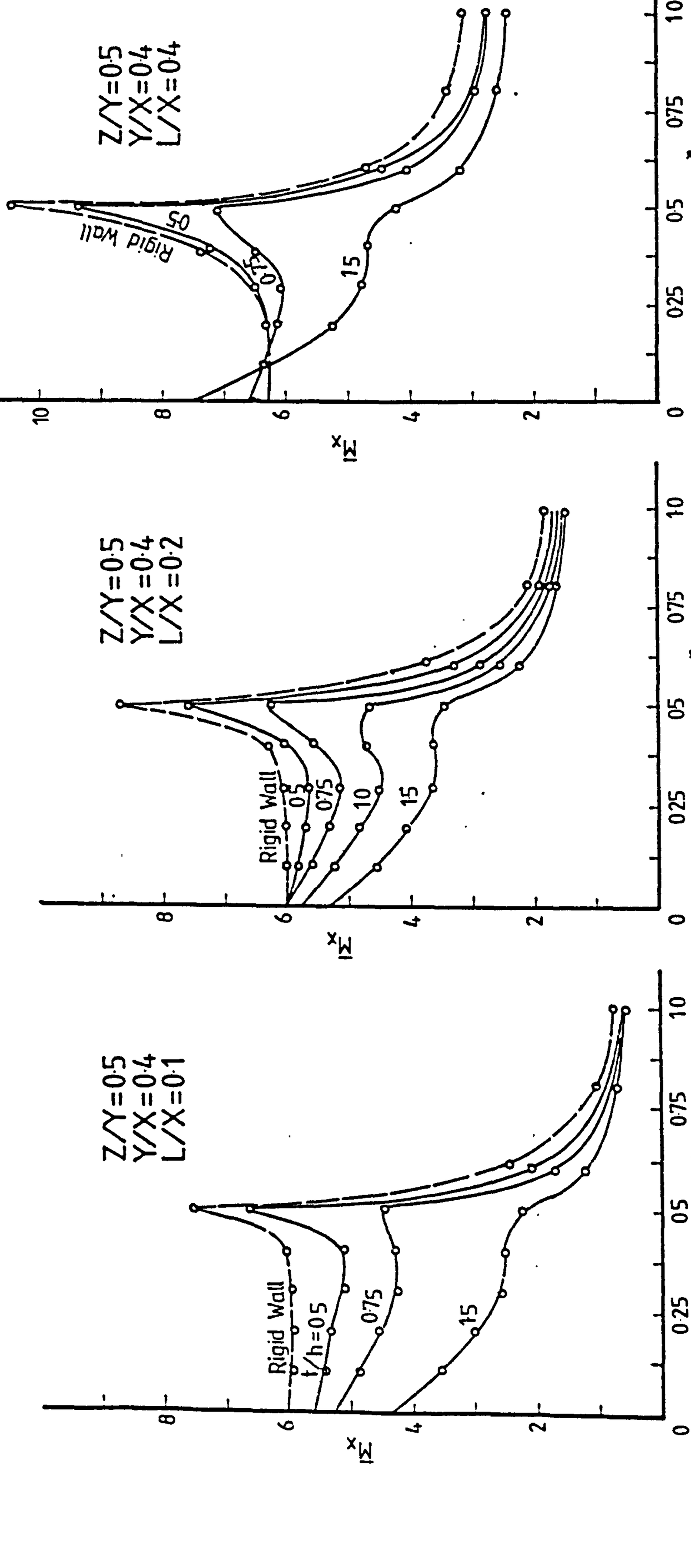

Fig. 5.15 (Contd) Distribution of Bending Moment Factor $\bar{M}_x$ at a Critical Section at x = -L/2, in Flanged Wall Configuration

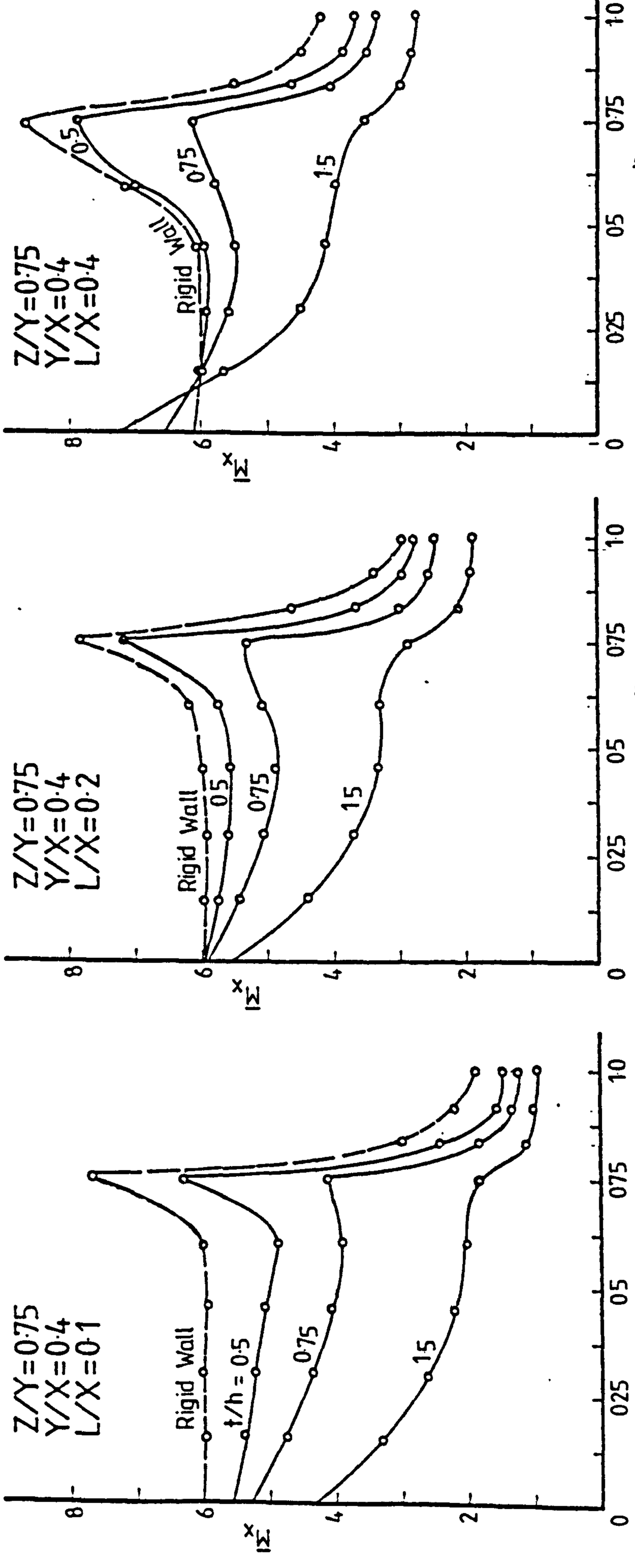

Fig. 5.15 (Contd) Distribution of Bending Moment Factor $\bar{M}_x$ at a Critical Section at x = -L/2, in Flanged Wall Configuration

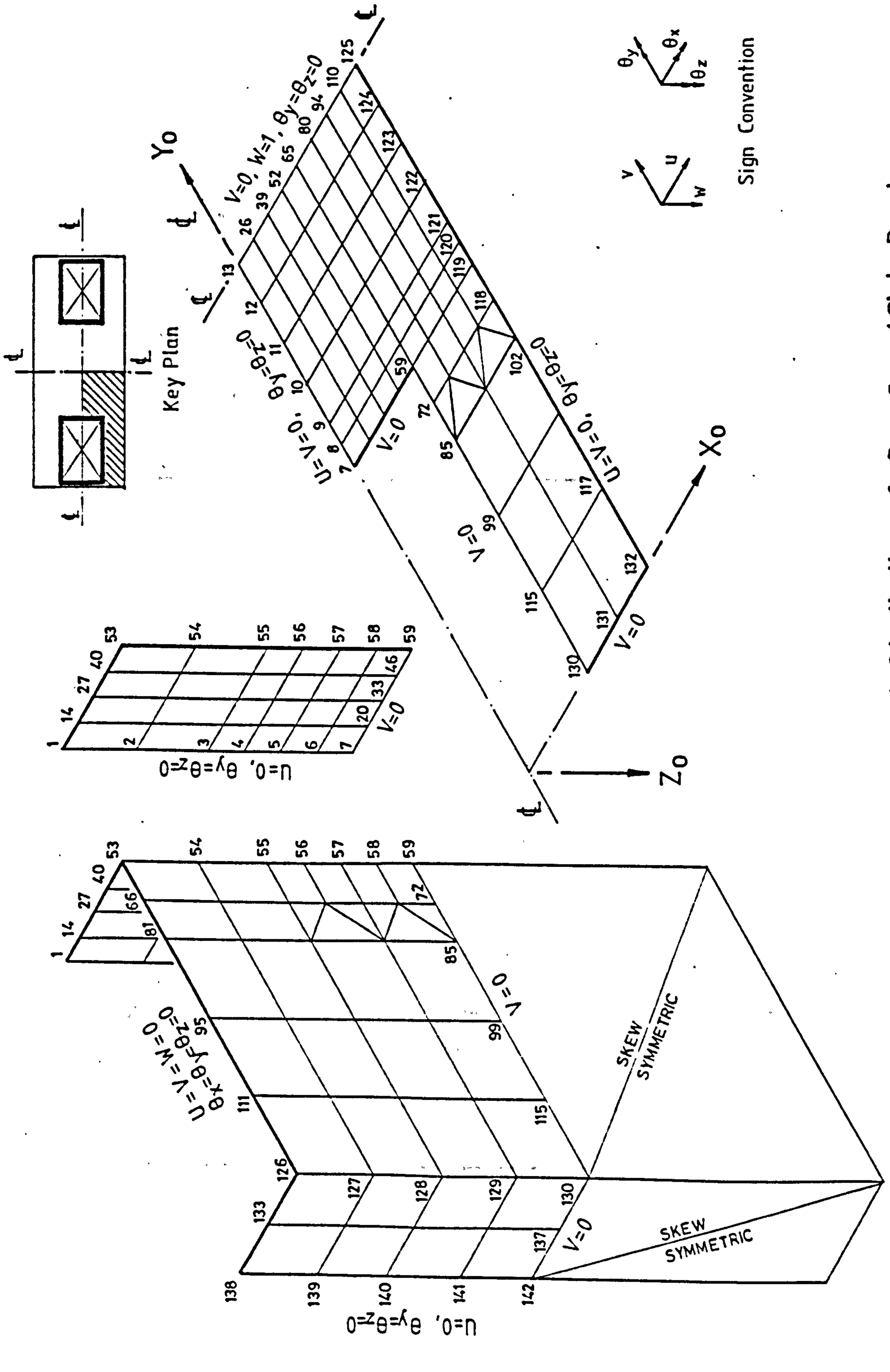

Fig. 5.16 Finite Element Idealisation of Box Core / Slab Panel

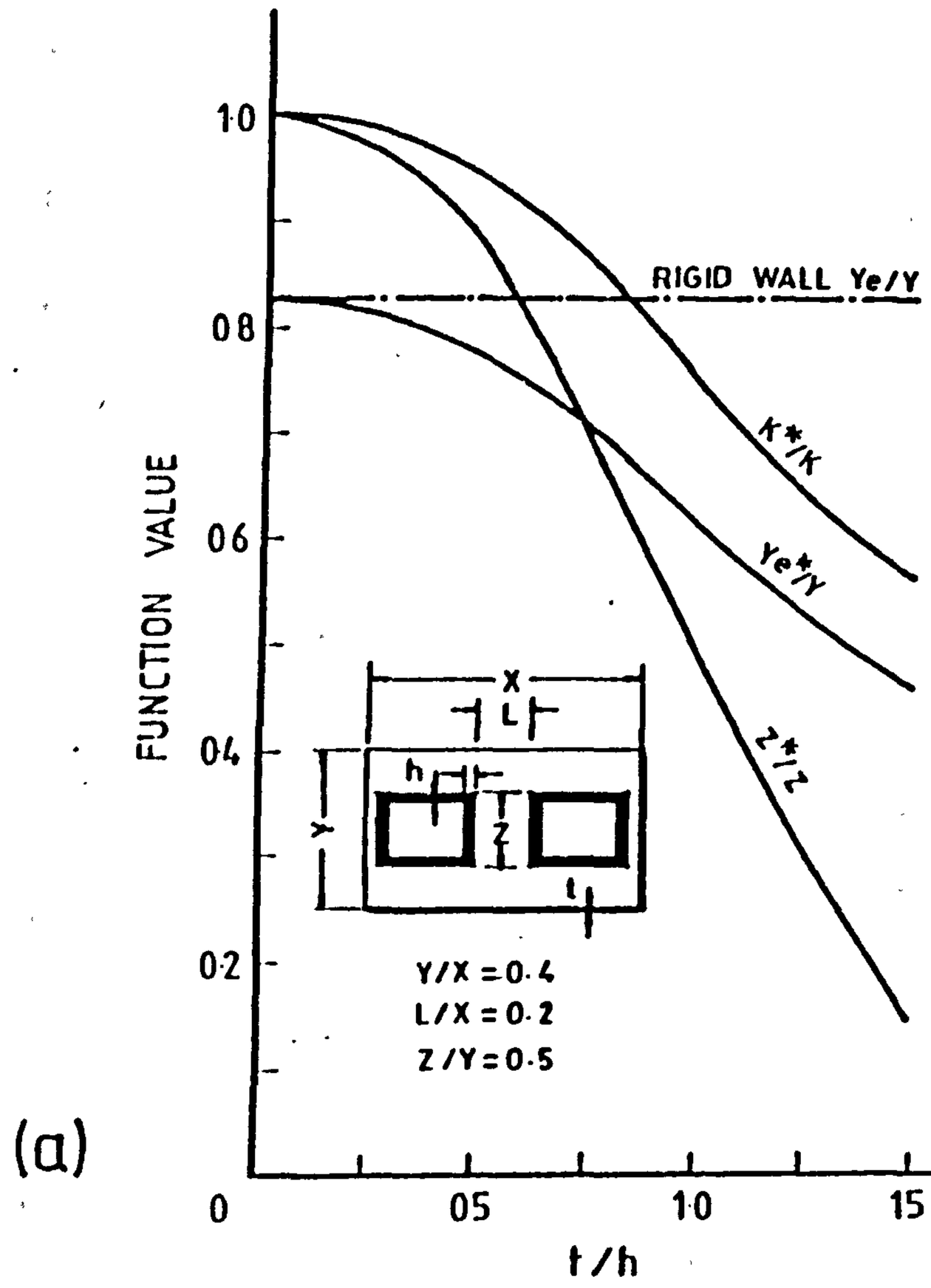

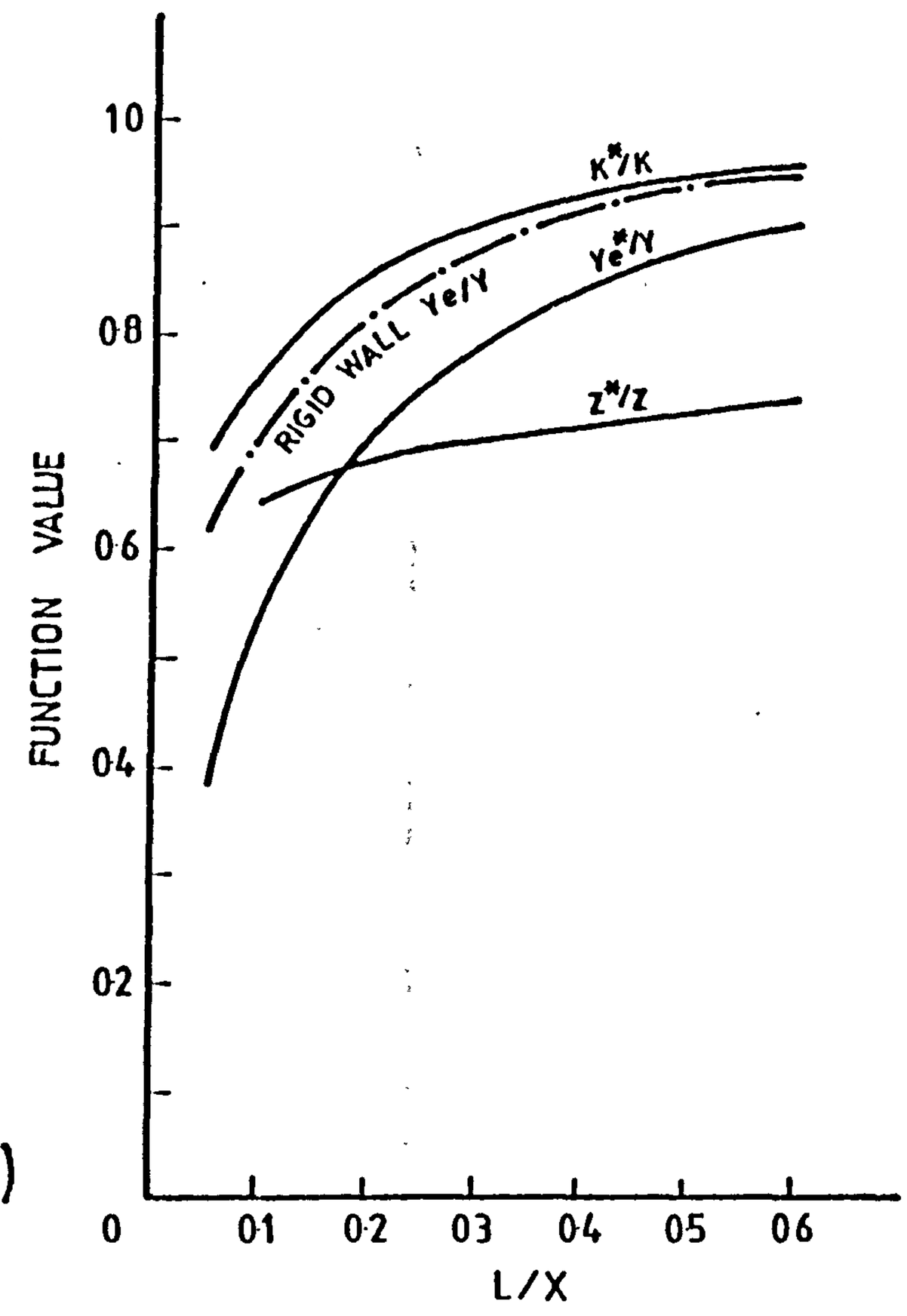

Fig. 5.17 Variations of Slab Effective Width, Stiffness Ratio and Effective Flange Width With (a) Slab/Wall Thickness Ratio and (b) Corridor Opening Ratio, in Box-Core Configuration

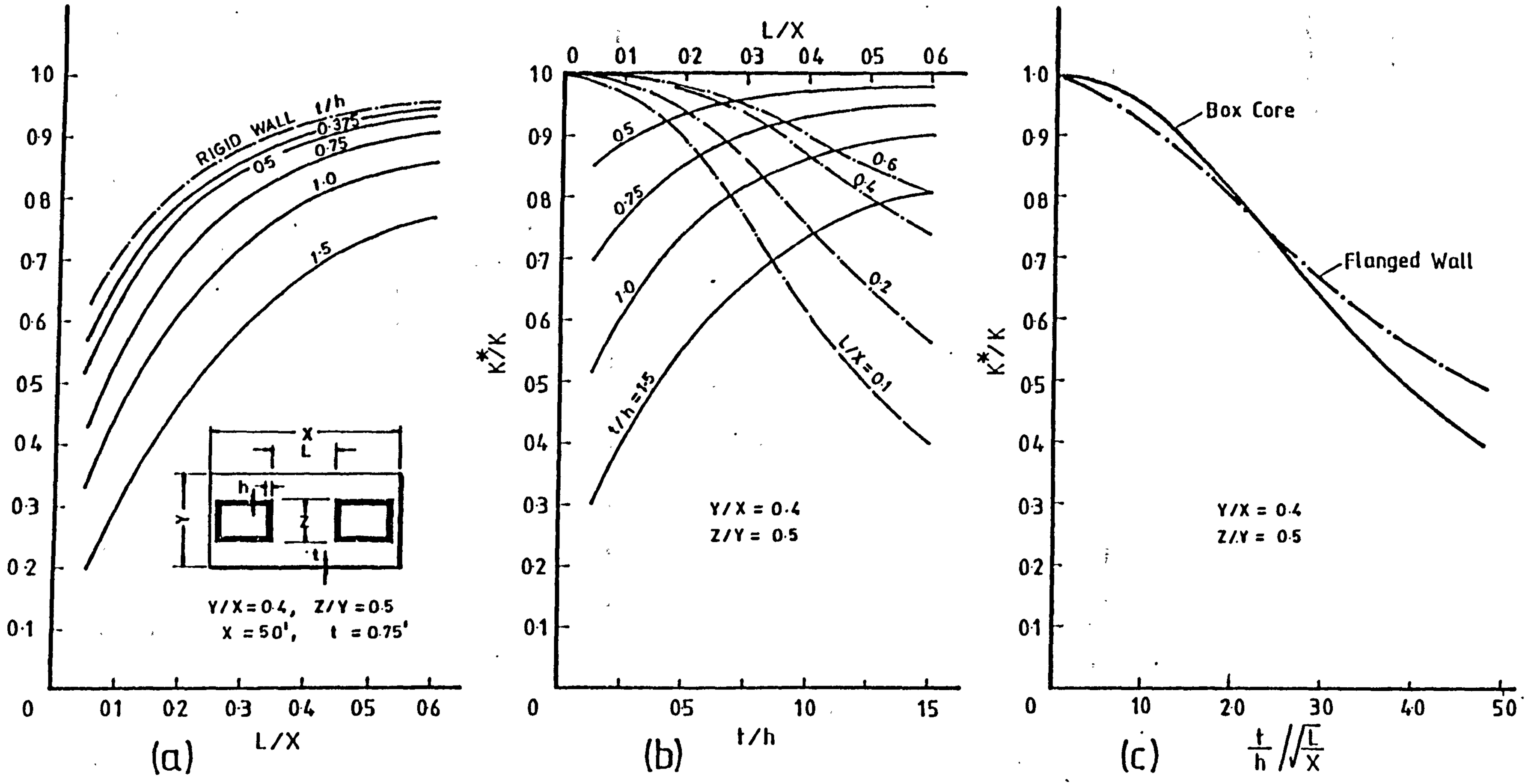

Fig. 5.18 Design Curves For (a) Slab Effective Width and (b) Stiffness Ratio, in Box-Core Configuration. (c) Variation of Stiffness Ratio With the Parameter $(t/h)/(L/X)^{\frac{1}{2}}$ For Box Core and Flanged Wall Configurations

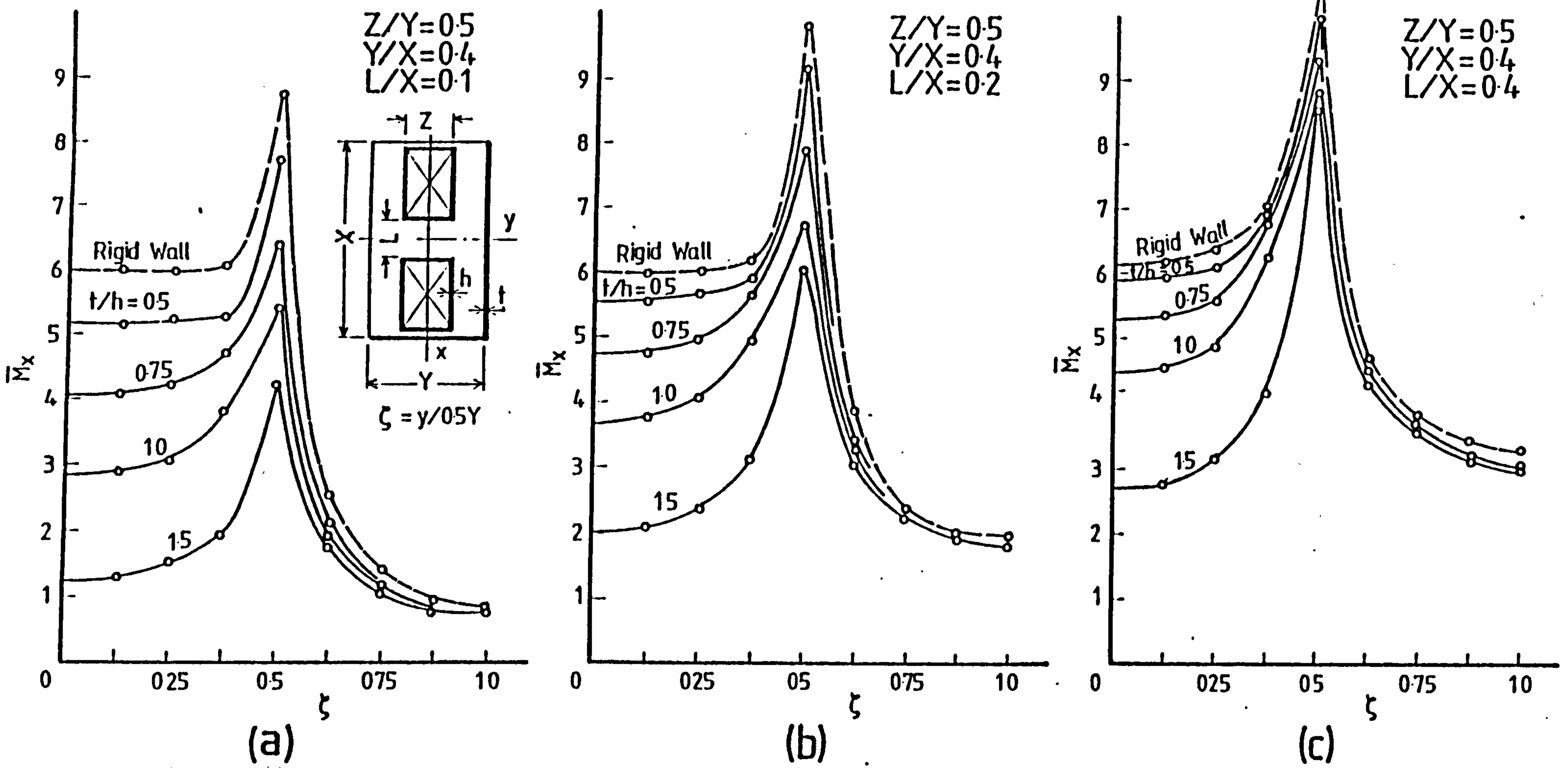

Fig. 5.19 (a)-(c) Distribution of Bending Moment Factor $\bar{M}_x$ at a Critical Slab Section at x = -L/2, in Box-Core Configuration

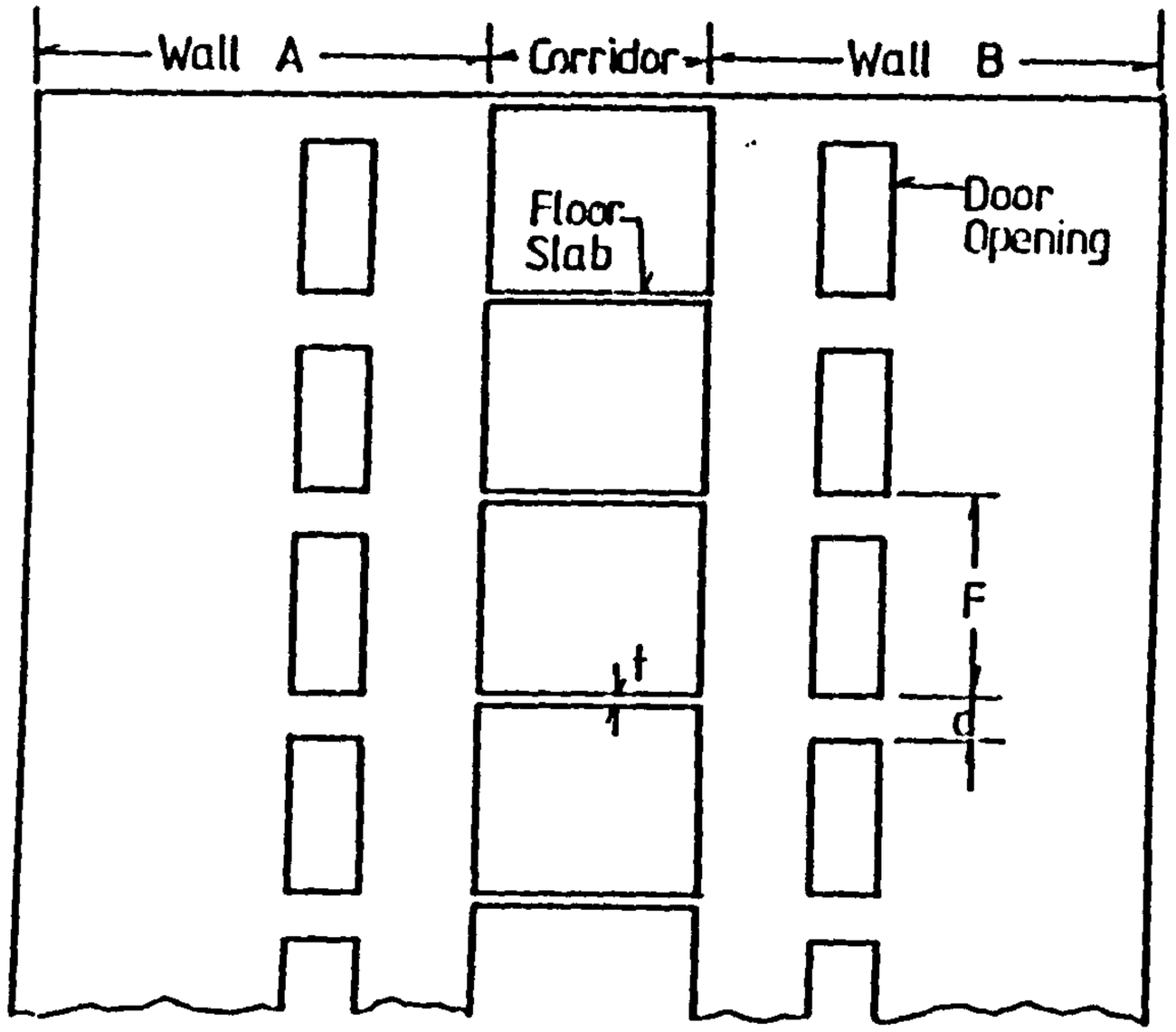

(a) Typical Wall Elevation

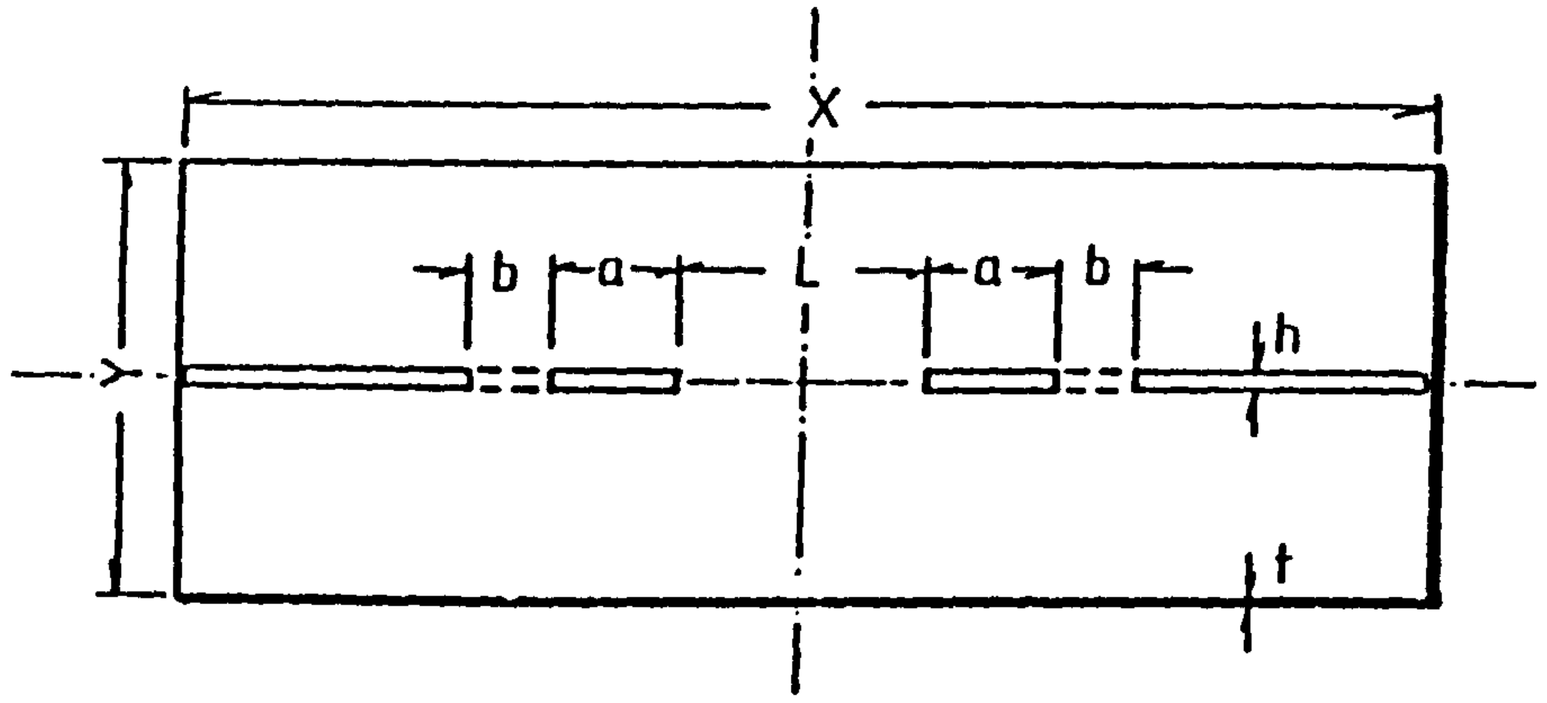

(b) Plan Of Typical Interior Floor Panel

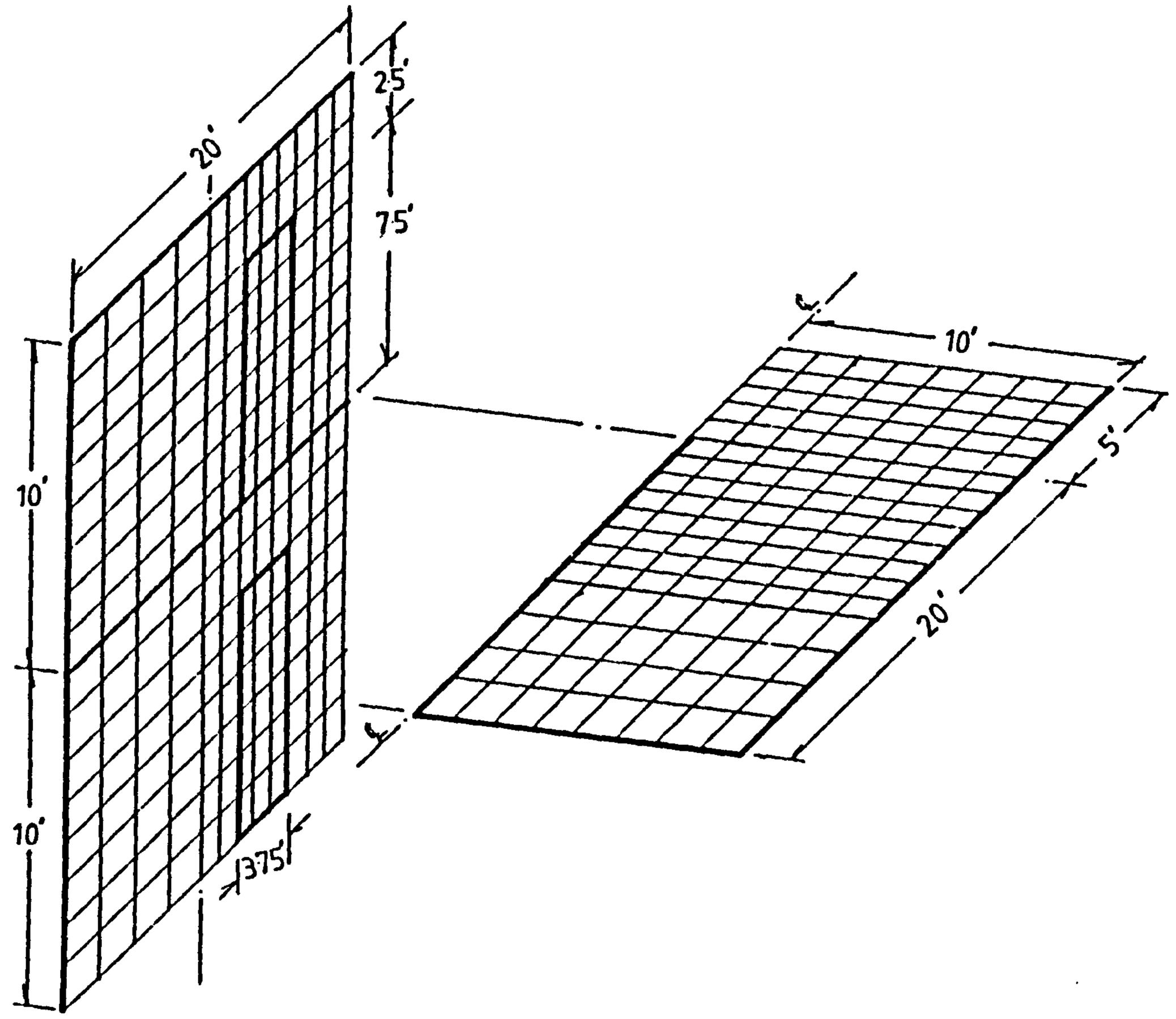

(c) Finite Element Idealisation Of 1/4 Perforated-Wall/Floor-Slab Panel

Fig. 5.20 Slab-Coupled Plane Walls With Door Openings

CHAPTER 6

COMPOSITE ACTION OF SLABS AND LINTEL BEAMS COUPLING A PAIR OF SHEAR WALLS

6.1 INTRODUCTION

Shear walls coupled by lintel beams monolithic with floor slabs are frequently encountered in practical shear wall buildings. The usual practice in the analysis of such coupled shear walls is to disregard the contribution of the slab and assume that the walls are coupled only by a prismatic lintel beam. In gravity load design it is common practice to include a portion of the slab as a flange for the floor beam so that a greater moment of resistance is obtained by the composite action. While under ultimate load conditions it may be sound practice to ignore the contribution of the slab on account of cracked flange sections at points of negative bending moments, there is no reason why under working load conditions in which the structural behaviour is sensibly linearly elastic, the beneficial stiffening effect of the slab should not be included in the analysis of the coupled shear walls.

In this Chapter the composite behaviour of the lintel and slab coupling a pair of shear walls is investigated by the finite element method. The stiffening effect and the effective width of the slab acting as the flange of a composite tee-beam are evaluated for a range of structural parameters. The significance of composite coupling action is assessed with reference to the calculation of critical design quantities for a typical coupled wall structure.

6.2 METHOD OF ANALYSIS

6.2.1 STIFFNESS OF COUPLING BEAM

Consider the elastic deformation of a coupling beam of span L coupling a pair of shear walls with centroidal

axes distant L_a apart, undergoing a parallel rotation θ under the actions of moments M (Fig. 6.1(a)). It is again assumed that plane sections of the wall remain plane in bending. The displacement δ due to the effects of flexure and shear deformation can be shown to be given by

$$\delta = \frac{M L^3}{6EI L_a} + \frac{2ML}{G A^* L_a}$$

which can be written simply as

$$\delta = \frac{ML^3}{6EI^* L_a}$$

where I* is the reduced moment of inertia given by

$$I^* = I/\left[1 + \frac{12EI}{GA^*L2} \right] \qquad (6.1)$$

in which I is the actual moment of inertia and A* is the effective shear area of the coupling beam, and E and G are respectively the elastic and shear moduli.

The wall rotation θ is given by

$$\theta = \frac{\delta}{L_a} = \frac{M L^3}{6EI^* L_a^2}$$

Hence the coupling stiffness of the beam, which may be defined in terms of the moment-rotation relationship of the wall, is given by

$$\frac{M}{\theta} = \frac{6EI^*}{L} \left(\frac{L_a}{L}\right)^2 \qquad (6.2)$$

The moment-rotation relationship for a pair of shear walls coupled by a lintel monolithic with the floor slab can be evaluated by a finite element analysis. Hence the effective moment of inertia for the composite coupling medium can be obtained using expression (6.2). Expressing the effective composite moment of inertia I_c^* as a ratio of the reduced moment of inertia of the lintel I_w^* provides a measure of the stiffening effect of the slab. The reduced moment of inertia of the lintel I_w^* is given by expression (6.1), with

$$I = I_w \text{ and } A^* = A_w/1.2$$

where I_w and A_w are the actual moment of inertia and cross-sectional area of the lintel.

6.2.2 EFFECTIVE FLANGE WIDTH OF COMPOSITE COUPLING BEAM

In common with gravity load design, a portion of the floor slab may be assumed to act as the flange of a tee-beam. In order to evaluate the effective flange width for the composite coupling beam, the effective shear area A^* must first be established. Results obtained by the finite element analysis indicate that where shear deformation is likely to be of some significance, the shear induced by coupling action is carried mainly (over 80%) by the web or lintel portion of the composite coupling beam. Hence it may be assumed, for convenience, that in the equivalent composite beam the whole of the shear is carried by the web, in which case, the shear area A^* can be taken as $A_w/1.2$. The absolute (un-reduced) moment of inertia I_c for the equivalent composite beam can then be evaluated from the effective composite moment of inertia I_c^* using expression (6.1), after which it is a relatively easy matter to obtain the effective flange width by a reverse process. It can be shown that the effective flange width Y_e is given by

$$Y_e = b + \frac{C + [\, C^2 + 48t^2\, A_w(I_c - I_w)\,]^{\frac{1}{2}}}{2t^3} \qquad (6.3)$$

where b is the width of the lintel, t is the slab thickness and $C = 12(I_c - I_w) - A_w(t^2 + 12e^2)$, in which e is the eccentricity between the centroids of the web and flange sections (Fig. 6.1(b)).

6.2.3 FINITE ELEMENT ANALYSIS OF SLAB AND LINTEL

The slab monolithic with the lintel beam is subjected to membrane as well as bending effects under composite coupling action. In order to model this behaviour adequately the slab and lintel beam are represented by

rectangular flat shell elements (RS24). By exploiting the conditions of symmetry and anti-symmetry, the analysis of the floor slab in an interior bay of a cross-wall structure is reduced to that for a typical slab quadrant. Fig. 6.2(a) shows a typical finite element idealisation of the slab and lintel beam, and the boundary conditions prescribed for the analysis. The wall is assumed rigid, and flexibility effects due to local elastic wall deformation at the beam-wall junction are disregarded, since it is expected that these effects could be allowed for in the overall analysis of the shear wall system following the procedures suggested for beam coupled shear walls.[65,66]

To obtain the moment-rotation relationship the nodes at the wall boundary are restrained completely against displacement, and the nodes along the corridor edge of the slab and beam are given a unit vertical displacement ($w = 1$, $\theta_x = 0$). The symmetry and anti-symmetry displacement boundary conditions are prescribed at the appropriate boundary nodes. The resultant vertical reaction Q at the deflected edge of the slab is evaluated by the finite element analysis. Since the resultant moment about the wall axis is given by $Q\ L_a/2$, and the effective wall rotation is given by $2/L_a$, the coupling stiffness of the composite beam is evaluated simply as $Q\ L_a^2/4$. The effective composite moment of inertia and the effective flange width of the equivalent tee-beam are then calculated according to equations (6.2) and (6.3). The finite element analysis also computes the membrane stresses and bending stress resultants at all the nodes.

6.3 EVALUATION OF ELEMENT MESH FOR LINTEL

In order to determine suitable mesh patterns for the discretisation of the lintel, a series of analyses has been carried out using various mesh patterns for a test problem involving an end-loaded prismatic cantilever beam. Two span-depth ratios were considered. The beams were

sub-divided along the depth into two and four element divisions. Along the span, the shorter and the longer beams were sub-divided respectively into five and eight element divisions as shown in Fig. 6.2(b). The span sub-divisions are considered reasonably fine and appropriate for the discretisation of the floor slab for the subsequent parameter study.

Table 6.1 shows the finite element results for the maximum deflection w_B at the tip, and the maximum fibre stress σ_A at the root of the cantilever, reduced to compare with unit values given by the engineer's beam theory, with allowance for shear deformation. The results show that by using the 2-element deep sub-division, values for the maximum deflection and fibre stress for both span-depth ratios are evaluated to within 5% of the values given by beam theory. Using the 4-element deep sub-division, the values for the maximum deflection are within 2% of the beam theory value, but the value of the maximum fibre stress for the smaller span-depth ratio is about 8% higher than the beam theory value. The poorer correspondence between the stress values in this case is due to the 'deep beam effect' which tends to increase the maximum fibre stresses beyond the values given by a linear stress distribution assumed in beam theory.

Since reasonably accurate results for deflections and stresses can be obtained using the 2-element deep sub-division, this discretisation scheme is employed for the lintel coupling beam in the parameter study.

6.4 PARAMETER STUDY ON COMPOSITE COUPLING ACTION

The variables which are involved in the structural geometry of a typical floor panel coupling a pair of shear walls include the slab width Y, the wall opening L, the wall length W, the slab thickness t, the lintel width b and the lintel depth d. Judging from the results obtained for slab-coupled shear walls (Chapters 3-5), the wall length W is not expected to have any significant influence on the composite action of lintel and slab and

therefore has not been considered as a variable in the present parameter study. The influences of the other variables on the lintel-slab composite coupling action have been evaluated with reference to a standard slab thickness. The main numerical results of the parameter study are given in Appendix A6.1.

6.4.1 INFLUENCE OF SLAB WIDTH

Fig. 6.3(a) shows the variations of composite stiffness ratio I_c^*/I_w^* and effective flange width Y_e/t with slab width Y/t for lintel depths d/t of 3.2 and 7.2 and wall opening width L/t of 13.3. The arrows denote to which axis the curve refers. It is seen that for the practical range of slab width considered, the composite stiffness ratio and the effective flange width are affected very little by variations in slab width.

6.4.2 INFLUENCE OF WALL-OPENING WIDTH

Fig. 6.3(b) illustrates the variations of composite stiffness ratio and effective flange width Y_e/Y with the wall opening width L/t for lintel depths d/t of 3.2 and 7.2. A lintel width b/t of 1.33 and slab width Y/t of 26.7 are considered in each case. The composite stiffness ratio and effective flange width Y_e/Y increase substantially with the wall opening width L/t over the range of values considered. The influence of wall opening width however tends to become less important with larger values.

6.4.3 INFLUENCE OF LINTEL WIDTH

The influence of lintel width on the composite stiffness ratio and effective flange width is assessed by comparing the results for lintel widths b/t of 1.33 and 2.67. Wall opening widths L/t of 13.3 and 26.7 are considered, and in each case the lintel depth d/t is 5.5 and the slab width Y/t is 26.7.

The numerical results given in Table 6.2 indicate that for the smaller wall opening width L/t, doubling the

width and hence stiffness of the lintel increases the effective flange width less than 2% and hence results in a reduction of the composite stiffness ratio I_c^*/I_w^* by about 16%. For the larger wall opening width, doubling the lintel width produces approximately an 8% increase in the effective flange width and a 5% increase in composite stiffness ratio. For practical purpose, therefore, the effect of variations in lintel width may be disregarded in the evaluation of effective flange width.

6.4.4 INFLUENCE OF LINTEL DEPTH

Fig. 6.4 shows the variations of composite stiffness ratio I_c^*/I_w^* and effective flange width Y_e/Y with lintel depth d/t for various wall opening widths L/t and slab widths Y/t. The three sets of curves are based on a lintel width b/t of 1.33. The results show that the composite stiffness ratio decreases with an increase in the lintel depth d/t over the whole range of values considered. The effective flange width Y_e/Y, on the other hand, is seen to decrease initially with increasing values of d/t, reaching a minimum value when d/t is between 3 and 4 generally. Thereafter, the effective flange width increases with lintel depth.

The effective flange width values for the practical range of relative lintel depths considered are substantially lower than the effective width for the limiting case of a flat slab floor without the lintel beam (cf. Chapter 3). The lower ends of the curves for Y_e/Y in Fig. 6.4 are seen to approach the limiting values obtained in Chapter 3. The curves may be used as design curves for evaluating rapidly the effective flange width or composite coupling stiffness in a practical situation. Although the curves are based on a particular relative lintel width b/t, the effective flange width values for other situations may be obtained reasonably accurately from the curves presented by disregarding the effect of practical differences in lintel widths.

6.4.5 DISTRIBUTION OF SHEAR ALONG LINTEL

For the calculation of effective flange width from the finite element results it has been assumed that the whole of the shear at a transverse slab section is carried by the web of the composite section. The accuracy of this assumption is immaterial so long as the effective coupling stiffness required in a shear wall analysis is calculated from the effective flange width using the same assumption. For the shear design of the lintel however, the actual shear carried by the web must be accurately known. Fig. 6.5 shows the span-wise variation of the percentage of the shear at transverse sections carried by the web, for two typical lintel depth-span ratios. It is seen that for the deeper lintel the percentage shear carried by the web is relatively constant along the span and is greater than 95% at any section. With the shallower lintel the web shear away from the wall support is significantly lower than the values close to the wall, but is still greater than 85% of the total shear at any section. In both cases, the web carries practically the full shear at points close to the wall support. Hence for shear design it is reasonable to assume that the whole of the shear at a transverse section is carried by the web alone.

6.4.6 INFLUENCE OF LOCAL ELASTIC WALL DEFORMATION

In evaluating the composite stiffness ratio and effective flange width in the preceding sections, the flexibility effect due to the local elastic wall deformation at the lintel and wall junction was disregarded by assuming that plane sections of the wall remain plane in bending. It has been anticipated that the junction flexibility effect could be allowed for in the calculation of composite coupling stiffness very simply by extending the flexible span of the coupling beam by an equivalent length equal to the lintel depth, as suggested by Michael[65] for prismatic lintel beams. In order to assess the accuracy

of the simple procedure, additional analyses which now include a segment of the wall with the lintel and slab in the finite element model have been carried out for a typical configuration which was considered in the previous parameter study.

Since the boundary conditions associated with the wall segment may have some influence on the results, the effective composite coupling stiffness of the lintel and slab has been evaluated for various assumed boundary conditions, as illustrated in Fig. 6.6, (a-d). In case 1 (Fig. 6.6(a)), the structure is simply supported along the corridor edge and at the wall axis at the level of the slab, and the wall is rotated by applying horizontal shear forces at its ends. The effective wall rotation for the calculation of composite coupling stiffness is assumed to be given by the chord rotation of the wall axis, and is evaluated from the computed horizontal displacements of the wall ends.

In the remaining three cases the walls are restrained in various ways and a constant vertical deflection is imposed along the corridor edge of the slab and lintel. In case 2 (Fig. 6.6(b)), the wall is restrained horizontally at the ends and vertically at a point on the wall axis at the level of the slab. In case 3 (Fig. 6.6(c)) each end of the wall is restrained horizontally along the whole edge and vertically only at a point on the wall axis. In the last case (Fig. 6.6(d)) the wall is completely clamped at its ends. In each of these three cases, the unknown resultant reaction at the corridor edge is evaluated by the finite element analysis to obtain the effective coupling stiffness of the composite coupling beam.

The configuration considered has a wall opening width of 26.67, a wall depth W/t of 13.33, a slab width Y/t of 26.67, a lintel width b/t of 1.33 and a lintel depth d/t of 5.50. The numerical results for the coupling stiffness, evaluated as $K = M/(D\Theta)$, are as follows:

Case 1 : K = 108.27

Case 2 : K = 108.15

Case 3 : K = 108.45

Case 4 : K = 111.77

It can be seen that the results are not significantly influenced by differences in the assumed boundary conditions for the wall.

In order to assess the accuracy of 'Michael's correction' for junction flexibility, the effective coupling stiffness for the same configuration has been evaluated from the 'rigid wall' results presented in Section 6.4.4, assuming an effective flexible span of $L^* = L + d$. The calculations have been performed in non-dimensional units in the following manner:

Effective span ratio $L^*/t = 26.67 + 5.50$ = 32.17

From Fig. 6.4, the composite stiffness ratio = 1.90

The effective M.I. of the lintel alone is given by $\frac{I_w^*}{t^4} = \frac{I_w}{t^4} / [\, 1 + \frac{E}{G}(\frac{d}{L^*})^2 \,]$ = 17.10

$\therefore$ The effective composite M.I. I_c^*/t^4

$= 1.9 \times 17.1$ = 32.49

The coupling stiffness K from equation (6.2)

is given by $\frac{M}{D\theta} = \frac{72(1-\nu^2)}{t^3} \frac{I_c^*}{L^*} (\frac{L_a}{L^*})^2$ = 109.89

This value of K agrees closely with the values obtained directly by the finite element analyses. Hence it would appear from the limited evidence available at the moment that 'Michael's correction' for junction flexibility is also applicable to the case of a composite coupling beam.

6.4.7 DISTRIBUTION OF STRESSES INDUCED BY COMPOSITE COUPLING ACTION

In order to illustrate the general distribution of stresses in the slab, lintel and wall induced by composite coupling action, stresses computed by the finite element analysis have been shown graphically in a number of cases.

Fig. 6.7, (a-c) show the distributions of membrane stresses N_x, N_y and N_{xy}, and bending stress resultants M_x and M_y in a quadrant of the slab induced by the parallel wall rotation shown in Fig. 6.7(h). Different scales have been used to plot the various stress components. The relative magnitudes of the various stress components may be judged from the maximum numerical values indicated for each diagram. Fig. 6.7(a) shows clearly the non-uniform transverse distributions of longitudinal membrane stresses N_x across the slab which account for the effective flange width being less than the full slab-width. The distribution of transverse membrane stress N_y (Fig. 6.7(b)) shows an unexpected existence of stresses at the exterior free edge of the slab which are considerably higher than the stresses near the inner edge of the wall where the coupling actions are expected to be highest. This unusual trend of results is not unique to the particular case considered, but is found to be a common feature with all the cases analysed, flexible and rigid wall cases included. The peak transverse stresses at the slab edge are much lower than the large longitudinal stresses induced around the inner edge of the wall, but may merit attention in the design when the stresses are tensile.

The distributions of bending stress resultants M_x and M_y (Fig. 6.7, (d-e)) show sharp peaks at the inner edge of the wall, but in practice the stress concentrations are expected to be less severe due to dispersion. Since there is a possibility that the critical bending moments may be theoretically singular it would be sensible to accept the critical finite element values only for the purpose of evaluating the integrated moment over a finite region, and not as absolute peak values.

Fig. 6.7, (f) and (g) show the distribution of longitudinal (horizontal) stresses N_x and vertical stresses N_z in the lintel and wall. The position of maximum lintel longitudinal fibre stress appears to be at a small distance from the junction with the wall and agrees with the

position of the maximum longitudinal membrane stress in the flange (Fig. 6.7(a)). Inside the wall, the longitudinal stresses diminish rapidly away from the root of the lintel beam, showing clearly that the lintel reaction has only a local effect on the wall.

The distribution of vertical wall stresses N_z shows distinct stress concentrations at the lintel-wall junction, and non-linear variations of stresses across wall sections close to the level of the lintel, but again these are essentially local effects. Clearly, special attention would be required in the detailing of the wall reinforcements to cater for the local stress concentrations induced by coupling action.

The local elastic rotation of the lintel-wall junction may be observed from the deflected shape of the structure illustrated in Fig. 6.7(h).

6.5 ALTERNATIVE MODELLING TECHNIQUE

An alternative method of modelling the lintel beam in a finite element analysis has been investigated since the completion of the work described in the preceding sections. In the alternative approach, the lintel is represented by space frame elements instead of flat shell elements. The slab is represented by flat shell elements as before. The space frame element includes axial, flexural, torsional and shear deformations.[90] The eccentric connection between the beam and slab is simulated numerically by relating the centroidal displacements of the beam to the middle-plane displacements of the slab above.[91,92] Referring to Fig. 6.8 which illustrates the displacements of the beam and slab in a composite section, the displacement relationships can be written as

$$u^B = u^S - e\theta_y^S$$

$$v^B = v^S + e\theta_x^S$$

$$w^B = w^S$$

$$\theta_x{}^B = \theta_x{}^S$$

$$\theta_y^B = \theta_y^S$$
$$\theta_z^B = \theta_z^S$$

or more simply as $\{\delta^B\} = [Z]\ \{\delta^S\}$

where the displacement vector $\{\delta\}^T = [u, v, w, \theta_x, \theta_y, \theta_z]$, the transformation matrix $[Z]$ is given by

$$[Z] = \begin{bmatrix} 1 & 0 & 0 & 0 & -e & 0 \\ & 1 & 0 & e & 0 & 0 \\ & & 1 & 0 & 0 & 0 \\ & & & 1 & 0 & 0 \\ & & & & 1 & 0 \\ & & & & & 1 \end{bmatrix}$$

ZEROS

and the superscripts B and S associate the displacement quantities u, v, w, θ_x, θ_y and θ_z with the beam and slab respectively, and e is the eccentricity between the neutral planes of the beam and slab sections.

The standard space frame element stiffness matrix can now be converted into an eccentric space frame element stiffness matrix by the orthogonal transformation

$$[K_S] = [T]^T\ [K_B]\ [T]$$

where $[K_B]$ and $[K_S]$ denote the standard and eccentric space frame element stiffness matrices respectively, and

$$[T] = \left[\begin{array}{c|c} Z & 0 \\ \hline 0 & Z \end{array}\right]$$

The alternative approach permits a considerable reduction in the number of shell elements required for the discretisation of the slab and lintel. The approach however cannot be used when the effects of local elastic wall deformation have to be included in the analysis, because the lintel element forces cannot be effectively transmitted to the wall elements.

6.5.1 VERIFICATION OF ALTERNATIVE MODELLING TECHNIQUE

In order to verify the accuracy of the alternative modelling technique, a standard cantilever tee-beam subjected to a point load at its free end has been analysed by the technique and the results obtained compared with those given by beam theory. Fig. 6.9(a) shows the dimensions and finite element idealisation of the cantilever. The width of the flange has been made relatively narrow to ensure that reasonably accurate results may be obtained by beam theory which assumes a fully effective composite section. The flange is represented by rectangular flat shell elements in its middle-plane and the web by eccentric space frame elements with a depth of (d-t/2). Space frame elements with and without shear deformation characteristics have been considered in this investigation. A separate analysis which idealises the flange and web as an assembly of flat shell elements has also been carried out for comparison with the other results. The shell element idealisation of a symmetric half of the cantilever for this analysis is shown in Fig. 6.9(b).

Table 6.3 shows the comparison between the finite element results and the beam theory results for the maximum deflection at the free end and the extreme fibre stresses at the supported end of the cantilever. The results have all been reduced to refer to unit values given by beam theory. In the calculation of shear deflection by beam theory, the shear is assumed to be carried by the web alone. Since the flange fibre stress evaluated by the finite element analysis at the centre-line is slightly higher than the value at the edge of the flange, an average value has been assumed for comparison with the uniform value given by beam theory.

The results show that with the space frame idealisation of the web, the maximum cantilever deflection and the maximum fibre stresses are evaluated respectively to within 1% and 6% of the values given by beam theory.

With the flat shell idealisation, the maximum deflection and stresses are evaluated respectively to within 6% and 9% of the beam theory values.

6.6 COMPARISON OF RESULTS OBTAINED BY SPACE FRAME AND FLAT SHELL IDEALISATIONS OF LINTEL

Results for the composite stiffness ratio and effective flange width of a composite coupling beam have been obtained using the eccentric space-frame idealisation of the lintel for a number of cases for the purpose of verifying the previous results obtained by the flat-shell idealisation. Table 6.4 shows the comparison of results evaluated by the two techniques for configurations with various wall opening widths L/t and lintel depths d/t. The values of composite stiffness ratio I_c^*/I_w^* evaluated by the two different techniques agree to within 3% whereas the effective flange width values Y_e/Y agree to within 10%.

6.7 SIGNIFICANCE OF COMPOSITE COUPLING ACTION

In order to assess the significance of composite coupling action on the overall behaviour of a coupled wall system, a typical 20-storeyed, 60 m high and 15 m deep cross wall building is analysed for wind load effects. A typical bay of the structure is assumed to consist of a pair of plane walls 230 mm thick coupled by 500 mm deep lintel beams monolithic with 150 mm thick floor slabs 5 m in width. A uniform wind pressure of 1.2 kN/m^2 is assumed acting on the building. Two wall opening widths, 2m and 4m, are considered. The effective flange width for the composite coupling beam in each case is obtained from the curves presented in Fig. 6.4, with due allowance for junction flexibility and shear deformation effects. The curves presented by Coull and Choudhury,[59] and Coull and Irwin[53] are used to evaluate the maximum lateral deflections δ_{max}, maximum extreme fibre wall stresses σ_A and σ_B, and maximum lintel shears Q_{max}. The design quantities evaluated assuming composite coupling action

are compared with those that disregard the influence of the slab, in Table 6.5. The percentage differences are shown in brackets in the table.

It is seen from the results that significant reductions in the maximum wall stresses and deflections can be achieved by considering composite coupling action, when the lintels are flexible (defined by a relative stiffness αH less than 3, specified in Reference 59). These reductions, however, are gained at the expense of increased lintel shears. With stiff lintel beams ($\alpha H > 5$) it is unlikely that any advantage can be gained by considering composite coupling action in the analysis and design of the wall system.

6.8 CONCLUSIONS

The composite action of the lintel and slab coupling a pair of shear walls has been investigated by a finite element method. The relative influences of a range of structural parameters on the composite stiffness and effective flange width of the composite coupling beam have been evaluated. For the normal range of structural dimensions encountered in practice, the slab width, lintel width and lintel depth have little influence on the effective flange width. The composite stiffness ratio and the effective flange width increase significantly with the wall opening width. Curves have been presented to allow the rapid evaluation of composite stiffness ratio or the effective flange width in a practical situation. The influence of elastic lintel-wall junction deformation may be allowed for in the calculation of the composite coupling stiffness by increasing the flexible span of the lintel by a length equal to the lintel depth. Significant reductions in the wind stresses and deflections in the coupled shear walls may be achieved by considering the composite action of the slab with the lintel in cases where the coupling by the lintel alone is relatively flexible (for instance $\alpha H < 3$).

TABLE 6.1 COMPARISON BETWEEN FINITE ELEMENT SOLUTION AND BEAM THEORY FOR PRISMATIC CANTILEVER BEAM DISCRETISED BY VARIOUS MESH PATTERNS

Span/Depth Ratio	2 Element Depth Sub-division		4 Element Depth Sub-division	
	w_B	σ_A	w_B	σ_A
1.33	0.9510	0.9664	0.9880	1.0832
2.67	0.9697	0.9656	0.9827	1.0168
Beam Theory	1.0000	1.0000	1.0000	1.0000

TABLE 6.2 EFFECT OF LINTEL WIDTH ON COMPOSITE COUPLING STIFFNESS

b/t	L/t = 13.33		L/t = 26.67	
	I_c^*/I_w^*	Y_e/Y	I_c^*/I_w^*	Y_e/Y
1.33	1.440	0.181	1.834	0.239
2.67	1.205	0.184	1.934	0.257

TABLE 6.3 COMPARISON BETWEEN FINITE ELEMENT SOLUTION AND BEAM THEORY FOR CANTILEVER TEE-BEAM

Idealisation of Web	Assumed Beam Depth	Shear Deformation Neglected			Shear Deformation Included		
		w	σ_T	σ_B	w	σ_T	σ_B
Space Frame Element	(d-t/2)	0.9985	0.9089	1.0596	0.9993	1.0352	1.0515
Flat Shell Element	(d-t/2)	-	-	-	0.9560	0.9224	0.9112
Beam Theory		1.0000	1.0000	1.0000	1.0000	1.0000	1.0000

TABLE 6.4 COMPARISON BETWEEN RESULTS FOR COMPOSITE COUPLING BEAM OBTAINED BY SPACE FRAME AND FLAT SHELL IDEALISATIONS OF LINTEL

d/t	Space Frame Model				Flat Shell Model			
	L/t = 13.33		L/t = 26.67		L/t = 13.33		L/t = 26.67	
	I_c^*/I_w^*	Y_e/Y	I_c^*/I_w^*	Y_e/Y	I_c^*/I_w^*	Y_e/Y	I_c^*/I_w^*	Y_e/Y
2.5	1.961	0.184	2.411	0.267	1.928	0.175	2.446	0.279
5.5	1.465	0.195	1.796	0.224	1.440	0.181	1.834	0.239
7.2	1.345	0.223	1.654	0.238	1.345	0.223	1.701	0.262

TABLE 6.5 EFFECT OF COMPOSITE COUPLING ACTION ON DESIGN QUANTITIES FOR COUPLED WALL STRUCTURE

L (m)	αH	σ_{A_2} (kN/m^2)	σ_{B_2} (kN/m^2)	δ_{max} (mm)	Q_{max} (kN)	Coupling Medium
2	4.04	2045.09	-1163.15	13.38	45.72	Lintel Alone
	5.03	1920.36	- 953.07	12.04	52.10	Lintel with Slab
	(25%)	(-6%)	(-18%)	(-10%)	(14%)	Percentage Diff.
4	2.40	3135.52	-2407.98	29.45	30.67	Lintel Alone
	3.21	2797.49	-1908.28	22.09	36.81	Lintel with Slab
	(34%)	(-11%)	(-21%)	(-25%)	(20%)	Percentage Diff.

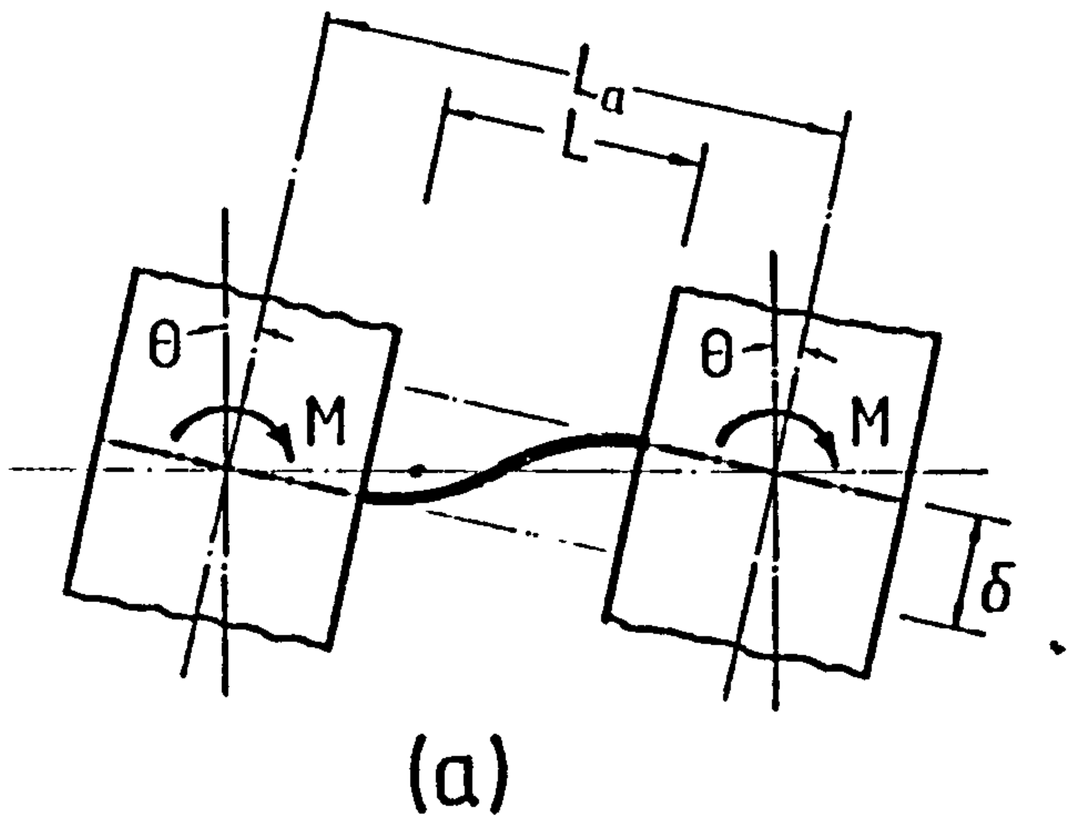

(a)

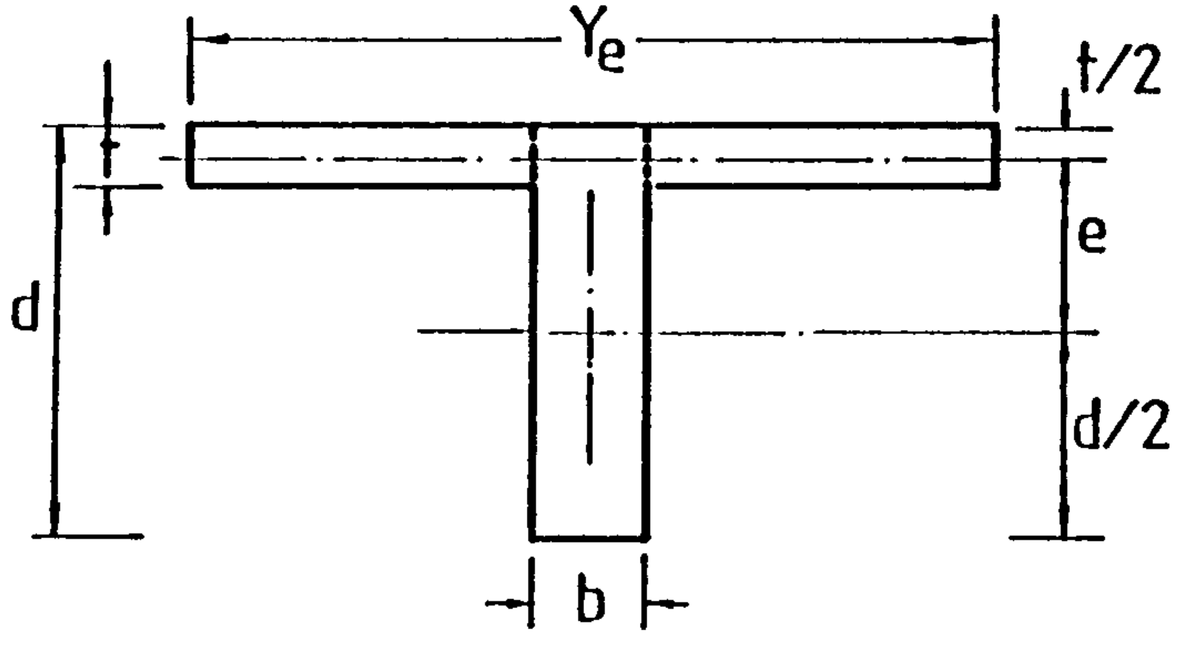

(b)

Fig. 6.1 (a) Deformation and (b) Cross-section of Composite Coupling Beam

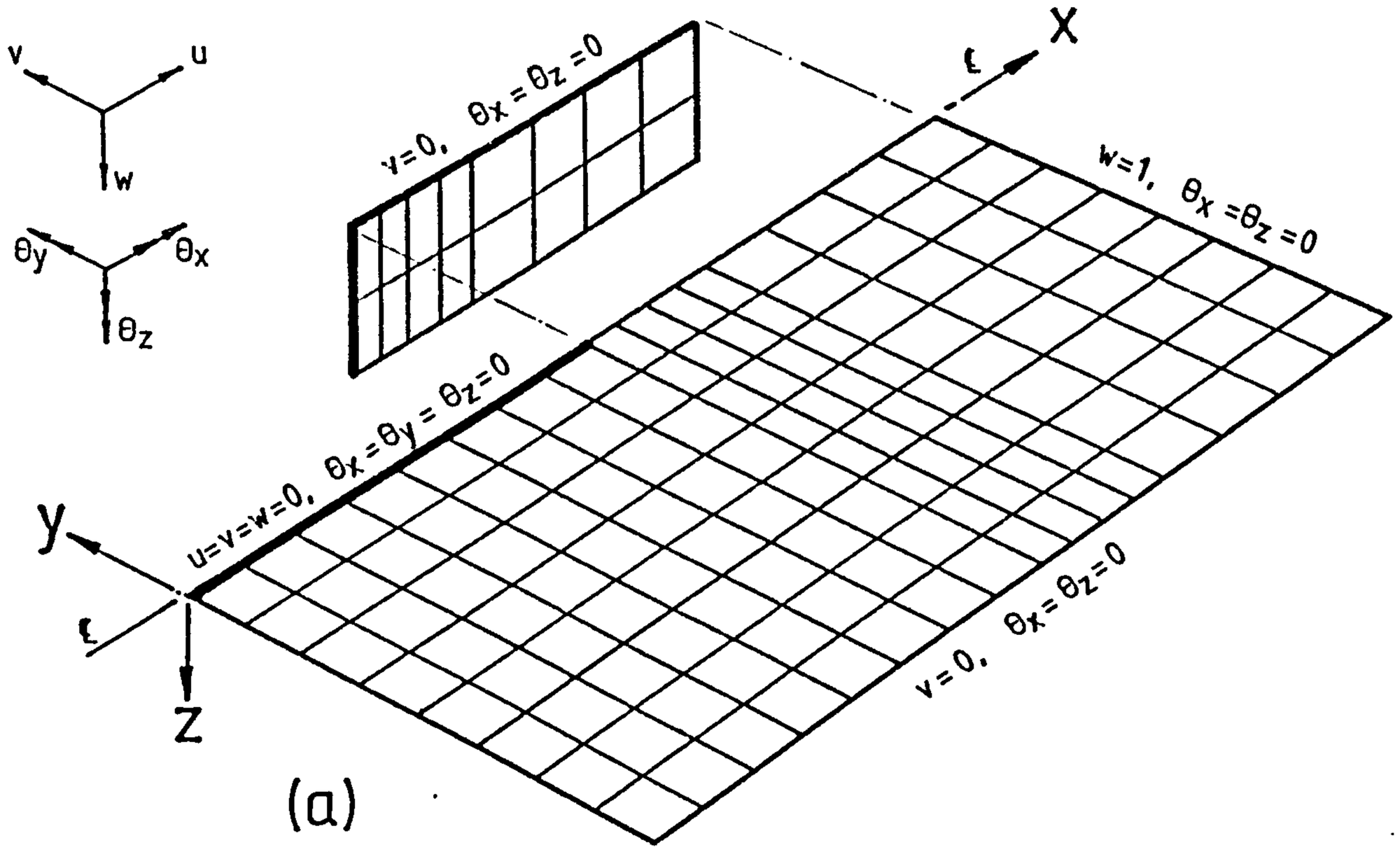

(a)

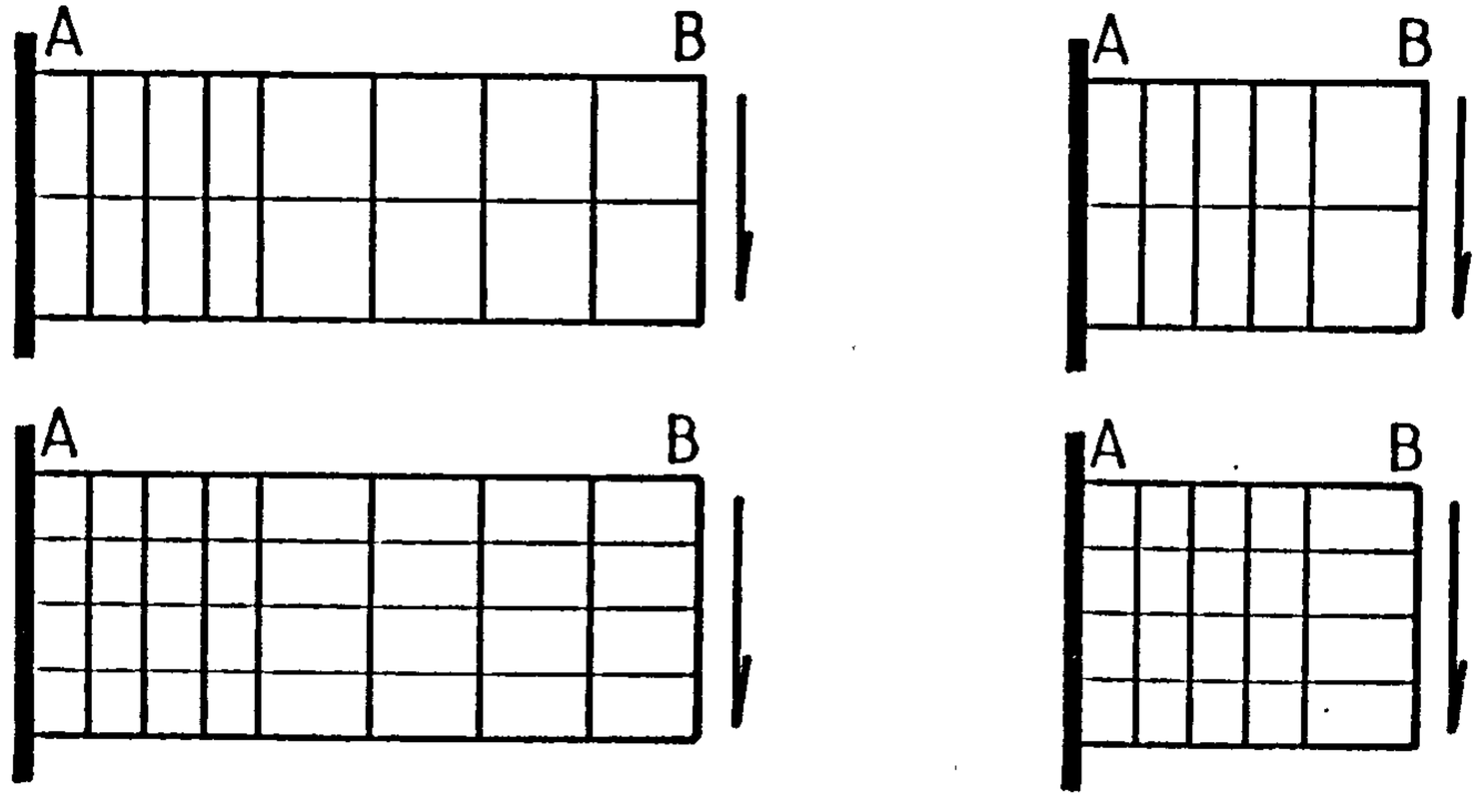

(b)

Fig. 6.2 (a) Typical Finite Element Idealisation of Lintel and Floor Slab. (b) Mesh Patterns for Cantilever Beam in Test Problem

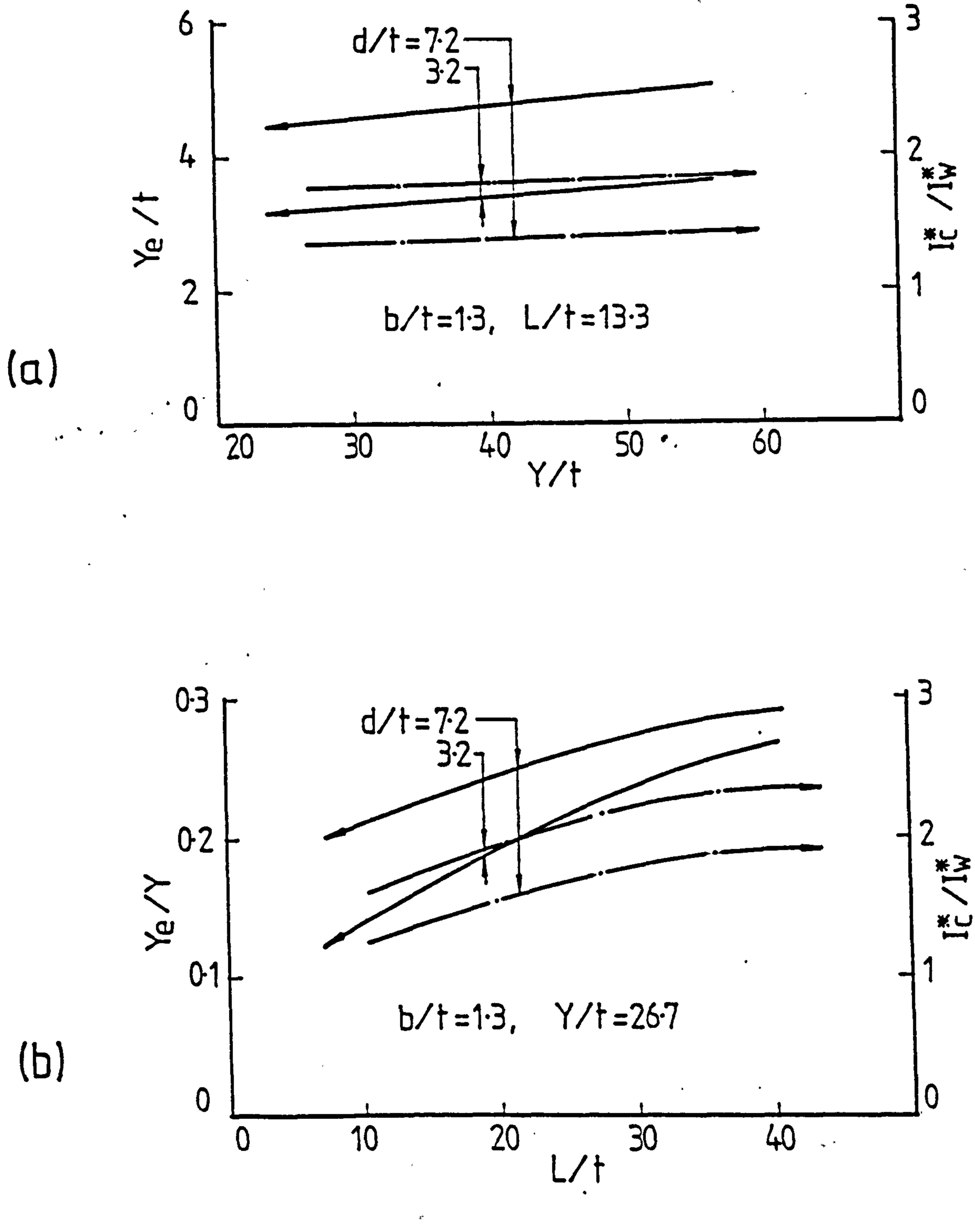

Fig. 6.3 Variations of Effective Flange Width and Composite Stiffness Ratio with (a) Slab Width and (b) Wall Opening Width

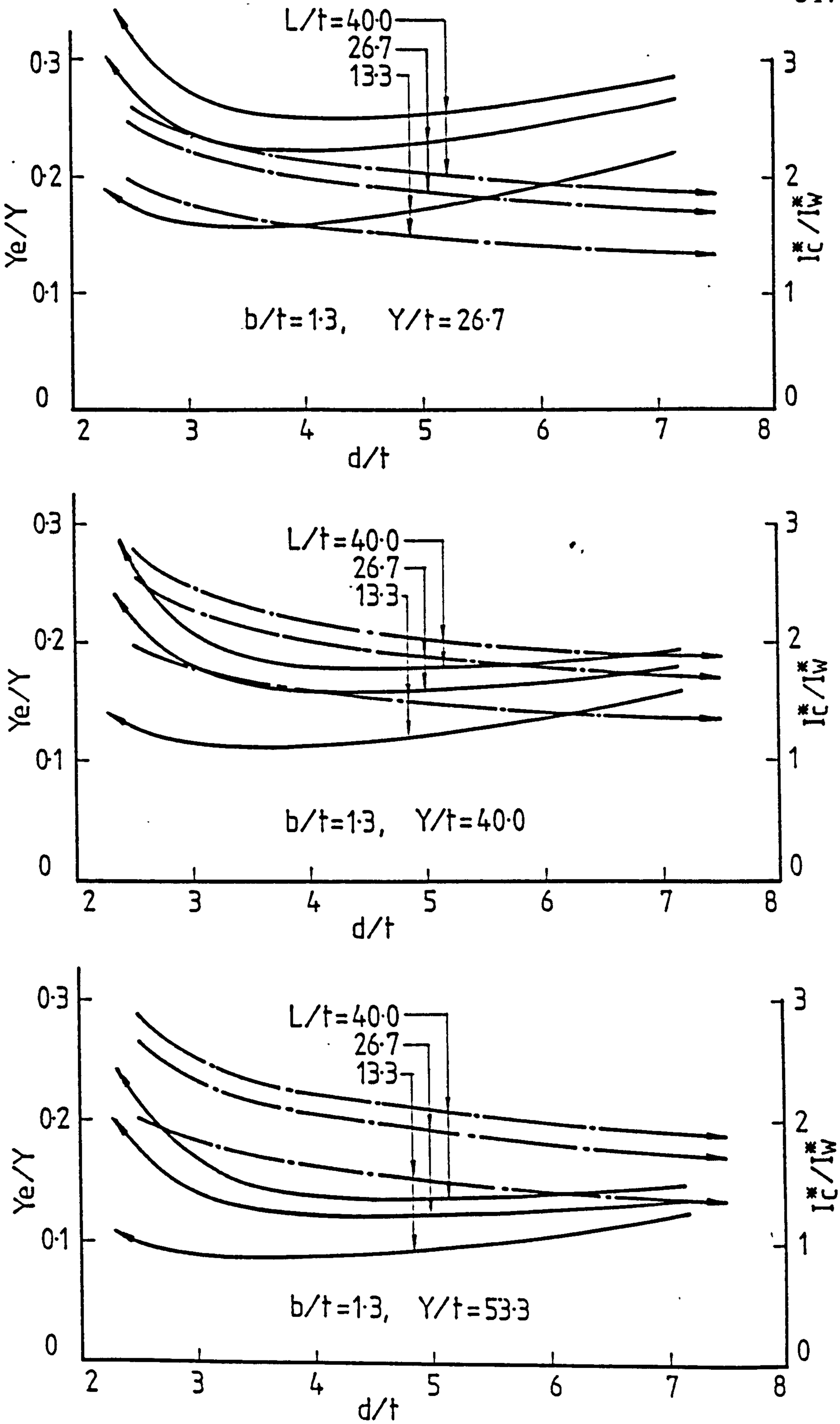

Fig. 6.4 Variations of Effective Flange Width and Composite Stiffness Ratio with Lintel Depth

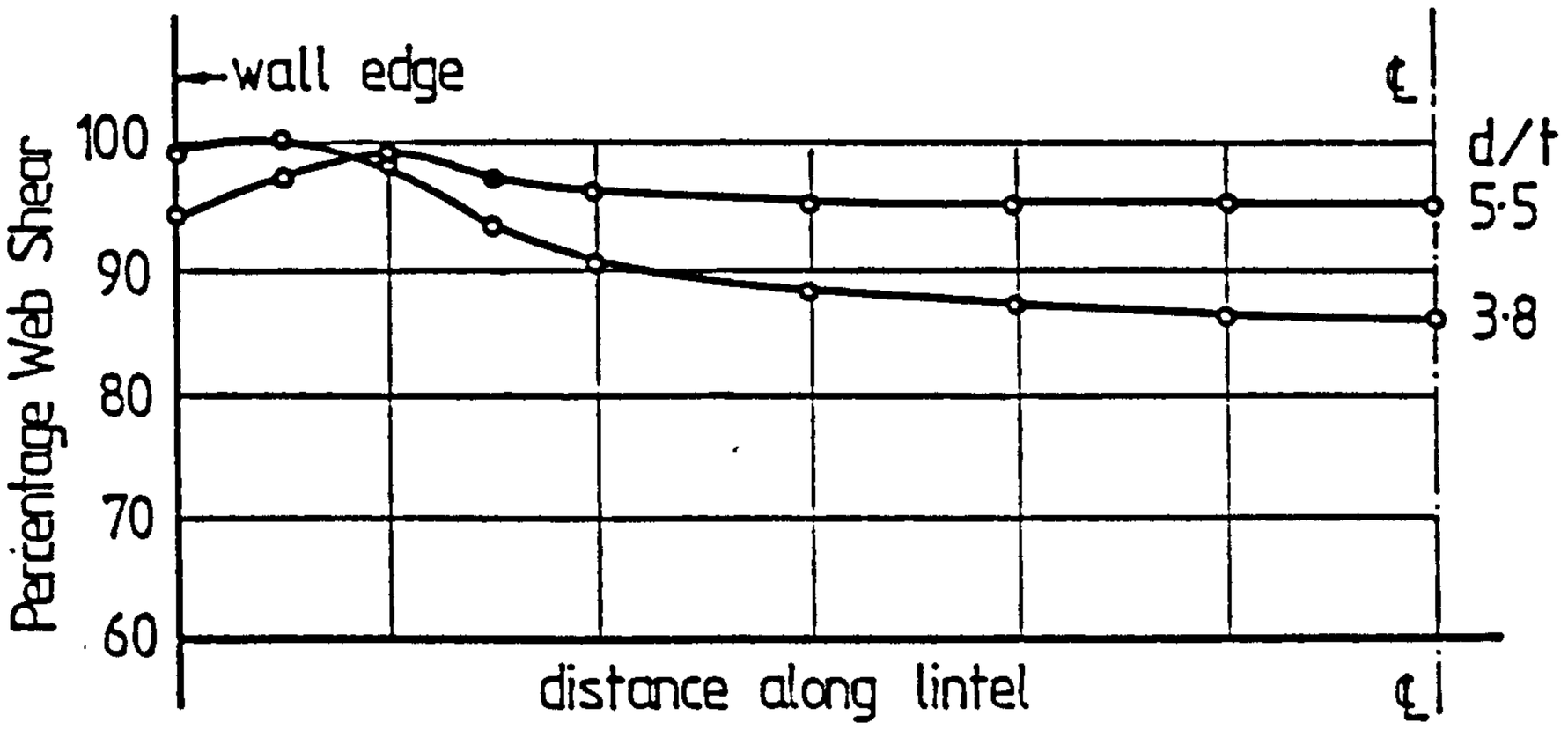

Fig. 6.5 Span-wise Variation of Percentage Shear Carried by Web of Composite Coupling Beam

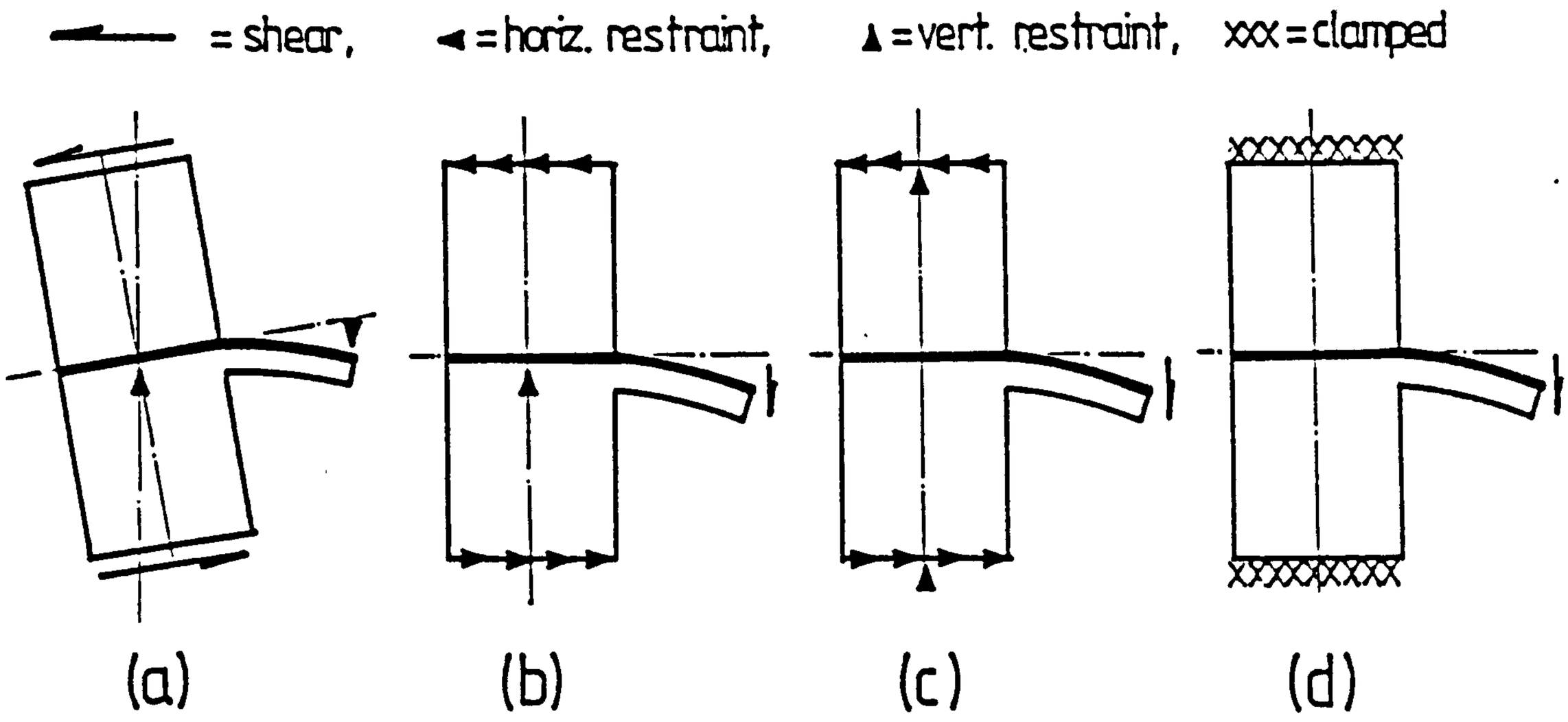

Fig. 6.6 Assumed Boundary Conditions of Coupled Wall

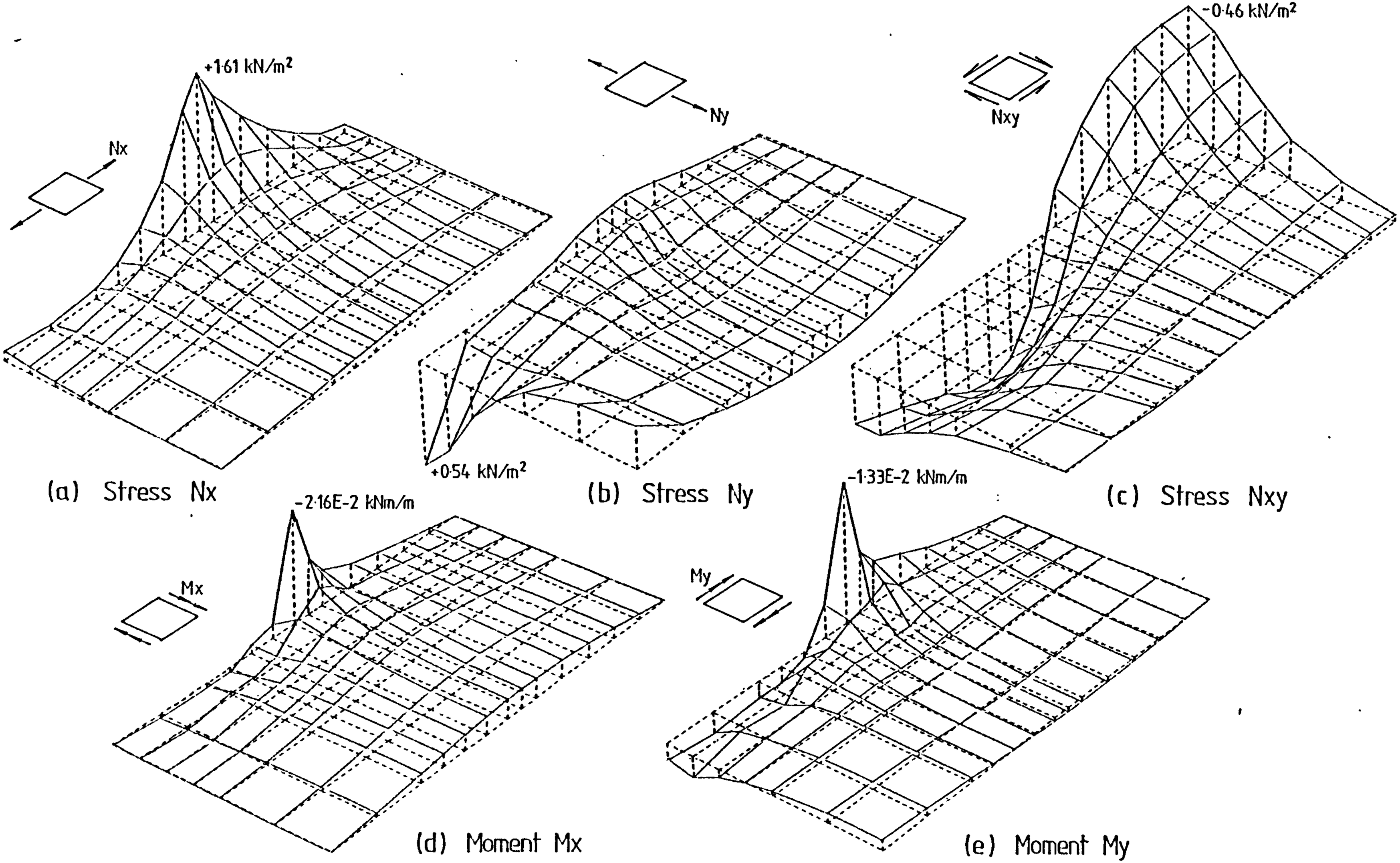

(a) Stress Nx (b) Stress Ny (c) Stress Nxy

(d) Moment Mx (e) Moment My

Fig. 6.7 Typical Distributions of Membrane Stresses and Bending Stress Resultants in Slab

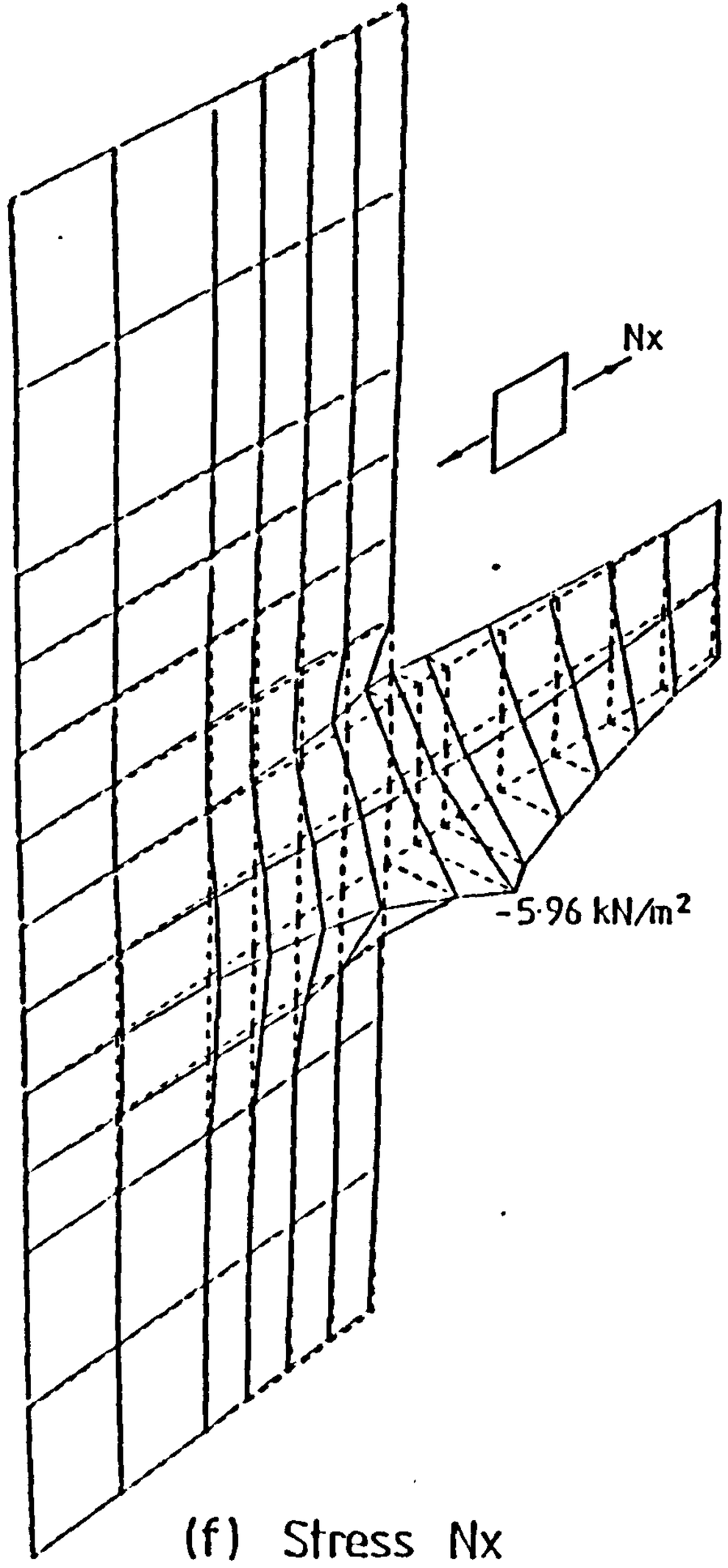

(f) Stress Nx

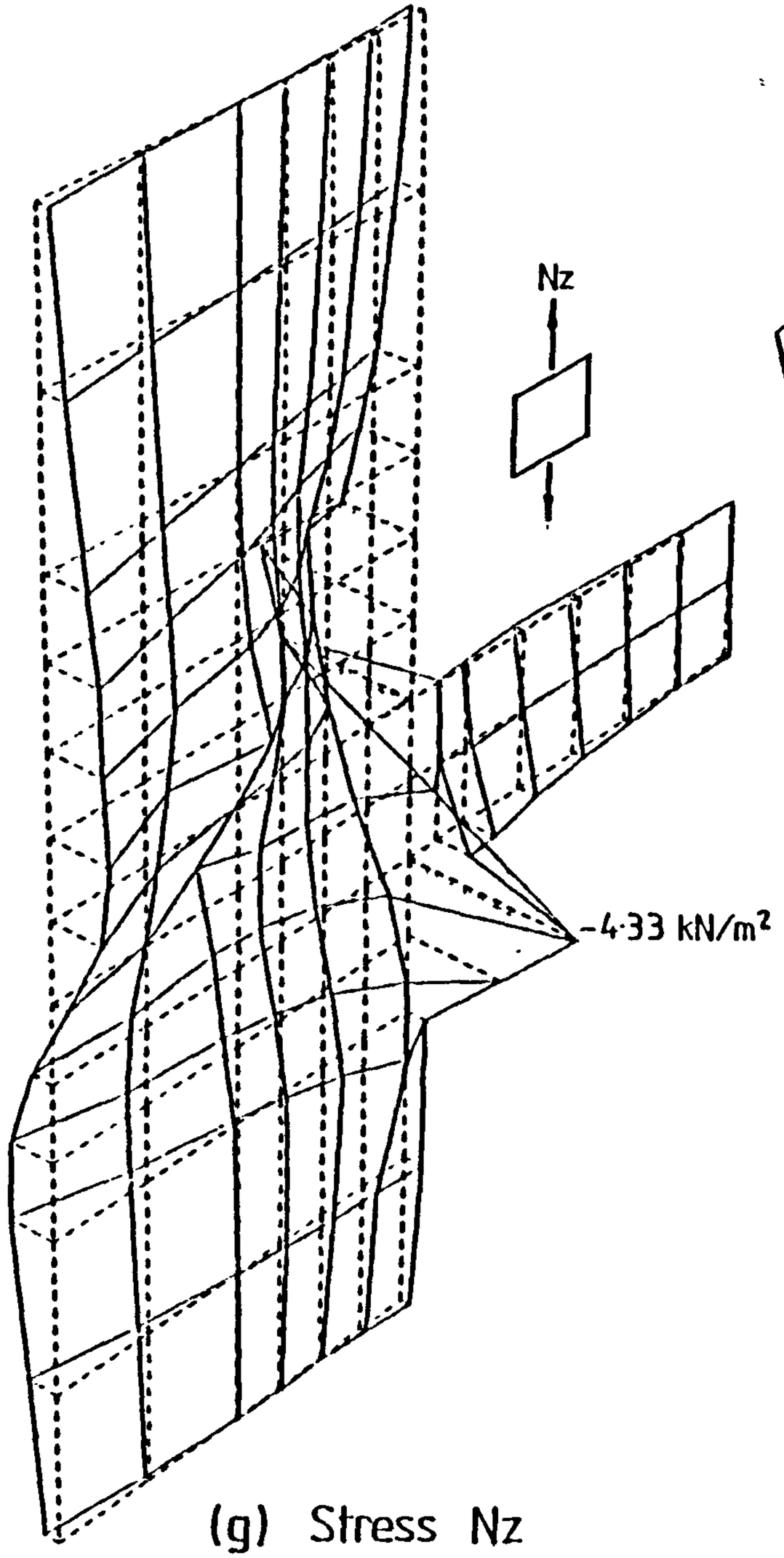

(g) Stress Nz

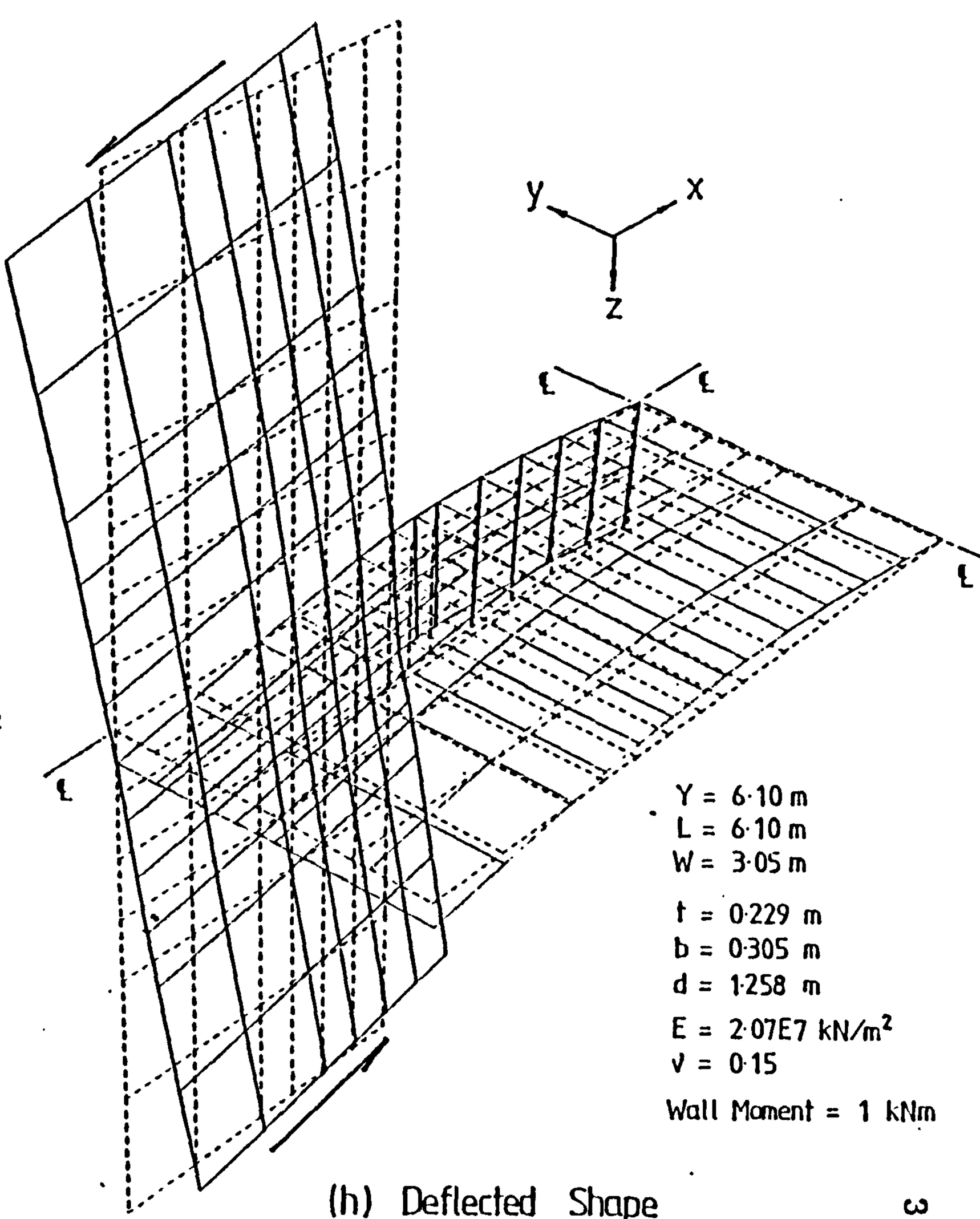

(h) Deflected Shape

Fig. 6.7 (Contd) Typical Distributions of Membrane Stresses in Lintel and Wall, and Deflected Shape of Structure

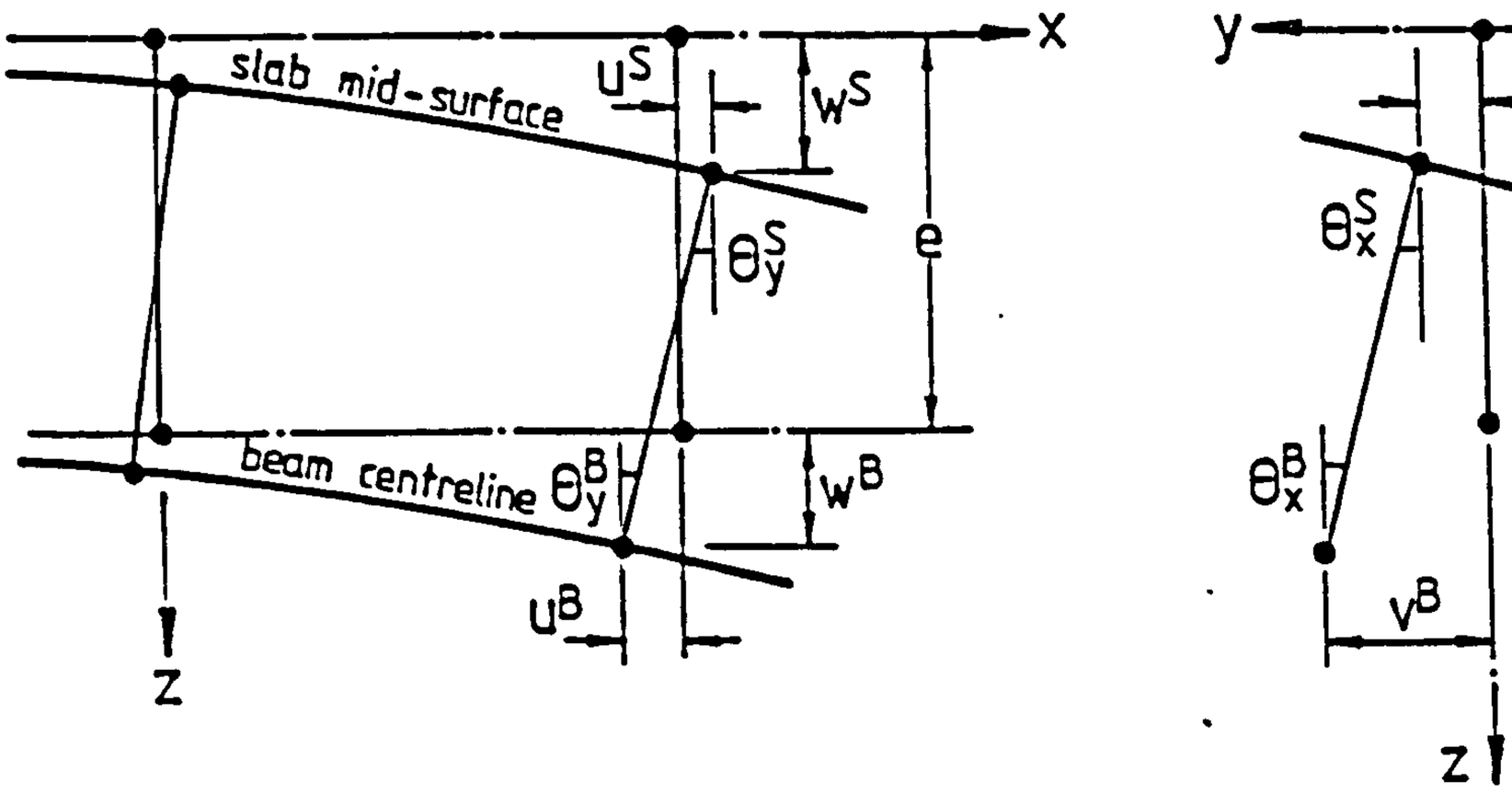

Fig. 6.8 Relationships Between Slab and Beam Nodal Displacements

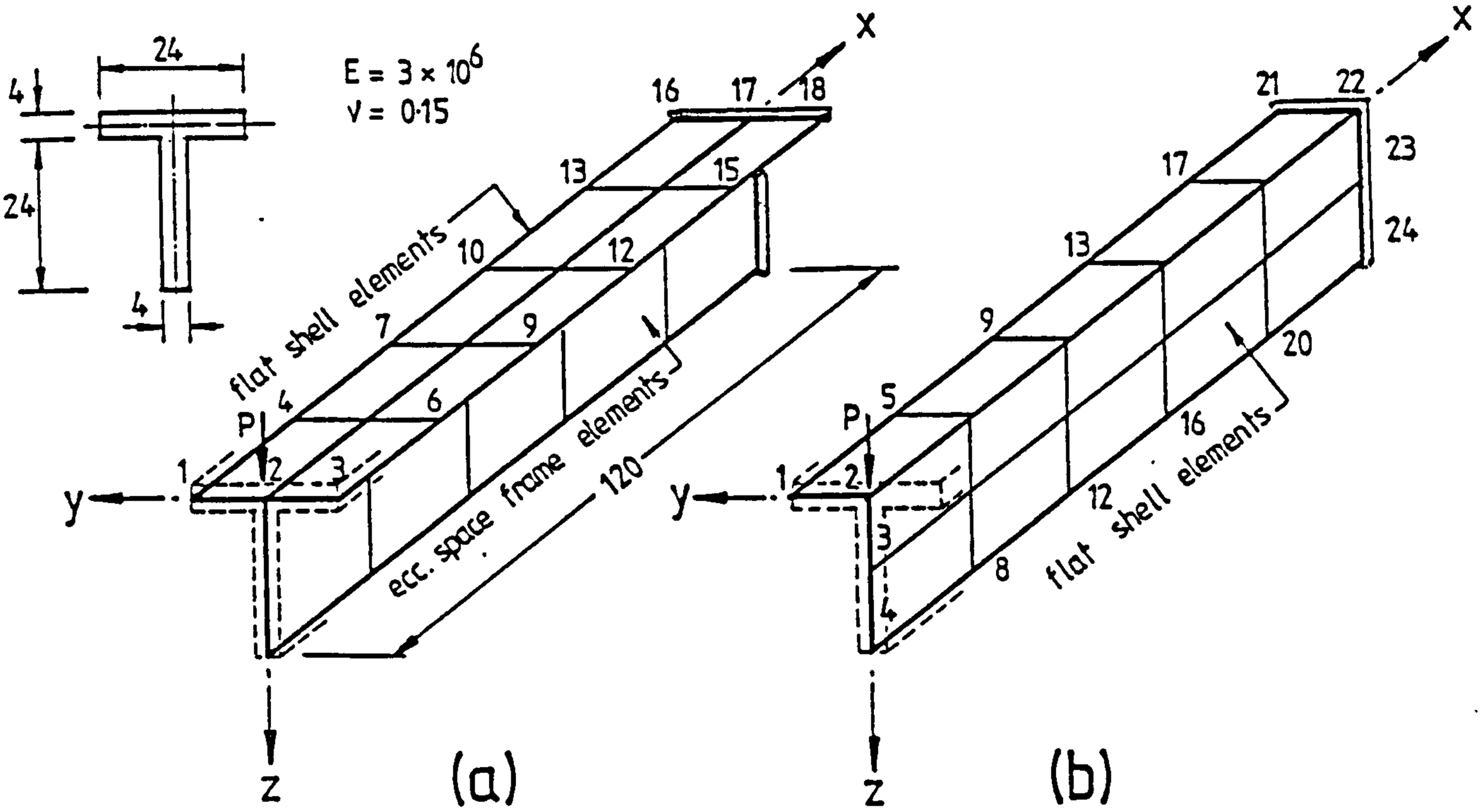

Fig. 6.9 Finite Element Idealisation of Cantilever Tee-Beam Using (a) Eccentric Space Frame Elements and (b) Flat Shell Elements for the Web

CHAPTER 7

TORSIONAL COUPLING OF SHEAR CORES BY FLOOR SLABS

7.1 INTRODUCTION

In many modern high rise buildings, the lateral resistance of the structure against wind or seismic forces is provided wholly or partly by a central core which houses the lift shaft, stair wells and service bays. The centre core consists essentially of open section shear walls connected by lintel beams or floor slabs at the floor levels to form a perforated thin walled box structure. Very often, due to the asymmetric structural layout or eccentric disposition of loads, the core is subjected to torsion in addition to bending under the action of the lateral loads.

An open section core, in contrast to a closed box structure, has a low torsional stiffness and undergoes large warping deformations under torsion. The restraint against free warping at the rigid base of the core induces throughout the height of the core walls axial and shearing warping stresses which may be large enough to merit consideration in the design. The presence of lintel beams or floor slabs, which act effectively as braces, stiffens the core against torsional deformations and reduces the warping stresses below the level of those which would be produced in the unbraced core.

The torsional behaviour of braced open cores has been studied recently by a number of investigators.[11-13,67-79] Various methods of torsional analysis have been presented. The majority are based on Vlasov's theory of thin walled beams[23] for describing the characteristic behaviour of the core walls. One popular approach to the torsional analysis uses the continuous medium technique whereby the discrete connecting lintel beams are replaced by a continuous medium of equivalent stiffness.[71-79] This yields closed form solutions, but is restricted to cores with uniform walls connected by regularly spaced uniform lintels

throughout the height of the core. In order to apply the continuous medium methods of analysis to cores braced by floor slabs, it becomes necessary to replace the slabs by an equivalent system of connecting beams at the core openings.

The second approach which is of more general application idealises the braced core as an assembly of discrete members consisting of beam or plate elements, or a combination of both, and uses a matrix formulation and computer solution in the analysis.[11-13,67-70] The various available discrete methods of torsional analysis are relatively efficient for cores connected by lintel beams. But for cores braced all round by the floor slabs, the necessary sub-structure analysis of the slab to evaluate its warping stiffness required for the analysis of the core involves a considerable amount of computational effort. Therefore, if the warping stiffness of the slab could be readily evaluated, or if the slab could be replaced by an equivalent system of connecting beams, the discrete methods of analysis could be used more easily to best advantage.

In this chapter, the slab surrounding a centre core is replaced by an equivalent system of lintel beams at the core openings such that the torsional behaviour of the core remains unaffected by the substitution. The finite element method is used to obtain the warping stiffness of the slab and hence the effective width for the equivalent beams. The core configurations considered include single U- or C-shaped cores and twin channel cores coupled by floor slabs (Fig. 7.1). The relative influences of various structural parameters on the warping stiffness and effective width of slab are examined and design curves are presented to enable these quantities to be evaluated rapidly for the torsional analysis of the core.

7.2 WARPING STIFFNESS AND EFFECTIVE WIDTH

7.2.1 WARPING STIFFNESS OF FLOOR SLAB

Shear cores in tall buildings behave essentially like thin wall beams of open sections. Under torsional loading

cross-sections of the core which were originally plane undergo warping deformation defined by equation (2.12). A slab rigidly connected to the core is forced to undergo out-of-plane deformation identical to the warping deformation of the core at the connection. The out-of-plane stiffness of the slab restrains the core against warping and induces longitudinal reactions which constitute a bimoment on the core. The warping stiffness of the slab may be defined in terms of the bimoment that is required to induce unit torsional warping ($\Theta' = 1$). The slab reactions and resultant bimoment due to unit warping displacements can be evaluated only by a plate bending analysis, which may be best performed by the finite element method. Assuming that the slab reactions are evaluated as a system of discrete forces P_i and couples M_{si} and M_{ni} acting respectively in the plane of, and normal to the plane of, the core wall (Fig. 7.2(a)), the bimoment resultants of these forces may be obtained using equations (2.25)-(2.27). The warping stiffness of the slab is then given by the sum of the bimoment resultants, thus

$$B_w = \sum_{i=1}^{N} P_i \Psi_i + \sum_{i=1}^{N} M_{si} \left(\frac{d\Psi}{ds}\right)_i + \sum_{i=1}^{N} M_{ni} \left(\frac{d\Psi}{dn}\right)_i \qquad (7.1)$$

where N is the number of nodes at which the slab reactions on the core are evaluated; Ψ_i is the sectorial coordinate, and $(d\Psi/ds)_i$ and $(d\Psi/dn)_i$ are the rates of change of sectorial co-ordinate function in the tangential and normal directions respectively.

7.2.2 WARPING STIFFNESS OF CONNECTING BEAM

A lintel beam connected at its ends to points on the warping core suffers the same warping displacements as the core at its ends and induces longitudinal reactions, and hence a resultant bimoment, on the core (Fig. 7.2(b)). The warping stiffness of the connecting beam may be defined in terms of the bimoment that is required to

produce unit warping displacements at its ends. These warping displacements consist of simultaneous vertical and rotational displacements equal respectively to the sectorial co-ordinate W_1 and its derivative $(dW/ds)_1$ at each end of the beam. The bimoment resulting from the imposed unit warping displacements is given by

$$B_w = 2 \left[P_1 W_1 + M_1 \left(\frac{dW}{ds}\right)_1 \right] \qquad (7.2)$$

The shear force P_1 and the moment M_1 can be obtained from the standard force-displacement relationship for a fixed ended beam (Fig. 7.2(c)) as

$$P_1 = \frac{12E\ I_b}{L^2} \left[\frac{2W_1}{L} + \left(\frac{dW}{ds}\right)_1 \right]$$

$$\text{and} \quad M_1 = \frac{6E\ I_b}{L^2} \left[\frac{2W_1}{L} + \left(\frac{dW}{ds}\right)_1 \right] \qquad (7.3)$$

where I_b is the second moment of area of the beam, and L is the core opening width. Equation (7.2) can therefore be written as

$$B_w = \frac{12E\ I_b}{L^3} \left[2W_1 + L\left(\frac{dW}{ds}\right)_1 \right]^2 \qquad (7.4)$$

7.2.3 EFFECTIVE WIDTH FOR EQUIVALENT BEAM IN SINGLE CORE CONFIGURATION

The single core configuration considered consists of a C-shaped core wall enclosed by the floor slab (Fig. 7.3(a)). For the purpose of the torsional analysis of the core, the slab enclosing the core may be replaced by an equivalent lintel beam connected across the core opening. If the equivalent beam is assumed to have the same depth t as the slab, then an effective width of slab Y_e can be evaluated for the equivalent beam by equating the warping stiffness of the slab to that of the beam.

The warping stiffness of the beam is given by equation (7.4), with the expression within the parenthesis equal to twice the area enclosed within the core (i.e. 2BD).

Denoting the double core area by Ω, equation (7.4) may be written simply as

$$B_w = \frac{12E\ I_b}{L^3}\ \Omega^2 \qquad (7.5)$$

with $I_b = Y_e\ t^3/12$.

The warping stiffness of the slab may be evaluated by the plate bending analysis in the form of a non-dimensional warping stiffness factor given by

$$K_w = \frac{B_w}{D^* \Omega} \qquad (7.6)$$

where B_w is evaluated according to equation (7.1), and D^* is the plate flexural rigidity. The effective width can then be expressed in terms of the warping stiffness factor, in non-dimensional form, as

$$\frac{Y_e}{S} = \frac{K_w}{12(1-\nu^2)}\ \frac{L^2}{\Omega}\ (\frac{L}{S}) \qquad (7.7)$$

where S is the width of the slab from the core to the facade.

7.2.4 EFFECTIVE WIDTH FOR EQUIVALENT BEAM IN TWIN-CORE CONFIGURATION

The twin-core configuration considered consists of two identical channel-section core walls interconnected and enclosed by floor slabs (Fig. 7.3(b)). Under torsional loading, the slabs constrain the walls to rotate about a common axis as a single core unit with unit warping displacements as shown in Fig. (7.2(d)). Since two equivalent connecting beams are now assumed to replace the floor slab, the total bimoment on the core resulting from unit warping displacements imposed at the ends of the connecting beams is given by

$$B_w = \frac{24E\ I_b}{L^3}\ [\ 2w_1 + L(\frac{dw}{ds})_1]^2 \qquad (7.8)$$

with the expression within the parenthesis equal to the

area within the core. Using the same symbol Ω to denote the double core area (i.e. 2BD), equation (7.8) may be written simply as

$$B_w = \frac{6E\ I_b}{L^3}\ \Omega^2 \qquad (7.9)$$

The effective width for each connecting beam is now given by

$$\frac{Y_e}{S} = \frac{K_w}{6(1-\nu^2)}\ \frac{L^2}{\Omega}\ \left(\frac{L}{S}\right) \qquad (7.10)$$

7.3 FINITE ELEMENT ANALYSIS OF SLAB

The analysis of torsional interaction between shear cores and floor slabs is very similar to that of the flexural interaction between coupled shear walls and floor slabs. Since the rectangular plate bending element RB12 (the Adini-Clough-Melosh element) has proved to be the best element among a large selection of elements evaluated for the analysis of shear wall-slab interaction (cf. Chapter 3), this element is again chosen for the present investigation of core-slab interaction.

In this investigation it is assumed that the slab is homogeneous, isotropic and linearly elastic, and its flexural behaviour can be described by thin plate theory. It is also assumed that the reaction of the slab on the core does not give rise to any local elastic wall deformation, i.e. the unit warping displacements of the core section remain distributed strictly in accordance with the variation of sectorial co-ordinates where the slab interacts with the core.

In the finite element analysis the slab is discretised into an assembly of plate bending elements. The element sub-division is generally made finer around the core opening than elsewhere to cater for the expected more severe bending deformation in this particular area. In the idealisation of the slab, no consideration is given to the finite thickness of the core wall, and the slab is considered to be connected to the middle plane of the core wall.

Conditions of anti-symmetry which exist in the deformed slab are taken into account to reduce the computational effort. In the single-core configuration, for instance, the warping displacements in the slab are anti-symmetric about a principal axis (Y-axis in Fig. 7.17(f)), and only half the slab is analysed. In the twin-core arrangement, the slab displacements are anti-symmetric about both principal axes (Fig. 7.25(f)), and in this case, only a quadrant of the slab is analysed.

The boundary conditions required for the solution of the problem are prescribed in terms of known displacements along the peripheral slab edges, if they are restrained, and along the lines of anti-symmetry and the wall-slab boundary. When the slab edges are connected to peripheral framing, then depending on the type of connection and on the relative stiffness of the frame members, the slab edges may be considered approximately as simply supported, clamped or elastically restrained. In the case of a simply supported edge, the transverse deflections and the slopes in the direction of the supported edge are prescribed as zero at the supported nodes. The normal slopes are also prescribed as zero in the case of the clamped edge. In the case of an elastically restrained edge, axial and rotational spring stiffnesses are prescribed at the restrained nodes.

The boundary conditions along the lines of anti-symmetry are identical to those of a simply supported edge, and zero transverse deflections and slopes in the direction of the anti-symmetry line are prescribed at the boundary nodes.

The displacements prescribed for the core-slab boundary correspond to a unit torsional warping of the core and consist of transverse deflections and rotations equal in magnitude and sense to the sectorial co-ordinates $\mathbb{W}$ and slopes of the sectorial co-ordinate function, $d\mathbb{W}/dx$ and $d\mathbb{W}/dy$, at the boundary nodes.

The sectorial co-ordinate and slope functions for single-core and twin-core configurations are shown in Fig. 7.4.

The equilibrium equations established at the nodes are solved by Gaussian elimination to yield the nodal displacements from which stresses and reactions are subsequently computed. The warping stiffness of the slab, which is equal to the bimoment defined by equation (7.1), is evaluated simply by summing up the products of the reaction and displacement vectors for the core-slab boundary nodes. The effective width for the equivalent connecting beam is then evaluated according to equation (7.7) or equation (7.10) depending on the core configuration considered.

7.4 CONVERGENCE STUDY

In order to determine suitable mesh patterns for the discretisation of the slab, a convergence check was carried out by comparing the solutions obtained from three different mesh patterns. A typical single-core configuration with core aspect ratio D/B of 1.0, core opening ratio L/B of 0.5 and slab span ratio S/B of 0.75 was considered for this purpose. Two types of restraint conditions were considered for the peripheral slab edges; in one case the slab edges were free and in the other they were simply supported. In each case the slab was assumed rigidly connected to the core. The three mesh patterns representing coarse, medium and fine mesh divisions were obtained by sub-dividing a half slab panel into 45, 88 and 180 elements respectively (Fig. 7.5).

The values of warping stiffness factor K_w and effective width Y_e/S evaluated for the various cases are shown in Table 7.1. The results obtained by the coarse and medium mesh patterns have been compared with those obtained by the fine mesh pattern. The 'coarse mesh' results are some 8 to 9% higher, while the 'medium mesh' results are 3 to 4% higher than the 'fine mesh' results.

The fine mesh pattern represents a relatively refined discretisation scheme and convergence errors in the ensuing solution should be very small. The solution however

requires a considerably large computational effort. The 'medium mesh' solution requires much less computational effort and the results obtained are reasonably accurate. The results obtained using the coarse mesh pattern are not very satisfactory although the computer requirements are minimal. The 'medium mesh' is considered the most suitable scheme and is adopted for subsequent parameter studies.

7.5 PARAMETER STUDY

Fig. 7.3 shows the idealised typical plan forms for single-core and twin-core configurations. In order to reduce the number of variables to a minimum, the slab is assumed to have a constant width S from the core wall to the peripheral or facade edge all round the centre core. The parameters which may influence the warping stiffness of the slab may be identified as the core configuration, the core aspect ratio D/B, the core opening ratio L/B, the slab width ratio S/B, and the support conditions for the interior and exterior edges of the slab. In order to evaluate the relative influence of the various parameters, a series of analyses has been carried out for both core configurations with various combinations of ratios D/B, L/B and S/B and with various forms of edge supports. The numerical results obtained for the warping stiffness factor K_w and effective width Y_e/S are given in Appendix A7.1-A7.9. The effective width values are presented in design curves in Fig. 7.6-7.14. Each of these Figures contains three sets of curves showing the variation of Y_e/S with L/B for various ratios S/B. Each set of curves refers to a particular set of support conditions for the slab. The first set of curves designated "Monolithic/Free" refers to the case where the slab is monolithic with the core and is free around its external peripheral edges. Such a case is applicable to the core-supported cantilevered-floor structure. The second set of curves, designated "Monolithic/S. Supported", refers to the case where the slab

is monolithic with the core and is simply supported around its periphery, while the last set of curves, designated "S.Supported/S.Supported", refers to the case where the slab is simply supported at the core and around its periphery. These two cases are applicable to hull-core, core-frame and core-supported base-cantilever structures where it is assumed that the peripheral columns are axially rigid and that the external framing does not offer any appreciable rotational restraint for the slab edges. As will be shown in a later section, these assumptions are reasonable for practical purpose.

Each Figure of three sets of curves refers to a particular core-slab configuration. Fig. 7.6-7.8 refer to the single-core configurations with core aspect ratios D/B of 0.5, 0.75 and 1.0. In each of these configurations it is assumed that the interior of the core is spanned by a strip of slab which forms the lift lobby in a practical core layout. The lobby slab is disregarded in similar core configurations for the next three Figures (Fig. 7.9-7.11).

Fig. 7.12-7.14 refer to twin-core configurations with lobby slabs. Curves have not been presented for similar core configurations without lobby slabs, but it will be shown later how the effective width values for such cases can be obtained approximately from the results presented for the other cases.

It is seen from the various Figures that the effective width Y_e/S increases considerably due to the peripheral slab restraint. The peripheral supports exert a greater influence with a larger core-opening to slab-width ratio L/S. The moment connection between slab and core provides a considerable stiffening effect for the slab. By releasing the moment restraint at the core the warping stiffness of the slab is reduced generally by between 30 and 40%.

For slabs unsupported around the periphery the absolute effective width Y_e increases with the slab width ratio S/B. In the case where the slab is restrained around the periphery the absolute effective width decreases

with an increase in the slab width S/B. In both cases the influence of slab width becomes less significant with larger slab width to core opening ratio S/L. With S/L greater than unity the influence of slab width is relatively insignificant.

The effective width Y_e/S decreases with an increase in the core aspect ratio D/B, the effect being relatively more significant with smaller core aspect ratios.

The effective width Y_e/S increases significantly with the core opening ratio L/B. Among the three geometric ratios D/B, L/B and S/B, the core opening ratio L/B has the greatest influence on the effective width Y_e/S for the slab.

It is seen that in the case where the slab edges are free, the effective width values for the single-core configurations without lobby slabs vary from 50 to 60% of the values for the same core configurations with lobby slabs, and in the other cases where the slab edges are simply supported, the corresponding percentage figures are 55 to 65%. The effective width values obtained for a limited number of cases for the twin-core configurations without lobby slabs when compared with corresponding results for similar configurations with lobby slabs (Table 7.2) appear to follow the same trends shown by the results for single-core configurations. Since design curves have not been presented for twin-core configurations without lobby slabs, it is suggested that the effective width values for these cases be obtained by taking 55 or 60% of the values for the case with a lobby slab, the value taken depending on whether the slab edges are free or restrained.

7.6 DISPLACEMENTS AND STRESS-RESULTANTS INDUCED BY WARPING ACTIONS

In order to illustrate the warping actions in the slab, transverse displacement and stress resultant fields induced by a unit torsional warping displacement have been

evaluated graphically by computer for typical core-slab configurations. The graphical results are presented in Fig. 7.15-7.26.

Fig. 7.15 and 7.16 show displacement contours while Fig. 7.17 and 7.18 show stress-resultant contours for a slab with free exterior edges and a slab with simply supported exterior edges in a typical "single-core without lobby" configuration with geometric ratios of D/B = 1.0, L/B = 0.5 and S/B = 0.75. To facilitate the interpretation of the contour diagrams and also to provide a quick qualitative picture of the general displacement and stress patterns throughout the slab, a complementary series of perspective diagrams have been presented in Figs. 7.19 and 7.20 for these cases. It is seen from the displacement contours and also from the perspective view of the deflected shape that the slab in all cases is deformed most severely in the area connecting the core-opening, giving rise to severe concentrations of bending moments and shearing forces in the slab around the coupled lips of the core section. The significant warping actions appear to be confined to the portion of the slab spanning the core opening. The other parts of the slab at the sides and back of the core appear to be practically unstressed especially when the slab edges are free. When the slab edges are restrained, a certain amount of bending is induced in these parts of the slab, but these actions are insignificant compared to the large actions at the core-opening.

The displacement and stress-resultant contours for the corresponding cases with lobby slabs have been presented in Fig. 7.21-7.24. It is seen that the lobby slab does not affect significantly the displacement and stress patterns in the slab outside the core. The significant warping actions in the lobby slab are confined to an area close to the lips of the core.

Fig. 7.25 and 7.26 show the stress-resultant contours for slabs in the "twin-core with lobby" configuration. Like the previous cases, the significant warping actions

are seen to be confined to the region around the lips of the core. The restraint at the exterior slab edges again does not affect the stress patterns significantly.

7.7 SLABS SUPPORTED BY A SMALL NUMBER OF PERIPHERAL COLUMNS

The previous section has considered the case of the slab supported around its periphery by closely spaced columns or by deep spandrel beams, whereby for an analysis of the warping action, the slab edges may be idealised as being simply supported throughout. Situations arise in which the peripheral columns are spaced relatively far apart and the slab is connected to the columns without spandrel supports. If the columns are assumed axially rigid but flexible in bending in comparison with the flexural stiffness of the slab, then the slab may be considered as point supported at the column positions. The warping stiffness of the slab in this case can be expected to vary according to the column arrangement but its value will lie between those for the two extreme cases in which the slab edges are free and simply supported throughout.

In order to illustrate the relative influence of discrete column supports on the warping stiffness of the slab, a square single-core configuration is considered. Two core-opening ratios L/B of 0.5 and 1.0 and three slab-width ratios S/B of 0.5, 0.75 and 1.0 are considered in order to include a reasonable range of variables in the evaluation of the slab's performance. Three column arrangements consisting of 4, 8 and 12 columns arranged symmetrically around the periphery of the slab are considered, together with the two extreme cases where the slab edges are unsupported and simply supported throughout. In all cases, the slab is assumed monolithic with the core wall. The lobby slab is assumed non-existent inside the core. The values for the warping stiffness factor K_w and effective width Y_e/S evaluated for the various cases are shown in Tables 7.3, (a) and (b). In order to

highlight the stiffening effect of the column supports, the results for the cases where the slab edges are restrained have been compared with those for the case where the slab edges are free and the percentage differences have been inserted below the effective-width values in the Table.

It is seen from the results that the stiffening effect of the peripheral supports increases significantly with the ratio of core-opening to slab width, L/S. The stiffening effect also increases with the number of column supports, but once the slab has been restrained by 8 columns arranged with pairs of columns in line with the core walls, then any further increase in the number of columns does not produce much further increase in the warping stiffness of the slab. The warping stiffness for the slab restrained by the 8-column arrangement is seen to differ by less than 10% from the limiting value given by the simply supported slab in the cases investigated. For practical purposes, the slab in the former case could well be assumed simply supported all around the periphery. It appears that although the slab is restrained only at a limited number of points around its periphery, the stiffening effect produced by the point supports is not substantially different from that produced by continuous simple supports.

7.8 EFFECT OF FINITE COLUMN STIFFNESS

The warping stiffness of a slab enclosing a centre core and supported by peripheral columns has been evaluated in the preceding section by assuming that the columns have infinite axial stiffness but zero flexural stiffness. The finite stiffness of actual columns will to a certain extent influence the warping stiffness of the slab. In order to evaluate the relative significance of the approximations involved in the previous assumptions, realistic column stiffnesses are now considered for two of the cases considered in the preceding section. These

cases consist of square single-core configurations with core-opening ratios L/B of 0.5 and 1.0 and a common slab width ratio S/B of 0.75. The slab in each case is connected to 12 columns arranged around the periphery. The cores are assumed to be 7.32 x 7.32 m (24 x 24 ft) square. It is estimated that column sizes will vary from 0.3x0.3 m (1 x 1 ft) square in the upper floors to 0.61 x 0.61 m (2 x 2 ft) square in the lower floors in a 60.98 m (200 ft) high, 20 storeyed building, with the column arrangement as assumed. The wall and slab thicknesses are assumed as 0.3 m (1 ft) and 0.23 m (0.75 ft.) respectively.

In order to simplify the analysis it is assumed that the effect of inter-floor interaction of various members can be disregarded in the evaluation of the warping stiffness for the slab. The columns at each floor can then be represented as elastic springs with axial and rotational stiffnesses. The axial spring stiffness is evaluated assuming a column length equal to the storey height. The rotational spring stiffness is evaluated assuming points of contraflexure at mid-storey heights. Stiffnesses corresponding to the two estimated column sizes are considered for the evaluation of warping stiffness and effective width for the slab.

Table 7.4 shows the values of warping stiffness factor K_w and effective width Y_e/S evaluated for the cases which account for finite column stiffnesses, compared with the results obtained assuming infinite axial and zero flexural column stiffnesses. It is seen from the results that the assumption of infinite axial column stiffness generally over-estimates the warping stiffness of the slab by less than one per cent, whereas the assumption of zero flexural stiffness under-estimates the warping stiffness by a few per cent. In the latter case, the errors may lead to a slightly conservative design of the core. Nevertheless, considering the possibility of cracking at the slab-column joint which tends to reduce the effectiveness of the column restraint it would appear reasonable to disregard

the rotational restraint of the column in evaluating the warping stiffness for the slab.

7.9 VERIFICATION OF RESULTS

There appears to be no reliable published data against which the results presented in this chapter could be compared. Although Stafford Smith and Taranath[11-13] have evaluated the warping stiffness of the slab for a limited number of cases using the finite element method, the results they obtained appear to be grossly in error, as will be shown later, and therefore cannot be used to check the author's results. A rigorous check on the finite element results by a classical plate solution does not appear possible due to the complicated boundary conditions presented by the slab cut-out at the core. Therefore, to prove the accuracy of the method of analysis, a simpler but rather similar problem of a slab without cut-out interacting with the core is considered and the results obtained by an influence coefficient method are used to verify the results obtained by the finite element method.

Two single-core configurations with opening ratios L/B of 0.5 and 1.0, and with a common slab-width ratio S/B of 0.75 were considered. The slab was assumed to be simply supported around its periphery and rigidly connected to the core in each case. Two finite element analyses were performed for each case using coarse and fine mesh patterns in order to obtain some indication of convergence. Similarly, the influence coefficient solutions were evaluated to two levels of refinement for each case. Seventy and 240 elements were used for the element discretisations of the slab. In the influence coefficient solutions, 9 nodal points were used for the representation of the core in all cases, but the influence coefficients were evaluated from 40 and 80 terms of the infinite series. In each method of analysis, advantage was taken of the anti-symmetry conditions about the Y-axis in the slab to reduce the computational effort.

The results for the warping stiffness factor K_w and effective width Y_e/S evaluated by the two methods of analysis are compared in Table 7.5. It can be seen that the finite element solution and influence coefficient solution are in good agreement. The minor discrepancies between the results evaluated by the two different methods are of such orders that they can be attributed to convergence errors. Since the accuracy of the finite element solution is verified by the influence coefficient solution for these test cases it is reasonable to assume that the finite element results for the real cases, which are essentially similar to the test cases except for the openings in the slab, are of similar accuracy.

The reliability of the finite element results can also be checked approximately using results which have been presented for slabs coupling shear walls in cross-wall structures. It may be recognised from the displacement and stress fields induced in the slab that the primary warping action of the slab arises from bending deformation produced by differential shearing action across the core opening similar to the action in a slab coupling a pair of plane walls. Therefore, if in the case where the slab is unsupported around its periphery, the portion of the slab connecting the side of the core with the opening is isolated from the rest of the panel, then the problem could be approximated as one similar to the end bay of a slab coupled cross wall structure. The results presented in Chapter 3 can therefore be used as a rough check to confirm that the effective width values evaluated for the core-slab structure are of the right order.

Consider for example the square single-core configuration with core-opening ratio L/B of 0.5 and slab-width ratio S/B of 0.75. The approximate 'end bay' equivalent will have the relevant ratios L/X of 0.5 and Y/X of 1.5. The effective width Y_e/Y for the end bay, which may be taken as 45% of that for an interior bay (Section 3.4.1.11), is evaluated by the empirical equations (3.4) and (3.6) as 0.130 which gives a value of 0.260 for the effective width

Y_e/S. This value compares very well with the value of 0.266 evaluated by the finite element analysis for the core-slab structure. The effective width values for slabs with other core-opening ratios and slab width ratios have also been checked and found to agree well generally with the 'end-bay' results.

As mentioned earlier on, Stafford Smith and Taranath's results for the warping stiffness of slab appear grossly in error. This can be seen from the results for a particular case which was presented in Reference 12. The case considered was a perspex model consisting of a 203 mm (8 in.) square core with a 102 mm. (4 in.) wide opening on one side, the core being enclosed by 508 mm (20 in.) square, 10 mm ($\frac{3}{8}$ in.) thick slabs. The elastic modulus and Poisson's ratio for the perspex were given as $E = 2930\ N/mm^2$ ($4.25 \times 10^5\ lb/in^2$) and $\nu = 0.35$ respectively. The warping stiffness of the slab was obtained as $2686\ Nm^2$ ($935,750\ lb\text{-}in^2$). Now this warping stiffness will give for an equivalent lintel an effective width of only 4.1 mm (0.16 in.), which is even thinner than the wall thickness or slab thickness and appears unreasonable. On the other hand, the warping stiffness for the same case determined by the author is $26355\ Nm^2$ ($9,180,000\ lb\text{-}in^2$) giving an effective width of 40.6 mm (1.60 in.), which is slightly more than four times the slab thickness and appears a much more reasonable figure. It was found that other cases presented by Taranath in Reference 13 show the same order of inaccuracy as the case quoted above.

7.10 EFFECT OF SLAB COUPLING ON OVERALL BEHAVIOUR OF CORE

The torsional behaviour of a thin-walled open-section core, which may or may not be coupled by a continuous medium across the core opening, can be described by the governing equation[23,75]

$$\frac{d^4\theta}{dz^4} - \alpha^2 \frac{d^2\theta}{dz^2} = \frac{t(z)}{E_1 I_w} \qquad (7.11)$$

where $\alpha = \sqrt{\frac{G\ J_w}{E_1 I_w}}$ and $E_1 = \frac{E}{1-\nu^2}$

For an uncoupled core $J_w = J$, the St. Venant torsional moment of inertia. When the core is coupled by uniform lintel beams at regular intervals along its height, the value of J_w is modified to $J_w = (J + J_d)$. In a single core configuration

$$J_d = \frac{\Omega^2}{Lh} \frac{1}{\left\{\frac{L^2 G}{12EI_b} + \frac{1.2}{A_b}\right\}} \qquad \text{(cf. Ref. 75)}$$

and in a twin core configuration

$$J_d = \frac{\Omega^2}{2Lh} \frac{1}{\left\{\frac{L^2 G}{12EI_b} + \frac{1.2}{A_b}\right\}} \qquad \text{(cf. Ref. 73-74)}$$

where I_b and A_b are the moment of inertia and cross-sectional area of the lintel, h is the lintel spacing and Ω and L are as defined earlier.

The solutions of the governing equation (7.11) for three standard load cases for a core on a rigid foundation are given by[73-75]

(a) Concentrated Torque P at the Top:

$$\Theta_z = \frac{P}{E_1 I_w} \frac{H^3}{(\alpha H)^3} \left\{ - \text{sh}(\alpha H.\frac{z}{H}) + \tanh \alpha H \left[\text{ch}(\alpha H.\frac{z}{H}) - 1 \right] + (\alpha H.\frac{z}{H}) \right\} \qquad (7.12)$$

(b) Uniformly Distributed Torque of Intensity m/unit height:

$$\Theta_z = \frac{mH^4}{E_1 I_w (\alpha H)^4} \left\{ -\alpha H\ \text{sh}(\alpha H.\frac{z}{H}) + \left[\alpha H \tanh \alpha H + \frac{1}{\text{ch}\alpha H} \right] \left[\text{ch}(\alpha H.\frac{z}{H}) - 1 \right] + (\alpha H)^2 \left[\frac{z}{H} - \frac{1}{2}(\frac{z}{H})^2 \right] \right\} \qquad (7.13)$$

(c) Triangular Distributed Torque of Maximum Intensity n/ unit height At Top:

$$\Theta_z = \frac{n\,H^4}{E_1 I_w (\alpha H)^4}\left\{ -\left(\frac{\alpha H}{2} - \frac{1}{\alpha H}\right)\mathrm{sh}\left(\alpha H.\frac{z}{H}\right) + \left[\left(\frac{\alpha H}{2} - \frac{1}{\alpha H}\right)\tanh \alpha H + \frac{1}{\mathrm{ch}\ \alpha H}\right]\left[\mathrm{ch}\left(\alpha H.\frac{z}{H}\right) - 1\right] + \left(\frac{\alpha H}{2} - \frac{1}{\alpha H}\right)\left(\alpha H.\frac{z}{H}\right) - \frac{\left(\alpha H.\frac{z}{H}\right)^3}{6\,\alpha H}\right\} \qquad (7.14)$$

With the solution for Θ_z known, the torsional stress-resultants and torsional stresses throughout the core can be evaluated using equations (2.13)-(2.22). The shear force distribution in the connecting medium may be obtained by[73-74]

$$q(z) = \frac{G\ J_d}{\Omega}\quad \frac{d\Theta}{dz} \qquad (7.15)$$

The overall torsional behaviour of a core structure is seen to be characterised by the parameter αH, the value of which reflects the coupling effect of the connecting beams. The value of αH is large when the core is coupled by stiff lintel beams and is small when the core is uncoupled. Fig. 7.27 illustrates the effect of coupling on two of the quantities which may control the torsional design of the core, namely, the maximum rotation Θ_H at the top and the maximum bimoment B_o at the base of the core. The percentage reductions in the values for Θ_H and B_o due to coupling effect have been plotted against values of αH and lintel depth to storey height ratio d/h for two standard load cases consisting of a concentrated torque at the top and a uniformly distributed torque along the height of the core. The core structure considered in the illustration isa7.32 x 7.32 m (24 x 24 ft) square core with an opening of 3.61 m (12 ft.) width coupled by lintel beams at 3.05 m (10 ft.) intervals along its total height of 60.96 m (200 ft.). The core walls are 0.30 m (1 ft.) thick.

While the curves in Fig. 7.27 are based on a

particular core structure, the trend of results they illustrate should be typical. It is seen that significant reductions in the maximum deflection Θ_H and maximum bimoment B_o can be achieved with relatively small values of αH associated with relatively flexible coupling beams. The design quantities Θ_H and B_o are not sensitive to αH when the coupling beams have appreciable stiffness ($\alpha H > 6$), but when the beams are flexible ($\alpha H < 4$), these quantities change rapidly with αH, and it is then important to evaluate accurately the stiffness of the coupling beams. This is particularly important when the core is coupled only by floor slabs which are relatively flexible, since a small error in the calculation of effective width for the equivalent lintel may have a significant effect on the behaviour of the core.

The effective width of slab and the value of αH for the core depends among other parameters on the shape of the core and on the core opening width L. The effectiveness of slab coupling is therefore dependent on these parameters. Fig. 7.28 shows values of αH and 'coupled/uncoupled' ratios of Θ_H and B_o plotted against core opening ratios L/B for four core configurations consisting of single-cores and twin-cores with aspect ratios D/B of 1.0 and 0.5 coupled by slabs with a width ratio S/B of 0.75. The 'coupled/uncoupled' ratio expresses the value of Θ_H or B_o evaluated assuming the core coupled by an effective width of slab, as a ratio of that for an uncoupled core, and serves as a measure of the effectiveness of slab coupling. The interior of the core in each case is assumed to be spanned by a lobby slab and calculations are based on a 60.96 m (200 ft.) high, 20-storeyed core-supported structure with a core width B of 7.32 m (24 ft) and wall and slab thicknesses of 0.3 m and 0.23 m (12 in. and 9 in.) respectively.

It is seen from Fig. 7.28 that although the core configurations differ considerably, the general trend of results showing the variations of αH and effectiveness of coupling with core opening ratio in each case is

similar. Throughout the possible range of wall opening ratios, significant coupling is provided by the slab, resulting in substantial reductions in the values of Θ_H and B_o. The coupling effects are relatively more significant with smaller core opening ratios. It is seen that as the core-opening ratio is reduced from 0.1 to the limit, the value of αH increases rapidly to an infinitely large value and the core becomes infinitely stiff, which is physically not possible. The anomaly is due to the limitations of open-section analysis in which some of the fundamental assumptions in the torsion theory become invalid when the coupling medium is very stiff. However, in practice, core-openings are relatively large and the situation where the validity of open-section analysis becomes questionable is unlikely to arise.

7.11 SIGNIFICANCE OF ERRORS IN EFFECTIVE WIDTH ON OVERALL CORE-PERFORMANCE

Inevitably, a certain amount of error is introduced into the evaluation of the effective width or warping stiffness of the slab due to the various approximations which have been assumed in order to simplify the analysis. However, errors in the estimation of effective widths for the connecting beams usually result in smaller errors in the calculation of design quantities associated with the overall torsional behaviour of the core-slab system. In order to illustrate the relative significance of these errors, the torsional behaviour of a 60.96 m (200 ft) high 20-storeyed core-supported structure is evaluated assuming various effective widths for the connecting beams. The 'correct' effective width is assumed to be given by the value obtained from the finite element analysis and effective widths which are $\pm$ 10% and $\pm$ 20% different from this value are considered for the other cases. Two typical core configurations are considered. These consist of a square single core with L/B = 0.5 and S/B = 0.75, and a square twin core with L/B = 0.33 and S/B = 0.75. The

lobby slab is assumed to be present only in the twin-core configuration. Both cores are assumed to be 7.32 m (24 ft.) square. Wall and slab thicknesses are assumed as 305 mm (12 in.) and 229 mm (9 in.) respectively. Two load cases are considered, namely, a concentrated torque of 1.36 kNm (1 kip-ft) at the top and a uniformly distributed torque of 4.45 kNm/m (1 kip-ft/ft).

The results for the rotation Θ_H at the top and the bimoment B_o at the base of the core for the various cases are shown in Table 7.6. The 'errors' in the calculation of these quantities due to the respective 'errors' in the effective widths Y_e have also been shown in the Table. It is seen from the results that the errors in the calculation of Θ_H and B_o are smaller than the errors in Y_e in every case. The negative error in Y_e has a larger influence on Θ_H and B_o than the positive error but in the former case, Θ_H and B_o are over-estimated and therefore err on the safe side for design. Errors in Y_e have a greater influence on Θ_H than on B_o and are more significant for the concentrated loading case than the distributed loading case.

It is seen from the cases considered that a 20% error in the estimation of effective width Y_e results in maximum error of about 10% in the calculation of bimoment B_o. The error in B_o results in a similar order of error in the calculation of longitudinal wall stresses induced by torsional loading. However, when these stresses are considered with the stresses due to gravity loading for design purpose, then the resultant error in the evaluation of critical design stresses will be much smaller than 10%. The cores considered here have relatively small opening ratios. With larger core-opening ratios, errors in the evaluation of effective widths will be less significant than the cases considered. It would appear that in most practical cases a 20% error in the estimation of the effective width is quite acceptable for design stress calculations.

The corresponding error in the calculation of torsional rotation Θ_H due to a 20% error in Y_e is seen to be of the order of 16-17% in more severe cases, and may not be acceptable when the design of the core is controlled by the lateral stiffness criterion. However, in most practical buildings, the design of the core to satisfy strength requirements often results in a structure of such stiffness that the torsional rotation or lateral drift criterion is easily satisfied, and a 20% error in the evaluation of Y_e may still be acceptable for stiffness calculations.

7.12 CONCLUSIONS

A rational method of replacing the slab enclosing a centre core by an equivalent system of lintel beams has been suggested to facilitate the torsional analysis of the core. The absolute effective width for the equivalent beam has been shown to be influenced strongly by the support conditions of the slab edges and by the core opening ratio, and less by the core aspect ratio and slab width ratio. Design curves showing the relative influence of the various parameters in the effective width have been presented to enable the effective width to be readily established for the torsional analysis of the core.

The significant warping actions in the slab have been shown to be confined to the area spanning the core opening. Severe stress concentrations arise around the coupled lips of the core section where special attention may be required in detailing the slab.

Effective coupling of the core walls can be achieved even with a relatively flexible slab system, and considerable economies may be gained in the design of the core by taking into account the contribution of the coupling slab.

TABLE 7.1 CONVERGENCE RESULTS FOR SINGLE-CORE CONFIGURATION (D/B = 1.0, L/B = 0.5, S/B = 0.75)

Mesh Type	Slab Edges Free			Slab Edges S.S.		
	K_w	Y_e/S	R^*	K_w	Y_e/S	R^*
Coarse Mesh 45 Elements, 192 DOF	40.147	0.2852	1.094	50.243	0.3569	1.074
Medium Mesh 88 Elements 345 DOF	38.045	0.2703	1.036	48.087	0.3416	1.028
Fine Mesh 180 Elements 651 DOF	36.705	0.2608	1.000	46.780	0.3323	1.000

R^* = Result normalised with respect to that for fine mesh.

TABLE 7.2 EFFECTIVE WIDTH VALUES FOR TWIN CORE CONFIGURATIONS WITH AND WITHOUT LOBBY SLAB

		D/B = 1, L/B = 0.25, S/B = 0.75			D/B = 0.75, L/B = 0.5 S/B = 0.5		
Boundary Conditions		M/F	M/S	S/S	M/F	M/S	S/S
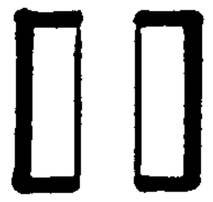	Case 1: Core With Lobby Slab	0.2760	0.2830	0.1787	0.7588	0.9928	0.6808
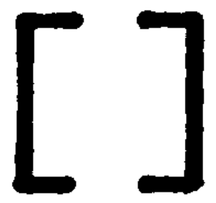	Case 2: Core Without Lobby Slab	0.1606	0.1714	0.1089	0.4205	0.5977	0.3742
Ratio:	Case 2 / Case 1	0.58	0.61	0.61	0.55	0.60	0.55

M = Monolithic, F = Free, S = Simply Supported

TABLE 7.3(a) EFFECT OF PERIPHERAL COLUMNS ON SLAB WARPING STIFFNESS

Square Single Core (L/B = 0.5)

Peripheral Support Conditions	Warping Stiff-ness and Eff. Width	Slab Width Ratio S/B		
		0.5	0.75	1.0
 Free Edges	K_w	34.8767	38.0447	40.3070
	Y_e/S	0.3717	0.2703	0.2148
	D%	0.0%	0.0%	0.0%
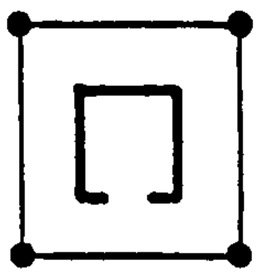 4 Columns	K_w	38.3153	40.6876	42.5428
	Y_e/S	0.4083	0.2891	0.2267
	D%	+9.86%	+6.95%	+5.55%
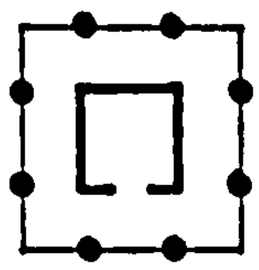 8 Columns	K_w	50.3482	47.3487	46.8080
	Y_e/S	0.5365	0.3369	0.2494
	D%	+44.36%	+24.46%	+16.13%
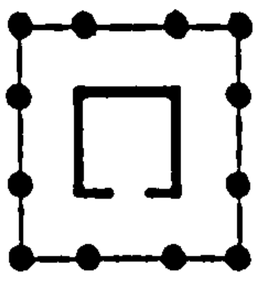 12 Columns	K_w	50.8744	47.4477	46.8284
	Y_e/S	0.5421	0.3371	0.2495
	D%	+45.87%	+24.72%	+16.18%
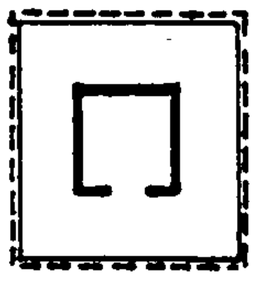 S.S. Edges	K_w	53.7696	48.0874	47.1025
	Y_e/S	0.5730	0.3416	0.2510
	D%	+54.17%	+26.40%	+16.86%

D% = Percentage difference in relation to case for free edges.

TABLE 7.3(b) EFFECT OF PERIPHERAL COLUMNS ON SLAB WARPING STIFFNESS

Square Single-Core (L/B = 1.0)

Peripheral Support Conditions	Warping Stiffness and Eff. Width	Slab Width Ratio S/B		
		0.5	0.75	1.0
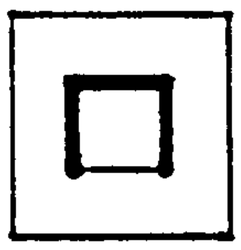 Free Edges	K_w	6.5078	7.5244	8.2172
	Y_e/S	0.5548	0.4276	0.3503
	D%	0.0%	0.0%	0.0%
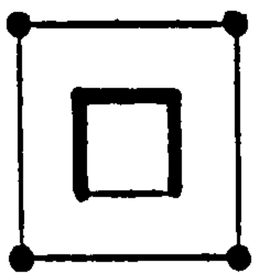 4 Columns	K_w	9.0291	9.4144	9.7819
	Y_e/S	0.7697	0.5351	0.4170
	D%	+38.74%	+25.12%	+19.04%
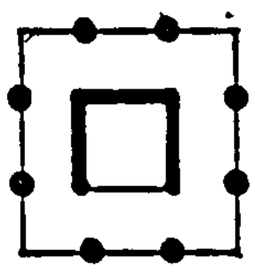 8 Columns	K_w	15.5857	13.1855	12.2704
	Y_e/S	1.3287	0.7494	0.5230
	D%	+139.45%	+75.24%	+49.33%
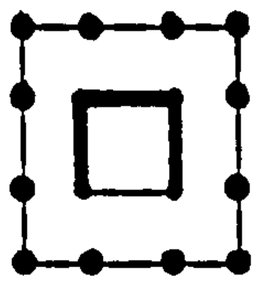 12 Columns	K_w	15.8084	13.2284	12.2797
	Y_e/S	1.3477	0.7518	0.5234
	D%	+142.91%	+75.81%	+49.44%
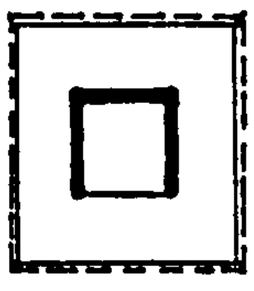 S.S. Edges	K_w	17.0364	13.6312	12.4824
	Y_e/S	1.4524	0.7747	0.5321
	D%	+161.78%	+81.16%	+51.91%

D% = Percentage difference in relation to case for free edges

TABLE 7.4 EFFECT OF FINITE COLUMN STIFFNESS ON SLAB WARPING STIFFNESS

CORE/SLAB CONFIGURATION		1'x1' Sq. Columns		2'x2' Sq. Columns		S.S.Edges
	Axial Stiffness *	4.320E4	4.320E4	1.728E5	1.728E5	∞
	Flex. Stiffness	0	4.320E4	0	7.912E5	0
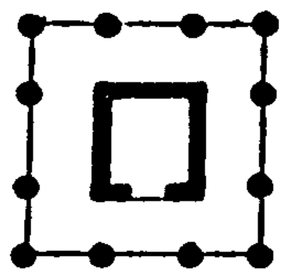	K_w	47.3947	48.8893	47.4343	49.7318	47.4477
	Y_e/S	0.3367	0.3474	0.3370	0.3533	0.3371
	D%	-0.11%	3.04%	-0.03%	4.81%	0%
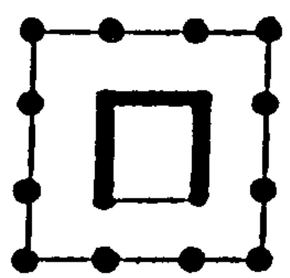	K_w	13.1961	14.1009	13.2203	14.5979	13.2285
	Y_e/S	0.7500	0.8014	0.7514	0.8297	0.7518
	D%	-0.24%	6.59%	-0.06%	10.35%	0%

D% = Percentage difference in relation to case for S.S. Edges

* In kip ft units

TABLE 7.5 : COMPARISON BETWEEN FINITE ELEMENT SOLUTION AND INFLUENCE COEFFICIENT SOLUTION

CORE CONFIGURATION	Finite Element Solution			Influence Coefficient Solution		
	Discretisation (Elem./DOF)	K_w	Y_e/S	Discretisation (Nodal Points/ Series Terms)	K_w	Y_e/S
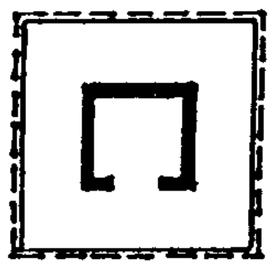 L/B = 0.5	70/264	93.050	0.6611	9/40	91.813	0.6523
	240/819	90.6178	0.6438	9/80	88.497	0.6287
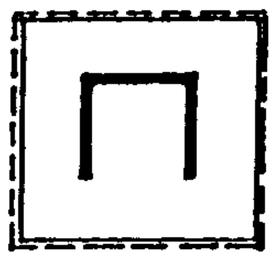 L/B = 1.0	70/264	24.9406	1.4175	9/40	23.953	1.3614
	240/819	24.3611	1.3845	9/80	22.324	1.2688

TABLE 7.6 SIGNIFICANCE OF ERROR IN EFFECTIVE WIDTH
(Figures in brackets refer to percentage errors)

Core Configuration	Effective Width Y_e (ft)	Conc. Torque at Top (1 kip-ft)		Uniformly Dist. Torque (1 kip-ft/ft)	
		$\Theta_H \times 10^6$	$B_o \times 10^{-1}$ (kip-ft^2)	$\Theta_H \times 10^4$	$B_o \times 10^{-4}$ (kip-ft^2)
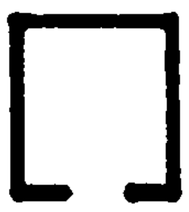 D/B=1.0 L/B=0.5 S/B=0.75	4.870 (0)	1.559 (0)	8.530 (0)	1.224 (0)	1.140 (0)
	4.383 (-10.0)	1.660 (6.5)	8.907 (4.4)	1.299 (6.1)	1.132 (3.0)
	5.357 (+10.0)	1.470 (-5.7)	8.194 (-3.9)	1.158 (-5.4)	1.070 (-2.7)
	3.896 (-20.0)	1.776 (13.9)	9.334 (9.4)	1.385 (13.1)	1.168 (6.3)
	5.844 (+20.0)	1.390 (-10.8)	7.893 (-7.5)	1.099 (-10.3)	1.043 (-5.1)
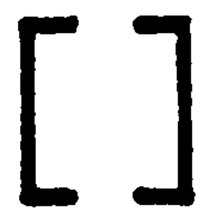 D/B=1.0 L/B=0.33 S/B=0.75	5.860 (0)	0.933 (0)	6.813 (0)	0.748 (0)	0.943 (0)
	5.274 (-10.)	1.006 (7.8)	7.151 (5.0)	0.802 (7.3)	0.975 (3.4)
	6.446 (+10.0)	0.871 (-6.7)	6.517 (-4.3)	0.700 (-6.3)	0.915 (-3.0)
	4.688 (-20.0)	1.091 (16.9)	7.543 (10.7)	0.866 (15.8)	1.011 (7.2)
	7.032 (+20.0)	0.816 (-12.6)	6.255 (-8.2)	0.659 (11.8)	0.890 (-5.7)

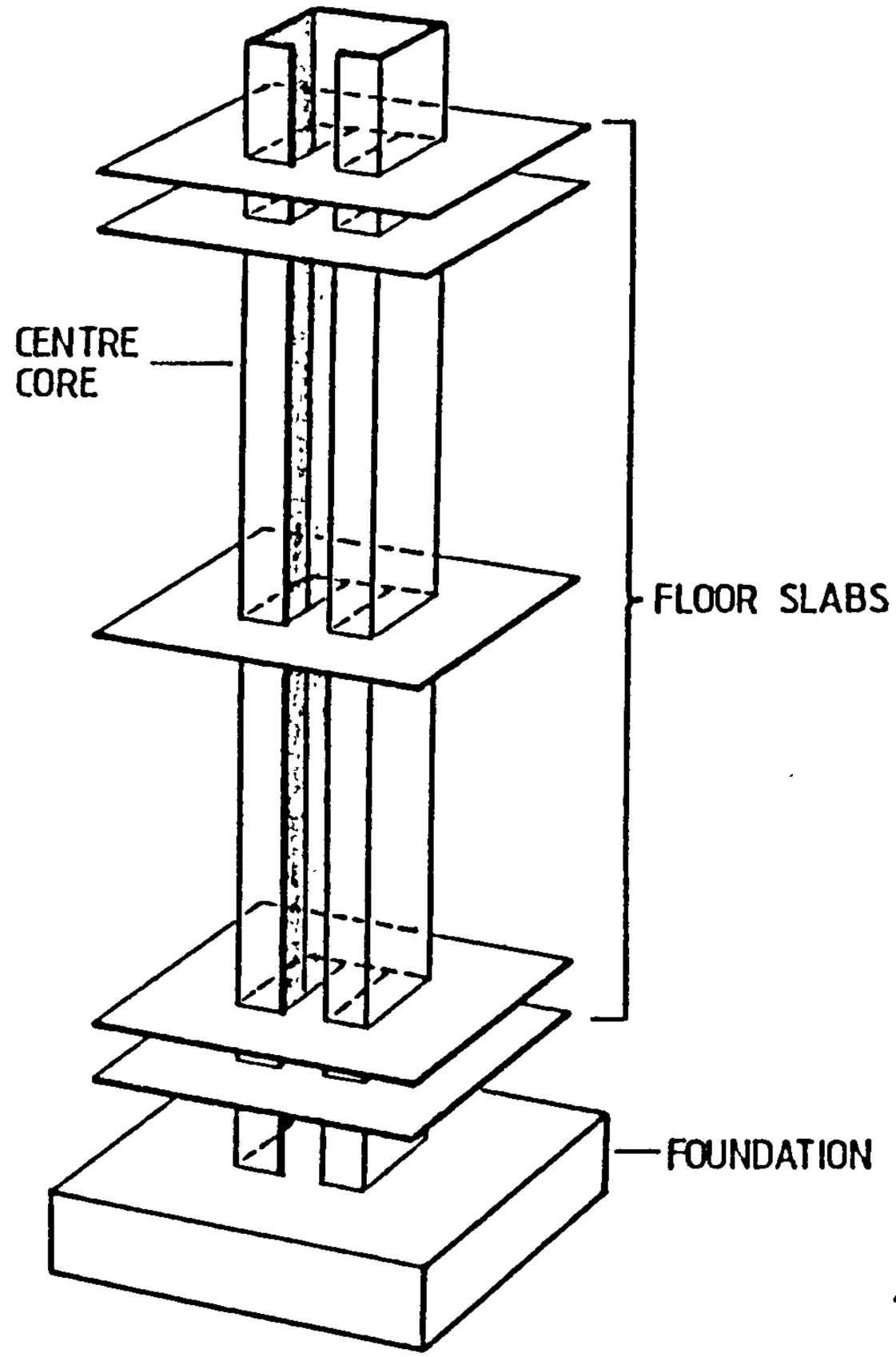

SINGLE-CORE STRUCTURE

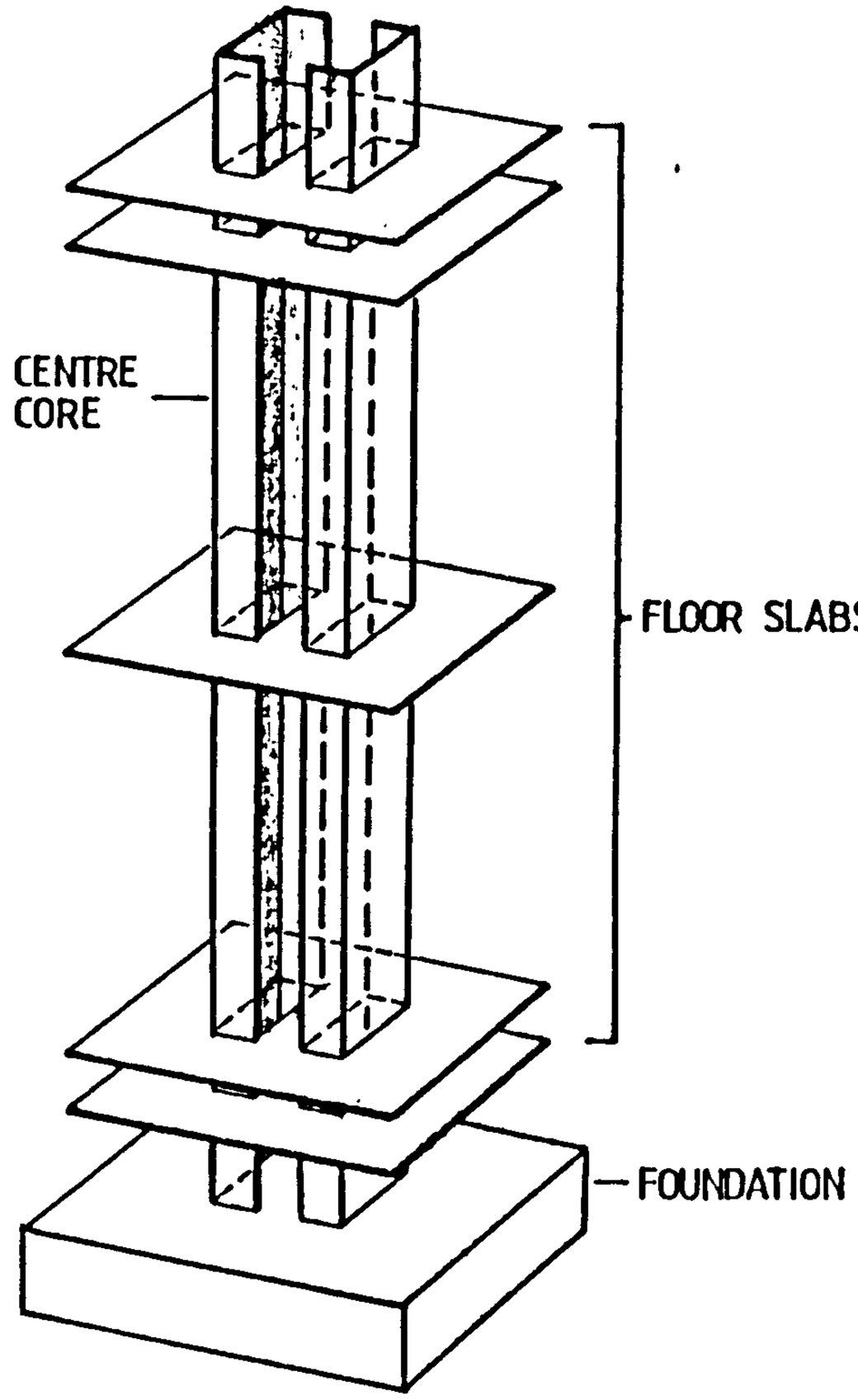

TWIN-CORE STRUCTURE

Fig. 7.1 Idealised Centre Core Structures

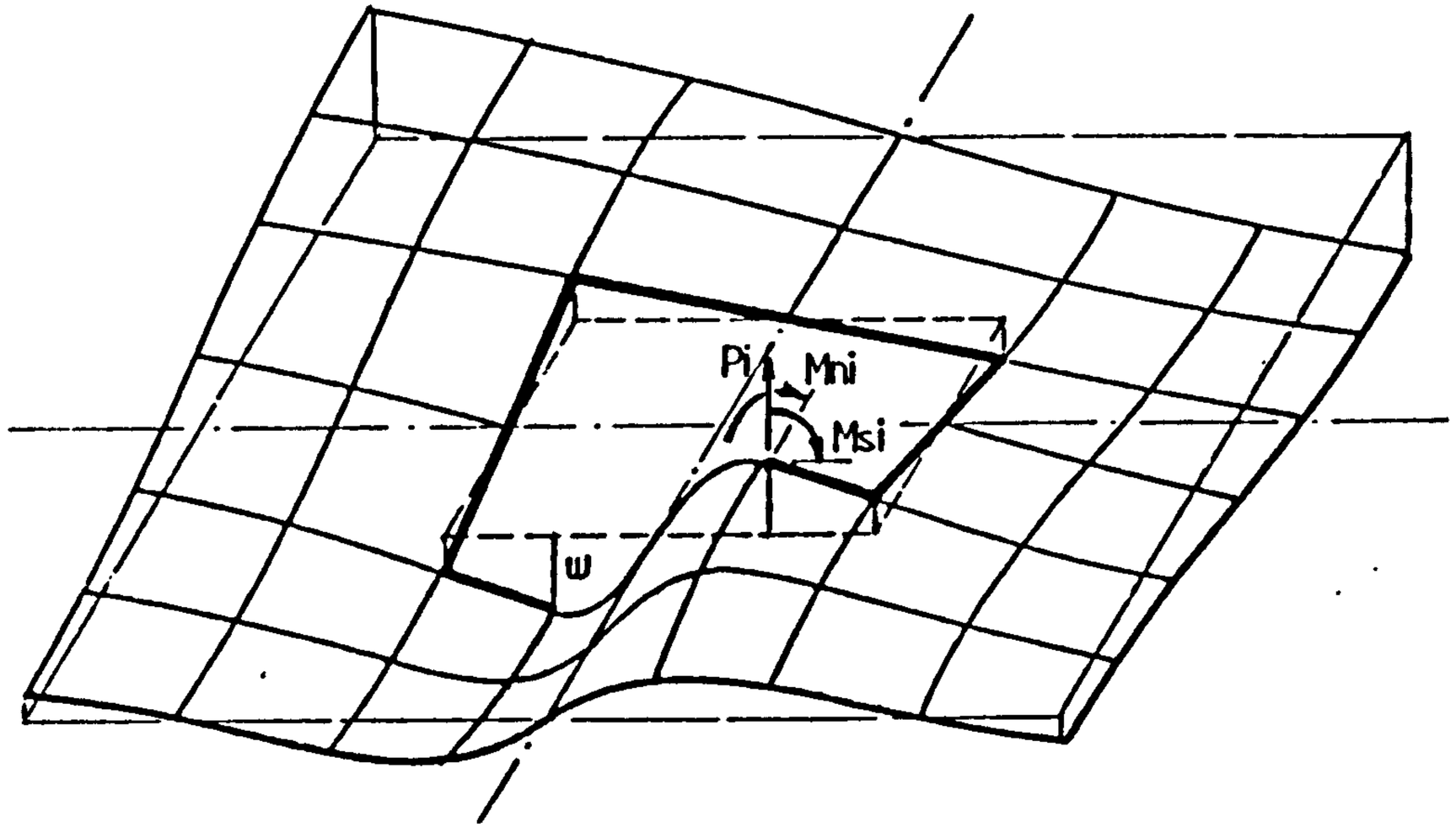

(a) Warping Displacements and Actions in Slab

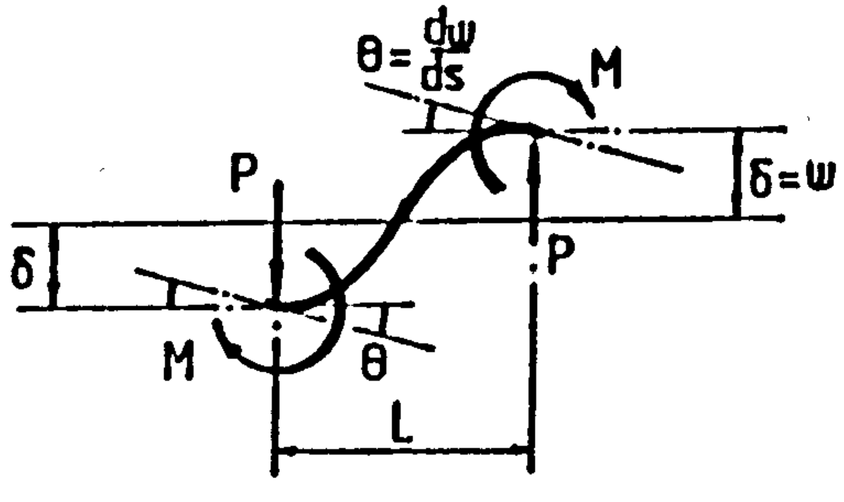

(c) Displacements and Actions in a Beam

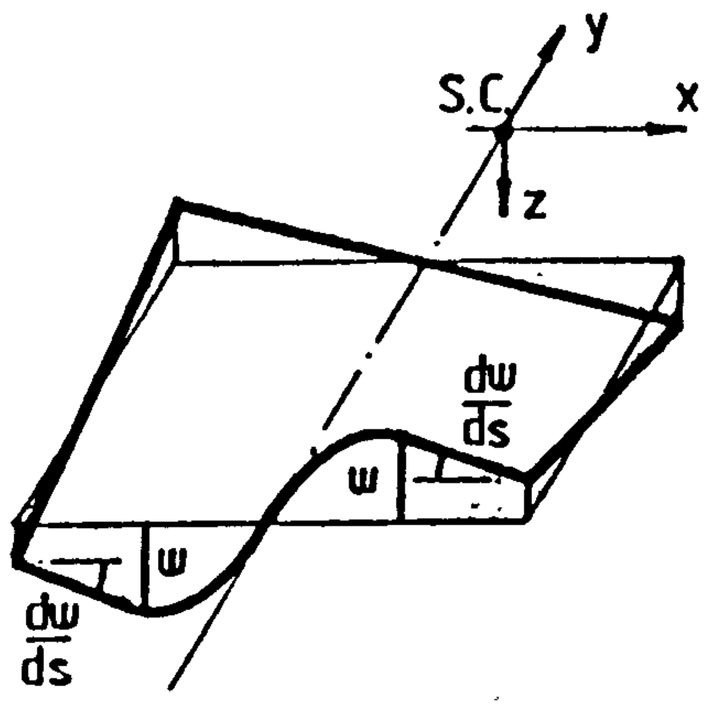

(b) Warping Displacements in Single-Core

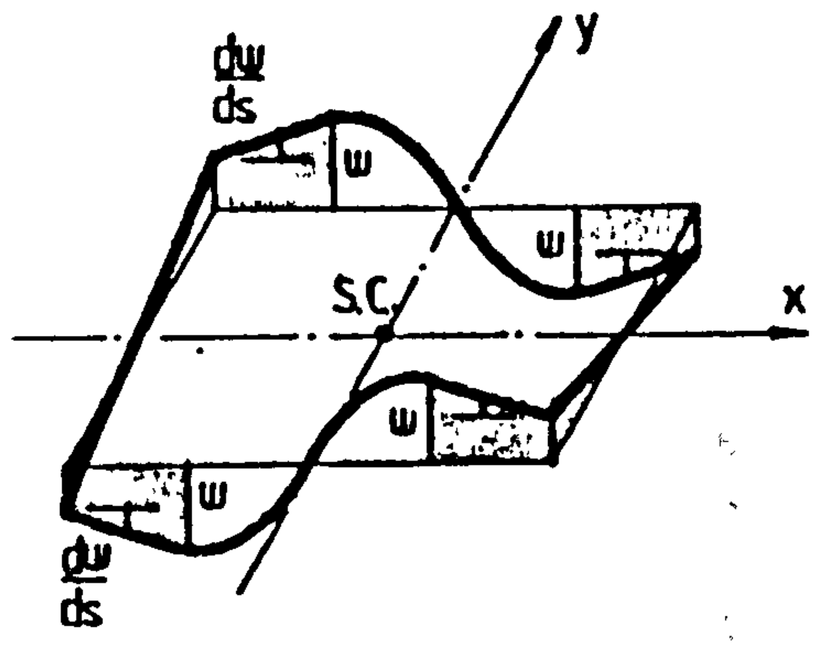

(d) Warping Displacements in Twin-Core

Fig. 7.2 Warping Displacements and Actions in Core, Slab and Beam

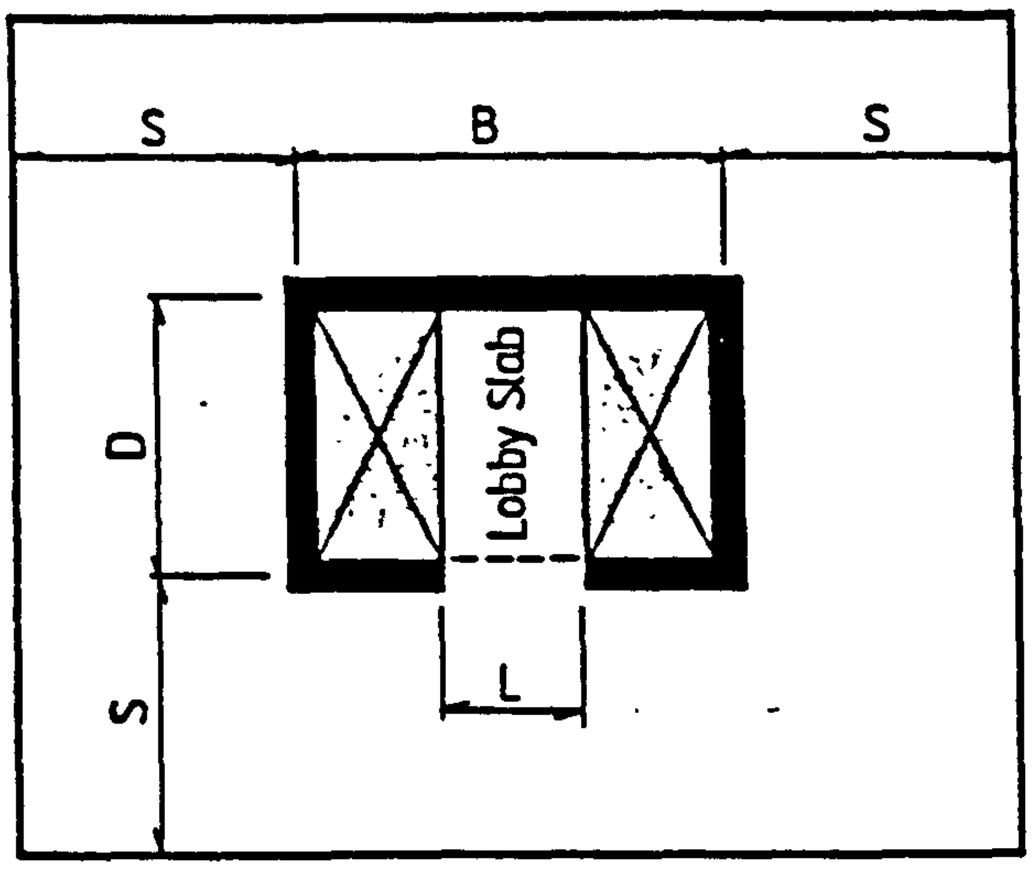

SINGLE - CORE WITH SLAB

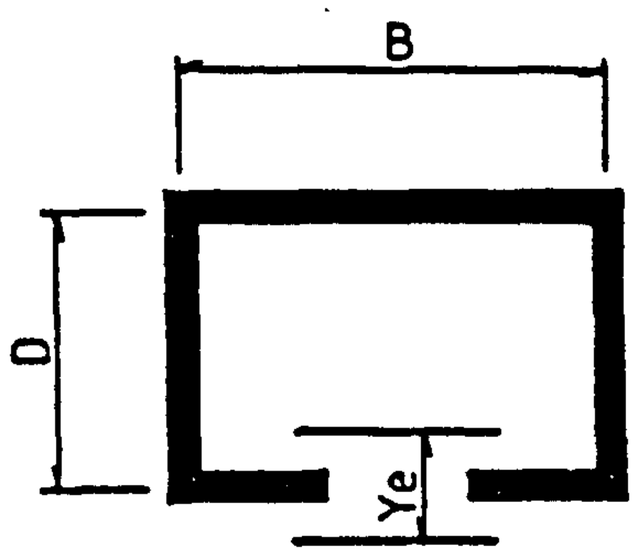

EQUIVALENT CORE
WITH LINTEL

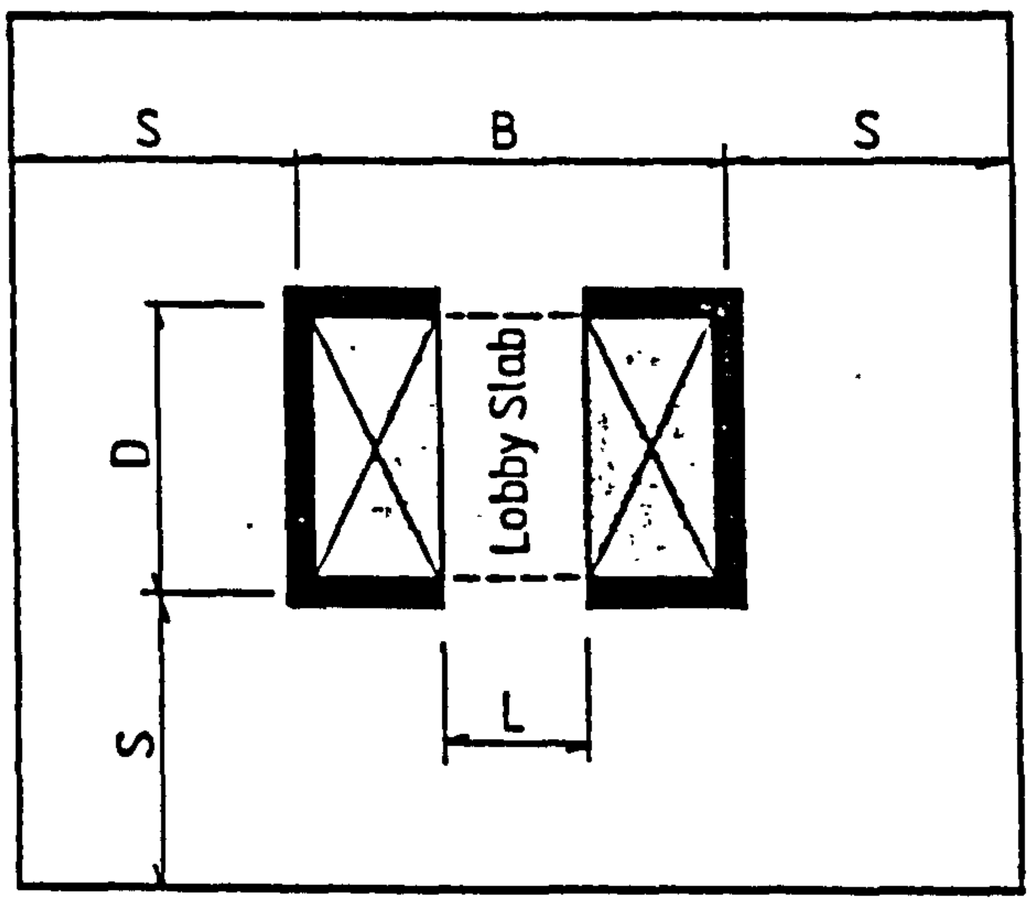

TWIN - CORE WITH SLAB

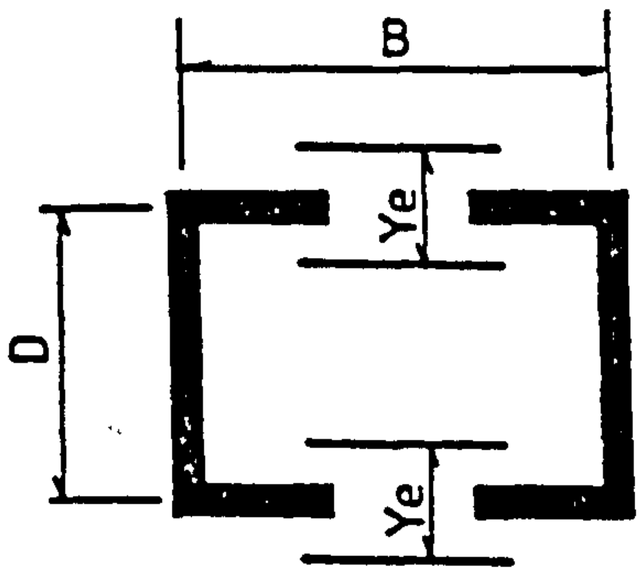

EQUIVALENT CORE
WITH LINTEL

Fig. 7.3 Idealised Plan-Forms for Single-Core and Twin-Core Configurations

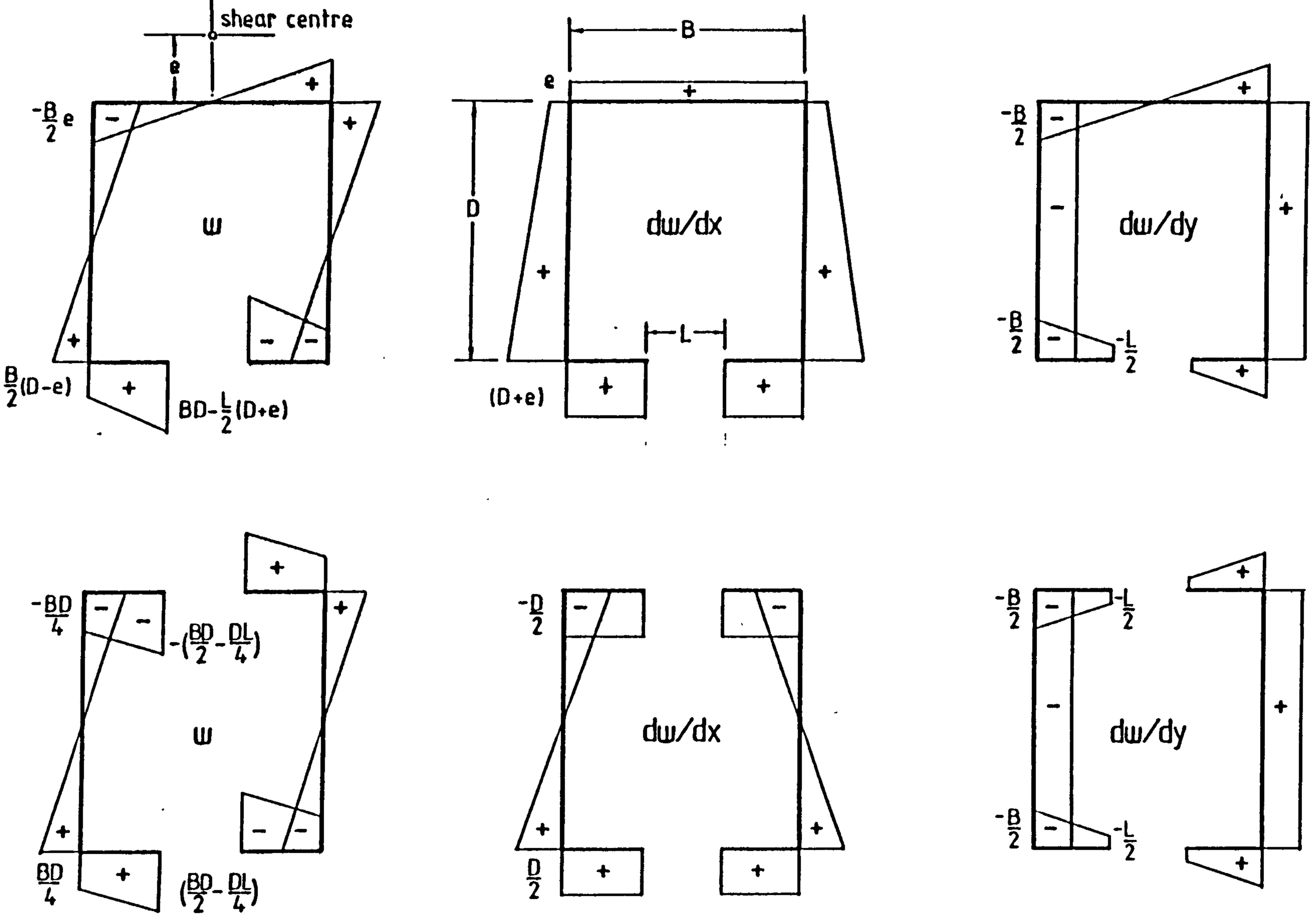

Fig. 7.4 Sectorial Co-ordinate and Slope Functions for Single-Core and Twin-Core Configurations

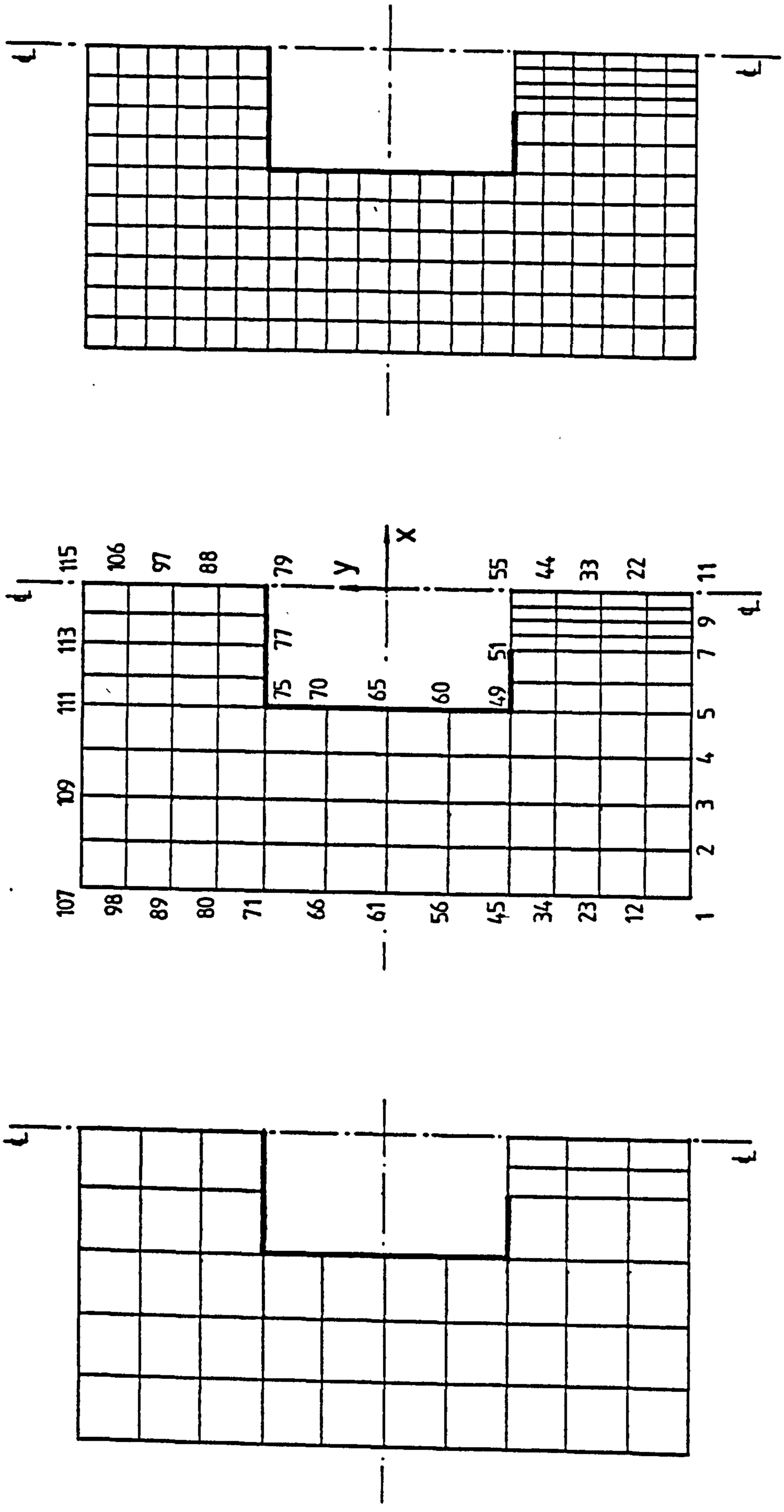

Mesh Patterns for Convergence Study

Fig. 7.5

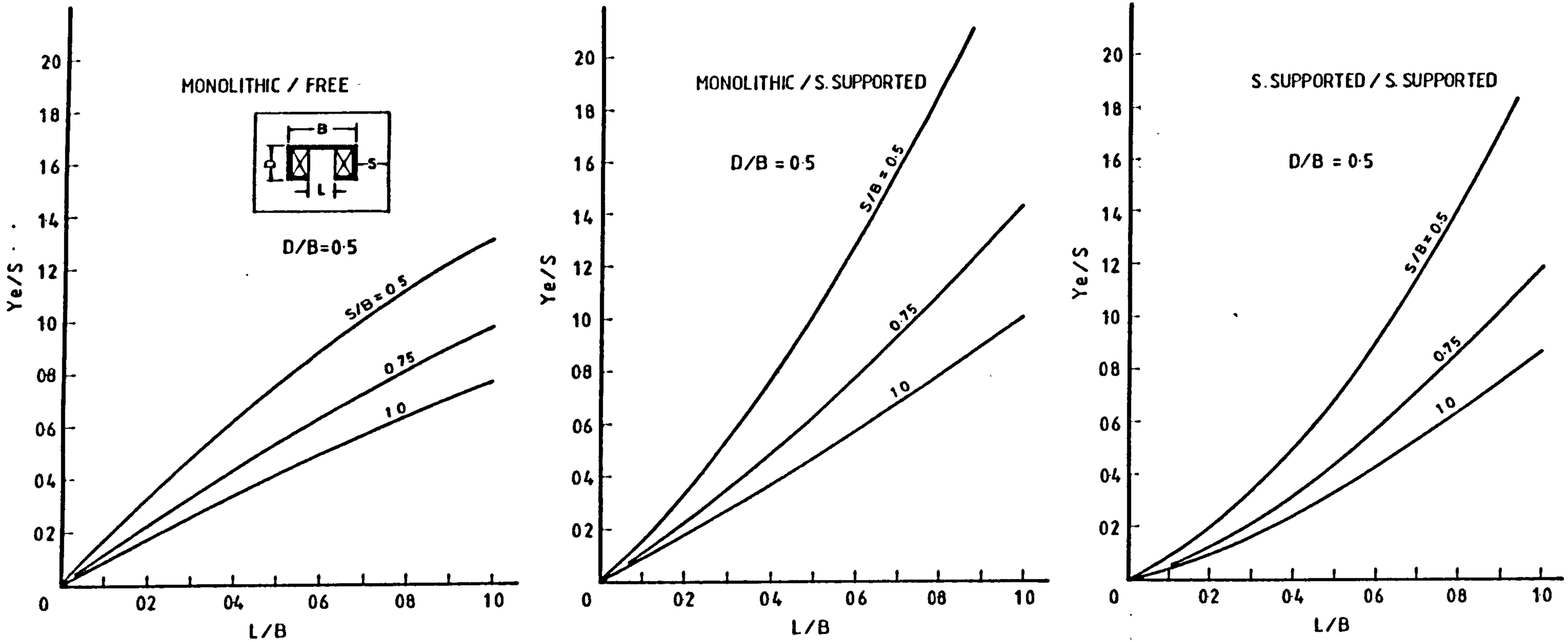

Fig. 7.6 Design Curves for Effective Width Values in Single-Core-With-Lobby Configuration (D/B = 0.5)

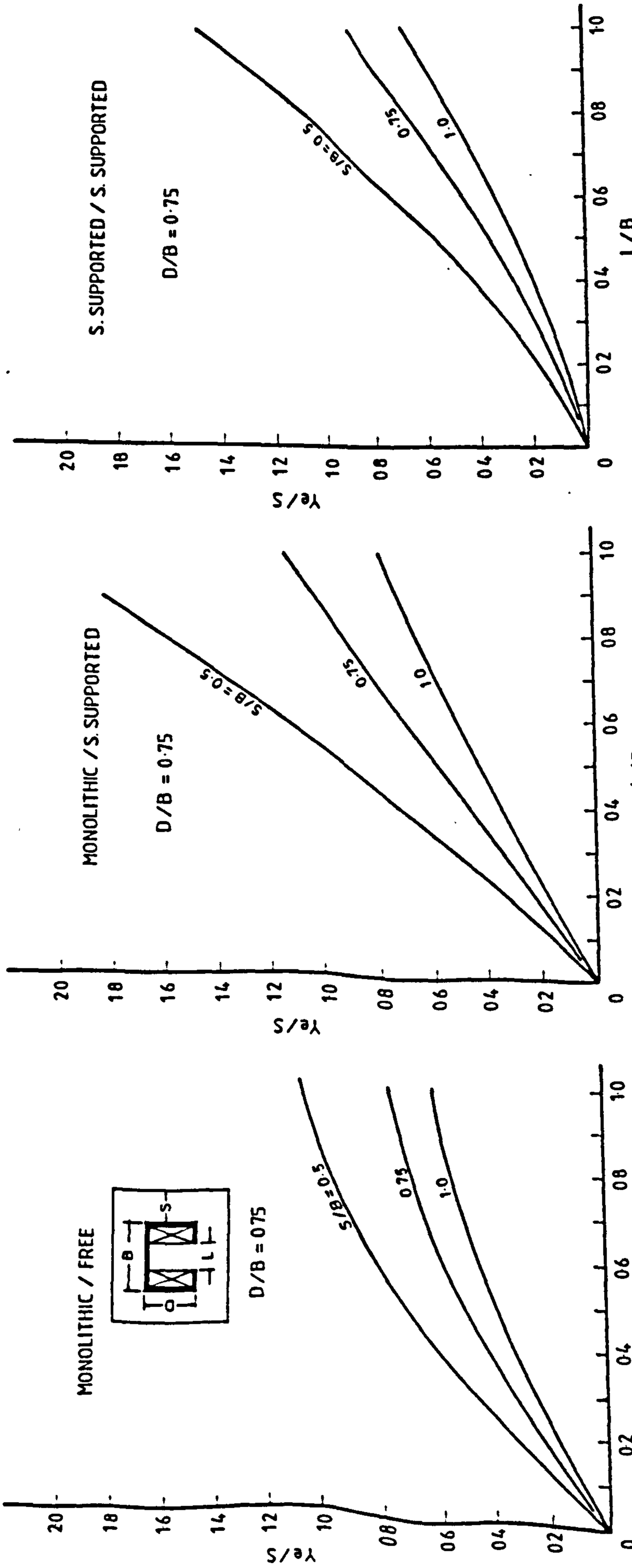

Fig. 7.7 Design Curves for Effective Width Values in Single-Core-Wall Lobby Configuration (D/B = 0.75)

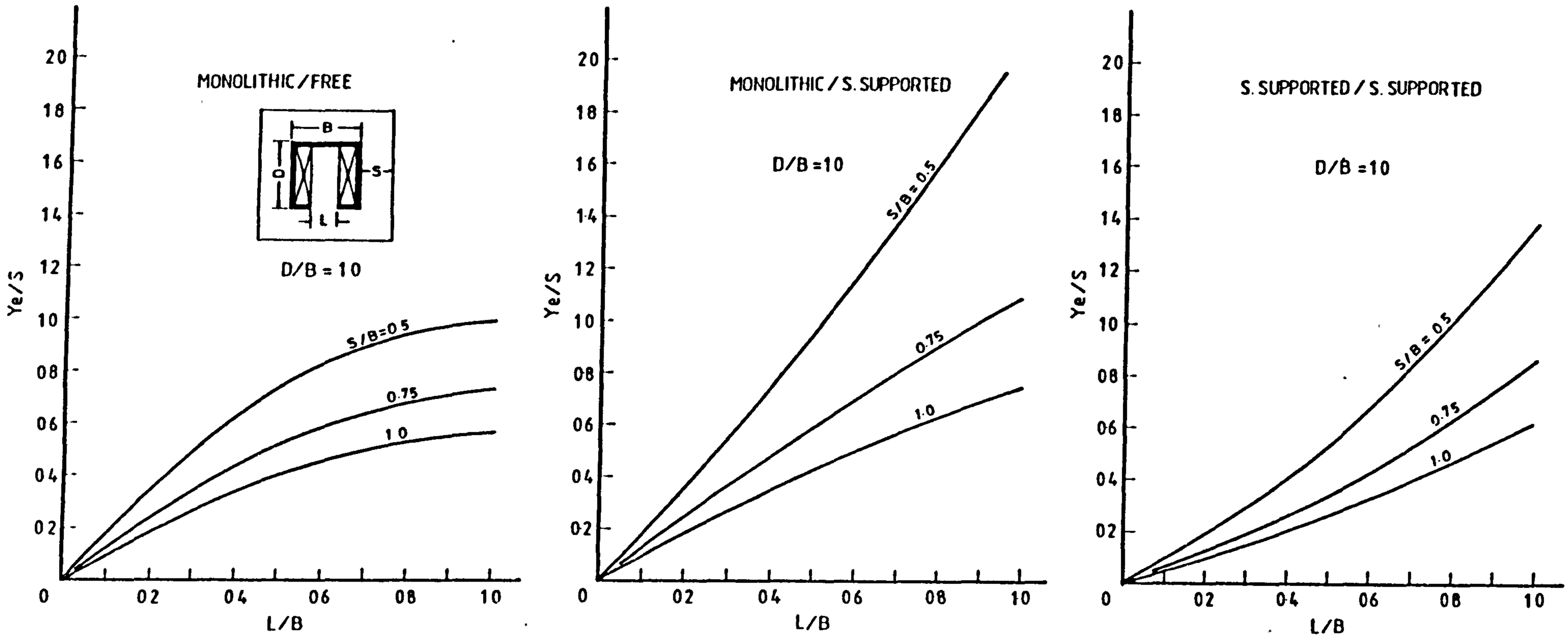

Fig. 7.8 Design Curves for Effective Width Values in Single-Core-With-Lobby Configuration (D/B = 1.0)

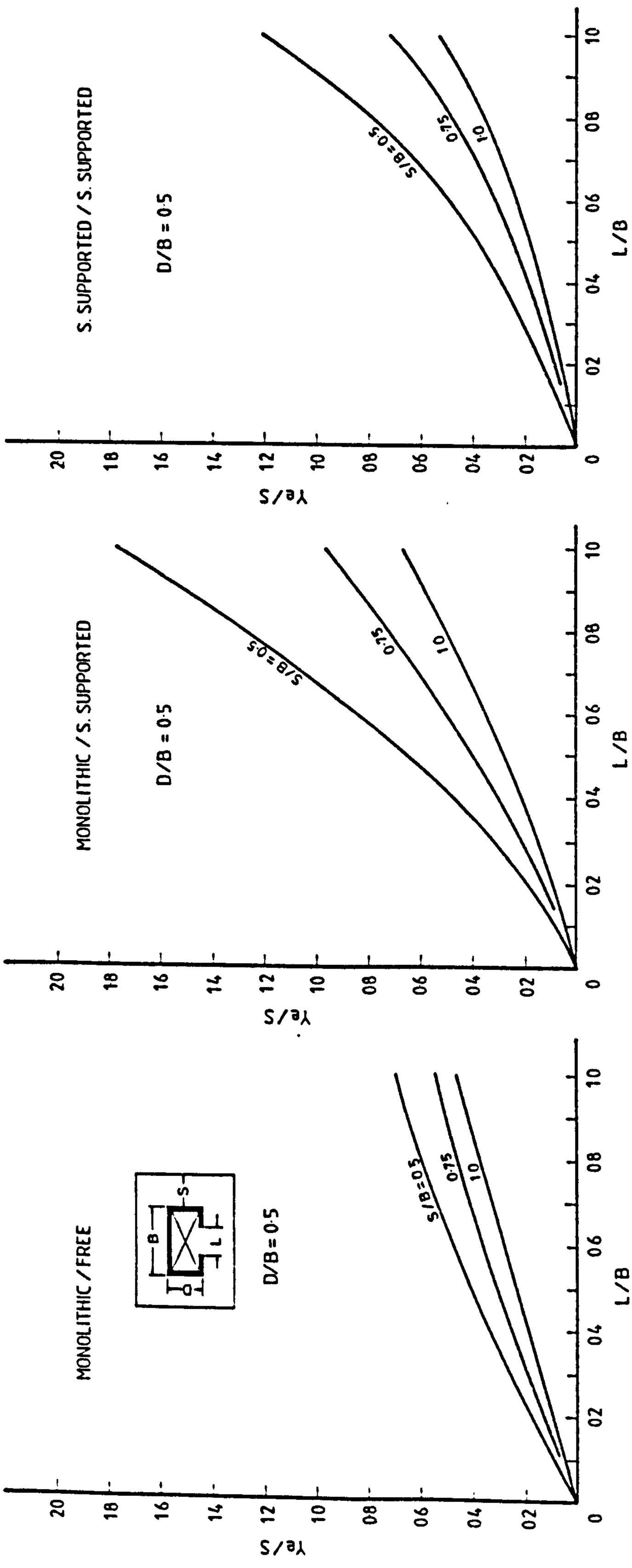

Fig. 7.9 Design Curves for Effective Width Values in Single-Core-Without-Lobby Configuration (D/B = 0.5)

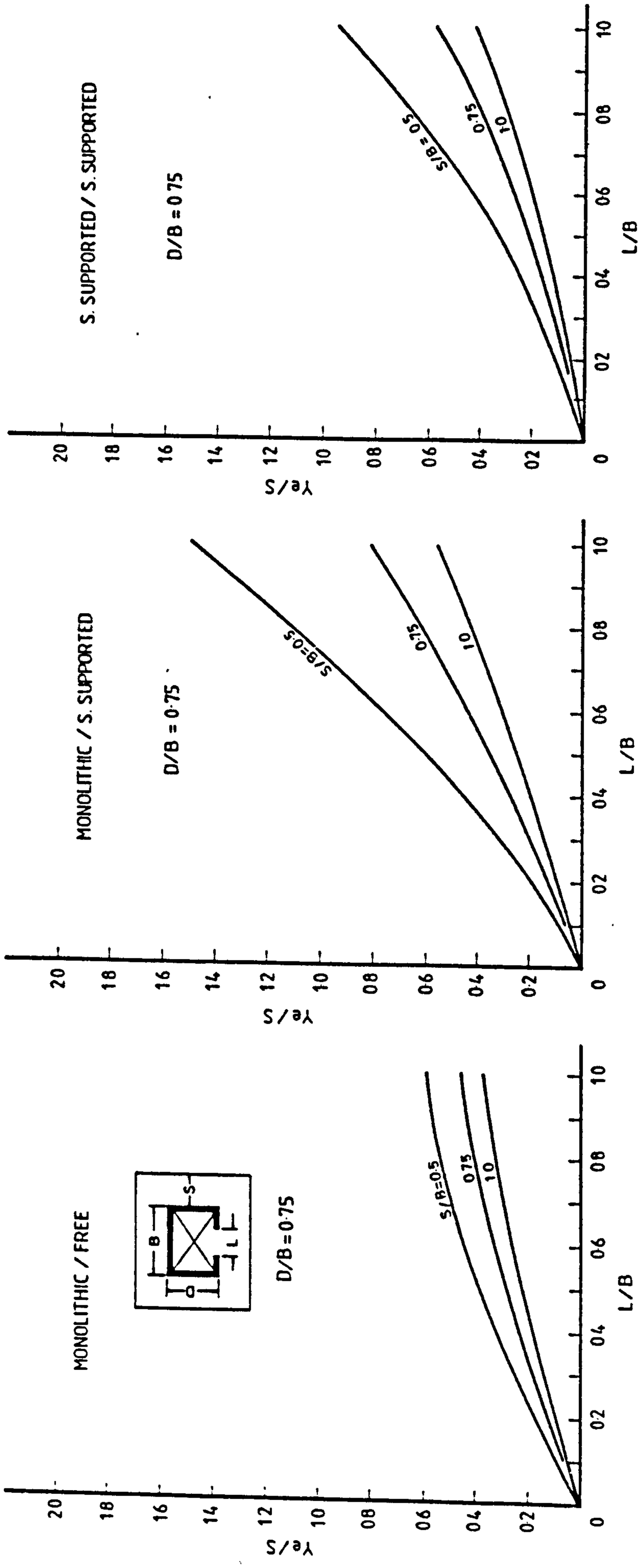

Fig. 7.10 Design Curves for Effective Width Values in Single-Core-Without-Lobby Configuration (D/B = 0.75)

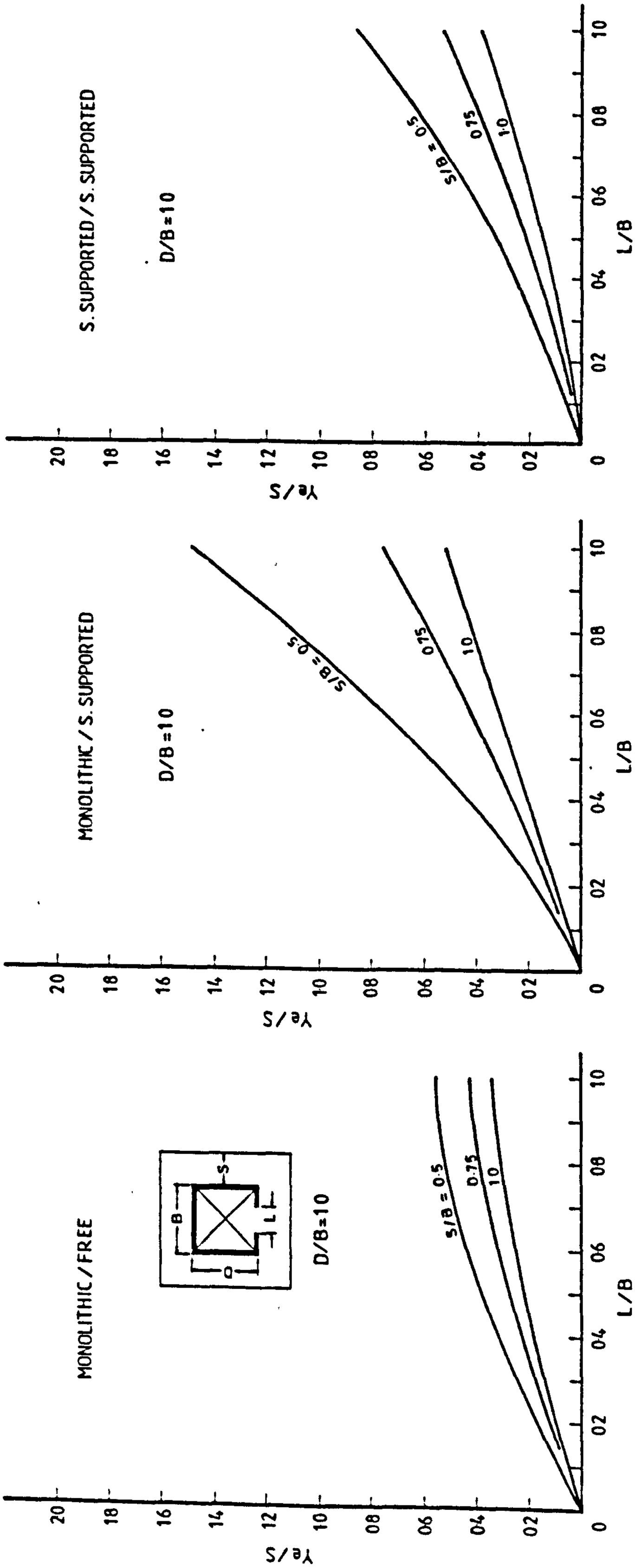

Fig. 7.11 Design Curves for Effective Width Values in Single-Core-Without-Lobby Configuration (D/B = 1.0)

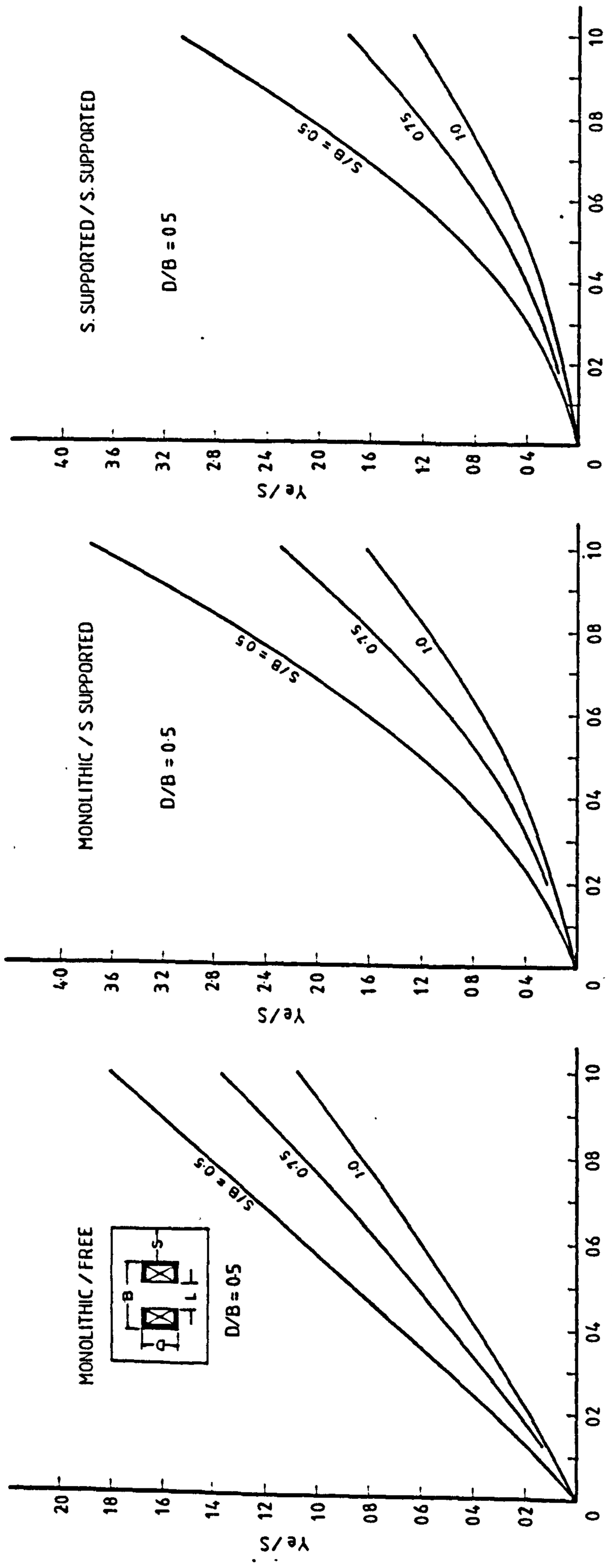

Fig. 7.12 Design Curves for Effective Width Values in Twin-Core-With-Lobby Configuration (D/B = 0.5)

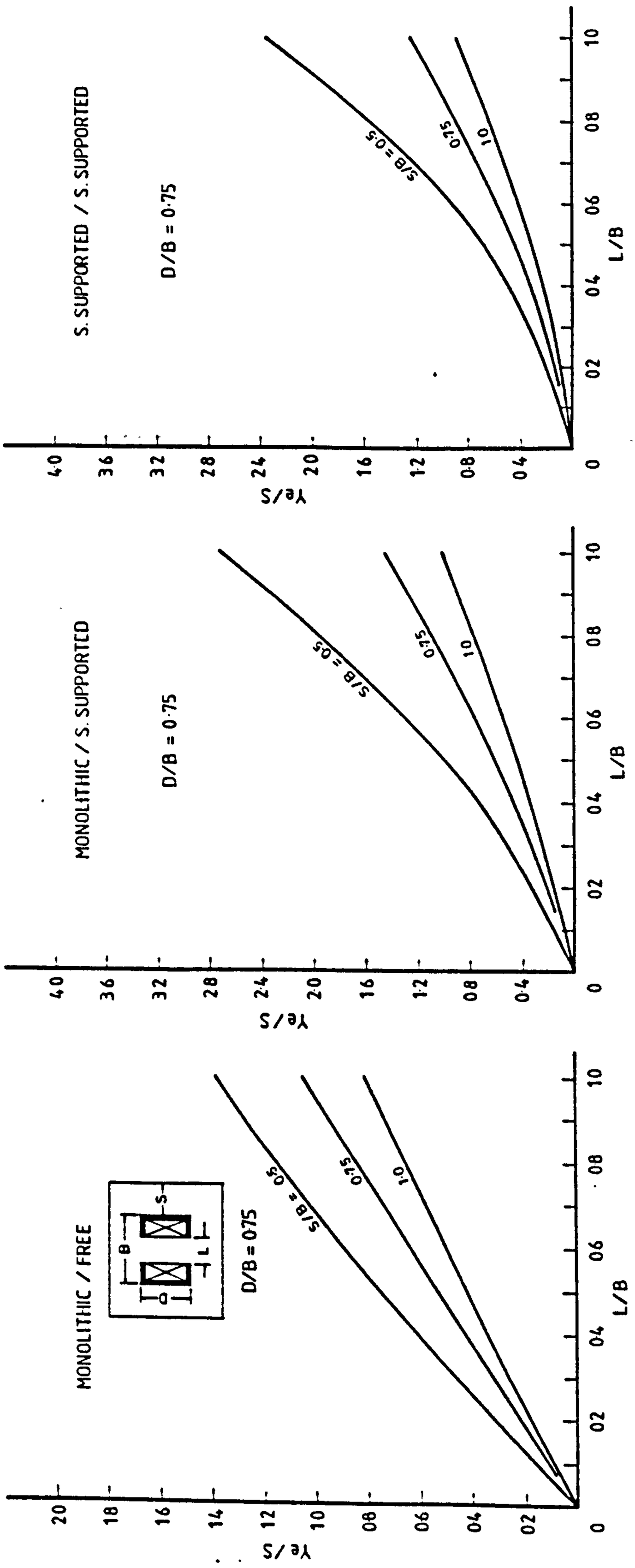

Fig. 7.13 Design Curves for Effective Width Values in Twin-Core-With-Lobby Configuration (D/B = 0.75)

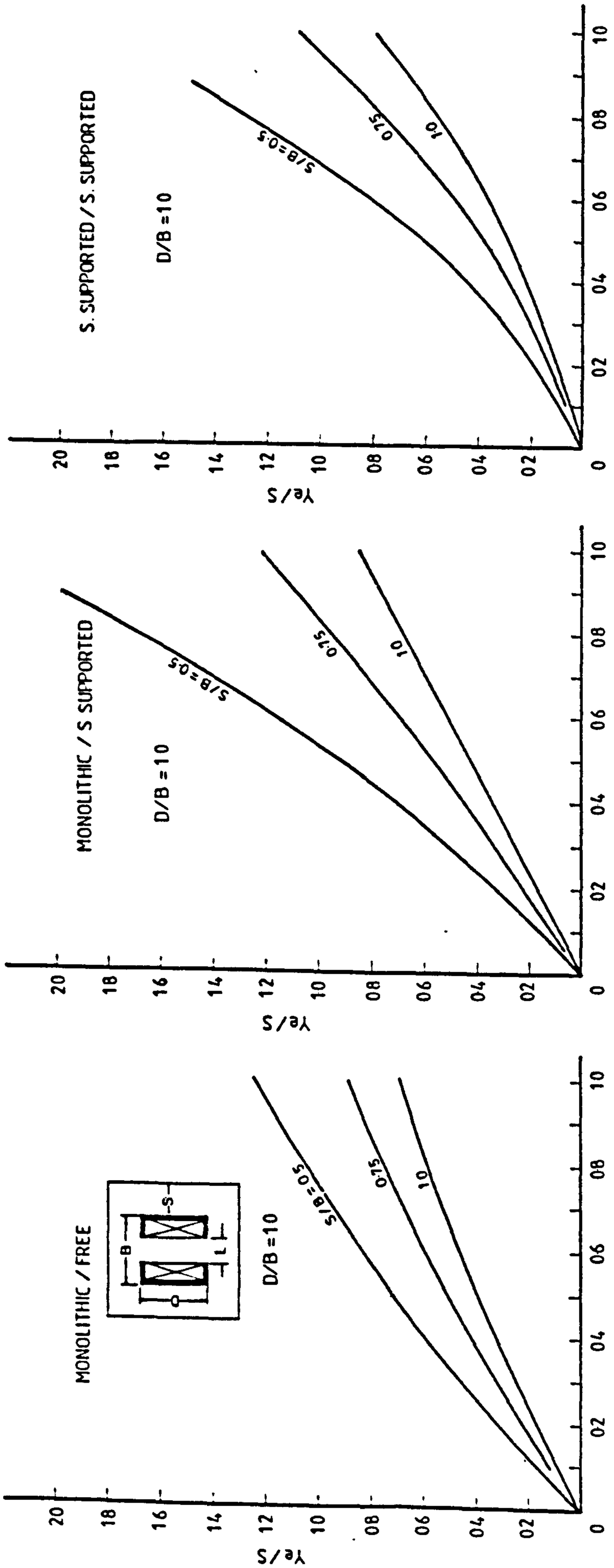

Fig. 7.14 Design Curves for Effective Width Values in Twin-Core-With-Lobby Configuration (D/B = 1.0)

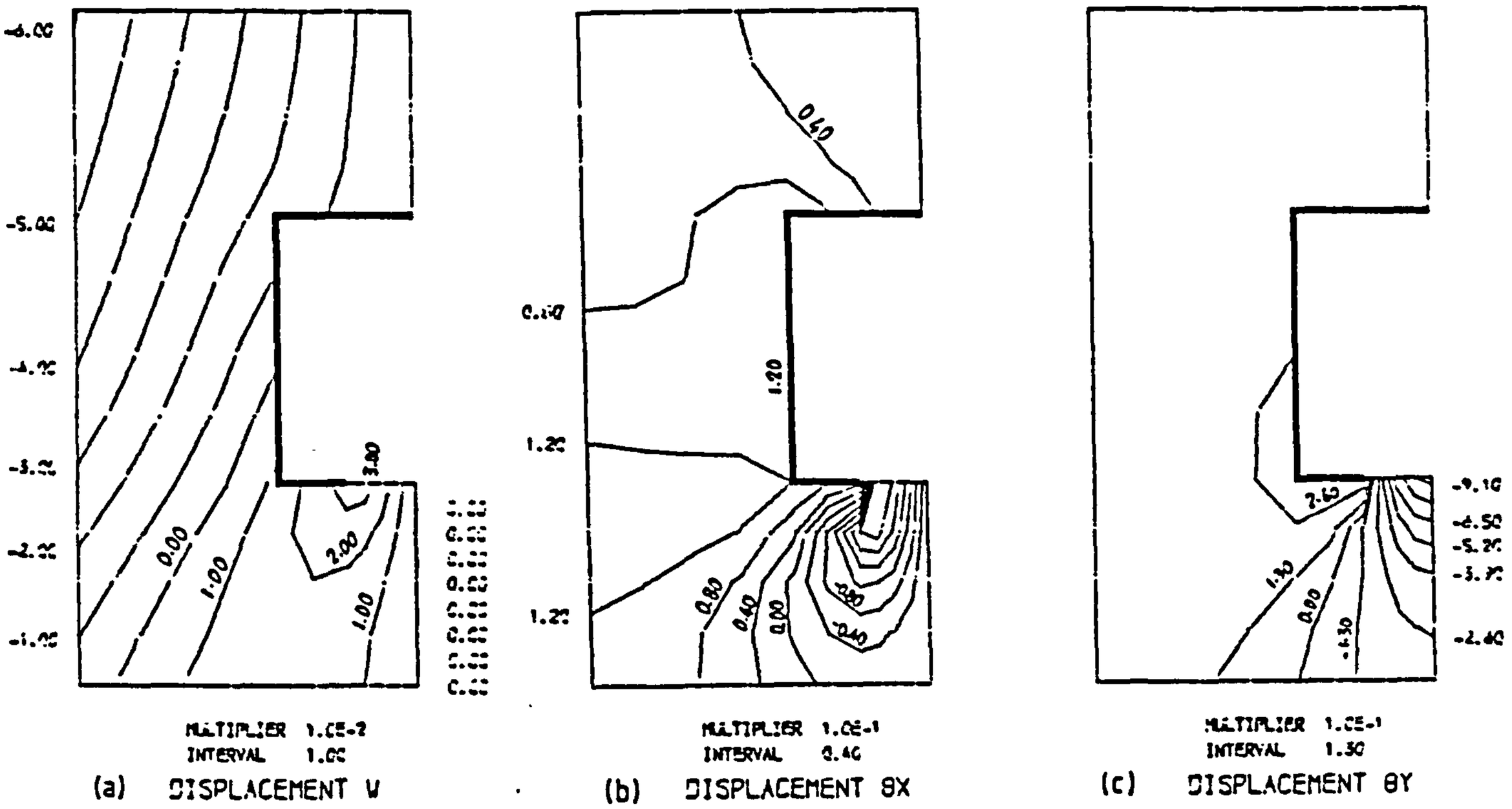

Fig. 7.15 Displacement Contours for Slab with Free Exterior Edges in Single-Core-Without-Lobby Configuration

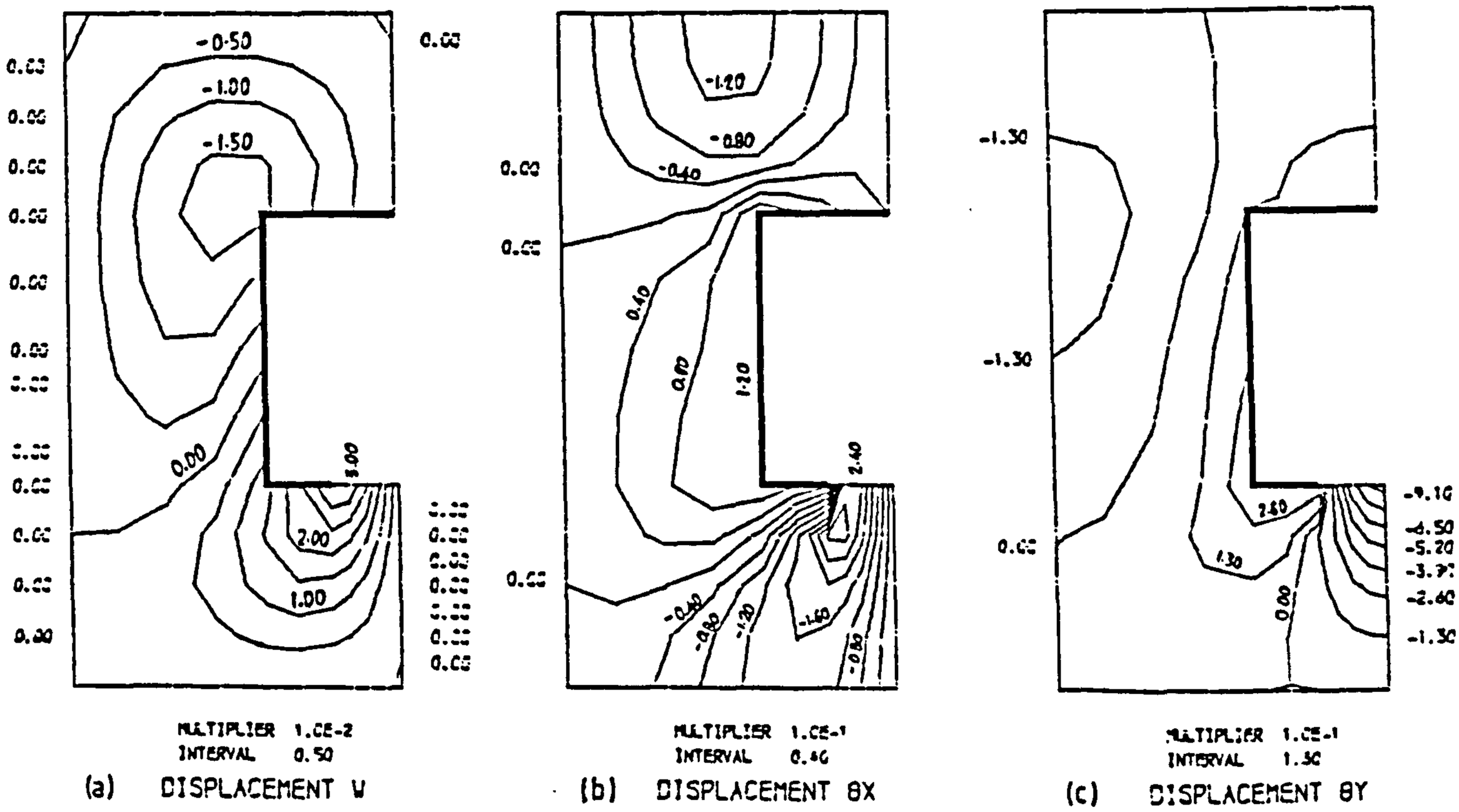

Fig. 7.16 Displacement Contours for Slab with Simply Supported Exterior Edges in Single-Core-Without-Lobby Configuration

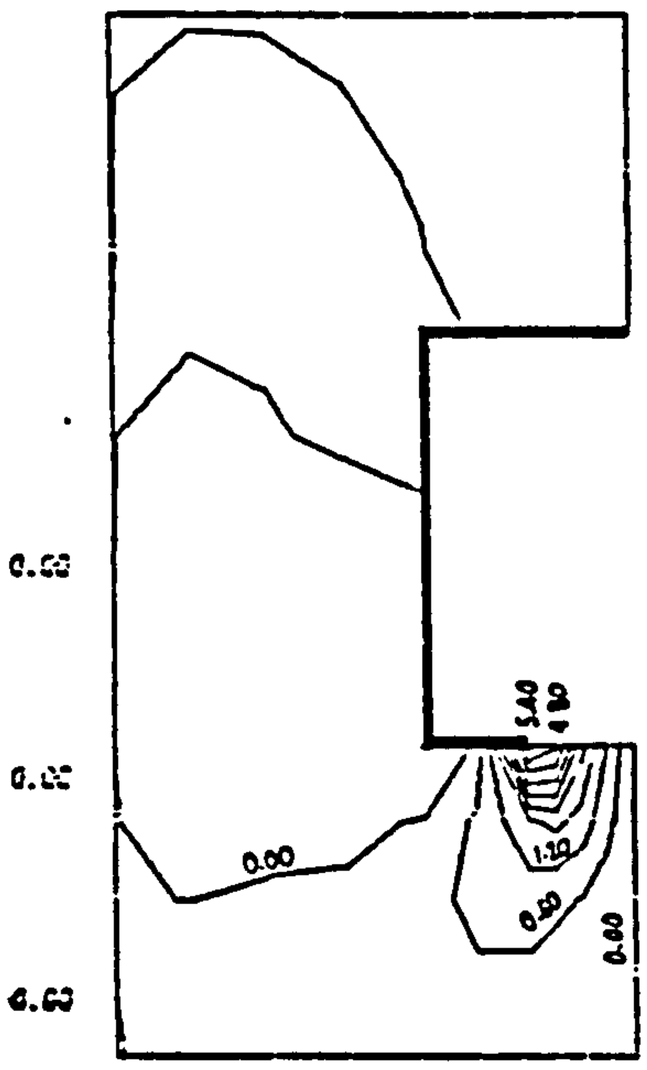

MULTIPLIER 1.0E-5
INTERVAL 0.40

(a) 'STRESS' CONTOURS MX

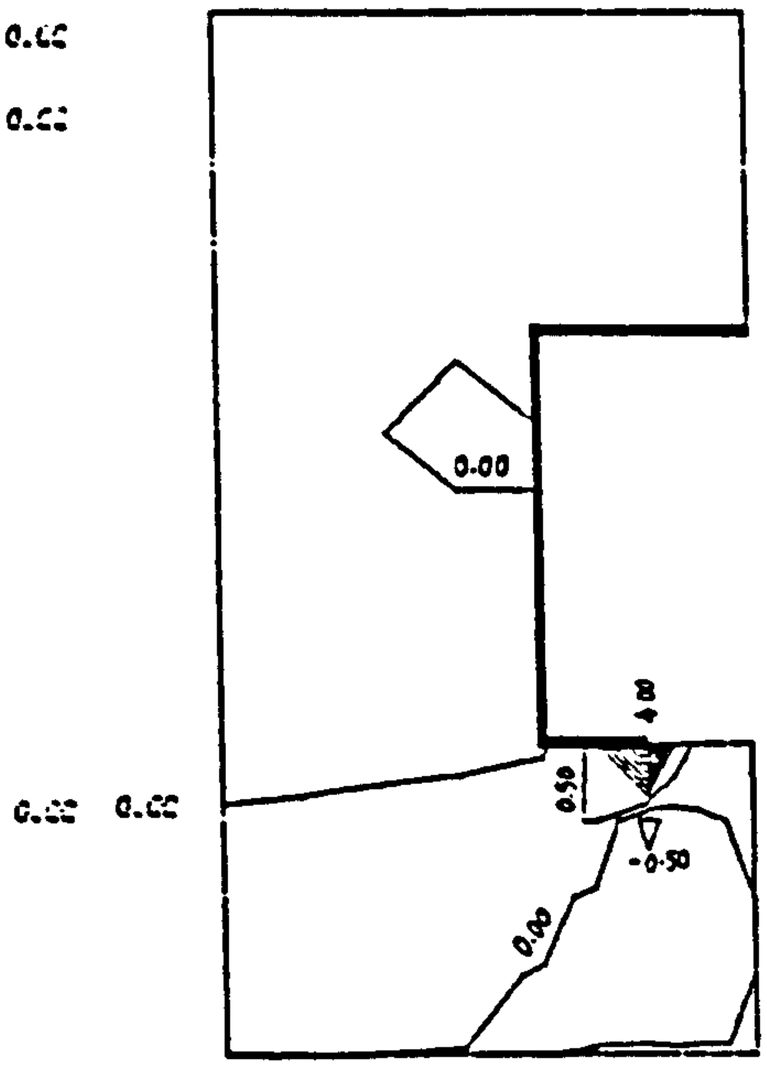

MULTIPLIER 1.0E-5
INTERVAL 0.50

(b) 'STRESS' CONTOURS MY

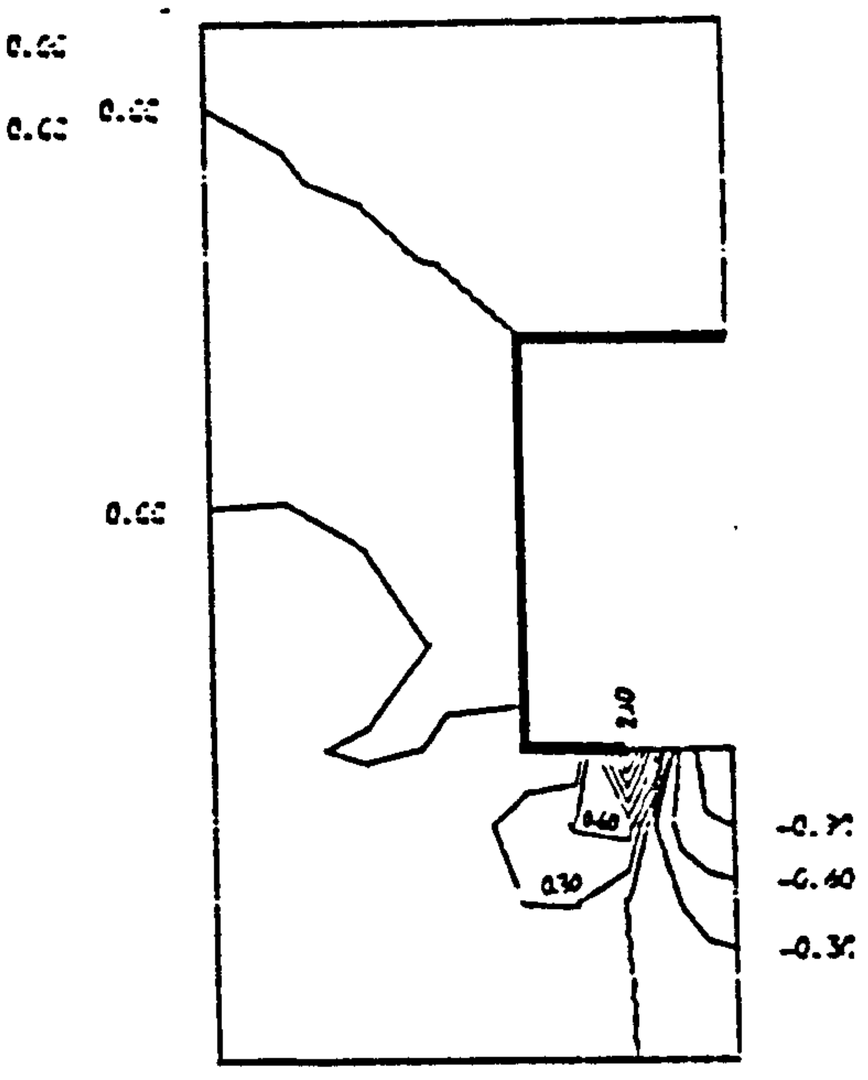

MULTIPLIER 1.0E-5
INTERVAL 0.3

(c) 'STRESS' CONTOURS MXY

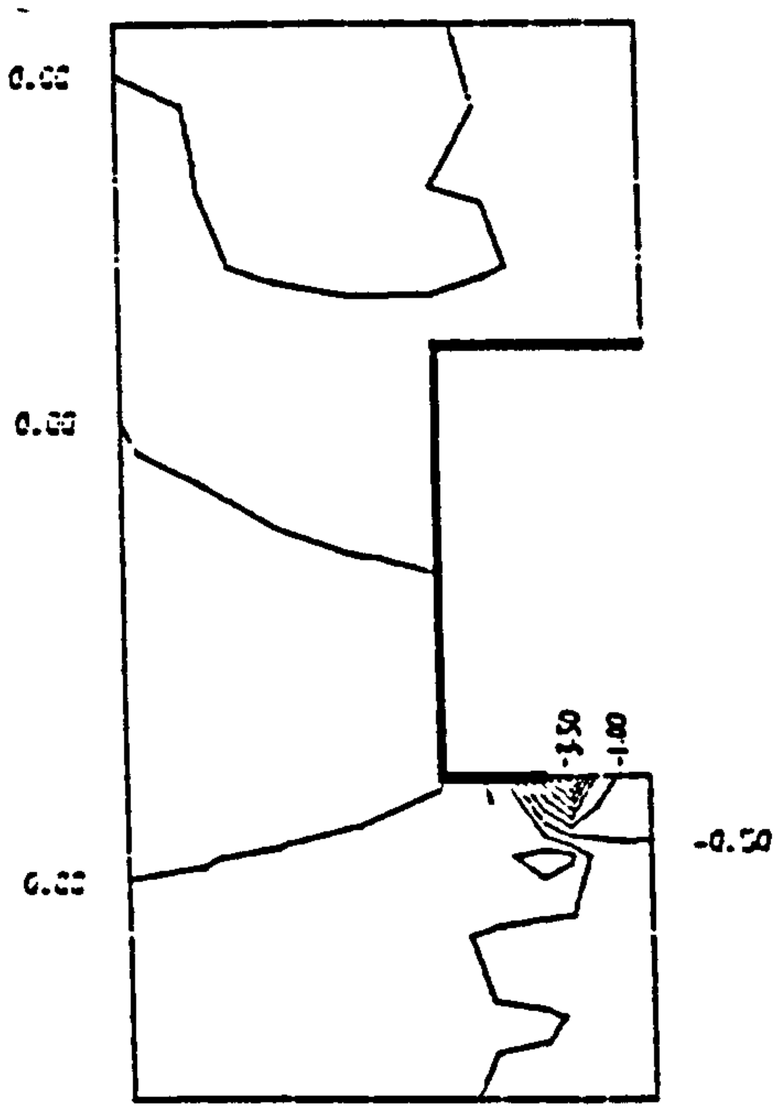

MULTIPLIER 1.0E-5
INTERVAL 0.50

(d) 'STRESS' CONTOURS QX

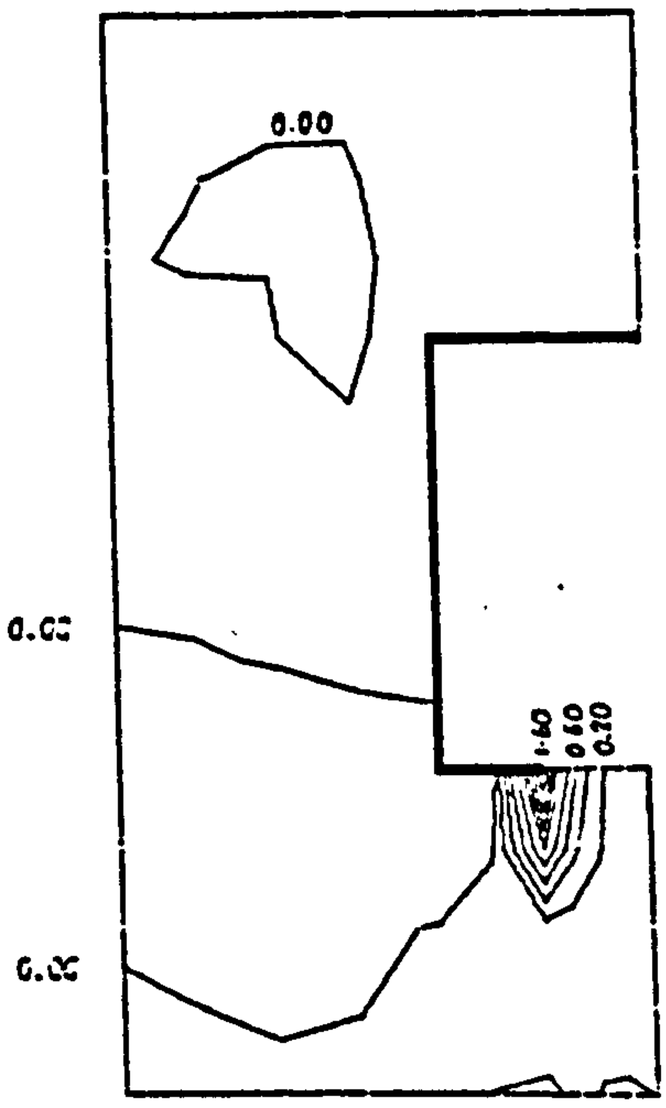

MULTIPLIER 1.0E-5
INTERVAL 0.2

(e) 'STRESS' CONTOURS QY

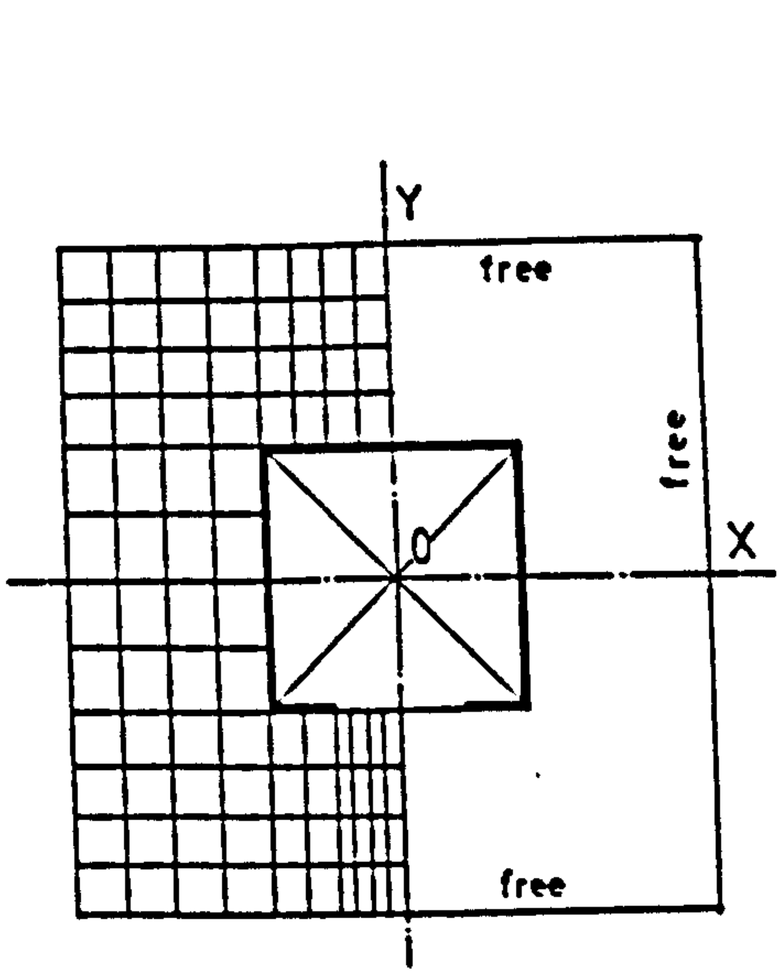

(f) KEY PLAN & ELEMENT MESH

Fig. 7.17 Stress Resultant Contours for Slab with Free Exterior Edges in Single-Core-Without-Lobby Configuration

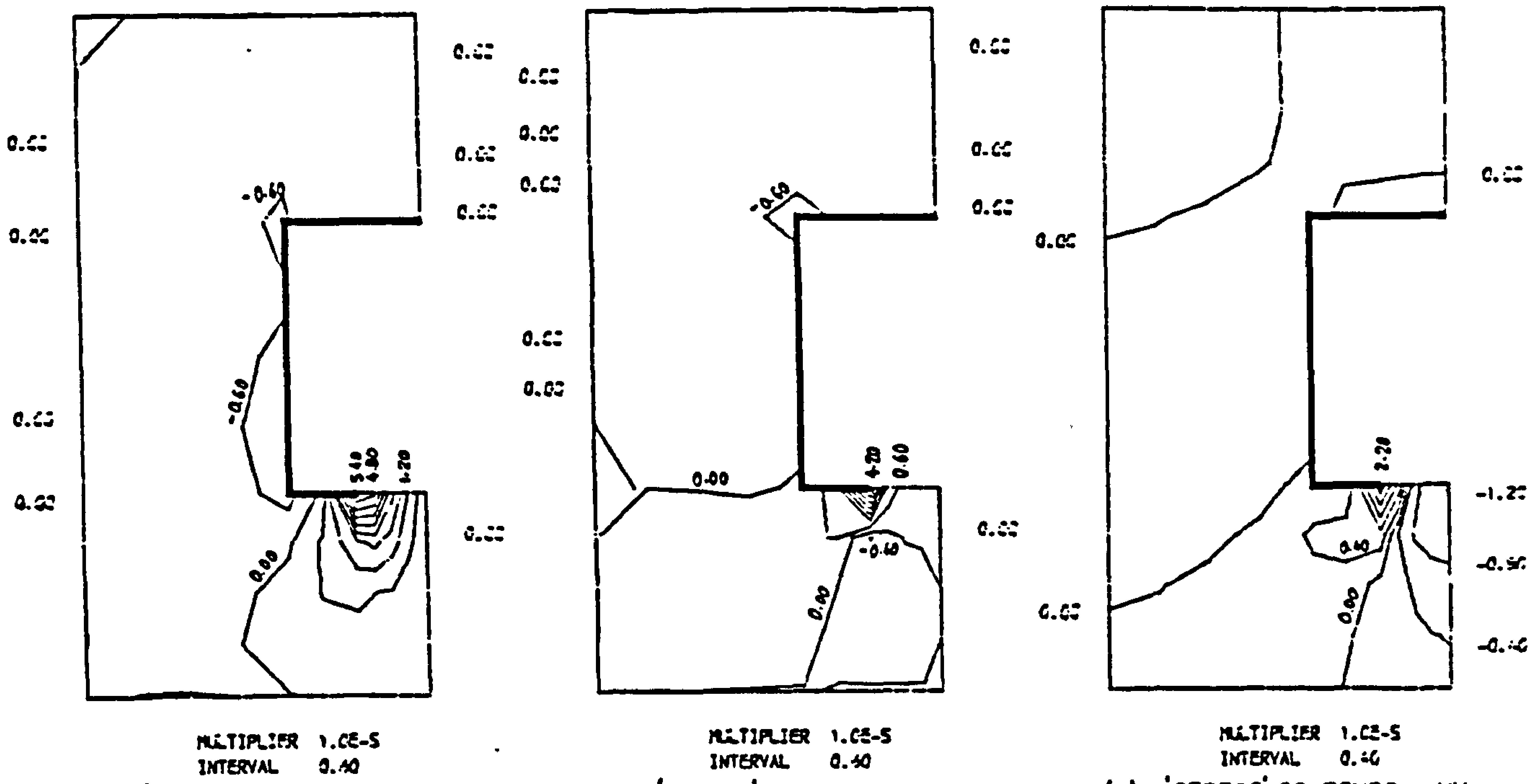

(a) 'STRESS' CONTOURS MX (b) 'STRESS' CONTOURS MY (c) 'STRESS' CONTOURS MXY

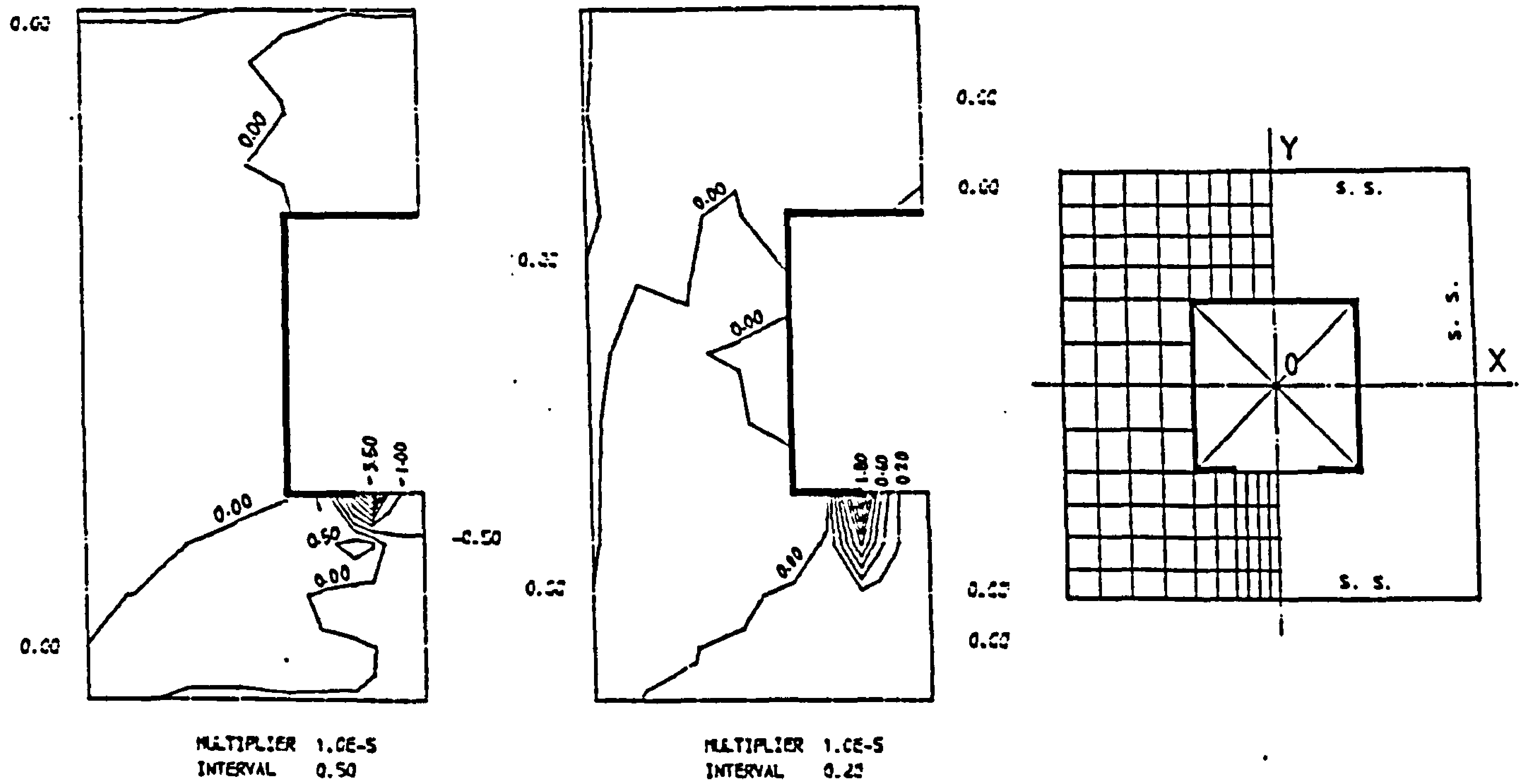

(d) 'STRESS' CONTOURS QX (e) 'STRESS' CONTOURS QY (f) KEY PLAN & ELEMENT MESH

Fig. 7.18 Stress Resultant Contours for Slab with Simply Supported Exterior Edges in Single-Core-Without-Lobby Configuration

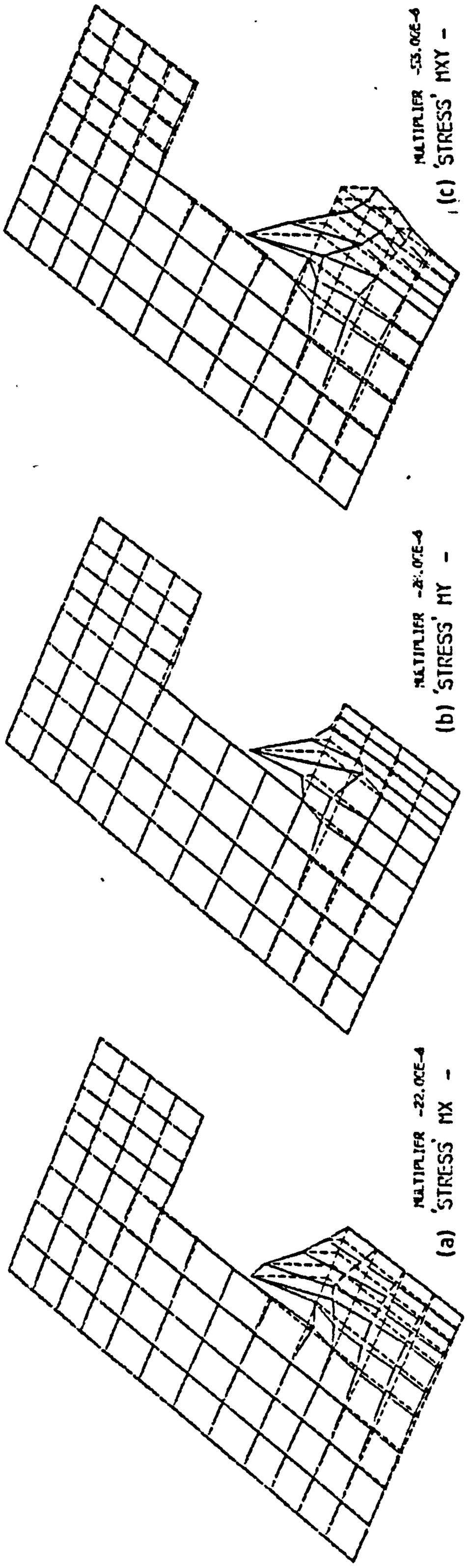

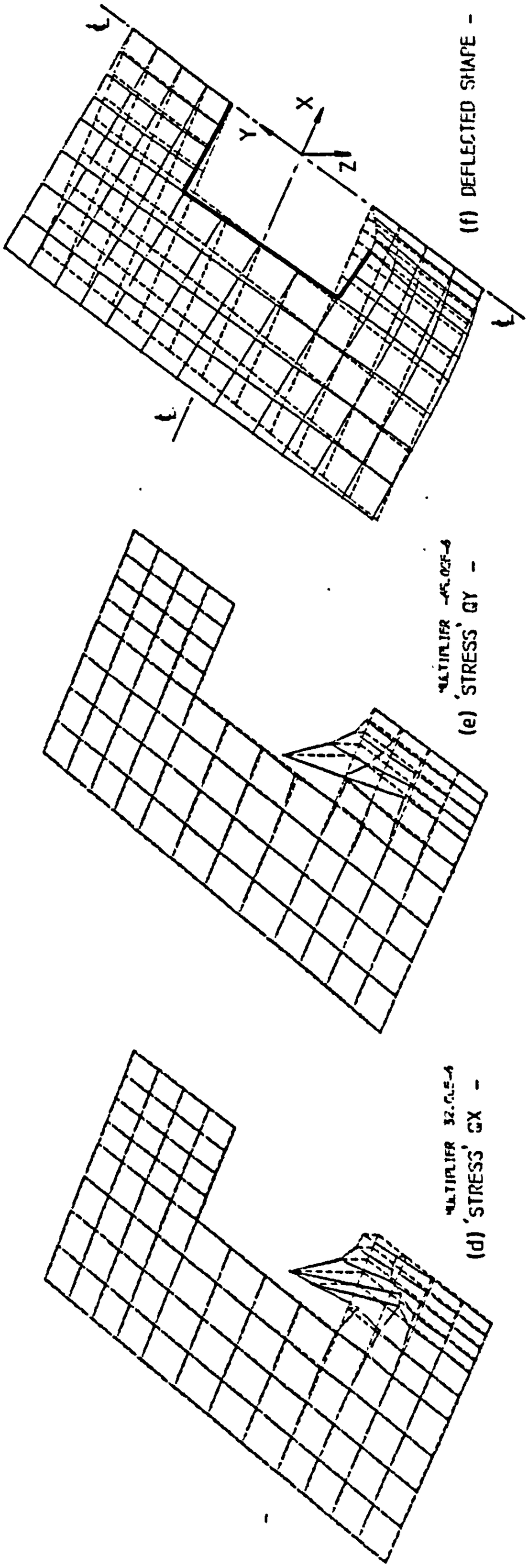

Fig. 7.19 Perspective View of General Stress Pattern in Slab with Free Exterior Edges in Single-Core-Without-Lobby Configuration

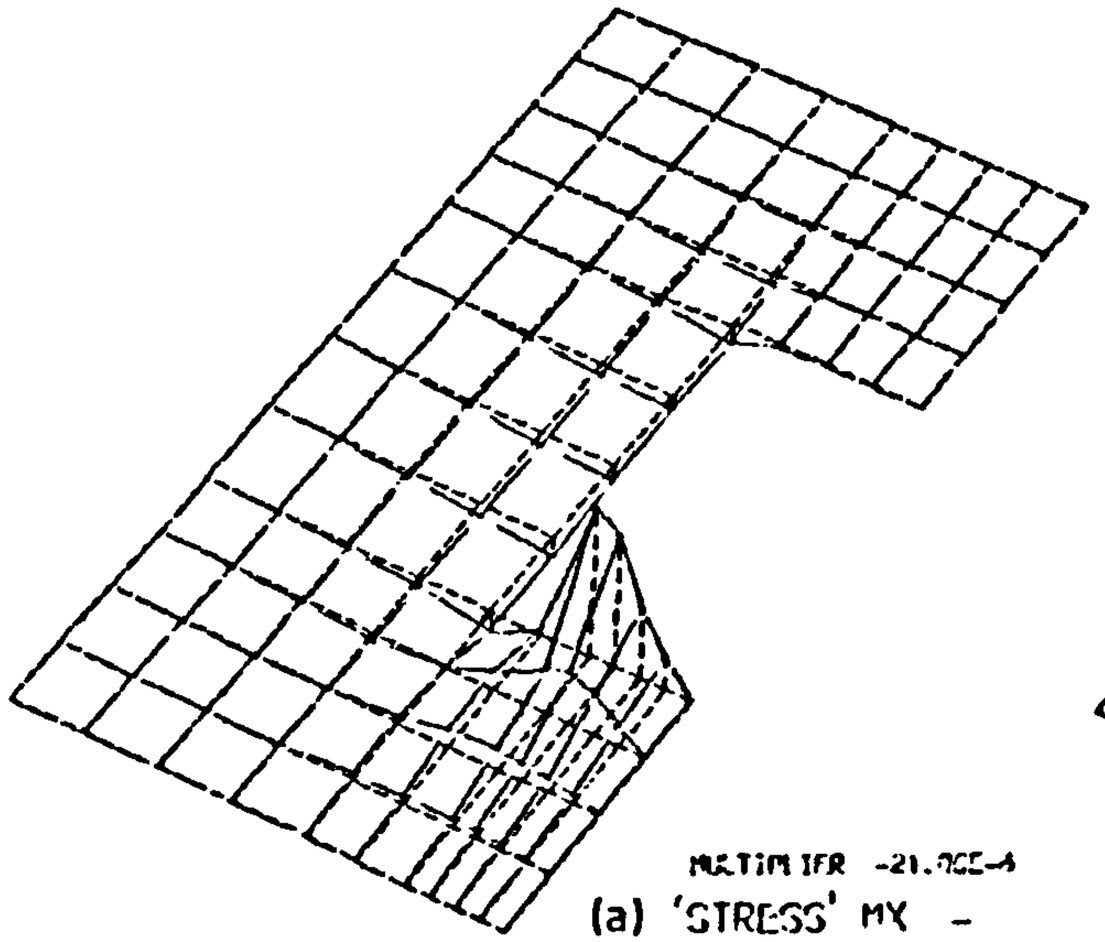

(a) 'STRESS' MY -

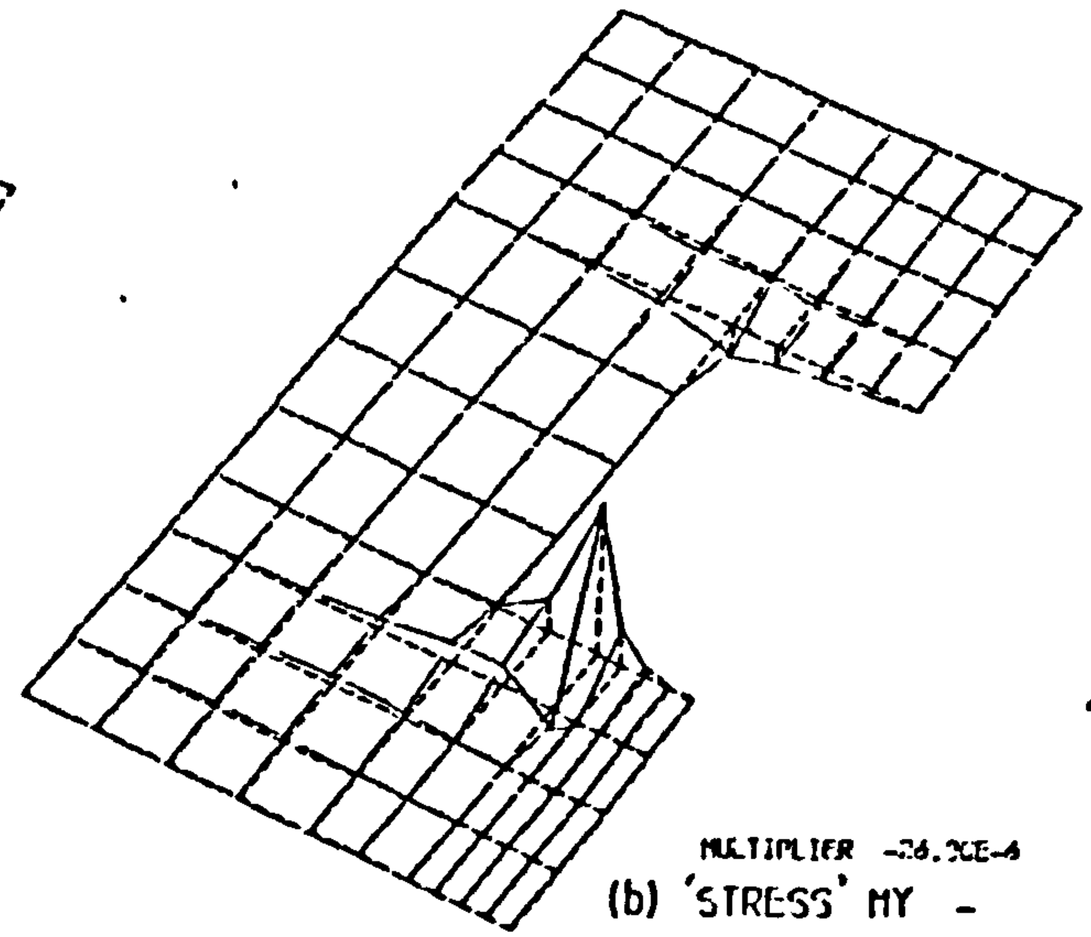

(b) 'STRESS' MY -

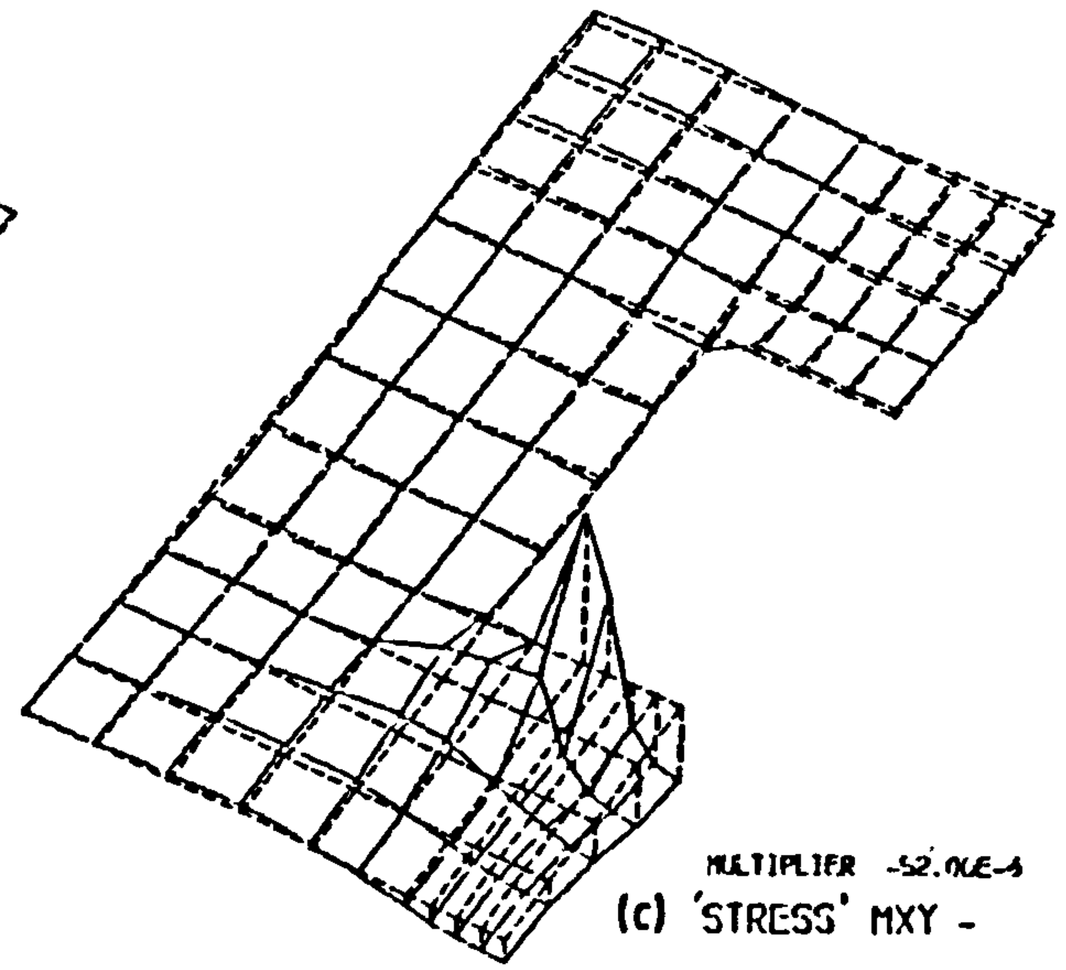

(c) 'STRESS' MXY -

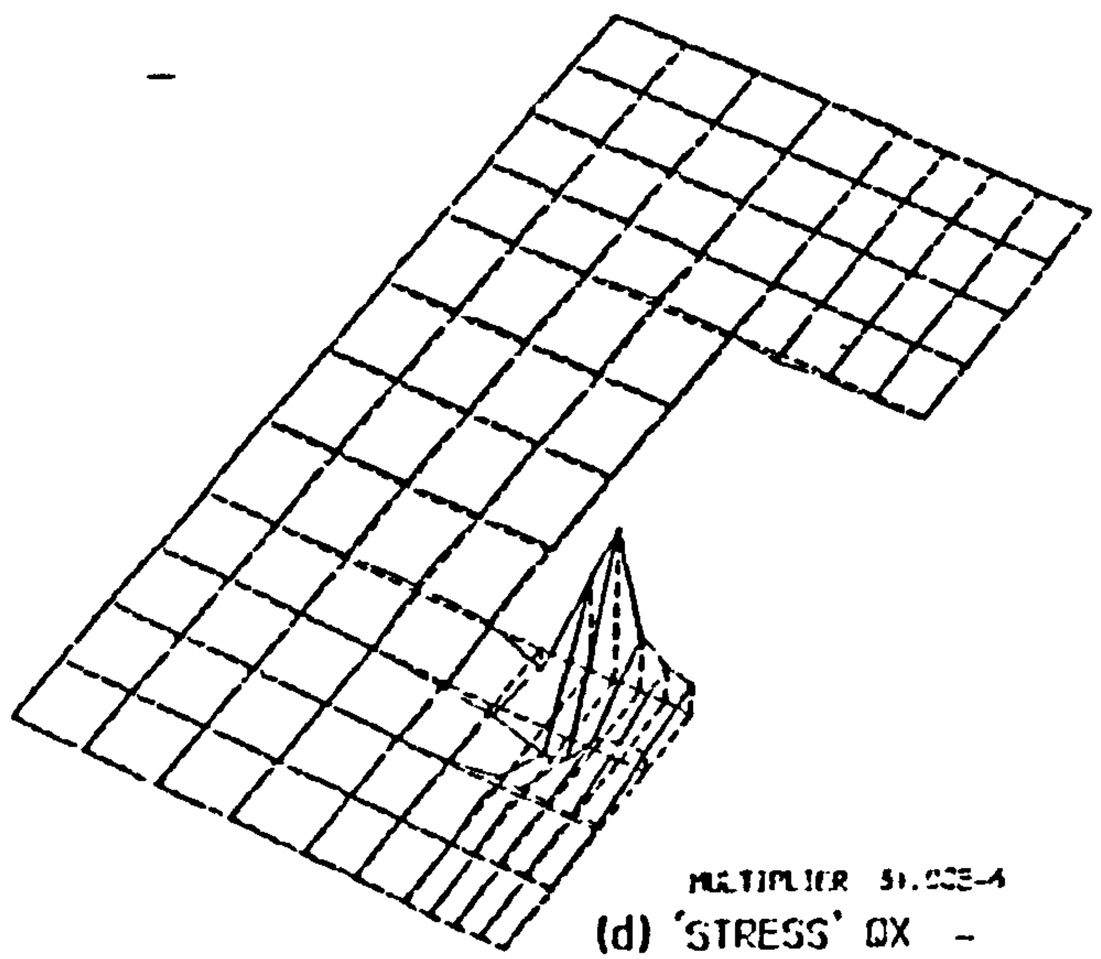

(d) 'STRESS' QX -

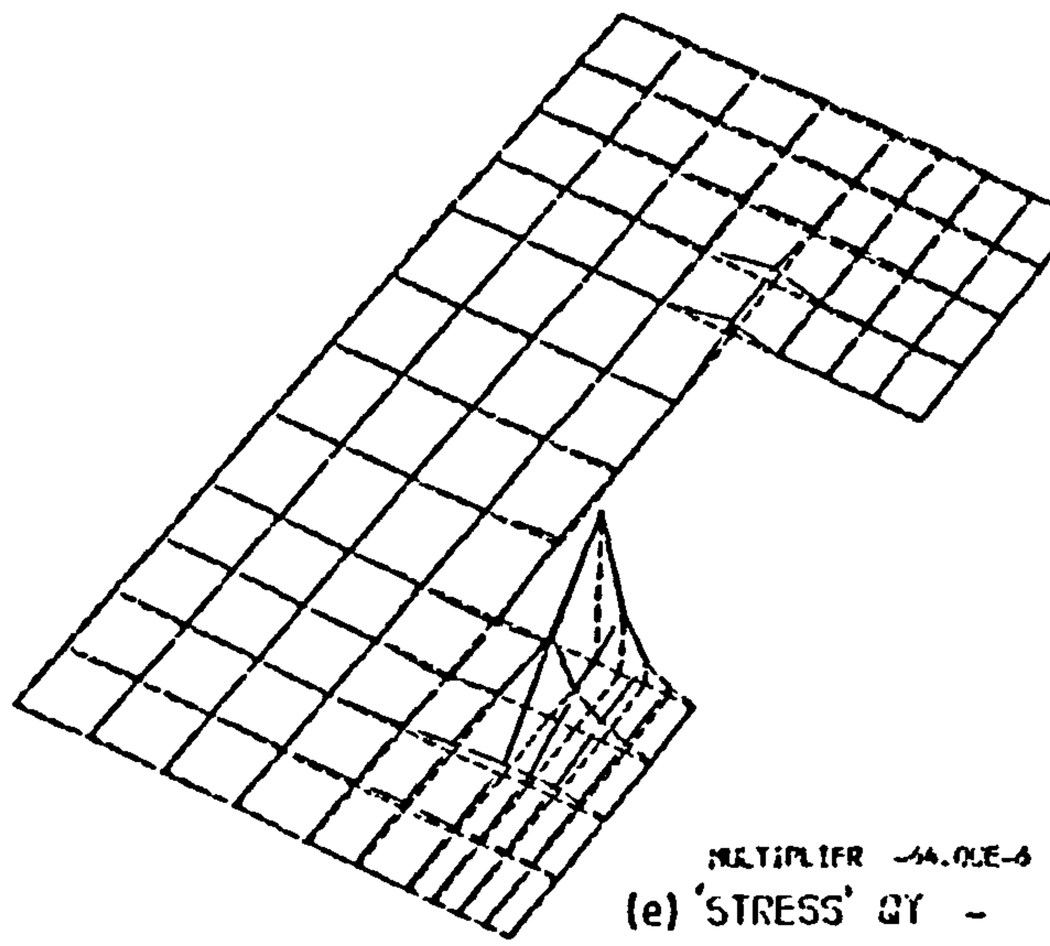

(e) 'STRESS' QY -

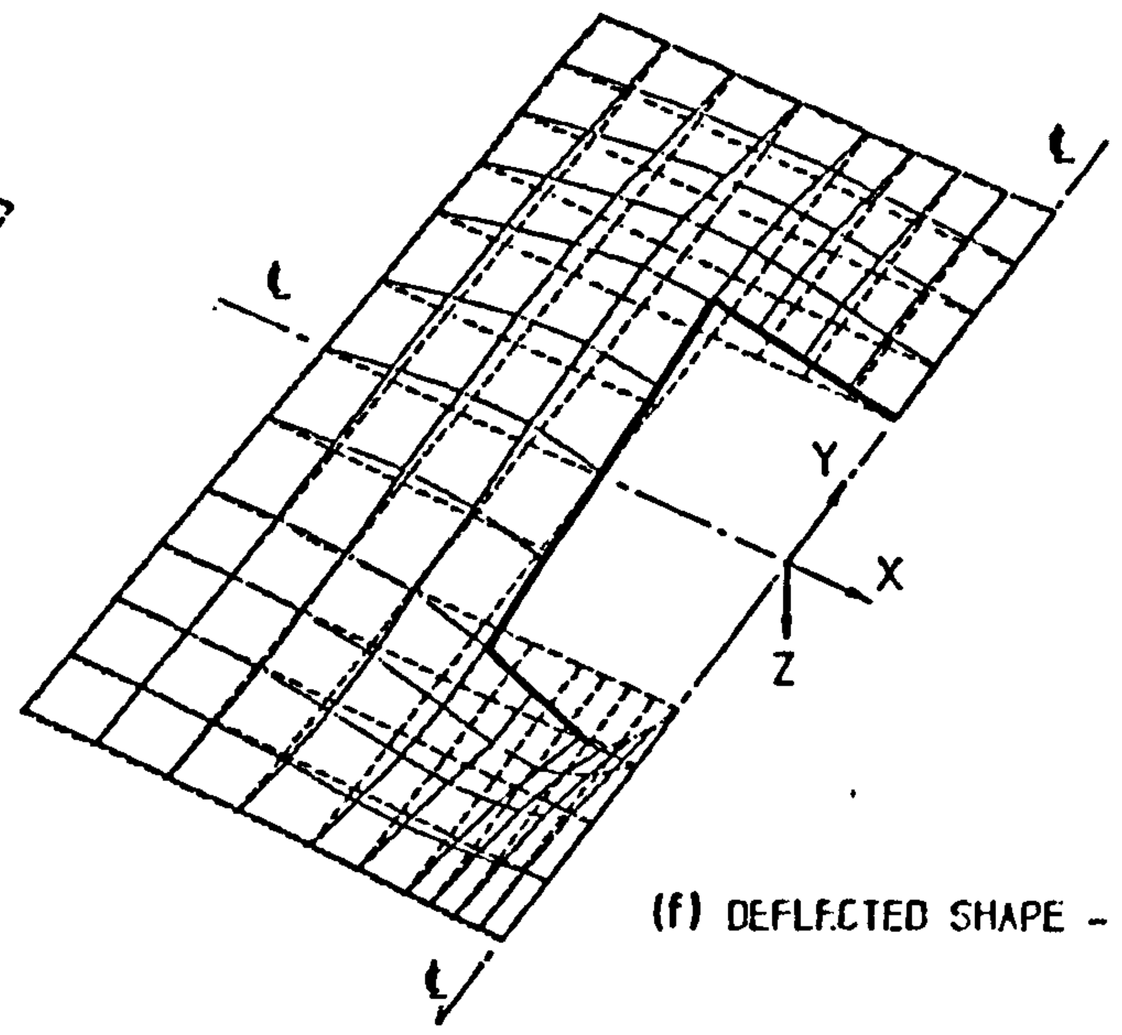

(f) DEFLECTED SHAPE -

Fig. 7.20 Perspective View of General Stress Pattern in Slab with Simply Supported Edges in Single-Core-Without-Lobby Configuration

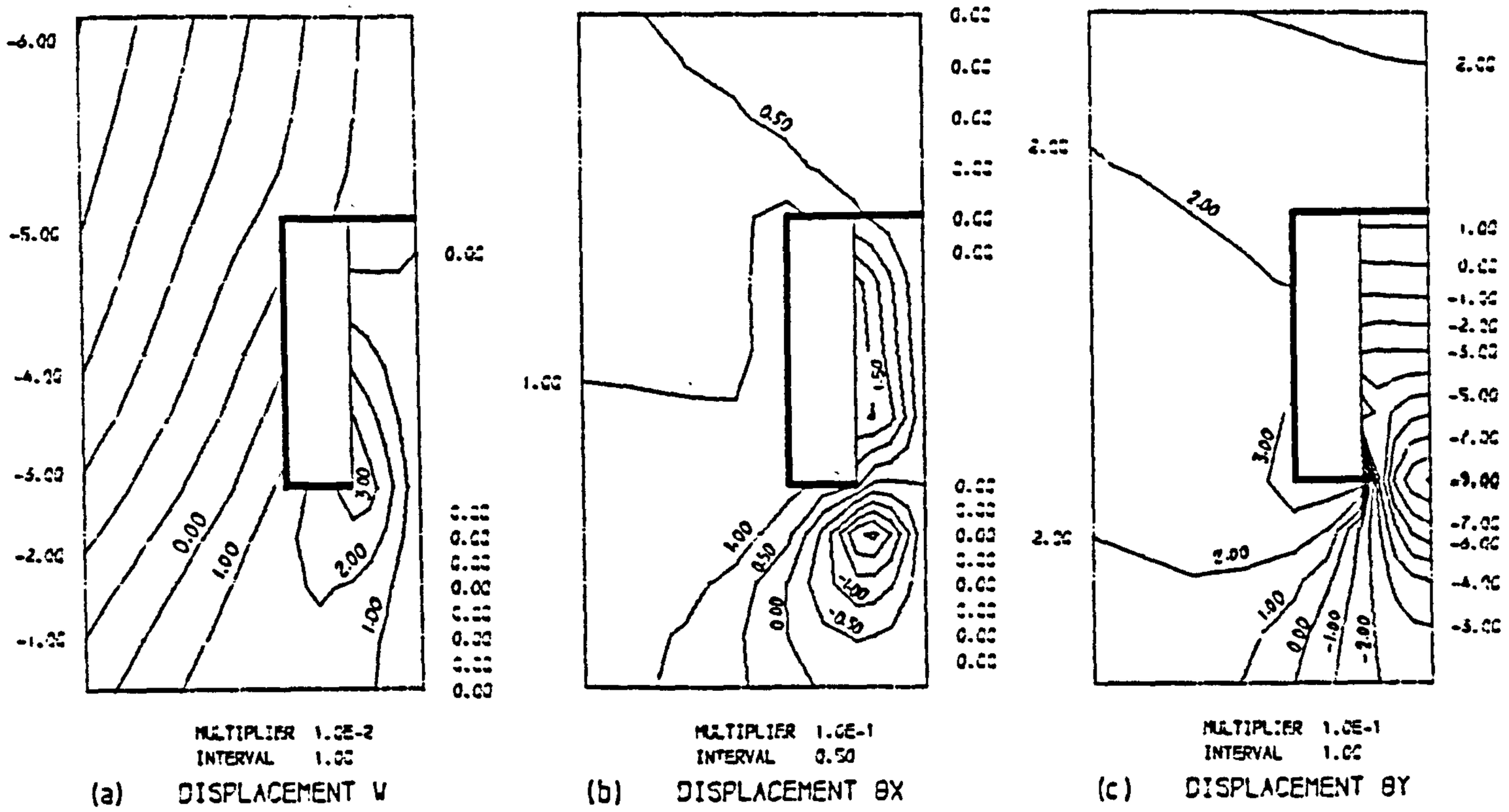

Fig. 7.21 Displacement Contours for Slab with Free Exterior Edges in Single-Core-With-Lobby Configuration

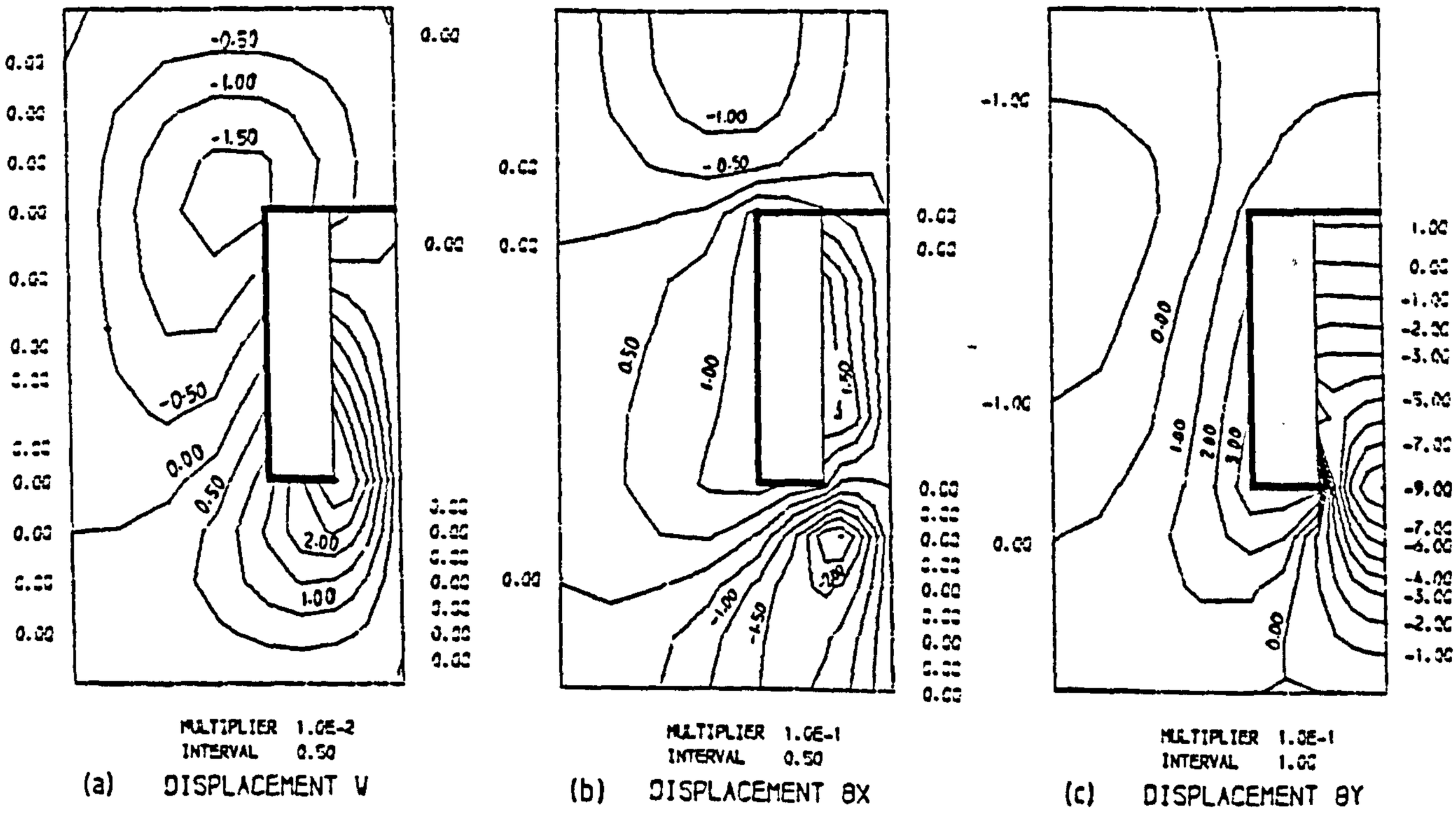

Fig. 7.22 Displacement Contours for Slab with Simply Supported Edges in Single-Core-With-Lobby Configuration

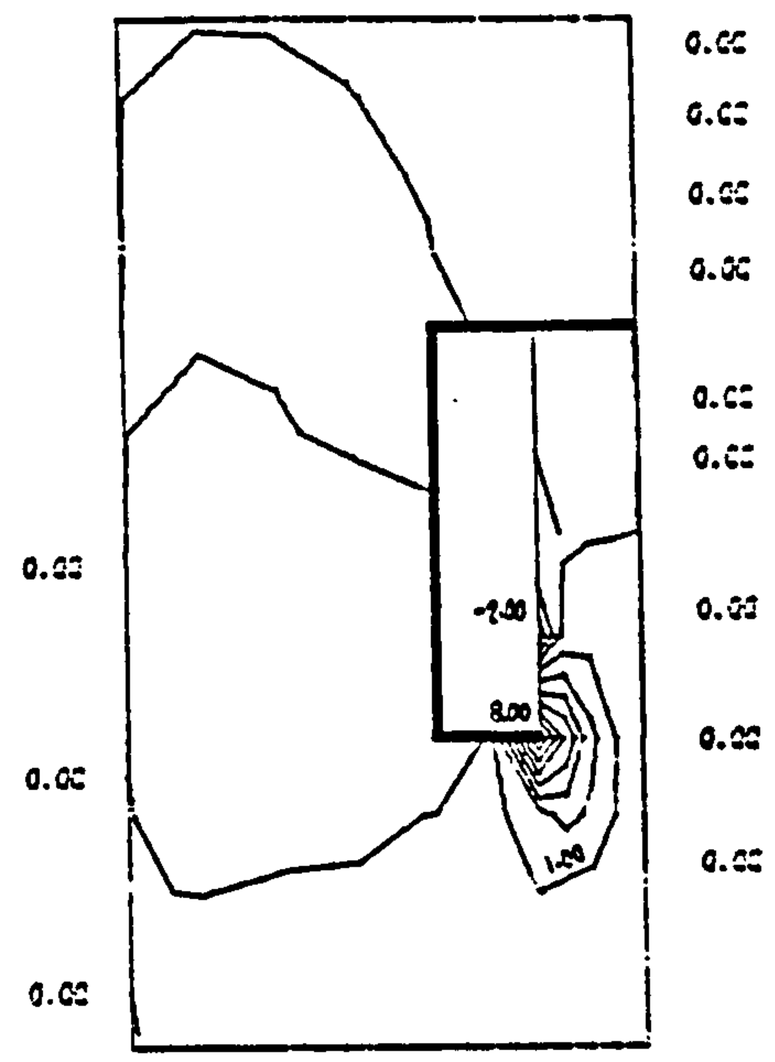

(a) 'STRESS' CONTOURS MX

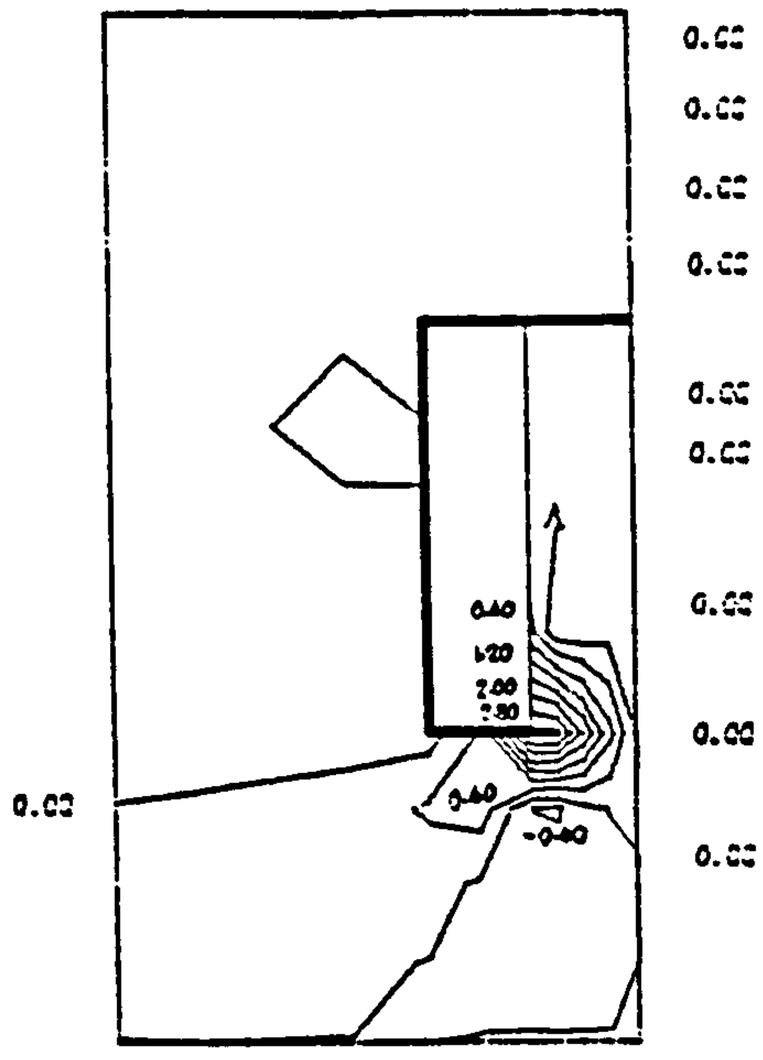

(b) 'STRESS' CONTOURS MY

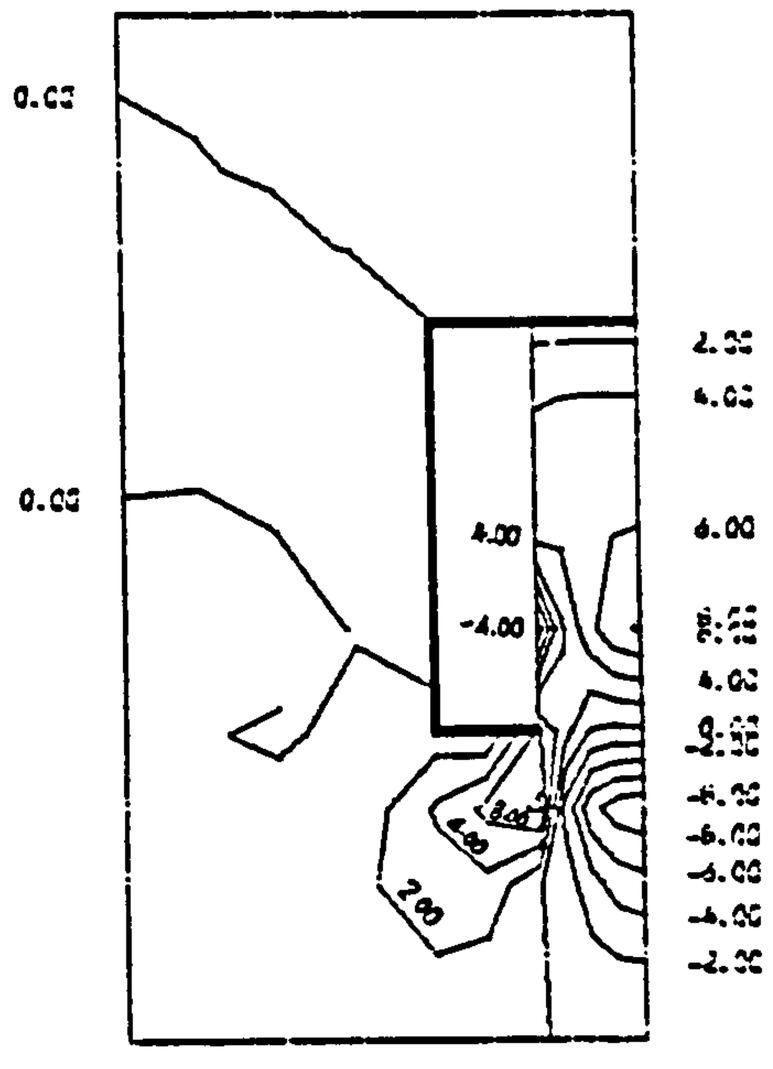

(c) 'STRESS' CONTOURS MXY

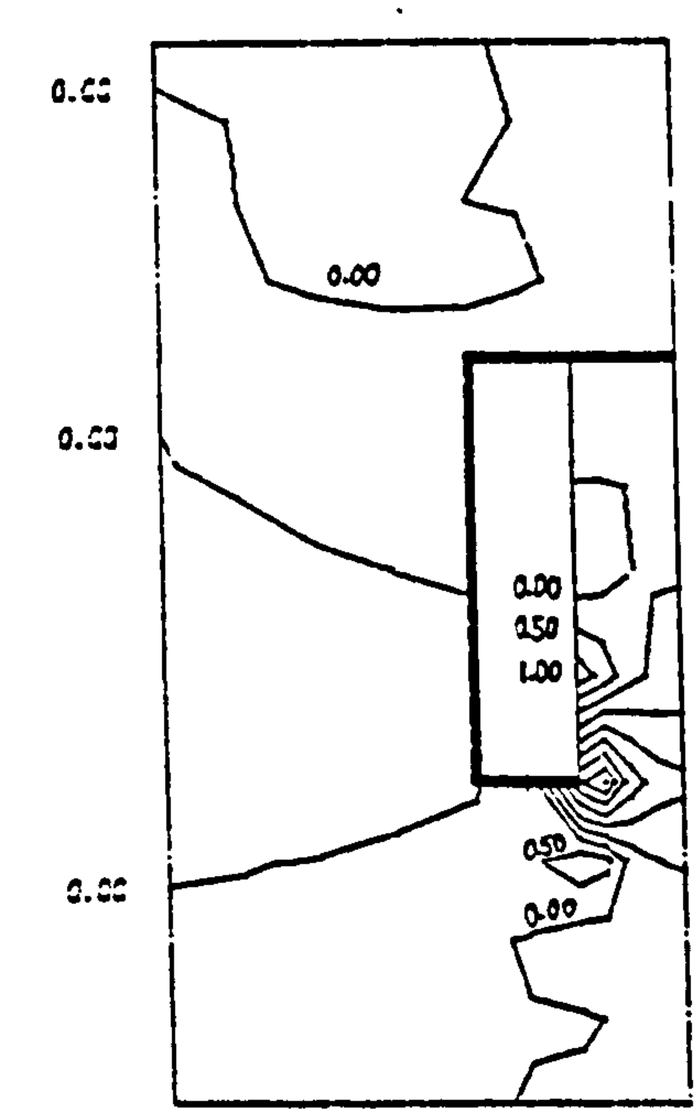

(d) 'STRESS' CONTOURS QX

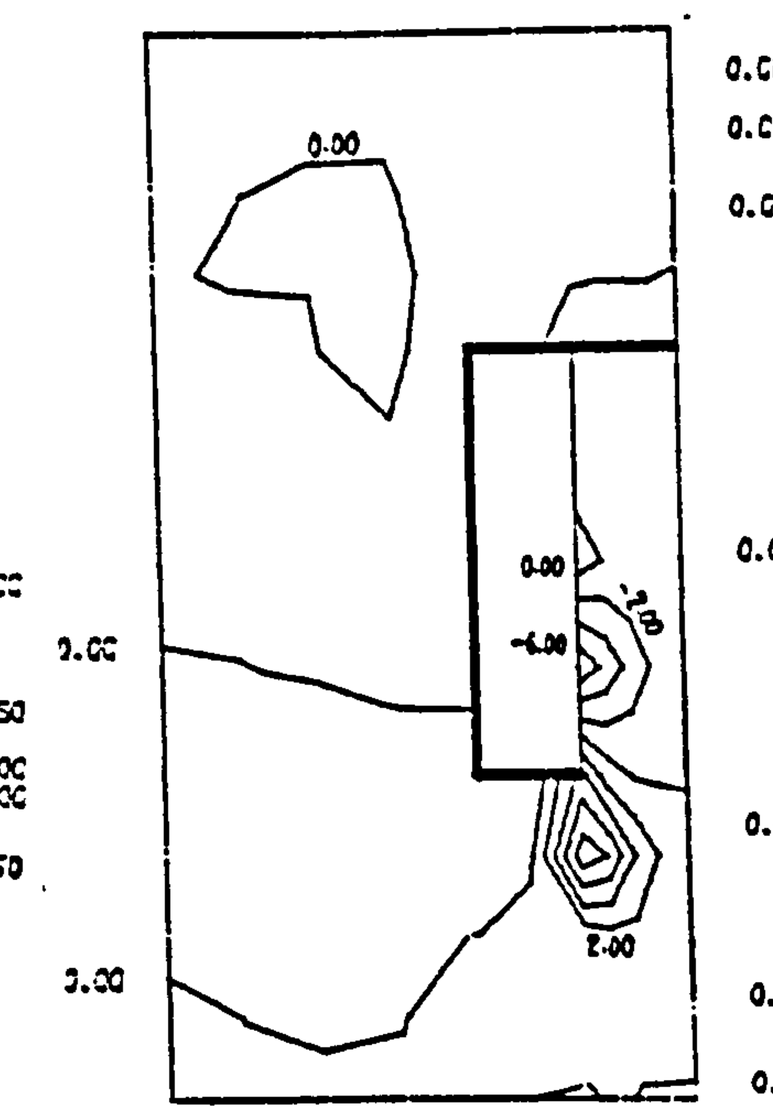

(e) 'STRESS' CONTOURS QY

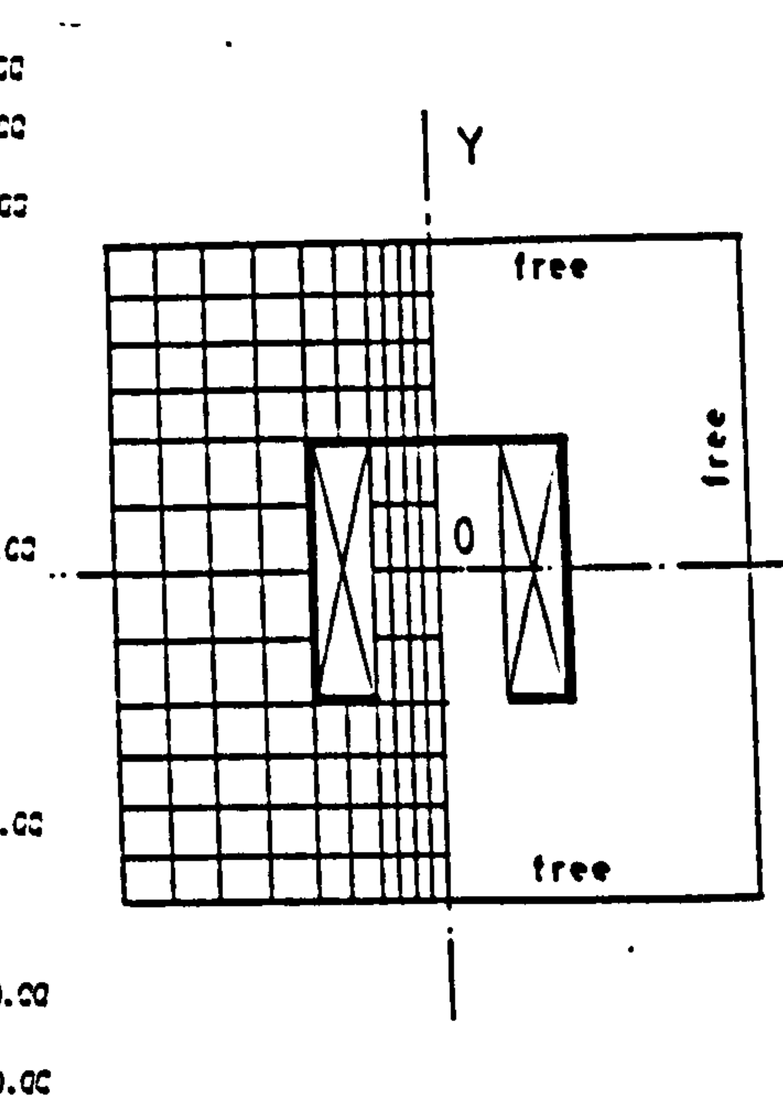

(f) KEY PLAN & ELEMENT MESH

Fig. 7.23 Stress Resultant Contours for Slab with Free Exterior Edges in Single-Core-With-Lobby Configuration

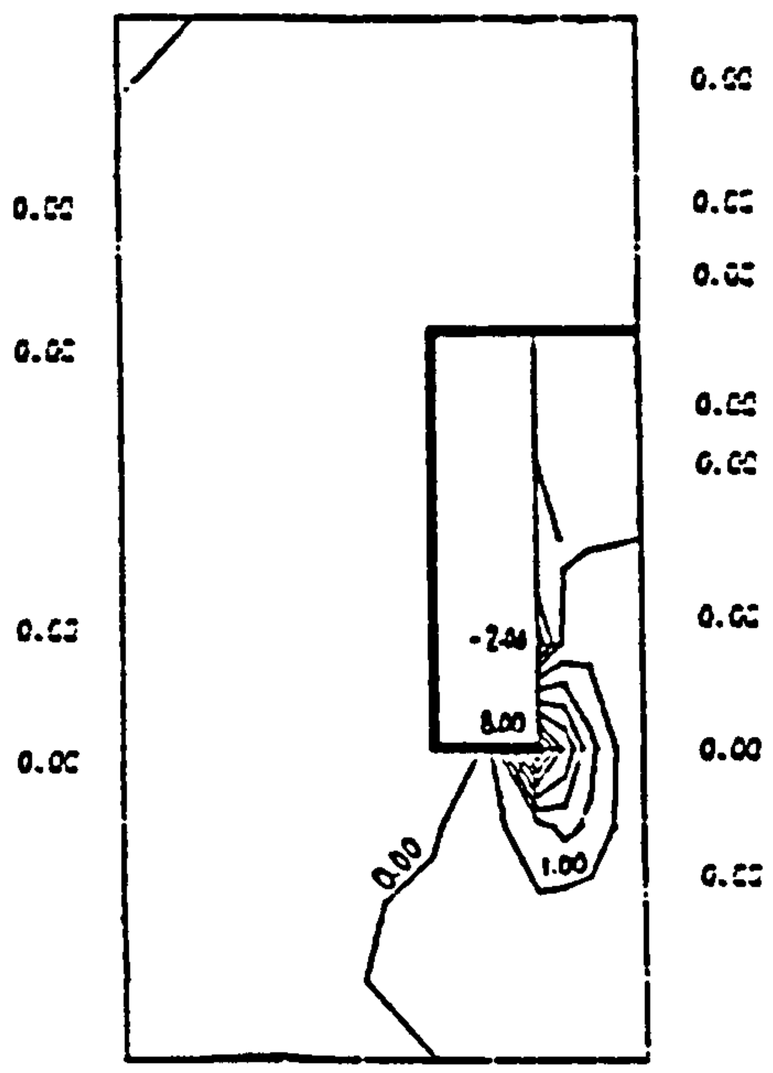

(a) 'STRESS' CONTOURS MX

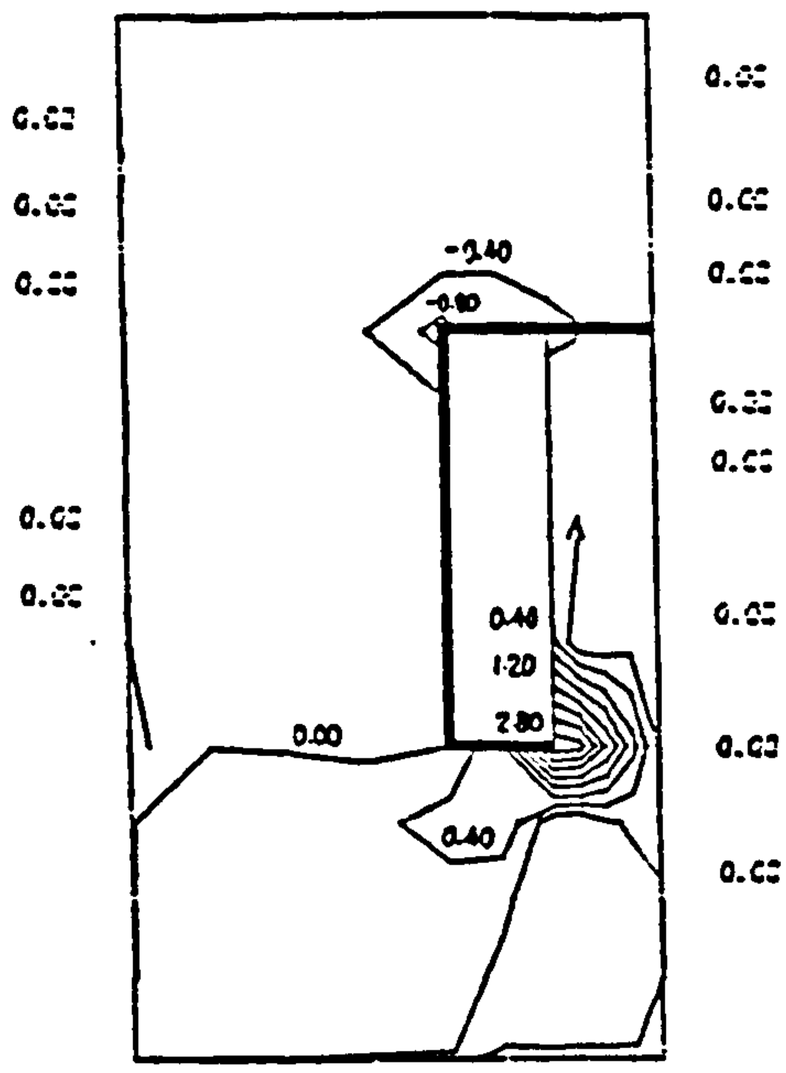

(b) 'STRESS' CONTOURS MY

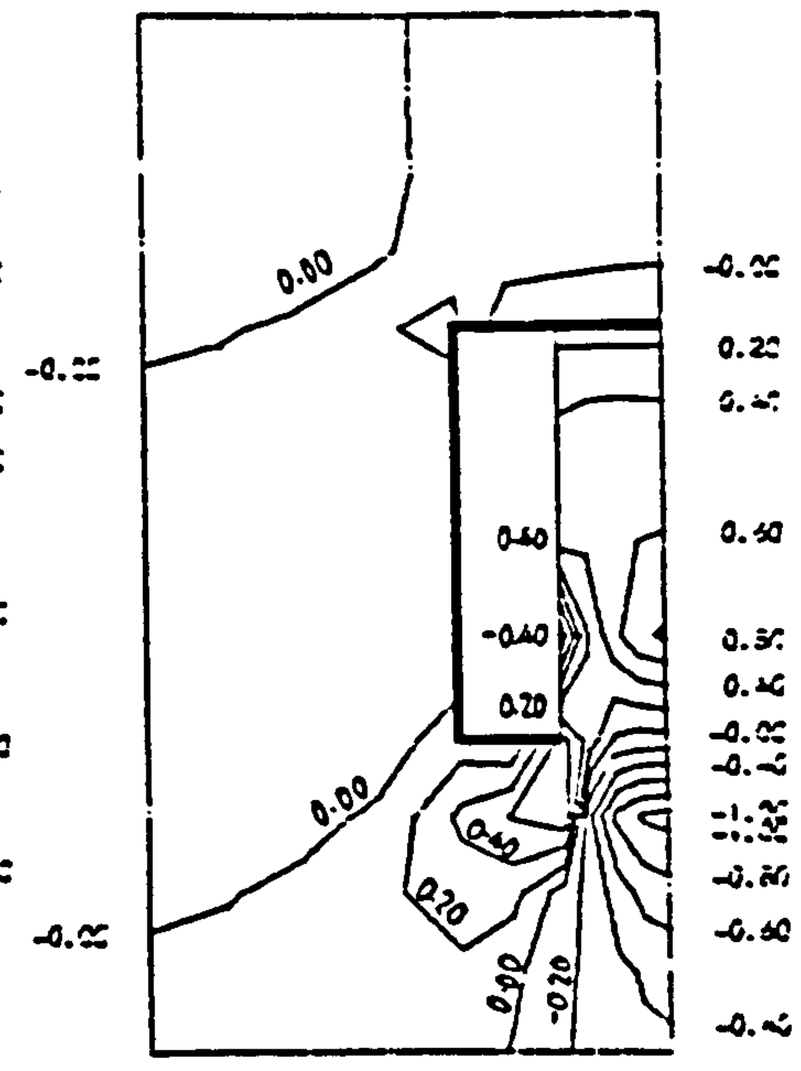

(c) 'STRESS' CONTOURS MXY

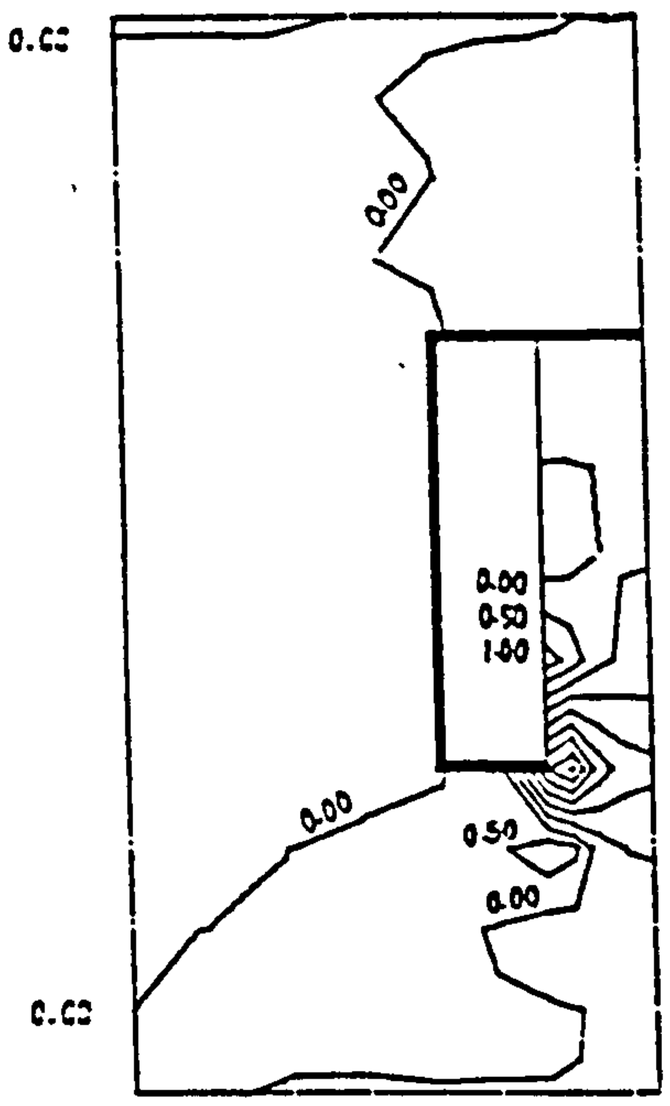

(d) 'STRESS' CONTOURS QX

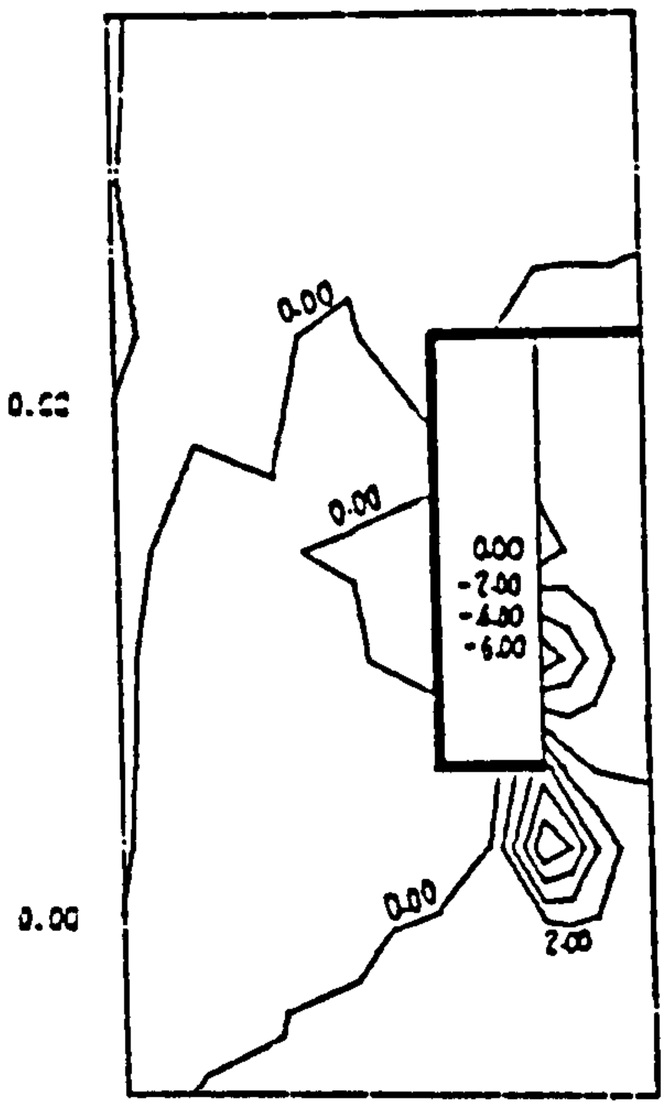

(e) 'STRESS' CONTOURS QY

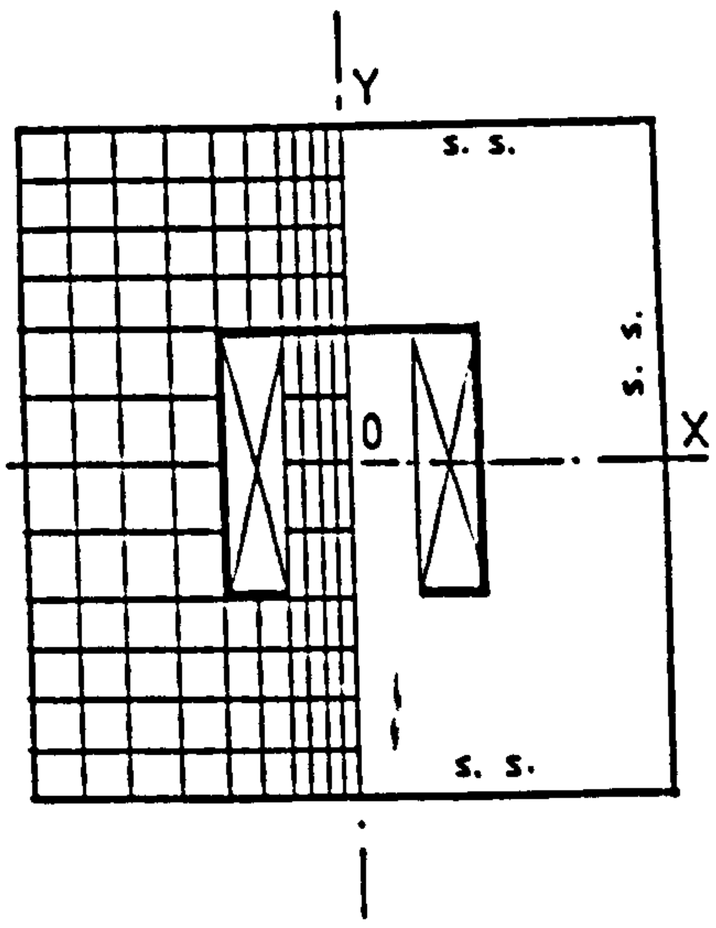

(f) KEY PLAN & ELEMENT MESH

Fig. 7.24 Stress Resultant Contours for Slab with Simply Supported Edges in Single-Core-With-Lobby Configuration

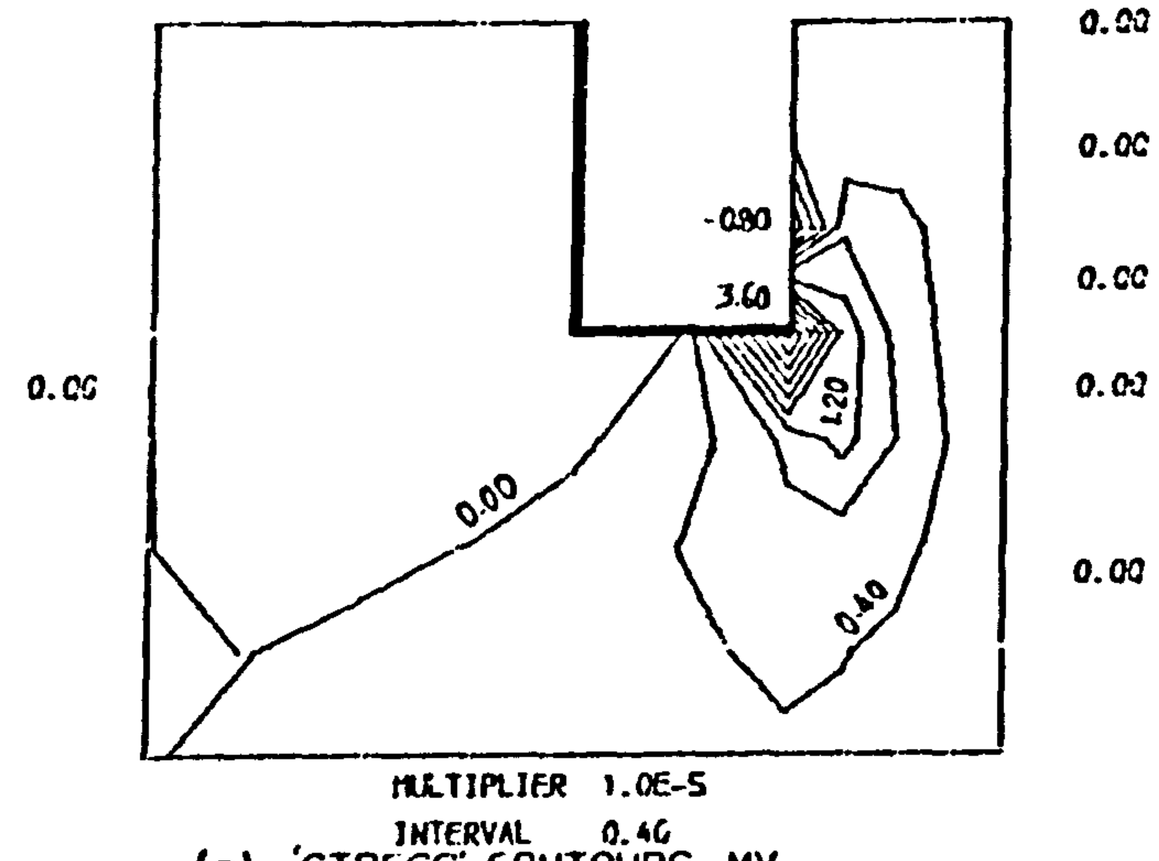

(a) 'STRESS' CONTOURS MX

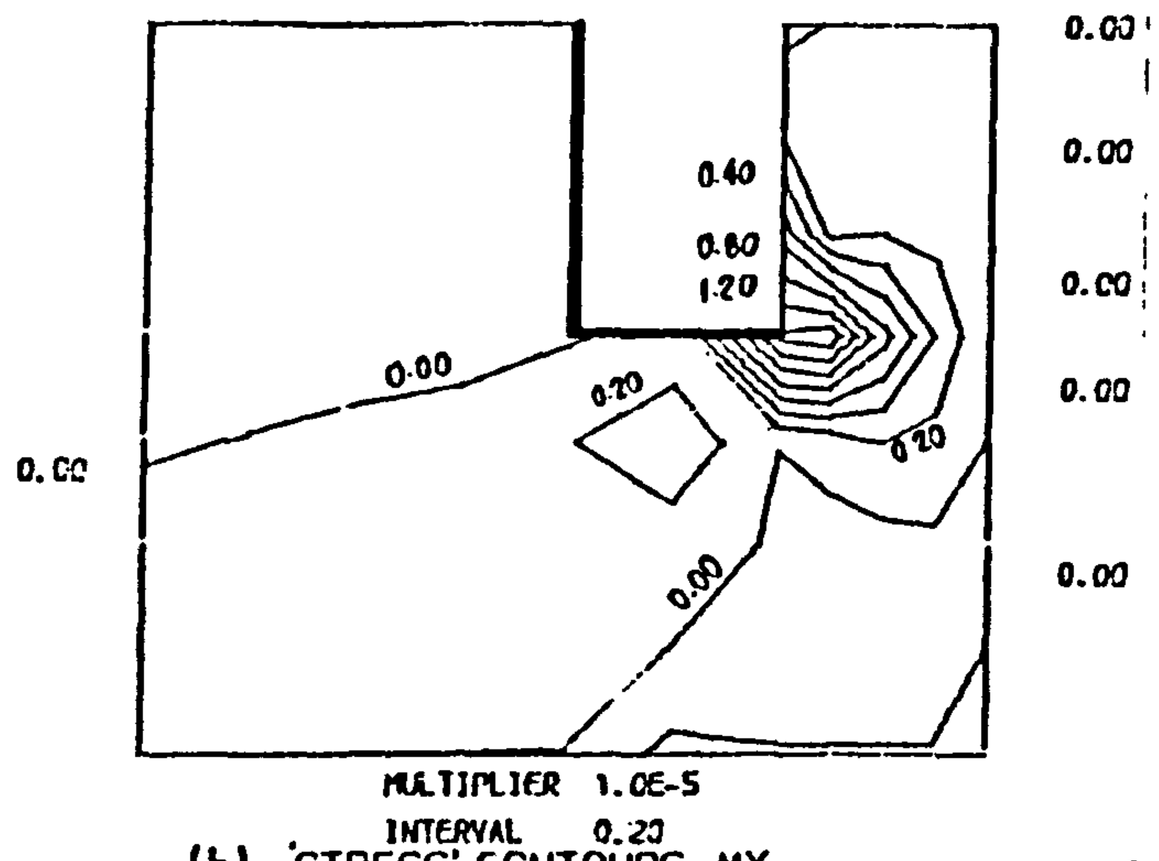

(b) 'STRESS' CONTOURS MY

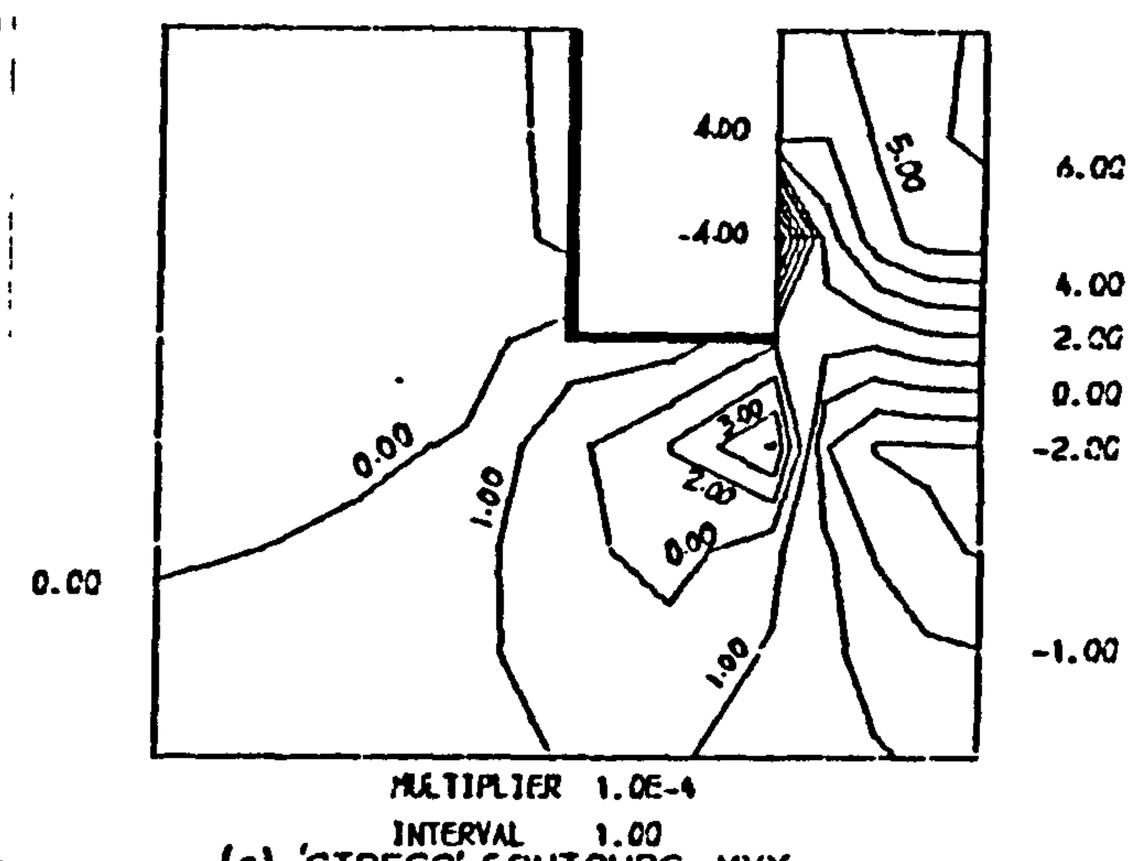

(c) 'STRESS' CONTOURS MXY

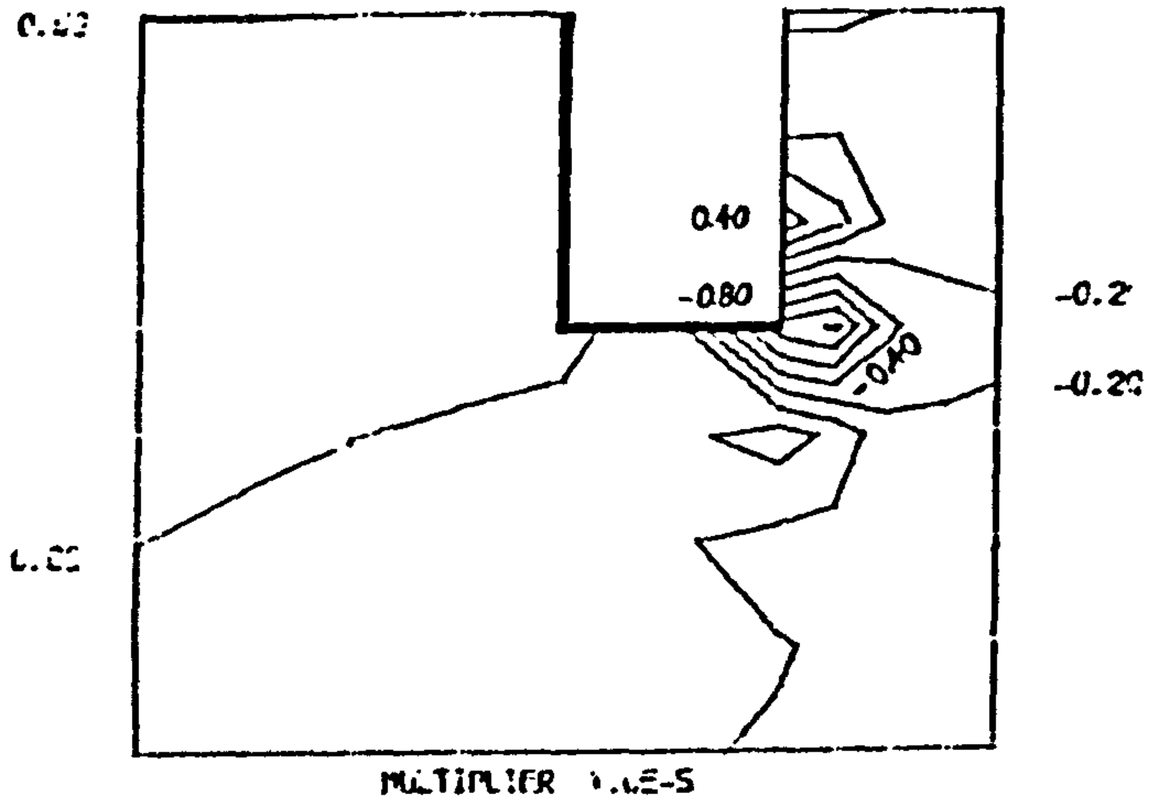

(d) 'STRESS' CONTOURS QX

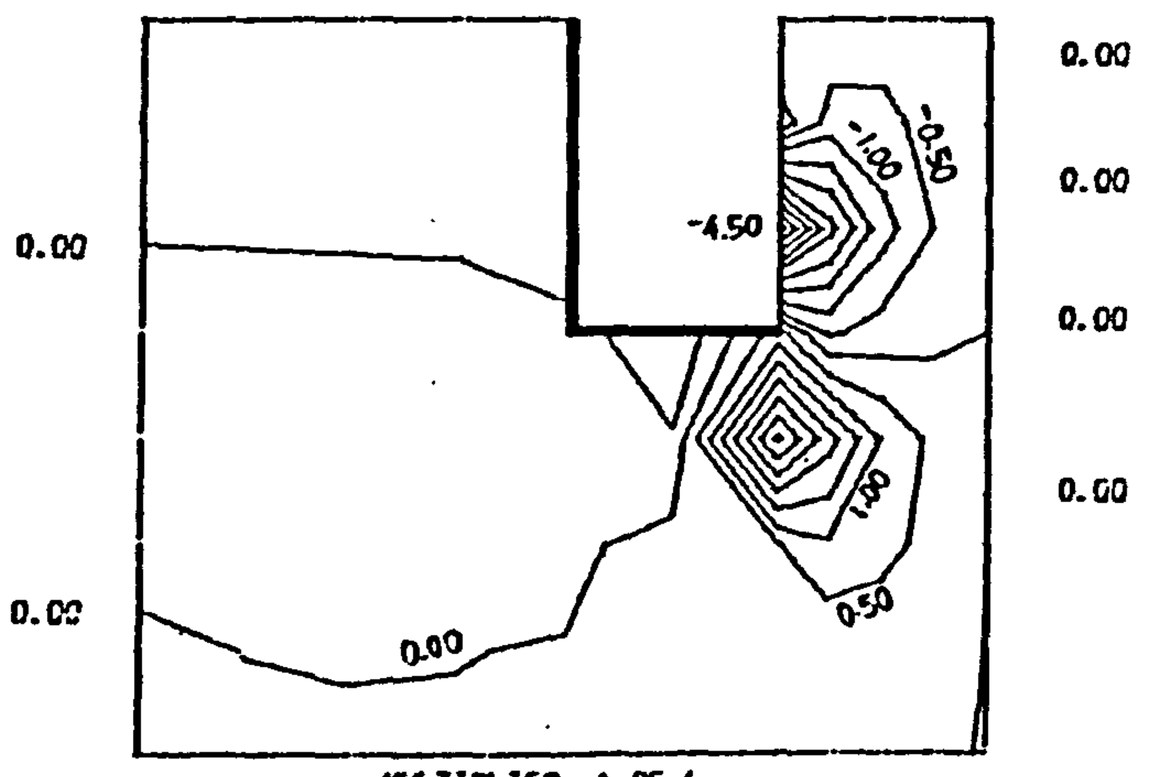

(e) 'STRESS' CONTOURS QY

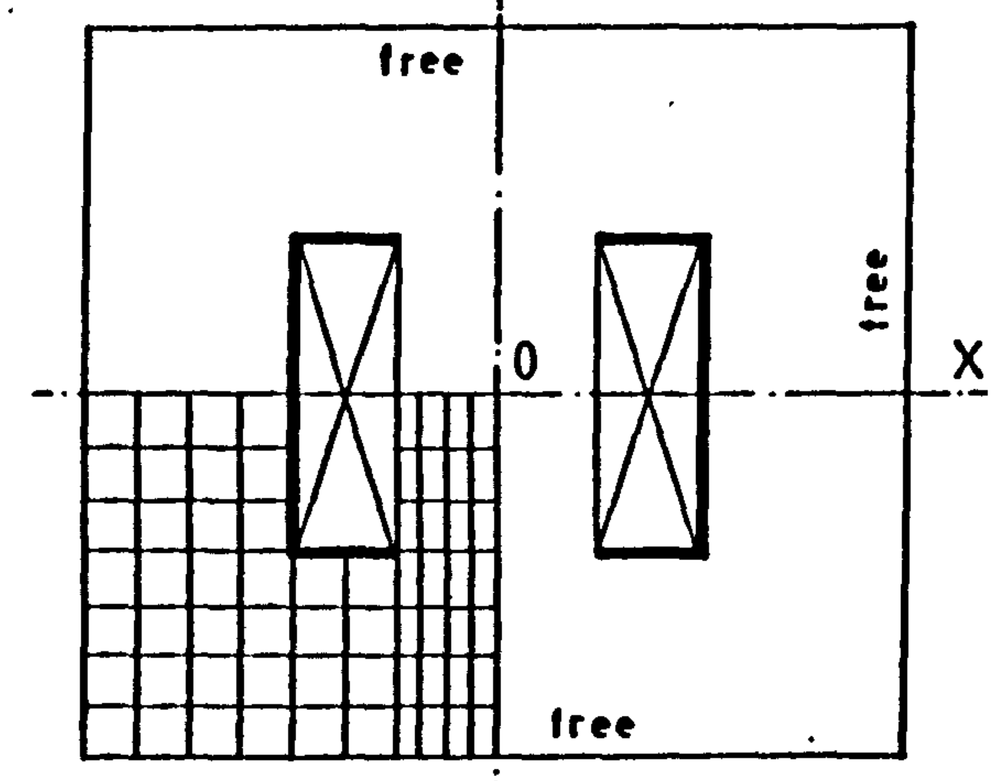

(f) KEY PLAN & ELEMENT MESH

Fig. 7.25 Stress Resultant Contours for Slab with Free Exterior Edges in Twin-Core-With-Lobby Configuration

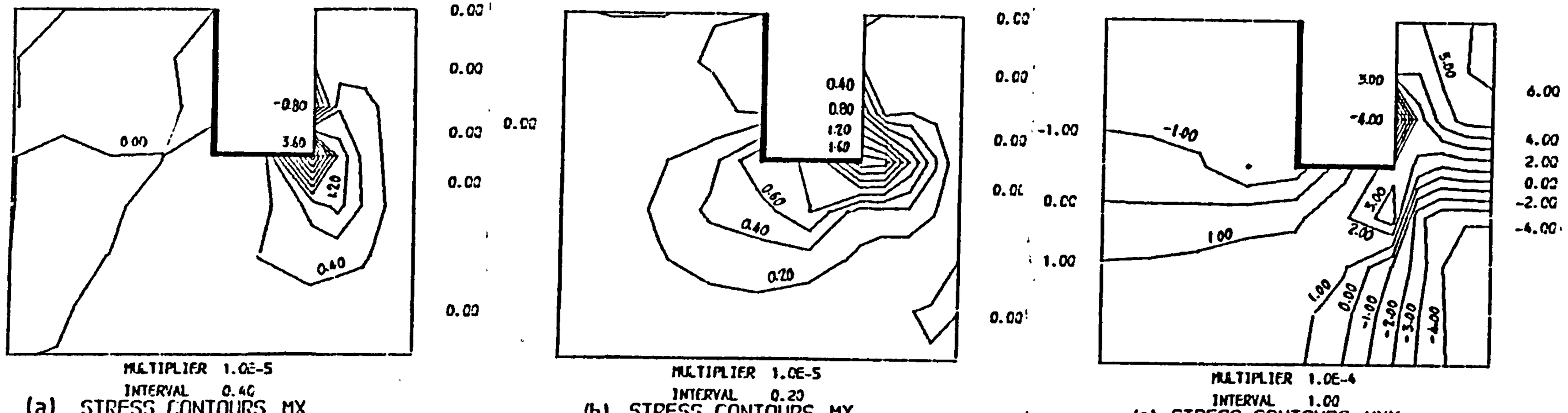

Fig. 7.26 Stress Resultant Contours for Slab with Simply Supported Exterior Edges in Twin-Core-With-Lobby Configuration

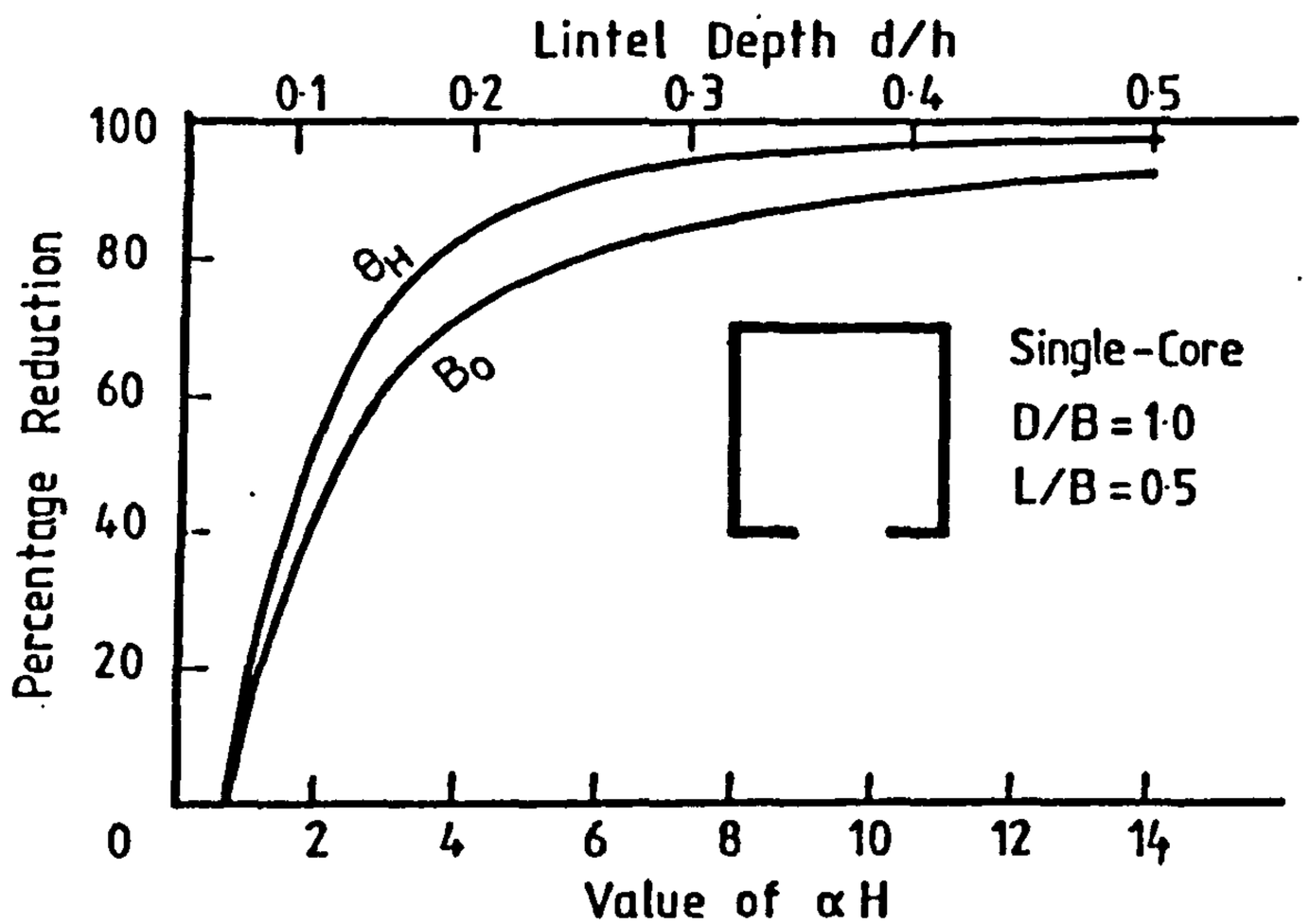

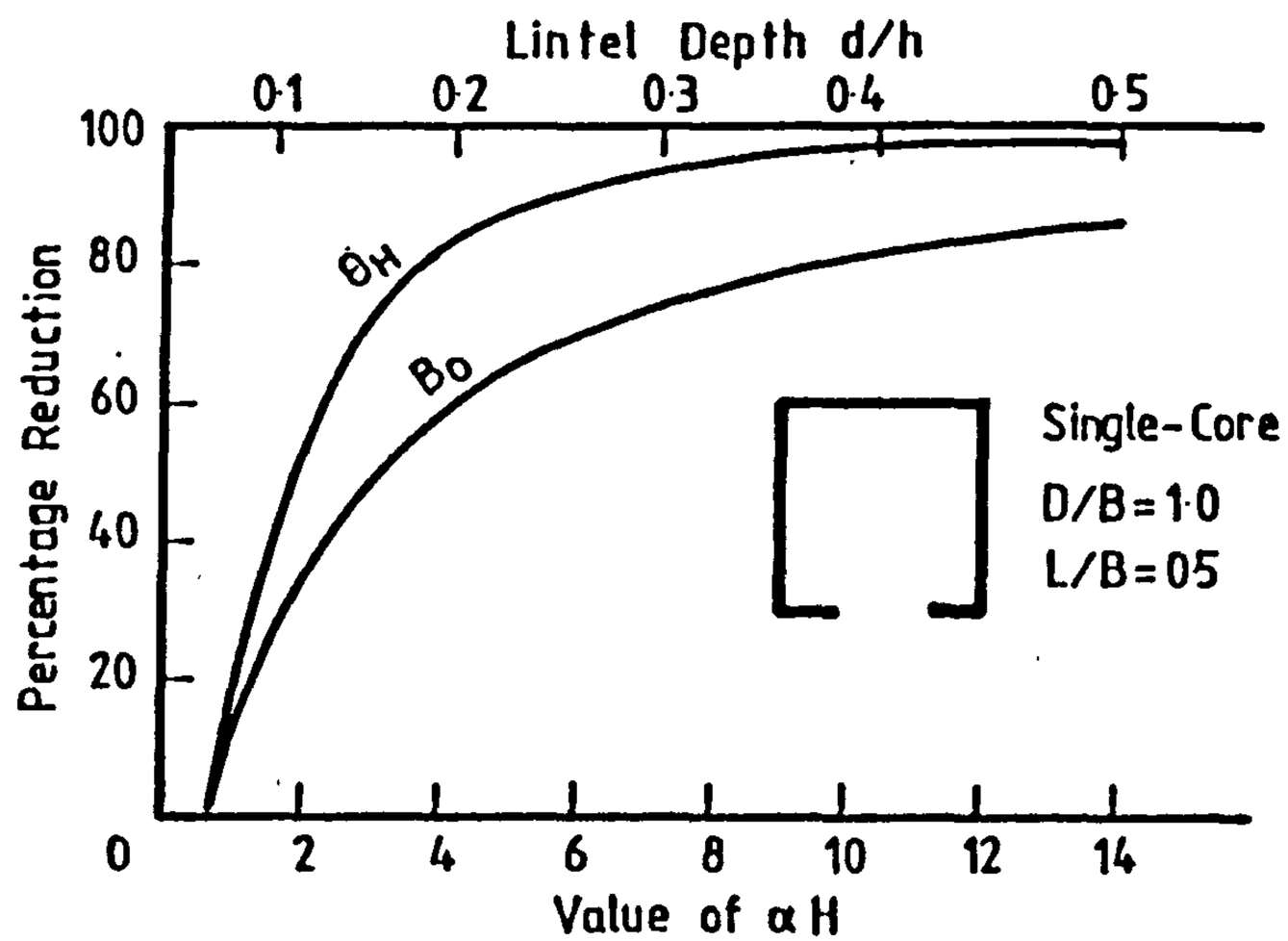

Fig. 7.27 Influence of αH on Overall Core Behaviour

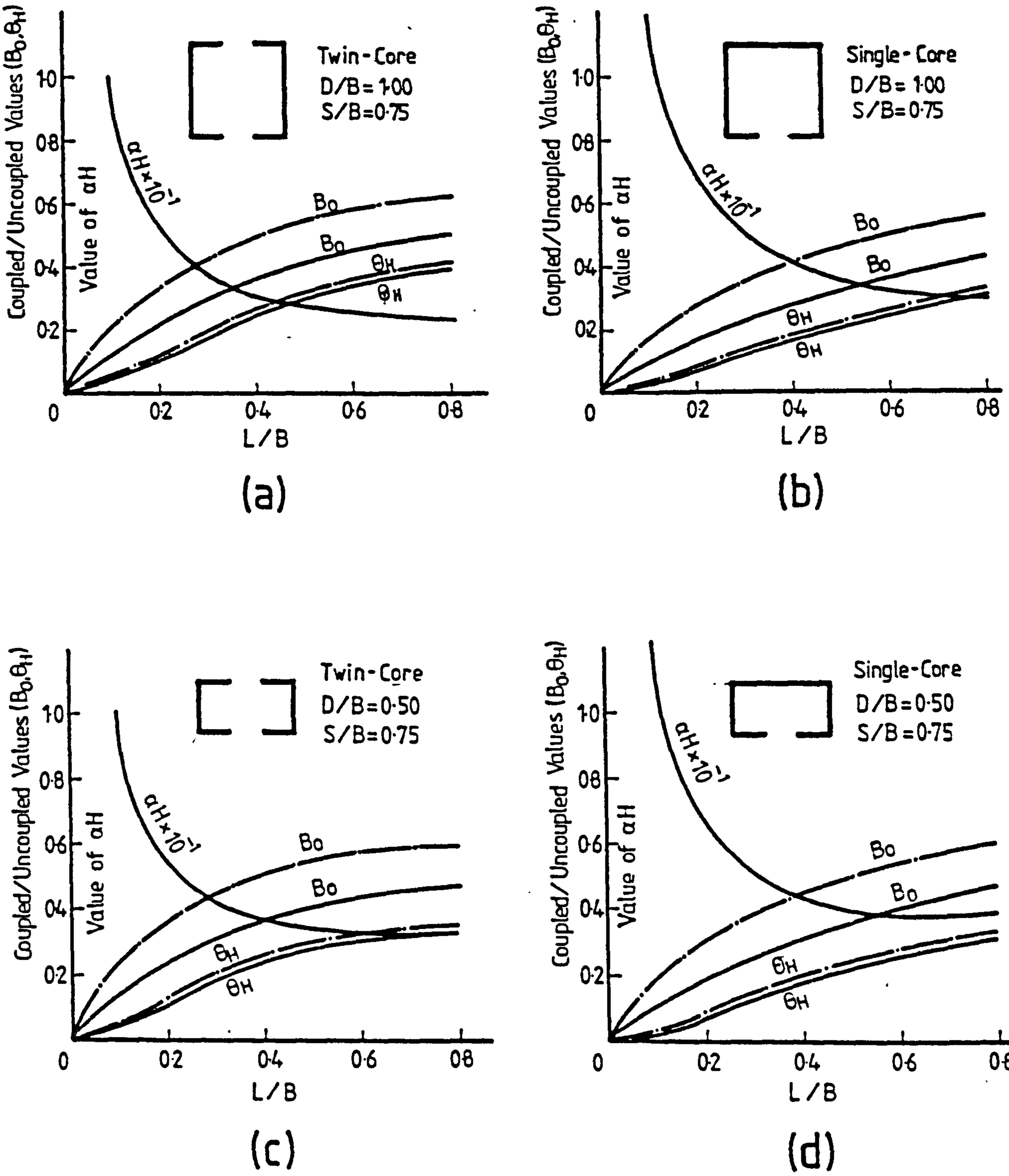

Fig. 7.28 Influence of Core-Opening Ratio on Effective Coupling

CHAPTER 8

COUPLING ACTION OF SLABS IN HULL-CORE STRUCTURES

8.1 INTRODUCTION

The hull-core structure has found considerable favour for the construction of tall commercial buildings.[82] This efficient structural system consists essentially of confining all the utilities, lifts, etc., within a central core which acts as the interior support to the floor system. The floor system is supported along the exterior by a series of columns which are usually closely spaced and connected by deep spandrel girders forming an exterior framed tube (Fig. 8.1(a)).

The success of the hull core system lies in the utilisation of the inner core and the outer hull to resist the lateral loads by tubular bending action. Due to the flexibility of the frame members the behaviour of the framed tube is strongly influenced by frame racking and shear lag effects.[83-86] The lateral behaviour of the centre core is essentially that of a vertical cantilever. Due to differences in structural behaviour between core and hull, a complex interaction between these two elements is effected through the floor slab when the structure is subjected to lateral loading. The structural behaviour of the composite tubular structure is then influenced by the stiffness of the floor system and by the rigidity of the connections between the floor and the tube systems. If the floors are effectively pin-connected to the core and hull, then under lateral loading the floor system transmits only horizontal forces between core and hull. A more efficient composite system can be achieved by having moment connections between core and hull so that axial forces are induced in the exterior columns by the cantilever bending of the core. These axial column forces not only reduce the shear lag effect but also increase

considerably the moment of resistance of the structure due to the large lever arm between the frame panels.

The interaction between the various structural components in the hull core structure is relatively complicated. An accurate analysis of the composite behaviour of the system under lateral loading would require a three dimensional finite element analysis of the complete structure which is both time consuming and expensive to carry out. An approximate analysis can be carried out by assuming that the complete behaviour of the structure can be built up of two primary component actions, a frame-tube action of the exterior hull and an interaction between the central core and the normal frame panels.[84] The latter system may be treated as a coupled shear wall system with flexible end walls,[87,88] or more conveniently, if the axial column deformation produced by the interaction forces can be neglected, as a vertical cantilever restrained by rotational springs at the floor levels.[89] The component systems may be analysed by available matrix or continuum techniques for plane systems. By using an influence coefficient technique[84,85] whereby compatibility of lateral deflections and equilibrium of lateral forces between the two component systems are enforced at various levels, the distribution of lateral loads to each system can be evaluated and hence the overall behaviour of the complete structure analysed.

This Chapter describes an investigation on the coupling action of the slab in the hull-core structure, using the techniques which have been employed for the investigations of shear wall slab interaction in cross-wall structures. The rotational stiffness and effective width of slab and the distribution of coupling actions, which are essential information for the analysis of the core-frame sub-system, are evaluated for a range of structural parameters.

8.2 ROTATIONAL STIFFNESS AND EFFECTIVE WIDTH OF SLAB

Fig. 8.1(b) shows a segment of a core coupled to the windward and leeward frame panels (normal frame panels) in a hull-core structure bending under lateral loading. It is assumed that plane sections of the core remain plane in bending. Since the in-plane stiffness of the floor slab constrains the core and frame panels to deflect equally laterally, the frame columns undergo a chord rotation equal to the wall rotation Θ. The wall rotation induces out-of-plane bending in the slab (Fig. 8.1(c)). Due to the flexural action of the slab, the relatively flexible frame column undergoes a local joint rotation at each floor resulting in points of contraflexure occurring in the columns generally at mid-storey height. Lines of contraflexure also occur in the floor slab at positions dependent on the relative column and slab stiffnesses.

The resistance of the slab against the wall rotation is a measure of its rotational stiffness in coupling a core with a hull. Thus the rotational stiffness of the slab may be defined in terms of the moment that is required to induce unit rotation of the core. The rotational stiffness may be evaluated, by a plate bending analysis, in the form of a non-dimensional stiffness factor K given by

$$K = \frac{M}{D\Theta} \qquad (8.1)$$

where D is the plate flexural rigidity.

For the purpose of overall analysis of the core sub-system, it is convenient to consider the core coupled only to the normal frame panels by a uniform width of slab in an equivalent wall-frame structure (Fig. 8.1(b)). The effective width of the slab can be established by equating the rotational stiffness of the slab to that of the beam in the equivalent wall-frame structure.

By an application of slope-deflection equations it can be shown that the rotational stiffness of the equivalent beam is given by

$$\frac{M}{\Theta} = \frac{6EI}{L} \cdot \beta$$

where $\beta = (1 + \frac{a}{L}) \left\{ (\frac{1 + 6\lambda_i}{1 + 3\lambda_i}) + (\frac{1 + 12\lambda_i}{1 + 3\lambda_i}) \frac{a}{L} \right\}$

in which a is the half depth of the core, L is the slab span and λ_i is a ratio of column to slab flexural stiffness given by

$$\lambda_i = \frac{I_c}{SH} / \frac{I_s}{L}$$

where I_c and I_s are the second moments of area of a column and a slab of unit width respectively, S is the column spacing and H is the storey height. Writing I, the second moment of area of the equivalent beam, as $I=Y_e t^3/12$, where t is the slab thickness, the effective width Y_e may be expressed in terms of the rotational stiffness factor K as

$$\frac{Y_e}{Y} = \frac{K}{6(1-\nu^2)} \cdot \frac{L}{Y} \cdot \frac{1}{\beta} \qquad (8.2)$$

where Y is the overall width of the slab and ν is Poisson's ratio.

8.3 FINITE ELEMENT ANALYSIS OF SLAB

The analysis of slab action must include the influence of the peripheral-frame column segments isolated by the points of contraflexure, since the rotational restraint at the slab edges depends largely on the relative column and slab flexural stiffnesses. In a straight forward finite element idealisation, a column segment can be represented by a space-frame element with six kinematic degrees of freedom at each end. This representation would require the slab to be represented by spatial or flat shell elements with nodal degrees of freedom compatible with those of the space frame element. The use of the flat shell element may be appropriate if the membrane or in-plane actions induced by eccentric spandrel edge beams, or the flexibility of the core walls have to be considered in the analysis; otherwise, the shell element is employed inefficiently, with superfluous in-plane degrees of freedom where the slab displacements consist of only three out-of-

plane degrees of freedom, namely the transverse deflection and two orthogonal rotations. In the latter case, a more economical but indirect two dimensional analysis can be carried out by simulating the action of a vertical column by the bending and torsional action of a horizontal beam in conjunction with the action of a vertical axial spring connected to the column slab junction. The axial spring stiffness is made equal to the axial stiffness of the column. The torsional stiffness of the beam is adjusted to the value of the flexural stiffness of the column in the direction normal to the direction of chord rotation and the free ends of the beam are restrained against torsional rotations. In the direction of chord rotation the flexural stiffness of the beam is identical to that of the column. The floor slab can then be represented by simple plate bending elements and the spandrel girder by beam elements.

In carrying out the finite element analysis, transverse displacements and slopes produced by a unit rigid core rotation are imposed at the interior edges of the slab. Simultaneously, the ends of every peripheral column (or substitute beam) are deflected to produce a unit chord rotation in the same direction as the wall rotation. The slab reactions at the wall nodes are evaluated by the finite element analysis to give a resultant moment about the rotational axis of the core. The slab rotational stiffness K and the effective width Y_e/Y are then evaluated according to equations (8.1) and (8.2). The finite element analysis also calculates the displacement and stress resultants at all the nodes in the discretised structure.

As usual, advantage can be taken of the conditions of symmetry and anti-symmetry in the structure to reduce the computational effort. Since the slab displacements are symmetric about the longitudinal centre-line (x-axis) and anti-symmetric about the transverse centre-line (y-axis), only a quadrant of the slab needs to be analysed. The

actions of a column are anti-symmetric about the middle plane of the slab when the spandrel beams are not eccentric (i.e. the beam and slab neutral planes are co-incident). In carrying out a three-dimensional analysis, either the upper or lower column stub may be omitted if the stiffness of the remaining column stub is doubled and the connected end of the column is restrained against horizontal translation. A similar reduction technique, strictly, cannot be used in the two-dimensional analysis if the performance of the slab is influenced by the axial stiffness of the column, since the omission of a beam stub simulating a column stub will then induce an extra vertical force in the axial spring when the end of the remaining beam stub is deflected vertically to simulate the column chord rotation. However, the axial stiffness of a practical-sized column is usually so large in relation to the flexural stiffness of the slab that the performance of the slab will not be significantly affected by replacing the axial spring support by a rigid support, in which case, the anti-symmetric conditions of the column may be incorporated by the reduction technique in the two-dimensional analysis without any significant loss of accuracy in the modelling.

Fig. 8.2 shows a typical finite element idealisation of the slab considered in a parameter study. The slab is modelled by the rectangular flat shell element RS24 in the three-dimensional analysis and by the rectangular plate bending element RB12 in the two-dimensional analysis.

8.4 PARAMETER STUDY

The factors which have to be considered in evaluating the coupling action of the slab are those which relate to the overall geometry of the hull-core system and those which relate to the structural properties of the components. The geometry of an idealised hull-core floor system may be described by the core dimensions a and b, the floor span L, the storey height H and the column spacing S. Since

the coupling action of the floor slab induces axial and flexural effects in the core and hull, the axial and flexural stiffnesses of the core walls and frame panels in relation to the flexural stiffness of the floor slab are relevant factors to be considered. In practical core structures, the core walls are relatively thick and are stiffened by a complex arrangement of internal walls (Fig. 8.1(a)). In this investigation, the core walls are assumed infinitely rigid in relation to the slab. The frame panels, on the other hand, are relatively flexible, particularly when bending out of plane. The rotational restraint that the frame panel offers to the coupling action of the slab depends on the relative flexural stiffness of the frame columns and on the relative torsional stiffness of the spandrels.

In this investigation, the relative influences of the following geometric and structural parameters are evaluated:

(a) Column spacing ratio S/L.

(b) Column axial stiffness ratio λ_a defined as $(E_c\ A_c/SH)/(E_s\ I_s/L^3)$, where A_c is the cross-sectional area of a frame column, I_s is the second moment of area of a slab strip of unit width, and E_c and E_s are the elastic moduli of the frame and slab materials.

(c) Spandrel torsional stiffness ratio λ_j defined as $(E_c\ J_c/S^2)/(E_s\ I_s/L)$ where J_c is the torsional constant of the spandrel beam.

(d) Column flexural stiffness ratio λ_i defined as $(E_c\ I_c/SH)/(E_s\ I_s/L)$ where I_c is the second moment of area of a frame column about an axis normal to the span direction of the slab.

(e) Core depth ratio a/L.

(f) Core width ratio b/L.

Although the final results are expressed in non-dimensional forms, for analysis, the slab is assumed as 305 mm (12 in.) thick and spanning 9.15 m (30 ft) between core and hull. The storey height is assumed as 3.66 m

(12 ft). Other structural dimensions are varied as required for parameter studies. Young's modulus and Poisson's ratio for the slab are assumed as 2.07×10^7 kN/m^2 (4.32×10^5 kip/ft^2) and 0.15 respectively.

8.4.1 INFLUENCE OF COLUMN SPACING

The relative influence of column spacing is assessed by comparing the values of slab rotational stiffness obtained for two practical column spacings S/L of 0.2 and 0.4 in a hull-core configuration with core ratios a/L and b/L of unity. The structural parameters for the frames, λ_a, λ_i and λ_j, which are dependent on the column spacing S, are maintained at the same values of 4500, 0.42 and 7.90 respectively when the column spacing is varied. The numerical results evaluated by a three-dimensional finite element analysis for the two cases are as follows:

	Column Spacing S/L	Slab Rotational Stiffness K
Case 1	0.20	175.41
Case 2	0.40	168.89

The slab rotational stiffness for the wider column spacing is less than 4% lower than that for the closer column spacing. Since the column spacing of most practical hull core or frame tube structures comes within or close to the range of values considered, it appears that for practical purposes, the influence of column spacing may be disregarded.

8.4.2 INFLUENCE OF COLUMN AXIAL STIFFNESS

The relative influence of column axial stiffness on the rotational stiffness of the slab is assessed by comparing the results obtained for a practical column stiffness with those for two extreme cases, where the column axial stiffness is reduced by a factor of 10^{-2} on one hand, and made infinitely large on the other. Core ratios a/L and b/L of unity, column spacing S/L of 0.4, and frame parameters λ_i and λ_j of 0.20 and 2.0

respectively are assumed in each case. The rotational stiffness values K evaluated by a three-dimensional analysis are as follows:

	Column Axial Stiffness Ratio λ_a	Slab Rotational Stiffness K
Case 1 - Practical Column	2250	168.89
Case 2 - Flexible Column	22.5	162.16
Case 3 - Rigid Column	∞	168.89

It is seen from the above results that the axial stiffness of a frame column is generally so large in relation to the flexural stiffness of the floor slab that any practical variations in the column axial stiffness will not have any significant effect on the performance of the slab. For the purpose of evaluating the rotational stiffness of the slab, therefore, the frame columns may be assumed axially rigid.

8.4.3 INFLUENCE OF SPANDREL TORSIONAL STIFFNESS

The same slab is analysed for four spandrel beam depths which give torsional stiffness ratios λ_j ranging in values from 0 to 11.24. The frame columns in each case are spaced at a distance S/L of 0.2 and have a flexural stiffness ratio λ_i of 0.42. The values of slab rotational stiffness K obtained for the various cases are as follows:

Spandrel Dimensions	Torsional Stiffness Ratio λ_j	Slab Rotational Stiffness K
0	0	174.97
0.3 x 0.6 m	4.57	175.30
0.3 x 0.9 m	7.90	175.52
0.3 x 1.2 m	11.24	175.62

It is seen from the results that the presence of the spandrel beam has negligible stiffening effect on the rotational stiffness of the slab for the configuration considered in which the frame columns are relatively

closely spaced. In order to assess the influence of spandrel beams for wider column spacings, additional results are obtained for a column spacing S/L of 0.4 for the two extreme spandrel sizes considered earlier. The column flexural stiffness ratio λ_i of 0.42 is maintained. The numerical results for these cases are as follows:

Spandrel Size	Torsional Stiffness Ratio λ_j	Slab Rotational Stiffness K
0	0	160.74
0.3 x 1.2 m	2.81	168.89

The spandrel beam in this case increases the rotational stiffness of the slab by less than 5%. Since the results show that the spandrel beam stiffness is not a significant factor in the evaluation of slab rotational stiffness, a constant spandrel beam size of 0.3 x 0.9 m is generally assumed for further parameter studies.

8.4.4 INFLUENCE OF COLUMN FLEXURAL STIFFNESS

The influence of column flexural stiffness is evaluated by varying the size of the frame columns from 0.229 x 0.229m (9 x 9 in.) to 0.61 x 0.61 m (24 x 24 in.) while maintaining a constant column spacing S/L of 0.2, thus obtaining values of λ_i varying from 0.13 to 6.67. Two core depth ratios a/L of 0.6 and 1.0 are considered, but the core width ratio b/L is maintained at 1.0 in each case.

Tables 8.1, (a) and (b) show the numerical values of the slab rotational stiffness K and effective width Y_e/Y for various cases analysed by a two-dimensional plate analysis. The results for the slab simply supported around its external periphery have been included for the limiting case in which the frame columns have zero flexural stiffness (i.e. pin-connected to slab). The results show that the rotational stiffness of the slab is increased considerably by the stiffness of the peripheral frame columns. The effective width, on the other hand, is reduced by a relatively small margin by increasing the

column stiffness. Doubling the column size, from 0.305 x 0.305 m to 0.61 x 0.61 m for instance, increases the rotational stiffness by about 30% but reduces the effective width by only about 4% for both core depth ratios.

Fig. 8.3 shows the numerical results for the slab rotational stiffness K and the effective width Y_e/Y plotted in a form convenient for the presentation of the design information. The parameter C_w expressed as $(\lambda_i-1)/(\lambda_i+1)$ has been used, in preference to the column flexural stiffness ratio λ_i, as the base for plotting the values K and Y_e/Y, since C_w gives a better spread of data points than λ_i for plotting the type of information obtained. Further, all values of λ_i from zero to infinity can be included within a compact range of values for C_w from -1 to +1. The curves presented in Fig. 8.3 may be used as design curves for evaluating rapidly the slab rotational stiffness or effective width in a practical situation.

8.4.5 INFLUENCE OF CORE DEPTH

The rotational stiffness of the slab is expected to increase with the core depth ratio a/L partly due to the increased rigid arm effect in the longitudinal direction of bending, and partly due to the increased length of side walls interacting with the side frame panels through transverse slab bending. The effective width of slab, on the other hand, is not affected by the rigid arm effect if there is no transverse bending, and hence any change in the effective width as a result of increasing the core depth ratio must reflect the increased effects of transverse interaction between the core and the side frames. Therefore in assessing the significant effects of core depth ratio, reference should be made to the effective width values rather than the rotational stiffness values.

As shown by the curves in Fig. 8.3 increasing the core depth ratio a/L from 0.6 to 1.0 increases the

effective width Y_e/Y by a relatively small and fairly constant margin over the whole range of column flexural stiffness ratios. The variations of effective width with core depth ratio for column stiffness ratios λ_i of 0 and 0.42 (C_w = -1 and -0.4) are shown in Fig. 8.4. The variation in each case is practically linear. On the basis of these results it appears that in a design situation, the effective width value may be interpolated or extrapolated linearly from the design curves for core depth ratios of 0.6 and 1.0 in Fig. 8.3.

8.4.6 INFLUENCE OF CORE WIDTH

The results presented in the design curves in Fig. 8.3 are based on a standard core width b/L of unity. Examination of slab actions induced by coupling (cf. Section 8.5) reveals that the portion of the slab panel in front of the core wall at a transverse distance of more than half the slab span from the ends of the core are practically unaffected by the transverse bending of the side panels. Therefore a change in the core width b/L should produce an almost equal change in the effective width of slab Y_e/L since the change in the core width affects only the inner fully effective portion of the slab if the core width is greater than half the slab span. Hence the effective width for any core width ratio b/L greater than 0.5 may be obtained from the value for the standard core width ratio by simply adding on an effective strip of slab equal to the difference between the core width under consideration and the standard core width. In order to illustrate this point, the effective width for a core width ratio b/L of 1.5 is evaluated from the result for the standard core width b/L of unity by the empirical method, and compared with the accurate value obtained by a finite element analysis. The frame column flexural stiffness ratio λ_i is taken as 0.42 (0.305 x 0.305 m columns at spacing S/L of 0.2), and the core depth a/L is taken as unity. The empirical calculations and the comparison of results are

performed in the following manner:

Standard core width b/L	= 1.000
Standard slab width Y/L	= 4.000
Standard effective width Y_e/Y (Fig. 8.3)	= 0.885
$\therefore$ Standard effective width Y_e/L = 0.885 x 4	= 3.540
Increase in core width when b/L increases from 1.0 to 1.5 = 0.5 x 2	= 1.000
Hence empirical effective width Y_e/L	= 4.540
Effective width obtained by finite element analysis Y_e/L	= 4.546
Percentage difference	= -0.13%

The effective width evaluated empirically from the 'standard' value is seen to be relatively accurate.

8.5 SLAB ACTIONS INDUCED BY COUPLING

The distributions of slab reactions and bending moments are examined for a typical hull-core configuration with core ratios a/L and b/L of unity and a relative column stiffness λ_i of 0.132 (0.23 x 0.23 m columns at spacing S/L of 0.2) for a unit rotation of the core.

8.5.1 SLAB REACTIONS

Fig. 8.5(a) shows the distributed slab reactions V_x and V_y acting on the normal and side frame panels in a typical quadrant of the structure. The results show that the interior columns in the normal frame panel opposite the core are more heavily loaded than the columns near the edge of the panel. The columns opposite the corner of the core are also slightly more heavily loaded than the rest of the interior columns. Relatively large reactions are also induced in the side frame by the transverse coupling action, which is expected to increase towards the corner of the core as the differential vertical displacement between the core and the side frame increases. Close to the leeward edge of the side frame the reactions act in the opposite direction producing uplift column forces. These reactions apparently result from the chord rotation imposed on the frame panels.

Under framed-tube action, the shear lag effect produced by spandrel flexibility tends to increase the loads in the corner columns and reduce the loads in the interior columns in the frame panels. The reactions induced by coupling action of the slab tend to offset the shear lag effect and produce a more efficient distribution of column loads under composite hull-core action.

Fig. 8.5(b) shows the theoretical slab reactions on the normal and side walls of the core. The distribution of reactions is marked by a high peak at the corner and a sharp drop a small distance away. Presumably the corner reaction is singular and the numerical values of the reactions evaluated at points close to the corner may not be absolutely reliable.

The value of the end reactions for an assumed uniform one-way slab strip connecting the normal core and frame panels has been indicated in Figs. 8.5, (a) and (b), to illustrate the deviation of the slab reactions from the uniform value. It is seen that the slab reactions V_x approach the uniform value some distance away from the corner disturbance.

8.5.2 SLAB MOMENTS

Fig. 8.6(a) shows the transverse distributions of longitudinal moments M_x along sections located at the leeward core face and normal frame panel positions (at $x = a$ and $x = a+L$ respectively) due to a unit rotation of the core. As discussed in Chapter 3 (Section 3.4.2.2) the peak bending moment at the corner of the core is theoretically singular, but the peak value evaluated by the finite element analysis though arbitrary in absolute value may be used in conjunction with adjacent values to obtain a valid estimate of the integrated moment in the critical region around the corner. Away from the corner disturbance, the bending moments at the core face and at the columns opposite are sensibly uniform and compare closely with the calculated uniform strip values (shown in broken line).

Fig. 8.6(b) shows the longitudinal distributions of transverse bending moments M_y at the core side wall and side frame panel positions (y = b and y = b+L respectively). Large transverse moments are induced in a region around the corner of the core. Again, although the peak bending moment value at the corner of the core is theoretically singular the finite element results can be used to evaluate the integrated bending moment in the critical region.

8.6 SLAB PIN-CONNECTED TO EXTERIOR FRAME PANELS

If the peripheral columns are very flexible in bending as when they are spaced widely apart, or if the floor slab is effectively pin-connected to the peripheral columns, then in the analysis of coupling action the slab may be idealised as being point supported around its periphery. As shown in section 8.4.2 the axial stiffness of even a minimum practical size column is so great in relation to the flexural stiffness of the slab that the column may be considered axially rigid. Fig. 8.7 shows the effect of column spacing on the rotational stiffness of the slab, The slab is assumed rigidly connected to the core as before. Two cases have been considered. In the first case the slab is restrained by columns on the normal and side frame panels, and the core ratios are a/L = 1 and b/L = 1. In the second case only the normal edges of the slab are restrained; the side edges are assumed free, and the core ratios are a/L = 0.5 and b/L = 1. The curves show that for the practical range of column spacing S/L generally less than 1, the column spacing has relatively little influence on the rotational stiffness of the slab. For practical purposes, therefore, the influence of column spacing may be disregarded and the slab edges assumed continuously simply supported when evaluating the rotational stiffness of the slab.

8.7 SLAB SIMPLY SUPPORTED AT ITS PERIPHERAL EDGES

When the slab is assumed simply supported at its edges the influence coefficient technique may be employed more conveniently than the finite element method to evaluate the rotational stiffness and effective width of slab. Fig 8.8 summarises the numerical results obtained by the influence coefficient method for cases in which the normal peripheral edges are simply supported and side edges are either simply supported or free. A comparison of corresponding results for these two cases should show the relative importance of transverse and longitudinal coupling between the core and the frame panels. Various core ratios a/L and b/L have been considered in order to illustrate further the influence of these parameters which have already been discussed in relation to slabs coupled to frames with finite column stiffness. The influence coefficient solution uses 6 nodes (2 web nodes and 4 flange nodes) and 30 harmonics for the configuration with b/L = 1, and 8 nodes (2 web nodes and 6 flange nodes) and 25 harmonics for the other configuration with b/L = 1.5.

It is seen from the curves that the transverse coupling effect accounts for a relatively small proportion of the coupling stiffness of the slab which is simply supported all round. This proportion varies generally between 3 and 20% over the range of core ratios considered. When the side edges of the slab are unrestrained the effective width Y_e/Y is practically unaffected by variations in core depth ratio a/L. With restrained side edges, the effective width of slab increases practically linearly with the core depth ratio; but this effect is relatively insignificant.

8.8 COMPARISON BETWEEN FINITE ELEMENT AND INFLUENCE COEFFICIENT RESULTS

In order to verify the general accuracy of the finite element and influence coefficient results, values of slab rotational stiffness K obtained by both techniques are

compared for slabs with simply supported peripheral edges ($\lambda_i = 0$) below:

a/L	b/L	Finite Element Solution	Influence Coeff. Solution
0.6	0.6	27.80	27.90
1.0	1.0	95.17	94.11

The results obtained by the two different techniques differ by less than 2%.

8.9 CONCLUSIONS

The coupling action of a slab moment-connected to the core and peripheral frames in a hull-core structure has been investigated by a finite element technique. The relative influences of a range of structural parameters have been evaluated. The column to slab flexural stiffness ratio λ_i has a significant influence on the rotational stiffness and effective width of the slab. With a constant column to slab flexural stiffness ratio, the influences of column spacing and spandrel beam stiffness are negligible. Practical variations in column axial stiffnesses have negligible effects on the rotational stiffness of the slab. The effective width of slab increases with the relative core width b/L and core depth a/L. Curves have been presented to facilitate the evaluation of rotational stiffness and effective width of slab for practical situations.

The slab reactions induced by coupling action have the effect of increasing the loads in the interior columns and reducing the loads in the corner columns in the external framed tube, thereby off setting to a certain extent the shear lag effect of the basic framed tube action.

Although not considered in the present investigation, the flexibility of the core walls and the presence of access openings in a practical core structure have the effect of reducing the coupling stiffness of the slab. Further parameter studies are required to assess the relative influence of these factors. These studies

could be carried out by employing the three-dimensional analysis described in this Chapter. If only approximate results are required, the influence of core opening and wall flexibility may be assessed from similar information presented in Chapter 3 (Section 3.9.1.1) and Chapter 5 for slabs coupling box cores in cross-wall structures.

TABLE 8.1 INFLUENCE OF COLUMN FLEXURAL STIFFNESS ON STIFFNESS AND EFFECTIVE WIDTH OF SLAB

(a) Core Ratios a/L = 1, b/L = 1

Column Size	λ_i	K	Y_e/Y
0	0	95.18	1.014
229 x 229 mm	0.132	136.85	0.931
305 x 305 mm	0.417	175.41	0.885
381 x 381 mm	1.017	203.21	0.864
458 x 458 mm	2.109	219.07	0.856
610 x 610 mm	6.667	231.78	0.850

(b) Core Ratios a/L = 0.6, b/L = 1

Column Size	λ_i	K	Y_e/Y
0	0	53.94	0.898
305 x 305 mm	0.417	96.64	0.816
458 x 458 mm	2.109	119.15	0.790
610 x 610 mm	6.667	125.77	0.785

(a)

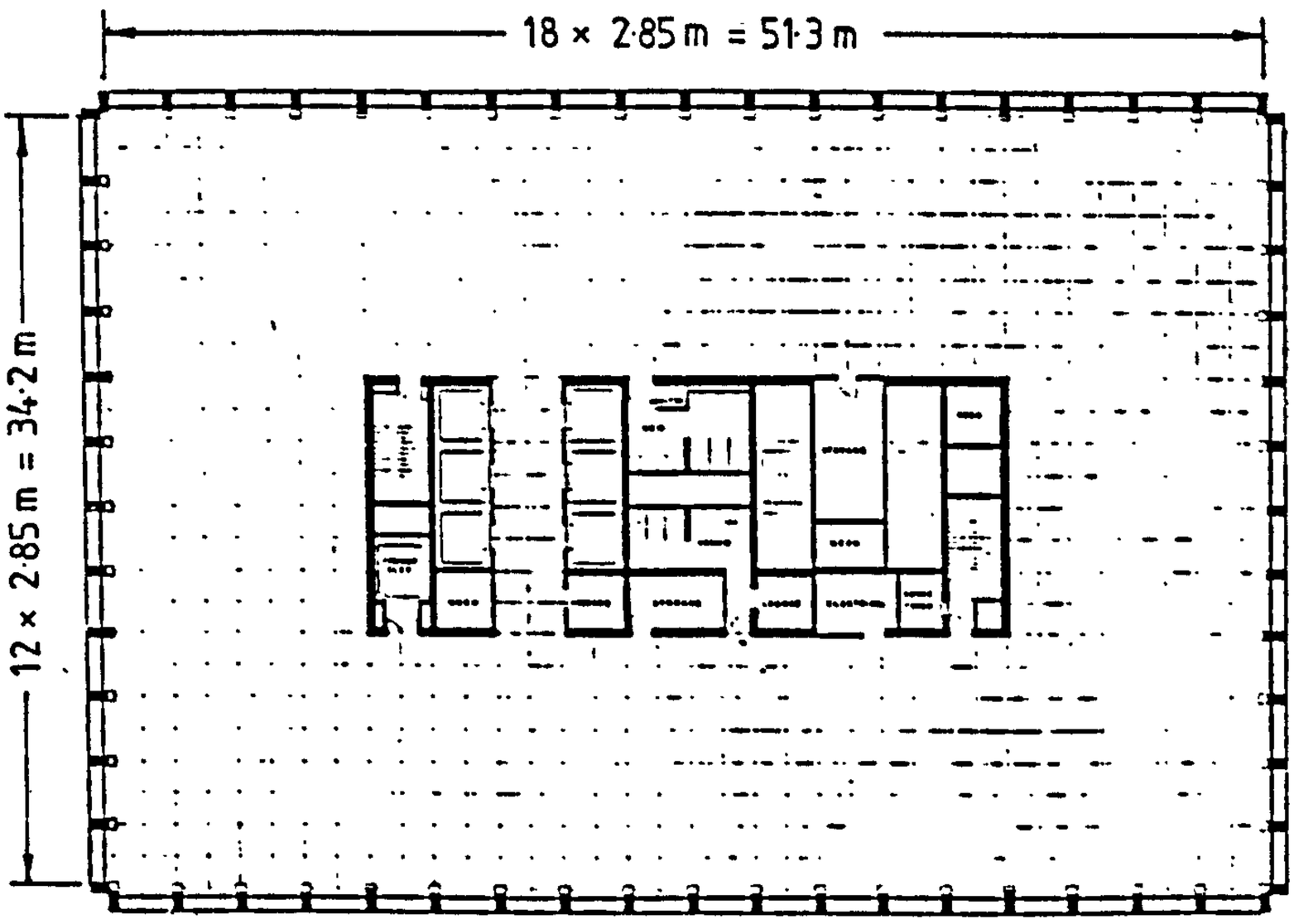

Typical floor plan of Brunswick Building.

(b)

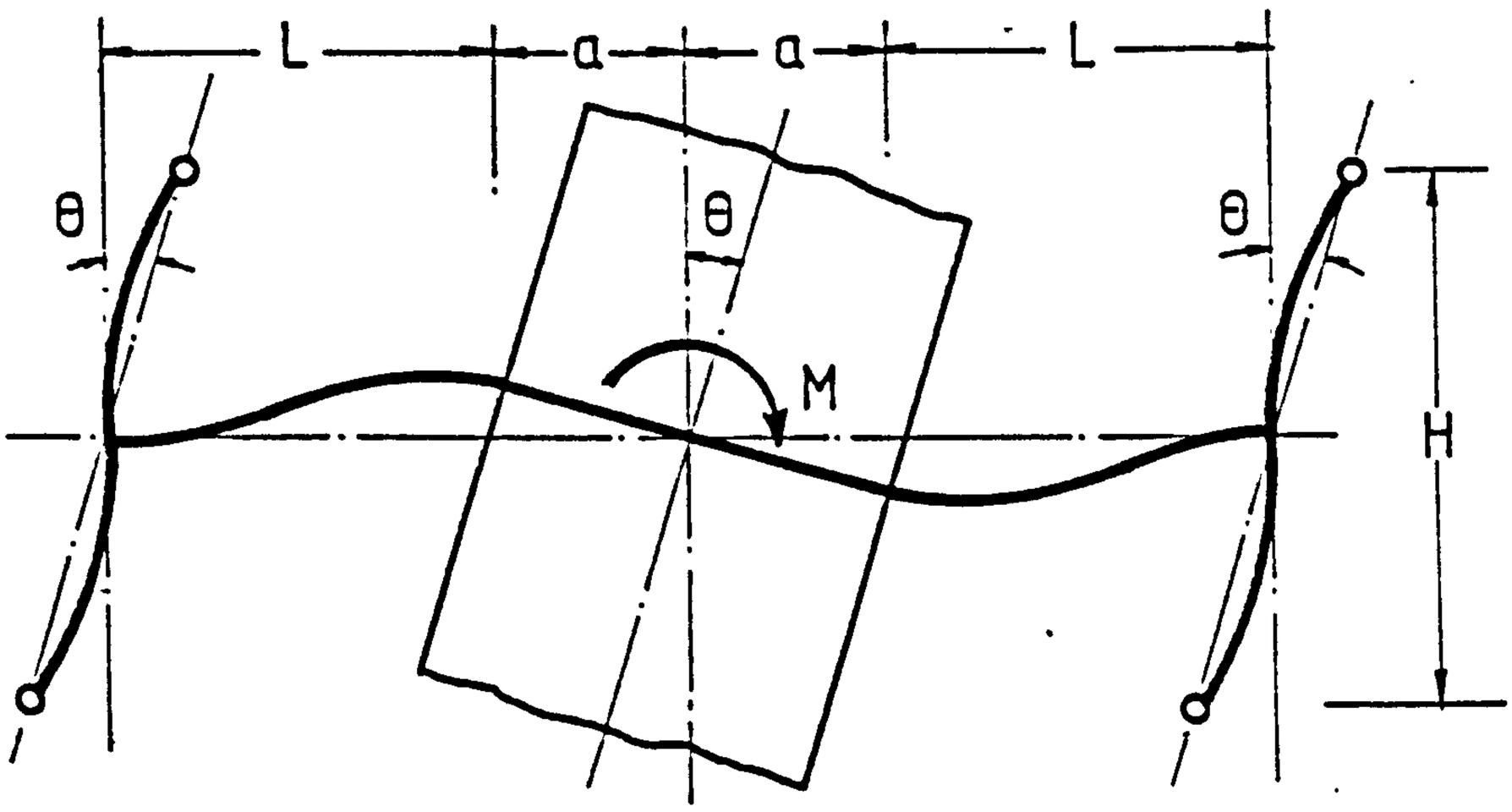

(c)

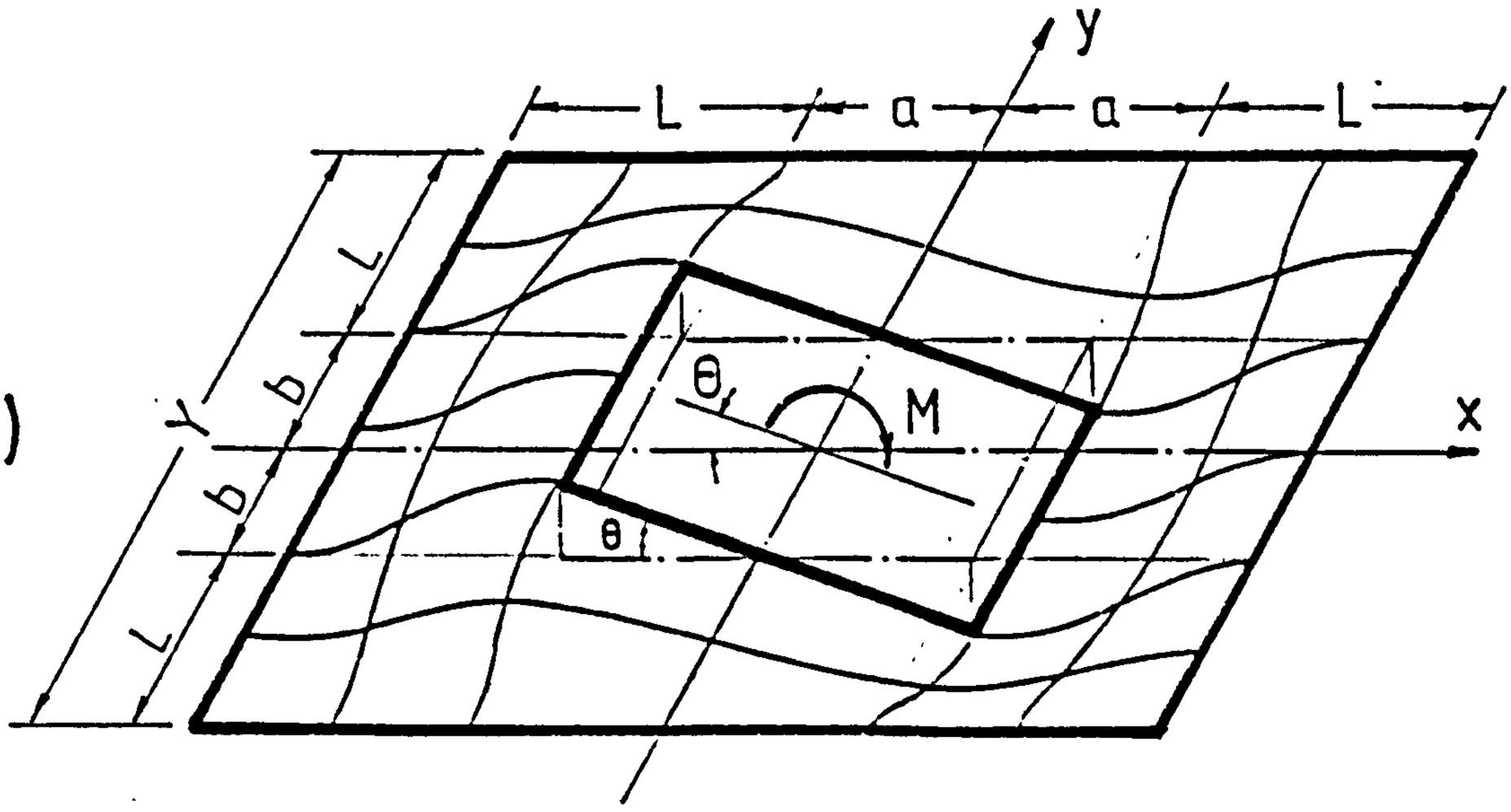

Fig. 8.1 Hull Core Structure (a) Typical Floor Plan, (b) Lateral Deformation Characteristics, and (c) Floor Deformation

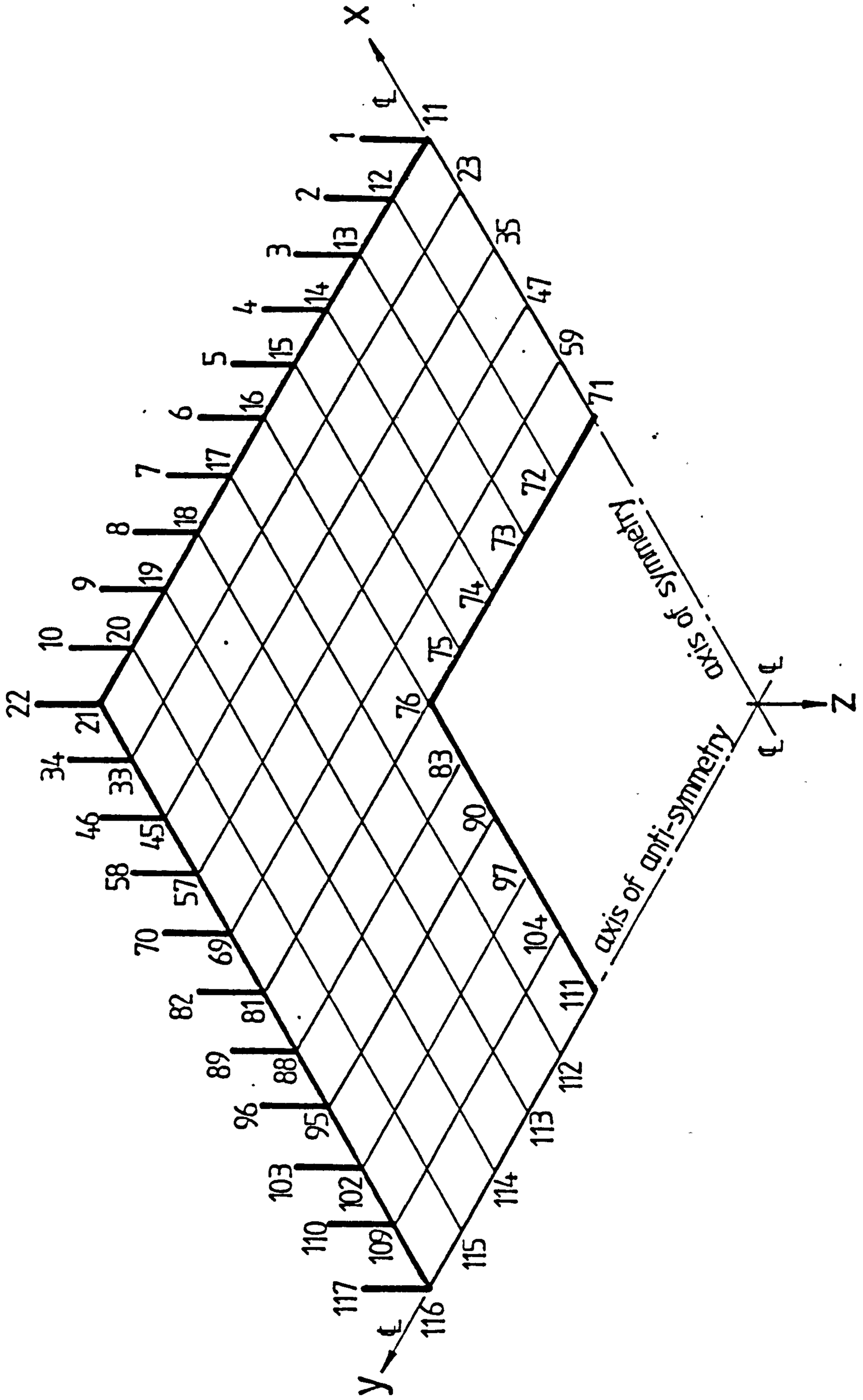

Fig. 8.2 Typical Finite Element Idealisation of Floor Slab

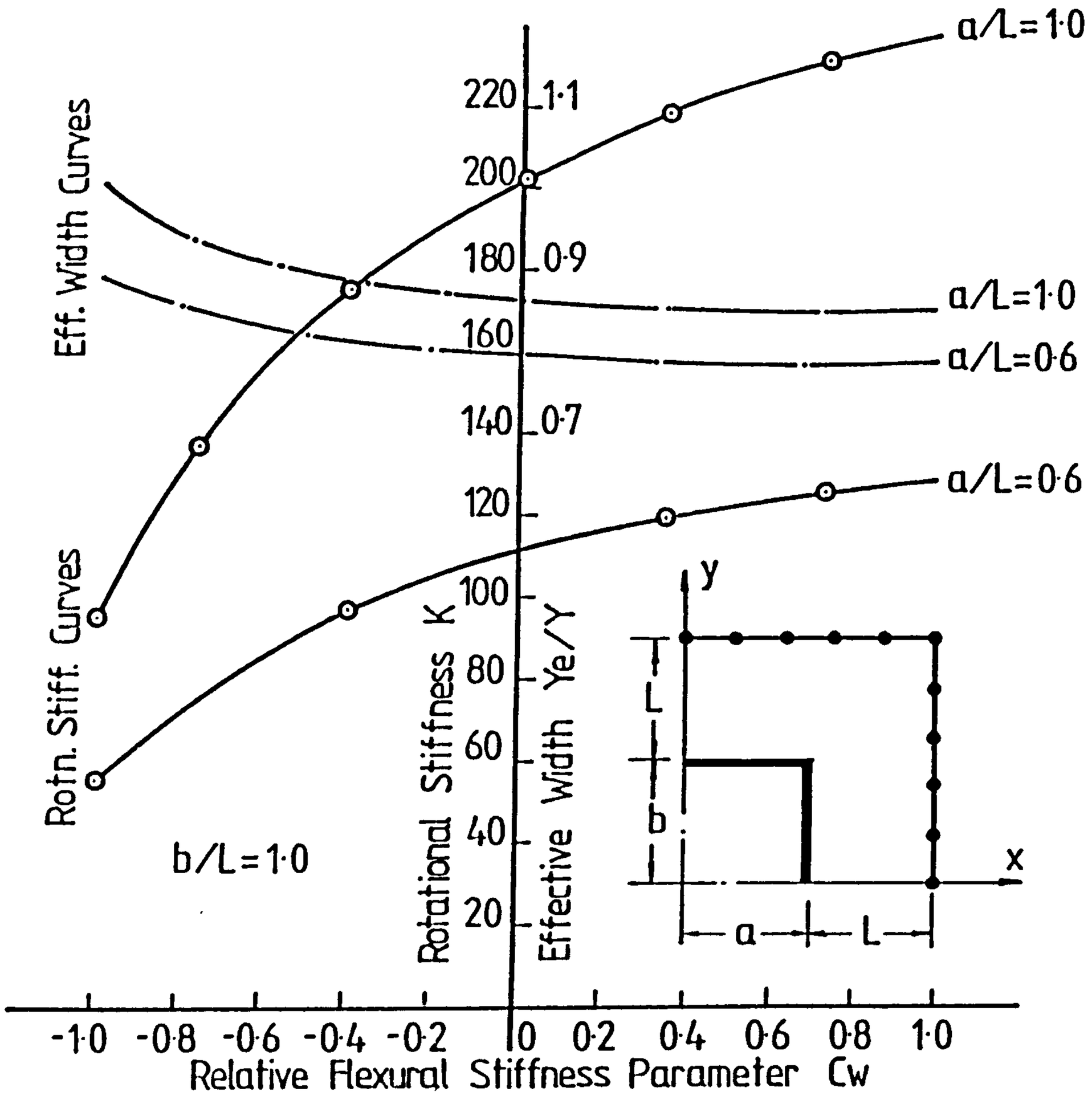

Fig. 8.3 Design Curves For Rotational Stiffness and Effective Width of Slab

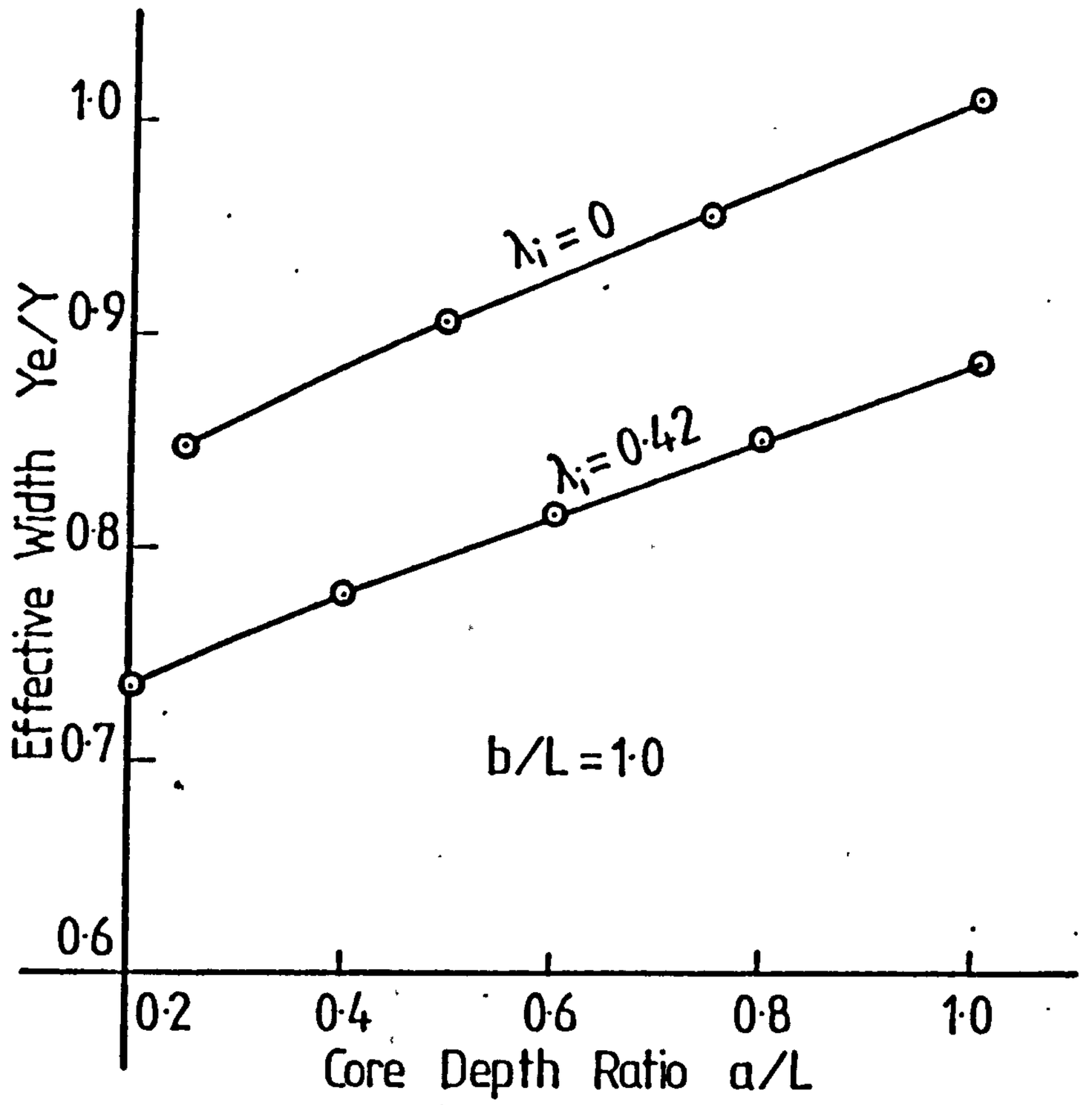

Fig. 8.4 Variation of Effective Width with Core Depth Ratio

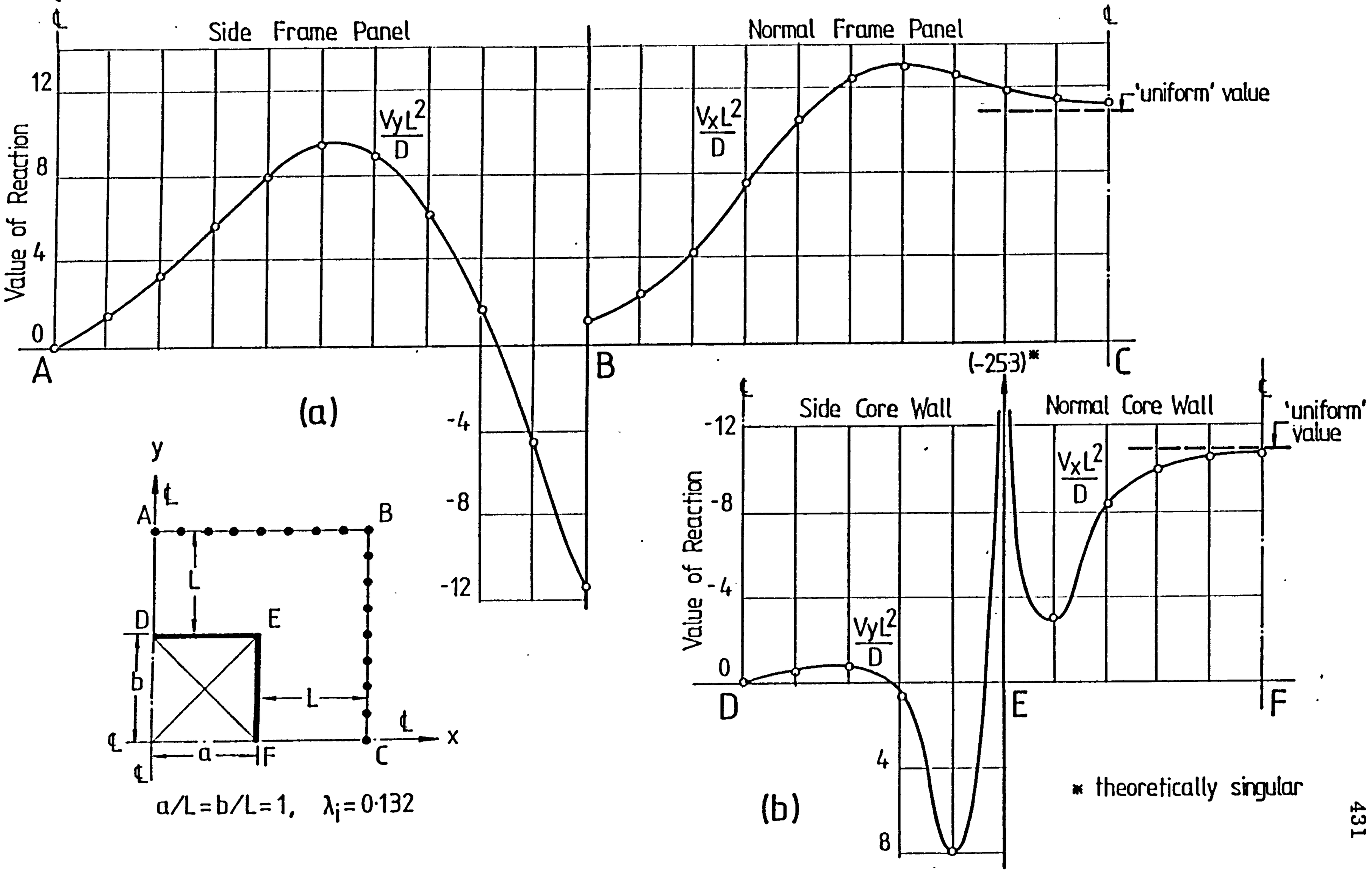

Fig. 8.5 Slab Reactions Induced by Unit Core Rotation, (a) Reactions on Frame Panels and (b) Reactions on Core Walls.

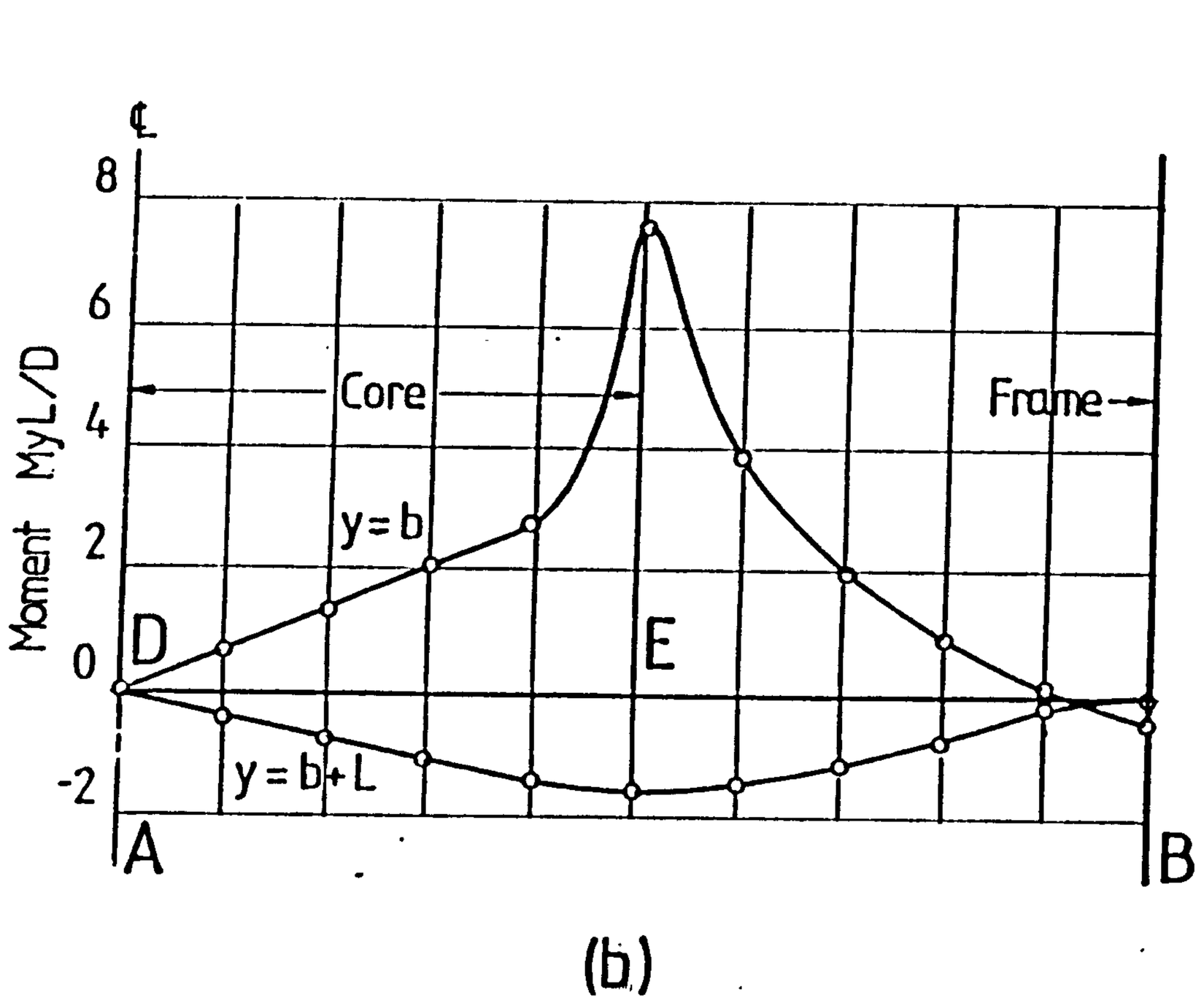

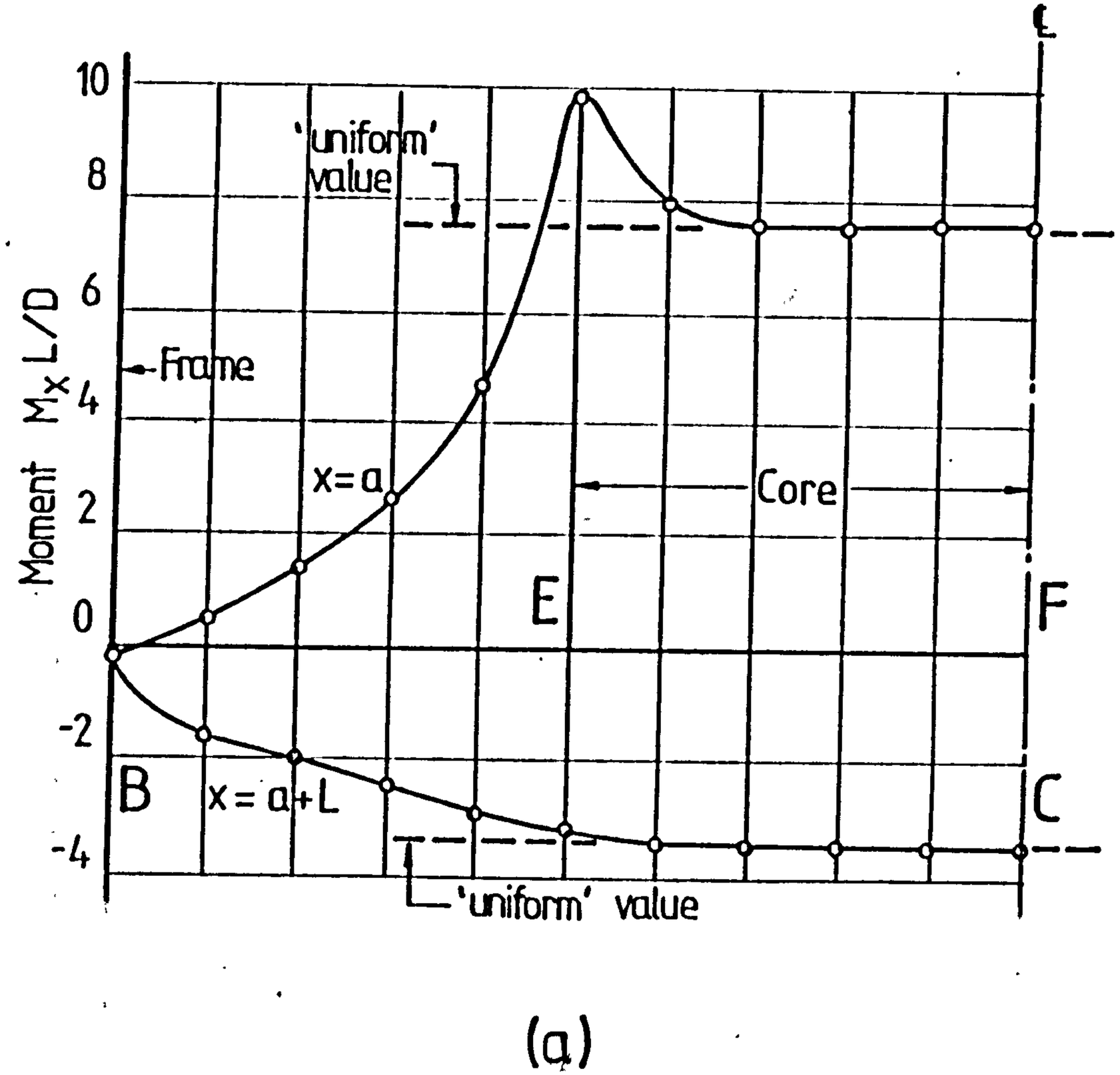

Fig. 8.6 Slab Moments Induced by Unit Core Rotation, (a) Transverse Moments and (b) Longitudinal Moments, at Critical Slab Sections.

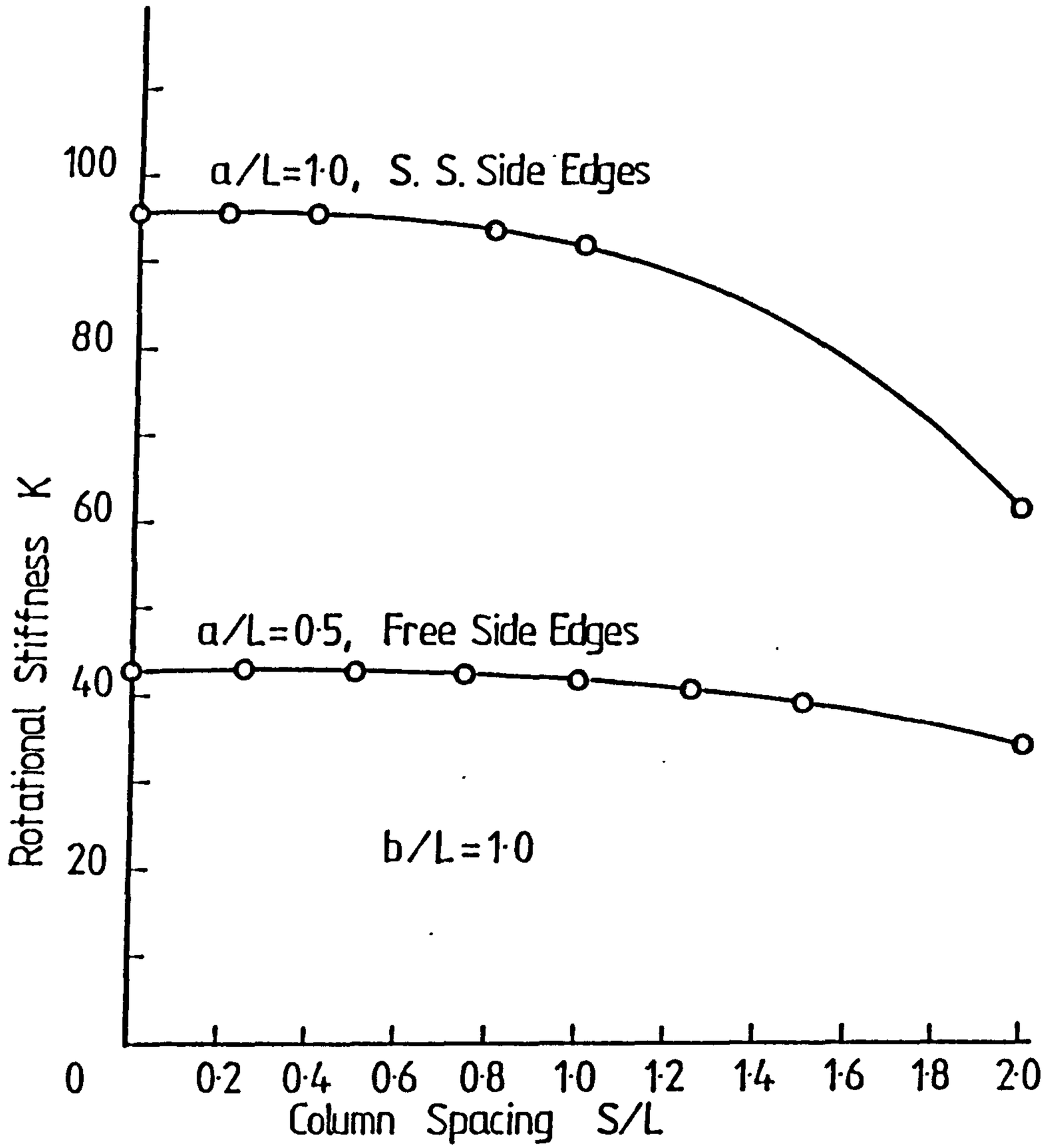

Fig. 8.7 Influence of Column Spacing on Rotational Stiffness of Slab Point-Supported at the Exterior Edges

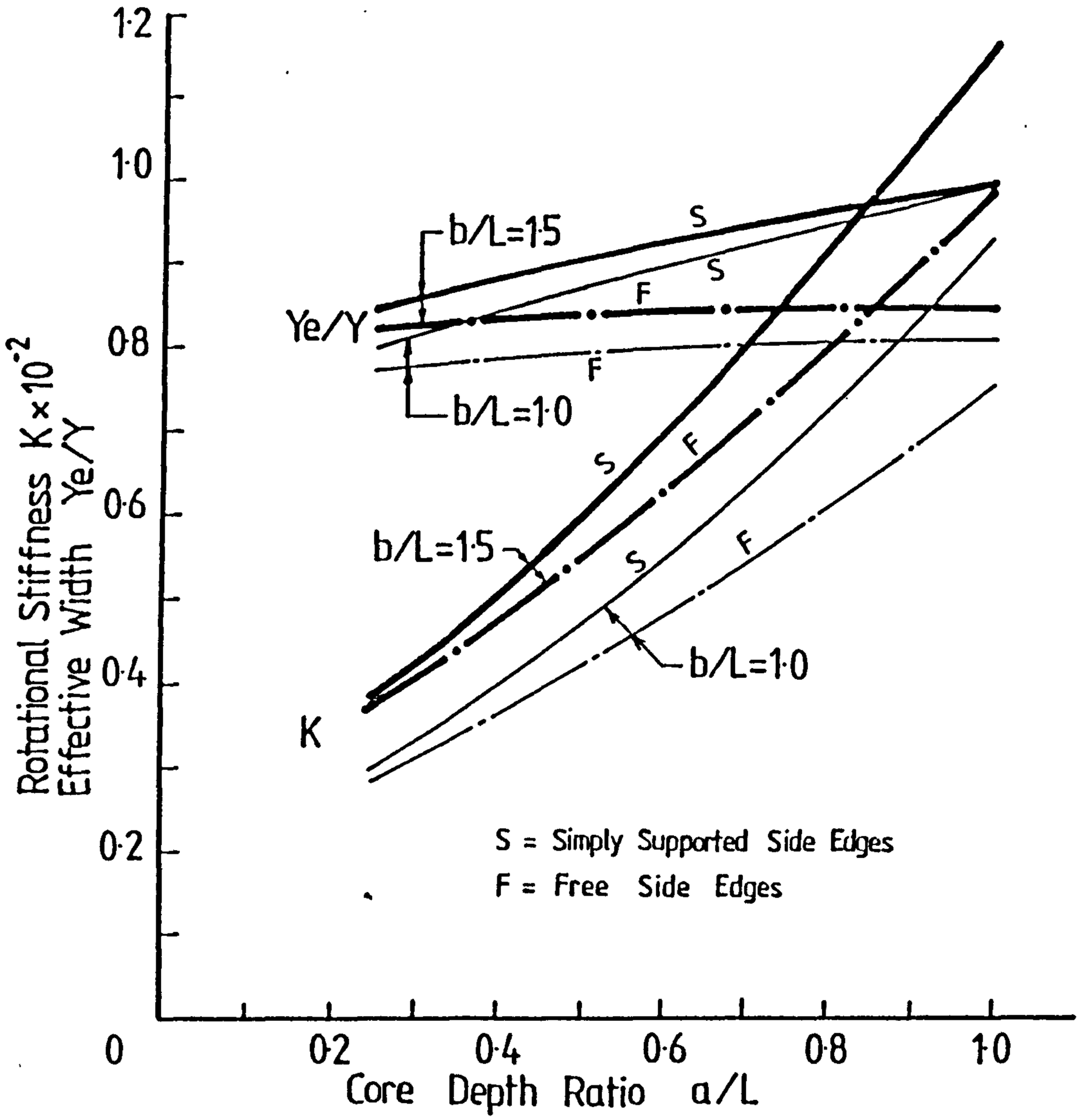

Fig. 8.8 Rotational Stiffness and Effective Width of Slab Simply Supported at the Exterior Edges

CHAPTER 9

EFFECTIVE WIDTH OF SLAB IN FLAT PLATE STRUCTURES

9.1 INTRODUCTION

A common form of framing for multi-storeyed office buildings consists of a regular arrangement of columns connected by flat plate floor slabs. Under lateral loading, the column-flat plate frame deforms with a deflected shape at the column line similar to that produced by a conventional column-beam frame, in which points of contraflexure generally occur in both beam and column segments (Fig. 9.1). The lateral load analysis for the column-flat plate frame may be carried out using any of the available methods of frame analysis by assuming an 'effective width' of slab to act as a beam in an equivalent frame. Since the lateral stiffness of the frame system depends largely upon the flexural stiffness of the beam members to develop the necessary 'portal action', it is important that the effective width of slab be assessed, reasonably accurately, for the frame analysis.

The effective width may be established by equating the rotational stiffness of the slab to that of an equivalent beam connected to the same column in a typical frame panel bounded by the assumed lines of contraflexure (Fig. 9.2). The rotational stiffness of the slab is influenced by the stiffening effect of the finite sized column and by the restraint along the slab edges. The amount of stiffening produced by the column depends on the axial stiffness of the column in relation to the bending stiffness of the slab, but in most practical cases, the relative column stiffness is very high, and so the column may be considered axially rigid.

In this Chapter the influence coefficient technique is employed for the analysis of column-slab interaction, and is shown to be particularly efficient for this class of problem. Values of slab stiffness and effective width, obtained by the method for a wide range of column-slab

geometrical proportions and slab boundary conditions, are presented, and shown to be accurate by comparing with results obtained by the finite element method.

9.2 METHOD OF ANALYSIS

The slab in a regular flat plate structure deflects with transverse lines of inflexion (or anti-symmetry) and longitudinal lines of zero slope (or symmetry lines) between columns (Fig. 9.3). A typical interior column-slab panel isolated by these two sets of lines is shown in Fig. 9.4. The slab panel may be considered as simply supported at the two transverse edges corresponding to the inflexion lines, for the purpose of analysis.

The moment applied by a column is transferred to the slab at points along the column periphery to which the slab is connected, in the form of continuously distributed unknown forces. These unknown forces are distributed in such a manner that the displacements induced in the slab are the same as the displacements of the column at the column-slab connection. The actual continuous system of forces transferred from column to slab cannot be exactly determined, but its effective action can be approximated to any reasonable degree of accuracy by an equivalent discretised force system consisting of point forces and moments acting at a discrete number of nodes on the column boundary (Fig. 9.5). The slab displacements (deflection and slopes) at each node can be written in terms of the unknown discrete nodal forces through the use of influence coefficients which were derived in Chapter 2. When these are equated to the known displacements produced by a unit rotation of the rigid column cross-section, the unknown nodal forces can be determined, leading to the calculation of the column moment M, which is numerically equal to the rotational stiffness of the slab. For convenience, the rotational slab stiffness may be expressed in the form of a non-dimensional stiffness factor K, given by

$$K = \frac{M}{D}$$

where D is the plate flexural rigidity. By equating the rotational stiffness of the slab to that of an equivalent beam of uniform width, having a depth equal to the slab thickness, the effective width B_e of the slab may be shown to be given, in non-dimensional form, by

$$\frac{B_e}{B} = \frac{K}{12(1-\nu^2)} \frac{A}{B} (1 - \frac{U}{A})^3 \qquad (9.1)$$

where A is the longitudinal slab length (i.e. in direction of rotation), or slab span between column centres, B is the transverse slab width, U is the column depth, and ν is the Poisson's ratio.

The displacements and stress resultants induced in the slab by unit column rotation can be calculated at any point by substituting the calculated nodal forces into the displacement and stress resultant influence functions for the slab (cf. Section 2.5.2).

The displacement pattern in the slab panel is symmetric about the x-axis and anti-symmetric about the y-axis (Fig. 9.4). The actual analysis of the slab can therefore be confined to a typical quadrant of the panel, in order to reduce the computational effort.

9.3 CONVERGENCE STUDY

The accuracy of the influence coefficient solution for the column-slab interaction problem is influenced by convergence errors introduced by the truncation of the infinite harmonic series in the evaluation of influence coefficients, and by the discretisation of the continuous interaction between column and slab. Since the series truncation leads to smaller influence coefficients and hence a stiffer slab, while the discretisation of the continuous column-slab connection results in a more flexible column connection, the truncation errors and discretisation

errors compensate to a certain extent. By having a proper balance between the number of series terms taken for the influence coefficient calculation and the number of nodes used to represent the column connection, accurate results may be obtained with less effort than would be required to obtain a truly convergent solution.

The convergence study described in Chapter 4 (Section 4.2) has shown that by taking between 20 and 40 terms of the infinite series for the evaluation of influence coefficients, sufficiently accurate solutions for shear wall-slab problems may be obtained using a very small number of discrete nodes (not more than 8 nodes) to represent the wall connection. Since a column generally is much smaller than a shear wall in cross-sectional dimensions, the number of nodes required to represent adequately its connection to the slab should be very much smaller than that required for the shear wall. A convergence study has been carried out to indicate the practical degree of refinement generally required in the evaluation of influence coefficients and in the representation of the column connection.

Table 9.1 shows values of the slab stiffness factor K and effective width B_e/B for a square slab with two relative column sizes U/A of 0.1 and 0.2, obtained using various numbers of nodes to represent the column-slab connection. Three force components P^i, M_x^i and M_y^i were used at each node to represent the interaction forces. The influence coefficients in each case were evaluated using 40 terms of the infinite series. The results obtained from finite element analyses using the element RB12 and discretisations of the slab quadrant into 36 and 144 elements (Fig. 9.6) have been included to provide a measure of the relative accuracy of the influence coefficient results. The percentage discrepancies between the influence coefficient results and the accurate finite element results are shown in brackets beneath the values of B_e/B. The discrepancy between the coarse mesh and fine mesh finite element results have also been shown, to give an idea of the

accuracy of the finite element results. It is seen that for the case of U/A = 0.1, the effective width obtained by the influence coefficient solution agrees best with the finite element result (-0.08% difference), when only one corner node is used to represent the column connection and 40 series terms are used to evaluate the influence coefficients. When more nodes are used, the results appear to depart further from the finite element results, because truncation errors show up more as the discretisation errors are reduced. For the case of U/A = 0.2, which represents a relatively large column, it appears that using one corner node plus a second node placed half way between the column corner and column axis, for the column representation, gives a result which agrees best with the finite element solution (-0.34% difference). When using one corner node alone for this case, the influence coefficient result is approximately 3½% below the finite element result, but is still reasonably accurate for practical purpose.

Having established that at most two nodes would be sufficient for the column representation, the convergence study is extended to indicate any possible further reduction in the computational effort by reducing the number of series terms for the influence coefficients and by omitting the transverse moment component M_y^i from the discrete nodal force vector. Table 9.2 shows the effective width values obtained using various numbers of series terms in combination with one and two column nodes with and without the moment M_y^i in the force vector. The finite element results have again been used to measure the relative accuracies of the various influence coefficient results. It is seen from the results that the omission of the moment M_y^i from the nodal force vector reduces the calculated effective width by less than 2%, whereas the reduction in the number of series terms from 40 to 20 terms increases the calculated effective width by less than 3%, in all cases. Increasing the number of series

terms from 40 to 50 terms reduces the calculated effective width less than 1%. Within the range of 20 to 40 series terms, the effective widths calculated with various degrees of refinement in the column representation are all within 5% of the accurate finite element result. With 10 series terms, the effective widths are seen to be significantly overestimated, but in the worst case, the discrepancy is still less than 10%. It appears that for practical purposes, the effective slab width may be calculated economically, to an acceptable degree of accuracy, using the influence coefficient technique with just one corner node and two force components, P^i and M_x^i, to represent the rigid column connection to the slab, and taking 20 terms of the infinite series to evaluate the influence coefficients. With exceptionally large columns (U/A greater than 0.2), it may be desirable to include an additional node to provide a better representation of the column connection.

9.4 TABLES FOR EVALUATING THE EFFECTIVE WIDTH

The remarkable economy in computation, resulting from the use of just one node to represent the column-slab connection in an influence coefficient solution, has made possible the calculation of effective widths for a wide range of parameters, at a fraction of the cost of computing one of the finite element results. Values of the slab stiffness K, and the effective width B_e/B, have been obtained for slabs with aspect ratios B/A, ranging from 0.50 to 2.0, and with column relative sizes, U/A and V/A, ranging from 0 to 0.2. Four standard types of edge support have been considered for the longitudinal slab edges, continuous, free, simply supported and clamped edges. To ensure that best overall results were obtained, the transverse moment component M_y^i was included in the nodal force vector, and 40 series terms were used for the evaluation of influence coefficients throughout the computation. The numerical results obtained are presented

in Tables 9.3(a-d) to 9.7(a-d). These should enable the rapid evaluation of the effective slab width or slab stiffness in a practical situation.

As a matter of interest, the computation of the effective widths for 121 cases shown in each table took about 42 seconds on the ICL 1904S computer. In contrast, the computation for a single case, by the finite element method, using a 12 x 12 mesh, takes about 52 seconds.

9.5 DISCUSSION OF RESULTS

9.5.1 EFFECT OF SLAB WIDTH AND LONGITUDINAL EDGE SUPPORT

Fig. 9.7 shows the variation of effective width B_e/A with slab width B/A for slabs supported in various ways along the longitudinal edges ($y = \pm B/2$), and connected to square columns with a constant relative dimension U/A of 0.2. It is seen from the results that the effective width B_e/A is virtually unaffected by the slab width and hence the edge supports when B/A is larger than 1.5. When the slab width B/A is reduced below a value of 0.75, the effective widths for the slabs with simply supported and clamped longitudinal edges increase rapidly due to the restraining effect of the longitudinal edges. The effective widths for the slabs with continuous and free longitudinal edges, on the other hand, decrease with the slab width. As can be seen from the single curve drawn, the results for slabs with continuous and free edges are virtually identical, even with very narrow slab widths, where longitudinal edge effects are expected to be more strongly felt. It would appear from this observation that the slab models frequently tested with free longitudinal edges[15,20] do in fact represent adequately the prototype interior slab panel, although it is traditionally believed that this may not be so.

9.5.2 EFFECT OF RELATIVE COLUMN WIDTH

The numerical results in Tables 9.3(a-d) to 9.7(a-d)

indicate clearly that irrespective of the type of longitudinal edge support and slab width, the effective width B_e/B increases significantly with the relative column width V/A, when the relative column depth U/A remains constant. This trend of results is to be expected, since increasing the column width will clearly stiffen the slab more against bending. The results obtained by Pecknold,[18] and Allen and Darvall,[19,20] however, do not indicate this trend. Pecknold found that varying the column width from half to two times the column depth changes the effective width less than 2% and according to Allen and Darvall's results (Tables 1 to 4, in Ref. 20), increasing the relative column width V/A, in most cases, results in a significant reduction in the effective width B_e/B, which is physically unreasonable, and can only be explained by defects in the method of solution used by these investigators.

In Fig. 9.8 are shown the results obtained by Allen and Darvall and by the author, showing the variation of the effective width B_e/B with the relative column width V/A, for continuous slabs with three aspect ratios B/A and a constant relative column depth U/A of 0.08. The results from accurate finite element analyses, using a 12 x 12 mesh over a quarter panel, have been included to establish the relative accuracies of the other results. It is seen from the curves that the contradictory trend of Allen and Darvall's results is due to a serious overestimation of the effective width when the relative column width V/A is small. For V/A = 0.03, Allen and Darvall's results appear to overestimate the effective width by 40 to 50% depending on the slab aspect ratio. On the other hand, the author's results obtained by the influence coefficient method are within about 4% of the accurate finite element results.

9.5.3 EFFECT OF RELATIVE COLUMN DEPTH

The numerical results presented in Tables 9.3(a-d) to 9.7(a-d) indicate that with any constant value of relative

column width V/A, an increase in the relative column depth U/A from zero up to a certain limit, has the effect of increasing the effective width B_e/B for all slabs. The rate at which B_e/B increases with U/A gradually diminishes until beyond a certain limit of U/A, which varies according to the column-slab proportions from 0.1 to 0.3, the effective width B_e/B begins to decrease with further increase in U/A, but the slab stiffness continues to increase. The influence of relative column depth on the effective width is better illustrated in Fig. 9.9, which shows the variation of B_e/B with U/A, for three slab aspect ratios B/A of 0.5, 1.0 and 2.0, and a constant relative column width V/A of 0.08. The same Figure also shows the comparison between the influence coefficient results and Allen and Darvall's results and the accurate finite element results included as a reference. Allen and Darvall's results appear to overestimate the effective width progressively more as the relative column depth U/A increases beyond about 0.06. With U/A = 0.12, these results differ from the finite element results by 18 to 22%, depending on the slab aspect ratio. The influence coefficient results, on the other hand, are within 2% of the finite element results.

Since the influence coefficient method works equally well for any wall or column configuration, results have been obtained by the method to illustrate the influence of the relative column depth U/A over the complete range of U/A from zero to unity, thus covering both column and shear wall cases. These results are shown graphically in Fig. 9.10, (a) and (b), for continuous and simply supported slabs with aspect ratios of 1.0 and 0.5 and a relative column width V/A of 0.05. The influence coefficient solutions used between one and five nodes, depending on the relative column depth, to represent the column or wall connection, and used 40 series terms to evaluate the influence coefficients. Accurate finite element results for the case of continuous slabs have again been included to verify the general accuracy of the influence coefficient results.

The curves illustrate clearly the comment made earlier that the effective width B_e/B increases with the relative column depth U/A only up to certain limit, after which it decreases with further increase in U/A. The second part of the curve, which shows B_e/B decreasing with larger values of U/A, is consistent with the trend of results for the shear wall-slab problem. The influence of longitudinal edge restraint on the effective width for the narrow slab (Fig. 9.10(b)) is seen to vary considerably over the range of ratios U/A. The finite element results again confirm the remarkable accuracy of the influence coefficient results and the versatility of the solution technique.

9.6 COMPARISON OF THEORETICAL RESULTS FROM VARIOUS INVESTIGATIONS

The results for the effective width of interior slab panels with square columns, obtained by the influence coefficient method, are compared in Fig. 9.11 with those from an accurace finite element analysis and from published sources. Although expressed differently in the original sources, the results of other investigators have all been reduced to the same form as the influence coefficient results for direct comparison. Thus Pecknold's effective width results,[18] which were originally defined in terms of an equivalent beam connected directly to the column axis without rigid arm effects, have been reduced by multiplying by a factor $(1-U/A)^3/(1-\nu^2)$. Allen and Darvall's effective width values[20] were expressed in the same form except for having a zero value of Poisson's ratio. The reduction here required only a multiplication by the factor $1/(1-\nu^2)$. Mehrain and Aalami's finite element results[17] were given in terms of the rotational stiffness K. The corresponding effective widths required for comparison were simply calculated using equation (9.1).

The results obtained by the various methods are seen to follow a very similar general trend which indicates

that the effective width B_e/B increases substantially as the relative column size (U/A or V/A) is increased. However, significant differences can be observed between corresponding values of the effective width obtained from the approximate and more accurate methods. The influence coefficient results agree very well with the finite element results obtained by the author, and by Mehrain and Aalami. The results obtained by Pecknold and by Allen and Darvall, on the other hand, are considerably higher than the finite element results, and appear to over-estimate the effective widths by 10 to 15% when the relative column dimension U/A is larger than 0.05.

The results presented by Khan and Sbarounis[15] have not been included in Fig. 9.11 for comparison, since they were obtained mainly by experiment. In any case, when compared with the accurate finite element results, after reduction to the same form, the effective widths obtained by Khan and Sbarounis were found to have been seriously under-estimated, especially with the larger column sizes, where discrepancies of up to 55% were observed.

9.7 COMPARISON OF RESULTS OBTAINED BY INFLUENCE COEFFICIENT METHOD AND FINITE ELEMENT METHOD

(a) Effective Width

The accuracy of the influence coefficient method in calculating the effective slab width has been shown in the previous sections, with particular reference to results obtained for slabs with continuous longitudinal edges. In order to verify the general accuracy of the method when applied to slabs with any other longitudinal edge supports, the effective width values obtained by the influence coefficient method for a square slab with the four standard longitudinal boundary conditions, viz., continuous, free, simply supported and clamped edges, are compared in Table 9.8, with the corresponding results obtained by the finite element method. A square column with a relative side

dimension U/A of 0.1 is considered for each case. The influence coefficient solution used one corner node with three force components to represent the column connection, and 40 series terms to evaluate the influence coefficients. The finite element solution used the element RB12, and a 12 x 12 variable mesh discretisation (Fig. 9.6). In both methods of solution, the plate analysis was performed on a typical slab quadrant. It can be seen from the tabulated results that the effective widths for the four cases have been calculated by the influence coefficient method to practically the same order of accuracy. In each case, the influence coefficient result is almost in exact agreement with the finite element result.

(b) Deflection

Fig. 9.12(a) shows, more convincingly, the remarkable accuracy of the influence coefficient solution, by comparing the deflections at a transverse slab section calculated by the two different methods, for the four cases considered. The agreement between the two sets of results is so close that the minute discrepancies are undiscernable on the curves plotted. The comparison of deflections for longitudinal slab sections has shown equally good agreement between the two methods, in all four cases. The results for the more usual case, i.e. the continuous slab, are shown graphically in Fig. 9.12(b) for illustration.

(c) Stress Resultants

The accuracy of the influence coefficient method in the evaluation of slab moments induced by the column rotation is illustrated in Fig. 9.13(a-c), by comparing the bending moments at a number of slab sections, evaluated by the method, with the results from an accurate finite element analysis. The influence coefficient results shown in the Figures were obtained using two nodes for the column representation and 40 series terms for the influence coefficients. The results obtained using one node are slightly less accurate (about 10% lower) than these

results, in respect of bending moments evaluated at points close to the column, and have not been considered for comparison with the finite element results. The finite element results were obtained with the usual 12 x 12 mesh discretisation. The case considered for this illustration refers to a square slab with longitudinal continuous edges, with a square column of relative dimension U/A of 0.1.

It is seen from the Figures that, very good agreement is generally obtained between the influence coefficient and finite element results. At the two sections located at y/b = 0.2 and 0.4, the results obtained by the two methods are almost indistinguishable. At the section located at y/b = 0, the peak values of the bending moments M_x and M_y obtained by the influence coefficient method are slightly lower than the finite element values, but are sufficiently accurate for practical purpose. If required, more accurate results may be obtained by using a higher level of refinement in the solution, at the expense of greater computational effort.

9.8 COMPARISON BETWEEN INFLUENCE COEFFICIENT RESULTS AND EXPERIMENTAL RESULTS

A series of tests have been performed by Allen and Darvall[20] on steel plate models to evaluate the effective width for slabs with various aspect ratios and relative column sizes. These experimental values of the effective width are compared with the results obtained by the influence coefficient method in Fig. 9.14. The influence coefficient results were obtained using one corner node for the column representation, and 40 series terms for the influence coefficients. Poisson's ratio for steel was assumed as 0.3 in the calculations. The longitudinal slab edges were considered as free edges in the analysis.

It can be seen from the Figure that reasonably good agreement is generally obtained between the theoretical and experimental results.

9.9 IMPLICATION OF RESULTS

A number of building Codes (for example, ACI 318-71[56]) permit the entire slab width between bay centre lines to be considered effective in an equivalent frame analysis for the column-flat plate structure. As is evident from the results presented in the preceding sections, the effective slab width, is generally less than the full slab width and varies according to various structural parameters. While for a very narrow slab the effective width may be close to the full slab width, for a wide slab the effective width is only a fraction of the entire slab width. In the latter case, the assumption of an effective full slab width will result in a serious over-estimation of the stiffness of the equivalent beam or frame. In order to illustrate this consequence, the lateral deflection of a practical flat plate building calculated assuming a full slab width for the equivalent frame is compared with that calculated assuming an effective width given by the design Tables presented in Section 9.4. The building considered (Fig. 9.15(a)) is a 20-storey, four-bay-deep office building with a 3.66 m (12 ft) floor height. Columns are 0.61 m (2 ft) square throughout the height of the building and are arranged in a 6.1m x 6.1m (20 ft x 20 ft) grid in plan. The floor slabs are of 254 mm (10 in.) thickness. A uniform static wind pressure of 1.2 kN/m^2 (25 lb/ft^2) is assumed acting on the building. Young's modulus and Poisson's ratio for concrete are assumed as 2.07×10^7 kN/m^2 (4.32×10^8 lb/ft^2) and 0.15 respectively. The approximate method of lateral load analysis for multi-storey multi-bay frames presented by Chan, Heidebrecht and Tso[80] is used to calculate the frame deflections. This simple hand method has been shown to give accurate results when compared with the stiffness matrix method.

The calculated lateral frame deflections at various levels for the two cases are compared in Fig. 9.15(b). It is seen from the results that by assuming the full slab width as effective, the effective width and stiffness of

the equivalent beam are over-estimated by 91% for the building in the example, and this results in the deflection at the top of the building being under-estimated by 34%.

9.10 CONCLUSIONS

The influence coefficient technique has been shown to be an efficient method for evaluating the slab stiffness or effective width required for the lateral load analysis of flat plate structures. Sufficiently accurate results can be obtained by the method, using a single node with two force components (2 unknowns) to represent the column-slab interaction, and taking 20 terms of the infinite series to evaluate the influence coefficients.

Values of the slab stiffness and effective width for a wide range of variables have been obtained by the method. The accuracy of the results have been confirmed by comparing with accurate finite element results and with available experimental data.

The assumption of an effective full slab width, allowed by some building Codes, over-estimates considerably the effective width, and hence the lateral stiffness of the building frame, in most cases.

TABLE 9.1 SLAB STIFFNESS AND EFFECTIVE WIDTH VALUES FOR A SQUARE SLAB, OBTAINED USING VARIOUS NUMBER OF NODES IN THE COLUMN REPRESENTATION.

(40 series terms used in influence coefficient. Figure in brackets refers to percentsge difference in relation to 12 x 12 mesh finite element result)

U/A	Rotational Stiffness and Effective Width	Influence Coefficient Solution					Finite Elem. Solution	
		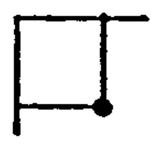 1	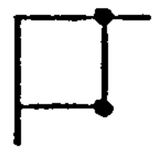 2	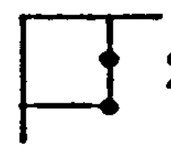 2	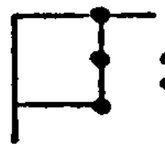 3	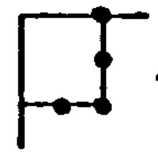 4	6 x 6 Mesh	12 x 12 Mesh
0.1	K	8.4080	8.4988	8.5276	8.5502	8.5528	8.4730	8.4160
	B_e/B	0.5226 (-0.08)	0.5282 (0.99)	0.5300 (1.34)	0.5314 (1.61)	0.5316 (1.64)	0.5266 (0.69)	0.5230
0.2	K	14.3432	14.6524	14.8070	14.9094	14.9254	14.9310	14.8574
	B_e/B	0.6261 (-3.45)	0.6396 (-1.37)	0.6463 (-0.34)	0.6508 (0.34)	0.6515 (0.46)	0.6517 (0.49)	0.6485

TABLE 9.2 EFFECTIVE WIDTH VALUES B_e/B FOR A SQUARE SLAB, OBTAINED USING VARIOUS NUMBER OF NODES, FORCE COMPONENTS AND SERIES TERMS IN THE SOLUTION

(Figure in brackets refers to percentage difference in relation to finite element solution)

U/A	No. of Nodes	Nodal Force Components	Influence Coefficient Solution					Finite Element Solution
			Number of Series Terms					
			10	20	30	40	50	
0.1	1	P^i, M_x^i	0.5594 (6.97)	0.5305 (1.43)	0.5207 (-0.44)	0.5155 (-1.43)	0.5121 (-2.08)	0.5230
		P^i, M_x^i, M_y^i	0.5695 (8.89)	0.5388 (3.02)	0.5282 (0.99)	0.5226 (-0.08)	0.5189 (-0.78)	
	2	P^i, M_x^i	0.5675 (8.51)	0.5391 (3.08)	0.5307 (1.47)	0.5263 (0.63)	0.5234 (0.08)	
		P^i, M_x^i, M_y^i	0.5706 (9.10)	0.5430 (3.82)	0.5345 (2.20)	0.5300 (1.34)	0.5270 (0.76)	
0.2	1	P^i, M_x^i	0.6655 (2.62)	0.6356 (-1.99)	0.6241 (-3.76)	0.6176 (-4.76)	0.6133 (-5.43)	0.6485
		P^i, M_x^i, M_y^i	0.6775 (4.47)	0.6455 (-0.46)	0.6331 (-2.37)	0.6261 (-3.45)	0.6213 (-4.19)	
	2	P^i, M_x^i	0.6826 (5.26)	0.6571 (1.33)	0.6469 (-0.25)	0.6408 (1.19)	0.6366 (-1.84)	
		P^i, M_x^i, M_y^i	0.6894 (6.31)	0.6634 (2.30)	0.6527 (0.65)	0.6463 (-0.34)	0.6419 (-1.02)	

TABLE 9.3(a) ROTATIONAL STIFFNESS AND EFFECTIVE WIDTH FOR SLAB WITH ASPECT RATIO OF 0.5 AND SIMPLY SUPPORTED/ CONTINUOUS EDGES

SLAB ROTATIONAL STIFFNESS FACTOR K
SLAB ASPECT RATIO B/A = 0.5000
S. SUPPORTED / CONTINUOUS EDGES

V/A U/A	C.COO	C.02C	C.040	0.06C	0.080	0.100	0.120	0.140	0.160	0.180	0.200
C.000	2.685	3.084	3.363	3.55C	3.690	3.801	3.891	3.963	4.021	4.066	4.099
0.02C	3.407	3.88C	4.129	4.341	4.520	4.671	4.798	4.903	4.988	5.054	5.104
C.040	4.177	4.429	4.656	4.852	5.031	5.189	5.327	5.443	5.540	5.616	5.674
C.060	4.733	4.969	5.183	5.37C	5.542	5.699	5.840	5.962	6.065	6.147	6.210
C.080	5.269	5.495	5.7C4	5.885	6.051	6.204	6.343	6.466	6.571	6.656	6.721
C.100	5.797	6.020	6.229	6.4C8	6.571	6.720	6.856	6.977	7.081	7.166	7.231
C.120	6.324	6.550	6.761	6.941	7.103	7.249	7.382	7.501	7.603	7.687	7.751
C.140	6.855	7.088	7.3C5	7.488	7.650	7.795	7.927	8.043	8.143	8.225	8.288
C.160	7.399	7.646	7.869	8.056	8.220	8.367	8.497	8.612	8.710	8.791	8.853
C.180	7.971	8.234	8.468	8.661	8.829	8.978	9.109	9.224	9.322	9.402	9.463
C.200	8.582	8.862	9.111	9.314	9.489	9.642	9.777	9.893	9.992	10.072	10.132

SLAB EFFECTIVE WIDTH Be/B
SLAB ASPECT RATIO B/A = 0.5000
S. SUPPORTED / CONTINUOLS EDGES

V/A U/A	C.COO	C.02C	C.040	0.06C	0.080	0.100	0.120	0.140	0.160	0.180	0.200
C.CCO	C.458	C.526	C.573	0.605	0.629	0.648	0.663	0.676	0.686	0.693	0.699
0.02C	C.579	C.623	C.663	0.697	0.725	0.750	0.770	0.787	0.800	0.811	0.819
C.040	C.630	C.668	C.7C2	0.732	0.759	0.783	0.804	0.821	0.836	0.847	0.856
C.060	C.670	C.704	C.734	0.76C	0.785	0.807	0.827	0.844	0.859	0.871	0.879
C.080	C.699	C.730	C.757	0.781	0.803	0.824	0.842	0.859	0.872	0.884	0.892
C.1CO	C.721	C.748	C.774	0.797	0.817	0.835	0.852	0.867	0.880	0.891	0.899
C.12C	C.735	C.761	C.786	0.807	0.825	0.842	0.858	0.872	0.883	0.893	0.901
C.140	C.743	C.769	C.792	0.812	0.830	0.845	0.860	0.872	0.883	0.892	0.899
C.160	C.748	C.773	C.795	0.814	0.831	0.846	0.859	0.870	0.880	0.888	0.895
C.180	C.749	C.774	C.796	0.814	0.830	0.844	0.856	0.867	0.876	0.884	0.890
C.200	C.749	C.774	C.795	0.813	0.828	0.842	0.853	0.864	0.872	0.879	0.885

TABLE 9.3(b) ROTATIONAL STIFFNESS AND EFFECTIVE WIDTH FOR SLAB WITH ASPECT RATIO OF 0.5 AND SIMPLY SUPPORTED/FREE EDGES

SLAB ROTATIONAL STIFFNESS FACTOR K
SLAB ASPECT RATIO B/A = 0.5000
S. SUPPORTED / FREE EDGES

V/A U/A	C.000	C.020	C.040	0.060	0.080	0.100	0.120	0.140	0.160	0.180	0.200
C.000	2.679	3.076	3.355	3.541	3.681	3.792	3.883	3.956	4.015	4.061	4.095
C.020	3.597	3.868	4.116	4.328	4.507	4.659	4.786	4.892	4.979	5.047	5.098
C.040	4.164	4.414	4.640	4.836	5.015	5.174	5.313	5.431	5.530	5.608	5.666
C.060	4.716	4.951	5.164	5.351	5.523	5.682	5.824	5.949	6.054	6.138	6.202
C.080	5.247	5.474	5.682	5.864	6.031	6.185	6.327	6.452	6.559	6.647	6.713
C.100	5.773	5.995	6.204	6.384	6.548	6.699	6.838	6.962	7.068	7.156	7.223
C.120	6.297	6.522	6.734	6.915	7.078	7.228	7.364	7.485	7.591	7.677	7.743
C.140	6.825	7.058	7.275	7.459	7.624	7.773	7.907	8.027	8.131	8.216	8.281
C.160	7.366	7.613	7.837	8.026	8.193	8.343	8.478	8.597	8.699	8.783	8.846
C.180	7.935	8.198	8.433	8.629	8.801	8.954	9.090	9.209	9.311	9.394	9.457
C.200	8.544	8.825	9.075	9.280	9.459	9.618	9.757	9.879	9.982	10.065	10.127

SLAB EFFECTIVE WIDTH Be/B
SLAB ASPECT RATIO B/A = 0.5000
S. SUPPORTED / FREE EDGES

V/A U/A	C.000	C.020	C.040	0.060	0.080	0.100	0.120	0.140	0.160	0.180	0.200
C.000	C.457	C.524	C.572	0.604	0.628	0.647	0.662	0.675	0.685	0.692	0.698
C.020	C.577	C.621	C.661	0.694	0.723	0.748	0.768	0.785	0.799	0.810	0.818
C.040	C.628	C.666	0.700	0.730	0.756	0.781	0.801	0.819	0.834	0.846	0.855
C.060	C.668	C.701	C.731	0.758	0.782	0.805	0.825	0.842	0.857	0.869	0.878
C.080	C.697	C.727	C.754	0.779	0.801	0.821	0.840	0.857	0.871	0.882	0.891
C.100	C.718	C.745	C.771	0.794	0.814	0.833	0.850	0.865	0.879	0.889	0.898
C.120	C.732	C.758	C.782	0.803	0.822	0.840	0.856	0.870	0.882	0.892	0.900
C.140	C.740	C.765	C.789	0.809	0.827	0.843	0.858	0.871	0.882	0.891	0.898
C.160	C.744	C.769	C.792	0.811	0.828	0.843	0.857	0.869	0.879	0.888	0.894
C.180	C.746	C.771	C.793	0.811	0.827	0.842	0.855	0.866	0.875	0.883	0.889
0.200	C.746	C.770	C.792	0.810	0.826	0.840	0.852	0.862	0.871	0.879	0.884

TABLE 9.3(c) ROTATIONAL STIFFNESS AND EFFECTIVE WIDTH FOR SLAB WITH ASPECT RATIO OF 0.5 AND SIMPLY SUPPORTED/SIMPLY SUPPORTED EDGES

SLAB ROTATIONAL STIFFNESS FACTOR K
SLAB ASPECT RATIO B/A = 0.5000
S. SUPPORTED / S. SUPPORTED EDGES

V/A / U/A	0.000	0.020	0.040	0.060	0.080	0.100	0.120	0.140	0.160	0.180	0.200
0.000	3.196	3.778	4.215	4.527	4.781	5.002	5.204	5.393	5.574	5.751	5.929
0.020	4.588	5.043	5.486	5.892	6.268	6.620	6.957	7.284	7.608	7.935	8.270
0.040	5.537	5.994	6.438	6.859	7.276	7.692	8.105	8.521	8.944	9.379	9.834
0.060	6.527	6.992	7.454	7.899	8.353	8.822	9.306	9.806	10.329	10.879	11.466
0.080	7.534	8.016	8.506	8.986	9.480	10.001	10.550	11.133	11.754	12.421	13.145
0.100	8.573	9.078	9.606	10.128	10.670	11.246	11.863	12.529	13.250	14.038	14.907
0.120	9.645	10.180	10.754	11.323	11.919	12.557	13.247	14.000	14.826	15.740	16.762
0.140	10.750	11.327	11.948	12.571	13.226	13.932	14.701	15.548	16.486	17.534	18.717
0.160	11.902	12.530	13.204	13.884	14.605	15.386	16.243	17.191	18.250	19.443	20.801
0.180	13.123	13.807	14.540	15.285	16.080	16.944	17.897	18.958	20.149	21.501	23.049
0.200	14.435	15.171	15.971	16.789	17.664	18.621	19.679	20.863	22.200	23.723	25.479

SLAB EFFECTIVE WIDTH Be/B
SLAB ASPECT RATIO B/A = 0.5000
S. SUPPORTED / S. SUPPORTED EDGES

V/A / U/A	0.000	0.020	0.040	0.060	0.080	0.100	0.120	0.140	0.160	0.180	0.200
0.000	0.545	0.644	0.719	0.772	0.815	0.853	0.887	0.919	0.950	0.981	1.011
0.020	0.736	0.809	0.880	0.946	1.006	1.062	1.116	1.169	1.221	1.273	1.327
0.040	0.835	0.904	0.971	1.035	1.098	1.160	1.223	1.285	1.349	1.415	1.483
0.060	0.924	0.990	1.056	1.119	1.183	1.249	1.318	1.389	1.463	1.541	1.624
0.080	1.000	1.064	1.129	1.193	1.259	1.328	1.401	1.478	1.561	1.649	1.745
0.100	1.066	1.128	1.194	1.259	1.326	1.398	1.475	1.557	1.647	1.745	1.853
0.120	1.121	1.183	1.249	1.316	1.385	1.459	1.539	1.627	1.723	1.829	1.948
0.140	1.166	1.228	1.296	1.363	1.434	1.511	1.594	1.686	1.788	1.902	2.030
0.160	1.203	1.266	1.334	1.403	1.476	1.555	1.641	1.737	1.844	1.965	2.102
0.180	1.234	1.298	1.367	1.437	1.512	1.593	1.682	1.782	1.894	2.021	2.167
0.200	1.260	1.324	1.394	1.466	1.542	1.626	1.718	1.821	1.938	2.071	2.224

TABLE 9.3(d) ROTATIONAL STIFFNESS AND EFFECTIVE WIDTH FOR SLAB WITH ASPECT RATIO OF 0.5 AND SIMPLY SUPPORTED/CLAMPED EDGES

SLAB ROTATIONAL STIFFNESS FACTOR K
SLAB ASPECT RATIO B/A = 0.5000
S. SUPPORTED / CLAMPED EDGES

V/A U/A	0.000	0.020	0.040	0.060	0.080	0.100	0.120	0.140	0.160	0.180	0.200
0.000	3.480	4.182	4.722	5.115	5.439	5.723	5.983	6.227	6.461	6.691	6.919
0.020	5.192	5.782	6.370	6.922	7.441	7.935	8.412	8.881	9.348	9.823	10.312
0.040	6.432	7.055	7.675	8.275	8.883	9.498	10.120	10.754	11.407	12.086	12.804
0.060	7.785	8.450	9.127	9.796	10.493	11.226	11.996	12.808	13.668	14.588	15.584
0.080	9.220	9.939	10.693	11.448	12.246	13.103	14.027	15.025	16.110	17.298	18.611
0.100	10.754	11.538	12.385	13.245	14.160	15.156	16.247	17.449	18.780	20.264	21.936
0.120	12.388	13.250	14.204	15.182	16.232	17.384	18.661	20.086	21.686	23.497	25.567
0.140	14.117	15.076	16.147	17.256	18.457	19.784	21.267	22.938	24.835	27.006	29.516
0.160	15.964	17.036	18.233	19.488	20.856	22.379	24.093	26.038	28.264	30.836	33.837
0.180	17.965	19.156	20.496	21.912	23.469	25.211	27.182	29.434	32.030	35.048	38.597
0.200	20.143	21.454	22.953	24.550	26.315	28.301	30.559	33.152	36.156	39.669	43.825

SLAB EFFECTIVE WIDTH Be/B
SLAB ASPECT RATIO B/A = 0.5000
S. SUPPORTED / CLAMPED EDGES

V/A U/A	0.000	0.020	0.040	0.060	0.080	0.100	0.120	0.140	0.160	0.180	0.200
0.000	0.593	0.713	0.805	0.872	0.927	0.976	1.020	1.062	1.102	1.141	1.180
0.020	0.833	0.928	1.022	1.111	1.194	1.273	1.350	1.425	1.500	1.576	1.655
0.040	0.970	1.064	1.158	1.248	1.340	1.433	1.527	1.622	1.721	1.823	1.932
0.060	1.102	1.197	1.293	1.387	1.486	1.590	1.699	1.814	1.936	2.066	2.207
0.080	1.224	1.320	1.420	1.520	1.626	1.740	1.862	1.995	2.139	2.297	2.471
0.100	1.337	1.434	1.539	1.646	1.760	1.884	2.020	2.169	2.334	2.519	2.727
0.120	1.439	1.540	1.650	1.764	1.886	2.020	2.168	2.334	2.520	2.730	2.971
0.140	1.531	1.635	1.751	1.871	2.002	2.146	2.306	2.488	2.693	2.929	3.201
0.160	1.613	1.722	1.843	1.969	2.108	2.262	2.435	2.631	2.856	3.116	3.419
0.180	1.689	1.801	1.927	2.060	2.206	2.370	2.555	2.767	3.011	3.295	3.629
0.200	1.758	1.873	2.004	2.143	2.297	2.471	2.668	2.894	3.156	3.463	3.826

TABLE 9.4(a) ROTATIONAL STIFFNESS AND EFFECTIVE WIDTH FOR SLAB WITH ASPECT RATIO OF 0.75 AND SIMPLY SUPPORTED/CONTINUOUS EDGES

SLAB ROTATIONAL STIFFNESS FACTOR K
SLAB ASPECT RATIO B/A = 0.7500
S. SUPPORTED / CONTINUOUS EDGES

V/A / U/A	0.000	0.020	0.040	0.060	0.080	0.100	0.120	0.140	0.160	0.180	0.200
0.000	2.867	3.326	3.656	3.881	4.056	4.200	4.322	4.427	4.518	4.598	4.668
0.020	3.941	4.270	4.577	4.846	5.081	5.287	5.469	5.630	5.773	5.900	6.012
0.040	4.427	4.939	5.228	5.487	5.730	5.955	6.161	6.349	6.519	6.672	6.808
0.060	5.311	5.611	5.893	6.148	6.392	6.625	6.846	7.052	7.242	7.417	7.574
0.080	5.979	6.275	6.558	6.814	7.059	7.297	7.526	7.744	7.948	8.138	8.312
0.100	6.643	6.944	7.233	7.494	7.743	7.985	8.220	8.446	8.661	8.863	9.050
0.120	7.320	7.622	7.921	8.189	8.445	8.693	8.933	9.166	9.389	9.600	9.797
0.140	7.99[illegible]	8.315	8.624	8.903	9.166	9.421	9.668	9.908	10.138	10.357	10.562
0.160	8.695	9.031	9.354	9.643	9.917	10.180	10.435	10.682	10.919	11.145	11.358
0.180	9.427	9.784	10.125	10.428	10.713	10.987	11.252	11.507	11.753	11.986	12.206
0.200	10.206	10.587	10.949	11.269	11.570	11.857	12.133	12.399	12.653	12.896	13.124

SLAB EFFECTIVE WIDTH Be/B
SLAB ASPECT RATIO B/A = 0.7500
S. SUPPORTED / CONTINUOUS EDGES

V/A / U/A	0.000	0.020	0.040	0.060	0.080	0.100	0.120	0.140	0.160	0.180	0.200
0.000	0.[illegible]26	0.378	0.416	0.441	0.461	0.477	0.491	0.503	0.514	0.523	0.531
0.020	0.422	0.457	0.490	0.518	0.544	0.566	0.585	0.602	0.618	0.631	0.643
0.040	0.469	0.497	0.526	0.552	0.576	0.599	0.620	0.638	0.656	0.671	0.685
0.060	0.501	0.530	0.556	0.580	0.603	0.625	0.646	0.666	0.684	0.700	0.715
0.080	0.529	0.555	0.580	0.603	0.625	0.646	0.666	0.685	0.704	0.720	0.736
0.100	0.551	0.575	0.599	0.621	0.642	0.662	0.681	0.700	0.718	0.734	0.750
0.120	0.567	0.590	0.614	0.634	0.654	0.673	0.692	0.710	0.727	0.744	0.759
0.140	0.57[illegible]	0.601	0.624	0.644	0.663	0.681	0.699	0.716	0.733	0.749	0.764
0.160	0.586	0.608	0.630	0.650	0.668	0.686	0.703	0.720	0.736	0.751	0.765
0.180	0.591	0.613	0.635	0.654	0.671	0.689	0.705	0.721	0.737	0.751	0.765
0.200	0.594	0.616	0.637	0.656	0.673	0.690	0.706	0.722	0.736	0.751	0.764

TABLE 9.4(b) ROTATIONAL STIFFNESS AND EFFECTIVE WIDTH FOR SLAB WITH ASPECT RATIO OF 0.75 AND SIMPLY SUPPORTED/FREE EDGES

SLAB ROTATIONAL STIFFNESS FACTOR K
SLAB ASPECT RATIO B/A = 0.7500
S. SUPPORTED / FREE EDGES

V/A U/A	C.000	C.020	C.040	0.060	0.080	0.100	0.120	0.140	0.160	0.180	0.200
C.000	2.359	3.316	3.644	3.868	4.042	4.185	4.307	4.412	4.504	4.584	4.654
C.020	3.927	4.253	4.558	4.825	5.059	5.264	5.445	5.606	5.749	5.877	5.990
C.040	4.608	4.918	5.204	5.462	5.703	5.926	6.131	6.318	6.489	6.642	6.780
C.060	5.286	5.584	5.863	6.116	6.358	6.590	6.810	7.016	7.206	7.381	7.540
C.080	5.949	6.242	6.522	6.776	7.019	7.255	7.484	7.701	7.906	8.097	8.273
0.100	6.611	6.904	7.190	7.449	7.696	7.937	8.171	8.397	8.613	8.816	9.004
C.120	7.276	7.575	7.871	8.138	8.391	8.638	8.878	9.111	9.335	9.547	9.746
C.140	7.947	8.260	8.567	8.844	9.106	9.359	9.606	9.846	10.077	10.298	10.505
C.160	8.636	8.969	9.289	9.577	9.849	10.111	10.366	10.613	10.852	11.081	11.296
C.180	9.361	9.715	10.052	10.354	10.638	10.911	11.175	11.432	11.679	11.916	12.139
C.200	10.132	10.509	10.868	11.187	11.485	11.772	12.049	12.316	12.573	12.819	13.051

SLAB EFFECTIVE WIDTH Be/B
SLAB ASPECT RATIO B/A = 0.7500
S. SUPPORTED / FREE EDGES

V/A U/A	C.000	C.020	C.040	0.060	0.080	0.100	0.120	0.140	0.160	0.180	0.200
C.000	C.325	C.377	C.414	0.440	0.459	0.476	0.490	0.502	0.512	0.521	0.529
C.020	C.420	C.455	0.488	0.516	0.541	0.563	0.583	0.600	0.615	0.629	0.641
C.040	0.463	C.495	C.523	0.549	0.573	0.596	0.617	0.635	0.653	0.668	0.682
C.060	C.499	C.527	C.554	0.577	0.600	0.622	0.643	0.662	0.680	0.697	0.712
C.080	C.527	C.552	C.577	0.600	0.621	0.642	0.662	0.682	0.700	0.717	0.732
C.100	C.548	C.572	C.596	0.617	0.638	0.658	0.677	0.696	0.714	0.731	0.746
C.120	C.564	C.587	C.610	0.630	0.650	0.669	0.688	0.706	0.723	0.740	0.755
C.140	C.575	C.597	C.619	0.639	0.658	0.677	0.695	0.712	0.729	0.745	0.760
C.160	C.582	C.604	C.626	0.645	0.664	0.681	0.698	0.715	0.731	0.747	0.761
C.180	C.587	C.609	C.630	0.649	0.667	0.684	0.700	0.716	0.732	0.747	0.761
0.200	C.590	C.612	C.633	0.651	0.668	0.685	0.701	0.717	0.732	0.746	0.760

TABLE 9.4(c) ROTATIONAL STIFFNESS AND EFFECTIVE WIDTH FOR SLAB WITH ASPECT RATIO OF 0.75 AND SIMPLY SUPPORTED/SIMPLY SUPPORTED EDGES

SLAB ROTATIONAL STIFFNESS FACTOR K
SLAB ASPECT RATIO B/A = 0.7500
S. SUPPORTED / S. SUPPORTED EDGES

V/A / U/A	0.000	0.020	0.040	0.060	0.080	0.100	0.120	0.140	0.160	0.180	0.200
0.000	3.009	3.519	3.893	4.153	4.360	4.535	4.688	4.826	4.953	5.070	5.180
0.020	4.213	4.592	4.953	5.276	5.566	5.828	6.068	6.290	6.499	6.697	6.887
0.040	5.004	5.373	5.722	6.043	6.351	6.647	6.929	7.198	7.456	7.705	7.947
0.060	5.807	6.171	6.521	6.847	7.167	7.486	7.799	8.107	8.409	8.706	8.999
0.080	6.606	6.972	7.331	7.668	8.002	8.339	8.678	9.018	9.358	9.698	10.038
0.100	7.414	7.787	8.163	8.516	8.868	9.224	9.587	9.956	10.330	10.709	11.094
0.120	8.235	8.622	9.017	9.391	9.763	10.141	10.528	10.926	11.333	11.750	12.177
0.140	9.069	9.479	9.898	10.294	10.689	11.091	11.505	11.931	12.372	12.826	13.296
0.160	9.931	10.370	10.814	11.235	11.656	12.086	12.528	12.986	13.461	13.955	14.468
0.180	10.840	11.310	11.784	12.234	12.684	13.144	13.619	14.112	14.625	15.160	15.718
0.200	11.809	12.312	12.821	13.304	13.787	14.281	14.792	15.323	15.878	16.457	17.065

SLAB EFFECTIVE WIDTH Be/B
SLAB ASPECT RATIO B/A = 0.7500
S. SUPPORTED / S. SUPPORTED EDGES

V/A / U/A	0.000	0.020	0.040	0.060	0.080	0.100	0.120	0.140	0.160	0.180	0.200
0.000	0.342	0.400	0.442	0.472	0.496	0.515	0.533	0.549	0.563	0.576	0.589
0.020	0.451	0.491	0.530	0.564	0.595	0.623	0.649	0.673	0.695	0.716	0.737
0.040	0.503	0.540	0.575	0.608	0.639	0.668	0.697	0.724	0.750	0.775	0.799
0.060	0.548	0.583	0.616	0.646	0.677	0.707	0.736	0.765	0.794	0.822	0.850
0.080	0.585	0.617	0.649	0.679	0.708	0.738	0.768	0.798	0.828	0.858	0.888
0.100	0.614	0.645	0.676	0.706	0.735	0.764	0.794	0.825	0.856	0.887	0.919
0.120	0.638	0.668	0.699	0.727	0.756	0.786	0.816	0.846	0.878	0.910	0.943
0.140	0.656	0.685	0.716	0.744	0.773	0.802	0.832	0.863	0.894	0.927	0.961
0.160	0.669	0.699	0.729	0.757	0.785	0.814	0.844	0.875	0.907	0.940	0.975
0.180	0.679	0.709	0.739	0.767	0.795	0.824	0.854	0.884	0.917	0.950	0.985
0.200	0.687	0.717	0.746	0.774	0.802	0.831	0.861	0.892	0.924	0.958	0.993

TABLE 9.4(d) ROTATIONAL STIFFNESS AND EFFECTIVE WIDTH FOR SLAB WITH ASPECT RATIO OF 0.75 AND SIMPLY SUPPORTED/CLAMPED EDGES

SLAB ROTATIONAL STIFFNESS FACTOR K
SLAB ASPECT RATIO B/A = 0.7500
S. SUPPORTED / CLAMPED EDGES

V/A / U/A	0.000	0.020	0.040	0.060	0.080	0.100	0.120	0.140	0.160	0.180	0.200
0.000	3.145	3.707	4.125	4.419	4.656	4.858	5.037	5.200	5.351	5.493	5.629
0.020	4.484	4.917	5.334	5.711	6.055	6.370	6.663	6.938	7.201	7.453	7.699
0.040	5.388	5.819	6.231	6.616	6.991	7.356	7.709	8.052	8.387	8.716	9.040
0.060	6.324	6.758	7.181	7.582	7.983	8.386	8.790	9.194	9.598	10.002	10.409
0.080	7.271	7.716	8.160	8.585	9.013	9.452	9.901	10.359	10.827	11.304	11.791
0.100	8.244	8.705	9.179	9.634	10.095	10.570	11.064	11.575	12.105	12.654	13.222
0.120	9.243	9.729	10.237	10.728	11.226	11.743	12.283	12.848	13.441	14.061	14.711
0.140	10.270	10.791	11.336	11.866	12.406	12.968	13.558	14.181	14.838	15.532	16.266
0.160	11.338	11.902	12.488	13.061	13.647	14.259	14.905	15.589	16.315	17.088	17.910
0.180	12.471	13.080	13.714	14.334	14.972	15.640	16.346	17.098	17.900	18.757	19.676
0.200	13.684	14.339	15.026	15.700	16.396	17.126	17.900	18.726	19.610	20.560	21.582

SLAB EFFECTIVE WIDTH Be/B
SLAB ASPECT RATIO B/A = 0.7500
S. SUPPORTED / CLAMPED EDGES

V/A / U/A	0.000	0.020	0.040	0.060	0.080	0.100	0.120	0.140	0.160	0.180	0.200
0.000	0.357	0.421	0.469	0.502	0.529	0.552	0.573	0.591	0.608	0.624	0.640
0.020	0.480	0.526	0.571	0.611	0.648	0.681	0.713	0.742	0.770	0.797	0.824
0.040	0.542	0.585	0.627	0.665	0.703	0.740	0.775	0.810	0.843	0.877	0.909
0.060	0.597	0.638	0.678	0.716	0.754	0.792	0.830	0.868	0.906	0.944	0.983
0.080	0.644	0.683	0.722	0.760	0.798	0.837	0.876	0.917	0.958	1.001	1.044
0.100	0.683	0.721	0.761	0.798	0.836	0.876	0.917	0.959	1.003	1.049	1.096
0.120	0.716	0.754	0.793	0.831	0.870	0.910	0.951	0.995	1.041	1.089	1.140
0.140	0.743	0.780	0.820	0.858	0.897	0.938	0.980	1.025	1.073	1.123	1.176
0.160	0.764	0.802	0.841	0.880	0.919	0.961	1.004	1.050	1.099	1.151	1.207
0.180	0.782	0.820	0.859	0.898	0.938	0.980	1.024	1.072	1.122	1.176	1.233
0.200	0.796	0.834	0.874	0.914	0.954	0.997	1.042	1.090	1.141	1.197	1.256

TABLE 9.5(a) ROTATIONAL STIFFNESS AND EFFECTIVE WIDTH FOR SLAB WITH ASPECT RATIO OF 1.0 AND SIMPLY SUPPORTED/CONTINUOUS EDGES

SLAB ROTATIONAL STIFFNESS FACTOR K
SLAB ASPECT RATIO B/A = 1.0000
S. SUPPORTED / CONTINUOUS EDGES

V/A / U/A	0.000	0.020	0.040	0.060	0.080	0.100	0.120	0.140	0.160	0.180	0.200
0.000	2.918	3.396	3.741	3.979	4.165	4.320	4.452	4.569	4.672	4.764	4.847
0.020	4.039	4.386	4.712	4.999	5.253	5.478	5.679	5.860	6.025	6.175	6.311
0.040	4.767	5.094	5.404	5.684	5.948	6.197	6.428	6.642	6.840	7.024	7.193
0.060	5.487	5.809	6.114	6.393	6.662	6.924	7.174	7.413	7.639	7.851	8.050
0.080	6.200	6.520	6.828	7.111	7.386	7.656	7.920	8.176	8.423	8.658	8.881
0.100	6.916	7.239	7.556	7.847	8.130	8.408	8.683	8.954	9.217	9.472	9.716
0.120	7.638	7.969	8.300	8.603	8.895	9.184	9.470	9.753	10.031	10.302	10.564
0.140	8.369	8.717	9.062	9.378	9.683	9.983	10.281	10.577	10.869	11.155	11.433
0.160	9.121	9.491	9.853	10.184	10.503	10.818	11.129	11.438	11.744	12.045	12.339
0.180	9.912	10.306	10.689	11.038	11.374	11.704	12.031	12.355	12.676	12.993	13.303
0.200	10.754	11.174	11.582	11.953	12.309	12.658	13.002	13.344	13.682	14.016	14.343

SLAB EFFECTIVE WIDTH, Be/B
SLAB ASPECT RATIO B/A = 1.0000
S. SUPPORTED / CONTINUOUS EDGES

V/A / U/A	0.000	0.020	0.040	0.060	0.080	0.100	0.120	0.140	0.160	0.180	0.200
0.000	0.249	0.290	0.319	0.339	0.355	0.368	0.380	0.389	0.398	0.406	0.413
0.020	0.324	0.352	0.378	0.401	0.421	0.440	0.456	0.470	0.483	0.495	0.506
0.040	0.359	0.384	0.408	0.429	0.449	0.467	0.485	0.501	0.516	0.530	0.543
0.060	0.389	0.411	0.433	0.453	0.472	0.490	0.508	0.525	0.541	0.556	0.570
0.080	0.412	0.433	0.453	0.472	0.490	0.508	0.526	0.543	0.559	0.575	0.590
0.100	0.430	0.450	0.470	0.488	0.505	0.523	0.540	0.556	0.573	0.589	0.604
0.120	0.444	0.463	0.482	0.500	0.517	0.534	0.550	0.567	0.583	0.599	0.614
0.140	0.454	0.473	0.491	0.509	0.525	0.541	0.558	0.574	0.589	0.605	0.620
0.160	0.461	0.480	0.498	0.515	0.531	0.547	0.562	0.578	0.593	0.609	0.623
0.180	0.466	0.484	0.502	0.519	0.535	0.550	0.566	0.581	0.596	0.611	0.625
0.200	0.469	0.488	0.506	0.522	0.537	0.552	0.568	0.582	0.597	0.612	0.626

TABLE 9.5(b) ROTATIONAL STIFFNESS AND EFFECTIVE WIDTH FOR SLAB WITH ASPECT RATIO OF 1.0 AND SIMPLY SUPPORTED/FREE EDGES

SLAB ROTATIONAL STIFFNESS FACTOR K
SLAB ASPECT RATIO B/A = 1.0000
S. SUPPORTED / FREE EDGES

V/A / U/A	C.CCO	C.020	C.040	0.06C	0.080	0.100	0.120	0.140	0.160	0.180	0.200
C.CCO	2.914	3.390	3.734	3.971	4.156	4.310	4.442	4.558	4.661	4.753	4.835
C.C2C	4.C3C	4.376	4.7C0	4.98C	5.238	5.462	5.662	5.843	6.006	6.156	6.291
0.040	4.750	5.080	5.388	5.667	5.930	6.177	6.407	6.620	6.817	6.999	7.168
0.060	5.472	5.792	6.095	6.372	6.640	6.899	7.149	7.386	7.610	7.821	8.018
C.C8C	6.181	6.499	6.805	7.086	7.359	7.626	7.889	8.143	8.388	8.622	8.844
0.100	6.893	7.213	7.528	7.817	8.097	8.374	8.647	8.915	9.176	9.429	9.672
C.120	7.610	7.939	8.267	8.567	8.858	9.144	9.428	9.708	9.984	10.253	10.514
C.140	8.336	8.681	9.024	9.337	9.640	9.938	10.233	10.526	10.816	11.100	11.376
C.160	9.083	9.450	9.809	10.138	10.454	10.766	11.075	11.381	11.684	11.983	12.275
C.180	9.869	10.260	10.640	10.986	11.319	11.646	11.970	12.291	12.610	12.924	13.232
C.200	10.705	11.122	11.527	11.894	12.247	12.593	12.934	13.273	13.608	13.939	14.264

SLAB EFFECTIVE WIDTH Be/B
SLAB ASPECT RATIO B/A = 1.0000
S. SUPPORTED / FREE EDGES

V/A / U/A	C.CCO	C.020	C.040	0.06C	0.080	0.100	0.120	0.140	0.160	0.180	0.200
C.CCO	C.248	C.289	C.318	0.339	0.354	0.367	0.379	0.389	0.397	0.405	0.412
0.020	C.323	C.351	C.377	0.40C	0.420	0.438	0.454	0.469	0.482	0.494	0.505
C.040	C.358	C.383	C.4C6	0.427	0.447	0.466	0.483	0.499	0.514	0.528	0.541
0.060	C.387	C.410	C.432	0.451	0.470	0.489	0.506	0.523	0.539	0.554	0.568
C.080	C.410	C.431	C.452	0.47C	0.488	0.506	0.524	0.541	0.557	0.572	0.587
0.100	C.428	C.448	C.468	0.486	0.503	0.520	0.537	0.554	0.570	0.586	0.601
C.120	C.442	C.461	C.480	0.498	0.515	0.531	0.548	0.564	0.580	0.596	0.611
C.140	C.452	C.471	C.489	0.506	0.523	0.539	0.555	0.571	0.586	0.602	0.617
C.160	C.459	C.477	C.496	0.512	0.528	0.544	0.560	0.575	0.590	0.605	0.620
0.180	C.464	C.482	C.5C0	0.516	0.532	0.547	0.563	0.578	0.593	0.607	0.622
C.200	C.467	C.485	C.5C3	0.519	0.535	0.550	0.565	0.579	0.594	0.608	0.623

TABLE 9.5(c) ROTATIONAL STIFFNESS AND EFFECTIVE WIDTH FOR SLAB WITH ASPECT RATIO OF 1.0 AND SIMPLY SUPPORTED/SIMPLY SUPPORTED EDGES

SLAB ROTATIONAL STIFFNESS FACTOR k
SLAB ASPECT RATIO B/A = 1.0000
S. SUPPORTED / S. SUPPORTED EDGES

V/A U/A	C.000	C.020	C.040	0.060	0.080	0.100	0.120	0.140	0.160	0.180	0.200
C.000	2.956	3.447	3.804	4.051	4.245	4.408	4.550	4.675	4.788	4.890	4.985
C.020	4.110	4.471	4.811	5.112	5.381	5.621	5.838	6.036	6.219	6.388	6.546
C.040	4.861	5.208	5.534	5.830	6.113	6.380	6.632	6.868	7.090	7.300	7.499
C.060	5.618	5.957	6.280	6.577	6.867	7.151	7.427	7.694	7.950	8.196	8.432
C.080	6.365	6.703	7.032	7.337	7.635	7.932	8.226	8.515	8.799	9.075	9.344
C.100	7.113	7.461	7.801	8.117	8.427	8.736	9.046	9.355	9.662	9.966	10.264
C.120	7.879	8.233	8.589	8.920	9.244	9.568	9.893	10.221	10.550	10.877	11.203
C.140	8.651	9.023	9.398	9.745	10.086	10.426	10.769	11.116	11.465	11.816	12.168
C.160	9.447	9.844	10.238	10.605	10.964	11.323	11.685	12.052	12.423	12.798	13.175
C.180	10.284	10.708	11.127	11.515	11.896	12.277	12.661	13.050	13.444	13.844	14.248
0.200	11.176	11.628	12.076	12.491	12.896	13.301	13.710	14.124	14.545	14.971	15.404

SLAB EFFECTIVE WIDTH Be/B
SLAB ASPECT RATIO B/A = 1.0000
S. SUPPORTED / S. SUPPORTED EDGES

V/A U/A	C.000	C.020	C.040	0.060	0.080	0.100	0.120	0.140	0.160	0.180	0.200
C.000	C.252	C.294	C.324	0.345	0.362	0.376	0.388	0.399	0.408	0.417	0.425
C.020	C.330	C.359	C.386	0.410	0.432	0.451	0.468	0.484	0.499	0.513	0.525
C.040	C.367	C.393	C.417	0.440	0.461	0.481	0.500	0.518	0.535	0.551	0.566
C.060	C.398	C.422	C.445	0.466	0.486	0.506	0.526	0.545	0.563	0.580	0.597
C.080	C.423	C.445	C.467	0.487	0.507	0.527	0.546	0.565	0.584	0.602	0.620
C.100	C.442	C.464	C.485	0.504	0.524	0.543	0.562	0.581	0.600	0.619	0.638
C.120	C.458	C.478	C.499	0.518	0.537	0.556	0.575	0.594	0.613	0.632	0.651
C.140	C.469	C.489	C.510	0.528	0.547	0.565	0.584	0.603	0.622	0.641	0.660
C.160	C.477	C.497	C.517	0.536	0.554	0.572	0.590	0.609	0.628	0.647	0.666
C.180	C.483	C.503	C.523	0.541	0.559	0.577	0.595	0.613	0.632	0.651	0.670
C.200	C.488	C.508	C.527	0.545	0.563	0.581	0.598	0.617	0.635	0.653	0.672

TABLE 9.5(d) ROTATIONAL STIFFNESS AND EFFECTIVE WIDTH FOR SLAB WITH ASPECT RATIO OF 1.0 AND SIMPLY SUPPORTED/CLAMPED EDGES

SLAB ROTATIONAL STIFFNESS FACTOR K
SLAB ASPECT RATIO B/A = 1.0000
S. SUPPORTED / CLAMPED EDGES

V/A U/A	C.000	C.020	C.040	0.C6C	0.080	0.100	0.120	0.140	0.160	0.180	0.200
C.000	3.C07	3.516	3.889	4.148	4.353	4.526	4.678	4.813	4.935	5.048	5.153
C.020	4.209	4.587	4.947	5.268	5.555	5.814	6.050	6.267	6.469	6.659	6.839
0.040	4.999	5.366	5.714	6.032	6.337	6.628	6.905	7.167	7.417	7.655	7.883
0.060	5.800	6.162	6.510	6.832	7.149	7.462	7.769	8.068	8.359	8.642	8.917
C.080	6.596	6.960	7.317	7.65C	7.980	8.310	8.640	8.969	9.295	9.618	9.936
C.100	7.403	7.773	8.146	8.495	8.840	9.188	9.540	9.896	10.253	10.611	10.970
C.120	8.221	8.605	8.997	9.366	9.730	10.098	10.473	10.854	11.241	11.633	12.029
C.140	9.053	9.46C	9.874	10.264	10.650	11.041	11.439	11.847	12.264	12.689	13.122
0.160	9.913	1C.348	1C.787	11.201	11.611	12.027	12.452	12.888	13.336	13.795	14.265
C.180	1C.819	11.286	11.753	12.194	12.632	13.076	13.531	13.999	14.480	14.975	15.485
C.200	11.785	12.284	12.785	13.258	13.728	14.204	14.692	15.194	15.712	16.247	16.799

SLAB EFFECTIVE WIDTH Be/B
SLAB ASPECT RATIO B/A = 1.0000
S. SUPPORTED / CLAMPED EDGES

V/A U/A	C.CO0	C.020	C.040	0.C6C	0.080	0.100	0.120	0.140	0.160	0.180	0.200
C.000	C.256	C.300	C.332	0.354	0.371	0.386	0.399	0.410	0.421	0.430	0.439
C.020	C.338	C.368	C.397	0.423	0.446	0.466	0.485	0.503	0.519	0.534	0.549
0.040	C.377	C.405	C.431	0.455	0.478	0.500	0.521	0.541	0.559	0.577	0.595
C.060	C.411	C.436	C.461	0.484	0.506	0.528	0.550	0.571	0.592	0.612	0.631
C.080	C.438	C.462	C.486	0.508	0.530	0.552	0.574	0.595	0.617	0.638	0.660
C.100	C.460	C.483	0.5C6	0.528	0.549	0.571	0.593	0.615	0.637	0.659	0.682
C.120	C.478	C.500	C.523	0.544	0.565	0.587	0.608	0.431	0.653	0.676	0.699
C.140	C.491	C.513	C.535	0.557	0.577	0.599	0.620	0.642	0.665	0.688	0.712
C.160	C.501	C.523	0.545	0.566	0.587	0.608	0.629	0.651	0.674	0.697	0.721
0.180	C.509	C.530	C.552	0.573	0.594	0.615	0.636	0.658	0.681	0.704	0.728
C.200	C.514	C.536	C.558	0.579	0.599	0.620	0.641	0.663	0.686	0.709	0.733

TABLE 9.6(a) ROTATIONAL STIFFNESS AND EFFECTIVE WIDTH FOR SLAB WITH ASPECT RATIO OF 1.5 AND SIMPLY SUPPORTED/CONTINUOUS EDGES

SLAB ROTATIONAL STIFFNESS FACTOR K
SLAB ASPECT RATIO B/A = 1.5000
S. SUPPORTED / CONTINUOUS EDGES

V/A U/A	C.CCO	C.020	C.040	0.06C	0.080	0.100	0.120	0.140	0.160	0.180	0.200
C.000	3.072	3.515	3.881	4.138	4.340	4.509	4.656	4.785	4.900	5.005	5.100
C.02C	4.254	4.58C	4.914	5.211	5.480	5.721	5.940	6.140	6.323	6.491	6.647
C.040	4.821	5.163	5.481	5.768	6.041	6.297	6.538	6.762	6.972	7.167	7.350
C.060	5.616	5.932	6.254	6.544	6.825	7.097	7.361	7.615	7.857	8.087	8.305
C.08C	6.348	6.663	6.991	7.29C	7.577	7.860	8.138	8.411	8.676	8.932	9.178
C.100	7.048	7.376	7.712	8.019	8.315	8.608	8.899	9.187	9.470	9.747	10.016
C.12C	7.799	E.133	8.484	8.805	9.115	9.422	9.726	10.030	10.331	10.628	10.919
C.140	8.561	8.910	9.279	9.617	9.943	10.264	10.584	10.904	11.222	11.538	11.849
0.160	9.328	9.702	10.089	10.445	10.787	11.125	11.461	11.797	12.132	12.466	12.798
C.180	10.161	10.554	10.967	11.345	11.708	12.066	12.422	12.777	13.132	13.487	13.839
C.200	11.037	11.454	11.896	12.299	12.686	13.066	13.444	13.821	14.198	14.574	14.949

SLAB EFFECTIVE WIDTH Be/B
SLAB ASPECT RATIO B/A = 1.5000
S. SUPPORTED / CONTINUOUS EDGES

V/A U/A	C.CCO	C.020	C.040	0.06C	0.080	0.100	0.120	0.140	0.160	0.180	0.200
C.000	C.175	C.200	C.221	0.235	0.247	0.256	0.265	0.272	0.279	0.284	0.290
C.02C	C.228	C.245	C.263	0.279	0.293	0.306	0.318	0.328	0.338	0.347	0.356
C.040	C.242	C.260	C.276	0.29C	0.304	0.317	0.329	0.340	0.351	0.360	0.370
C.060	C.263	C.280	C.295	0.309	0.322	0.335	0.348	0.359	0.371	0.382	0.392
C.080	C.281	C.295	C.309	0.323	0.335	0.348	0.360	0.372	0.384	0.395	0.406
C.100	C.292	C.306	C.320	0.332	0.345	0.357	0.369	0.381	0.392	0.404	0.415
C.120	C.302	C.315	C.329	0.341	0.353	0.365	0.377	0.388	0.400	0.412	0.423
C.140	C.309	C.322	C.335	0.348	0.359	0.371	0.383	0.394	0.406	0.417	0.428
0.160	C.314	C.327	C.340	0.352	0.363	0.375	0.386	0.397	0.409	0.420	0.431
C.180	0.318	C.331	C.344	0.356	0.367	0.378	0.389	0.400	0.412	0.423	0.434
C.200	C.321	C.333	C.346	0.358	0.369	0.380	0.391	0.402	0.413	0.424	0.435

TABLE 9.6(b) ROTATIONAL STIFFNESS AND EFFECTIVE WIDTH FOR SLAB WITH ASPECT RATIO OF 1.5 AND SIMPLY SUPPORTED/FREE EDGES

SLAB ROTATIONAL STIFFNESS FACTOR K
SLAB ASPECT RATIO B/A = 1.5000
S. SUPPORTED / FREE EDGES

V/A U/A	C.000	C.020	C.040	0.060	0.080	0.100	0.120	0.140	0.160	0.180	0.200
C.000	3.071	3.514	3.880	4.137	4.339	4.508	4.654	4.783	4.898	5.003	5.097
C.020	4.253	4.578	4.912	5.209	5.477	5.719	5.937	6.137	6.319	6.488	6.643
C.040	4.819	5.161	5.479	5.766	6.038	6.294	6.534	6.758	6.967	7.163	7.345
C.060	5.614	5.929	6.251	6.541	6.821	7.093	7.357	7.610	7.852	8.081	8.299
C.080	6.345	6.659	6.987	7.286	7.573	7.855	8.133	8.405	8.670	8.925	9.171
C.100	7.044	7.372	7.707	8.014	8.310	8.603	8.893	9.180	9.463	9.739	10.007
C.120	7.794	8.128	8.478	8.800	9.109	9.415	9.719	10.022	10.322	10.618	10.909
C.140	8.556	8.904	9.273	9.611	9.936	10.257	10.576	10.895	11.212	11.527	11.838
C.160	9.322	9.696	10.082	10.437	10.779	11.116	11.451	11.787	12.121	12.454	12.784
C.180	10.155	10.547	10.959	11.336	11.699	12.056	12.411	12.765	13.120	13.473	13.824
C.200	11.029	11.446	11.887	12.289	12.676	13.055	13.432	13.808	14.184	14.559	14.932

SLAB EFFECTIVE WIDTH Be/B
SLAB ASPECT RATIO B/A = 1.5000
S. SUPPORTED / FREE EDGES

V/A U/A	C.000	C.020	C.040	0.060	0.080	0.100	0.120	0.140	0.160	0.180	0.200
C.000	C.175	C.200	C.221	0.235	0.247	0.256	0.264	0.272	0.278	0.284	0.290
C.020	C.227	C.245	C.263	0.279	0.293	0.306	0.318	0.328	0.338	0.347	0.355
C.040	C.242	C.259	C.275	0.290	0.304	0.316	0.329	0.340	0.350	0.360	0.369
C.060	C.265	C.280	C.295	0.309	0.322	0.335	0.347	0.359	0.371	0.381	0.392
C.080	C.281	C.295	C.309	0.322	0.335	0.348	0.360	0.372	0.384	0.395	0.406
C.100	C.292	C.305	C.319	0.332	0.344	0.356	0.368	0.380	0.392	0.403	0.415
C.120	C.302	C.315	C.328	0.341	0.353	0.365	0.376	0.388	0.400	0.411	0.422
C.140	C.309	C.322	C.335	0.347	0.359	0.371	0.382	0.394	0.405	0.417	0.428
C.160	C.314	C.327	C.340	0.352	0.363	0.374	0.386	0.397	0.408	0.420	0.431
C.180	C.318	C.331	C.343	0.355	0.367	0.378	0.389	0.400	0.411	0.422	0.433
C.200	C.321	C.333	C.346	0.358	0.369	0.380	0.391	0.402	0.413	0.424	0.435

TABLE 9.6(c) ROTATIONAL STIFFNESS AND EFFECTIVE WIDTH FOR SLAB WITH ASPECT RATIO OF 1.5 AND SIMPLY SUPPORTED/SIMPLY SUPPORTED EDGES

SLAB ROTATIONAL STIFFNESS FACTOR K
SLAB ASPECT RATIO B/A = 1.5000
S. SUPPORTED / S. SUPPORTED EDGES

V/A U/A	C.CCO	C.020	C.040	0.06C	0.080	0.100	0.120	0.140	0.160	0.180	0.200
C.000	3.C75	3.519	3.885	4.143	4.346	4.515	4.662	4.792	4.908	5.013	5.109
C.020	4.259	4.585	4.920	5.219	5.488	5.731	5.951	6.151	6.336	6.506	6.663
C.040	4.827	5.170	5.489	5.777	6.051	6.309	6.550	6.776	6.987	7.185	7.370
C.060	5.624	5.941	6.264	6.556	6.838	7.112	7.378	7.633	7.877	8.109	8.330
C.080	6.358	6.674	7.004	7.304	7.593	7.877	8.158	8.433	8.700	8.959	9.208
C.100	7.060	7.390	7.727	8.036	8.334	8.629	8.922	9.212	9.498	9.778	10.051
C.120	7.814	8.149	8.502	8.825	9.137	9.446	9.753	10.060	10.364	10.665	10.960
C.140	8.579	8.929	9.300	9.640	9.969	10.292	10.615	10.938	11.260	11.580	11.897
C.160	9.348	9.724	10.113	10.471	10.816	11.157	11.496	11.836	12.176	12.515	12.852
C.180	10.185	10.579	10.994	11.375	11.741	12.102	12.462	12.821	13.182	13.542	13.900
C.200	11.063	11.483	11.926	12.333	12.723	13.107	13.489	13.871	14.253	14.636	15.017

SLAB EFFECTIVE WIDTH Be/B
SLAB ASPECT RATIO B/A = 1.5000
S. SUPPORTED / S. SUPPORTED EDGES

V/A U/A	C.CCO	C.020	C.040	0.06C	0.080	0.100	0.120	0.140	0.160	0.180	0.200
C.000	C.175	C.200	C.221	0.235	0.247	0.257	0.265	0.272	0.279	0.285	0.290
C.020	C.223	C.245	C.263	0.279	0.294	0.307	C.318	0.329	0.339	0.348	0.356
C.040	C.243	C.260	C.276	0.291	0.304	0.317	0.329	0.341	0.351	0.361	0.371
0.060	C.265	C.280	C.296	0.309	0.323	0.336	0.348	0.360	0.372	0.383	0.393
C.080	C.281	C.295	C.310	0.323	0.336	0.349	0.361	0.373	0.385	0.396	0.408
0.100	C.293	C.306	C.320	0.333	0.345	0.358	0.370	0.382	0.394	0.405	0.416
C.120	C.303	C.316	C.329	0.342	0.354	0.366	0.378	0.390	0.401	0.413	0.424
C.140	C.310	C.323	C.336	0.348	0.360	0.372	0.384	0.395	0.407	0.419	0.430
C.160	0.315	C.328	C.341	0.353	0.364	0.376	0.387	0.399	0.410	0.422	0.433
C.180	C.319	C.332	C.345	0.356	0.368	0.379	0.391	0.402	0.413	0.424	0.436
C.200	C.322	C.334	C.347	0.359	0.370	0.381	0.393	0.404	0.415	0.426	0.437

TABLE 9.6(d) ROTATIONAL STIFFNESS AND EFFECTIVE WIDTH FOR SLAB WITH ASPECT RATIO OF 1.5 AND SIMPLY SUPPORTED/CLAMPED EDGES

SLAB ROTATIONAL STIFFNESS FACTOR K
SLAB ASPECT RATIO H/A = 1.5000
S. SUPPORTED / CLAMPED EDGES

V/A U/A	C.000	C.020	C.040	0.060	0.080	0.100	0.120	0.140	0.160	0.180	0.200
C.000	3.080	3.526	3.894	4.153	4.357	4.528	4.676	4.807	4.924	5.031	5.128
C.020	4.269	4.597	4.934	5.235	5.506	5.750	5.973	6.175	6.362	6.535	6.695
C.040	4.840	5.185	5.506	5.797	6.072	6.333	6.577	6.805	7.019	7.220	7.408
C.060	5.642	5.961	6.286	6.581	6.865	7.142	7.411	7.670	7.917	8.154	8.379
C.080	6.380	6.699	7.031	7.334	7.626	7.914	8.198	8.477	8.749	9.012	9.267
0.100	7.087	7.420	7.760	8.072	8.373	8.672	8.969	9.264	9.556	9.841	10.120
C.120	7.746	8.184	8.540	8.867	9.183	9.496	9.808	10.120	10.431	10.738	11.041
C.140	8.417	8.970	9.344	9.689	10.022	10.351	10.679	11.008	11.337	11.665	11.989
C.160	9.392	9.771	10.165	10.527	10.877	11.223	11.569	11.916	12.263	12.611	12.957
0.180	10.234	10.633	11.053	11.438	11.810	12.177	12.544	12.911	13.280	13.650	14.020
0.200	11.119	11.543	11.992	12.404	12.801	13.192	13.582	13.972	14.364	14.757	15.151

SLAB EFFECTIVE WIDTH Be/B
SLAB ASPECT RATIO B/A = 1.5000
S. SUPPORTED / CLAMPED EDGES

V/A U/A	C.000	C.020	C.040	0.060	0.080	0.100	0.120	0.140	0.160	0.180	0.200
C.000	0.175	C.200	C.221	0.236	0.248	0.257	0.266	0.273	0.280	0.286	0.291
C.020	C.228	C.246	C.264	0.280	0.295	0.308	0.319	0.330	0.340	0.350	0.358
C.040	C.243	C.261	C.277	0.291	0.305	0.318	0.331	0.342	0.353	0.363	0.373
C.060	C.266	C.281	C.297	0.311	0.324	0.337	0.350	0.362	0.374	0.385	0.396
C.080	C.282	C.296	C.311	0.325	0.337	0.350	0.363	0.375	0.387	0.399	0.410
C.100	C.294	C.307	C.322	0.334	0.347	0.359	0.372	0.384	0.396	0.408	0.419
0.120	C.304	C.317	C.331	0.343	0.356	0.368	0.380	0.392	0.404	0.416	0.428
0.140	C.311	C.324	C.338	0.350	0.362	0.374	0.386	0.398	0.410	0.422	0.433
C.160	C.316	C.329	C.342	0.355	0.366	0.378	0.390	0.401	0.413	0.425	0.436
C.180	C.321	C.333	C.346	0.358	0.370	0.382	0.393	0.405	0.416	0.428	0.439
0.200	C.324	C.336	C.349	0.361	0.372	0.384	0.395	0.407	0.418	0.429	0.441

TABLE 9.7(a) ROTATIONAL STIFFNESS AND EFFECTIVE WIDTH FOR SLAB WITH ASPECT RATIO OF 2.0 AND SIMPLY SUPPORTED/CONTINUOUS EDGES

SLAB ROTATIONAL STIFFNESS FACTOR K
SLAB ASPECT RATIO B/A = 2.0000
S. SUPPORTED / CONTINUOUS EDGES

V/A / U/A	0.000	0.020	0.040	0.060	0.080	0.100	0.120	0.140	0.160	0.180	0.200
0.000	3.293	3.674	4.055	4.335	4.558	4.745	4.907	5.051	5.180	5.297	5.404
0.020	4.595	4.880	5.215	5.517	5.796	6.053	6.290	6.508	6.710	6.897	7.072
0.040	4.984	5.291	5.620	5.913	6.191	6.454	6.703	6.936	7.154	7.359	7.551
0.060	5.692	6.003	6.335	6.631	6.912	7.186	7.451	7.706	7.951	8.185	8.407
0.080	6.434	6.736	7.075	7.381	7.672	7.957	8.238	8.513	8.781	9.041	9.291
0.100	7.155	7.467	7.816	8.136	8.439	8.735	9.028	9.319	9.605	9.885	10.158
0.120	7.897	8.218	8.582	8.916	9.233	9.544	9.852	10.159	10.462	10.762	11.057
0.140	8.663	8.999	9.381	9.734	10.069	10.397	10.721	11.043	11.365	11.684	11.999
0.160	9.453	9.806	10.210	10.582	10.937	11.283	11.625	11.966	12.306	12.645	12.980
0.180	10.294	10.668	11.097	11.494	11.871	12.239	12.603	12.964	13.325	13.684	14.041
0.200	11.163	11.563	12.021	12.443	12.844	13.236	13.622	14.006	14.388	14.770	15.150

SLAB EFFECTIVE WIDTH Be/B
SLAB ASPECT RATIO B/A = 2.0000
S. SUPPORTED / CONTINUOUS EDGES

V/A / U/A	0.000	0.020	0.040	0.060	0.080	0.100	0.120	0.140	0.160	0.180	0.200
0.000	0.140	0.157	0.173	0.185	0.194	0.202	0.209	0.215	0.221	0.226	0.230
0.020	0.184	0.196	0.209	0.221	0.233	0.243	0.252	0.261	0.269	0.277	0.284
0.040	0.188	0.200	0.212	0.223	0.233	0.243	0.253	0.262	0.270	0.278	0.285
0.060	0.202	0.213	0.224	0.235	0.245	0.254	0.264	0.273	0.282	0.290	0.298
0.080	0.214	0.224	0.235	0.245	0.255	0.264	0.273	0.283	0.291	0.300	0.308
0.100	0.222	0.232	0.243	0.253	0.262	0.271	0.281	0.290	0.298	0.307	0.316
0.120	0.229	0.239	0.249	0.259	0.268	0.277	0.286	0.295	0.304	0.313	0.321
0.140	0.235	0.244	0.254	0.264	0.273	0.282	0.291	0.299	0.308	0.317	0.325
0.160	0.239	0.248	0.258	0.267	0.276	0.285	0.294	0.302	0.311	0.319	0.328
0.180	0.242	0.251	0.261	0.270	0.279	0.288	0.296	0.305	0.313	0.322	0.330
0.200	0.244	0.252	0.262	0.272	0.280	0.289	0.297	0.306	0.314	0.322	0.331

TABLE 9.7(b) ROTATIONAL STIFFNESS AND EFFECTIVE WIDTH FOR SLAB WITH ASPECT RATIO OF 2.0 AND SIMPLY SUPPORTED/FREE EDGES

SLAB ROTATIONAL STIFFNESS FACTOR K
SLAB ASPECT RATIO B/A = 2.0000
S. SUPPORTED / FREE EDGES

V/A U/A	C.000	C.020	C.040	0.060	0.080	0.100	0.120	0.140	0.160	0.180	0.200
C.000	3.293	3.674	4.055	4.335	4.557	4.744	4.907	5.051	5.180	5.297	5.403
C.020	4.595	4.879	5.215	5.516	5.795	6.053	6.289	6.508	6.710	6.897	7.071
C.040	4.984	5.291	5.620	5.913	6.191	6.454	6.702	6.935	7.154	7.358	7.550
C.060	5.692	6.003	6.335	6.631	6.912	7.185	7.450	7.706	7.951	8.184	8.406
C.080	6.434	6.735	7.074	7.381	7.672	7.957	8.237	8.513	8.780	9.040	9.290
C.100	7.154	7.467	7.816	8.135	8.438	8.735	9.028	9.318	9.604	9.884	10.157
C.120	7.897	8.217	8.581	8.915	9.233	9.544	9.852	10.158	10.462	10.761	11.056
C.140	8.662	8.999	9.381	9.733	10.068	10.396	10.720	11.043	11.364	11.683	11.997
C.160	9.452	9.806	10.210	10.582	10.936	11.282	11.624	11.965	12.305	12.643	12.979
C.180	10.293	10.667	11.096	11.493	11.870	12.238	12.602	12.963	13.324	13.683	14.040
C.200	11.162	11.562	12.021	12.442	12.843	13.234	13.621	14.004	14.387	14.768	15.148

SLAB EFFECTIVE WIDTH Be/B
SLAB ASPECT RATIO B/A = 2.0000
S. SUPPORTED / FREE EDGES

V/A U/A	C.000	C.020	C.040	0.060	0.080	0.100	C.120	0.140	0.160	0.180	0.200
C.000	C.140	C.157	C.173	0.185	0.194	0.202	0.209	0.215	0.221	0.226	0.230
C.020	C.184	C.196	C.209	0.221	0.233	0.243	0.252	0.261	0.269	0.277	0.284
C.040	0.188	C.200	C.212	0.223	0.233	0.243	0.253	0.262	0.270	0.278	0.285
C.060	0.202	C.213	C.224	0.235	0.245	0.254	0.264	0.273	0.281	0.290	0.298
C.080	C.214	C.224	C.235	0.245	0.255	0.264	0.273	0.283	0.291	0.300	0.308
C.100	C.222	C.232	C.243	0.253	0.262	0.271	0.281	0.290	0.298	0.307	0.316
0.120	0.229	C.239	C.249	0.259	0.268	0.277	0.286	0.295	0.304	0.313	0.321
C.140	C.235	C.244	C.254	0.264	0.273	0.282	0.291	0.299	0.308	0.317	0.325
C.160	C.239	C.248	C.258	0.267	0.276	0.285	0.294	0.302	0.311	0.319	0.328
C.180	0.242	C.251	C.261	0.270	0.279	0.288	0.296	0.305	0.313	0.322	0.330
C.200	C.244	C.252	C.262	0.272	0.280	0.289	C.297	0.306	0.314	0.322	0.331

TABLE 9.7(c) ROTATIONAL STIFFNESS AND EFFECTIVE WIDTH FOR SLAB WITH ASPECT RATIO OF 2.0 AND SIMPLY SUPPORTED/SIMPLY SUPPORTED EDGES

SLAB ROTATIONAL STIFFNESS FACTOR K
SLAB ASPECT RATIO B/A = 2.0000
S. SUPPORTED / S. SUPPORTED EDGES

V/A U/A	0.000	0.020	0.040	0.060	0.080	0.100	0.120	0.140	0.160	0.180	0.200
0.000	3.293	3.674	4.055	4.335	4.558	4.745	4.907	5.051	5.180	5.297	5.404
0.020	4.594	4.880	5.216	5.517	5.796	6.053	6.290	6.509	6.711	6.898	7.073
0.040	4.985	5.291	5.621	5.914	6.192	6.455	6.703	6.936	7.155	7.360	7.552
0.060	5.493	6.003	6.336	6.632	6.913	7.186	7.452	7.707	7.952	8.186	8.408
0.080	6.434	6.736	7.075	7.382	7.673	7.958	8.239	8.514	8.783	9.042	9.292
0.100	7.155	7.468	7.817	8.137	8.440	8.736	9.030	9.320	9.607	9.887	10.160
0.120	7.898	8.218	8.583	8.917	9.235	9.546	9.854	10.160	10.464	10.765	11.059
0.140	8.664	9.000	9.382	9.735	10.070	10.398	10.723	11.045	11.367	11.686	12.001
0.160	9.454	9.808	10.212	10.584	10.938	11.285	11.627	11.969	12.309	12.647	12.983
0.180	10.295	10.669	11.099	11.495	11.873	12.241	12.605	12.967	13.328	13.687	14.045
0.200	11.164	11.565	12.023	12.445	12.846	13.238	13.624	14.009	14.392	14.773	15.154

SLAB EFFECTIVE WIDTH Be/B
SLAB ASPECT RATIO B/A = 2.0000
S. SUPPORTED / S. SUPPORTED EDGES

V/A U/A	0.000	0.020	0.040	0.060	0.080	0.100	0.120	0.140	0.160	0.180	0.200
0.000	0.140	0.157	0.173	0.185	0.194	0.202	0.209	0.215	0.221	0.226	0.230
0.020	0.184	0.196	0.209	0.221	0.233	0.243	0.252	0.261	0.269	0.277	0.284
0.040	0.188	0.200	0.212	0.223	0.233	0.243	0.253	0.262	0.270	0.278	0.285
0.060	0.202	0.213	0.224	0.235	0.245	0.254	0.264	0.273	0.282	0.290	0.298
0.080	0.214	0.224	0.235	0.245	0.255	0.264	0.273	0.283	0.292	0.300	0.308
0.100	0.222	0.232	0.243	0.253	0.262	0.271	0.281	0.290	0.299	0.307	0.316
0.120	0.229	0.239	0.249	0.259	0.268	0.277	0.286	0.295	0.304	0.313	0.321
0.140	0.235	0.244	0.254	0.264	0.273	0.282	0.291	0.299	0.308	0.317	0.325
0.160	0.239	0.248	0.258	0.267	0.276	0.285	0.294	0.302	0.311	0.320	0.328
0.180	0.242	0.251	0.261	0.270	0.279	0.288	0.296	0.305	0.313	0.322	0.330
0.200	0.244	0.252	0.262	0.272	0.280	0.289	0.297	0.306	0.314	0.322	0.331

TABLE 9.7(d) ROTATIONAL STIFFNESS AND EFFECTIVE WIDTH FOR SLAB WITH ASPECT RATIO OF 2.0 AND SIMPLY SUPPORTED/CLAMPED EDGES

SLAB ROTATIONAL STIFFNESS FACTOR K
SLAB ASPECT RATIO B/A = 2.0000
S. SUPPORTED / CLAMPED EDGES

V/A U/A	C.000	C.020	C.040	0.060	0.080	0.100	0.120	0.140	0.160	0.180	0.200
C.000	3.294	3.675	4.056	4.336	4.559	4.746	4.908	5.052	5.182	5.299	5.406
C.020	4.597	4.881	5.217	5.515	5.798	6.055	6.292	6.511	6.713	6.901	7.076
C.040	4.986	5.293	5.622	5.915	6.193	6.457	6.706	6.939	7.158	7.363	7.555
C.060	5.694	6.005	6.337	6.634	6.915	7.189	7.454	7.710	7.955	8.189	8.412
C.080	6.436	6.738	7.078	7.384	7.676	7.961	8.242	8.518	8.786	9.046	9.297
C.100	7.157	7.470	7.820	8.139	8.443	8.740	9.034	9.324	9.611	9.892	10.166
C.120	7.901	8.221	8.586	8.920	9.238	9.550	9.858	10.165	10.470	10.770	11.066
C.140	8.667	9.003	9.386	9.735	10.075	10.403	10.728	11.051	11.373	11.693	12.009
C.160	9.457	9.811	10.216	10.588	10.943	11.290	11.633	11.975	12.316	12.655	12.992
C.180	10.299	10.674	11.103	11.500	11.879	12.247	12.612	12.974	13.336	13.696	14.055
0.200	11.168	11.569	12.028	12.450	12.853	13.245	13.632	14.017	14.400	14.783	15.164

SLAB EFFECTIVE WIDTH Be/B
SLAB ASPECT RATIO B/A = 2.0000
S. SUPPORTED / CLAMPED EDGES

V/A U/A	C.000	C.020	C.040	0.060	0.080	0.100	0.120	0.140	0.160	0.180	0.200
0.000	C.140	C.157	C.173	0.185	0.194	0.202	0.209	0.215	0.221	0.226	0.230
C.020	C.184	C.196	C.209	0.221	0.233	0.243	0.252	0.261	0.269	0.277	0.284
C.040	C.188	C.200	C.212	0.223	0.234	0.244	0.253	0.262	0.270	0.278	0.285
C.060	C.202	C.213	C.224	0.235	0.245	0.255	0.264	0.273	0.282	0.290	0.298
C.080	C.214	C.224	C.235	0.245	0.255	0.264	0.274	0.283	0.292	0.300	0.309
0.100	C.227	C.232	C.243	0.253	0.262	0.272	0.281	0.290	0.299	0.307	0.316
C.120	0.230	C.239	C.249	0.259	0.268	0.277	0.286	0.295	0.304	0.313	0.321
C.140	C.235	C.244	C.254	0.264	0.273	0.282	0.291	0.300	0.308	0.317	0.326
C.160	C.239	C.248	C.258	0.268	0.276	0.285	0.294	0.303	0.311	0.320	0.328
C.180	C.242	C.251	C.261	0.270	0.279	0.288	0.296	0.305	0.313	0.322	0.330
C.200	C.244	C.252	C.263	0.272	0.280	0.289	0.298	0.306	0.314	0.323	0.331

TABLE 9.8 EFFECTIVE WIDTH VALUES FOR SQUARE SLABS WITH VARIOUS LONGITUDINAL EDGE SUPPORTS AND A SQUARE COLUMN OF RELATIVE DIMENSION U/A OF 0.1 - COMPARISON BETWEEN INFLUENCE COEFFICIENT AND FINITE ELEMENT RESULTS

Longitudinal Slab Edges	Effective Width B_e/B		Percentage Difference
	I.C. Method	F.E. Method	
Continuous	0.5226	0.5230	-0.08%
Free	0.5204	0.5208	-0.08%
S. Supported	0.5430	0.5428	+0.04%
Clamped	0.5710	0.5701	+0.16%

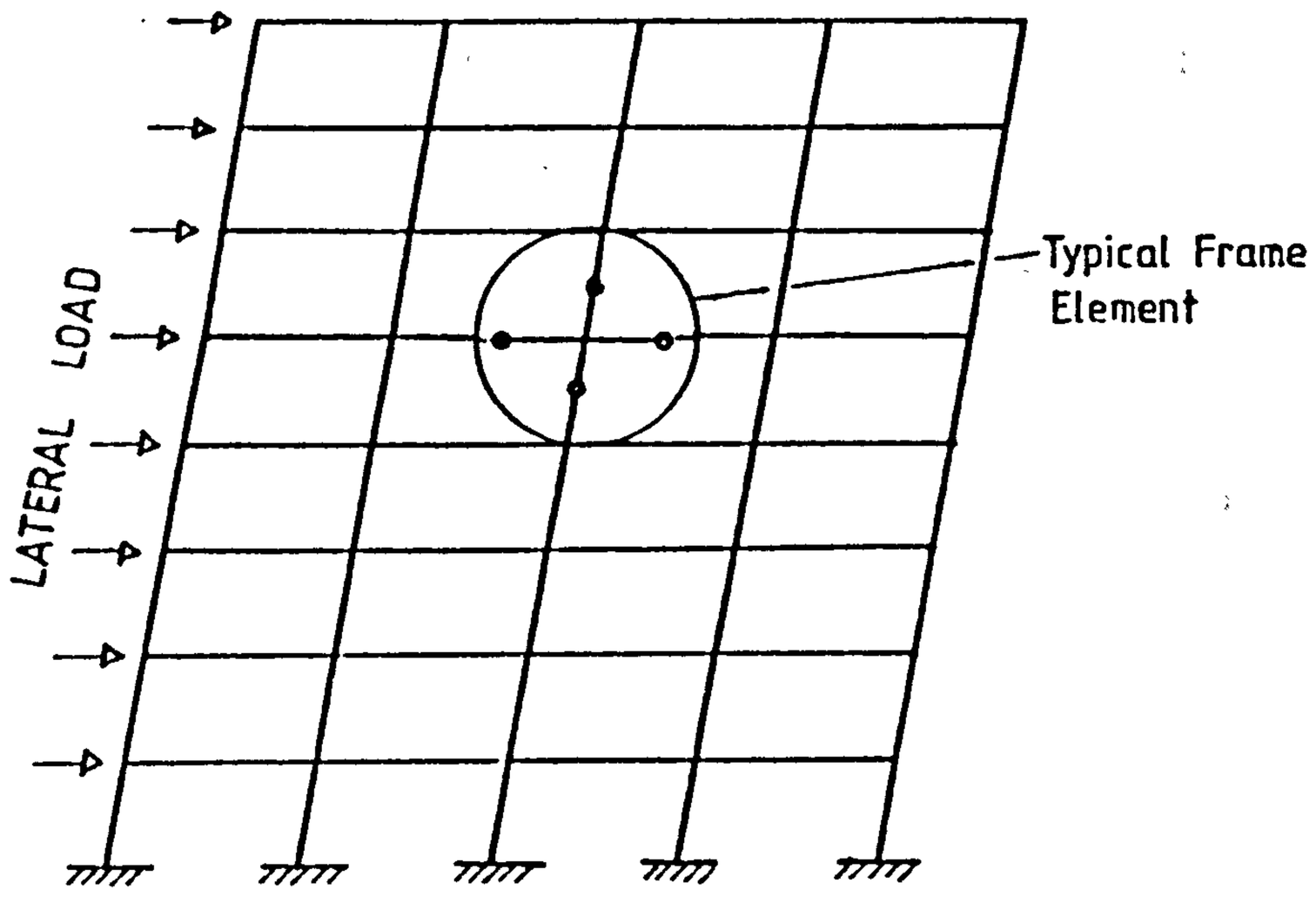

FIG. 9.1 DEFLECTION OF FRAME UNDER LATERAL LOADING

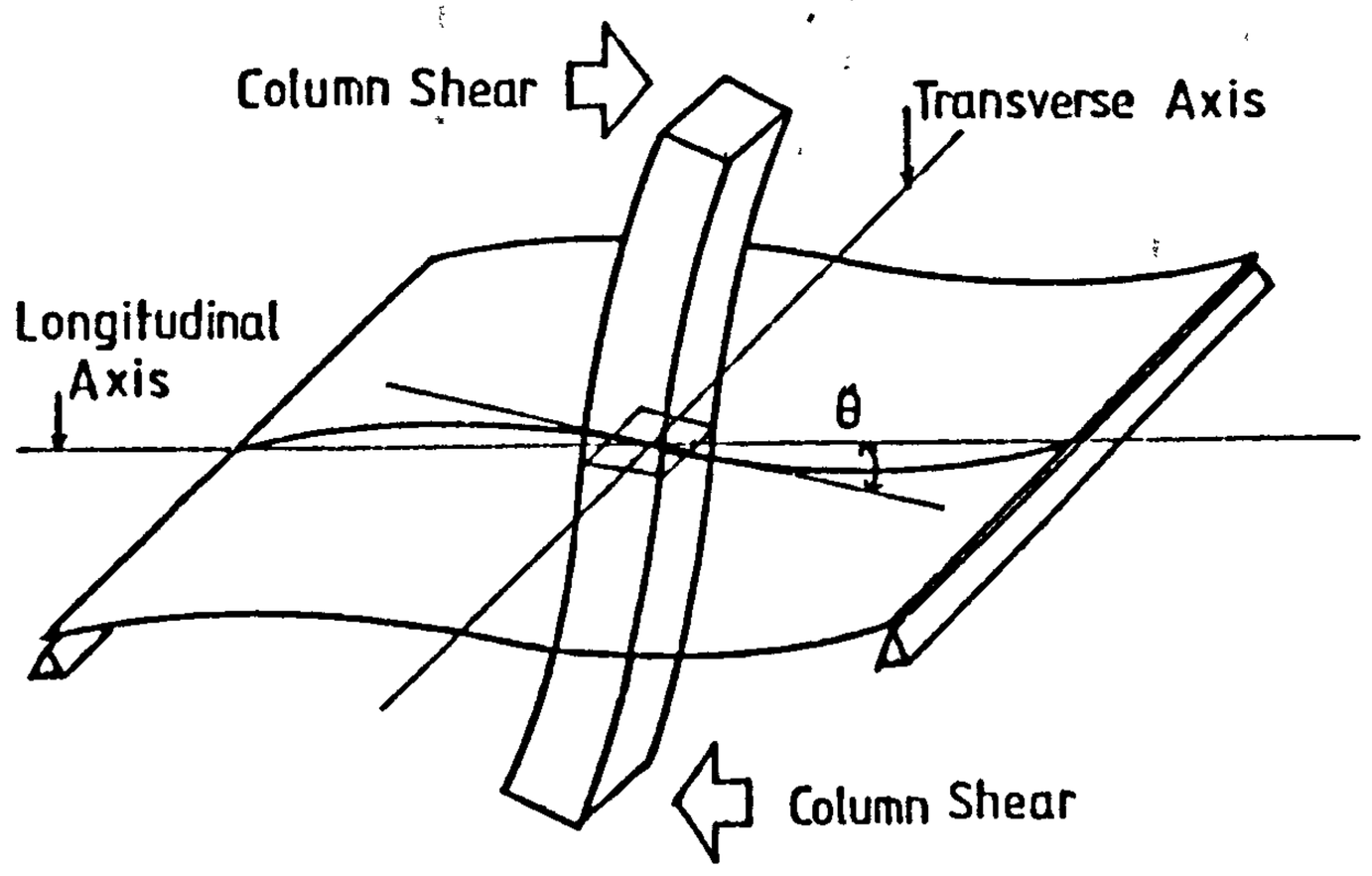

FIG. 9.2 TYPICAL PLATE/COLUMN FRAME ELEMENT

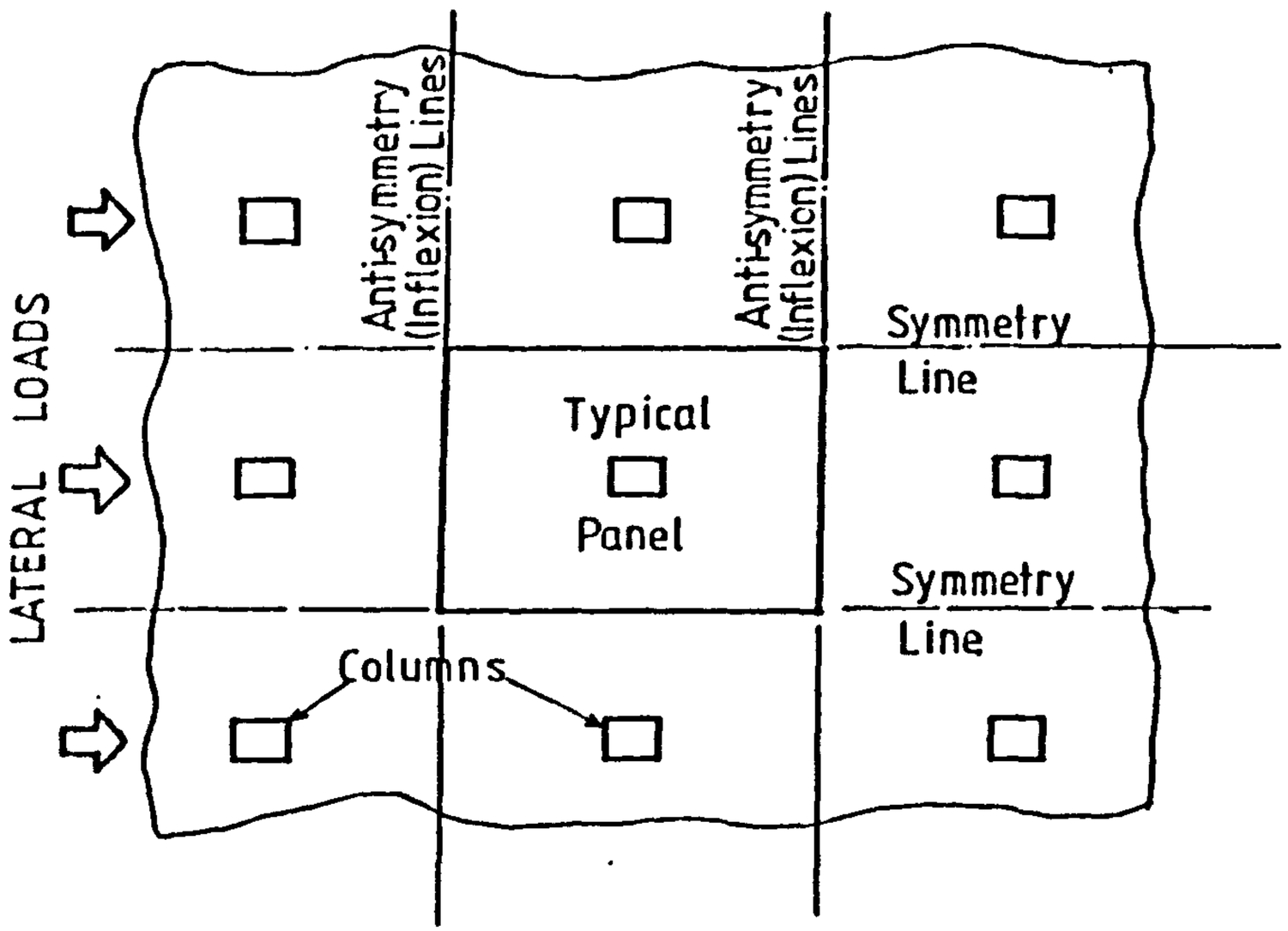

FIG. 9.3 LINES OF SYMMETRY AND ANTI-SYMMETRY IN A TYPICAL FLAT PLATE FLOOR

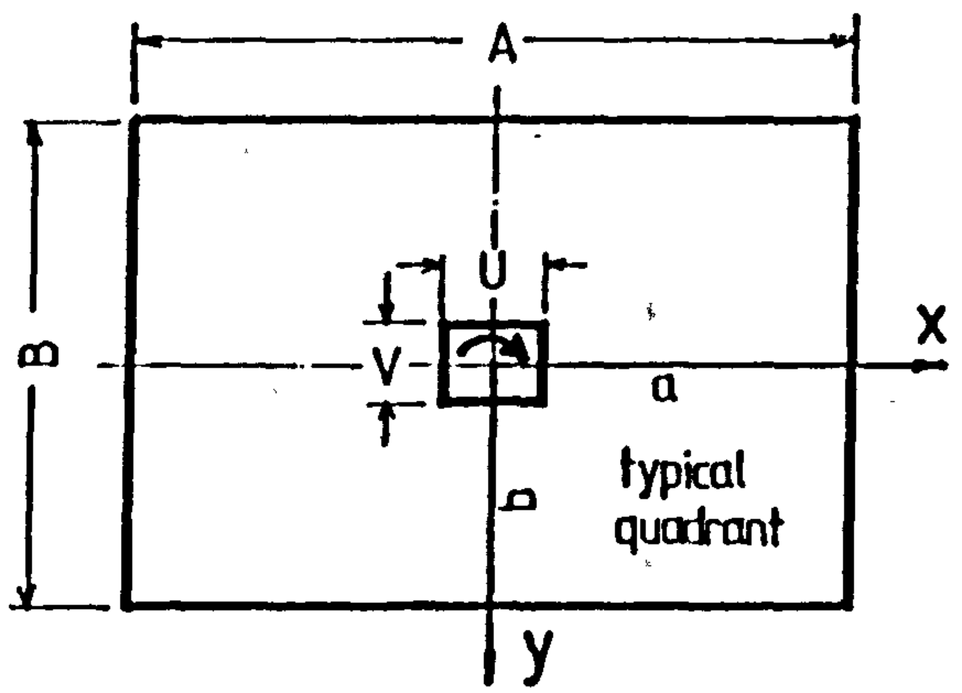

FIG. 9.4 TYPICAL INTERIOR FLOOR PANEL

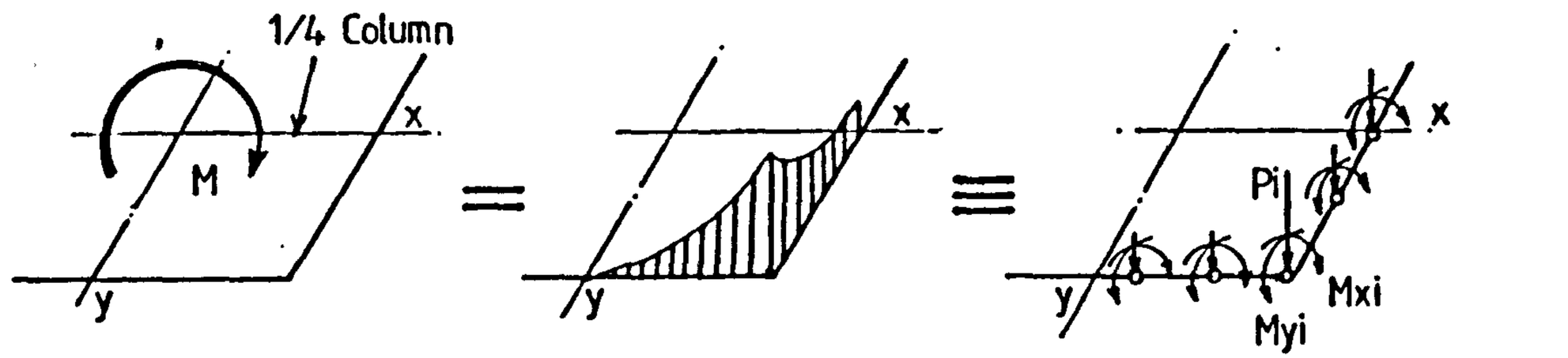

COLUMN MOMENT DISTRIBUTED FORCES DISCRETE LOADS AND MOMENTS

FIG. 9.5 DISCRETISATION OF COLUMN MOMENT TRANSFER

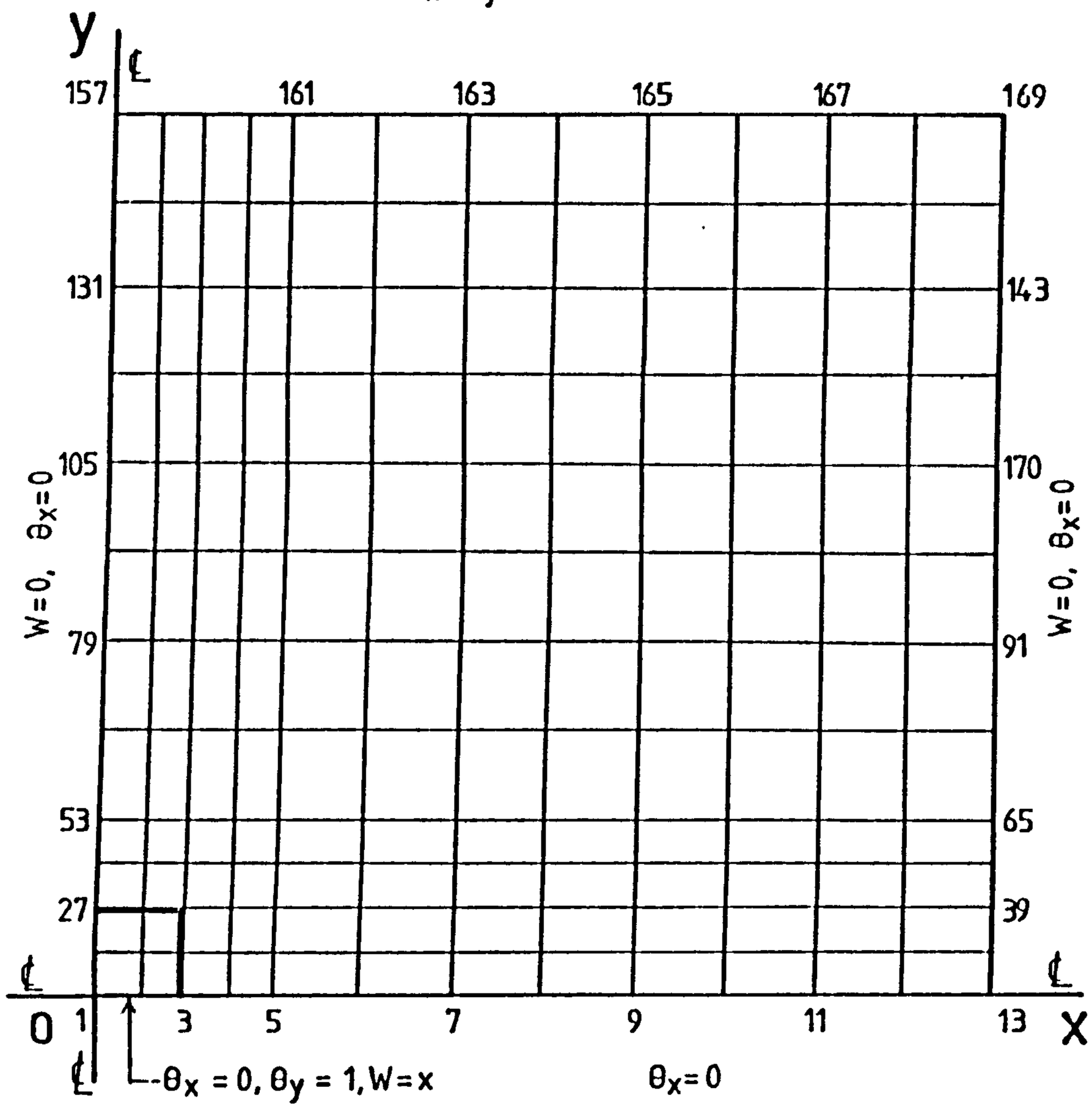

Fig. 9.6 Finite Element Idealisation of a Slab Quadrant

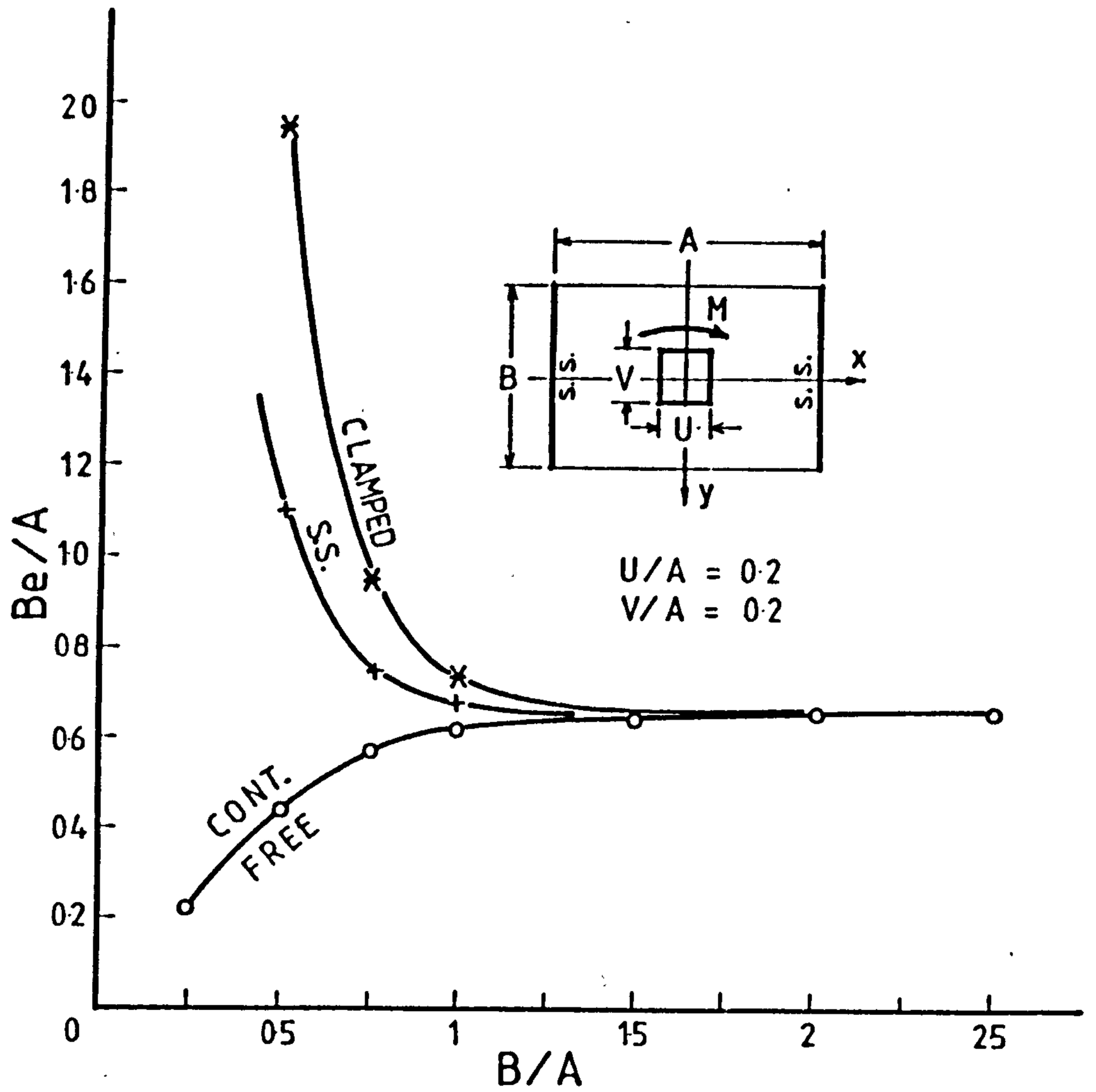

Fig. 9.7 Influence of Slab Width and Longitudinal Edge Supports on Effective Width

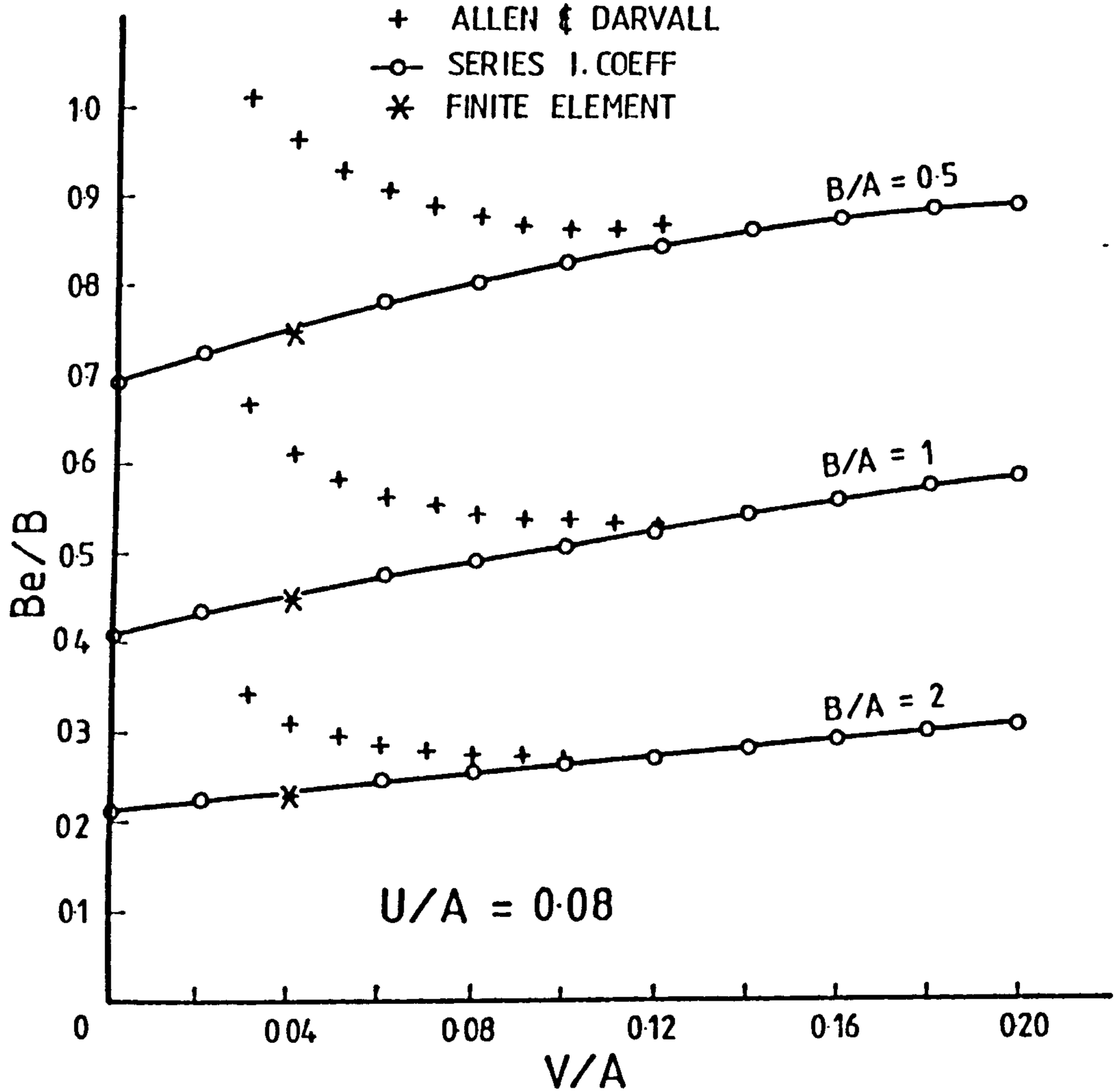

Fig. 9.8 Influence of Relative Column Width on Effective Width

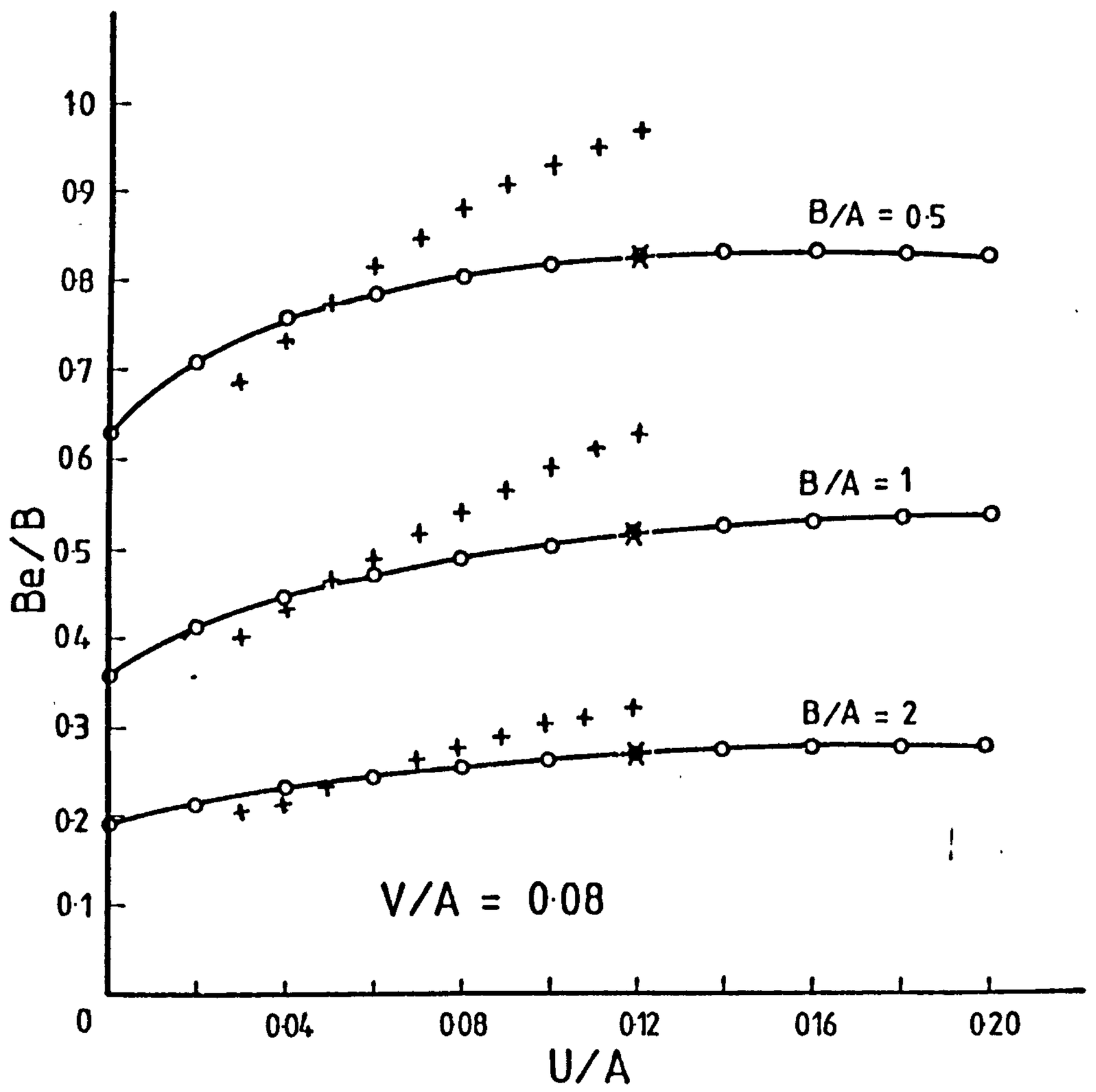

Fig. 9.9 Influence of Relative Column Depth on Effective Width

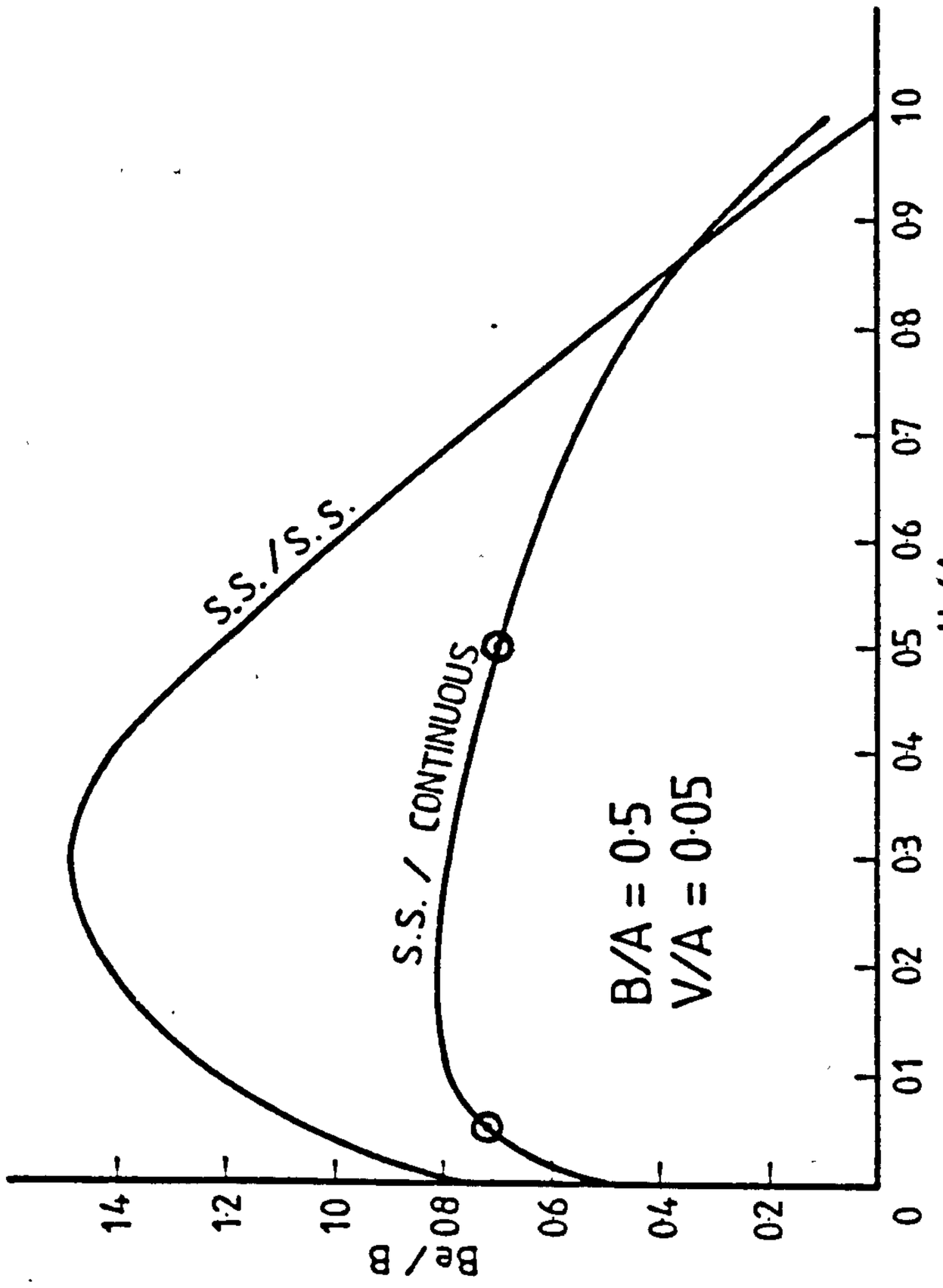

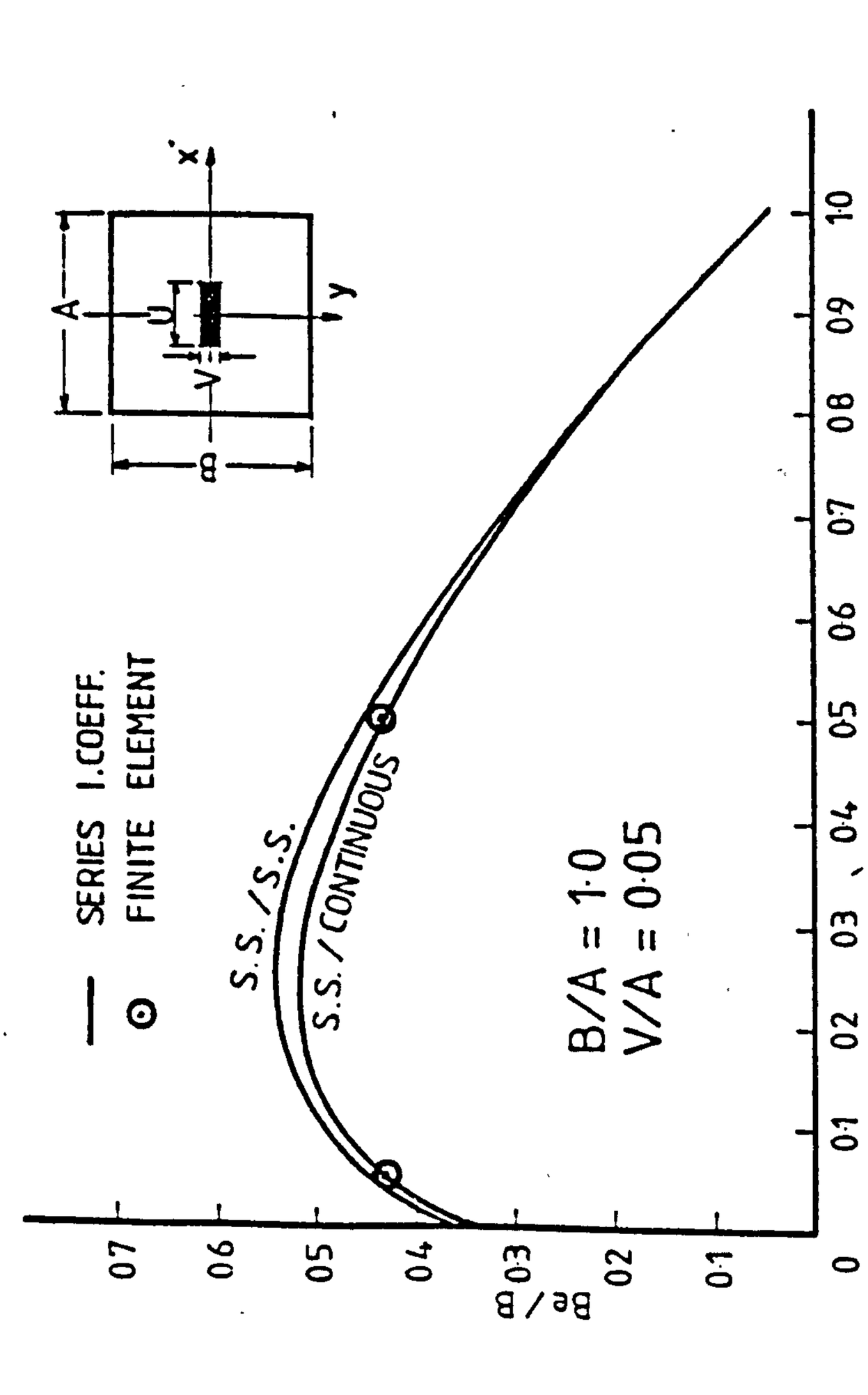

Fig. 9.10 Variation of Effective Width with Relative Column Depth. (a) Slab with Aspect Ratio of 1, and (b) Slab with Aspect Ratio of 0.5

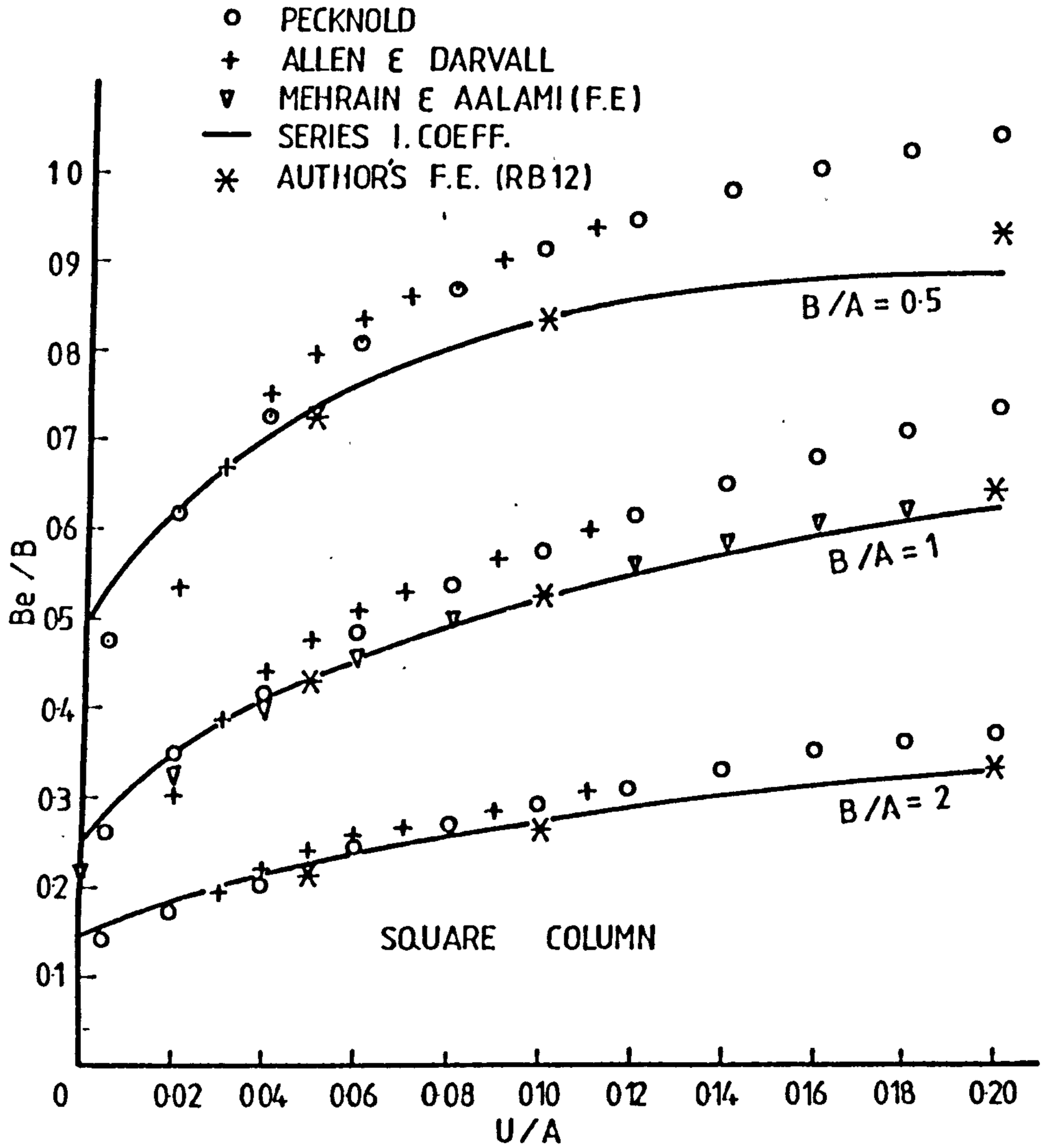

Fig. 9.11 Comparison between Effective Width Values Obtained by Various Theoretical Methods

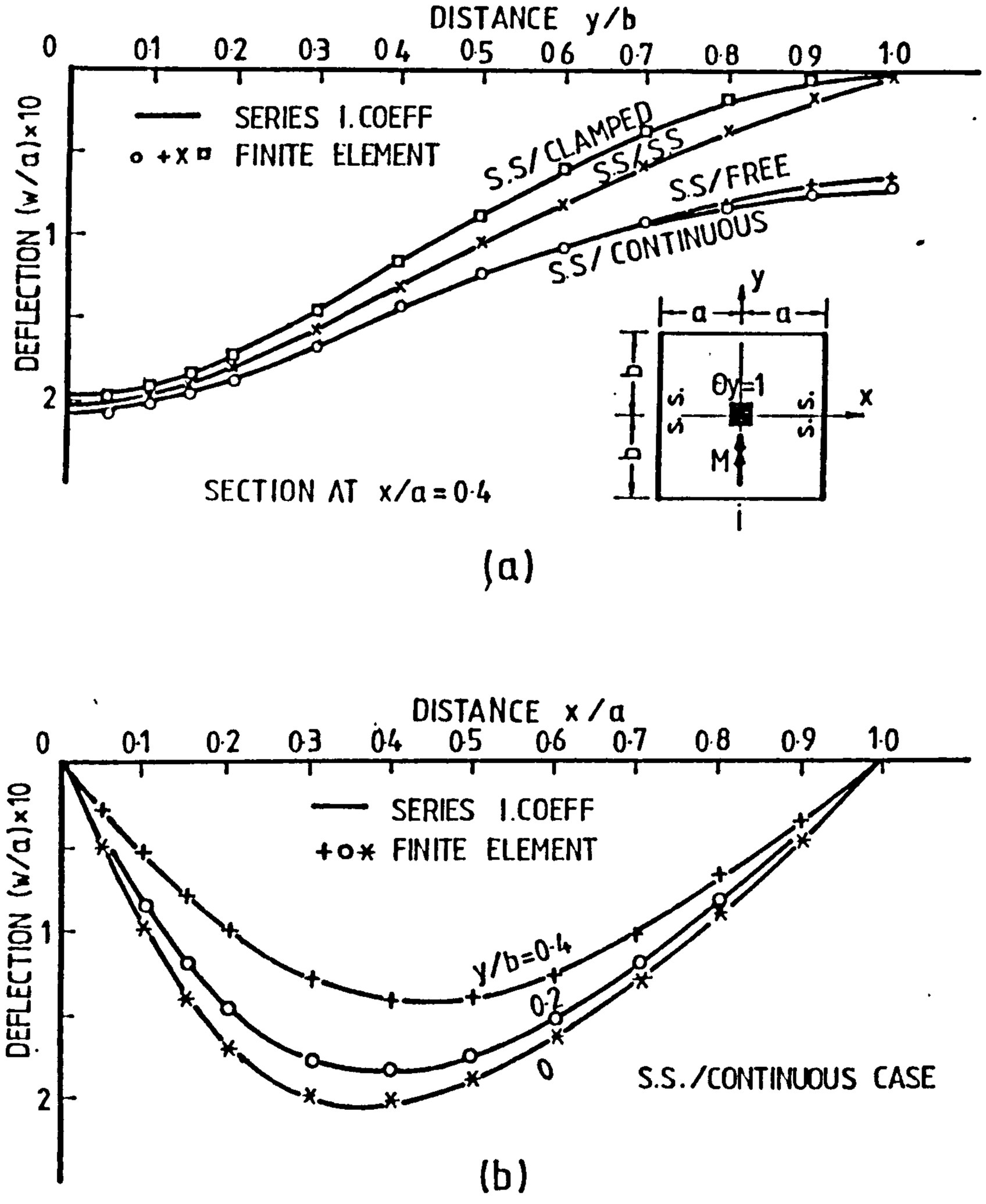

Fig. 9.12 Comparison between Deflections Obtained by Influence Coefficient Method and Finite Element Method

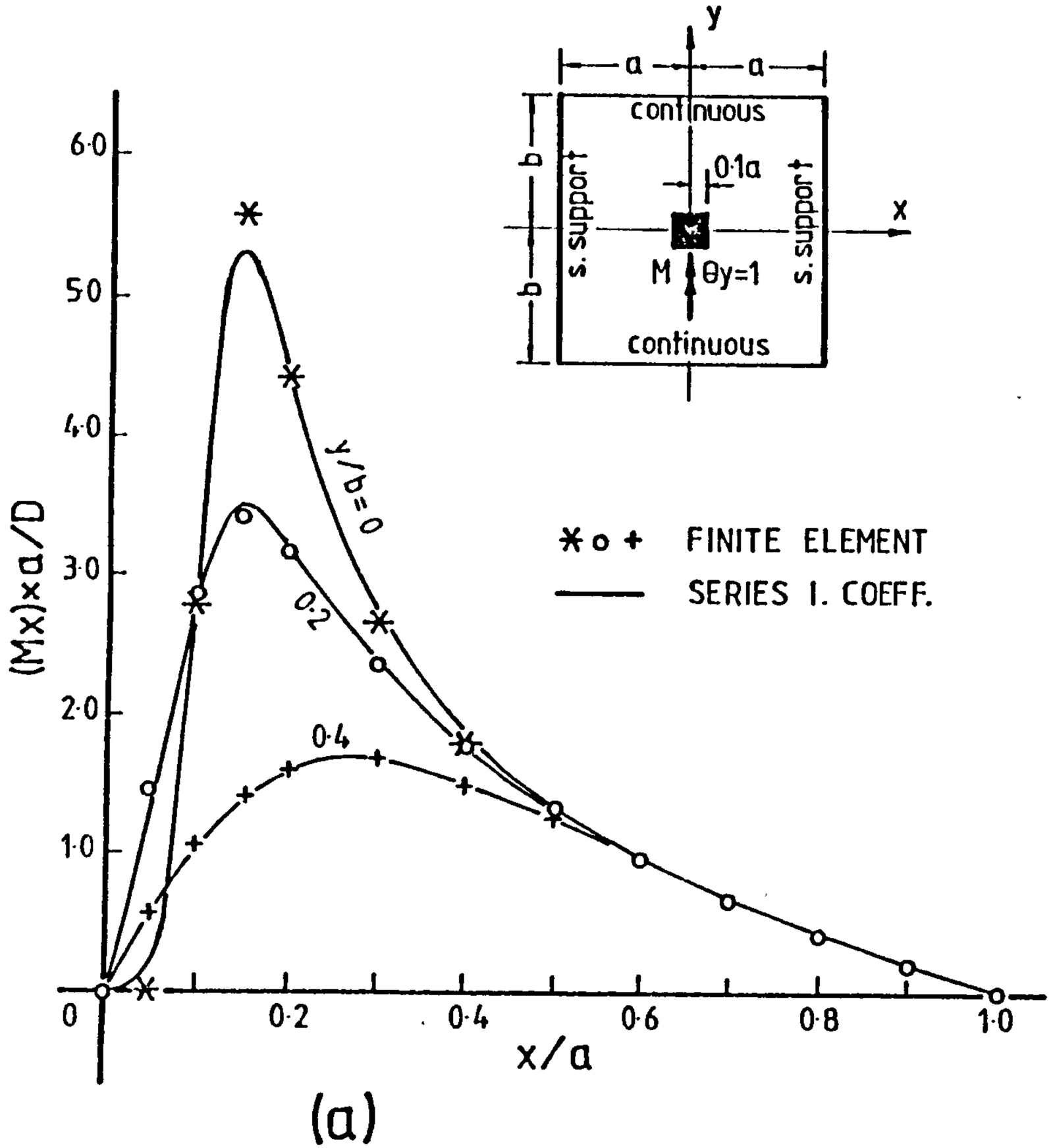

* o + FINITE ELEMENT

—— SERIES I. COEFF.

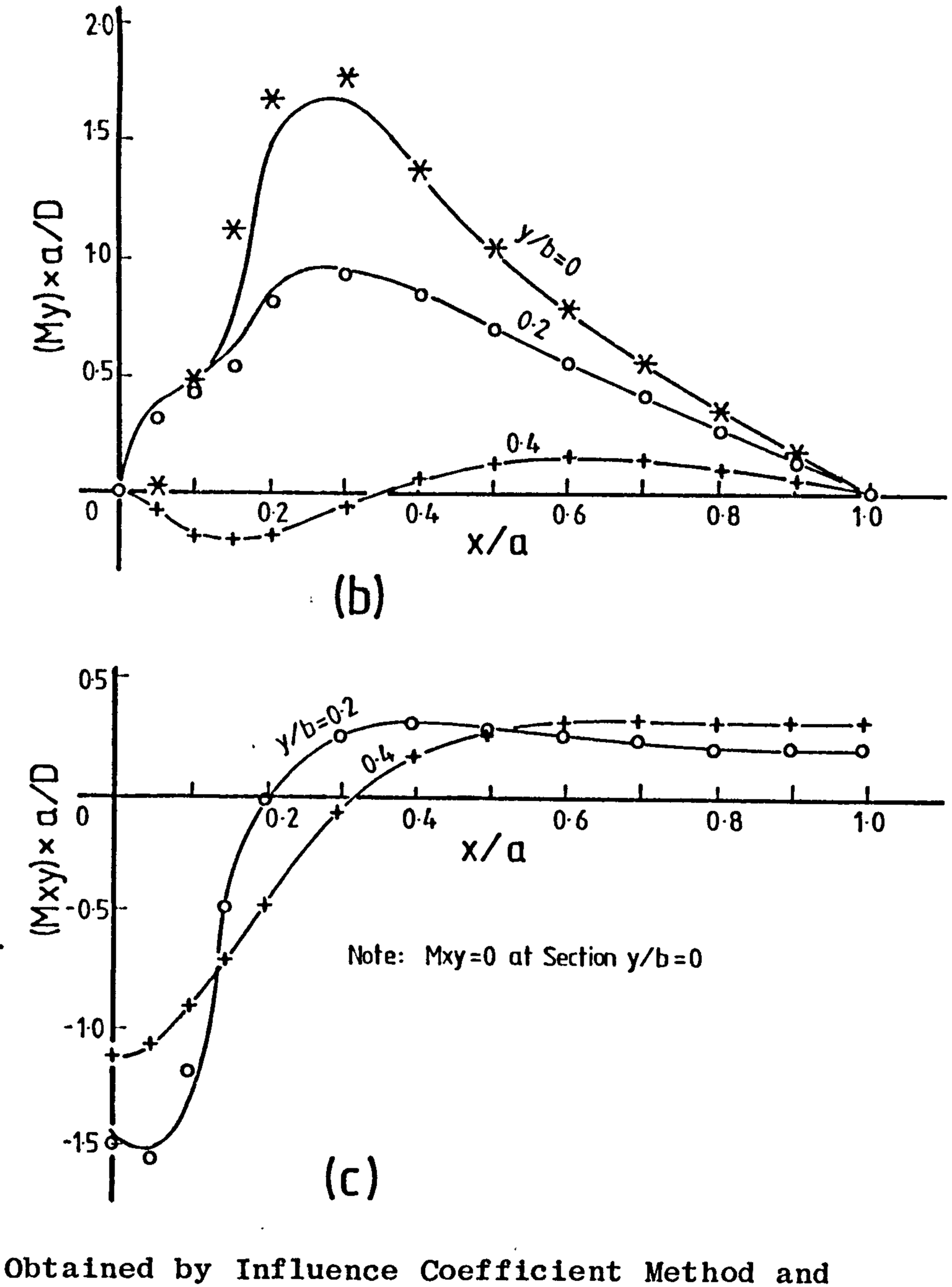

Fig. 9.13 Comparison between Slab Moments Obtained by Influence Coefficient Method and Finite Element Method, at Various Longitudinal Sections, (a) Longitudinal Bending Moment Mx, (b) Transverse Bending Moment My, and (c) Twisting Moment Mxy

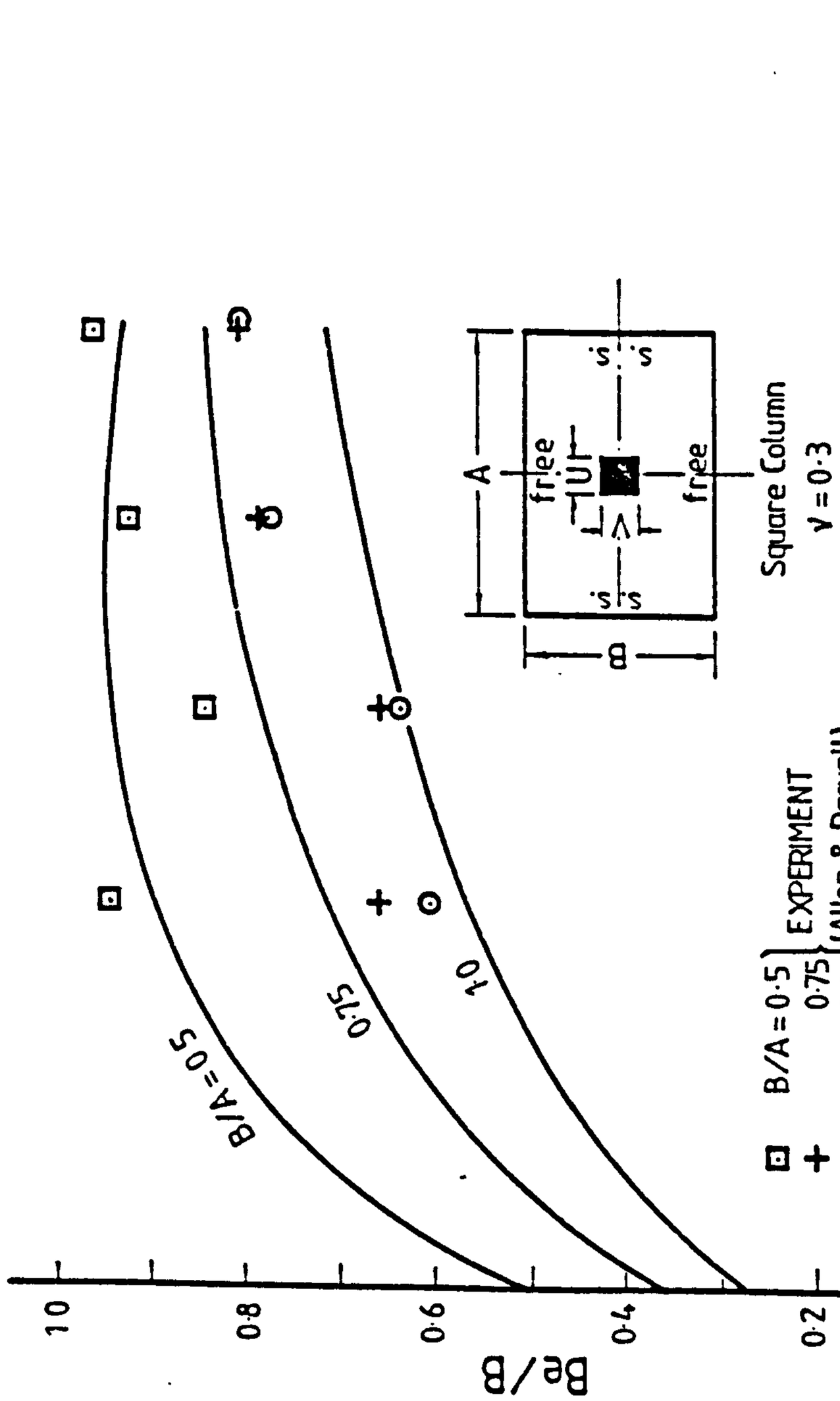

Fig. 9.14 Comparison between Effective Width Values Obtained by Influence Coefficient Method and by Experiment

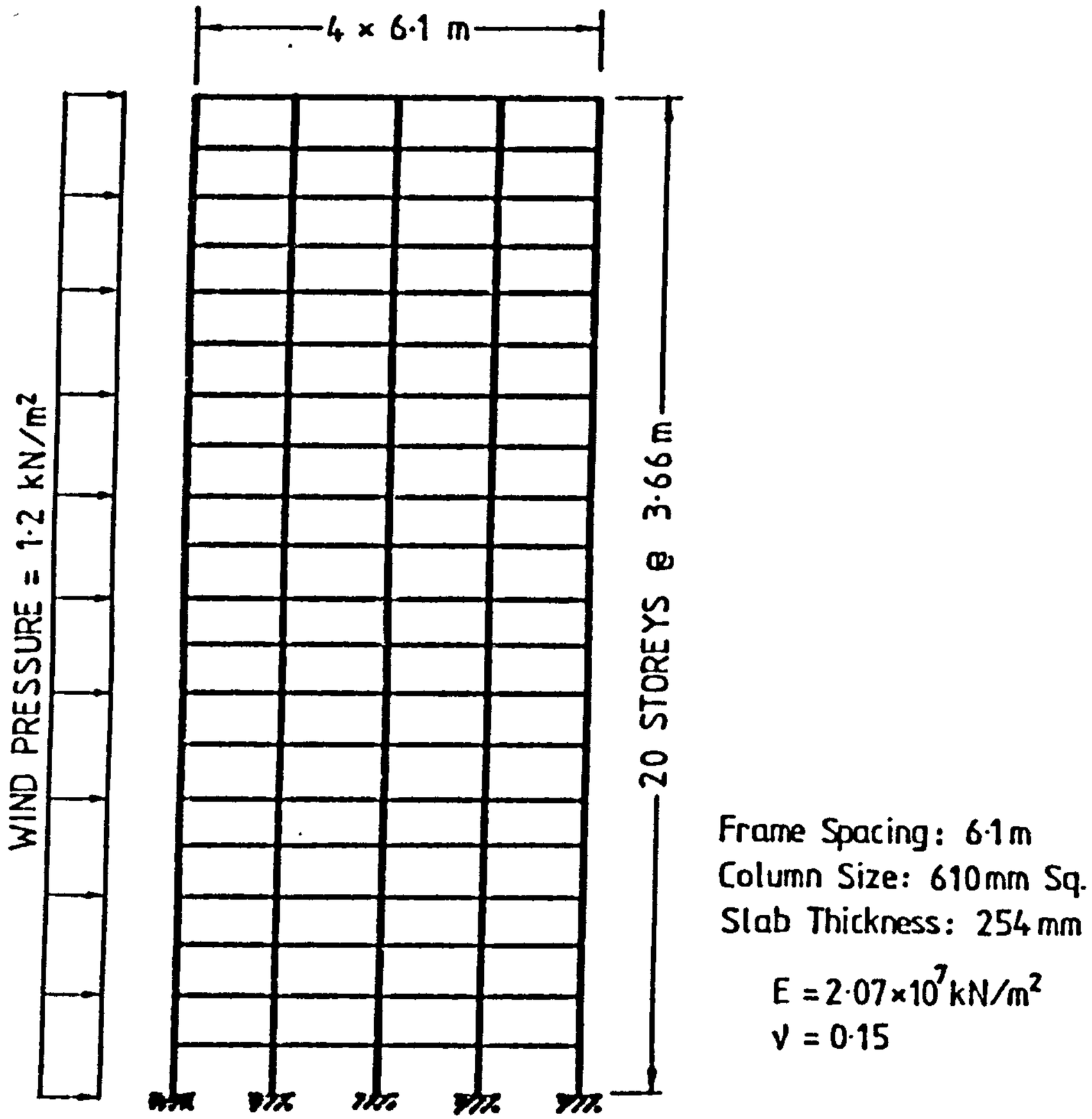

FIG. 9.15 (a) TYPICAL FRAME OF EXAMPLE FLAT PLATE BUILDING

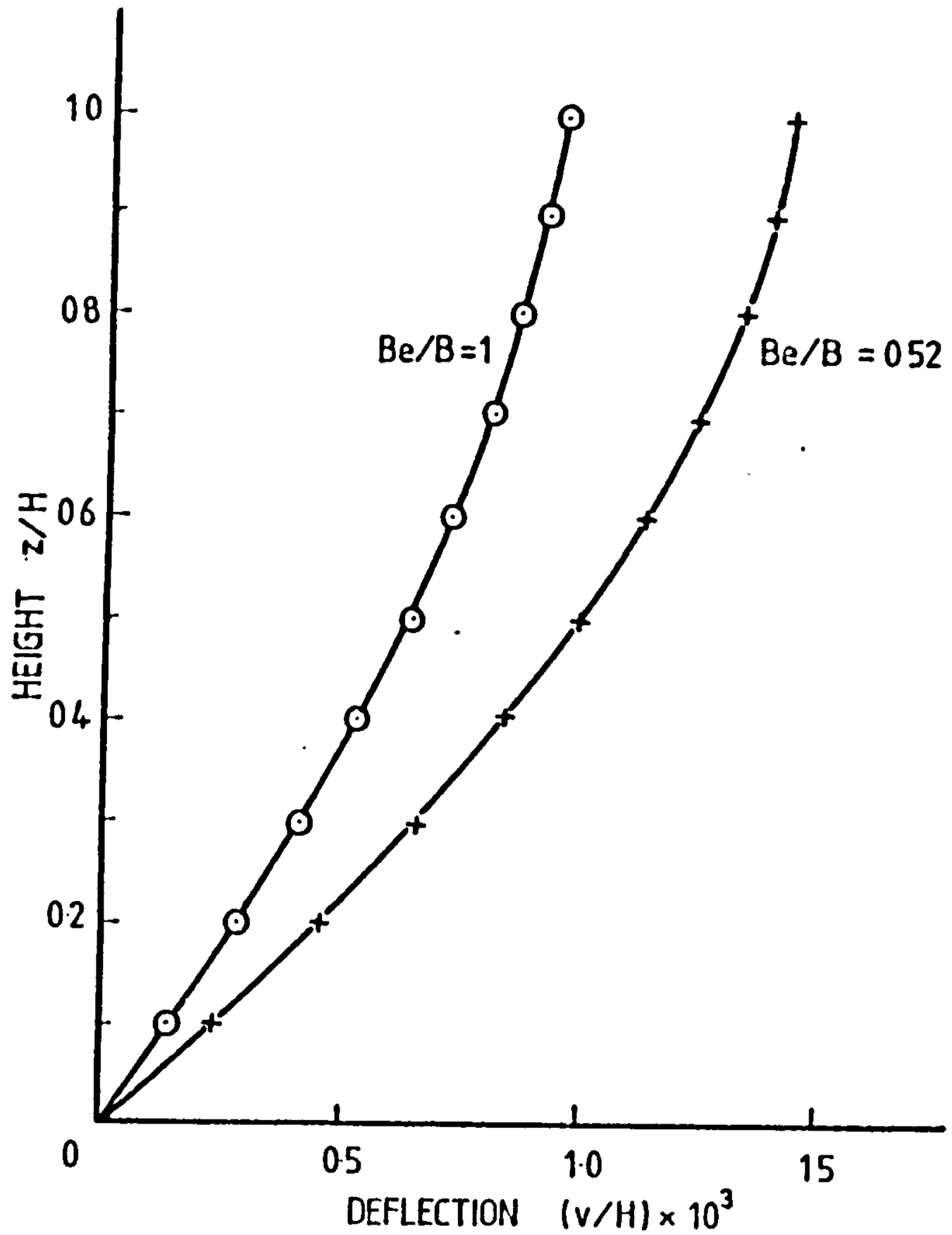

FIG. 9.15 (b) LATERAL DEFLECTION OF EXAMPLE FLAT PLATE BUILDING

CHAPTER 10

EXPERIMENTAL INVESTIGATION

10.1 INTRODUCTION

The accuracy of the numerical results obtained by a theoretical method of structural analysis is limited to the accuracy of the mathematical modelling of the prototype structure and to the accuracy of the method of solution of the mathematical problem formulated. The mathematical modelling of the shear wall-slab structure involves the use of plate and beam theories to describe its structural behaviour. The idealisation of prototype behaviour in these theories involves a certain amount of approximation to the real behaviour of the structure, although experience has shown that the approximations involved are reasonable. The idealised structural problem has been solved numerically either by the finite element method or by the influence coefficient method in the author's theoretical investigations. The discretisation process in the numerical solution involves a certain degree of approximation to the exact mathematical solution for the problem. Therefore, it is inevitable that the numerical results which have been presented in the previous Chapters will contain a certain amount of error, the significance of which can only be assessed by prototype or model testing.

In order to verify the accuracy of the methods of analysis and of the numerical results which have been presented, tests have been performed on small scale shear wall-slab models and the experimental results obtained have been compared with the corresponding numerical results evaluated by the theoretical methods of analysis. Two separate groups of tests have been carried out. The first series of tests has been conducted to substantiate the methods of analysis employed in Chapters 3 and 4 for calculating the slab stiffness or effective width assuming that plane sections of the coupled walls remain plane in

bending. The second series of tests has been carried out to verify the method of analysis which considers the local elastic wall deformation effects in the wall-slab interaction. The various aspects of the experimental investigation are described in this Chapter.

10.2 CHOICE OF MODEL MATERIAL

In order to give a good representation of prototype behaviour, the model should ideally be constructed of a similar material to the prototype structure. For modelling the shear wall-slab structure, concrete appears to be the obvious choice as model material. The concrete model, unfortunately, gives a poor response to test loading and unless it is constructed to a suitable scale, the limitations of the loading and monitoring equipment available may well prevent any useful results from being obtained from the test.

Various alternative materials are available for the construction of the model, which after all is in this case required only to simulate the elastic response of the prototype structure to applied loading. The alternative material should clearly be chosen so that the deflections and strains developed in the model are measurable under the test load without overstraining the material. Apart from possessing suitable elastic properties, the model material should also be inexpensive, readily available and easy to fabricate.

Metals and alloys have often been used for constructing slab models. These materials have very consistent and practically linear stress/strain elastic properties, and test results obtained from the models are generally very good. They are, however, expensive for model construction and require large test loads to produce the required response. To test the model requires large loading equipment and strong supports for the model, which may not be readily available in the laboratory.

Various sheet plastics have also been used for model

construction. Araldite and perspex, in particular, have found favourable use in shear wall and slab models. These materials have reasonably linear stress/strain properties and low elastic moduli, which give rise to large deflections and strains under load. Sheets are readily available in a wide range of sizes and thicknesses, and they can be easily cut, machined and fabricated. Araldite exhibits negligible creep under stress in the elastic range but is expensive. Perspex, on the other hand, is relatively cheap, but has the undesirable tendency to creep under load. It is also sensitive to humidity and temperature change, and sheets of perspex often show anisotropic material properties and variation in thickness across the sheet. Nevertheless, by making careful measurements of the thickness and elastic properties and by adopting a rigorous procedure of testing whereby all necessary precautions are taken to minimise the adverse effects, reasonably accurate test results can be obtained with the use of a perspex model.

10.3 SERIES 1 TESTS

10.3.1 DESIGN AND CONSTRUCTION OF MODEL:

Experimental tests have been carried out by Qadeer and Stafford Smith[2], Coull and El-Hag[7,40] and El-Buluk[8] using small scale slab-wall models to evaluate directly the coupling stiffness and effective width values for slabs with various wall configurations. The design of the model and the test procedure adopted by these investigators were essentially similar. The model consisted essentially of a pair of steel wall sections pivoted at their bases and rigidly coupled to the slab specimen at the top. By applying a horizontal load at the level of the slab, the wall rotation induced by the effective wall moment was obtained for evaluating the slab stiffness and effective width. The experimental results obtained by these investigators, unfortunately, do not agree well with theoretical results, particularly for configurations with

small corridor opening ratios or large flange width ratios. In some instances, discrepancies of up to 60% difference have been noted between these experimental results and the author's finite element results. The poor experimental results appear to be due to inherent defects in the model and test apparatus. These defects arise from the unavoidable slackness in the pivots and possibly in the bolted connections between wall and slab.

Recognising the shortcomings of the previous relatively elaborate yet unreliable test model a simpler model which could be more positively loaded and monitored was devised for the author's experimental investigation. The test set up is illustrated in Fig. 10.1 and Plates 10.1, (a) and (b). The model was designed to represent a typical half of the slab panel since it is known that the deformation of the prototype slab panel is anti-symmetric about the corridor centre-line. The line of anti-symmetry (or line of inflexion) in the prototype was simulated by a simply supported slab edge in the model.

The slab specimen was cut from a 3/16 in. (5 mm) (nominal) thick perspex sheet. The connection to a rigid wall was simulated by sandwiching the slab between a pair of steel pieces ($\frac{3}{4}$ in. (19.05 mm) deep by $\frac{1}{4}$ in. (6.35 mm) wide), cut to the shape of the wall and bolted through the slab with $\frac{1}{8}$ in. (3 mm) diameter brass bolts at 1 in. (25.4 mm) centres. The slab was supported across an opening in a test bench with a rocker bearing at the outer end of the wall and a long roller and holding down device at the corridor edge of the slab. The holding down device consists of a row of needles held on a 1 in. (25.4 mm) square rectangular hollow section clamped at its ends to the test bench. The needles could be individually adjusted and locked in position such that the points bear on the slab surface directly over the roller support, thus preventing possible up-lift due to transverse bending but allowing free rotation of the supported slab edge during the test. By positioning the roller and holding down device at various distances from the inner end of the wall

section, coupling slabs with various corridor opening ratios could be simulated using the same model.

A wall moment could be applied to the model by hanging weights at the inner end of the wall section. The induced wall rotation could be monitored effectively by measuring the deflections at the ends of the wall section and at the simply supported slab edge using three dial gauges suspended from a dexion frame clamped to the test bench. The effective slab width could then be evaluated in the following manner:

Referring to Fig. 10.2 which shows the deflected slab model with δ_1, δ_2 and δ_3 as the measured deflections, P as the applied load, and x_1, x_2 and x_3 as measured distances, the effective wall rotation about the supported end is given by

$$\theta_1 = \left(\frac{\delta_2 - \delta_1}{x_1}\right) - \left(\frac{\delta_3 - \delta_1}{x_2}\right) \qquad (10.1)$$

The applied wall moment about the supported end is given by

$$M_1 = P.x_3 \qquad (10.2)$$

Writing $K_1 = M_1/(D\ \theta_1)$, where D is the flexural rigidity of the slab, the rotational stiffness factor K for the slab coupling a pair of walls rotating about their centroidal axes a distance c apart is given by

$$K = K_1 \left(\frac{0.5c}{x_2}\right)^2 \qquad (10.3)$$

The effective width Y_e/Y is then given by

$$\frac{Y_e}{Y} = \frac{K}{6(1-\nu^2)} \left(\frac{L}{Y}\right)\left(\frac{L}{c}\right)^2 \qquad (10.4)$$

where Y is the width of the slab panel, L is the corridor width and ν is Poisson's ratio for the slab.

10.3.2 TEST PROGRAMME

Altogether, 35 wall-slab combinations (Tables 10.1a and b) were tested. The combinations were obtained by

varying the wall length W and the flange width Z from 3 in. (76.2 mm) to 7 in. (177.8 mm) and the corridor width L from 2 in. (50.8 mm) to 8 in. (203.2 mm). The slab width Y was kept at a constant value of 10 in. (254 mm). The wall thickness h and the slab overhang width C were kept at constant values of $\frac{1}{4}$ in. (6.4 mm).

10.3.3 TEST PROCEDURE

The model was set up with the supports and dial gauges at their respective marked positions on the model and with the weight hanger on. The loads were applied in five increments to a maximum test load of 10 or 15 kg. depending on the stiffness of the model. The dial gauges were read 10 minutes after each load increment to allow time for the gauge readings to stabilise. The model was then unloaded in equal decrements and gauge readings similarly taken at each stage until the model was completely unloaded. The complete test was repeated half an hour later to obtain a second set of results for averaging.

To enable the calculation of the flexural rigidity of the slab, the average slab thickness was obtained by micrometer measurements on the model. The elastic constants E and ν, were obtained from the perspex supplier's specification as the actual values were not expected to be significantly different from the recommended values.

10.3.4 EVALUATION OF TEST RESULTS

The two corresponding sets of gauge readings taken at the loading and unloading stages in a test were averaged to minimise the effects of creep in the perspex. The effective wall rotation and applied wall moment at each load stage were calculated from equations (10.1) and (10.2), using for the calculations, the distances measured before the commencement of the test. A straight line was fitted to the moment-rotation relationship by the method of least squares and the gradient of the line obtained for the

calculation of the coupling stiffness and effective width in accordance with equations (10.3) and (10.4). The corresponding results from the two tests on the same model were averaged for the final results. The processing of the experimental data was carried out by computer.

The experimental results for the various tests are shown in Tables 10.1, (a) and (b).

10.3.5 THEORETICAL RESULTS

The slab models were analysed theoretically by the finite element method and by the influence coefficient method. In the theoretical analysis, the slab edges parallel to the direction of bending were treated as free edges, and the finite wall thickness was disregarded. The material constants, E and ν, for the analysis were the values assumed for the experiments. The slab thickness in all cases was taken as the 3/16 in. (5 mm) nominal thickness since the theoretical effective width is unaffected by the slab thickness.

The order of refinement adopted for the analysis of the model was comparable to that used for the parametric studies described in Chapters 3 and 4. The finite element analyses used between 72 and 104 elements for the discretisation of the slab, depending on the configuration. The influence coefficient solutions used four discrete nodes for the discretisation of plane walls. For flanged walls, two web nodes and between two and six flanged nodes were used depending on the flange width. Forty terms of the series were used for the evaluation of the influence coefficients.

The effective width values evaluated by the two theoretical methods are shown in Tables 10.2-10.3, (a) and (b).

10.3.6 COMPARISON BETWEEN EXPERIMENTAL AND THEORETICAL RESULTS

Values of the effective width Y_e/Y obtained from the tests have been compared with the theoretical results in

Fig. 10.3. For the cases with plane walls, the experimental results generally agree well with the theoretical results. The agreement appears particularly good for cases with small ratios L/Y. With the larger ratios L/Y, the experimental results are slightly higher than the theoretical results and indicate the possible stiffening effect of the finite wall thickness which has not been considered in the theoretical analysis. This stiffening effect in cases with small ratios L/Y appears to have been offset by flexibility effects due to possible transverse shear deformation of the slab and unavoidable slackness of the wall-slab connection which are expected to become more significant when the slab is stiff and large loads are used to induce the necessary wall rotation in the test.

The correspondence between the experimental and theoretical results for the cases with flanged walls appears less good. With walls of small sections (3 x 5 in. Tee, 5 x 5 in Tee and 5 x 3 in. Tee), the experimental results agree reasonably well with the theoretical results, but with larger wall sections (7 x 5 in. Tee and 5 x 7 in. Tee), the experimental results are significantly lower than the theoretical results, the discrepancy becoming greater as the ratio L/Y is decreased. It appears that these experimental results are significantly influenced by the flexibility effects. In these flanged wall cases, in addition to the effects of transverse shear deformation and wall-slab connection flexibility, bending of the wall pieces may be a significant contributing factor for the poor experimental results.

10.4 SERIES 2 TESTS

10.4.1 DESIGN OF MODEL

In the first series of tests described, the wall was assumed infinitely stiff in comparison with the slab and it was possible to simulate the presence of the wall in the model by clamping steel pieces cut to the shape of the

wall on to the slab. In the second series of tests, the wall and slab were modelled as an integral unit, since the influence of wall flexibility on the performance of the slab was being considered. For convenience, the case of a slab interacting with a pair of walls undergoing differential axial movement was considered for the investigation. Since it is difficult to reproduce in a simple model the continuous boundary conditions of a typical interior slab panel, free slab edges were considered for the prototype and model, for the purpose of verification of the method of analysis. On account of conditions of anti-symmetry about the corridor centre-line, the model was designed to represent only one half of the prototype wall-slab panel. The line of anti-symmetry in the prototype slab panel was simulated by a free edge subjected to a constant deflection in the model. The wall was assumed fully restrained at the floor levels above and below the slab under investigation.

Six different models were considered for this series of tests to provide sufficient variety of the parameters for the general accuracy of the method of analysis to be verified. The six models (Fig. 10.4) were obtained essentially from a single model constructed in stages and tested at each stage before some component parts were added for the next model. The models illustrated in Fig. 10.4 represent, in the order in which they were tested, the following configurations:

(1) Plane wall-slab panel with large corridor opening
(2) Plane wall-slab panel with small corridor opening
(3) Flanged wall-slab panel with small corridor opening
(4) Flanged wall-slab panel with large corridor opening
(5) Flanged wall-lintel-slab panel with large corridor opening
(6) Flanged wall-lintel-slab panel with small corridor opening.

The dimensions of the models were chosen from preliminary theoretical analyses to ensure that strains

and deflections induced by a reasonable test load on the model would be large enough to be reliably measured with the available apparatus.

10.4.2 CONSTRUCTION OF MODEL

The basic model (Fig. 10.5(a)) consisted essentially of an intersection of two plates representing the floor slab and the plane shear wall. The slab and wall components were cut from a $\frac{3}{8}$ in. (10 mm) thick perspex sheet to approximate dimensions using a band saw. The plates were then machined along their edges to the required dimensions. A slit was cut in the slab at one end where the wall would penetrate. The slit was milled to a width 1/16 in. (1.6 mm) narrower than the wall thickness. The wall was recessed at mid-height to a depth of 1/16 in. (1.6 mm) on each face and at the inner edge to provide a key for the slab. I.C.I. Tensol Cement No. 7, which has properties similar to perspex when cured, was applied to the joint surfaces and the wall unit slotted into the slab unit. The assembled units were squared and clamped in position, and an additional quantity of cement was run in to completely fill up the joint. After the cement had hardened sufficiently for the model to be handled safely any excess cement which had overrun the joint was carefully scraped off, and the corners were finished neatly. The end-blocks for the wall were built up by cementing on $\frac{3}{8}$ in. (10 mm) thick perspex pieces. The end blocks were eventually drilled to accept three $\frac{1}{2}$ in. (12.7 mm) diameter clamping bolts at each end of the wall. The slab was provided with a row of $\frac{1}{4}$ in. (6.4 mm) diameter bolt holes along the cantilevered edge representing the line of anti-symmetry in the prototype, for receiving the stiffening and loading unit (Fig. 10.5(c)). This consisted essentially of a pair of aluminium angles designed to restrain the clamped edge of the slab from transverse bending and at the same time transmit the concentrated load applied through a hanger attached to the unit, as a distributed shear on the slab.

The model with a smaller corridor opening was obtained by clamping the aluminium angles nearer to the wall (Fig. 10.5(b)). To accommodate them, four $\frac{1}{4}$ in. (6.4 mm) diameter bolt holes were drilled through the slab when required. These holes were refilled with I.C.I. Tensol Cement No. 7 when the aluminium angles were repositioned back at the outer edge for the next model having a larger corridor opening.

The wall flange required for Models 3 and 4 was added in the second stage of construction. The flange was assembled in four quadrants. The flange pieces were cut from the $\frac{3}{8}$ in. (10 mm) thick perspex sheet and were individually shaped to provide a tight fit between the wall and slab when cemented on.

The lintel beam was added in the last stage of construction for Models 5 and 6. The lintel piece was also cut from the $\frac{3}{8}$ in. (10 mm) thick perspex sheet, machined to the correct dimensions and cemented to the underside of the slab and to the wall.

The plane wall and flanged wall models under test are shown in Plates 10.2, (a) and (b), respectively.

10.4.3 STRAIN GAUGES

Japanese Type PL 10 electrical resistance strain gauges were used for measuring the surface strains in the model. The gauges were positioned at regular intervals along three slab sections and a wall section (Fig. 10.6) to enable the strain distributions to be picked up accurately. In addition to these regular gauges, a few random gauges were positioned at points where strains were expected to be similar, on account of symmetry, to those monitored by the regular gauges. These served as control gauges to enable any possible deviation from symmetry during test to be detected. The gauges and terminal strips for wire leads were glued on to the model at accurately marked positions with M Bond 200 adhesive. The lead wires were soldered on to the gauge terminals and

the gauges varnished over with M Coat A for insulation and protection. The resistance of each gauge was checked with a Solarton 4440 Digital Multimeter for fault in the gauge and connection before being wired to the monitoring equipment.

Strain gauges attached to disused perspex models were used as dummy gauges for compensating for the effects on strain measurement produced by humidity and temperature changes in the laboratory and by local heating caused by the gauge circuit.

10.4.4 STRAIN MEASUREMENT

The strain monitoring equipment was made up of Balwin-Lima-Hamilton BLH Model 220 switching units connected to a BLH Type 20 strain indicator (Plate 10.2(a)). Each switching unit allowed ten strain gauge outputs to be monitored in succession on the strain indicator. A number of switching units were connected in parallel to enable the monitoring of the large number of gauge outputs required in the test. Each gauge and its dummy compensator were wired to one channel of the 10-channel switching unit.

The BLH Portable Type 20 strain indicator used a self-contained battery power pack for the gauge circuit. For strain measurement, it used a manually operated null-balance system with digital readout for fast accurate reading. The indicator could be operated over a range of 0 to $\pm$ 30,000 micro-inch per inch strains with a resolution of 5 microstrains in the digital readout. Gauges of different gauge factors could be accommodated with adjustment of a control on the indicator.

10.4.5 DEFLECTION MEASUREMENT

John Bull dial gauges Type 2S with a maximum travel of 25 mm and a sensitivity of 0.01 mm were used for deflection measurements on the model. The dial gauges were supported on a light dexion frame clamped to the test

stand. The gauges were positioned at points along the centreline of the slab (Fig. 10.7) for measuring deflections which could be conveniently compared with the theoretical results. In addition to these gauges, two others were placed at the extremities of the loaded slab edge. These together with the one in the centre provided a means of checking that the load was symmetrically disposed and the edge uniformly deflected. Other gauges were placed to monitor possible support movements and asymmetric bending in the slab.

10.4.6 TEST FRAME

The test frame (Plate 10.2a) consisted of a pair of mounting units set one metre apart, connected by horizontal and inclined bracing members to form a stiff self-supporting box frame. The end of the frame which was intended for supporting the model was further stiffened by bracing an additional mounting unit to it at a short distance apart.

Each mounting unit consisted of two vertical legs of 3 x 1½ in. (76 x 38 mm) steel channels welded to 6 x 6 in. (152 x 152 mm) base plates and set apart by welding to two ½ in. (12.7 mm) thick by 6 in. (152 mm) wide steel plates. These steel plates were provided with a regular array of holes for use in fixing the model to the frame and were set near the upper ends of the support legs to provide adequate clearance below the model to hang the weights. The bracing consisted of cut lengths of 2 x 1 in. (50 x 25 mm) rectangular hollow sections with welded end plates which were tapped for bolting to the mounting units.

To strengthen the mounting units, ½ in. (12.7 mm) diameter screwed rods and short lengths of hollow sections were used to bolt and brace the horizontal steel plates of the two adjacent mounting units to make them act together more effectively as a unit.

The mounting plates were originally designed for horizontal mounting of the model set into a base plate,

and were not suitable for direct vertical mounting of the shear wall-slab model. An auxiliary mounting piece was connected to the mounting unit to provide a means of support for the model shear wall. The auxiliary mounting piece consisted of 2 x 1 in. (50 x 25 mm) RHS horizontal arms welded to a 3 x 2 in. (76 x 50 mm) RHS vertical trunk bolted to the mounting plates. The horizontal arms were provided with $\frac{1}{2}$ in. (12.7 mm) diameter screwed rods with lock nuts and $\frac{3}{8}$ in. (9.5 mm) thick backing plates for effective clamping of the end blocks of the model shear wall (Fig. 10.5, (d)-(e)).

10.4.7 TEST PROCEDURE

The model was set up with the strain gauges wired to the monitoring equipment, and the dial gauges and weight hanger in position. The three dial gauges in line at the loading edge were set to similar or nearly similar initial readings so that any uneven deflection of the loaded edge could be immediately detected from differences in the gauge readings, at all stages of the test. Before commencing the actual testing, the model was pre-loaded with the full test load for 10 minutes and then unloaded, to take up any initial relaxation of the model and supporting parts. The actual testing was commenced half an hour later in order to allow the gauges to stabilise for the initial readings to be taken.

The test loads were applied by hanging weights on the weight hanger suspended by a cord attached to the mid-point of the aluminium stiffening angles. For loading in the reversed (upward) direction, the cord was passed over an overhead pulley carried on a heavy steel angle clamped to the test frame (Plate 10.2 (a)). The loads were applied in four or five increments to a maximum test load which varied from 5 to 12 kg according to the model tested. The maximum test load for each model was predetermined to ensure that the strains induced in the model would be large enough to be satisfactorily measured but not too large as

to cause distress in the model. The strain gauges and dial gauges were read in a fixed sequence, commencing 10 minutes after each load increment, in order to allow the gauge readings to settle to reasonably stable values.

The test was repeated the following day in order to allow enough time for the model to recover from creep effects. For models 1 to 4, tests were performed with upward loading in addition to the tests carried out with downward loading to minimise errors due to possible asymmetry in material properties, model geometry or fixity conditions. The upward loading tests were omitted for Models 5 and 6 for fear of damage to the lintel-wall butt joint which could be subjected to large tensile forces during the test.

10.4.8 DETERMINATION OF MODULUS OF ELASTICITY AND POISSON'S RATIO

Values of the elastic modulus and Poisson's ratio for the model material were required for the theoretical analysis of the model. These were determined from tests made on specimens cut from the same sheet of perspex used to make the models. Two beam specimens measuring $1\frac{1}{2}$ in. (38.1 mm) wide by 15 in. (381 mm) long were strain-gauged in the longitudinal and transverse directions at mid-span. The beams were then tested in flexure by supporting them over a span of 14.1 in. (360 mm) and applying incremental loading at one-third points on the span. A predetermined maximum test load of 2.5 kg was used to ensure a maximum strain level similar to the model test conditions. In addition to strain measurements, mid-span deflections were also monitored on the test specimens. Each specimen was tested twice and then turned over for two repeat tests to minimise errors due to anisotropic tendencies of the perspex.

The thickness of each specimen was measured by a micrometer at quarter points for the calculation of cross-sectional properties.

The averaged values of the elastic constants determined from the tests were

Modulus of elasticity:

(a) By strain measurement = 3138 N/mm^2 (4.54×10^5 lb/in^2)

(b) By deflection measurement = 2940 N/mm^2 (4.26×10^5 lb/in^2)

Average value = 3039 N/mm^2 (4.40×10^5 lb/in^2)

Poisson's ratio = 0.375

10.4.9 EVALUATION OF TEST RESULTS

The rigorous test routine of incremental loading and unloading, test repetition and load reversal had been adopted so as to provide sufficient sets of test results from which a reliable set could be evaluated statistically. In processing the test results, the corresponding strain or deflection readings obtained at each gauge station during the loading and unloading stages in a test were averaged to reduce errors due to creep effects in the perspex. A straight line was then fitted by the method of least squares through the points which would be obtained by plotting the averaged strain or deflection readings against the applied load. The gradient of the fitted straight line gave the strain or deflection induced at the gauge station by a unit shear (1 kg) applied at the cantilevered slab edge. The corresponding results from the various tests performed on the same model were finally averaged for comparison with the theoretical results. Any particular result which was suspect on account of its large deviation from the normal trend of the other corresponding results was disregarded in the averaging process. (Faults were actually detected, after the test, at some terminals on the switching units to which a number of 'suspect' gauges were wired.)

Due to the large number of tests performed and the enormous number of gauge readings obtained for each test,

manual processing of the test results would have been extremely time-consuming. The test results were therefore processed on a computer using one of the author's programs. The evaluated test results are shown in Tables 10.4, (a)-(f), and 10.5, (a)-(f).

10.4.10 THEORETICAL ANALYSIS

In order to provide a comparison between theoretical and experimental results, the shear wall-slab models were analysed by the finite element method as described in Section 5.2. The finite element idealisations for Models 2, 3 and 5 are shown in Fig. 10.8-10.10. The idealisations for Models 1, 4 and 6 differed from those shown only in the sub-division of the corridor slab in the span-wise direction. In the idealisation, advantage was taken of the symmetry or anti-symmetry conditions where they existed to reduce the computational effort.

In the finite element analysis, the walls were treated as fully restrained at the level of the end block. The edge of the slab representing the line of anti-symmetry in the full slab panel was prescribed with a unit deflection and zero transverse slope. The remaining edges of the slab were treated as free edges.

The modulus of elasticity for the finite element analysis was assumed as the averaged value determined by the strain and deflection measurements in the tests. The value of Poisson's ratio determined by the tests was also used for the theoretical analysis. The wall and slab thickness was assumed as $\frac{3}{8}$ in. (10 mm) since this nominal value was in close agreement with the average value of 0.377 in. determined by micrometer measurements at a number of points on the model.

In order to allow a direct comparison between theoretical and experimental results, surface strains were computed from the averaged nodal membrane and bending stresses in the finite element analysis. The computed strains and deflections at various sections were normalised with respect to the applied shear computed from nodal

reactions at the deflected slab edge. The theoretical results are compared with the test results in Fig. 10.11-10.16.

10.4.11 DISCUSSION OF RESULTS

In comparing results obtained by theoretical analyses and model tests it must be appreciated that the degree of correspondence obtainable is influenced by errors which are present in both sets of results. Good correspondence between theoretical and experimental results does not necessarily mean that the theory is accurate and the experimental technique is sound, unless both sets of results are accurate, since good correspondence can also be obtained between two erroneous sets of results when errors are of similar sense and order. Poor correspondence, on the other hand, may be due to deficiencies in the experiments and not due to any inaccuracy of the theory. It is important to be able to identify all possible sources of errors which may be present in both the theoretical and experimental investigations and be able to assess their sense and relative importance if the results are to be correctly interpreted.

Errors arise in any experimental investigation due to unavoidable deficiencies in the test equipment. Some of these errors may be minimised with a rigorous test procedure when their cause and effects are understood, but some others remain undetermined.

The electrical resistance strain gauges and strain indicator are precision scientific equipment, and provided they are in good working order, errors in strain measurement will be very small. However, through regular use and occasional manhandling, defects can develop in the strain monitoring equipment which may affect its precision. One possible defect which is seldom recognised is due to the gauge factor calibrating unit drifting out of correct adjustment. This defect which was detected in a strain indicator in regular use resulted in errors of up to 30%

in the strain readings. But since the strain indicator used in the tests had been specifically checked to ensure that the calibration control was correctly set this source of error can be discounted. Errors in strain measurements can also arise through defects in some channels of the switching units to which the gauges and strain indicator are connected. These errors can usually be detected during the test by the erratic strain readings or by the rapid drift of the null-balance indicator. This source of error when it was detected in the test was eliminated in the next test by reconnecting the affected gauges to other channels which were in good order. The affected strain readings were discarded in the averaging process when the results were being processed. Therefore errors from this source should not be present in the processed experimental results unless they are very small and have escaped detection during the test.

The effects of changes in temperature and humidity which affect the properties of the perspex were minimised by using compensating dummy strain gauges. Nevertheless, errors due to these effects could show up in the strain readings for the wall which was restrained at its ends against movement. These errors, however, are not expected to be significant, with the reasonably well controlled laboratory atmospheric conditions during the tests.

The local stiffening effect of the perspex due to the presence of the strain gauge and adhesive may, to a certain extent, influence the accuracy of the measured strain. However, the errors involved should be negligible, with the modern construction of the strain gauges.

Creeping of the perspex under load increases with time the deflections and strains in the model. By reading the gauges in the same sequence at a fixed time interval after each load increment or decrement, and by averaging the readings obtained during the loading and unloading stages, the effects of creep were minimised in the test results.

Movement in the wall supports, which will tend to make measured deflections appear larger but will not affect the strain measurements, was just discernable with a very sensitive dial gauge (John Bull Type 2U), and will therefore not influence the test results noticeably.

The models were of simple construction with very few parts and joints, and could be fabricated to a high standard of finish. Nevertheless, dimensional inaccuracy due to the inherent thickness variation of the perspex sheet could still be a source of error which could influence the degree of correspondence between theoretical and experimental results. Judging from the micrometer measurements of the wall and slab thickness, which indicated possible deviations from nominal sheet thickness of $\pm$ 5%, differences between calculated and observed strains up to an order of $\pm$ 10% can be expected at some points on the model.

The stiffened edge of the slab which was supposed to undergo a constant deflection along its length to simulate the line of anti-symmetry in the prototype slab panel was deflected by applying a central load. An eccentric application of the load with respect to the centre line will affect the accuracy of the test results due to unsymmetrical bending. However, in all the tests, fairly symmetric loading was achieved, as indicated by the control dial gauges and strain gauges symmetrically located on the slab. The dial gauges 1, 2 and 3 (Fig. 10.7) located along the loaded edge showed discrepancies of less than 2% in deflection measurements in all the tests. Similarly, the symmetrically placed strain gauges 17 and 36 (Fig. 10.6) indicated differences less than 2% in the longitudinal strain measurements in all the tests. Therefore, errors due to eccentric loading should be small.

Inaccuracies associated with the finite element analysis arise in the modelling and discretisation processes. In idealising the slab as a thin plate, the effects of transverse shear deformation are being neglected.

This would result in calculated slab deflections being underestimated to a certain extent depending on the slab thickness in relation to its span. In the models analysed, the slab was relatively thin and errors from this source should be very small.

A second source of inaccuracy which arises in the modelling process is due to the idealisation of the wall panels as thin membrane members. The idealisation results in the intersection of wall and slab being represented as a line, whereas in the actual situation the wall and slab intersect through a finite volume of material. This means that the wall and slab become more severely loaded locally, through mutual interaction, in the idealised model than in the real model. Therefore theoretical stresses or strains at points on the wall and slab close to the intersection will, to a certain extent, be overestimated, depending on the relative wall and slab dimensions and on the location of the points where these quantities are evaluated.

The discretisation of the continuum into a finite number of elements introduces errors of convergence into the numerical results. The nature of these errors depends not only on the element mesh division of the structure but also on the type of problem being solved and on the element characteristics. The finite element analyses for the wall-slab models employed the rectangular shell element RS24 together with the triangular shell element TS18 and used reasonably refined element mesh patterns for the discretisation. Convergence studies have indicated that under such circumstances, convergence errors will tend to make calculated slab deflections appear smaller and make calculated slab stresses appear larger than the 'true' theoretical results. These errors should be quite small at most places in the model except at points of severe stress concentration where the errors in the calculated stresses or strains could be significantly large.

10.4.11.1 Comparison Between Experimental and Theoretical Results

(a) Slab Centre-line Deflections (Fig. 10.6, 10.11-10.16)

The experimental results for the slab centre-line deflections for Models 1 to 4 (Fig. 10.11-10.14) generally agree very well with the theoretical results, with discrepancies in the maximum deflections varying from ½ to 5½%. The larger discrepancies are associated with the two models having the smaller slab span (corridor width), for which, measured deflections at all points are larger than the predicted values and appear to reflect the influence of shearing deformation and discretisation errors. Shearing deformation tends to increase the slab deflection and is more significant when the shear span is small. Discretisation errors, on the other hand, tend to make calculated deflections appear smaller, and in the present case these errors are likely to be larger for the slab with the smaller span, where the element sub-division of the slab, in relation to its span, is coarser than that of the slab with the larger span.

The correspondence between the experimental and theoretical deflections for Models 5 and 6 (Fig. 10.15-10.16) is poorer than that for the first four models. The theoretical results in this case are 9% and 14½% lower than the experimental results, and again the larger discrepancy is associated with the model with the smaller slab span. The calculated deflections for these models should be less affected by the effects of shearing deformation than the previous models because the lintel beam, which carries a substantial portion of the shear load, has been modelled as plane stress elements capable of undergoing shearing deformation. However, discretisation errors are likely to be more significant here since the lintel beam has been discretised using a rather coarse two-element-deep mesh sub-division. These last two models have more components and joints in their construction than the previous models and so the experimental results for these models are more

likely to be affected by joint flexibility. The effects of various experimental errors also tend to show up more significantly when the measured deflections are small, which is the case with these last two models.

(b) Slab Strains at Section A-A (Fig. 10.6, 10.11-10.16)

The measured longitudinal strain ε_y in Models 1, 4 and 5, which have the larger slab span, agree very well with the theoretical results. At most points along the section, the plotted experimental and theoretical results almost coincide. In the other three models which have the shorter slab span, the experimental strains ε_y generally agree less well with the theoretical results. In Model 3, the experimental strains all lie below the theoretical strain curve for ε_y (Fig. 10.13), but in Models 2 and 6 the experimental results straddle the theoretical curves (Fig. 10.12 and 10.16).

The experimental and theoretical transverse strains ε_x agree reasonably well in all six models. In Models 1 and 2 which have plane walls and therefore relatively large transverse slab strains, the measured strains at most points are significantly lower than the calculated values, but in the four flanged wall models where transverse slab strains are low, the experimental and theoretical strains are in better agreement. The discrepancies in the plane wall models are to be expected. Since the finite wall thickness has not been represented in the discretisation of the slab, the transverse bending moments and strains would be overestimated to a certain extent along the slab centre line (i.e. at section A-A).

(c) Slab Strain at Section B-B (Fig. 10.6, 10.11-10.16)

The longitudinal strains ε_y, measured in Models 1 and 2 agree fairly well with the theoretical results at most points, except where the strains reach peak values. The calculated peak strain value in each model is approximately 16% higher than the experimental value and

is clearly influenced significantly by the discretisation errors in the finite element analysis, but the irregular strain pattern predicted is reasonably well reflected in the experimental results. In the other four models (Fig. 10.13 to 10.16) the measured longitudinal strains generally agree well with the calculated results. In models 3 and 4 the experimental results are generally lower than the theoretical results, but in Models 5 and 6, this trend is reversed.

The transverse strains ε_x obtained experimentally in all six models agree very well with the theoretical results. In each case, the peculiar strain pattern predicted is accurately picked up by the strain measurements, in spite of the fact that the strains at most points are relatively small, and therefore more difficult to measure accurately.

The overall accuracy of the strain measurements may be assessed by carrying out a statical check on the equilibrium between the internal bending moments and the external applied moment at this section. The areas under the experimental strain curves for ε_x and ε_y are used together with the sectional and elastic properties of the slab to evaluate the internal bending moments at the section. The results of the statical check for the first four models are shown in Table 10.7. The statical check could not be performed for the last two models due to insufficient strain measurements required to separate the membrane from the bending effects in the measured strain. It may be concluded from the results of the various statical checks that the strains have generally been measured reasonably accurately, probably with a maximum error of only $\pm$ 5% in the reading.

(d) Slab Strains at Section C-C (Fig. 10.6, 10.15-10.16)

In all six models, the experimental and theoretical longitudinal strains ε_y are generally in good agreement. A comparison between the highest measured strain and the corresponding theoretical value in each case shows that discrepancies are less than 4% for the first three models

and varies from 5 to 8% for the remaining models.

(e) Wall Strains at Section D-D (Fig. 10.6, 10.11-10.16)

In the plane wall models (i.e. Models 1 and 2) the correspondence between experimental and theoretical results for the vertical wall strains is not as good as that for the slab strains already discussed. Although absolute experimental and theoretical strain values generally do not agree very well, the predicted and observed strain patterns indicating severe stress concentration at the inner edge of the wall are very similar. The peak theoretical compressive strains in the two models are substantially higher than the experimental values and indicate discrepancies of 15 to 30%. The large discrepancies may be explained by the presence of not only theoretical errors but also experimental errors. As may be observed from the results of the convergence study in Fig. 5.2 (Chapter 5) the calculated peak strain value at the inner edge of the wall is likely to have been affected by convergence errors which tend to make it appear larger than the correct analytical result. It can also be observed in Figs. 10.11 and 10.12 that the positive wall strains measured at the inner positions in the wall are substantially higher than the predicted values and this seems to indicate, from a static check at the section, the presence of an axial tension, which may have been produced by the restraint of the wall ends. This axial tension has the effect of lowering the high compressive strains at points near the edge of the wall produced by the applied loading on the slab.

In Models 3 and 4 the experimental strains in the web and flange sections agree well with the theoretical results, and discrepancies vary from 3 to 7% in respect of strains compared near the edge of the flange. In Models 5 and 6, although the correspondence between experimental and theoretical strains is reasonably good in the web section and a larger part of the flange section,

there appears to be a serious discrepancy between the experimental and theoretical strain distributions in the central portion of the flange. In this particular region, the theoretical results show a sharp rise in the strain distribution which does not appear to be shown by the available experimental measurements. In order to find an explanation for the apparent discrepancy it is necessary to take a closer look at the way in which the inconsistent strains have been calculated. It is observed that the large strain value predicted at the centre of the flange was produced primarily by bending in the flange at the root of the lintel beam. This local bending in the flange appears to have been produced as a result of the severe local horizontal in plane deformation of the wall web induced by the large lintel beam reaction. The local bending of the flange can only happen in the theoretical model where the flange has been idealised as being connected to the middle plane of the web. In the real model, what has been idealised as a part of the flange which is able to bend is, in fact, a part of the web. Therefore, the calculated flexural strains in the flange at the centre line of the web is imaginary rather than real.

(f) Lintel Strains at Section E-E (Fig. 10.6, 10.11-10.16)

The longitudinal strains measured at the soffits of the lintel beams in Models 5 and 6 agree extremely well with the theoretical results. Discrepancies between the experimental and theoretical results are less than 2% in all cases.

10.5 CONCLUSIONS

A reasonably wide range of shear wall-slab models has been tested. Although the models in the first series of tests were relatively unsophisticated, reasonably good correspondence between theoretical and test results was obtained in most cases where the slab was not excessively

stiff. In cases where the slabs were very stiff, the test results appeared to be influenced considerably by various secondary effects not considered in the theoretical analysis and also by inherent defects in the test apparatus. Consequently, in these cases, correspondence between theoretical and test results was less satisfactory.

The models in the second series of tests were relatively more sophisticated and so was the theoretical method of analysis which was intended to be verified. In all these cases good agreement was obtained between the theoretical and test results for deflections and strains at most points on the model. However at certain points close to regions of stress concentration, the theoretical strains were considerably higher than the measured values as a result of the finite element idealisation which neglected the effect of finite wall thickness. Clearly, in these regions care must be exercised in interpreting the finite element results.

On the whole, the experimental tests provide strong evidence to support the validity of the various theoretical analyses.

TABLE 10.1(a) - EXPERIMENTAL RESULTS FOR SERIES 1 MODELS IN PLANE WALL CONFIGURATION

Plane Wall	Effective Width Y_e/Y				
W \ L	2 in.	3 in.	4 in.	6 in.	8 in.
3 in.	0.192	0.282	0.379	0.523	0.638
5 in.	0.196	0.262	0.347	0.556	0.671
7 in.	0.181	0.280	0.360	0.500	0.618

TABLE 10.1(b) - EXPERIMENTAL RESULTS FOR SERIES 1 MODELS IN FLANGED WALL CONFIGURATION

Flanged Wall	Effective Width Y_e/Y			
W x Z \ L	2 in.	4 in.	6 in.	8 in.
3 x 5 in.	0.609	0.817	0.949	1.039
5 x 5 in.	0.583	0.770	0.929	1.006
7 x 5 in.	0.492	0.703	0.786	0.879
5 x 3 in.	0.416	0.643	0.754	0.854
5 x 7 in.	0.676	0.856	0.998	1.063

TABLE 10.2(a) - FINITE ELEMENT RESULTS FOR SERIES 1 MODELS IN PLANE WALL CONFIGURATION

Plane Wall	Effective Width Y_e/Y				
W \ L	2 in.	3 in.	4 in.	6 in.	8 in.
3 in.	0.191	0.273	0.347	0.471	0.566
5 in.	0.194	0.278	0.355	0.485	0.584
7 in.	0.194	0.279	0.356	0.487	0.587

TABLE 10.2(b) - FINITE ELEMENT RESULTS FOR SERIES 1 MODELS IN FLANGED WALL CONFIGURATION

Flanged Wall	Effective Width Y_e/Y			
W x Z \ L	2 in.	4 in.	6 in.	8 in.
3 x 5 in.	0.734	0.832	0.894	0.935
5 x 5 in.	0.739	0.840	0.903	0.943
7 x 5 in.	0.741	0.844	0.907	0.947
5 x 3 in.	0.522	0.652	0.745	0.810
5 x 7 in.	0.943	1.006	1.037	1.053

TABLE 10.3(a) - INFLUENCE COEFFICIENT RESULTS FOR SERIES 1 MODELS IN PLANE WALL CONFIGURATION

Plane Wall	Effective Width Y_e/Y				
W \ L	2 in.	3 in.	4 in.	6 in.	8 in.
3 in.	0.192	0.269	0.343	0.469	0.574
5 in.	0.197	0.282	0.362	0.500	0.610
7 in.	0.202	0.289	0.374	0.519	0.627

TABLE 10.3(b) - INFLUENCE COEFFICIENT RESULTS FOR SERIES 1 MODELS IN FLANGED WALL CONFIGURATION

Flanged Wall	Effective Width Y_e/Y			
W x Z \ L	2 in.	4 in.	6 in.	8 in.
3 x 5 in.	0.721	0.855	0.930	0.984
5 x 5 in.	0.720	0.860	0.932	0.982
7 x 5 in.	0.726	0.862	0.938	0.986
5 x 3 in.	0.522	0.675	0.772	0.853
5 x 7 in.	0.869	0.978	1.017	1.048

TABLE 10.4(a) - STRAIN MEASUREMENTS FOR

PERSPEX MODEL NO. 1 - (PLANE WALL/FLOOR SLAB INTERACTION)

SURFACE STRAINS (MICROSTRAIN/KG)

GAUGE	DOWNWARD LOADING		UPWARD LOADING		AVERAGE
	TEST 1	TEST 2	TEST 3	TEST 4	
1	43.74	45.46	-45.54	-44.00	44.69
2	0.00	9.71	-12.97	-9.96	8.16
3	62.11	67.16	-65.23	-63.69	64.55
4	9.51	27.40	-22.54	-20.86	20.08
5	83.01	102.83	-90.63	-85.54	90.50
6	20.61	32.11	-33.64	-28.34	28.68
7	103.39	109.59	-105.56	-103.84	105.59
8	34.54	44.79	-50.81	-45.66	43.95
9	141.39	177.21	-157.30	-146.04	155.48
10	81.26	94.94	-100.70	-96.30	93.30
11	171.46	188.31	-192.99	-188.01	185.19
12	-160.04	-160.01	171.81	174.21	-166.52
13	-19.47	-10.49	13.11	14.63	-14.43
14	47.10	50.29	-51.19	-49.93	49.63
15	170.39	179.77	-180.81	-178.26	177.31
16	-19.49	-17.77	19.29	18.81	-18.84
17	126.77	128.89	-134.51	-133.81	130.99
18	-34.50	-25.47	22.76	24.69	-26.85
19	103.83	106.99	-113.46	-113.36	109.41
20	-37.10	-24.49	28.21	29.74	-29.89
21	96.74	104.83	-103.10	-103.33	102.00
22	61.70	67.79	-72.33	-68.20	67.50
23	102.39	105.34	-110.69	-110.87	107.32
24	65.01	67.47	-71.31	-71.76	68.89
25	14.07	28.91	-23.93	-22.09	22.25
26	-63.49	-56.33	49.69	50.59	-55.02
27	-27.83	-23.03	28.70	28.29	-26.96
28	10.61	10.47	-8.73	-7.71	9.38
29	11.74	15.06	-15.71	-15.50	14.50
30	2.33	15.74	-13.96	-9.83	10.46
31	-0.63	11.03	-8.86	-6.47	6.43
32	0.00	4.07	-5.83	-4.83	3.68
33	7.69	13.13	-9.86	-7.41	9.52
34	0.00	0.00	0.00	0.00	0.00
35	41.77	44.04	-44.24	-44.00	43.51
36	126.59	128.86	-133.04	-132.33	130.20
37	190.13	189.66	-187.57	-187.10	188.62
38	0.00	0.00	0.00	0.00	0.00
39	0.00	0.00	0.00	0.00	0.00
40	0.00	0.00	0.00	0.00	0.00
41	0.00	0.00	0.00	0.00	0.00
42	0.00	0.00	0.00	0.00	0.00
43	0.00	0.00	0.00	0.00	0.00
44	0.00	0.00	0.00	0.00	0.00
45	0.00	0.00	0.00	0.00	0.00

TABLE 10.4(b) - STRAIN MEASUREMENTS FOR

PERSPEX MODEL NO. 2 - (PLANE WALLS/ FLOOR SLAB INTERACTION)

SURFACE STRAINS (MICROSTRAIN/KG)

GAUGE	DOWNWARD LOADING		UPWARD LOADING		AVERAGE
	TEST 1	TEST 2	TEST 3	TEST 4	
1	0.00	0.00	0.00	0.00	0.00
2	0.00	0.00	0.00	0.00	0.00
3	0.00	0.00	0.00	0.00	0.00
4	0.00	0.00	0.00	0.00	0.00
5	0.00	0.00	0.00	0.00	0.00
6	5.36	5.54	-6.78	-5.94	5.90
7	22.91	22.54	-21.73	-19.91	21.77
8	24.37	24.63	-25.91	-22.64	24.39
9	58.53	57.07	-57.59	-47.99	55.29
10	55.83	55.02	-55.75	-50.89	54.37
11	85.52	86.11	-86.80	-78.72	84.29
12	-96.49	-96.42	106.29	102.31	-100.38
13	-6.09	-5.90	6.64	8.63	-6.81
14	32.09	32.06	-32.11	-31.08	31.84
15	79.69	79.26	-79.92	-76.57	78.86
16	-6.88	-7.72	7.43	6.69	-7.18
17	53.47	52.93	-56.39	-54.45	54.31
18	-9.34	-10.14	10.55	12.75	-10.69
19	39.71	39.50	-42.26	-40.36	40.46
20	-10.88	-11.35	11.42	12.97	-11.66
21	35.34	34.57	-37.34	-36.41	35.92
22	0.00	0.00	0.00	0.00	0.00
23	26.20	25.80	-27.99	-27.18	26.79
24	33.01	31.86	-33.43	-32.67	32.74
25	10.39	8.84	-10.94	-5.87	9.01
26	-32.94	-33.35	27.77	28.31	-30.59
27	-15.17	-15.81	19.06	18.74	-17.20
28	3.39	3.50	0.00	-0.42	1.83
29	6.18	6.70	-6.51	-6.67	6.51
30	3.91	3.41	-4.26	-2.29	3.47
31	1.77	2.36	-2.61	-0.94	1.92
32	0.75	0.64	-1.28	-1.55	1.05
33	5.31	4.80	-3.58	-2.69	4.10
34	2.81	2.44	-1.16	-0.83	1.81
35	24.09	23.94	-25.26	-24.08	24.34
36	52.71	52.51	-54.69	-52.59	53.12
37	85.89	85.40	-84.96	-82.12	84.59
38	0.00	0.00	0.00	0.00	0.00
39	0.00	0.00	0.00	0.00	0.00
40	0.00	0.00	0.00	0.00	0.00
41	0.00	0.00	0.00	0.00	0.00
42	0.00	0.00	0.00	0.00	0.00
43	0.00	0.00	0.00	0.00	0.00
44	0.00	0.00	0.00	0.00	0.00
45	0.00	0.00	0.00	0.00	0.00

TABLE 10.4(c) - STRAIN MEASUREMENTS FOR

PERSPEX MODEL NO.3 - (FLANGED WALL/FLOOR SLAB INTERACTION)

SURFACE STRAINS (MICROSTRAIN/KG)

GAUGE	DOWNWARD LOADING		UPWARD LOADING		AVERAGE
	TEST 1	TEST 2	TEST 3	TEST 4	
1	0.00	0.00	0.00	0.00	0.00
2	0.00	0.00	0.00	0.00	0.00
3	0.00	0.00	0.00	0.00	0.00
4	0.00	0.00	0.00	0.00	0.00
5	0.00	0.00	0.00	0.00	0.00
6	-0.70	1.03	-4.86	-2.76	1.99
7	27.42	27.11	-28.75	-28.14	27.86
8	-2.94	1.64	-11.54	-9.95	5.05
9	47.98	53.24	-71.04	-65.30	59.39
10	0.00	3.40	-11.93	-9.33	6.16
11	87.12	85.84	-86.80	-88.06	86.95
12	-4.97	-4.05	3.34	5.54	-4.47
13	2.05	4.35	-8.17	-7.34	5.48
14	5.62	6.31	-6.74	-6.53	6.30
15	71.72	72.41	-76.87	-77.14	74.54
16	4.37	4.81	-5.66	-4.76	4.90
17	57.06	56.54	-57.02	-57.50	57.03
18	-14.31	-9.19	-1.09	0.00	-5.60
19	41.06	40.90	-41.76	-41.84	41.39
20	-13.13	-10.72	2.02	7.54	-8.35
21	32.33	32.48	-35.95	-35.83	34.15
22	0.00	0.00	0.00	0.00	0.00
23	26.00	25.05	-26.21	-26.22	25.87
24	13.46	14.57	-18.09	-16.94	15.76
25	-10.03*	0.00	-22.08*	-6.82	4.72*
26	-5.08	-5.35	4.13	5.05	-4.90
27	0.00	1.11	-2.81	-3.50	1.86
28	5.04	5.29	-6.82	-6.19	5.83
29	3.71	2.93	-6.09	-5.81	4.64
30	-1.94	-0.43	-5.08	-4.37	1.77
31	-2.68	-1.05	-4.27	-2.23	0.69
32	-1.56	-0.54	-1.76	-1.14	0.20
33	0.00	2.45	-13.94	-5.39	5.45
34	-5.40	-4.53	4.00	4.85	-4.69
35	6.34	5.91	-6.99	-6.22	6.36
36	56.41	55.35	-57.44	-56.76	56.49
37	77.99	77.17	-77.31	-77.66	77.53
38	-48.79	-48.08	47.16	48.80	-48.21
39	-4.14	-3.27	2.92	3.49	-3.45
40	-30.20	-28.92	28.44	28.85	-29.10
41	-25.11	-23.94	23.42	25.22	-24.42
42	-18.96	-18.37	18.76	19.36	-18.86
43	-11.57	-10.72	9.71	12.25	-11.06
44	0.00	0.00	0.00	0.00	0.00
45	0.00	0.00	0.00	0.00	0.00

* Switching Unit Suspect

TABLE 10.4(d) - STRAIN MEASUREMENTS FOR
PERSPEX MODEL NO. 4 - (FLANGED WALL/ FLOOR SLAB INTERACTION)

SURFACE STRAINS (MICROSTRAIN/KG)

GAUGE	DOWNWARD LOADING		UPWARD LOADING		AVERAGE
	TEST 1	TEST 2	TEST 3	TEST 4	
1	44.76	45.99	-44.14	-45.63	45.13
2	1.79	1.80	-6.63	-3.24	3.36
3	62.83	64.86	-63.29	-64.14	63.78
4	0.00	7.33	-6.66	-7.04	5.26
5	82.37	84.34	-80.19	-83.44	82.59
6	12.03	13.86	-16.61	-15.10	14.40
7	107.53	110.17	-104.31	-108.96	107.74
8	5.90	12.10	-21.97	-16.71	14.17
9	153.43	149.63	-142.47	-148.10	148.41
10	0.00	0.00	-18.66	-16.34	8.75
11	191.03	194.97	-192.47	-193.77	193.06
12	-9.96	-9.73	12.14	9.63	-10.36
13	2.34	4.34	-2.10	-5.71	3.63
14	12.71	13.39	-14.16	-14.51	13.69
15	168.10	171.54	-168.84	-171.14	169.90
16	4.00	5.19	0.00	-6.27	3.86
17	135.04	136.97	-136.14	-137.84	136.50
18	-29.89	-29.89	18.74	25.04	-25.89
19	103.26	103.94	-103.00	-105.49	103.92
20	-27.71	-26.40	30.13	27.51	-27.94
21	91.91	93.36	-90.47	-93.36	92.27
22	61.89	63.46	-64.87	-63.31	63.38
23	101.71	104.19	-103.06	-104.51	103.37
24	34.30	35.04	-33.01	-38.07	35.11
25	8.94	16.16	87.44 *	-16.07	-11.57*
26	-10.97	-10.24	11.70	9.91	-10.71
27	2.70	6.06	-4.56	-7.10	5.10
28	12.21	13.07	-12.77	-13.91	12.99
29	9.37	9.49	-13.23	-12.74	11.21
30	2.84	4.20	-3.69	-6.89	4.40
31	0.00	1.99	0.00	-4.04	1.51
32	0.40	0.30	-3.99	-2.99	1.92
33	0.00	0.00	0.00	0.00	0.00
34	0.00	0.00	0.00	0.00	0.00
35	13.00	14.31	-12.54	-13.96	13.45
36	134.27	136.00	-134.36	-137.29	135.48
37	176.30	178.70	-174.67	-177.69	176.84
38	-119.63	-120.31	119.47	116.94	-119.09
39	0.00	0.00	0.00	0.00	0.00
40	-61.27	-61.44	62.34	59.99	-61.26
41	-54.07	-53.67	53.69	54.34	-53.94
42	-51.63	-53.93	58.91	54.80	-54.82
43	-14.84	-16.16	14.73	15.13	-15.21
44	0.00	0.00	0.00	0.00	0.00
45	0.00	0.00	0.00	0.00	0.00

* Switching Unit Faulty

TABLE 10.4(e) - STRAIN MEASUREMENTS FOR
PERSPEX MODEL NO. 5 - (FLANGED WALL/LINTEL/SLAB/ INTERACTION)

SURFACE STRAINS (MICROSTRAIN/KG)

GAUGE	DOWNWARD LOADING TEST 1	TEST 2	AVERAGE
1	23.87	24.25	24.06
2	-3.60	-1.70	-2.65
3	35.40	35.52	35.46
4	1.90	1.40	1.65
5	48.75	49.27	49.01
6	1.07	0.00	0.54
7	63.90	63.60	63.75
8	-3.67	0.00	-1.84
9	85.50	86.80	86.15
10	-11.87	-13.80	-12.84
11	111.97	111.17	111.57
12	0.00	0.00	0.00
13	0.00	-33.67 *	-16.84 *
14	-1.93	-1.27	-1.60
15	83.50	82.80	83.15
16	0.47	0.72	0.60
17	64.67	64.65	64.66
18	-16.12	-12.85	-14.49
19	49.33	48.80	49.06
20	-15.07	-14.47	-14.78
21	42.08	42.15	42.11
22	32.87	33.25	33.06
23	51.90	50.62	51.26
24	20.02	19.82	19.92
25	4.03	3.80	3.91
26	0.00	0.00	0.00
27	34.00	34.67	34.34
28	32.33	32.87	32.60
29	16.20	17.10	16.65
30	6.60	6.80	6.70
31	0.00	2.45	1.23
32	-1.15	0.70	-0.22
33	0.00	0.00	0.00
34	0.00	0.00	0.00
35	12.60	13.82	13.21
36	64.17	63.75	63.96
37	93.22	92.53	92.87
38	-49.30	-47.92	-48.61
39	0.00	0.00	0.00
40	-29.68	-26.62	-28.15
41	-23.93	-23.07	-23.50
42	-50.42 *	-19.40	-34.91*
43	-19.07	-18.85	-18.96
44	-328.45	-326.57	-327.51
45	-243.72	-241.37	-242.54

* Switching Unit Faulty

TABLE 10.4(f) - STRAIN MEASUREMENTS FOR
PERSPEX MODEL NO. 6 - (FLANGED WALL/LINTEL/SLAB INTERACTION)

SURFACE STRAINS (MICROSTRAIN/KG)

GAUGE	DOWNWARD LOADING		AVERAGE
	TEST 1	TEST 2	
1	0.00	0.00	0.00
2	0.00	0.00	0.00
3	0.00	0.00	0.00
4	0.00	0.00	0.00
5	0.00	0.00	0.00
6	2.22	1.87	2.04
7	15.40	15.03	15.22
8	-1.28	-3.78	-2.53
9	34.48	34.35	34.42
10	-6.92	-6.27	-6.59
11	52.10	52.67	52.38
12	0.00	0.00	0.00
13	2.87	3.02	2.94
14	0.00	-0.75	-0.38
15	35.93	36.20	36.07
16	2.47	2.23	2.35
17	26.35	26.87	26.61
18	-2.03	-1.92	-1.98
19	19.30	19.12	19.21
20	-4.65	-5.23	-4.94
21	15.30	15.42	15.36
22	0.00	0.00	0.00
23	12.68	12.73	12.71
24	10.12	9.60	9.86
25	2.67	2.63	2.65
26	0.00	0.00	0.00
27	16.40	15.85	16.12
28	15.12	14.73	14.92
29	7.90	7.48	7.69
30	2.72	1.97	2.34
31	1.15	0.45	0.80
32	0.67	0.00	0.33
33	0.00	0.00	0.00
34	0.00	0.00	0.00
35	7.07	6.58	6.83
36	26.22	26.12	26.17
37	39.97	41.12	40.54
38	-19.60	-20.28	-19.94
39	0.00	0.00	0.00
40	-13.35	-14.05	-13.70
41	-10.82	-11.15	-10.98
42	-8.62	-9.67	-9.14
43	-8.82	-9.28	-9.05
44	-135.80	-137.97	-136.89
45	-60.15	-61.33	-60.74

TABLE 10.5(a) - DEFLECTION MEASUREMENTS FOR MODEL NO. 1

Deflection x 100 (mm)

Gauge	Downward Loading		Upward Loading		Average
	Test 1	Test 2	Test 3	Test 4	
1	222.040	223.120	222.510	221.830	222.380
2	222.630	223.600	222.370	222.060	222.670
3	223.140	223.980	222.880	222.700	223.180
4	110.360	110.720	109.370	108.99	109.860
5	48.943	49.312	48.432	48.139	48.707
6	7.057	7.236	7.663	7.181	7.284
7	12.659	12.789	12.835	12.313	12.549
8	9.914	9.725	10.012	9.554	9.801
9	7.857	7.614	8.239	7.371	7.770
10	0.428	0.235	0.345	0.339	0.337

TABLE 10.5(b) - DEFLECTION MEASUREMENTS FOR MODEL NO. 2

Deflection x 100 (mm)

Gauge	Downward Loading		Upward Loading		Average
	Test 1	Test 2	Test 3	Test 4	
1	32.779	32.286	32.736	31.471	32.318
2	32.614	32.400	33.650	32.779	32.861
3	32.143	32.143	33.307	33.550	32.786
4	17.950	17.743	18.464	18.007	18.014
5	8.264	8.164	7.943	7.521	7.973
6	4.236	4.179	4.457	4.393	4.316
7	7.686	7.807	8.479	8.300	8.068
8	7.636	7.736	8.807	8.729	8.227
9	0.236	0.350	0.736	0.743	0.316

TABLE 10.5(c) - DEFLECTION MEASUREMENTS FOR MODEL NO. 3

Deflection x 100 (mm)

Gauge	Downward Loading		Upward Loading		Average
	Test 1	Test 2	Test 3	Test 4	
1	23.057	24.593	22.536	22.786	23.243
2	23.329	25.000	23.093	23.300	23.681
3	22.814	24.729	22.993	23.229	23.441
4	11.693	11.514	11.400	11.657	11.566
5	2.693	2.493	2.464	2.614	2.566
6	2.321	2.321	2.200	2.271	2.278
7	3.114	3.107	2.950	2.964	3.034
8	3.000	2.963	2.850	2.943	2.939
9	0.129	0.000	0.000	0.000	0.032

TABLE 10.5(d) - DEFLECTION MEASUREMENTS FOR MODEL NO. 4

Deflection x 100 (mm)

Gauge	Downward Loading		Upward Loading		Average
	Test 1	Test 2	Test 3	Test 4	
1	189.170	191.700	191.160	189.640	190.593
2	190.710	192.200	191.110	189.570	190.898
3	190.400	191.940	191.710	189.890	190.985
4	105.530	106.730	107.340	105.290	106.223
5	47.586	48.257	48.586	48.143	48.143
6	1.600	1.857	1.614	1.571	1.661
7	4.257	4.114	4.271	4.043	4.171
8	1.857	2.114	1.759	1.786	1.879
9	0.000	0.428	0.000	0.443	0.218

TABLE 10.5(e) - DEFLECTION MEASUREMENTS FOR MODEL NO. 5

Deflection x 100 (mm)

Gauge	Downward Loading		Average
	Test 1	Test 2	
1	86.325	85.525	85.925
2	86.425	85.525	85.975
3	86.300	85.625	85.963
4	48.200	47.625	47.913
5	21.775	21.525	21.650
6	1.075	1.175	1.125
7	2.200	2.200	2.200
8	1.275	1.250	1.263
9	0.125	0.000	0.063

TABLE 10.5(f) - DEFLECTION MEASUREMENTS FOR MODEL NO. 6

Deflection x 100 (mm)

Gauge	Downward Loading		Average
	Test 1	Test 2	
1	10.533	10.600	10.567
2	10.550	10.683	10.617
3	10.683	10.800	10.742
4	5.483	5.583	5.533
5	1.533	1.517	1.525
6	1.400	1.400	1.400
7	1.467	1.550	1.509
8	0.250	0.267	0.259

TABLE 10.6 STATICAL CHECK AT SLAB SECTION BB IN MODELS 1-4

	Model Number			
	1	2	3	4
$\int \varepsilon_y \, dx$ (in. x 10^6)	2637	1071	1049	2549
$\int \varepsilon_x \, dx$ (in. x 10^6)	-189	- 10	- 73	-261
$D_o = Et^2/ 6(1-\nu^2)$ (lb)	12053	12053	12053	12053
$M_i = D_o(\int \varepsilon_y dx + \nu \int \varepsilon_x dx)$ (Internal moment) (lb-in.)	30.93	12.87	12.31	29.53
M_e (External moment) (lb-in.)	30.86	12.50	12.50	30.86
$100 \times (M_i - M_e)/M_i$ (Percentage)	0.23	2.96	-1.52	-4.30

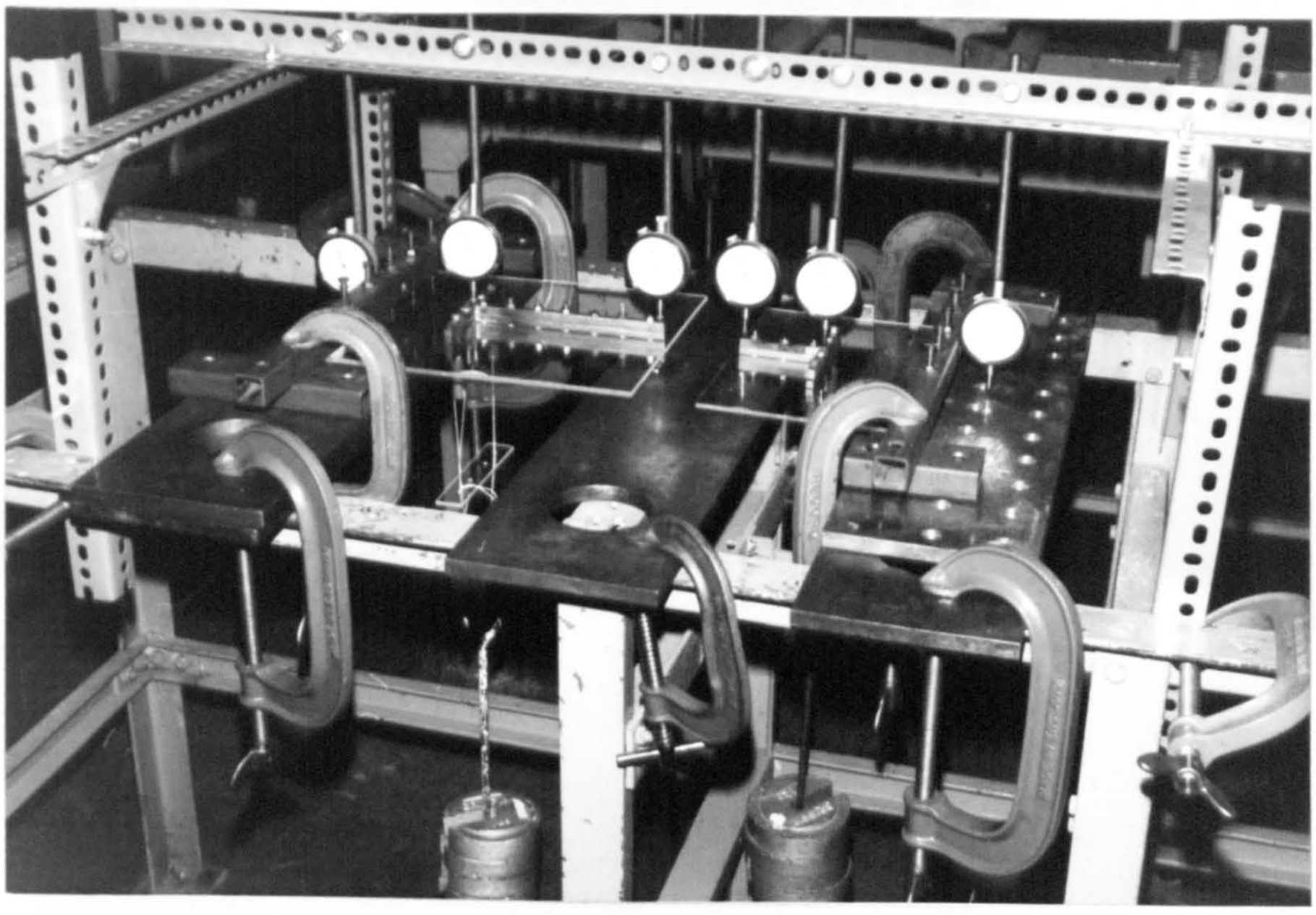

Plate 10.1(a) Pair of Flanged Wall-Slab Models Under Test

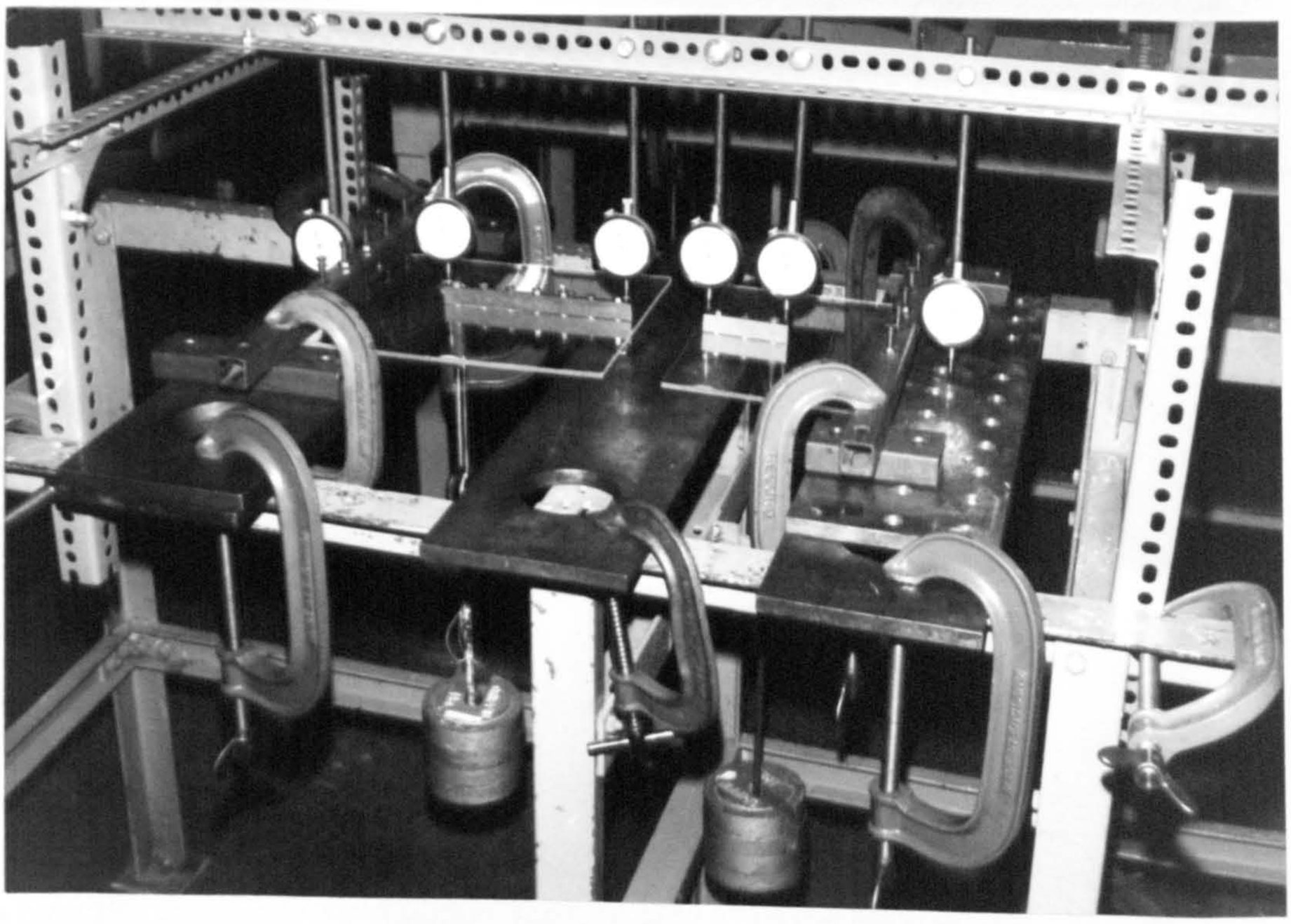

Plate 10.1(b) Pair of Plane Wall-Slab Models Under Test

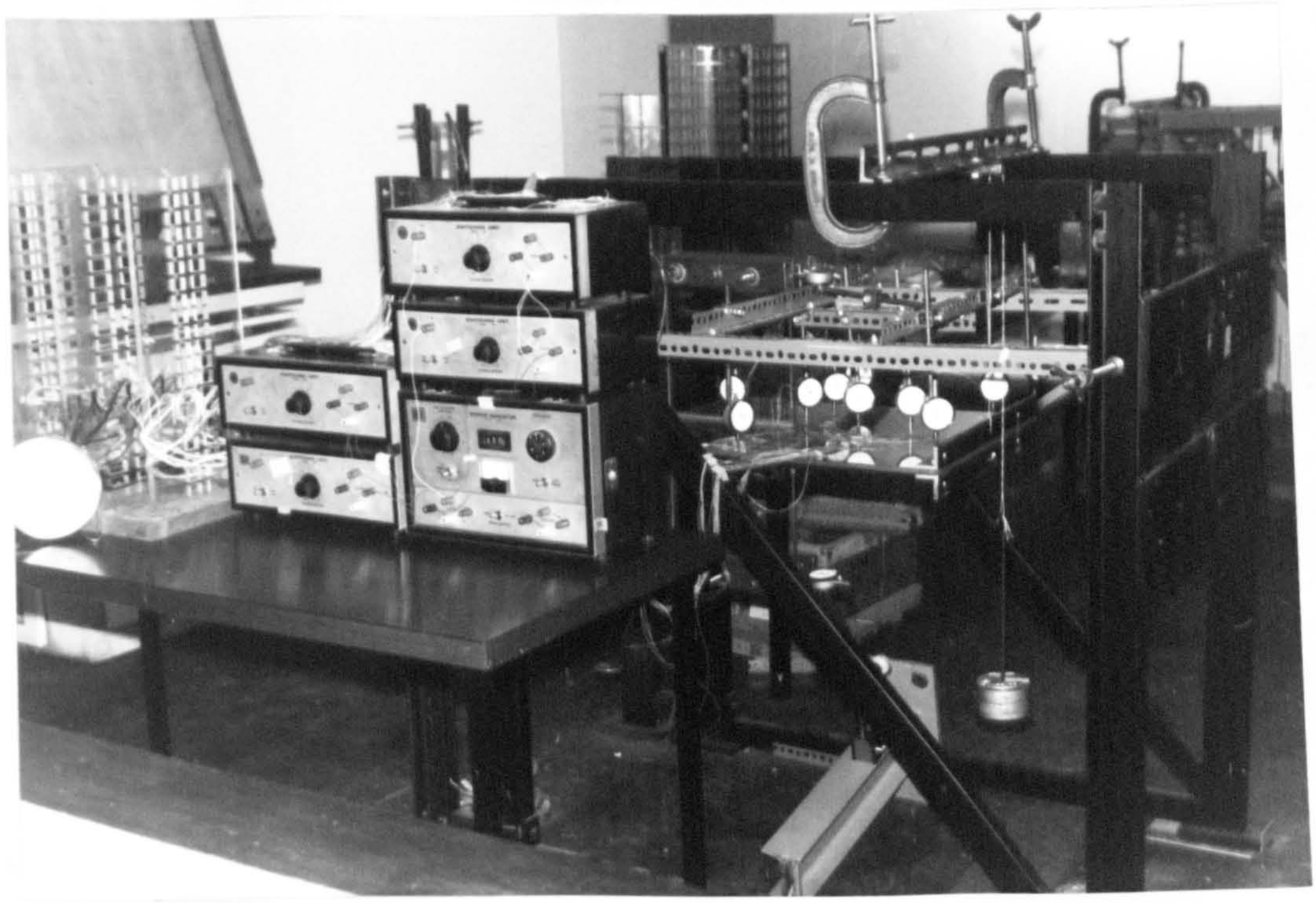

Plate 10.2(a) Plane Wall-Slab Model Under Test
(Upward Loading)

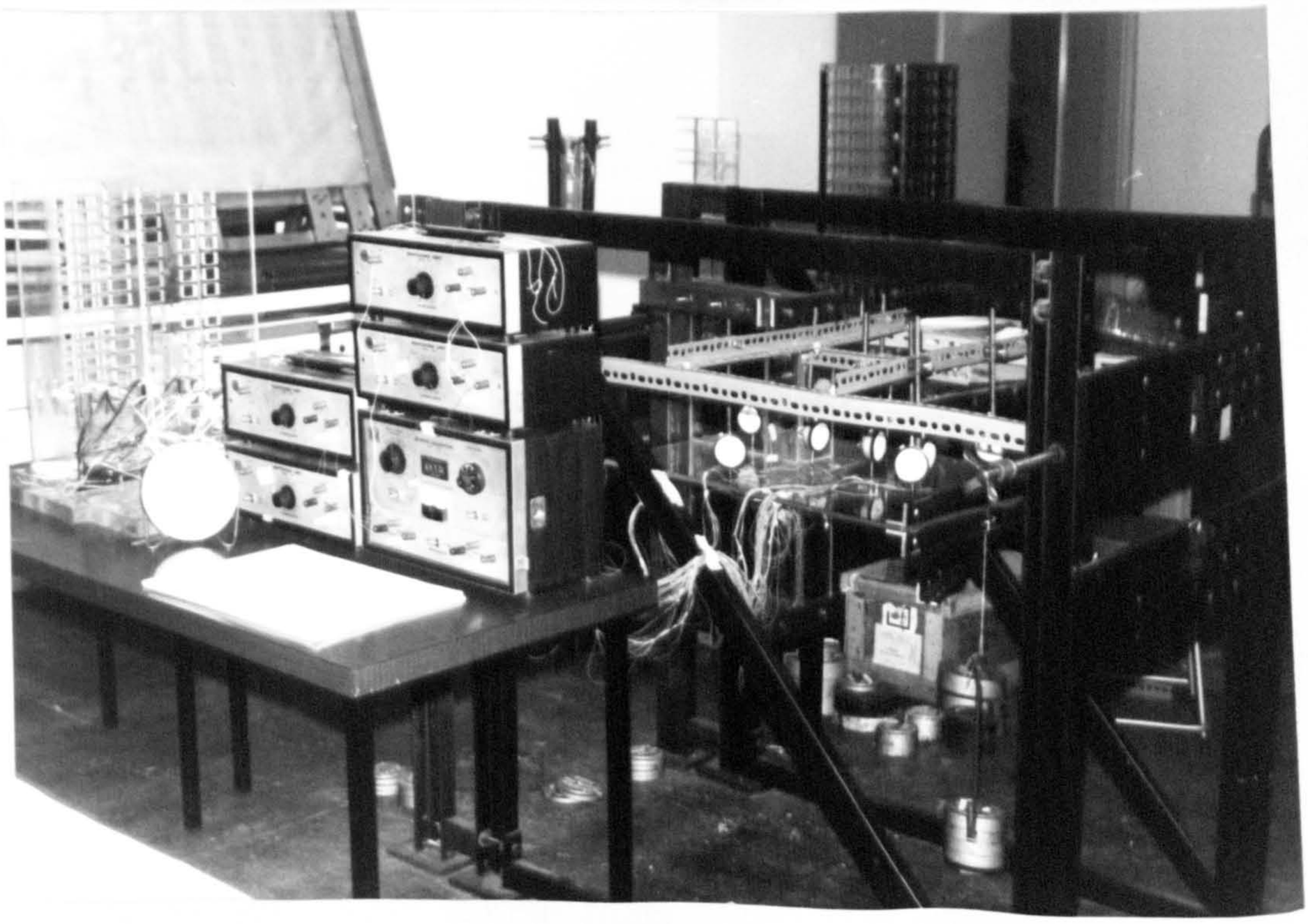

Plate 10.2(b) Flanged Wall-Slab Model Under Test
(Downward Loading)

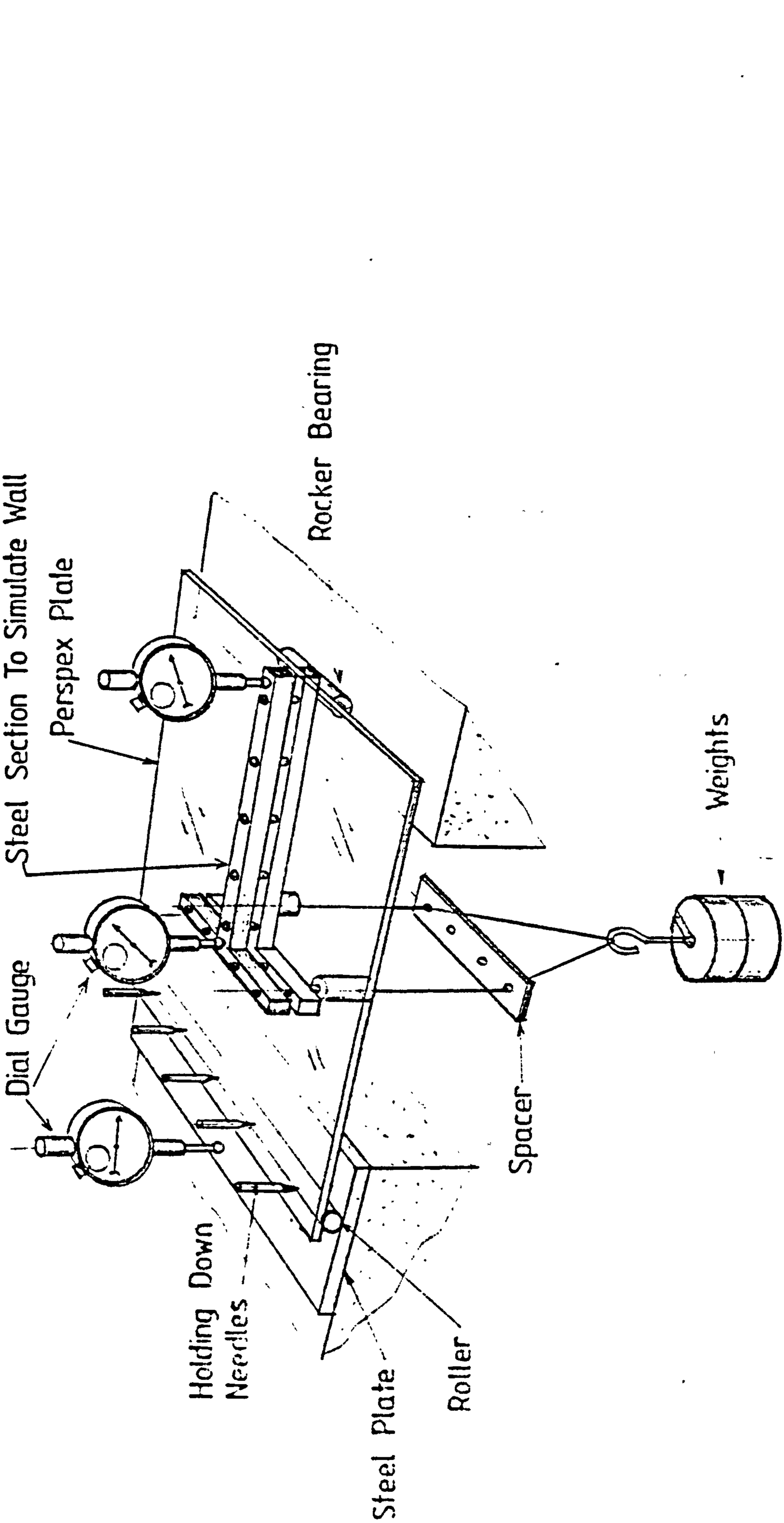

FIG. 10.1 - MODEL OF SLAB COUPLING FLANGED WALLS UNDER TEST

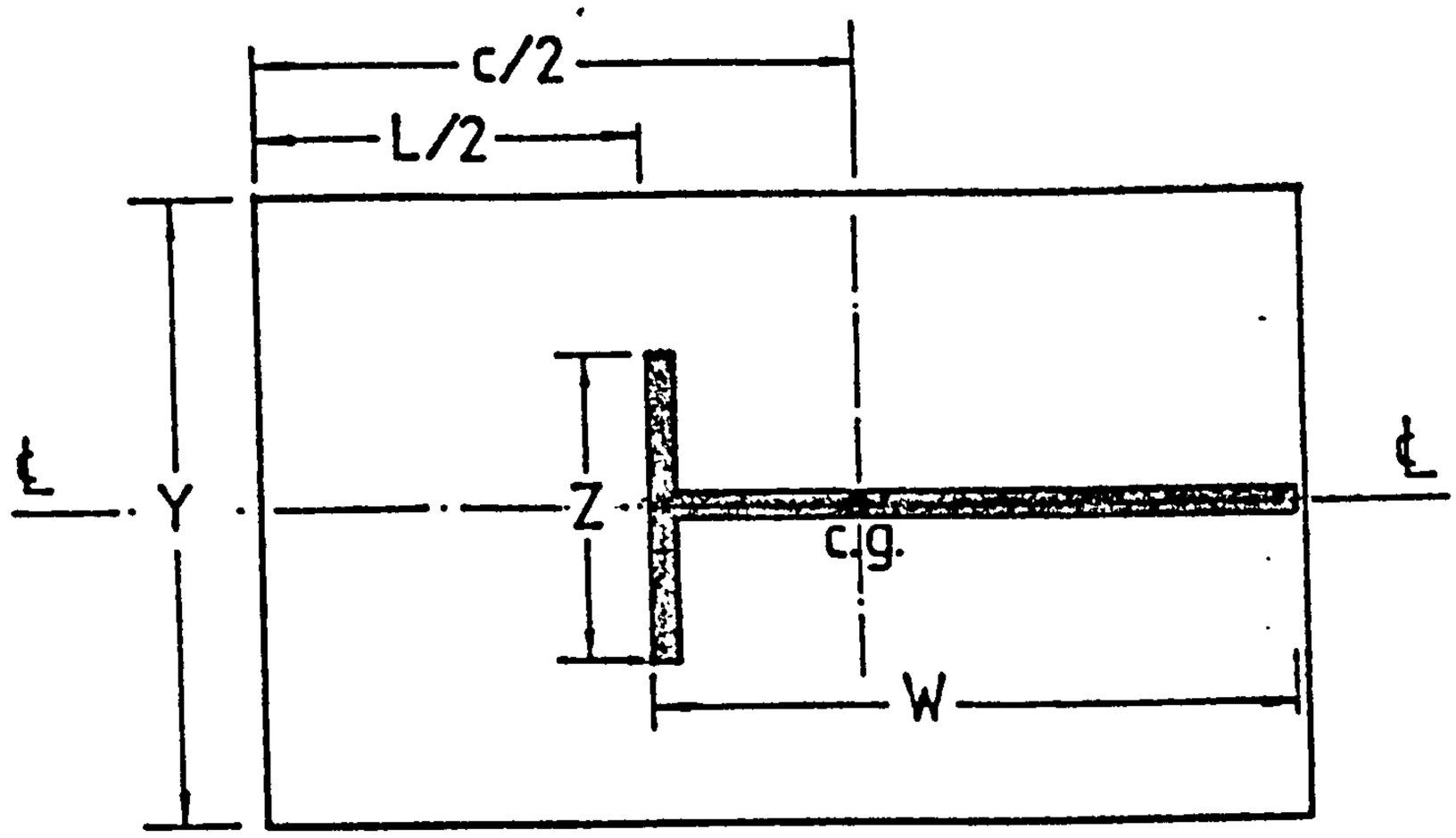

Typical Plan

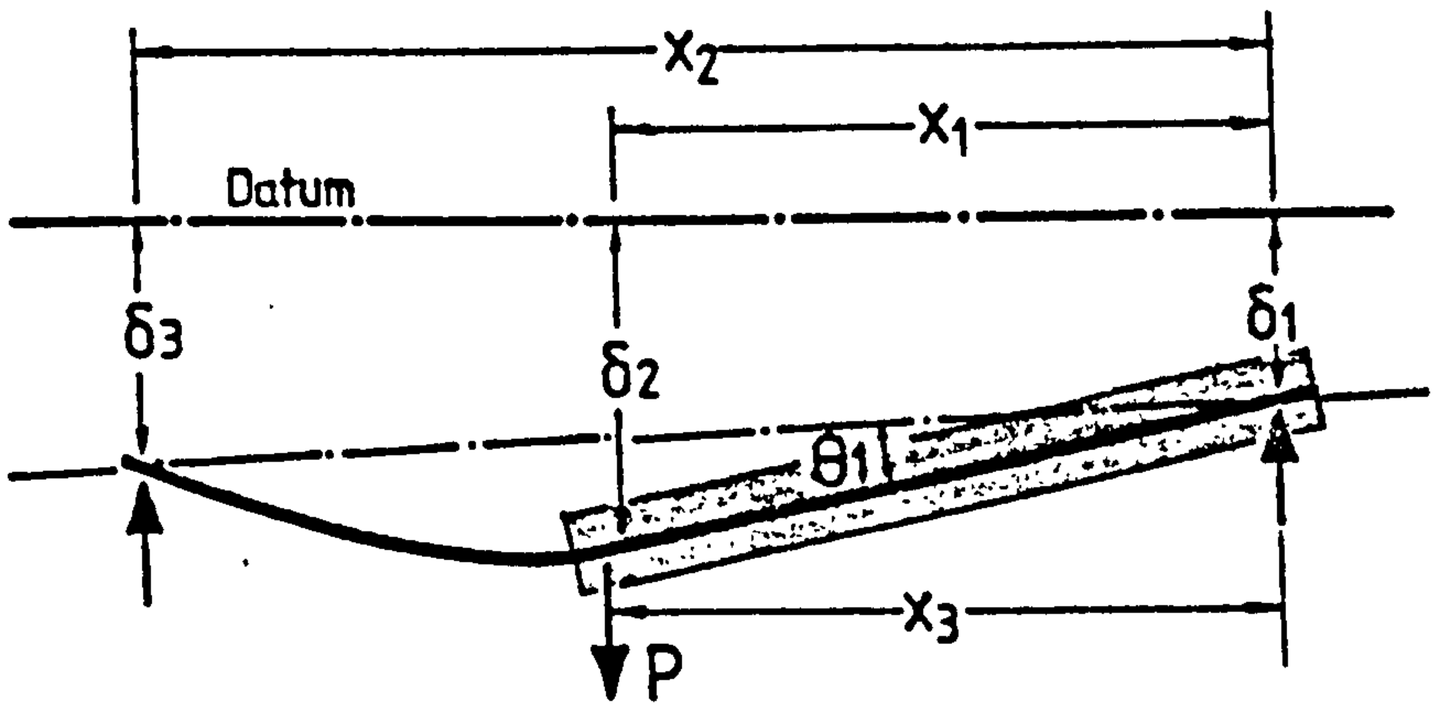

Load & Deflections

FIG. 10.2 - TYPICAL PLAN & LOAD-DEFLECTION RELATIONSHIP OF SERIES 1 TEST MODELS

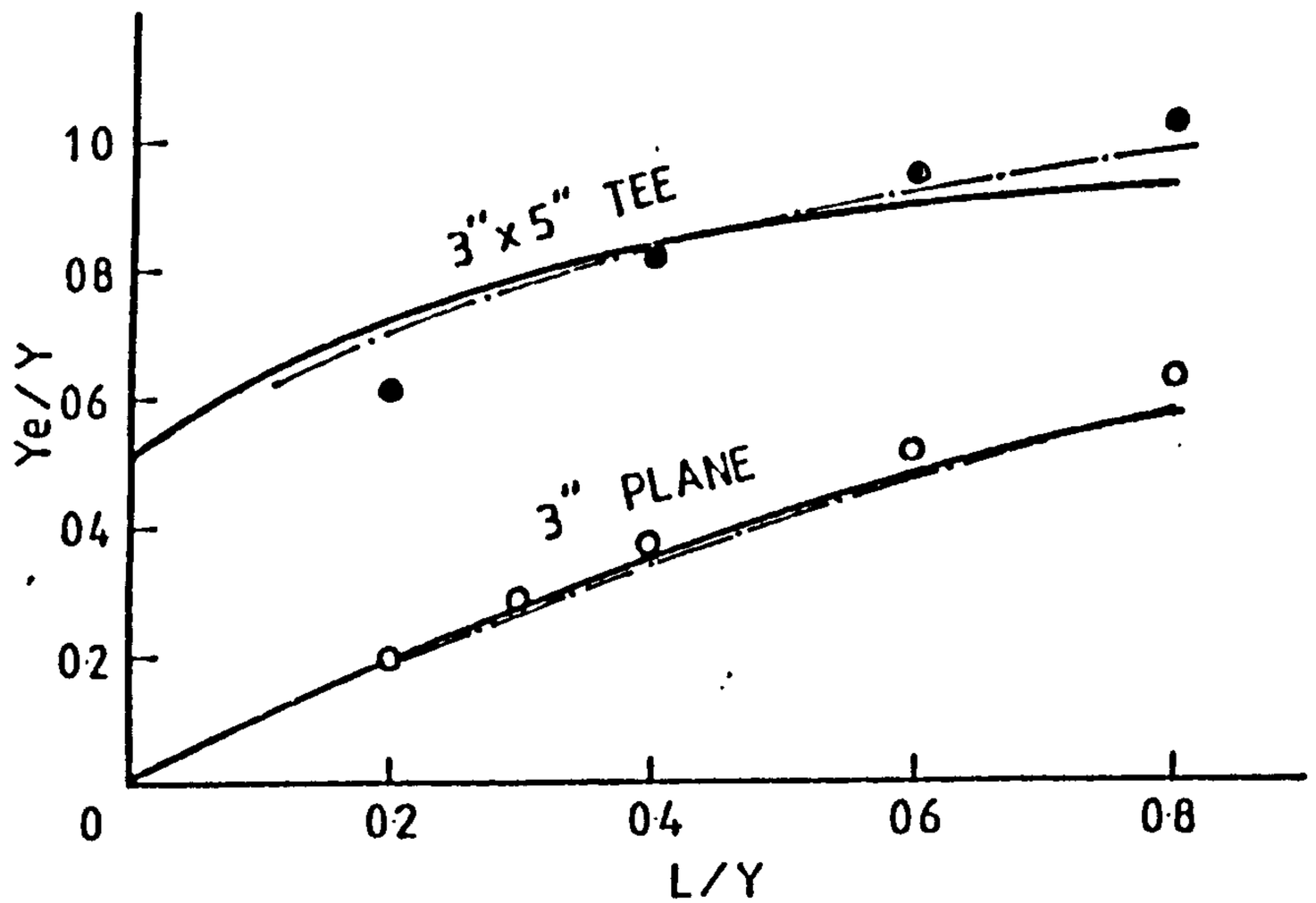

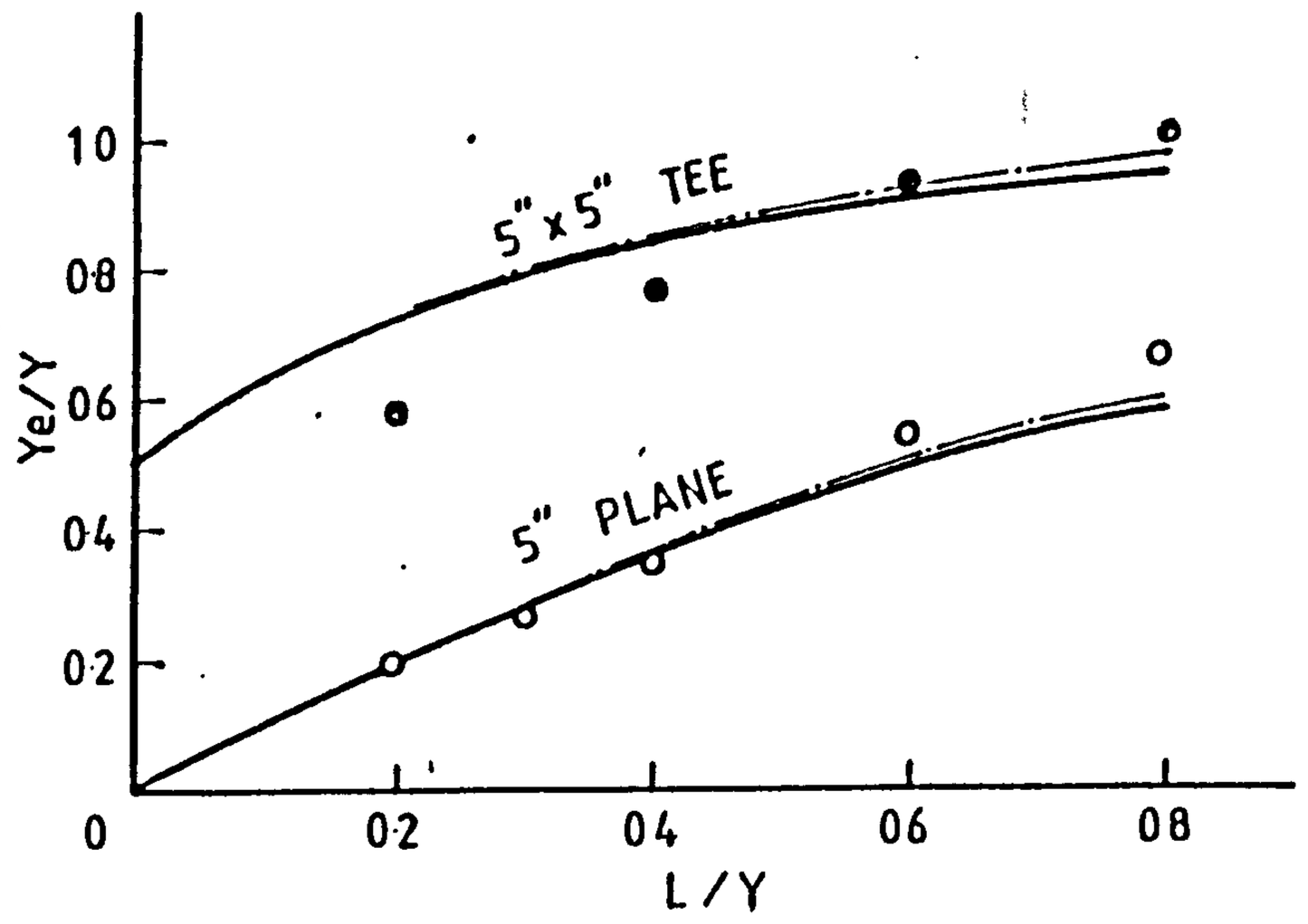

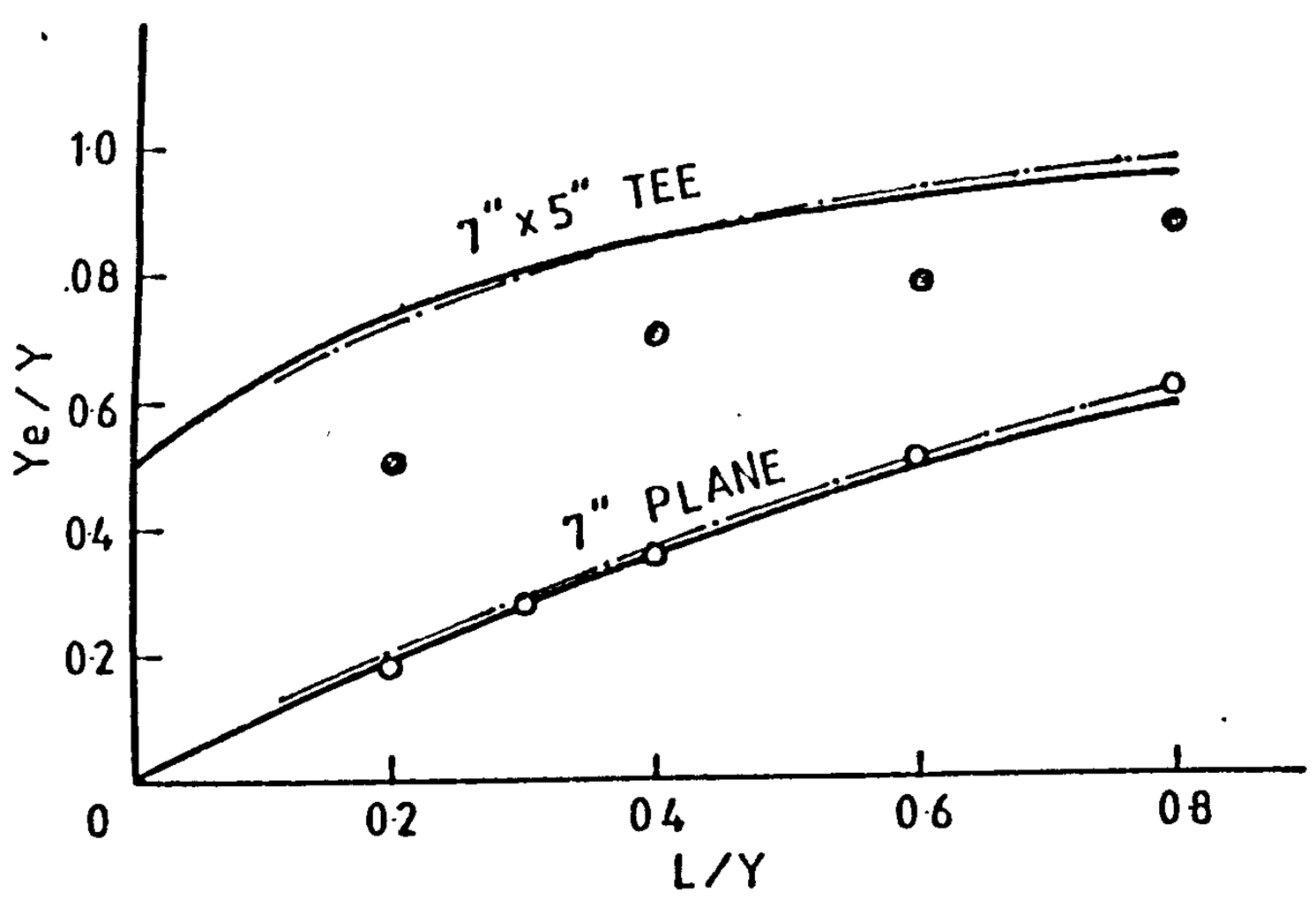

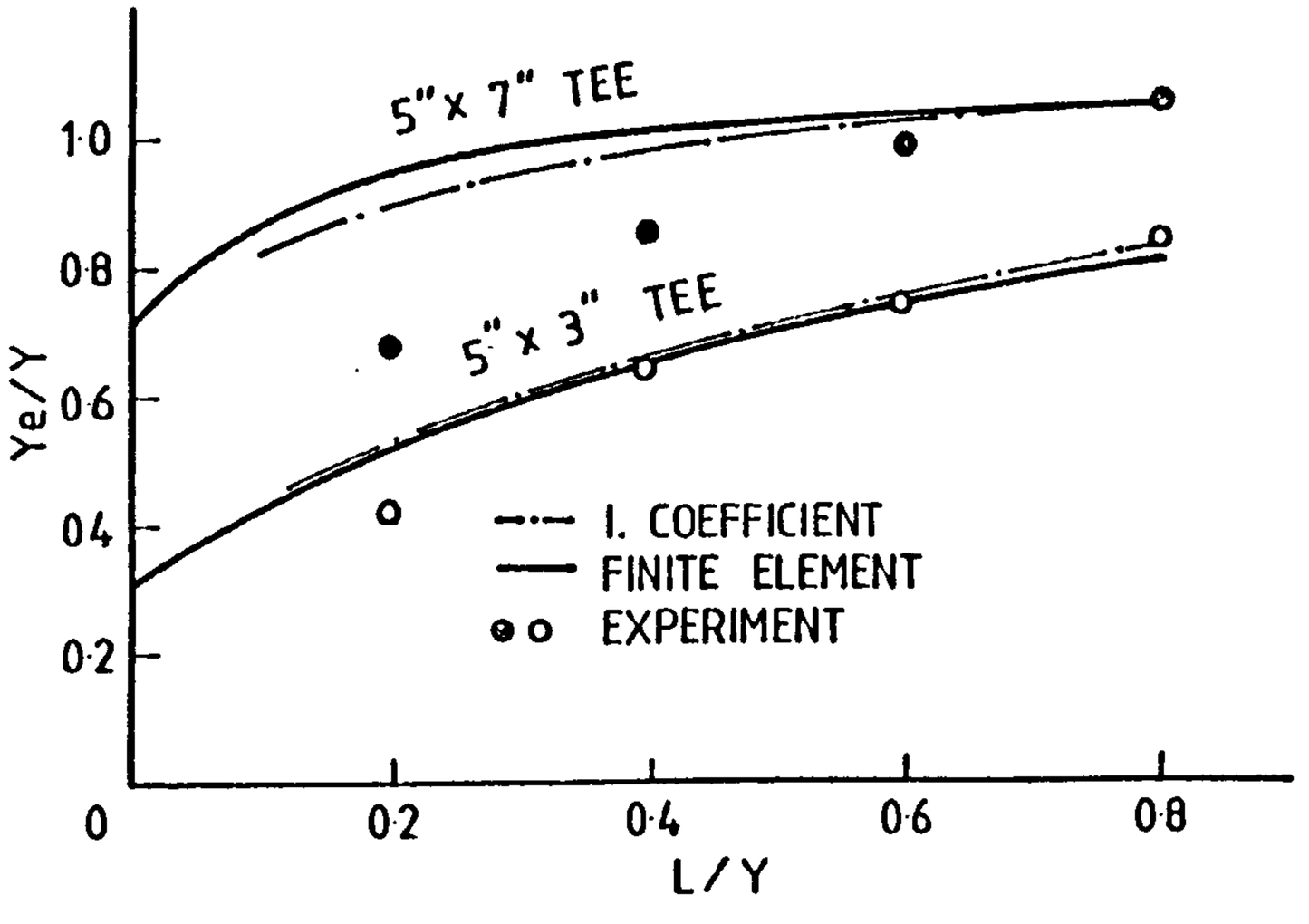

FIG. 10.3 - COMPARISON BETWEEN EXPERIMENTAL AND THEORETICAL RESULTS

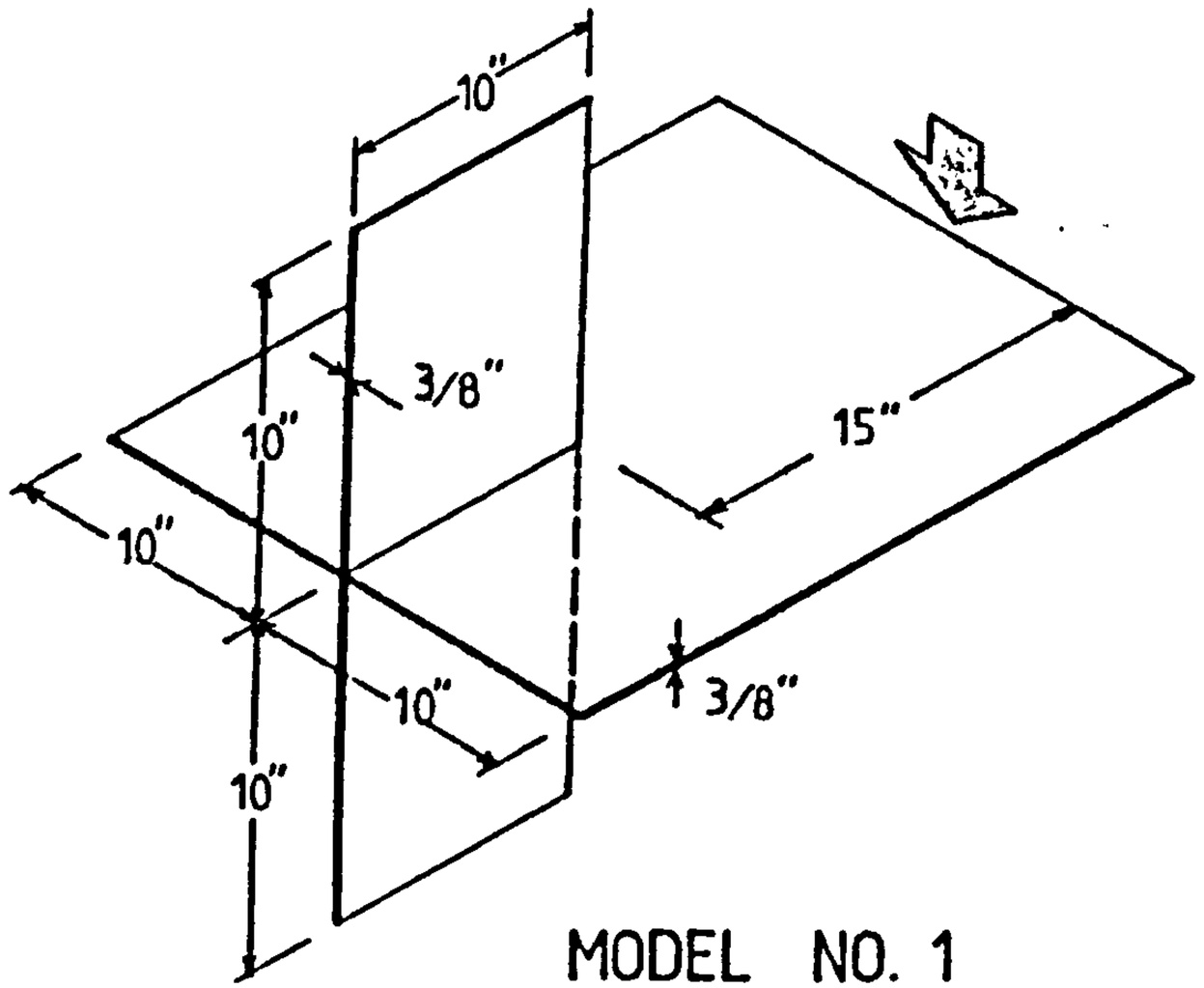

MODEL NO. 1

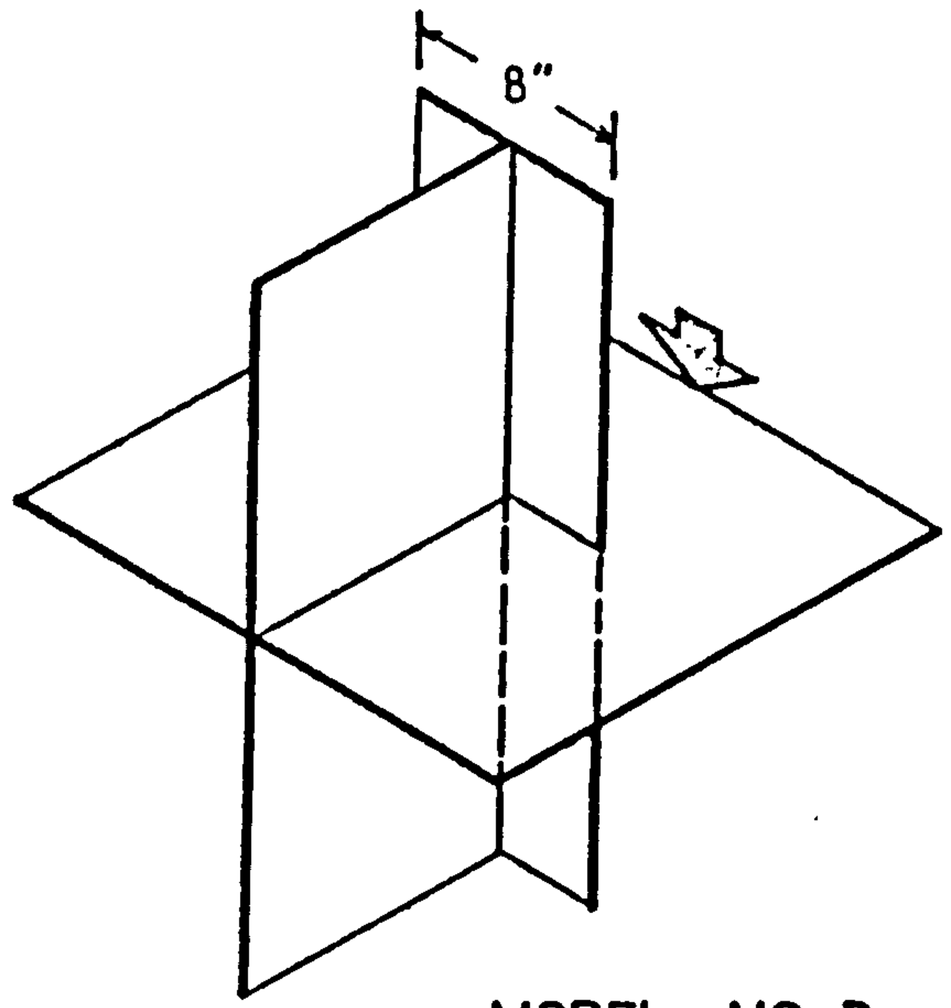

MODEL NO. 3

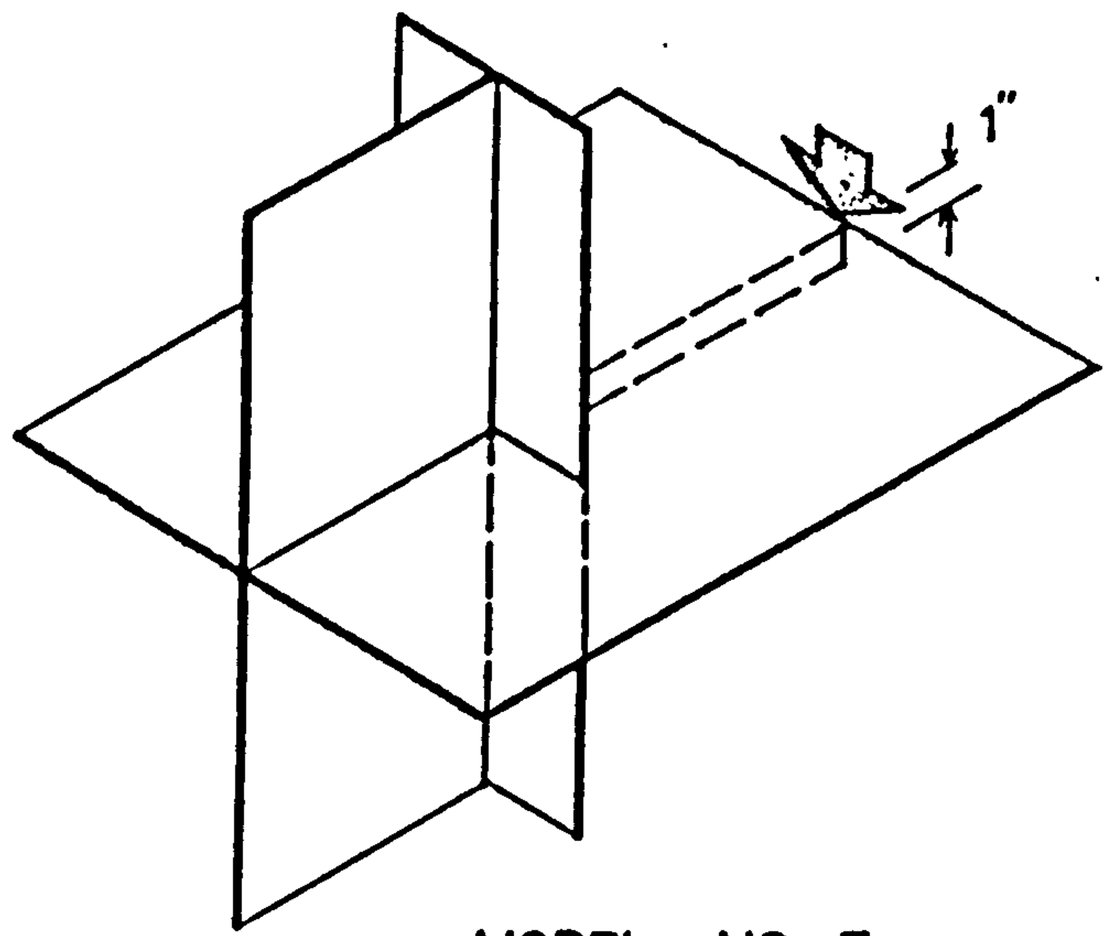

MODEL NO. 5

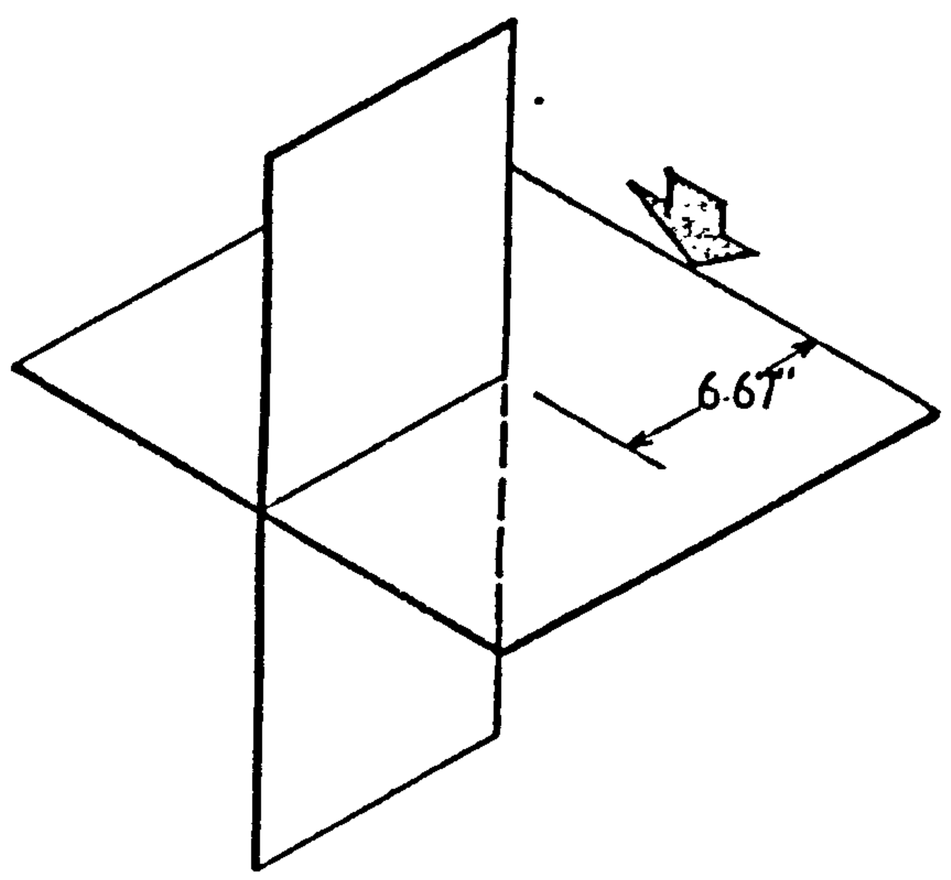

MODEL NO. 2

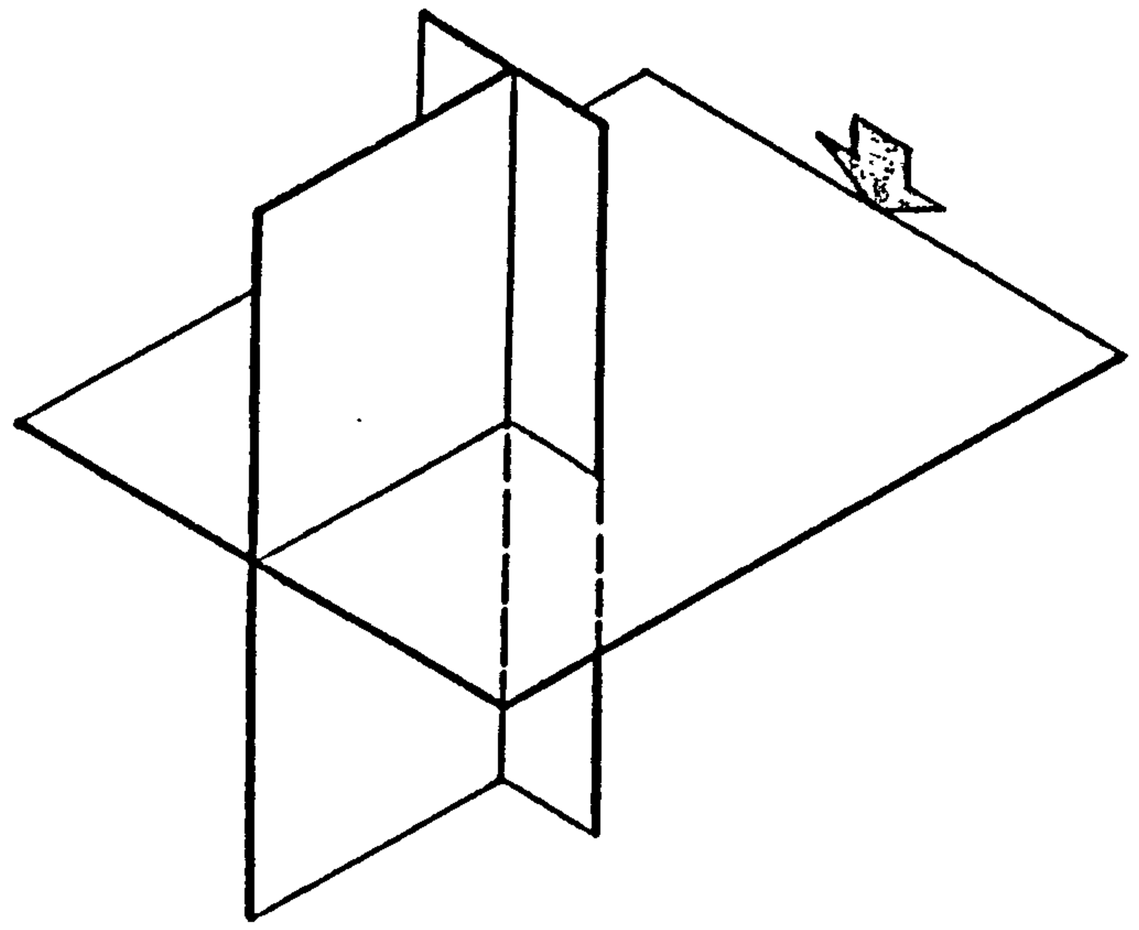

MODEL NO. 4

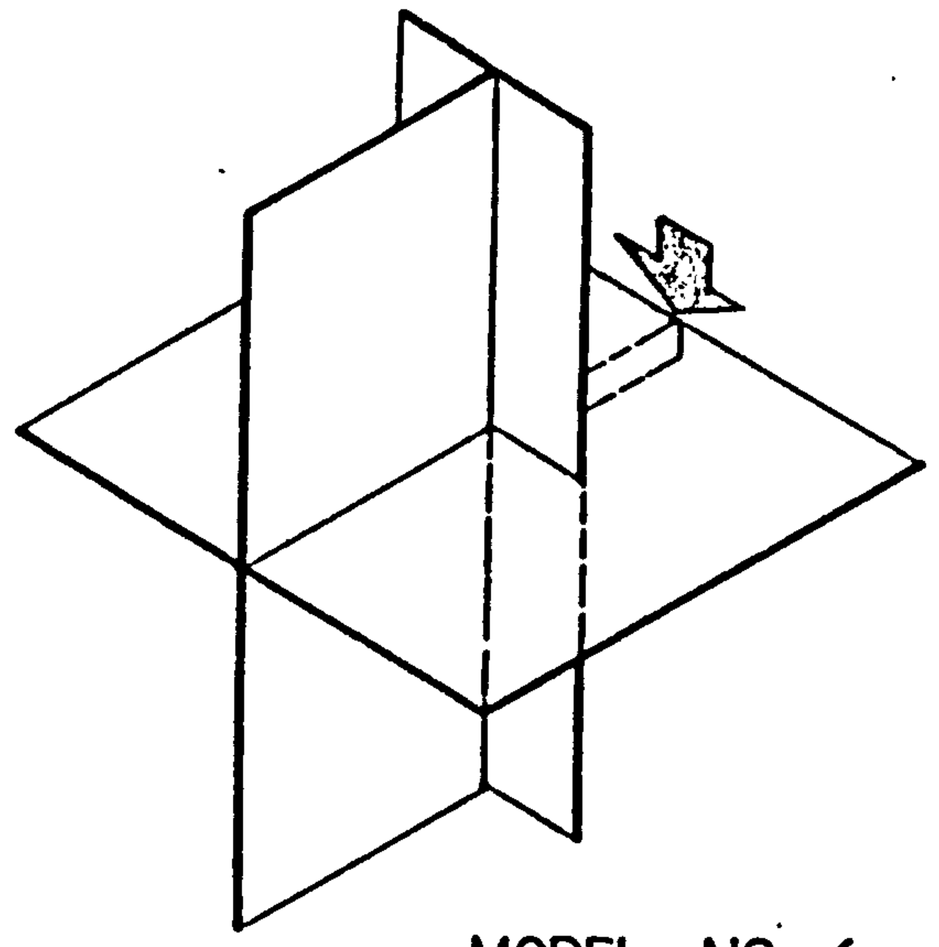

MODEL NO. 6

FIG. 10.4 - MODELS IN SERIES 2 TESTS

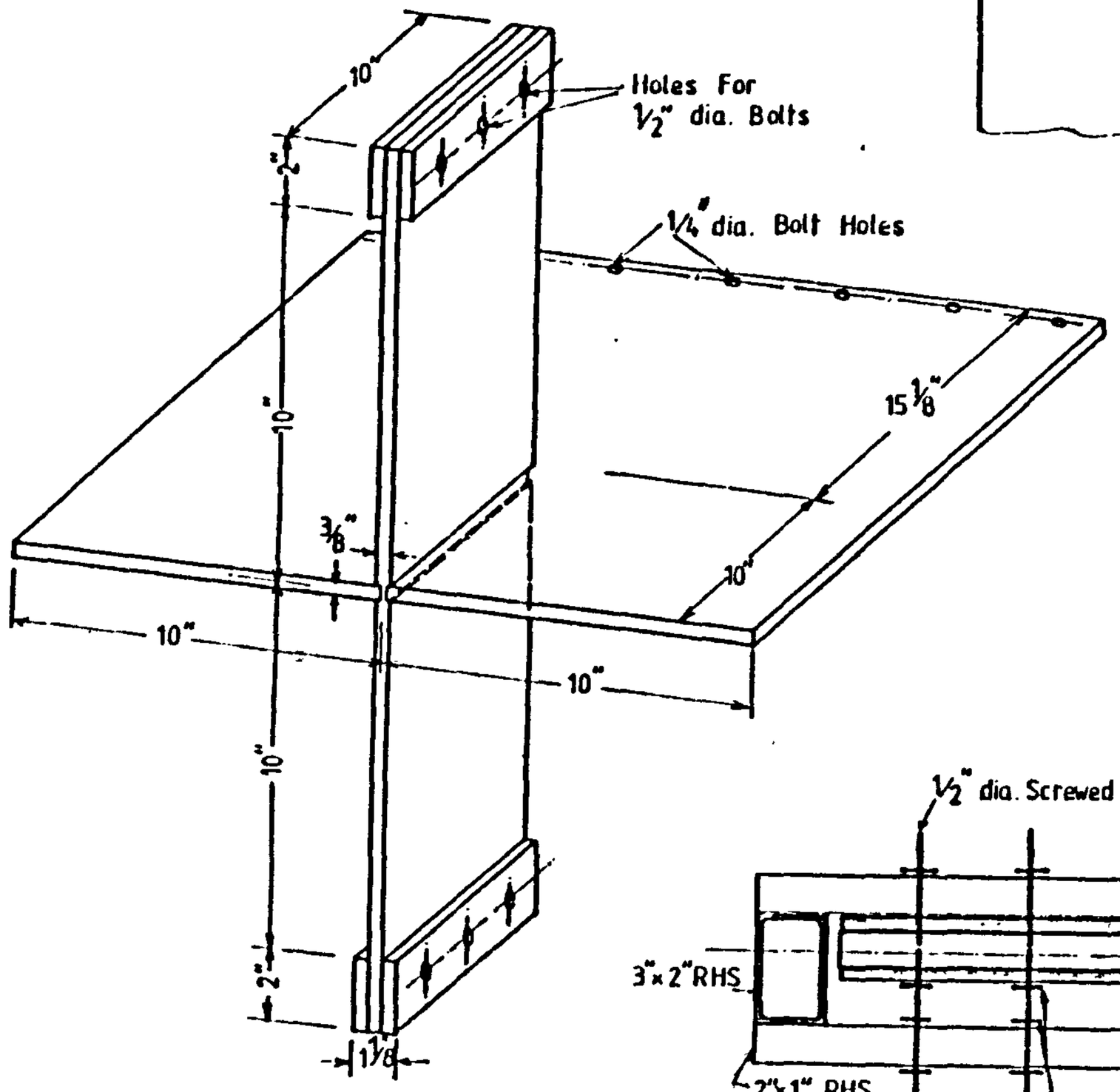

(a) BASIC MODEL CONSTRUCTION

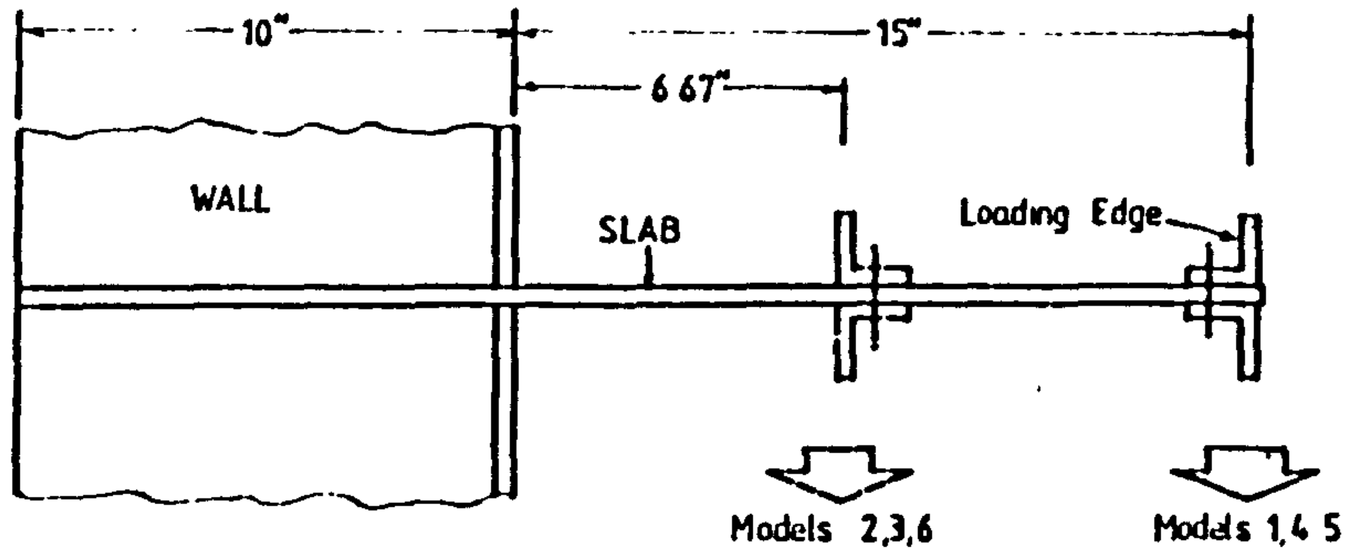

(b) POSITIONS OF LOADING EDGE

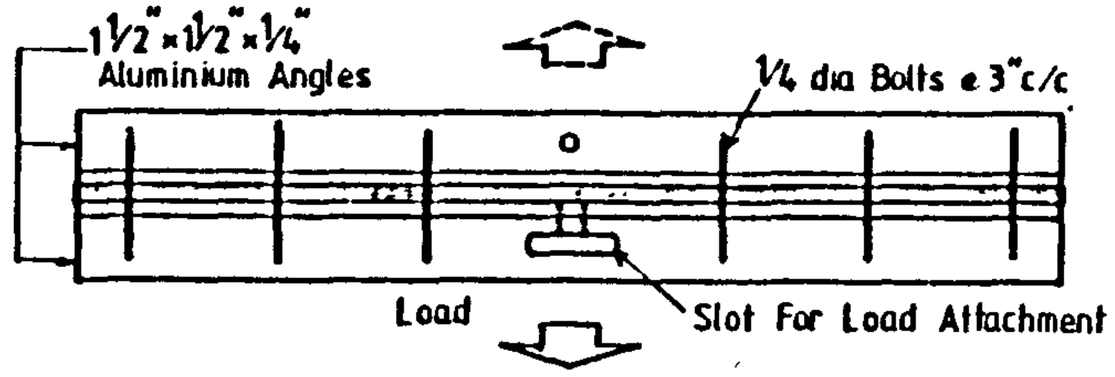

(c) LOADING EDGE DETAIL

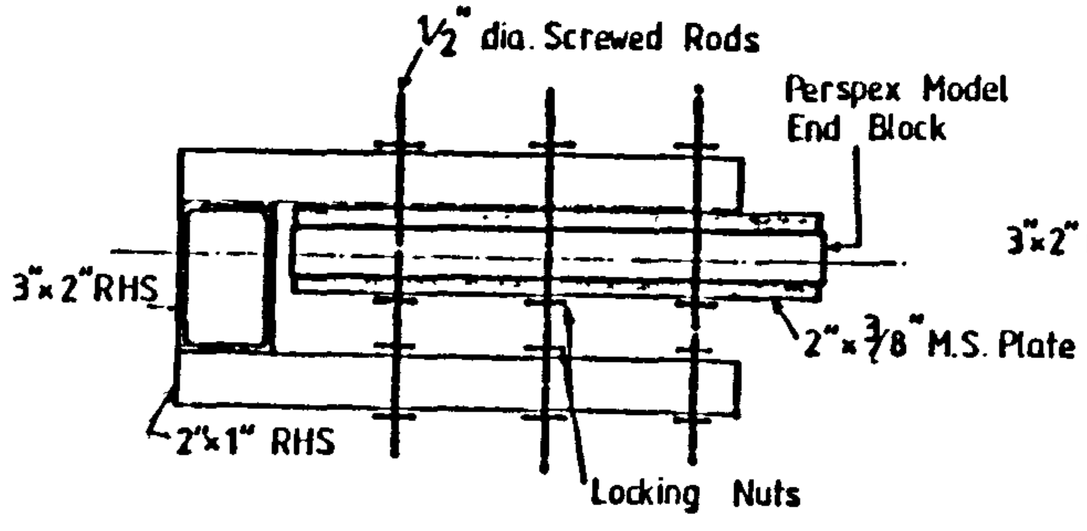

(d) MOUNTING DETAIL FOR PLANE WALL MODELS

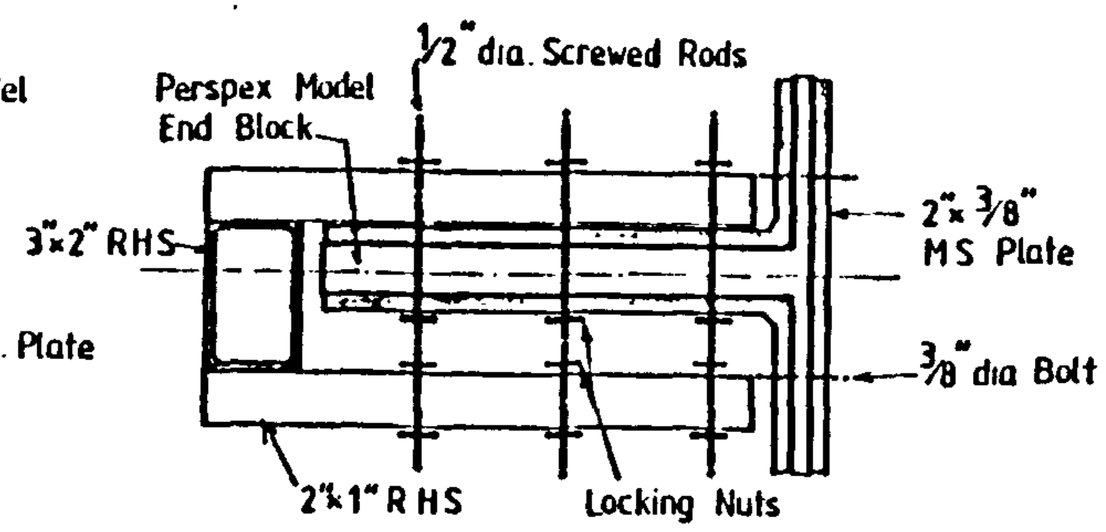

(e) MOUNTING DETAIL FOR FLANGED WALL MODELS

FIG. 10.5 - MODEL CONSTRUCTION, MOUNTING AND LOADING DETAILS

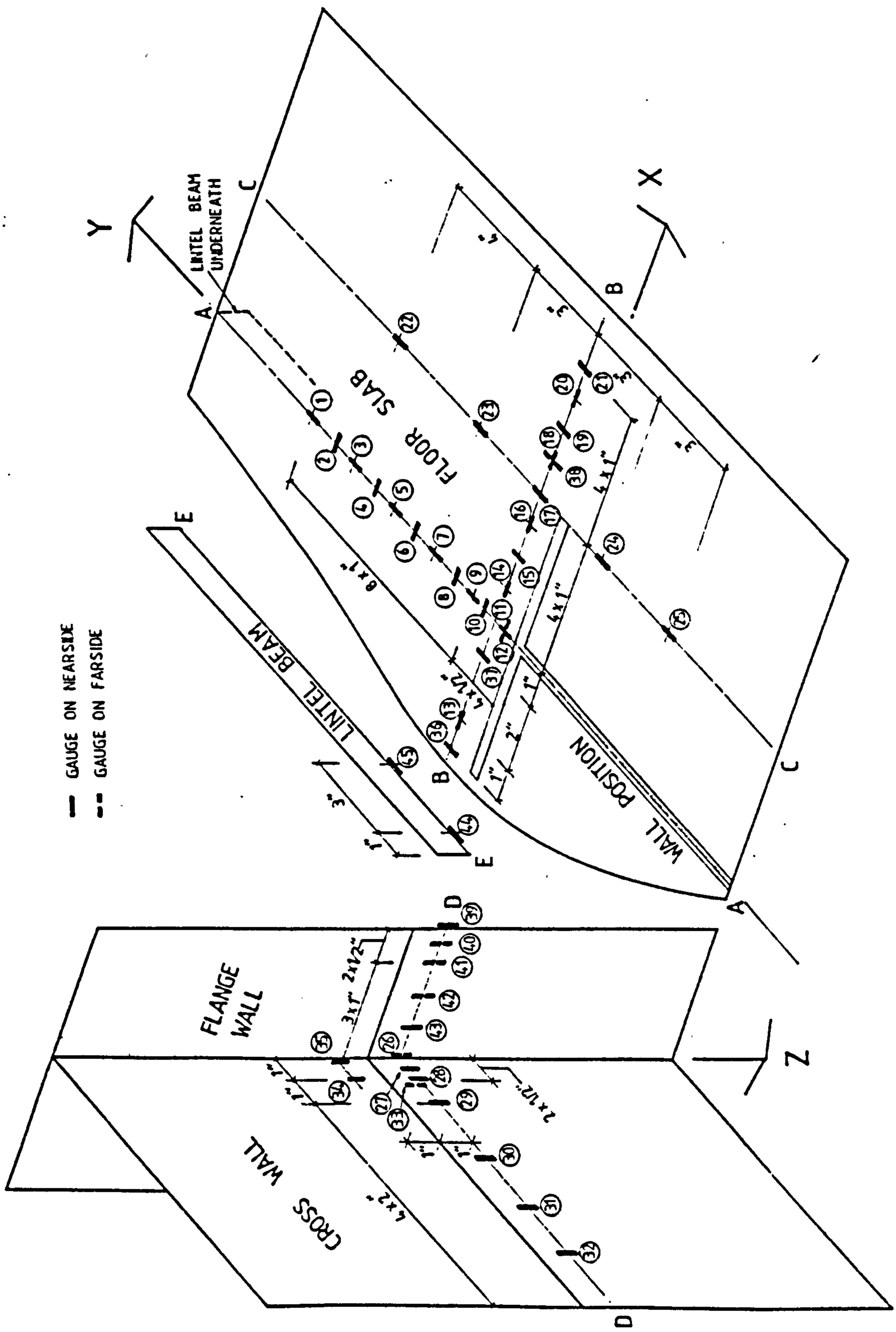

FIG. 10.6-STRAIN GAUGE LOCATION

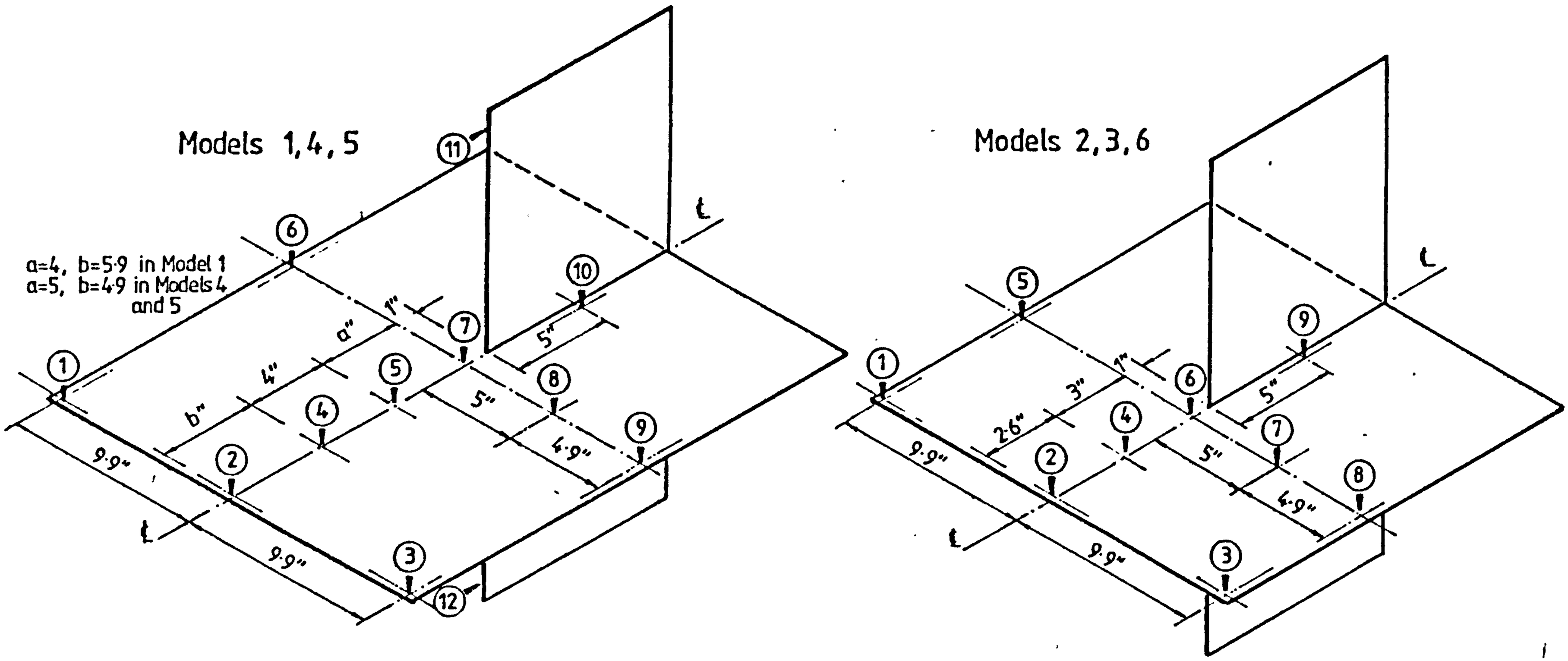

FIG. 10.7 - DIAL GAUGE LOCATION

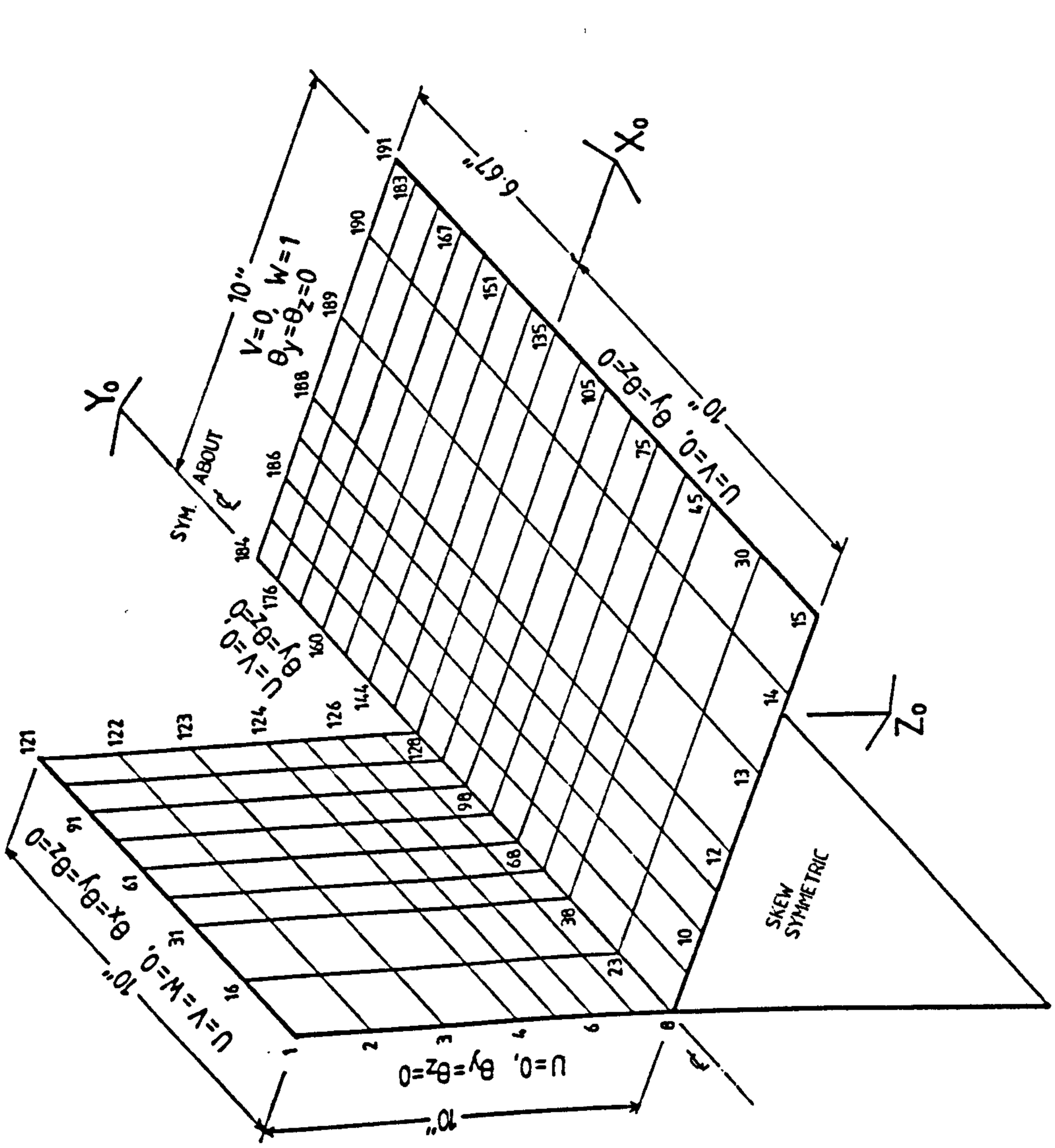

FIG. 10.8 - FINITE ELEMENT IDEALISATION OF MODEL NO.2

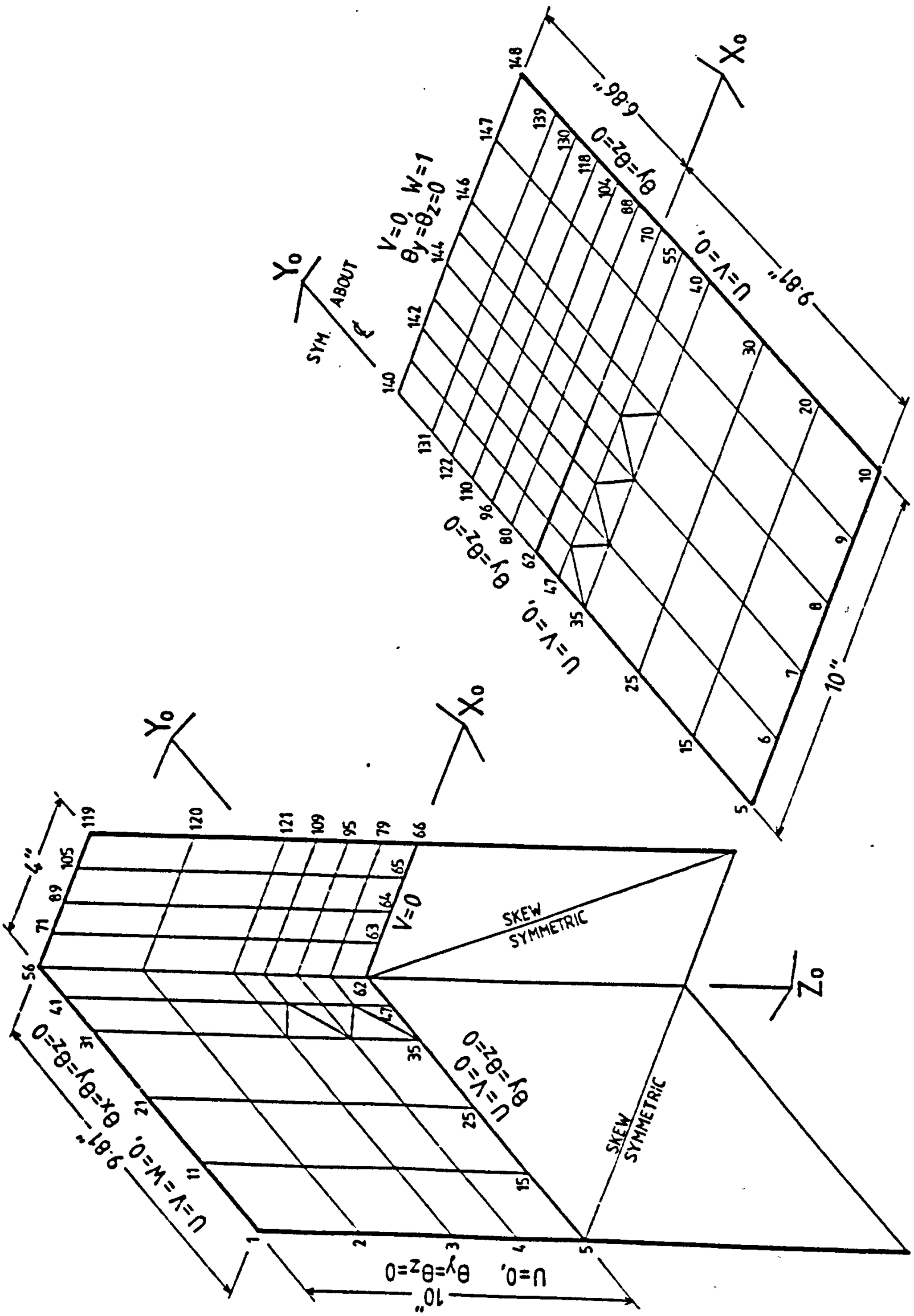

FIG. 10.9 - FINITE ELEMENT IDEALISATION OF MODEL NO.3

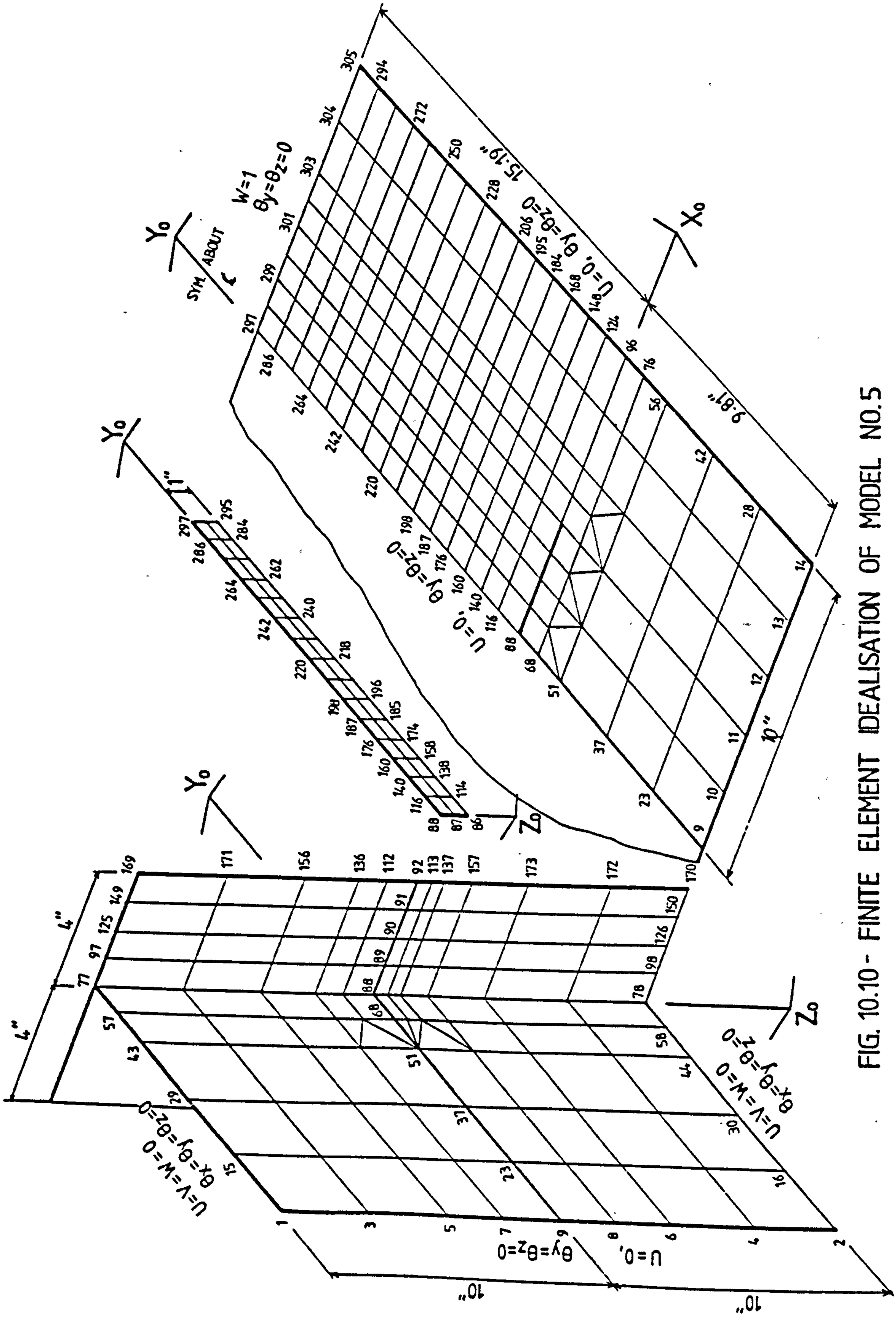

FIG. 10.10 - FINITE ELEMENT IDEALISATION OF MODEL NO.5

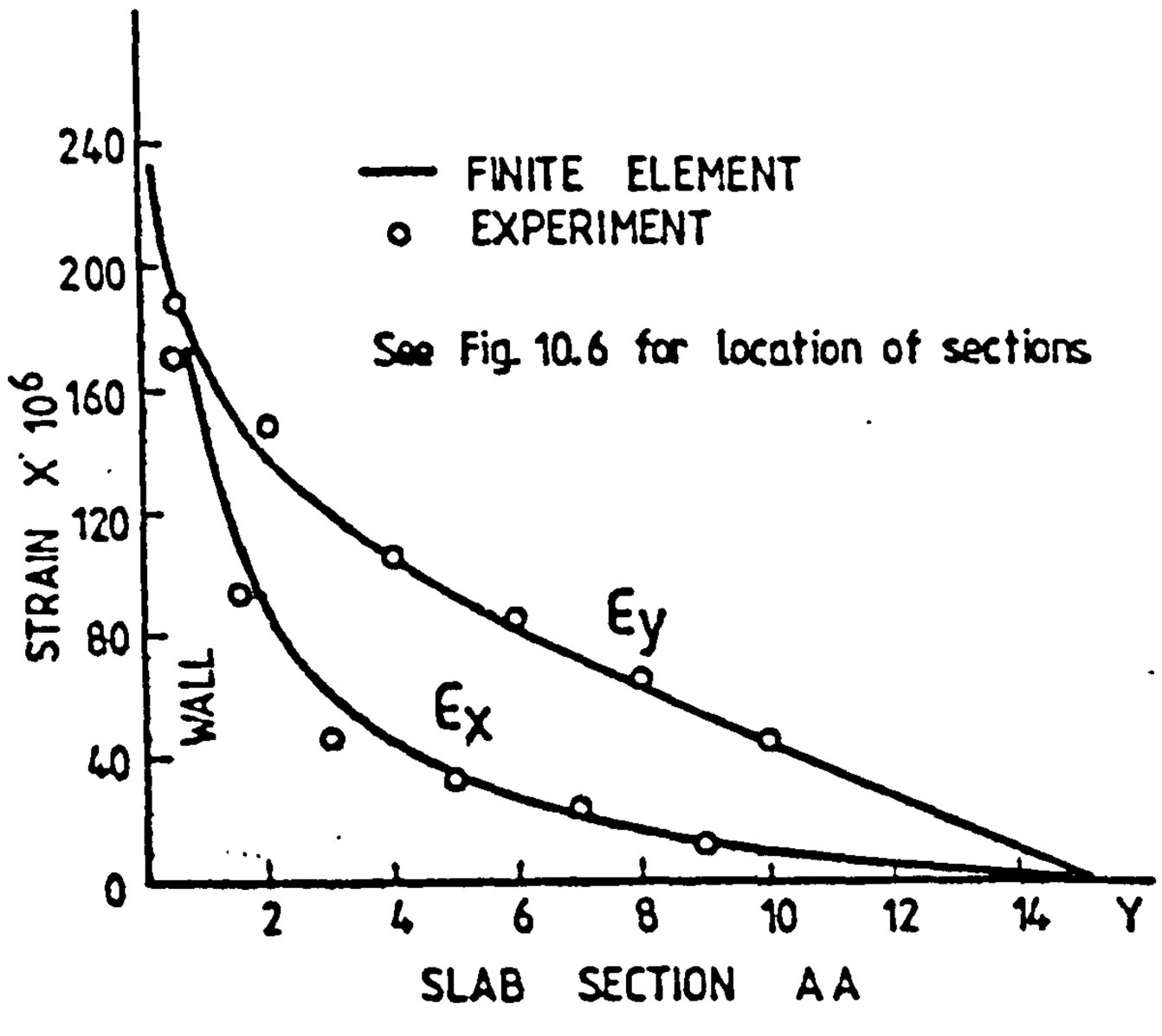

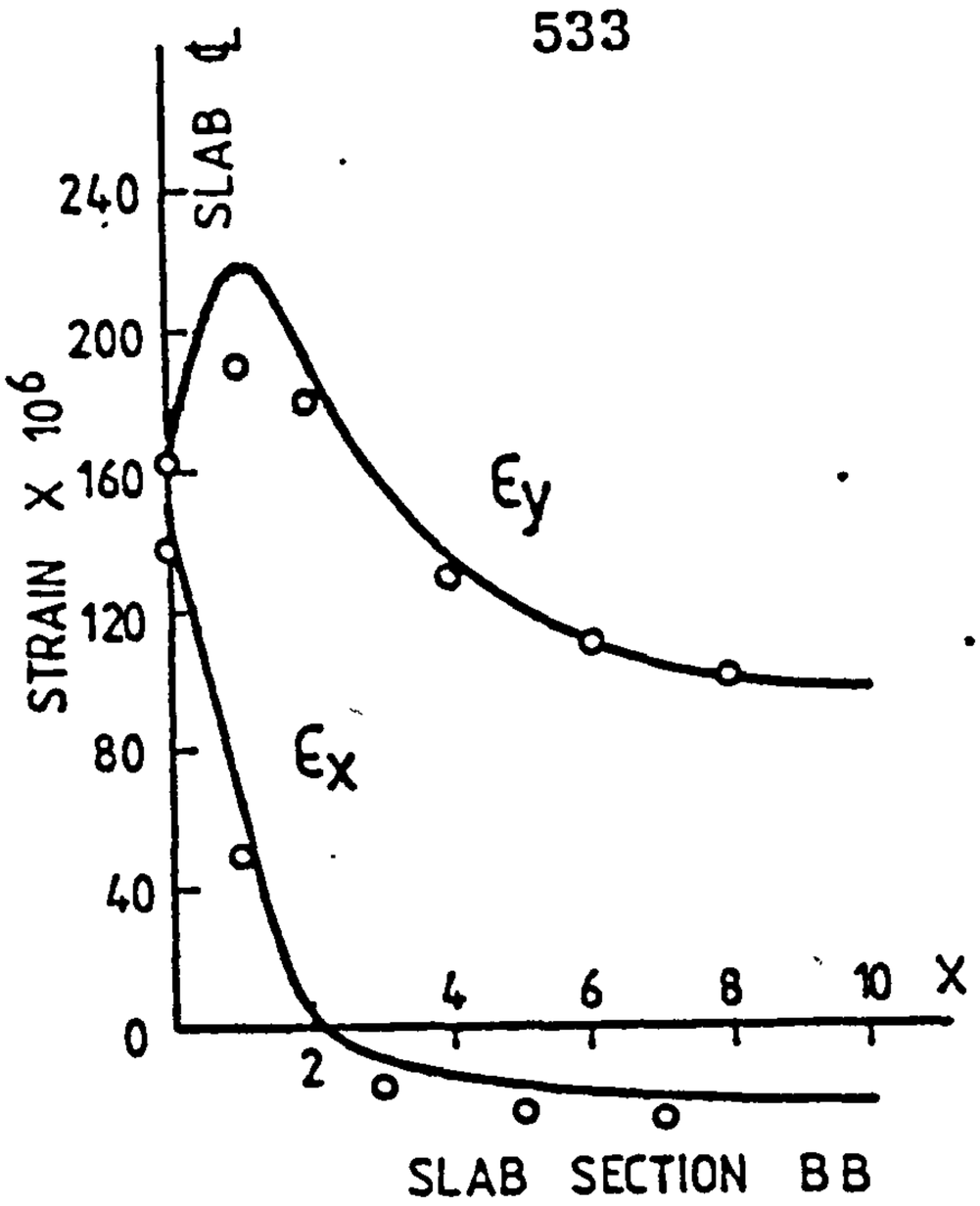

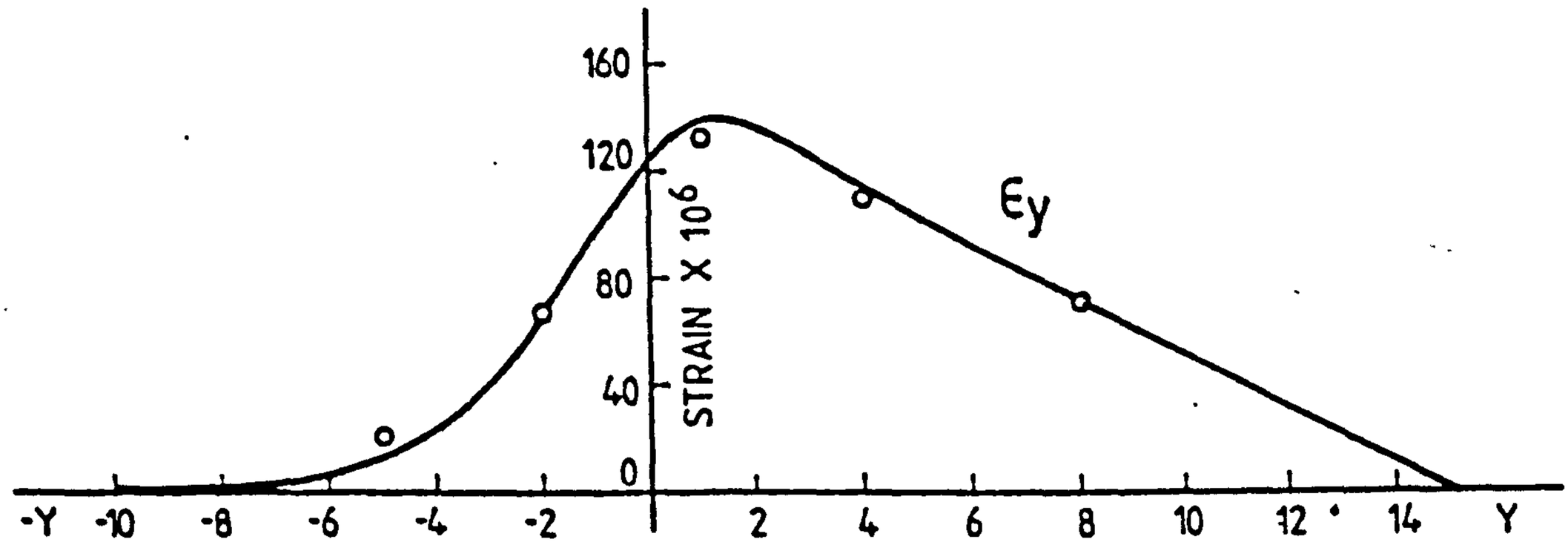

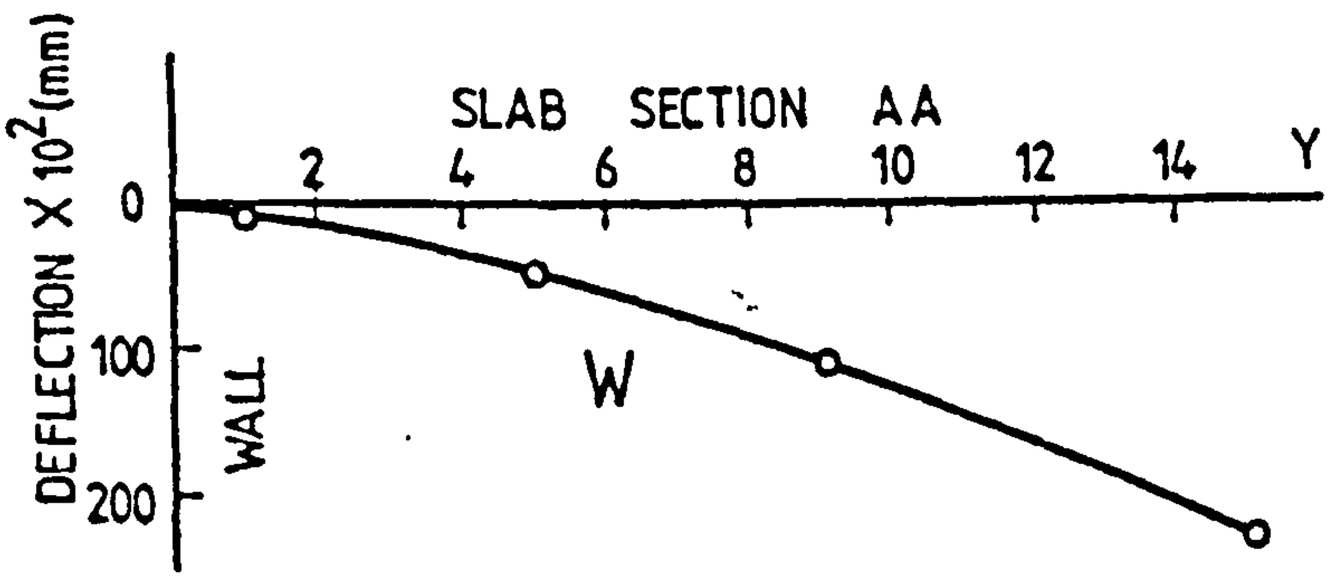

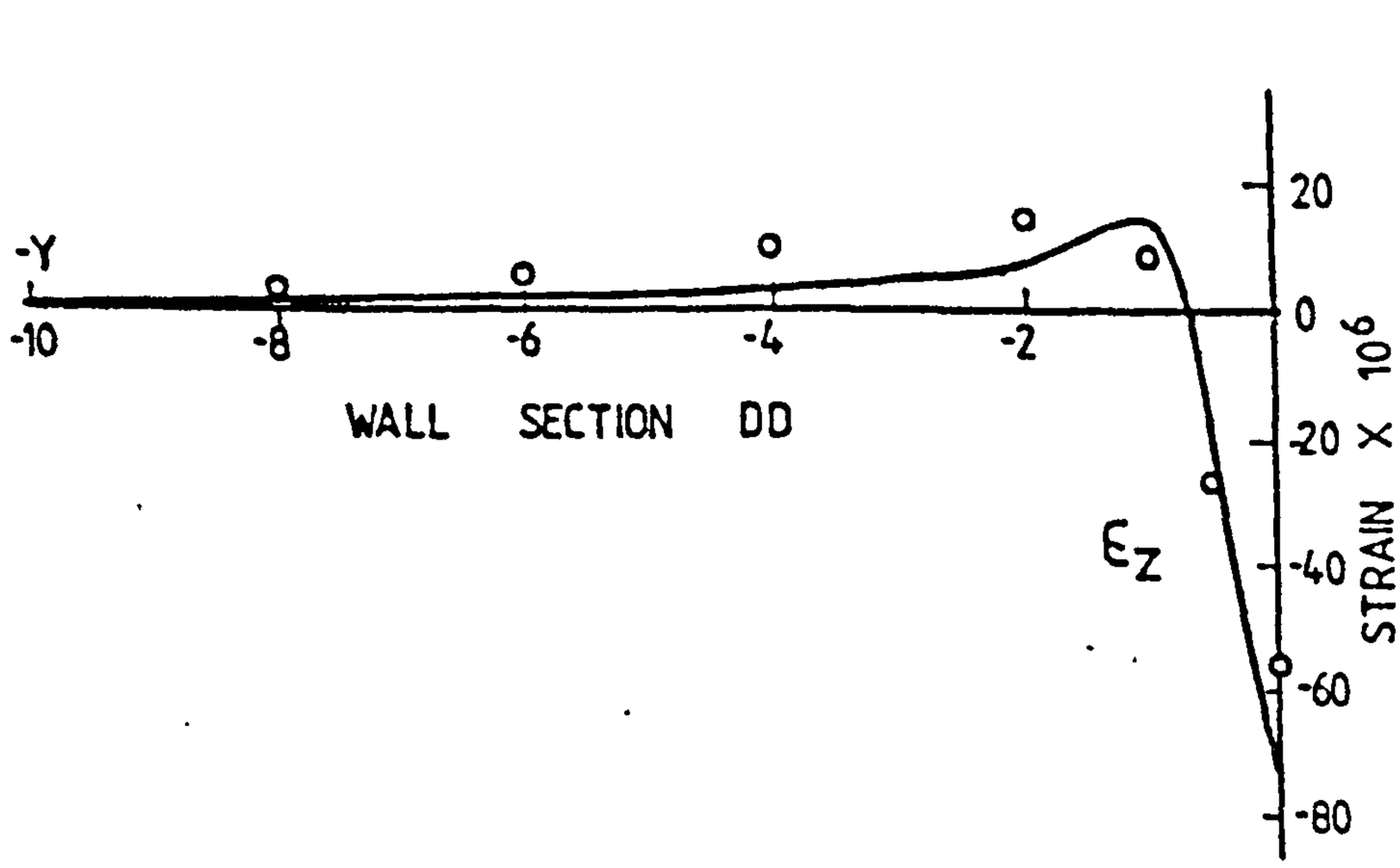

FIG. 10.11 - STRAINS AND DEFLECTIONS IN MODEL NO. 1

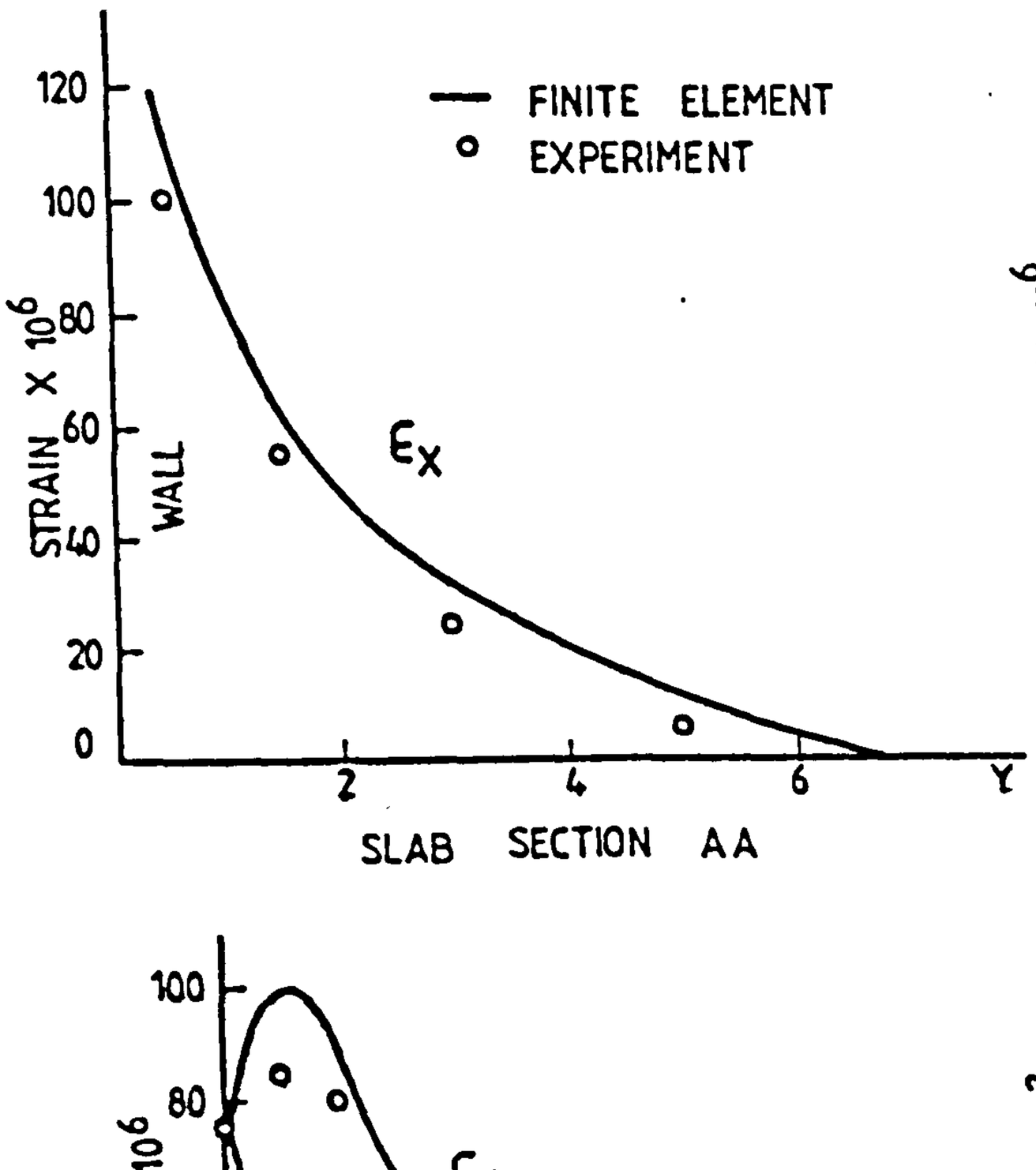

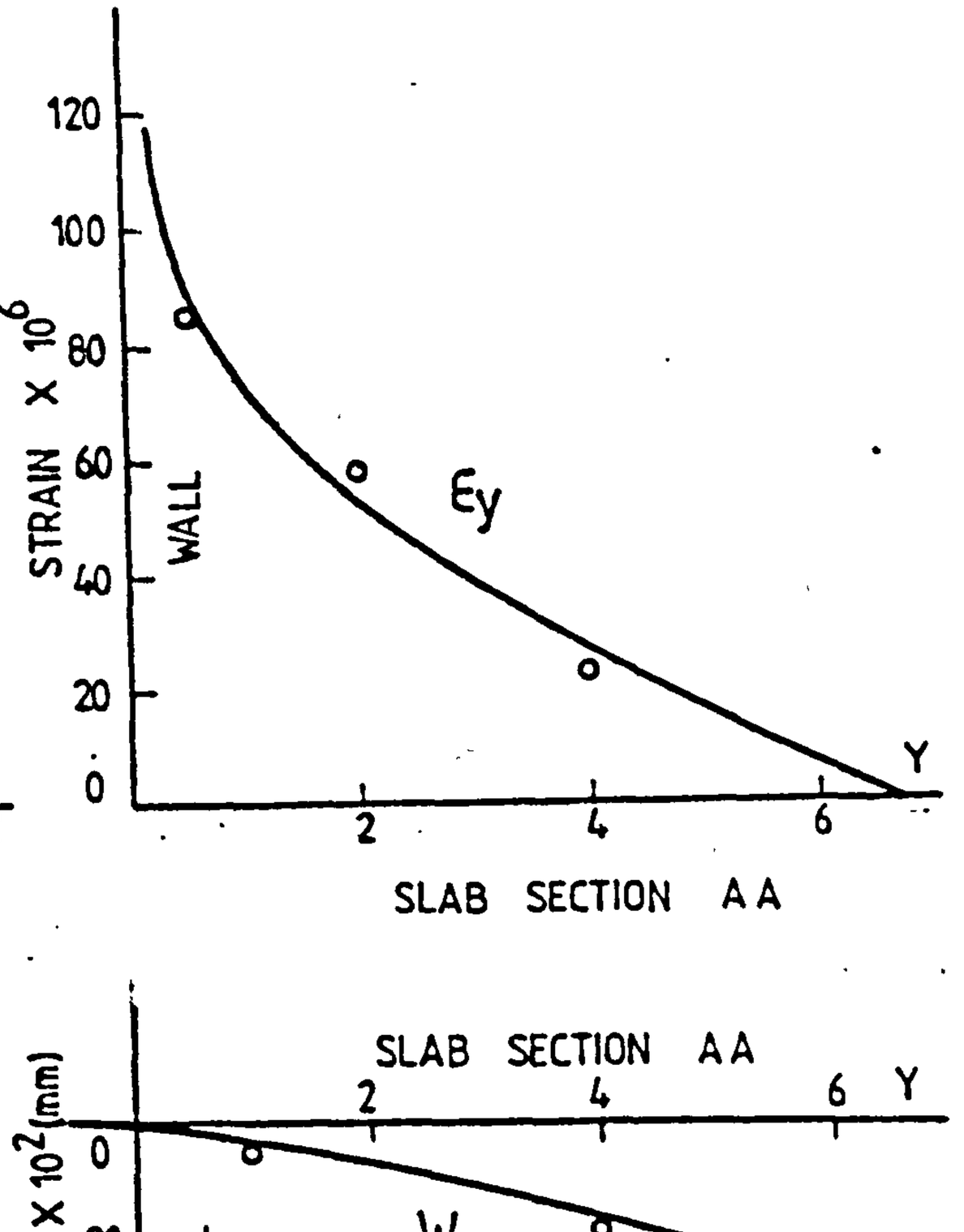

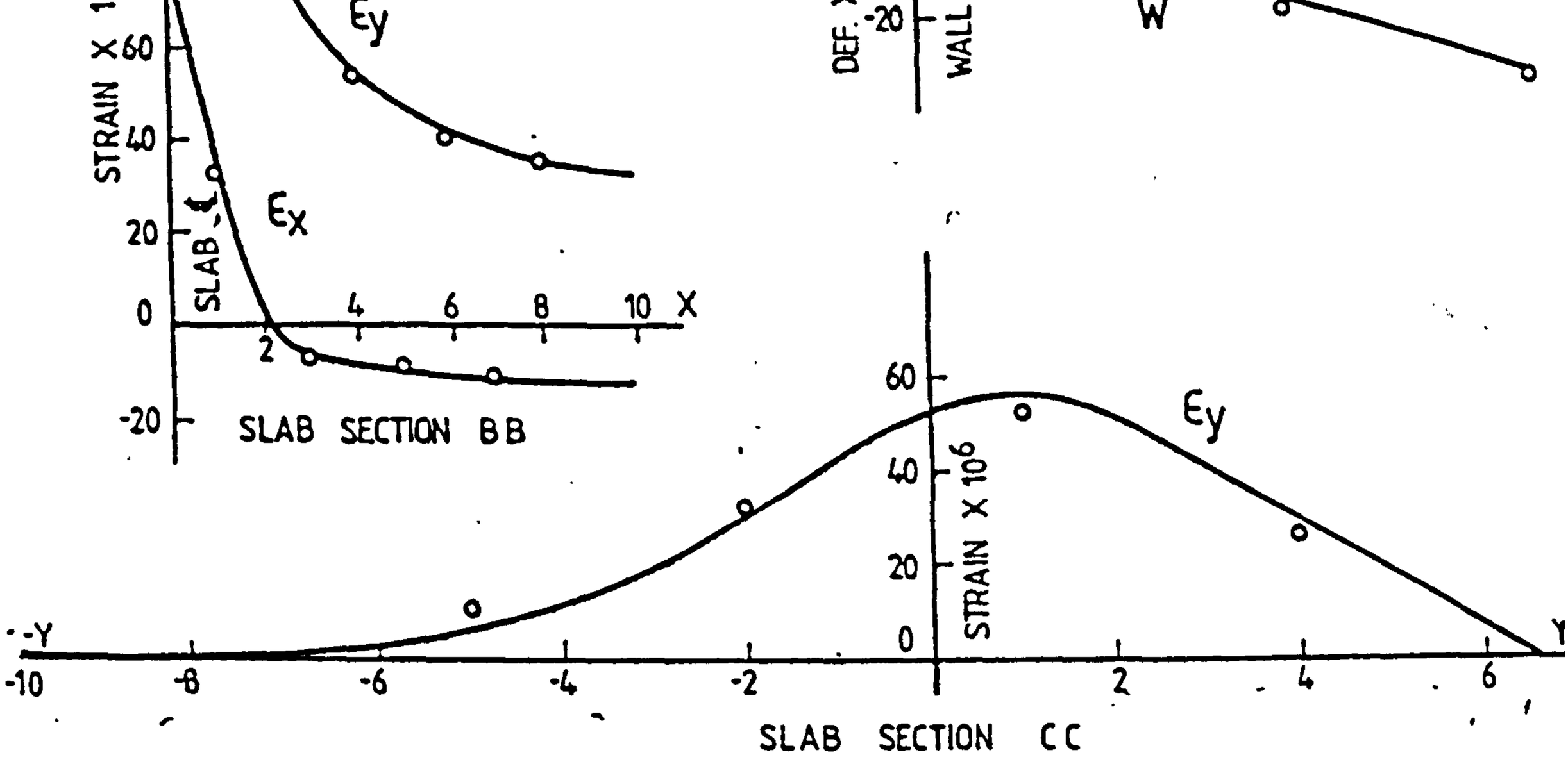

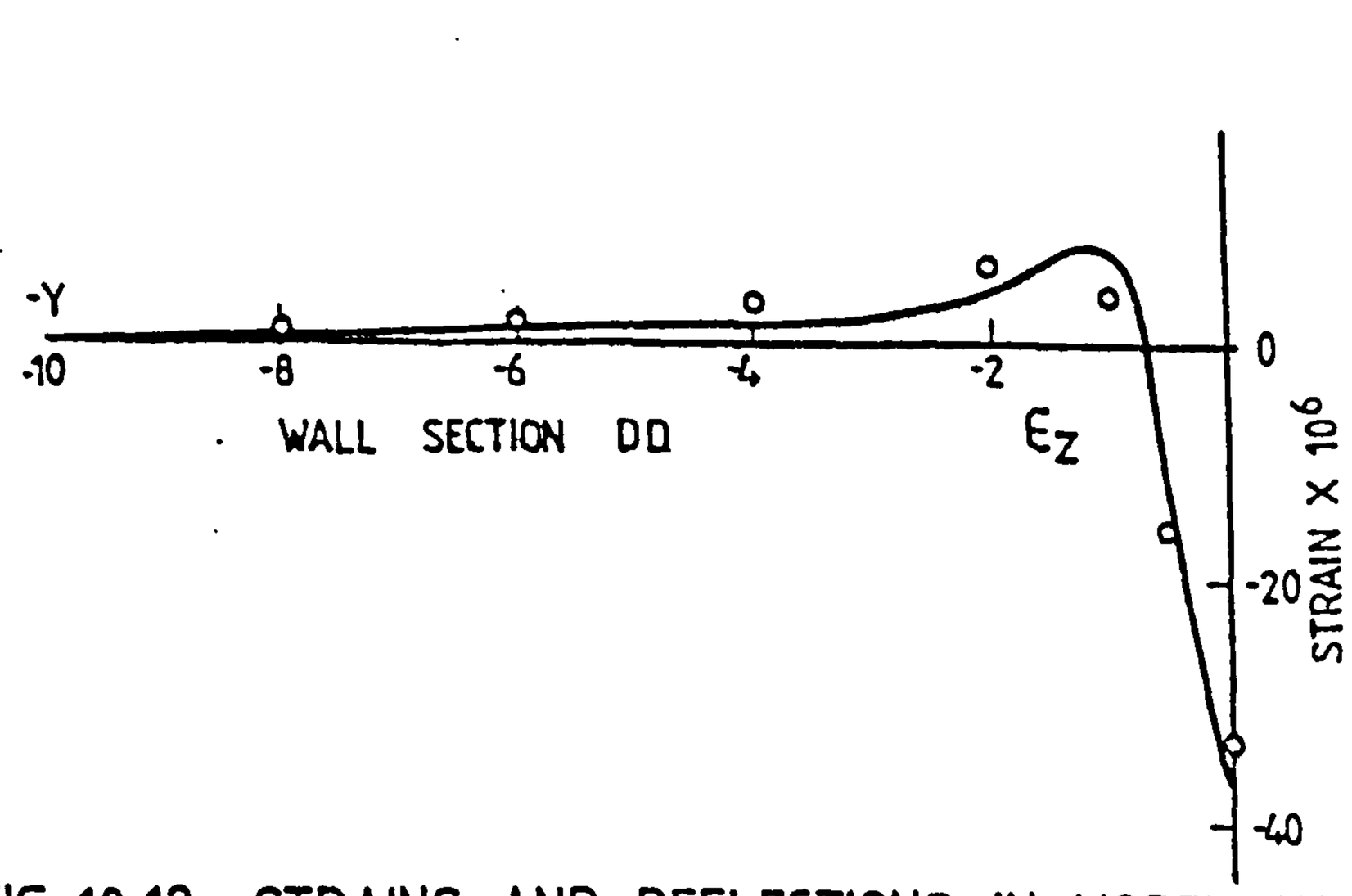

FIG. 10.12 - STRAINS AND DEFLECTIONS IN MODEL NO.2

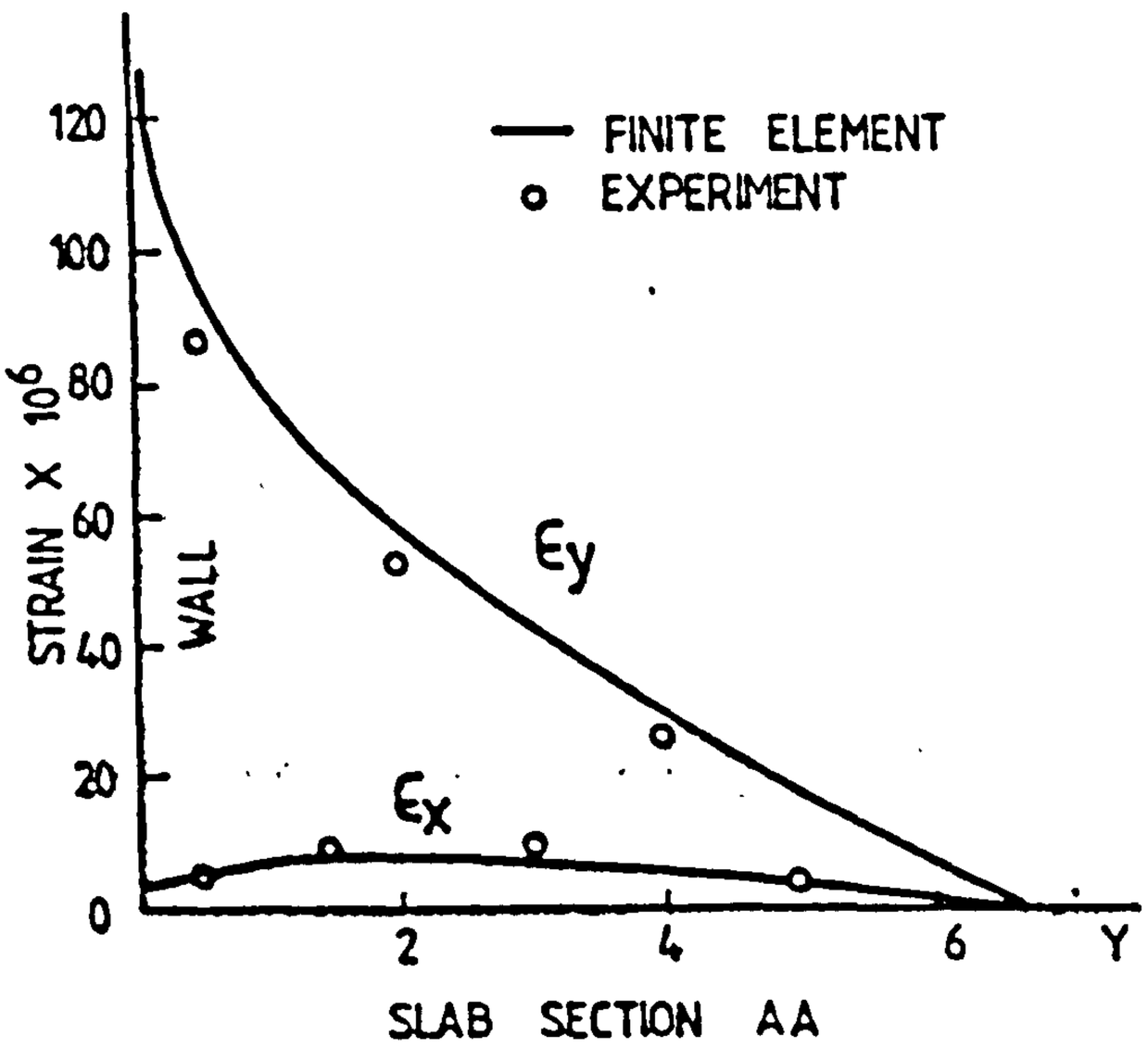

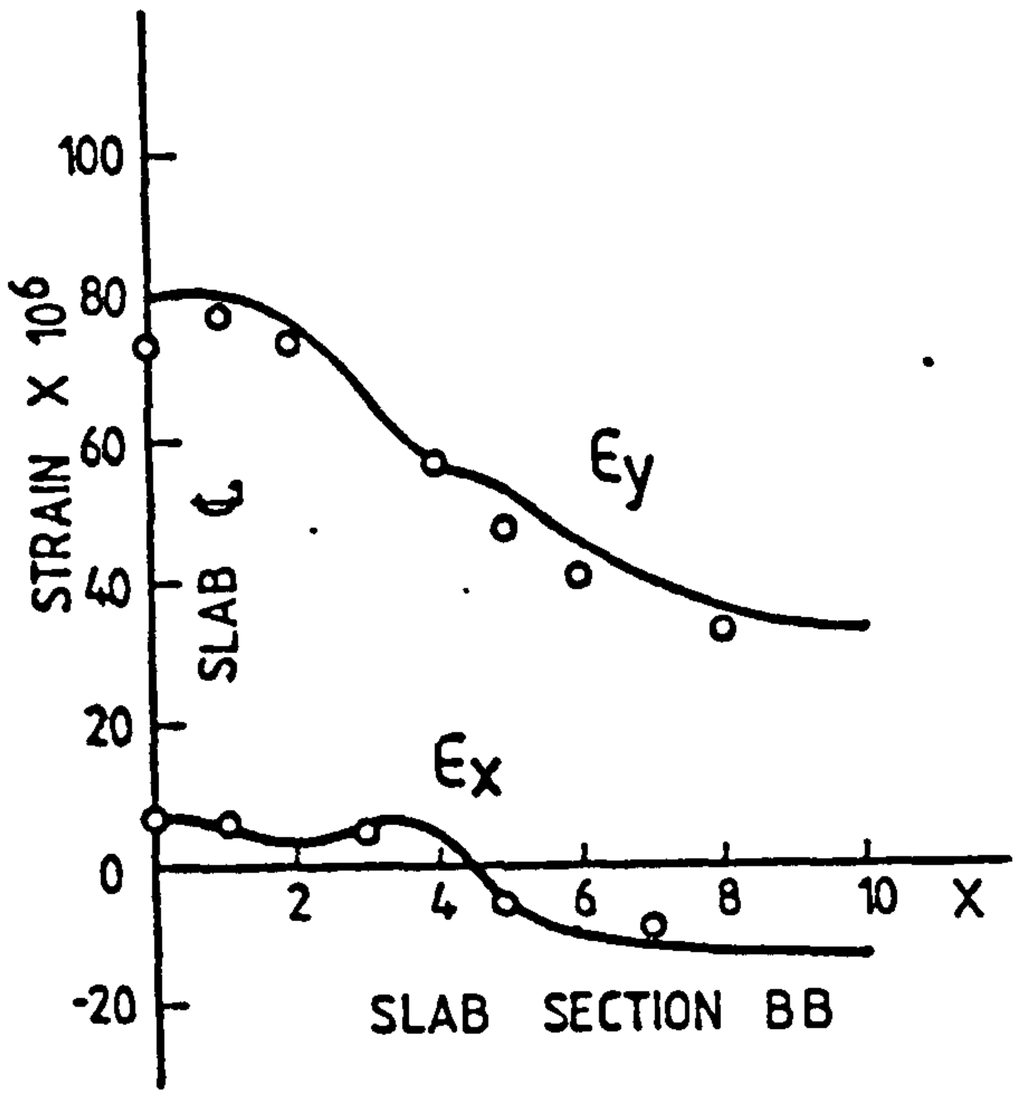

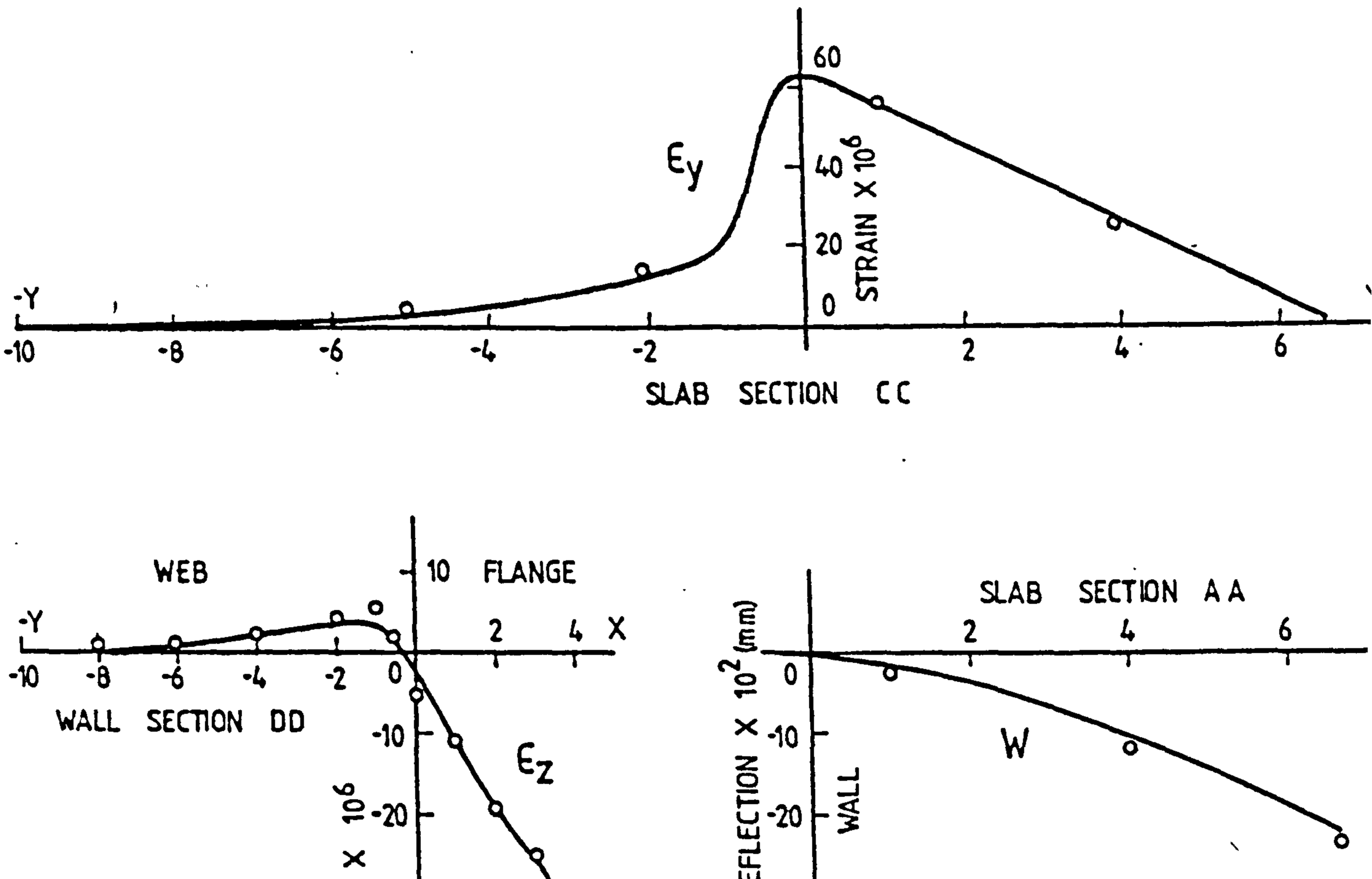

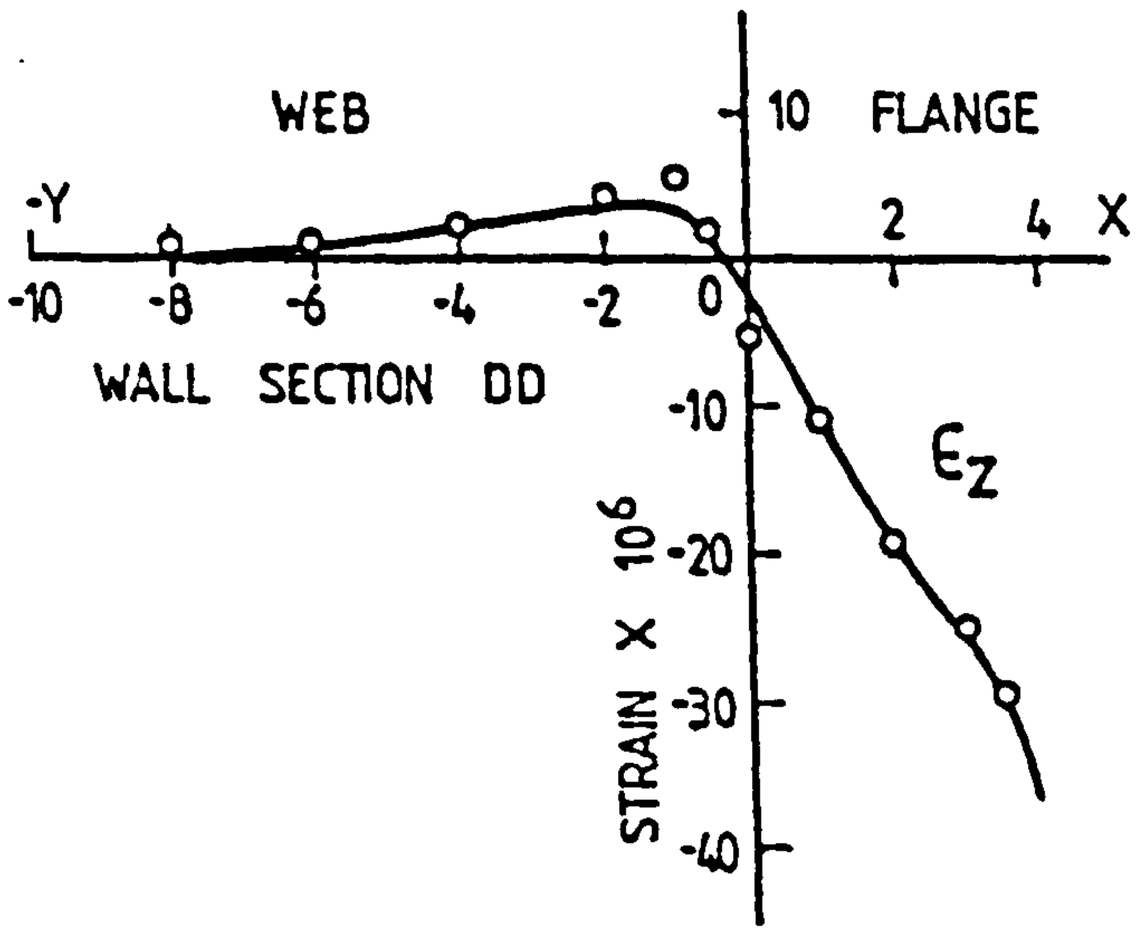

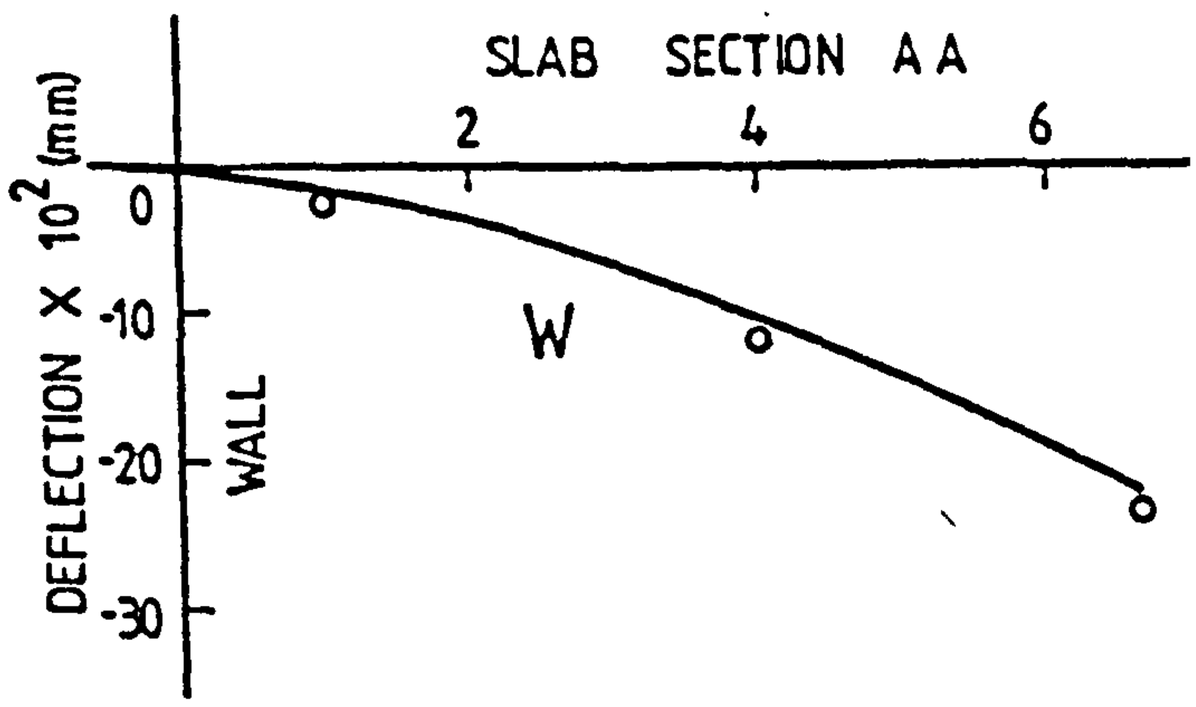

FIG. 10.13- STRAINS AND DEFLECTIONS IN MODEL NO. 3

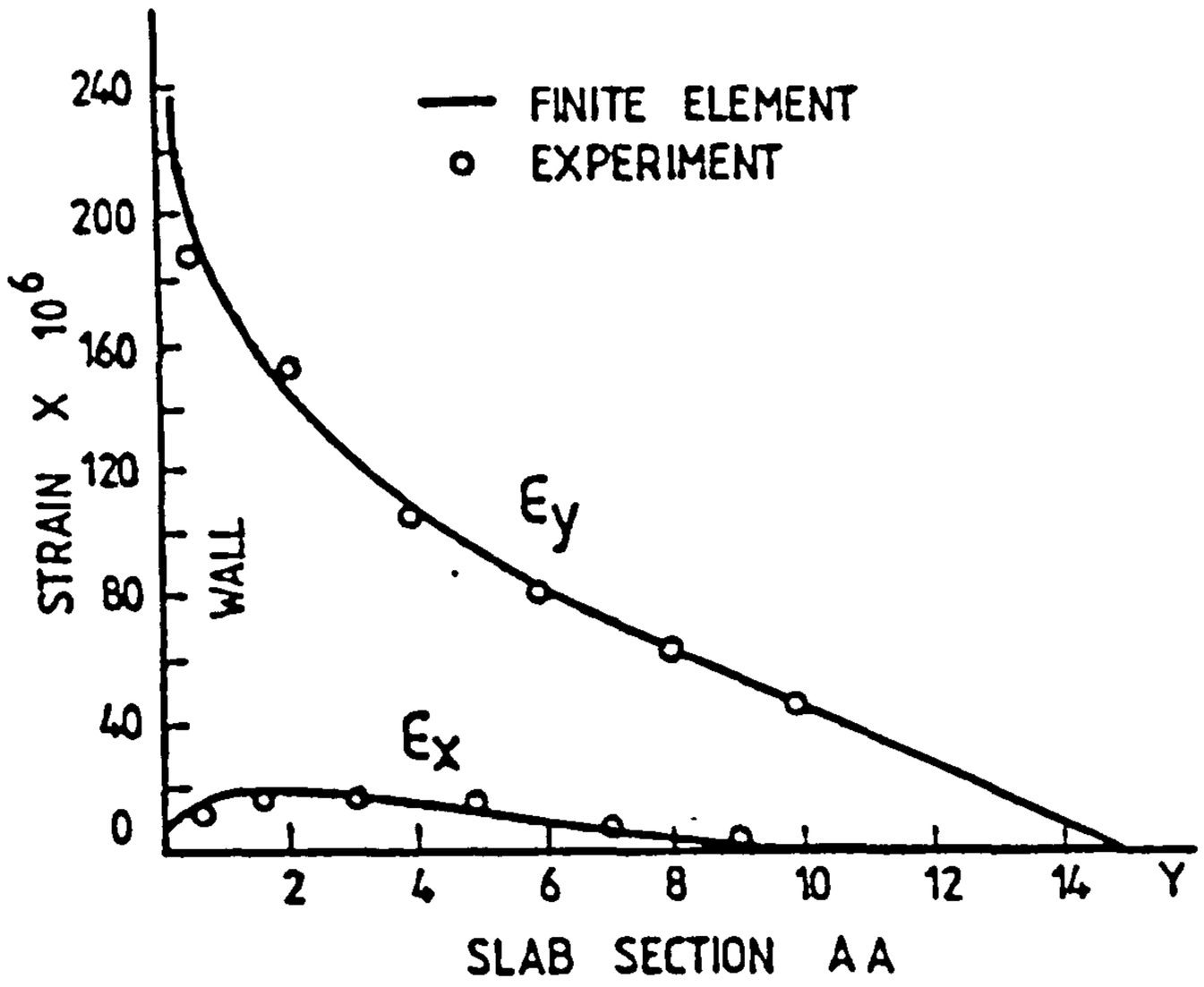

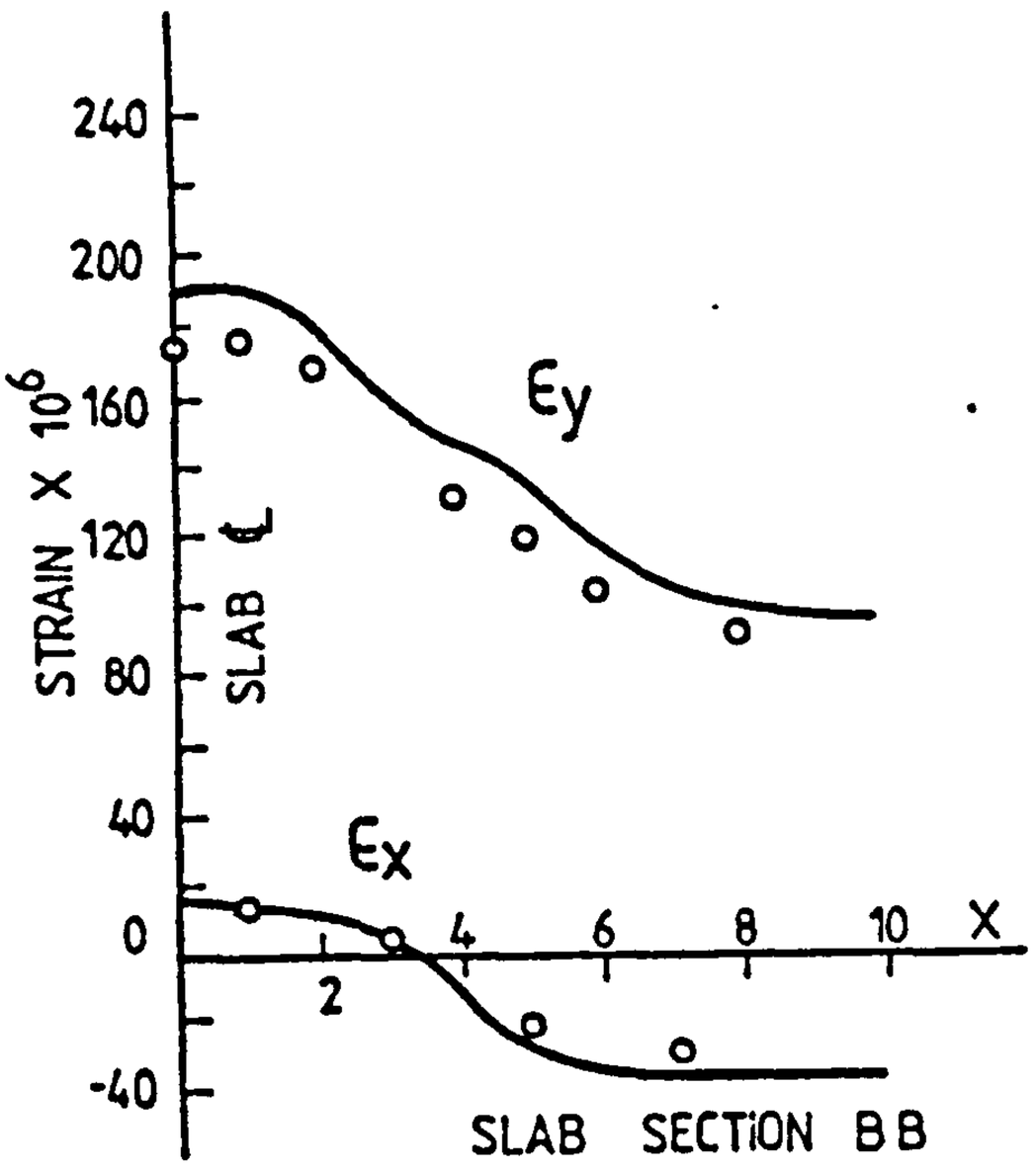

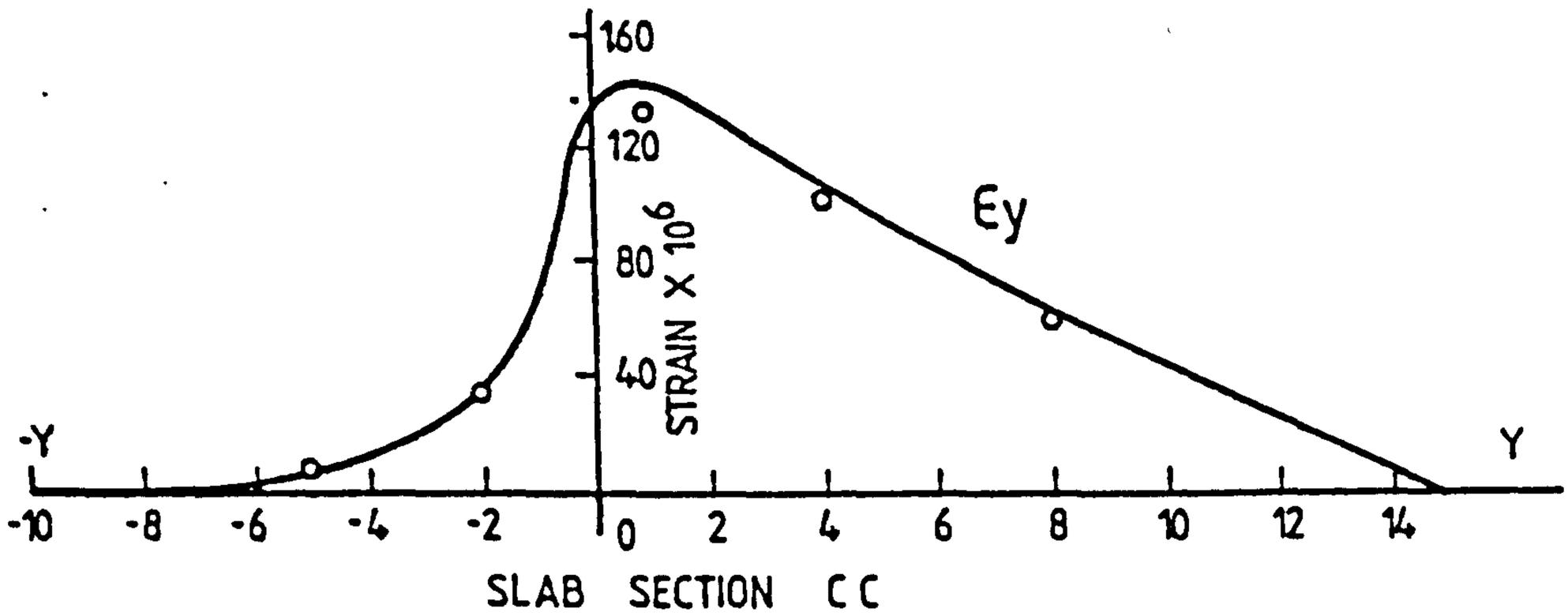

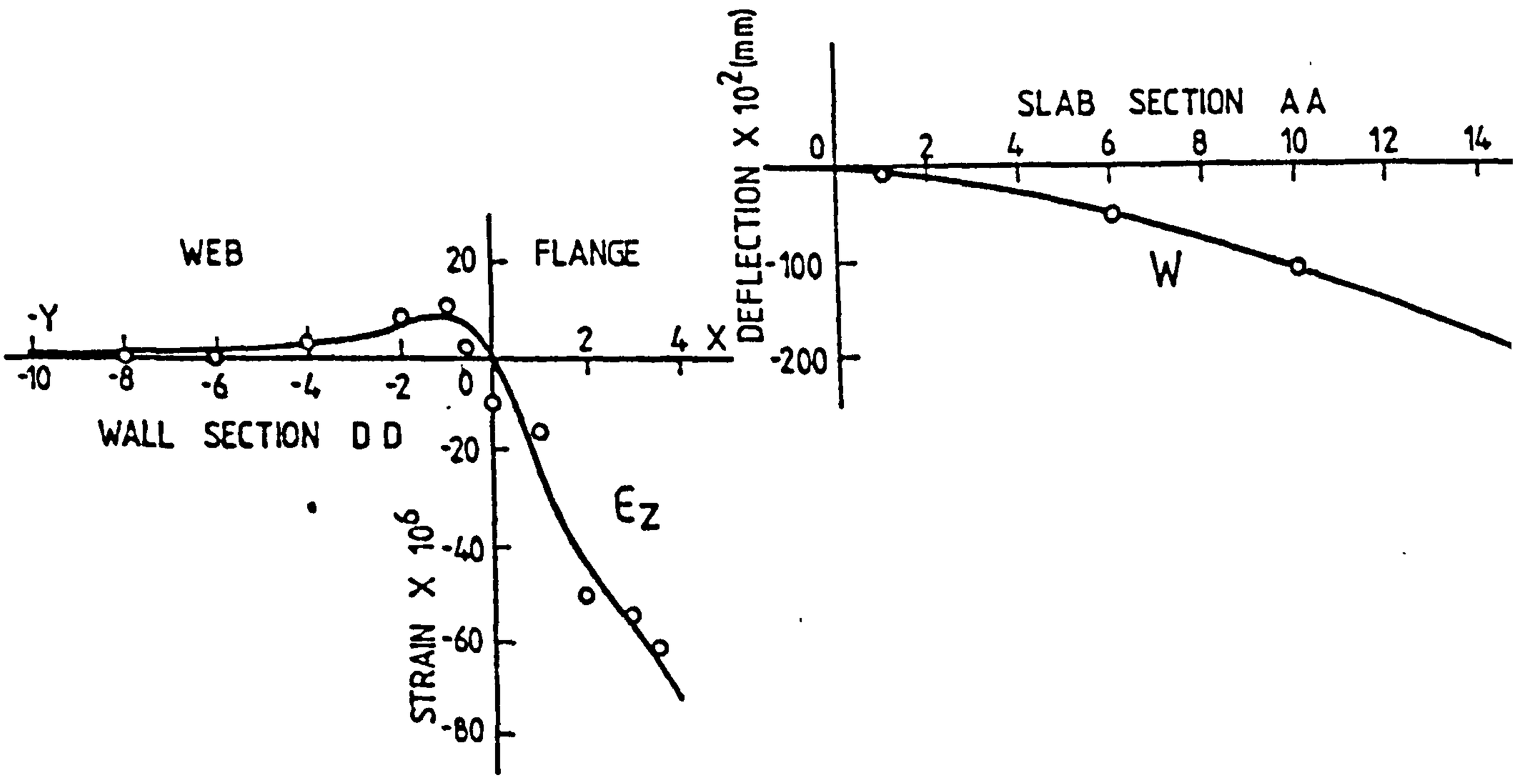

FIG. 10.14 - STRAINS AND DEFLECTIONS IN MODEL NO. 4

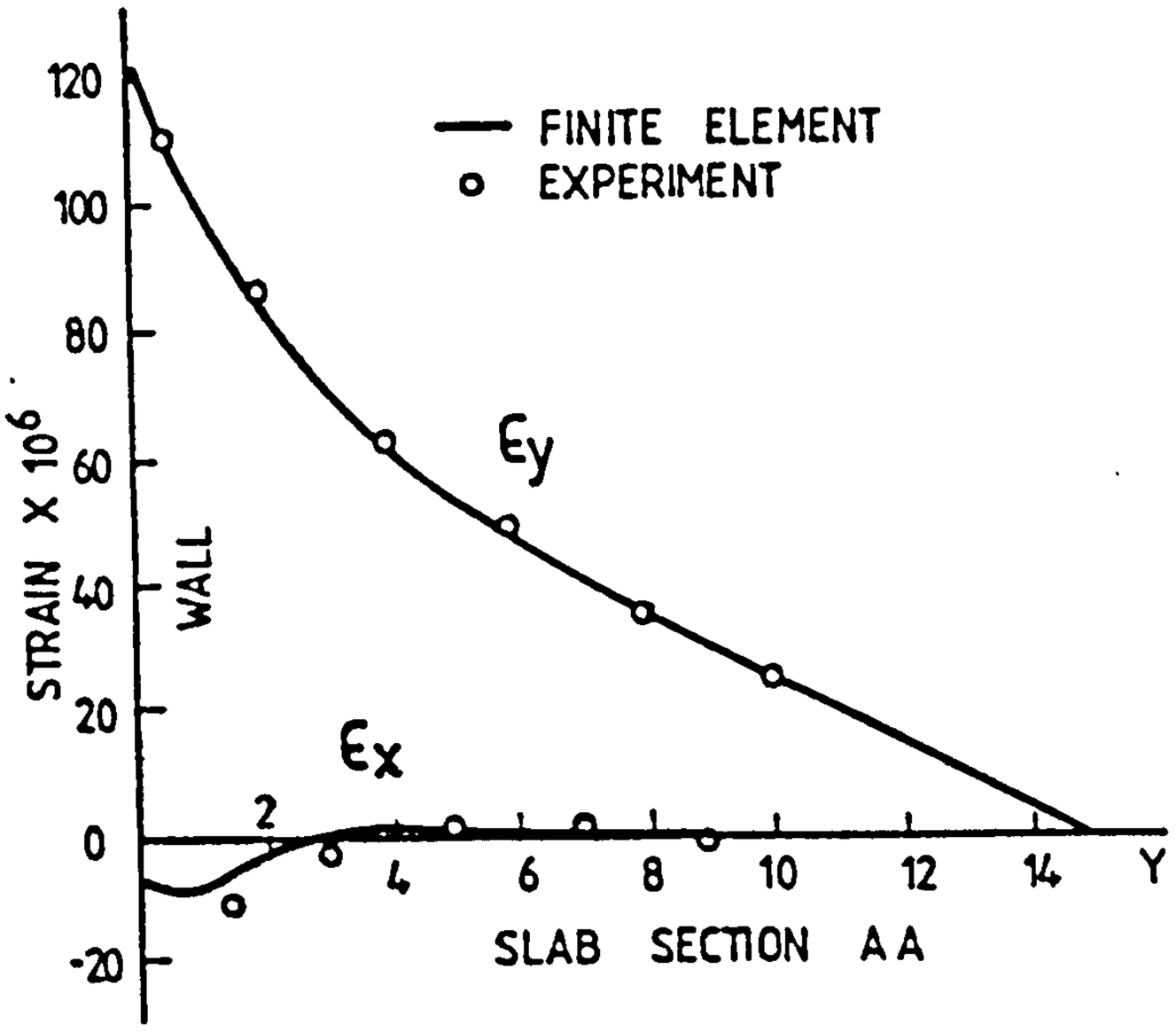

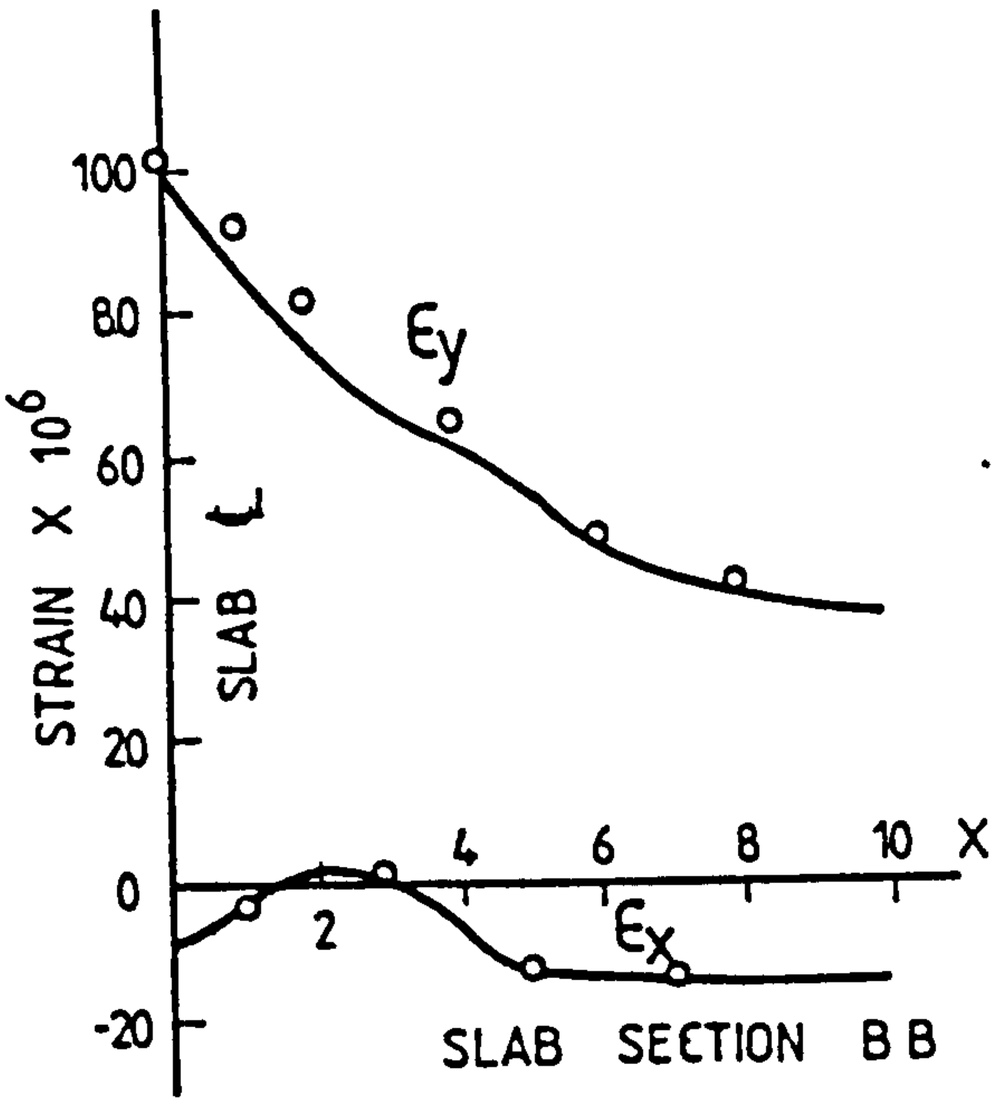

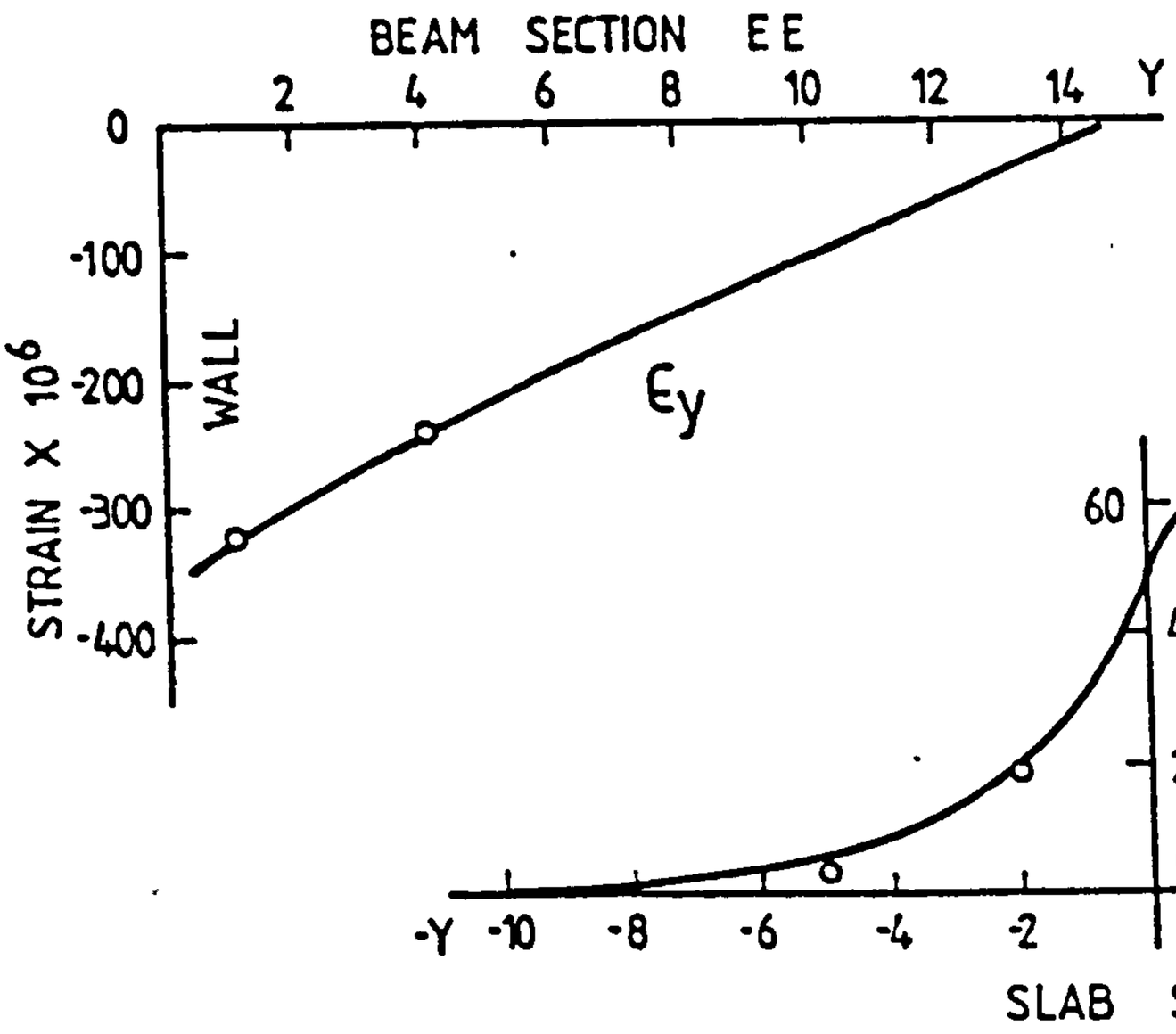

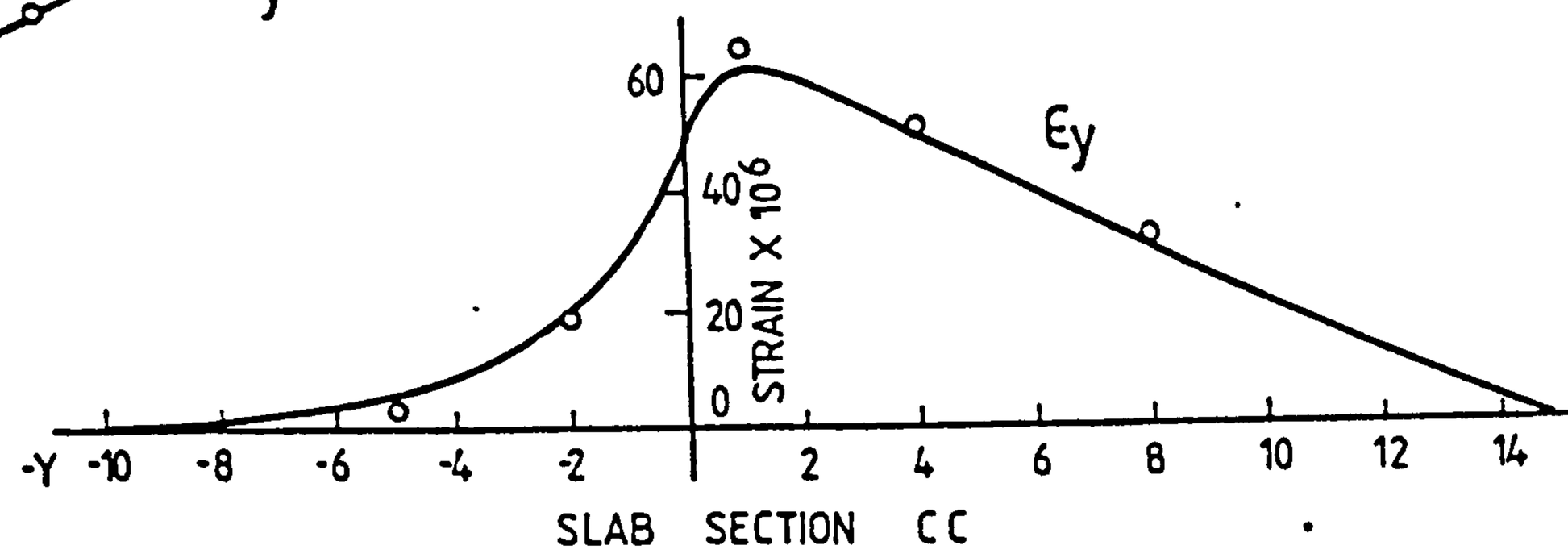

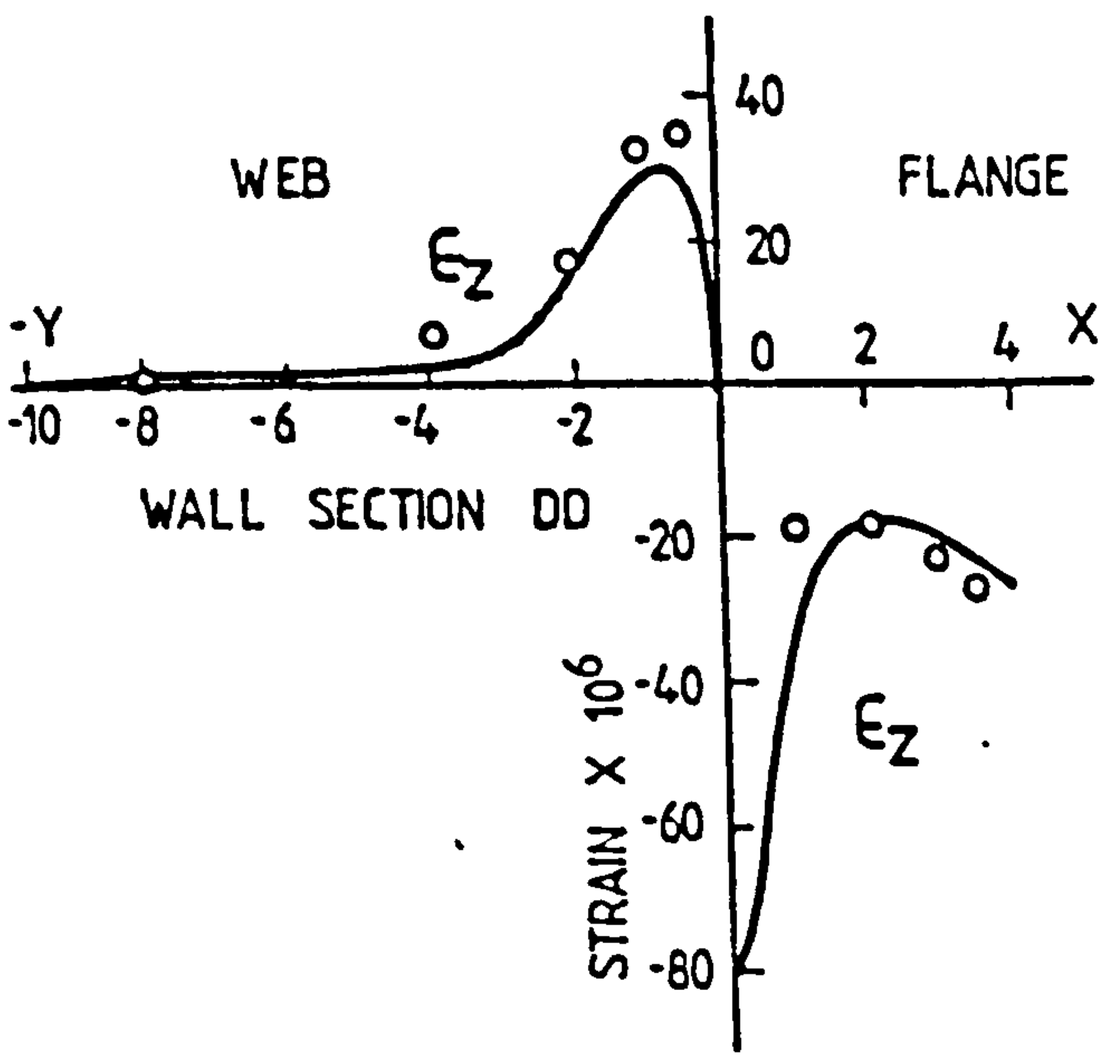

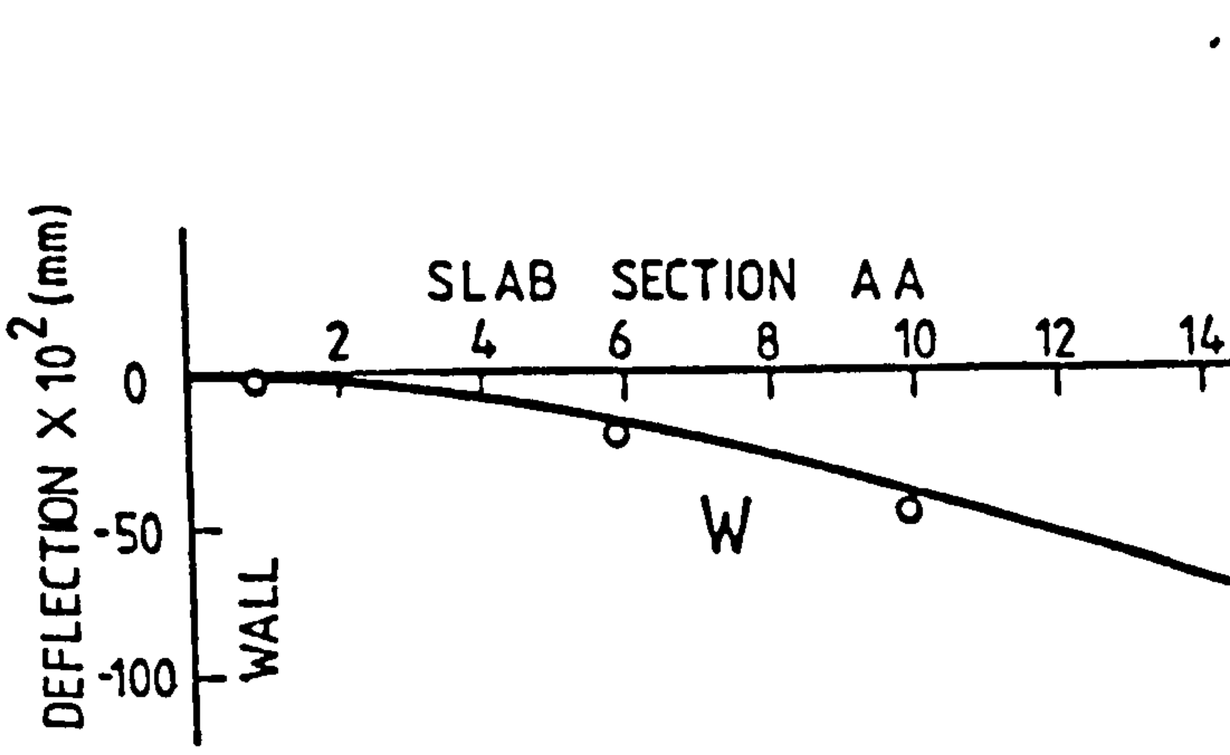

FIG. 10.15 - STRAINS AND DEFLECTIONS IN MODEL NO. 5

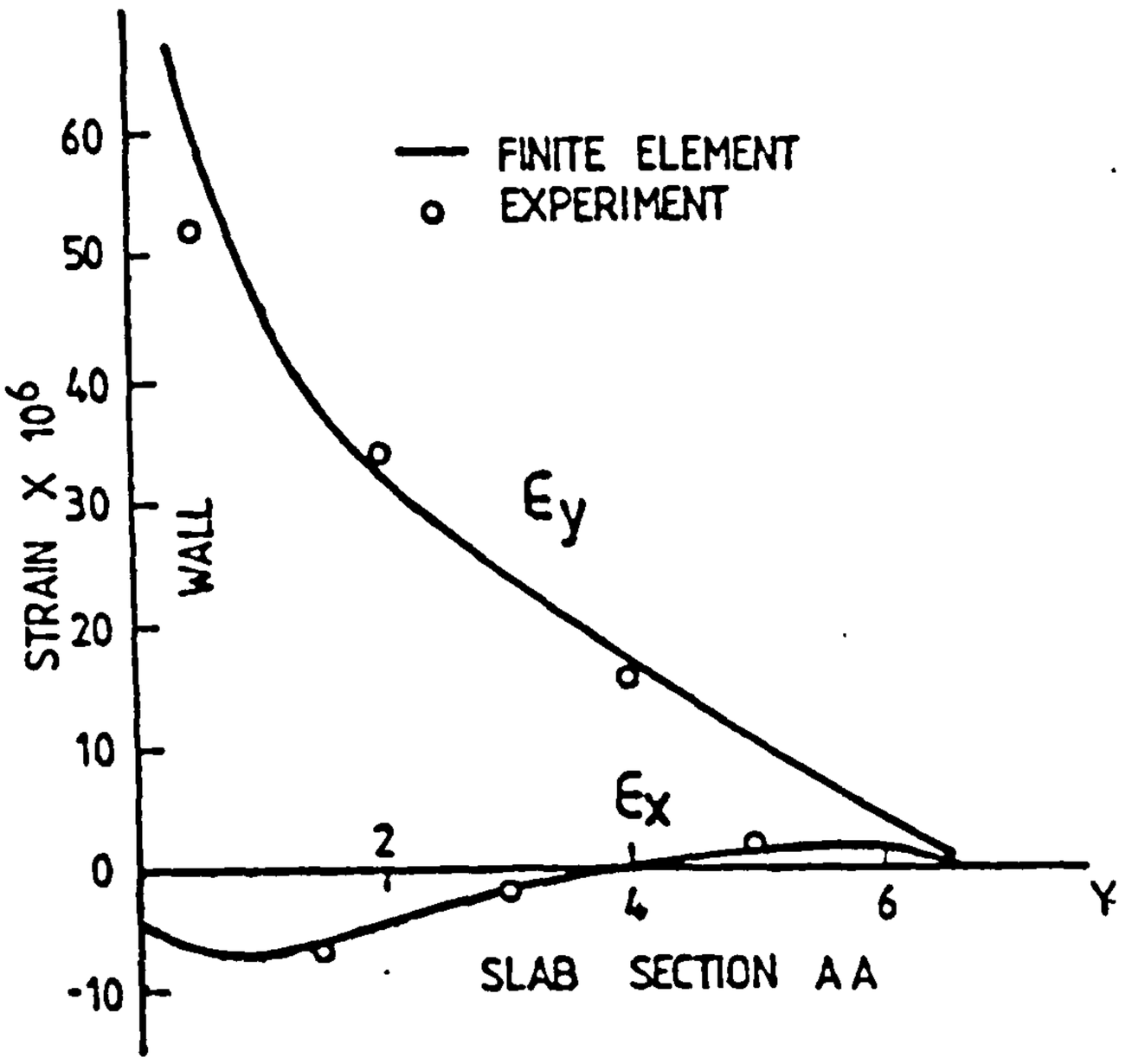

FIG. 10.16 - STRAINS AND DEFLECTIONS IN MODEL NO.6

CHAPTER 11

COMPUTER PROGRAMS

11.1 INTRODUCTION

Although the concepts behind the finite element method are relatively straightforward, the real application of the theory requires a considerable amount of computer programming effort. Thus although the author's main concern was with the investigation of various structural problems, a large portion of the effort was expended in the writing of computer programs to get the established finite element concepts implemented as a means for attacking the structural problem.

In this Chapter, the more important programs which have been used for the investigation of various structural problems reported in the preceding Chapters are described. Although a number of the programs are modified from an existing finite element program suite in the Department of Civil Engineering, University of Strathclyde, the majority of the programs were written by the author from scratch.

11.2 FINITE ELEMENT PROGRAM SYSTEM

A primary consideration in programming for the finite element method is a systematic organisation of the various computational and data handling processes. Typically, a finite element solution system is composed of a series of routine computational processes, typified by data input, element stiffness generation, structure stiffness assembly, equation solution, stress calculation and output display. It is therefore convenient for program development and application to build up the complete program system as a series of program modules, each performing a distinct function. If the interfaces and data structure of the modules are sufficiently standardised, it is possible to assemble appropriate modules according to the need in a given application.

The program modules can be written as sub-routines which are run by a master driving program, or as a series of short programs run by a job description macro and interfacing through peripheral data storage. The latter system has the important advantage of reduced core requirements because the programs can be made relatively small. The author's programs are based on the macro system and use disc backing store for data storage.

Tables 11.1, (a) and (b), list in sequential order the author's program suites for the implementation of various finite element schemes for the analysis of plate structures. Except for the equation solving programs, which are written in FORTRAN, all the other programs are written in ALGOL. The programs are written for implementation in the ICL 1904S computer of the University of Strathclyde. The source programs (program listings) and operating instructions are available from the Department of Civil Engineering, University of Strathclyde, and only the general features of the various programs will be described.

11.2.1 BASIC SOLUTION PROGRAMS

(i) Data Input

All the input programs listed in Table 11.1(a) perform a similar function of reading in the essential data for the description of the problem, verifying the data where possible, printing out the data supplied or generated and storing them on backing store where they can be accessed by subsequent programs. The data input consists typically of the following information:

(a) Control data
(b) Material properties
(c) Element connections
(d) Element geometry
(e) Boundary conditions
(f) Spring conditions
(g) Applied loads

The control data consist of information on the total number of nodes, elements, stiffnesses, boundary conditions, etc., and are used for allocating storage spaces for various arrays in core as well as on backing store, and for the control of cycling of input, output and arithmetic operations.

The programs listed allow for constant isotropic material properties defined by Young's modulus and Poisson's ratio. In an alternative suite of programs (consisting of programs RE01, RE02 and RE05), written for the element RB12, allowance is made for any number of orthotropic material properties.

The element connection data list in sequence the nodal numbers and the stiffness reference of each element. The stiffness reference identifies elements having the same stiffness properties. The element connection numbers provide the essential reference for the assembly of the structure stiffness matrix. The element connection data can be either read in element by element, in the case of irregular mesh patterns, or automatically generated for groups of elements from generation data for regular mesh patterns. The data generation reduces not only the data preparation effort but also the chances of data input error.

The element geometry data are required for the construction of the stiffness matrix for each element stiffness reference. For the rectangular bending elements (RB12 and RB24), the element geometry is specified by the lengths of the element sides and the plate thickness. For the other elements, the nodal co-ordinates and the plate thickness provide the necessary information for describing the geometry and orientation of the element.

A known boundary condition is identified by the boundary node number and the direction and value of the known displacement. The displacement direction is identified by the sequential order of the displacement parameter in the displacement vector for the node. The

boundary condition data can be read in node by node or generated for strings of regular numbered nodes by the input programs.

An externally connected axial or rotational spring is identified by the nodal number of the restrained node and the direction and stiffness of the spring. The identification of spring direction is similar to that for boundary conditions.

A concentrated load is specified in the data input by the nodal number and direction and value of the load. With patch loading, the tributary loads are assigned to the element nodes as concentrated loads. Loads uniformly distributed over the whole plate, however, do not need this treatment and require only the specification of the intensity of loading.

(ii) Stiffness Generation

Although all the stiffness generation programs listed in Table 11.1(a) perform the same basic function of creating for each stiffness reference an element stiffness matrix (and a consistent load vector in the case of plate bending elements), the program structure varies considerably from one program to the other since the element stiffness matrix is highly dependent on the mathematical formulation of the element.

In programs REC2 and TRJ2 for the simple plate bending elements (RB12 and TB9), the element stiffness matrices are constructed using explicit expressions given in References 30 and 45.

In program REW2 (element RB24) the generalised stiffness matrix is constructed using the explicit expressions given in Appendix A2.1. The matrix [C] relating the generalised parameters to the displacement parameters is generated and inverted numerically to obtain the transformation matrix which transforms the generalised stiffness matrix into the element stiffness matrix.

In program TRB2 (element TB18), the generalised

stiffness matrix for a 21-degree of freedom element is constructed using the explicit expressions given in Reference 33. The displacement-parameter transformation matrix $[C]^{-1}$ is obtained in a similar manner to program REW2 but in addition to this transformation matrix a transformation matrix for eliminating the mid-side nodal parameters is also generated. The element stiffness matrix for the 18-degree of freedom element is then obtained from the generalised matrix through an appropriate transformation.

In program QUB2 (element QB16), the four partial stiffness matrices for the four triangular fields are constructed using explicit expressions given in Reference 34, and then assembled into a generalised stiffness matrix by direct address. The condensation matrix and the co-ordinate transformation matrix are generated and the generalised stiffness matrix transformed into the operational element stiffness matrix.

In programs SHE2 and SHI2 for the shell elements RS24 and TS18, the plane stress and plate bending element stiffness matrices are constructed using explicit expressions[30,35,37,45] and then assembled into a shell element stiffness matrix in local co-ordinates. The direction cosines are generated from the element nodal co-ordinates and the local element stiffness matrix transformed to a global one.

(iii) Stiffness Assembly

The assembly programs assemble the structure stiffness matrix and load vector and inserts the boundary conditions. Six of the program suites use a common assembly program REC3 modified from a departmental program suite. The program assembles the banded structure stiffness matrix in rectangular form (band-matrix technique). In order to conserve core store, the band matrix is assembled and modified for any boundary conditions in segments. A boundary condition is incorporated by replacing the

diagonal stiffness coefficient of the boundary equation by a large number (10^{70}) and replacing the corresponding load term by the newly formed diagonal coefficient multiplied by the value of the prescribed displacement.

The program REC3 can be used only for elements having the same number of nodal parameters at all the element nodes. The program QUB3 written by the author is a more sophisticated version which can be used for the assembly of elements with unequal numbers of parameters at corner and side nodes, a well-known problem.[26] In this program, the addressing of the element stiffness coefficients is facilitated by reference to a pointer array (generated in program QUB1) which registers the nodal degree of freedom and equation number for each node.

The program RES3 differs from REC3 only in that the structure stiffness matrix assembled by RES3 can be stored in multiple disc files, if required to overcome storage capacity problem, whereas in REC3 the structure stiffness matrix is stored in one single disc file, the capacity of which can be easily exceeded for large problems.

The program RJS3 is a modified version of RES3 and permits the assembly of elements with skewed boundary conditions. In this program, the stiffness matrix of any element having skew boundary nodes is modified so that the boundary degrees of freedom are referred to a local skewed direction before the stiffness matrix is assembled. This allows the direct application of skewed boundary conditions in the assembled boundary equations.[33]

(iv) Equation Solution

The equation solver SOV4 is used in most of the author's program suites. The program is a modified version of a Departmental program and has program steps added by the author to omit arithmetic operations on zero coefficients in the forward elimination and back substitution processes, thus improving considerably the efficiency of the equation solver. The solver is based on an out-of-core Gaussian

elimination scheme which requires only a portion of the band matrix to be in core store during the elimination and back substitution processes. The solver handles multiple load vectors and operates on data assembled by program REC3 or program QUB3. The version RES4 is used when the structure stiffness matrix and load vectors are assembled by program RES3 or program RJS3.

(v) 'Stress' Calculation

Like the stiffness generating programs, the stress calculation programs differ considerably from one another due to the different mathematical formulations of the elements. However all these programs perform the basic function of computing the element 'stresses' (plate stress resultants and membrane stresses) and printing out the results for displacements and stresses at all the nodes.

Typically, in programs REC5, TRJ5 and QUB5 the element 'stress' matrix (for plate stress resultants) is constructed for each element stiffness reference. The nodal stress resultants are computed for each element by multiplying the element displacement vector with the appropriate 'stress' matrix, and the nodal 'stress' values from elements connected to a common node are accumulated and averaged.

In programs REW5 and TRB5 for the higher order bending elements, the element displacement vectors contain curvature terms, and the bending stress resultants are computed directly from these values using the standard moment-curvature relationships in plate theory.[22] The shearing forces and Kirchhoff's supplemented shears are computed by first constructing the 'shear stress' matrices and then multiplying these with the element displacement vector.

In programs SHE5, SHI5 and RJS5 for the shell elements, the bending and the membrane stress matrices are constructed separately in local co-ordinate reference. For stress calculation the element displacement vector in

global co-ordinates is first transformed to local co-ordinates and then the bending and membrane displacement components are separated for multiplication by the appropriate stress matrices.

(vi) Reaction Calculation

The programs compute the nodal reactions by computing first the element force vector given by the product of the element stiffness matrix and the element displacement vector. The element nodal forces from elements connected to a common node are accumulated for each node and the load vector subtracted from the accumulated force vector to obtain the resultant nodal reactions. The nodal reactions computed have finite values only at restrained nodes. At other nodes the resultant nodal reactions will be computed to values close to zero (of the order of 10^{-10} to 10^{-12} times the finite reaction values), reflecting the round-off errors.

11.2.2 GRAPHICAL OUTPUT DISPLAY PROGRAMS

A major problem faced by the stress analyst using the finite element solution is the interpretation and analysis of the large volume of numerical results in the computer print-out. The use of computer graphics for the display of the results alleviates this difficulty to a great extent.

Depending on the intended use of the graphical display, the numerical results may be displayed in the form of scaled vectors, contour lines or three dimensional surfaces in perspective. Any of these forms of display should give the analyst an instant overall picture of the distribution of stresses throughout the structure analysed, and highlight areas requiring special attention.

Table 11.1(b) lists the programs written by the author for plotting by an automatic graph plotter the results produced by a finite element solution. The programs use the 'GHOST' plotting routines from the ICL computer soft-

ware library for the drawing of lines and characters dictated by the written programs.

(i) Nodal Co-ordinates Data Input

Programs REC20, SHE20 and RJS20 are used for the input of absolute global co-ordinates for the nodes of the discretised structure. The data can be read in node by node, or generated for groups of nodes in regularly sub-divided regions. The nodal co-ordinates are stored in the disc file containing the finite element results (produced by the stress calculation program), for use by subsequent plotting programs.

(ii) Vector Plotting

Program REC22 computes the principal bending moments and directions, and plots these as scaled vectors at the nodal points. The program requires for input only the specification of the height of the picture, and the maximum vector length as a ratio of the picture height. The program automatically sets all the other essential plotting dimensions in relation to the input data.

(iii) Contour Plotting

Program REC23 plots contours of deflection and slopes and program REC24 plots contours of stress resultants from the results produced by the RECP suite of solution programs. Two versions of each of the programs are available. In the first version, the program automatically sets the contour interval and the number of contours to provide between 8 and 15 lines evenly spaced over the complete range of nodal values. In the second version, the choice of the contours is left to the user. Both versions allow the user a choice of any number of plots for any of the displacement and stress functions.

Program SHE27 allows the plotting of contours for the bending stress resultants and membrane stresses evaluated by the SHEP suite of programs. Again, versions of the

program are available for automatic or user prescribed selection of contours for plotting.

(iv) Perspective Plotting

Each of the programs REC28, SHE28 and RJS28 allows a choice of plotting either the finite element mesh or the deflected shape of the structure in perspective view. A typical program can be used in one run to produce any number of displays of the structure viewed from any angle or position specified by the user. The plotted deformations are exaggerated to accentuate the deflected shape.

The programs REC29 and SHE29 plot the distribution of stress resultants in the form of a surface in perspective view. Again these programs allow the choice of any number of displays of any of the stress functions viewed from any angle or position.

11.2.3 ELEMENT COMBINATION PROGRAMS

The finite element program system adopted allows different element types such as beam and plate elements to be combined in the same solution.

(i) Beam and Plate Elements

Programs BEA1 and BEA2 enable beam elements to be incorporated into the primary solution using plate bending elements (RB12 or TB9). In a combined program run, the program BEA1 is inserted between the stiffness assembly and equation solution programs for the primary system. The program reads in the beam element data, generates the beam stiffnesses and assembles them into the overall structure stiffness matrix. The program BEA2 can be inserted in the primary solution system at any point after the equation solver, and calculates the beam forces.

(ii) Space Frame and Shell Elements

Programs SPF1 and SPF2 enable eccentric space frame

elements to be combined with flat shell elements (RS24 or TS18) in a combined program run. The programs function in a similar manner to programs BEA1 and BEA2. Modified versions of Programs SPF1 and SPF2, which are designated as programs SPF1S and SPF2S, include shear deformation in the element stiffness formulation.

(iii) Triangular and Rectangular Elements

Triangular and rectangular elements are often used together to obtain the best discretisation scheme for the given situation. With minor modifications to the data structure, the programs listed in Table 11.1(a) for the triangular and rectangular elements can be easily assembled for a combined solution system for such a situation.

11.3 INFLUENCE COEFFICIENT SOLUTION PROGRAMS

In addition to the finite element programs described in this Chapter, a number of computer programs have been written for the influence coefficient method of analysis for slabs coupling shear walls. The various programs are similar in program structure, and differ only in the evaluation of integration constants for different boundary conditions. All these programs are written in ALGOL.

Program SER1 is for the analysis of a typical quadrant of a slab panel coupling a pair of symmetrical shear walls undergoing parallel rotation. The same program can be used for any of the four standard boundary conditions, continuous, free, simply supported and clamped conditions, at the edges of the slab parallel to the direction of wall rotation. The program reads in the bare minimal amount of data required to define the problem, generates the flexibility matrix and nodal displacement vector, and solves the assembled compatibility equations for the unknown nodal force vector, by Cholesky decomposition. The program then calculates the coupling stiffness and effective width of the slab, and proceeds to calculate the plate stress-resultants at the points specified by the user.

Program SER2 is used for the analysis of a typical half of a slab coupling a pair of dissimilar walls symmetric about the longitudinal centreline. Program SER3 is used for the analysis of a full slab panel coupling a pair of shear walls of any individual shape. In their present forms, both programs allow for only the most usual case of a slab with continuous longitudinal edges, as the need to consider other cases did not arise. If required, the programs can be easily expanded to include the cases of free, simply supported and clamped longitudinal edges.

TABLE 11.1(a) BASIC FINITE ELEMENT SOLUTION PROGRAMS

Element Type	RB12	TB9	RB24	TB18	QB16	RS24		TS18	
Program Suite	RECP	TRJP	REWP	TRBP	QUBP	SHEP	RESP	SHIP	RJSP
Data Input	REC1	TRJ1	REW1	TRB1	QUB1	SHE1	RES1	SHI1	RJS1
Stiffness Generation	REC2	TRJ2	REW2	TRB2	QUB2	SHE2	SHE2	SHI2	SHI2
Stiffness Assembly	REC3	REC3	REC3	REC3	QUB3	REC3	RES3	REC3	RJS3
Equation Solution	SOV4	SOV4	SOV4	SOV4	SOV4	SOV4	RES4	SOV4	RES4
Stress Calculation	REC5	TRJ5	REW5	TRB5	QUB5	SHE5	SHE5	SHI5	RJS5
Reaction Calculation	REC6	REC6	TRB6	TRB6	QUB6	SHE6	SHE6	SHE6	-
Graphical Output Display									

TABLE 11.1(b) GRAPHICAL OUTPUT DISPLAY PROGRAMS

Element Type	RB12	RS24	TS18
Program Suite	RECP	SHEP	RJSP
Nodal Co-ordinates Input	REC20	SHE20	RJS20
Vector Plot	REC22	-	-
Displacement Contour	REC23	-	-
Stress Contour	REC24	SHE27	-
Deflected Shape	REC28	SHE28	RJS28
Stress Perspective	REC29	SHE29	-

CHAPTER 12

CONCLUSIONS AND SUGGESTIONS FOR FUTURE WORK

The contribution of floor slabs interacting with the vertical structural elements in a variety of tall building systems is frequently disregarded, or at best approximated by rule of thumb methods, in the lateral load analysis, due to lack of understanding of the behaviour of the slab. The work described in this thesis not only helps the designer achieve a better understanding of the behaviour of the slab, but also allows him to use the relatively simple existing techniques to analyse the complicated slab-coupled structural elements.

The interaction between the floor slabs and the vertical elements in cross-wall, centre core, hull-core and flat-plate frame structures under lateral loading has been studied using finite element and influence coefficient techniques. The general accuracy of these techniques has been substantiated by experimental tests on small scale shear wall-slab models, and by the comparison of results with other investigations reported in the literature. The influence coefficient technique yields results of comparable accuracy to those given by the finite element technique, and has distinct computational advantages, but the technique as developed in this thesis is restricted to the analysis of regular slabs coupling rigid shear walls or columns. The finite element technique, on the other hand, is extremely versatile and has been used conveniently to analyse slabs with openings and slabs integral with floor beams, flexible walls and columns, which are beyond the scope of the simple influence coefficient technique.

The finite element technique employed the simple and most popular Adini-Clough-Melosh rectangular element for modelling plate behaviour. The convergence study for a wide range of established simple and refined elements

used in the analysis of a slab coupling a pair of shear walls has shown that this simple element provides the best results with the least computational effort.

The relative influences of a wide range of structural parameters on the structural behaviour of the slab coupling a pair of rigid (locally non-deformable) shear walls in a cross-wall structure have been examined. The effective width of slab and the important coupling actions are influenced significantly only by the interior structural features of the wall and slab. The slab overhang, the wall length and the exterior wall flanges have very little influence, whereas the wall opening width, the interior flange width or wall thickness and the slab width have a strong influence on the behaviour of the slab.

The difference in wall shapes between a flanged wall and a box core has a negligible effect on the behaviour of the slab when the flange width and core width are the same.

The stiffness of the slab in a coupled planar-flanged (T-shaped) wall configuration is very similar to that in a skew-coupled L-shaped wall configuration when the two different configuration have the same overall length of wall flanges. The distributions of coupling actions are however different in the two configurations.

Access openings in the corridor core walls reduce the coupling stiffness of the slab to an extent dependent on the relative size of the core-opening. Access openings in the side walls have negligible effect on the slab.

In the orthotropic coupling slab, the effective width defined in terms of the longitudinal flexural rigidity, increases with the ratio of transverse to longitudinal flexural rigidities, but for normal reinforced concrete floor slabs the orthotropic effect due to reinforcement ratios is insignificant.

Design curves and simple empirical equations have

been presented to enable the effective width and coupling stiffness of the slab to be readily obtained for different wall configurations. Once the effective stiffness of the slab is determined the overall analysis of the coupled wall structure may be carried out using an equivalent frame or continuum solution.

The structural design of the slab requires an accurate knowledge of the distribution and magnitude of slab stresses induced by the coupling action. The coupling action results in a non-uniform distribution of bending moments and shearing forces in the slab, with severe concentrations of slab actions around the extremities of the interior wall edges. The bending and shearing stress resultants at these critical points are likely to be theoretically infinite when the behaviour of the slab is modelled by plate theory. The plate bending finite element solution yields non-convergent values of stress resultants at the critical points. The calculated critical nodal values of bending stress resultants can however be used for calculating the integrated moment across the critical zone. The shearing force distribution is discontinuous close to the critical points and the critical integrated positive and negative shearing forces cannot be determined from the divergent calculated nodal shearing stress resultant values. The critical punching shear at the critical sections located according to code provisions for gravity load design however can be evaluated reasonably accurately from the calculated nodal shearing force values.

A set of accurate contour diagrams for non-dimensional bending moment factors has been presented for slabs coupling plane walls. These contours allow the bending moments induced by coupling action to be rapidly evaluated at any point on the slab in a design situation. For other wall configurations only approximate curves showing the variation of bending moment factors at the

critical sections have been presented. It would be desirable in future studies to produce design contours for these configurations, similar to those presented for the plane-wall configuration.

The dimensions and shape of the critical section for punching shear design has been recommended, and design curves for evaluating rapidly the critical punching shear have been presented, for plane wall and flanged wall configurations. Punching shear is likely to be important for slabs coupling plane walls or flanged walls with narrow flanges.

The interaction between the slab and a coupled wall produces local elastic axial wall deformation and local bending of wall flanges. The effects of local wall deformation reduce the coupling stiffness of the slab and influence the distribution of slab actions, to an extent dependent on the structural geometry. The flexibility effect has been measured by the ratio of flexible wall to rigid wall slab stiffness. The relative influences of a range of structural parameters on the stiffness ratio have been examined for plane wall, flanged wall and box-core configurations. The wall length, storey height, slab width and flange width have relatively little influence on the stiffness ratio, compared to the influence of relative wall and slab thicknesses and wall opening width. In the plane wall configuration, the stiffness ratio varies essentially with a single geometrical parameter $t/(L^2h)^{1/3}$; in the flanged wall and box-core configurations, the stiffness ratio varies approximately as a function of $(t/h)/(L/x)^{\frac{1}{2}}$.

Design curves have been presented to enable the stiffness ratio to be rapidly determined for plane wall, flanged wall and box-core configurations. Once the stiffness ratio is determined, the coupling stiffness evaluated from rigid wall design data can be corrected for the local elastic wall deformation effect.

Curves have also been presented for evaluating the distribution of bending moments at the critical slab

section for the various flexible wall configurations. Future work directed at preparing more comprehensive design curves in the form of non-dimensional contours for evaluating rapidly the stresses induced not only in the slab but also in the coupled walls is envisaged. Since the actual shear transfer and local stress concentrations at the slab-wall junction cannot be satisfactorily determined using two dimensional plane elements to model the structure, it would be desirable in future studies to supplement the overall analysis of the slab wall panel modelled by two-dimensional plane elements, with a detailed local analysis of the slab-wall junction area modelled more accurately by three-dimensional solid elements. The actual area of interest and the necessary boundary conditions (in terms of displacements or forces) for the local analysis could be determined from the overall analysis.

Although normally disregarded, the composite action of the floor slab increases considerably the coupling stiffness of the lintel beam, and may merit consideration in cases where the coupled wal ls are relatively flexible. The relative influences of a range of geometrical ratios on the effective flange width and coupling stiffness of the composite lintel beam have been examined. The effective flange width, defined in terms of composite flexural stiffness rather than membrane stress distribution normally favoured for gravity load design, is influenced little by the overall slab width and lintel width, but more strongly by the lintel depth and wall opening width, in relation to the slab thickness.

Curves have been presented to enable the effective flange width and composite coupling stiffness of the lintel and slab to be rapidly determined for the analysis of the coupled wall system. The curves do not account for junction flexibility produced by local elastic wall deformation. The limited results available for a typical wall configuration indicate that junction

flexibility may be satisfactorily allowed for in the calculation of composite coupling stiffness by extending the clear span of the lintel by a distance equal to the lintel depth. Further studies are however required to establish the range of wall configurations over which this empirical procedure is generally applicable.

The floor slabs in a centre core structure subjected to torsional loading restrain the core against warping deformation and torsional rotation. For the overall torsional analysis of the core, it is possible to replace the slab effectively by an equivalent system of connecting beams at the core openings. The influences of a range of geometrical ratios and boundary conditions on the warping stiffness and effective width of slab have been examined for idealised box cores with single and double access openings. The warping stiffness and absolute effective width of the slab are influenced strongly by the core opening ratio and fixity conditions at the slab edges, and less by the core aspect ratio and slab width ratio.

Design curves have been presented for various core configurations to enable the warping stiffness of the slab or equivalent connecting beams to be readily determined for the torsional analysis of the core structure using an existing matrix or continuum technique. Although the curves are based on idealised box core configurations, it is usually possible in a practical design situation to disregard the coupling of internal core walls and so reduce the complicated core configuration to the simple form considered, for evaluating the warping stiffness of the slab. The internal core walls should however be considered in the calculation of torsional properties of the core walls for the overall analysis.

The significant slab actions induced by warping of the core are confined to the portions of the slab spanning the core openings. Large actions are concentrated around the coupled lips of the core where considerable local deformation of the core wall and redistribution of slab

actions can be expected. Further studies are required to examine the effects of local wall deformation as well as obtain detailed information on slab and wall stresses which are required for the design of the structural members.

In a hull-core structure the coupling of the centre core to the peripheral framed tube by the floor slabs increases the cantilever bending stiffness of the structure. The relative influences of a range of geometrical ratios and relative frame to slab stiffness ratios on the coupling stiffness of the slab with a rigid box core configuration have been examined. The coupling stiffness of the slab is influenced significantly by the core dimensions in relation to the slab span, and by the relative frame panel to slab flexural stiffness ratio. The relative frame column spacing, the frame axial to slab flexural stiffness ratio and the spandrel torsional to slab flexural stiffness ratio have very little influence on the coupling stiffness of the slab.

Curves showing the influence of the significant parameters have been presented to enable the coupling stiffness of the slab to be readily determined. Further work is required to examine the effects of local elastic wall deformation and the presence of core access openings which are expected to reduce the coupling stiffness of the slab. The techniques which were employed for the evaluation of such effects in the cross-wall structure could be adopted for any future work in this connection.

In a flat plate frame structure, the effective width of slab for the equivalent frame for lateral load analysis is only a fraction of the full bay width normally permitted by building codes for gravity load analysis, and the effective width varies according to the relative column and slab dimensions. An assumption of a fully effective bay width can in most practical cases result in a considerable overestimation of the lateral stiffness of the equivalent frame. A comprehensive set of tables has

been presented in this thesis to enable the effective width of slab to be readily obtained in a practical design situation. The tables are considerably more accurate than the design curves and tables presented in a number of recent papers on this subject.

SUGGESTIONS FOR FUTURE WORK

In addition to the earlier suggestions for future work in connection with the problems examined, a number of related topics of practical interest deserve examination in future studies. In system construction of cross wall structures, the precast wall and slab panels are connected by in situ concrete joints which have to serve the primary function of transmitting shear forces between the components. The detailing of the joint is often such that the moment connection between the floor and wall panels cannot be fully achieved, and the joint then provides essentially a pin or elastic connection for the slab. The effects of joint flexibility on the coupling performance of the slab need to be examined.

The study on the slab in the cross-wall structure has considered only the bending action of the slab coupling a pair of in-line shear walls. Torsional deformations of the structure due to non uniform lateral loading or structural asymmetry produce warping in the floor slabs connecting adjacent wall assemblies undergoing differential deflections. Since the warping stiffness of the slab provides a certain amount of restraint against the torsional deformation of the walls it is desirable to examine the warping action of the slab and assess its contribution to the overall torsional behaviour of the structure.

The structures considered in the present study have an orthogonal arrangement of walls and frames most commonly encountered in traditional building forms. The behaviour of the slabs coupling curved shear walls, circular cores and triangular cores require examination,

as architectural fancies and aesthetic considerations sometimes produce plan forms with these unusual wall shapes.

The present work has been concerned purely with linear elastic analysis which is still generally being accepted as the basis for the design of the concrete structure, although its limitations in this respect are well known. Effects of cracking of the concrete section and plastic yielding of the steel and concrete are known to produce a non-linear structural response and re-distribution of actions in the slab. With the increasing popularity of the limit state design philosophy and the emergence of elasto-plastic methods of shear wall analysis, the need for extending the present study to the investigation of non-linear elasto-plastic slab behaviour is apparent. In considering elasto-plastic behaviour, the influence of slab reinforcement detailing and the effects of gravitational forces, which have not been considered in the present study, become important and require due examination in future studies.

APPENDIX A1 - REFERENCES

1. ACI Committee 442, "Response of Buildings to Lateral Forces", ACI Jnl., Proc. Vol. 68, No. 2, Feb., 1971, pp.81-106.

2. Qadeer, A. and Stafford-Smith, B., "The Bending Stiffness of Slabs Connecting Shear Walls", ACI Jnl., Proc. Vol. 66, No. 6, June 1969, pp.464-472.

3. Qadeer, A. and Stafford-Smith, B., "Actions in Slabs Connecting Shear Walls", Proc. Symposium on Tall Buildings, Planning, Design and Construction, Vanderbilt University, Nashville, Tenn., Nov., 1974, pp.315-338.

4. Chang, Y.C., "Slabs in Shear Wall Buildings", M.Sc. Thesis, Dept. of Civil Engineering, University of Toronto, Sept. 1969.

5. Petersson, H., "Bending Stiffness of Slabs in Shear Wall Structure", Draft Report, Division of Structural Design, Chalmers University of Technology, Gothenberg, Sweden, 1972.

6. Black, D., Pulmano, V.A. and Kabaila, A.P., "Stiffness of Flat Plates in Cross-Wall Structures", UNICIV Report No. R-133, University of New South Wales, Kensington, Australia, 1974.

7. Coull, A. and El-Hag, A.A., "Effective Coupling of Shear Walls by Floor Slabs", ACI Jnl., Proc. Vol. 72, No. 8, Aug. 1975, pp.429-431.

8. El-Buluk, M.A., "Interaction Between Shear Walls and Floor Slabs", M.Sc. Thesis, University of Strathclyde, Glasgow, 1975.

9. Tso, W.K. and Mahmoud, A.A., "Effective Width of Coupling Slab in Shear Wall Buildings", Proc. ASCE, Vol. 103, No. ST3, March 1977, pp.573-586.

10. Wong, Y.C. Discussion of "Effective Width of Coupling Slab in Shear Wall Buildings", by Wai K. Tso and Adel A. Mahmoud, Proc. ASCE, Vol. 103, No. ST12, Dec., 1977.

11. Stafford-Smith, B. and Taranath, B.S., "Analysis of Tall Core-Supported Structures Subject to Torsion", Proc. ICE, Part 2, Vol. 53, 1972, pp.173-187.

12. Taranath, B.S. and Stafford-Smith, B., "Torsion Analysis of Shear Core Structures," 'Analysis of Structural Systems for Torsion', ACI SP35, 1972, pp.239-263.

13. Taranath, B.S., "The Torsional Behaviour of Open Section Shear Wall Structures", Ph.D. Thesis, University of Southampton, 1968.

14. Zbirohowski-Korsia, K., "Thin Walled Beams - From Theory to Practice", Crosby-Lockwood, London, 1967.

15. Khan, F.R. and Sbarounis, J.A., "Interaction of Shear Walls and Frames", Proc. ASCE, Vol. 90, No. ST3, June 1964, pp.285-335.

16. Aalami, B., "Moment-Rotational Relationship Between Column and Slab", ACI Jnl., Proc. Vol. 69, No. 5, May 1972, pp.263-269.

17. Mehrain, M. and Aalami, B., "Rotational Stiffness of Concrete Slabs", ACI Jnl., Proc. Vol. 71, No. 9, Sept. 1974, pp.429-435.

18. Pecknold, D.A., "Slab Effective Width for Equivalent Frame Analysis", ACI Jnl., Proc. Vol. 72, No. 4, Apr. 1975, pp.135-137.

19. Allen, F.H. and Darvall, P., Discussion of "Slab Effective Width for Equivalent Frame Analysis" by David A. Pecknold, ACI Jnl., Proc. Vol. 72, No. 10, Oct. 1975, pp.583-585.

20. Allen, F.H. and Darvall, P., "Lateral Load Equivalent Frame", ACI Jnl., Proc. Vol. 74, No. 7, July 1977, pp.294-299.

21. Pecknold, D.A., "Effective Width of Orthotropic Plate", Proc. ASCE, Vol. 104, No. ST5, May 1978, pp.855-872.

22. Timoshenko, S.P. and Woinosky-Kreiger, S., 'Theory of Plates and Shells', 2nd Edition, McGraw-Hill, New York, 1959, pp.257-258.

23. Vlasov, V.Z., 'Thin Walled Elastic Beams', English Translation, National Science Foundation, Washington D.C., London, Old Bourne Press, 1961.

24. Wood, R.H., 'Plastic and Elastic Design of Slabs and Plates', Thames and Hudson, Limited, London 1961.

25. Coull, A. and Rao, K.S., "The Analysis of Reinforced Concrete Bridge Decks by the Line-Solution Technique", 1st Int. Symposium on Concrete Bridge Design, ACI SP23, 1969, pp.19-37.

26. Zienkiewicz, O.C., 'The Finite Element Method in Engineering Science', McGraw-Hill, London, 1971.

27. Cheung, Y.K., 'Finite Strip Method in Structural Analysis,' Pergamon, Oxford, 1976.

28. Adini, A. and Clough, R.W., "Analysis of Plate Bending by the Finite Element Method", Report, National Science Foundation Washington D.C., 1961.

29. Bazeley, G.P., Cheung, Y.K., Irons, B.M. and Zienkiewicz, O.C., "Triangular Elements in Bending-Conforming and Non-Conforming Solutions", Proc. Conf. Matrix Methods in Struct. Mech., Wright-Patterson A.F., Ohio, 1965.

30. Cheung, Y.K., King, I.P. and Zienkiewicz, O.C., "Slab Bridges with Arbitrary Shape and Support Conditions - A General Method of Analysis Based on Finite Elements", Proc. ICE, Vol. 40, 1968, pp.9-36.

31. Wegmuller, A.W., "A Refined Plate Bending Finite Element", Int. J. Solids Struct., Vol. 10, No.11, 1974, pp.1173-1178.

32. Bell, K., "A Refined Triangular Plate Bending Element", Int. J. Num., Meth. Eng. Vol. 1 No. 1 , 1969, pp.101-122.

33. Holland, I. and Bell, K., 'Finite Element Methods in Stress Analysis', Tapir, Trondheim, 1969, pp.213-252.

34. Fraeijs de Veubeke, B., "A Conforming Finite Element For Plate Bending", In. J. Solids Struct., Vol.4, No. 1, 1968, pp.95-108.

35. Turner, M.J., Clough, R.W., Martin, H.C. and Topp, L.J., "Stiffness and Deflection Analysis of Complex Structures", J. Aero. Sci. Vol. 23, 1956, pp.805-823.

36. Cheung, Y.K., "Finite Element Method in the Study of Plane Stress, Plates and Shells," Ph.D. Thesis, University of Wales, Swansea, 1964.

37. Marshall, J., "Aspects of Torsion of Structural Rectangular Hollow Sections", Ph.D. Thesis, University of Strathclyde, Glasgow, 1972.

38. Parekh, C.J., "Finite Element Solution System", Ph.D. Thesis, University of Wales, Swansea, 1969.

39. Jaeger, L.G., 'Elementary Theory of Elastic Plates', Pergamon, 1964.

40. El-Hag, A.A., "Coupling of Shear Walls by Floor Slabs in Tall Buildings", M.Sc. Thesis, University of Strathclyde, Glasgow, 1973.

41. Brebbia, C.A. and Connor, J.J., 'Fundamentals of Finite Element Techniques', Butterworth, 1973, pp.194-195.

42. Clough, R.W. and Felippa, C.A., "A Refined Quadrilateral Element for Analysis of Plate Bending", Proc. 2nd Conf. Matrix Methods in Struct. Mech., Wright-Patterson A.F. Base, Ohio, 1968.

43. Clough, R.W. and Tocher, J.L., "Finite Element Stiffness Matrices for Analysis of Plate Bending", Proc. 1st Conf. Matrix Methods in Struct. Mech., Wright-Patterson A.F. Base, Ohio, 1965.

44. Bogner, F.K., Fox, R.L. and Schmidt, L.A., "The Generation of Interelement Compatible Stiffness and Mass Matrices by the Use of Interpolation Formulas", Proc. 1st Conf. Matrix Methods in Struct. Mech., Wright-Patterson A.F. Base, Ohio, 1965.

45. Zienkiewicz, O.C. and Cheung, Y.K., "The Finite Element for Analysis of Elastic Isotropic and Orthotropic Slabs", Proc. ICE, Vol. 28, 1964, pp.471-488.

46. Salvadori, M.G. and Baron, M.L., 'Numerical Methods in Engineering', Prentice-Hall, 1961.

47. Walz, J.E., Fulton, R.E. and Cyrus, N.J., "Accuracy and Convergence of Finite Element Approximation", Proc. 2nd Conf. Matrix Methods in Struct. Mech., Wright-Patterson A.F. Base, Ohio, 1968.

48. Michael, D., Discussion of "Bending Stiffness of Slabs Connecting Shear Walls" by Aslan Qadeer and Bryan Stafford-Smith, ACI Jnl., Proc. Vol. 66, No. 12, Dec., 1969, pp.1021.

49. Keer, L.M. and Sve, C., "On the Bending of Cracked Plates", Int. J. Solids Struct., Vol. 6, No.12, 1970, pp.1545-1559.

50. Kiattikomol, K., Keer, L.M. and Dundurs, J., "Application of Dual Series to Rectangular Plates", Proc. ASCE, Vol. 100, No. EM2, Apr. 1974, pp.433-444.

51. Stahl, B. and Keer, L.M., "Vibration and Buckling of a Rectangular Plate with an Internal Support", Int. J. Solids Struct. Vol. 8, 1972, pp.69-91.

52. Salvadori, M.G. and Reginni, H.C., "Simply Supported Corner Plate", Proc. ASCE, Vol. 68, No. ST11, Nov. 1960.

53. Coull, A. and Irwin, A.W., "Design of Connecting Beams in Coupled Shear Wall Structures", ACI Jnl., Proc. Vol. 66, Mar. 1969, pp.205-209.

54. Schwaighofer, J. and Collins, M.P., "Experimental Study of the Behaviour of Reinforced Concrete Coupling Slabs", ACI Jnl., Proc. Vol. 74, No. 3, Mar. 1977, pp.123-127.

55. British Standards Institute CP110 : Part 1, "The Structural Use of Concrete", 1972.

56. ACI Committee 318, "Building Code Requirements for Reinforced Concrete (ACI 318-71), American Concrete Institute, Detroit, 1971.

57. Pama, R.P., Imsom-Somboon, S. and Lee, S.L., "Elastic Rigidities of Circularly Voided Slabs", Building Science, Vol. 10, 1975, pp.207-212.

58. Cusens, A.R. and Pama, R.P., "Bridge Deck Analysis", Wiley, London, 1975.

59. Coull, A. and Choudhury, J.R., "Stresses and Deflections in Coupled Shear Walls", ACI Jnl., Proc. Vol. 64, No. 2, Feb. 1967, pp.65-72.

60. Coull, A. and Choudhury, J.R., "Analysis of Coupled Shear Walls", ACI Jnl., Proc. Vol. 64, No. 9, Sept. 1967, pp.587-593.

61. Marshall, M.G., "The Analysis of Shear Wall Structures", M.Sc. Thesis, University of Waterloo, Ontario, Sept. 1968.

62. Pearce, D.J. and Matthews, D.D., "An Appraisal of the Design of Shear Walls in Box Frame Structures", Report, Dept. of the Environment, Property Services Agency, Croydon.

63. Rockey, K.C. and Evans, H.R., "A Finite Element Solution for Folded Plate Structures", 'Space Structures' R.M. Davies ed., Blackwell Scientific Publication, Oxford and Edinburgh, 1967.

64. Timoshenko, S.P. and Goodier, J.N., 'Theory of Elasticity', McGraw-Hill, 1951.

65. Michael, D., "The Effect of Local Wall Deformation on the Elastic Interaction of Cross Walls Coupled by Beams", 'Tall Buildings', A. Coull and B. Stafford Smith ed., Pergamon Press, 1967, pp.253-272.

66. Bhatt, P. "Effect of Beam-Shearwall Junction Deformations on the Flexibility of the Connecting Beam", Building Science, Vol. 8, 1973, pp.149-151.

67. Heidebrecht, A.C. and Swift, R.D., "Analysis of Asymmetrical Coupled Shear Walls", Proc. ASCE, Vol. 97, No. ST5, May 1971, pp.251-257.

68. Liauw, T.C. and Leung, K.W., "Torsion Analysis of Core Wall Structures by Transfer Matrix Method", Struct. Engineer, Vol. 53, No. 4, Apr. 1975, pp.187-194.

69. Liauw, T.C., "Torsion of Multi-Storey Spatial Core Walls", Proc. ICE, Part 2, Vol. 65, Sept. 1978, pp.601-609.

70. Mallick, D.V. and Dungar, R., "Dynamic Characteristics of Core Wall Structures Subjected to Torsion and Bending", Struct. Engineer, Vol. 55, No. 6, June 1977, pp.251-261.

71. Michael, D., "Torsional Coupling of Core Walls in Tall Buildings", Struct. Engineer, Vol. 47, No. 2, Feb. 1969, pp.67-71.

72. Rosman, R., "Torsion of Perforated Concrete Shafts", Proc. ASCE, Vol. 95, No. ST5, May 1969, pp.991-1010.

73. Tso, W.K. and Biswas, J.K., "Analysis of Core Wall Structure Subject to Applied Torque", Building Science, Vol. 8, 1973, pp.251-257.

74. Tso, W.K. and Biswas, J.K., "Torsional Analysis of Core Wall Structures", Proc. 5th World Conf. on Earthquake Engineering, 1972.

75. Heidebrecht, A.C. and Stafford Smith, B., "Approximate Analysis of Open-Section Shear Walls Subject

to Torsional Loading," Proc. ASCE, Vol. 99, No.ST12, Dec. 1973, pp.2355-2373.

76. Coull, A. and Irwin, A.W., "Torsional Analysis of Multi-Storey Shear Wall Structures", 'Analysis of Structural Systems for Torsion', ACI SP36, pp.211-237.

77. Coull, A., "Torsion of Structural Cores on Deformable Foundations," Building Science, Vol. 10, 1975, pp.57-64.

78. Rutenberg, A.V. and Tso, W.K., "Torsional Analysis of Perforated Core Structure", Proc. ASCE, Vol. 101, No. ST3, Mar. 1975, pp.539-550.

79. Khan, M.A.H. and Stafford Smith, B., "Restraining Action of Bracing in Thin-Walled Open Section Beams", Proc. ICE, Part 2, Vol. 59, Mar. 1975, pp.67-78.

80. Chan, P.C.K., Heidebrecht, A.C. and Tso, W.K., "Approximate Analysis of Multistory Multibay Frames", Proc. ASCE, Vol. 101, No. ST5, May 1975, pp.1021-1035.

81. Wong, Y.C. and Coull, A., "Interaction Between Floor Slabs and Shear Walls", To be published in forth-coming symposium volume on Response of Buildings to Lateral Forces by ACI Committee 442.

82. Khan, F.R., "Current Trends in Concrete High-rise Buildings", 'Tall Buildings', A. Coull and B.Stafford Smith, ed., Pergamon Press, 1967, pp.571-590.

83. Coull, A. and Subedi, N.K., "Frame-Tube Structures for High-Rise Buildings", Proc. ASCE, Vol. 97, No. ST8, Aug. 1971, pp.2097-2105.

84. Coull, A. and Subedi, N.K., "Hull-Core Structures Subjected to Lateral Forces", Proc., 3rd Int. Conf. on Wind Effects on Buildings and Structures, SAIKON, Co. Ltd., Tokyo, 1971, pp.569-577.

85. Coull, A. and Subedi, N.K., "Hull-Core Structures Subjected to Bending and Torsion", Proc., 9th Congress, IABSE, Amsterdam, May, 1972, pp.613-632.

86. Khan, F.R., and Amin, N.R., "Analysis and Design of Framed Tube Structures for Tall Concrete Buildings", Struct. Engineer, Vol. 51, 1973, pp.85-92.

87. Coull, A. and Irwin, A.W., "Analysis of Load Distribution in Multi-storey Shear Wall Structures", Struct. Engineer, Vol. 48, Aug. 1970, pp.301-306.

88. Arvidsson, K., "Shear Walls With Door Openings Near the Edge of the Wall", ACI Jnl., Proc. Vol. 71, No.7, July 1974, pp.353-357.

89. Cardan, B., "Concrete Shear Walls Combined With Rigid Frames in Multi-storey Buildings Subjected to Lateral Loads", ACI Jnl., Vol. 58, No. 9, Sept. 1961, pp. 299-315.

90. Przemieniecki, J.S., 'Theory of Matrix Structural Analysis', McGraw-Hill, 1968.

91. Davies, J.D., Somervaille, I.J. and Zienkiewicz, O.C., "Analysis of Various Types of Bridges by the Finite Element Method", 'Recent Developments in Bridge Design and Construction', Crosby Lockwood, 1971, pp.217-236.

92. Ansourian, P., "An Application of the Method of Finite Elements to the Analysis of Composite Floor Systems", Proc. ICE, Part 2, Vol. 59, Dec. 1975, pp.699-726.

APPENDIX A2.1

THE GENERALISED ELEMENT STIFFNESS MATRIX $[K_\alpha]$ FOR ELEMENT RB24

The non-zero elements of the generalised element stiffness matrix on and above the main diagonal are listed below for the case of an isotropic material and constant element thickness. For convenience the elements of the matrix are denoted only by their row and column indices, thus

$$(k_\alpha)_{ij} = (i,j)$$

The following symbols are used in the expressions:

ν = Poisson's ratio

$u = (1-\nu)/2$

a and b= element dimensions (Fig. 2.6)

All expressions are to be multiplied by the factor (4abD), where D is the flexural rigidity.

$$(4,4) = \frac{4}{a^4} \qquad (4,6) = \frac{4\nu}{a^2b^2}$$

$$(4,11) = \frac{8}{a^4} \qquad (4,13) = \frac{4}{3a^4} + \frac{4\nu}{3a^2b^2}$$

$$(4,15) = \frac{8\nu}{a^2b^2}$$

$$(5,5) = (5,12) = (5,14) = (5,22) = (5,23) = (5,24) = \frac{4u}{a^2b^2}$$

$$(6,6) = \frac{4}{b^4} \qquad (6,11) = \frac{8\nu}{a^2b^2}$$

$$(6,13) = \frac{4}{3b^4} + \frac{4\nu}{3a^2b^2} \qquad (6,15) = \frac{8}{b^4}$$

$$(7,7) = \frac{12}{a^4} \qquad (7,9) = \frac{4\nu}{a^2b^2}$$

$$(7,16) = \frac{24}{a^4} \qquad (7,18) = \frac{4}{a^4} + \frac{12\nu}{5a^2b^2}$$

$$(7,20) = \frac{8\nu}{a^2b^2}$$

$$(8,8) = \frac{4}{3a^4} + \frac{16u}{3a^2b^2}$$

$$(8,10) = \frac{4\nu}{a^2b^2}$$

$$(8,17) = \frac{8}{3a^4} + \frac{32u}{5a^2b^2}$$

$$(8,19) = \frac{4}{5a^4} + \frac{4\nu}{3a^2b^2} + \frac{16u}{3a^2b^2}$$

$$(8,21) = \frac{8\nu}{a^2b^2}$$

$$(9,9) = \frac{4}{3b^4} + \frac{16u}{3a^2b^2}$$

$$(9,16) = \frac{8\nu}{a^2b^2}$$

$$(9,18) = \frac{4\nu}{3a^2b^2} + \frac{4}{5b^4} + \frac{16u}{3a^2b^2}$$

$$(9,20) = \frac{8}{3b^4} + \frac{32u}{5a^2b^2}$$

$$(10,10) = \frac{12}{b^4}$$

$$(10,17) = \frac{8\nu}{a^2b^2}$$

$$(10,19) = \frac{12\nu}{5a^2b^2} + \frac{4}{b^4}$$

$$(10,21) = \frac{24}{b^4}$$

$$(11,11) = \frac{144}{5a^4}$$

$$(11,13) = \frac{8}{3a^4} + \frac{24\nu}{5a^2b^2}$$

$$(11,15) = \frac{16\nu}{a^2b^2}$$

$$(12,12) = \frac{4}{a^4} + \frac{36u}{5a^2b^2}$$

$$(12,14) = \frac{4\nu}{a^2b^2} + \frac{4u}{a^2b^2}$$

$$(12,22) = \frac{8}{a^4} + \frac{60u}{7a^2b^2}$$

$$(12,23) = \frac{12}{5a^4} + \frac{12\nu}{5a^2b^2} + \frac{36u}{5a^2b^2}$$

$$(12,24) = \frac{8\nu}{a^2b^2} + \frac{4u}{a^2b^2}$$

$$(13,13) = \frac{4}{5a^4} + \frac{8\nu}{9a^2b^2} + \frac{4}{5b^4} + \frac{64u}{9a^2b^2}$$

$$(13,15) = \frac{24\nu}{5a^2b^2} + \frac{8}{3b^4}$$

$$(14,14) = \frac{4}{b^4} + \frac{36u}{5a^2b^2}$$

$$(14,22) = \frac{8\nu}{a^2b^2} + \frac{4u}{a^2b^2}$$

$$(14,23) = \frac{12\nu}{5a^2b^2} + \frac{12}{5b^4} + \frac{36u}{5a^2b^2}$$

$$(14,24) = \frac{8}{b^4} + \frac{60u}{7a^2b^2}$$

$$(15,15) = \frac{144}{5b^4}$$

$$(16,16) = \frac{400}{7a^4}$$

$$(16,18) = \frac{8}{a^4} + \frac{40\nu}{7a^2b^2}$$

$$(16,20) = \frac{16\nu}{a^2b^2}$$

$$(17,17) = \frac{48}{5a^4} + \frac{64u}{7a^2b^2}$$

$$(17,19) = \frac{8}{5a^4} + \frac{24\nu}{5a^2b^2} + \frac{32u}{5a^2b^2}$$

$$(17,21) = \frac{16\nu}{a^2b^2}$$

$$(18,18) = \frac{12}{5a^4} + \frac{8\nu}{5a^2b^2} + \frac{4}{7b^4} + \frac{48u}{5a^2b^2}$$

$$(18,20) = \frac{24\nu}{5a^2b^2} + \frac{8}{5b^4} + \frac{32u}{5a^2b^2}$$

$$(19,19) = \frac{4}{7a^4} + \frac{8\nu}{5a^2b^2} + \frac{12}{5b^4} + \frac{48u}{5a^2b^2}$$

$$(19,21) = \frac{40\nu}{7a^2b^2} + \frac{8}{b^4}$$

$$(20,20) = \frac{48}{5b^4} + \frac{64u}{7a^2b^2}$$

$$(21,21) = \frac{400}{7b^4}$$

$$(22,22) = \frac{400}{21a^4} + \frac{100u}{9a^2b^2}$$

$$(22,23) = \frac{24}{5a^4} + \frac{40\nu}{7a^2b^2} + \frac{60u}{7a^2b^2}$$

$$(22,24) = \frac{16\nu}{a^2b^2} + \frac{4u}{a^2b^2}$$

$$(23,23) = \frac{12}{7a^4} + \frac{72\nu}{25a^2b^2} + \frac{12}{7b^4} + \frac{324u}{25a^2b^2}$$

$$(23,24) = \frac{40\nu}{7a^2b^2} + \frac{24}{5b^4} + \frac{60u}{7a^2b^2}$$

$$(24,24) = \frac{400}{21b^4} + \frac{100u}{9a^2b^2}$$

APPENDIX A2.2

'STRESS' MATRIX FOR VEUBEKE'S QUADRILATERAL BENDING ELEMENT QB16

This appendix shows the author's derivation of the 'stress' matrix not included in Veubeke's paper.[34] The original paper should be consulted for the nomenclature followed in this Appendix. The general quadrilateral element with the local oblique co-ordinate axes x and y, and the global cartesian co-ordinate axes X and Y is shown in Fig. 2.8(a) and (b).

The bending stress resultants are related to the curvatures, in cartesian co-ordinate directions, by

$$\begin{Bmatrix} M_x \\ M_y \\ M_{xy} \end{Bmatrix} = [D] \begin{Bmatrix} \partial^2 w/\partial X^2 \\ \partial^2 w/\partial Y^2 \\ \partial^2 w/\partial X \partial Y \end{Bmatrix} \quad \text{where}$$

$$[D] = \frac{Et^3}{12(1-\nu^2)} \begin{bmatrix} -1 & -\nu & 0 \\ -\nu & -1 & 0 \\ 0 & 0 & 1-\nu \end{bmatrix} \quad \text{for an isotropic material.}$$

For brevity, we may write

$$\{\sigma\} = [D]\{\varepsilon\}$$

The cartesian derivatives are related to the oblique derivatives by the rules of partial differentiation giving

$$\begin{Bmatrix} \frac{\partial^2 w}{\partial x^2} \\ \frac{\partial^2 w}{\partial y^2} \\ \frac{\partial^2 w}{\partial x \partial y} \end{Bmatrix} = \begin{bmatrix} (\frac{\partial X}{\partial x})^2 & (\frac{\partial Y}{\partial x})^2 & 2\frac{\partial X}{\partial x}.\frac{\partial Y}{\partial x} \\ (\frac{\partial X}{\partial y})^2 & (\frac{\partial Y}{\partial y})^2 & 2\frac{\partial X}{\partial y}.\frac{\partial Y}{\partial y} \\ \frac{\partial X}{\partial x}.\frac{\partial X}{\partial y} & \frac{\partial Y}{\partial x}.\frac{\partial Y}{\partial y} & (\frac{\partial X}{\partial x}.\frac{\partial Y}{\partial y} + \frac{\partial X}{\partial y}.\frac{\partial Y}{\partial x}) \end{bmatrix} \begin{Bmatrix} \frac{\partial^2 w}{\partial X^2} \\ \frac{\partial^2 w}{\partial Y^2} \\ \frac{\partial^2 w}{\partial X \partial Y} \end{Bmatrix}$$

or, more concisely,

$\{\epsilon_o\} = [G] \{\epsilon\}$, giving

$$\{\epsilon\} = [G]^{-1} \{\epsilon_o\}$$

The terms in G can be easily evaluated from the nodal co-ordinates of the quadrilateral. For instance, we can write

$$\frac{\partial X}{\partial x} = \frac{x_{10}}{a} \quad , \quad \frac{\partial X}{\partial y} = \frac{x_{20}}{b}$$

$$\frac{\partial Y}{\partial x} = \frac{y_{10}}{a} \quad , \quad \frac{\partial Y}{\partial y} = \frac{y_{20}}{b}$$

where $x_{ij} = x_i - x_j$ and $y_{ij} = y_i - y_j$.

Consider triangular field 1, where the deflection field is expressed in the form of interpolation functions

$$w = [\, W_{0,1} \; \emptyset_{0,1} \; \psi_{0,1} \; W_{1,1} \; \emptyset_{1,1} \; \psi_{1,1} \; W_{1,2} \; \emptyset_{1,2} \; \psi_{1,2} \; \emptyset_{12} \,] \{q_1\}$$

Performing the differentiation with respect to x and y, the second derivatives $\{\epsilon_{01}\}$ may be expressed in terms of the nodal displacements $\{q_1\}$, as

$$\{\epsilon_{01}\} = [Q_1] \{q_1\}$$

The nodal displacement vector $\{q_1\}$ for field 1 is related to the element displacement vector $\{q\}$ by the transformation.

$$\{q_1\} = [L_1] [N] [P] \{q\}$$

in which $[L_1]$ is the localising matrix,
$[N]$ is the condensation matrix,
and $[P]$ is the co-ordinate transformation matrix, defined in Reference 34.

The 'stresses' in field 1 can now be expressed as

$$\{\sigma_1\} = ([D] [G]^{-1} [Q_1] [L_1] [N] [P]) \{q\}$$

and the stress matrix for field 1 becomes

$$[S_1] = [D] [G]^{-1} [Q_1] [L_1] [N] [P]$$

The 'stress' matrices for triangular regions 2, 3 and 4 can be similarly evaluated by an appropriate change of parameters in $[Q_1]$ and $[L_1]$.

APPENDIX A2.3

INTEGRATION CONSTANTS FOR EVALUATION OF INFLUENCE FUNCTIONS

Expressions for the influence functions for the slab were given in Section 2.5.3 for one specific set of boundary conditions. The corresponding values of the integration constants $A_m - S_m$ of equations (2.53) and (2.54), for other commonly encountered boundary conditions, are as follows:-

(i) Rectangular slab. Sides x = o, x = a, simply supported, side y = o continuous, side y = b free.

$$A_m = \frac{1}{\Delta}\left\{ \beta\left[(4-\mu)\,sh\alpha\, ch(\alpha-\beta) - 2sh\beta\right] + \mu\alpha^2\left[(\alpha-\beta)\,ch\beta + sh\beta\right] + (4-\mu)\,sh\alpha\, sh(\alpha-\beta) + \frac{4}{\mu}\,ch\beta\right\}$$

$$B_m = -\frac{1}{\Delta}\left\{(4-\mu)\,sh\alpha\, sh(\alpha-\beta) + \mu(\alpha-\beta)sh\beta + 2ch\beta\right\}$$

$$C_m = D_m = 0$$

$$P_m = \frac{1}{\Delta}\left\{(4-\mu)\,sh^2\alpha\,\left[ch\beta - \beta sh\beta\right] - 2\,\beta\, sh\beta + \left(\mu\alpha^2 + \frac{4}{\mu}\right)ch\beta\right\}$$

$$Q_m = -\frac{1}{\Delta}\left\{(4-\mu)\,sh^2\alpha\; ch\beta - \mu\beta\, sh\beta + 2ch\beta\right\}$$

$$R_m = \beta sh\beta - ch\beta$$

$$S_m = ch\beta$$

where $\mu = (1-\nu)$ and $\Delta = (4-\mu)sh\alpha\; ch\alpha - \mu\alpha$

(ii) Rectangular slab. Sides x = o, x = a, simply supported, side y = o continuous, side y = b simply supported.

$$A_m = \frac{1}{ch\alpha}\left[-\frac{\alpha ch\beta}{ch\alpha} + \beta ch(\alpha-\beta) + sh(\alpha-\beta)\right]$$

$$B_m = -\frac{sh(\alpha-\beta)}{ch\alpha}$$

$$C_m = D_m = 0$$

$$P_m = \frac{1}{ch\alpha}\left[\frac{-\alpha ch\beta}{ch\alpha} - \beta sh\alpha\, sh\beta + sh\alpha\, ch\beta\right]$$

$$Q_m = -\frac{sh\alpha\ ch\beta}{ch\alpha}$$

$$R_m = \beta sh\beta - ch\beta$$

$$S_m = ch\beta$$

(iii) Rectangular Plate. Sides x = o, x = a simply supported, side y = o continuous, side y = b clamped.

$$A_m = \frac{1}{\Delta_1}\left[sh\alpha\, sh(\alpha-\beta) + \beta sh\alpha\, ch(\alpha-\beta) - \alpha sh\beta - \alpha(\alpha-\beta)ch\beta\right]$$

$$B_m = \frac{1}{\Delta_1}\left[(\alpha-\beta)sh\beta - sh\alpha\ sh(\alpha-\beta)\right]$$

$$C_m = D_m = 0$$

$$P_m = -\frac{1}{\Delta_1}\left[(\alpha^2 - sh^2\alpha)ch\beta + \beta sh^2\alpha\, sh\beta\right]$$

$$Q_m = -\frac{1}{\Delta 1}\left[sh^2\alpha\ ch\beta + \beta sh\beta\right]$$

$$R_m = \beta sh\beta - ch\beta$$

$$S_m = ch\beta$$

where $\Delta_1 = ch\alpha\ sh\alpha + \alpha$

(iv) Rectangular Plate. Sides x = o, x = a, y = o, y = b simply supported

$$A_m = B_m = 0$$

$$C_m = \frac{1}{sh\alpha}\left[-\frac{\alpha sh\beta}{sh\alpha} + \beta ch(\alpha-\beta) + sh(\alpha-\beta)\right]$$

$$D_m = - \frac{sh(\alpha - \beta)}{sh\,\alpha}$$

$$P_m = sh\,\beta - \beta\,ch\,\beta$$

$$Q_m = - sh\,\beta$$

$$R_m = \frac{1}{sh\,\alpha}\left[- \frac{\alpha\,sh\,\beta}{sh\,\alpha} + \beta\,ch\,\alpha\;\;ch\,\beta - ch\,\alpha\;\;ch\,\beta \right]$$

$$S_m = \frac{ch\,\alpha\;\;sh\,\beta}{sh\,\alpha}$$

APPENDIX A3.1 RICHARDSON'S EXTRAPOLATION: (h, h^2) - EXTRAPOLATION FORMULA

The discretisation error series is assumed in the form

$$e = c_1 h + c_2 h^2 + c_3 h^3 + \ldots\ldots$$

in which c_1, c_2, c_3, etc. are constants, and h is the mesh size which can be expressed in terms of the number of mesh divisions n on one side of the plate thus

$$h = b/n$$

With three approximations A_1, A_2, A_3 obtained for mesh divisions n_1, n_2, n_3 the respective approximation errors are, neglecting error terms higher than h^2, given by

$$e_1 = A - A_1 = c_1 b/n_1 + c_2 b^2/n_1^2$$

$$e_2 = A - A_2 = c_1 b/n_2 + c_2 b^2/n_2^2$$

$$e_3 = A - A_3 = c_1 b/n_3 + c_2 b^2/n_3^2$$

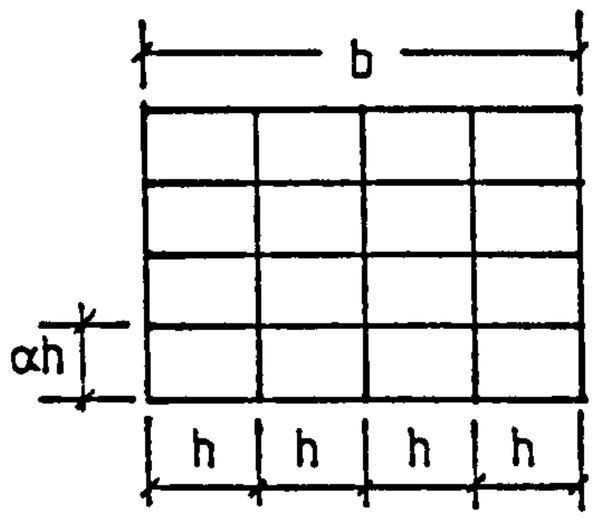

Eliminating the unknown constants $c_1 b$ and $c_2 b^2$ between these three equations and solving for the true value A, we obtain the (h, h^2)-extrapolation formula in the form

$$A = \frac{n_1^2 A_1}{(n_1-n_2)(n_1-n_3)} - \frac{n_2^2 A_2}{(n_1-n_2)(n_2-n_3)} + \frac{n_3^2 A_3}{(n_1-n_3)(n_2-n_3)},$$

which may be written in more compact form as

$$A = \sum_{i=1,2,3} \left(\frac{n_i^2}{n_{ij}\, n_{ik}}\right) A_i$$

with $n_{ij} = (n_i - n_j)$, etc, with a cyclic permutation of indices.

APPENDIX A3.2 EFFECTIVE WIDTH OF SLAB FOR COUPLED PLANE WALL CONFIGURATION

	Effective Width Y_e/Y						
Y/X \ L/X	0.10	0.15	0.20	0.30	0.40	0.50	0.60
0.10	0.6160	0.7123	0.7879	0.8514	0.8933	0.9137	0.9351
0.20	0.3903	0.5195	0.6082	0.7187	0.7836	0.8236	0.8550
0.30	0.2800	0.3929	0.4822	0.6098	0.6915	0.7460	0.7860
0.40	0.2175	0.3116	0.3923	0.5199	0.6101	0.6740	0.7198
0.50	0.1781	0.2573	0.3282	0.4480	0.5394	0.6077	0.6559
0.60	0.1511	0.2189	0.2812	0.3908	0.4790	0.5473	0.5953
0.70	0.1315	0.1905	0.2455	0.3448	0.4276	0.4933	0.5392
0.80	0.1168	0.1687	0.2178	0.3079	0.3846	0.4465	0.4898
1.00	0.0936	0.1356	0.1757	0.2504	0.3154	0.3688	0.4061

APPENDIX A3.3 EFFECTIVE WIDTH OF SLAB FOR COUPLED THICK WALL OR COUPLED BOX CORE CONFIGURATION

		Effective Width Y_e/Y					
Y/X	Z/Y / L/X	0.000	0.125	0.250	0.375	0.500	0.75
0.2	0.1	0.3903	0.5062	0.6178	0.7240	0.8210	0.9688
	0.2	0.6082	0.7025	0.7817	0.8514	0.9106	0.9952
	0.4	0.7836	0.8465	0.8943	0.9334	0.9651	1.0081
	0.6	0.8550	0.9014	0.9354	0.9625	0.9841	1.0131
0.4	0.1	0.2175	0.3405	0.4656	0.5891	0.7099	0.9271
	0.2	0.3923	0.5067	0.6182	0.7243	0.8212	0.9703
	0.4	0.6101	0.7031	0.7825	0.8523	0.9109	0.9955
	0.6	0.7198	0.7879	0.8440	0.8947	0.9386	1.0047
0.6	0.1	0.1511	0.2759	0.4030	0.5295	0.6549	0.8950
	0.2	0.2812	0.4011	0.5227	0.6415	0.7548	0.9482
	0.4	0.4790	0.5868	0.6871	0.7793	0.8596	0.9834
	0.6	0.5953	0.6864	0.7686	0.8424	0.9047	0.9966
0.8	0.1	0.1168	0.2427	0.3703	0.4976	0.6244	0.8726
	0.2	0.2178	0.3402	0.4653	0.5885	0.7084	0.9281
	0.4	0.3846	0.5000	0.6129	0.7188	0.8136	0.9713
	0.6	0.4898	0.5963	0.6986	0.7921	0.8721	0.9884

APPENDIX A3.4 EFFECTIVE WIDTH OF SLAB FOR COUPLED T-SHAPED FLANGED WALL CONFIGURATION

		Effective Width Y_e/Y					
Y/X	Z/Y / L/X	0.000	0.125	0.250	0.375	0.500	0.750
0.2	0.1	0.3903	0.5025	0.6080	0.7092	0.8047	0.9627
	0.2	0.6082	0.6966	0.7711	0.8391	0.9003	0.9934
	0.4	0.7836	0.8396	0.8836	0.9224	0.9566	1.0067
	0.6	0.8550	0.8956	0.9268	0.9542	0.9779	1.0121
0.4	0.1	0.2175	0.3388	0.4603	0.5804	0.6985	0.9176
	0.2	0.3923	0.5029	0.6080	0.7088	0.8039	0.9636
	0.4	0.6101	0.6950	0.7666	0.8325	0.8918	0.9906
	0.6	0.7198	0.7879	0.8440	0.8947	0.9384	1.0015
0.6	0.1	0.1511	0.2748	0.3998	0.5242	0.6478	0.8871
	0.2	0.2812	0.3986	0.5154	0.6298	0.7403	0.9393
	0.4	0.4790	0.5802	0.6732	0.7605	0.8388	0.9766
	0.6	0.5953	0.6864	0.7686	0.8424	0.9047	0.9924
0.8	0.1	0.1168	0.2418	0.3679	0.4938	0.6194	0.8665
	0.2	0.2178	0.3383	0.4601	0.5806	0.6981	0.9196
	0.4	0.3846	0.4948	0.6020	0.7036	0.7945	0.9641
	0.6	0.4898	0.5963	0.6986	0.7921	0.8721	0.9841

APPENDIX A3.5 EFFECTIVE WIDTH OF SLAB FOR COUPLED PLANAR - FLANGED WALL CONFIGURATION

		Effective Width Y_e/Y				
Y/X	Z/Y / L/X	0.000	0.125	0.250	0.500	0.750
0.2	0.1	0.3903	0.4398	0.4787	0.5324	0.5614
	0.2	0.6082	0.6476	0.6796	0.7306	0.7642
	0.4	0.7836	0.8104	0.8312	0.8641	0.8858
	0.6	0.8550	0.8746	0.8897	0.9137	0.9292
0.4	0.1	0.2175	0.2659	0.2955	0.3205	0.3283
	0.2	0.3923	0.4378	0.4761	0.5300	0.5590
	0.4	0.6101	0.6492	0.6808	0.7319	0.7655
	0.6	0.7198	0.7507	0.7754	0.8164	0.8435
0.6	0.1	0.1511	0.1951	0.2137	0.2238	0.2261
	0.2	0.2812	0.3278	0.3631	0.4017	0.4171
	0.4	0.4790	0.5239	0.5609	0.6185	0.6539
	0.6	0.5953	0.6335	0.6653	0.7200	0.7557
0.8	0.1	0.1168	0.1558	0.1668	0.1712	0.1721
	0.2	0.2178	0.2637	0.2932	0.3182	0.3259
	0.4	0.3846	0.4317	0.4698	0.5250	0.5551
	0.6	0.4898	0.5318	0.5680	0.6310	0.6703

APPENDIX A3.6 EFFECTIVE WIDTH OF SLAB FOR COUPLED L-SHAPED FLANGED WALL CONFIGURATION

		Effective Width Y_e/Y			
Y/X	Z/Y / L/X	0.000	0.125	0.250	0.375
0.2	0.1	0.3903	0.4771	0.5242	0.5491
	0.2	0.6082	0.6873	0.7412	0.7756
	0.4	0.7836	0.8370	0.8761	0.9023
	0.6	0.8550	0.8940	0.9230	0.9423
0.4	0.1	0.2175	0.2877	0.3086	0.3153
	0.2	0.3923	0.4770	0.5239	0.5485
	0.4	0.6101	0.6860	0.7391	0.7732
	0.6	0.7198	0.7815	0.8282	0.8593
0.6	0.1	0.1511	0.2060	0.2148	0.2169
	0.2	0.2812	0.3586	0.3907	0.4038
	0.4	0.4790	0.5616	0.6149	0.6463
	0.6	0.5953	0.6698	0.7272	0.7637

APPENDIX A3.7 EFFECTIVE WIDTH OF SLAB FOR COUPLED BOX CORES WITH OPENINGS

L/X = 0.6, W/Z = 1.0

		Effective Width Y_e/Y				
Y/X	B/Z / D'/Z	0.25	0.50	0.75	1.0	Closed Core
0.4	0.0	0.9388	0.8958	0.8216	0.7074	0.9494
	0.1	0.9436	0.9132	0.8547	0.7607	
	0.3	0.9471	0.9320	0.8974	0.8368	
	0.5	0.9481	0.9380	0.9133	0.8701	
0.6	0.0	0.8221	0.7919	0.7386	0.6532	0.8297
	0.1	0.8254	0.8042	0.7626	0.6932	
	0.3	0.8278	0.8173	0.7929	0.7488	
	0.5	0.8285	0.8215	0.8041	0.7711	
0.8	0.0	0.6987	0.6759	0.6350	0.5676	0.7072
	0.1	0.7012	0.6852	0.6535	0.5993	
	0.3	0.7030	0.6951	0.6767	0.6427	
	0.5	0.7036	0.6983	0.6852	0.6596	

APPENDIX A3.8 STIFFNESS AND EFFECTIVE WIDTH OF CRACKED SLAB

Plane Wall Configuration, Y/X = 0.4

L/X		Crack Length λ/Y				
		0	0.125	0.25	0.5	0.75
0.1	K	154.78	83.57	48.75	22.80	12.92
	Y_e/Y	0.218	0.118	0.069	0.032	0.018
0.2	K	41.38	29.36	20.37	11.42	6.90
	Y_e/Y	0.392	0.278	0.193	0.108	0.065
0.4	K	11.03	9.00	7.04	4.56	2.94
	Y_e/Y	0.614	0.501	0.392	0.254	0.164

APPENDIX A4.1 - EFFECTIVE WIDTH OF SLAB FOR COUPLED PLANE-WALL CONFIGURATION EVALUATED BY SERIES SOLUTION

(a) Walls of Zero Thickness

	Effective Width Y_e/Y						
Y/X \ L/X	0.1	0.15	0.2	0.3	0.4	0.5	0.6
0.2	0.4049	0.5329	0.6255	0.7401	0.8053	0.8470	0.8776
0.3	0.2868	0.3983	0.4913	0.6251	0.7110	0.7690	0.8106
0.4	0.2201	0.3134	0.3972	0.5316	0.6270	0.6938	0.7394
0.5	0.1780	0.2564	0.3294	0.4542	0.5494	0.6182	0.6642
0.6	0.1512	0.2182	0.2812	0.3918	0.4806	0.5469	0.5914
0.7	0.1314	0.1896	0.2442	0.3428	0.4234	0.4848	0.5262
0.8	0.1165	0.1675	0.2158	0.3029	0.3760	0.4325	0.4708
1.0	0.0954	0.1366	0.1747	0.2455	0.3051	0.3520	0.3844

(b) Walls of 12 in. (305 mm) Thickness

	Effective Width Y_e/Y						
Y/X \ L/X	0.1	0.15	0.2	0.3	0.4	0.5	0.6
0.2	0.4895	0.6092	0.6927	0.7917	0.8493	0.8828	0.9076
0.3	0.3459	0.4546	0.5438	0.6702	0.7482	0.8020	0.8395
0.4	0.2650	0.3571	0.4391	0.5687	0.6603	0.7247	0.7680
0.5	0.2141	0.2918	0.3639	0.4868	0.5800	0.6471	0.6920
0.6	0.1819	0.2483	0.3106	0.4163	0.5158	0.5733	0.6175
0.7	0.1581	0.2157	0.2697	0.3677	0.4477	0.5087	0.5502
0.8	0.1402	0.1905	0.2382	0.3201	0.3951	0.4541	0.4926
1.0	0.1148	0.1551	0.1929	0.2589	0.3203	0.3696	0.4023

APPENDIX A4.2 - EFFECTIVE WIDTH OF SLAB FOR COUPLED THICK-WALL OR BOX-CORE CONFIGURATION EVALUATED BY SERIES SOLUTION

		EFFECTIVE WIDTH Y_e/Y					
Y/X	Z/Y / L/X	0.0	0.125	0.25	0.375	0.50	0.75
0.2	0.1	0.4049	0.5059	0.6194	0.7260	0.8240	0.9787
	0.2	0.6255	0.7035	0.7846	0.8556	0.9166	1.0034
	0.4	0.8053	0.8556	0.9026	0.9416	0.9735	1.0165
	0.6	0.8776	0.9141	0.9458	0.9718	0.9929	1.0204
0.4	0.1	0.2201	0.3498	0.4789	0.6060	0.7299	0.9439
	0.2	0.3972	0.5094	0.6108	0.7133	0.8070	0.9876
	0.4	0.6239	0.7114	0.7831	0.8501	0.9071	1.0088
	0.6	0.7350	0.8069	0.8613	0.9086	0.9465	1.0161
0.6	0.1	0.1512	0.2768	0.4049	0.5322	0.6584	0.8983
	0.2	0.2818	0.4028	0.5264	0.6467	0.7616	0.9540
	0.4	0.4809	0.5801	0.6820	0.7714	0.8505	0.9923
	0.6	0.5905	0.6857	0.7727	0.8495	0.9069	1.0123
0.8	0.1	0.1165	0.2400	0.3668	0.4934	0.6193	0.8644
	0.2	0.2159	0.3365	0.4627	0.5872	0.7080	0.9226
	0.4	0.3761	0.4928	0.6118	0.7247	0.8253	0.9722
	0.6	0.4710	0.5869	0.6984	0.8001	0.8855	0.9930

APPENDIX A4.3 - EFFECTIVE WIDTH OF SLAB FOR COUPLED T-SHAPED FLANGED WALL CONFIGURATION EVALUATED BY SERIES SOLUTION

		Effective Width Y_e/Y					
Y/X	L/X \ Z/Y	0.0	0.125	0.25	0.375	0.50	0.75
0.2	0.1	0.4049	0.5044	0.6167	0.7227	0.8210	0.9783
	0.2	0.6255	0.7010	0.7805	0.8512	0.9133	1.0031
	0.4	0.8053	0.8527	0.8978	0.9368	0.9702	1.0163
	0.6	0.8776	0.9119	0.9420	0.9680	0.9901	1.0202
0.4	0.1	0.2201	0.3491	0.4770	0.6060	0.7247	0.9426
	0.2	0.3972	0.5070	0.6025	0.6997	0.7907	0.9857
	0.4	0.6239	0.7085	0.7756	0.8398	0.8961	1.0074
	0.6	0.7350	0.8056	0.8583	0.9049	0.9425	1.0152
0.6	0.1	0.1512	0.2764	0.4038	0.5303	0.6553	0.8941
	0.2	0.2818	0.4021	0.5243	0.6429	0.7556	0.9486
	0.4	0.4809	0.5789	0.6774	0.7662	0.8427	0.9881
	0.6	0.5905	0.6849	0.7705	0.8473	0.9042	1.0037
0.8	0.1	0.1165	0.2396	0.3659	0.4920	0.6175	0.8610
	0.2	0.2159	0.3358	0.4610	0.5849	0.7050	0.9178
	0.4	0.3761	0.4920	0.6104	0.7229	0.8230	0.9690
	0.6	0.4710	0.5865	0.6979	0.7996	0.8849	0.9920

APPENDIX A4.4 - EFFECTIVE WIDTH OF SLAB FOR COUPLED PLANAR-FLANGED WALL CONFIGURATION EVALUATED BY SERIES SOLUTION

		Effective Width Y_e/Y				
Y/X	Z/Y / L/X	0.0	0.125	0.25	0.50	0.75
0.2	0.1	0.4165	0.4680	0.5095	0.5648	0.5921
	0.2	0.6395	0.6794	0.7131	0.7657	0.7974
	0.4	0.8151	0.8393	0.8599	0.8925	0.9119
	0.6	0.8965	0.9121	0.9266	0.9489	0.9614
0.4	0.1	0.2259	0.2739	0.3026	0.3259	0.3330
	0.2	0.4048	0.4532	0.4924	0.5450	0.5721
	0.4	0.6337	0.6727	0.7054	0.7547	0.7851
	0.6	0.7549	0.7869	0.8137	0.8510	0.8727
0.6	0.1	0.1527	0.1931	0.2096	0.2186	0.2208
	0.2	0.2840	0.3321	0.3664	0.4012	0.4142
	0.4	0.4852	0.5326	0.5723	0.6263	0.6546
	0.6	0.6043	0.6493	0.6878	0.7396	0.7653
0.8	0.1	0.1163	0.1561	0.1594	0.1638	0.1649
	0.2	0.2159	0.2613	0.2891	0.3113	0.3180
	0.4	0.3770	0.4265	0.4674	0.5181	0.5396
	0.6	0.4795	0.5300	0.5742	0.6340	0.6607

APPENDIX A4.5 - EFFECTIVE WIDTH OF SLAB FOR COUPLED L-SHAPED FLANGED WALL CONFIGURATION EVALUATED BY SERIES SOLUTION

		Effective Width Y_e/Y			
Y/X	L/X \ Z/Y	0.0	0.125	0.25	0.375
0.2	0.1	0.4165	0.5434	0.5890	0.6035
	0.2	0.6395	0.7474	0.7998	0.8231
	0.4	0.8151	0.8837	0.9193	0.9363
	0.6	0.8965	0.9289	0.9546	0.9664
0.4	0.1	0.2259	0.3164	0.3382	0.3393
	0.2	0.4048	0.5073	0.5583	0.5796
	0.4	0.6337	0.7168	0.7754	0.8071
	0.6	0.7549	0.8140	0.8619	0.8908
0.6	0.1	0.1527	0.2201	0.2235	0.2286
	0.2	0.2840	0.3741	0.4084	0.4146
	0.4	0.4852	0.5734	0.6392	0.6644
	0.6	0.6043	0.7010	0.7694	0.7997

APPENDIX A5.1 INFLUENCE OF WALL THICKNESS, SLAB THICKNESS AND WALL/SLAB THICKNESS RATIO ON SLAB COUPLING STIFFNESS.

Plane Wall Configuration (L/X = 0.2, Y/X = 0.4)

t/h	ξ	η	K*	Y_e^*/Y	K*/K	$\xi/\eta^{1/3}$
0.25	0.125	0.50	37.71	0.3572	0.920	0.16
	0.188	0.75	37.66	0.3567	0.919	0.21
	0.25	1.00	37.58	0.3559	0.917	0.25
	0.375	1.50	37.36	0.3539	0.912	0.33
	0.50	2.00	37.07	0.3511	0.905	0.40
0.50	0.25	0.50	37.40	0.3543	0.913	0.32
	0.375	0.75	36.98	0.3503	0.903	0.41
	0.50	1.00	36.41	0.3448	0.888	0.50
	0.75	1.50	35.09	0.3324	0.856	0.66
	1.00	2.00	33.56	0.3180	0.819	0.79
0.75	0.375	0.50	36.63	0.3470	0.894	0.47
	0.563	0.75	35.46	0.3359	0.865	0.62
	0.75	1.00	34.07	0.3227	0.831	0.75
	1.125	1.50	31.21	0.2957	0.762	0.98
	1.50	2.00	28.54	0.2703	0.696	1.19
1.00	0.50	0.50	35.34	0.3347	0.862	0.63
	0.75	0.75	33.19	0.3144	0.810	0.83
	1.00	1.00	30.99	0.2936	0.757	1.00
	1.50	1.50	27.03	0.2560	0.660	1.31
	2.00	2.00	23.75	0.2251	0.580	1.59
Rigid Wall Case			40.97	0.3881	1.0	

$\xi = 50t/X, \qquad \eta = 50h/X.$

APPENDIX A5.2(a) VARIATION OF SLAB STIFFNESS FACTOR K* WITH VARIOUS GEOMETRIC RATIOS

Plane Wall Configuration

Y/X	t/h / L/X	Stiffness Factor K* 0.5	1.0	1.5	2.0	Rigid Wall K
0.4	0.1	124.56	89.99	60.11	41.59	153.95
	0.2	36.40	31.00	24.47	19.34	40.97
	0.4	10.27	9.42	8.30	7.29	10.96
	0.6	4.78	4.51	4.16	3.84	5.00
0.6	0.1	127.63	91.55	62.70	44.28	160.91
	0.2	39.03	32.89	26.36	21.12	44.44
	0.4	12.01	11.01	9.71	8.68	12.91
	0.6	5.90	5.57	5.15	4.73	6.21
0.8	0.1	130.41	93.25	64.30	45.84	166.86
	0.2	40.70	34.45	27.88	22.59	46.66
	0.4	11.86	11.74	10.45	9.34	13.81
	0.6	6.45	6.07	5.61	5.16	6.81

APPENDIX A5.2(b) VARIATION OF EFFECTIVE SLAB WIDTH Y_e^*/Y WITH VARIOUS GEOMETRIC RATIOS

Plane Wall Configurations

Y/X	t/h / L/X	Effective Width Y_e^*/Y 0.5	1.0	1.5	2.0	Rigid Wall Y_e/Y
0.4	0.1	0.1755	0.1268	0.0847	0.0586	0.2169
	0.2	0.3448	0.2936	0.2318	0.1832	0.3881
	0.4	0.5715	0.5243	0.4622	0.4060	0.6101
	0.6	0.6879	0.6492	0.5989	0.5517	0.7198
0.6	0.1	0.1199	0.0860	0.0589	0.0416	0.1512
	0.2	0.2465	0.2076	0.1665	0.1334	0.2806
	0.4	0.4458	0.4086	0.3602	0.3223	0.4790
	0.6	0.5661	0.5345	0.4938	0.4537	0.5953
0.8	0.1	0.0919	0.0657	0.0453	0.0323	0.1174
	0.2	0.1928	0.1631	0.1321	0.1071	0.2210
	0.4	0.3568	0.3267	0.2908	0.2600	0.3846
	0.6	0.4640	0.4370	0.4039	0.3709	0.4898

APPENDIX A5.3 INFLUENCE OF SLAB/WALL THICKNESS RATIO ON SLAB COUPLING STIFFNESS.

Flanged Wall Configuration (L/X = 0.2, Y/X = 0.4, Z/Y = 0.5)

t/h	K*	Y_e^*/Y	K*/K	Z*/Z
1.50	54.01	0.5116	0.64	0.25
1.00	62.85	0.5953	0.74	0.46
0.75	70.28	0.6657	0.83	0.63
0.50	77.59	0.7349	0.91	0.81
0.375	80.65	0.7640	0.95	0.89
0.25	82.80	0.7843	0.98	0.95
Rigid Wall	84.87	0.8039	1.00	1.00

APPENDIX A5.4 INFLUENCE OF CORRIDOR OPENING RATIO ON SLAB COUPLING STIFFNESS

Flanged Wall Configuration (Y/X = 0.4, Z/Y = 0.5, t/h = 0.75)

L/X	K*	Y_e^*/Y	K*/K	Z*/Z
0.1	355.20	0.5005	0.72	0.58
0.2	70.28	0.6657	0.83	0.63
0.4	14.50	0.8074	0.91	0.65
0.6	6.04	0.8687	0.93	0.63

APPENDIX A5.5 INFLUENCE OF FLANGE WIDTH RATIO ON SLAB COUPLING STIFFNESS

Flanged Wall Configuration (L/X = 0.2, Y/X = 0.4, t/h = 0.75)

Z/Y	K*	Y_e^*/Y	K*/K	Y_e/Y
0.00	34.07	0.3227	0.83	0.3881
0.25	55.31	0.5239	0.86	0.6080
0.50	70.28	0.6657	0.83	0.8039
0.75	82.82	0.7845	0.81	0.9636

APPENDIX A5.6(a) VARIATION OF SLAB STIFFNESS FACTOR K* WITH VARIOUS GEOMETRIC RATIOS

Flanged Wall Configuration

Y/X	L/X	Stiffness Factor K*					Rigid Wall K
		Z/Y \ t/h	1.5	0.75	0.50	0.375	
0.4	0.1	0.25	186.19	248.08	280.11	295.01	326.69
		0.50	240.61	355.20	420.59	450.32	495.67
		0.75	272.77	445.42	546.72	591.27	651.17
	0.2	0.25	47.02	55.31	59.09	60.70	64.18
		0.50	54.01	70.28	77.59	80.65	84.87
		0.75	60.11	82.82	93.17	97.17	101.72
	0.4	0.25	11.51	12.67	13.16	13.36	13.77
		0.50	12.31	14.50	15.33	15.68	16.02
		0.75	12.90	15.86	17.01	17.40	17.79
0.6	0.1	0.25	225.08	312.33	360.27	382.33	425.54
		0.50	294.09	469.58	574.76	622.08	689.55
		0.75	341.46	616.14	780.61	851.60	944.31
	0.2	0.25	56.78	68.63	74.33	76.71	81.62
		0.50	68.00	93.16	105.65	110.63	117.23
		0.75	76.40	115.97	134.22	140.99	148.74
	0.4	0.25	14.73	16.49	17.28	17.59	18.14
		0.50	16.11	19.82	21.44	22.05	22.60
		0.75	17.36	22.89	24.94	25.63	26.31

APPENDIX A5.6(b) VARIATION OF EFFECTIVE SLAB WIDTH Y_e^*/Y WITH VARIOUS GEOMETRIC RATIOS

Flanged Wall Configuration

Y/X	L/X	t/h / Z/Y	Effective Width Y_e^*/Y				Rigid Wall Y_e/Y
			1.5	0.75	0.50	0.375	
0.4	0.1	0.25	0.2624	0.3496	0.3947	0.4157	0.4603
		0.50	0.3391	0.5005	0.5927	0.6346	0.6985
		0.75	0.3844	0.6276	0.7704	0.8332	0.9176
	0.2	0.25	0.4454	0.5239	0.5598	0.5750	0.6080
		0.50	0.5116	0.6657	0.7349	0.7640	0.8039
		0.75	0.5694	0.7845	0.8825	0.9204	0.9636
	0.4	0.25	0.6409	0.7052	0.7326	0.7436	0.7666
		0.50	0.6856	0.8074	0.8538	0.8731	0.8918
		0.75	0.7180	0.8832	0.9468	0.9689	0.9906
0.6	0.1	0.25	0.2114	0.2934	0.3384	0.3592	0.3998
		0.50	0.2763	0.4411	0.5399	0.5844	0.6478
		0.75	0.3208	0.5788	0.7333	0.8000	0.8871
	0.2	0.25	0.3586	0.4334	0.4694	0.4844	0.5154
		0.50	0.4294	0.5881	0.6670	0.6986	0.7403
		0.75	0.4824	0.7323	0.8476	0.8903	0.9393
	0.4	0.25	0.5466	0.6119	0.6413	0.6530	0.6732
		0.50	0.5980	0.7356	0.7959	0.8182	0.8388
		0.75	0.6444	0.8496	0.9256	0.9512	0.9766

APPENDIX A5.7 INFLUENCE OF SLAB/WALL THICKNESS RATIO ON SLAB COUPLING STIFFNESS

Box-Core Configuration (L/X = 0.2, Y/X = 0.4, Z/Y = 0.5)

t/h	K*	Y_e^*/Y	K*/K	Z*/Z
1.50	48.27	0.4573	0.56	0.14
1.00	64.87	0.6145	0.75	0.49
0.75	74.30	0.7038	0.86	0.69
0.50	81.81	0.7750	0.94	0.88
0.375	84.27	0.7982	0.97	0.93
0.25	85.83	0.8130	0.99	0.98
Rigid Wall	86.88	0.8230	1.00	1.00

APPENDIX A5.8 INFLUENCE OF CORRIDOR OPENING RATIO ON SLAB COUPLING STIFFNESS.

Box-Core Configuration (Y/X = 0.4, Z/Y = 0.5, t/h = 0.75)

L/X	K*	Y_e^*/Y	K*/K	Z*/Z
0.1	380.58	0.5363	0.76	0.64
0.2	74.30	0.7038	0.86	0.69
0.4	15.16	0.8440	0.93	0.71
0.6	6.26	0.9006	0.96	0.75

APPENDIX A5.9 INFLUENCE OF CORRIDOR OPENING RATIO AND SLAB/WALL THICKNESS RATIO ON SLAB COUPLING STIFFNESS

Box Core Configuration (Y/X = 0.4, Z/Y = 0.5)

L/X	t/h	K*	Y_e^*/Y	K*/K	Z*/Z	$(\frac{t}{h})/(\frac{L}{X})^{\frac{1}{2}}$
0.1	1.50	203.90	0.2873	0.40	0.14	4.74
	1.00	308.67	0.4349	0.61	0.44	3.16
	0.75	380.58	0.5363	0.76	0.64	2.37
	0.50	447.21	0.6302	0.89	0.83	1.58
	0.375	471.85	0.6649	0.94	0.91	1.19
	Rigid Wall	503.79	0.7099	1.00	1.00	-
0.2	1.50	48.27	0.4573	0.56	0.14	3.35
	1.00	64.87	0.6145	0.75	0.49	2.24
	0.75	74.30	0.7038	0.86	0.69	1.68
	0.50	81.81	0.7750	0.94	0.88	1.12
	0.375	84.27	0.7982	0.97	0.93	0.84
	Rigid Wall	86.88	0.8230	1.00	1.00	-
0.4	1.50	12.14	0.6757	0.74	0.16	2.37
	1.00	14.31	0.7969	0.87	0.52	1.58
	0.75	15.30	0.8520	0.94	0.73	1.19
	0.50	16.00	0.8908	0.98	0.89	0.79
	0.375	16.22	0.9028	0.99	0.94	0.59
	Rigid Wall	16.44	0.9153	1.00	1.00	-
0.6	1.50	5.31	0.7648	0.81	0.16	1.94
	1.00	5.95	0.8557	0.90	0.54	1.29
	0.75	6.26	0.9006	0.95	0.75	0.97
	0.50	6.49	0.9344	0.98	0.91	0.65
	0.375	6.54	0.9411	0.99	0.95	0.48
	Rigid Wall	6.60	0.9496	1.00	1.00	-

APPENDIX A6.1 VARIATIONS OF COMPOSITE STIFFNESS RATIO I_c^*/I_w^* AND EFFECTIVE FLANGE WIDTH Y_e/Y WITH RELATIVE WALL OPENING WIDTH L/t, SLAB WIDTH Y/t AND LINTEL DEPTH d/t. (FIXED LINTEL WIDTH b/t = 1.33)

L/t	Y/t	d/t					
		2.50	3.17	3.83	5.50	7.17	
13.33	26.67	1.928	1.717	1.604	1.440	1.345	I_c^*/I_w^*
		0.175	0.158	0.159	0.181	0.223	Y_e/Y
	40.00	1.983	1.753	1.631	1.457	1.356	I_c^*/I_w^*
		0.127	0.112	0.112	0.127	0.156	Y_e/Y
	53.33	2.013	1.780	1.655	1.474	1.369	I_c^*/I_w^*
		0.099	0.088	0.088	0.100	0.125	Y_e/Y
26.67	26.67	2.446	2.151	2.017	1.834	1.701	I_c^*/I_w^*
		0.279	0.232	0.224	0.239	0.262	Y_e/Y
	40.00	2.583	2.221	2.059	1.850	1.709	I_c^*/I_w^*
		0.220	0.171	0.159	0.164	0.178	Y_e/Y
	53.33	2.638	2.254	2.082	1.863	1.719	I_c^*/I_w^*
		0.177	0.134	0.123	0.126	0.136	Y_e/Y
40.00	26.67	2.628	2.301	2.166	1.985	1.884	I_c^*/I_w^*
		0.326	0.263	0.251	0.258	0.286	Y_e/Y
	40.00	2.806	2.393	2.219	2.020	1.892	I_c^*/I_w^*
		0.267	0.198	0.180	0.181	0.193	Y_e/Y
	53.33	2.880	2.433	2.246	2.035	1.902	I_c^*/I_w^*
		0.217	0.157	0.140	0.139	0.148	Y_e/Y

APPENDIX A7.1 WARPING STIFFNESS AND EFFECTIVE WIDTH VALUES FOR SLABS IN SINGLE-CORE-WITH-LOBBY CONFIGURATION (D/B = 0.5)

(a) Slab Edges: Monolithic/Free

	Stiffness Factor K_w			Effective Width Y_e/S		
L/B \ S/B	0.50	0.75	1.00	0.50	0.75	1.00
0.25	142.90	150.69	159.05	0.3807	0.2676	0.2119
0.50	36.45	38.48	39.83	0.7768	0.5468	0.4244
0.75	14.83	16.08	16.86	1.0666	0.7711	0.6064

(b) Slab Edges: Monolithic/S.Supported

	Stiffness Factor K_w			Effective Width Y_e/S		
L/B \ S/B	0.50	0.75	1.00	0.50	0.75	1.00
0.25	156.50	157.70	163.71	0.4169	0.2801	0.2181
0.50	48.13	44.59	43.87	1.0257	0.6335	0.4675
0.75	24.24	21.14	20.21	1.7433	1.0139	0.7267

(c) Slab Edges: S.Supported/S.Supported

	Stiffness Factor K_w			Effective Width Y_e/S		
L/B \ S/B	0.50	0.75	1.00	0.50	0.75	1.00
0.25	98.89	102.46	108.00	0.2634	0.1820	0.1439
0.50	31.79	30.24	30.12	0.6776	0.4296	0.3209
0.75	18.04	16.39	16.01	1.2929	0.7861	0.5758

APPENDIX A7.2 WARPING STIFFNESS AND EFFECTIVE WIDTH VALUES FOR SLABS IN SINGLE-CORE-WITH-LOBBY CONFIGURATION (D/B = 0.75)

(a) Slab Edges: Monolithic/Free

	Stiffness Factor K_w			Effective Width Y_e/S		
L/B \ S/B	0.50	0.75	1.00	0.50	0.75	1.00
0.25	221.39	232.11	243.99	0.3932	0.2748	0.2167
0.50	51.84	54.37	56.01	0.7366	0.5150	0.3979
0.75	19.73	21.19	22.06	0.9462	0.6776	0.5289

(b) Slab Edges: Monolithic/S.Supported

	Stiffness Factor K_w			Effective Width Y_e/S		
L/B \ S/B	0.50	0.75	1.00	0.50	0.75	1.00
0.25	239.37	241.25	250.08	0.4251	0.2857	0.2221
0.50	67.08	62.27	61.27	0.9531	0.5898	0.4353
0.75	32.64	27.57	26.32	1.5171	0.8815	0.6311

(c) Slab Edges: S.Supported/S.Supported

	Stiffness Factor K_w			Effective Width Y_e/S		
L/B \ S/B	0.50	0.75	1.00	0.50	0.75	1.00
0.25	138.90	145.93	155.21	0.2467	0.1728	0.1378
0.50	39.73	38.38	38.65	0.5645	0.3635	0.2746
0.75	21.46	19.83	19.59	1.0291	0.6340	0.4697

APPENDIX A7.3 WARPING STIFFNESS AND EFFECTIVE WIDTH VALUES FOR SLABS IN SINGLE-CORE-WITH-LOBBY CONFIGURATION (D/B = 1.0)

(a) Slab Edges: Monolithic/Free

	Stiffness Factor K_w			Effective Width Y_e/S		
S/B / L/B	0.50	0.75	1.00	0.50	0.75	1.00
0.25	313.66	327.29	342.70	0.4178	0.2906	0.2282
0.50	69.89	72.97	74.93	0.7448	0.5184	0.3992
0.75	25.62	27.38	28.38	0.9214	0.6566	0.5103

(b) Slab Edges: Monolithic/S.Supported

	Stiffness Factor K_w			Effective Width Y_e/S		
S/B / L/B	0.50	0.75	1.00	0.50	0.75	1.00
0.25	337.03	339.19	350.63	0.4489	0.3012	0.2335
0.50	89.72	83.29	81.83	0.9561	0.5917	0.4360
0.75	41.13	35.76	34.02	1.4794	0.8573	0.6119

(c) Slab Edges: S.Supported/S.Supported

	Stiffness Factor K_w			Effective Width Y_e/S		
S/B / L/B	0.50	0.75	1.00	0.50	0.75	1.00
0.25	181.82	192.89	206.38	0.2422	0.1713	0.1375
0.50	48.82	47.66	48.35	0.5203	0.3386	0.2576
0.75	25.79	24.15	24.06	0.9275	0.5791	0.4326

APPENDIX A7.4 WARPING STIFFNESS AND EFFECTIVE WIDTH VALUES FOR SLABS IN SINGLE-CORE-WITHOUT-LOBBY CONFIGURATION (D/B = 0.5)

(a) Slab Edges: Monolithic/Free

	Stiffness Factor K_w			Effective Width Y_e/S		
L/B \ S/B	0.50	0.75	1.00	0.50	0.75	1.00
0.25	81.35	89.81	98.60	0.2167	0.1595	0.1313
0.50	18.48	20.35	21.69	0.3939	0.2891	0.2312
0.75	7.89	8.94	9.63	0.5677	0.4285	0.3463
1.00	4.10	4.87	5.42	0.6991	0.5531	0.4617

(b) Slab Edges: Monolithic/S.Supported

	Stiffness Factor K_w			Effective Width Y_e/S		
L/B \ S/B	0.50	0.75	1.00	0.50	0.75	1.00
0.25	94.68	96.76	103.23	0.2523	0.1718	0.1375
0.50	29.52	26.24	25.63	0.6292	0.3728	0.2731
0.75	16.43	13.63	12.78	1.1815	0.6538	0.4597
1.00	10.40	8.47	7.85	1.7734	0.9630	0.6695

(c) Slab Edges: S.Supported/S.Supported

	Stiffness Factor K_w			Effective Width Y_e/S		
L/B \ S/B	0.50	0.75	1.00	0.50	0.75	1.00
0.25	60.77	64.53	70.13	0.1619	0.1146	0.0934
0.50	17.32	16.44	16.51	0.3692	0.2335	0.1759
0.75	9.82	8.97	8.85	0.7063	0.4301	0.3185
1.00	14.48	12.88	12.57	1.2066	0.7153	0.5239

APPENDIX A7.5 WARPING STIFFNESS AND EFFECTIVE WIDTH VALUES FOR SLABS IN SINGLE-CORE-WITHOUT-LOBBY CONFIGURATION (D/B = 0.75)

(a) Slab Edges: Monolithic/Free

	Stiffness Factor K_w			Effective Width Y_e/S		
L/B \ S/B	0.50	0.75	1.00	0.50	0.75	1.00
0.25	120.87	133.22	146.16	0.2147	0.1577	0.1298
0.50	26.59	29.07	30.84	0.3779	0.2753	0.2191
0.75	10.72	12.03	12.84	0.5163	0.3845	0.3078
1.00	5.20	6.06	6.66	0.5914	0.4590	0.3784

(b) Slab Edges: Monolithic/S.Supported

	Stiffness Factor K_w			Effective Width Y_e/S		
L/B \ S/B	0.50	0.75	1.00	0.50	0.75	1.00
0.25	138.52	142.30	152.23	0.2460	0.1685	0.1352
0.50	41.06	36.72	36.00	0.5834	0.3478	0.2557
0.75	21.77	18.07	16.94	1.0440	0.5777	0.4063
1.00	13.15	10.62	9.80	1.4946	0.8047	0.5571

(c) Slab Edges: S.Supported/S.Supported

	Stiffness Factor K_w			Effective Width Y_e/S		
L/B \ S/B	0.50	0.75	1.00	0.50	0.75	1.00
0.25	88.48	94.63	103.21	0.1571	0.1120	0.0917
0.50	23.56	22.63	22.89	0.3348	0.2144	0.1626
0.75	12.53	11.57	11.50	0.6009	0.3699	0.2758
1.00	11.44	10.29	10.13	0.9532	0.5716	0.4222

APPENDIX A7.6 WARPING STIFFNESS AND EFFECTIVE WIDTH VALUES FOR SLABS IN SINGLE-CORE-WITHOUT-LOBBY CONFIGURATION (D/B = 1.0)

(a) Slab Edges: Monolithic/Free

	Stiffness Factor K_w			Effective Width Y_e/S		
L/B \ S/B	0.50	0.75	1.00	0.50	0.75	1.00
0.25	160.54	176.88	194.02	0.2139	0.1571	0.1292
0.50	34.88	38.04	40.31	0.3717	0.2703	0.2148
0.75	13.83	15.39	16.36	0.4973	0.3690	0.2942
1.00	6.51	7.52	8.22	0.5548	0.4276	0.3503

(b) Slab Edges: Monolithic/S.Supported

	Stiffness Factor K_w			Effective Width Y_e/S		
L/B \ S/B	0.50	0.75	1.00	0.50	0.75	1.00
0.25	183.50	188.69	201.95	0.2444	0.1676	0.1345
0.50	53.77	48.09	47.10	0.5730	0.3416	0.2510
0.75	28.28	23.39	21.85	1.0172	0.5608	0.3929
1.00	17.04	13.63	12.48	1.4524	0.7747	0.5321

(c) Slab Edges: S.Supported/S.Supported

	Stiffness Factor K_w			Effective Width Y_e/S		
L/B \ S/B	0.50	0.75	1.00	0.50	0.75	1.00
0.25	116.42	124.97	136.57	0.1551	0.1111	0.0910
0.50	30.06	29.10	29.56	0.3203	0.2068	0.1575
0.75	15.54	14.49	14.48	0.5588	0.3475	0.2604
1.00	10.11	9.20	9.11	0.8619	0.5227	0.3883

APPENDIX A7.7 WARPING STIFFNESS AND EFFECTIVE WIDTH VALUES FOR SLABS IN TWIN CORE WITH LOBBY CONFIGURATION (D/B = 0.5)

(a) Slab Edges: Monolithic/Free

	Stiffness Factor K_w			Effective Width Y_e/S		
S/B / L/B	0.50	0.75	1.00	0.50	0.75	1.00
0.25	75.90	80.22	84.70	0.4044	0.2849	0.2256
0.50	20.65	21.96	22.83	0.8801	0.6240	0.4866
0.75	9.38	10.26	10.83	1.3500	0.9839	0.7792

(b) Slab Edges: Monolithic/S.Supported

	Stiffness Factor K_w			Effective Width Y_e/S		
S/B / L/B	0.50	0.75	1.00	0.50	0.75	1.00
0.25	84.02	84.03	87.03	0.4477	0.2985	0.2318
0.50	28.40	25.74	25.18	1.2105	0.7314	0.5366
0.75	16.50	13.94	13.17	2.3739	1.3375	0.9472

(c) Slab Edges: S.Supported/S.Supported

	Stiffness Factor K_w			Effective Width Y_e/S		
S/B / L/B	0.50	0.75	1.00	0.50	0.75	1.00
0.25	58.56	59.44	61.83	0.3120	0.2111	0.1647
0.50	20.89	19.29	18.94	0.8904	0.5482	0.4038
0.75	13.27	11.63	11.16	1.9087	1.1156	0.8024

APPENDIX A7.8 WARPING STIFFNESS AND EFFECTIVE WIDTH VALUES FOR SLABS IN TWIN-CORE-WITH-LOBBY CONFIGURATION (D/B = 0.75)

(a) Slab Edges: Monolithic/Free

	Stiffness Factor K_w			Effective Width Y_e/S		
L/B \ S/B	0.50	0.75	1.00	0.50	0.75	1.00
0.25	109.67	115.47	121.70	0.3896	0.2734	0.2162
0.50	26.70	28.19	29.17	0.7588	0.5341	0.4145
0.75	11.38	12.27	12.83	1.0912	0.7846	0.6151

(b) Slab Edges: Monolithic/S.Supported

	Stiffness Factor K_w			Effective Width Y_e/S		
L/B \ S/B	0.50	0.75	1.00	0.50	0.75	1.00
0.25	118.52	119.28	123.95	0.4210	0.2825	0.2201
0.50	34.94	31.92	31.42	0.9928	0.6048	0.4464
0.75	18.73	15.86	15.05	1.7968	1.0140	0.7218

(c) Slab Edges: S.Supported/S.Supported

	Stiffness Factor K_w			Effective Width Y_e/S		
L/B \ S/B	0.50	0.75	1.00	0.50	0.75	1.00
0.25	76.91	79.17	83.23	0.2732	0.1875	0.1478
0.50	23.95	22.29	22.06	0.6808	0.4223	0.3135
0.75	14.35	12.62	12.19	1.3764	0.8068	0.5844

APPENDIX A7.9 WARPING STIFFNESS AND EFFECTIVE WIDTH VALUES FOR SLABS IN TWIN-CORE-WITH-LOBBY CONFIGURATION (D/B = 1.0)

(a) Slab Edges: Monolithic/Free

	Stiffness Factor K_w			Effective Width Y_e/S		
S/B L/B	0.50	0.75	1.00	0.50	0.75	1.00
0.25	148.12	155.40	163.39	0.3946	0.2760	0.2176
0.50	33.83	35.58	36.69	0.7209	0.5055	0.3910
0.75	13.90	14.91	15.49	0.9999	0.7149	0.5572

(b) Slab Edges: Monolithic/S.Supported

	Stiffness Factor K_w			Effective Width Y_e/S		
S/B L/B	0.50	0.75	1.00	0.50	0.75	1.00
0.25	157.96	159.35	165.62	0.4208	0.2830	0.2206
0.50	42.84	39.40	38.92	0.9130	0.5598	0.4147
0.75	21.79	18.55	17.69	1.5676	0.8894	0.6362

(c) Slab Edges: S.Supported/S.Supported

	Stiffness Factor K_w			Effective Width Y_e/S		
S/B L/B	0.50	0.75	1.00	0.50	0.75	1.00
0.25	96.85	100.63	106.48	0.2580	0.1787	0.1418
0.50	27.89	26.12	26.01	0.5944	0.3712	0.2771
0.75	16.14	14.27	13.87	1.1613	0.6843	0.4987